Vol. 63, No. 1 / 2021

e: ISSN 2068 – 2239
p: ISSN 2068 – 4215

INMATEH –

AGRICULTURAL ENGINEERING

JANUARY - APRIL

***INMATEH - Agricultural Engineering* journal is indexed in the next international databases:**
ELSEVIER /SciVerse SCOPUS, CLARIVATE ANALYTICS - WEB of SCIENCE- Emerging Sources Citation Index (ESCI), ULRICHS Web: Global Serials Directory, CABI, Index COPERNICUS International, EBSCO Publishing, Elektronische Zeitschriftenbibliothek

INMATEH - Agricultural Engineering
vol. 63, no.1 / 2021
e-ISSN: 2068 – 2239; p: ISSN: 2068 – 4215

https://inmateh.eu/ *E-mail: inmatehjournal@gmail.com*

Edited by: INMA Bucharest

National Institute for Research-Development of Machines and Installations
Designed for Agriculture and Food Industry - INMA Bucharest
6, Ion Ionescu de la Brad Bvd., sector 1, Bucharest, ROMANIA

CONTENT

DETECTION SYSTEM FOR FEEDING QUANTITY OF MOBILE STRAW GRANULATOR BASED ON POWER OF SCREW CONVEYOR
/
基于螺旋输送器功率的移动式秸秆制粒机喂入量检测系统

Wei Wang, YuanJuan Gong*), XueWei Bai [1)] [1]
[1)] Shenyang Agricultural University, College of Engineering, Shenyang / China;
Tel: +86-024-88487057; E-mail: gongyjSYND@126.com
DOI: https:// doi.org/10.35633/inmateh-63-01

Keywords: *straw granulator, power measurement, screw conveyor, feeding quantity, butterworth filter*

ABSTRACT
At present, straw harvesting operation is performed according to artificial experience, and there is no scientific method to detect the feeding quantity of the mobile straw granulator. This paper designed a feeding quantity detection system based on the power of the motive power shaft of the screw conveyor of the mobile straw granulator. The detection system includes the detection device and the detection method. The detection device consists of torque sensor, rotation speed sensor and on-board industrial computer. The detection method obtains the feeding quantity with the power that can be computed according to torque and rotation speed. The detection system was evaluated on the mobile straw granulator of Liaoning Ningyue agricultural machinery company. The field experiment shows that the average error of feeding quantity detection system is 7.5%, and the detection accuracy can meet the actual needs of the field application.

摘要
目前，秸秆收获作业靠人工经验判断，没有科学的方法来检测移动式秸秆制粒机的喂入量，本文设计了基于移动式秸秆制粒机螺旋输送器动力轴功率的喂入量检测系统。喂入量检测系统包括喂入量检测装置和喂入量检测方法。喂入量检测装置由扭矩传感器、转速传感器、车载工控机构成；喂入量检测方法中使用功率预测秸秆喂入量，功率通过扭矩与转速间接求取；本文以辽宁宁越农机公司的移动式秸秆制粒机为试验平台对检测系统进行了验证。田间试验表明，采用喂入量检测方法的平均误差为7.5%，检测精度能够满足实际田间应用需求。

INTRODUCTION

China is rich in all kinds of crop straw resources, of which the annual yield of corn straw can reach 180 million tons *(Zhao et al, 2019)*. Mechanized harvesting of corn straw in the field is very important, and the feeding quantity, as an important parameter in harvesting operation, determines the efficiency of corn straw harvesting. If the feeding quantity is too large, the key parts of the mobile straw granulator will be blocked. If the feeding quantity is too small, the harvesting efficiency of corn straw will be seriously restricted. How to use modern information technology to detect feeding of mobile straw granulator and improve the harvest efficiency is particularly urgent.

There have been many important theoretical results in the research on the feeding quantity of the mechanical equipment. According to the working principle of combine harvester, relevant scholars put forward the feeding quantity detection model and designed the feeding quantity detection system *(Savoie, et al, 2014)*. For example, the torque of the driving shaft and fuzzy neural network technology are used to detect the feeding quantity and adjust the speed of the combine harvester respectively *(Ji, 2005)*. A monitoring method to detect the feeding quantity of peanut was proposed based on the torque of the power input shaft of the pickup platform *(Wang et al, 2019)*. Through the dynamic analysis of the pickup, the mathematical model of the peanut harvester pickup is designed according to the torque and feeding quantity of the power input shaft of the peanut harvester pickup. The relationship between the feeding quantity of the combine harvester and the loss rate of the harvesting process was analysed to establish the mathematical model of them *(Siemens and Hulick, 2008)*. However, there are many factors that affect the change of feeding quantity, and the actual working environment is complicate, which lead to a large measurement error. And, these researches are mostly aiming at combine harvesters. Hence, the detection of feeding quantity of the mobile straw granulator is an urgent demand.

[1] *Wei Wang, Ph.D. Stud.; YuanJuan Gong, Prof. Ph.D.; XueWei Bai, Ph.D.*

This paper proposed an embedded feeding quantity detection system. The relationship between the screw conveyor and the feeding quantity of the mobile straw granulator is analysed to build the correlation model. The embedded hardware system was constructed based on the STM32 and ZigBee, and had a low power consumption and high communication efficiency.

MATERIALS AND METHODS

Feeding quantity detection system

The mobile straw granulator is shown in Fig.1 (a), and the specific feeding device is shown in Fig.1 (b). During the harvesting of the mobile straw granulator, the corn straw is crushed and picked up by the front-end pickup device, and then the straw is sent to the screw conveyor. Then, the material is fed into the straw conveying equipment through the screw conveyor. Finally, the material enters the straw granulator silo.

This paper analysed the screw conveyor power shaft to establish the mathematical model between the power of the power shaft and the feeding quantity of the mobile straw granulator to detect the feeding quantity. The system includes detection device and detection method. As an important parameter of the mobile straw granulator, power can not only detect the feed quantity, but also reflect the power required by the straw granulator in the harvesting process. The detection of power parameters is significant to the detection system.

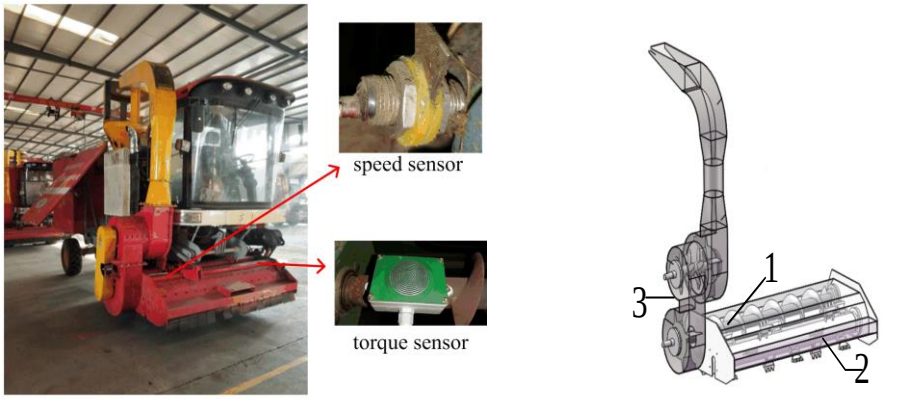

a. Test equipment *b. Structure diagram of feeding device*

Fig. 1 - Mobile straw granulator

1. Screw conveyor; 2. Picking up and crushing equipment; 3. Conveying equipment

Detection device

The detection system includes torque sensor, speed sensor and the on-board industrial computer. The overall scheme of the detection system is shown in Fig. 2. The on-board industrial computer is composed of microcontrollers, CAN (Controller Area Network) controller *(Harmon et al, 2018)*, display module, ZigBee RF (Radio Frequency) module *(Partal et al, 2019)* and 4G data transmission module. The speed sensor and the on-board industrial computer vehicle terminal adopt CAN bus protocol. Torsion sensor and on-board industrial computer communicate through ZigBee RF module; 4G data transmission module provides remote control interface. ZigBee RF module has advantages of low power consumption *(Bihl et al, 2017)*, Ad-hoc network *(Amer et al, 2020)* and stable communication, so ZigBee communication is used in the torque sensor communication module.

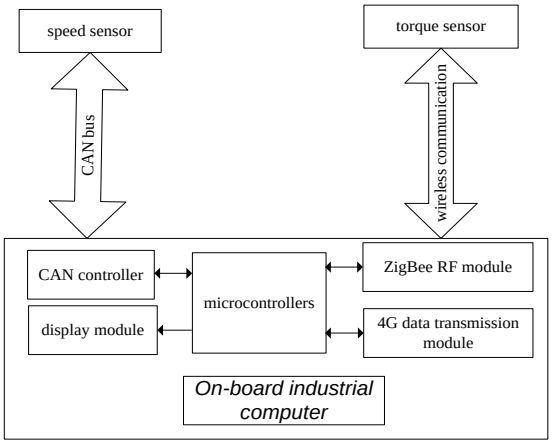

Fig. 2 – The detection system

The torque sensor which is used to detect the torque is shown in Fig. 3. Lithium battery with voltage of 3.7V and capacity of 3000mAh is used for power supply. The hardware circuit is shown in Figure 4. And the torque sensor was mounted on the mobile straw granulator as Fig. 1(a). Low-power chip stm32f030f4p6 is the core of data acquisition. ZigBee module which uses CC2530 RF with 2400Mhz as the working frequency is used to communicate information. The strain bridge (R8, R9, R2, R16) is used to generate voltage signal *(Feng and Wang, 2020)*. After being amplified by differential operational amplifier (U1B: lm358), buffered and isolated by voltage follower (U1A: lm358), voltage signal is sent to the fifth-order Butterworth low-pass filter composed of LM324 (U2A, U2B, U2C). The filter has the function of gain adjustment and filtering high-frequency signal *(Mahata et al, 2020)*. The parameters of resistance and capacitance in the filter are calculated according to the cut-off frequency and quality factor in the normalization table of low-pass filter. The frequency response curve is shown in Fig. 5. After the process of the filter, the required low-frequency signal is retained while the high-frequency signal generated by vibration is filtered out. With these components, the strain gauge deformation is converted into the voltage signal corresponding to the transmission shaft torque, and the voltage signal is converted into torque value. The single chip microcomputer sends the torque value to the ZigBee module (U4) through the pins (P0.2, P0.3). Then, the ZigBee module transmits the torsion value to the on-board industrial computer in the cab of the harvester through the spring antenna.

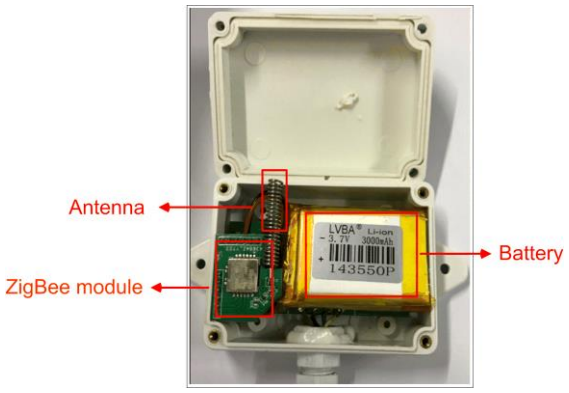

Fig. 3 – Torque sensor communication module

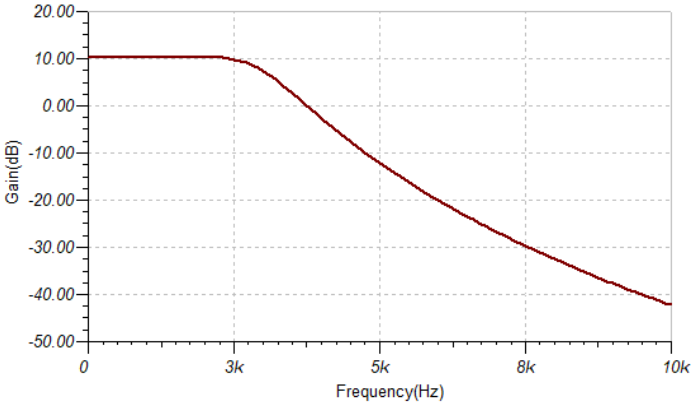

Fig. 5 –Frequency response curve of filter

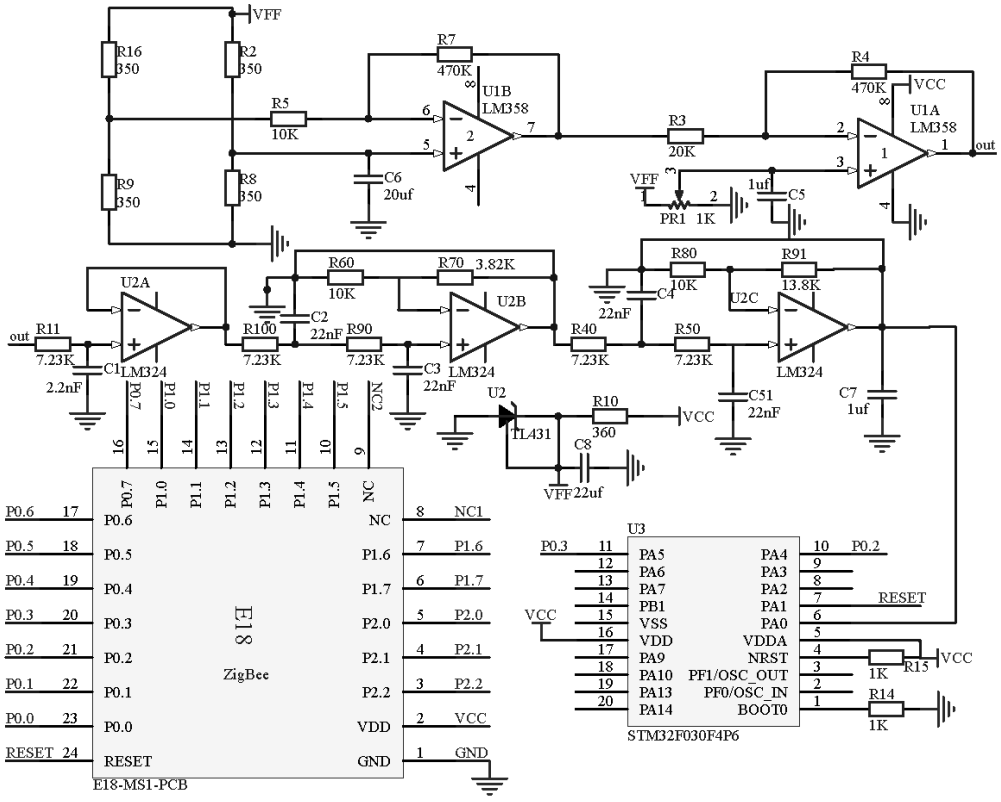

Fig. 4 – Hardware circuit of torque sensor

The on-board industrial computer device and the specific circuit are shown in Figure 6 and Figure 7, respectively.

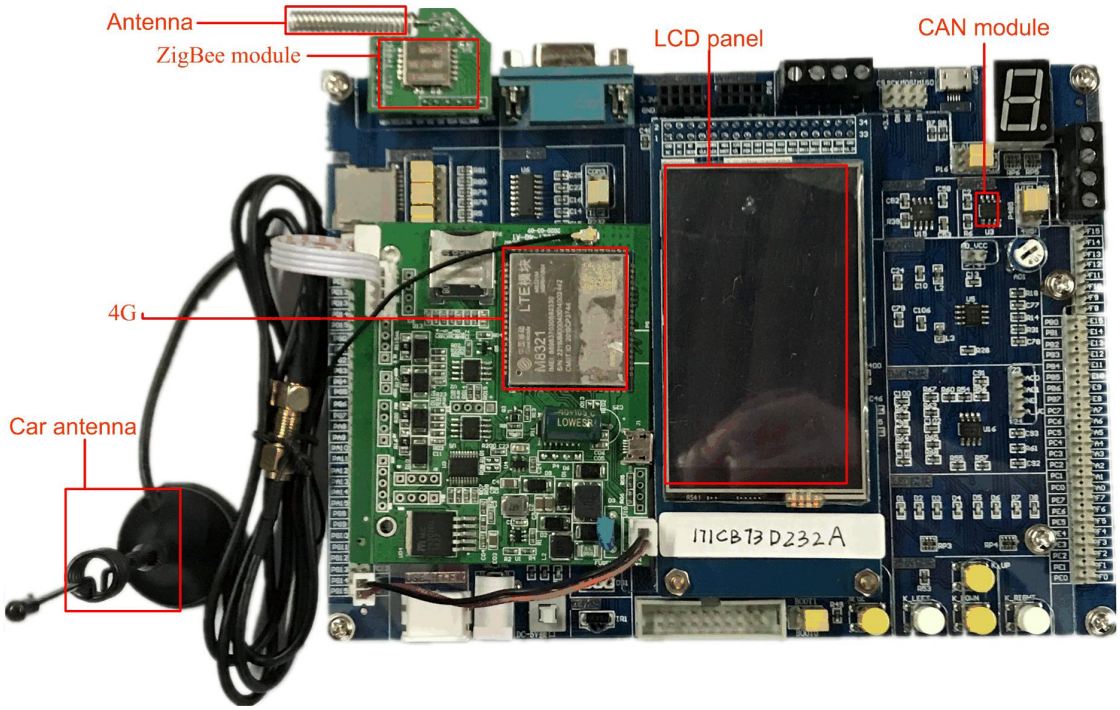

Fig. 6 – On board industrial computer

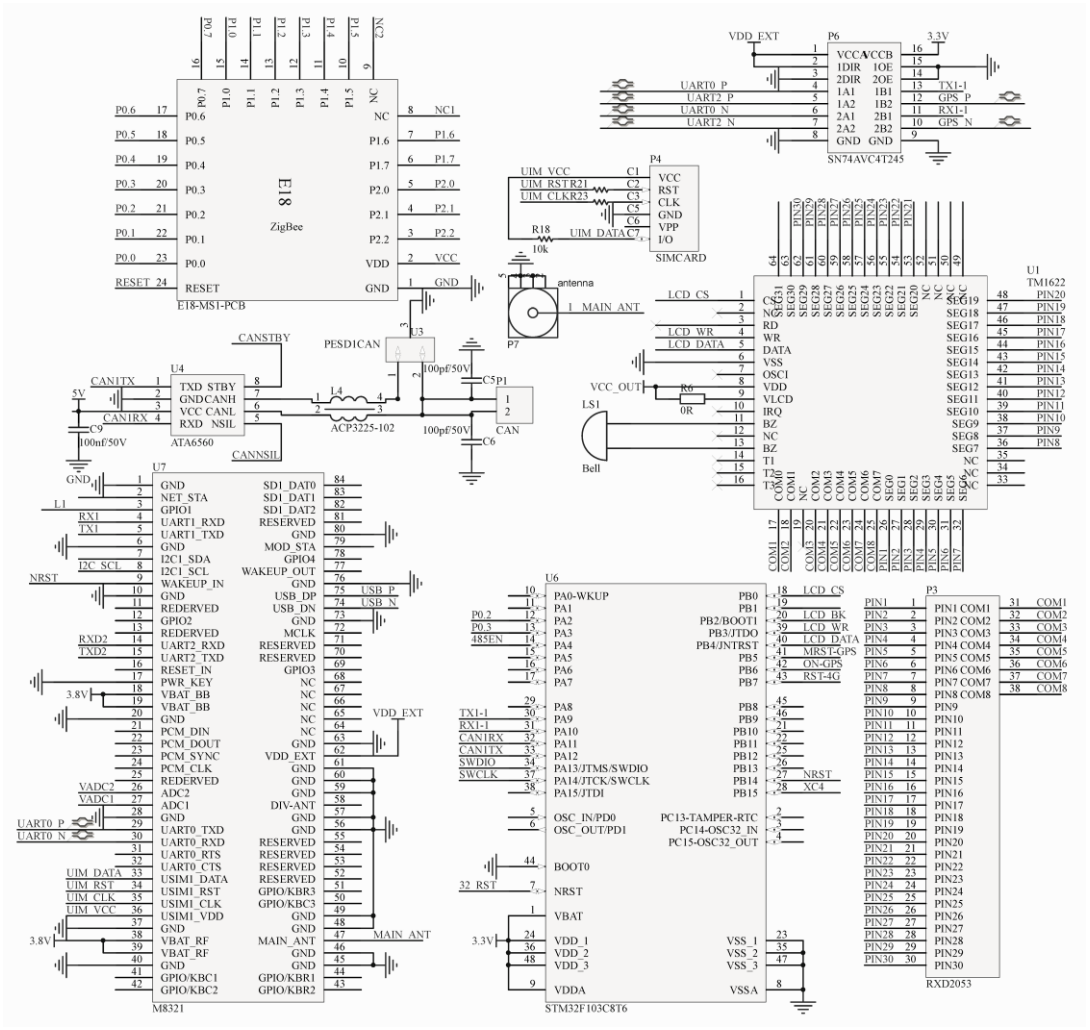

Fig. 7 – Circuit diagram of on-board industrial computer

When communicating with torque sensor, U6 (stm32f103c8t6) transmits command information to ZigBee module by USART communication through pins (P0.2, P0.3). Then, it is sent to the torque sensor. The on-board industrial computer communicates with the speed sensor through CAN controller U4 (ata6560). The capacitor C9 can filter out the high frequency interference of power supply. In order to improve the anti-electromagnetic interference ability of CAN bus interface, the anti-interference circuit is designed. U3 (PESD1CAN) is used to eliminate electrostatic interference. Transient power of U3 between 8 and 20us can reach 200W. The common mode filter L4 (WCM-3216-222T) can resist common mode interference. P3 (LCD) is driven by special driver chip U1 (TM1622) to display information such as torque, speed, power and feeding quantity. When the straw granulator is working, the microcontroller communicates with the 4G chip U7 (M8321); U7 interacts with SIM card P4, and the parameters related to the feeding quantity are transmitted to the background server by the antenna P7. P6 (SN74AVC4T245) is used to match the level of USART signal.

Detection method

In the detection of the feeding quantity, the power cannot be measured directly as there is no measuring equipment for agricultural machinery used in field operation. The power is related to speed and torque, so it is necessary to calculate the speed and torque of screw conveyor and measure the power indirectly. The voltage signal of the strain gauge can be collected by the electronic circuit, and the torque value corresponding to the voltage signal can be calibrated by the professional torque sensor. The speed is obtained by the speed sensor. The feeding quantity can be predicted by fitting the above power with the actual feeding value.

Power detection

The strain method is used for torque detection. As shown in Fig. 8, the main plane is the grey square whose perpendicular is 45 degrees relative to the X axis. σ_1 and σ_2 represent tensile stress and compressive stress, respectively. And they are equal in value. According to Hooke's law *(Kaanta et al, 2018)*, the tensile strain and compressive strain along the principal stress direction are expressed as Eq. (1) and (2), respectively.

$$\varepsilon_{45^\circ} = \varepsilon_1 = \frac{\sigma_1}{E} - \mu\frac{\sigma_2}{E} = (1+\mu)\frac{\sigma_1}{E} = \frac{16(1+\mu)}{\pi E D^3} \quad (1)$$

$$\varepsilon_{-45^\circ} = \varepsilon_2 = \frac{\sigma_2}{E} - \mu\frac{\sigma_1}{E} = (1+\mu)\frac{\sigma_2}{E} = -\frac{16(1+\mu)}{\pi E D^3} \quad (2)$$

In the above expression, E denotes the elastic modulus of the material and μ is the Poisson's ratio of the material. Under the influence of torque, the strain in the direction of plus or minus 45 degrees is equal and the direction is opposite. If $\varepsilon_{45^\circ} = \varepsilon_{-45^\circ} = \varepsilon(\varepsilon > 0)$, the torque can be obtained by Eq. (3), in which, $G=E(2(1+\mu))$ is the shear modulus, $\gamma=2\varepsilon$ is the shear strain, and D is the outer diameter of the drive shaft.

$$T_1 = \frac{\pi D^3}{16} G\gamma \quad (3)$$

Therefore, the torque of the shaft can be obtained by applying strain gauges on the axial direction of plus or minus 45 degrees and the torque of the shaft $T_1(\varepsilon)$ can be obtained by detecting the maximum strain change of the transmission shaft. There is a linear relationship between T_1 and ε.

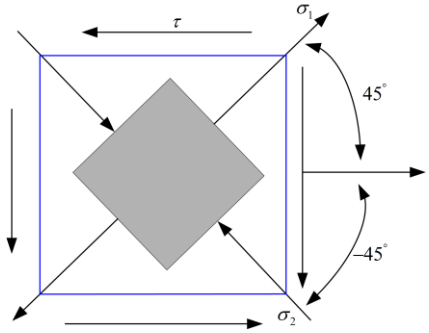

Fig. 8 – Schematic diagram of torque principle

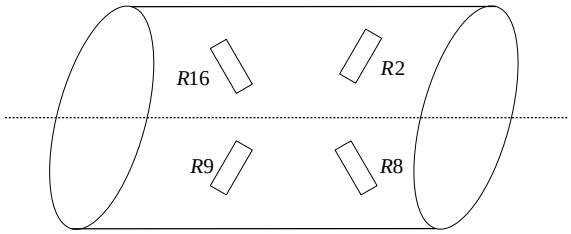

Fig. 9 – Schematic diagram of strain gauge mounting method

The mounting method of strain gauge of torque sensor is shown in Fig. 9. The torque sensor uses strain gauges to form Huygens bridge, and four strain gauges (R_8, R_9, R_2, R_{16}) form an equal arm full bridge, and they form an angle of 90 degrees respectively. When the transmission shaft is strained by torque, the resistance value of the strain gauge changes with the surface stress of the driving shaft. And this leads to the change of the output voltage. Through the calibration and measurement of the output voltage signal, the torque T_1 of the driving shaft of the screw conveyor can be obtained. The speed sensor is designed according to Hall Effect *(Kumar and Ganguli, 2020)*. It was mounted on the mobile straw granulator as shown in Fig. 1(a). The magnetic steel is pasted on the side of the driving wheel of the screw conveyor. When the magnetic steel passes through the hall element, the Hall Effect will be generated to form a pulse signal. The rotational speed denoted by n_1 of the driving shaft of the screw conveyor is calculated according to the number of pulses recorded in unit time multiplied by 60 seconds. By detecting the torque T_1 and speed n_1 of the driving shaft of the screw conveyor, the power P of the driving shaft is calculated, as shown in Eq. (4).

$$P = (n_1 * T_1) / 9559 \tag{4}$$

Calculation of actual feeding quantity

The actual feeding quantity is related to the moisture content of straw, the picking width of straw granulator, the height of screw conveyor and its walking speed. The density of straw in the test plot was uniform, and the moisture content was basically the same at harvest. The actual feeding quantity q could be obtained by calculating the weight m of straw per unit area and the area S of straw picked up by the straw granulator in unit time. The area S of straw harvested in unit time can be calculated by walking speed v of straw granulator and width d of the straw. In the working process of the straw granulator, if the picking width and the height of screw conveyor remain unchanged, the walking speed and the quantity of straw per unit area become the main factors affecting the feed quantity. The calculation of the actual feeding quantity is shown in Eq. (5), in which, q represents the actual feeding quantity, S represents the straw area per unit time, d is the actual picking width at harvest, v denotes the walking speed of straw granulator, and m denotes the mass of the straw per unit area.

$$q = Sm = dvm \tag{5}$$

RESULTS AND DISCUSSION

Field experiment and verification of straw granulator

The power and feeding quantity were obtained by experiments. The relationship between the predicted feeding quantity and the measuring power was obtained by linear model fitting. In order to verify the effectiveness of the power measurement method, it is necessary to verify and compare the feeding quantity predicted by power with the actual feeding quantity through field test.

Test conditions and methods

In order to establish the prediction model of screw conveyor power, straw harvest simulation experiment was conducted in Liaoning Ningyue Agricultural Machinery Co., Ltd. Xiaguang 560xg type straw granulator was used, and the on-board industrial computer device was installed in the cab. In this experiment, the moisture content of straw was the same, the length of rectangular crushed straw was 10 meters, the width was 2.0 meters, and the weight of unit straw was 1 kg. The pickup device and screw conveyor were 10cm above the ground. The frequency of data frame transmitted by ZigBee wireless communication was set to 400 Hz.

Test data processing and analysis

The accuracy of torque measurement is very important in this detection system. In this paper, the single chip microcomputer is used to collect the deformation signal. Before collecting the deformation signal, the hardware circuit of the fifth-order Butterworth filter *(Mahata et al, 2020)* is used to pass the noises. The function of the filter is verified by experiments.

Fig.10 shows the voltage waveform collected without Butterworth filter. It can be seen from the figure that there is more noise. The signal error range is large and it will affect the stability of the whole detection system.

The signal processing curve of Butterworth filter is shown in Fig.11 with less noise signal and stable voltage signal.

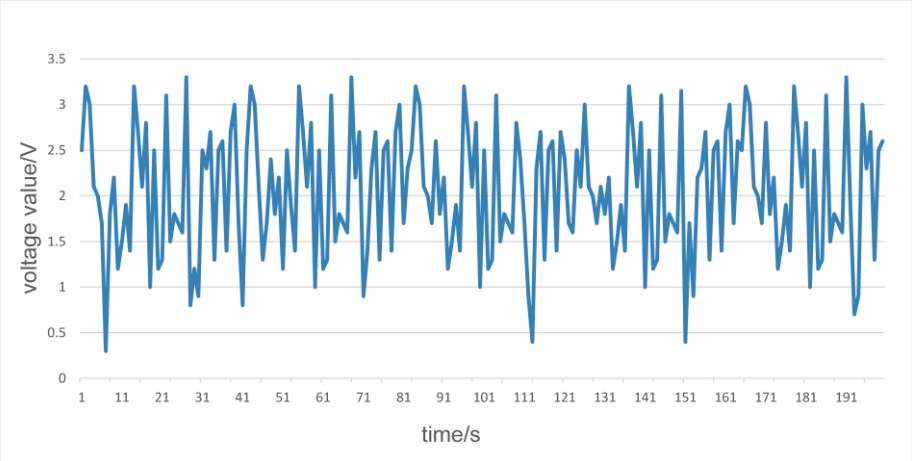

Fig. 10 – Voltage curve before noise filtering

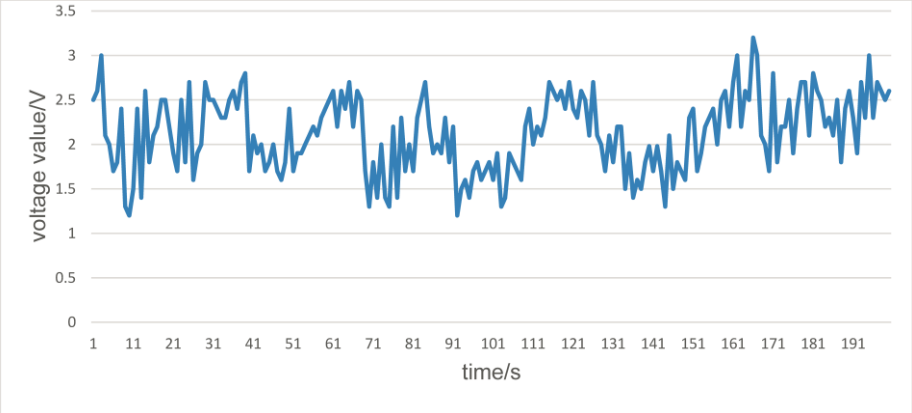

Fig. 11 – Voltage curve after noise filtering

The A/D module of single chip microcomputer collects the voltage signal value which is converted into torque value after arithmetic average filtering algorithm in software. The specific calibration data is shown in Table 1, and the calibration Eq. (6) can be obtained from the calibrated data.

$$y = 47.6x - 57.2 \quad (6)$$

Table 1

Torque sensor calibration test data

Torque (N.m)	Measured mean voltage (V)	Theoretical voltage (V)	Voltage prediction error (V)
0	1.202	1.202	0
25	1.718	1.728	0.011
50	2.260	2.252	0.008
75	2.791	2.777	0.014
100	3.291	3.300	0.009

The torque value detected by the calibrated torque sensor is shown in the second column of Table 2. The power of screw conveyor obtained by Eq. (4) through speed and torque is shown in the fourth column of Table 2. The actual feeding quantity is calculated by Eq. (5), as shown in the fifth column of Table 2.

According to table 2, the on-line monitoring power data of screw conveyor and the feeding data are linearly fitted. The fitted regression curve is shown in figure (12), and the correlation coefficient is 0.964.

The fitted linear model is shown in Eq. (7).

$$y = 0.2139x - 0.435 \quad (7)$$

Table 2

Test data obtained by online monitoring system

Speed of screw conveyor (r/min)	Torque (N.m)	Vehicle speed (m/s)	Power of screw conveyor (kW)	Feeding quantity (kg/s)
1406	48.9	0.5435	7.196	1.087
1423	48.6	0.5595	7.245	1.119
1456	48.1	0.5680	7.328	1.136
1487	48.0	0.5985	7.482	1.197
1489	48.4	0.6050	7.543	1.210
1510	48.1	0.5855	7.601	1.171
1534	48.6	0.5975	7.807	1.195
1544	49.5	0.6605	7.993	1.321
1564	50.1	0.6620	8.208	1.324
1585	50.1	0.6685	8.308	1.337
1596	50.5	0.6730	8.442	1.346
1601	51.3	0.6840	8.565	1.368
1608	51.2	0.6835	8.612	1.367
1600	52.0	0.7035	8.712	1.407
1599	52.8	0.7365	8.812	1.473
1612	54.8	0.7445	9.233	1.489
1605	53.3	0.7535	8.945	1.507
1612	53.7	0.7625	9.064	1.525
1590	55.1	0.7780	9.165	1.556
1589	55.8	0.7890	9.283	1.578

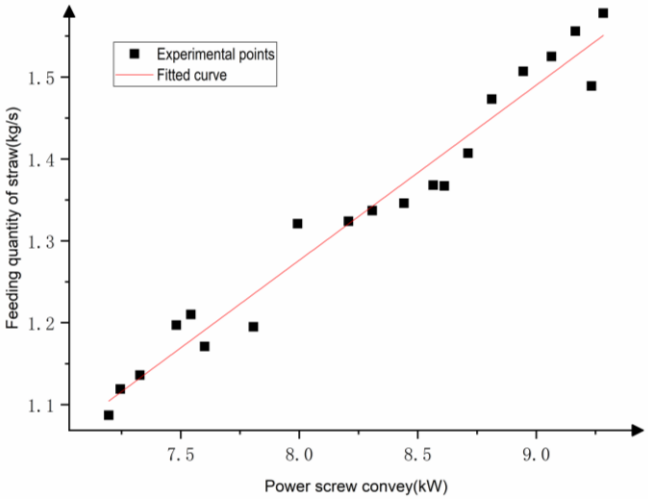

Fig. 12 – Regression curve after fitting

Field experiment

After the establishment of the model, the actual harvest experiment was carried out in the field, as shown in Fig. 13. Some experimental data are shown in Table 3. The mean error is equal to 7.5%. The measured value and the actual value of the feeding quantity are in the acceptable range. In conclusion, there is a linear relationship between the power of screw conveyor of straw granulator and the feeding quantity, and the feeding quantity can be predicted by power. The feeding quantity detection method based on power measurement proposed in this paper is effective. It can be used in the mobile straw granulator which integrates crushing, picking up and briquetting. It provides a method for the automatic control of the mobile straw granulator.

Fig. 13 –Field experiment

Table 3

Field test monitoring data

Power of screw conveyor (kW)	Calculated feed quantity (kg)	Actual feeding quantity (kg)	Error (%)
7.056	1.074	1.174	-8.5%
7.189	1.013	1.123	-9.7%
7.213	1.108	1.091	1.5%
7.402	1.148	1.099	4.4%
7.489	1.167	1.237	-5.6%
7.672	1.206	1.123	7.3%
7.834	1.241	1.356	-8.4%
7.939	1.263	1.316	-4.0%
7.589	1.188	1.099	8.0%
8.103	1.298	1.123	15.6%
8.246	1.329	1.298	2.3%
8.465	1.376	1.452	5.2%
8.378	1.357	1.278	6.1%
7.982	1.272	1.367	6.9%
7.843	1.243	1.146	8.5%
8.726	1.431	1.278	12.0%
8.894	1.467	1.325	10.7%
9.046	1.500	1.423	5.4%
8.905	1.415	1.612	12.2%
9.248	1.543	1.432	7.7%
Average error			7.5%

CONCLUSIONS

This paper proposed a system to detect the feeding quantity of the mobile straw granulator. The contributions are mainly embodied in three aspects:

(1) The linear relationship model between the screw conveyor and the feeding quantity was established. And the effectiveness of the model has been verified in the field experiment. It showed that predicting the feeding quantity by the power of the screw conveyor is feasible.

(2) The detection device including data acquisition, Butterworth filter, torque sensor, communization module, and control module was designed. It has the advantages of low power consumption and high signal noise ratio.

(3) The circuit of the main detection device was described in the paper. The scheme of this paper can be duplicated according to the circuit and the descriptions of the system.

Due to the bad working environment of straw crushing and picking up, in the future work, it is necessary to further study the methods to improve the working stability of strain gauge, such as improving materials, improving installation methods and other measures to further improve the detection accuracy.

ACKNOWLEDGEMENT

The results of the work are obtained using the straw granulator provided by Liaoning Ningyue Agricultural Machinery Equipment Co., Ltd.

REFERENCES

[1] Amer H., Al-Kashoash H., Khami M.J., et al, (2020), Non-cooperative game based congestion control for data rate optimization in vehicular Ad Hoc networks, *Ad Hoc Networks*, vol. 107, pp. 102-181, Elsevier, Amsterdam/Netherlands;

[2] Bihl T.J., Bauer K.W., Temple M.A., (2017), Feature selection for RF fingerprinting with multiple discriminant analysis and using ZigBee device emissions, *IEEE Transactions on Information Forensics and Security*, vol. 11, no. 8, pp.1862-1874, Institute of Electrical and Electronics Engineers Inc., Piscataway/U.S.A.;

[3] Feng Y., Wang Q., (2020), Adjusting ankle angle measurement based on a strain gauge bridge for powered transtibial prosthesis, *Journal of Dynamic Systems Measurement and Control*, online, Amer Soc Mechanical Eng, New York/U.S.A (DOI: 10.1115/1.4046158);

[4] Harmon J.D., Luck B.D., Shinners K.J. et al, (2018), Time-motion analysis of forage harvest: a case study, *Transactions of the Asabe*, vol. 61, no. 2, pp. 483-491, American Society of Agricultural and Biological Engineers, North Carolina State/U.S.A.;

[5] Ji B.B., (2005), *Research of predictive system for feed quantity of combine based on fuzzy neural network*, (*基于模糊神经网络的联合收割机喂入量预测系统研究*), MSc dissertation, Jiangsu university, Jiangsu/China;

[6] Kaanta, L., Kasper, G., Piirainen-Marsh, A., (2018), Explaining Hooke's Law: definitional practices in a CLIL physics classroom, *Applied Linguistics*, vol. 39, no. 5, pp. 694-717, Oxford University Press, Oxford/England;

[7] Kumar A., Ganguli S., (2020), A new Hall-effect enabled voltage amplifier device based on magnetic and thermal properties of materials [J]. *Journal of Magnetism and Magnetic Materials*, vol. 514, pp.167054, Ed. Elsevier, Oxford/England.

[8] Mahata S., Kar R., Mandal D., (2020), Optimal approximation of asymmetric type fractional-order bandpass Butterworth filter using decomposition technique, *International Journal of Circuit Theory and Applications*, online, Wiley Online Library, State of New Jersey/USA (DOI: 10.1002/cta.2835);

[9] Partal H.P., Belen M.A., Partal S.Z., (2019), Design and realization of an ultra-low power sensing RF energy harvesting module with its RF and DC sub-components, *International Journal of RF and Microwave Computer-Aided Engineering*, vol. 29, no. 1, pp. e21622.1-e21622.12, John Wiley and Sons Inc., Hoboken/U.S.A.;

[10] Savoie P., Hébert P.L., Robert F.S., (2014), Novel willow header adapted to a pull-type forage harvester: development and field experiments, Applied Engineering in Agriculture, vol. 30, no. 5, pp. 741-750, American Society of Agricultural and Biological Engineers, St. Joseph/U.S.A.;

[11] Siemens M.C., Hulick D.E, (2008), A new grain harvesting system for single-pass grain harvest, biomass collection, crop residue sizing, and grain segregation, *Transactions of the Asabe*, vol. 51, no.5, pp.1519-1527, American Society of Agricultural and Biological Engineers, North Carolina State/U.S.A.;

[12] Wang S.Y, Hu Z.C, Wu F., (2019), Modeling and experiment of feeding rate for full-feed peanut pickup harvester, (*全喂入花生捡拾收获机喂入量建模与试验*), *Transactions of the Chinese Society of Agricultural Engineering*, vol. 35, no. 23, pp. 29-36, Chinese Society of Agricultural Engineering, Beijing/China;

[13] Zhao B., Wang X., Ata-Ul-Karim S.T. et al, (2019), Effect of straw incorporation on corn yield in north China: a meta-analysis, *Journal of Bio-based Materials and Bioenergy*, vol. 13, no. 4, pp. 532-536, American Scientific Publishers, Los Angeles/U.S.A.

CALCULATION OF FIELD CAPACITY AND FUEL CONSUMPTION OF MOBILE MACHINERY WITH BUNKERS, TANKS OR OTHER CONTAINERS FOR AGRICULTURAL GOODS
/
ОПРЕДЕЛЯНЕ НА ПРОИЗВОДИТЕЛНОСТ И РАЗХОД НА ГОРИВО НА СЕЛСКОСТОПАНСКА ТЕХНИКА С ВМЕСТИМОСТИ

Vezirov Ch. Z. *[1)]., Atanasov At. Z. [1)]., Vlăduț V. [2)] [1]
[1)]University of Ruse, Agro-industrial Faculty / Bulgaria,
[2)]INMA Bucharest/ Romania
Tel: +359 082888442; E-mail: vezirov@uni-ruse.bg
DOI: https://doi.org/10.35633/inmateh-63-02

Keywords: *field capacity, fuel consumption, spread sheets, calculation, field operations*

ABSTRACT

A method and procedure for automatic calculation of field capacity and fuel consumption of mobile machinery with tanks, hoppers and bunkers is suggested. They are based on a combination of two well-founded approaches: East-European and North-American. To increase its calculation area some applications for machines with containers as grain, fertilizer, solution, etc. are added. An example of five linked field operations, namely potato transportation, fertilization, spraying, planting and harvesting is presented. A list of needed information with relations between them and main indices of agricultural aggregates is prepared. For convenience and objectivity calculations are automated with spreadsheets.

РЕЗЮМЕ

Предложени са метод и процедура за автоматично изчисляване на производителността и разхода на гориво от мобилни машини с резервоари, бункери, други вместимости. Те са комбинация от два добре обосновани подхода: източноевропейски и североамерикански. За да се увеличи обхвата на нейното използване, са добавени някои приложения за машини с контейнери за зърно, тор, разтвор и др. Представен е пример за пет свързани полеви операции, а именно транспортиране на картофи, торене, пръскане, засаждане, прибиране на реколтата. Направен е списък на необходимата информация за връзките между тях и основните показатели на селскостопанските агрегати. За удобство и обективност изчисленията са автоматизирани с електронни таблици.

INTRODUCTION

As other areas of management, the agricultural machinery one is about choices. That's why a good decision must be based on well-founded and interrelated steps to a global optimum. To be a choice informed, the potential buyer needs to have enough data including that about technical characteristics of farm machinery (*Spiridonov V., 2018*). Usually, manufactures and traders offer only some information presenting the machines positively, i.e. higher productivity and velocity.

Typically, a statement of the task for effective mechanized agriculture includes as a target machinery work with enough field capacity, required quality, minimum labour and fuel consumption (*Vezirov Ch., 2013*). In principle and in-depth solution of these problems is discussed in (*ASAE 496.3, 2006, ASAE 497.7, 2011, Tutorial, 1978*). The recent research in this area are concerns to the clarification of the proposed dependences for the mechanics of agricultural units (forces, velocities, powers) (*Blinsky Y.N., 2015; Arzhenovskiy A.G., 2017; Vezirov Ch. et al, 2014*). Furthermore with the help of generalized dependencies it becomes possible to calculate fuel consumption more accurately, including for throttle down mode of diesel engines (*Grisso R.D. et al, 2006, Schreiber M., 2006*).

Unfortunately, the practical application of some of these proposals is only possible for a small list of machines and specific operating conditions. For example, there is a lack of enough data to estimate the required power when operating spraying machines, for fertilizing with mineral fertilizers.

[1] *Vezirov Ch. Z., Assoc. Prof. Ph.D. Eng.; Atanasov At. Z., Assoc. Prof. Ph.D. Eng., Vlăduț V., PhD. Eng.*

Incorrect results for energy and fuel consumption can be obtained due to the use of equipment with different capacities for harvested products, fertilizers, solutions etc. The situation is similar with different degrees of use of these volumes. Determining the appropriate volume of hoppers and tanks is done from the aspect of the design of such machines without taking into account the specific production conditions (*Dyachkov A.P. et al, 2014*). Other researchers offer various resources to objectify the computational process, which undoubtedly facilitates obtaining the necessary information (*Zaied M.B. et al., 2014; Kumar N. et al, 2015; Revanth K. et al, 2018*).

The positive experience in the application of modern information technologies as well as the need for more accurate determination of the productivity and fuel consumption of equipment with capacities prompted us to try to solve the described task.

MATERIALS AND METHODS

The comparison of the formulas for determining the required power (*ASAE 496.3, 2006, ASAE 497.7, 2011, Tutorial, 1978*) shows similarity. The draft power requirement is

$$P_d = F_i[A + BS + CS^2\,]WTS \tag{1}$$

where:

F_i is dimensionless soil texture adjustment parameter,
i is 1 for fine, 2 for medium and 3 for coarse textured soils,
A, B, C are machine-specific parameters (*ASAE 497.7*, *2011*),
S is field (working or forward) speed,
W is machine working width, or number of rows or tools,
T is tillage depth for major tools, 1 for minor tillage tools and seeding implements.

Accordingly, the required power take-off

$$P_{pto} = a + bW + cWS \tag{2}$$

where:

a, b, c are machine-specific parameters (*ASAE 497.7, 2011*),
WS is material feed rate.

In such a way F_iAWTS and cWS are functions of working width and forward speed. Furthermore F_iCWTS is different from 0 only for Subsoiler/Manure injector and Mouldboard plough, while in other sources (*Tutorial, 1978*) it is reported directly by an F_iBWTS. Another problem is the impossibility to report idle-power by P_d. To overcome these problems, we propose the machine-specific parameters to be entered with a formula whose velocity is in the denominator.

Regarding the measurement of the influence of the weight of the transported load in the tank or the hopper dependency can be used through resistance force.

$$\frac{Mgf}{(SW)} \tag{3}$$

where:

M is mass of machine including the product in tank or bunkers,
g is gravitational acceleration,
f is motion/rolling resistance ratio for specific terrain.

If the idle-power (only when towing machines from the tractor) does not depend on the speed and working width, then $F_i = 1,\ T = 1$ and

$$P_d = \left(\frac{V}{W}\right)\Psi\rho gf \tag{4}$$

where:

V is volume of tank or bunker,
Ψ is rate of volume use,
ρ is bulk density of the product in tank or bunker.

Since in some data, sources of the traction resistance are given only as a function of the working width, formula (1) assumes the form

$$P_d = \left(\frac{V}{W}\right)\Psi\rho gf + F_iAWTS \tag{5}$$

Additionally, calculations can be made for 1, 2 or 3 types of machines behind the tractor or for up to 2 types of machines together with the self-propelled harvester. Examples: squadron hitch, cultivators and seeders or header, self-propelled grain harvester and straw baler.

Important question in solving the task is the ability to use aggregated data. Such data are available, even before specifying the machines (from which company, what model and modification) for which field capacity and fuel consumption will be calculated. Such summary data for trailers (*Ivanov S., 2019*) are shown in Figure 1.

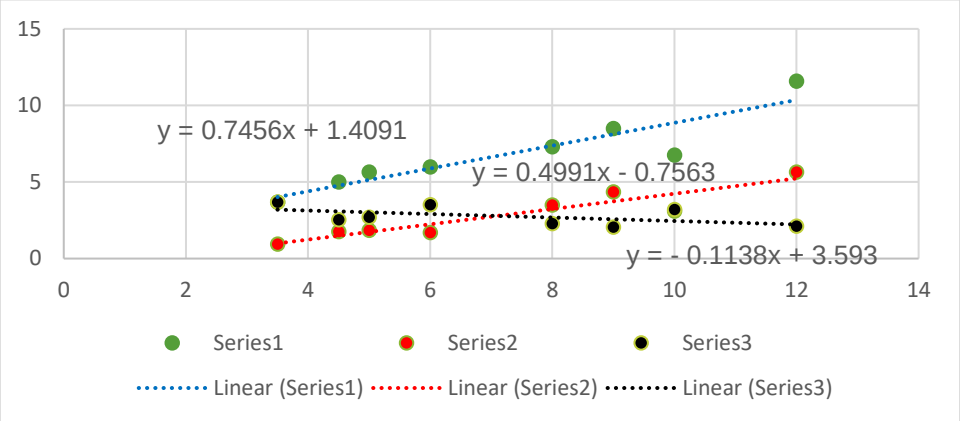

Fig. 1 - Relations for agricultural trailers between x - carrying capacity and y: volume of bodywork - Series1; empty trailer's mass (tare) - Series2; ratio between empty trailer's mass and carrying capacity – Series3

Naturally, the larger volume of the trailer provides greater load capacity - Series1. Greater load capacity also requires more material for trailer body - Series2. At the same time, greater load capacity is achieved with less tare weight, and therefore with lower energy consumption for movement - Series3. For load capacity up to 9 t the dependence is very close to linear. This allows for calculation of Pd through the volumes of trailer's capacities.

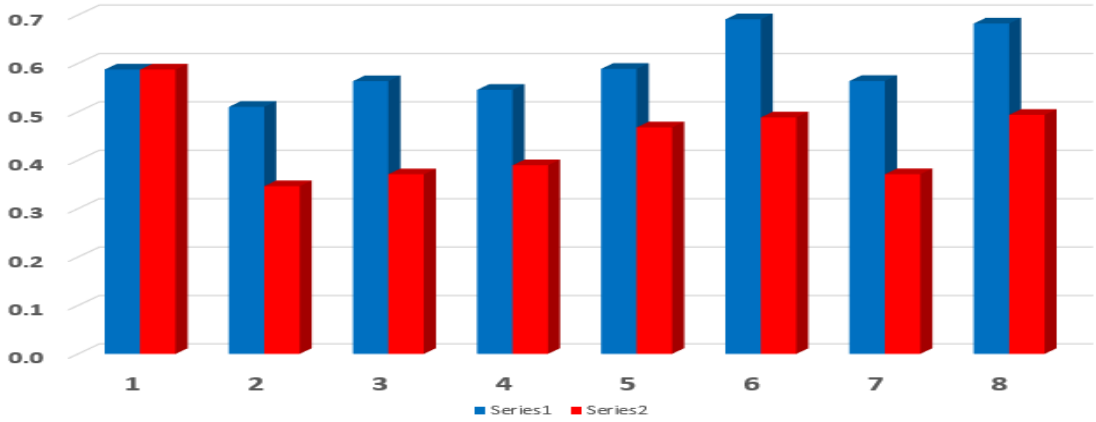

Fig. 2 - Ratios between trailer's volumes: blue colour with blind side extensions to without extensions, red colour with mesh side extensions to without extensions.
Number under the bars means respectively carrying capacity in tons: 1 – 3.5; 2 – 4.5; 3–5; 4–6; 5–8; 6–9; 7–10; 8–12

The Fig. 2 shows that the use of dense and mesh superstructures allows better use of the volume of trailers for loads with lower bulk density. This increase is not enough for straw, hay, tobacco and other plant stems. However, averaged volume data for upgraded trailers can be used.

In a similar way, data are obtained on the ratios of volumes of capacities, own weight to working widths for fertilizers, sprayers, seeders and to engine power of harvesting machines.

RESULTS AND DISCUSSION

We use spreadsheets to perform the calculations. They are suitable due to the following features:

- the change of the entered data and in one cell immediately allow comparison of the result,
- information with formulas can be set in the cells,
- the formulas used and the results shown allow an intermediate verification of the data,
- the formulas are visible and can be updated if necessary, according to the available information.

To implement above mentioned ideas a spread sheet was created, see figure 3.

INITIAL DATA is presented in 2 groups:

A. Input direct in cells with light green background colour;

Operation (column A); distance of transportation (column B); fertilization, spraying, sowing rate, yield (column C); tractors, power machines: brand, model, modification, type of undercarriage, rated engine power (columns D, E, F); implements, other machines, up to 3 types; for each of them: numbers in aggregate/unit, width, volume, rate of volume use of materials in tanks, bunkers, approximately 1; squadron hitch for 2 or more implements together in an aggregate/unit: brand, model, modification, mass/quantity of matter, width of bar for hitching (columns AJ, AK, AL); tilling, sowing or planting depth respectively for 1st, 2nd and 3rd machine/implement (columns AN, AO, AP); type of terrain/soil (ASAE 497.7) (column AR); 1 for machines/implements with information according to ASAE 497.7 about width units in “tools” or “rows” (columns AS, AT, AU); material feed rate (column BP);

B. Input indirect in cells with light yellow background colour by links of a cell in specific sheet. The names of such sheets are shown above related column or columns in row 11.

Specific sheets are for: bulk density of grain, solution, fertilizer, manure, seeds, etc. (columns S, T, U) – “density”; motion resistance rate for undercarriage on specific terrain (columns Y, Z, AA) – “Femc”; field width efficiency (column AB) – “β§η”; maximum speed for specific operation and machine or squadron hitch (columns AF, AH, AG, AI) – “V&χm&ao”; motion resistance rate for squadron hitch (column AM) - “Femc”; field time efficiency (column AQ) - “T”; soil parameter Fi (*ASAE 497.7, 2011*) (column AV); machine-specific parameters for 1st, 2nd and 3rd machine/implement for draft power requirement (*ASAE 497.7, 2011*) (columns AW, AX, AY; BB, BC, BD; BG, BH, BI respectively); machine-specific parameters for PTO power requirement (*ASAE 497.7, 2011*) (columns BM, BN, BO); maximum acceptable energy use rate less than 1 (column BQ);

RESULTS are presented in 3 groups:

C. In cells with white background colour - intermediate data:

To check the numbers obtained before the final results (columns AZ, BA; BE, BF; BJ, BK); calculated specific draft/drawbar resistance for aggregate/unit (column BL); acceptable forward field speed (column BR); real working width of aggregate/unit (column BS); power take-off (column BT); draft power requirement (column BU); sum of two powers mentioned before (column BV); required power for aggregate/unit including tractive one and needed for PTO (column BW); engine power according to type of undercarriage and tractive condition (column BX); ratio of numbers in previous two columns BW and BX (column BY); specific fuel consumption (column BZ); fuel consumption for entire shift time (column CA);

D. In cells with light pink background colour:

Field efficiency and specific fuel consumption for autonomous operation without relation with transportation (exception for fuel for tractors and self-propelled harvesters) (columns CB, CC);

E. In cells with light blue background colour:

Field efficiency and specific fuel consumption for linked operations (columns CE, CF). The columns CD, CE, CF are not used in this example because of the nature of specific agricultural operations.

Result of above-described procedure for five linked field operations, namely potato transportation, fertilization, spraying, planting, harvesting is presented in the same figure 3. First step was to select tractor, trailer, planter, sprayer, spreader and harvester, i.e. (*Complex, 2020*). They have to be compatible, as appropriate hitch system, PTO with equal rotational speed and numbers of splines etc. For example, trailer’s mass with full load has to be less than tractor’s mass for off road transportation. On the other hand, there is a relation between tractor’s rated tractive force on unpaved farm road, and maximum trailer’s carrying capacity: 0.9–4 t, 1.4–6 t, 2–9 t, 3–12 t, 5–21 t (*Ivanov S., 2019*).

	A	B	C	D	E	F	G	H	I	J	K	L	M	N	O	P	Q	R
10																		
11				rated effective power ↓														
12				tractors, power machines														
13	agricultural operations	distance of transportation, km	fertilization, spraying, sowing rate, yield, t/dka	brand, model	type: 1 - 4x2 2 - MFDW 3 - 4x4 4 - crawler	Pen, W	brand, model			numbers in aggregate			width, m			volume, m³		
14										n1	n2	n3	B1	B2	B3	1.	2.	3.
15	Transportation of fertilizer	3.4	0.1	Tractor	2	60000	Trailer	Telescopic crane		1	1		1.0			6.15		
16	Spreading of fertilier		0.1	Tractor	2	60000	Spreader			1			10.8			5		
17																		
18	Transportation of potato	3.4	0.25	Tractor	2	60000	Trailer	Telescopic crane		1	1		1.0			6.15		
19	Potato planting		0.25	Tractor	2	60000	Planter			1			3.0			4		
20																		
21	Transportation of solution for spraying	3.4	0.03	Tractor	2	60000	Tank semi trailer			1			1.0			4		
22	Spraying		0.03	Tractor	2	60000	Sprayer			1			10.8			1.2		
23																		
24	Transportation of fertilizer	3.4	0.015	Tractor	2	60000	Trailer	Telescopic crane		1	1		1.0			6.15		
25	Under root fertilisation		0.015	Tractor	2	60000	Row dependent soil cultivator			1			0.75			0.9		
26																		
27	Potato harvest		2.5	Tractor	2	60000	Harvester			1			1.5			4		
28	Transportation of potato	3.5	2.5	Tractor	2	60000	Trailer			1			1.0			6.15		
29																		
30	Fig. 3. Segment of spreadsheet for calculation of field capacity and fuel consumption - part 1																	
31																		

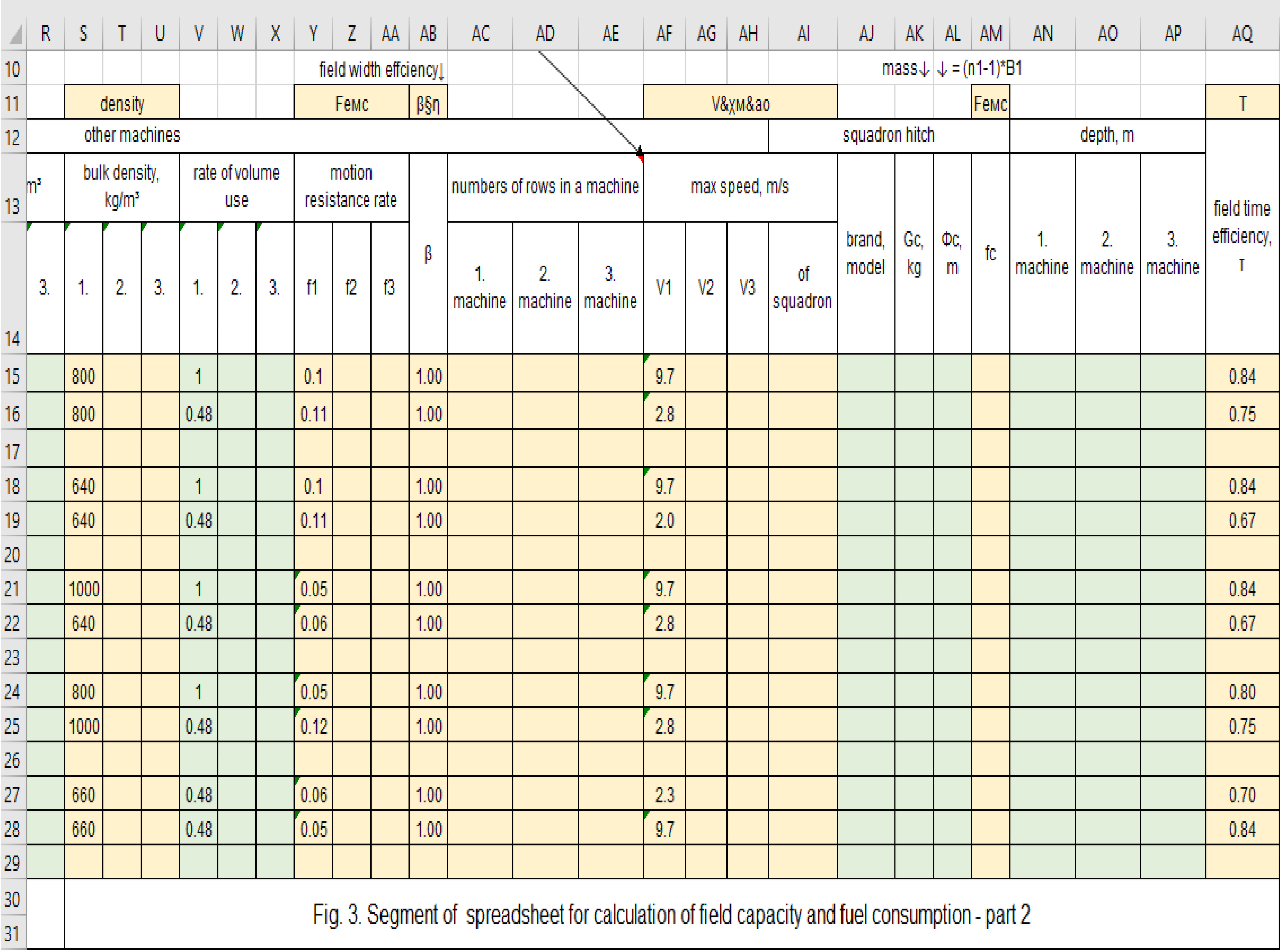

	R	S	T	U	V	W	X	Y	Z	AA	AB	AC	AD	AE	AF	AG	AH	AI	AJ	AK	AL	AM	AN	AO	AP	AQ
10								field width effciency↓											mass↓ ↓ = (n1-1)*B1							
11		density						Fемс			β§η				V&χм&ao							Fемс				T
12		other machines																squadron hitch					depth, m			
13	m³	bulk density, kg/m³			rate of volume use			motion resistance rate			β	numbers of rows in a machine			max speed, m/s				brand, model	Gc, kg	Φc, m	fc	1. machine	2. machine	3. machine	field time efficiency, T
14	3.	1.	2.	3.	1.	2.	3.	f1	f2	f3		1. machine	2. machine	3. machine	V1	V2	V3	of squadron								
15		800			1			0.1			1.00				9.7											0.84
16		800			0.48			0.11			1.00				2.8											0.75
17																										
18		640			1			0.1			1.00				9.7											0.84
19		640			0.48			0.11			1.00				2.0											0.67
20																										
21		1000			1			0.05			1.00				9.7											0.84
22		640			0.48			0.06			1.00				2.8											0.67
23																										
24		800			1			0.05			1.00				9.7											0.80
25		1000			0.48			0.12			1.00				2.8											0.75
26																										
27		660			0.48			0.06			1.00				2.3											0.70
28		660			0.48			0.05			1.00				9.7											0.84
29																										
30																										
31																										

Fig. 3. Segment of spreadsheet for calculation of field capacity and fuel consumption - part 2

	AR	AS	AT	AU	AV	AW	AX	AY	AZ	BA	BB	BC	BD	BE	BF	BG	BH	BI	BJ
10					V&χM&ao RM = Fi * (A + B * V + C * V²) * Ba * ao														
11					Fi	1. machine					2. machine					3. machine			
12		1 - small machines, seeders				A	B	C			A	B	C			A	B	C	
13	terrain: 1 - firm 2 - tilled 3 - soft 4 - concrete	1. machine	2. machine	3. machine	–	N/ (m*cm)	N*s/ (m²*cm)	N*s²/ (m³*cm)	inter mediate	N/m	N/ (m*cm)	N*s/ (m²*cm)	N*s²/ (m³*cm)	inter mediate	N/m	N/ (m*cm)	N*s/ (m²*cm)	N*s²/ (m³*cm)	inter mediate
14																			
15	1				1.00	1760			1760	6587				0	0				0
16	1				1.00	140			140	332				0	0				0
17									0	0				0	0				0
18	1				1.00	1760			1760	5621				0	0				0
19	2				0.94	840			790	1232				0	0				0
20									0	0				0	0				0
21	1				1.00	670			670	2632				0	0				0
22	1				1.00	40			40	60				0	0				0
23									0	0				0	0				0
24	1				1.00	880			880	3293				0	0				0
25	3				0.94	2190			2059	2737				0	0				0
26									0	0				0	0				0
27	1				1.00	1490			1490	1987				0	0				0
28	1				1.00	880			880	1836				0	0				0
29																			

30
31

Fig. 3. Segment of spreadsheet for calculation of field capacity and fuel consumption - part 3

	BK	BL	BM	BN	BO	BP	BQ	BR	BS	BT	BU	BV	BW	BX	BY	BZ	CA	CB	CC	CD	CE	CF	CG	CH
10		Ppto ≈ a + b* Ba + c * F				↓maximum acceptable energy use level																		
11			Ppto			0	ββη					power engine load ↓									for linked operations		ΔV	Δη
12		χм	a	b	c	F	ηmax	Vmax	Ba*β	Ppto	Pd	Pd+Ppto	Peo	Pen	η	gp	Gcм	Wcм	g	is enough width of squdron hitch bar	Wcм, dka/ shift	9, g/dka		
13	N/m	N/m	kW	kW/m	kWs/kg	kg/s	–	m/s	m	kW	kW	kW	kW	kW	–	kg/kWh	kg/ shift	dka/ shift	g/dka					
14																								
15	0	6587					0.96	5.45	1.0	0	36	36	49	51	0.96	0.226	74	119	620				4.27	0.00
16	0	332			11	2.89	0.90	2.68	10.8	31.8	10	41	46	51	0.90	0.226	62	563	110				0.10	0.00
17	0	0					0.00			0	0	0												
18	0	5621					0.96	6.40	1.0	0	36	36	49	51	0.96	0.226	74	139	530				3.32	0.00
19	0	1232					0.88	2.00	3.0	0	7	7	12	51	0.23	0.590	36	104	340				0.00	0.65
20	0	0					0.00			0	0	0												
21	0	2632					0.96	9.72	1.0	0	26	26	35	51	0.68	0.261	61	212	280				0.00	0.28
22	0	60			4.4	0.9	0.94	2.78	10.8	3.96	2	6	6	51	0.13	0.745	26	521	40				0.00	0.81
23	0	0					0.00			0	0	0												
24	0	3293					0.96	9.72	1.0	0	32	32	43	51	0.85	0.229	64	202	310				0.00	0.11
25	0	2737			5	0.03	0.92	2.78	0.8	0.16	6	6	10	51	0.19	0.640	37	41	910				0.00	0.73
26	0	0					0.00			0	0	0												
27	0	1987		10.7			0.85	2.30	1.5	16.1	7	23	27	51	0.52	0.326	49	63	770				0.00	0.33
28	0	1836					0.96	9.72	1.0	0	18	18	24	51	0.47	0.354	57	212	270				0.00	0.49
29																								
30																								
31																								

Fig. 3. Segment of spreadsheet for calculation of field capacity and fuel consumption - part 4

Some problems arose because of aggregated information about time efficiency, soil and terrain (only 3 or 4 condition), calculation for only one mode (soil and plants processing), exclude: turning, run idle (no load), loading or unloading of materials, etc. The specific input values, i.e. machine-specific parameters, was changed by coefficients taking into account soil cone index, field length, coherence of agricultural and transport machinery, etc. Part of input data has been verified by comparing different sources. The other one has been adjusted based on formal experience with similar operations and machinery.

Because some data for machine-specific parameters are with width units in “tools” or “rows”, the tillage depth was relatively precise.

To comply with the requirements for operation’s forward speed and maximum engine power use level, values have been changed in columns BR manually or by Solver add-in. Optimization criteria was the closeness of calculated forward speed and rate engine power use to the acceptable values. This Microsoft Excel program can be used for what-if analysis too. Other way to meet these requirements was reducing the rate of volume use for trailer, tank, bunker capacity (columns V, W, X) or increasing the trailer volume by using blind or mesh side extensions (columns P, Q, R). The possibility of transportation with more than one trailer in aggregate/unit was checked also (it is not shown in the figure).

This procedure and spreadsheet were used for calculations for other crops and technologies too. It was found that there is no enough data in most recommended sources *Tutorial, 1978, ASAE 496.3, 2006, ASAE 497.7, 2011*, for such operations like spraying, fertilization, gathering up and loading straw, root crops from field, a lot of stationary systems, cargo handling, with electrical engines. It is obviously that collecting large volume of information of this kind is practically impossible. Our practice shows that in such situation analogy approach may be effective.

In few cases, field experiments are required. They are aimed at determining the appropriate forward speed to ensure quality work, effective load of engine and undercarriage, wheel slip or speed reducing ratio of tractor, car or self-propelled harvester. The simplest way to evaluate these indicators is by tachometer, speedometer, even by naked eye. Of course, these experiments can be realized with available similar machinery in analogical soil and plants conditions. If selected machines are bought such trials make sense to precise machine-specific parameters and other input data.

Finally, we must emphasize that only by these two indices, namely filed capacity and fuel consumption, it is not possible to evaluate machines’ efficiency of machine and tractor fleet. It is important to find the global extremum for all farm operations.

The fact that above-described procedure is realized by such widespread software Excel as a part of Microsoft Office makes it even easier to use. Furthermore, each cell with formulas is visible and may be changed by users. Similarly, more than 12 sheets with specific data are available and may be supplemented and improved. In other words, this free computer software can be distributed under terms that allow users to run the software for any purpose as well as to study, change, and distribute it in any adapted versions.

CONCLUSIONS

The above presented procedure for determination of field capacity and fuel consumption of mobile machinery with tanks, hoppers, bunkers allows a semi-automated informed choice. By it, the effect of main factors such as type of tractor, harvester, trailer and their technical parameters, goods, terrain, on field speed, energy consumption and time efficiency is reproduced. All this information can be achieved from official standards, manuals or simple experiments. The procedure allows specifying concrete values and relations according to practice. Application of spreadsheets makes the process easier, quicker and well-founded.

ACKNOWLEDGEMENT

The study was supported by contract 2020-FNI-01, funded by the Research Fund of the University of Ruse.

REFERENCES

[1] Arzhenovskiy A.G., (2017), Methods of determination of power and fuel-economic rates of machine and tractor units, (Методы определения энергетических и топливо-экономических показателей машинно-тракторных агрегатов), *Agricultural Machinery and Technologies*, № 6, 36-40, https://doi.org/10.22314/2073-7599-2017-6-36-4;

[2] Blinsky Y. N., Voronin D.M., Kemelev V. S., (2015), *The basics of mechanized processes in agricultural sector, (Основы проектирования механизированных процессов в АПК)*;
[3] Dyachkov A.P. et al, (2014), Technique for determining the optimal capacity of sowing units, (Методика определения оптимальной грузоподъемности бункеров посевных агрегатов), *Forestry Journal,* № 3*;*
[4] Grisso R.D., Vaughan D.H., Roberson G., (2006), Method for Fuel Prediction for Specific Tractor Models, https://www.researchgate.net/publication/240620349_Method_for_Fuel_Prediction_for_Specific_Tractor_Models;
[5] Ivanov S., (2019), *Fineness of tractor trailers selection (Тонкости подбора тракторных прицепов)*, https://zen.yandex.ru/media/russianengineering/tonkosti-podbora-traktornyh-pricepov-5cae4deb7c77b000b28b81a0;
[6] Kumar N., Pandey K. P., (2015), A visual basic program for predicting optimum gear and throttle position for best fuel economy for 32 kW tractor, *Computers and Electronics in Agriculture*, 119, 217–227;
[7] Fere N. E. et al., (1978), *Tutorial for machine and tractor fleet exploitation.* (*Пособие по эксплуатации машинно-тракторного парка*);
[8] Revanth K. et al, (2018), Decision Support System for Matching Tractor – Implement System, International *Journal of Current Microbiology and Applied Sciences*, ISSN: 2319-7706, Volume 7, Number 11. DOI: 10.20546/ijcmas.2018.711.076.
[9] Schreiber M., (2006), *Fuel consumption when using agricultural tractors, especially with regard to CO_2 emissions; (Kraftstoffverbrauch beim Einsatz von Ackerschleppern im besonderen Hinblick auf CO_2 – Emissionen)*, Dissertation, Universität Hohenheim, Deutschland;
[10] Spiridonov V., (2018), About informed choice of machinery for field crop growing, (За информирания избор на техника за полевъдството), *57th Science Conference of Ruse University*, Bulgaria;
[11] Vezirov Ch.Z., (2013), *Using of agricultural resources*, (*Използване на ресурсите в земеделието*), https://e-learning.uni-ruse.bg/index.php;
[12] Vezirov Ch. Z Atanasov, At. Z. Hristov, H. Y. Vlăduț, V. (2014), Approach, limits and criteria for farm machinery replacement in agriculture*, ISB-INMA TEH' 2014. International Symposium: Agricultural and Mechanical Engineering, Bucharest, Romania, 30-31 October 2014*, pp.57-64;
[13] Zaied M.B., Ahmed M. El Naim, Tarig E. Mahmoud, (2014), Computer Modelling for Prediction of Implement Field Performance Variables, *World Journal of Agricultural Researc*h, Volume 2, № 2, 37-41;
[14] Zavrazhnov A.I. et al., (2019), *Exploitation of machine and tractor fleet, (Эксплуатация машинно-тракторного парка)*;
[15] Zhou K. et al., (2015), Performance of machinery in potato production in one growing season, *Spanish Journal of Agricultural Research*, 13(0215):12-2171;
[16] ***ASAE 496.3, (2006), *Agricultural Machinery Management*;
[17] ***ASAE 497.7, (2011), *Agricultural Machinery Management Data*;
[18] ****Complex machinery for potato growing by the company GRIMME*., https://www.techagro.ru/read/potatos_making.

EXPERIMENT AND PARAMETERS OPTIMIZATION OF SEED DISTRIBUTOR OF MECHANICAL WHEAT SHOOTING SEED-METERING DEVICE

/

机械式小麦射播排种器分种装置参数优化与试验

Wang Yingbo[1)], Li Hongwen*[1)], Wang Qingjie[1)], He Jin[1)], Lu Caiyun[1)], Liu Peng[1)], Yang Qinglu[1)] [1]

[1)]College of Engineering, China Agricultural University, Beijing/China

Tel: +8610 62737300; *E-mail: lhwen@cau.edu.cn*

DOI: https://doi.org/10.35633/inmateh-63-03

Keywords: *Shooting seed; seed metering device; seed distributor; structural optimization*

ABSTRACT

In order to solve problems of lower seed-filling stability and wheat seed damage of mechanical shooting seed-metering device, the filling structure of the shooting device was optimized. The effects of seed movement were obtained through analysing the kinematics and dynamics of wheat seed through seed distributor. The influence factors were the inner diameter of seed distributor, the rotational speed of seed distributor and the inclination angle of distributor window. The discrete element software (DEM) was used to simulate the motion process to explore the different factors on the wheat seeds' movement characteristics in the shooting device. The coefficient of variation of shooting uniformity and shooting speed of wheat seed were selected as test indicators. A verification experiment was conducted, and a high-speed camera was taken to obtain wheat seed's movement and shooting speed. The verification test showed that the constant uniform variation coefficient of seed amount and average shooting depth was 8.6% and 32 mm, respectively.

摘要

针对机械式小麦射播排种器充种效果较差，导致播种均匀度、排种稳定性不佳的问题，对排种器分种结构进行优化，通过对小麦种子经过分种装置时的运动学与动力学分析，得出影响种子运动状态的因素，并对分种轮的结构参数进行优化，采用开口侧壁后倾形式以提升充种效果，并结合 EDEM 软件对排种器的充种、排种过程进行仿真试验。试验结果表明：在内径为 125 mm，开口倾斜角度为 25°，转速为 1100 r/min 时，排种量均匀度变异系数为 8.6%，排种速度为 34.7 m/s，平均播种深度为 32 mm，满足华北地区小麦播种作业要求。

INTRODUCTION

Wheat is one of the important crops in China, which has widely distributed planting area and yield production, and ranks no.2 in the production of crops. As one of the main grain production bases in China, North China plain covers an area of 6 million hectares for winter wheat (*Olaf E. et al, 2008, Bassu S et al, 2009*). In the growth of wheat, planting quality is an essential process. Thus, the seeding effect of the planter has a crucial influence on the growth and wheat yield (*Cui Qingliang et al., 2001*).

Mechanical and precision vacuum seed-metering device were wildly used in wheat seeders. The seed was pressed on the hole under the action of the internal air pressure and filled in a vertical disc, which was wildly used for precision vacuum seed-metering device (*Ahmet Çelik et al., 2016*). The device was more efficient in plot area sowing operations. However, the seed filling and seeding uniformity were influenced largely during wheat sowing operations in field a*reas (Matin M A et al., 2014).* Some other wheat seeders were using mechanical seed metering devices. For instance, the grooved wheel seed-metering devices were generally used. The structures of seeders were simple, which can be conveniently adjusted. Specifically, the seeding uniformity and stability were worse than that of a pneumatic seed-metering device (*Li Chaosu et al, 2012*). Furthermore, a furrow opener cuts a furrow and allows seed or seedlings to be deposited before being covered with soil. The coverer installed on the rear of the seeder covered seedlings drilled from a seed-metering device (*Wang Chao et al, 2019*). Critical components of the seed-metering device and soil-touching parts such as coverers significantly influenced sowing performance (*Wang Chao et al, 2020*).

[1]*Wang Yingbo, Ph.D. Stud. Eng.; Li Hongwen, Prof. Ph.D.; Wang Qingjie, Prof. Ph.D.; He Jin, Prof. Ph.D.; Lu Caiyun, Prof. Ph.D.; Liu Peng, Yang Qinglu, Ph.D. Stud. Eng.*

This study aimed to improve the variation coefficient of seeding amount of a non-contact mechanical shooting seed-metering device. Seed could be accelerated by the blade and shot into the soil layer. In this study, the structure and parameter of seed distributor were optimized. A Central-Composite three-factor simulation experiment was also conducted to optimize the independent variables.

MATERIALS AND METHODS

ANALYSIS OF WHEAT SEED MOVEMENT

Structure and working principle

The overall structure of the seed-metering device is shown in Fig.1. It consists of a seeding tube, a device shell, a seed distributor, a seeding control cage, a rotating shaft and eight blades. The seed entered into the seed distributor through the seed tube, fell into the windows of seed distributor, and rotated with the seed distributor. While window of the seed distributor matched on the window of seeding control cage, wheat seeds were rotated into the inner cavity of shooting device, and moved along with blades at a high speed. Eight blades were evenly distributed on the surface of seeding control cage. Meanwhile, seeds were accelerated by blades, which causes seed being continuously and uniformly shot into the field. The rotational speed of blades was equalled to that of the rotating shaft because of the fixed connection among blades, turntable and shaft. The rotary speed of blades was adjusted by sprocket to adapt different operating speeds for wide-row wheat planting.

a) Side view of the shooting device; b) Inner view of the shooting device

Fig. 1 - Structure of shooting seed-metering device

1. Seeding tube; 2. Device shell; 3. Rotating shaft; 4. Seeding control cage; 5. Seed distributor; 6. Blade; 7. Shooting exit

Analysis of seed process

The seed metering device is a critical component in the sowing process, and has a significant impact on the seeding effect. The sowing process of the seed-metering device was divided into four working processes: seed cleaning, seed filling, seed carrying and seed shooting. The operation of filling and cleaning of mechanical shooting metering device was conducted by seed distributor and seeding control cage, which could constantly keep the number of wheat seed in rotation area. Furthermore, the carrying and shooting process was conducted by blade rotating at high speed. The state of seed movement was directly affected by seed movement through the seed distributor. Thereby, subsequent movement process and shooting performance were also affected.

Seed falls into the inner cavity of seed distributor for filling stage and moves out of seeding control cage. The structure of seed distributor is shown in Fig.2. The cleaning process was located in the window of seed distributor. The relative position relationship between seeding control cage and seed distributor is shown in Fig.3. Seed could move out of the seeding control cage through the seed distributor under a certain speed and position (*Zhang Boping, 1982*). The critical conditions were analysed to find the limited position of wheat seeds that could move out of the seeding control cage.

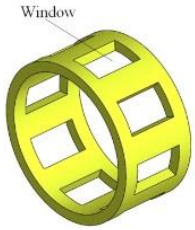

Fig. 2 - Structure of seed distributor

Fig. 3 - Relative position of seeding control cage and seed distributor

Initially, the linear motion equation of seed acceleration process inside the window of seed distributor was established. As shown in Fig.4, the radial direction of window was represented by the *X* axis.

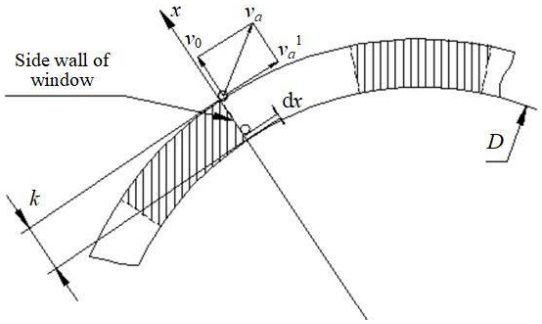

Fig. 4 - Model of seed movement on the window of seed distributor

The acceleration of wheat seed moving radially outward on the inner side of the window:

$$a = \frac{\mathrm{d}v}{\mathrm{d}t} = \frac{\mathrm{d}^2 x}{\mathrm{d}t^2} = \omega^2 (\frac{D}{2} + x) \tag{1}$$

where: ω is the rotational speed of seed distributor, rpm;

D is the diameter of seed distributor, mm;

a is the acceleration velocity of seed, m/s².

With initial conditions, the radial velocity when the seed moves to the outmost layer of seed distributor:

$$v_0 = \omega\sqrt{k^2 + kD} \tag{2}$$

where: v_0 is the radial seed velocity, m/s; k is the thickness of seed distributor, mm.

The speed is shown in Equation (3), while seeds move to the outer edge of seed distributor.

$$v_a = \sqrt{v_0^2 + (v_a^1)^2} = \omega\sqrt{2Dk + 2k^2 + \frac{D^2}{4}} \tag{3}$$

where: v_0 is the absolute velocity, m/s; v_a^1 is the tangential speed; m/s.

Analysis of seed cleaning process

Wheat seeds enter the rotation area in sequential order from the seed distributor, because wheat seeds were idealized as spherical particles for theoretical analysis afterward. Other seed particles could enter the window of seed distributor while all seeds in the window need to move out of the seeding control c*age (Jiang Qinghe 2001)*. Wheat seed collides with the end of sidewall of seeding control cage while moved out of seed distributor. The centroid of the seed coincides with intersection point B, a critical state where seeds could move out of the seeding control cage. The first and last seed moved out of seed distributor was seed at point A and point C, respectively. Moreover, point D is the position where seed and blade collided. Specifically, the whole process was the cleaning stage of sowing seed.

The radial velocity of seed while moving out of seed distributor was not affected by position, because the initial radial velocity of the seed was 0. The movement of the seed at extreme position C should be discussed. As shown in Fig.5, the angle β between its absolute velocity and radial velocity was shown in Equation (4).

$$\beta = \arccos\frac{v_0}{v_a} \tag{4}$$

The seed couldn't get into the rotation area and be accelerated since the motion angle of seeds moved to the seeding control cage was less than β. The seed on the left side needed to move a circle between the seeding control cage and seed distributor before moving into the rotation area. Thus, shooting performance was affected.

Therefore, Equation (5) needs to be satisfied:

$$\beta < \beta' \tag{5}$$

where:

β' is the angle between the radial direction and tangential direction of the seeding control cage, (°).

$$\beta' = \arctan\left[\frac{D}{2r} - \cos\left(\sqrt{(2r - D)2r} - 30°\right)\right] \quad (6)$$

The initial installation angle of the blade and seeding control cage is 30°. According to the geometric relationship, the last seed in the window could move out of directional seeding cage while the outer diameter *r* of the seed distributor was greater than 0.75 times the inner diameter. Therefore, all seeds in the window could move out of the seeding control cage while the seed distributor was rotated once.

The inner diameter *r* of the seed distributor was selected to be 0.75 to 0.85 times outer the diameter because the thickness of the seed distributor couldn't be too small.

The rotation angle of seed distributor (λ) was obtained in Equation (7) by geometric relationship.

$$\tan\lambda = l_{CD} / D \quad (7)$$

where: l_{CD} is the straight distance between two positions of C and D, mm.

Through analysis of Equation 7 and results, it can be concluded that all seeds could move out of the seeding control cage from the opening window of the seed distributor rotated within 30°.

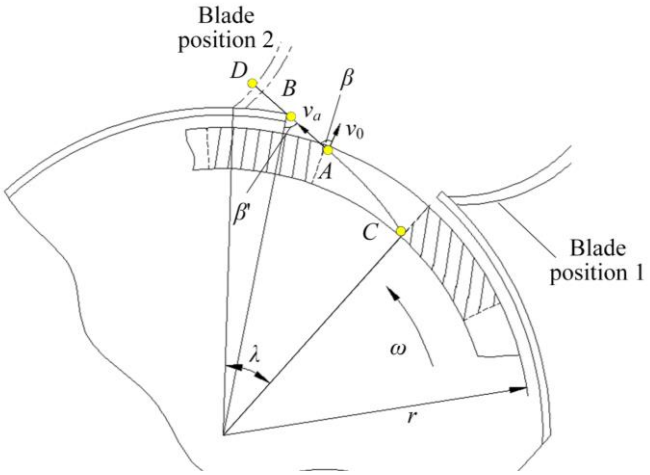

Fig. 5 - Model of seed movement at the limited position

Note: The dotted blade is the position of blade contact with the seed

Principle analysis of seed distributor on seed movement

Determination of the inner diameter of the seed distributor

Some seed particles could not move out of the seed distributor during a rotation process, which could affect the filling process and sowing performance caused by a smaller diameter of the seed distributor (*Zeng Hui, 1990*). The low sowing efficiency was also conducted by the larger diameter of the seed distributor. Therefore, seeds in the seed distributor window were analysed.

The first and last seed particle moved out of seed distributor was a_2 and b_1, respectively, which was two limited position seed (as shown in Fig.6 and Fig.7).

The tangential speed of the seed (a_2) moving out of the seed distributor is shown as Equation (8).

$$v_1 = \omega r \quad (8)$$

where: *r* is the outer diameter of seed distributor, mm.

The rotation angle of blade during the contact between wheat seed and blade was obtained in Equation (9).

$$\omega t = \theta + \delta \quad (9)$$

where: *t* is movement time while the wheat seed is in contact with the blade, s;

δ is the angle between sidewall of window and initial position (blade position 1) of the blade, (°);

θ is the angle between sidewall of window and the contact position of the blade, (°).

The rotation centre angle of seed (φ) from the initial point to contact point is shown in Equation (10).

$$\varphi = \omega t - (\gamma + \delta) \quad (10)$$

where: γ is the angle between two sidewalls of window, (°);

φ is the rotation centre angle of the seed, (°).

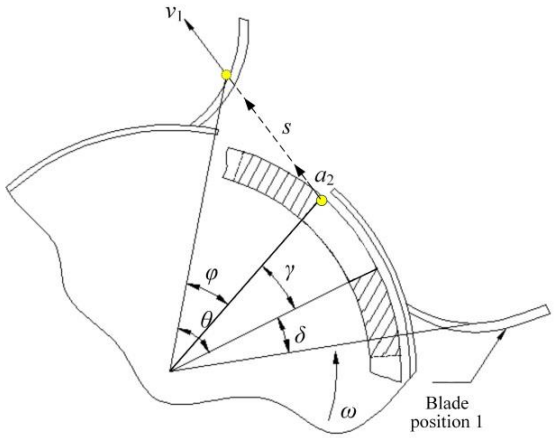

Fig. 6 - Seed movement process of a_2 position

Seed moved out of seed distributor and made a motion in a straight line. The movement distance of seed from the initial point to (a_2) the contact point is shown in Equation (11).

$$s=v_1 t=\omega t r \tag{11}$$

where: s is movement distance of the seed from the initial point to (a_2) the contact point, mm;

v_1 is the tangential velocity of the seed particle at a_2 position flying out of seed distributor, m/s.

The rotation angle of seed could be calculated by Equation (12) according to geometric relationship.

$$\tan\varphi=\frac{s}{r}=\omega t \tag{12}$$

The line speed at which seeds moved to the outermost side at position a_2 is shown in Equation (13).

$$v_{a1}=\sqrt{v_1^2+2\omega(r\omega-2fv_1)(l-r_0)} \tag{13}$$

where: l is the radial position of wheat seed on the blade, mm;

f the coefficient of friction;

r_0 is position radius of wheat seed on the blade, mm.

The movement of seed inside the metering device was affected by the parameters of seed distributor. Thereby subsequent sowing effect was affected, according to analysis of Equation (11), (12) and (13), respectively.

Determination of outer diameter of seed distributor

In order to enhance the stability of shooting depth, seed velocity at the outer and inner layers of the window should be consistent. Therefore, seed velocity at two limited positions was analysed. The movement of seed of the rest of seed distributor was the same as the limited position.

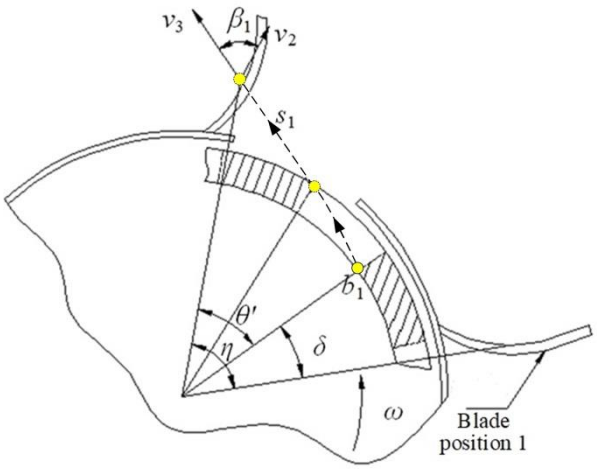

Fig. 7 - Seed movement process of b_1 position

As shown in Fig.7, the movement distance of the seed at inner layer of seed distributor moved to outer edge of seed distributor was the thickness of seed distributor (k). The tangential speed of seed at b_1 position while seed contacted with blade is shown in Equation (14).

$$v_2 = \omega\sqrt{s^2 + r(r-0.75r)D} \tag{14}$$

The rotation angle of the blade is shown in Equation (15), while wheat seed was in contact with blade.

$$\eta = \sqrt{2(r-r_0)/r_0} \tag{15}$$

where: η is the rotation angle of blade, (°).

The rotation centre angle θ' of seed from the initial point (b_1) to the collision point is shown in Eq. (16).

$$\omega t = \theta' + \delta \tag{16}$$

where: θ' is the rotation centre angle of wheat seed from the initial point (b_1) to the collision point, (°).

The geometric relationship of the seed moved out of seed distributor is shown in Equation (17).

$$\frac{s_1}{\sin\theta'} = \frac{R_0}{\sin(\pi-\beta_1)} \tag{17}$$

where: β_1 is the angle between radial velocity and absolute velocity of wheat seed at position b_1, (°);

s_1 is the movement distance of seed from the initial point (b_1) to contact point, mm.

The absolute speed of seed motion at position b_1 to the outermost of shooting device was obtained by Equation (18).

$$v_{a2} = \sqrt{\omega^2 r^2 + 2\omega(r\omega - 2fv_2) + R^2} \tag{18}$$

where: R is rotation radius of the blade of seed metering device, mm.

Equation (13) and (18) show that two limited positions of seed move out of shooting device at same speed, while outer diameter (r) of seed distributor was 0.3 times the gyration radius (R) of the blade. Therefore, the outer diameter of that was determined to be 150 mm to ensure the shooting speed of seed at each position in seed distributor was consistent.

Optimization of structure parameters of seed distributor

The connection line between the centre point with upper and lower endpoints M and T of the seed distributor sidewall, respectively, was optimized into a non-collinear line. Therefore, a certain angle between MT and OM was conducted, which was shown in Fig.8. The direction of centrifugal force of seed was at a certain angle to sidewall of the seed distributor window.

The acceleration differential equation of motion for seed moves on sidewall with the inclination angle of α and acceleration velocity a_1, respectively, is shown in Equation (19).

$$a_1 = \omega^2[(\sqrt{\frac{D^2}{4} - (\frac{D}{2}+k)^2\sin^2\alpha} + x_0) - f(\frac{D}{2}+k)\sin\alpha] \tag{19}$$

where: α is the inclination angle of seed distributor window, (°);

x_0 is the distance between seed on the sidewall and the bottom line of the window of seed distributor, mm.

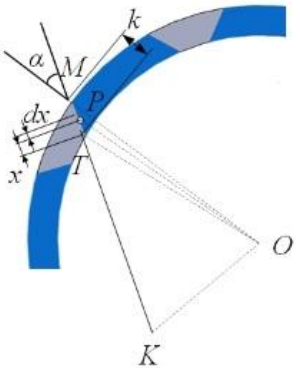

Fig. 8 - Seed movement form at the inclination window

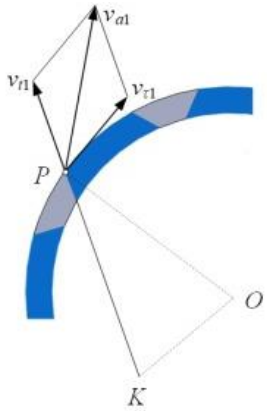

Fig. 9 - Speed diagram at the inclination window

The radial velocity v_{t1} of seed moving to the outer edge of seed distributor was obtained by Equation (20), according to the initial speed.

$$v_{t1}=\omega\sqrt{(2\sqrt{\frac{D^2}{4}-(\frac{D}{2}+k)^2\sin^2\alpha}+x_0{}^2)-2f(\frac{D}{2}+k)x_0\sin\alpha} \quad (20)$$

The sidewall of the opening window with inclined backward could increase the speed of seed under the same rotational speed, according to the analysis of Equation 20 and Fig.9.

Therefore, the shooting performance and shooting velocity were increased with an inclined backward window. The inclination angle (α) shouldn't exceed 45°, while combined with the overall size of window.

The factors that affect seed velocity out of seed distributor was the inner diameter of seed distributor (D), rotational speed of seed distributor (ω), and inclination angle of distributor window (α), which resulted from the analysis of Equation (18), (19) and (20), respectively. Thereby, the shooting performance was also influenced.

RESULTS

Simulation model

The model of seed was built with bonding particles, which because of seed shape was similar to an ellipsoid. The bulk density and 1000-seed weight were 780 kg·m^{-3} and 42.3 g, respectively. The average seed size was 5.1×2.3×2.1 mm. The soil model and seed model were established by EDEM *(Philippe Traoré et al, 2015*). The multiple seed-metering devices were conducted by SolidWorks.

The generation rate of seed particles was set as 5000 per second while the sowing rate was selected as 200 kg/ha.

The simulation parameters and characteristics (soil, steel and seed) were set as shown in Table 1 and Table 2 (*Lei Xiaolong et al, 2018*), in which the material of seed-metering device was set as steel.

Table 1

Simulation parameters

Items	Poisson's ratio	Shear modulus [Pa]	Density [kg·m^{-3}]
Wheat seed	0.4	5.1×10^7	780
Soil	0.4	1×10^6	1,350
Steel	0.3	7.8×10^{10}	7,850

Table 2

Simulation characteristics of soil and wheat seed

Items	Coefficient of static friction	Coefficient of dynamic friction	Coefficient of restitution
Seed-Soil	0.42	0.43	0.07
Seed-Seed	0.61	0.55	0.35
Soil-Soil	0.41	0.35	0.14
Seed-steel	0.40	0.40	0.10

The wheat seed selected in red mark showed the seed moved out of seed distributor as shown in Figure 10c. The shooting process was shown in Fig.10a and Fig.10b.

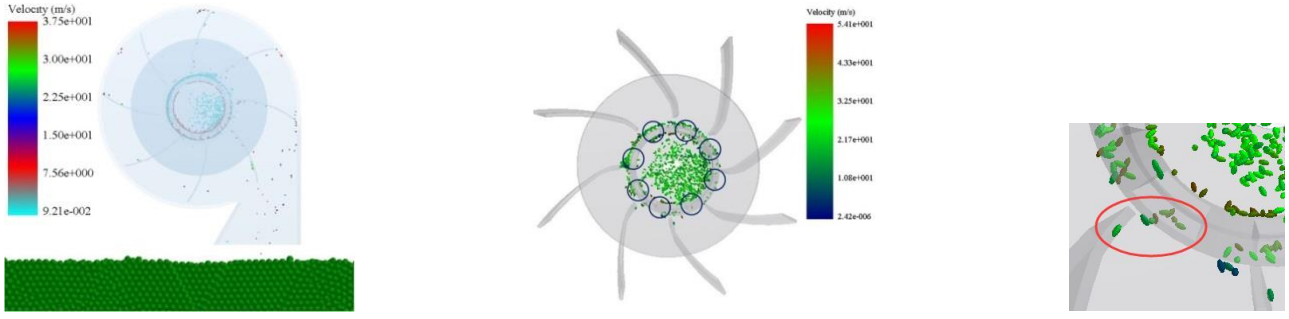

a. Simulation process *b. Velocity map* *c. Enlarged view of window*

Fig. 10 - Simulation process for seed-metering device

The seed distributor with different inclination angles (10°, 14°, 20°, 26° and 30°) was shown in Fig.11.

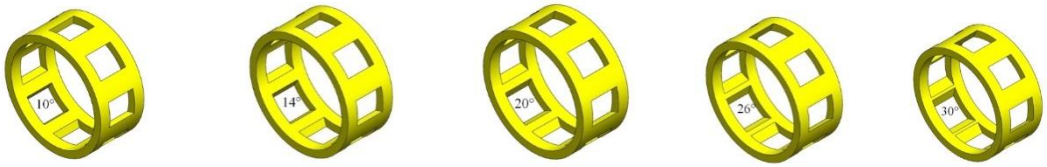

a.10° **b. 14°** **c.20°** **d. 26°** **e. 30°**

Fig. 11 - Structure of seed distributor with different inclination angles

Experiment procedure and results

Experiment plan

A Central-Composite three-factor experiment was carried out to understand the interactions and optimize the independent variables. The factors and levels are shown in Table 3.

Table 3·

Experiment factors and levels

Levels	Rotational speed of seed distributor x_1 [r·min^{-1}]	Inner diameter of seed distributor x_2 [mm]	Inclination angle of distributor window x_3 [°]
+γ	1,200	130	30
+1	1,118	126	26
0	1,000	120	20
-1	882	114	14
-γ	800	110	10

In this study, the performance of the shooting seed-metering device was evaluated in terms of uniform variation coefficient of the seeding amount (*VCSA*), average shooting depth (*ASD*) and shooting velocity (*SV*), according to GB/T 9478-2005 "Test methods of single seed drills (precision drills)" in China.

The soil bin used for sowing in the simulation experiment was divided into ten areas in length (number 1 to 10), as shown in Fig.12. The shooting depth was the vertical distance between soil surface and bottom of shooting hole by high-speed seed. Five seeds were randomly selected in each area (total 50 seed) for the calculation of *ASD*.

The calculation equation was given in Equation (21):

$$h_0 = \frac{1}{5} \times \frac{\sum_{i=1}^{50} h_i}{10} \tag{21}$$

where: h_0 is *ASD*, mm; h_i is shooting depth of seed number i (from number 1 to number 50), mm.

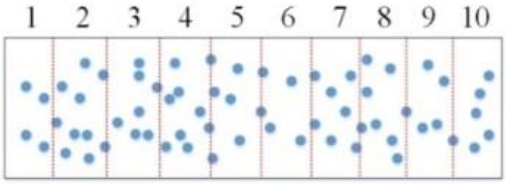

Fig. 12 - Schematic diagram of seed amount

The calculation equation for *VCSA* was given in Equation (22):

$$\lambda = \sqrt{\frac{1}{M} \sum_{i=1}^{M} (n_i - \xi)^2} \times 100\% \tag{22}$$

where:

λ is *VCSA*, %;

n_i is seeding amount in seeding area number i (width 50 mm, length 200 mm);

ξ is the average amount in five seeding areas;

M is the total number of all seeding areas, M=5.

The *SV* was captured by a post processor of EDEM. 50 seeds were randomly selected in each experiment for calculation.

The test plan and experiment data are shown in Table 4.

Table 4·

Test plan and experimental data

Test No.	Rotational speed of seed distributor x_1 [rpm]	Inner diameter of seed distributor x_2 [mm]	Inclination angle of distributor window x_3 [°]	VCSA Y_1 [%]	SV Y_2 [m·s^1]
1	882	114	14	8.6	27.7
2	1.118	114	14	10.1	38.6
3	882	126	14	6.4	26.5
4	1.118	126	14	7.1	35.3
5	882	114	26	6.2	33.5
6	1.118	114	26	8.1	39.6
7	882	126	26	5.8	30.1
8	1.118	126	26	6.8	38.2
9	800	120	20	5.4	26.3
10	1200	120	20	10.4	37.7
11	1.000	110	20	8.3	35.5
12	1.000	130	20	5.2	30.3
13	1.000	120	10	7.8	32.4
14	1.000	120	30	6.3	36.7
15	1.000	120	20	7.2	33.6
16	1.000	120	20	6.9	32.5
17	1.000	120	20	8.3	33.8
18	1.000	120	20	7.2	31.6
19	1.000	120	20	8.4	33.4
20	1.000	120	20	7.5	33.9
21	1.000	120	20	7.7	32.8
22	1.000	120	20	8.4	33.9
23	1.000	120	20	8.0	34.4

Results analysis

As showed in Table 4 and Table 5, all parameters were significantly ($p < 0.01$) related to *VCSA*. The final regression math model was given in Equation (23):

$$Y_1 = -76.847\,58 + 8.317\,90\times10^{-3}x_1 + 1.698\,70x_2 - 1.581\,26x_3 + 0.012\,374x_2x_3 - 8.730\,47\times10^{-3}x_2^2 \quad (23)$$

Table 5·

Variance analysis for *VCSA*

Variation source		Sum of squares	df	Mean square	*F* value	*P* value
	Model	32.87/31.63	9/5	3.65/6.33	9.02/16.55	0.0003***/<0.0001***
	x_1	13.36/13.36	1/1	13.36/13.36	32.99/34.95	< 0.0001***/ < 0.0001***
	x_2	10.74/10.74	1/1	10.74/10.74	26.53/28.10	0.0002***/<0.0001***
	x_3	4.48/4.48	1/1	4.48/4.48	11.06/11.72	0.0055***/<0.0032***
	x_2x_3	1.53/1.53	1/1	1.53/1.53	3.78/4.01	0.0738*/0.0616*
	x_2^2	1.52/1.51	1/1	1.52/1.51	3.76/3.96	0.0747*/0.0629*
Residual	Lack of fit	2.67/3.90	5/9	0.53/0.43	1.64/1.33	0.2541/0.3479
Total		38.13/38.13	22/22			

SV was an essential indicator for sowing performance and shooting depth of the shooting device.

As showed in Table 4 and Table 6, all parameters were significantly ($p < 0.01$) related to *SV*.

The final regression math model was given in Equation (24):

$$Y_2 = 8.790\,32 + 0.051\,24x_1 - 0.222\,22x_2 + 0.602\,43x_3 - 9.722\,72\times10^{-4}x_1x_3 + 0.015\,567x_3^2 \quad (24)$$

Table 6·

Variance analysis for the coefficient of shooing velocity

Variation source		Sum of squares	df	Mean square	F value	P value
Model		271.57/269.55	9/5	30.17/53.91	31.44/63.22	＜0.0001***/＜0.0001***
x_1		206.25/206.25	1/1	206.25/206.25	214.89/241.87	＜0.0001***/＜0.0001***
x_2		23.84/23.84	1/1	23.84/23.84	24.84/27.96	0.0002/＜0.0001***
x_3		30.8730.87	1/1	30.8730.87	32.16/36.20	＜0.0001***/＜0.0001***
x_1x_3		3.78/3.78	1/1	3.78/3.78	3.94/4.43	0.0687*/0.0504*
x_3^2		4.77/4.81	1/1	4.77/4.81	4.97/5.64	0.0441**/0.0295**
Residual	Lack of fit	6.42/8.44	5/9	1.28/0.94	1.70/1.24	0.2410/0.3866
Total		284.05/284.05	22/22			

Figure 13 shows the effect of x_2 and x_3 on *VCSA*. The value was decreased with increasing x_2 and x_3. A larger inner diameter of the seed distributor led to a greater *VCSA*. In summary, a lower indicator value occurred within the range of 16° > x_3 < 25° of x_3, and 116 > x_2 < 125 mm of x_2, respectively.

Fig.14 shows the effect of x_1 and x_3 on the shooting velocity. The value was increased with increasing x_3 and increasing x_1, respectively. A greater indicator value occurred within the range of 18° > x_3 < 25° of x_3, and 976 > x_2 < 1120 rpm of x_1, respectively.

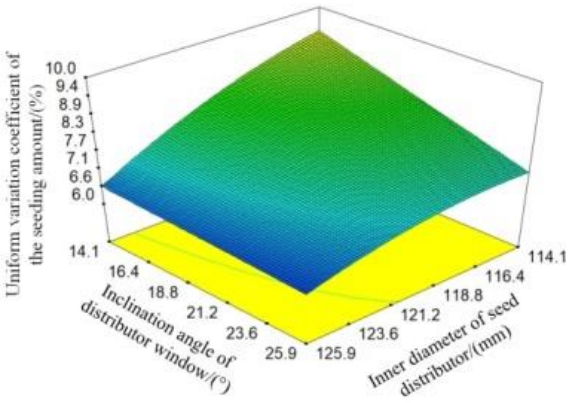

Fig. 13 - Response surface of *VCSA*

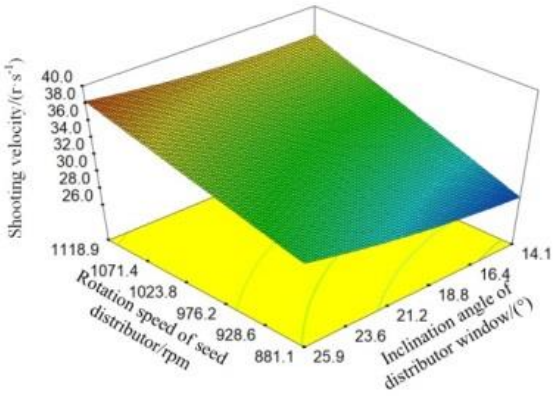

Fig. 14 - Response surface of *SV*

Design-Expert V8.0.6 was used for optimization analysis (*Păun A et al, 2018*). The optimization solution indicated that *VCSA* and shooting velocity was 7.9% and 36.8 m/s, respectively, while inner diameter, inclination angle of distributor window and rotational speed was 125 mm, 25° and 1,100 rpm, respectively.

Verified experiment

A validation experiment was conducted, in which a high-speed camera was used for calculation of *SV*. The shooting device was assembled by parts with resin material. The experiment process and photos captured by high-speed camera was shown in Figure 15 and 16.

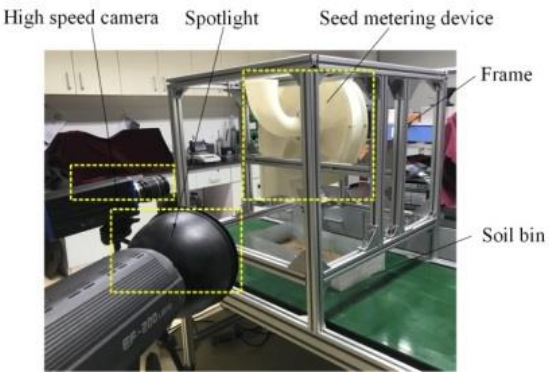

Fig. 15 - Bench experiment

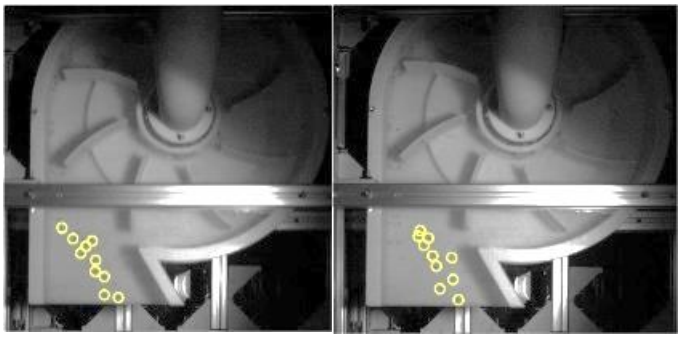

Fig. 16 - Analysis of high-speed camera picture

The experiment data under optimized parameters are shown in Fig.17.

The results show *SV*, *ASD* and *VCSA* were in the range of 32 to 36 m/s, 31 to 39 mm and 7% to 10%, respectively. Therefore, *ASD* was over 30 mm while shooting depth was over 30 m/s, which could achieve requirements for winter wheat sowing.

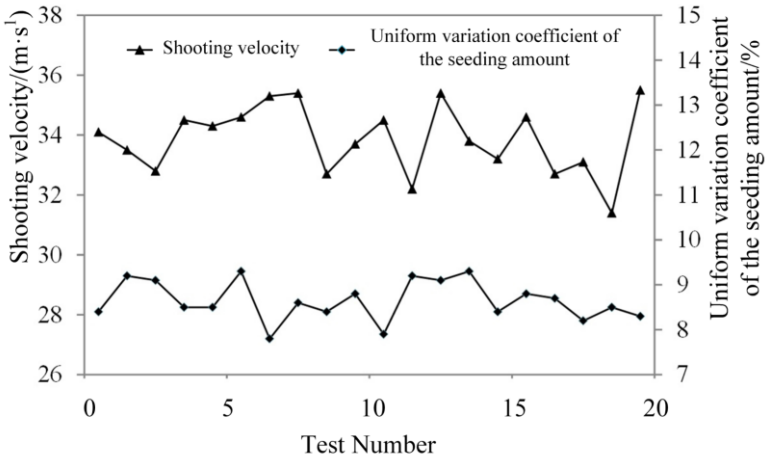

a. Shooting velocity and uniform variation of seed amount

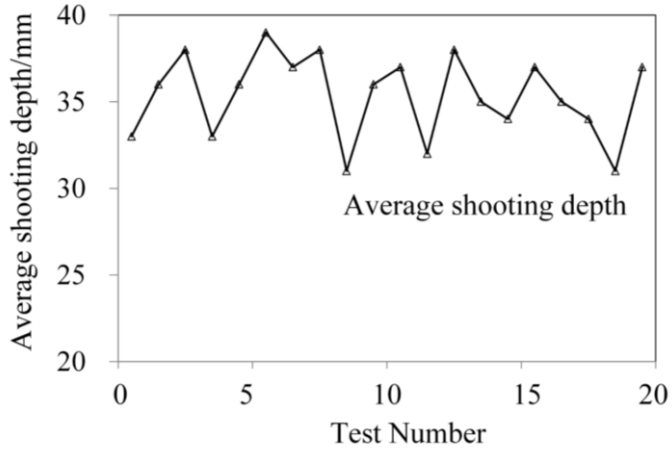

b. Average shooting depth

Fig. 17 - Results of verification experiment

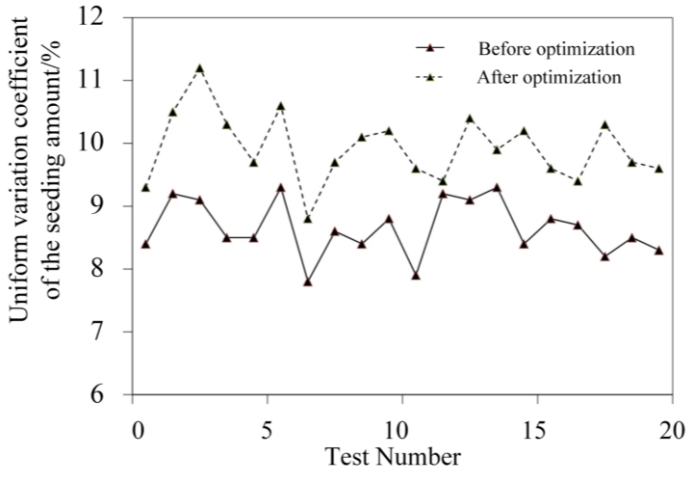

Fig. 18 - Results of the coefficient of uniform variation of seed amount before and after optimization

The results of seed metering device with two different seed distributors (before and after parameter optimized) was obtained in Fig.18. The results show *SV* and *VCSA* for the seed distributor with inclination angle was improved. Therefore, the *VCSA*, *SV* and *ASD* were 8.6%, 34.7 m/s and 32 mm, respectively. These results fully meet the sowing requirement in North China Plain.

CONCLUSIONS

1. In this study, the seed distributor of mechanical shooting seed-metering device was optimized. Theoretical analysis and two experiments were conducted to obtain the connections between factors and shooting performance. Furthermore, the operation parameters of the shooting device were optimized. The main conclusions were obtained. The speed of seed out of seed distributor and shooting performance were affected by the inner diameter of seed distributor (*D*), rotational speed of seed distributor (*ω*), and inclination angle of distributor window (*α*).

2. The shooting performance was primarily influenced by variations in the rotational speed of seed distributor x_1, inclination angle of distributor window x_2 and inclination angle of distributor window x_3.

3. The validation experiment was conducted as the inner diameter of the seed distributor, inclination angle of the distributor window, and rotational speed was 125 mm, 25° and 1,100 rpm, respectively. The results show that *VCSA*, *SV* and *ASD* were 8.6%, 34.7 m/s and 32 mm, respectively, which could meet the winter wheat planting requirements in North China Plain.

ACKNOWLEDGEMENT

This study was financially supported by the Program for China Agriculture Research System (CARS-03) and ChangJiang Scholars.

REFERENCES

[1] Ahmet Çelik, Sefa Altikat, (2016), Seeding Performances of No-Till Seeders Equipped with Different Furrow Openers, Covering Components and Forward Speeds for Winter Wheat, *Journal of Agricultural Science*, Vol.18, Issue 3, pp. 226-238, Istanbul / Turkey.

[2] Bassu S., Asseng S., Motzo R. et al, (2009), Optimising sowing date of durum wheat in a variable Mediterranean environment. *Field Crops Research*, Vol.111, Issue 1-2, pp. 109-118, Paris/France.

[3] Cui Qingliang, Qiu Zurong, He Junlin et al, (2001), Study on the pneumatic non-tillage precision seeder (2BQYF-6A), *Transactions of the CSAM*, Vol.32, Issue 4, pp. 31-33, Taiyuan / China.

[4] Jiang Qinghe, Zhao Pengcheng, (2001), Motion Study on Shots Passing through Windows on Shot Blasting impellers, *Trans IMF*, Vol.79, Issue 4, pp. 151-153, Jinan / China.

[5] Lei Xiaolong, Liao Yitao, Cong Jinling et al, (2018), Parameter optimization and experiment of air-assisted centralized seed-metering device of direct seeding machine for rape and wheat, *Transactions of the CSAE*, Vol.34, Issue 12, pp. 16-26, Wuhan / China.

[6] Li Chaosu, Tang Yonglu, Wu Chun et al, (2012), Effect of sowing patterns on growth, development and yield formation of wheat in rice stubble land, *Transactions of the CSAE*, Vol.28, Issue 18, pp. 36-43, Chengdu / China.

[7] Matin M.A., Fielke J.M., Desbiolle J.M.A., (2014), 2 Furrow parameters in rotary strip-tillage: Effect of blade geometry and rotary speed, *Biosystems Engineering*, Vol.118, Issue 1, pp. 7–15, Adelaide / Australia.

[8] Olaf E., Umar F., Malik R. K. et al, (2008), On-farm impacts of zero tillage wheat in south Asia's rice-wheat systems, *Field Crops Research*, Vol.105, Issue 3, pp. 240-252, New Delhi / India.

[9] Păun A., Stroescu Gh., Vişan A.L. et al, (2018), Researches regarding the optimization of impurities removal technology from the cereal and industrial plant seeds for establishing ecological crops, *INMATEH Agricultural Engineering*, Vol.56, Issue 3, pp. 83-90, Bucharest / Romania.

[10] Traoré Philippe, Laurentie Jean-Charles, Dascalescu Lucian, (2015), An efficient 4 way coupling CFD–DEM model for dense gas–solid particulate flows simulations, *Computers and Fluids*, Vol.113, Issue 31, pp. 65-76.

[11] Wang Chao, Li Hongwen, He Jin et al, (2019), Effect of incident angle on wheat soil-ripping parameters by pneumatic seeding, *Transactions of the CSAE*, Vol.35, Issue 16, pp. 32-39, Beijing/China.

[12] Wang Chao, Lu Caiyun, Li Hongwen et al, (2020), Preliminary bench experiment study on working parameters of pneumatic seeding mechanism for wheat in rice-wheat rotation areas, *Int J Agric & Biol Eng*, Vol.13, Issue 1, pp. 66–72, Beijing / China.

[13] Zhang Boping, (1982), Design principles of planting machines, *Machinery Industry Press,* 389-403, Beijing/China.

[14] Zeng Hui, (1990), Calculation of the diameter of the blasting wheel, *China Foundry Machinery & Technology*, Vol.146, Issue 2, pp.40-44, Jinan/China.

DEM SIMULATION AND EVALUATION OF WELL CELLAR MAKING PERFORMANCE OF OPENER WITH LARGE SOCKET

/

大窝套小孔成穴器对井窖成穴性能的离散元仿真和评价

Xie Q.J., Liu F.Y., Yang M.J., Liu J., Yang S.H., Xie S.Y.*) [1]

Southwest University, College of Engineering and Technology, Chongqing Key Laboratory of Agricultural Equipment for Hilly and Mountainous Regions / P. R. China

**Correspondence: Tel: +86-13509417936; E-mail: xsyswu@163.com*

DOI: https://doi.org/10.35633/inmateh-63-04

Keywords: *opener with large socket, discrete element method, well cellar making, simulation, optimization*

ABSTRACT

Well cellar seedling transplanting can effectively avoid series of problems such as long recovery time and poor uniformity of seedlings caused by the server climate conditions outside. Well cellar making is quite difficult in the upland with low moisture content. An opener with large socket was newly designed for the well cellar making. The well cellar making process was simulated by means of discrete element method (DEM), and its verification was qualified by soil bin test, with a relative error 7.46%. Taking arc radius of the opener socket, rotation speed and penetration speed as control factors, and collapse rate of the cellar hole as evaluation index, the influence of control factors on the collapse rate and their significance were obtained by Box-Behnken Design (BBD) test and analysis of variance (ANOVA). A quadratic regression equation of collapse rate with control factors was established, and the optimal parameters of the control factors were obtained as arc radius 128 mm, rotation speed 380 r/min and penetration speed 0.15 m/s, with the minimum collapse rate 22.70%. The collapse rate of the newly designed well cellar opener decreased much compared to the traditional one.

摘要

井窖式移栽可有效避免气候条件引起的还苗期长、秧苗均匀性差等一系列问题，为改善土壤墒情较差时井窖成穴难的现状，本文提出了一种大窝套小孔成穴器。采用离散元法对井窖制作过程进行数值模拟并通过土槽试验验证，相对误差为7.46%。以成穴器的圆弧半径、转速和入土速度为试验因素，以孔穴垮塌率为评价指标，通过 Box-Behnken 试验和方差分析得出各因素对孔穴塌陷率的影响及其显著性。建立各因素与孔穴垮塌率的二次回归模型，得到的最优参数为圆弧半径128 mm、转速380 r/min、入土速度0.15 m/s，最小垮塌率为22.70%。与传统的井窖式成穴器相比，其垮塌率明显降低。

INTRODUCTION

Transplanting, as a crucial link of tobacco planting, has a great influence on the survival of tobacco seedlings and the final yield of tobacco leaves (*Zhang, P. C. et al, 2007*). Planting depth of tobacco seedlings can directly affect nutrient-taking during the whole growth process. Studies have shown that the well cellar transplanting can avoid a series of problems such as weak seedlings in the best transplanting period, long recovery time and poor uniformity of seedlings due to the severe climate conditions outside (*Jia, R.L. et al, 2013; Luo, H. B. et al, 2012*). At present, the well cellar making machine is mainly of the backpack type, the opener is composed of a cylinder and a cone, and local structures were added to improve the efficiency (*Yu, L. H. et al, 2018*). As the soil is loose and porous, it will be compressed and move along the axial direction and radial direction during the well cellar making process. Soil type, soil moisture content, structure and working parameters of the opener are the key factors affecting the quality of well cellar (*Yu, L. H. et al, 2018*). Loose soil is not conducive to forming for the traditional well cellar opener with low soil moisture (the moisture content is less than 11%) (*Liu, G. H. et al, 2018*), which is an urgent problem to be solved.

Accurate descriptions of soil-tool interaction would be a major step forward in agricultural machinery design, which can effectively reduce the design cycle and manufacturing cost. As the soil is granular and discontinuous, deformation and breakage will occur when it contacts with the tools (*Shmulevich. I., 2010*). Discrete element method (DEM) allows granular materials to be treated as a collection of particles with certain shape and mass (*Hu, G. M., 2010*), and it is widely used to simulate soil-tool interaction.

[1] *Xie QJ, Ms.; FY Liu, Dr.; MJ Yang, Prof.; J Liu, Dr.; SH Yang, Ms.; SY Xie, Prof.*

Han C. J. et al (2019) applied DEM to simulate the hole-forming process of the opener of watermelon seedling transplanter. Then, the effects of the small-end diameter and the theoretical working depth on the hole-forming effect were discussed. *Ji Y.J. et al (2014)* used DEM to study the effect of the inclination angle of the opener on hole size and said that the working speed and soil moisture content will affect the hole-forming effect.

In this study, an opener with large socket was proposed based on the requirement of well cellar making for tobacco seedlings. A soil model was established within EDEM to explore the optimal parameters of the opener, the micro-behaviour of the soil, and the quantitative evaluation of performance of well cellar making. The aim was to reduce the design cycle of the machine and provide technical support for the improvement of the transplanters.

MATERIALS AND METHODS

Opener design and test platform

Design of opener with large socket

To improve the performance of well cellar making with low soil moisture content, an opener with large socket was proposed, as shown in Fig. 1a. Compared with the traditional well cellar opener (Fig. 1b), a large socket was formed in the loose soil layer and a small hole was formed in the compacted soil layer in view of the differences in compactness and moisture content at different soil layers. The large socket functioned as wind prevention and heat preservation, rain collection and drought resistance, as well as watering and fertilization.

To help the tool penetration and ensure the uprightness of the seedlings, the bottom and the middle were designed to be conical, the diameter D_1 was 40 mm, and the height H_1 was 30 mm. Considering that the best well cellar specification for seedlings was circular with a diameter of 80-90 mm (*Luo, H. B. et al, 2012*), the diameter D_2 was 80 mm, and the height H_2 was 120 mm. Combined with agricultural requirements (*Chen, W. et al, 2015*), the height H_3 was 100 mm and the curve was an arc. A coordinate system was established with the centre of the circle as the origin. For any point A (x, y) on the arc, $x^2 + y^2 = R^2$ was satisfied. Then, the relationship between θ and R is expressed as:

$$\theta = \arctan\frac{x}{\sqrt{R^2 - x^2}}, \text{ [deg]} \quad (1)$$

Where:

θ is the angle of soil particle along tangent direction of the wall of the cellar hole, [degree].

According to the theoretical analysis, the smaller θ was, the smaller the tangent force was, and the less likely the particle slipped downward.

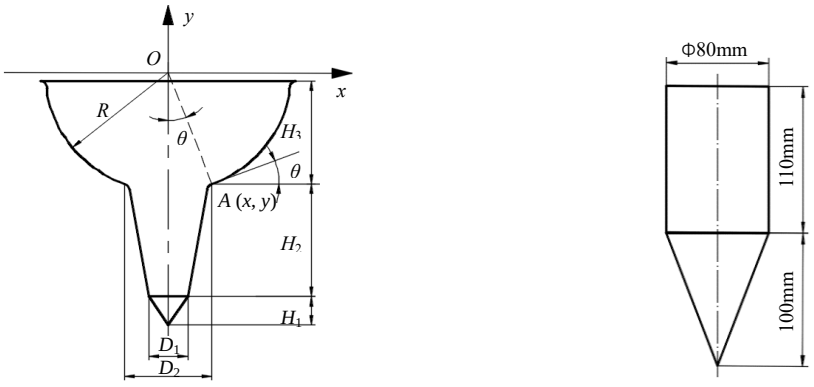

(a) Opener with a large socket (b) Traditional well cellar opener

Fig. 1 - Structure diagram

Test platform

In order to verify the working performance of the opener and the accuracy of the simulation, a test platform was designed, as shown in Fig. 2a. The test platform was mainly composed of lifting mechanism, power transmission mechanism, an opener with a large socket, soil bin, and rack, etc. The rotation speed and penetration speed of the opener can be adjusted to the specified values through speed control module. The basic dimensions of the soil bin were sides 600 mm and height 320 mm.

To ensure that the soil conditions in the soil bin were consistent with the field soil, a layered method was used to prepare soil (*Hang, C. G. et al, 2017*). As a result, the average moisture content of 0-120 mm (upper soil) and that of 120-320 mm (lower soil) soil layers were 7.6% and 12.8%, respectively.

The well cellar making performance has a significant effect on the growth of tobacco seedlings. For the well cellar made by the opener with large socket, large hole formed by the large socket was convenient for wind protection and water fertilization, the small hole of the lower part was used for seedling transplanting. In view of this effect, after the experiment was completed, the effective depth of the cellar hole was measured, which was the depth that was used for transplanting after soil particle slip, as shown in Fig. 2b, the collapse rate of cellar hole can be expressed as:

$$S = \frac{H - h}{H} \times 100\% \text{ , [\%]} \quad (2)$$

where:

S is the collapse rate, [%]; *H* is the theoretical transplanting depth (150 mm, i.e. H_1+H_2), [mm];

h is the effective transplanting depth, [mm].

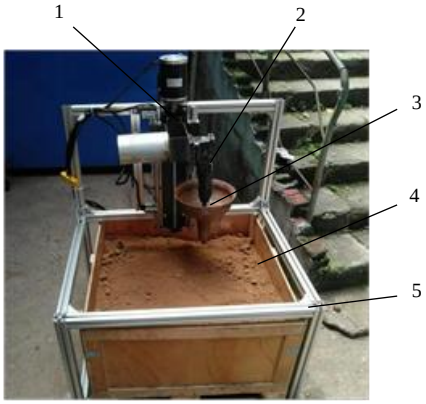

(a) Test platform

(b) Effective transplanting depth measurement

Fig. 2 - Soil bin test

1- lifting mechanism; 2 - power transmission mechanism; 3 - opener; 4 - soil bin; 5 - rack

Discrete element modeling

Properties of the materials

Establishing a correct model is an essential precondition for the accuracy of simulation results. It requires the use of contact models that can represent the characteristics of the materials as reliably as possible. Due to the deformation and the intermolecular forces between particles, Hertz-Mindlin (no slip) was defined as contact model between soil and machine, and Hertz-Mindlin with Johnson-Kendall-Roberts was defined as contact model between soil particles. The later contact model considers the cohesion between particles on the basis of Hertz contact theory. Even if particles are not in direct contact, there is attractive cohesion under this model, and the maximum cohesion of particles can be described as (*Johnson, K. L. et al,1971*):

$$F_{max} = -\frac{3}{2}\pi\gamma R^*, \text{ [N]} \quad (3)$$

where:

$F_{\max}$ is the maximum cohesion of particles, [N]; γ is the surface energy, [J/m^2];

R^* is the equivalent radius, [m].

Because moisture content differs at different soil layers, the cohesive strength between the soil particles and the ability to resist the movement of the soil particles are also different. Taking the soil of Weining tobacco area in Guizhou Province as the research object, in order to balance the calculation speed and simulation accuracy, sphere with particle radius of 2 mm was used to simulate soil particles in this study. The parameters involved in the simulation were shown in Table 1, which were mainly divided into the intrinsic parameters and the contact parameters. On the macroscopic scale, the repose angle of the material can reflect the flow and friction characteristics of the granular material, then coefficient of static friction, coefficient of rolling friction and surface energy of soil particles were calibrated by the repose angle test.

In this study, the lifting method (*Shi, L. R. et al, 2017*) was used to measure the repose angle. The soil was filled with a cylinder with diameter of 40 mm and height of 120 mm, then the cylinder was lifted at a speed of 0.02 m/s to form a cone-like pile on the plane. The simulation was carried out according to the physical test and the parameters was continually adjusted until the repose angle obtained by simulation was in accordance with the measured value. Then parameters of friction and surface energy of the soil particles were calibrated.

Table 1

Simulation parameters

Item	Top soil	Sub soil	Steel	Topsoil-topsoil	Topsoil-steel	Subsoil-subsoil	Subsoil-steel	Data source
Intrinsic parameters								
Density [kg/m^3]	1720	1870	7850	-	-	-	-	Measurement
Shear modulus [MPa]	10^6	10^6	7.9×10^{10}	-	-	-	-	*Fang, H. M. et al, 2016* *Yuan, Q. C. et al, 2018*
Poisson's ratio	0.38	0.38	0.3	-	-	-	-	
Contact parameters								
Coefficient of restitution	-	-	-	0.6	0.6	0.6	0.6	*Ucgul, M. et al, 2015*
Coefficient of static friction	-	-	-	0.45(1)	0.5(1)	0.6(2)	0.6(2)	(1) Calibration (2) *Fang, H. M. et al, 2016*
Coefficient of rolling friction	-	-	-	0.2(1)	0.31(1)	0.05(2)	0.05(2)	
Surface energy [J/m^2]	-	-	-	0.42	-	1.36	-	Calibration

Working model of an opener with large socket

Based on the soil contact model and parameters, a virtual soil bin of sides 600 mm and height 320 mm was built, in which the subsoil depth was 200 mm and the topsoil depth was 120 mm. To ensure the consistency of simulation and reality, soil particles were generated randomly and the sizes followed a normal distribution. The 3D model of an opener with large socket was established in Creo 3.0 and imported into EDEM. The simulation model was shown in Fig. 3. The opener moves down at a certain speed while rotating. In all simulations, the time step was 20% of Rayleigh time, and the grid cell size was $4R_{min}$, where R_{min} is the value of the minimum particle radius in the simulation.

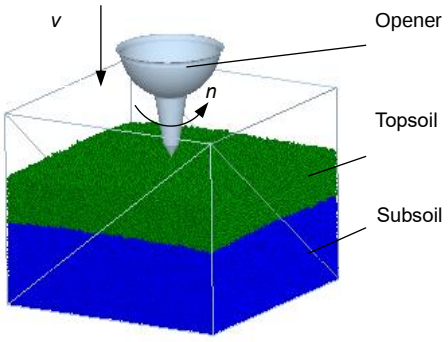

Fig. 3 - Virtual soil bin and geometric model of opener

Response surface optimization

The effects of main control factors on the performance of well cellar making were the opener's structure parameters and working parameters. Taking the arc radius (X_1), rotation speed (X_2) and penetration speed (X_3) as control factors and the collapse rate as the evaluation index, levels of control factors were determined according to Box-Behnken design (BBD), as shown in Table 2. And the detailed simulation experiment arrangement was shown in Table 3, with a total of 17 treatments, including 5 centre point repeated treatments. At last, a multiple quadratic regression equation was used to establish the functional relationship between control factors and the collapse rate.

Table 2

Control factors and levels

Level	Control factors		
	X_1 [mm]	X_2 [r/min]	X_3 [m/s]
-1	100	200	0.1
0	114	350	0.15
1	128	500	0.2

Table 3

Experiment arrangement of BBD and results

Treatment	Level of control factors			collapse rate (%)
	X_1	X_2	X_3	
1	-1	-1	0	24.5
2	1	-1	0	34.8
3	-1	1	0	23.5
4	1	1	0	33.3
5	-1	0	-1	26.6
6	1	0	-1	36.2
7	-1	0	1	25.0
8	1	0	1	36.0
9	0	-1	-1	32.5
10	0	1	-1	31.7
11	0	-1	1	35.0
12	0	1	1	29.0
13	0	0	0	25.3
14	0	0	0	25.4
15	0	0	0	26.0
16	0	0	0	25.8
17	0	0	0	24.8

RESULTS

Soil model validation by repose angle test

The test results of topsoil and subsoil were shown in Fig. 4. Repose angles of the physical test and the simulation were measured in image process software of ImageJ. It could be seen that their outlines of repose angles were extremely similar, with relative errors of 1.17% and 1.38%, respectively. It indicated that the parameters of the soil model were accurate and reliable, which can be used for the optimization in this study. The parameter calibration results were shown in Table 1.

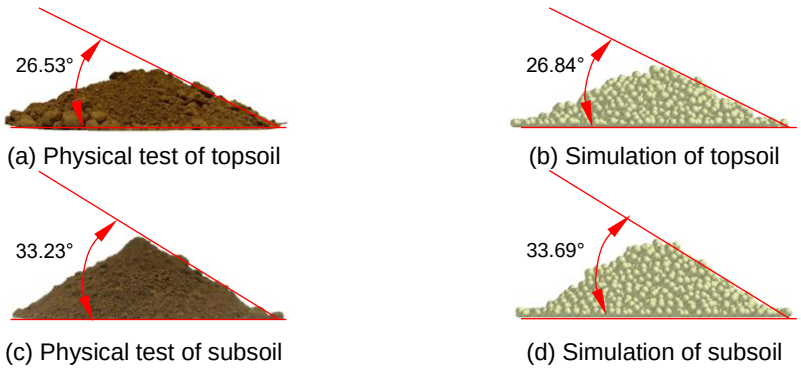

(a) Physical test of topsoil (b) Simulation of topsoil

(c) Physical test of subsoil (d) Simulation of subsoil

Fig. 4 - Repose angle

Statistics analysis

Regression model and analysis of variance

BBD experiment results of the collapse rate were obtained, as shown in Table 3. The regression analysis was applied to the experiment results with Design-Expert 8.0 and the regression equation, with a coefficient of determination R^2 0.9897, was obtained as:

$$S = 25.46 + 5.09X_1 - 1.16X_2 - 0.25X_3 - 0.13X_1X_2 + 0.35X_1X_3 - 1.30X_2X_3 + 1.23X_1^2 + 2.33X_2^2 + 4.26X_3^2 \quad (4)$$

The analysis of variance (ANOVA) result of quadratic polynomial model was shown in Table 4. According to ANOVA, arc radius of the opener (X_1) had the highest significant level of impact on the collapse rate of the cellar hole, and it was followed by rotation speed (X_2) and penetration speed (X_3), sequentially. Meanwhile, the interaction between X_2 and X_3 had an impact on the collapse rate1% probability level by F test of ANOVA. The P value of the regression model was less than 0.0001 and P value of the lack of fit was more than 0.05, showing that the regression model agreed with the experiment results.

Table 4

ANOVA of quadratic polynomial model

Source of variation	Quadratic sum	Degree of freedom	Mean square	F value	P value	Significance
Model	340.43	9	37.83	74.91	<0.0001	**
X_1	207.06	1	207.06	410.08	<0.0001	**
X_2	10.81	1	10.81	21.41	0.0024	**
X_3	0.50	1	0.50	0.99	0.3528	ns
X_1X_2	0.063	1	0.063	0.12	0.7353	ns
X_2X_3	6.76	1	6.76	13.39	0.0081	**
X_1X_3	0.49	1	0.49	0.97	0.3574	ns
X_1^2	6.40	1	6.40	12.67	0.0092	**
X_2^2	22.91	1	22.91	45.37	0.0003	**
X_3^2	76.32	1	6.32	151.15	<0.0001	**
Residual	3.53	7	0.50	-	-	
Lack of fit	2.66	3	0.89	4.07	0.1043	ns
Pure error	0.87	4	0.22	-	-	
Sum	343.96	16	-	-	-	

Notes: Significance:

*** means significant at 1% probability level by F test, ns means non-significant at 5% probability level.*

Parameter optimization

The response surface of collapse rate of the cellar hole as function of rotation speed (X_2) and penetration speed (X_3) was shown in Fig. 5. Control factor of X_2 was significant at 0.24% probability level by F test, and their interaction was at 0.1% probability level. As seen from response surface, with the increase of X_2 and X_3, the collapse rate decreased at first and then increased. While X_3 was close to 0.15 m/s, the collapse rate reached the minimum value. Control factor of arc radius (X_1) was significant at 0.1% probability level, and the collapse rate decreased while increasing X_1. Therefore, for the purpose of reducing the collapse rate, the optimized parameters were determined as: arc radius 128 mm, rotation speed 380 r/min and penetration speed 0.15 m/s. And the theoretical collapse rate of the cellar hole was 21.45% according to the regression equation.

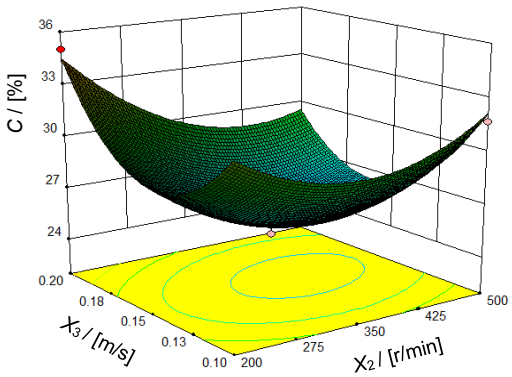

Fig. 5 - Response surface of collapse rate of the cellar hole as function of X_2 and X_3

Comparative analysis

To verify the correctness of the optimization results and the advantages of the optimized opener, simulation test was carried out based on the optimized parameters, compared with that of the traditional well cellar opener.

Well cellar making process

(1) Penetration process

The force and velocity distributions of the soil in penetration process were shown in Fig. 5. As seen from Figs. 5a and 5b, when the optimized well cellar opener was just entering the soil (0.2 s), the tip exerted constant shear and compression on the soil, which made the soil particles in contact with the tool move sideways. As the opener moved downward, the disturbance of soil increased. When the arc was in contact with the soil (0.9 s), the soil moved along the normal direction of the arc under the compression, and the force was mainly concentrated on the tip of the opener. When the opener penetrated completely into the soil (1.6 s), the arc, especially the lower part, compressed the surrounding soil obviously. The particles of equal velocity were mainly distributed along the arc of the opener, and the particles closer to the arc had a higher velocity. Meanwhile, some particles moved along the tangential direction of the arc to the ground to form an uplift. In contrast, as shown in Figs. 5c and 5d, the force and velocity of soil particles were distributed along the conical wall during the operation of the traditional well cellar making, and the cylindrical wall basically did not exert longitudinal compression on the surrounding soil.

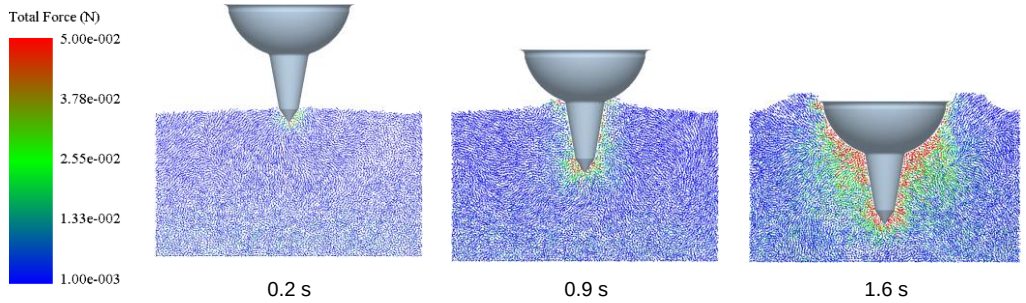

(a) Soil force distribution of the optimized well cellar opener

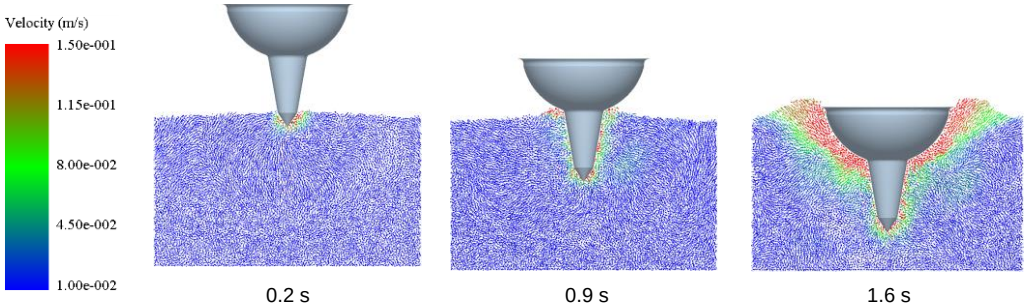

(b) Soil velocity distribution of the optimized well cellar opener

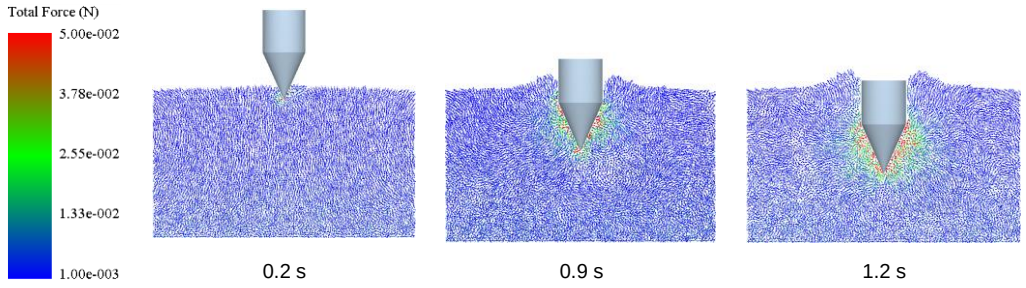

(c) Soil force distribution of the traditional well cellar opener

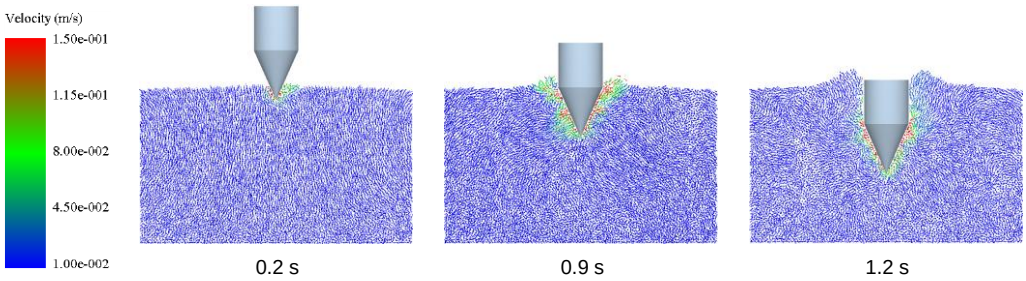

(d) Soil velocity distribution of the traditional well cellar opener

Fig. 5 –Soil force and velocity distribution at different time in penetration process

(2) Retraction process

The soil velocity distribution during retraction process were shown in Fig. 6. The soil velocity of the cellar hole formed by the optimized well cellar opener was lower than the traditional one and the particles moved along the tangential direction of the wall. While the soil velocity of the cellar hole formed by the traditional well cellar opener, especially that close to ground, was quite higher, and the particle moved toward the centre of the cellar hole, which was due to the fact that there was no longitudinal compression on the topsoil when the traditional well cellar opener was introduced into the soil. Under the action of gravity, the force chain between particles was more likely to be destroyed, thus it caused the soil to slip downward with a higher speed.

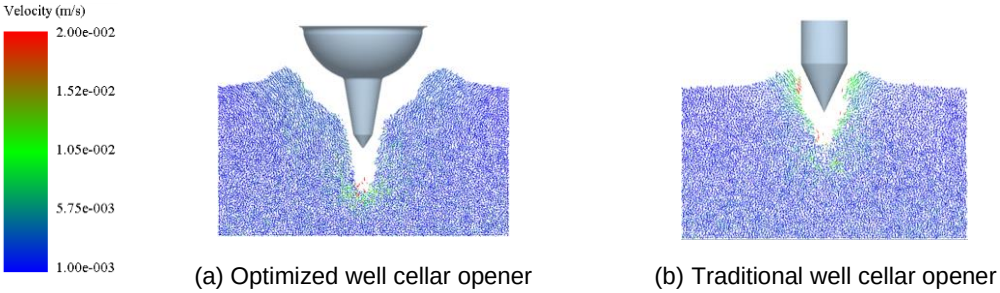

(a) Optimized well cellar opener (b) Traditional well cellar opener

Fig. 6 - Soil velocity distribution in retraction process

Quality of well cellar making

When the well cellar openers were completely removed from soil, part of the soil slipped downward to fill the cellar holes under action of gravity, as shown in Fig. 7. The red curve was the slide track of soil particles. The quality of the optimized well cellar opener was better and the upper layer of soil basically did not slide, with the collapse rate of 22.70%, while the cellar hole formed by the traditional well cellar opener was almost filled with the topsoil, and the collapse rate was as high as 63.20%. It is to be mentioned that compared with the theoretical value, the error of the simulation value of the optimized well cellar opener was 5.83%, indicating that the regression equation was correct.

(a) Optimized well cellar opener (b) Traditional well cellar opener

Fig. 7 - Quality of well cellar making

Soil bin test verification

The optimized well cellar opener was obtained and the soil bin test was carried out on the test platform. The experiment was repeated for 5 times, and the average value was taken as the reference value of collapse rate. The results showed that the average effective transplant depth of the holes was 113.2 mm, collapse rate was 24.53%, standard deviation was 0.79 mm, and the relative error between the soil bin test and simulation test was 7.46%. The errors were mainly due to the complex soil conditions, the influence of soil bin boundary and the vibration of the mechanical structure. The results of the soil bin test and the simulation test had good consistence.

CONCLUSIONS

In this study, a well cellar opener with a large socket was proposed. Well cellar making simulation and parameter optimization of the opener with a large socket were conducted. Main conclusions were drawn as follows:

- DEM is an effective way to animate interaction between the opener and the soil, and as a result, soil particle disturbance and quantitative evaluation of well cellar making can be obtained. The correctness of the simulation model was verified by repose angle and soil bin test.

- By statistical analysis of BBD test results, arc radius of the opener had the highest significant level of impact on the collapse rate of the cellar hole, and it was followed by rotation speed and penetration speed, sequentially. The optimized parameters of the opener were arc radius 128 mm, rotation speed 380 r/min, penetration speed 0.15 m/s.

- Compared with the traditional well cellar opener, the arc of the optimized well cellar opener had a remarkable compaction effect on the soil, and performance of well cellar making was improved significantly. The collapse rate had been greatly reduced from 63.20% to 22.70%.

ACKNOWLEDGEMENTS

The study was funded by the intelligent agricultural equipment project, national key technologies R&D program in the 13th Five-year plan period (NO. 2017YFD0701100) and Fundamental Research Funds for Central Universities, P. R. China (No. XDJK2018AC001).

REFERENCES

[1] Chen, W., Pan, W.J., Li, H.X., Lin, Y. C., Chen, Y. (2015). *Deep planting with shallow-socket method and tool for tobacco (烤烟浅窝套小孔深栽方法及掏窝打孔一体化工具).* Patent. CN201510482723.4. P.R.C.;

[2] Fang, H. M., Ji, C. Y., Tagar, A. A., Zhang, Q. Y., Guo, J. (2016). Simulation analysis of straw movement straw-soil-rotary blade system (秸秆-土壤-旋耕刀系统中秸秆位移仿真分析). *Transactions of the Chinese Society for Agricultural Machinery*, Vol.47, Issue 1, pp.60-67, Ed. Chinese Society of Agricultural Engineering, Beijing/P.R.C.; http://doi.org/10.6041/j.issn.1000-1298.2016.01.009;

[3] Han, C. J., Xu, Y., Zhang, J., You, J., Guo, H. (2019). Design and experiment of semi-automatic transplanter for watermelon seedlings raised on compression substrate (半自动压缩基质型西瓜钵苗移栽机设计与试验). *Transactions of the Chinese Society of Agricultural Engineering*, Vol.35, Issue 11, pp.48-56, Ed. Chinese Society of Agricultural Engineering, Beijing/P.R.C.; http://doi.org/10.11975/j.issn.1002-6819.2018.13.00;

[4] Hang, C. G., Huang, Y. X., Zhu, R. X. (2017). Analysis of the movement behaviour of soil between subsoilers based on the discrete element method. *Journal of Terramechanics*, Vol.74, Issue 12, pp.35-43, Ed. Elsevier Sci Ltd, Oxford/England; http://doi.org/10.1016/j.jterra.2017.10.002;

[5] Hu, G. M. (2010). *Analysis and simulation of particle system by discrete element method (颗粒系统的离散元素法分析仿真).* Wuhan University of Technology Press, Wuhan/P.R.C.;

[6] Ji, Y.J., Yu, M., Li, H C. (2014). Simulation analysis of cavitation performance for spade soil opener based on discrete element method (铲式成穴器成穴性能的离散元法仿真). *Journal of Jiangsu University (Nature Science Edition)*, Vol.35, Issue 1, pp.40-43, Ed. Jiangsu University, Zhengjiang/P.R.C.; http://doi.org/10.3969/j.issn.1671-7775.2014.01.008;

[7] Jia, R. L., Sun, C. Y., Wang, J. M., Wei, D. F., Pei, J. (2013). Effects of Different Transplanting Methods on Growth of Flue-cured Tobacco in Field (不同移栽方式对烤烟田间长势的影响). *Modern Agricultural Science and Technology*, Issue 23, Ed. Anhui Academy of Agricultural Sciences, Hefei/P.R.C.; http://doi.org/10.3969/j.issn.1007-5739.2013.23.004;

[8] Johnson, K. L., Kendall, K., Roberts, A. D. (1971). Surface energy and the contact of elastic solids. *Proceedings of the Royal Society of London*, Vol.324, Issue 1558, pp.301-313, Ed. The Royal Society, London/England; https://doi.org/10.1098/rspa.1971.0141;

[9] Luo, H. B., Long, P. Z., Ma, J., Tian, J. S., Ai, Y. F. (2012). Research and application of tobacco plantlet transplanting in well cellar (烤烟井窖式小苗移栽技术研究与应用). *Guizhou Agricultural Sciences*, Vol.40, Issue 8, pp.101-107, Ed. Guizhou Academy of Agricultural Sciences, Guiyang/P.R.C.; http://doi.org/10.3969/j.issn.1001-3601.2012.08.030;

[10] Liu, G. H., (2018). *Analysis and test of hole-forming effect in dry and wet soil environment (干湿两种土壤环境成穴性分析及试验*). Master dissertation, Guizhou University, Guizhou/P.R.C.;

[11] Shi, L. R., Zhao, W. Y., Sun, W. (2017). Parameter calibration of soil particles contact model of farmland soil in northwest arid region based on discrete element method *(*基于离散元的西北旱区农田土壤颗粒接触模型和参数标定). *Transactions of the Chinese Society of Agricultural Engineering*, Vol.33, Issue 21, pp.181-187, Ed. Chinese Society of Agricultural Engineering, Beijing/P.R.C. http://doi.org/10.11975/j.issn.1002-6819.2017.21.021;

[12] Shmulevich, I. (2010). State of the art modeling of soil-tillage interaction using discrete element method. *Soil and Tillage Research*, Vol.111, Issue 1, pp.41-53, Ed. Elsevier Sci Ltd, Oxford/England; http://doi.org/10.1016/j.still.2010.08.003;

[13] Ucgul, M., Fielke, J. M., Saunders, C. (2015). Three dimensional discrete element modeling DEM of tillage accounting for soil cohesion and adhesion, *Biosystems Engineering,* Vol.34, Issue 18, pp. 298-306, Ed. Academic Press Inc., London/England; http://doi.org/10.1016/j.biosystemseng.2014.11.006;

[14] Yu, L. H., Liu, G. H., Zhang, F. G., Wu, X. M., Hu, C. S. (2018). Test and analysis for performance on the knapsack well cellar making machine for seedling transplanting (背负式幼苗移栽井窖制作机性能测试分析). *Journal of Agricultural Mechanization Research*, Vol.35, Issue 1, pp.40-43, Ed. Heilongjiang Society of Agricultural Machinery, Harbin/P.R.C.; http://doi.org/10.3969/j.issn.1003-188X.2018.03.028;

[15] Yuan, Q. C., Xu, L. M., Xing, J. J., Duan, Z. Z., Ma, S. (2018). Parameter calibration of discrete element model of organic fertilizer particles for mechanical fertilization (机施有机肥散体颗粒离散元模型参数标定). *Transactions of the Chinese Society of Agricultural Engineering*, Vol.34, Issue 18, pp.21-27, Ed. Chinese Society of Agricultural Engineering, Beijing/P.R.C. http://doi.org/10.11975/j.issn.1002-6819.2018.18.003;

[16] Zhang, P. C., Lu, Y. G., Yuan, H. W., Zhang, Z. Z., Cui, B. W. (2007). Effect of different methods of transplanting on the growth condition in field and the yield and quality of flue- cured tobacco (不同移栽方式对烤烟田间长势和产质影响的研究). *Journal of Anhui Agricultural Sciences*, Vol.35, Issue 35, pp.11491, 11516, Ed. Anhui Academy of Agricultural Sciences, Hefei / P.R.C.; http://doi.org/10.3969/j.issn.0517-6611.2007.35.072.

INVESTIGATION OF SUBSTRATE MIXING PROCESS IN ROTATING DRUM REACTOR
/
ДОСЛІДЖЕННЯ ПРОЦЕСУ ЗМІШУВАННЯ КОМПОНЕНТІВ СУБСТРАТУ В ОБЕРТОВОМУ РЕАКТОРІ БАРАБАННОГО ТИПУ

Golub Gennadii[1)], Tsyvenkova Nataliya[1,2)], Holubenko Anna[2)], Chuba Vyacheslav[1)], Tereshchuk Marina[2)]
[1)] National University of Life and Environmental Sciences of Ukraine / Ukraine;
[2)] Zhytomyr National Agroecological University / Ukraine
Tel: +380503138903; E-mail: nataliyatsyvenkova@gmail.com
DOI: https://doi.org/10.356.33/inmateh-63-05

Keywords: *fermentation, reactor, substrate, composting process, drum blades, mixing process*

ABSTRACT
The results of the research on the influence of the drum type reactor design-technological parameters and the substrate`s physical-chemical parameters on the substrate`s components mixing evenness, that influence the quality of the received compost, are presented in this paper. By the method of the multifactor experiment rational values of the drum rotation speed, the blades (mounted on the inner drum surface) angle and the substrate`s moisture content are defined at which the components distribution homogeneity in the substrate reaches maximal value. The abovementioned, in turn, provides high compost quality by the agrichemical indices. The recommendations are given to pick the design parameters and operational modes of the drum type reactor.

РЕЗЮМЕ
Представлено результати дослідження впливу конструкційно-технологічних параметрів реактора барабанного типу і фізико-хімічних властивостей субстрату на рівномірність змішування компонентів у субстраті, що впливає на якість виробленого компосту. Методом проведення багатофакторного експерименту визначено раціональні значення частоти обертання барабану реактора, кута нахилу нерухомих лопатей, розташованих на внутрішній поверхні барабану, та вологості субстрату, при яких рівномірність розподілу компонентів в субстраті досягає максимальних значень. Зазначене, в свою чергу, забезпечує високу якість компостів за агрохімічними показниками. Наведені рекомендації щодо вибору конструктивних параметрів та режимів реактора барабанного типу.

INTRODUCTION

Widespread use of pesticides and fertilizers in agricultural production has provided a significant increase in crop yields. In Western Europe the yield of cereals has reached 5-6 t/ha due to the agrochemicals usage *(Fernández et al., 2010; Golub et al., 2017)*. However, the excessive fertilizer application and unbalanced plant nutrition constantly reduce the quality of crop products, and improper chemicals storage and usage leads to reduction of the natural soil fertility and its degradation, and as a result – to environmental pollution *(Golub et al., 2017)*. One way to improve soil fertility is to use organic fertilizers *(Toledo et al., 2020).*

Composting is one of the most important technological methods of high-quality organic fertilizers production. It is necessary to preserve nutrients in some fertilizers during their mineralization (manure, etc.) and to improve nutrients' accessibility in a more complex ones like peat, straw or other inert organic *(Geethamani et al., 2020).*

Although composting technologies have been developing intensively in the last few decades, the main obstacle of its wide application is its low efficiency because of how long it takes to produce it especially when composting in compost bins *(Liu et al., 2020).*

One of main methods of composting process intensification is a compost production in closed chambers *(Fahad et al., 2018; Liu et al., 2020).* Process intensification is reached by keeping optimal thermal conditions on each stage, use of aeration and development of rational parameters and modes of operation *(Jiang-Ming, 2017; Kalamdhad and Kazmi, 2008).*

Creating horizontal rotating drum reactors was a determinative step in the modernization and mechanization of composting in closed chambers *(Aboulam et al., 2006; Jain and Kalamdhad, 2018).* Inner reactor space often equipped with bulkheads, mixing shaft or welded scrapers *(Arora et al., 2018).* Process intensification is reached by the use of contraflow aeration that provides thermophilic bio-thermal composting mode *(Jain et al., 2019).* At such conditions and adequate thermal insulation the overall composting cycle can only take seven days *(Kalamdhad et al., 2008; Wang et al., 2016*). In reactors 200…300 litre big a periodic aeration is used, as a rule. It is done to provide even substrate saturation with the oxygen and to avoid the process from becoming anaerobic *(Kalamdhad et al., 2008*). Daily productivity of a single reactor is 20–50 t (*Kauser et al., 2020).* Nevertheless, use of the rotating reactors has some disadvantages. In some cases, this technology involves an extra stage of treatment in bins from several weeks to three months. Also, a high requirement is set for initial raw material, especially to agricultural biomass. The abovementioned leads to significant grow of investment in this technology which, in some cases, exceeds 5-10 times composting in compost bins *(Arora et al., 2018; Kalamdhad and Kazmi, 2008).*

In modern times creating and setting-up new technologies is narrowed to find optimal parameters of technological process and modes of correspondent equipment *(Liu et al., 2020).* Solving this type of problems requires a row of experiments since only practical experience gives possibility to objectively estimate process on any stage and is a basis for the creation of adequate mathematical models.

Papers *(Arora et al., 2018; Golub et al., 2019; Kauser et. al., 2020)* analysis indicates that reaching high evenness of component`s mixing is one of the methods of reaching the high quality of the end product.

Hence, it is actual the question of reactor design development and the optimal operational parameters definition, according to the physical-chemical substrate composition, at which the maximal mixing evenness and, as a consequence, high compost quality by the agrochemical indicators are reached.

MATERIALS AND METHODS

The goal of the work is to research the influence of the drum speed, the blades angle and the substrate`s moisture content on the substrate components distribution unevenness. In the same time, a requirement of agrichemical quality of compost should be maintained. To achieve this goal, the functional dependencies between factors of compost production should be found. Rational values of composting process which provide proper compost quality and minimal energy consumption should be defined.

To run experiments an experimental specimen of a drum type reactor was designed, which is shown in Figure 1. The reactor is designed for composting organic waste of agricultural origin.

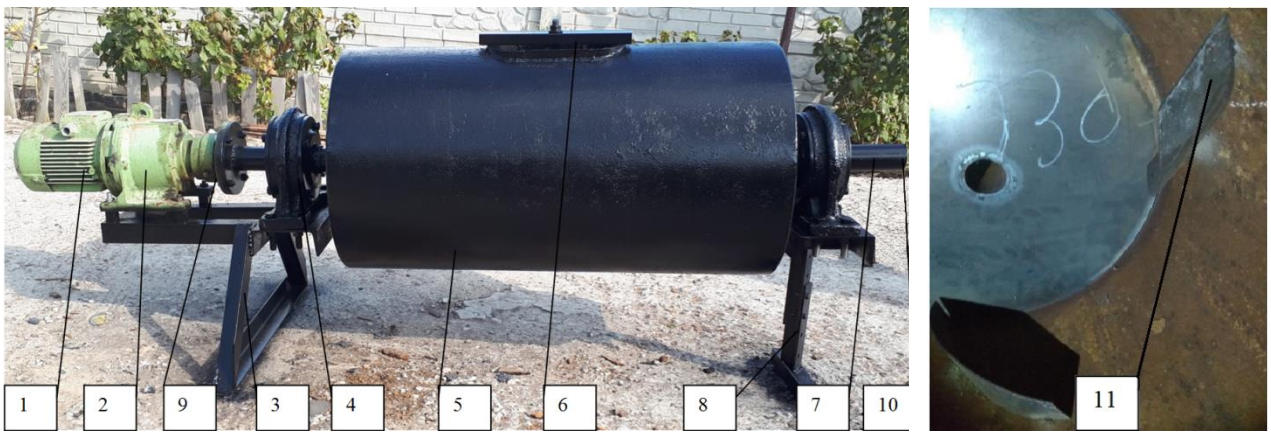

a *b*

Fig. 1 – Experimental installation: *a* – general view of a drum type reactor; *b* – blades installation

1 – electric motor; 2 – gear; 3 – frame; 4 –bearing support; 5 – reactor; 6 – loading lid; 7 – axle; 8 – regulated stand; 9 – coupling; 10 – connector with inner threads; 11 – blades (pipes with jets unmounted)

The experimental installation consists of an air-tight drum type reactor *5*, that have a cylindrical shape and is installed horizontally on hollow axles *7*. The reactor *5* is equipped with the lid *6* for loading substrate and unloading treated compost. Thanks to the lid *6* the reactor *5* is easy to maintain, clean from residues, wash, etc. Loading the substrate and unloading the compost is done periodically, which is acceptable for an experimental installation.

Also, the lid *6* is equipped with a check valve set at *2* bar. To mix the substrate on an inner surface of the reactor *5* concave blades *11* and four longitudinally located tubes with jets for substrate aeration are fixed.

Axles *7* with bearings are installed in supports *4*. The axle where the electromechanical power train is connected by the coupler is blind; the other axle has a connector *10* with inner threads. A coupler *9* serves also for feeding air into reactor during its rotation. The drum type reactor *5* is actuated with the electromechanical power train that is mounted on a frame *3*. The electromechanical power train consists of a 3.5 kW electric motor *1*, a planetary gear *2* and a variable frequency drive (not shown) to adjust reactor RPM.

During reactor rotation, due to the combined action of its working units, substrate components experience mixing. The concave blades and four longitudinally located pipes with jets create contraflow particles movement that helps even distribution of components in the substrate.

To improve the substrate saturation with air, the mixing process is combined with the periodical forced aeration. The forced air supply into the reactor helps avoiding a negative phenomenon of anaerobic zones appearance, that is responsible for the nitrogen loses in the compost. Also, oxygen is necessary for the metabolism and breathing of the aerobic microorganisms and for the organic molecules' oxidation in a fermented substrate. At the beginning, the O_2 concentration in the pores is around 20% that corresponds to its normal concentration in the air. The same time the CO_2 concentration varies between 0.5…5%. With the rise of the microbiological activeness the O_2 concentration drops, and the CO_2 concentration – rises. When the O_2 concentration drops to 5% the anaerobic processes become prevalent. According to *(Rabinovich, 2006)* the air to substrate ratio is chosen as 4:1. The substrate mixing happens every 55 min and lasts for 5 min. The time between consequent aerations should be sufficient for the oxygen concentration to drop to 5…12%, in the thermophilic stage *(Kalamdhad et al., 2008)*. The air is supplied into the drum via the hollow axis by the compressor. Air supply is controlled. During the pumping, the bypass valve opens automatically so that the pressure inside the drum does not exceed 1.1 bars. In case if bypass valve is stuck, due to debris, and pressure rises, the relief valve is activated to drop pressure. After the mixing and aeration stopped the relief valve opens momentarily to equalize pressure inside the drum with the atmospheric one.

Stand *8* is regulated and that makes possible to change the height of reactor support. Such design provides changing reactor rotation axle tilt between 0…20 degrees from horizontal plane. The angle regulation is discrete with *5* degrees step. Due to this the substrate can be moved along the reactor that provides additional mixing during composting process. Overall net weight of an installation is 92 kg, reactor`s volume is 220 L.

At the beginning of experiments, to minimize thermal loses into the environment, a reactor was thermally insulated. Experimental installation was located in small room with minimal air flow. The room temperature was +18…+20°C, humidity was 40…60%, the wind speed was less than 0.1 m/s. When the reactor was not rotating the check valve was connected to the ventilation system.

For research, a substrate consisting of 50% of manure with chopped straw (moisture content 45%), 20% bird guano and 30% plant raw material (15% peat and 15% deciduous trees wood shavings). Research was done for the abovementioned substrate with three different moisture contents. The substrate moisture content had the following values W – 50%; 60% and 70%. The reactor *5* was filled with a substrate of abovementioned composition by 50%.

Temperature measurement during the experiment was only for reference to know what phase of fermentation was, and served as an indication of the end of the experiment. To measure the composted substrate temperature thermal probes TCP 1-8 was mounted on an inner surface of the reactor, which were providing temperature in different zones. Measurement results were averaged. Whereas the reactor was rotating the thermocouple connection and temperature measurements were done periodically. For the lag phase the temperature was between 18…20°C; for the mesophilic phase – 20…42°C; for the thermophilic phase – 42…65°C; for the maturation phase – the temperature was dropping to the ambient temperature. In general, on the thermophilic phase the maximal temperature did not exceed 65°C and varied between 62…64°C.

To provide substrate movement in longitudinal direction a reactor`s axle tilt changed periodically, setting the angle in a range from 0 to 10 degrees alternately.

A dependence of the coefficient of variation *k* of the control component`s distribution in the substrate on the substrate moisture content *W*, the reactor`s rotation speed *n* and blades angle α were researched.

To determine the connection between independent factors (*W, n,* α) and a dependent factor (*k)*, to find a mathematical equation to describe this connection a multifactor experiment was done *(Golub et al., 2018; Melnikov et al., 1980)*.

At the beginning of experiment substrate moisture content was *W=50%.* The substrate moisture content was defined according to EN 14774-2:2009. Blades *11* on the inner surface of drum were fixed at angle α=15°. Whereas drum rotation speed was *n*=5 rpm. Experiments were repeated for drum rotation speeds *n*=10 rpm and *n*=15 rpm. Then, blades' angle was changed to α=27°, then to α=39° and experiments were repeated for the same rotation speeds. According to the plan of experiment, the investigations were repeated for substrates with moisture content *W=60%* and *W=70%.*

Red granules of the polyphenylsulphide 1.5 mm in diameter were taken as a controlled component for determination of mixing unevenness. Polyphenylsulphide granules' density was equal to a substrate density and was around 300–360 kg/m^3 depending on the substrate moisture content 50, 60 or 70 %. Controlled component distribution was defined from 42 samples, 50 gr each. Samplings were made in different points of the drum on each stage of composting. Samplings were made over equal time periods, namely every 6 hours. Samplings were made according to GOST 13496.0-80. Controlled component content in samples was determined according to GOST 21560.0.

The content of the nitrogen, potassium, phosphor, total carbon of the humus acids, ash and moisture were defined according to DSTU ISO 4176-2003, DSTU ISO 5310-2003, DSTU EN 15922:2015, DSTU 8454:2015, GOST 26714-85 and GOST 26713-85 respectively. Investigations were done in a certified laboratory of the educational-scientific centre of ecology and environmental protection of the Polissya National University.

As an indicator of mixing unevenness a coefficient of variation of controlled component actual distribution in samples (%) was taken. Measurements were done with 3% of controlled component in the total mass of material in the drum (*Golub et al., 2019*).

The coefficient of variation *k* of the control component's distribution was defined by calculating the:

$$k = \bar{l} \cdot 100\% / \overline{C}_m \quad (1)$$

where:

$\bar{l} = \sum_{i=1}^{n} \left| C_{mi} - \bar{C}_m \right| / n$ – is mean linear deviation of the control component concentration in samples;

C_{mi} – control component concentration in the i-th sample within each sampling session;

$\overline{C}_m$ – mean control component concentration, C_m=3%.

Factors encoding: $X_1=W$, $X_2=n$, $X_3=\alpha$. Variation levels of factors are given in table 1.

Table 1

Variable factors and limits of their variation for definition of evenness of substrate components mixing

Factor variation level	Substrate moisture content *W*	Drum speed *n*	The blades angle α
	[%]	[rpm]	[degree]
Lower level (-)	50	5	15
Middle level (0)	60	10	27
Upper level (+)	70	15	39

To hold an experiment, a 5-level plan of second order was used. Experiments for plan realization were repeated tree times *(Golub et al., 2018; Melnikov et al., 1980).* The experimental plan included variation of three independent factors, which influence the unevenness of the mixing process.

Planning stage included the following steps: factor encoding, scheduling, randomization tests, implementation plan of the experiment, testing of reproducibility of the experiments, calculation of regression coefficients, assessment of the significance of regression coefficients and adequacy of the test model *(Melnikov et al., 1980)*. The experiment consisted of 15 tests at threefold repetition in each of them.

The main measuring equipment was: the sample weight was measured with a laboratory scales FEH-320; substrate moisture content with an instrument ZD-05 (error 0.2 %); substrate temperature was measured with the thermal probe TCP 1-8 (error 0.15 %); blades angle was measured with the laser goniometer Bosch

GAM 220 MF (0 601 076 200) (error 0.1 %); drum rotation speed with the portable optical tachymeter Testo 465 (error 0.02 %).

According to the plan of multifactor experiment the values of the model`s relative error are lower than 1.83% *(Melnikov et al., 1980)*. This is the case for all experiments. The values of mean relative deviation are lower than 0.9% *(Melnikov et al., 1980)*. Thus the relative error value is less than 5 % *(Melnikov et al., 1980)*. Such relative error value is considered acceptable in modelling. Therefore, it can be concluded that presented model predicts a degree of substrate components mixing unevenness with high accuracy.

RESULTS

As a result of laboratory experiments and statistical computation, the coefficient of variation *k* of controlled component distribution in samples was obtained and it is shown in table 2.

Table 2

Planning matrix of a multifactor experiment

№	Experiment planning method			Experiments results				Model adequacy check		
	X_1	X_2	X_3	k_1	k_2	k_3	k_{med}	$k_{med.com}$	$(k_{med} - k_{med.com})$	$k_{med} - k_{med.com})^2$
1	+	+	0	19.882	19.659	19.473	19.671	21.546	-1.874	3.513
2	+	–	0	21.211	21.478	21.673	21.454	20.621	0.833	0.693
3	–	+	0	20.103	20.682	20.421	20.402	21.235	-0.833	0.693
4	–	–	0	22.848	22.633	22.779	22.753	20.879	1.874	3.513
5	0	0	0	11.320	11.264	11.857	11.480	11.417	0.064	0.004
6	+	0	+	19.278	19.032	19.013	19.108	18.538	0.570	0.324
7	+	0	–	21.214	21.106	21.041	21.120	20.669	0.451	0.204
8	–	0	+	19.853	19.359	19.482	19.565	20.016	-0.451	0.204
9	–	0	–	18.674	18.573	18.456	18.568	19.137	-0.570	0.324
10	0	0	0	11.541	11.838	11.952	11.777	11.417	0.360	0.130
11	0	+	+	16.973	16.871	16.736	16.860	15.734	1.126	1.267
12	0	+	–	17.087	17.163	17.222	17.157	15.914	1.244	1.547
13	0	–	+	13.474	13.026	13.712	13.404	14.648	-1.244	1.547
14	0	–	–	14.372	14.678	14.734	14.595	15.720	-1.126	1.267
15	0	0	0	10.979	10.987	11.012	10.993	11.417	-0.424	0.180

Regression coefficients: b_0=11.417; b_1=0.013; b_2=0.32; b_3=-0.313; b_{12}=0.142; b_{13}=-0.752; b_{23}=0.223; b_{11}=6.87; b_{22}=2.784; b_{33}=1.304.

After processing the experimental data in “Statistica” a regression equation in a coded form was obtained and the correlation coefficient was determined:

$$k_{(W,\,n,\,\alpha)} = 11.417 + 0.013 \cdot W + 0.32 \cdot n - 0.313 \cdot \alpha + 0.142 \cdot W \cdot n - \\ -0.752 \cdot W \cdot \alpha + 0.223 \cdot n \cdot \alpha + 6.87 \cdot W^2 + 2.784 \cdot n^2 + 1.304 \cdot \alpha^2 \quad (2)$$

where:

W – substrate moisture content, [%];

n – drum reactor rotation speed, [rpm];

α – blades angle, [degree];

k – coefficient of variation of controlled component distribution in samples, [%].

The coefficient of correlation is R^2=0.9613.

The Cochrane criterion and Student test were used to determine the homogeneity of variances and the confidence intervals for regression coefficients respectively. In our case we have a 5% level of significance for the number of freedom degrees f_2=2 and number of experiments f_1=15.

For these values, the tabulated value of Cochrane criterion was G^{tabl}=0.3346 and the tabulated value of Student coefficient was t=4.3 *(Melnikov et al. 1980)*. As we have got that G^{com}=0.203<G^{tabl}(0.05; 15; 2)=0.3346 the process is reproduced. The significance of regression coefficients was tested according to the established confidence intervals and covariance. Adequacy test of hypotheses of obtained regression equation was performed by the Fisher criterion. The estimated value of the Fisher criterion in the dispersion of inadequacy S^2_{inadeq}=1.078 was F^{com}=6.88, since F^{com}=6.88<F^{tabl}(0.05; 15; 2)=19.38. The hypothesis by the adequacy of the regression equation is confirmed.

After processing the experimental data in "Statistica", graphs were built to show dependencies of optimization criterions from factors variation levels, which are quadratic response surfaces. In particular, dependencies of the coefficient of variation k of the control component`s distribution in the substrate on its moisture content W, reactor rotation speed n and blades angle α were built. Graphical representations of the abovementioned equation are given in Figures 2–4.

According to Eq. (1) the biggest influence on the coefficient of variation of controlled component distribution k in samples, namely an unevenness of substrate components mixing, has drum rotation speed n, blades angle α has a little less influence, and moisture content W has the lowest influence.

According to the graphs in Figure 2, between substrate moisture content *W=50…70%* rational drum rotation speed is n=10 rpm. Rational blades angle is α=27…29°. Lower blade angles works better with lower moisture content. When moisture content rises to *W=70%*, to provide less mixing unevenness, blade angle should be set at α=29°.

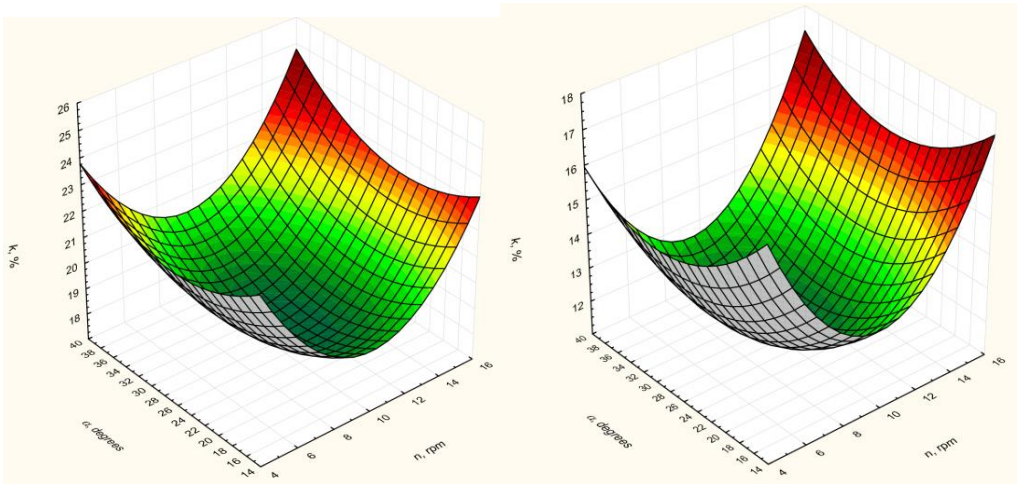

a) *b)*

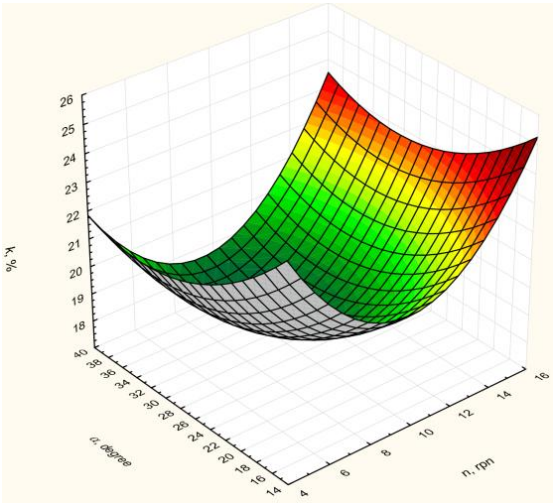

c)

Fig. 2 – Response surfaces of the change in the values of k from the simultaneous change of two factors *k=f(n, α):* a – *W=50%*; b – *W=60%*; c – *W=70%*

According to the graphs in Figure 3, between drum rotation speed *n*=5…15 rpm, the best substrate components mixing was observed at moisture content *W*=62% with blades angle changing between α=27…29°.

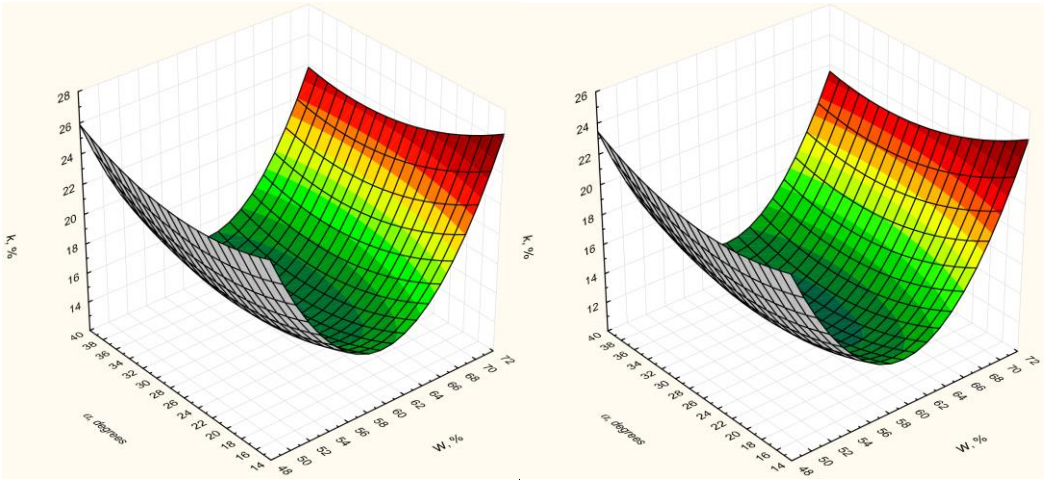

a) *b)*

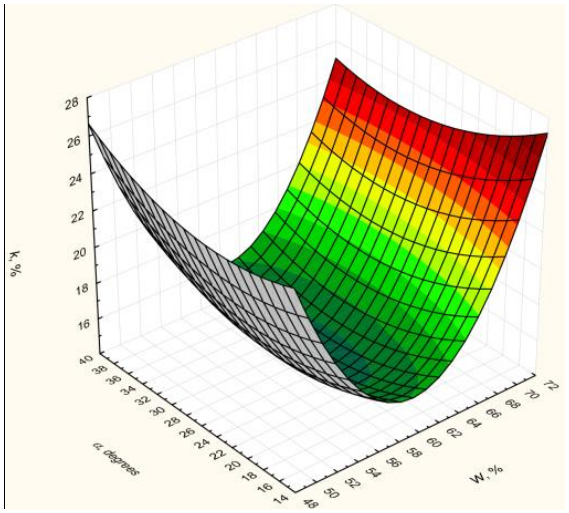

c)

Fig. 3 – Response surfaces of the change in the values of k from the simultaneous change of two factors *k=f(W, α):* a – *n=5%*; **b –** *n=10%*; **c –** *n=15%*

According to the graphs in Figure 4, for blades angles α=15…39°, the best mixing was observed for moisture content *W*=57…62% while drum rotation speed was within *n*=9…11°rpm.

By analysing the received dependencies it was found that while rising drum rotation speed up to *n*=9 rpm the substrate unevenness is lowering, however further rising above 11 rpm leads to the raising of the substrate unevenness. This could be due to predominance of component segregation over mixing.

The range of rational values of substrate moisture content is *W*=57…62%. At this values of moisture content, while rising blades angle to α=27° substrate unevenness is lowering. However rising blades angle over 29° leads to raising substrate unevenness. This is explained by the fact that rising blades angle on reactor working surface improves holding substrate components in ascendance zone preventing it from sliding and widening mixing zone due to involving space over sliding surface. When rising angle above 29° partial substrate sliding is observed, it is returned into general flow instead of spraying in drums' free space hence degrading component distribution.

It should be marked that reactor rotation speed *n* has the biggest influence compared to substrate moisture content *W* and blades angle α. The lowest substrate unevenness (coefficient of variation of controlled component distribution in samples *k*=11%) was observed at substrate moisture content *W*=61%, reactor rotation speed *n*=10 rpm and blades angle equal to α=28°.

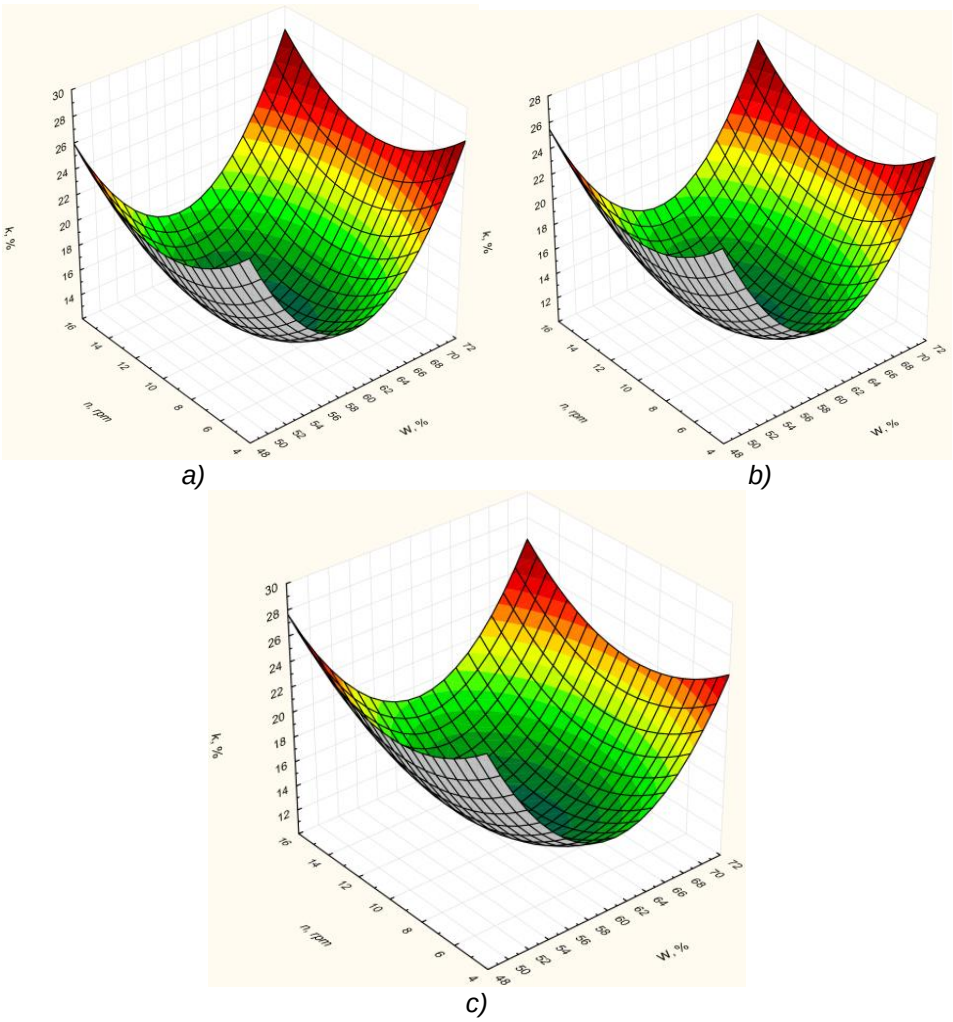

Fig. 4 – Response surfaces of the change in the values of k from the simultaneous change of two factors *k=f(n, W)*: a – α=15%; b – α=27%; c – α=39%

From the graphs in Figures 2–4, it can be concluded that: to provide even mixing of substrate and receive high bio-chemical quality of compost the substrate moisture content should be between *W*=57…62%, rotation speed *n*=9…11°rpm and blades angle equal to α=27…29°.

To estimate the fertilizing characteristics of the fermentation product, the following agrichemical criteria were used: total nitrogen (N) content, mobile forms of phosphorus (P_2O_5) and potassium (K_2O) content, total carbon of the humus acids (C_{HA}) content, ash and moisture content in compost. The content was defined in % to dry weight. So, nitrogen content in the compost was 2.4% (initial substrate – 1.87%); P_2O_5 – 2.12% (init. sub. – 1.53%); K_2O – 1.68% (init. sub. – 1.2%); C_{HA} – 16.5% (init. sub. – 11.8%); ash – 14.27% (init. sub – 10.17%). Compost moisture content was 54% for the substrate moisture content 61%. This compost quality was received at parameters like: mixing with forced aeration was going at drum speed 10 rpm and blades angle 28°; the air to substrate ratio was 4:1; pressure inside was near equal to the atmospheric one; ambient temperature was +18°C. The process duration was 252 hours.

For the minimal drum speed and blades angle (*n*=5°rpm and α=15°C) and other conditions being identical, the produced compost had poorer agrichemical characteristics. Content per dry weight was: N=1.62%; P_2O_5=1.84%; K_2O=1.44; C_{HA}=16.3%; ash – 12.7%; moisture 50%.

For the maximal drum speed and blades angle values (*n*=15°rpm and α=39°C) and other conditions being identical, the produced compost was worse. Content per dry weight was: N=1.54%; P_2O_5=1.71%; K_2O=1.36; C_{HA}=15.8%; ash – 11.8%; moisture 45%.

In the future, basing on the dependencies of influence of the design-technological parameters of the fermentation process and substrate`s moisture content on mixing unevenness (final compost quality), it is planned to find optimal time of the process. Also, to find the influence of mixing time and amount of aeration air on the substrate`s maturation process and the change of its temperature modes on every fermentation phase.

CONCLUSIONS

The rational parameters and modes of reactor operation are substantiated by multifactor experiment. Namely, the influence of substrate moisture content, drum rotation speed and blades angle on substrate components mixing evenness and specific energy consumption of the process:

a) Substrate components mixing evenness is more dependent on rotation speed *n* opposed to moisture content *W* and blades angle α;

b) Even mixing of substrate components was observed at such rational factors ranges: *W*=57…62%, *n*=9…11°rpm, α=27…29°;

c) Minimal value of the coefficient of variation *k* of control component distribution in samples was 11% at substrate moisture content *W*=61%, rotation speed *n*=10 rpm and blades angle α=28°;

For the abovementioned rational factors ranges the compost with high agrichemical characteristics was produced: N=2.4%; P_2O_5=2.12%; K_2O=1.68; C_{HA}=16.5%; ash – 14.27%; moisture – 54%. The reactor`s operation beyond the mentioned parameters range results in worse mixing quality. This, in turn, leads to the need of changing the mixing modes: either reducing the time between consequent mixing or rising the periodical mixing duration.

REFERENCES

[1] Aboulam, S., Morvan, B., & Revel, J.-C. (2006). Use of a Rotating-Drum Pilot Plant To Model the Composting of Household Waste On an Industrial Scale. *Compost Science & Utilization,* 14(3), 184–190. https://doi.org/10.1080/1065657x.2006.10702282

[2] Arora, S., Rani, R., & Ghosh, S. (2018). Bioreactors in solid state fermentation technology: Design, applications and engineering aspects. *Journal of Biotechnology*, 269, 16–34.

[3] Fahad, N., Ahmed, M., Mohamed, A., et al. (2018). Energy Analysis of a Rotary Drum Bioreactor for Composting Tomato Plant Residues. *Energies*, 11(2), 449. https://doi.org/10.3390/en11020449

[4] Fernández, F.J., Sánchez-Arias, V., Rodríguez, L., & Villaseñor, J. (2010). Feasibility of composting combinations of sewage sludge, olive mill waste and winery waste in a rotary drum reactor. *Waste Management*, 30(10), 1948–1956. https://doi.org/10.1016/j.wasman.2010.04.00

[5] Geethamani, R., Soundara, B., Kanmani, S., et al. (2020). Production of cost affordable organic manure using institutional waste by rapid composting method. *Materials Today: Proceedings.* https://doi.org/10.1016/j.matpr.2020.02.803

[6] Golub, G. A., Kukharets, S. M., Tsyvenkova, N. M., Golubenko, A. A., Kalenichenko, P. S. (2018). Research on a boiler furnace module effectiveness working on small fracture wastes. *INMATEH – Agricultural Engineering*, 55, 2, 7–16.

[7] Golub, G., Myhailovych, Ya., Achkevych, O., Chuba, V. (2019). Optimization of angular velocity of drum mixers. *Eastern-European Journal of Enterprise Technologies*, 3, 7(99), 64–72. https://doi.org/10.15587/1729-4061.2019.166944

[8] Golub, G., Pavlenko, S. & Kukharets, S. (2017). Analytical research into the motion of organic mixture components during formation of compost clamps. *Eastern-European Journal of Enterprise Technologies,* 3, 1(87), 30–35.

[9] Jain, M. S., & Kalamdhad, A. S. (2018). Efficacy of batch mode rotary drum composter for management of aquatic weed (Hydrilla verticillata (L.f.) Royle). *Journal of Environmental Management,* 221, 20–27. https://doi.org/10.1016/j.jenvman.2018.05.055

[10] Jain, M. S. & Kalamdhad, A. S. (2019). Drum composting of nitrogen-rich Hydrilla Verticillata with carbon-rich agents: Effects on composting physics and kinetics. *Journal of Environmental Management,* 231, 770–779. https://doi.org/10.1016/j.jenvman.2018.10.111

[11] Jiang-Ming, Z. (2017). Effect of turning frequency on co-composting pig manure and fungus residue. *Journal of the Air and Waste Management Association*, 67(3), 313–321.

[12] Kalamdhad, A. S. & Kazmi, A. A. (2008). Mixed organic waste composting using rotary drum composter. *International Journal of Environment and Waste Management,* 2(1/2), 24–36. https://doi.org/10.1504/ijewm.2008.016989

[13] Kalamdhad, A. S., Pasha, M., Kazmi, A. A. (2008). Stability evaluation of compost by respiration techniques in a rotary drum composter. *Resources, Conservation and Recycling*, 52, 829–834.

[14] Kauser, H., Pal, S., Haq, I. & Khwairakpam, M. (2020). Evaluation of rotary drum composting for the management of invasive weed Mikania micrantha Kunth and its toxicity assessment. *Bioresource Technology,* 313, 123678. https://doi.org/10.1016/j.biortech.2020.123678

[15] Liu, Z., Wang, X., Wang, F. (2020). The progress of composting technologies from static heap to intelligent reactor: Benefits and limitations. *Journal of Cleaner Production*, 270, 122328. https://doi.org/10.1016/j.jclepro.2020.122328

[16] Melnikov, S. V., Atselkin, V. R., Roshchin, P. M. (1980). *Planning experiment of agricultural process research (Планирование эксперимента в исследованиях сельскохозяйственных процессов),* Kolos, 168 p., Leningrad/S.U.

[17] Toledo, M., Gutiérrez, M. C., Peña, A., Siles, J. A. & Martín, M. A. (2020). Co-composting of chicken manure, alperujo, olive leaves/pruning and cereal straw at full-scale: Compost quality assessment and odour emission. *Process Safety and Environmental Protection,* 139, 362–370. https://doi.org/10.1016/j.psep.2020.04.048

[18] Wang, Y., Niu, W. & Ai, P. (2016). Assessing thermal conductivity of composting reactor with attention on varying thermal resistance between compost and the inner surface. *Waste Management,* 58, 144–151. https://doi.org/10.1016/j.wasman.2016.09.018

[19] Golub, G., Tregub, M., Holubenko, A., Tsyvenkova, N., Chuba, V., Tereshchuk, M. (2020). Determining of the influence of reactor parameters on the uniformity of mixing substrate components. *Eastern-European Journal of Enterprise Technologies*, 6, 7(108), 60–70. https://doi.org/10.15587/1729-4061.2020.217159

[20] Rabinovich, R. (2006). *Improvement of aerobic solid phase fermentation of organic raw materials by optimization of production process technological parameters (Совершенствование аэробной твердофазной ферментации путем оптимизации технологических параметров производственного процесса)*. PhD dissertation 05.20.01 – Technologies and means of agricultural mechanization, Tver, 151 p.

CFD-BASED SIMULATION AND MODEL VERIFICATION OF PEACHES FORCED AIR COOLING ON DIFFERENT AIR SUPPLY TEMPERATURES
/
基于CFD 的不同送风温度对蜜桃强制风冷的仿真与模型验证

Yingmin Chen, Haiyan Song*), Rui Zhao, Qin Su [1]
College of Agricultural Engineering, Shanxi Agricultural University, Taigu / China
Tel: +86-0354-6288316; E-mail: haiyansong2003@163.com, chenyingmin137@126.com
DOI: https://doi.org/10.35633/inmateh-63-06

***Keywords*:** *postharvest peach, computational fluid dynamics (CFD), forced air cooling (FAC), precooling, simulation, model verification*

ABSTRACT

To ensure optimum peach quality during precooling, air supply temperature within the precooled facility should be precisely controlled. Three-dimensional unsteady computational fluid dynamics (CFD) model was established in this research, taking air supply temperature as an influencing factor, a dynamic simulation of this model was performed based on Fluent, and its reliability was verified through experiments. Simulation results showed that the decrease of air supply temperature did not affect the 7/8ths cooling time (SECT) significantly, but shortened the cooling time of the fruit which was cooled from the initial temperature to a fixed temperature, especially when air supply temperature dropped below 4°C, its corresponding cooling time showed a trend of steady variation. Meanwhile, respiration rate of 6-8 °C was about twice as high as that of 2-4 °C, its corresponding moisture loss was also increased by 34.71-39.74%. Thus, the range of 2-4 °C was more suitable for quick precooling peaches after harvest. Experiments showed that the root mean square error (RMSE) of 0.7 and 2.7 m·s^{-1} were 0.747 and 0.836 °C, respectively. It could be seen that simulation results were in good agreement with experimental results, which fully verified the feasibility and high accuracy of this new modeling method. Finally, this study can provide a reliable reference for establishing an accurate precooling numerical model, and rationally optimizing air supply temperature range of fruits precooling experiment to maintain its high quality.

摘要

为保证蜜桃在预冷过程中的最佳品质，预冷设备内的送风温度须精确控制。本研究建立了三维果品非稳态的 CFD 数学仿真模型，以送风温度为影响因素，基于 Fluent 对该模型进行了动力学仿真，并通过实验进一步验证了该模型的可靠性。仿真结果表明：风温的减小并不会显著影响果品的 7/8 预冷时间，反而会缩短果品从初始温度降温至某一固定温度的冷却时间。当风温减小到低于 4℃时，其对应的冷却时间将呈现平稳变化的趋势，而且风温为 6-8 ℃时果品的呼吸速率约为 2-4 ℃的两倍，其水分损失量也增大了 34.71-39.74 %。由此可知，2-4 ℃的风温范围更适合蜜桃采后预冷。此外，模型验证实验表明：该模型在风温为 2 ℃时，0.7 和 2.7 m·s^{-1} 的仿真和实验的均方根误差分别为 0.747 和 0.836 ℃，模拟与实验结果的高度吻合充分证明了该新型建模方法的可行性和高准确性。该研究为建立高精准度预冷数值模型，合理优化果品预冷实验送风温度范围，保持其高品质提供了可靠的参考依据。

INTRODUCTION

Postharvest peach carries an amount of field heat, which makes the fruit breathe vigorously. According to the relevant statistics, the rate of quality loss is as high as 13 to 38% when the fruit reaches the consumers through the supply chain after harvest (*Kummu et al., 2012)*. Therefore, the most crucial step for freshly harvested fruits is to remove field heat via prompt precooling, which retards after-ripening and minimizes mass loss, prior to the refrigerated storage or transportation (*Becker et al., 2011; Wang et al., 2019)*. Moreover, forced-air cooling (FAC) is a typical and effective industrial postharvest handling technique.

During the forced-air cooling (FAC), the complexity of the air movement inside a single fruit-packing crate makes it difficult to measure temperature variations solely via field tests. More importantly, extending the test cycle requires significant human and material resources.

[1] *Yingmin Chen, As. Ph.D. Stud. Eng.; Haiyan Song*, Prof. Ph.D. Eng.; Rui Zhao, As. Ph.D. Stud. Eng.; Qin Su, As. M.E. Stud. Eng.*

However, these difficulties can be avoided by using computational fluid dynamics (CFD) to create a three- dimensional numerical model. This is because the transient coupling effect of fluid-solid can be simulated by CFD, and it can also obtain the distribution of airflow and temperature at a high spatiotemporal resolution (*Norton et al., 2007*). Therefore, actual measurements in experiments are required only at specific locations to verify the accuracy of the simulation. However, some of these models do not take into account the effect of these heat sources on heat flow inside the fruit zone *(Ferrua et al., 2008a and 2008b; Berry et al., 2016; Han et al., 2017)*, which leads to the reduced reliability of the simulation results from such studies. From this, a new modelling method is proposed to improve the accuracy of simulation results in peaches cooling, and these heat sources are coded as detailed procedures by a user-defined function (UDF) written in C programming language.

In addition, CFD has been widely applied to research the cooling phenomena of various horticultural food products for optimizing the design of precooling packing crates or finding the optimal air-inflow velocity (*Delele et al., 2013a and 2013b; Han et al., 2017).* Unfortunately, few studies have analysed the comprehensive effects of different air supply temperatures on postharvest peaches during precooling.

Therefore, the objective of this study is to determine the optimal range of air supply temperature and to verify the feasibility of this new modeling method. This modelling method can accurately predict the temporal and spatial temperature distribution in the fruit cooling process, and can also save an amount of manpower and material resources consumed in the precooling experiments, so that this method can be widely applied in precooling research. Moreover, this study does not only provide a new modelling method to simulate airflow and heat transfer for different precooling strategies during fruits cooling, but offers a reference for optimizing the air supply temperature range for improving the peaches precooling performances.

MATERIALS AND METHODS

Geometry and meshing

We used Design Modeler of ANSYS19.2 to create a packaging corrugated carton packed with three layers of peaches. The thickness of this container and trays were 7 and 4 mm, and the structure design was shown in Fig.1, among them, the tray was a single corrugated cardboard of 368×256 mm^2.

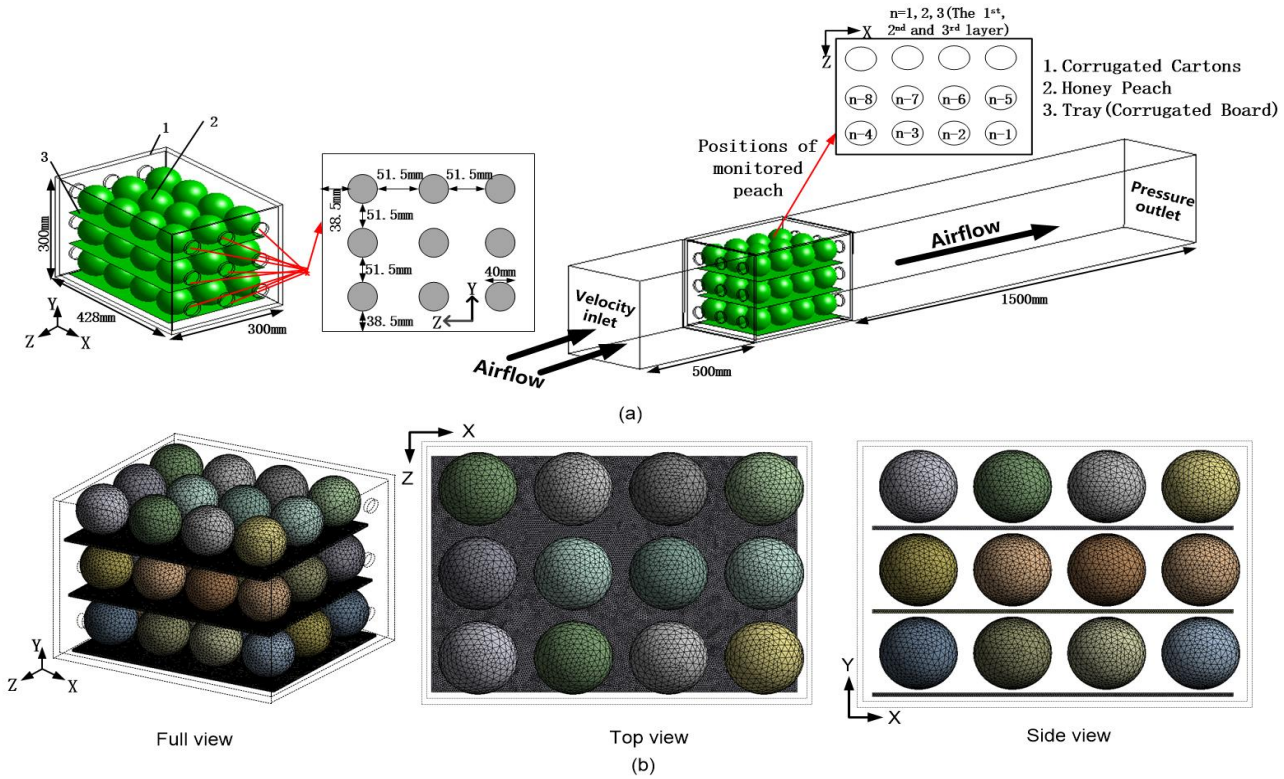

Fig. 1 - (a) Schematic diagram of precooling simulation: positions of monitored peaches inside an individual package *(from n-1 to n-8, where n=1,2,3)***, (b) computational grids of numerical model**

This model was divided into unstructured grids through Meshing software of ANSYS19.2. The number of grid cells after meshing in this model was about 6.93×10^6, with a space step of 1 mm. Through grid quality examination, the mesh skewness of this model was below 0.9, which presented a high and rational mesh quality of this model.

New modeling method of mathematical model

Assumptions in mathematical model: To simplify the mathematical model and facilitate the numerical calculation, necessary assumptions were made for the actual precooling process: The thermal-physical properties of peaches are constant, their heat conduction is isotropic, and their internal texture is uniform; Ignore the dissipating heat generated by the viscous dissipation; The precooling-air is regarded as an incompressible fluid with constant thermal properties; The precooling-air is considered to be a Newtonian fluid and a Boussinesq fluid.

Airflow and heat transfer model: For this study, we created a 3D model of peaches and air around it. The governing differential equations describing the fluid flow were solved with a general purpose fluid-flow solver (Fluent, ANSYS 19.2) in the 3D computational domain, which was divided into three parts: the air flow zone, the peach internal flow field and the coupling interfacial zone. The heat and momentum transfer in precooling process was performed with an unsteady state.

(1) The air flow zone

Mass conservation equation

$$\mathrm{div(U)}=0 \tag{1}$$

Momentum conservation equation:

$$\begin{aligned}
\rho_a\frac{\partial u}{\partial t}+\rho_a\mathrm{div(uU)}&=\mathrm{div}(\mu_a\mathrm{gradu})-\frac{\partial P_a}{\partial x}+S_u\\
\rho_a\frac{\partial v}{\partial t}+\rho_a\,\mathrm{div(vU)}&=\mathrm{div}(\mu_a\mathrm{gradv})-\frac{\partial P_a}{\partial y}+S_v\\
\rho_a\frac{\partial w}{\partial t}+\rho_a\mathrm{div(wU)}&=\mathrm{div}(\mu_a\mathrm{gradw})-\frac{\partial P_a}{\partial z}+S_w
\end{aligned} \tag{2}$$

Energy conservation equation:

$$\frac{\partial T_a}{\partial t}+\mathrm{div}(UT_a)=\mathrm{div}\left(\frac{\lambda_a}{\rho_a c_a}\mathrm{grad}T_a\right) \tag{3}$$

where: U is the velocity vector, u, v, w is the velocity component [m·s^{-1}] in the x, y, z direction, respectively. ρ_a and μ_a are the air density [kg·m^{-3}] and dynamic viscosity [Pa·s], respectively. c_a and λ_a are the air-specific heat capacity [J·kg^{-1}·K^{-1}] and thermal conductivity [W·m^{-1}·K^{-1}], respectively. P_a is water vapor pressure inside the carton [Pa], T_a is the air temperature [K], t is the precooling time for fruits [s]. S_u, S_v, S_w are generalized source terms in the x, y and z directions. Since air is an incompressible fluid, only the gravity effect of cold air is deemed to be $g=9.81$ [m·s^{-2}] in precooling, so $S_u=0$, $S_v=0$, $S_w=-\rho g$.

(2) Flow field internal to the peach

Heat sources internal to peaches (Q_{int}, [W·m^{-3}]) are mainly made up of respiration heat (Q_r, [W]) and transpiration heat (Q_t, [W]). Internal heat source is loaded into the heat conduction differential equation of the peach zone by an user-defined function (UDF) written in the C programming language.

$$\lambda_P\left(\frac{\partial^2 T_{P,t}}{\partial r^2}+\frac{2}{r}\frac{\partial T_{P,t}}{\partial r}+\frac{\cos\theta}{r^2\sin\theta}\cdot\frac{\partial T_{P,t}}{\partial\theta}+\frac{1}{r^2}\frac{\partial^2 T_{P,t}}{\partial\theta^2}\right)+Q_{int}=c_P\rho_P\frac{\partial T_{P,t}}{\partial t} \tag{4}$$

$$Q_{int}=\frac{Q_r-Q_t}{V_P} \tag{5}$$

where: $T_{p,t}$ is the peaches temperature at time t [K], c_P is peach-specific heat capacity [J·kg^{-1}·K^{-1}], λ_P and ρ_P are peach thermal conductivity [W·m^{-1}·K^{-1}] and density [kg·m^{-3}], respectively. V_P and A_p are the volume [m^3] and surface area of the peach [m^2].

Additionally, its heat of respiration and transpiration can be described as following formula (*Dehghannya et al., 2008*):

$$Q_r/V_P=\rho_P\times f_P \tag{6}$$

In this equation, f_p is the respiratory heat generation per unit mass of commodity [W·kg^{-1}], i.e., $f_P = (10.7/3600) \times m_1 \times [1.8(T_{P,t} - 273.15) + 32]^{m_2}$, where the respiration coefficients m_1 and m_2 are given in *Becker et al*. 2011 and successfully applied in many previous researches (*Delele et al. 2013a; Zhao et al. 2016*), i.e., 1.2996×10^{-5} and 3.6417 for peach.

$$Q_t/V_P = L_P m_P A_P/V_P = 3L_P m_P/r \quad (7)$$

Among them, $L_P = 9.1T_{P,t}^2 - 7512.9T_{P,t} + 3875100$, which presents evaporative latent heat [J·kg^{-1}], r is the vector radius of the peach (0.04 m).

When $P_p > P_a$ and $P_w > P_a$, $m_p = k_t(P_p - P_a)$, where k_t is the transpiration coefficient [kg·m^{-2}·s^{-1}·Pa^{-1}], and $P_p = VPL \cdot P_W$, $P_a = RH \cdot P_W$, $VPL = 0.99$ is the vapor pressure lowering effect of peaches (*Becker et al., 2011*) and $RH = 0.9$ is air relative humidity. P_P is the partial pressure of water vapor at the evaporating surface and P_W is the partial water vapor saturation pressure in air [Pa]:

$$P_W = \exp\left(23.4735 - \frac{3990.5}{T_a - 39.317}\right) \quad (8)$$

$$k_t = \frac{1}{1/k_a + 1/k_s} \quad (9)$$

where:

k_s and k_a are the skin mass-transfer coefficient and the air film mass-transfer coefficient, respectively, for peaches, k_s=14.2×10^{-9} [kg·m^{-2}·s^{-1}·Pa^{-1}] (*Becker et al., 2011*).

The value of k_t and k_a can be estimated by using the Sherwood- Reynolds-Schmidt correlations:

$$Sh = \frac{k_a \cdot 2r}{\delta M_{H_2O}} = 2.0 + 0.552Re^{0.53}Se^{0.33} \quad (10)$$

$$\delta = \frac{9.1 \times 10^{-9} \times T_a^{2.5}}{T_a + 245.18} \quad (11)$$

where:

δ is the diffusion coefficient of water vapor in air [m^2·s^{-1}].

Due to the low flow speed of the wet-cold air in the carton, $Re=0$ can be assumed (*Rennie et al., 2009*).

$$k_a = \frac{\delta M_{H_2O}}{R_{H_2O} T_a r} \quad (12)$$

For different precooling-air temperature, the values of δ, k_t and k_a were calculated by Eq. 9-12 and shown in Table 1.

$M_{H2O}=0.018$ is the molecular mass of water vapor [kg·mol^{-1}], $R_{H2O}=8.314$ is the water vapor constant [J·mol^{-1}·K^{-1}].

Table 1

Various parameters of different precooling-air temperature in simulation

Precooling-air temperature [°C]	Diffusion coefficient of water vapor	Air film mass transfer coefficient	Skin mass transfer coefficient
	δ ×10^{-5} [m^2·s^{-1}]	k_a ×10^{-9} [kg·m^{-2}·s^{-1}·Pa^{-1}]	k_t ×10^{-9} [kg·m^{-2}·s^{-1}·Pa^{-1}]
0	2.16490	4.28982	3.29454
2	2.19627	4.32035	3.31252
4	2.22784	4.35082	3.33040
6	2.25960	4.38123	3.34819
8	2.29155	4.41157	3.36588

(2) The coupling interfacial zone

According to the conservation of energy, the peach-air heat balance equation is obtained as (*Rennie et al., 2009*):

$$(\lambda_a \nabla T_a - \lambda_P \nabla T_{P,0}) n_{ap} = L_P (m_{con} - m_P) - \alpha_P (T_{P,0} - T_a) \quad (13)$$

where:

n_{ap} is an unit vector perpendicular to the peach-air interface,

α_P is the surface convective heat transfer coefficient of peach [W·m^{-2}·K^{-1}],

m_{con} is the condensation coefficient [kg·m^{-2}·s^{-1}].

Initial conditions and boundary conditions: The initial temperature of peach and the precooling-air temperature were set to 26 °C and 2 °C, respectively. The velocity-inlet boundary condition was used to define the airflow velocity at the inflow boundary (see Fig.1), and the airflow velocity was set to 2.5 m·s^{-1}. The pressure-outflow boundary condition was adopted at the outflow boundary. The surface of the peach, the inner and outer surfaces of the package, and the surface of trays were all taken as a no slip wall boundary.

Numerical simulation setting: Realizable k-ε turbulence model was used to simulate the whole precooling process. A pressure-based split solver was used, and the discrete format of momentum, energy, turbulent kinetic energy and diffusivity were set to second-order upwind scheme. We utilized semi-implicit method for pressure-linked equations (SIMPLE) to couple pressure to velocity, and used a transient simulation with a time step of 10 s and 20 iterations per time step.

The convergence criteria for continuity, momentum and turbulence were set to 10^{-4} and that for the energy equations was 10^{-6}. The thermal-physical parameters of each object in this model were shown in Table 2. The simulation was implemented in a 64-bit Windows10 computer with a 2.30 GHZ Inter®Core E5-2697 V4 CPU and 256GB RAM.

Table 2

Parameters of thermal-physical properties

Parameters	Density	Specific heat capacity	Thermal conductivity	Dynamic viscosity
	[kg·m^{-3}]	[J·kg^{-1}·K^{-1}]	[W·m^{-1}·K^{-1}]	[Pa·s]
Cooling air	1.293	1006	0.02343	1.73E-5
Honey Peach	691.95	3898.3	0.472	-
Corrugated Carton	220	1700	0.065	-
Tray (Corrugated Board)	260	1700	0.065	-

Parameters of precooling performance assessment

Cooling rate and SECT: The dimensionless temperature Y is used to analyse the cooling kinetics of the fruit. The formula for Y is expressed as (*Dincer, 1995):*

$$Y = \frac{T_{p,t} - T_a}{T_{P,0} - T_a} \quad (14)$$

where:

$T_{P,0}$ is the initial temperature of peaches (299.15 K).

The half (Y=1/2, HCT, min) cooling time is usually used to measure whether the fruit reaches the cooling average level.

The 7/8ths cooling time (Y=1/8, SECT, min) is used to measure whether the fruit is close to the commercial storage temperature.

The temperature of SECT is suitable for subsequent refrigerated transportation and storage. Therefore, the selection of SECT point is the most appropriate inflection point for refrigerated transfer.

Cooling uniformity: A variation curve of ΔY is a novel representation of cooling uniformity as a function with the dimensionless cooling time (Y_{avg}). Compared with temperature variability which has been reported as the relative standard deviation (*Defraeye et al., 2015*), the new heterogeneity index not only can observe the instantaneous uniformity (HI_t) at single time points, but also intuitively judge the overall heterogeneity index ($OHI=\Delta Y_{max}-\Delta Y_{min}$) by using a specific value.

A lower value of OHI represents a high level of temperature homogeneity, conversely, the worse precooling uniformity is (*Olatunji et al., 2017*):

$$Y_{avg,t} = \sum_{n=1}^{m} Y_{n,t} \Big/ m \tag{15}$$

$$\Delta Y_{n,t} = Y_{n,t} - Y_{avg,t} \tag{16}$$

$$HI_t = \Delta Y_{max-P,t} - \Delta Y_{min-N,t} \tag{17}$$

where:

$Y_{avg,t}$ is the average dimensionless temperature of all monitored fruits (n=24),

$\Delta Y_{max-P,t}$ and $\Delta\ Y_{min-N,t}$ are the maximum and minimum values of ΔY_n which reflects horticultural commodity higher or colder than the average temperature, thereby cooling slowly (hot spots) or faster (cold spots).

Moisture loss: Integrated evaluation of precooling efficiency is essential for optimizing cooling strategies of horticultural products and ensuring optimum fresh quality and safety. Thus, an influence of various precooling-air temperature on mass degradation should be taken into consideration.

$$-\frac{\partial M}{\partial t} = m_P \times A_P \tag{18}$$

Peaches mass loss (M, [mg]) mainly occurs by transportation driving force, which is estimated by Eq. 18 (*Hoang et al., 2003; Nalbandi et al., 2020*), among them, the rate of moisture loss m_p [kg·m^{-2}·s^{-1}] is calculated with Eq. 8-12.

Experimental verification

To determine the validity of this mathematical model, predicted (S_i) and measured (E_i) temperatures are compared based on the root-mean-square error ($RMSE$) and mean absolute percentage error ($MAPE$).

$$RMSE = \sqrt{\frac{1}{n}\sum_{i=1}^{n}(E_i - S_i)^2} \tag{19}$$

$$MAPE = \frac{1}{n}\sum_{i=1}^{n}\frac{|E_i - S_i|}{E_i} \times 100\% \tag{20}$$

Freshly Okubo peaches were harvested in July from Taigu of Shanxi Province (112º55′E, 37º43′N). Then peaches were immediately cooled in a self-made precooling device, where the precooling-air and relative humidity were set as 2℃ and 80-90%, respectively. At the same time, the air-inflow velocities were set to 0.7 and 2.7 m·s^{-1}, respectively.

The fruits' temperature was measured with a temperature digital recorder (SSN-13E, YOWEXA, Inc., Shenzhen, China). The accuracy of this sensor is ± 0.3℃. The fog making capacity of ultrasonic humidifier (HS-05-3, LUOSHE HUASHENG, Inc., Wuxi, China) is 0.3 KW.

RESULTS

Effect of air supply temperature on cooling rate

The effect of air supply temperature on cooling rate was examined by using the turbulence simulations for five different air supply temperatures: 0, 2, 4, 6 and 8℃. Fig. 2 compared the variation in the average temperature of peaches as a function of cooling time for different air supply temperatures.

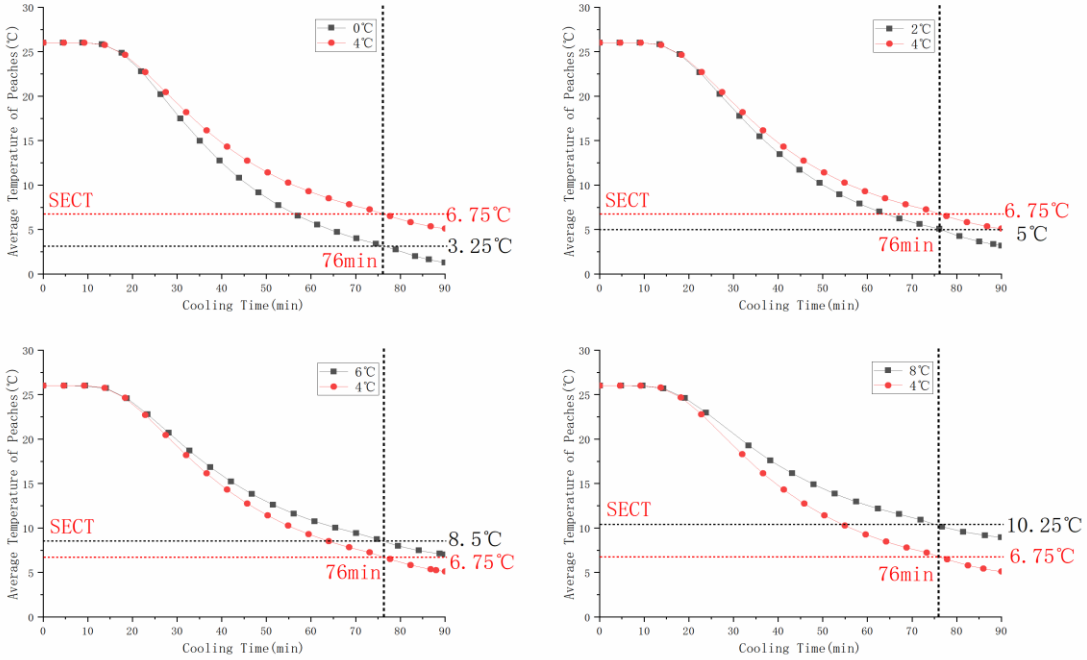

Fig. 2 - The average cooling temperature of peaches inside the container as a function of different air supply temperature: the monitoring position is the core temperature of peach

As it was clear in Fig. 2, its average temperature decreased gradually with the prolongation of cooling time. However, when air-inflow velocity was constant, the values of SECT did not increase as air supply temperature increased. For example, when air-inflow velocity was equal to 2.5 $m \cdot s^{-1}$, the SECT focused on ~76 mins. This meant that air supply temperature had no significant influence on the variations of SECT. This result was attributed to the fact that increasing the air supply temperature increased peaches transfer temperature in cold storage, and their transfer temperature was 3.25, 5, 6.75, 8.5 and 10.25°C, respectively, observed from Fig. 2. However, the substantial increase in air supply temperature made the precooling effect of fruit have certain limitations, especially for fruits (like peach) with high respiration intensity and perishability, which was mentioned in the following section. Therefore, we also needed to further study its corresponding variation trend of cooling time when the fruit was cooled from initial temperature (26°C) to fixed temperature on different precooling conditions. As could be seen from Fig. 3, the cooling time decreased with the decrease of air supply temperature, especially when its temperature was below 4°C, the variation range of cooling time was significantly reduced, as well as the same variation trend.

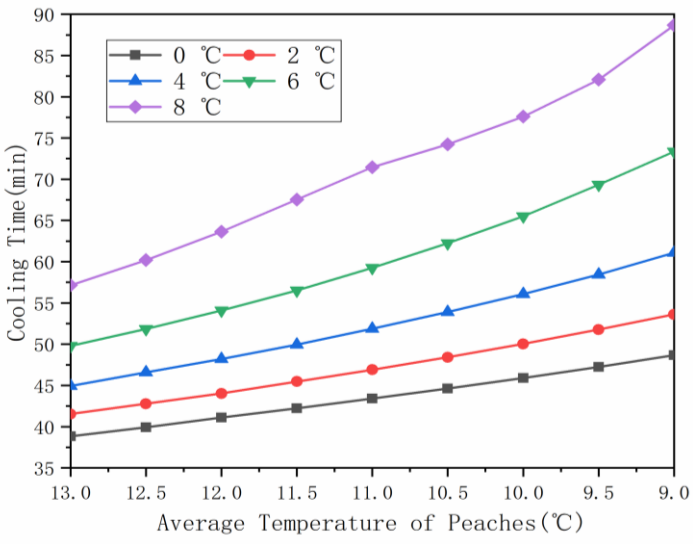

Fig. 3 - Relationship between air supply temperature and cooling time

In the actual precooling operation process, although too low air temperature shortened the cooling time, it was also easy to cause chilling injury to the fruit, thus affecting its sales quality. The specific magnitude of peaches chilling injury could be seen directly from Fig. 5, which showed the variation function curve of ΔY_{min} value and dimensionless temperature (Y_{avg}) at each precooling-air temperature.

According to Fig. 5, the maximum value of $|\Delta Y_{min}|$ at 8°C was 0.058, and the magnitude of its chilling injury effect was 30.12, 23.68, 17.14 and 9.38 % lower than other air supply temperatures (0-6°C). Based on this observation, blindly lowering the air supply temperature in precooling device gradually increased the chilling injury rate of peach. Therefore, it was recommended that the air supply temperature should not be lower than 2°C.

Effect of air supply temperature on cooling uniformity and quality loss

Observing Fig. 4, it was found that when air-inflow velocity was 2.5 m·s^{-1}, the increase in air supply temperature gradually reduced the instantaneous temperature distribution gradient, namely, from 0.8 to 0.6°C. In addition, the curve variation trend of hot spot (ΔY_{max}) and cold point (ΔY_{min}) of the peach gradually developed as an "eye" shape (see Fig. 5), and its size also gradually decreased with the increase of air supply temperature, which was specifically reflected in the overall heterogeneous index value (OHI) of the peach inside the container, namely, 0.152, 0.137, 0.125, 0.117 and 0.106, respectively.

These analysis results fully demonstrated that its cooling uniformity was continuously improved with the increase of air supply temperature. Meanwhile, the overall heterogeneity index (OHI) of 8 °C is 30.26, 22.63, 15.20 and 9.40 % lower than other air supply temperatures (0-6 °C).

According to this result, air supply temperature of 4°C was a demarcation point that affected the uniformity of fruits. When air supply temperature was lower than 4°C, its size of "eye" increased significantly and asymmetrically. But when air supply temperature was increased to over 4°C, its variation range of "eye" was small and began to be distributed symmetrically.

This indicated that when air supply temperature exceeded 4°C, its temperature distribution began to be stable. Any further increase in air supply temperature did not improve the cooling uniformity obviously.

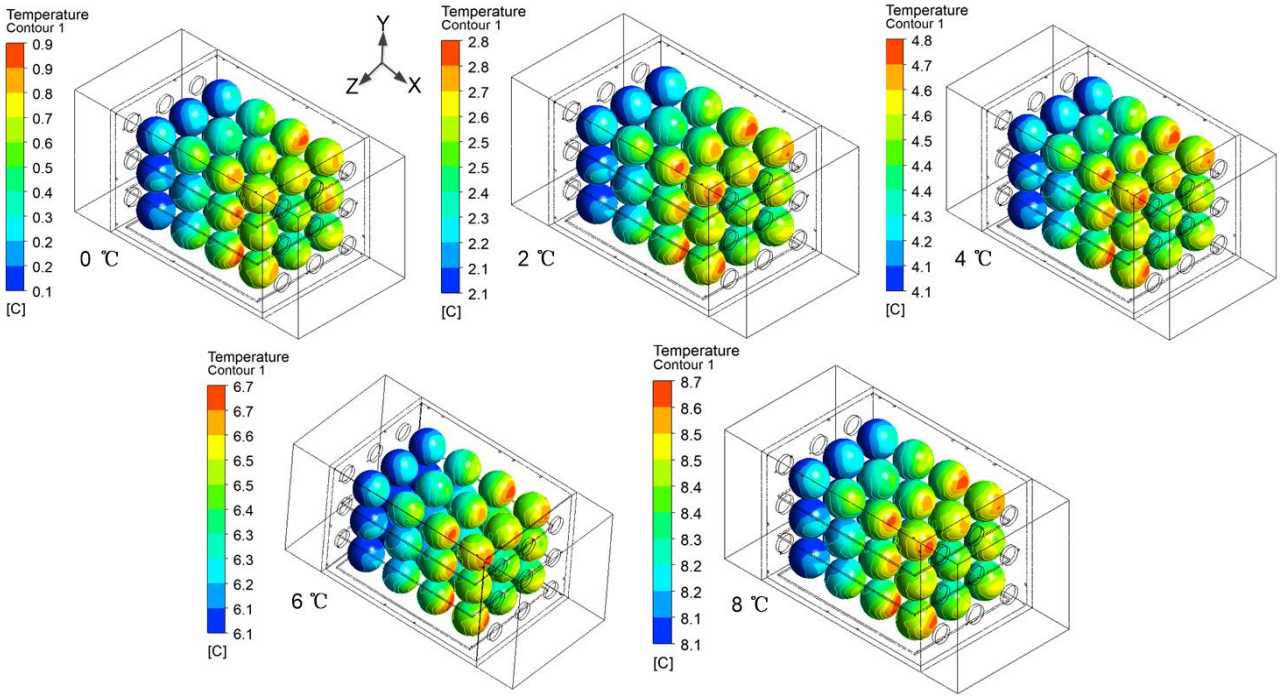

Fig. 4- Instantaneous static temperature (°C) contours of peaches inside an individual carton for different precooling-air temperatures at the simulation time of 90 min when air-inflow velocity is equal to 2.5 m·s^{-1}

However, blind improvement of air supply temperature had a certain effect on the quality of peaches during precooling. This was because the increase of air supply temperature enhanced its respiration rate. For example, when the moment was at 90 mins, the instantaneous respiratory heat generated by peach per unit mass (f_p, calculated by Eq. 6) at 6-8°C is 0.041-0.053 W·kg^{-1}, twice as much as that at 2-4 °C (0.022-0.027 W·kg^{-1}) (see Fig. 6).

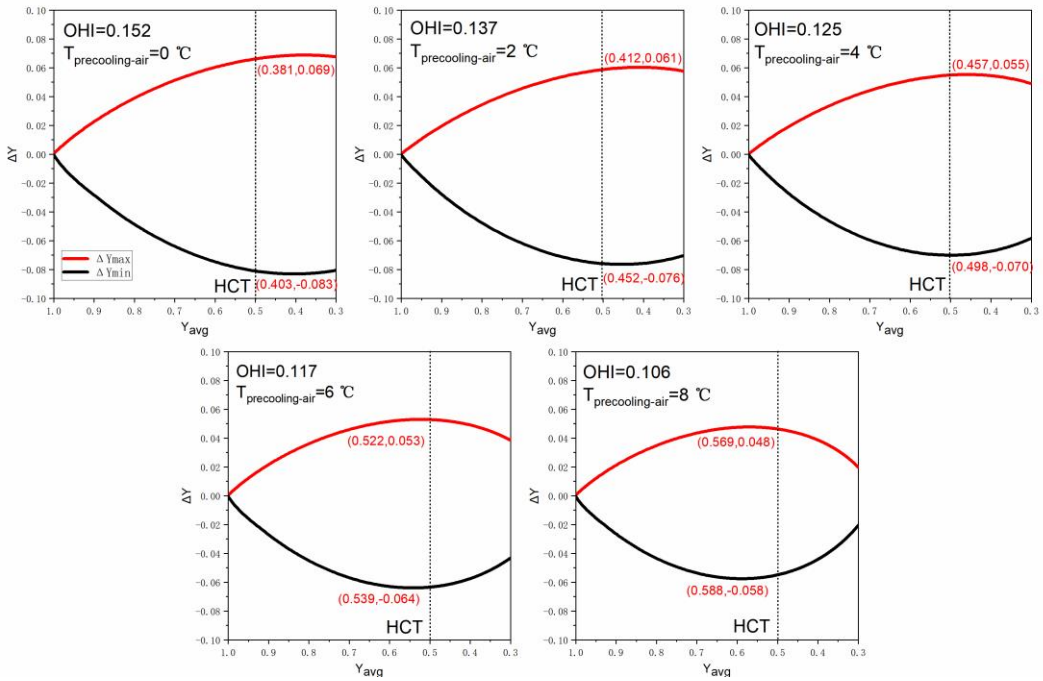

Fig. 5- Cooling heterogeneity curves of different precooling-air temperatures

Moreover, the continuous increase of respiration heat consumed fruit nutrients, accelerated its ripening speed and promoted the growth of microorganisms internal to the fruit, which was mentioned in previous study (*Dehghannya et al., 2012; Ngcobo et al., 2012*). These phenomena greatly improved peaches rotten rate, shortened their shelf life and commercial edible value. Meanwhile, the increase in respiration rate also increased their heat transfer resistance, forcing the cooling time to be prolonged continuously.

More importantly, the moisture loss at 2-4 °C was the lowest among that of all air supply temperatures (i.e., 73.85 and 76.61 mg), among them, the moisture loss at 6 °C was 39.74 and 34.71 % higher than that at 2 and 4°C. According to this result, the improvement of air supply temperature would reduce the taste and freshness of peaches. Thus, based on the comprehensive analysis of the above precooling performances, it was found that air supply temperature of 2-4 °C was the most appropriate range to maintain the quality of peaches during precooling.

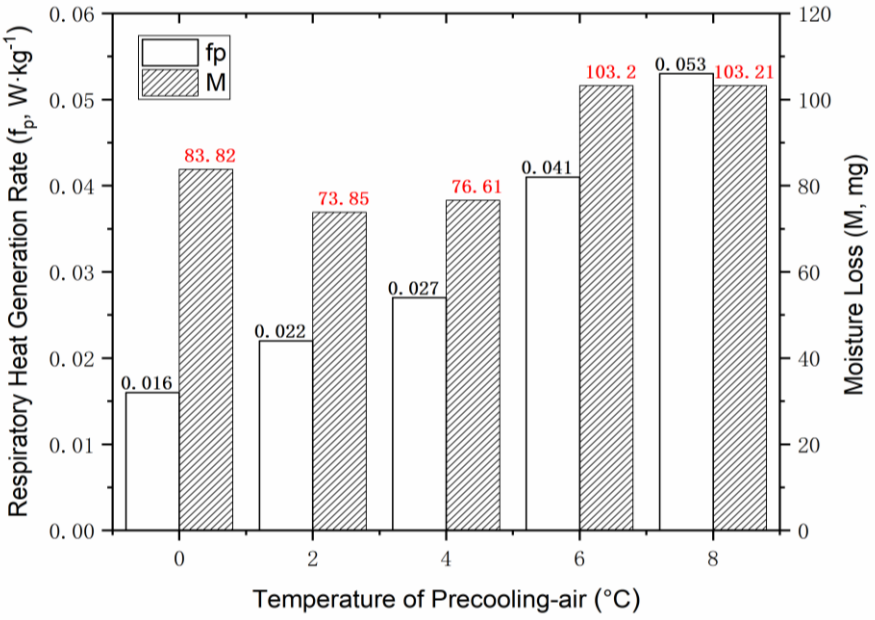

Fig. 6- Instantaneous respiratory heat generation rate (f_p) and cumulative moisture loss (M) at different precooling-air temperatures when peaches precooled for 90 mins

Validation of the established numerical model by experiment

The curve of experimental temperature and the simulated temperature were shown in Fig.7.

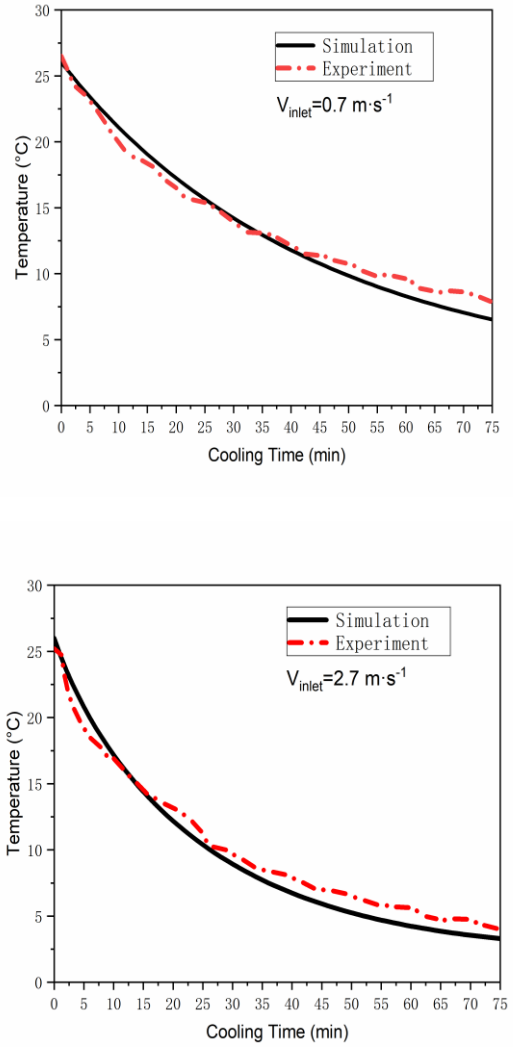

Fig. 7- Numerical simulation and experimental verification curve of peaches temperature with two air-inflow velocities: monitored position at peach 1-1

Overall, the simulated temperature was basically consistent with the measurement results. For the CFD model for 0.7 and 2.7 m·s^{-1}, their corresponding values of RMSE were 0.747 and 0.836 °C, respectively, as well as the MAPE values of 5.44 and 10.70%, respectively. The deviations could be considered satisfactory in view of the various parameters controlling the simulation and experiment. The results demonstrated that this new modeling method can predict the peaches convective heat transfer phenomenon accurately during the whole precooling process, thereby saving a lot of labour and material costs in the experiment.

CONCLUSIONS

In this study, the heat and mass transfer model of peaches forced air cooling (FAC) was established by CFD, and the heat source term was loaded into the Fluent model by UDF function. Then, the effect of various air supply temperatures on precooling performances was investigated and the following conclusions were obtained:

(1) The increase of air supply temperature had no remarkable effect on SECT when air-inflow velocity was constant, but significantly affected the cooling time when the air supply temperature exceeded 4 °C.

(2) In the actual precooling operation, too low air supply temperature resulted in higher chilling injury rate and poor cooling uniformity.

However, although the increase of air supply temperature could improve the cooling uniformity, it could also increase the respiration heat and moisture loss. Its respiration rate at 6-8 °C was about twice as high as that at 2-4 °C, and its corresponding moisture loss also increased by 34.71-39.74%. Thus, the air supply temperature in the range of 2-4℃ was proposed as optimum for quickly precooling peaches after harvest.

(3) This numerical model was highly consistent with the experiment (RMSE<1°C), so that this new modeling method with 3D simulator could be widely used for the simulation of precooling process of the peach, for which the cooling process inside the container was carried out in a turbulence airflow regime.

ACKNOWLEDGEMENTS

This work was funded by the National Key Research and Development Program of China (No. 2018YFD0700300).

REFERENCES

[1] Becker, B. R., Misra, A., Fricke, B. A., (2011), Bulk Refrigeration of Fruits and Vegetables Part I: Theoretical Considerations of Heat and Mass Transfer, *HVAC and R Research*, 2(2): 122-134.

[2] Berry, T. M., Defraeye, T., Nicolaï, B. M., Opara, U. L., (2016), Multi-parameter Analysis of Cooling Efficiency of Ventilated Fruit Cartons using CFD: Impact of Vent Hole Design and Internal Packaging, *Food and Bioprocess Technology*, 9(9): 1481-1493. https://doi.org/10.1007/s11947-016-1733-y

[3] Dincer, I., (1995), Air flow precooling of individual grapes, *Journal of Food Engineering*, 26(2): 243-249. https://doi.org/10.1016/0260-8774(94) 00049-F

[4] Dehghannya, J., Ngadi, M., Vigneault, C., (2008), Simultaneous Aerodynamic and Thermal Analysis during Cooling of Stacked Spheres inside Ventilated Packages, *Chemical Engineering Technology*, 31(11): 1651-1659.

[5] Dehghannya, J., Ngadi, M., Vigneault, C., (2012), Transport phenomena modelling during produce cooling for optimal package design: Thermal sensitivity analysis, *Biosystems Engineering*, 111(3): 315-324. https://doi.org/10.1016/j.biosystemseng.2012.01.001

[6] Delele, M. A., Ngcobo, M. E. K., Getahun, S. T., Chen, L., Mellmann, J., Opara, U.L., (2013a), Studying airflow and heat transfer characteristics of a horticultural produce packaging system using a 3-D CFD model. Part I: Model development and validation, *Postharvest Biology and Technology*, 86: 536-545. https://doi.org/10.1016/j.postharvbio.2013.08.014

[7] Delele, M. A., Ngcobo, M. E. K., Getahun, S. T., Chen, L., Mellmann, J., Opara, U.L., (2013b), Studying airflow and heat transfer characteristics of a horticultural produce packaging system using a 3-D CFD model. Part II: Effect of package design, *Postharvest Biology and Technology*, 86: 546-555. https://doi.org/10.1016/j.postharvbio.2013.08.015

[8] Defraeye, T., Cronjé, P., Berry, T., Opara, U.L., East, A., Hertog, M. & Nicolai, B., (2015), Towards integrated performance evaluation of future packaging for fresh produce in the cold chain, *Trends in Food Science & Technology*, 44(2): 201-225. https://doi.org/10.1016/j.tifs.2015.04. 008

[9] Ferrua, M.J., Singh, R.P., (2008a), Modeling the forced-air cooling process of fresh strawberry packages, Part II: Experimental validation of the flow model, *International Journal of Refrigeration*, 32(2): 349-358. https://doi.org/ 10.1016/j.ijrefrig.2008.04.009

[10] Ferrua, M.J., Singh, R.P., (2008b), Modeling the forced-air cooling process of fresh strawberry packages, Part III: Experimental validation of the energy model, *International Journal of Refrigeration,* 32(2): 359-368. https://doi.org/10.1016/j.ijrefrig.2008.04.011

[11] Hoang, M. L., Verboven, P., Baelmans, M., Nicolaï, B. M., (2003), A continuum model for airflow, heat and mass transfer in bulk of chicory roots, *Transaction of the ASAE*, 46(6): 1603-1611.

[12] Han, J.W., Qian, J.P., Zhao, C.J. & Fan, B.L., (2017), Mathematical modelling of cooling efficiency of ventilated packaging: Integral performance evaluation, *International Journal of Heat and Mass Transfer*, 111: 386-397. https://doi.org/10.1016/j.ijheatmasstransfer.2017.04.015

[13] Kummu, M., de Moel, H., Porkka, M., Siebert, S. & Ward, P.J., (2012), Lost food, wasted resources: Global food supply chain losses and their impacts on freshwater, cropland, and fertiliser use, *Science of the Total Environment*, 438: 477-489. https://doi.org/10.1016/j.scitotenv.2012.08. 092

[14] Norton, T., Sun, D. W., Grant, J., Fallon, R., Dodd, V., (2007), Applications of computational fluid dynamics (CFD) in the modelling and design of ventilation systems in the agricultural industry: A review, *Bioresource Technology*, 98(12): 2386-2414.

[15] Ngcobo, M.E.K., Delele, M.A., Opara, U.L., Zietsman, C.J. and Meyer, C.J., (2012), Resistance to airflow and cooling patterns through multi-scale packaging of table grapes, *International Journal of Refrigeration*, 35(2): 445-452. https://doi.org/10.1016/j.ijrefrig.2011.11.008

[16] Nalbandi, H., Seiiedlou, S., (2020), Sensitivity analysis of the precooling process of strawberry: Effect of package designing parameters and the moisture loss, *Food Science & Nutrition*, 8(5): 2458-2471. https://doi.org/10.1002/fsn3.1536

[17] Olatunji, J. R., Love, R. J., Shim, Y. M., Ferrua, M. J., East, A.R., (2017), Quantifying and visualising variation in batch operations: A new heterogeneity index, *Journal of Food Engineering*, 196: 81-93. https://doi.org/10.1016/j.jfoodeng. 2016.10.004

[18] Rennie, T.J., Tavoularis, S., (2009), Perforation-mediated modified atmosphere packaging: Part I. Development of a mathematical model, *Postharvest Biology and Technology*, 51(1) :1-9. https://doi.org/10.1016/j.postharvbio. 2008. 06. 007

[19] Wang, D., Lai, Y. H., Zhao, H.X., Jia, B.G. & Yang, X.Z, (2019), Numerical and Experimental Investigation on Forced-Air Cooling of Commercial Packaged Strawberries, *International Journal of Food Engineering*, 15(7). https://doi.org/10.1515/ijfe-2018-0384

[20] Zhao, C. J., Han, J. W., Yang, X. T., Qian, J. P., Fan, B. L., (2016), A review of computational fluid dynamics for forced-air cooling process, *Applied Energy*, 168: 314-331. https://doi.org/10.1016/j.apenergy.2016.01.101

THE EFFICIENCY OF USING CAM MECHANISMS TO OPERATE THE EQUIPMENT FOR OPENING AND INTERRUPTING WATERING FURROWS
/
EFICIENȚA UTILIZĂRII MECANISMELOR CU CAMĂ PENTRU ACȚIONAREA ECHIPAMENTELOR DE DESCHIS ȘI COMPARTIMENTAT BRAZDE DE UDARE

Oprescu R.*[1)], Biris S.[2)], Voicea I.[1)], Ungureanu L.[2)], Ungureanu N[2)]., Grădilă M.[3)]

[1)] National Institute for Research - Development of Machines and Installations designed for Agriculture and Food Industry – INMA Bucharest; [2)] University POLITEHNICA of Bucharest – UPB Bucharest;

[3)] Research Development Institute for Plant Protection - ICDPP Bucharest

Tel: 0766580791; E-mail: oprescu.remusmarius@gmail.com; biris.sorinstefan@gmail.com

DOI: https://doi.org/10.356.33/inmateh-63-07

Keywords: *soil, mathematical modeling, irrigation, tillage*

ABSTRACT

Due to climate change, there have been changes in temperature, distribution and precipitation, phenomena that have led to the development of technologies that increase the efficiency of precipitation water use and support the preservation of soil quality. The paper presents some theoretical considerations on the cam mechanisms for actuating the working parts the equipment for opening and interrupting watering furrows are provided with; setting the optimal dimensions of the blades of the equipment for furrow opening through the experiments performed is also made. By using the cam mechanisms in the equipment for opening and interrupting watering furrows both superior quality indices in the execution of the work but also a quiet operation of the equipment are obtained and by optimizing the size of the working part, the volume of water accumulated between furrows increases significantly.

REZUMAT

În ultima perioadă, din cauza schimbărilor climatice, au avut loc modificări ale temperaturii, distribuției și cantității de precipitații, fenomene ce au condus la elaborarea de tehnologii care să sporească eficiența utilizării apei din precipitații și să susțină conservarea calității solului. În lucrarea de față sunt prezentate câteva considerente teoretice asupra mecanismelor cu camă pentru acționarea organelor de lucru cu care sunt prevăzute echipamentele de deschis și compartimentat brazde de udare, adoptarea dimensiunilor optime pentru paletele echipamentului de deschis rigole prin experimentările efectuate. Prin utilizarea mecanismelor cu camă în componența echipamentelor de deschis și compartimentat brazde de udare se obțin atât indici calitativi superiori în executarea lucrării dar și o funcționare silențioasă a echipamentului iar prin optimizarea dimensiunii organului de lucru crește semnificativ volumul de apă acumulat între minibaraje.

INTRODUCTION

The agricultural plots may lose a large quantity of rainwater by surface drainage and also large quantities of soil by erosion (*Duley, 1940*). Rainwater collection has the potential of reducing soil erosion and increasing the productivity of these areas.

Rainwater harvesting is a general term used to describe the collection and the concentration of the surface draining for different uses, including agricultural and household use (*FAO, 1993*). The “on-site” systems are the simplest and the cheapest approaches for rainwater harvesting and they can be used in many agricultural systems. Also named *water conservation work systems,* they involve some methods to increase the quantity of water stored in the soil profile by capturing or maintaining the rainwater (*Brhane et al., 2006*).

A concept referring to the “on-site” capture of rainwater through different techniques is known under the name of “*Reservoir Tillage*” (RT).

This approach, has been developed considering that the soil work may offer an increase of the surface water storage capacity and can represent one of the most efficient means to fight against both surface draining and soil erosion. RT creates basins or cavities for water retention, allowing it to infiltrate the soil, thus avoiding the drainage (*Rochester et al., 1994*).

[1] *Oprescu R., PhD. Stud. Eng.; Biris S., Prof. PhD. Eng.; Voicea I., PhD. Eng.; Ungureanu L., PhD. Eng.; Ungureanu N., Lect.PhD. Eng.; Gradila M., PhD. Eng*

RT has been defined as a system in which numerous, small surface hollows are made in order to collect and retain the rainwater and thus avoid the surface draining (*Patrick et al., 2007*). Currently, RT is used mainly against the soil erosion in areas with large volume annual rainfalls but of reduce intensities.

Along the areas with quick but small volume rainfalls and also with increased droughts, an interrupted-furrows system is used to collect the rainfall water (*Kronen M., 1994*).

The rainfalls are drained in small basins through these capture works, allowing longer times for infiltration, which further reduces the drainage and the erosion potential of soil erosion and soil particles transportation (*Ventura et al., 2005*).

By this method, the large infiltration surface created by cavities and the depth of the still water within, lead to increased infiltration speeds and therefore to the decrease of losses through surface drainages and evaporation (*Patrick et al., 2007*).

Current scenarios foresee that the climate changes will increase the water deficit in Southern Romania (Marica and Busuioc, 2004). The climate changes have the potential to affect the agriculture by rainfall changes on temperature, distribution and quantity. Rainfall changes will be one of the most critical factors that will determine the global impact of the climate changes. This problem shows the necessity to elaborate integrated technologies that will increase the efficient use of rainfall water and to sustain the soil and environment quality, ensuring greater agricultural yields at lower costs.

In order to produce the interruption, the equipment that opens and interrupts the watering furrows use different mechanisms that produce these repetitive moves.

The interrupted furrow is the result of a mechanical work of the soil that leaves furrows behind, interrupted by soil heaps, at adjustable intervals, in order to create small basins for water accumulation. During the rain, the excess water is accumulated in these basins, so that it can be slowly absorbed by the soil, eliminating the possibility of streaming outside the cultivated perimeter. This is very important, as during the rain showers the intensity of the rainfalls often overcomes the speed of water infiltration into the soil (*Biolan I. et al., 2015*). The purpose of the present study was to look for a system of actuation of the working parts of this equipment so as to obtain the optimum form of the furrow necessary to capture a maximum volume of water from the rainfalls.

Researches on the analysis of mechanisms used in the construction of agricultural machinery were carried out by (*Croitoru Şt. et al., 2017; Ivan Gh. et al., 2017; Moise V. et al., 2017; Vlăduţ V. et al., 2017)*, aiming to optimize the assemblies and subassemblies within these equipment (*Croitoru Şt. et al., 2015; Vlăduţoiu L. et al., 2017*), verified by analysis using finite element (*Biriş S., et al., 2007*), simulated and accelerated regime on hydropulse installation (*Vlăduţ V., et al., 2007*) or in real-field and simulated laboratory (*Matache M., et al., 2015; Vlăduţ V., et al., 2009*), in order to obtain the desired qualitative indices (*Cujbescu D. et al., 2016; Vlăduţ D.I. et al., 2017*).

MATERIALS AND METHODS

In the case of agricultural machines for soil processing, their working parts are controlled by the operator or, if repetitive operations are required along the work, a rigid memory can be used.

Because the cam mechanisms have the great advantage that they can carry out very complicated transmission functions, in order to obtain an optimum form of the furrow, a mechanism with a rotating cam and a rotating roller cam follower is chosen for the machine in question.

The synthesis of the rigid memory for the control of the working parts involves several phases, namely: choosing the type of mechanism for control; establishing the functions of transmission from the cam to the cam follower; determining the minimum size of the mechanism; the synthesis of the cam profile.

The transmission functions used for the control of the cam follower are chosen so that the operation of the mechanism is silent, so there are no shocks in operation, so the reduced accelerations do not exceed certain limits and finally to lead to a convenient shape for the furrows. For the present case, the transmission functions whose diagrams of the reduced accelerations are of sinusoidal and cosine form were considered.

Among the different types of cam mechanisms, a mechanism with a rotating cam and a rotating roller cam follower is chosen, for the machine concerned, according to Figure 1.

The optimization of the dimensions of this mechanism consists in determining the length *L* of the cam follower and the size of the angle ψ_o, so that in the process of the mechanism operation the permissible pressure angles α_{max} and α_{min} are not exceeded. The angle ψ_o is the angle between the vectors $\overline{BC}_0$ and $\overline{BA}$, Figure 2, (*Lasdon S.L., 1975; Marica and Busuioc, 2004; Moise et al., 2016*).

For the synthesis of the cam profile, the Pelecudi-Sava method is used (*Pelecudi and Sava, 1966*).

The synthesis of the profile of the rotating cam and the rotating roller cam follower

Figure 1 shows the kinematic diagram of the mechanism with rotating cam and the rotating roller cam follower. For the synthesis of the cam profile, the Pelecudi-Sava method is used (*Pelecudi and Sava, 1966*).

Let consider the profiles 1 and 2 of two bodies considered rigid (Fig. 1).

A system of coordinate axes is attached to the two profiles, namely: the system Ax_1y_1 for profile 1 and the system Bx_2y_2 for the profile 2. The parametric equations of the cam profile are:

$$x_1 = (XB - XA)\cos\varphi + (YB - YA)\sin\varphi + L\cdot\cos(\theta - \varphi) + r[\cos\vartheta\cdot\cos(\theta - \varphi) - \sin\vartheta\cdot\sin(\theta - \varphi)] \quad (1)$$

$$y_1 = -(XB - XA)\sin\varphi + (YB - YA)\cos\varphi + L\cdot\sin(\theta - \varphi) + r[\cos\vartheta\cdot\sin(\theta - \varphi) + \cos\vartheta\cdot\sin(\theta - \varphi)] \quad (2)$$

where:

$$XA = const, YA = const, \varphi = \varphi(t), XB + L\cos\varphi, XB + L\cdot\cos\varphi, \theta = \theta(t) \quad (3)$$

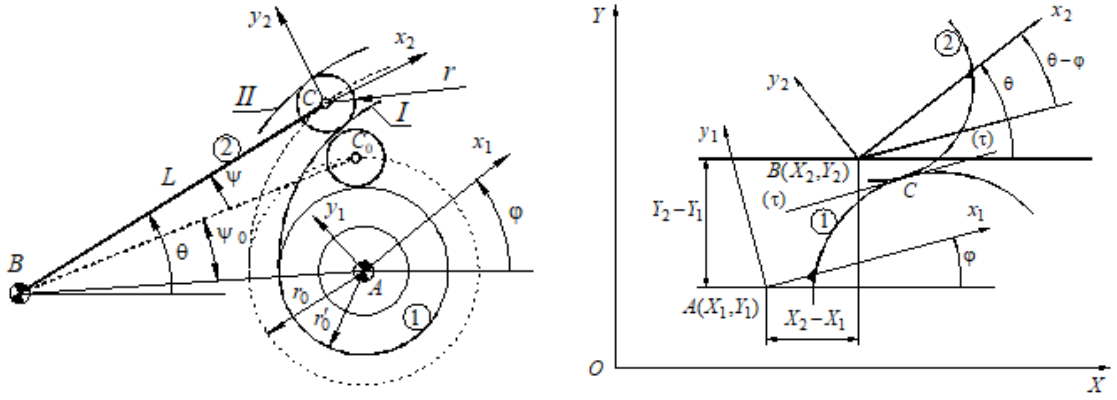

Fig. 1 - The kinematic diagram of the mechanism with rotating cam and the rotating roller cam follower

The expressions of the trigonometric functions *cos v* and *sin v*, from the relations (1) and (2), are determined using the condition of tangency between the cam and the cam follower, according to the relations (4), (5), (6), (7).

$$\sin\vartheta = \pm\frac{B}{\sqrt{A^2 + B^2}} \quad (4)$$

$$\cos\vartheta = \pm\frac{A}{\sqrt{A^2 + B^2}} \quad (5)$$

where:

$$A = \omega_1[(XB - XA)\cos\theta + (YB - YA)\sin\theta] - L(\omega_2 - \omega_1) \quad (6)$$

$$B = \omega_1[-(XB - XA)\sin\theta + (YB - YA)\cos\theta] \quad (7)$$

If the numerator and the denominator of the functions *sin v* and *cos v*, from the relations (4) and (5), are divided by ω_1, it results (8) and (9):

$$\sin\vartheta = \pm\frac{B_1}{\sqrt{A_1^2 + B_1^2}} \quad 8)$$

$$\cos\vartheta = \pm\frac{A_1}{\sqrt{A_1^2 + B_1^2}} \quad (9)$$

where:

$$B_1 = -(XA - XB)\sin\theta + (YB - YA)\cos\theta \quad (10)$$

In the end, the parametric equations of the cam profiles are, (11) and (12):

$$x_1 = (XB - XA)\cos\varphi + (YB - YA)\sin\theta + L\cdot\cos(\theta - \varphi) \pm \frac{r}{\sqrt{A_1^2 + B_1^2}}[A_1\cdot\cos(\theta - \varphi) - B_1\sin(\theta - \varphi)] \quad (11)$$

$$y_1 = -(XB - XA)\sin\varphi + (YB - YA)\cos\varphi + L \cdot \sin(\theta - \varphi) \pm \frac{r}{\sqrt{A_1^2 + B_1^2}}[A_1 \sin(\theta - \varphi) + B_1 \cdot \cos(\theta - \varphi)] \quad (12)$$

Taking into account the expressions of the parametric equations of the theoretical profile (punctiform cam follower), according to (13) and (14):

$$x_{1p} = (XB - XA)\cos\varphi + (YB - YA)\sin\varphi + L \cdot \cos(\theta - \varphi) \quad (13)$$

$$y_{1p} = -(XB - XA)\sin\varphi + (YB - YA)\cos\varphi + L \cdot \sin(\theta - \varphi) \quad (14)$$

The parametric equations of the two profiles *I* and *II*, of the form, (15), (16), respectively (17), (18) are:

- for profile *I*:

$$x_{1I} = x_{1p} - \frac{r}{\sqrt{A_1^2 + B_1^2}}[A_1 \cdot \cos(\theta - \varphi) - B_1 \cdot \sin(\theta - \varphi)] \quad (15)$$

$$y_{1I} = y_{1p} - \frac{r}{\sqrt{A_1^2 + B_1^2}}[A_1 \cdot \sin(\theta - \varphi) + B_1 \cdot \cos(\theta - \varphi)] \quad (16)$$

- for profile *II*:

$$x_{1II} = x_{1p} + \frac{r}{\sqrt{A_1^2 + B_1^2}}[A_1 \cdot \cos(\theta - \varphi) - B_1 \cdot \sin(\theta - \varphi)] \quad (17)$$

$$y_{1II} = y_{1p} + \frac{r}{\sqrt{A_1^2 + B_1^2}}[A_1 \cdot \sin(\theta - \varphi) + B_1 \cdot \cos(\theta - \varphi)] \quad (18)$$

The equipment for modelling the soil in interrupted furrows, which uses the analysed mechanism with simple cam and cam follower for forming the furrows, has the following main components, showed in Fig. 2: the cam drive-wheel *1*, the ridge plough for opening the watering channel *R*, the chain drive *2*, the cam *3*, the roller *4*, the cam follower *5*, the cam follower holder *6*, the interruption blade *7*.

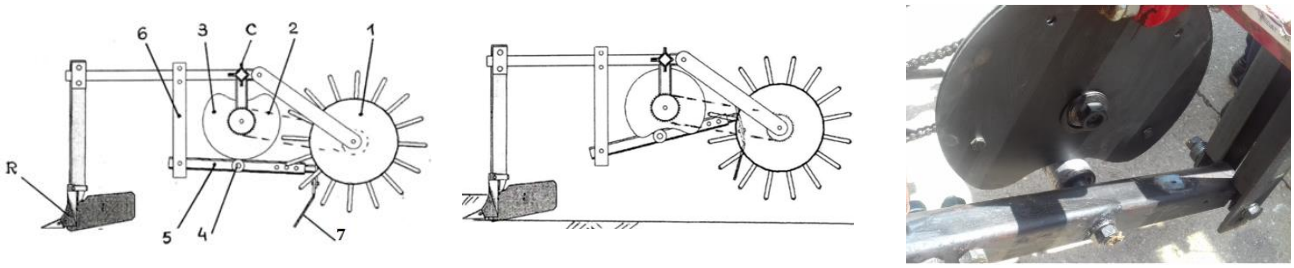

Fig. 2 - The equipment for soil modelling in interrupted furrows

In order to carry out the experiments with the equipment for modelling the soil in interrupted furrows, the mechanism with the simple rotating cam and cam follower for the formation of the furrows, was mounted on a plough for interrupting the watering furrows in vineyards, symbol PCVM 2.2, which was operated by a 45HP vegetable tractor, L445. In Fig.3 are presented aspects during the experiments.

Fig. 3 - Tractor unit L445 and the Plow PCVM 2,2b during the experiments

The qualitative indices of the work performed with the equipment for modelling the soil in furrows, during the experiments are identified in Fig.4a, and the values determined are shown in Table 1.

The dimensions of the interrupting blade are those indicated in Fig.4b.

- *The absolute mean,* V_{ma}, is calculated by the following formula (23):

$$V_{ma} = \frac{\sum_1^n \vartheta_i}{n}, \text{ [cm]} \quad (23)$$

where: v_i – the measured value, cm;

n – the number of measurements made.

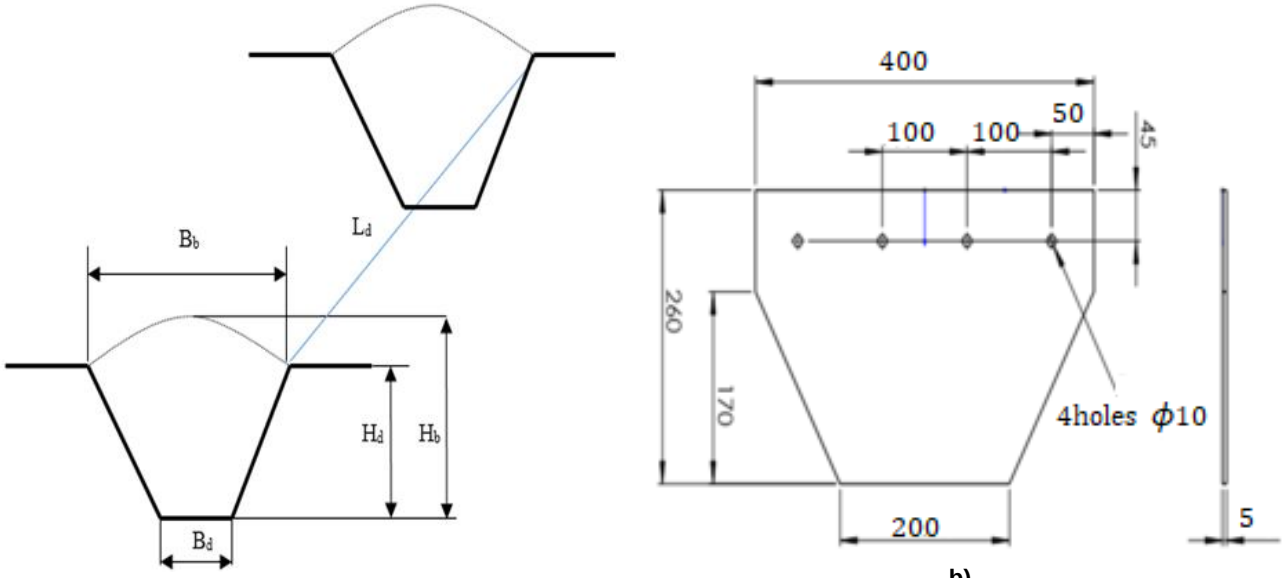

a) b)

Fig. 4 a) The dimensions of the ditch and of the soil stopper; b) The dimensions of the blade

RESULTS

For the equipment for opening and interrupting watering furrows, the optimal synthesis has been done for the mechanism with rotating cam and roller cam follower, Fig.5, knowing the following data:

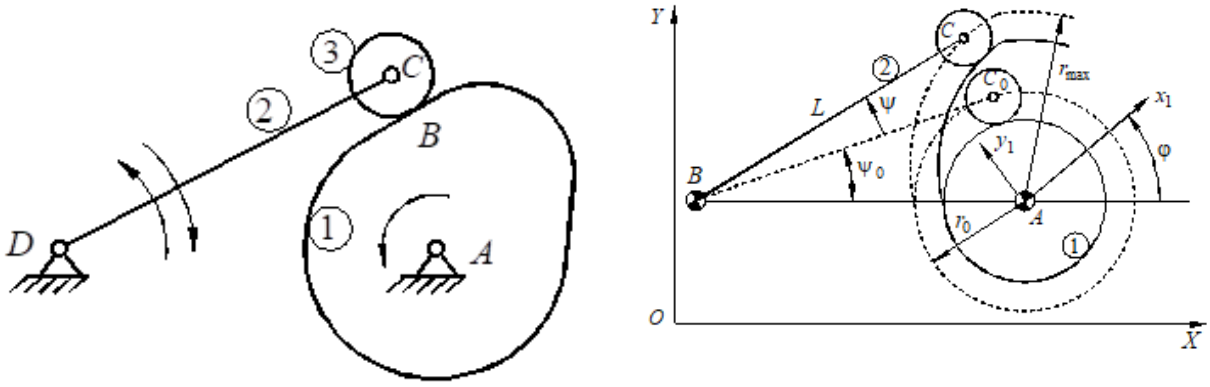

Fig.5 - Mechanism with rotating cam and rotating roller cam follower

Ψ_{max} rad or $\Psi_{max}{}^{o}$ – maximum oscillation angle of the cam follower; α_{max} rad or $\alpha_{max}{}^{o}$ – maximum pressure angle; α_{max} rad or $\alpha_{max}{}^{o}$ – minimum pressure angle; Φ_1=0.785398 rad or Φ_1=45°–cam rotation angle, corresponding to the lifting phase; Φ_2=260 rad–cam rotation angle, corresponding to the upper stationary phase; Φ_3=0.872665 rad or Φ_3=50° – cam rotation angle, corresponding to the descent phase; Φ_4=0.0872665 rad or Φ_4=5°–cam rotation angle, corresponding to the lower stationary phase; $XA=0$ mm, $YA=0$ mm – the coordinates of the base cam joint in relation to the base; $XB=-300$ mm, $YB=-200$ mm–the coordinates of the cam follower joint in relation to the base.

Following the synthesis of the rigid memory, it results:

$$L_{\,cam\ follower} = BC_2 = 327 \text{ mm} \quad (19)$$

$$r_{max}=198.223 \text{ mm} \quad (20)$$

$$r_{min}=107.499 \text{ mm} \quad (21)$$

$$r_{\,cam\ follower\ roller} = 33 \text{ mm} \quad (22)$$

Fig.6 presents the kinematic diagram of the single cam mechanism, resulting from the synthesis and the dimensions of the blade for interrupting watering furrows.

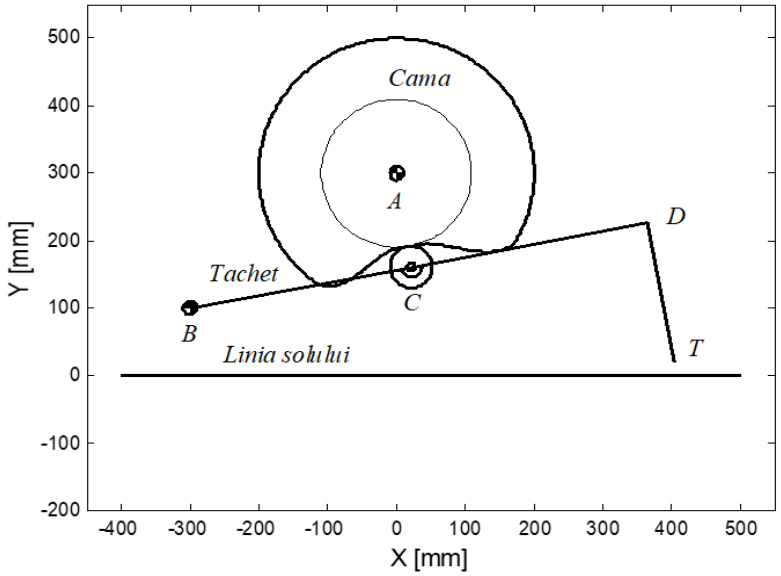

Fig.6 - Kinematic diagram of the mechanism with a simple rotating cam

- *The average square deviation*, σ_a is determined by the relation (24):

$$\sigma_a = \pm\sqrt{\frac{\sum_{i=1}^{n}(\vartheta_i - \vartheta_{ma})^2}{n-1}}, \text{ [cm]} \quad (24)$$

- *The variation index,* V_a, is calculated with the relation (25):

$$V_a = \frac{\sigma_a}{\vartheta_{ma}} \text{x} 100 \text{ [\%]} \quad (25)$$

Table 1

Qualitative working indices of the equipment with blades

Test	Qualitative working indices				
	Soil stopper height, H_b, [cm]	Ditch depth H_d, [cm]	Ditch' upper width, B_b, [cm]	Ditch' bottom width, B_d, [cm]	Intervals between stoppers L_d, [cm]
1	26.00	19.50	50.00	19.50	280.50
2	27.00	19.00	51.00	19.00	281.00
3	26.50	18.50	50.00	20.00	279.50
4	27.50	20.00	50.50	19.00	278.00
5	26.00	18.50	51.00	19.50	281.00
6	26.60	19.00	50.50	19.40	280.00
The absolute mean, V_{ma}, [cm]	26.60	19.08	50.50	19.40	280.00
The average square deviation, σ_a, [cm]	0.584	0.584	0.447	0.374	1.14
The variation index, V_a, [%]	2.19	3.10	0.90	1.90	0.40

CONCLUSIONS

Following the theoretical considerations and the results of the experiments, the following conclusions are drawn:

- the mechanism that activates the equipment with blades must have a quiet operation, and without shocks, reduced accelerations within certain limits and lead to the achievement of the convenient forms of the furrows;

- from the performed analysis, it was found that the mechanism with the rotating cam and cam follower performs the requirements mentioned in the previous paragraph in very good conditions;
- the values of the qualitative working indices, which actually represent the dimensions made by the equipment blade to make the earth stoppers are almost equal to those of the blade itself, which indicates a high precision of the equipment fit with the mechanism with rotation cam and cam follower that actuates the equipment with blades;
- the average square deviation, σ_a and the variation index, V_a, have very small values, which means that the mechanism used on the working equipment from the experiments is appropriate.

ACKNOWLEDGEMENT

This work was supported by Romanian Education and Research Ministry, through *Programme 1 – Development of the national research-development system, sub-programme 1.2 – Institutional performance – Projects for financing excellence in RDI, contract no. 16PFE* and Romanian Ministry of Research and Innovation CCDI -UEFISCDI, "Complex system of integral capitalization of agricultural species with energy and food potential", project number PN-III-P1-1.2-PCCDI-2017-0566, Contract no. 9PCCDI/2018.

REFERENCES

[1] ***Aquaproiect SA (2017), Project Furrow soil modelling device divided into two constructive solutions, Financing contract no. 4639/2017;

[2] Biolan, I., Serbu, I., Mardare, F., Biolan, C., (2017), *Modern techniques for irrigating agricultural crops*, AGIR Publishing House, Bucharest / Romania;

[3] Biriş, S., Maican, E., Faur, N., Vladut, V., Bungescu S., (2007), Fem model for appreciation of soil compaction under the action of tractors and agricultural machines, *Proceedings of the 35 International Symposium on Agricultural Engineering "Actual Tasks on Agricultural Engineering"*, pp. 271…280, Opatija / Croatia

[4] Brhane, G., Wortmann, C.S., Marno, M., Gebrekidan, H., Belay, A., (2006), Micro basin tillage for grain sorghum production in semiarid areas of northern Ethiopia, *Agron. J.,* 98: pp.124-128;

[5] Croitoru, St., Marin, E., Badescu, M., Manea, D., Vladut, V., Ungureanu, N., Manea, D., Boruz, S., Matei Gh., (2015), Researches regarding the minimum work for improving soil fertility by deep loosening, *Proceedings of the 43 International Symposium on Agricultural Engineering "Actual Tasks on Agricultural Engineering",* pp. 165-176, Opatija / Croaţia;

[6] Croitoru, Şt., Vladut, V., Voicea, I., Gheorghe, Gh., Marin, E., Vladutoiu, L., Moise, V., Boruz, S., Pruteanu, A., Andrei, S., Păunescu, D., (2017), Structural and kinematic analysis of the mechanism for arable deep soil loosening, *Proceedings of the 43 International Symposium on Agricultural Engineering "Actual Tasks on Agricultural Engineering",* pp. 207-216, Opatija / Croatia;

[7] Cujbescu, D., Vladut, V., Voicu, Gh., Ungureanu, N., (2016), Researches on obtaining higher qualitative indices for the sowing work, *15th International Scientific Conference "Engineering for Rural Development"*, Proceedings vol. 15, pp. 1305-1311, Jelgava / Latvia;

[8] Duley, F.L. (1990), Surface factors affecting the rate of intake of water by soils, *Soil Sci. Soc*. Am. 4: pp.60-64;

[9] FAO (1993), Soil tillage in Africa: needs and challenges, *FAO Soils Bulletin* 69. Rome;

[10] Ivan, Gh., Vladut, V., Ciuperca, R., Moise, V., (2017), Kinematic scheme of the equipment to reed harvesting machine MRS, *16th International Scientific Conference " Engineering for Rural Development "*, Proceedings vol. 16, pp. 841-847, Jelgava / Latvia;

[11] Kronen, M. (1994), Water harvesting and conservation techniques for small-holder crop production. *Soil Tillage Res*. 32: pp.71-86;

[12] Lasdon, S.L., (1975), Theory of optimization of large systems, *Technical Publishing House*, Bucharest / Romania;

[13] Marica, A.C., Busuioc, A., (2017), The potential of climate change on the main components of water balance relating to maize crop, *Romanian J. Meteor.* 6(1-2): pp.50-57, Bucharest / Romania;

[14] Matache, M., Voicu, Gh., Cardei, P., Vladut, V., Persu, C., Voicea, I., (2015) - Accelerated test of MAS 65 deep soil loosening machine frame, *Proceedings of the 43 International Symposium on Agricultural Engineering "Actual Tasks on Agricultural Engineering",* pp. 131-140, Opatija / Croatia;

[15] Moise, V., Maican, E., Moise, St. I., (2018), *Numerical methods. Applications in MATLAB*, Printech Publishing House, Bucharest / Romania;

[16] Moise, V., Simionescu, I., Ene, M., (2016), *Optimal synthesis of cam mechanisms*, Printech Publishing House, Bucharest / Romania;

[17] Moise, V., Vladut, V., Tabara, I., Adir, G., Moise, Şt.I., Dudici, L., Niculae, E., Rotaru, Al., (2017), The synthesis of the digging pits mechanisms for shrubs with the precise-mathematical drawing of a curve, *Proceedings of the 45 International Symposium on Agricultural Engineering "Actual Tasks on Agricultural Engineering",* pp. 239-248, Opatija / Croatia;

[18] Patrick, C., Kechavarzi, C, James, I.T., Dogherty, M.O., Godwin, R.J. (2007), Developing reservoir tillage technology for semi-arid environments, *Soil Use and Management,* 23: pp.185-191;

[19] Pelecudi, Chr., Sava, I., (1976), On the unitary analysis and synthesis of the mechanisms with superior couplings, *Studies and researches of Applied Mechanics,* Bucharest / Romania*;*

[20] Pelecudi, Chr., (1967), Basics of mechanism analysis*, Publishing House of the Academy of the Socialist Republic of Romania*, Bucharest / Romania;

[21] Rochester, E.W., Hill, D.T., Yoo, K.H. (1994), Impact of reservoir tillage on run-off quality and quantity, *Trans. ASABE* 37(4): 1183-1186;

[22] Ventura, E., Norton, L.D., Ward, K., Lopez-Bautista, M., Tapia-Naranjo, A. (2005), A new reservoir tillage system for crop production in semi-arid areas, *ASAE Annual Meeting ASABE*.

[23] Vladut, D.I., Vladut, V., Grigore, I., Biris, S., (2017), Experimental research on qualitative indices of work for equipment for seedbed preparation in conservative system, *16th International Scientific Conference " Engineering for Rural Development "*, Proceedings vol. 16, pp. 1174-1179, Jelgava / Latvia;

[24] Vladut, V., Gangu, V., Pirna, I., Bajenaru, S., Biria, S., Bungescu, S., (2007), Complex tests of the resistance structures in simulated and accelerated regime on hydropulse installation, *Proceedings of the 35 International Symposium on Agricultural Engineering "Actual Tasks on Agricultural Engineering",* pp. 393-404, 2007, Opatija / Croaţia;

[25] Vladut, V., Popa, L., Danciu, A., Bungescu, S., Biris, S., Paraschiv, G., (2009), Soil pressure determination in real-field and simulated laboratory, *Proceedings of the 37 International Symposium on Agricultural Engineering "Actual Tasks on Agricultural Engineering",* pp. 107-116, Opatija / Croaţia;

[26] Vladut, V., Gheorghe, G., Marin, E., Biris, S.Șt., Paraschiv, G., Cujbescu, D., Ungureanu, N., Gageanu, I., Moise, V., Boruz, S., (2017), Kinetostatic analysis of the mechanism of deep loosening system of arable soil, *Proceedings of the 45 International Symposium on Agricultural Engineering "Actual Tasks on Agricultural Engineering",* pp. 217-228, Opatija / Croaţia;

[27] Vladutoiu, L., Cardei, P., Vladut, V., Fechete, L., (2017), Modern trends in designing and selecting the machine / equipment for soil deep tillage, *16th International Scientific Conference " Engineering for Rural Development "*, Proceedings vol. 16, pp. 1415-1420, Jelgava / Latvia.

IMPROVEMENT OF THE STRUCTURAL LAYOUT OF POTATO PLANTERS' COULTER GROUP
/
УСОВЕРШЕНСТВОВАНИЕ КОНСТРУКТИВНОЙ СХЕМЫ СОШНИКОВОЙ ГРУППЫ КАРТОФЕЛЕСАЖАЛОК

Dorokhov Alexey Semenovich, Ponomarev Andrey Grigoryevich, Zernov Vitaly Nikolaevich, Petukhov Sergey Nikolaevich, Aksenov Alexander Gennadievich, Sibirev Aleksey Viktorovich
FSBSI "Federal Scientific Agronomic and Engineering Centre VIM"/ Russian
Telephone: 89645843518; E-mail: sibirev2011@yandex.ru
DOI: https://doi.org/10.356.33/inmateh-63-08

Keywords: *morphological features, potato plant, potato planters, coulter groups, angle of attack, coulter suspension*

ABSTRACT
Structural layouts of coulters and their groups in potato planters are justified in the article based on the morphological features of the potato plant, its requirements for growing conditions and ensuring the quality of the planting process. The purpose of coulter groups is to form a bed for placing tubers with a loose layer of soil in 5-8 cm and sealing them with loosened soil to a certain depth. To substantiate the type of potato planter coulters that meet the requirements for potato growing conditions to the maximum extent possible, optimize the parameters of coulter groups that automatically ensure the stability of the coulter travel depth when imitating irregularities of the field microrelief. A comparative analysis of the impact on the soil of the most common anchor coulters with a blunt angle of soil entry and a sharp angle with an individual floating suspension is given, and indicators of the quality of their operation are described. It was found that coulters with an individual floating suspension and an acute angle of soil entry meet the requirements for potato growing conditions to the maximum extent possible. In order to ensure travel stabilization of such a coulter at a given depth when imitating field irregularities, a version of the coulter group has been developed that provides automatic correction of the coulter's angle of attack when changing its travel depth. Experimental studies have optimized the parameters of the coulter suspension that ensure automatic imitation of field microrelief irregularities up to 20 cm deep within the initial requirements for potato planting machines. Coulters with an individual floating suspension and a sharp angle of soil entry most fully meet the requirements for potato growing conditions to the maximum extent possible. A coulter group with a suspension aspect ratio of 150:200:400:400 cm and an acute angle of coulter entry into the soil provides automatic maintenance of the set coulter travel depth within the initial requirements (±2 cm) for irregularities in the field microrelief of up to 200 mm. In this case, the bottom and walls of the furrow are not compacted.

РЕЗЮМЕ
Конструктивные схемы сошников и в целом сошниковых групп картофелесажалок в статье обосновываются исходя из морфологических особенностей картофельного растения, его требований к условиям произрастания и обеспечения качественного выполнения технологического процесса посадки. Назначение сошниковых групп - формировать ложе для размещения посадочных клубней с рыхлой прослойкой почвы в 5 – 8 см. и заделки их разрыхленной почвой на определенную глубину. Обосновать тип сошников картофелесажалки наиболее полно удовлетворяющих требованиям к условиям произрастания картофельного растения. Оптимизировать параметры сошниковых групп, автоматически обеспечивающих стабильность глубины хода сошника картофелесажалки при копировании неровностей микрорельефа поля. Дан сравнительный анализ воздействия на почву наиболее распространенных анкерных сошников с тупым углом вхождения в почву и острым с индивидуальной плавающей подвеской, приведены показатели качества их работы. Установлено, что наиболее полно удовлетворяют требованиям к условиям произрастания картофельного растения сошники с индивидуальной плавающей подвеской и острым углом вхождения в почву.

С целью обеспечения стабилизации хода такого сошника на заданной глубине при копировании неровностей поля разработана версия сошниковой группы, обеспечивающей автоматическую коррекцию угла атаки сошника при изменении глубины его хода. Экспериментальными исследованиями оптимизированы параметры подвески сошника обеспечивающие автоматическое копирование неровностей микрорельефа поля глубиной до 20 см. в пределах исходных требований на картофелепосадочные машины. Наиболее полно удовлетворяют требованиям к условиям произрастания картофельного растения сошники с индивидуальной плавающей подвеской и острым углом вхождения в почву. Автоматическое поддержание заданной глубины хода сошника в пределах исходных требований (±2 см) при неровностях микрорельефа поля до 200 мм обеспечивает сошниковая группа с соотношением сторон подвески 150:200:400:400 см и острым углом вхождения сошника в почву. При этом дно и стенки борозды не уплотняются.

INTRODUCTION

Coulter groups of potato planters include coulters with furrow-closing working bodies intended to form a bed for placing tubers and sealing them to a certain depth. Currently, the most common are anchor coulters with a blunt angle of soil entry and a rigid or individual floating suspension (foreign planters). Soviet-made planters were equipped with coulters with a sharp angle of soil entry and an individual floating suspension *(Aldoshin N.V. et al, 2015; Aldoshin N.V. et al, 2014; Kukharev O.N. et al, 2018; Kurdyumov V.I. et al, 2019; Kurdyumov V.I. et al, 2016)*.

Substantiation of the structural layout of coulters and coulter groups in general should be carried out based on the morphological features of the potato plant and its requirements for growing conditions.

The root system of potatoes grown from tubers is fibrous. The roots initially spread mainly deep into the soil and to the sides. The main mass of roots (60–80 %) extends deep into the arable layer under the mother tuber. In highly compacted soils (up to 1.35 – 1.50 g/cm^3), the root system develops very poorly and is concentrated in the surface layer of the soil, which leads to late emergence of crops and loss of yield. The root system of potatoes develops much better on loose soils with a density of 1.10–1.20 g/cm^3*(Bashkirtsev V.I. et al, 2017; Lobachevsky Ya.P. et al, 2016; Laryushin N.P. et al, 2015).*

An important factor is the effect of the coulter on the density of soil – compaction of the furrow bottom and walls or loosening. The loose soil layer in the furrow provides normal emerging crops. When the furrow bottom is loosened sufficiently well, the rolling of tubers during planting decreases, the power of the root system increases and this ensures higher yields *(Sibirev A.V. et al, 2019).*

Thus, based on biological characteristics of potato plants, the basic requirements for coulter groups of potato planters are as follows: the furrow bottom should not be compacted; a layer of loose soil at the furrow bottom should be 4 to 5 cm; when placing mineral fertilization between potatoes and fertilizers, a layer of loose soil with a minimum thickness of 2 cm should be provided; the coulter suspension must satisfactorily replicate field roughness up to 200 mm high; the deviation from a predetermined depth of tubers should not exceed 2 cm *(Zykin E.S. et al, 2017; Kukharev O.N., 2006; Kalinin A.B. et al, 2015; Kalinin A.B. et al, 2016; Kukharev O.N. et al, 2018).*

The purpose of our research is to justify the type of potato planter coulters that meet the requirements for potato growing conditions to the maximum extent possible. Optimize the parameters of coulter groups that automatically ensure the stability of the coulter travel depth within initial requirements for potato planters when imitating irregularities of the field microrelief up to 20 cm deep.

MATERIALS AND METHODS

A coulter with a blunt angle of entry tends to dig out under the action of the soil from the force P_2 (Figure 1). At the defined depth, it is held by the weight of the planters significantly unloading the support and driving wheels of the machine.

This reduces the grip of the drive wheel on the ground and its slippage while increasing the set planting pitch until the formation of gaps.

Minor fluctuations in the values of soil density in different parts of the field significantly change the value of the traction force P_1, and, consequently, the reaction of the soil from the force P_2, which also changes its value (as a component of the resulting force P). All this affects the depth of the coulter travel and can even result in that tubers are not covered with soil and emerge on the field surface. In addition, the uneven depth of tuber planting is affected by the field roughness; especially this affects the rigid suspension of the coulter.

A coulter with a blunt angle of soil entry pushes soil particles into the furrow bottom and shifts them to the sides. As a result, the bottom and walls of the furrow are compacted. This phenomenon is especially seen on heavy soils with variable humidity along the rut length.

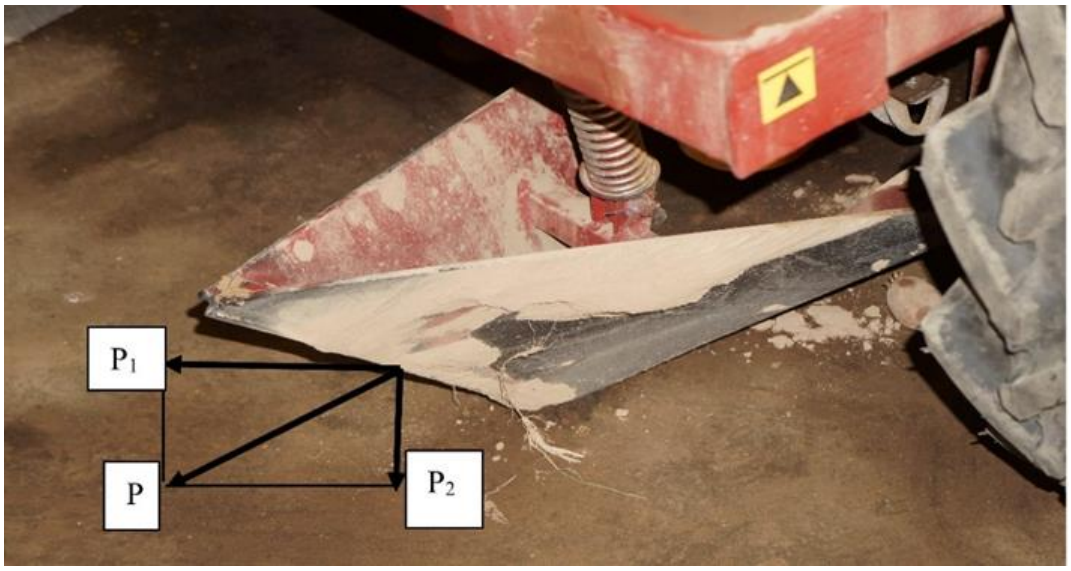

Fig. 1 – Coulter with a blunt angle of soil entry of L-202 potato planter
P_1 – is the tractor pulling force; P_2 – is the force of the planter weight; P – is the resulting force

The coulter with an acute angle of soil entry works in a self-deepening mode. The coulter tries to go deeper into the soil under the action of the soil from the force P_2 (Fig. 2) – the vertical component of the resulting force *P* when the tractor applies the pulling force P_1. The gauge wheel limits the depth of the coulter travel. In this case, the coulter does not compact, but loosens the bottom and walls of the furrow.

To increase the thickness of the loose layer at the furrow bottom, and to form a soil layer between fertilizers and tubers when working with fertilizers, *8* blades are usually provided in the front part of the coulter body, or a V-shaped sweep is installed *(Kukharev O.N. et al, 2018; Sibirev A.V. et al, 2018).*

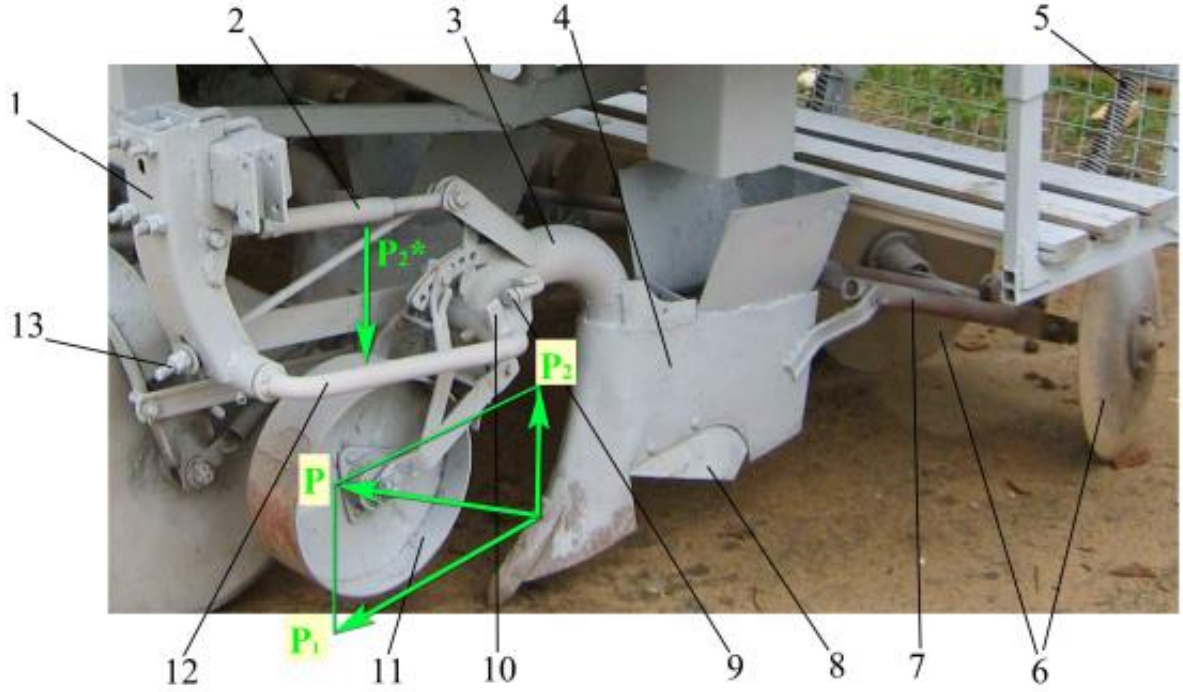

Fig. 2 – Coulter group of the KSU-4 clone potato planter (VIM)
1 – bracket attaching the coulter to the planter frame; 2 – upper link of the suspension; 3 – coulter bracket; 4 – coulter; 5 – push-rod; 6 – burrow-closing discs; 7 – disc mounting frame; 8 – blade; 9 – stop's adjusting bolt; 10 – stop; 11 – gauge wheel; 12 – lower suspension; 13 – Panhard rod

Figure 2 shows a coulter group for machines used to plant potato clones designed by the Federal State Budgetary Research Institution “Federal State Agricultural Centre VIM” (FGBNU FNAC VIM) with self-deepening coulters and an individual floating suspension of parallelogram type, pos. *5, 6, 7*. Such coulters were installed on Soviet-made potato planters SN-4B, SKS-4, KSM-4, etc.

The angle of soil entry of coulter *4* depending on soil density is set by the length of upper rod *2* of the suspension. The depth of the coulter travel is changed by turning the fork of gauge wheel *11* relative to the coulter bracket. In the front part of the coulter body there is a shield that forms a channel for directing mineral fertilizers into the bed formed by the coulter tip. Blades *8* form a loose layer of soil at the furrow bottom and provide a soil layer between the fertilizer and tubers.

To limit the coulter lowering when transferring the planter to the transport position, there is stop *10* at the end of rod *12*. Adjustment bolt *9* is installed in front of the stop in coulter bracket *3*. This bolt touches thrust stop *10* when lifting the planter to the transport position.

The parallelogram provides diagonal rod *13*, one end of which is pivotally attached to the coulter bracket and the other one, having a threaded and screwed nut, is passed through the slot of front bracket *1*. The rod restricts the coulter raising preventing the coulter body from resting against structural elements of the planter during operation.

Frame *7* is pivotally attached to the coulter sidewalls for mounting through the curved half-axes of furrow-closing disks *6* and clamping telescopic rod *5*. The upper part of rod *5* is pivotally attached to the planter frame. Semi-axes of the furrow-closing disks can be rotated relative to the frame in order to regulate the angle of attack of the disks, which determines the shape of the ridge. Rod *5* provides holes for adjusting the compression of the pressure spring, and, consequently, the pressure of the disks onto the soil, which affects the depth of tubers and the height of ridges.

A coulter with a sharp angle of soil entry, a gauge wheel and a floating parallelogram suspension with a length of longitudinal rods of 400 mm satisfactorily imitate the field irregularities with a height up to 150 mm. Blades *8* in the front part of the coulter body provide a loose layer of soil at the furrow bottom up to *5* cm. The disadvantage of the potato planter coulters considered is that, despite imitating field irregularities, the depth of tuber planting in the soil is not always uniform. This is due to the fact that when imitating field irregularities while moving the coulter down vertically, the tip of the coulter falls into denser soil layers, and since the parallelogram suspension mechanism keeps the coulter's angle of attack constant, the reaction of the soil under the action of the vertical component of the resultant force *P* (Figure 2) increases.

The vertical component of the force pressing the wheel to the soil P_2^* is proportionally increased, this force makes the wheel pressed into the loose surface layer of soil, the planting depth of tubers increased (uneven depth of planting along the rut length, depending on the soil density, up to ±4 cm). Uneven depth of the coulter travel affects the seedling vigour, especially when planting mini-tubers in elite potato seed production.

The value and direction of the resultant force *P* (Figure 2) depends on the operating speed of the planting machine, the coulter travel depth, the soil density, its humidity, coefficient of friction of the coulter surface with the soil and the angle of soil entry of the coulter (angle of attack). In the design of the coulter group, we can adjust the value of the coulter angle of soil entry. When the angle of attack increases, the coulter tries to go deeper into the soil, which is prevented by the force P_2^* on the side of the gauge wheel *11* (Figure 2), pushing it into the soil. When the coulter angle of attack decreases, the force P_2^* decreases and the gauge wheel is less pressed into the ground.

To stabilize the coulter travel at a given depth, when imitating irregularities, it is necessary to automatically change the value of the angle of attack β (Figure 4), depending on the change in the field microrelief.

The stated technical problem is achieved by that the individual floating suspension of the coulter in the coulter group of planters (Figure 3 and Figure 4) is not a parallelogram, but a hinge quadrilateral with the sides formed by the mounting bracket of the coulter group of planters to frame *1* (side AB), coulter body *5* (side CD) and longitudinal upper *2* (side BC) and bottom *4* (side AD) rods.

In this case, the distance between the hinges of side *1* is less than that of side *5*, and the upper rod *2* and lower rod *4* are equal to each other. Moreover, the straight line passing through the attachment points of the longitudinal rods to the mounting bracket of the coulter group is perpendicular to the field surface, and the upper suspension rod has telescopic coupling *3* for setting the initially set coulter angle of attack.

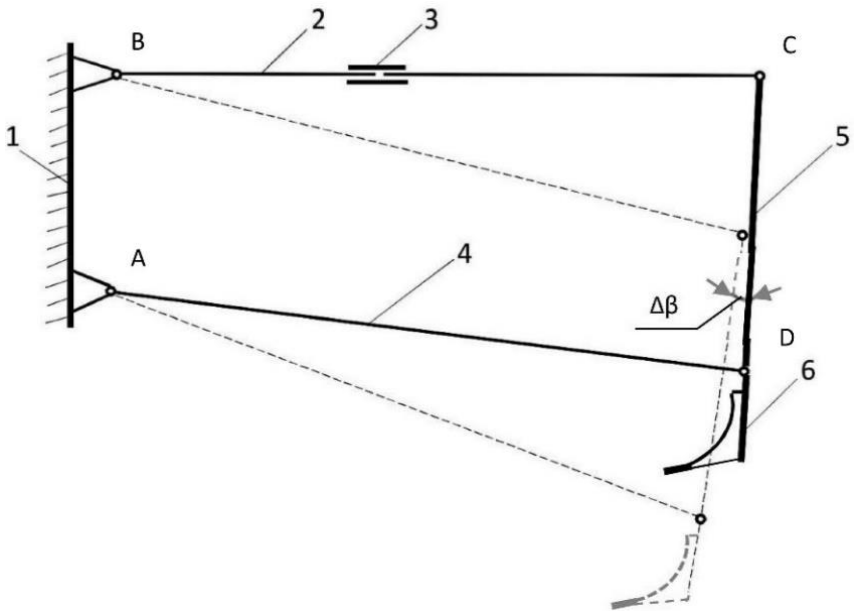

Fig. 3 – Schematic diagram of the coulter individual floating suspension operation

1 – planters to frame; 2 – longitudinal upper rods; 3 – telescopic coupling; 4 – longitudinal bottom rods; 5 – coulter body; 6 – coulter

The value of change in the angle of attack ∆β depending on the change in the coulter travel depth is achieved by reducing the distance between the hinges of the quadrilateral of side *1* (AB) in relation to side *5* (CD) (Figure 3).

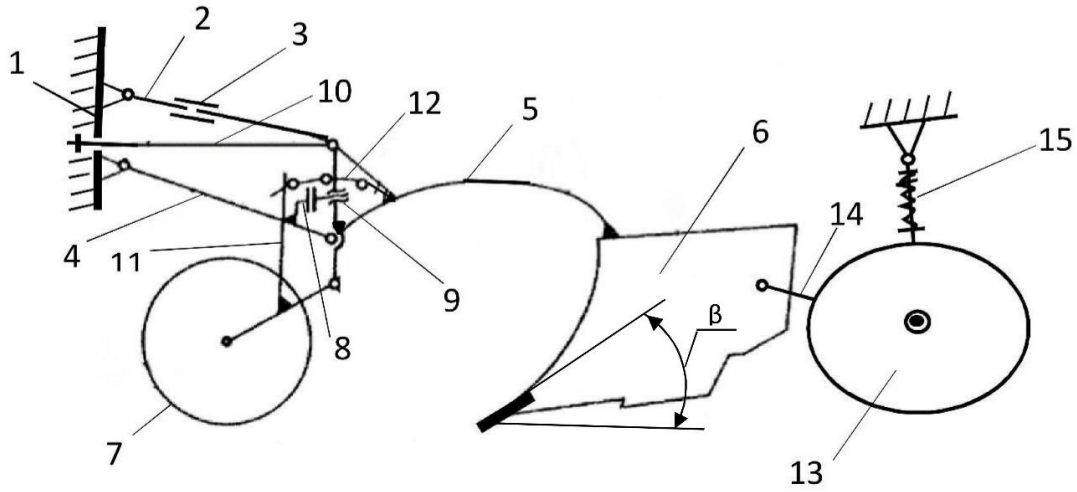

Fig. 4. – Coulter group of potato planters with automatic stabilization of planting depth

1 – frame; 2 – upper rod; 3 – telescopic coupling; 4 – lower thrust; 5 – coulter body; 6 – coulter; 7 – gauge wheel; 8 – stop of coulter lowering limiter; 9 – stop's adjusting bolt; 10 – diagonal thrust of coulter raising limiter; 11 – plug of gauge wheel; 12 – adjustment sector for coulter depth; 13 – burrow-closing disks; 14 – disk fixing frame; 15 – spring-loaded push rod

The developed coulter group of planters with automatic stabilization of planting depth (Figure 4) contains the bracket attaching the coulter to planter frame *1*, upper rod *2* of coulter suspension with telescopic coupling *3* to set the initial angle of attack *β* of the coulter, lower thrust *4* of coulter suspension, coulter body *5*, coulter *6*, gauge wheel *7*, stop of coulter lowering limiter *8*, stop's adjusting bolt *9*, diagonal thrust of coulter raising limiter *10*, plug *11* of gauge wheel, adjustment sector *12* for coulter depth, burrow-closing disks *13*, disk fixing frame *14*, spring-loaded push rod *15*.

Preparing the coulter group for operation and imitation of field irregularities is as follows.

The initially set angle of soil entry of coulter *6* is provided by the length of upper rod *2* of the suspension using telescopic coupling *3*. The travel depth of coulter *6* is set by turning fork *11* of gauge wheel *7* relative to sector *12* fixed to the coulter body. The sharp angle of the coulter entering into the soil loosens the furrow bottom.

By adjusting the length of bolt *9* and changing the position of the nut on rod *10*, the necessary amount of the coulter travel in vertical direction is achieved, which makes it possible to imitate field irregularities.

The travel depth of coulter *6* is set and maintained by the gauge wheel. When the coulter group overcomes field irregularities and moves the coulter down vertically, the coulter tip falls into denser soil layers. In this case, the resultant of soil resistance forces on the coulter increases, but due to the pre-set aspect ratio of the four-link suspension mechanism, the angle of attack of coulter *6* decreases (Figure 3), and the vertical component of the resultant of soil resistance forces remains approximately constant. The vertical component of the force pressing the gauge wheel to the soil remains a constant value.

As a result, the gauge wheel is pressed into the surface layer of the soil by about the same amount, and the tuber bed formed by the coulter at the furrow bottom is automatically stabilized at a given depth.

RESULTS AND DISCUSSION

In order to optimize the ratio of sizes of suspension rods that provide the most stable coulter depth travel, four variants of side lengths of the four-link mechanism were adopted in experimental studies (Figure 3) with the following AB:CD:BC:AD ratio, respectively:

a) 4:4:8:8 or 200:200:400:400 in mm - parallelogram;
b) 3:4:8:8 or 150:200:400:400 in mm;
c) 2:4:8:8 or 100:200:400:400 in mm;
d) 1:4:8:8 or 50:200:400:400 in mm.

Researches of experimental coulter groups were carried out on a two-row clone planting machine developed and manufactured by the FGBNU FNAC VIM experimental plant (Figure 5).

The test site is the experimental field of Redkinskaya Agro-Industrial Complex LLC in Koshelevo village, Konakovsky District, Tver Region. During the tests, the planter was combined with MTZ-82 tractor of traction class 1.4.

Fig. 5 – Experimental coulter group on VIM clone landing machine

Soil type during testing – sod-podzolic (light loam), structure – small-lumpy, relief – smooth, microrelief-ridged with a difference of ridges up to 200 mm (*Sibirev A.V. et al, 2018, Sibirev A.V. et al, 2019).*

Soil moisture and hardness in the layers, respectively:

0 to 5 cm.	14.5 %	0.35 MPa
5 to 10 cm.	16.7 %	0.54 MPa
10 to 15 cm.	19.5 %	1.29 MPa
15 to 20 cm.	22.8 %	1.34 MPa

Soil temperature during testing in the layer from 0 to 20 cm was + 10.0°C, air temperature was +12.0°C.

In order to obtain correctly comparable experimental data, a section of the field with a specially cut microrelief was prepared for testing (Figure 6).

Fig. 6 – Experimental field section

Express assessment of the surface microrelief of the experimental field section was carried out for test sections 5 meters long (Figure 7). This made it possible to carry out a reliable comparative assessment of the tested coulter groups of potato planters (*Sorokin A.A., 2006*).

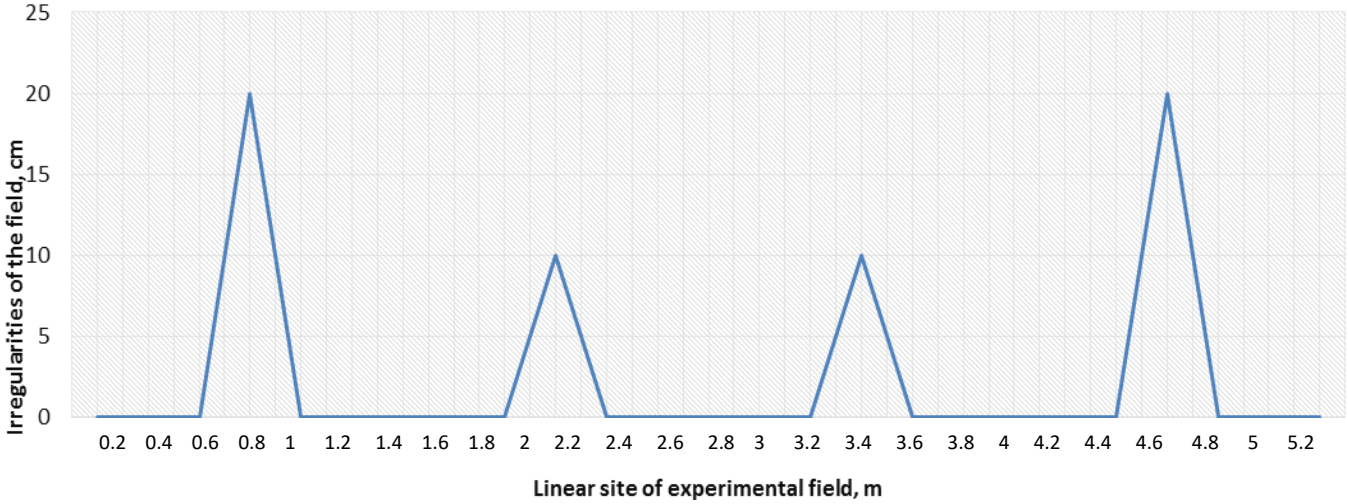

Fig. 7 – Microrelief of the experimental field

During the research, four pairs of coulters with different ratios of suspension rod lengths were alternately installed on a two-row clone planter in accordance with the experiment plan and the planter was rolled three times over the experimental field section in the direction perpendicular to the cut irregularities with a constant movement speed of 3.0 km/h.

The coulter travel depth was the distance from the surface of the field formed after running planters with raised sealing disks (edges of the formed bed for tubers) to the loose layer of the furrow bottom. Measurements of the coulter travel depth on a linear section of the experimental field were made every 20 cm. From six repetitions of measurements at each point (2 coulters with 3 repetitions), the average value was determined and graphs of the coulter depth were drawn for each suspension typical size (Figure 8).

For each coulter group, average values of the coulter travel depth, average square deviations and coefficients of variation were then determined from measurements that were average for points.

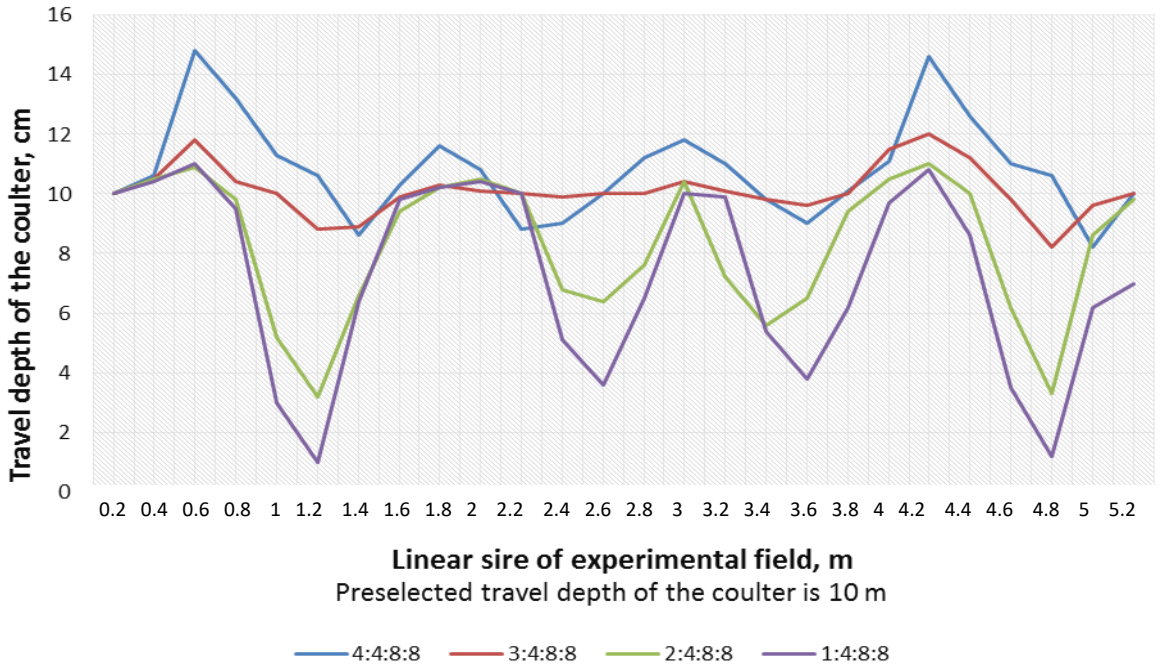

Fig. 8 – The effect of the coulter suspension ratio AB CD BC AD to the uniformity of the coulter travel when passing rough spots

The test results after mathematical processing of the obtained data are shown in Table 1.

Table 1

Uniformity of the coulter travel depth depending on the aspect ratio of its suspension

Aspect ratio of the coulter suspension mm	Δβ at the height of irregularities mm		Coulter travel depth cm					
	100	200	defined	max	min	av.	ϭ±cm	V %
200:200:400:400	0°	0°	10.0	15.0	8.0	10.8	3.67	34.0
150:200:400:400	6°	7°	10.0	12.0	8.0	10.0	1.78	17.8
100:200:400:400	10°	16°	10.0	11.0	3.0	8.1	3.92	48.4
50:200:400:400	18°	29°	10.0	11.0	0.5	6.8	5.28	77.6

Δβ is the change of the coulter angle of attack when overcoming irregularities
ϭ - *standard deviation*
V - *the coefficient of variation*

The graphic images in Figure 8 clearly show the effect of the coulter suspension aspect ratio on the deviation of its travel depth from the set depth when passing rough spots of the field surface.
The deviation of the coulter travel depth with a conventional parallelogram suspension (200:200:400:400) is observed to be increased within 4 cm from the depth defined for field irregularities up to 20 cm, which exceeds the initial requirements by 2 cm. For field irregularities up to 10 cm, this coulter group easily meets the initial requirements.

In a coulter group with a suspension aspect ratio of 150:200:400:400, the deviation of the travel depth from the set one does not exceed 2 cm, even if the field is uneven, the average travel depth of the coulter remains at the set level.

Travel of the coulter with the third type of suspension (100:200:400:400) deviates from a predetermined value decreasing to a depth of 6 cm for field irregularities of 10 cm and to a depth of 3 cm for microrelief irregularities of 20 cm, which exceeds the limit of tolerances defined by initial requirements for potato planting machine.

The travel depth of the coulter with the fourth type of suspension (50:200:400:400) deviates even more from the set point, and for irregularities of 20 cm the furrow bottom almost reaches the field surface.

The travel deviation of the coulter of the third and fourth types of suspensions in terms of depth decrease from the set point is explained by a decrease in the coulter angle of attack β to a negative value, which causes its abrupt deflection and a tendency to reach the field surface due to inertia forces. It is obvious that with an increase in the planting machine speed, the operation quality of the last two types of coulter suspensions will deteriorate further and the machine will have oscillatory movements. Therefore, the third and fourth types of suspensions are unacceptable, as they do not meet the initial requirements for potato planting machines.

Conclusions from the analysis of graphs (Figure 8) are confirmed by averaged probabilistic indicators (Table 1). Thus, the average value of the coulter travel depth with a parallelogram suspension deviates slightly (by 0.8 cm) from the set value since it increases with an average square deviation of ±3.67 cm and a coefficient of variation of 77.6%. The average value of the coulter travel depth with a suspension aspect ratio of 150:200:400:400 corresponds to its set value with a much less significant mean square deviation of ±1.78 cm and a coefficient of variation of 17.8 %. The average values and variational indicators of suspensions with an aspect ratio of 100:200:400:400 and 50:200:400:400 are far beyond the initial requirements for potato planting machines and therefore cannot be applied to planters in the practice of potato planting.

CONCLUSIONS

Coulters with an individual floating suspension and an acute angle of soil entry meet the requirements for potato growing conditions to the maximum extent possible.

A coulter group with a suspension aspect ratio of 150:200:400:400 cm and an acute angle of coulter entry into the soil provides automatic maintenance of the set coulter travel depth within the initial requirements (±2 cm) to potato planting machines for irregularities in the field microrelief of up to 200 mm. In this case, the bottom and walls of the furrow are not compacted.

Coulters with a parallelogram suspension (ratio of rod lengths is 200:200:400:400 cm) ensure uniformity of the coulter travel depth along the rut length within ±2 cm with irregularities in the field microrelief of up to 100 mm.

Reducing the length of the AB rod (Figure 3 position 1) of the coulter suspension up to 100 cm or less causes oscillating movements of the coulter, which results in its travel depth uniformity going far beyond the initial requirements.

REFERENCES

[1] Aldoshin N.V., Didmanidze O.N., (2015), *Engineering and technical support for the quality of mechanized work: Monograph (Инженерно-техническое обеспечение качества механизированных работ*: *Монография),* State Agrarian University - Moscow Agricultural Academy named after K.A. Timiryazev. 188 p. Moscow / Russia;

[2] Aldoshin N.V., Gorbachev I.V., Zolotov A.A. and others. (2014), *Agricultural machines (Сельскохозяйственные машины),* State Agrarian University - Moscow Agricultural Academy named after K.A. Timiryazev. 149 p. Moscow / Russia;

[3] Bashkirtsev V.I., Aldoshin N.V., (2017), *Mechanized work quality assurance during the operation of agricultural machinery (Обеспечение качества механизированных работ при эксплуатации сельскохозяйственной техники, Учебное пособие),* State Agrarian University - Moscow Agricultural Academy named after K.A. Timiryazev. 96 p., Moscow / Russia;

[4] Kalinin A.B., Smelik V.A., Teplinsky I.Z., Pervukhina O.N., (2015), Selection and substantiation of the parameters of an agroecosystem ecological state for monitoring technological processes of crop cultivation, *IOP conference series: materials science and engineering.* no. 39. pp. 315-319. St. Petersburg / Russia;

[5] Kalinin A.B., Teplinsky I.Z., Kudryavtsev P.P., (2016), Soil condition in intensive technology (Почвенное состояние в интенсивной технологии). *Potatoes and vegetables (Картофель и овощи),* no. 2. pp. 35–36. St. Petersburg / Russia;

[6] Kukharev O.N., (2006), *Energy-saving technologies for oriented planting of crops (by the example of onions and sugar beets) (Энергосберегающие технологии ориентированной посадки сельскохозяйственных культур: на примере лука и сахарной свеклы),* dis. Ph. D. in Eng. Science. 414 p., Penza / Russia;

[7] Kukharev O.N., Larushin N.P., (2018), A device for guiding bodies of irregular shape, *Research Journal of Pharmaceutical, Biological and Chemical Sciences*. vol. 9. no 3. pp. 30–33. India;

[8] Sibirev A.V., Aksenov A.G., Mosyakov M.A., (2018), *Experimental Laboratory Research of Separation Intensity of Onion Set Heaps on Rod Elevator*, Journal of Engineering and Applied Sciences. no. 23. pp. 10086–10091. Islamabad / Pakistan;

[9] Sibirev A.V., Aksenov A.G., Dorokhov A.S., (2019), Results of laboratory investigations of soil screening ability of a chain digger with asymmetric vibrator arrangement, *INMATEH — Agricultural Engineering*, no.57(1), pp. 9–18. Bucharest / Romania;

[10] Sorokin A.A., (2006), *Theory and calculation of potato harvesters (Теория и расчет картофелеуборочных машин)*, Monograph, VIM.159 p. Moscow / Russian.

REAL-TIME COMPARISON OF SEVERAL TRANSPIRATION METHODS FOR ESTIMATING GREENHOUSE VENTILATION RATE VIA WATER VAPOUR BALANCE METHOD

/

PERBANDINGAN METODE PENGUKURAN TRANSPIRASI UNTUK MENGHITUNG LAJU VENTILASI GREENHOUSE DENGAN METODE KESEIMBANGAN UAP AIR

Ahmad Tusi[1,2], Teruaki Shimazu[3] [1]
Faculty of Agriculture, University of Lampung, Bandar Lampung / Indonesia;
[2] Graduate School of Agricultural Science, Gifu University, Gifu / Japan;
[3] Faculty of Applied Biological Sciences, Gifu University, Gifu / Japan
Tel: +62 8128890680; E-mail: ahmad.tusip@fp.unila.ac.id
DOI: https://doi.org/10.356.33/inmateh-63-09

Keywords: *transpiration rate, electronic weighing device, sap flow, water level, flow rate, water vapor balance method*

ABSTRACT

Transpiration rate is an essential factor in the water vapor balance method for estimating the ventilation rate in a greenhouse continuously. Several methods of transpiration measurement, i.e., electronic weighing device (Control), the sap flow measurement (SF), water level measurement (WL), and water flow rate measurement (WF) tested and evaluated on tomato crops in a naturally ventilated greenhouse. The objective was to compare these methods and establish the most affordable one to be used in a greenhouse condition to determine the ventilation rate using the water vapor balance approach. Results obtained with the SF particularly have a strong correlation and are not statistically different from the Control (r=0.89). The WF method gave good results and reliable for predicting the total of transpiration in the greenhouse. However, in our conditions, this method generally had a lag time of the transpiration rate in a short time interval basis (minute and hourly). But it had an excellent predicted transpiration rate in daily evapotranspiration. The WL suffered weak agreement to the Control due to the scattering data. It was affected by the very high sensitivity of the device, and it is not recommended to use on the farm level, like in a greenhouse. It appears that measurements with the control and the SF could be considered for monitoring the ventilation rate in the greenhouse using a water vapor balance technique.

ABSTRAK

Transpirasi merupakan faktor yang sangat penting untuk menghitung laju ventilasi dengan metode keseimbangan uap air di dalam greenhouse. Beberapa metode pengukuran transpirasi tanaman, diantaranya: metode timbang elektronik (Kontrol), Sap flow (SF), pengukuran muka air (WL), dan pengukuran laju aliran air (WF), telah diujikan dan dievaluasi pada tanaman tomat di greenhouse dengan ventilasi udara secara alami. Tujuan penelitian adalah untuk membandingkan semua metode tersebut dan menetapkan jenis alat yang sesuai untuk menghitung laju ventilasi dengan metode keseimbangan uap air. Hasil menunjukkan bahwa metode SF memiliki hubungan korelasi yang sangat bagus dan tidak berbeda secara statistik dengan Kontrol (r=0.89). Metode WF memberikan hasil yang cukup baik dan mampu mengukur laju transpirasi di dalam greenhouse. Namun, metode ini secara umum diperoleh adanya waktu jeda dalam pengukuran transpirasi untuk interval waktu pengukuran yang singkat (per menit dan jam), tetapi metode tersebut dapat mengukur laju transpirasi tanaman harian. Sedangkan metode WL mengalami korelasi yang rendah terhdap Kontrol disebabkan oleh penyebaran data. Hal ini dipengaruhi oleh tingkat sensitivitas alat tersebut, dan alat ini tidak direkomendasikan untuk penggunaan di dalam greenhouse. Metode Kontrol dan SF dapat dipertimbangkan untuk keperluan monitoring laju ventilasi di dalam greenhouse dengan metode keseimbangan uap air.

INTRODUCTION

Monitoring the photosynthetic rate of plants by the CO_2 balance method requires precise measurement of greenhouse ventilation rate.

[1] *Ahmad Tusi, Ph.D..; Teruaki Shimazu, Prof. Ph.D.*

Previous studies indicated photosynthesis using the CO_2 balance method with short time interval measurement from 1 to 15 min *(Chalabi and Fernandez, 1994; Zekki et al., 1999; Takakura et al., 2017*). It certainly requires the ability of the sensor to monitor the ventilation rate in real-time properly. One of the methods to estimate the ventilation rate is the water vapor balance method (WVB), as mentioned by *Li et al. (2012),* and *Mashonjowa et al. (2013).* The primary source of water vapor in the greenhouse is from leaf transpiration. *Tusi and Shimazu (2020)* reported that the reliability of WVB method depends on the accuracy of short-term transpiration measurements. Hence, an accurate measurement of transpiration is needed to quantify water vapor present in the greenhouse for predicting the ventilation rate based on this technique.

There are various types of transpiration recording devices used by greenhouse engineers, i.e., electronic weighing balance *(Boulard and Draoui, 1995; Kittas et al., 2002; Li et al., 2012)*, sap flow sensor *(Mashonjowa et al., 2010)*, water flow sensor *(Harmanto et al., 2006).* There is another method that has been developed by *Shimomoto et al. (2020)* using an open bottom chamber to monitor photosynthesis and transpiration. Among the different methods for direct measurement of the transpiration rate, the electronic weighing device is standard and has been widely used in a Dutch commercial greenhouse *(De Koning and Tsafaras, 2017).* It measures the changing of fresh weight of plants either in 1 plant or several plants in a device per time unit, i.e. 4 plants/device *(Boulard and Draoui, 1995),* and 3 plants per device *(Kittas et al., 2002).*

Laperen and Madery (1994) promoted a new weighing lysimetric system to measure transpiration and water uptake simultaneously on one plant in short time intervals (min). The previous study showed that the interval time for measuring ventilation rate based the WVB was 10 min, 1 h, and daily, as mentioned in *Kittas et al. (2002), Boulard and Draoui (1995),* and *Harmanto et al. (2006),* respectively. Hence, this technique can monitor quick responses to changing environmental conditions.

In terms of the sap flow technique, it is measured based on heat flow. This method is ideally suited to applications requiring routine determinations of plant water use, and it is very useful in studies of plant responses to environmental conditions in either the field or laboratory (*Smith and Allen, 1*996). Also, the sap flow had a close correlation with the leaf area index *(Cohen and Li, 1996)* and suggested that the results were free of external environmental noise.

Mashonjowa et al. (2010) estimated the ventilation rate using water vapor balance by the sap flow sensor. They observed water vapor in a large greenhouse (1,267 m^2) via two the sap flow sensors only recorded every 5 s and averaged over 30 minutes. Furthermore, *Harmanto et al. (2006)* recorded data on an hourly basis and average over nine h or daily ventilation rate (daylight). This technique allows us to measure water consumption either in one row/bed system or one greenhouse. It is different from the previous method that measured only one or several plants per device. However, plant physiological measuring is highly inhomogeneous in a greenhouse system, which means that a large number of sensors will be required for getting reliable means. So far, no sensors for data logging right on the plant have been used in practical horticulture due to limited information, especially for monitoring of ventilation rate value using the WVB approach in a greenhouse system. There is no information about the suitable transpiration device for estimating the ventilation rate using the water vapor balance method. It has been mainly affected due to the high cost of such measuring instruments and the difficulty of attaching them to the plant. This paper presented a comparison and evaluation of the applicability of different direct transpiration devices for use in greenhouse experiments to predict and monitor the ventilation rate in real-time. The research aimed to compare and evaluate the other method of transpiration measurement either in the technical aspect and interval time measurement capability; also, to provide recommendations or suggestions that could be used for monitoring the ventilation rate using the WVB technique.

MATERIALS AND METHODS

For computing the transpiration rate, the experiment was conducted in a naturally ventilated greenhouse to generate water vapor during the day time in a single-span experimental greenhouse at a research field site of Faculty of Applied Biological Science, Gifu University, Japan. The greenhouse was made of glass (glasshouse) with dimensions of 3.25 m × 5.00 m × 2.80 m. It had a supported roof and double flap side ventilations, which was covered with screen-net materials (pore size 0.4 mm and porosity 52.2%).

The greenhouse was occupied by mature tomato crops (*Lycopersicon esculentum* Mill., variety 'Momotaro'), cultivated on 14 modified Wagner pots with a volume of 10 L (one plant per pot) filled with light sandstones (diameters ranging from 1 to 5 mm) and supplied with hydroponic nutrient solutions (EC= 1 dS

m^{-1} and pH range of 5.5–6.5) in the lower part of the pot system with a maximum water level of 10 cm (capillary irrigation system). A net area of surface pot was 180 cm^2, and the growing medium on the pot system was covered with plastic mulch.

The transpiration rate (g h^{-1}) of cultivated tomatoes in the greenhouse was measured by the different methods, as presented in Table 1. The method as control was using an electronic weighing device (Model SW-15KS, A&D Company, Japan) with an accuracy of 2 g (Fig. 1a). The control measurement was compared with other methods, i.e., the Sap flow measurement (SF), water level measurement (WL), and water flow meter device (WF). The SF and WL were compared with the control, but the WF was compared with the SF. All measurements were conducted and recorded every minute during the daytime, then, a 15-minutes interval averaging data basis due to the time lag of direct methods for measuring transpiration. All the above measurements were recorded in a data logger (CR1000, Science Campbell, USA).

The transpiration from the Control device was computed as below equation:

$$Tr = \frac{W_{(t-1)} - W_{(t)}}{dt} \; x \; 60 \quad (1)$$

where T_r is transpiration rate (g h^{-1}); $W_{(t-1)}$ is pot weight before t time of measurement, and $W_{(t)}$ is pot weight in *t* time of measurement; d_t is the time interval (15 minutes); 60 is converter coefficient from minute to hours.

The Sap Flow measurement

The SF rate (Fig. 1b) was measured continuously at the base of the stem of selected tomato plants with Dynagage Sap Flow sensors (Model SGA13-WS, Dynamax Inc., Houston, USA), installed according to the operation manual. It was enclosed in a thermally insulated sheath and wrapped around the stem to prevent direct sunlight and adverse environmental effects. It works based on the energy balance method, where the amount of heat carried by the SF is converted into real-time sap flow in grams per hour. Even the stem of the plant is heated, but it is non-intrusive and not harmful since the plants are heated 1 – 5°C.

Detailed calculation with the SF method was presented in *(Smith and Allen, 1996).* Daily observation of the SF was conducted at an interval of 1 min, a CR1000 datalogger (Campbell, Co., USA) was used to measure the SF output during the tomato growth seasons. Transpiration rate using the SF was observed in late winter until spring seasons, from March to April 2019, and compared with the control device.

Table 1

Transpiration measurement devices observation

Measurement Methods	Device	Specification	
Control (C)	Electronic weighing	SW-15KS Model Capacity max. 15kg Minimum display 2 g	A&D Company, Japan
Sap Flow (SF)	The Sap flow sensor	SGA13-WS Sensor Stem diameter= 12-16 mm	Dynamax Inc. USA
Water level (WL)	Water level measurement	FL-001 Pulse Type Level Sensor Tank pressure= -0.1 to 0.5 MPa Resolution 1 mm	Keyence, Japan
Water Flow (WF)	Water flow rate measurement	FD-XS8 Clamp-On Micro Flow Sensor Tolerance: + 8mL Rate= 0 – 8000 mL/min	Keyence, Japan

Water Level Measurement Devices

The water level device was measured by a water level sensor (FL-001 Pulse-type level sensor, Keyence, Japan) continuously (Fig. 1c). It measured the water level of nutrient solution on the below part of the pot system using the stick with an accuracy of 1 mm. Decreased water in the pot system was recorded in 1 min interval basis, then averaged every 1 hour. The transpiration rate was calculated by observing the changes in water level over the time interval of measurement (Eq. 2). The transpiration measurement period was observed in the fall season, between October – December 2019. Also, it was compared with the control device.

$$Tr = \frac{[WL_{(t-1)} - WL_{(t)}]}{dt \; . \; 10} \times \rho \times A_p \quad (2)$$

Where T_r is transpiration (g h^{-1}); $WL_{(t-1)}$ is water level in the pot before t time of measurement, and $WL_{(t)}$ is water level in t time of measurement (mm); d_t is the time interval (1 h); ρ is water mass density (1 g cm^{-3}), and A_p is the net surface area of pot system (cm^2).

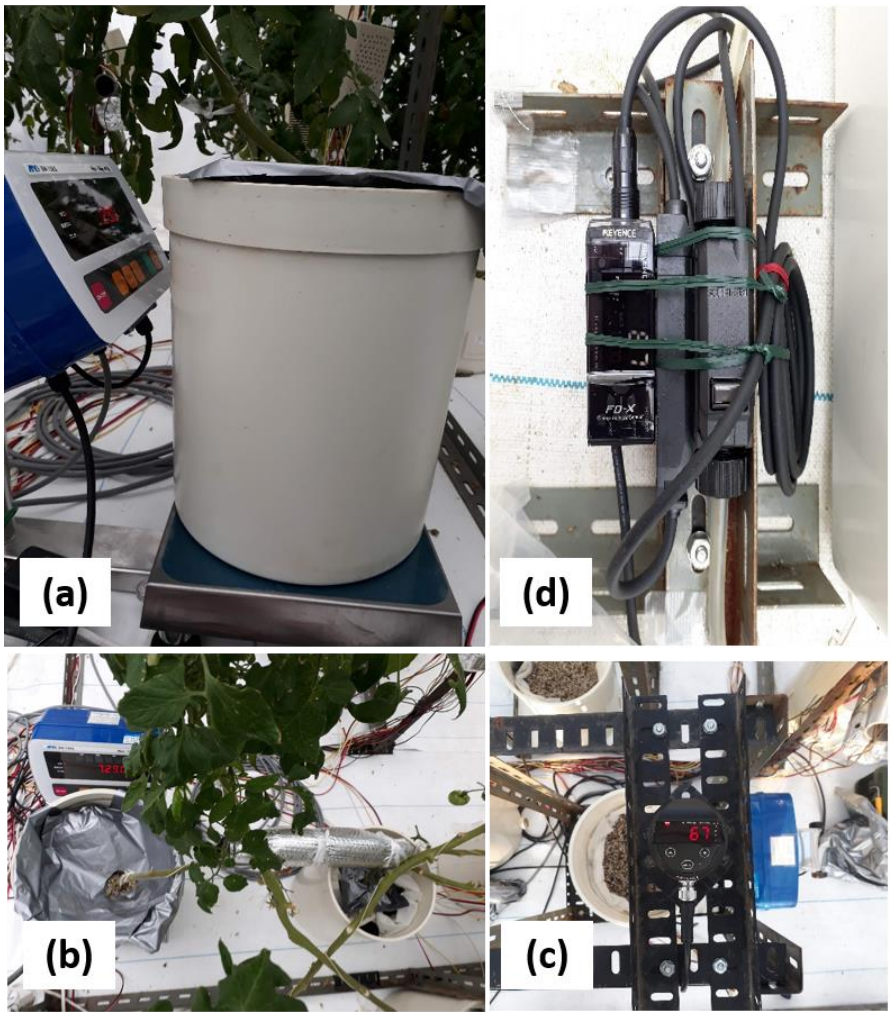

Fig. 1 - Transpiration measurement devices

(a) Electronic weighing device (Control), (b) Sap flow sensor (SF), (c) Water level sensor (WL), and (d) Water flow sensor (WF)

Water Flow Measurement Devices

For water flow measurement, it was conducted in a plastic house at a research field site of Faculty of Applied Biological Science, Gifu University, Japan. The greenhouse was covered using plastic material with dimensions of 5 m × 10 m × 3 m. The total of greenhouse floor area was 50 $m^{2,}$ and the greenhouse volume was 120 m^3. It had supported the roof and side ventilation, which was covered with screen-net materials (mesh opening 0.8 mm with porosity 62%). The greenhouse was occupied by mature tomato crops (*Lycopersicon esculentum* Mill., variety 'Momotaro'), cultivated on the two-bed system using substrate culture technique (light sandstones with a diameter ranging from 1 to 5 mm) and supplied with hydroponic nutrient solutions (EC= 1.1 – 1.3 dS m^{-1} and pH range of 5.5–6.5).

The substrate surface was covered with plastic mulch. During the measurement periods in early spring seasons 2020, and the tomato crops were cultivated at an average height of about 1.5 m. The plants were laid out 0.45 m apart in double rows on each bed, and each bed has dimension 6.0 m x 0.65 m. The total number of tomato plants was 46 plants (23 plants per bed) in the greenhouse. The nutrient solution was supplied from the water tank under the cultivation bed by capillarity, and the liquid level in the water tank was adjusted by the float liquid valve. The flow rate from the storage medium tank to the cultivation bed via the main pipe was measured using the micro-flow sensor (FD-XS8 Clamp-On Micro Flow Sensor, Keyence, Japan) attached to the outside of the pipe, as presented in Fig. 1d. The outside diameter plastic tube used 8 mm, hence the 1.27 cm diameter of the mainline should be converted to 8 mm for a measurement. This device was calibrated before applied in the greenhouse, and it has good performance with the measurement based on the volumetric method.

Because it was cultivated on bed systems (not in pot system), it had compared with the SF technique after the SF was calibrated with the Control. All data collected have been statistically analysed by linear regression between the reference method and the other methods using R software.

RESULTS

The transpiration rate of a tomato measured by a SF sensor was in the range of 10 to 150 g h-1 in the spring season. The SF had a similarly good result with the Control as close with the target line, as shown in Fig 2(a). The graph showed that the SF measurement (15-min interval) was remarkably accurate and had a strong correlation to the Control with the corresponding value of the Pearson correlation coefficient (r) of 0.89, as presented in the figure (***p = 2.2 × 10^{-6}). *Lascano et al. (2016)* reported that there were no statistical differences between hourly and daily values of sap flow measurement with the lysimetric. The measured transpiration rate by the Control was slightly higher than the sap flow sensor due to evaporation from the substrate from the pot system even if it was covered by plastic mulch. The evaporation from the growing media was too small by 6.3% from the total of evapotranspiration. Even if it was small, it should be considered to calculate the total water vapor balance method in the greenhouse for predicting the ventilation rate.

Based on the result, it can be directly used in the SF measurement for further monitoring of the ventilation rate using the WVB method. Practically, the SF device should be regularly checked and calibrated. Also, it was recommended to change the position of the sensor on stem plants to other plants.

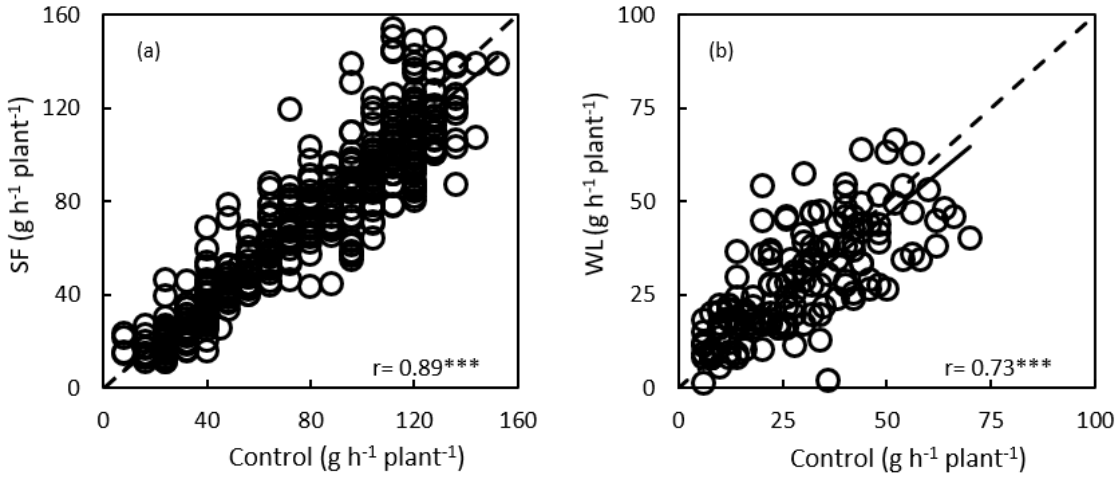

Fig. 2 - Transpiration rate correlation value between (a) the SF measurement with the Control during the spring season, March – April 2019 (n=404 data), and (b) the WL measurement with the Control during October – November 2019 (n=163 data). The r value is the corresponding value of the Pearson correlation coefficient (*p=2.2 ×10^{-16} <0.001)**

The WL measurement has slightly smaller transpiration compared to the SF because it was conducted in the fall season with lower radiation than in the spring season (data not presented), between October and November 2019, with the value from 5 to 60 g h^{-1} per plant. The WL measurement exhibited a good correlation to the Control with the r value being 0.73, as presented in Fig 1b. It was lower than the SF because there was a scattered data linearly with an increase in transpiration rate. The fluctuated data was affected by the very high sensitivity of the device to the activities in a greenhouse (shaking to the pot system during the cultivation process). Also, the low transpiration rate has influenced the accuracy due to the lag time of measurement in the short time interval measurement.

Akutsu et al. (2015) also reported that the water level with the manometer type for potted tomato plants had a time lag of measurement, whereas they refilled to maintain a certain level in the tube every 2 hr. In this observation, even the WL device accuracy of measurement is 1 mm. Still, if it is converted to a weight unit (in gram), it was found that 1 mm of precision device equals 18 g at 180 cm^2 of the pot tomato cultivation area that is used. It means that the Control (2 gr of accuracy) was higher than the WL device. It is one of the reasons why the WL suffered the lag time of the direct measurement of the transpiration rate. Contrary to the WF method, it measured the total amount of water consumption of tomato crops in the greenhouse.

During observation in March 2020 (spring season, with n=375 data), the transpiration rate varied between 50 – 150 g h^{-1} per plant. This value was the same transpiration rate as a measurement in spring 2019 by sap flow and weighing device measurement.

Fig 3a showed that the WF measurement had a lower correlation compared to the SF with r = 0.59. The water flow measurement has a lower correlation than the sap flow and the water level measurement devices.

This problem can be elucidated with diurnal changes in the transpiration rate both in a cloudy day (Fig 3b) and in a sunny day (Fig 3c).

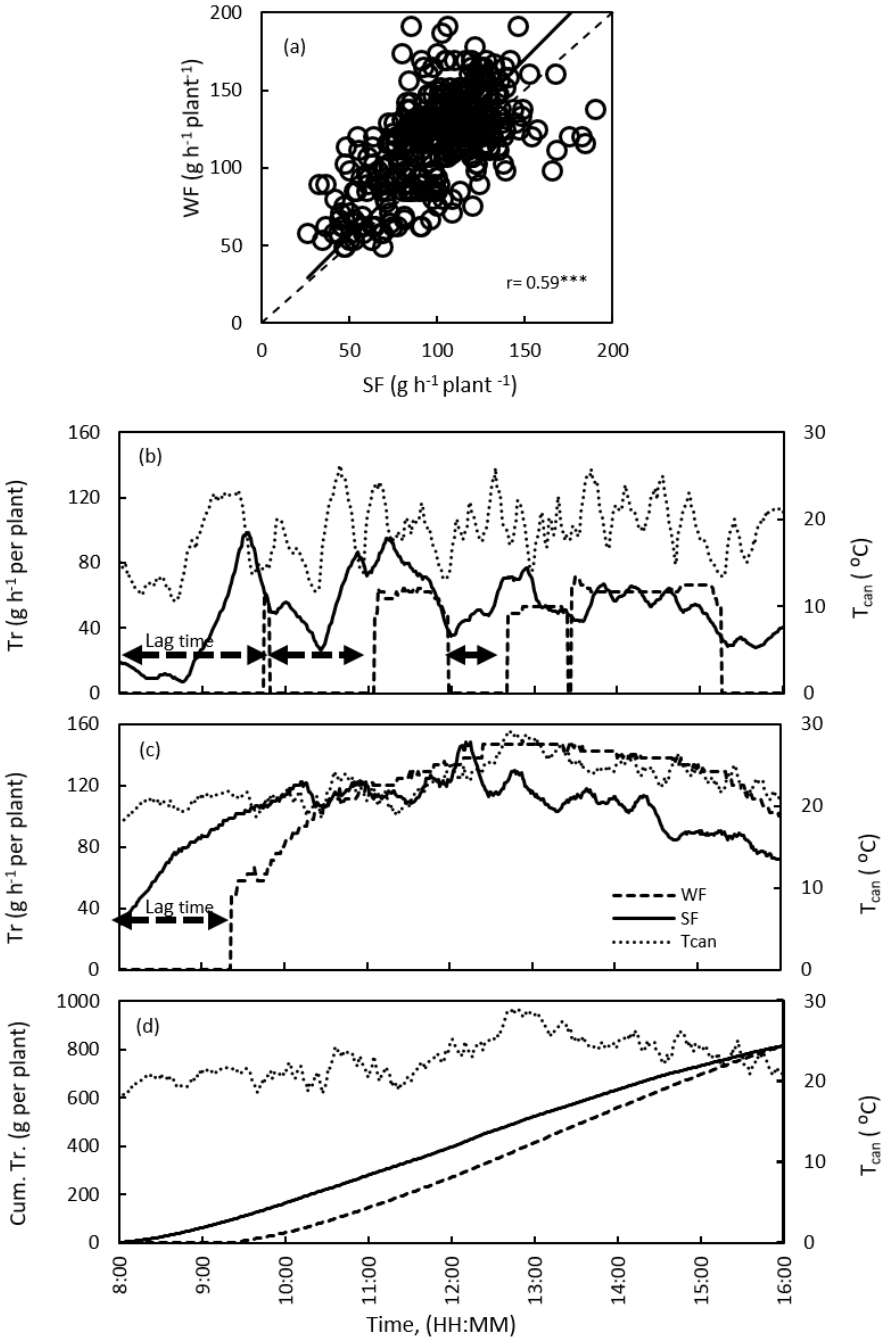

Fig 3. (a) Correlation of transpiration rate measurement between the WF and the SF measurement; b) the diurnal changes in transpiration rate during (b) cloudy day, March 5, 2020 (c) sunny day, March 6, 2020. (d) the accumulation of transpiration during the measurement day on March 6, 2020

The water flow measurement in the greenhouse experienced several time lags in the direct measurement of transpiration on a cloudy day. This condition was often encountered during cloudy conditions (Fig 3b) than when it was a sunny day (Fig 3c).

The fluctuation of transpiration data at a different time in the day should be related to the variable conditions of irradiance recorded that are related to the canopy temperature condition (Tcan). An increase of irradiance in the greenhouse caused enhancement of transpiration rate consequently.

Thus, the time lags of measurement were fewer in number in high radiation condition than lower radiation, like in cloudy condition. *Wei et al. (2020)* noted that the SF rate was primary controlled by

photosynthetically active radiation (PAR) and varied with time scales. On sunny days, the time lag appeared in the morning only. After that, the transpiration rate measurement by water flow was similar to the sap flow in mid-day. However, when the transpiration rate was accumulated in the measurement day, as presented in Fig 3d, it shows the same level of total transpiration rate during the day. It indicated that the water flow measurement has a reasonably measured transpiration in daily measurement, not in a short time interval. It should be noticed that in this experiment, the water flow device measured the total of water consumption of the tomato crops supplied by a passive system with an automatic floating valve to supply water in the bed cultivation system. It might be another reason for the time lag of transpiration measurement. Further research about the implementation of the water flow device with a drip irrigation system or others should be performed.

Table 2

Transpiration measurement devices observation

Description	Transpiration measurement devices			
	Electronic Weighing (Control)	**Sap Flow (SF)**	**Water Level (WL)**	**Water Flow (WF)**
Measurement of time record	10-15 minutes*	per minute	hourly and daily	daily
Scale of measurement	One plant or several plants per device	One plant only	One plant or per tank	A large community of plant (per greenhouse)
Advantageous	High accuracy	Good agreement with the Control	Knowing real-time of water uptake measurement	Measuring of total water consumption in a greenhouse
Disadvantageous	Sensitive to human activities	Need calibration regularly and change position	Sensitive to human activities; time lag of measurement	The time lag of measurement
WVB technique application**	√√√	√√√	√√	√√

**) it depends on the accuracy level of a measurement device. It was conducted with 2 g of accuracy level.*

***) Transpiration devices recommendation for monitoring ventilation rate via the WVB method.*

(√ = not good, √√ = enough, √√√ = good, √√√√ = very good)

Overall, among the four different methods used in this study, the sap flow and an electronic weighing device (with 2 g of accuracy) were recommended for estimating the ventilation rate in the greenhouse, as needed to calculate the photosynthetic rate via CO_2 balance method. The detail of the measurement methods was presented in Table 2. It shows the advantages and disadvantageous of several different transpiration measurement devices. 2 g of accuracy level of measurement via an electronic weighing device was enough to measure transpiration rate with the time lag of measurement between 10-15 minutes. Also, it was enough for estimating the photosynthetic rate via the CO_2 balance approach. As we know, an increase in the accuracy level of measurement devices will contribute to the cost that should be paid.

Leperen and Madery (1994) observed the transpiration and water uptake by an electronic weighing lysimeter with an accuracy level of 0.03 g min^{-1} $plant^{-1}$ that may be made for short time intervals (min). The high accuracy level makes it possible to monitor quick responses to changing environmental conditions.

CONCLUSIONS

Transpiration rate could be monitored directly and continuously by the electronic weighing lysimetric and the sap flow measurement in a short time interval (minute). The measured transpiration rate via the sap flow gave a better result than the water level and water flows measurement approaches. Also, it has the same level of transpiration rate with the Control. The Control and the sap flow can be used for real-time monitoring in short time interval (per minute) compared to the water level and the water flow devices which need hourly and daily interval, respectively. The electronic weighing device and the sap flow may permit continuous real-time monitoring of the crop transpiration rate in a greenhouse, which is a primary parameter of the WVB method for estimating the ventilation rate.

ACKNOWLEDGEMENT

One of the authors (Mr. Ahmad Tusi) would like to thank the Indonesia Endowment Fund for Education (LPDP, BUDI-LN), Ministry of Finance, and Ministry of Education and Culture, the Republic of Indonesia for funding the doctoral program at Gifu University, Japan.

REFERENCES

[1] Akutsu, M., Sunagawa, H., Usui, T., Tamaki, M., Hirata, M., Kaiho, A., & Takakura, T. (2015). Non-destructive, real time, and automatic measurement of transpiration from a plant canopy stand. *Journal of Advances in Agriculture*, 5(2), 677–683. https://doi.org/10.24297/jaa.v5i2.5083

[2] Boulard, T., & Draoui, B. (1995). Natural ventilation of a greenhouse with continuous roof vents: measurement and data analysis. *Journal of Agricultural Engineering Research,* 61(1), 27–36.

[3] Chalabi, Z. S., & Fernandez, J. E. (1994). Estimation of net photosynthesis of a greenhouse canopy using a mass balance method and mechanistic models. *Agricultural and Forest Meteorology,* 71(1-2), 165–182

[4] Cohen, Y., & Li, Y. (1996). Validating sap flow measurement in field-grown sunflower and corn. *Journal of Experimental Botany*, 47(11), 1699–1707. https://doi.org/10.1093/jxb/47.11.1699

[5] De Koning, A.N.M., & Tsafaras, I. (2017). Real-time comparison of measured and simulated crop transpiration in greenhouse proceses control. *Acta Horticulturae*, 1170, 301-307

[6] Ehler, N. (1991). An autocalibrating model for simulating and measuring net canopy photosynthesis using a standard greenhouse climate computer. *Computers and Electronics in Agriculture*, 6(1), 1–20. https://doi.org/10.1016/0168-1699(91)90019-6

[7] Hand, D. W., Clark, G., Hannah, M.A., Thornley, J.H.M., & Wilson, J. W. (1992). Measuring the canopy net photosynthesis of glasshouse crops. *Journal of Experimental Botany*, 43(3), 375–381. https://doi.org/10.1093/jxb/43.3.375

[8] Harmanto, Tantau, H. J., & Salokhe, V. M. (2006). Microclimate and air exchange rates in greenhouses covered with different nets in the humid tropics. *Biosystem Engineering,* 94(2), 239–253. https://doi.org/10.1016/j.biosystemseng.2006.02.016

[9] Kittas, C., Boulard, T., Bartzanas, T., Katsoulas, N., & Mermier, M. (2002). Influence of an insect screen on greenhouse ventilation. *Transactions of the ASAE,* 45(4), 1083–1090

[10] Lascano, R.J., Goebel, T.S., Booker, J., Baker, J.T., & Gitz, D.C. (2016). The stem heat balance method to measure transpiration: evaluation of a new sensor. *Agricultural Sciences*, 7(9), 604-620. http://dx.doi.org/10.4236/as.2016.79057

[11] Leperen, W. V., & Madery, H. (1994). A new method to measure plant water uptake and transpiration simultaneously. *Journal of Experimental Botany*, 45(1), 51–60. https://doi.org/10.1093/jxb/45.1.51

[12] Li, M., Kozai, T., Niu, G., & Takagaki, M. (2012). Estimating the air exchange rate using water vapor balance method as a tracer gas in a semi-closed growth chamber. *Biosystems Engineering*, 113(1), 94–101. https://doi.org/10.1016/j.biosystemseng.2012.06.010

[13] Mashonjowa, E., Ronsse, F., Milford, J., Lemeur, R., & Pieters, J.G. (2010). Measurement and simulation of the ventilation rates in naturally ventilated azrom type greenhouse in Zimbabwe. *Journal of Applied Engineering in Agriculture,* 26(3), 475–488.

[14] Mashonjowa, E. Ronsse, F., Milford, J., Lemeur, R., & Pieters, J.G. (2013). Modelling the thermal performance of a naturally ventilated greenhouse in Zimbabwe using a dynamic greenhouse climate model. *Solar Energy*, 91, 381–393. https://doi.org/10.1016/j.solener.2012.09.010

[15] Shimomoto, K., Takayama, T., Takahashi, N., Nishina, H., Inaba, K., Isoyama, Y., & Oh, S-C. (2020). Real-time monitoring of photosynthesis and transpiration of a fully-grown tomato plant in greenhouse. *Environmental Control in Biology*, 58(3), 65-70. https://doi.org/10.2525/ecb.58.65.

[16] Smith, D. M., & Allen, S. J. (1996). Measurement of sap flow in plant stems. *Journal of Experimental Botany*, 47(12), 1833–1844. https://doi.org/10.1093/jxb/47.12.1833

[17] Takakura, T., Sunagawa, H., Tamaki, M., Usui, T., & Taniai, N. (2017). In site net photosynthesis measurement of a plant canopy in a single-span greenhouse. *Journal of Advances in Agriculture,* 7(2): 1015-1020. https://doi.org/10.24297/jaa.v7i2.6092

[18] Tusi, A., & Shimazu, T. (2020). The essential factor of ventilation rate in prediction of photosynthetic rate using the CO2 balance method. *Reviews in Agricultural Science*, 8, 279-299. https://doi.org/10.7831/ras.8.0_279

[19] Wei, X., Fu, S., Chen, D., Zheng, S., Wang, T., & Bai, Y. (2020). Grapevine sap flow in response to physio-environmental factors under solar greenhouse conditions. *Water*, 12(3081), 1-17. . https://doi.org/10.3390/w12113081

[20] Zekki, H., Garry, C., Gosselin, A., & Gauthier, L. (1999). Validation of a photosynthesis model through the use of the CO_2 balance of a greenhouse tomato canopy. *Annals of Botany*, 84(5), 591–598.

DESIGN AND EXPERIMENT OF SEGMENTED TYPE MIXER WITH DOUBLE SPIRAL RIBBON FOR AGRICULTURAL WASTE
/
分段式双螺带农业废弃物搅拌装置设计与试验

Wang Tiejun [1)], Wang Tieliang [1)], Wang Ruili [2)], Liu Kai [2)], Gong Yuanjuan *[2)] [1]
[1)] Shenyang Agricultural University, College of Water Conservancy, Shenyang / China;
[2)] Shenyang Agricultural University, College of Engineering, Shenyang / China
Tel: +8613998240253; E-mail: 1985500005@syau.edu.cn
DOI: https://doi.org/10.356.33/inmateh-63-10

Keywords: *agricultural waste; segmented type; double spiral ribbon; mixing uniformity; residual rate of material; response surface*

ABSTRACT
In this study, a segmented type mixer with double spiral ribbon was designed to destroy choking and accumulation of agricultural waste in the mixing process, by improving the mixing uniformity and reducing the residual amount of maize straw and cow dung. To determine the optimal working parameters of the mixer, the ternary quadratic regression orthogonal rotation combined experiment was carried out by using the mixing uniformity and residual rate of material as the evaluation indexes and the spindle speed, full coefficient and mixing time as the influencing factors. The results showed that the order of the influences on the mixing uniformity was spindle speed>mixing time>fullness coefficient, and the order of the influences on the residual rate of material was fullness factor>spindle speed>mixing time. The study established a regression model of influencing factors and evaluation indexes, and analysed the influence of significant factors and their interaction on evaluation indexes. The optimum combination after parameter optimization based on response surface method was determined to be as follows: spindle speed of 38.00rad/min, full coefficient of 55.00%, mixing time of 9.33min. While the mixing uniformity and residual rate of material corresponding to the verification test were 91.25% and 95.19%, respectively, the relative error of the predicted result was less than 0.5%. The study meets the requirements of mixing agricultural waste materials to make fertilizers, and provides technical solutions for improving the localized resource utilization of agricultural waste.

摘要
针对农业废弃物搅拌过程壅堵和积料的问题，本研究为提高玉米秸秆和牛粪混合均匀性、降低物料残留量，设计了一种分段式、双螺带搅拌装置。为确定装置最佳工作参数，以主轴转速、充满系数和混合时间为试验因素，以混合均匀度和物料残留率为评价指标，采用三元二次回归正交旋转组合试验方法进行试验与响应面分析。结果表明：影响混合均匀度的主次因素为：主轴转速＞混合时间＞充满系数，影响物料残留率的主次因素为：充满系数＞主轴转速＞混合时间。建立试验因素与评价指标的回归模型，分析显著因素及其交互作用对评价指标的影响。基于响应面法进行参数优化，确定最终优化参数组合为：主轴转速 38.00rad/min，充满系数 55.00%，混合时间 9.33min，对应验证试验的混合均匀度和物料残留率分别为 91.25%和 95.19%，与模型预测结果相对误差小于 0.5%。该研究满足农业废弃物料制肥的混配要求，为提高农业废弃物属地化资源利用提供技术方案。

INTRODUCTION
With the high-quality development of China's agriculture and rural areas, more and more attention has been paid to the agricultural ecological environmental problems caused by agricultural wastes from non-intensive planting and breeding, and the decrease in the quality of cultivated land caused by long-term large-scale use of chemical fertilizers (*Wang et al., 2020; Wang et al., 2017*). Decomposing and returning the solid biomass such as straw and livestock manure to the field is a significant means to coordinate agricultural waste pollution and soil nutrient deficiency (*Chai et al., 2019; Zhang et al., 2020*). By using local straws and livestock manure to produce organic fertilizer or soil amendments through small-scale compost decomposing, the agricultural organic waste can be returned to the field accelerated, which is brought by decentralized small and medium agricultural production.

[1] *Tiejun Wang, Ph.D. Stud. Eng.; Tieliang Wang, Prof. Ph.D. Eng.; Ruili Wang, Assoc. Prof. Ph.D. Eng.; Kai Liu, M.S. Stud. Eng.; Yuanjuan Gong, Prof. Ph.D. Eng.*

It is a technological method to increase the conversion efficiency of agricultural waste resources and improve the physical and chemical properties of the soil. The mixing effect, during the small-scale compost decomposing technology, affects the working process of fertilizer spreading machine and the quality of fertilizer (*Ştefan et al., 2019; Cârdei et al., 2019*). Intermittent low-speed mixing can reduce energy consumption and improve the fermentation effect, by studying the influence of different mixing parameters on the power consumption of the equipment and the fermentation effect of cow manure (*Peter et al., 2020; Li et al., 2013*). The medium-speed mode of the equipment can speed up the mixing process of bulk materials, by studying the flow characteristics of straw materials of the conveying process over a rough surface, which provides help for the design of spiral screw mixing system (*Pylypaka et al., 2017; Xue et al., 2017; Naumenko et al., 2018*). The research on the mechanical behaviour of maize straw pith and the bulk particle motion kinematics in the screw conveyor-mixer provided theoretical support for the design of crop-mechanical mixing-system (*Ştefan et al., 2018; Hewko et al., 2015; Zhang et al., 2017*). Continuous-flow conveyors could transport simultaneously during mixture process, which provided a mean of choosing cost-effective operating modes of a conveyor-mixer (*Hevko et al., 2017*).

In order to effectively improve the applicability of agricultural waste mixing equipment, this paper designs a segmented type mixer with double spiral ribbon, which is able to improve the mixing uniformity and reduce the residual. On the basis of performed finite element analysis on the mixing mechanism, from the material mixing mechanism point of view, the material-mechanical interaction is analysed, whereby the whole machine structure and key components is designed. Moreover, through the three-dimensional quadratic regression orthogonal rotation combined experiment and field verification test, the working parameters of the prototype were optimized, and the working performance was verified.

MATERIALS AND METHODS

The whole design and working principle

The segmented type mixer is mainly composed of the spiral ribbon structure, mixing chamber, transmission system, motor, and reducer. Its structure is as shown in Fig.1. The overall design dimensions are 1660mm×600mm×1100mm (length × width × height) and the overall mass is 160kg. The capacity of the mixing chamber is 0.40m^3, the power of the motor is 3.0kW, and the productivity is about 500kg/h.

The mixing chamber is composed of a rectangular parallelepiped in upper part and a semi-cylinder in lower part. According to the research on the length-to-width ratio of the mixing chamber (*Chen et al., 2004*), when the capacity of the mixing chamber is determined, the length-to-width ratio of the mixing chamber is one of the main parameters. The length of the mixing chamber is 1000mm, the width and lower diameter are all 500mm, and the upper part is 550mm high.

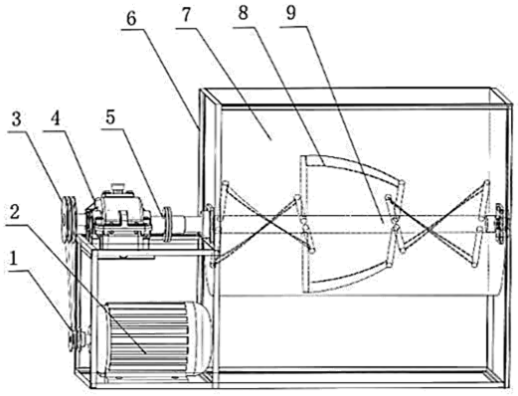

Fig. 1 - Diagram of the overall structure for the mixer
1- The first belt wheel; 2- The motor; 3- The second belt wheel; 4– Reducer; 5– Coupling; 6– Frame; 7- Mixing chamber;8- Spiral ribbon structure; 9- Mixing spindle

Belt transmission is the main transmission mode of the mixer, while the motor transmits power to the mixing spindle through the reducer and coupling. The machine's transmission scheme is shown in Fig.2. During work, the filamentous straw and the cow dung after cleaning are fed from the opening in the upper part of the mixing chamber. The segmented and reversed double spiral ribbon mixing structure on the mixing spindle makes the material produce three-dimensional reciprocating mixing motion. In the mixing chamber, the mixing structure was divided into three segments in the horizontal direction: left, middle and right, and in

the vertical direction, which was divided into two rotations: left-hand and right-hand. The direction of rotation is opposite in the same segment, and the left and middle segments are opposite to the right segment. Straw and cow dung are driven by the reverse spiral ribbon in the horizontal direction to produce convective motion, and are continuously divided by the rotating spiral ribbon in the vertical direction to produce shearing motion. Simultaneously, the different gravity of the straw and cow dung causes different movement speed and direction, which results in diffusion movement. That is, the left and right mixing ribbons push the material to the middle position of the mixing chamber, and the middle mixing ribbon pushes the material to both sides of the mixing chamber, whereby the material is gradually mixed in the mixing chamber, as shown in Fig.3. After the mixing is completed, open the discharge port at the lower part of the mixing chamber, and the material is discharged out of the chamber under the force of the spiral ribbon and its own gravity.

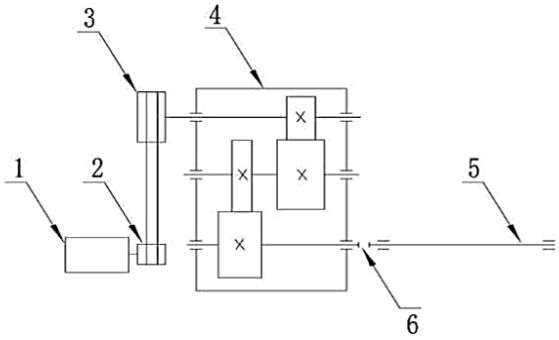

Fig. 2 - Structural diagram of the machine transmission scheme

1- Motor; 2- Small pulley; 3- Large pulley; 4- Reducer; 5- Stirring spindle; 6- Coupling

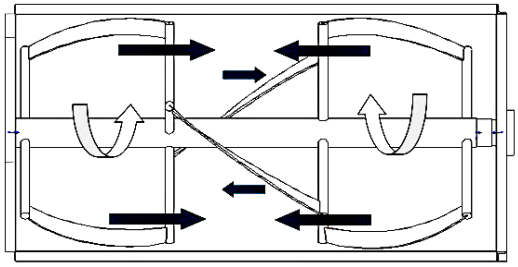

Fig. 3 - Schematic diagram of material mixing process

Design of key structural parameters

Design of mixing arm

Redundancy of mixing arms will affect the flow of materials in the mixing chamber, and increase the design length of the mixing spindle, thereby reducing the structural strength. When the number of mixing arms is small, the force of the mixing arms and mixing ribbons will increase when the material is pushed, which will affect the mixing quality and working efficiency of the mixer (*Liu et al., 2019*). Considering the relationship between the phase angle of the mixing arm and the number of mixing arms, as shown in Fig.4, the design value of the phase angle of the mixing arm is 60°, and the number of mixing arms is 4 groups.

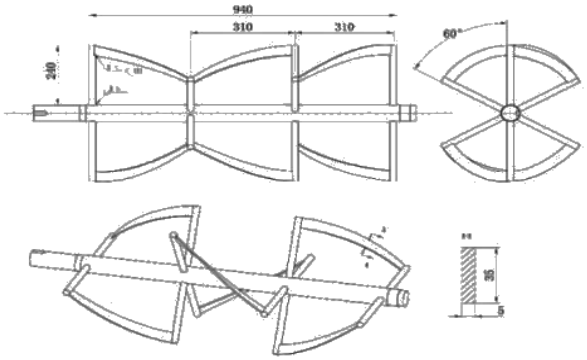

Fig. 4 - Mixing arm and ribbon arrangement

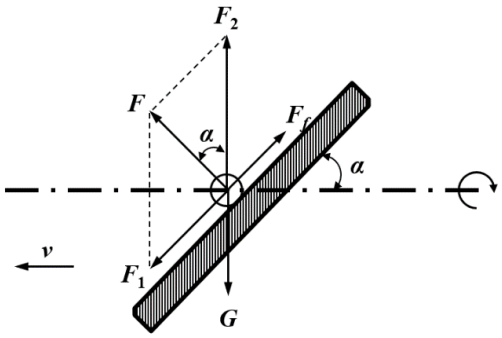

Fig. 5 - Material point force diagram

Design of spiral ribbon

Referring to the design of the spiral ribbon stirring device, the spiral ribbon is a single strip, and the design blade width is 35mm, the thickness is 5mm, and the length is 320mm. As it is shown in Fig.5, the installation angle of the ribbon refers to the acute angle α between the inclined surface of the ribbon and the stirring axis. Simplify the material into a mass point, then the force on the mass point is: gravity G, driving force F and friction force F_f, f is the friction coefficient, decomposing F into the surface direction force F_1 and the vertical axis direction force F_2. To achieve axial movement of the material, F_1 must be greater than or equal to F_f, that is:

$$F \cdot tan\,\alpha - F \cdot f \geq 0 \quad (1)$$

then, the installation angle of the ribbon $\alpha \geq \arctan \cdot f$. Take the friction coefficient as 0.55, so $\alpha \geq 29°$. In order to increase the movement of the material in the mixing chamber, the design value of the installation angle of the ribbon α is 45°.

Static stress analysis

In this design, the mixing structure and mixing shaft were made of No. 45 steel. The finite element analysis model of the mixing equipment had a total of 17,878 units and 33841 nodes. As it is shown in Fig.6, the main stress parts, main deformation and displacement areas of the mixing equipment were the power input position and the connection between two mixing arms. The maximum stress was 232MPa, which meted the requirements of the material permission range, where the mixing arm and the mixing spindle would not bend and break under the jamming condition.

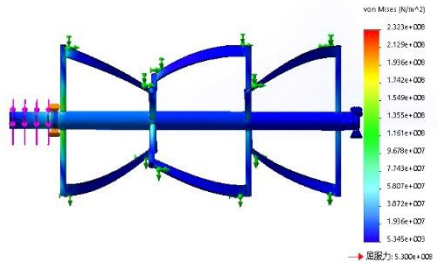

a. Stress diagram of stirring device

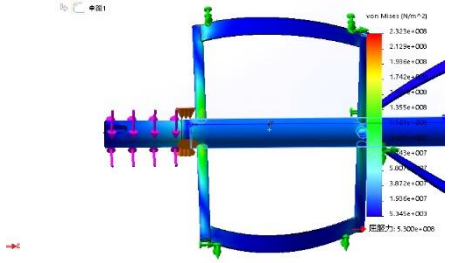

b. Stress concentration area diagram of mixing device

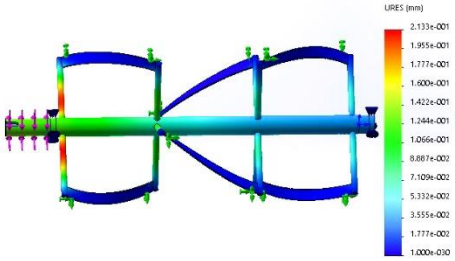

c. Deformation diagram of stirring device

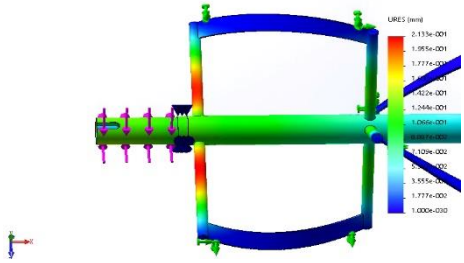

d. Deformation concentration area of mixing device

Fig. 6 - Static stress analysis results of mixing mechanism

Modal analysis

Because of the presence of vibration sources during work, it is necessary to conduct a modal analysis of the mixing equipment, as shown in Fig.7.

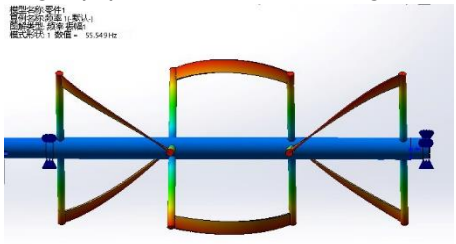

a. First-order modal vibration diagram

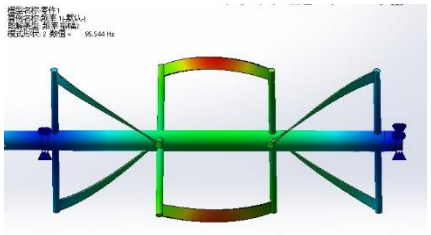

b. Second-order mode vibration diagram

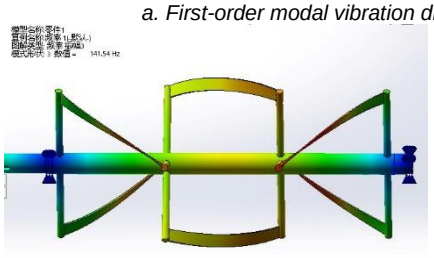

c. Third-order mode vibration diagram

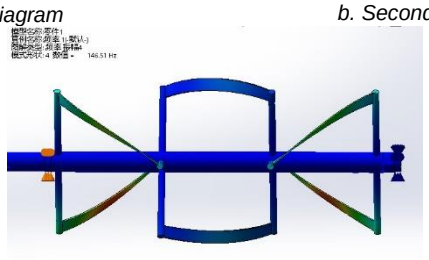

d. Fourth-order mode vibration diagram

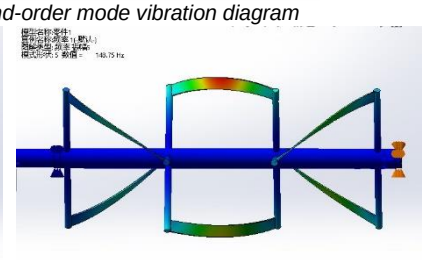

e. Fifth-order mode vibration diagram

Fig. 7 - Modal vibration pattern of the first five orders for the stirring mechanism

The first five orders natural frequencies of the extraction were 55.549 Hz, 95.544 Hz, 141.54 Hz, 146.51 Hz, and 148.75 Hz. It shown that with the increase of the mode order, the natural frequency of the mixing equipment also increased, but the increase speed was gradually reduced. The design maximum speed of the mixing equipment was 45 rad/min, which was much smaller than the critical speed of 3332.94r/min under the minimum natural frequency, so the mixing equipment would not cause resonance in the actual working process.

Experiment design

The experiment was conducted at the Northeast Facility Horticultural Engineering Scientific Observation and Experimental Station of Shenyang Agricultural University. The experiment maize straw was harvested in 2018 at North Mountain Scientific Research Base of Shenyang Agricultural University, and the experiment cow dung was taken from surrounding farmers.

Before the experiment, it was randomly sampled and determined the moisture content range of maize straw and cow dung stored under natural conditions, using an electronic analytical balance (Germany Sartorius QUINTIX224-1CN) and a digital display electric heating constant temperature drying oven (Shanghai Yangguang Experimental Instrument Co., Ltd. 101-0A) and other equipment. The moisture content of maize straw was 15.36%, and the moisture content of cow dung was 65.12%. The ratio of straw to cow dung was 3:2 during the experiment. The experiment selects mixing uniformity and material residual rate as experiment indicators. According to the study of the detection methods and mixing characteristics of mixing uniformity (*Yu et al., 2015; Wang et al., 2013*), physical method was used in the experiment, and the bean with relatively small particle size and mass as tracers to detect mixing uniformity. The corresponding value of the tracer mass was measured each time $X_1, X_2, X_3, \ldots, X_{10}$ calculating the mean and standard deviation. The mixing uniformity was calculated according to formula (2).

$$M = (1 - \frac{S}{\overline{X}}) \times 100\% \quad (2)$$

where M is the mixing uniformity, %; S is the sample standard deviation; $\overline{X}$ is the sample marker average.

The detection method of the material residue rate is to measure the quality of the material put into the mixer and the quality of the material discharged from the mixer, and calculate the material residue rate according to formula (3).

$$E = (1 - \frac{T_1 - T_2}{T_1}) \times 100\% \quad (3)$$

where E is material residual rate, %; T_1 is the quality of the material put into the mixer, kg;

T_2 is the quality of the material discharged from the mixer, kg.

The experiment selected the spindle speed, the full coefficient and the mixing time as the experiment factors, and carries out the ternary quadratic regression orthogonal rotation combination experiment. According to the analysis of the aforementioned documents and the mixing process, the value range of each factor and the experiment factor levels were shown in Table 1. The experiment equipment and materials were shown as Fig.8.

Factors and levels of combination experiment **Table 1**

Levels	Factors		
	Spindle speed	Full coefficient	Mixing time
	[rad·min^{-1}]	[%]	[min]
	x_1	x_2	x_3
1.682	45.00	80.00	11.00
1	40.95（41.00）	71.89 (72.00)	9.78（9.80）
0	35.00	60.00	8.00
-1	29.05（29.00）	48.11（48.00）	6.22（6.20）
-1.682	25.00	40.00	5.00
△j	5.95（6.00）	11.89（12.00）	1.78（1.80）

Note: The parameters in parentheses were the parameters taken in the experiment. Adjusted the calculation results according to the feasibility of actual operation, and taken the values in parentheses.

Fig. 8 - Experimental equipment and materials

RESULTS

Experiment results and inspection

A total of 23 groups of experiment were considered, and each group was repeated three times. The results were taken as the average value. The experiment scheme design and result analysis were shown in Table 2.

The quadratic polynomial regression models among the spindle speed (x_1), full factor (x_2), mixing time (x_3), mixing uniformity (Y_M) and material residue rate (Y_E) were established. The following regression equations were obtained:

$$Y_M=-21.814+4.054x_1+1.859x_2-3.830x_3+0.014x_1x_2+0.025x_1x_3+0.080x_2x_3-0.071x_1^2-0.025x_2^2-0.090x_3^2 \quad (4)$$

$$Y_E=+49.791-1.193x_1-0.361x_2-3.021x_3+0.004x_1x_2-0.016x_1x_3+0.016x_2x_3+0.014x_1^2+0.001x_2^2+0.145x_3^2 \quad (5)$$

Significance test and analysis of variance were performed on the obtained ternary quadratic regression equation, and the results were shown in Table 3. The correlation coefficient R_M=0.98, R_E=0.95, the regression equation significance level F_{RM}=74.49, F_{RE}=28.05, the lack of fit test F_{LfM}=1.84, F_{LfE}=2.23, P_M=0.2115, P_E=0.1497 were all greater than 0.05 and the difference was not significant, indicating that the regression equations Y_M and Y_E was significantly with statistically significant.

The optimized regression equation after excluding insignificant terms such as x_1x_3 and x_3x_3 of Y_M and x_1x_3 of Y_E at the significance level of P=0.05 was:

$$Y_M=-21.814+4.054x_1+1.859x_2-3.830x_3+0.014x_1x_2+0.080x_2x_3-0.071x_1^2-0.025x_2^2 \quad (6)$$

$$Y_E=+49.791-1.193x_1-0.361x_2-3.021x_3+0.004x_1x_2+0.016x_2x_3+0.014x_1^2+0.001x_2^2+0.145x_3^2 \quad (7)$$

It can be seen from Table 3 that the spindle speed (x_1) and mixing time (x_3) had extremely significant effects on the uniformity of mixing and the residual rate of materials (P<0.01); the full coefficient (x_2) had a significant effect on the uniformity of mixing (P<0.05), which had extremely significant impact on the residual rate of materials (P<0.01); the interaction of spindle speed and full coefficient (x_1x_2), the interaction of fullness coefficient and mixing time (x_2x_3) had extremely significant impact on the uniformity of mixing (P<0.01), and significant impact on the residual rate of materials (P<0.05) .

Table 2

Experimental plan and results

No.	Spindle speed	Full coefficient	Mixing time	*M*	*E*
	[rad·min^{-1}]	[%]	[min]	[%]	[%]
1	1	1	1	90.25	93.16
2	1	1	-1	84.86	93.10
3	1	-1	1	86.31	96.69
4	1	-1	-1	87.44	94.48
5	-1	1	1	85.67	92.30
6	-1	1	-1	81.06	92.11
7	-1	-1	1	85.40	93.86
8	-1	-1	-1	87.87	93.13
9	1.682	0	0	85.47	94.59
10	-1.682	0	0	84.57	92.15
11	0	1.682	0	81.72	92.05
12	0	-1.682	0	82.32	96.22
13	0	0	1.682	92.37	94.72
14	0	0	-1.682	90.23	92.12
15	0	0	0	92.34	94.44
16	0	0	0	92.18	94.27
17	0	0	0	92.45	95.15
18	0	0	0	91.82	94.96
19	0	0	0	92.93	94.82
20	0	0	0	93.02	95.20
21	0	0	0	90.98	94.70
22	0	0	0	92.48	94.62
23	0	0	0	92.76	94.56

Table 3

Data significance experiment and analysis of variance

Source of variation	Mixing uniformity *M*				Material residual rate *E*			
	SS	DF	*F value*	*P value*	SS	DF	*F value*	*P value*
Model	350.62	9	74.49	<0.0001**	36.64	9	28.05	<0.0001**
x_1	7.88	1	15.07	0.0019**	7.53	1	51.89	<0.0001**
x_2	2.80	1	5.36	0.0375*	15.43	1	106.31	<0.0001**
x_3	7.32	1	14.00	0.0025**	4.20	1	28.91	0.0001**
x_1x_2	7.80	1	14.92	0.0020**	0.68	1	4.68	0.0497*
x_1x_3	0.56	1	1.07	0.3189	0.23	1	1.60	0.2276
x_2x_3	23.12	1	44.21	<0.0001**	0.90	1	6.21	0.0270*
x_1x_1	99.87	1	190.98	<0.0001**	3.66	1	25.19	0.0002**
x_2x_2	202.26	1	386.75	<0.0001**	0.71	1	4.89	0.0456*
x_3x_3	1.31	1	2.50	0.1379	3.39	1	23.38	0.0003**
Remaining	6.80	13			1.89	13		
Lack of Fit	3.64	5	1.84	0.2115	1.10	5	2.23	0.1497
Pure Error	3.16	8			0.79	8		
Sum	357.42	22			38.53	22		

Analysis of influencing factors

The calculation results of the response surface of each experiment factor and its interaction on the experiment index were shown in Fig.9. It can be seen from the figure that the primary and secondary order of the influence of each experiment factor on the mixing uniformity was spindle speed>mixing time>fullness coefficient, and the primary and secondary order of the influence of each experiment factor on the material residual rate was fullness coefficient>spindle speed>mixing time.

Figure 9a was the response surface diagram of the influence of the interaction between the spindle speed and the fullness coefficient on the mixing uniformity and the residual rate of the material when the mixing time was 0 level. It showed that when the spindle speed was constant and the fullness coefficient gradually increased within the experiment range, the mixing uniformity first increased and then decreased, and the material residue rate gradually increased. When the full coefficient was constant and the spindle speed gradually increased within the experiment range, the mixing uniformity first increased and then decreased, and the material residual rate gradually decreased. The peaks of the mixing uniformity and the material residual rate both appeared in the middle level range. This was because the fullness coefficient determined the total amount of material in the same time. When the fullness coefficient was at low level, the total amount of material was smaller, which caused the weakly active diffusion movement between the material, and the reduced shearing effect on the material of the ribbon, thereby the mixing effect was poor and the material was less attached to the inner wall of the mixing chamber and the mixing arms. When the fullness coefficient was at high level, there was more material in the mixing chamber, where the diffusion effect between materials was limited by the movement space. At the same time, under the same spindle speed, the spiral ribbon would disperse more the driving force of the material, thus affecting the convective mixing process and reducing the mixing effect, attaching more material to the mixing chamber wall and mixing arms. When the fullness coefficient was constant, appropriately increasing the spindle speed to increase the power input can improve the mixing effect. When the spindle speed was too high, during a larger input of power, the material moving speed was increased and the material residue was little. However, the material with different bulk densities was prone to form different mixed material areas in the mixing chamber, resulting in uncoordinated convection and diffusion conditions of the material in the horizontal and vertical directions, reducing the mixing effect.

Figure 9b was the response surface diagram of the influence of the interaction between the fullness coefficient and the mixing time on the mixing uniformity and the residual rate of the material when the spindle speed was 0 level. When the fullness coefficient was constant, and the mixing time was within the experiment range, the uniformity of mixing increased with the increase of mixing time, and the residual rate of material decreased with the increase of mixing time. When the mixing time was constant and the fullness coefficient gradually increased within the experiment range, the mixing uniformity first slowly increased and then decreased, and the residual rate of materials gradually increased. This is because when the spindle speed was constant and the input power was constant, the same fullness coefficient and the same material had the same force per mixing time; the mixing time increasing improved the mixing movement time of the material in

the mixing chamber, further improving the mixing effect. But it also increased the time for the material to attach to the inner wall of the mixing chamber, which improved the adhesion strength and reduced the amount of material discharged.

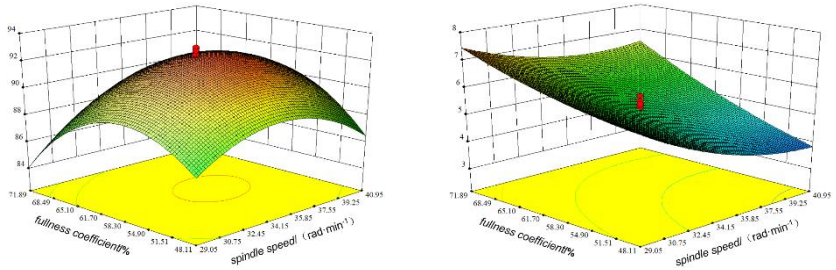

a. The effect of the interaction between the spindle speed and the fullness coefficient on the uniformity of mixing (left) and the residual rate of material (right)

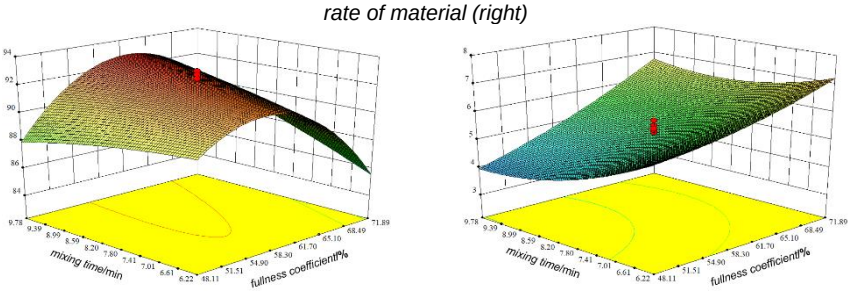

b. The effect of the interaction between fullness coefficient and mixing time on mixing uniformity (left) and material residual rate (right)

Fig. 9 - Response surface analysis of the factors interaction effect on the index

Parameter optimization and verification test

Set the target parameter the mixing uniformity and the material residual rate to maximize, and the factors parameter to the range of experiment to obtain the optimal working parameter combination of the segmented type mixer with double spiral ribbon: the spindle speed was 37.63rad/min, the fullness coefficient was 55.77%, and the mixing time was 9.33min, the overall operation effect being the best. The predicted mixing uniformity will be 91.7445% and the material residue rate will be 95.6798%.

In order to further verify the reliability and applicability of the mathematical model, the optimization results were tested and verified under the same experiment conditions, while the actual test results and the model prediction values were analysed for error. Considering the operability of the test, the optimization results were adjusted as follows: the spindle speed was 38.00rad/min, the fullness coefficient was 55.00%, and the mixing time was 9.33min, and three repeated tests were carried out to obtain the best working parameter combination. The average values of the test values of uniformity and material residue rate were 91.25% and 95.19%, respectively, which were close to the predicted values of the model. The relative error between the actual and predicted values didn't exceed 0.5%, indicating the established model and analysis results were valid.

CONCLUSIONS

In this paper, the mixing uniformity and material residue rate were used as the evaluation indicators of the mixing effect of the segmented type mixer with double spiral ribbon, and the influence of the spindle speed, fullness coefficient and mixing time under the mixing condition of maize straw and cow dung was studied. A response surface model was established, and the equipment's best working parameters were optimized through experiments, with the following conclusions:

1) Through the analysis of the mixing process of agricultural wastes, the segmented type mixer with double spiral ribbon was divided into three sections in the left, middle and right anti-spiral direction in the horizontal direction, and two sections in the anti-rotation direction in the vertical direction, so that the material in the three-dimensional reciprocating mixing movement was realized in the mixer to enhance the mixing effect of the material. The finite element analysis of the mixing mechanism was carried out to verify the feasibility of equipment design and operational reliability.

2) Through the ternary quadratic regression orthogonal rotation combination experiment, the mixer parameter optimization and verification tests were carried out, and the regression equation between the impression factors and the indexes was established and optimized. The influence of the factors and their interaction on the mixing effect and the law were analysed too.

The best working parameters of the equipment were: spindle speed 38rad/min, fullness coefficient 55%, mixing time 9.33min, upon which the mixing effect was the best, when the time mixing uniformity and material residue rate reached 91.25% and 95.19%. Respectively, it met the requirements of agricultural waste fertilizer production technology and had better performance.

This study only conducted related research on the mixing parameters and mixing effects of maize straw and cow dung under the experimental conditions. In the later stage, it is necessary to increase different types of straw and livestock manure and their interaction with mechanical structures and materials to conduct in-depth research to improve equipment applicability and reliability.

ACKNOWLEDGEMENT

The study was supported by the Key R&D Guidance Plan Project of Liaoning Province (2019JH8/10200019) and the Higher Education Research Budget Project of Liaoning Province (LSNFW201909). The authors thank relevant scholars for their assistance in the literature.

REFERENCES

[1] Cârdei P., Stefan V., Popa L. et al., (2019), Statistical models for the working process carried out by the organic fertilizer spreading machine. *INMATEH-Agricultural Engineering*, Vol.58, Issue 2, pp.121-128, Bucharest/Romania;

[2] Chai Rushan, Wang Qingyun, Ye Xinxin et al., (2019), Nitrogen resource quantity of main grain crop straw in China and the potential of synthetic nitrogen substitution under straw returning (我国主要粮食作物秸秆还田替代化学氮肥潜力). *Journal of Agro-Environment Science*, Vol.38, Issue 11, pp. 2583-2593, Tianjin/China;

[3] Chen Zhiping, Zhang Xuwen, Lin Xinghua, et al., (2004), Selection manual for mixing and mixing equipment design (搅拌与混合设备设计选用手册). *Chemical Industry Press*, Beijing/China.

[4] Hevko R.B., Yazlyuk B.O., Liubin M.V., Tokarchuk O.A., Klendii O.M., Pankiv V.R., (2017), Feasibility study of mixture transportation and stirring process in continuous-flow conveyors. *INMATEH-Agricultural Engineering*, Vol.51, Issue 1, pp.49-58, Bucharest/Romania;

[5] Hevko B.M., Popovich P.V., Diachun A.Y., Lyashuk O.L., Liubachivskyi R.O., (2015), The study of bulk material kinematics in a screw conveyor-mixer. *INMATEH-Agricultural Engineering*, Vol.47, Issue 3, pp.155-162, Bucharest/Romania;

[6] Li Daoyi, Li Shujun, Liu Tianshu et al., (2013), Effect of mixing on dry anaerobic digestion of dairy manure (搅拌对牛粪干式厌氧发酵效果的影响). *Transactions of the Chinese Society for Agricultural Machinery*, Vol.44, Issue 2, pp.117-120, Beijing/China;

[7] Liu Dejun, Wang Bin, Liu Yongbiao et al., (2019), Design and experiment of horn comb-type adhesive-material mixing device for straw boards. *IOP Conf. Series: Materials Science and Engineering*, Vol.490, Issue 5, 052029;

[8] Naumenko M., Sokol S., Filipenko D., Guridova V., Kharytonov M., (2018), Numeric model of the grain mixture flow in a cylindrical sieve which revolves around the inclined axis. *INMATEH-Agricultural Engineering*, Vol.56, Issue 3, pp.67-74, Bucharest/Romania;

[9] Pankiv V.R., Tokarchuk O.A., (2017), Investigation of constructive geometrical and filling coefficients of combined grinding screw conveyor. *INMATEH-Agricultural Engineering*, Vol.51, Issue 1, pp.59-68, Bucharest/Romania;

[10] Peter S, Alexey A, Nikolai T., et al., (2020), Investigation of impact of technological and structural parameters upon energy indicators of work of mixer. *19th International Scientific Conference Engineering for Rural Development, Engineering for Rural Development*, Vol.19, pp.1338-1348, Jelgava/Latvia;

[11] Pylypaka S.F., Klendii M.B., Klendii O.M., (2017), Particle motion over the surface of a rotary vertical axis helicoid. *INMATEH-Agricultural Engineering*, Vol.51(1), pp.15-28, Bucharest/Romania;

[12] Stefan V., Cardei P., Popa L. et al., (2019), Influence of the manure spreading machines' working parameters on the qualitative performances of the fertilization process. *INMATEH-Agricultural Engineering*, Vol. 58, Issue 2, pp.115-120, Bucharest/Romania;

[13] Stefan V., Cardei P., Vladut V.N. et al., (2018), Mathematical model for particle motion applied on a manure spreading apparatus used in environmentally friendly technology. *Environmental Engineering and Management Journal*, Vol.17, pp.217-227, Iasi / Romania;

[14] Wang Jinwu, Tang Han, Wang Jinfeng, (2017), Comprehensive utilization status and development analysis of crop straw resource in northeast China (东北地区作物秸秆资源综合利用现状与发展分析). *Transactions of the Chinese Society for Agricultural Machinery*, Vol.48, Issue 5, pp.1-21, Beijing/China;
[15] Wang Nong, Liu Baocun, Sun Yuebing, (2020), Problems in the agricultural environment of China and innovation of future science and technology (我国农业生态环境领域突出问题与未来科技创新的思考). *JAES.*, Vol.37, Issue 1, pp.1-5, Tianjin/China;
[16] Wang Ruifang, Li Zhanyong, Dou Rubiao, et al., (2013), Simulation on random motion and mixing characteristic for soybean in rotary drum (水平转筒内大豆颗粒随机运动与混合特性模拟). *Transactions of the Chinese Society for Agricultural Machinery*, Vol.44, Issue 6, pp.93-99, Beijing/China;
[17] Xue Zhiping, Bai Xuewei, Zhang Bo, et al., (2017), Analysis on flow features for screw feeder based on discrete element model (基于离散元法的螺旋进料器物料流动特性分析). *Journal of Shenyang Agricultural University*, Vol.48, Issue 1, pp.63-69, Shenyang/China;
[18] Yu Keqiang, He Xun, Li Liqiao, et al., (2015), Experimental study on mixing uniformity detection method of total mixed ration (全混合日粮混合均匀度检测方法的试验研究). *Journal of Shenyang Agricultural University*, Vol.46, Issue 4, pp.440-448, Shenyang/China;
[19] Zhang Feng, Yu Wei, Liu Wenhe, et al. (2020), The mixed fermentation technology of solid wastes of agricultural biomass. *Frontiers in Energy Research*, Vol.8: 50, Lausanne/Switzerland;
[20] Zhang Lixian, Yang Zhongping, Zhang Qiang, Zhu Xinhua, Hu Haijun, (2017), Mechanical behaviour of corn stalk pith: an experimental and modelling study. *INMATEH-Agricultural Engineering*, Vol.51, Issue 1, pp.39-48, Bucharest/Romania.

INTELLIGENT AQUACULTURE ENVIRONMENT MONITORING SYSTEM BASED ON LORA COMMUNICATION TECHNOLOGY
/
基于LoRa 通信技术的智能水产养殖环境监控系统

Huiying Cai*[1)], Fangzhen Li[1)], Peng Lv[1)], Lingqiang Ran[1)], Lida Zou[1)] [1)]
[1)] Shandong University of Finance and Economics, school of computer science and technology, Jinan / China;
Tel: +86-0531-88596229; E-mail: caihuiying323@163.com
DOI: https://doi.org/10.356.33/inmateh-63-11

Keywords: *aquaculture, monitoring system, LoRa, PLC Intelligent controller, variable universe*

ABSTRACT
*In view of the nonlinearity and large time delay characteristics of the aquaculture, this paper proposes an environment monitoring system based on low long range (LoRa) communication technology. The system integrates sensor nodes, dissolved oxygen regulation node, LoRa communication network and personal computer (PC) platform to realize real-time monitoring, storage and data sharing. The environmental parameters were processed by programmable logic controller (PLC) intelligent controller, in which, the dissolved oxygen was adjusted with the variable universe fuzzy PID algorithm. The system was tested in a fish pond with an area of 110*120 square meters. The results show that the system can obtain temperature, pH and dissolved oxygen in real time and it has the advantages of high measurement accuracy, stable and reliable data transmission, and can satisfy the needs of aquaculture intelligent management.*

摘要
*针对水产养殖非线性与大时滞的特点，本文提出了基于 LoRa 通信技术的水产养殖环境监测系统设计，系统集传感器节点、溶解氧调控节点、LoRa 通信网络、上位机平台于一体，实现了数据的实时监控、存储与共享。PLC 智能控制器对传感器采集到的环境参数进行处理并通过变论域模糊 PID 算法对水中溶解氧浓度进行智能调节。该监控系统在面积为 110*120 平方米的鱼塘进行了实验，试验结果表明：该系统可实时获取温度、pH 值、溶解氧等养殖环境参数信息系统，优势是测量精度高，数据传输稳定可靠，满足了水产养殖智能化管理的需要.*

INTRODUCTION

In recent years, the aquaculture industry of China has developed rapidly, but it still faces the problems of low efficiency and high labour intensity, and has not fully realized the intelligent management mode. The amount of aquaculture cannot meet the demand of consumption. Temperature, pH and dissolved oxygen are important water environmental parameters in aquaculture. Traditionally, the farmers obtain environmental parameters with manual sampling and chemical analysis which is time-consuming and the accuracy of the parameters is low.

The rapid development of Internet of things technology has played an important role in changing the current extensive breeding mode. Researchers have carried out a variety of related research work and achieved important results. The android platform aquaculture remote monitoring system based on the Internet of things was designed to realize the remote monitoring of water quality sensor parameters with good real-time performance (*Sang Q.S., 2018*).

Through the integration of internet of things and GIS technology, a centralized management of regional aquaculture management was proposed and can promote the development of aquaculture to the direction of intelligence and information (*Zhao R.Y., 2020*).

A smart data gathering system for monitoring several parameters in aquaculture tanks was designed using a wireless sensor network (*Parra L., Sendra S., 2017*).

A low-cost water-quality monitoring system based on ZigBee is reported to measure the important variables in precision aquaculture (*López R.A.B., Cordova L.R.M. et al, 2020*). This paper puts forward an aquaculture environment monitoring system based on LoRa communication technology which is a popular communication protocol of Internet of things technology.

[1] *Huiying Cai, Ph.D.; Fangzhen Li, Ph.D.; Peng Lv, Ph.D.; Lingqiang Ran, Ph.D.; Lida Zou, Ph.D.;*

The system, which is composed of hardware part and upper computer platform, realizes the remote collection function of aquaculture environmental parameters (pH, temperature, dissolved oxygen) and the regulation function of dissolved oxygen in water. The hardware part is composed of sensor node, dissolved oxygen regulation node and LoRa communication network. The sensor node uses ARM cortex m3 core based stm32f103c8t6 processor to collect breeding environment information and upload gateway free data through LoRa communication module. LoRa communication protocol has the advantages of low power consumption, long communication distance, automatic frequency hopping and rate adaptive function. The dissolved oxygen regulation node adopts Siemens smart controller to control the on-site aerator and feeding equipment. The PC platform can monitor the signal strength of the sensor node LoRa antenna, which provides a basis for on-site layout of sensor nodes and the evaluation of the quality of communication links.

MATERIALS AND METHODS

System architecture

The parameters detected by the aquaculture environment monitoring system include temperature, dissolved oxygen and pH. The architecture of the monitoring system is shown in Figure 1. It consists of the physical layer, communication layer and application layer. The physical layer is used to collect breeding environment parameters and receive control signals to control dissolved oxygen concentration. The circuits to collect the temperature, dissolved oxygen and pH are designed on the stm32f103c8t6 based sensor nodes of the physical layer. The dissolved oxygen concentration and the feeding equipment are controlled through the digital quantity interface by the PLC controller. LoRa communication module with RS485 interface is equipped between PLC controller and server of host computer to receive data command. The communication layer is used to transmit breeding environment information and dissolved oxygen regulation information. The application layer is used to query, storage and share data.

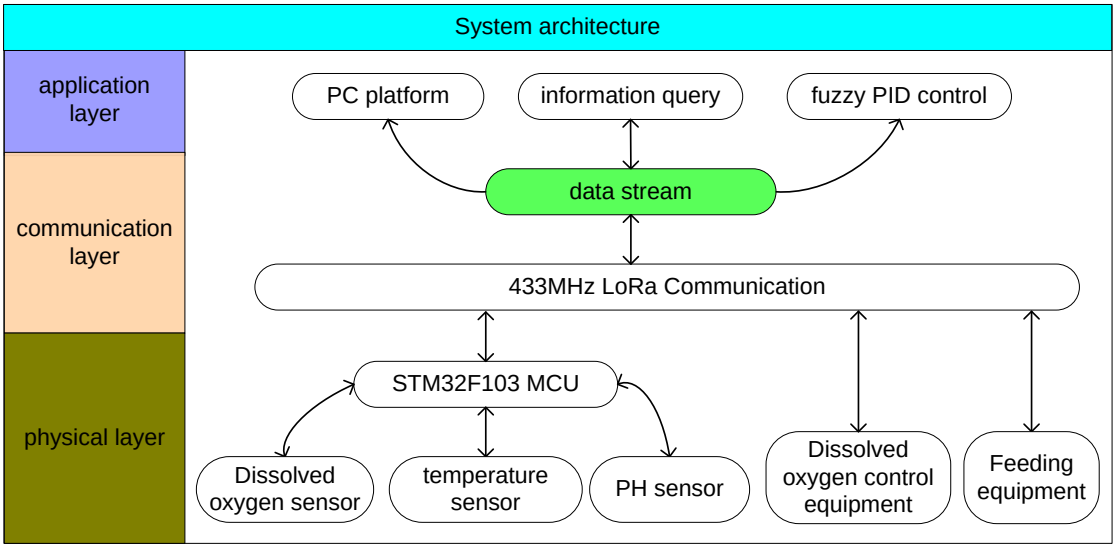

Fig.1 - System framework

Design of the sensor nodes

Hardware structure design of wireless sensor network node

The hardware structure design of sensor network node is shown in Figure 2. The sensor network node includes the temperature sensor, dissolved oxygen sensor, pH sensor, A/D conversation circuit, processor, LoRa module and flash memory. The wireless sensor network node is powered by solar cells which are widely used in the control system of agriculture (*Ravishankar E., Booth R.E. et al, 2020*) and aquaculture (*El-Atab N., Almansour R., 2020*).

The core processor is ARM cortex m3 core based stm32f103c8t6 which has Serial Peripheral Interface (SPI) interface and A/D conversation interface to acquire, analyse, store and upload data. LoRa module and flash memory communicate with processor through the SPI interface. Temperature, dissolved oxygen and pH are acquired by the temperature sensor, dissolved oxygen sensor and pH sensor respectively. The sensors are processed by the information analysis module and connected with the A/D interface of the processor.

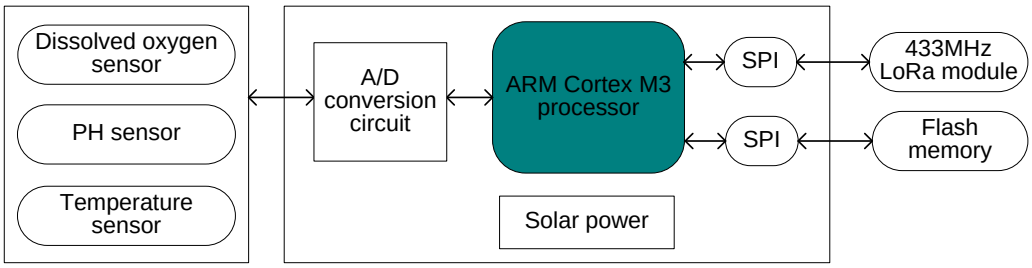

Fig.2 – Design of sensor network node

The hardware circuit of sensor network node is shown in Figure 3. Figure 3a is the power supply module which adopts 12V power supply. The power interface is protected by high reliability devices. The first level protection adopts varistor 14d470k (MOV1), 1.1A/60V fuse (FUSE1), transient voltage suppressor (TVS) SMCJ36CA (D4). The varistor 14d470k whose action voltage is 47 V and peak current is 1 KA (8/20us pulse) can absorb strong energy interference. The response speed of TVS SMCJ36CA is fast. Benefit from these components, the first level protection is used to absorb large current and voltage generated by electromagnetic interference. The second level protection includes TVS SMCJ36CA (D60), common mode inductor acp3225-102 and ceramic air discharge tube smd1812-151 (D50) group. In the case that the primary protection fails or cannot absorb interference completely, the secondary protection will play a significant role in absorbing interference. The asynchronous buck power chip mp1482 converts the input 12-18 V into 3.3 V for sensor nodes, and can provide 2A load current. In this power supply system, the anti-power supply surge differential mode interference can reach 1 KV voltage while anti-common mode interference can reach 1 KV voltage.

The main control module stm32f103c8t6 interacts with LoRa communication module through SPI communication interface. LoRa communication module uses lsd4rf-2r717n10 of which working frequency band is 860-935 MHz. It adopts LoRa modulation mode and is compatible with and supports 2FSK and GFSK traditional modulation mode. Hardware frequency hopping technology is combined with LoRa spread spectrum technology, which can achieve better communication concealment and security. W25x16 is selected as the flash memory of which the storage space is 16 MB**,** the communication rate can reach 72 MHz, and the current consumption is 0.5 mA under normal working condition. The memory communicates with stm32f103c8t6 through SPI interface.

The dissolved oxygen acquisition circuit is shown in Figure 3b. It uses the polarographic film dissolved oxygen electrode composed of platinum electrode and silver electrode. Dissolved oxygen electrode generates current type signal when 0.7 V excitation voltage is applied to platinum electrode and silver electrode. In the circuit, two-stage operational amplifier circuits (U1, U2) with ±3.3 V power supply are used to process the current signal. U1 converts the current generated by dissolved oxygen electrode into voltage through resistance R1, and U2 further filters and amplifies the voltage. The calculation formula of dissolved oxygen voltage is shown in Equation (1), in which, V_{ab}, I, R_1, R_2, R_6 represents the dissolved oxygen voltage, the output current of the dissolved oxygen electrode, and the fixed resistances respectively.

$$V_{do} = \frac{R_1 R_2}{R_6} I \tag{1}$$

The pH acquisition circuit is shown in Figure 3c. It uses a composite electrode composed of calomel electrode and glass electrode to measure pH. When the concentration of hydrogen ion changes, the electromotive force between calomel electrode and glass electrode will change, and the weak voltage signal will be output. This module uses two-stage operational amplifier circuits (U3, U4) with ±3.3 V power supply. U3 is a reverse amplifying circuit, and the voltage magnification is adjusted by sliding resistance. U4 reverses the output voltage signal of U3 to meet the input range of 0-3.3 V. The resistors R3 and R4 can adjust the reference of adjustable output voltage signal. The power filter capacitor C4, C5, C6, and C7 can filter out the high-frequency interference and make the power supply stable. The voltage signal of pH can be calculated by Equation (2), in which, V_{ph} is the voltage signal of pH and R_1, R_2, R_3, R_4, R_5, R_6, R_8 are resistors with fixed value.

$$V_{ph} = \frac{3.3R_3}{R_3 + R_4}\left(1 + \frac{R_8}{R_6}\right) - \frac{R_8}{R_6}\left(1 + \frac{R_1 + R_2}{R_5}\right) \tag{2}$$

Temperature acquisition circuit is shown in Figure 3d. The bridge circuit is composed of R1, R2, R3, and R4, in which, R4 is the built-in thermistor (NTC-MF52AT). U5A, U5B is the two stage operational amplifier to amplify the voltage signal. U5A is a differential operational amplifier which can effectively amplify the differential mode voltage and suppress the common mode voltage. U5B can further process the voltage signal processed by U5A to make it fall in the A/D converter range. PR1 and PR2 can adjust the output reference voltage and output magnification voltage respectively. The collected temperature signal can be computed by Equation (3), in which, V_t is the voltage of the temperature signal and the other symbols with R as superscript are resistors with fixed value.

$$V_t = \frac{3.3R_{PR1}}{R_{16}+R_{PR1}}\left(1+\frac{R_{PR2}}{R_6}\right)-\frac{R_{PR2}}{R_6}\left(\frac{3.3R_3R_7(R_{11}+R_{12})}{R_{11}(R_2+R_3)(R_7+R_8)}-\frac{R_4R_{12}}{R_{11}(R_1+R_4)}\right) \quad (3)$$

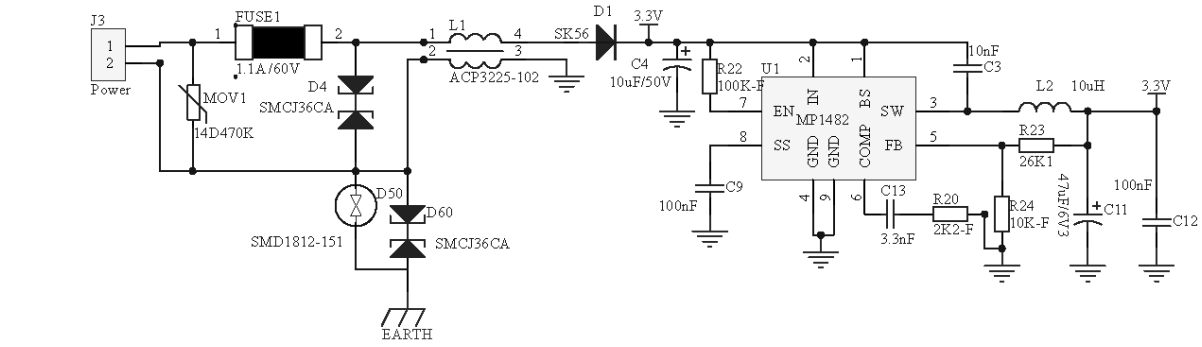

(a) power supply circuit

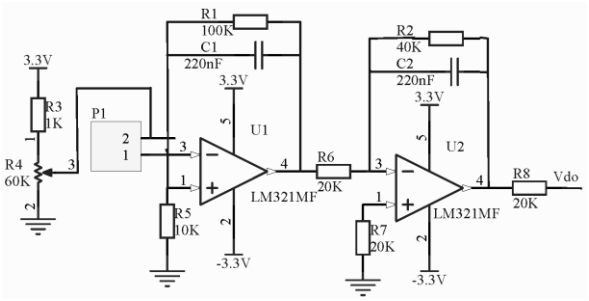

(b) Dissolved oxygen acquisition circuit

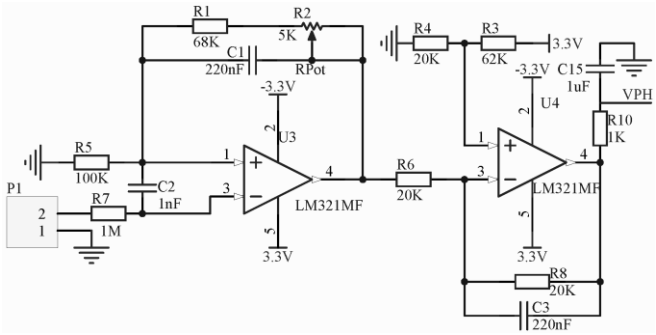

(c) pH acquisition circuit

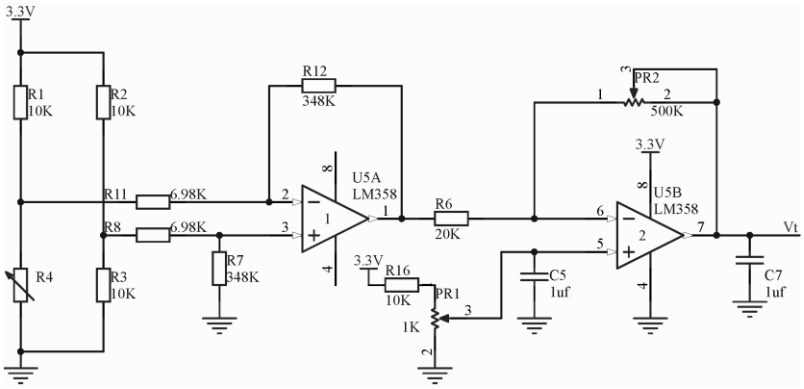

(d)Temperature acquisition circuit

Fig. 3 – Hardware design of sensor nodes

Software design of wireless sensor network node

The software of sensor network node is based on the embedded UC/OS-II operation system which has the advantages of preemptive, multi task and real-time (*Ungurean, I., 2020*). It can create 64 tasks. The tasks, priority, stack size and function established in the monitoring system are listed in table 1. The sensor network nodes are powered and the operation system and outside devices are initialized firstly. Then the task control function establishes the temperature, pH, dissolved oxygen, LED flashing, upload communication tasks, and assign priority and stack space to them. Sensor network node uses CRC verification and can transmit, receive, and converse data.

Table 1

The tasks of the operating system

Task	Priority	Stack size (K)	Function
WenDuTaskTCB	5	512	read temperature
PHTaskTCB	6	512	read pH
RongJieYangTaskTCB	7	512	read dissolved oxygen
LEDTaskTCB	9	128	LED flashing indication
TongXinTaskTCB	4	1024	communication

Calibration of sensors

As temperature, dissolved oxygen, and pH are represented through voltage which is susceptible to temperature, it is necessary to calibrate the relationship between output voltage and temperature of each sensor. Different solutions are put into the constant temperature magnetic stirrer. It was cooled into 1℃. And then the temperature was increase by 1℃ every 10 minutes. Fifty values were acquired during this process. Each value was sampled ten times by the corresponding modules and the average value was used.

The correlation coefficient of the output voltage and temperature was computed. The dissolved oxygen sensor and pH sensor use saturated sodium sulphite solution and standard solution with pH = 7 respectively.

The calibration curves are shown in Figure 4. Figure 4a and figure 4b show linear relationship between the independent variable and dependent variable of dissolved oxygen and pH. The correlation coefficient of dissolved oxygen sensor and pH sensor are 0.994 and 0.9969 respectively.

Figure 4c shows that there is an inflection point in the fitted curve where the slope of the curve is the largest. In the range of [1, 25] and [25, 50], there is a piecewise linear relationship respectively, and the correlation is strong. The linear correlation function is shown in Figure 4c.

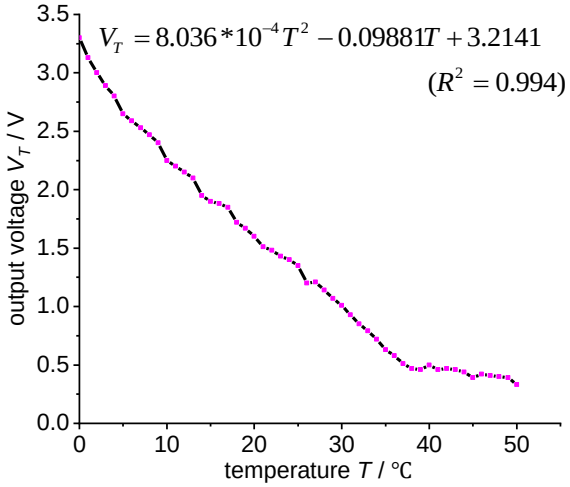

(a) The relationship between voltage and temperature of dissolved oxygen

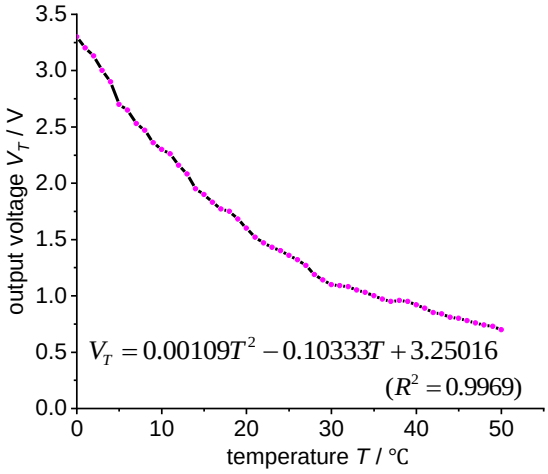

(b) The relationship between voltage and temperature of pH

Fig. 4 - Calibration curves

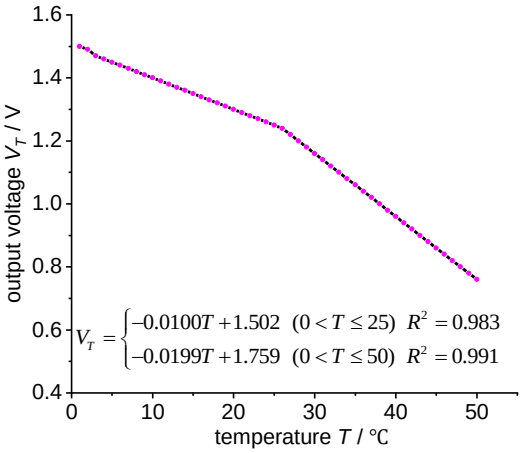

(c) The relationship between voltage and temperature

Fig. 4 c - Calibration curves

Design of the dissolved oxygen regulation equipment

The dissolved oxygen regulation equipment adopts Siemens PLC controller S7-200 which is equipped with RS485 communication interface and supports Modbus RTU, USS and free port communication protocol (*Liu T., Zhao K. et al, 2020*). The system structure of dissolved oxygen regulation equipment is shown in Figure 5. The dissolved oxygen regulation equipment adopts 380 V three-phase AC motor (M1), and the feeding equipment adopts 220 V AC motor (M2). QS1 and QS2 are power switch circuit breakers, FU1 and FU2 are fuses, KM1 and KM2 are AC contactors, FR1 and FR2 are thermal relays. The output ports Y0 and Y1 control the dissolved oxygen regulation equipment and the feeding equipment respectively. LoRa communication equipment and PLC controller are connected through RS485 interface. In the automatic control mode, QS1 and QS2 are closed. When the LoRa communication equipment receives the command to open the dissolved oxygen regulation equipment or feeding equipment, the information is transmitted to the PLC controller through RS485 interface. The corresponding output ports Y0/Y1 of PLC acts, and the coil KM1/KM2 is powered on. Then, the main contact KM4/KM3 is closed, and the motor M1/M2 rotates. KM4/KM3 is used as the auxiliary contact of AC contactor to judge the closed state of contactor.

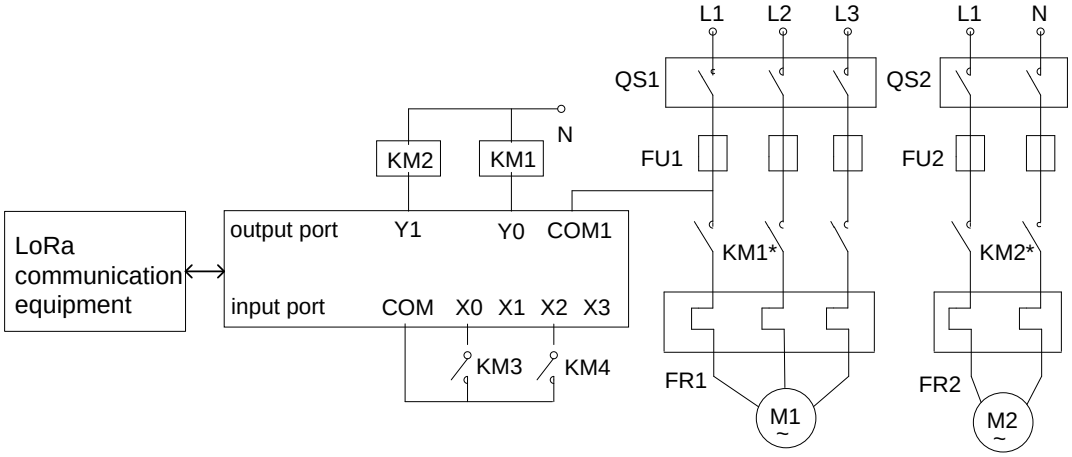

Fig. 5 - Schematic diagram of dissolved oxygen regulation equipment

Communication design

Data transmission of communication layer depends on wireless communication module lsd4rf-2r717n10 with 433MHz. The main chip is SX1278 which can adjust the transmission power. The sensor node adopts monitoring mode and is in sleep mode when there is no data acquisition command.

The PC software platform will measure the RSSI value of each communication to evaluate the link communication quality. The RSSI value can be used to optimize the deployment of field nodes. Unreliable communication will happen as occasionally as there are co frequency interference and plant occlusion in the complex outdoor environment. In this case, the platform sets the RSSI value according to the actual needs to make it in the right range. And the platform will issue the corresponding command to adjust the node

transmission power to ensure the best communication quality. The transmission distance between sensor node and platform terminal and the relationship between receiving power and transmitting power are computed according to Equation (4).

$$P_R = P_T / r^n \tag{4}$$

In which, P_R, P_r, r, n represents wireless signal receiving power, wireless signal transmitting power, transmission distance and propagation factor, respectively.

The other form of Equation (4) can be expressed as Equation (5). Equation (5) shows that the received power changes in an inverse exponential curve.

$$P_R = B - 10 \cdot n \cdot \lg(r) \tag{5}$$

Remote monitoring terminal

Communication between sensor network nodes and host computer

There are two ways to upload the data: the node actively reports the data and the software platform queries the data. The data is communicated through LoRa. If the upload is successful, the sensor network nodes will sleep in the low-power mode after feedback. When the software platform queries the pH, the command denoted by 09 02 00 00 00 02 F8 8C is send. In the command, 09 represent device address, 02 represents function code, 00 00 and 00 02 represents starting address of the register and the number of bytes to read respectively, F8 8C represents the CRC verification. The returned data frame is 09 03 04 XX XX 00 02 22 74. In the frame, the first, second and third bytes represent the device address, function code and the total number of bytes of returned pH respectively, the fourth and fifth bytes are pH, the sixth and seventh bytes represent decimal places, and the eighth and ninth bytes represent CRC verification. XX XX represents the value of pH in hexadecimal system. 00 02 represents that pH has two decimal places. For example, 03 09 can be converted into decimal number 1411 and the value of pH is 14.11.

In order to improve the efficiency of communication, the temperature information is uploaded together with the data of dissolved oxygen. When the software platform queries the dissolved oxygen and temperature values, it sends the command: 03 03 00 00 00 04 45 EB, in which, the first 03 is the device address, the second 03 is the function code, 00 00 is the starting address of the register, 00 04 is the number of bytes to read, and 45 EB is the CRC check. The returned data is: 03 02 08 XX XX 00 02 YY YY 00 01 5C 45, in which, 03, 02, and 08 represent device address, function code, and number of returned bytes respectively. XX XX represents the value of dissolved oxygen. 00 02 denote the number of decimal places. YY YY is the value of temperature. 00 01 denote the number of decimal places. 5C 45 is the CRC verification.

Dissolved oxygen regulation

Variable universe fuzzy control has shown significant potential in real-time control (*Yang S.M., Deng B. et al, 2019*). So, it is adopted to solve the large time delay problem of dissolved oxygen in pond. The control diagram is shown in Figure 6. The dissolved oxygen sensor sends the collected data to the PLC controller through LoRa communication protocol, and the PLC controls the aerator according to the variable universe fuzzy PID control algorithm.

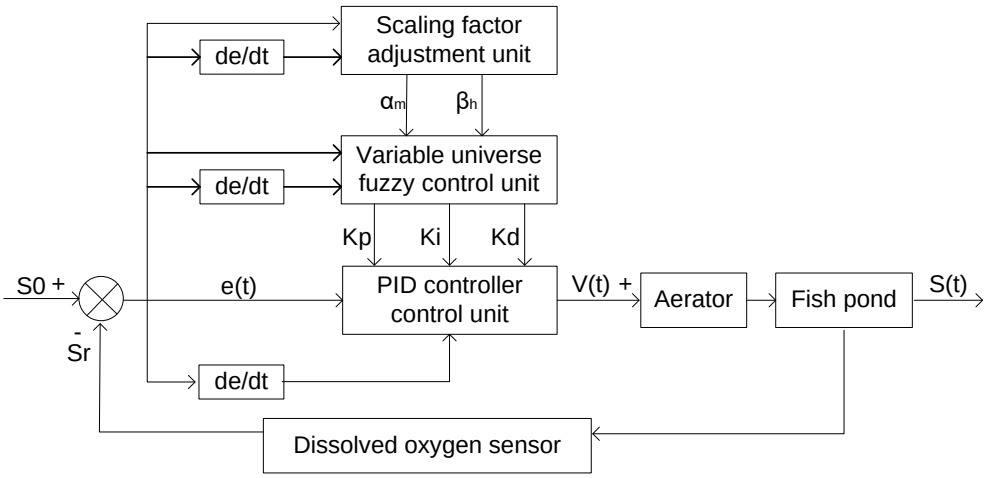

Fig. 6 - Diagram of the variable universe fuzzy control

Fuzzy PID control algorithm

The fuzzy PID algorithm (*Ren Q., 2020*) is adopted to adjust the dissolved oxygen. The fuzzy subsets of input variables e, ec and out variables $\triangle K_P$, $\triangle K_I$, $\triangle K_D$ are {NB, NM, NS, ZO, PS, PM, PB}, representing negative big, negative middle, negative small, zero, positive small, positive middle, positive big, respectively. The basic domains of e, ec, $\triangle K_P$, $\triangle K_I$, $\triangle K_D$ are [-9, 9], [-2, 2], [-10, 10], [-0.5, 0.5], [-10, 10], respectively. The fuzzy domains of input and output are {-6, -5, -4, -3, -2, -1, 0, 1, 2, 3, 4, 5, 6}. The quantification factors of e, ec, $\triangle K_P$, $\triangle K_I$, $\triangle K_D$ are K_e=6/9=0.67, K_{ec}=6/2=3, K_{rP}=10/6=1.67, K_{rI} =0.5/6=0.083, K_{rD}=10/6=1.67, respectively.

Membership function is an important factor to determine the control effect of fuzzy controller (*Mani P., Rajan R. et al, 2021*). In order to better restrain the change of dissolved oxygen, this paper uses trapezoidal function as the input and output membership function of fuzzy controller, as shown in Equation (6), in which, F_{trapmf} is the membership value, x is the universe value of fuzzy controller, and a, b, c, d is the parameter of trapezoidal membership function.

$$F_{trapmf} = \begin{cases} 1 & (c \le x \le b) \\ \dfrac{a-x}{a-b} & (b \le x \le a) \\ \dfrac{c-x}{c-d} & (d \le x \le c) \\ 0 & (a \ge x \ or \ x \le d) \end{cases} \tag{6}$$

Based on the experience of breeding operators and the technical knowledge of dissolved oxygen regulation design experts, a fuzzy control unit with two-dimensional input (e, ec) and three-dimensional output ($\triangle K_P$, $\triangle K_I$, $\triangle K_D$) is constructed. The fuzzy rules of the fuzzy control unit are shown in Table 2.

Table 2

Adjusting rules of KP/KI/KD for fuzzy PID controller

$\triangle K_P$ /$\triangle K_I$ /$\triangle K_D$		error variation: e						
		NB	NM	NS	ZO	PS	PM	PB
ec	NB	PB/NB/PS	PM/NB/ZO	PM/NM/ZO	PM/NM/ZO	PS/NS/ZO	PS/ZO/PB	ZO/ZO/PB
	NM	PM/NB/NS	PM/NM/NS	PM/NM/NS	PM/NS/ZO	PS/NS/ZO	ZO/ZO/NS	ZO/ZO/PM
	NS	PM/NM/NB	PM/NM/NB	PS/NS/NM	PS/NS/NS	ZOZO/ZO	ZO/ZO/ZO	NS/PS/PM
	ZO	PM/NS/NB	PS/NS/NM	PS/NS/NM	ZO/ZO/NS	NS/ZO/ZO	NS/PS/PS	NS/PS/PM
	PS	PS/NS/NB	PS/NS/NM	ZO/ZO/NS	NS/PS/NS	NS/PS/ZO	NM/PM/PS	NM/PM/PM
	PM	ZO/ZO/NM	ZO/ZO/NS	NS/PS/NS	NM/PS/NS	NM/PM/ZO	NM/PM/PS	NM/PB/PS
	PB	ZO/ZO/PS	NS/ZO/ZO	NS/PS/ZO	NM/PM/ZO	NM/PM/ZO	NM/PB/PS	NB/PB/PM

Variable universe scaling factor adjustment unit

In fuzzy PID control, the scope of universe is not changed, which cannot solve the problem of low control accuracy and affect the overall performance of the control system. Based on Fuzzy PID control, a variable universe adaptive fuzzy PID controller is designed, which can effectively solve the problem of low control accuracy and overshoot. After the expansion of variable universe, the scope of universe is shown in Equation (7), in which, α_m, β_h, denotes the expansion factors of input and output universe respectively. The scope of universe $E(e_1)$, $E(e_2)$ decreases with the decrease of deviation and expands with the increase of deviation. For the nonlinear dissolved oxygen system, the time-varying error is effectively suppressed and the control accuracy is improved.

$$\begin{cases} E(e_1) = \left[-\alpha_e(e_1)\times 9, \alpha_e(e_1)\times 9\right] \\ E(e_2) = \left[-\alpha_{ec}(e_2)\times 2, \alpha_{ec}(e_2)\times 2\right] \\ U(e_1,e_2) = \left[-\beta(e_1,e_2)u_1, \beta(e_1,e_2)u_2\right] \end{cases} \tag{7}$$

The variable universe expansion factor must satisfy the duality and coordination in the design. In this paper, the proportional expansion factor based on function design is adopted.

It is shown in Equation (8), where, λ is the proportional constant $\lambda \in (0, 1)$, $\beta(0)$ is the initial value, k_m is the design parameter.

$$\begin{cases} \alpha_m(x) = 1 - \lambda \exp(-k_m x^2) & (m = e, ec) \\ \beta_h(y) = K \sum_{i=1}^{n} p_i \int_0^t e_i(\tau) d\tau + \beta(0) & (n = p, i, d) \end{cases} \quad (8)$$

According to the characteristics of dissolved oxygen regulation combined with practical work experience, the input and output expansion factors are taken respectively, as shown in Equation (9).

$$\begin{cases} \alpha_1(e) = 1 - 0.61\exp(-0.55e^2) \\ \alpha_2(ec) = 1 - 0.61\exp(-0.63ec^2) \\ \beta_p = 3.5|e| \\ \beta_i = \dfrac{1}{|e| + 0.55} \\ \beta_d = 4.2|e| \end{cases} \quad (9)$$

RESULTS

The experiments of LoRa communication, acquisition of water quality parameter data and dissolved oxygen regulation were conducted in a fish pond whose area is 110*120 square meters. The LoRa communication experiment is used to verify the stability and reliability of LoRa communication network transmission. The data acquisition experiment is used to verify the accuracy of parameter acquisition and the correctness of transmission. The dissolved oxygen regulation experiment is to verify the control accuracy of dissolved oxygen content in fish ponds.

LoRa communication experiment

In order to test the performance of LoRa communication module, the communication experiment was carried out in the open environment and the occluded environment. The occluded environment refers to the environment with tree sheltered or telegraph poles or something that blocks the signal. The results are shown in Fig 7.

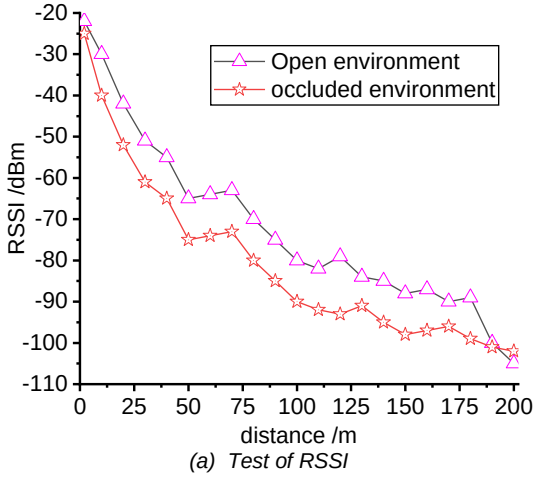

(a) Test of RSSI

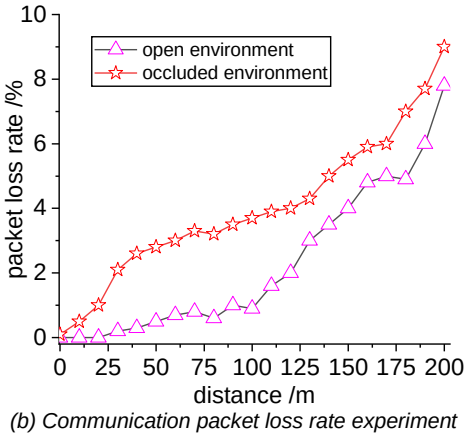

(b) Communication packet loss rate experiment

Fig. 7 – Communication performance experiment of LoRa

Figure 7a shows the performance of LoRa RSSI. In the open environment, when the transmission distance varies from 0 meter to 25 meters, RSSI changes slowly and decreases from – 24 dBm to – 60 dBm gradually. RSSI decreases to -100 dBm when the transmitting and receiving distance reaches 170 meters. In the occluded environment, RSSI will also decrease with the increase of communication distance. Compared with the open environment, the RSSI will be lower at the same distance. The experimental results are consistent with the theoretical relationship that the intensity of LoRa signal changes with the increase of transmission distance.

Figure 7b shows the result of communication packet loss rate experiment. In the open environment, the packet loss rate is higher than 4% when the transmission distance exceeds 150 meters and the RSSI value is – 95 dBm. The packet loss rate increases with the further increase of distance. The packet loss rate reaches 8% when the communication distance is 200 meters and RSSI value is – 105 dBm. Compared with the open environment, the overall change trend of packet loss rate in the occluded environment is slower. The packet loss rate reaches 9% when the transmission distance is 200 meters.

Therefore, an open environment should be chosen and the distance should be controlled within 100 meters to get better signal strength and lower packet loss rate.

Data acquisition experiment

In order to verify the accuracy of aquatic parameter, the data of sensor network nodes were collected in different weather (sunny, cloudy, light rain), different time periods (8:30, 12:00, 19:30). The parameters measured by hash MS5 Hydrolab water quality monitor were taken as the standard values. The results are shown in table 3, from which, it can be seen that: the temperature acquisition accuracy is less than or equal to 0.15, the average relative error is 0.1%; the dissolved oxygen acquisition accuracy is less than or equal to 0.29, the average relative error is 0.8%; the pH value acquisition accuracy is less than or equal to 0.17, the average relative error is 0.81%.

Table 3

Results of Data acquisition experiment

Date	Parameter	Time	Standard value	Actual value	Relative error (%)
September 20, 2020 (sunny)	Temperature (℃)	8: 00	26.86	26.84	-0.07
		12: 00	27.82	27.80	-0.07
		19: 30	27.32	27.35	0.12
	Dissolved oxygen (mg/L)	8: 30	4.62	4.91	6.2
		12: 00	7.60	7.64	0.53
		19: 30	5.72	5.63	-1.57
	pH	8: 30	8.32	8.32	0
		12: 00	6.89	6.92	0.44
		19: 30	8.32	8.33	0.12
September 22, 2020 (cloudy)	Temperature (℃)	8: 30	25.12	25.11	-0.04
		12: 00	25.02	25.13	0.44
		19: 30	24.98	24.96	-0.08
	Dissolved oxygen (mg/L)	8: 30	4.97	5.08	2.21
		12: 00	8.21	8.06	-1.83
		19: 30	4.72	4.88	3.39
	pH	8: 30	6.98	7.12	2.01
		12: 00	6.62	6.72	1.51
		19: 30	7.02	6.98	-0.57
September 24, 2020 (light rain)	Temperature (℃)	8: 30	25.12	25.11	-0.04
		12: 00	26.56	26.58	0.08
		19: 30	25.61	25.46	0.58
	Dissolved oxygen (mg/L)	8: 30	4.89	4.68	-4.29
		12: 00	6.12	6.27	2.45
		19: 30	5.88	5.89	0.17
	pH	8: 30	8.35	8.47	1.44
		12: 00	7.18	7.20	0.28
		19: 30	7.98	8.15	2.13

Dissolved oxygen experiment

In order to verify the regulation accuracy of field control equipment for dissolved oxygen in pond, the regulation test was conducted in pond. Four node sensors, whose average value was taken as the dissolved oxygen amount, were placed in the four corners of the pond. 5 KW impeller aerator is placed in the centre of the pond. The control target value of dissolved oxygen is set to be 7.1 mg/L. In order to verify the control effect of variable universe fuzzy PID controller of dissolved oxygen, self-organizing fuzzy neural controller and fuzzy PID controller are used for comparison. The software platform is set to collect data every 30 minutes, and the collection time is 24 hours. Figure 8 shows the data curve of dissolved oxygen regulated by three controllers. The fluctuation of variable universe fuzzy PID controller is the minimum after the regulation becomes stable. Table 3 shows the comparison data of the performance of the three controllers. From the table, it can be seen that each index of the variable universe fuzzy PID controller has obvious advantages: the regulation time is 53 minutes; the minimum overshoot is 4.89%; the standard deviation is 0.056; and the average error is 0.2. The variable universe fuzzy PID controller has the best performance.

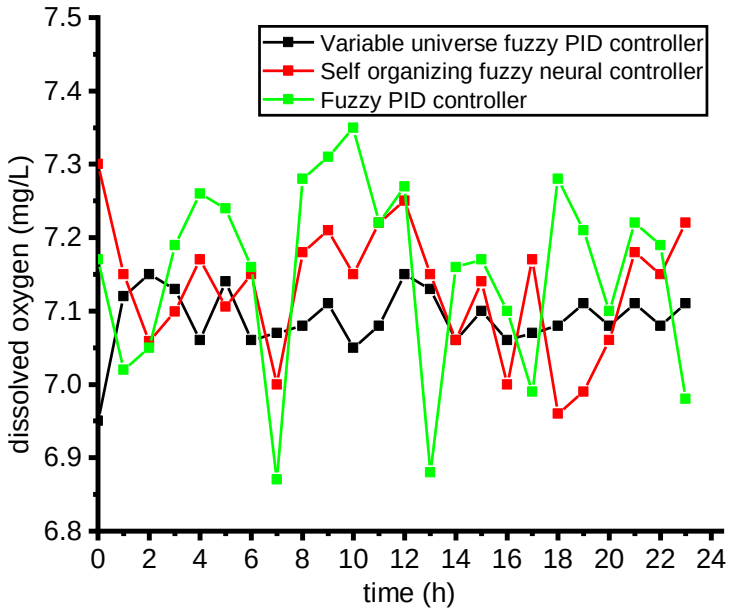

Fig. 8 - Performance test of dissolved oxygen regulation

Table 4

Comparison of controller performance parameters

Parameter	Variable universe fuzzy PID control	Self-organizing fuzzy neural controller	Fuzzy PID control
Adjustment time /min	53	80	120
Overshoot /%	4.89	8.25	16.49
Standard deviation	0.056	0.125	0.223
Average error	0.02	0.05	0.10

CONCLUSIONS

According to the characteristics of aquaculture environment, this paper designed an aquaculture environment monitoring system which integrates advanced technologies LoRa communication technology, variable universe fuzzy PID control and PLC control technology. The system realized the accurate measurement of water quality parameters (temperature, dissolved oxygen, pH) in aquaculture environment and the regulation of dissolved oxygen in water. It can effectively restrain the disturbance caused by uncertain factors in aquaculture environment and has high steady-state precision and strong regulation ability.

ACKNOWLEDGEMENT

This work was financially supported by the Department of Education of Shandong Province, grant no. KJ2018BAN058.

REFERENCES

[1] EI-Atab N., Almansour R. et al., (2020), Heterogeneous cubic multidimensional integrated circuit for water and food security in fish farming ponds, *Small*, vol. 16, no. 4, article number: 1905399, Weinheim/Germany (DOI: 10.1002/smll.201905399);

[2] Liu T.R., Zhao K., Sun C.L. et al., (2020), Real-time flow control of blade section using a hydraulic transmission system based on an H-Inf controller with LMI design, *Energies*, vol. 13, no. 19, article number: 5029, Basel/Switzerland (DOI: 10.3390/en13195029);

[3] Lopez R.A.B., Cordova L.R.M., Nunez J.C.G. et al., (2020), Implementation and evaluation of open-source hardware to monitor water quality in precision aquaculture, *Sensors*, vol. 20, no. 21, article number: 6337, Basel/Switzerland (DOI: 10.3390/s20216112);

[4] Mani P., Rajan R., Joo Y.H., (2021), Integral sliding mode control for T-S fuzzy descriptor systems, *Nonlinear Analysis Hybrid Systems*, vol. 39, article number: 100953, Netherlands (DOI: 10.1016/j.nahs.2020.100953);

[5] Parra L., Sendra S., Llore J., Rodrigue, J.J.P.C., (2017), Design and deployment of a smart system for data gathering in aquaculture tanks using wireless sensor networks, *International Journal of Communication Systems*, vol. 30, no. 16, article number: e3335, Chichester/England (DOI: 10.1002/dac.3335);

[6] Ravishankar E., Booth R.E., Saravitz C. et al., (2020). Achieving net zero energy greenhouses by integrating semitransparent organic solar cells, *Joule*, vol. 4, no. 2, pp. 490-506, Cambridge/USA;

[7] Ren Q., (2020), Intelligent control technology of agricultural greenhouse operation robot based on Fuzzy PID path tracking algorithm, *INMATEH Agricultural Engineering*, vol. 62, no. 3, pp. 181-190. Bucharest/ Romania;

[8] Sang Q.S., (2018), *Aquaculture remote monitoring system based on Internet of things and mobile terminal (基于物联网和移动终端的水产养殖远程监控系统)*, MSc dissertation, Wuhan Institute of Technology, Wuhan/China;

[9] Ungurean I., (2020), Timing comparison of the real-time operating systems for small microcontrollers, *Symmetry-Basel*, vol. 12, no. 4, article number: 592, Basel/Switzerland (DOI: 10.3390/sym12040592);

[10] Yang S., Deng B., Wang J. et al., (2019), Design of hidden-property-based variable universe fuzzy control for movement disorders and its efficient reconfigurable implementation, *IEEE Transactions on Fuzzy Systems*, vol. 27, no. 2, pp. 304-318, NJ/USA;

[11] Zhao R.Y., (2020), Design of remote monitoring system for aquaculture boat based on SuperMap GIS and Android platform *(基于超图GIS 和Android 平台的水产养殖船远程监控系统设计)*, MSc dissertation, Jiangsu University, Jiangsu/China.

DESIGN AND EXPERIMENT OF ADJUSTABLE SOCKET-WHEEL PRECISION FERTILIZER APPARATUS FOR DRY DIRECT-SEEDING RICE

/

可调窝眼轮式旱直播水稻精量穴施排肥器设计与试验

Liu Jun [1], Zhu Dequan[*1,2], Tai Qilei[1], Yu Congyang[1], Wang Tingjue[1], Xue Kang[1], Zhang Shun[1], Liao Juan[1] [1]

[1] School of Engineering, Anhui Agricultural University, Hefei 230036, China;

[2] Anhui Province Engineering Laboratory of Intelligent Agricultural Machinery and Equipment, Hefei 230036, China;

[*] *Corresponding author, E-mail: zhudequan@ahau.edu.cn*

DOI: https://doi.org/10.356.33/inmateh-63-12

Keywords: *hole fertilization, fertilizer apparatus, socket-wheel, numerical simulation, test*

ABSTRACT

To solve problems of non-adjustable fertilizer and low fertilization precision in the precision hole fertilization of dry direct-seeding rice, an adjustable socket-wheel precision hole fertilizer apparatus for rice was designed. The basic structure and working principle of the fertilizer apparatus were expounded, the structural parameters of key components were determined. The numerical simulation experiments based on the discrete element method were carried out by using sulfurized urea as the research object. Selecting the rotation speed of the socket-wheel, the length of the trough, the depth of the socket as the experimental factors, and taking the average amount of fertilizer discharging and the coefficient of variation of fertilization uniformity as evaluation indicators, the orthogonal rotation combined experiments with three factors and five levels were carried out. A multi-objective optimization method was used to determine the best parameter combination under the constraint of the target value of the hole fertilizer discharging of 1.500 g. The simulation results show that the coefficient of variation of fertilizer uniformity was the smallest and the coefficient of variation was 15.80% when the rotation speed of socket-wheel was 26.57 r/min, the length of the trough was 5.36 mm and the depth of socket was 5.64 mm. By using slow-release urea, sulfurized urea and bio-organic fertilizer as test materials, the bench test and field test was carried out on the fertilizer apparatus and the reliability of the simulation results and the adaptability of the fertilizer apparatus were verified.

摘要

针对旱直播水稻精量穴施肥中存在施肥量不可调节、施肥精度低等问题，设计了一种可调窝眼轮式水稻精量穴施排肥器。阐述了排肥器基本结构与工作原理，确定了关键零部件结构参数。以加硫尿素为试验材料，利用离散元法，选取窝眼轮转速、料槽长度、窝眼深度为试验因素，以排肥量均值、排肥均匀性变异系数为评价指标，进行 3 因素 5 水平正交旋转组合试验。在穴排肥量目标值为 1.500 g 的约束条件下，确定了最佳参数组合。仿真结果表明：在窝眼轮转速为 26.57 r/min、料槽长度为 5.36 mm、窝眼深度为 5.64 mm 时，排肥均匀性变异系数最小，变异系数为 15.80%。以缓释尿素、加硫尿素、生物有机肥为试验材料，对排肥器进行台架验证试验与田间施肥试验，验证了仿真结果的可靠性与排肥器的适应性。

INTRODUCTION

At present, banding and broadcasting are the main ways of fertilization for chemical fertilizer in dry direct-seeding rice, and there are problems such as the over-usage of fertilizer and poor uniformity, which not only affect the yield and quality of rice, but also increase production cost and cause environmental pollution *(Zheng et al., 2019, Hu et al., 2020, Wang et al., 2018).*

Precision fertilization can effectively improve the utilization rate of fertilizer, reduce the usage of fertilizer, and help improve the yield and quality of rice *(Fan et al., 2020, Zhang et al., 2018, Wang et al., 2020, Zhang et al., 2019)*. Alameen et al. developed a variable fertilization control system for the granular fertilizer, which could automatically set the required fertilizer amount and improve the fertilization accuracy *(Alameen et al., 2019).* Yang et al. designed a bivariate fertilization machine with an outer groove-wheel, which greatly improved the stability of fertilizer discharging compared with the common outer groove-wheel

[1] *Jun liu, As. M.S. Stud. Eng.; Dequan Zhu, Prof. Ph.D. Eng.; Qilei Tai, As. M.S. Stud. Eng.; Congyang Yu, As. M.S. Stud. Eng.; Tingjue Wang, As. Ph.D. Stud. Eng.; Kang Xue, As. Ph.D. Stud. Eng.; Shun Zhang, Lec. Ph.D. Eng.; Juan Liao, Lec. Ph.D. Eng.*

fertilizer apparatus *(Yang et al., 2019)*. Xue et al. used EDEM software to simulate the fertilizer discharging process, analysed the movement law of granular fertilizer, and improved the fertilization effect of the spiral fertilizer distributor *(Xue et al., 2019)*. Lei et al. designed a horizontal pneumatic screw combination adjustable quantitative fertilizer feeding device for a granular fertilizer, which improved the performance of fertilizer filling and fertilizer discharging *(Lei et al., 2018)*. Yuan et al. designed a spoon wheel fertilizer applicator, which improved the fertilizer utilization rate and reduced the production cost *(Yuan et al., 2018)*. All the above researches have improved the fertilization performance to a certain extent, but there are still some problems such as non-adjustable fertilizer and low fertilization precision, which are difficult to meet the requirements of precision hole fertilization of dry direct-seeding rice at present.

Therefore, aiming at the problems mentioned above in the hole fertilization process, an adjustable socket-wheel precision hole fertilizer apparatus was designed and the discrete element method was used to evaluate the performance of the fertilizer apparatus. Selecting the rotation speed of the socket-wheel, the length of the trough, the depth of the socket as the experimental factors, and taking the average amount of fertilizer discharging and the coefficient of variation of fertilization uniformity as evaluation indicators, the orthogonal rotation combined experiments with three factors and five levels were carried out. A multi-objective optimization method was used to determine the best parameter combination under the constraint of the target value of the hole fertilizer discharging of 1.500 g. The reliability of the simulation results was verified through bench tests, and the working performance of the fertilizer apparatus was tested through field tests, which can provide a theoretical basis for the structure optimization and performance improvement of the fertilizer apparatus.

MATERIALS AND METHODS

- **Structure and working principle**

The adjustable socket-wheel precision hole fertilizer apparatus for rice mainly consists of fertilizer shaft, adjustment plate, isolation ring, fertilizer protection belt and others, as shown in Fig.1.

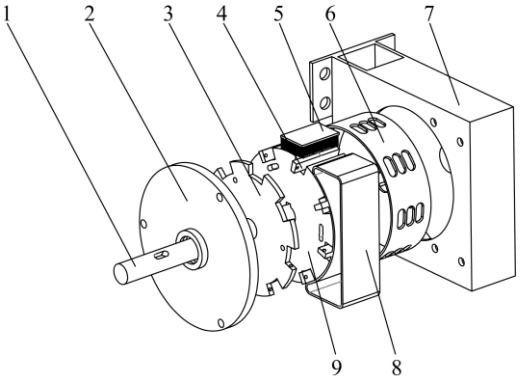

Fig. 1 - Diagram of structure and working principle of fertilizer apparatus
1 – Fertilizer shaft; 2 – Flange; 3 – Adjusting disc; 4 – Adjustment plate; 5 – Brush; 6 – Isolation ring; 7 – Shell; 8 – Fertilizer protection belt; 9 – Socket-wheel

According to the type of fertilizer and the requirement of the amount of rice fertilization, the adjustment disc will be rotated to drive the adjustment plate to move synchronously in the axial direction before working, so as to adjust the volume of the socket to meet the requirement of fertilization. When working, fertilizer will be charged from the fertilizer tank into the fertilizer apparatus firstly, then the fertilizer shaft drives the socket-wheel to rotate, and the fertilizer particles are filled into the socket in the end. In the fertilizer clearing area, excess fertilizer particles are removed by brushes and the fertilizer particles will be fertilized for a second time. In the fertilizer protection area, due to the role of the fertilizer protection belt, the fertilizer particles in the socket will not fall in advance. When reaching the fertilizer discharging area, the fertilizer particles fall into the fertilizer ditch by their gravity and centrifugal force to complete a precision fertilizer discharging operation.

- **Design of key component parameters**

Design of adjustment plate parameters

To meet the agronomic requirements of different fertilization amounts, an adjusting plate was designed to adjust the volume of the socket. One end of the adjusting plate is in the socket of the socket-wheel, the socket-wheel provided with the material trough communicating with the socket, and the space for containing fertilizer is formed by the material trough and the socket.

The other end of the adjusting plate can slide along the outside of the circle of the sliding groove of the socket-wheel, and the outside of the adjusting plate is flushed with the outside of the socket-wheel. After the position of the adjusting plate has been adjusted, the adjusting plate is fixedly connected with the socket-wheel. To meet the requirements of different types of fertilizer particles and different fertilizer amounts for the fertilizer apparatus, an adjustable trough is set on the side of the hemisphere of the socket. The number of sockets is limited by the distance between the socket-wheel and the socket, and the way to increase the number of sockets is to increase the width of the socket-wheel or to use the three rows of uniform equal distance distribution.

The structure of the adjusting plate is shown in Fig.2.

(a) Schematic diagram of adjustment plate (b) Assembly diagram of adjustment plate and socket-wheel

Fig. 2 - Schematic diagram of adjusting plate structure

1 – Adjustment plate; 2 – Trough; 3 – Socket

The material trough of the adjustment plate is installed in conjunction with the socket of the socket-wheel, and the shape of the material trough consists of a hemisphere and a semi-cylinder.

- **Design of adjustment plate parameters**

To ensure the fertilizer filling performance of the socket and the adaptability of the fertilizer apparatus, three varieties of granular fertilizer of the slow-release urea, sulfurized urea, and bio-organic fertilizer were selected as the study objects. Each variety of fertilizer was randomly selected with 500 grains to measure the triaxial size of the fertilizer particles. The equivalent diameter (D_e) and sphericity rate (φ) of the fertilizer particles can be calculated by the formula (1)*(Dun et al., 2020)*.

$$\begin{cases} D_e = (LWT)^{1/3} \\ \varphi = \dfrac{D_e}{L} \times 100\% \end{cases} \quad (1)$$

where:

L is the average length, [mm];

W is the average width, [mm];

T is the average thickness, [mm].

The triaxial size, equivalent diameter and sphericity rate of the three kinds of fertilizer particles are shown in Table 1.

Table 1

Triaxial size, equivalent diameter and sphericity rate of fertilizer particles

Fertilizer varieties	Average length (mm)	Average width (mm)	Average thickness (mm)	Equivalent diameter (mm)	Sphericity rate (%)
Slow-release urea	4.25	4.04	3.83	4.04	95.06
Sulfurized urea	5.39	4.74	4.27	4.78	88.68
Bio-organic fertilizer	4.21	4.10	3.99	4.10	97.39

The fertilizer particles may accumulate in the socket after the fertilizer particles are filled into the socket. Gaps will be formed between fertilizer particles socket and fertilizer particles-fertilizer particles because of the high sphericity rate of fertilizer particles *(Zhang et al., 2003)*. Due to the existence of gaps, the actual volume of the fertilizer in the socket is smaller than the volume of the socket, so the porosity of the fertilizer particles should be considered when designing the socket size. The porosity (ε) can be calculated by the formula (2).

$$\begin{cases} \varepsilon = \dfrac{v_b}{v_a} \times 100\% \\ v_b = v_a - v_b \\ v_a = \dfrac{m}{\rho_a} \\ v_p = \dfrac{m}{\rho_p} \end{cases} \quad (2)$$

where:

v_a is the accumulated volume of fertilizer particles, [cm^3];

v_b is the interstitial volume of fertilizer particles, [cm^3];

v_p is the real volume of fertilizer particles, [cm^3];

m is the mass of the accumulated fertilizer particle, [g];

ρ_a is the density of the accumulated fertilizer particle, [g/cm^3];

ρ_p is fertilizer particle density, [g/cm^3].

The porosities and densities of the fertilizer particles of the three varieties are shown in Table 2.

Table 2

Porosities and densities of fertilizer particles

Fertilizer varieties	Slow-release urea	Sulfurized urea	Bio-organic fertilizer
Porosity (%)	43.44	59.23	54.88
Density (g cm^{-3})	1.214	1.330	1.936

Since the fertilizer particles of the three varieties are all similar to spheres, the shape of the sockets was selected as a circle. The structure parameters of the socket are shown in Fig.3.

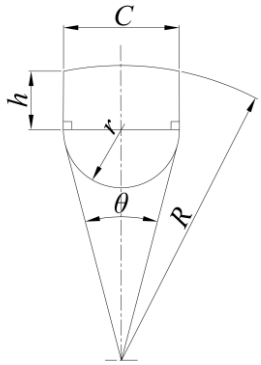

Fig. 3 - Structure parameters of the socket

where:

h is the depth of the socket, [mm];

r is the radius of the socket, [mm];

C is the diameter of the socket, [mm];

R is the radius of the socket-wheel, [mm];

θ is the outer arc angle of the socket, [rad].

According to the agronomic requirements of precision hole fertilization of dry direct-seeding rice, the standard of the amount for fertilization was selected to be 285-700 kg/hm^2. It was calculated that the amount of fertilizer per hole is 0.875-2.150 g.

Assuming that the radius of the fertilizer particles is A [mm], the volume of a single fertilizer particle can be calculated by formula (3).

$$v = \frac{4}{3}\pi A^3 \quad (3)$$

where: *v is* the volume of fertilizer particles, [mm^3].

Due to the different densities of the three kinds of fertilizer particles, the sulfurized urea with moderate density was selected as the research object in the design. The actual volume of fertilizer per hole can be calculated according to formula (4).

$$V_1 = \frac{m_1}{\rho_p} \quad (4)$$

where:

V_1 is the actual volume of fertilizer particles, [mm^3];

m_1 is the mass of fertilizer per hole, [g];

ρ_p is the density of fertilizer particle, [g cm^{-3}].

It can be calculated by formula (4) that the volume of fertilizer per hole was 0.66-1.62 cm^3, and the volume of fertilizer per hole was 0.22-0.54 cm^3.

The socket radius was set as 4.5 mm, and V_2 can be calculated by formula (5).

$$V_2 = \left(51.71\pi + 77.56h\pi + 10.13\pi l + 9hl\right)\left(1-\varepsilon\right) \quad (5)$$

where:

V_2 is the volume of fertilizer particles in the socket, [mm^3];

l is the length of the trough, [mm].

- **Fertilizer discharging performance simulation**

Model building and parameter setting

After the assembly model of the fertilizer apparatus was completed in the SolidWorks, save the model as a *.step* format document and import it into the EDEM for simulation. A conveyor belt was set directly below the fertilizer outlet, and the direction was horizontal to the left so as to simulate the movement of the ground. A detection device was set directly below the fertilizer outlet to detect the quantity of fertilizer particles discharging from each hole. The process of the simulation was shown in Fig.3. Define the material properties of fertilizer particles, stainless steel, resin and soil *(Zhu et al., 2018)*, respectively, as shown in Table 3.

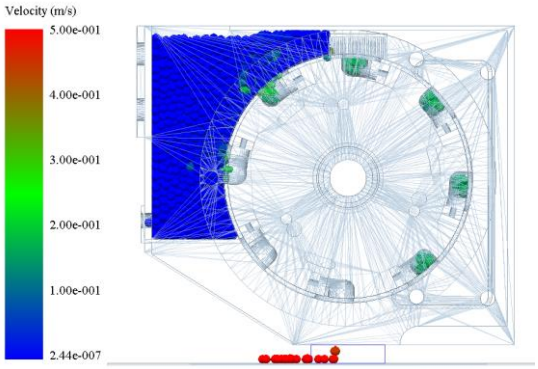

Fig. 4 - Process of simulation

Table 3

Material properties

Items	Shear modulus (Pa)	Poisson's ratio	Density (kg·m^{-3})
Fertilizer particles	1×10^7	0.25	1330
Stainless steel	7×10^{10}	0.30	7800
Resin	1.×10^6	0.45	1150
Soil	1.×10^8	0.49	2350

The material contact parameters of fertilizer-fertilizer, fertilizer-resin and fertilizer-soil are shown in Table 4. The simulation time was set as 15 s, and fertilizer particles were generated in 1 s. The value of the fixed time step was set as the 20% in simulation.

Table 4

Material contact parameters

Items	Coefficient of restitution	Coefficient of static friction	Coefficient of rolling friction
Fertilizer -fertilizer	0.11	0.32	0.24
Fertilizer-resin	0.45	0.28	0.19
Fertilizer-soil	0.04	1.25	1.28

The sphericity of sulfurized urea is greater than 88%, so the sulfurized urea fertilizer particles can be viewed as spheres in the EDEM software. Therefore, the diameter of the sulfurized urea was set as 4.78 mm in the numerical simulation model.

Model building and parameter setting

The average amount of fertilizer discharging ($\bar{X}$) and the coefficient of variation of fertilizer uniformity (CV) can be calculated by the following formulas *(Wang et al., 2018)*.

$$\bar{X} = \frac{\sum_{i=1}^{m} X_i}{N} \tag{6}$$

$$CV = \sqrt{\frac{\sum_{i=1}^{m}(X_i - \bar{X})^2}{(m-1)\bar{x}^2}} \times 100\% \tag{7}$$

where:

X_i is the mass of fertilizer of the i-th hole, [g];

N is the number of holes.

Test factors coding and levels setting are shown in Table 5.

Table 5

Test factors coding and levels setting

Code	Rotating speed of socket-wheel X_1 (r·min^{-1})	Length of trough X_2 (mm)	Depth of socket X_3 (mm)
1.682	35.00	8.00	7.00
1	30.94	6.38	6.19
0	25.00	4.00	5.00
-1	19.06	1.62	3.81
-1.682	15.00	0.00	3.00

- **Bench verification tests**

Test materials and equipment

The test site was the precision seeding laboratory of Anhui Agricultural University, and the test materials were slow-release urea, sulfurized urea and bio-organic fertilizer. The test equipment was the JPS-12 type seed-metering device performance test bench developed by the Heilongjiang Agricultural Machinery Engineering Research Institute. The fertilizer apparatus was installed on a fixed supporter, and the motor was controlled to drive the fertilizer apparatus device to rotate. The fertilizer bed belt was coated with a certain width of sticky oil, and the fertilizer particles were dropped from the fertilizer apparatus port onto the sticky oil layer. Data was collected through artificial observation and measurement.

The bench test process was shown in Fig.5.

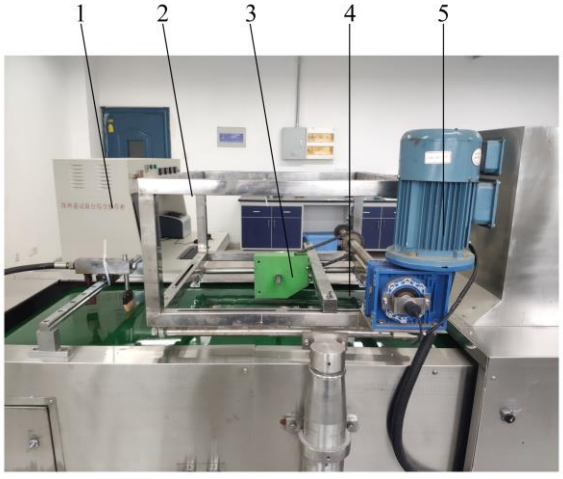

Fig. 5 - Diagram of bench tests

1 – Control console; 2 – Fixed supporter; 3 – Fertilizer apparatus; 4 – fertilizer bed belt; 5 – Motor

- **Field fertilization tests**

Test materials and conditions

To further test the performance of the fertilizer apparatus, the field fertilization tests were carried out in the agricultural field of Anhui Agricultural University. The test materials were slow-release urea, sulfurized urea and bio-organic fertilizer. Before the tests, a rotary tiller was used to smooth the surface of the test field, and the height difference of the ground in the field after the rotary tillage was within 5 cm.

RESULTS

- **Simulation test results**

The simulation test results are shown in Table 6.

Table 6

Simulation test results

Codes	Rotating speed of socket-wheel X_1 (r·min^{-1})	Length of trough X_2 (mm)	Depth of socket X_3 (mm)	Average amount of fertilizer discharging Y_1 (g)	Coefficient of variation of fertilizer uniformity Y_2 (%)
1	-1	-1	-1	0.678	14.00
2	1	-1	-1	0.732	13.14
3	-1	1	-1	1.102	21.03
4	1	1	-1	1.258	19.87
5	-1	-1	1	0.895	14.50
6	1	-1	1	1.013	13.48
7	-1	1	1	1.535	21.55
8	1	1	1	1.721	20.26
9	-1.682	0	0	1.079	17.00
10	1.682	0	0	1.069	16.48
11	0	-1.682	0	0.725	8.99
12	0	1.682	0	1.702	21.55
13	0	0	-1.682	0.921	17.54
14	0	0	1.682	1.465	19.84
15	0	0	0	1.268	13.78
16	0	0	0	1.266	12.45
17	0	0	0	1.174	12.56
18	0	0	0	1.248	11.95
19	0	0	0	1.159	11.75
20	0	0	0	1.262	13.15
21	0	0	0	1.277	13.25
22	0	0	0	1.123	12.89
23	0	0	0	1.288	12.05

Analysis of simulation results

These regression equations among the experimental factors and the evaluation indicators were obtained by using Design-Expert software to analyse the data in Table 6:

$$\begin{cases} Y_1 = -0.936 + 0.081X_1 + 0.015X_2 + 0.179X_3 + 1.503\times10^{-3}X_1X_2 \\ \quad + 1.622\times10^{-3}X_1X_3 + 0.018X_2X_3 - 1.788\times10^{-3}X_1^2 - 2.431\times10^{-3}X_2^2 - 0.015X_3^2 \\ Y_2 = 71.965 - 2.089X_1 + 0.279X_2 - 14.728X_3 - 5.040\times10^{-3}X_1X_2 \\ \quad - 5.128\times10^{-3}X_1X_3 + 3.089X_2X_3 + 0.041X_1^2 + 0.166X_2^2 + 1.519X_3^2 \end{cases} \quad (8)$$

The analysis of variance of model variables are shown in Table 7.

Table 7

Variance analysis of model variables

Source of variation	Average amount of fertilizer discharging				Coefficient of variation of fertilizer uniformity			
	Sum of squares	Degree of freedom	F value	P value	Sum of squares	Degree of freedom	F value	P value
Model	1.64	9	47.59	<0.0001	298.23	9	83.64	<0.0001
X_1	0.018	1	4.72	0.0489*	1.98	1	5.01	0.0434*
X_2	1.14	1	296.47	<0.0001**	173.76	1	438.56	<0.0001**
X_3	0.39	1	101.75	<0.0001**	2.31	1	5.83	0.0312*
X_1X_2	3.613×10^{-3}	1	0.94	0.3496	0.041	1	0.10	0.7539
X_1X_3	1.105×10^{-3}	1	0.29	0.6006	0.011	1	0.027	0.8731
X_2X_3	0.020	1	5.16	0.0407*	6.125×10^{-4}	1	1.546×10^{-3}	0.9692
X_1^2	0.063	1	16.49	0.0014**	33.94	1	85.66	<0.0001**
X_2^2	3.012×10^{-3}	1	0.79	0.3917	14.09	1	35.57	<0.0001**
X_3^2	7.018×10^{-3}	1	1.83	0.1993	73.51	1	185.54	<0.0001**
Residual	0.050	13			5.15	13		
Lack of fit	0.021	5	1.12	0.4192	1.50	5	0.66	0.6664
Pure error	0.029	8			3.65	8		
Total	1.69	22			303.38	22		

*Note: The "**" indicates the highly significance at 0.01 level; the "*" indicates significance at 0.05 level.*

According to the analysis of Table 7, it can be obtained that the order of the model variables affecting the average amount of fertilizer discharging was as follows: $X_2 > X_3 > X_1^2 > X_2X_3 > X_1 > X_3^2 > X_1X_2 > X_2^2 > X_1X_3$. Among these model variables, X_2、X_3、and X_1^2 all have a very significant impact, X_2X_3 and X_1 both have a significant impact. It can be obtained that the order of the model variables affecting the coefficient of variation of fertilizer uniformity was as follows: $X_2 > X_3^2 > X_1^2 > X_2^2 > X_3 > X_1 > X_1X_2 > X_1X_3 > X_2X_3$, Among these model variables, X_2、X_3^2、X_1^2 and X_2^2 all have a very significant impact, X_3 and X_1 both have a significant impact.

In order to more intuitively analyse the relationship between influencing factors and the performance of the fertilizer apparatus, the response surface graphs were obtained by processing the data of the orthogonal test, as shown in Fig. 6.

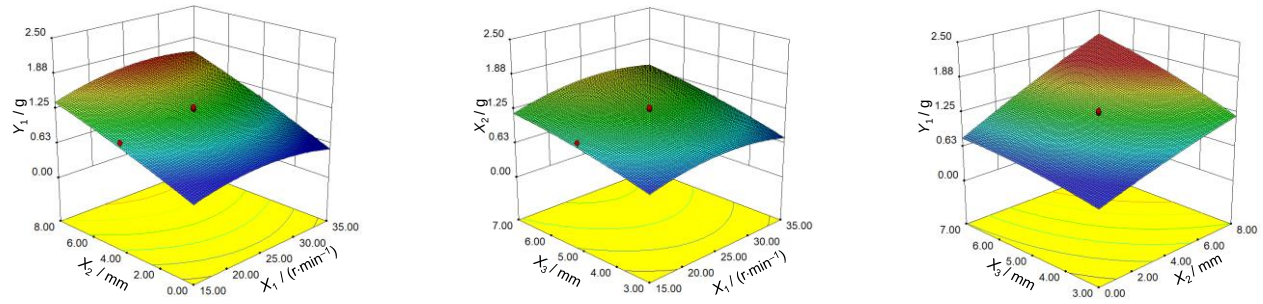

(a) The influence of various factors on the average amount of fertilizer discharging

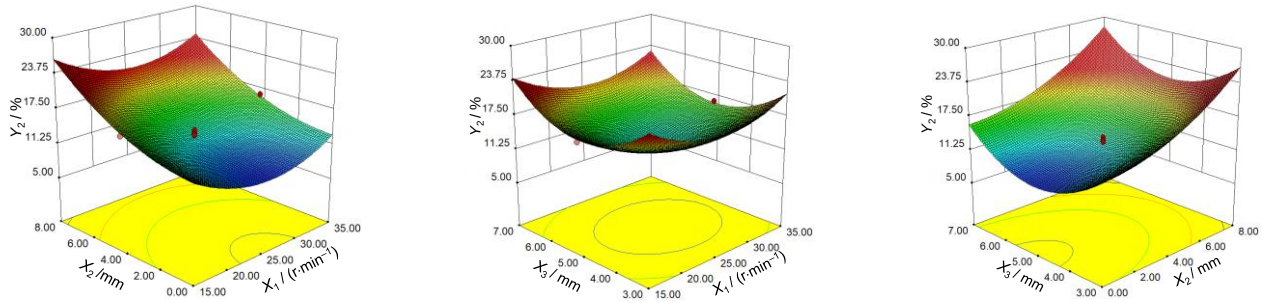

b) The influence of various factors on the coefficient of variation of fertilizer uniformity

Fig. 6 - Influences of various factors on evaluation indexes

It can be seen from Fig.6(a) that the average amount of fertilizer discharging increases with the increase of the trough length, and increases with the increase of the socket depth. When the length of the trough and the depth of the socket increase, the volume of the socket increases, the average amount of fertilizer discharging particles filled into the socket increases. It can be seen from Fig.6(b) that the coefficient of variation of fertilizer uniformity first decreased and then increased with the increase of the socket depth when trough length was constant. When the socket depth is too large, the time for the fertilizer particles to fall increases, which results in an increase in the coefficient of variation of fertilizer uniformity. When the socket depth is constant, the coefficient of variation of fertilizer uniformity increases with the trough length. When the trough length increases, some of the fertilizer particles do not fill the socket in time, resulting in an increase in the coefficient of variation of fertilizer uniformity.

Simulation parameter optimization

During the fertilization process, the coefficient of variation of fertilizer uniformity is as better as small. The parameters were optimized at the target value of the hole fertilizer discharging of 1.500 g, and the constraints were shown as formula (9).

$$\begin{cases} 15.00 \ \ r/min \le X_1 \le 35.00 \ \ r/min \\ 0.00 \ \ mm \le X_2 \le 8.00 \ \ mm \\ 3.00 \ \ mm \le X_3 \le 7.00 \ \ mm \\ 0.875 \ \ g \le Y_1(X_1, X_2, X_3) \le 2.105 \ \ g \\ 0 \le Y_2(X_1, X_2, X_3) \le 40\% \end{cases} \quad (9)$$

According to the constraint model, the Design-Expert software was used to optimize the solution, and obtain the optimal parameter combination that affects the coefficient of variation of fertilizer uniformity. When the rotating speed of the socket-wheel was 26.57 r/min, the trough length was 5.36 mm and the socket depth was 5.64 mm, the coefficient of variation of fertilizer uniformity was the smallest, with a value of 15.80%.

- **Bench verification results**

The fertilizer apparatus worked under the conditions of the optimal parameters combination obtained by the simulation test, and the mass of each hole of fertilizer discharging per 15 s was measured. The test was repeated three times in each group and the average values were taken as the results. The results are shown in Table 8.

Table 8

Test results of the bench

Fertilizer varieties	Average amount of fertilizer discharging Y_1 (g)	Coefficient of variation of fertilizer uniformity Y_2 (%)
Slow-release urea	1.739	17.35
Sulfurized urea	1.472	16.40
Bio-organic fertilizer	2.216	15.29

From Table 8, it can be seen that sulfurized urea has the lowest average amount of fertilizer discharging, while bio-organic fertilizer has the highest average amount of fertilizer discharging. Bio-organic fertilizer has the lowest coefficient of variation of fertilizer uniformity, while sulfurized urea has the highest coefficient of variation of fertilizer uniformity. The error between the bench test results and the simulation parameter optimization results was less than 5%, so the simulation results were reliable.

- **Field fertilization results**

The structure parameters of the fertilizer apparatus were the optimal parameters, and the traveling speed of the walking tractor was about 3.6 km/h. The quality of 50 holes of fertilizer was counted consecutively for each group of trials, and each trial was repeated three times. The results are shown in Table 9.

Table 9

Test results of the field

Fertilizer varieties	Average amount of fertilizer discharging Y_1 (g)	Coefficient of variation of fertilizer uniformity Y_2 (%)
Slow-release urea	1.750	19.75
Sulfurized urea	1.512	18.44
Bio-organic fertilizer	2.168	17.86

From Table 9, it can be seen that the average amount of fertilizer discharging of the three types of fertilizers was different from the bench test results due to the influence of field vibration on the working performance of the fertilizer apparatus, which cause the changing of the fluidity the irregularly movement of fertilizer particles. Field vibration also led to the instability of the fertilizer particles filling and increased the coefficient of variation of fertilizer uniformity, which was higher than the results of the bench test.

CONCLUSIONS

(1) In order to solve problems of non-adjustable fertilizer and low fertilization precision in the precision hole fertilization of dry direct-seeding rice, an adjustable socket-wheel precision hole fertilizer apparatus for rice was designed. According to the working performance requirements of the fertilizer apparatus, the structural parameters of the key components of the adjustment plate and the socket were determined.

(2) Sulfurized urea was selected as the test material, and the EDEM software was used to simulate the process of the fertilizer discharging in the three factors and five levels of orthogonal rotation combination test. The simulation results were optimized under the conditions that the target value of the hole fertilizer discharging of 1.500 g, the rotating speed of socket-wheel was 26.57 r/min, the depth of socket was 5.36 mm, and the depth of socket was 5.64 mm, and obtained the coefficient of variation of fertilizer uniformity was 15.80%.

(3) The bench test results showed that the average amount of fertilizer discharging of slow-release urea, sulfurized urea and bio-organic fertilizer were 1.739 g, 1.472 g and 2.216 g, respectively,

and the coefficient of variation of fertilizer uniformity were 17.35%, 16.40%, and 15.29%, respectively. Field test results showed the average amount of fertilizer discharging of slow-release urea, sulfurized urea and bio-organic fertilizer were 1.750 g, 1.512 g and 2.168 g, respectively, and the coefficient of variation of fertilizer uniformity were 19.75%, 18.44%, and 17.86%, respectively. The coefficient of variation of fertilizer uniformity of the three varieties of fertilizers were all less than 20% whether the bench test or the field test, which met the requirements of the precision hole fertilization of dry direct-seeding rice, and the fertilizer apparatus had good adaptability to different varieties of granular fertilizers.

ACKNOWLEDGEMENT

This work was supported by the Scientific and Technological Special Project of Anhui Province (No. 17030701045) and the Funding Project of Scientific Research Activities for Academic and Technical Leaders and Reserve Candidates in Anhui Province (No. 2019D223).

REFERENCES

[1] Alameen, A. A., Al-Gaadi, K. A.， Tola, E. (2019), Development and performance evaluation of a control system for variable rate granular fertilizer application, *Computers and Electronics in Agriculture,* vol. 160, pp.31-39;

[2] Dun, G., Yu, C.， Guo, Y., et al. (2020), Design and Experiment of double-gear type fertilizer apparatus, *Transactions of the Chinese Society for Agricultural Machinery,* vol. 51, issue 3, pp. 87-96;

[3] Fan, J., Lu, X.， Gu, S., et al. (2020), Improving nutrient and water use efficiencies using water-drip irrigation and fertilization technology in Northeast China, *Agricultural Water Management,* vol. 241, article. 106352;

[4] Hu, J., He, J.， Wang, Y., et al. (2020), Design and study on lightweight organic fertilizer distributor, *Computers and Electronics in Agriculture,* vol. 169, article. 105149;

[5] Lei, X., Li, M.， Zhang, L., et al. (2018), Design and experiment of horizontal pneumatic screw combination adjustable quantitative fertilizer feeding device for granular fertilizer, *Transactions of the Chinese Society of Agricultural Engineering,* vol. 34, issue 19, pp. 9-18;

[6] Wang, J., Gao, G.， Wang, J., et al. (2018), Design and test of adjustable blades side deep fertilizing device for paddy field, *Transactions of the Chinese Society for Agricultural Machinery,* vol. 49, issue 03, pp. 68-76;

[7] Wang, J., Li, R.， Zhang, H., et al. (2020), Beneficial bacteria activate nutrients and promote wheat growth under conditions of reduced fertilizer application, *BMC Microbiology,* vol. 20, issue 1, pp. 1-12;

[8] Xue, Z., Zhao, L.， Wang, F., et al. (2019), Performance simulation test of the spiral fertilizer distributor based on discrete element method, *Journal of Hunan Agricultural University (Natural Sciences),* vol. 45, issue 5, pp. 548-553;

[9] Yang, H., Zhang, L.， Dong, W., et al. (2019), Analysis and experiment of fertilizer device for bivariate fertilizer based on discrete element method, *Machine Design and Research,* vol. 35 (5), pp. 179-183;

[10] Yuan, W., Li, K.， Jin, C., et al. (2018), Design and experiment of hill placement fertilizer applicator, *Journal of Agricultural Mechanization Research,* vol. 40, issue 1, pp. 145-149+165;

[11] Zhang, J., Hou, S.， Wang, R., et al. (2018), Design of variable-rate liquid fertilization control system and its stability analysis, *International Journal of Agricultural and Biological Engineering,* vol. 11, issue 1, pp. 109-114;

[12] Zhang, J., Liu, G.， Luo, C., et al. (2019), MOEA/D-DE based bivariate control sequence optimization of a variable-rate fertilizer applicator, *Computers and Electronics in Agriculture,* vol.167, art. 105063;

[13] Zhang, Y.， Hu, Y. (2003), Study on measurement method of porosity of friction material, *Non-Metallic Mines,* vol.26, issue 3, pp. 48-51;

[14] Zheng, W., Jiang, Y.， Ma, X., et al. (2019), Development of a liquid-jet nozzle for fertilizer injection in paddy fields using CFD, *Computers and Electronics in Agriculture,* vol. 167, article. 105061;

[15] Zhu, Q., Wu, G.， Chen, L., et al. (2018), Influences of structure parameters of straight flute wheel on fertilizing performance of fertilizer apparatus, *Transactions of the Chinese Society of Agricultural Engineering,* vol. 34, issue 18, pp. 12-20.

DEVELOPMENT OF PADDY-FIELD WATER LEVEL GAGE CORRESPONDING TO A SENSOR-NETWORK
/
センサーネットワークに対応した水田水位計の開発

Ryoei Ito[*1)]; Takamitsu Kajisa[1)] [1]
[1)]Graduate school of Bioresources, Mie University, Mie 514-8507, Japan
Tel: +81-59-231-9577; Email: itou-r@bio.mie-u.ac.jp
DOI: https://doi.org/10.35633/inmateh-63-13

Keywords: *e-Tape, Arduino, XBee, paddy, irrigation*

ABSTRACT
This study proposes a measurement system that comprises an e-Tape water level sensor, Arduino and XBee. The system was considered a success because of the linear relation between measured voltage signals and water depths obtained by it. This linearity was essential because Arduino does not have non-linear calculation ability. As a result, the numerical order of RMSE in measuring water depth using this system was obtained as 3.52 mm. For measuring water consumption for 1 day at the standard scale of paddy fields in Japan, water consumption can be estimated using the system below non-flowing water surfaces. However, when there is water flow, it will be difficult to estimate water consumption because discharge errors may be cumulative.

摘要
この研究では，e-Tape 水位センサーと Arduino および XBee で構成される測定システムを提案している。 このシステムは，測定された電圧信号とそれによって得られた水深との間の線形関係のために妥当と見なされた。 Arduino には非線形計算機能がないため，この線形性は不可欠であった。結果的に，このシステムを使用して水深を測定した際の誤差 RMSE の数値の大きさは 3.52㎜ であった。日本の標準規模の水田で 1 日の減水深を測定する場合，それは流れのない水面下でシステムを使用して推定できることが示された。ただし，流れがある場合には，流量の誤差が累積する可能性があるため，減水深の推定が困難になると考察された。

INTRODUCTION

The importance of monitoring and predicting the impact of multiple factors in situ is often discussed. The charging of electric vehicles in smart grid cities can be monitored using predictive models, which can be used to manage energy distribution and lead to effective and efficient use of energy (*Park et al., 2011*). An energy distribution system (SMAS) will be beneficial to the industry and for home energy management. Sometimes, the prediction of solar-powered off-grid surface water quality is discussed for power management purposes (*Khalid et al., 2016*). In this regard, a wireless sensor grid is recommended for monitoring purposes. Wireless sensor network technology is used in water tank filling and management applications (*Mughal et al., 2014*). As one of the merits of predictive models, tidal movements can be accurately monitored.

Moreover, modeling in lowland paddy fields is proposed. For this discussion, sometimes, for the paddy, the development of the model is shown by a partially urbanized agricultural watershed. Presently, the use of water varies because of changes in cropping systems and the consolidation of farmworkers. Hence, these changes should be considered when constructing irrigation systems for paddy fields. From a water manager's viewpoint, the management of water resources is changing from the conventional supply-driven type to an end-user-based demand-driven type. Furthermore, farmers who are end users are increasingly cultivating their land in a centralized manner, thus making it difficult to achieve accurate water management and circulation was performed in the past. Moreover, in their rice fields, farmers may be uncertain whether there is water, thus increasing the requirement for the remote monitoring of farmlands. *Tanji et al, (2010),* proposed a smart grid for paddy field irrigation to prevent possible drought, reduce water costs, and ensure the availability of water at any time. The smart grid used information technology to efficiently operate and manage energy distribution. Paddy field meters were also used in the smart grid to monitor water distribution and drainage in the paddy field irrigation system and to select appropriate water contents for the paddy field. Furthermore, *Hirafuji et al.*

[1] *Ryoei Ito, Assistant Prof. Ph.D Ag.; Takamitsu Kajisa, Prof. Ph.D Agr*

(2013) developed an open source field server (Open-FS) using Arduino, which is an open-source hardware. The authors aimed to collect, visualize, and share measured data using the Open-FS at a low cost. The authors proposed a "sensor cloud system," which comprises an existing cloud service (Twitter, etc.) and browser written in HTML5.

By installing JPEG cameras and XBee on an Arduino board, an inexpensive smart sensor was built that has a wireless communication function that can be practically used even in agriculture (*Ito and Kawakita, 2013*). "Arduino" is an open-source hardware and software company, project, and user community that designs and manufactures single-board microcontrollers and microcontroller kits for building digital devices. Its products are licensed under the GNU Lesser General Public License or the GNU General Public License, thus permitting the manufacture of Arduino boards and software distribution by anyone. Arduino boards are commercially available in a preassembled form or as do-it-yourself kits. Digi XBee is the brand name of a family of form factor compatible radio modules from Digi International. e-Tape is the name of a water level sensor made by Milone Technologies.

This study is a reprint of a previous study (*Ito, 2014*). Note that approximately six years have elapsed since this worked was examined. The demand and spread of information and communication technology (ICT) is on the rise. However, the practical use of ICT in actual fields is still extremely low (such as, *Kameoka et al., 2017, Madushanki et al., 2019, Ito and Yamaguchi, 2019, Tsukahara et al., 2020*). Particularly, the use of image processing in farmlands, as introduced in this study, is unpopular. One of the most important tasks for farmers is to monitor the growing condition of crops. Therefore, this study is a contribution to agriculture. However, certain researchers who are not directly involved in agriculture do not see the merits of using ICT in this regard. To that end, we introduce our research contents and hope to receive the opinions of multiple readers. In future, if a multi-node system is developed, it can be used for both water-saving irrigation and automatic gate operation associated with rotary irrigation. As a premise for the provision of a multi-node system, a single system must be constructed.

MATERIALS AND METHODS

OBJECTIVE

To perform water-saving irrigation, an Arduino board is installed at each node to monitor water depth. However, the conversion of water depth information to voltage information using complex equations is challenging (nonlinear calculation is impossible to handle). Therefore, the aim in this study is to construct a system in which a personal computer is used to remotely receive water depth information from the e-Tape-Arduino-XBee set. Furthermore, we require to measure the relationship between the output voltage from the A-D conversion system in Arduino (digitalized analog value) and water depth information to examine the linearity of this relationship.

This research aims to develop a water level gage for the management and monitoring of water level in paddy fields using the abovementioned technologies by developing and analysing the detail of the paddy field system, which is based on Arduino and XBee. The second aim of this study is to assess the potential of the system for measuring water consumption by discussing the methodology used by the system.

Although the system's monitoring and management capabilities using input information and radio information can be expected, the implementation of the e-Tape water depth sensor for measuring water depth in paddy fields was not very clear. Therefore, the detail between water depth and analog voltage for this system is carefully measured and explained in the following experiment section.

EXPERIMENTS

During the design process, several interviews were conducted to understand the requirements of the study site managed by the legal entity of Mie Prefecture's Land-Improvement-District (LID). This district has a beneficiary area of ~3,183 ha, which is classified as a medium-sized land improvement zone and has many small-scale farmers as inhabitants, and there are blocks with open channel sections to the end. Based on interviews with the staff of LID in Mie Prefecture, it was stated: "We cannot grasp the flow rate, especially, in the open channel section, so the number of patrols of the branch water channel will increase in a drought year like last year." Accordingly, "The needs for a function to automatically measure the water intake at the terminal paddy field transfer data to the management office is high." To develop a paddy water level gage, Arduino and XBee were adopted as before (Fig. 1). Moreover, this information is reported in the reference (*Ito and Kawakita, 2013*). e-Tape from Milone Technologies was used to measure water levels.

This water level sensor has a resistance value that varies by water level and is priced at ~5,000 yen (~$50), which can be characterized as inexpensive (Fig. 2).

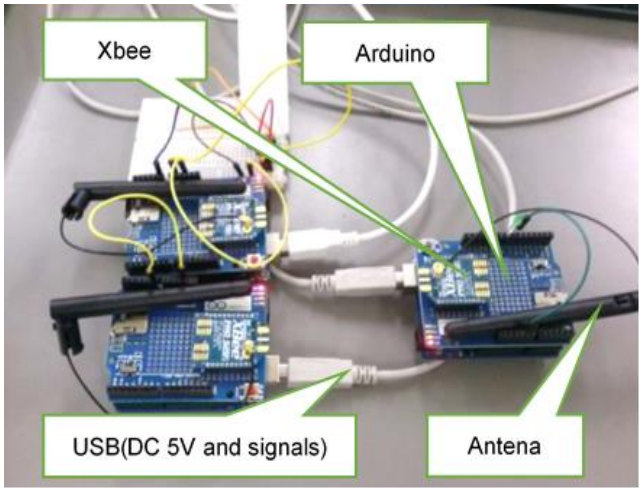

Fig. 1 - The example of the system prototype multi-nodes

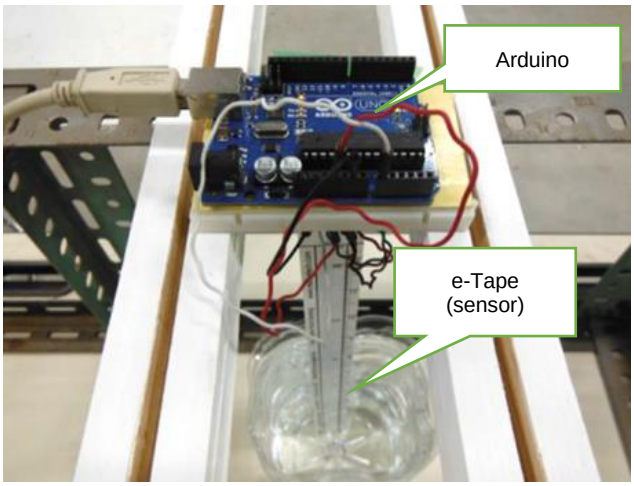

Fig. 2 - The water level sensor

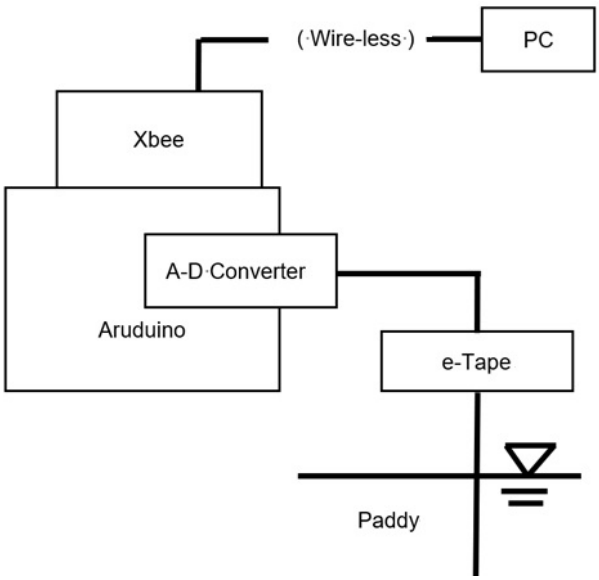

Fig. 3 - Conceptual illustration of the system for paddy

As shown in Fig. 3, the water level sensor and Arduino were connected; moreover, the water level sensor was attached to a polyethylene terephthalate bottle filled with water. The amount of water in the bottle was increased and the water level was read using a digital point gage.

Furthermore, the voltage value of the water in the bottle was measured 100 times at intervals of 1 s using Arduino. XBee, which is used to realize a one-to-one connection, can sufficiently register the individual identification (ID) number of each node and agree with the PAN ID. However, when multiple nodes are displayed as mesh networks, it is necessary to have a mechanism to identify individual nodes because this is required to broadcast packets.

RESULTS AND DISCUSSION

Using equation (1) of the A-D converter, input raw data i can be converted to an input voltage. At that time, water depth Y_{mes} will be measured, where i is the digitalized number of input voltage x (mV) obtained by the A-D converter.

$$x = 500 \times \frac{i}{i_{max}} \tag{1}$$

Fig. 4 shows the actual measurement result. The obtained ratio R^2 was 0.9951. Therefore, the liminality between water depths and voltage could be confirmed. Consequently, the following equation (3) is provided to ensure that water depth Y_{cal} is consistent with the water depth Y_{mes}.

$$Y_{mes} = the\ measured\ water\ depth\ by\ hand \tag{2}$$

$$Y_{cal} = -0.143x + 75.401 \tag{3}$$

Fig. 4 shows the relation between x and the measured water depth Y_{mes}. obtained by plots, where the obtained correlation coefficient is −0.997 (Table 1). Therefore, Fig. 4 shows a very strong negative relation between X and Y_{mes}. The *p*-value of n and R is 0.000, indicating that the relation is meaningful and significant.

By substituting measured raw data of x into equation (1), the simulated water depth Y_{cal}. (cm) can be obtained. In this manner, we can compare and discuss the difference between Y_{mes}. and Y_{cal}. Table 1 shows that the root mean square error (RSME) of Y_{mes}. and Y_{cal}. is 0.352 cm. The greatest absolute difference of Y_{mes}. and Y_{cal}. is 0.937 cm.

We connected e-Tape water level sensor to the core system using Arduino and XBee and developed a paddy level sensor corresponding to a sensor network for the management and monitoring of water levels in paddy fields. The standard order of the seepage at paddy fields seeps through at 2–3 cm/day. Therefore, in a case we obtain water depth Y_{cal}. daily, the order of the errors of 0.352 or 0.937 cm might be evaluated small.

In certain cases, it will be recommended to evaluate the obtained order of error of the calculated discharge. For this purpose, we use the following equations (4) and (5) for illustration. We can obtain the RSME or maximum error of Q_{mes}. and Q_{cal} using these equations.

$$Q_{mes} = 1.7 \times B \times (Y_{mes} - Y_{base})^{1.5} \tag{4}$$

$$Q_{cal} = 1.7 \times B \times (Y_{cal} - Y_{base})^{1.5} \tag{5}$$

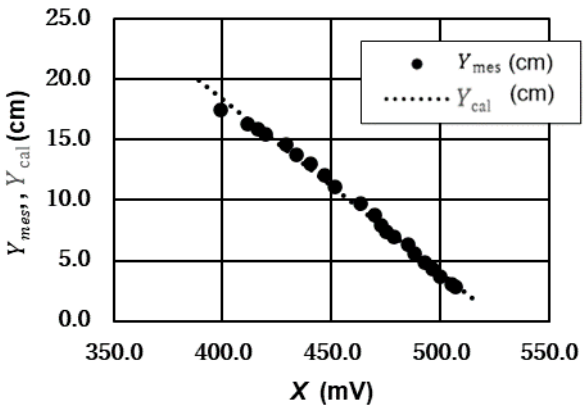

Fig. 4 - Test results

Note: black circles are the measured water depth Y_{mes} ; the dot-line is the approximate straight line of Y_{cal}

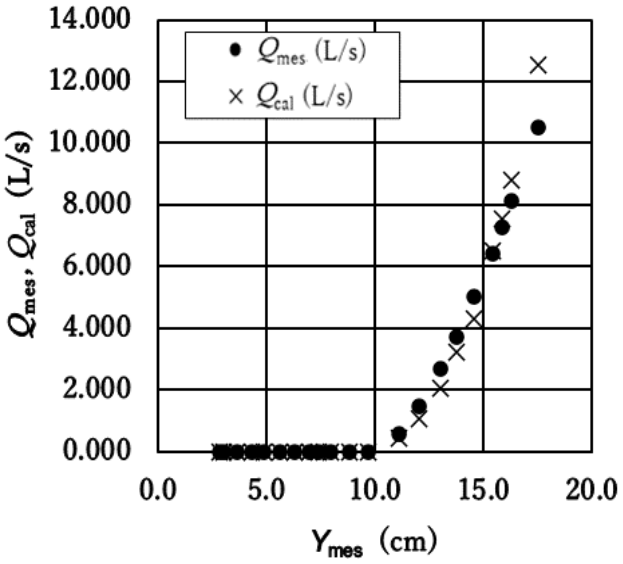

Fig. 5 - An example of the measured results

Note: Dots are Q_{mes} using equation (4), the cross marks are Q_{cal} using equation (5)

Table 1
Examples of obtained indexes in which width *B* of 0.3 (m) and Y_{base} of 0.1 m were used

Data number *n* of Y_{mes}	21	
R of *x* and Y_{mes}	−0.997	
p-value of *x* and Y_{mes}	0.000	
n of Y_{mes} or Y_{cal}	21	
RMSE of Y_{mes} and Y_{cal}	0.352	[cm]
Maximum value of | Y_{cal} - Y_{mes} |	0.937	[cm]
n of Q_{mes} or Q_{cal}	9	
RMSE of Q_{mes} and Q_{cal} (B =0.3 m, Y_{base}=0.1m)	0.812	[L/s]
Maximum value of | Q_{cal} - Q_{mes} | (B=0.3 m, Y_{base} =0.1m)	2.026	[L/s]

In Table 1, the RSME of Q_{mes}. and Q_{cal} is obtained as 0.812 L/s. The greatest absolute difference of Q_{mes}. and Q_{cal} is 2.026 (L/s). If we assume the area of the typical paddy field is 3000 m^2, these errors (0.812 and 2.026 L/s) will become 2.339 and 5.835 cm/day, respectively.

The order of the errors of 2.339 or 5.835 cm is almost the same compared to the standard order of the seepage at the paddy field, which is distributed from 2 to 3 cm/day.

CONCLUSIONS

We can convert input raw data to input voltage using the experimental equation of the A-D converter in Arduino. This could validate the linearity between water depth and voltage. The possibility of obtaining water depth needs to be confirmed because this system cannot perform non-linear calculations.

Consequently, the first aim of this study is to examine the potential of this system, and this was achieved with a high degree of feasibility. The numerical order of RMSE in measuring water depth using this system was obtained as 3.52 mm. To achieve the second aim of this study, we discussed the possibility of using this system to measure water consumption for 1 day based on the standard scale of paddy fields in Japan. Estimating water consumption will be possible if we can use the system below non-flowing water surfaces. Where there is water flow, it will be difficult because the error of discharge may be cumulative.

The equation shown in Fig. 3 can be used in a personal computer after a measured analog value has been inputted into the PC using Arduino and Xbee. Analysis can be conducted simply because the equation did not display the curving line. Moreover, a sensor network can be constructed by assigning and transmitting an identification (ID) number to each sensor node so that data from several sensor nodes can be identified. Therefore, high accuracy for practical use has been obtained. Moreover, a sensor network can be constructed by assigning and transmitting an ID number to each sensor node so that data from several sensor nodes can be identified. Moreover, the accuracy in measuring water levels was sufficiently high, and data communication between multiple nodes was possible. Furthermore, the model that was prototyped in this study achieved the initial target price.

ACKNOWLEDGEMENT

Part of this research was supported by the JT problem-solving service science research and development program “Quantitative Evaluation of Agricultural Water Usage Service and Development of Demand-Driven Provision Method” (representative: Toshiaki Iida). Henceforth, achieving self-sustaining operation using solar panels will be focused on in a future study.

REFERENCES

[1] Hirafuji M., Yoichi H., Miki Y., Kiura T., Fukatsu T., Tanaka K., Matsumoto K., Hoshi N., Nesumi H., Shibuya Y., Itoh A., Ninomiya S., J. Adinarayana J., Sudharsan D., Saito Y., Kobayashi K., Suzuki T. (2013), Development of an open field server and sensor cloud system. *Agricultural Information Research*, 22(1), pp.60-70 (in Japanese).

[2] Ito R., Kawakita K. (2013), Development of smart sensor for agriculture using physical computing device. *Proceeding of the Conference of Agricultural and Rural Engineering Meeting*, 2(35) (in Japanese).

[3] Ito R. (2014), Development of paddy field water level gage corresponding with a sensor-network. *Proceeding of the Conference of Agricultural and Rural Engineering Meeting*, 5(23) (in Japanese).

[4] Ito R., Yamaguchi C. (2019), A Field Image Monitoring System Based on Embedded Linux, *International Journal of GEOMATE*, 17, issue 62, pp.181-187; doi:10.21660/2019.62.25814.

[5] Kameoka S., Isoda S., Hashimoto A., Ito R., Miyamoto S., Wada G., Watanabe N., Yamakami T., Suzuki K., Kameoka T. (2017), A Wireless Sensor Network for Growth Environment Measurement and Multi-Band Optical Sensing to Diagnose Tree Vigor, *Sensors*, 17(5), 966, doi:10.3390/s17050966.

[6] Khalid R. R., A. Meyer, J. Meiers, P. H. Beck, G Frey. (2016), Predictive power management for a solar-powered off-grid surface water quality monitoring system, *2016 IEEE 11th Conference on Industrial Electronics and Applications (ICIEA)*, doi:10.1109/ICIEA.2016.7603614.

[7] Madushanki R., Wirasagoda H., Halgamuge M. (2019), Adoption of the Internet of Things (IoT) in Agriculture and Smart Farming towards Urban Greening: A Review. *International Journal of Advanced Computer Science and Applications*, 10 (4), pp.11-28, doi:/10.14569/IJACSA.2019.0100402.

[8] Mughal H. M., Shaikh A. Z., Shamsi A. J. (2014), WaterGrid: A wireless sensor grid for riverine water management. *17th IEEE International Multi Topic Conference 2014*, doi: 10.1109/INMIC.2014.7097353.

[9] Park K, Kim Y., Kim S., Kim K., Lee W., Park H. (2011), Building Energy Management System based on Smart Grid. (2011), *IEEE 33rd International Telecommunications Energy Conference (INTELEC), IEEE*, doi: 10.1109/INTLEC.2011.6099782.

[10] Tanji H., Kobayashi S., Kiri H. (2010), Exhibition of paddy field irrigation system responding to future energy supply changes, *Journal of the Hydrology and Water Resources Association*, 23(1), pp.43-56 (in Japanese).

[11] Tsukahara A., Kameoka S., Ito R., Hashimoto A., Kameoka T. (2020), Evaluation of Freshness of Lettuce using Multi-Spectroscopic Sensing and Machine Learning, *Journal of Applied Botany and Food Quality*, 93, pp.136-148, doi:10.5073/JABFQ.2020.093.018.

DESIGN OPTIMIZATION AND PERFORMANCE TEST OF MAGNETIC PICKUP FINGER SEED METERING DEVICE

磁力指夹式排种器优化设计及性能试验

Fei Liu, Zhen Lin, Dapeng Li, Tao Zhang*)
College of Mechanical and Electrical Engineering, Inner Mongolia Agricultural University, Hohhot/China
Tel: +86-471-5964308 E-mail: ztde163163@163.com
DOI: https://doi.org/10.35633/inmateh-63-14

Keywords: *Magnetic pickup finger，seed metering device，magnetic induction intensity，seeding performance，vibration*

ABSTRACT

As the core part of precision seeder, the performance of pickup finger seed metering device directly affects the seeding quality. Aiming at the problem that the traditional pickup finger seed metering device can be easily affected by the performance of spring material, and the reliability of spring decreases with the increase of service time, a magnetic pickup finger seed metering device is designed to open and close the pickup finger by magnetic force, so as to improve the stability of seed metering performance. Through the design and optimization of permanent magnet structure, cam structure and seed taking pickup finger structure, the magnetic force distribution of ring magnet is analysed by using ANSYS Maxwell magnetic simulation software. Under the working speed of 3.9km/h, the vibration frequency, vibration amplitude and magnetic induction intensity were selected for orthogonal test. The experimental results show that the optimal combination of factors is vibration frequency 6Hz, vibration amplitude 3.1mm and magnetic induction intensity 316.34mT. Under the condition of the combination of operation parameters, the seed arrangement performance is 91.7% of the qualified rate, 6.2% of the replant rate and 2.1% of the missed rate, which meets the requirements of the national standard for the performance of the seeder. This study can provide a reference for the optimization of the structure and the improvement of the seed metering performance of the pickup finger seed metering device.

摘要

指夹式排种器作为精密播种机核心工作部件，其性能直接影响播种质量。针对传统指夹式排种器易受弹簧材料性能影响，随使用时间增加排种性能下降的问题，设计一种由磁力完成指夹开启与闭合的磁力指夹式排种器，提高指夹式排种器排种性能稳定性。通过设计优化永磁体结构、凸轮结构及取种指夹结构，应用 Ansys-Maxwell 磁力仿真软件分析环形磁铁磁力分布；在作业速度 3.9km/h 条件下，选取振动频率、振动幅值、磁感应强度 3 因素进行正交试验。试验结果表明：较优因素水平组合为振动频率 6Hz、振动幅值 3.1mm、磁感应强度 316.34mT；该组合作业参数条件下，排种合格率 91.7%、重播率 6.2%、漏播率 2.1%，满足国家标准对精密播种机性能要求。该研究可为指夹式排种器结构优化与排种性能提高提供参考。

INTRODUCTION

As a major corn planting region, the Inner Mongolia Autonomous Region is among the top regions in China in terms of corn planting area and output. The Inner Mongolia Region consists mostly of alpine arid areas where vibrations from machines and tools cause disturbances during the no-tillage surface operation in the case of heavy straw coverage. Therefore, suction-type and spoon-wheeled metering devices may exhibit poor metering performance (*Wang et al, 2019*; *Yang et al, 2016*). The pickup finger metering device is a mechanical precision metering device extensively used for precision seeding operation on no-tillage surfaces due to its stable metering performance and strong adaptability to operating environments (*Searle et al, 2008; Tang et al, 2020*).

In recent years, *Abdolahzare et al.,* (*2018*), used high-speed camera systems to study factors affecting the seed distribution uniformity, thereby reducing the seed spacing variation coefficient. *Cortez et al.,* (*2020*), studied the effect of seeding speed on operation quality and found that the seed spacing distribution stability decreases with the increase in the forward speed of the seeder, with an operating speed of 5 km/h providing an optimal operating performance.

Weidong et al., (*2004*), *Zhang et al.*, (*2020*) and *Yazgi et al.,* (*2014*), investigated the metering performance and miss-seeding monitoring system of precision metering devices for crops, such as corn, rape and rice. In addition, some researchers have studied the structure of the pickup finger precision metering device. For instance, Geng *et al.*, (*2016*), designed a telescopic pickup finger corn seed metering device.

Li et al., (*2018*), designed a pickup spoon precision broad bean seed metering device incorporating the advantages of a spoon-wheeled metering device and a pickup finger metering device; they studied the optimal operating parameters of seed pickup length, seed pickup width and bending angle, thereby improving the operating performance of the precision seeding of broad bean.

Wang et al., (*2019)*, optimized the design of the pickup finger precision corn seed metering device, simplifying the structure of the mechanical metering device and improving the operation quality. *Wang et al.*, (*2015; 2017)*, optimized the structure parameters of the precision corn seed metering device and improved the adaptability of the metering device to seeds.

Zhou et al., (*2019*), performed tests on the operating performance of metering devices that use rubber and plastic as additional materials for the seed plate and reported that the operating performance of the metering device can be improved by changing the contact material.

Fu et al., (*2011)*, proposed a precision metering technique featuring mechanical forced gripping of corn, performed theoretical analysis of the metering process and built relevant mechanical models, providing the theoretical basis for improvement in the operating performance of metering devices. By optimizing the cleaning brush and jounce belt structures, the U.S. Kinze no-tillage seeder achieves decreased seed spacing, decreased re-seeding rates and improved seed metering accuracy. Precision Planting (*Trimont, Boston,* USA) designed a cushion device at the seeding opening of the metering device pickup finger, which prevents seed collision and rebounds miss-seeding when seeds enter the lead-in chamber.

Chinese and foreign scholars have studied the pickup finger, cam, seed plate, jounce belt and other structures through theoretical analyses, numerical simulations and experimental investigations, thereby improving the operating performance of metering devices. However, there are few studies on the performance of the helical compression spring in the pickup finger. It is impossible to avoid the effect of spring material performance on metering performance. Moreover, it is difficult to study the spring material performance stability in pickup finger metering devices. Therefore, the present paper designed a magnetic pickup finger-type precision metering device, in which the magnetic force enables the pickup finger to hold the seeds to avoid the poor metering performance resulting from the degradation of spring material.

MATERIALS AND METHODS

Structure and operating principle of the metering device

The structure of the magnetic pickup finger-type precision metering device is shown in Figure 1. During the seeding operation, seeds enter the metering chamber from the seed box, and the ground wheel powers the pickup finger pressure plate that drives the pickup finger to rotate through the seed filling area, seed guiding area, seed clearing area and seed charging area.

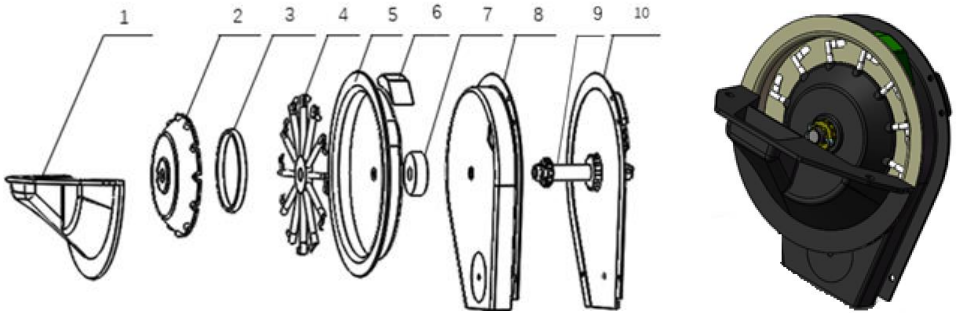

Fig. 1 - Structure of magnetic pickup finger seed metering device

1. Feeding inlet; 2. Refers to the pressure plate; 3. Permanent magnet; 4.Pickup finger; 5. Discharge plate; 6. Hairbrush; 7. Cam; 8. End cap; 9. Feed shaft; 10. Conductor shield

The permanent magnet attracts the pickup finger tail tab to a certain extent so that the pickup finger tab fits tightly on the surface of the seed plate. The pickup finger rotates around a fixed axis at the seed plate surface. A cam is placed under the seed plate, and the cam is designed with a pickup finger opening area and a pickup finger closing area. The pickup finger tail tab slides on the cam surface, and when the pickup finger rotates to the opening area of the cam surface, the supporting force of the cam surface for the pickup finger

tail tab overcomes the attraction of the permanent magnet. At this moment, the pickup finger opens and forms a definite opening angle with the seed plate, and the seeds enter the pickup finger to complete seed filling. When the pickup finger rotates to the closed area of the cam surface, the attraction of the permanent magnet to the pickup finger tail tab provides torque for the pickup finger, thus allowing it to clamp the seeds. The seeds rotate with the pickup finger to complete seed guiding. When the pickup finger tab holding the seeds passes through the seed clearing belt, the jounce belt vibrates slightly to remove excess seeds, which completes the seed clearing. When the pickup finger rotates to the seed exit, the magnetic action of the permanent magnet causes the pickup finger to push the seeds into the seed exit, and the seeds fall into the seed guide belt. All four seeding processes, i.e., seed filling, guiding, clearing and charging, are then completed.

Permanent magnet structure design and numerical simulation

In a pickup finger precision metering device, a fine-tuning spring provides the pickup finger tab with holding force, the stability of which has an immediate effect on the seed filling, seed guiding and seed clearing performance. Performance degradation of the spring material develops as time passes, which changes the spring stiffness coefficient, thereby impairing the stability of the metering performance. In the present paper, a permanent magnet is used to replace the fine-tuning spring, and the attraction of the permanent magnet to the pickup finger tail tab replaced the spring force for the pickup finger. Compared to the fine-tuning spring, the permanent magnet has a more stable force and a longer life span. Moreover, the permanent magnet is reusable. The structure of the designed permanent magnet is a ring with an outer diameter of 110 mm, an inner diameter of 93 mm, and a thickness of 6 mm. The magnetization direction is radial magnetization. Permanent magnet is a hard magnet, which is not easy to lose magnetism or magnetize. Ferrite material can maintain its original magnetism for a long time (*Hu et al, 2011; Hu et al, 2010*).

To identify the effect of the magnetic field distribution on the attraction to the pickup finger tail tab, Ansys-Maxwell software was used for computer simulation analysis of the magnetic induction intensity and the magnetic field intensity. Because the permanent magnet is circular with a symmetrically distributed magnetic field, the solution type is a static magnetic field when the axisymmetric 3D model is imported into Ansys-Maxwell. A permanent magnet is defined as a boundary condition under which the tangential component of the magnetic field intensity is always zero. The insulation boundary condition is used for the metering device housing, while the symmetric boundary condition is used for the cam. The cam material property is defined as steel, and the pickup finger material property is defined as iron. The simulation results of permanent magnet magnetic field are shown in Figure 2.

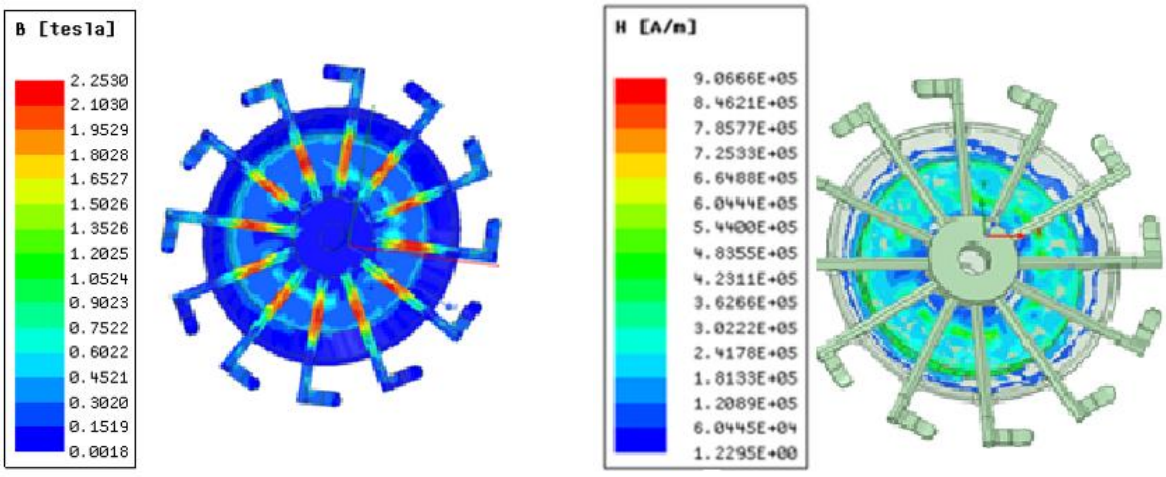

a) Distribution of magnetic induction intensity b) Distribution of magnetic field strength

Fig. 2 - Magnetic field simulation results of permanent magnet

According to the cloud chart of the magnetic induction intensity numerical simulation result, the magnetic density at the yoke is larger and the distribution is more concentrated, and the magnetic density at the outer side is smaller. The uneven distribution of radial magnetization and material density results in uneven lateral yoke distribution, and the largest magnetic force occurs at the contact point between the permanent magnet and pickup finger. The change in permanent magnet shape significantly affects the peripheral flux density value characteristics, thereby affecting the attraction to the pickup finger tail tab.

Metering control mechanism design

The seed filling performance has an important effect on the overall operating performance of the magnetic pickup finger metering device. The seed filling performance is affected by the opening/closing time point and opening angle of the pickup finger as well as the tail tab attraction. The magnetic pickup finger metering device is designed with a cam mechanism that controls the opening/closing time point and opening angle of pickup finger and a permanent magnet that changes the attraction of the pickup finger tail tab. Thus, the operating angle of the cam has an immediate effect on seed filling performance. Based on the motion pattern desirable for the pickup finger, the cam working surfaces are divided into a constantly open plane, constantly closed plane, closed slope and progressively opened slope. Figure 3 shows the cam structure.

The pickup finger tail tab is in contact with the cam slope. When the pickup finger tail tab moves to the progressively opened slope of the cam, the supporting force of the progressively opened slope for the pickup finger tail tab is greater than the attraction of the permanent magnet to the pickup finger tail tab. As a result, the pickup finger opens, and the seeds enter the space formed by the pickup finger and seed plate to complete seed filling. Hence, the opening angle and structure of the pickup finger affect the seed filling quantity and stability. When the pickup finger tail tab moves to the closed slope of the cam, the attraction of the permanent magnet to the pickup finger tail tab causes the pickup finger to close, and the pickup finger holds the seeds for seed guiding and clearing. The closed slope and constantly closed plane of the pickup finger affect the seed guiding stability and seed clearing process. Both vibration frequency and vibration amplitude may significantly affect the seed filling performance, seed guiding stability and seed clearing process during the metering operation.

To effectively fill the seeds and keep them steady, the pickup finger opens and closes steadily in the filling area. The closed slope of the cam is smooth and stable, ensuring that the corn grains are accurately pushed to the guiding port. The maximum finger opening angle is 20°, the constant filling angle is 160°, the finger hold angle is 30°, and the finger push angle is 150°.

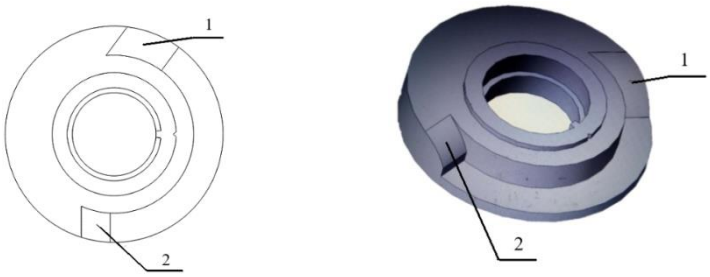

a) Closed slope b) Inclined slope

Fig. 3 - Cam structure

Pickup finger design

The pickup finger consists of a pickup finger tab, pickup finger lever, magnet and pickup finger tail tab. The pickup finger structure is shown in Figure 4. During operation of the metering device, the pickup finger rotates with the pickup finger pressure plate around a fixed axis under the driving force of the pickup finger lever to hold the seeds. The cam structure and permanent magnet control the pickup finger to complete seed filling, seed guiding, seed clearing and seed charging. The structure and motion pattern of the pickup finger affect the action of the pickup finger on seeds. Figure 5 shows the analysis of the force applied during the pickup finger holding.

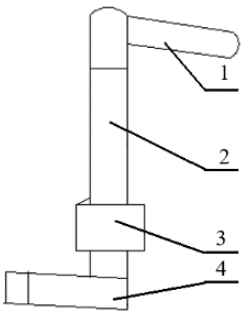

Fig. 4 - Seeding pickup finger structure diagram

1. Pickup finger; 2. Pickup finger pole; 3. Magnet; 4. Pickup finger tail

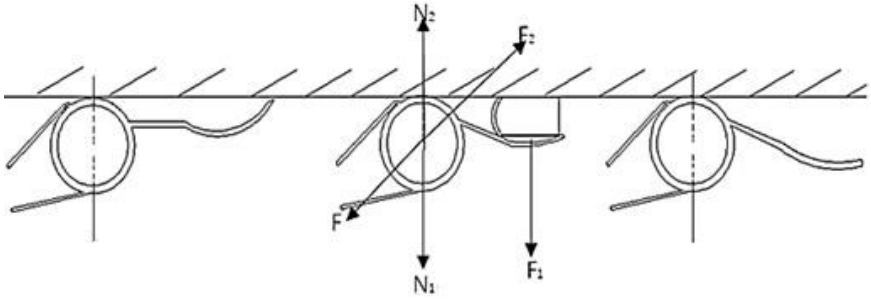

a) Closed state b) Clamped state c) Opened state

Fig. 5 - Stress analysis of finger clamp

Because corn seeds cannot rotate in the process of carrying seeds, Equations (1), (2), (3) are reached.

$$\sum M = 0 \tag{1}$$

$$fr + F(u_1 + u_2) = F_1 b_1 \tag{2}$$

$$F_1 = \frac{fr + F(u_1 + u_2)}{b_n} \tag{3}$$

where: M is torque of the pickup finger pole axle centre, N·m;

f is friction between the planter plate and the finger clamp, N;

F_1 is clamping force of pickup finger, N;

F is magnetic of permanent magnet, N;

u_1 is force arm of the left magnetic force, mm;

u_2 is force arm of the right magnetic force, mm;

r is radius of pickup finger, mm;

b_n is width of the corn seeds that are clamped, mm.

Seed stress analysis indicated that the pickup finger holding force is associated with the magnetic force of the permanent magnet, the frictional force of the seed plate against the pickup finger lever, the pickup finger lever radius, the left magnetic force arm, the right magnetic force arm and the width of the held corn seed. In the condition of the pickup finger structure and seed plate material are invariants, the magnetic force of the permanent magnet significantly affects the holding force of the pickup finger.

Test method

The test was performed with Yulong-9 corn seeds with a moisture content of no more than 15.0%, a thousand grain weight of 288.48 g and a rest angle of 30.84°. The metering performance test was performed using a JPS-12 metering device performance test stand (developed by Heilongjiang Research Institute of Agricultural Machinery Engineering). The test unit was an optimized magnetic pickup finger-type precision metering device. A computer controlled the rotation speed of the pickup finger pressure plate and the seed bed belt velocity during the test. The seeds from the metering device fell onto viscous oil on the surface of the seed bed belt. The data were collected as per the Chinese National Standard (GB), and the metering performance index of the metering device was calculated.

According to above-noted structure optimization and theoretical analysis, the dominant factor affecting the metering performance was the vibration frequency of the metering device. The metering qualification index, re-seeding index and miss-seeding index were calculated based on the Chinese National Standard GB/T6973-2005 "Testing Methods of Single Seed Drills (Precision Drills)" with reference to the agronomic requirements on corn seeding.

RESULTS

In order to find a better parameter combination, three-factor and three-level orthogonal test was carried out on the three selected factors, and L_9 (3^4) orthogonal table was used for the test and analysis. According to the single-factor test results in the early stage, the factors and horizontal setting are shown in Table 1, the test results of seeding performance are shown in Table 2, and the variance analysis of seeding performance is shown in Table 3.

Table 1

Factors and levels of orthogonal test

Level	Vibration frequency (Hz)	Vibration Amplitude (mm)	Magnetic induction intensity (mT)
1	5	2.4	316.34
2	6	3.1	226.48
3	7	3.7	200.36

Table 2

Test results of seed metering performance

	Factors				Performance values		
Test number	**Vibration frequency (Hz) A**	**Vibration Amplitude (mm) B**	**Magnetic induction intensity mT C**	**Error D**	**Qualified rate (%)**	**Multiple rate (%)**	**Miss rate (%)**
1	1	1	1	1	65.0	35.0	0
2	1	2	2	2	78.0	22.0	0
3	1	3	3	3	64.9	35.1	0
4	2	1	2	3	88.9	11.1	0
5	2	2	3	1	91.7	6.2	2.1
6	2	3	1	2	84.4	13.3	2.3
7	3	1	3	2	73.0	24.4	2.6
8	3	2	1	3	78.0	18.0	4.0
9	3	3	2	1	77.3	18.2	4.5
Qualified rate *R*	0.19	0.07	0.06	0.01			
Important order			A B C				
Optimization scheme			$A_2B_3C_1$				
Multiple rate *R*	0.62	0.24	0.15	0.05			
Important order			A B C				
Optimization scheme			$A_1B_3C_2$				
Miss rate *R*	0.07	0.04	0.02	0.03			
Important order			A B C				
Optimization scheme			$A_3B_3C_1$				

Table 3

Variance analysis of seeding performance

Test indexes	Sources	SS	df	MS	F	P-value	Significant
Qualified rate	A	558.162	2	279.081	254.224	99	**
	B	97.549	2	48.774	44.430	19	**
	C	55.582	2	27.791	25.316	9	*
	Error e	2.196	2	1.098			
Multiple rate	A	630.500	2	315.250	130.809	99	**
	B	113.540	2	56.770	23.556	19	*
	C	48.080	2	24.040	9.975	9	(*)
	Error e	4.820	2	2.410			
Miss rate	A	20.829	2	10.414	23.001	18	**
	B	3.376	2	1.688	3.728	6.94	
	C	0.649	2			4.32	
	Error e	1.162	2				
	New error e	1.811	4	0.453			

According to the outcome of the range analysis, the factors affecting the grain spacing qualification index were vibration frequency, vibration amplitude and magnetic induction intensity. The grain spacing qualification index was quite favourable at a vibration frequency of 6 Hz, an amplitude of 3.7 mm and a magnetic induction intensity of 316.34 mT.

Variance analysis indicated that vibration frequency significantly affected the grain spacing pass rate, re-seeding rate and miss-seeding rate. The vibration amplitude also significantly affected the abovementioned metering performance indicators, and the magnetic induction intensity imposed a relatively weak effect on the metering performance indicators. These facts further indicated that the magnetic pickup finger metering device does not require the permanent magnet to have high magnetization performance, which, to some extent, helps reduce the cost of this type of metering device, making it suitable for wide promotion.

Integration of the range and variance analyses and the analysis shown in Table 3 indicated that the three factors affecting the metering performance were as follows, in decreasing order: vibration frequency > vibration amplitude > magnetic induction intensity. The optimal operation parameter combination is vibration frequency 6Hz, vibration amplitude 3.1mm and magnetic induction intensity 316.34MT. Under the conditions of the combined operation parameters, the performance of the seeding operation was 91.7%, 6.2% and 2.1% respectively.

CONCLUSIONS

This study presents a novel magnetic pickup finger-type precision metering device and analyses and optimizes its primary structure and operating parameters. This study also investigates the dominant factors affecting metering performance through the orthogonal test. The findings are shown below.

(1) The stress analysis for the pickup finger in the operating state indicates that its metering performance is associated with the magnetic field distribution and the coefficient of friction between the seed plate and pickup finger.

(2) According to the numerical simulation outcome of the permanent magnet, the magnetic field is strong at both ends and weak in the middle. The material density distribution and magnetizing direction of the permanent magnet affect the magnetic induction intensity. The RbFeB permanent magnet offers evenly distributed magnetic induction and a favourable metering result.

(3) The magnetic induction intensity has a less significant effect on metering performance indicators, and the magnetic pickup finger metering device does not require the magnetization performance of the permanent magnet to be high, which reduces the cost of the metering device.

(4) The orthogonal test for metering performance indicates that the parameter combination offering optimal metering performance consists of a vibration frequency of 6 Hz, an amplitude of 3.7 mm and a magnetic induction intensity of 316.34 mT.

ACKNOWLEDGEMENTS

The authors were funded for this project by the National Natural Science Foundation of China (NSFC) (No. 32060418), Program for Young Talents of Science and Technology in Universities of Inner Mongolia Autonomous Region (No. NJYT-20-B03).

REFERENCES

[1] Abdolahzare Z., Mehdizadeh S.A., (2018), Real time laboratory and field monitoring of the effect of the operational parameters on seed falling speed and trajectory of pneumatic planter, *Computer and Electronics in Agriculture*, vol.44, no.1, pp.187-198, Oxford / England;

[2] Cortez J.W., Anghinoni M., Arcoverde SNS., (2020), Seed metering mechanisms and tractor-seeder forward speed on corn agronomic components, *Engenharia Agricola*, vol.40, no.1, pp.61-68, Jaboticabal / Spain;

[3] Duanyang Geng, Yuhuan Li, Pengxiang Meng et al., (2016), Design and Test on Telescopic Clip Finger Type of Metering Device (玉米伸缩指夹式排种器设计与试验), *Transactions of the Chinese Society for Agricultural Machinery*, vol.47, no.5, pp.38-45, Beijing / China;

[4] Han Tang, Changsu Xu, Jinwu Wang, et al., (2020), Design and experiment of finger-clip maize no-tillage precision planter, *International Agricultural Engineering Journal*, vol.29, no.1, pp.86-97, Beijing / China;

[5] Jianping Hu, Xun Wang, Jun et al., (2011), Magnetic field analysis and structure optimization of magnetic seeding element (磁力排种元件磁场分析与结构优选), *Transactions of Chinese Society for Agricultural Machinery*, vol.42, no.2, pp.67-70, Beijing / China;

[6] Jianping Hu, Qirui Wang, Xiuping Shao, (2010), Simulation on Magnetic Precision Seed-metering Device, *Transactions of Chinese Society for Agricultural Machinery*, vol.41, no.12, pp.35-38, 34, China;

[7] Jinwu Wang, Han Tang, Rui Guan, et al., (2017), Optimization design and experiment on clamping static and dynamic finger-spoon maize precision seed metering device (动定指勺夹持式玉米精量排种器优化设计与试验), *Transactions of Chinese Society for Agricultural Machinery*, vol.48, no.12, pp.48-57, Beijing / China;

[8] Jinwu Wang, Han Tang, Qi Wang et al., (2015), Numerical simulation and experiment on seeding performance of pickup finger precision seed-metering device based on EDEM (基于 EDEM 软件的指夹式精量排种器排种性能数值模拟与试验), *Transactions of the Chinese Society of Agricultural Engineering*, vol.31, no.21, pp.43-50, Beijing / China;

[9] Jinwu Wang, Han Tang, Wenqi Zhou et al., (2015), Improved design and experiment on pickup finger precision seed metering device(指夹式精量玉米排种器改进设计与试验), *Transactions of the Chinese Society for Agricultural Machinery*, vol.46, no.9, pp.68-76, Beijing / China;

[10] Jinwu Wang, Han Tang, Jinfeng Wang et al., (2017), Analysis and experiment of guiding and dropping migratory mechanism on pickup finger precision seed metering device for corn (指夹式玉米精量排种器导种投送运移机理分析与试验), *Transactions of the Chinese Society for Agricultural Machinery*, vol.48, no.1, pp.29-37, Beijing / China;

[11] Jinwu Wang, Han Tang, Jinfeng Wang et al., (2017), Optimization design and experiment on ripple surface type pickup finger of precision maize seed metering device, *International Journal of Agricultural and Biological Engineering*, vol.10, no.1, pp.61-71, Beijing / China;

[12] Kaixing Zhang, Yuanyuan Sun, Lei Liu et al., (2020), Design and test of variable diameter pneumatic drum type bean seed metering device, *INMATEH Agricultural Engineering*, vol.60, no.1, pp.9-18, Bucharest/ Romania;

[13] Li Yang, Bingxin Yan, Dongxing Zhang, et al., (2016), Research Progress on Precision Planting Technology of Maize (玉米精密播种技术研究进展), *Transactions of the Chinese Society for Agricultural Machinery*, vol.47, no.11, pp.38-48, Beijing / China;

[14] Peng Zhou, Manquan Zhao, Fei Liu et al., (2019), Experimental Research on the Finger-type Corn Precision Seed-metering Device(指夹式玉米精密排种器试验优化研究), *Journal of Agricultural Mechanization Research*, vol.41, no.8, pp.153-157, Harbin / China;

[15] Qi Wang, Longtu Zhu, Mingwei Li et al., (2019), Vibration characteristics of corn no-tillage finger-type precision planter and its effect on seeding performance (指夹式玉米免耕精密播种机振动特性及对排种性能的影响), *Transactions of the Chinese Society of Agricultural Engineering*, vol.35, no.9, pp. 9-18, Beijing / China;

[16] Searle C. L., Kocher M. F., Smith J. A., et al., (2008), Field Slope Effects on Uniformity of Corn Seed Spacing for Three Precision Planter Metering Systems, *Applied Engineering in Agriculture*, vol.24, no.5, pp. 581-586, St. Joseph / Michigan;

[17] Wei Fu, Shufeng Li, Jiayi Sun, Hongying Yang, Za Kan, (2011), Design of Forced Clamping Precision Corn Seed Metering Device (强制夹持式玉米精量排种器的设计), *Transactions of the Chinese Society of Agricultural Engineering*, vol.27, no.12, pp. 38-42, Beijing / China;

[18] Weidong L., Matthijs T., Greg S. et al., (2004), Impact of Planter Type, Planting Speed, and Tillage on Stand Uniformity and Yield of Corn, *Agronomy Journal*, vol.96, no.6, pp.1668-1672, Madison/ Wisconsin;

[19] Yazgi A., Degirmencioglu A., (2014), Measurement of seed spacing uniformity performance of a precision metering unit as function of the number of holes on vacuum plate, *Measurement*, vol.56, pp.128-135, Oxford/England;

[20] Yecheng Wang, Yunpeng Gao, Wenshuo Tai et al., (2019), Design and Test of clamping Maize Precision seed metering device (夹持式玉米精密排种器设计与试验), *Transactions of Chinese Society for Agricultural Machinery*, vol.50, no.9, pp.40-46, Beijing/ China;

[21] Yuhuan Li, Li Yang, Ying Han et al., (2018), Design and experiment of spoon-clamping type metering device for faba beans(勺夹式蚕豆精量排种器设计与试验), *Transactions of Chinese Society for Agricultural Machinery*, vol.49, no.S, pp.108-116, Beijing/ China.

OPTIMIZATION DESIGN OF AN AIR-PRESSURE SUBSOILER TYPE
/
气吹式深松铲优化与设计

Hongjie Su, Hongmei Cui*, Feiyu Li, Teng Fan
College of Mechanical and Electrical Engineering, Inner Mongolia Agricultural University, Hohhot, China
Tel：+86 18686001276；E-mail: chm123m@126.com
DOI: https://doi.org/10.35633/inmateh-63-15

Keywords: *subsoiler, soil bulk density, air-pressure subsoiler, specific draft force*

ABSTRACT
Through the mechanical analysis of air-pressure subsoiler, it is found that the main factors affecting its tractive resistance are the air pressure injected into the soil, the soil cohesion, the length and width of the shovel surface, the soil disturbance coefficient, and moving speed of the subsoiler. The traditional air-pressure subsoiler was redesigned to solve the problem of large tractive resistance. In the soil trench experiment, the subsoiling shovel's shape, the air pressure, and the position of air hole were used as test factors, and the ratio of the traction resistance of the shovel to the soil disturbance, namely SDF (Specific Draft Force), was used as the evaluation index. By the response surface test method and analysing the soil disturbance and the tractive resistance, it is determined that rectangular subsoiling shovel with the air hole in the upper part of the shovel is the optimal under the pressure of 1.2 MPa.

摘要
针对气吹式深松铲阻力大的问题，通过对气压式深松铲力学分析，确定影响牵引阻力的因素主要有，注入土壤内部的气压大小、土壤的内聚力、铲面的长度与宽度、土壤扰动系数以及深松铲行进速度。重新设计气压式深松铲，在土槽实验室中以深松铲铲形，气压大小，与气孔位置为试验因素，以深松铲牵引阻力与深松土壤扰动量的比值即比阻 SDF 为评价指标，使用响应面试验方法，综合深松土壤的扰动量与深松铲的牵引阻力进行优化分析，最终确定凿式深松铲加压 1.2Mpa 气孔位置在上部时为相对最优的深松铲。

INTRODUCTION

Since the soil plough pan and soil compaction are becoming increasingly serious (*An Jing, 2016*), it is urgent to improve soil compaction and break the plough pan. Air-Pressure subsoilers (*Zuo Shengjia et al., 2017*) can not only break the plough pan, but also reduce the soil bulk density, improve soil compaction, and provide suitable conditions for crop growth.

European countries adopted subsoil technology early (*Zhang Si, 2018*). In the 1930s, vibrating subsoilers, combined working machines and other agricultural machinery and tools were widely applied in most European countries. A large number of studies have shown (*Bandalan E.P. et al., 1999; Niyamapa T. et al., 2000; Wang Y.X. et al., 2019*) that the vibrating subsoiler can reduce the resistance of the subsoiler, and the forced vibrating subsoiler can reduce the tractive resistance. The self-excited vibrating subsoiler, despite being capable of reducing the tractive resistance, is subject to unstable tillage depth and easy deviation of the frame, so its structural reliability needs to be improved.

Since the 1960s, some scholars and institutions in China have begun to study the structure and mechanism of subsoilers. Based on domestic and foreign subsoiling technology research, China has developed a new type of subsoiling machine—Air-Pressure subsoiler. This subsoiler solves the problems of large subsoil resistance, high energy consumption, unstable subsoil depth and poor structural reliability of traditional subsoilers. The first application of high-pressure gas permeation was by the HSMRC team of NJIT in the United States. They injected high-pressure gas into the rock and soil to remove pollutants. Sehuring's experimental research on injecting high-pressure gas into the soil showed that the air flow rate and the pollutant penetration rate in the soil were increased by 6 times after the high-pressure gas was injected into the soil (*Zuo Shengjia et al., 2017; He Jin, 2005; Gao Xiaodong et al., 2015; Schuring J.R. et al., 1991*).

*Hongjie Su, MS.Stud. Eng.; Hongmei Cui *, Associate Prof, Ph.D. Eng.; Feiyu Li, MS.Stud.Eng；Teng Fan，MS.Stud.Eng.*

In 2016, Zuo developed a new type of air-pressure subsoiling machine. Air-Pressure subsoiling means to create cracks in the soil with high pressure gas during subsoiling so as to improve the porosity of the soil, thereby better crushing the soil. Studies have shown that subsoiling can not only break the plough pan, but also reduce the soil bulk density (*Zuo Shengjia et al., 2017*). In 2018, Liu et al. (*Liu Mingcai, 2018*) designed an air-pressure subsoiler suitable for clay in southern China.

At present, the studies on subsoilers mostly focus on vibrating subsoilers (*Hilal Y.Y et al., 2021; Wang Y. et al., 2019*), few of them being on air-pressure subsoilers. Air-Pressure subsoiling technique is in its infancy, and air-pressure subsoiler also has the problem of large subsoil resistance. To address this problem, it is urgent to optimize the original air-pressure subsoiler.

MATERIALS AND METHODS

Stress analysis of air-pressure subsoiler

It can be seen from Figure 1 that when the subsoiling shovel moves towards the left at a constant speed of v, the soil is pushed forward by it, which produces a shearing force that acts on the soil. And this shearing force will result in an instantaneous cohesion force CS and a friction force $\mu' N$ generated by the movement between the soil, as well as a friction force μN_2 between the soil and the shovel surface generated by the movement of the soil along the shovel surface. Different from traditional subsoiler, the proposed Air-Pressure subsoiler generates air pressure P that acts on the soil, and at the same time produces a reaction force of the same magnitude on the shovel surface.

When the Air-Pressure subsoiler moves forward, the force balance equation can be expressed as:

$$F = N_2 \cdot \sin\alpha + \mu N_2 \cdot \cos\alpha + R \cdot L + P \cdot L \cdot A \cdot \sin\alpha \quad (1)$$

where:

F is the tractive resistance, (N);

N_2 is the normal force on the shovel surface, (N);

μ is the friction coefficient between soil movement and the shovel surface;

R is the cutting force generated by the shovel surface moving forward on the soil, (N);

L is the width of the shovel surface, (m);

α is the angle between the shovel surface and the soil surface, (°);

A is the length of the air pressure distribution on the shovel surface when the air-pressure subsoiler is working, (m).

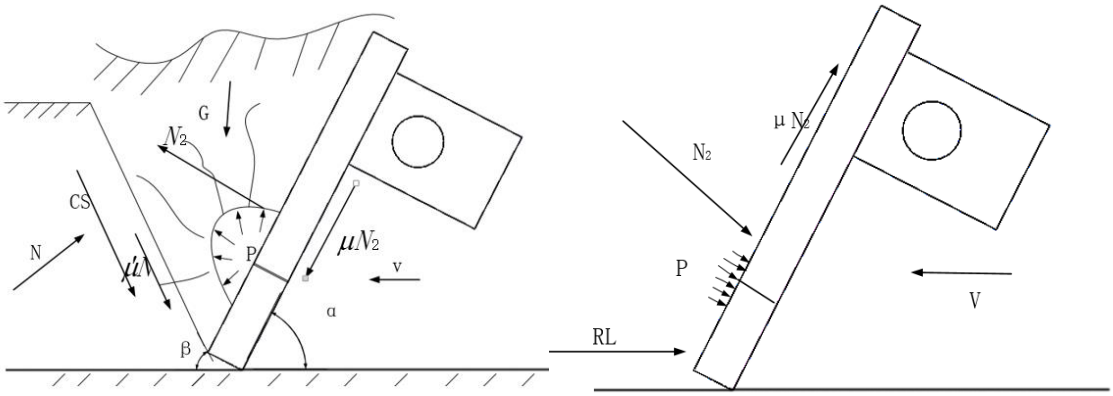

Fig. 1 - The force model of the shovel surface and the soil during the movement of the air-pressure subsoiler

If the soil block on the shovel surface during the movement of the Air-Pressure subsoiler is taken as the research object, the horizontal balance equation of the soil block at this time can be expressed as:

$$N_2(\sin\alpha + \mu'\cos\alpha) - N(\sin\beta + \mu L\cos\beta) - (CS + B - PS_1)\cos\beta = 0 \quad (2)$$

The vertical balance equation of the soil block can be written as:

$$G - N_2(\cos\alpha - \mu\sin\alpha) - N(\cos\beta - \mu'\sin\beta) + (CS + B - PS_1)\sin\beta = 0 \quad (3)$$

where: G is the gravity of the soil block on the shovel surface, (N);

N is the normal load acting on the front failure surface, (N);

B is the acceleration force generated by the movement of the soil block, (N);

β is the inclination of the front failure surface of the soil, (°);

μ' is the soil' internal friction coefficient;

CS is the cohesive force generated when the soil fails (N);

P is the air pressure of the air tube (Pa);

S_1 is the effective soil area raised by the air pressure (m²).

By establishing the simultaneous equations of the above formulas, N_0 and N_1 can be eliminated. Then we get:

$$M_2 = \frac{\cos\alpha - \mu\sin\alpha}{\sin\alpha + \mu\cos\alpha} + \frac{\cos\beta - \mu\sin\beta}{\sin\beta + \mu\cos\beta} \tag{4}$$

The tractive resistance of the subsoiler is finally obtained as:

$$F = \frac{G}{M_2} + \frac{CS + B - PS_1}{M_2(\sin\beta + \cos\beta)} + PLA\sin\alpha \tag{5}$$

According to the experimental study of soil pressure characteristics conducted by Zuo (*Zuo Shengjia et al., 2019*), the effective area of soil lifted by the shovel surface can be expressed as:

$$S_1 = \pi R^2 \tag{6}$$

where: R is a radius.

Based on the above formula and Guo's (*Guo Jinlong, 2016)* research on the relationship between soil velocity and geometry, the expression of the soil block's acceleration and that of the failure area of the soil block's front section can be derived:

$$G = f \cdot L \cdot d \frac{\sin(\alpha+\beta)}{\beta}\left[L1 + \frac{1}{2}\left(\frac{d\cdot\cos(\alpha+\beta)}{\beta} + L1\right)\right] \tag{7}$$

$$A = \frac{f}{g} L \cdot d \cdot t \cdot v^2 \frac{\sin\alpha}{\sin(\alpha+\beta)} \tag{8}$$

$$S = \frac{L\cdot d}{\sin\beta} \tag{9}$$

where: g is the acceleration of gravity (m/s²),

t is the time (s),

v is the speed of subsoiler (m/s),

f is the soil bulk density (kg/m³),

$L1$ is the length of shovel surface (m);

d is the soil disturbance coefficient (m).

The above formula is reorganized and brought into the formula of tractive resistance to get:

$$F = \frac{fLd\frac{\sin(\alpha+\beta)}{\beta}\left[L1 + \frac{1}{2}\left(\frac{d\cos(\alpha+\beta)}{\beta} + L1\right)\right]}{M_2} + \frac{\frac{CLd}{\sin\beta} + \frac{f}{g}Ld\cdot tv^2\frac{\sin\alpha}{\sin(\alpha+\beta)} + P\pi R^2}{M_2(\sin\beta + \mu\cos\beta)} + PL\sin\alpha\frac{f}{g}Ldtv^2\frac{\sin\alpha}{\sin(\alpha+\beta)} \tag{10}$$

When the high-pressure gas enters the soil through the air tube of the Air-Pressure subsoiler, the air pressure acting on the soil partly counteracts the soil's cohesive force and the acceleration force on the shovel surface. It can be known from formula (10) that the main influencing factors of tractive resistance are: the air pressure injected into the soil, the cohesion of the soil, the length and width of the shovel surface, the soil disturbance coefficient, and the speed of the subsoiler.

Aiming at the problem of the large tractive resistance of the Air-Pressure subsoiler, a new type of air-pressure subsoiler is designed.

According to the above-mentioned mechanical analysis, the shape of the shovel, the magnitude of the air pressure, and the position of the air hole are the design factors, as shown in Figure 2. Three types of subsoiling shovel (rectangular, triangular, and rhombic) are designed. The magnitude of the Air-Pressure subsoiler's air pressure, the shape of the shovel, and the position of air hole on the shovel were used as test factors.

The soil trench test was conducted in the laboratory of Inner Mongolia Agricultural University. The disturbance of the soil after the soil was subsoiled by the air-pressure subsoiler was recorded. In the meantime, the tractive resistance of each group of subsoiling shovels was recorded through the force sensor installed on the six force suspension on the trolley.

The specific draft force (SDF) was calculated by Formula (11) which can be found on the next page.

Test Scheme

According to the above analysis, the shape of subsoiling shovel *A,* the magnitude of air pressure B (MPa), and the position of air hole C were chosen as the three test factors/levels.

The specific factors/levels in the test are shown in the table below.

Table 1

Levels of test factors

Level/factor	Shape of shovel	Air pressure (MPa)	Position of ventilation hole
1	Rectangular	0	upper
2	Triangular	0.6	middle
3	Rhombic	1.2	lower

A total of three shovel shapes were designed for the new Air-Pressure subsoiler, as shown in Figure 2.

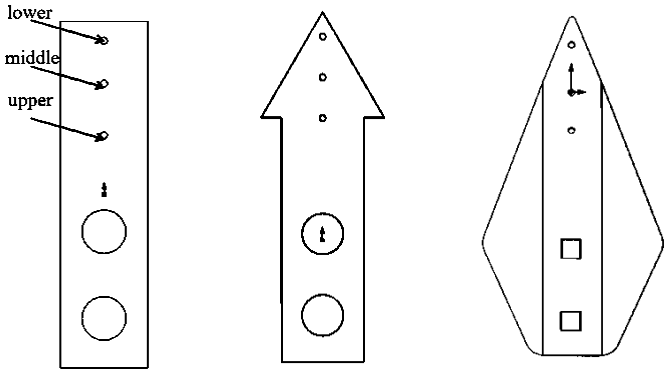

(a) Rectangular *(b) Triangular shovel* *(c) Rhombic shovel*

Fig. 2 - Shapes of shovel

From the *Agricultural Machinery Design Manual (Mechanical Research Institute of the First Ministry of Machinery*), it can be known that the subsoiling shovel's entry angle ranges from 18° to 24°. The research of Liu et al. (*Liu Jun 'an et al., 2018*) showed that when the shovel's entry angle is 21°, the subsoiling effect is the best and the tractive resistance is the smallest. Therefore, the shovel tip is fixed on the shovel shaft, so that the entry angle into the soil is 21°. The specific parameters are shown in Figure 3.

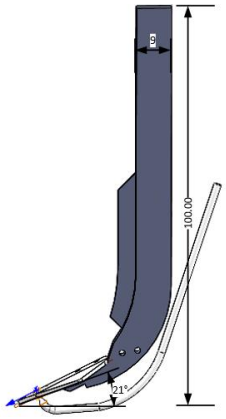

Fig. 3 - Structure of the Air-Pressure subsoiler

The 3D modelling software SolidWorks is applied to model the subsoiling shovel. It can be seen from Figure 3 that the rear of the shovel is connected to the air tube. The length is 100 cm, and the shovel handle is 9 cm in width.

SDF was selected as the evaluation index to evaluate the subsoiling effect of the shovel. With reference to the established groove area, the SDF was calculated by the formula of SDF.

$$SDF = F / A \tag{11}$$

where: SDF is the specific draft force to be calculated, (N/cm^2);

F is the tractive resistance, (N);

A is the soil disturbance area, (cm^2).

It can be known from the specific resistance formula that the smaller the tractive resistance and the larger the disturbance area, the smaller the corresponding SDF. This means that the smaller the SDF, the higher the working efficiency of the subsoiler.

Experiment preparation and testing

Test location: School of Mechanical and Electrical Engineering, Inner Mongolia Agricultural University.

The equipment used for providing traction was a trolley. The test takes the Air-Pressure subsoiling shovel as the research object, as shown in Figure 5.

Before the test, the parameters of the soil in the field were measured. Then the soil in the soil trough was treated with a layered treatment method to ensure that the soil parameters in the trough were consistent with those in the field. In this way, the accuracy of the soil trough test could be ensured.

First, 15 cm of soil in the top soil layer was removed and the remaining soil was sprayed with tap water. After the moisture was fully penetrated into the soil, the surface soil was tilled 3 times, and then compacted with rollers. After compaction, the removed soil was backfilled on the soil surface, and the soil was sprayed with tap water in an appropriate amount. After the water has penetrated completely, the soil was repeatedly compacted with roller. In the test, the soil moisture measurement sensor was used to test the humidity of the soil, and the average soil moisture content was maintained at 13%. A firmness sensor was used to measure the soil firmness after each compaction. The soil was compacted repeatedly and the average soil firmness was kept at 2000 N for 0-20 cm soil, and 2500 N for 20-40 cm soil. Soil samples obtained from the trough were taken to the laboratory for determination of soil bulk density.

Fig. 4 - Picture of soil preparation

During the test, the speed of the trolley was 0.5 m/s, and the depth of the subsoiling shovel into the soil was 35 cm. The total length of the soil tank laboratory is 54 m. To leave room for the acceleration and deceleration of the trolley, the soil trough was divided into 3 areas. The actual effective measurement area was 30 m, with 12 m at both ends of the soil trough for acceleration and deceleration.

The test process is shown in Figure 5. In the test, the pressure was provided by the air compressor, connected to the tip of the subsoiling shovel through the air tube, and finally injected into the soil. As shown in Figure 5, the shovel of the Air-Pressure subsoil was fixed on six force suspensions, and connected with the upper pull rod and the trolley by the left and right suspensions. The force sensor on the suspension was connected to the computer on the trolley to transmit tractive resistance data in real time. The air compressor was connected with the shovel by a 6 m air tube.

While the trolley was moving forward and backward, the air compressor was manually pushed to move at the same speed of the trolley, so that the air pressure can be smoothly injected into the soil via the tube. The maximum exhaust pressure was 2.5 MPa, and the rated working pressure was 1.2 MPa.

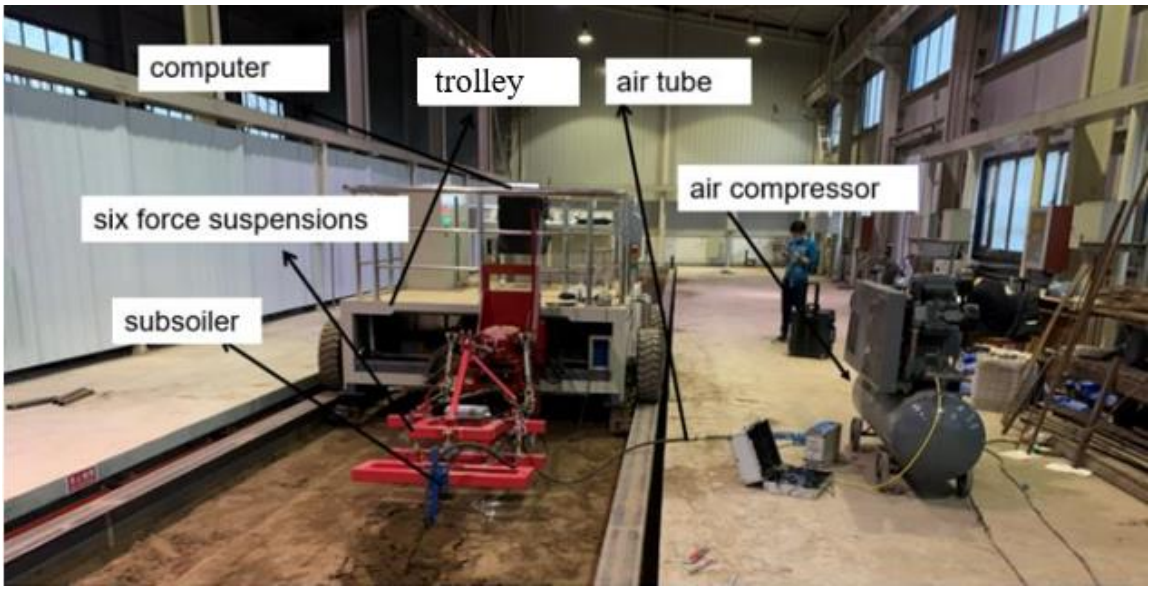

Fig. 5 - Test process

In order to accurately obtain the actual soil disturbance profile of the subsoiling shovel, white ash was marked on the subsoiled ditch according to the soil disturbance test method of Chen et al. (*Hasimu A et al., 2014; Chen Y et al., 2013*) for easy observation. Subsequently, a transparent board was placed on the subsoiled surface and the profile of the soil groove was plotted on the board with a marker. After that, the transparent board was placed on a piece of coordinate paper with an interval of 1 mm, and then the profile was drawn on the paper as shown in Fig. 6(a). The number of squares within the soil groove was the area of the groove. During the test, the tractive resistance of each group of subsoiling shovels was recorded through the six force suspension on the trolley, and the SDF was calculated by the specific resistance formula.

In order to obtain an accurate soil disturbance profile, each measurement was repeated 3 times with an interval of 2 m. To evaluate the subsoiling effect of the Air-Pressure subsoiler more accurately, soil samples before and after subsoiling were taken for soil bulk density determination. Specifically, a pit with a length of 30 cm, a width of 30 cm, and a depth of 50 cm was dug in the soil. Then a cutting ring was used to take three soil samples on the tillage layer, plough pan, and subsoil layer respectively. The cutting ring was then taken out and sealed in a test bag. After subsoiling, the soil samples were taken on both sides of the subsoiling groove with the same method. Each group of tests was repeated 3 times, and the specific sampling process is shown in Figure 6 (b).

(a) (b)

Fig. 6 - Measurement of soil disturbance profile and determination of soil bulk density

RESULTS

The Box-Behnken test was designed based on the above analysis results, and a total of 17 groups of tests were performed, each of which was repeated 3 times. Table 2 shows the design parameters and results of Box-Behnken test. According to the test results, the Design Expert software was applied to establish the second-order regression equation of SDF and variables A (shovel shape), B (pressure magnitude), and C (position of air hole).

The equation is given by:

$$SDF = 4.27 + 0.0065A - 0.4600B + 0.1750C - 0.2550AB - 0.3550AC - 0.0250BC - 0.3035A^2 - 0.2485B^2 + 0.1365C^2 \quad (12)$$

Table 2

Design parameters and results of Box-Behnken test

Serial number	Parameter A (shovel shape)	Parameter B (pressure magnitude)	Parameter C (position of air hole)	SDF (N/cm²)
1	0 (Triangular)	0	0 (The middle part of the shovel)	4.31
2	0	1 (1.2)	-1 (The lower part of the shovel)	3.61
3	-1 (Rectangular)	0	-1	2.91
4	0	0	0	4.01
5	1 (Rhombic)	0 (0.6)	1 (The upper part of the shovel)	4.59
6	0	0	0	4.62
7	-1	1	0	2.79
8	0	-1 (0)	-1	4.36
9	-1	0	1	3.97
10	-1	-1	0	3.32
11	0	0	0	4.31
12	1	0	-1	4.95
13	1	-1	0	5.16
14	1	1	0	3.61
15	0	-1	1	4.76
16	0	0	0	4.11
17	0	1	1	3.91

Analysis of variance was performed on Table 2, and the results are shown in Table 3.

Box-Behnken test analysis of variance **Table 3**

Source of variance	Mean square	Degree of freedom	Sum of squares	P value
Model	0.7748	9	6.97	0.0003
A	3.54	1	3.54	< 0.0001**
B	1.69	1	1.69	0.0002*
C	0.2450	1	0.2450	0.0338*
AB	0.2601	1	0.2601	0.0301*
AC	0.5041	1	0.5041	0.0069*
BC	0.0025	1	0.0025	0.7980
A²	0.3878	1	0.3878	0.0129*
B²	0.2600	1	0.2600	0.0302*
C²	0.0785	1	0.0785	0.1801
Residual	0.0354	7	0.2477	
Lack of Fit	0.0096	3	0.0288	0.9078
Pure Error	0.0547	4	0.2189	
Cor Total	7.22	16		

R2=0.9657; R2adj=0.9216; CV=4.61%; Adeq Precision=15.5959

*Note: ** indicates that the item is extremely significant (p<0.01), and * indicates that the item is significant (p<0.05).*

It can be seen from Table 3 that the shape of the subsoiling shovel (parameter A) has an extremely significant influence on the SDF. The magnitude of air pressure (parameter B) and the position of air hole (parameter C) have a significant impact on the SDF. The effects of interaction terms AB and AC, and the quadratic terms A and B on the SDF are significant. From the perspective of single factor analysis, the influence of each factor on the SDF in descending order is as follows: the shape of the subsoiling shovel (parameter A)> the magnitude of air pressure (parameter B)> the position of air hole (parameter C).

Interaction effect analysis of regression model

The variance analysis results of Box-Behnken test shows that the interaction terms AB and AC have a significant impact on the SDF. Design Expert software was used to draw two interactive response surfaces, as shown in Figure 7.

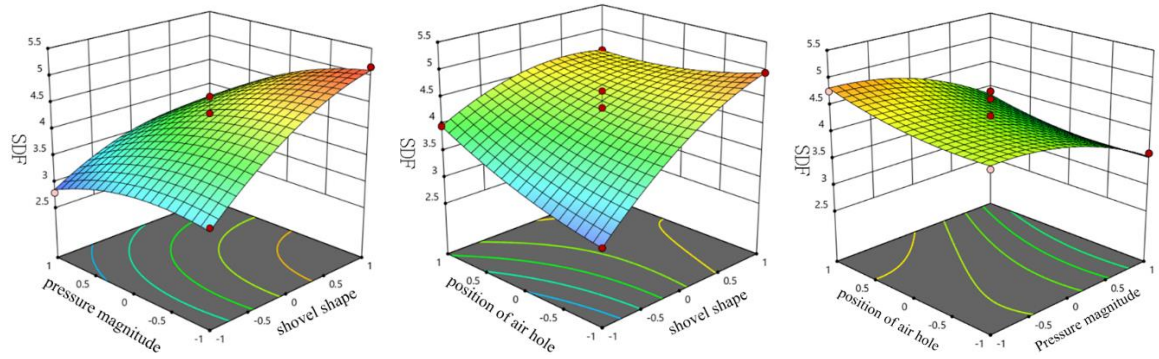

a. A and B interaction *b. A and C interaction* *c. B and C interaction*

Fig. 7 - Interactions between parameters

It can be seen from Figure 7a that the shape of the subsoiling shovel (parameter A)-air pressure magnitude (parameter B) corresponds to a large slope of the curved surface, which causes a large change in the SDF. And the contour line shows a large curvature. These indicate a strong interaction between parameter A and parameter B. Figure 7b shows that the surface slope corresponding to the shape of subsoiling shovel (parameter A)-air hole position (parameter C) is relatively large, indicating that parameters A and C have a great impact on SDF. The contour line in Figure 7b shows a large curvature, indicating that the interaction between the shovel shape (parameter A) and the magnitude of air pressure (parameter B) is significant. It can be seen from Figure 7c that the position of air hole (parameter C) and the magnitude of air pressure (parameter B) are flat, indicating that the interaction effect is insignificant.

Optimal parameters and comparative analysis

The optimization function of Design Expert was used to obtain the minimum SDF, and several groups of solutions were obtained. The optimal solution is as follows: The shape of the subsoiling shovel is rectangular, the air pressure is 1.2 MPa, and the air hole is located on the upper part of the subsoiling shovel.

The new Air-Pressure subsoiler was compared with the traditional Air-Pressure subsoiler by the soil tank test method under the same test factors. The tractive resistance and soil disturbance after subsoiling were recorded, as shown in Figure 8.

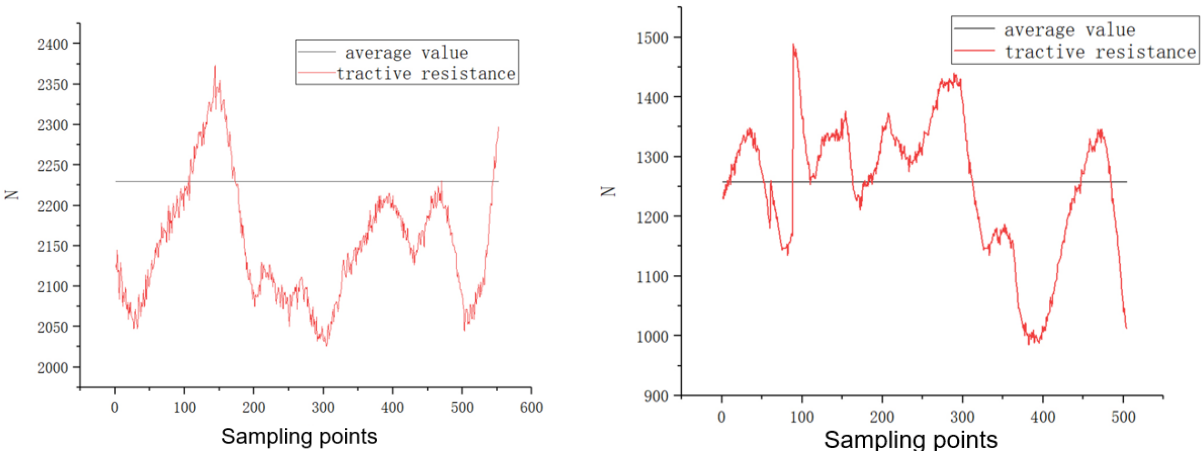

The traditional Air-Pressure subsoiler *The new Air-Pressure subsoiler*

Fig. 8 - Tractive resistance

It can be clearly seen from Figure 8 that the traction resistance of the new subsoiler is reduced by 44.08% compared to the traditional one. It can be calculated that the SDF of subsoiling is reduced by 12.7%.

The soil bulk density before and after subsoiling by the new Air-Pressure subsoiler is shown in the table below. It can be seen from the table that the average bulk density of soil before subsoiling is 11.1% lower than that after subsoiling.

Change of soil bulk density **Table 4**

Soil bulk density (g/cm^3)	The first time	The second time	The third time	Mean
Before subsoiling	1.32	1.36	1.38	1.35
After subsoiling	1.19	1.22	1.21	1.20

CONCLUSIONS

This paper establishes the force model of the shovel surface of the Air-Pressure subsoiler and the soil under the action of air pressure, and analyses the mechanism of the Air-Pressure subsoiler in soil splitting and resistance reduction. Moreover, this paper deduces the formula for calculating the tractive resistance of this proposed subsoiler during operation. It is found that increasing the air pressure can effectively reduce the tractive resistance.

Through a comprehensive analysis of factors such as soil characteristics, groove area, and subsoiling resistance F, it is found that the shape of the subsoiling shovel has the most significant influence on the SDF. Among the three types of shovel, the Air-Pressure subsoiler with a rectangular subsoiling shovel has the largest disturbance to the soil and the smallest tractive resistance. The bulk density decreases by 11.1% on average.

Under the test conditions of this study, the Air-Pressure subsoiler with a rectangular shovel and an entry angle α of 21° is the best subsoiler.

When the pressure is 1.2 MPa and the air hole is in the upper part of the shovel, the subsoiling performance is the best. Compared with the original Air-Pressure subsoiler, the newly-designed Air-Pressure subsoiler reduces the tractive resistance by 44.08%, and the SDF by 12.7%.

ACKNOWLEDGMENT

The supports of the National Natural Science Foundation of China (NSFC) (No. 51905277), and the financial support the Inner Mongolia Natural Science Foundation (No. 2019BS05014), High-level Talent Scientific Research Project of Inner Mongolia Agricultural University (No. NDYB2018-7) for this research are greatly appreciated.

REFERENCES

[1] An Jing, (2016). *Soil compaction mechanisms of black soil and brown earth in the Northeast of China* (*东北地区棕壤和黑土旱田土壤板结机理研究*) Ph.D. Thesis, Shenyang Agricultural University.

[2] Bandalan, E. P., Salokhe, V. M., & Gupta, C.P. (1999). Performance of an oscillating subsoiler in breaking a hardpan. *Journal of Terramechanics*, 36(2), 117-125.

[3] Chen Y., Munkholm L.J., & Nyord T. (2013). A discrete element model for soil–sweep interaction in three different soils. *Soil & Tillage Research*, 126(none), 34-41.

[4] Guo Jinlong. (2016). *Design and research of vibration subsoiler* (master's degree thesis, Shihezi University)

[5] Gao Xiaodong. & Pei Xinmin. (2015). Current situation and problems of subsoilers at home and abroad. (玉米免耕播种深松联合作业机研究). *Agricultural Machinery* (21), 89-91.

[6] He Jin. (2005). *Study on Drilling and Subsoiling Combined Machine for No-till Maize (玉米免耕播种深松联合作业机研究)* (Master's Degree Thesis, China Agricultural University).

[7] Hilal Y.Y., Al-rajabo Saad Abdul Jabbar & Dahham G. A. (2021). The effects of vibrating wings subsoiler plough on driver's seat of agricultural tractors and mechanization performance. *Soil and Tillage Research*, 205, 104806.

[8] Hasimu A., & Chen Y. (2014). Soil disturbance and draft force of selected seed openers. *Soil & Tillage Research*, 140, 48-54.

[9] Liu Mingcai. (2018). *The design and research of the dry land pressure deep pine machine (旱作耕地气压深松机的设计与研究)* (master's thesis, Fujian Agriculture and Forestry University).

[10] Liu Jun'an, Wang Xiaoyan, Li Hongwen, He Jin, Wang Qingjie & Li Wenying. (2017). Structural parameter optimization of subsoiler based on soil disturbance and traction resistance (基于土壤扰动与牵引阻力的深松铲结构参数优化). *Journal of Agricultural Machinery* (02), 60-67.

[11] Mechanical Research Institute of the First Ministry of Machinery. (1973). *Agricultural Machinery Design Manual（农业机械设计手册）*. Mechanical Industry Press.

[12] Schuring J.R., Jurka V., & Chan P.C. (2010). Pneumatic fracturing to remove VOCS *Remediation Journal, 2*(1), 51-68.

[13] Niyamapa T. and Salokhe V.M. (2000). Force and pressure distribution under vibratory tillage tool. *Journal of Terramechanics*, 37(3), pp. 139-150.

[14] Wang Y., Osman A.N., Zhang D., Yang L., & Zhong X. (2019). Optimized design and field experiment of a staggered vibrating subsoiler for conservation tillage. International *Journal of Agricultural and Biological Engineering*, 12(1), 59-65.

[15] Zuo Shengjia, Kong Degang, Chinese, Chen Haixia, Zhang Yong & Han Fuao, (2017). Research status and development trend of pneumatic subsoiling technology (气压深松技术研究现状和发展趋势). *Chinese Journal of Agricultural Machinery Chemistry* (06), 99-103.

[16] Zhang Siyuan. (2018). *Design and Experimental study on the Forced Vibration Subsoiler (受迫振动深松机的设计与研究)* (master's degree thesis, Shihezi University).

[17] Zuo Shengjia, Kong Degang, Chen Haixia, Chinese, Zhang Yong & Liu Chunsheng. (2017). Pneumatic subsoiler design based on pneumatic fracturing theory (基于气压劈裂原理的气压深松机设计). *Journal of Chinese Agricultural Mechanization* (04), 5-10.

FRUIT VIBRATION HARVESTING TECHNOLOGY AND ITS DAMAGE. A REVIEW
/
果品振动收获技术及其果实损伤-综述

Hou Junming, Hu Weixue, Wang Wei, Zhu Hongjie, Rende Zhi [1]
Shenyang Agricultural University, College of Engineering / China
Tel: +8618202412618; E-mail: junming_hou@163.com
DOI: https://doi.org/10.35633/inmateh-63-16

Keywords: *vibration harvest, vibration mode, fruit damage, harvest efficiency, tree modeling*

ABSTRACT

Manual harvesting of large area fruits is inefficient, which consumes manpower and resources. Mechanized harvesting is the inevitable trend of fruit harvest. Vibration harvesting is one of the important forms in terms of fruit mechanized harvesting. According to the different striking parts of fruit trees, the vibration modes were classified as trunk, crown, and branch types. The harvesting efficiency of fruit is an important index to measure the quality of all fruit harvesting machines. The reduction of fruit damage is considered in the harvesting of vulnerable fruits. In this study, the development of vibration harvesting technologies were studied in terms of vibration mode. The development of fruit damage, harvesting efficiency, and fruit tree modeling were discussed. Finally, the development direction of fruit vibration mechanized harvesting was looked forward. Machinery instead of manpower, fully mechanized harvesting is the inevitable development direction of fruit harvesting.

摘要

人工收获大面积果品效率低下，耗费人力，浪费资源。机械化收获是果品收获的必然趋势，振动收获方式是果品机械化收获的重要形式之一。按对果树打击部位的不同位置，对振动方式进行分类，包括树干、树冠、树干三种振动方式。果实的收获效率是衡量所有果品收获机械优劣的重要指标，易损果实的收获还需考虑降低果实损伤。本文从振动方式（树干、树冠、树干）综述了振动收获技术的发展历程以及发展现状，分别对果实损伤分析，收获效率分析以及果树建模分析的发展现状作出综述,并做出总结评论。最后，对果品振动式的机械化收获发展方向进行展望。机械代替人力，全机械化收获是果品收获的必然发展方向。

INTRODUCTION

Fruit is the essential food in human daily life, which plays an important role in the human dietary structure. Human demand for fruit is increasing. All kinds of fruits are grown in huge areas worldwide. Moreover, fruit harvesting is the most critical part of the whole fruit production process. It is a labour-intensive work with strong seasonality. In the fruit production process, the labour force accounts for 30%-45% (*Chen Du et al, 2011*). If they are not harvested timely, it will directly affect the quality of fruits and cause a lot of economic losses. Mechanized harvesting is the best way for fruit production. It can not only reduce production costs, save resources, but also improve production efficiency and improve fruit quality.

At present, compared with the other crops, the development of mechanized harvesting for fruits is slow. There are fewer machines used in actual production. In the process of research, improving harvesting efficiency and reducing fruit damage are two major problems. Vibration harvesting is one of the important forms of fruit harvesting. It is of great value to improve the production efficiency and reduce the damage rate to study the harvesting machine with different vibration forms.

In this study, the development status of vibration harvesting technology was discussed. The development of fruit damage, harvesting efficiency, and fruit tree modeling were summarized. Finally, the prospect of fruit vibratory mechanization harvesting development direction was analysed.

PRINCIPLE AND STATUS OF VIBRATORY HARVESTER

The principle of vibration harvesting is that the fruit trees are shaken by a vibration device. Then the fruit trees will vibrate with a certain frequency and amplitude.

[1] *Hou Junming, Associate Prof., Ph.D. Eng.; Hu Weixue., MS. Stud. Eng.; Wang Wei, Prof., Ph.D. Eng.; Zhu Hongjie, MS. Stud. Eng., Rende Zhi,AP., Ph.D. Eng.*

When the inertia force is greater than the binding force of the fruit handle, the fruit stalk will break, and the fruit will fall off. There are three types of vibration: trunk vibration, crown vibration, and branch vibration (*Sanders, 2005; Li et al, 2011*).

Branch vibration harvester

The principle of the branch vibration is to use the clamping device to hold the branch with fruit, and to use the crank connecting rod mechanism to achieve the effect of vibrating the branch, so that the fruits and branches are separated. As shown in Fig.1, the prototype of a hand-held jujube harvester designed (*Meng, 2014*) drives an eccentric vibration mechanism to enable the forward clamp head to reciprocate back and forth.

Fig. 1 - Prototype of hand-held jujube harvester

At present, this kind of harvester has a simple structure and relatively perfect development. For example, *Adrian et al* designed the first inertial shaker for citrus harvesting in 1965. *Yibo Ma* et al developed a dual motor-driven hand-held fruit harvester in 2018. The device includes a chuck, a motor-driven exciter, a controller, and a battery pack, which can adjust the operating frequency and excitation mode (*Ma et al, 2018*). However, this kind of harvesting machine is only suitable for harvesting a single or small number of fruit trees in the family. and is not suitable for large-scale harvesting.

Crown vibration harvester

The vibration harvesting of tree crown is to hit the tree crown by percussion device to achieve the effect of tree branch vibration and separate the fruit and branches. At present, compared with the tree branch and trunk vibration harvester, the crown vibration harvester is not perfect. Fig.2 shows the harvesting mechanism of the tree crown vibration harvester, which drives the lever roller to move horizontally or vertically to achieve the purpose of tree crown vibration. Fig.3 shows the self-propelled dwarf close planting jujube harvester; Fig.4 shows the straddle coffee harvester; Fig.5 shows the enclosed raspberry vibration harvester.

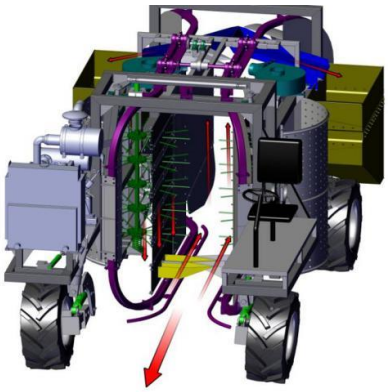

Fig. 2 - Harvesting mechanism of the tree crown vibration harvester

Fig. 3 - Self-propelled dwarf close planting jujube harvester

Fig. 4 - Straddle coffee harvester

Fig. 5 - Enclosed raspberry vibration harvester

The crown vibration harvesting is suitable for large-area fruit harvesting, which can significantly save manpower and improve efficiency. The method is suitable for fruits, which are not easy to be damaged, such as walnut, jujube, etc. However, the fruit will be damaged seriously during the beating process, which will reduce the economic and edible value. Therefore, it is still difficult to harvest vulnerable fruits and reduce fruit damage.

Trunk vibration harvester

Trunk vibration is to use the clamping device to clamp the trunk part of the fruit tree and then vibrate the trunk to achieve the vibration of the fruit tree, so that the fruit and branches are separated. At present, development is relatively perfect. Fig.6 shows the model of vibration harvesting system (*Luo et al, 2017*). Its principle is to drive an eccentric rotating mechanism or crank slider mechanism to make the vibrating head vibrate repeatedly. When the trunk vibrates, the mechanical energy is transferred to the fruit. Fig 7 shows the walnut tree shaking machine. Fig. 8 shows the 4ys-24 red jujube harvester (*Tang et al, 2010*).

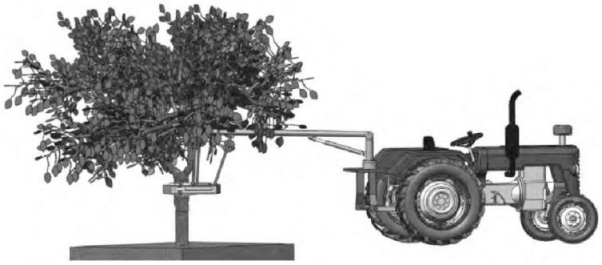

Fig. 6 - Model of vibration harvesting system

Fig. 7 - Walnut tree shaking machine

Fig. 8 - 4ys-24 red jujube harvesting machine

The clamping vibration harvesting machine has been applied in practice. It has high harvesting efficiency, which can save a lot of manpower and material resources. The method is suitable for harvesting fruit on a single tall tree. For example, FMC-400, a citrus harvesting machine designed, works on the principle of reciprocating movement of the clamping head to achieve the purpose of tree trunk vibration. However, the clamping vibration machine is only suitable for single fruit trees, not for the large-scale and large-scale fruit harvesting.

Table 1

Comparison of different harvesting methods

Harvesting way	Suitable type of fruit tree	Advantages	Disadvantages
Branch vibration harvester	Single fruit tree	Simple structure, easy operation, and low cost	Low harvesting efficiency
Crown vibration harvester	Suitable for large area dwarf dense planting fruit trees	Full mechanization, high efficiency, can complete a large area of fruit harvesting	Complex structure, easy to cause fruit damage
Trunk vibration harvester	Single fruit tree (tall, thick)	Full mechanization, high harvesting efficiency, can complete high tree harvesting	Complex structure, not suitable for a large-scale, large area of fruit harvesting

Table 1 shows the comparison of different harvesting methods. Tree branch vibration harvesting is the most popular method in practical production and application at present.

However, compared with the other two methods, the harvesting efficiency is low. Fruit tree planting can gradually develop into large-scale planting mode, so the tree branch vibration harvesting mode is a transitional stage of mechanized fruit harvesting. The trunk vibration harvesting method is suitable for tall, single trees with thicker trunks. Under the planting mode of large-area dwarf dense planting, crown vibration harvesting mode is the mainstream direction. Still, this kind of mechanical structure is complex, how to reduce fruit damage in the harvesting process is a problem. At present, this kind of method is rarely used in the actual harvesting, basically in the theoretical test stage.

FRUIT HARVESTING EFFICIENCY

Harvesting efficiency is one of the important indexes to measure the harvesting quality. The factors that affect the efficiency mainly include vibration frequency, amplitude, and exciting position.

Fruit harvest

There are many related researches on fruit harvesting efficiency. Scholars have done a lot of research on the cherry harvesting. These studies mainly focused on energy transfer efficiency with different vibration frequencies. Different excitation positions were used to test the fruit removal rate. It was concluded that the farther away from the excitation position, the higher the fruit removal rate. The dynamic response of cherry trees under vibration was studied. The frequency of 2-40hz was used to obtain the resonance frequency of tree vibration. The results showed that the cherry tree with simple structure and few branches had higher harvesting efficiency (*He et al, 2013; Zhou et al, 2014; Du et al, 2010*). The effects of frequency, excitation location and branch structure of fruit trees on harvesting efficiency were analysed. The main movement patterns of cherry during shedding were studied by high-speed camera. It can provide reference for the design of cherry harvester. But the vibration excitation system of fruit trees is complex. In the actual harvesting process, many external factors have not been considered. Fig. 9 shows the cherry harvesting analysis test.

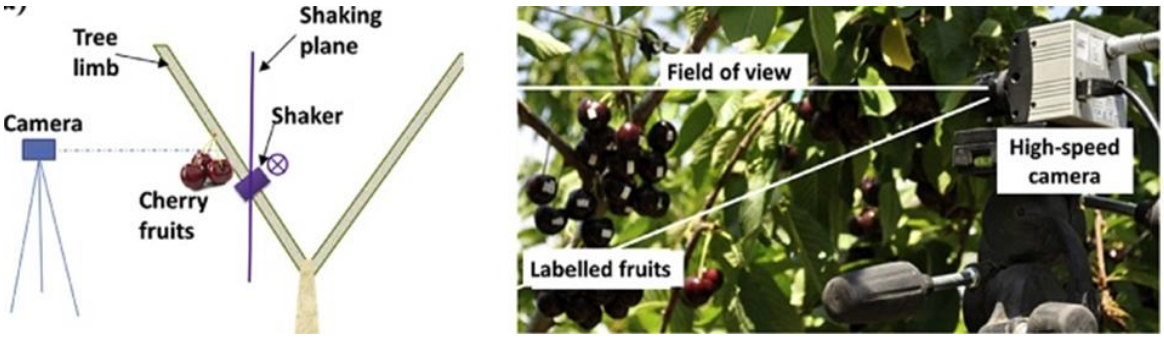

Fig. 9 - Cherry harvesting analysis test

To improve the efficiency of the mechanical harvesting apple, *Liu et al* designed a harvesting mode for high fruit trees. The results showed that when the change rate of vibration frequency was 8Hz, a higher harvesting rate could be obtained. When the frequency was greater than 12Hz, the harvesting rate was higher than that of the traditional fixed frequency harvesting mode (*Ming et al, 2018*). The experiment showed that it was feasible to harvest apple with a frequency conversion mode, which provided a new method for fruit harvesting mode.

Hamidreza H et al took olive as the object, simulated the influence of vibration frequency, loading mode, and loading height on the olive harvest. They compared the simulation results with field test results, and carried out an accurate 3D analysis of mechanized olive harvesting (*Hoshyarmanesh et al, 2017*). The ideal harvesting parameters and harvesting efficiency were obtained. Rafael R et al made a study on the dynamic response of olive trees with vibration parameters. 44 points were randomly measured on the tree with different heights from the ground. The dynamic response and vibration characteristics of the olive tree under different vibration parameters were analysed. This study provides a reference for the design of straddle olive harvester and is also applicable to other similar harvesting machines. Fig.10 shows the dynamic response test analysis of olive (*Sola Guirado et al, 2019*).

Peng et al studied, on winter, jujube harvesting, and analysed the dynamic response of jujube trees under different frequencies (5, 10, 15, 20, 25 Hz) with finite element method, and found the relation between acceleration and frequency (*Peng et al, 2017*).

Liu et al studied the influence of vibration frequency on citrus fruit abscission, then obtained that vibration frequency and penetration depth had extremely significant effects on fruit removal efficiency (*Liu et al, 2018*). *Spain A. et al* obtained the influence law of vibration frequency and other parameters on citrus fruit abscission, and obtained that almost all fruits can fall off with the amplitude of 15Hz and the vibration time of 5s (*Torregrosa et al, 2009*). This study provided a reference for the design of mechanical parameters of tree trunk vibration harvesting, but the problem of fruit damage was not considered in the experiment. The high-speed camera and the image processing method can analyse the movement of citrus in the vibration harvesting process, and better understand the vibration separation mechanism of citrus and other fruits. *Torregrosa A. et al* studied the vibration response of citrus fruit. The vibration rod had an amplitude of 60~180mm and a frequency of 3~18Hz. Based on the high speed camera, the main parameters of fruit detachment were determined (*Torregrosa et al, 2014*). *Castro-Garcia et al* applied the experiment on 22 secondary branches of Valencia sweet orange. In the branch, three natural frequency values were determined, which were 2, 7 and 11Hz respectively. The effects of fruit and leaf on the dynamic response of secondary branches were studied (*Castro-Garcia et al, 2020*). The results were as follows: in the process of mechanical harvesting, the number and quality of leaves and fruits of fruit trees had an important impact on the harvesting efficiency, which provided a reference to optimize the parameters of harvesting machinery.

Erdogan D et al studied the mechanical harvesting of apricot with the amplitude of different distance (20, 30, 40, 50, 60 mm) then the vibration frequency of 10, 15, and 20 Hz, and studied the influence of vibration parameters on the harvesting efficiency (*Erdoğan et al, 2003*). It provided a reference for the parameter design of the inertial vibration device. *Pezzi F. et al* used five frequency settings to record the grape yield, Furthermore, they studied the vibration transmission in the process of grape mechanized harvesting (*Pezzi et al, 2009*). *Wang et al* studied the vibration harvesting efficiency of litchi and found that 90% of the fruits shed at the speed of 1.2s, 0.9s, and 0.5s at 18Hz, 25Hz, and 32Hz, respectively (*Wang et al, 2019*). *He et al* developed an intelligent vibrating screen system to measure the multiple natural frequencies of fruit trees. It also conducted an acceleration response test under different vibration frequencies to obtain the optimal vibration frequency (*He et al, 2020*). Table 2 shows the analysis of the harvesting efficiency of some fruits.

Fig. 10 - Dynamic response analysis test of the olive tree

Table 2

Analysis of fruit harvesting efficiency test (some fruits)

Fruits	Factors affecting the	Conclusion	Reference
Cherry	Frequency	The fruit removal rate was higher at the frequency of 18Hz.	*(He et al, 2013; Zhou et al, 2014; Du et al, 2010)*
	Vibration position	The farther the distance from the excitation location, the higher the fruit removal rate in each region.	
Apricot	Frequency	In the amplitude of 40mm, the frequency of 15hz vibrating screen work can be the greatest degree of fruit.	*(Erdoğan et al, 2003)*
	The amplitude		
Litchi	Frequency	90% of the fruits were fruited at 1.2s, and 90% of the fruits were fruited at 1.2s, 0.9s, and 0.5s at 18Hz, 25Hz, and 32Hz, respectively.	*(Wang et al, 2018)*
Citrus	The amplitude	With an amplitude of 15Hz and a vibration time of 5s, almost all the fruit can be shed.	*(Torregrosa et al, 2009)*
	Vibration time		

Yang et al studied the influence of vibration time, vibration frequency, and amplitude of vibration excitation point on vibration acceleration of apricot tree. Moreover, the dynamic response during the apricot abscission process was studied. They established response equations of different test points, and optimized multi-objective parameters. (*Yang et al, 2019*). *San et al* studied the influence of vibration mode and frequency on the vibration harvesting response of apricot trees. Through the vibration transmission upward from the clamping position along the trunk, the acceleration vibration response curves of different positions were obtained. At the same time, it was concluded that the acceleration value of each detection point was the maximum when the apricot tree was excited by 11.56 Hz. (*San et al, 2018*). The research provides theoretical reference for the design of apricot or other fruit harvesting machine parameters.

Yang made a study on the mechanical harvesting of dwarf and dense planting jujube. Taking the fruit removal rate as the index, the parameters of the harvesting parts and dense planting jujube harvesting device were designed. The parameters were optimized by orthogonal test, and the parameters of the optimal fruit removal rate were obtained (*Yang, 2013*).

Huo established the vibration model of the blueberry picking system. The frequency, amplitude, time, and area of action were taken as the factors affecting the efficiency of blueberry picking. The primary, secondary order, and the optimal combination of picking parameters were obtained through simulation, (*Huo, 2013*). Ding carried out research on mulberry fruit abscission characteristics. Then they studied the main influencing factors of inertial force during mulberry vibration picking, obtained the vibration parameters of vibration picking device when mulberry fell off and designed a portable mulberry vibration picking device according to the experimental parameters (*Ding, 2016*).

Many scholars have studied the harvesting efficiency of mechanized harvesting fruits. However, there are still problems. First of all, most of the experiments extract part of the parameter values for research; whether the parameter values beyond the test value range can get better optimization results is still to be discussed. Secondly, the effects of the harvesting season, environmental factors, and fruit tree parameters were not considered. However, the experiment of large-area and large-scale fruit harvesting efficiency has been done less, so this kind of experiment is still a big problem.

Non-fruit harvesting

There are also related studies on the harvesting efficiency of pistachio and walnut. *Polat et al* studied the effect of vibration frequency and amplitude on pistachio fruit harvesting. The amplitudes of 40, 50 and 60mm and the frequencies of 10, 15 and 20Hz were adopted. The optimal amplitude was 50mm and the optimal frequency was 20Hz. It was concluded that the efficiency of mechanical harvesting was far greater than that of manual harvesting. Through the comparison between manual harvesting and mechanical harvesting, it was concluded that the inertia vibrating screen is feasible. The influence of fruit tree structure on the test results was fully considered (*Polat et al, 2007*).

Wang et al applied different harvesting methods to analyse the harvesting efficiency of *Lycium barbarum* fruit. The results showed that the picking rate reached 85%, while the fruit damage rate was low (*Wang et al, 2018*). It is the best method to harvest the *Lycium barbarum* by vibration.

Du et al analysed the different incentive modes produced by the combination of different eccentric mass for dwarf Chinese hickories. It was concluded that orthogonal eccentric mass could effectively and evenly transfer vibration and improve harvesting efficiency (*Du et al, 2018*).

Ferreira et al studied the dynamic response of coffee tree during picking and obtained the frequency and amplitude of coffee tree vibration (*Ferreira et al, 2020*).

There are kinds of dried fruits and non-fruit fruits such as *Lycium barbarum* and coffee. However, compared with fruits, there are few studies on the harvesting efficiency of such fruits.

FRUIT DAMAGE

Mechanical damage will cause fruit aging, decay, loss of nutritional value, and greatly reduce the economic and edible value of the fruit. Therefore, for the mechanical vibration harvesting of fragile fruits, the damage of fruits is an important index. The influencing factors include vibration parameters, such as frequency, amplitude, etc., as well as the drop height, picking plate angle, and so on.

Vibration parameters

The parameters such as excitation frequency are the main factors affecting fruit damage for vibration harvesting. *Zhou et al* used a high-speed camera to capture 18 fruit trajectories at different frequencies, and concluded that the main motion modes were tilt and cylinder motion.

This experiment also analysed the movement pattern of cherry fruit during harvesting and its relation with fruit damage. As shown in Fig. 11, the cherry damage can be divided into four levels.

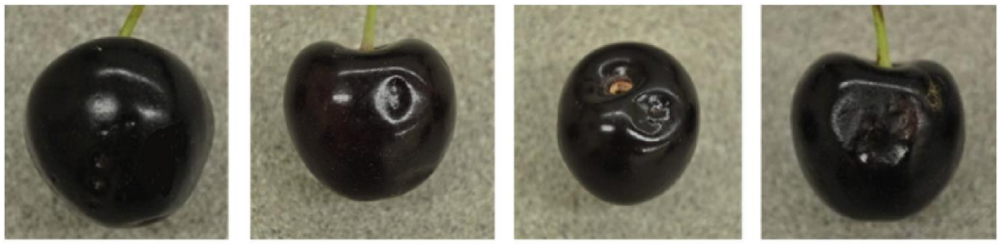

(a) *(b)* *(c)* *(d)*

Fig. 11 - Cherry damage grading

Cherry damage classification is shown in Table 3 (*Zhou et al, 2016*). *He L. et al* made the relevant research on the cherry damage principle. Four different excitation positions were used to test the fruit damage. The damage of different excitation positions from low to high was 20%, 28%, 20%, and 23% respectively. It was concluded that there was no significant difference in the damage of fruits at different excitation locations (*He et al, 2017*).

Table 3

Damage grading of cherry

Fruit	Number	Level	Damage	Reference
Cherry	a	Level 1 damage	There are small dents	(*Zhou et al, 2014*)
	b	Level 2 damage	There are depressions	
	c	Level 3 damage	The diameter of the damaged area is larger than 6.4mm	
	d	Level 4 damage	The diameter of the damaged area is larger than 9.5mm	

Wang et al made a study on litchi collision damage and found that when the vibration frequency was 32 Hz, the minimum damage degree was 5.69%. It was feasible to harvest litchi fruit with high speed and low damage under appropriate frequency (*Wang et al, 2019*). However, this test is a mechanical shedding test conducted in the laboratory, which does not consider the influence of environmental factors and fruit tree structure, which is a common problem in the current test.

Sergio Castro Garcia et al studied the use of vibrating tree trunk to harvest olive. To achieve 85% harvesting efficiency, acceleration greater than 183.4m/s^2 and vibration frequency of 28.1Hz is required. However, the damage of olive is 3.5 times that of manual harvesting (*Sergio Castro-Garcia et al, 2015*). *Pezzi F. et al* used five frequency settings, 370-450 times per minute, to record the loss of yield and plant defoliation. They studied the mechanical vibration transmission of mechanical harvesting grapes (*Pezzi et al, 2009*). The straddle type harvester was used to test, which provided a reference for the parameter design of the harvester.

Sergio Castro-Garcia et al analysed the abscission process of "Valencia" orange fruit, adopted low-frequency and high amplitude movement to improve the vibrating screen system to reduce the damage of trees and fruits in the process of harvesting. In this experiment, three different vibrating screens were applied to obtain the vibration frequency and vibration time during the fruit harvesting process, which can improve the harvesting efficiency and reduce the damage of the fruit. It provides a reference for the design of harvesting machine parameters (*Sergio Castro-Garcia et al, 2018*). *Han et al* designed a vibrating screen with an adjustable vibration amplitude for harvesting apple. The vibration frequency of 20Hz and the vibration time of 5 s was adopted. The results showed that the vibration amplitude of 30 mm was enough to make the fruit fall off and get high-quality fruit (*Han et al, 2019*).

Table 4, vibration parameters affecting fruit damage (some fruits). A large number of experiments showed that the vibration parameters affecting fruit damage include frequency and amplitude, while the excitation position had little effect on fruit damage. However, the appropriate frequency or amplitude can reduce the fruit damage in the harvesting process, and does not affect the harvesting efficiency.

Table 4

Vibration parameters affecting fruit damage (some fruits)

Fruit	Vibration parameters	Conclusion	Reference
Cherry	Frequency	At the vibration frequency of 10, 14, and 18, the fruit damage caused by 14Hz was at the lowest of 47.1%.	(*Zhou et al, 2016*)
Litchi	Frequency	The lowest average damage at 32Hz was 5.69%.	(*Wang et al, 2019*)
Apple	Amplitude	The fixed frequency was 20Hz and the vibration time was 5. Among the four amplitudes of 20, 25, 30, 35, and 40mm, the amplitude of 30mm could not reduce the harvesting efficiency and obtain high-quality fruits.	(*Han et al, 2019*)

Impact parameters

The drop height, impact angle, and other parameters also affect fruit damage. *Salarikia et al* used a drop test to analyse the dynamic characteristics of pear under impact load, to reduce the impact damage of pear during harvesting (*Salarikia et al, 2016*). *Stropek* selected two pear varieties as experimental materials to study the relation between the internal damage energy and the impact speed of pear. The result is that the higher the impact speed, the higher the internal damage energy (*Stropek et al, 2020*).

P. Komanicki et al analysed the impact of impact load on pear impact damage by measuring the surface pressure of pear under different drop heights and specific impact times (*Komarniki et al, 2016*). All of the above are aimed at the pear damage test. The influence of the drop height, impact times, and other parameters on the pear damage and the energy transfer in the process were analysed. It can not only provide a reference for pear damage reduction in the harvest process but also provide a theoretical basis for material damage principle in other production processes such as transportation.

Zhou et al studied the effects of fruit drop height and grip angle on cherry collision damage. The results showed that there was a positive linear correlation between fruit impact force and fruit drop height, and fruit bruise could be reduced when the tilt angle was 60 degrees (*Zhou et al, 2016*).

Wang et al took litchi as the research object. When the impact velocity was 2.8 m/s, 15 times of impact on the fruit was obvious, and 5 times of impact on the fruit damage was small. When the velocity was 0.98m/s, there was no obvious damage after 15 times of impact. So, increasing the impact speed or times would cause greater damage to the fruit (*Wang et al, 2018*). *Wang et al* used litchi fruits of "Nuomici" and "Guiwei" varieties as experimental materials to study the collision behaviour between fruit and rigid plate. With the increase of drop from 200 mm to 800 mm, the damage degree of litchi varieties increased. However, when the drop increased from 600 mm to 800 mm, "Nuomici" was more resistant to fruit damage than "Guiwei" (*Wang et al, 2020*). The studies showed that in addition to the impact parameters, there was also an important relation between the variety of fruit and the damage.

Öztekin et al carried out impact tests on Peach Cultivars of “Glohaven”, “J.H. Hale”', and “Loring”. Through the analysis of the relation among impact peak acceleration, impact velocity change and impact area, the damage boundary values of three peach varieties were determined (*Öztekin et al, 2020*).

Bao et al made a study on impact damage assessment of mechanically harvested blueberry fruit based on collision deformation energy. It was concluded that when the distance between the blueberry growth concentration area and blueberry harvester fruit plate was close to 600 mm, and the angle of the picking plate was close to 15^{o}, the impact deformation energy of fruit was less than 0.68×10-3J, and the fruit damage was the least (*Bao et al, 2017*).

Table 5m shows impact parameters affecting fruit damage. It can be seen from the relevant literature that the impact parameters of fruit damage mainly include fruit drop height, fruit drop angle, impact speed, and impact times. The purpose of changing the impact parameters is to reduce the impact load during the harvesting process and reduce the damage of the fruit. The height of fruit drop, impact speed, and impact times were positively correlated with fruit damage. Therefore, in the case of little effect on the fruit harvesting efficiency, the appropriate impact parameters can effectively reduce the fruit damage. At present, the purpose of relevant tests is mostly to find out the relation between relevant parameters and impact load. Therefore, the relevant impact parameters should be optimized in the experimental study to obtain the optimal impact parameters without affecting the harvesting efficiency.

Table 5

Impact parameters affecting fruit damage (some fruits)

Fruit	The impact parameters	conclusion	reference
Cherry	Fruit drop height	There was a linear positive correlation between the impact force of the fruit and the height of the fruit, which could reduce the bruising of the fruit when the tilt angle was 60°.	(*Zhou et al, 2016*)
	Tilt angle		
Litchi	Impact velocity	When the impact velocity was 2.8 m/s, the damage to the fruit was obvious in the 15 impacts, but less in the 5. When the speed was 0.98 m/s, no obvious damage was seen in the 15 impacts.	(*Wang et al 2018*)
	Number of impacts		

Colliding materials

Material is also an important factor affecting fruit damage. *Zhou et al* studied the effect of buffer materials on cherry damage. The thick enough cushion material could reduce the impact force of fruit and reduce the damage of fruit (*Zhou et al, 2016*).

Lin et al studied the effect of colliding material on peach damage by a vibration test. The results showed that PU +CFB was better than EPE + CFB and CFB as packaging buffer material (*Lin et al, 2020*).

Öztekin et al put three kinds of peach such as "Glohaven", "J.H. Hale" and "Loring" on three steel impacting surfaces that did not cover any material, and covered the porous plastic or rubber foam on the impact surface. The results showed that porous plastics could reduce the damage of fruit (*Öztekin et al, 2020*).

Fernando I. et al evaluated the effectiveness of two types of corrugated paperboard packaging, reusable plastic creates (RPC) and vacuum tightening for their protective performance in reducing damage of bananas under simulated transport vibration. (*Fernando et al, 2019*).

It can be seen that the study on collision materials in the harvesting process mainly include the fruit picking device and the hitting device. The changing on the materials is also to reduce the impact load of the fruit when contacting the fruit picking device and beating device. Selecting the appropriate flexible material through the test can effectively reduce the damage of the fruit in the harvesting process, and obtain high-quality fruit. The experiments can not only provide a reference for the selection of materials in the harvesting process but also provide a reference for the selection of other production process materials such as fruit transportation and packaging.

FRUIT TREE MODELING

Fruit tree modeling can analyse the dynamic response characteristics of fruit trees in the process of vibration harvesting, to provide a theoretical basis for the design of harvesting machinery. The accuracy of the test can be verified by comparing the modeling results with the test results.

Peng carried out the study on the vibration harvesting of winter jujube by modeling on the jujube tree. As shown in Fig.12, the tree model was divided into two parts of branch and trunk. The response of trees to vibration excitation was predicted. The relation between the response and the excitation frequency was studied. It was concluded that the changing trend of simulation and measurement was better (*Peng et al, 2017*). This method has certain reference value for studying the dynamic response of fruit trees under the excitation of the vibration device.

For the citrus harvest, *Liu et al* established a cantilever branch model with a periodic vibration force to simulate the vibration process of citrus canopy. The results showed that there was a positive correlation between the vibration frequency and the maximum stress at the end of the fruit stalk. When the vibration frequency was 5 Hz, the fruit could be removed (*Liu et al, 2018*). This method is aimed at the vibration process of the canopy and provides a reference for improving the design of the canopy vibration device.

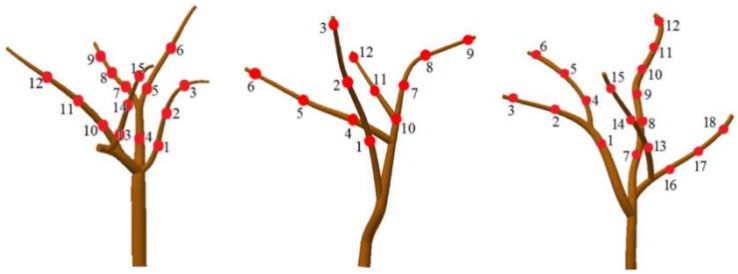

Fig. 12 - Three jujube tree models

Du et al established the finite element model of a dwarf Chinese hickory tree. Then, ADAMS software was used to analyse the model to simulate the response of a dwarf Chinese hickory tree to different eccentric mass combination excitation. It was concluded that the orthogonal eccentric mass could effectively and evenly vibrate the branches and improved the harvesting efficiency (*Du et al, 2018*).

Salarikia et al studied the impact damage of pears. The drop test was applied to analyse the pear samples by the finite element method. The pear model was made by non-contact optical scanning technology, and the simulation analysis was carried out on the three-dimensional entity (*Salarikia et al, 2016*). Using non-contact optical scanning technology to make a 3D model can not only detect and analyse the shape and appearance of real objects in detail but also avoid the tedious process of manual modeling.

Kursat Celik H. used the simulation method to analyse the damage sensitivity of Ankara pear to impact load (*Kursat Celik H., 2017*).

Du established the finite element model of kiwifruit falling and simulated the falling scene. It was concluded that the sensitivity of using the finite element method to predict fruit damage was reliable (*Du et al, 2019*).

Villibor et al established a flexible model of coffee fruit stem system for dynamic analysis. The model included oblique branch, fruit stem, and fruit. The fruit stem was modeled as a flexible beam and discretized into four elements (*Villibor et al, 2019*).

Yang et al studied the dynamic response of apricot tree vibration, established the model of the apricot tree by ANSYS software, obtained relevant parameters through finite element analysis (*Yang et al, 2019*), The results were shown in Figure 13. Wang et al applied three typical plastic fruit trees to establish fruit tree models. Then, the natural frequencies and modal shapes of the fruit trees in the low-frequency range of 1 ~ 50 Hz were obtained by using the finite element method.

The simulation test of vibration response characteristics was carried out (*Wang et al, 2017*).

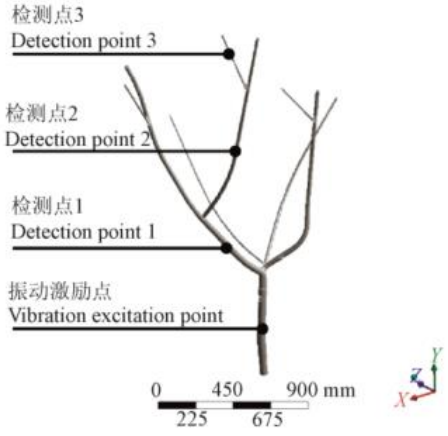

Fig. 13 - Finite element model of apricot tree established by Autodesk Inventor 2014

Bao obtained the theoretical value of deformation and deformation energy of blueberry through finite element simulation and studied the damage principle. It was concluded that the drop height and the angle of the fruit receiving plate were the main factors affecting the deformation energy of blueberry (*Bao et al, 2017*).

Through research on fruit tree modeling, it can be concluded that fruit harvest is dynamic rather than static. So, the modeling of fruit tree and fruit is dynamic model, the modeling must be a flexible model. Most of the researches adopt the method of finite element modeling. Through the method of fruit tree modeling, we can simulate the dynamic response characteristics of fruit trees in the process of vibration harvesting, predict the factors affecting the fruit picking efficiency, and analyse the damage mechanism of fruits in the process of picking. The simulation results can also be compared with the experimental results to further verify the accuracy of the test results. But the fruit system is very complex, mechanical harvest will be affected by many factors of fruit trees and fruit itself, such as the height of trees, the shape and size of fruit. There are many external factors in the process of harvesting, such as geographical and environmental factors. The results obtained by modeling may have some errors with the experimental results. How to improve the reliability and accuracy of fruit tree modeling needs further research.

DEVELOPMENT PROSPECT

Fruit vibration harvesting is the mainstream development of fruit mechanized harvesting. It is a kind of harvesting method with relatively high harvesting efficiency. Among the three harvesting methods, branch vibration harvesting is inefficient and will be replaced by full mechanization. Trunk vibration harvesting is suitable to harvest fruit on tall fruit trees, but it is not suitable for large-scale and large-area fruit harvesting. Crown vibration harvesting is suitable for large-scale fruit harvesting, but it is easy to cause fruit damage. Therefore, fruit vibration harvesting may have breakthroughs in the future:

(1) The main direction of fruit harvesting development in the future is a large-scale fruit harvesting. The crown vibration harvesting is the most suitable method, so the development of the crown vibration harvesting machinery should be strengthened. If the fruit tree trunk is thin, the application of crown vibration to the tree trunk can not only improve the harvesting efficiency of traditional tree trunk vibration harvester, but also reduce the damage of fruit.

(2) Make a breakthrough in improving the efficiency of fruit harvesting. Optimize the parameters of mechanical operation, to improve the efficiency of fruit harvesting and reduce the production cost.

(3) Make a breakthrough in reducing fruit damage. The mechanism of fruit damage was analysed. Without affecting the harvesting efficiency, the impact times and impact force of fruits were reduced, so as to reduce the damage of fruits. In the vulnerable fruit, the harvest aspect makes the breakthrough unceasingly.

CONCLUSIONS

The vibration harvesting for fruit is one of the development ways to realize the full mechanized harvesting of fruits. This research has been carried out for decades. At present, a lot of research has been done on apple, cherry, pistachio, and other fruits all over the world. A large number of patents on harvesting machinery have been obtained. But it is seldom applied in the production of harvesting machinery. At present, most of the machines are still in the theoretical stage. There is still a big gap between fruit harvesting and crop harvesting. There is still a long way to go to realize the full mechanized harvesting of fruits. We should carry out further research based on previous studies to promote the development of fruit mechanization.

ACKNOWLEDGEMENT

This research was supported by Natural Science Foundation of Liaoning Province of China, (2019-ZD-0718), the authors thank relevant scholars for their assistance in the literature.

REFERENCES

[1] Bao Y.D., Yang C., Zhao Y.L., Liu X.L., Guo Y.L., (2017), Impact damage assessment of mechanically harvested blueberry fruit based on collision deformation energy. *Transactions of the Chinese Society of Agricultural Engineering*, Vol.33, Issue 16, pp.283-292;

[2] Castro-Garcia S., Aragon-Rodriguez F., Arias-Calderón R., Sola-Guirado R. R., Gil-Ribes J. A., (2020), The contribution of fruit and leaves to the dynamic response of secondary branches of orange trees. *Biosystems Engineering*, Vol.193, pp.149-156;

[3] Chen D., Du X.Q., Wang S.M., Zhang Q., (2011), Mechanism analysis and research progress of vibratory fruit harvesting technology. *Transactions of the CSAE*, Vol.27, Issue 08, pp.195-200;

[4] Ding H.X., (2016), *Study on vibration shedding characteristics of mulberry and design of picking device*. Northwest agricultural and Forestry University/China, 2016;
[5] Du D.D., Wang B., Wang J., Yao F.Q., Hong X.Z., (2019), Prediction of bruise susceptibility of harvested kiwifruit (Actinidia chinensis) using finite element method. *Postharvest Biology and Technology*, Vol.152, pp.36-44;
[6] Du X., Chen D., Zhang Q., Pierce F. J., Scharf P. A., (2010), Dynamic Response of Sweet Cherry Tree to Oscillating Excitations for Mechanical Harvest. *IFAC Proceedings Volumes*, Vol.43, Issue 26, pp.83-88;
[7] Du X., Jiang F., Li S., Xu N., Li D., Wu C., (2019), Design and experiment of vibratory harvesting mechanism for Chinese hickory nuts based on orthogonal eccentric masses. *Computers and Electronics in Agriculture*, Vol.156, pp.178-186;
[8] Erdoğan D., Güner M., Dursun E., Gezer I., (2003), Mechanical Harvesting of Apricots. *Biosystems Engineering*, Vol.85, Issue 01, pp.19-28;
[9] Fernando I., Fei J., Stanley R., Rouillard V., (2020), Evaluating packaging performance for bananas under simulated vibration. *Food Packaging and Shelf Life*, Vol.23, 100428;
[10] Ferreira Júnior Luis da Gonzaga, Silva Fabio Moreida, Ferreira Danton Diego et al., (2020), Dynamic behaviour of coffee tree branches during mechanical harvest. *Computers and Electronics in Agriculture*, Vol.173, 105415;
[11] Fu H., Duan J.L., Manoj K., He L., Xia H.M., Li J., Zhang Q., (2019), Effect of Shaking Amplitude and Capturing Height on Mechanical Harvesting of Fresh Market Apples. *IFAC-PapersOnLine*, Vol.52, Issue 30, pp.306-311;
[12] He L., Liu X., Du X., Wu C., (2020), In-situ identification of shaking frequency for adaptive vibratory fruit harvesting. *Computers and Electronics in Agriculture*, Vol.170, 105245;
[13] He L., Zhou J., Du X., Chen D., Zhang Q., Karkee M., (2013), Energy efficacy analysis of a mechanical shaker in sweet cherry harvesting. *Biosystems Engineering*, Vol.116, Issue 04, pp.309-315;
[14] Hoshyarmanesh H., Dastgerdi H. R., Ghodsi M., Khandan R., Zareinia K., (2017), Numerical and experimental vibration analysis of olive tree for optimal mechanized harvesting efficiency and productivity. *Computers and Electronics in Agriculture*, Vol.132, pp.34-48;
[15] Huo Q., (2013), Simulation analysis of blueberry picking system and plant vibration model [D]. Northeast Forestry University/China;
[16] Komarnicki P., Stopa R., Szyjewicz D., Młotek M., (2016), Evaluation of bruise resistance of pears to impact load. *Postharvest Biology and Technology*, Vol.114, pp.36-44;
[17] Kursat Celik H., (2017), Determination of bruise susceptibility of pears (Ankara variety) to impact load by means of FEM-based explicit dynamics simulation. *Postharvest Biology and Technology*, Vol.128, pp.83-97;
[18] Li P., Lee S., Hsu H., (2011), Review on fruit harvesting method for potential use of automatic fruit harvesting systems. *Procedia Engineering*, Vol.23, pp.351-366.;
[19] Li Z., Thomas C., (2014), Quantitative evaluation of mechanical damage to fresh fruits. Trends in Food Science & Technology, Vol.35, Issue 02, pp.138-150;
[20] Lin M., Chen J., Chen F., Zhu C., Wu D., Wang J., Chen K., (2020), Effects of cushioning materials and temperature on quality damage of ripe peaches according to the vibration test. *Food Packaging and Shelf Life*, Vol.25,100518;
[21] Liu M., Wang F.L., Xing H.Q., Ke W.L., Ma S.C., (2018), The Experimental Study on Apple Vibration Harvester in Tall-spindle Orchard. *IFAC PapersOnLine*, Vol.51, Issue 17, pp.152-156;
[22] Liu T.H., Luo G., Ehsani R., Toudeshki A., Zou X.J., Wang H J., (2018), Simulation study on the effects of tine-shaking frequency and penetrating depth on fruit detachment for citrus canopy-shaker harvesting. *Computers and Electronics in Agriculture*, Vol.148, pp.54-62;
[23] Luo G., Liu T.H., Zeng W., Yang Z., Liu X.H., (2017), Analysis and Simulation of trunk vibration in fruit vibration harvesting. *Journal of Machine Design*, Vol.34, Issue 01, pp.47-51;
[24] Ma Y.B., Chen D., Zhang M.C., Zhang Y.Y., Wang S.M., (2018), Research on hand-held dual motor driven harvester for tree fruit. *IFAC-Papers on line*, Vol.51, Issue 17, pp.268-273;
[25] Meng X.J., (2014), *Design and research of hand-held jujube vibration harvester*. Shihezi University / China;
[26] Opara U. L., Pathare P. B., (2014), Bruise damage measurement and analysis of fresh horticultural produce—A review. *Postharvest Biology and Technology*, Vol.91, pp.9-24;

[27] Öztekin Y. B., Güngör B., (2020), Determining impact bruising thresholds of peaches using electronic fruit. *Scientia Horticulturae*, Vol.262, 109046;
[28] Peng J., Xie H., Feng Y., Fu L., Sun S., Cui Y., (2017), Simulation study of vibratory harvesting of Chinese winter jujube (Zizyphus jujuba Mill. cv. Dongzao). *Computers and Electronics in Agriculture*, Vol.143, pp.57-65;
[29] Pezzi F., Caprara C., (2009), Mechanical grape harvesting: Investigation of the transmission of vibrations. *Biosystems Engineering*, Vol.103, Issue 03, pp.281-286;
[30] Polat R., Gezer I., Gune M., Dursun E., Erdogan D., Bilim H. C., (2007), Mechanical harvesting of pistachio nuts. *Journal of Food Engineering*, Vol.79, Issue 04, pp.1131-1135;
[31] Salarikia A., Miraei A.S., Golzarian M. R., Mohammadinezhad H., (2017), Finite element analysis of the dynamic behaviour of pear under impact loading. *Information Processing in Agriculture*, Vol.4, Issue 01, pp.64-77;
[32] San J.L., Yang H.M., Wang X.N., Niu C.H., Guo W.S, Hou S.L., (2018), Effects of vibration mode and frequency on vibration harvesting response of apricot. *Transactions of the Chinese Society of Agricultural Engineering*, Vol.34, Issue 08, pp.10-17;
[33] Sanders K. F., (2005), Orange Harvesting Systems Review. Biosystems Engineering, Vol.90, Issue 02, pp.115-125;
[34] Sergio C., Francisco J.C., Francisco J., Jesus A.G., Gregorio L.B., (2015), Suitability of Spanish 'Manzanilla' table olive orchards for trunk shaker harvesting. *Biosystems Engineering*, Vol.125, pp.388-395;
[35] Sergio C., Rafael R. S., Jesus A.G., (2018), Vibration analysis of the fruit detachment process in late-season 'Valencia' orange with canopy shaker technology. *Biosystems Engineering*, Vol.170, pp.130-137;
[36] Sola-Guirado R. R., Aragon-Rodriguez F., Castro-Garcia S., Gil-Ribes J., (2019), The vibration behaviour of hedgerow olive trees in response to mechanical harvesting with straddle harvester. *Biosystems Engineering*, Vol.184, pp.81-89.;
[37] Stropek Z., Gołacki K., (2013), The effect of drop height on bruising of selected apple varieties. *Postharvest Biology and Technology*, Vol.85, pp.167-172;
[38] Stropek Z., Gołacki K., (2020), Bruise susceptibility and energy dissipation analysis in pears under impact loading conditions. *Postharvest Biology and Technology*, Vol.163,111120;
[39] Tang Z.H., Shen C.J., Meng X.J., Jia S.X., Zhou Y., Zheng X., (2010), Development of 4ys-24 jujube harvester. *Xinjiang Agricultural Mechanization*, Issue 01, pp.30-32;
[40] Torregrosa A., Albert F., Aleixos N., Ortiz C., Blasco J., (2014), Analysis of the detachment of citrus fruits by vibration using artificial vision. *Biosystems Engineering*, Vol.119, pp.1-12;
[41] Torregrosa A., Ortí E., Martín B., Gil J., Ortiz C., (2009), Mechanical harvesting of oranges and mandarins in Spain. *Biosystems Engineering*, Vol.104, Issue 01, pp.18-24;
[42] Villibor G. P., Santos F. L., de Queiroz D. M., Khoury Junior J. K., Pinto F. d. A. d. C., (2019), Dynamic behaviour of coffee fruit-stem system using modeling of flexible bodies. *Computers and Electronics in Agriculture*, Vol.166,105009.;
[43] Wang D, Chen D, Wang S.M., Chen Z., Zhang F., (2017), Vibration harvesting mechanism analysis of plastic fruit trees based on finite element method. *Transactions of the Chinese Society of Agricultural Engineering*, Vol.33, Issue S1, pp.56-62;
[44] Wang J.P., Mei S., Xiao H.R., Zhao Y., Zhou H.P., (2018), Research on Mechanized Harvesting Methods of Lycium barbarum Fruit. *IFAC-PapersOnLine*, Vol.51, Issue 17, pp.223-226;
[45] Wang W., Lu H., Zhang S., Yang Z., (2019), Damage caused by multiple impacts of litchi fruits during vibration harvesting. *Computers and Electronics in Agriculture*, Vol.162, pp.732-738;
[46] Wang W., Zhang S., Fu H., Lu H., Yang Z., (2020), Evaluation of litchi impact damage degree and damage susceptibility. *Computers and Electronics in Agriculture*, Vol.173,105409;
[47] Wang W.Z., Yang Z., Lu H.Z., Fu H., (2018), Mechanical damage caused by fruit-to-fruit impact of litchis. *IFAC-PapersOnLine*, Vol.51, Issue 17, pp.532-535;
[48] Yang H.M., San J.L., Chen Y.F., Wang X.N., Niu C.H., Hou S.L., (2019), Influence of different vibration characteristic parameters on vibration response of apricot. Transactions of the Chinese Society of Agricultural Engineering, Vol.35, Issue 02, pp.10-16;
[49] Yang H.Y., (2013), *Design and experimental study on harvesting components of dwarf close planting jujube harvesting device*. Shihezi University/China;

[50] Zhou J., He L., Karkee M., Zhang Q., (2016), Analysis of shaking-induced cherry fruit motion and damage. *Biosystems Engineering*, Vol.144, pp.105-114;
[51] Zhou J., He L., Zhang Q., Karkee M., (2014), Effect of excitation position of a handheld shaker on fruit removal efficiency and damage in mechanical harvesting of sweet cherry. *Biosystems Engineering*, Vol.125, pp.36-44;
[52] Zhou J.F., He L., Karkee M., Zhang Q., (2016), Effect of catching surface and tilt angle on bruise damage of sweet cherry due to mechanical impact. *Computers and Electronics in Agriculture*, Vol.121, pp.280-289;
[53] Zulkifli N., Hashim N., Harith H. H., et al, (2020), Finite element modelling for fruit stress analysis - A review. *Trends in Food Science & Technology*, Vol.97, pp.29-37.

NAVIGATION, VALIDATION AND EVALUATION OF FOUR-WHEELED ROBOT FOR GREENHOUSE SPRAYING

/

پیمایش، اعتبارسنجی و ارزیابی ربات چهار چرخ برای سمپاشی گلخانه ای

Hossein Mosalanejad[1)], Saeid Minaei*[2)], Alimohammad Borghei[3)], Behfar Farzaneh[4)] [1]

[1)] Biosystems Engineering Department, Science and Research Branch, Islamic Azad University, Tehran / Iran

[2)] Biosystems Engineering Department, TarbiatModares University, Tehran / Iran

[3)] Biosystems Engineering Department, Science and Research Branch, Islamic Azad University, Tehran / Iran

[4)] Department of Agricultural Mechanization Engineering, Islamic Azad University, Eghlid / Iran

Tel:++982148292466 E-mail: minaee@modares.ac.ir

https://doi.org/10.35633/inmateh-63-17

Keywords: *Four-wheeled robot; Greenhouse sprayer; Infrared sensor; Ultrasonic sensor; Automatic spraying; Backpack sprayer*

ABSTRACT

This study investigates the potential of using a sprayer robot for the greenhouse with bell-pepper plants and compares its performance with the backpack sprayer. The infrared sensors were used to navigate the robot and the ultrasonic sensors were used to distinguish the beginning of each row for automatic spraying. Results showed that the robot's guidance was done well by the infrared sensor. It was capable for spraying plants on both sides of the greenhouse simultaneously with ultrasonic sensor. The sprayer robot had better spray quality and lower solution consumption and spraying time and spray loss than the backpack sprayer.

چکیده

این مطالعه، پتانسیل استفاده از ربات سمپاش برای گلخانه با گیاهان فلفل دلمه ای را بررسی کرده و عملکرد آن را با سمپاش پشتی مقایسه می کند.از حسگرهای فروسرخ برای جهت یابی ربات و از حسگرهای فراصوتی برای تشخیص ابتدای هر ردیف برای سمپاشی اتوماتیک استفاده شده است. نتایج نشان داد که هدایت ربات توسط حسگر فروسرخ به خوبی انجام شده است. این ربات قادر به پاشش همزمان گیاهان در دو طرف گلخانه با حسگر فراصوتی بود. ربات سمپاش نسبت به سمپاش پشتی از کیفیت پاشش بهتر و مصرف محلول، زمان پاشش و اتلاف کمتری برخوردار بود.

INTRODUCTION

Similar to other industries, agriculture has been affected by technological advances (*Ko et al., 2014*). In the late 20th century, precision agriculture showed increasing attention in the agricultural community (*Jafari Malekabadi et al., 2019; Cantelli et al., 2019*). Precision agriculture is a new concept that founded based on a series of technological breakthroughs such as GPS, humidity-soil fertility controlling sensors, remote sensing and GIS. It allows higher variability in agricultural products through comprehensive management in the sites of a project (*Bengochea-Guevara et al., 2016; Hernandez et al., 2016; Zaman et al., 2019*). Deficiencies such as lack of human workforce and replacing automated machines are the motivations for the introduction of robotic systems in agriculture and especially the greenhouse environment (*Sanz-Cortiella et al., 2011a, 2011b*).

In the modern period, each activity is described with its benefits and efficiency, so greenhouses produce better crops with higher quality (*Rincón et al., 2020*). The function of a greenhouse is the measurement and control of any factor to achieve its predetermined goals (*Roldan et al., 2015; Pahuja et al., 2013; Rodríguez et al., 2015; Zeng et al., 2012*). Some of the most fundamental applied sciences in the greenhouses are soil sciences, climate control and combination of other methods such as modern irrigation and nutrition supply techniques, carbon dioxide enrichment and pollination with bees (*Roldan et al., 2016; Sharma and Borse, 2016*). Studies show that considerable part of total investments in greenhouse units is consumed by the owner and employees (30% of the total cost or even more). Agricultural researchers have an agreement on such a conclusion that higher profit can be achieved by using higher efficiency of work or reducing the number of active workforces (*Sánchez-Hermosilla et al., 2013a*). The common benefits of such systems are more timeliness, higher accuracy and coordination and lower costs (*Sezen, 2003*). In the greenhouse, any

[1] *Hossein Mosalanejad, Ph. D Student; Saeid Minaei, Professor; Alimohammad Borghei, Professor; Behfar Farzaneh, Assistant Professor*

agricultural activity using automated systems needs more effort. Robots (rail and ground robots), sensors (cameras and laser scanners) and actuators (manipulation and grasping systems) are three main systems that are used widely in any modern greenhouse (*Sezen, 2003; Younse and Burks, 2007; Sánchez-Hermosilla et al., 2013a; Bengochea-Guevara et al., 2016; Hernandez et al., 2016; Moreno et al., 2016*).

Sammons et al. (2005) evaluated inductive sensors for the navigation unit of automatic spraying. They concluded that this sensor was able to track the underground metal pipes. In another study, a fuzzy logic algorithm was used to control functions in the greenhouse mini-robot (*Subramanian et al., 2005*). The distance and relative location of objects (metallic and non-metallic devices and plants) are measured using proximity sensors. Other types of sensors are useful for such purposes such as capacitive, optical and ultrasound. *Harik and Korsaeth (2018)* studied a combination of the hector simultaneous localization and mapping and an artificial potential field controller to estimate the robot's position and to perform autonomous navigation inside the greenhouse.

Sánchez-Hermosilla et al. (2013a) investigated the navigation of a robot using laser system. They reported that this system was very reliable, but required several lasers to be mounted in the proximity of corridors. *Kalantari et al. (2014)* used a robot to spray in greenhouses. They concluded that the uniformity of the spray was better. Mean droplet size at the centreline of the spray was much smaller than dose in the outer side of the full cone spray. The drop size by the nozzle was less than 60 μm which was suitable for insecticide or fungicide applications. *Cantelli et al. (2019)* used a robot for autonomous spraying in vineyards and greenhouses. Positions were measured integrating the measures of the encoders. The laser scanner and ultrasonic sensor were mounted in the upper-front part of the vehicle. They were used to detect static and dynamic obstacles.

Masoudi et al. (2012) evaluated the ability of ultrasonic sensors to produce guidance signals for greenhouse application robots. Results showed that the accuracy of the sensor was good for distances between 15 and 215 cm and angles between 0 and 30°. Sensors of flat surfaces and round surfaces had the maximum width of view 17.15 cm and 33.20 cm respectively. Also, from comparison with data from reference sensors, the maximum error and RMSE for orientation and position were 11.23°, 4.036° and 3 cm, 0.714 cm, respectively. *Osadcuks et al. (2014)* compared various sensors for application in mobile robotics in greenhouse environment. Ultrasound sensors were the most reliable for long-range obstacle detection in a greenhouse environment. Although the statistically significant influence of environmental conditions were observed, changes in maximum detection distances did not exceed 5 mm or 2.5% and there was no correlation with temperature and humidity. Also, short-range capacitive and inductive type sensors were not significantly affected by a greenhouse environment, however, the obstacle detection range of a capacitive decreased when moisture condensing occurred during temperature and humidity transients.

Although studies have been done on robot in the greenhouse, the study and evaluation of four-wheel robot have not reported yet in literatures for greenhouse spraying in Iran. The aim of this study was effective handling of human health challenges which somehow relates to working conditions in greenhouses. So, a four-wheel sprayer robot was designed for automatic spraying that had the ability of free movement between rows of plants. Navigation was evaluated based on acquired data from infrared sensors and the ultrasonic sensor was used to detect plants for spraying. Finally, the proposed sprayer robot was compared with traditional backpack sprayers. The effect of the speed (levels of 7, 14 and 21 m/min) on the spraying quality coefficient (Q_C) was investigated. Also, solution consumption, spray height, spraying time, and spray loss were calculated and compared in a greenhouse with bell pepper plants.

MATERIALS AND METHODS

1. Designing and Constructing the sprayer robot

Sprayer robot was designed and simulated using Autodesk inventor professional 2018 software (Fig. 1).

It was developed based on the following goals:

- Detection of the path drawn on the greenhouse floor by the infrared sensor.
- Detection of the plant by ultrasonic sensors installed on the sides of the robot.
- Send ultrasonic sensor signals to the control unit.
- Send command to sprayer unit operators by the control unit to start spraying operation.
- Stop spraying at the end of the crop row and follow the curved path at the end of the path, to enter the next row of greenhouses.
- Continue this operation until the end of the greenhouse.

So, the robot had three main parts including control and processing, drive and sprayer units. These parts were mounted on the chassis (Fig. 2).

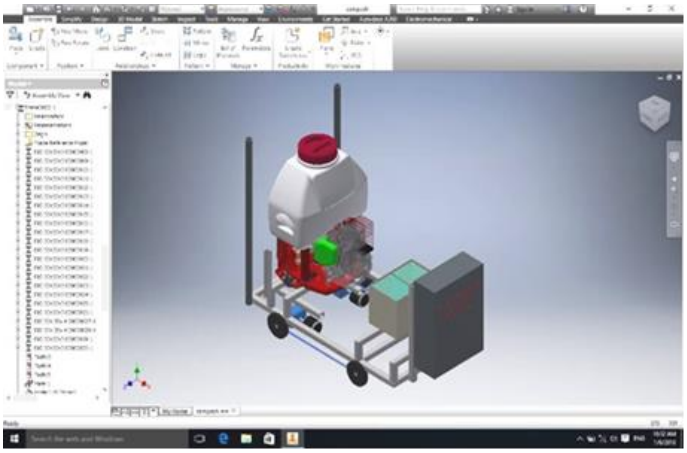

Fig.1 - The sprayer robot in the software environment

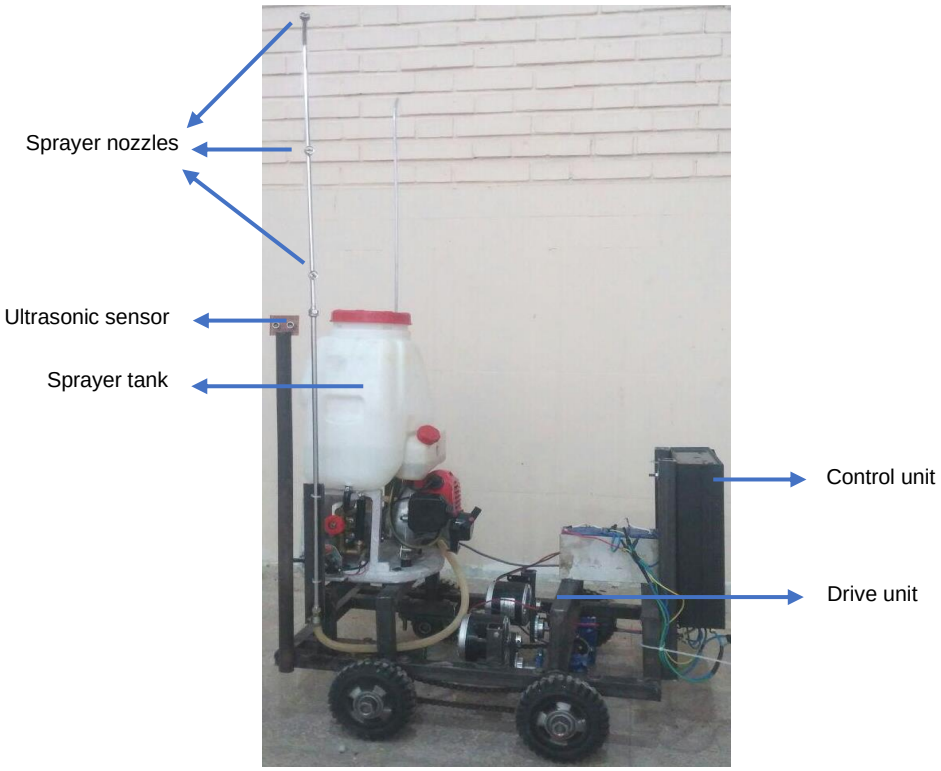

Fig. 2 - Different parts of the prototype robot

1.1 Control and processing unit

Fig. 3 and 4 show the control system implemented and various connections and units. The user interfaces had control over the running of the control unit (microcontroller) and were feedback data about the status of the robot. The control unit read the information and, after processing it, controlled the movements of the robot and the spraying system. The function of the microcontroller is any logical/calculation task that might be necessary for the spraying cycle. AVR microcontroller (ATmega-32 model) was used as the main control unit. Dynamic basic software was used as operational software. Microcontroller programming and circuit simulation were done in BASCOM-AVR 11 and PROTEUS 7 respectively.

The spraying system requires correct information as inputs, so the proper function of a robot (its controlling and spraying units) mostly depends on the efficiency of external sensors (Fig. 4). Therefore, a combination of infrared, ultrasonic and level sensors was installed. Another important subject was the effect of mechanical structural and other environmental factors, so analysis of advanced position was performed to find the best possible locations and encoder sensor was used. The LCD/Keypad module shows the user relevant

information on the status of the robot and allows the user to control the robot directly with ease. Further controlling operations were done through this module.

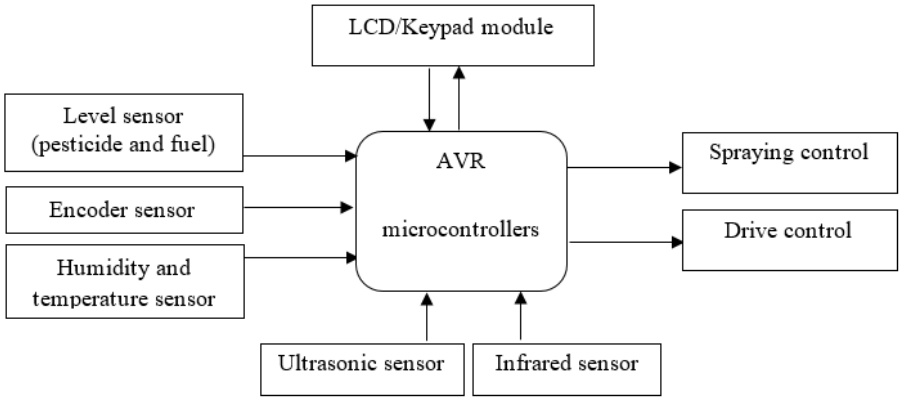

Fig. 3- Control system of the sprayer robot

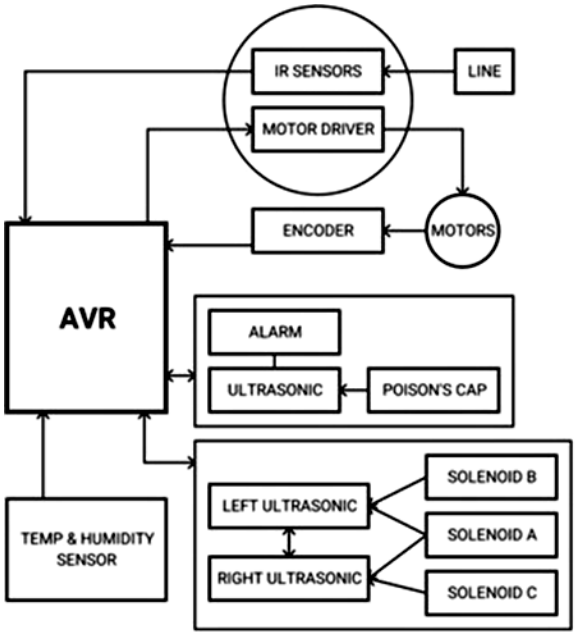

Fig. 4- Schematic of various connections and units

1.2 Drive unit

The robot was designed to be highly manoeuvrable in different directions. The cost was also considered as another factor. The drive unit consisted of a chassis, four wheels, a DC-type motor, a gearbox, and a belt and pulley. To select the engine, the moment of force for the wheel must be calculated to move the robot. So, the maximum weight of the robot, its centre of gravity and its distance from the wheels were calculated. Then, by considering the beam model with two simple supports and the concentrated forces applied to it, the free body diagram was drawn and the moment of force was calculated.

After the beginning of a movement, information about the location of the robot should be sent to the control unit, so the encoder sensor was used. Also, further adjustments were made by a user interface that controlled operational feedback. Lines in the greenhouse were marked to automatically guide the robot. The infrared sensor was used to navigate. It enabled the robot to track the lines between rows of plants.

1.3 Sprayer unit

The sprayer unit consisted of a 25-liter tank, a 1.7-liter/min centrifugal pump, a two-stroke engine (to operate the centrifugal pump), two vertical booms, three valves and three solenoids. Each boom had three nozzles. The distance of each nozzle was 25 cm from each other. The first nozzle had 90 cm high from the ground .

According to Fig. 5, the robot must perform the spraying operation according to its position in both one-way and two-way modes. The one-way spraying was related to the first and last rows of the greenhouse where

the cultivated plants were located on only one side of the robot. For this purpose, two solenoid control valves and ultrasonic sensors on the sides of the robot were used to determine the spraying state.

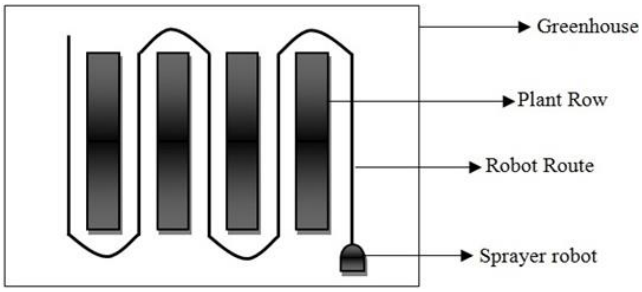

Fig. 5- The robot moving in the greenhouse

The SRF05 ultrasonic sensor with precision of 2 mm was used to detect the start and end of the plant row. An ultrasonic level sensor was used to control and measure the amount of solution in the tank. It alarmed the lack of solution as soon as the tank solution level reached a certain level. Also, this sensor measured the amount of solution consumed over a specified distance by measuring the height of the solution in the tank. Fig. 6 and 7 show the sprayer hydraulic circuit and schematic circuits of solenoids A, B and C, respectively.

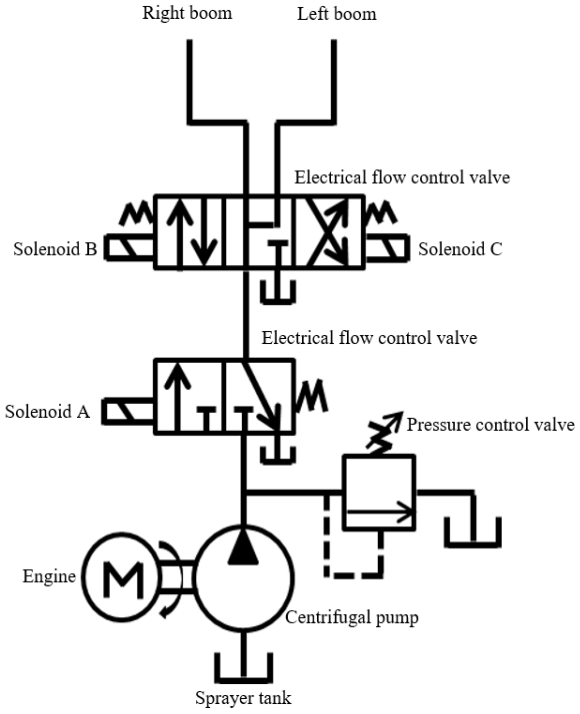

Fig. 6- Hydraulic circuit in sprayer unit

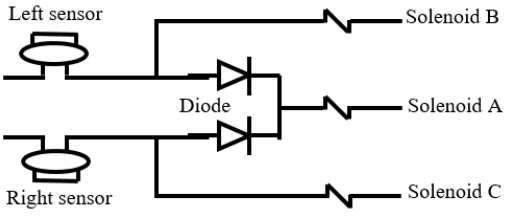

Fig. 7 - Schematic of the circuit of solenoids A, B and C

2. Evaluation of the sprayer robot

Sensors are not adjusted in the greenhouse environment, so in the first step, ultrasonic and infrared sensors were used in an initial experiment and calibrated by the experimental line follower robot (temperature=22^{0}C, humidity = 67%). Another problem was the movement of the robot in the correct direction. Therefore unloaded chassis was tested separately from the controlling unit, and the movement angle was measured.

The sprayer robot was evaluated in a greenhouse in Dehaghan city of Isfahan province, with the specifications listed in Table 1.

Table 1

Characteristics of the greenhouse used for evaluating the sprayer robot

Product type	Area (m^2)	Corridor Length (m)	Width of corridors (cm)	Plant height (cm)	Temperature (°C)	Humidity (%)
Bell pepper	4500	40	90	250	22	67

Experiments were conducted to examine the effects of the speed (levels of 7, 14 and 21 m/min) on the spraying quality coefficient (Q_C) and also assessed solution consumption, spray height, spraying time, and spray loss in comparison with the conventional sprayer (the back sprayer/ TU26 /China). The experiments were performed in a completely randomized design with three replications. The data were analysed by SPSS and Excel software.

2.1 The optimal speed of the sprayer robot

To determine the optimal speed of the robot, spraying operations were performed in a 10 m path at three-speed levels of 7, 14 and 21 m/min in three replications. Then, the spraying quality coefficient (Q_C) was measured and evaluated using water-sensitive papers. The optimal speed was selected based on the best spraying quality.

Spraying quality was evaluated based on the standards of Institute of Standards and Industrial Research of Iran (*Anon., 2008*). The sensitive papers (dimensions: 3 x 7 cm) were placed at a distance of 50 and 25 cm in the direction of the sprayer movement and the plant height, respectively. Q_C was calculated based on *Jafari Malekabadi et al., (2016)*. ACDSee Pro 3 software was used to analyse the papers.

2.2 Spray Height

To evaluate spray height, sensitive papers placed on the plant were assessed. The papers of height 175 to 250 cm were collected and numbered. At each height, 10 papers were randomly selected and those that had been discoloured as a result of the droplets sitting were distinguished.

2.3 Spraying Time

A digital timer was set to measure time every 10 meters.

2.4 Spray Loss

The spray loss causes pollution of soil. The sensitive papers were placed under every plant according to Fig. 8. The papers were collected and the number and diameter of the droplets were measured in 1 cm^2. Then the area of the droplets was calculated. ACDSee Pro 3 software was used to analyse the papers.

Fig. 8 - Position of sensitive cards to measure spray loss

2.5 Solution Consumption

After spraying, the amount of remained volume was measured, and then the sprayer tank was refilled for re-spraying. The solution consumption was also measured using the level sensor.

RESULTS

1. Evaluating the sprayer robot and determining the optimal speed

Investigation of ultrasonic sensor showed that the sprayer robot was capable for spraying plants on both sides of the greenhouse simultaneously, similar to the results obtained by *Cantelli et al. (2019)* and *Osadcuks et al. (2014)*. Evaluation of the robot's movement in the straight path showed that the 4 m displacement had a rightward deviation of 2.5 cm. Wheels were the main elements of movement, so front wheels were adjusted again. The new system had a deviation of 1.5 cm in the 4 meters and the sensors repeatedly corrected this deviation and did not increase cumulatively as the displacement continued. Therefore, the robot's guidance was done well by the infrared sensor.

Unlike some other research (for example *Sánchez-Hermosilla et al., 2013a*), this method did not require the installation of several sensors in the proximity of the corridor, especially at the end of the corridor, and accuracy was better than studies of *Younse and Burks, (2007)*. On the other hand, the sprayer robot used a simple system in this study. In contrast, in some studies, such as *Zhang et al. (2019)*, used a complex and expensive system.

The optimal speed was obtained based on the spraying quality coefficient, Q_C. The closer the coefficient is to 1, the better the quality. Fig. 9 shows the results of the evaluation of different speeds. The effect of speed was significant at 99% confidence level on Q_C. The speed of 14 m/min had better Q_C (2.56) and was the optimal speed. This result was similar to the results obtained by *Sammons et al. (2005)*.

At low speed, the Q_C was large and the quality decreased, because the leaves spray more time and the number of sprayed drops to the plant increases. So, the droplets cohere together and create a larger diameter. Also, when the speed of the robot exceeded the optimum value, the quality decreased. Because, the number of sprayed droplets to the plant decreases and, in the computation relation of the quality, with the decrease of the denominator of the fraction (the numeric median diameter), the Q_C becomes larger. Another reason could be that as the speed increased, the vibration rate of the sprayer boom increased.

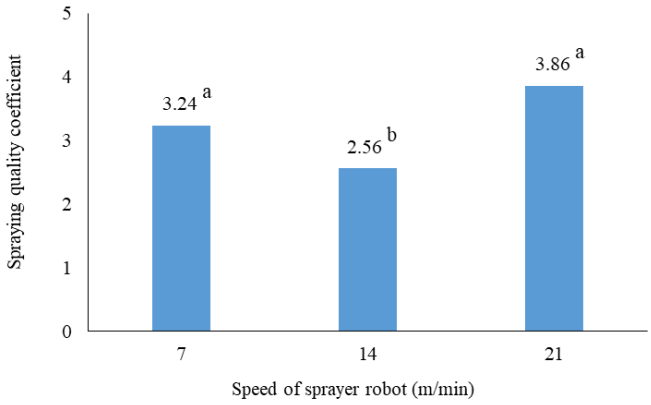

Fig. 9 - Spraying quality coefficient for different speeds
(The means with the same letter were not significant at 1% level)

2. Comparison of a robot with a conventional sprayer

In this section, experiments were performed at a robot speed of 14 m/min.

2.1 Spraying quality coefficient (Q_C)

Fig. 10 shows samples of the water sensitive papers for both types of sprayer. The results of the analysis of the papers showed that there was significant difference between the sprayers at 1% significance level on Q_C. The means of Q_C were 2.56 and 4.30 for sprayer robot and back sprayer, respectively (Table 2).

The nozzles of both types of sprayers were the same. The reason for the uniformity and better quality of the sprayer robot was: 1) the uniformity of movement and the constant speed of the robot, 2) unchanging the distance and displacement of the boom and its nozzles in the robot. In contrast, in the back sprayer, the operator speed was not the same and the boom distance from the plant varied. This result was similar to the results obtained by *Sammons et al. (2005)* and *Kalantari et al. (2014)*.

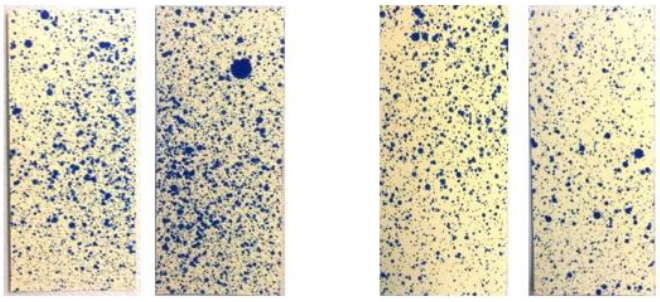

a b

Fig. 10 - The water sensitive papers: a) back sprayer and b) sprayer robot

Table 2

Mean comparison of spray quality coefficient, solution consumption, spray height (number of wetted papers), spraying time and spray loss (area of droplets,) for sprayers

Parameters			Sprayer robot	Back sprayer
Spray quality coefficient			2.56 [b]	4.30 [a]
Solution consumption [litres]			5.26 [a]	4.06 [b]
Spray height [cm]	Height [cm]	175	10 [a]	9.67 [a]
		200	9.67 [a]	9.67 [a]
		225	6.67 [b]	9.67 [a]
		250	6 [b]	9.34 [a]
Spraying time [s]			22.66 [b]	68.26 [a]
Spray loss [mm^2]			5.57 [b]	7.31 [a]

Note: The means with the same letter were not significant.

2.2 Solution Consumption

The mean comparison of solution consumption demonstrated that the sprayer robot used approximately 30% less solution than the back sprayer, in a 10 m path. Some of the factors that caused to higher consumption by the back sprayer were the following: irregular and non-uniform movement of the operator, lack of skill and inaccuracies in spraying two-way modes, long working time and fatigue.

2.3 Spray Height

After spraying, the sensitive papers were collected at different heights (175, 200, 225 and 250 cm). The number of wetted papers was counted and their averages were compared. According to Table 2, there was no significant difference between the sprayers at the height of 175 and 200 cm. Therefore, the treatments were able to spray up to 2 m above ground level.

But there was a significant difference between the two sprayers at height 225 and 250 cm. Thus, the robot did not perform well in terms of spray height more than 2 m compared to the back sprayer. The reasons were the shortness of the sprayer robot boom and the low pressure of the sprayer pump. This problem will be resolved in further research and development of the robot for other activities and the results will be presented in the following articles.

2.4 Spraying Time

Analysis of spraying time results indicated that there was statistically significant difference at 1% level between different treatments. Comparison of means showed that the spraying time by the back sprayer was three times more than that of the sprayer robot (Table 2). So, the robot's performance was better than the conventional sprayer in terms of spraying time. The reasons were 1) the possibility of two-way spraying by the robot, 2) more robot nozzles than the back sprayer, and 3) operator fatigue and rest for the back sprayer.

2.5 Spray Loss

The area of droplets on the sensitive papers placed on the ground was calculated and there was significant difference between the sprayers (1% level). The means of spray loss area were obtained 5.57 and 7.31 mm for sprayer robot and back sprayer, respectively (Table 2). Therefore, the spray loss of the sprayer robot was less than that of the back sprayer and it had less soil contamination. On the other hand, the robot had better spraying quality coefficient Q_C. Thus, these two parameters had an inverse relationship. *Li et al. (2009)* and *Kalantari et al. (2014)* reported that the use of the robot would improve the uniformity of spraying and reduce drift and spray loss on the ground. The results of *Sánchez-Hermosilla et al. (2013b)* show that spraying at the high pressure (2000 kPa), the average deposit was between 22.5% and 34.6% less than at the lower pressures (1000 or 1500 kPa).

CONCLUSIONS

The main aim of this study was to investigate the potential of a four-wheel sprayer robot for spraying greenhouse with maximum efficiency, lower costs and simpler utilization. Navigation was evaluated based on acquired data from infrared sensors and the ultrasonic sensor was used to detect plants for spraying. Also, the proposed sprayer robot was compared with traditional backpack sprayers. The effect of the speed (levels of 7, 14 and 21 m/min) on the spraying quality coefficient (Q_C) was investigated. Solution consumption, spray height, spraying time, and spray loss were calculated and compared in a greenhouse with bell pepper plants in Iran. Although more study is needed, the results were promising and showed some benefits that can be achieved with robotic automation. From the obtained results, it can be concluded that:

- Sprayer robot had a rightward deviation of 1.5 cm in the 4 m displacement. Therefore, the robot's guidance was done well by the infrared sensor.
- Sprayer robot was capable for spraying plants on both sides of the greenhouse simultaneously with ultrasonic sensor, and its movement was uniform.
- The optimal speed was 14 m/min that had better spraying quality coefficient Q_C.
- The sprayer robot had better spraying quality than the back sprayer, while its solution consumption (30%) and spraying time (three times) were lower.
- The spray loss of the sprayer robot was less than that of the back sprayer and it had less soil contamination.
- The robot did not perform well in terms of spray height more than 2 m compared to the back sprayer. This problem will be resolved in further research.
- As a future work, the development of the sprayer robot can be using a hydraulic robot system to adjust the amount of spraying, toxin dose and the spray height. The camera or/and sensor can also be used to detect pests and spray only areas of the greenhouse that was infected by the pest.

REFERENCES

[1] Anon, (2008). *Field measurement of spray distribution in tree and bush crops*. Institute of Standards and Industrial Research of Iran. No. 10347.www.isiri.org.

[2] Bengochea-Guevara, J.M., Conesa-Muñoz, J., Andújar, D., Ribeiro, A. (2016). Merge fuzzy visual servo and GPS-based planning to obtain a proper navigation behaviour for a small crop-inspection robot. *Sensors*.16 (3), 276.Doi: 10.3390/s16030276.

[3] Cantelli, L., Bonaccorso, F., Longo, D., Melita, C.D., Schillaci, G., Muscato, G. (2019). A small versatile electrical robot for autonomous spraying in agriculture. *Agri Engineering*. 1: 391-402. Doi: 10.3390/agriengineering1030029.

[4] Harik, E.H.C., Korsaeth, A. (2018). Combining hector SLAM and artificial potential field for autonomous navigation inside a greenhouse. *Robotics*, 7 (22).

[5] Hernandez, A.C., Gomez, C., Crespo, J., Barber, R. (2016). Object detection applied to indoor environments for mobile robot navigation. *Sensors*. 16 (1180).

[6] JafariMalekabadi, A., Khojastehpour, M. and Emadi, B. (2019). Disparity map computation of tree using stereo vision system and effects of canopy shapes and foliage density. *Computers and Electronics in Agriculture*. 156: 627-644. DOI: 10.1016/j.compag.2018.12.022.

[7] JafariMalekabadi, A., Sadeghi, M. and ZakiDizaji, H. (2016). Comparing sprayer quality equipped with a telescopic boom with conventional sprayers in orchards in Iran. *Journal of Agricultural Science and Technology*. 18 (3): 585-599.

[8] Kalantari, D., Shayanmehr, M., Refigh, A. (2014). Evaluation of the spray generated by a greenhouse spraying robot Agricultural Engineering International: *CIGR Journal*. 16 (1): 55-60.

[9] Ko, M.H., Ryuh, B., Kim, K.S., Suprem, A., Mahalik, N. 2014. Autonomous greenhouse mobile robot driving strategies from system integration perspective: review and application, *IEEE.* 1705-1716. DOI: 10.1109/TMECH.2014.2350433.

[10] Li, V., Xia, Ch., Lee, J. (2009). Vision-based pest detection and automatic spray of greenhouse plant. *International conference on (ISIE)*, Korea. Doi:10.1109/ISIE.2009.5218251.

[11] Masoudi, H., Alimardani, R., Omid, M., Mohtasebi, S.S., Noguchi, N. (2012). Determination of ultrasonic sensor ability for use as guidance sensors of mobile robots. *Sensors and Materials*, 24 (3): 115–126.

[12] Moreno, J., Clotet, E., Lupiañez, R., Tresanchez, M., Martínez, D., Pallejà, T., Casanovas, J., & Palacín, J. (2016). Design, implementation, and validation of the three-wheel holonomic motion system of the assistant, personal robot. *Sensors*. 16(10): 1658. DOI: 10.3390/s16101658.

[13] Osadcuks, V., Pecka, A., Lojans, A., Kakitis, A. (2014). Experimental research of proximity sensors for application in mobile robotics in greenhouse environment. *Agronomy Research*, 12(3), 955–966.

[14] Pahuja, R., Verma, H.K., Uddin, M. 2013. Wireless sensor network for greenhouse climate control, *IEEE*, 12 (2). DOI: 10.1109/MPRV.2013.26

[15] Rincón, V.J., Grella, M., Marucco, P., Alcatrão, L., Sánchez-Hermosilla, J., Balsari, P. (2020). Spray performance assessment of a remote-controlled vehicle prototype for pesticide application in greenhouse tomato crops, *Science of the Total Environment*. Doi: 10.1016/j.scitotenv.2020.138509.

[16] Rodríguez, F., Berenguel, M., Guzman, J.L., Ramírez-Arias, A. (2015). *Modeling and control of greenhouse crop growth*. Springer, London, UK.

[17] Roldan, J.J., Garcia-aunon, P., Garzon, M., Leon, J., Cerro, J., Barrientos, A. (2016). Heterogeneous multi-robot system for mapping environmental variables of greenhouses. *Sensors*. 16 (7). Doi: 10.3390/s16071018.

[18] Roldan, J.J., Joossen, G., Sanz, D., Cerro, J., Barrientos, A. (2015). Mini-UAE based sensory system for measuring environmental variables in greenhouses. *Sensors*. 15, 3334-3350.

[19] Sammons, P.J., Tomonari, F. and Bulgin, A. (2005). Autonomous pesticide spraying robot for use in a greenhouse. *Australian conference on robotics and automation*, pp:1-9, IBSN 0-9587583-7-9, December, Sydney, Australia.

[20] Sánchez-Hermosilla, J., González, R., Rodríguez, F., Donaire, J.G. (2013a). Mechatronic description of a laser auto-guided vehicle for greenhouse operations. *Sensors*. 13, 769-784.

[21] Sánchez-Hermosilla, J., Paez, J., Rincon, V.J., Carvajal, F., (2013b). Evaluation of the effect of spray pressure in hand-held sprayers in a greenhouse tomato crop. *Crop Protection*. 54, 121-125. Doi.org/10.1016/j.cropro.2013.08.006

[22] Sanz-Cortiella, R., Llorens-Calveras, J., Escolà, A., Arnó-Satorra, J., Ribes-Dasi, M., Masip-Vilalta, J., Camp, F., Gràcia-Aguilá, F., Solanelles-Batlle, F., Planas-DeMart, S., Pallejà-Cabré, T., Palacin-Roca, J., Gregorio-Lopez, E., Del-Moral-Martínez, I., Rosell-Polo, JR. (2011a). Innovative lidar 3D dynamic measurement system to estimate fruit-tree leaf area. *Sensors*. 11, 5769–5791.

[23] Sanz-Cortiella, R., Llorens-Calveras, J., Rosell-Polo, JR., Gregorio-Lopez, E., Palacin-Roca, J. (2011b). Characterisation of the LMS200 laser beam under the influence of blockage surfaces. Influence on 3D scanning of tree orchards. *Sensors*. 11(3):2751–2772. doi: 10.3390/s110302751.

[24] Sezen, B. (2003). Modeling automated guided vehicle systems in material handling. Dogus University Journal. 4(2), 207-216.

[25] Sharma, S., Borse, R. (2016). Automatic agriculture spraying robot with smart decision making. *Intelligent Systems Technologies and Applications*. DOI: 10.1007/978-3-319-47952 1_60.

[26] Subramanian, V., Burks, T.F., Singh, S. (2005). Autonomous greenhouse sprayer using machine vision and radar for steering control. *Applied engineering in agriculture*. 21, 935-943.

[27] Younse, P. J., Burks, T. F. (2007). Greenhouse robot navigation using KLT feature tracking for visual odometry. *Agricultural engineering international: the CIGR Ejournal*. Manuscript ATOE 07 015. Vol. IX.

[28] Zaman, S., Comba, L., Biglia, A., RicaudaAimonino, D., Barge, P., Gay, P., (2019). Cost-effective visual odometry system for vehicle motion control in agricultural environments. *Computers and Electronics in Agriculture*. 162, 82-94. Doi.org/10.1016/j.compag.2019.03.037

[29] Zeng, S., Hu, H., Xu, L., Li, G. (2012). Nonlinear adaptive PID control for greenhouse environment based on RBF network. *Sensors*. 12, 5328-5348.

[30] Zhang, T., Zhou, W., Meng, F., Li, Z. (2019). Efficiency analysis and improvement of an intelligent transportation system for the application in greenhouse. *Electronics*. 8, 946. Doi: 10.3390/electronics8090946.

DESIGN AND EXPERIMENT OF SEED AGITATOR FOR VERTICAL DISK SEED METERING DEVICE
/
垂直圆盘排种器搅种装置的设计与试验

Chen Yulong[1,2], Zhang Meng [1], Liu Zeqi [1], Lan Yubin [1,2], Yi Lili [1,2], Ji Pengqiang [3], Yin Xiang [*1,2] [1]
[1] School of Agricultural Engineering and Food Science, Shandong University of Technology, Zibo 255000, China;
[2] Shandong Provincial Collaborative Innovation Centre of Dry-farming Intelligent Agricultural Equipment, Zibo, China;
[3] Shandong Agricultural Machinery Research Institute, Jinan 255000, China 250000, China
Tel: +86 18369916558; E-mail: 666513@163.com
DOI: https://doi.org/10.35633/inmateh-63-18

Keywords: *seed metering device, agitator, discrete element method, seed filling force*

ABSTRACT
In order to improve the seed filling performance of mechanical hole type seed metering device with high speed, a vertical disc metering device was designed with seed agitator to improve the seed filling probability. Discrete element simulation method and physical prototype bench tests were used to simulate and analyse the seed metering process. The structure parameters of the seed agitators were optimized by the quadratic orthogonal rotation central composite design test. The results showed that: 1) the addition of seed agitator had a significant influence on the MIS (miss index), among which the concave type had the lowest MIS, and it was the highest without agitator; 2) for concave type agitator, the optimal value of depth and angle were 3.1 mm and 60.5°, respectively; 3) the physical prototype tests showed that the QFI (quality of feed index) was more than 95% under the speed of 2-10 km/h, and the MIS was less than 1%, which meets the requirements of precision sowing.

摘要
为了提高机械式排种器的高速作业性能，设计了一种垂直圆盘排种器，通过搅种装置提高种子填充率。采用离散元仿真和台架试验对排种过程进行仿真和分析。采用二次正交旋转中心组合设计试验对搅种装置的结构参数进行优化分析。结果表明：1）搅种装置对漏播指数有显著影响，其中凹式搅种槽的漏播率最低，没有搅种槽时漏播率最高；2）凹式搅种槽的最佳深度和倾角分别为 3.1mm 和 60.5°；3）台架试验表明，在 2～10km/h 转速下，排种器的合格率大于 95%，漏播率小于 1%，满足精量播种的要求。

INTRODUCTION

Precision seeding is one of the most important research branch of smart agriculture. Seed metering device is the core mechanism of the planter (*Yang et al., 2016*). Mechanical metering device was the firstly developed and also the most popular precision metering device in the past decades (*Liu et al., 2015; Vianna, Reis, & Machado, 2014; Wang et al., 2017*). Compared with pneumatic seed metering devices, mechanical seed metering devices still occupies an important proportion in the field of sowing at home and abroad because of its simple structure, low cost and convenient operation (*Singh, Singh, & Saraswat, 2007*). But the mechanical seed metering device cannot complete the filling operation smoothly because of its poor filling performance under high-speed.

To improve the seed filling performance of the metering device under high-speed conditions, some scholars have carried out a lot of research work. Researchers designed linear and guided stirring teeth on the metering plate to make the seeds flip to improve the seed fluidity and to reduce the probability of missing filling (*Zhang et al., 2014*). A kind of convex table seed metering disk was designed to support the seeds while stirring the seed group, which can assist to fill seed and to improve the high-speed operation performance of seed metering device (*Ding et al., 2018*). Aiming at the horizontal disc wheat seed metering device, a cone surface diversion scheme was proposed. Influence of guide strip type, number of holes, cone speed and cone angle on seed filling performance was studied.

[1] *Yulong Chen, Lecture Ph.D. Eng.; Meng Zhang, M.S. Stud. Eng.; Zeqi Liu, M.S. Stud. Eng.; Yubin Lan, Prof. Ph.D. Eng.; Lili Yi, As. Ph.D. Eng.; Pengqiang Ji, Ph.D. Eng.; Xiang Yin, As. Ph.D. Eng.*

The results showed that the guide seed metering device was better than the original seed metering device in seed metering performance and crushing rate (*Liu et al., 2018*). It was found that the internal friction force between seeds would be reduced by stirring the seed group, thus, to improve the seed filling affection (*Shi et al., 2019*). A self-disturbance inner filling corn precision metering device was designed (*Du et al., 2019*), in which the involute type stirring strip was added on the inner surface of the inner filling metering device to improve the kinetic energy of the seed group. The optimized stirring strip can effectively improve the seed metering performance.

The literature review results show that reasonable disturbance to the seed group can effectively improve the seed filling performance. A lateral filling device of vertical disc was designed to improve the seed filling performance while the stirring groove was designed to stir the seeds. Theoretical analysis, key parameters optimization and simulations of the seed filling and agitator of the seed metering device were carried out. After that the theoretical results were verified by bench tests, which provides a useful exploration for the high-speed adaptive design and development of mechanical precision seed metering device.

MATERIALS AND METHODS

Vertical disc metering device

The vertical disc metering device was composed of shell, flexible unit, metering plate, flange, bearing, base, shaft and other parts (Fig. 1). The outer ring of the metering plate was evenly distributed with multiple seed taking holes while the inner side of the seed taking hole was designed with a seed agitator.

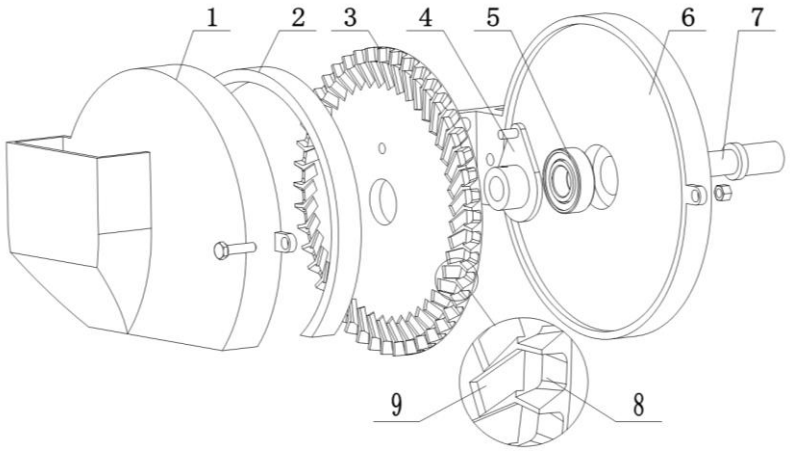

1. Shell; 2. Flexible seed cleaning part; 3. Disk; 4. Flange; 5. Bearing; 6. Base; 7. Shaft; 8. Hole; 9. Seed agitator

Fig. 1 - Structure diagram of seed metering device

During operation, seeds will be sent to the seed chamber surrounded by the disk and the shell through the seed inlet on the shell. The disk makes a circular movement under the drive of the main shaft to complete the seed metering operation. The working process can be divided into four stages: seed filling, seed cleaning, seed transportation and seeding. When the hole enters the seed group, the filling process will be started by. The seeds will be sent to the seed hole by the lateral component of the internal force of the seed group. When the seed hole overlaps with the flexible unit, the flexible unit starts to clean seeds until only one seed stayed in the reasonably designed hole. The seed hole and the seed in it continue to move under the flexible unit. At this time, the flexible unit plays a role to maintain the seed preventing the seed to separate from the hole, and the seed is transported to the seed dropping area. When the hole leaves the flexible unit, it starts the seed dropping process, and the seeds are separated from the hole under the action of gravity and centrifugal force.

A number of seed taking holes were evenly designed on the edge of the seed disk.

According to the design experience (*Liu et al, 2015*), the radius of the seed hole of the seed metering device was set as follows:

$$d = l_{max} + (1 \sim 1.5) \text{ [mm]} \tag{1}$$

where l_{max} is the maximum size of seed.

Here, the radius of disk was set as 100 mm. Forty holes were drilled on each disk with radius of 4mm.

The relationship between the rotation speed of disk and the forward speed of planter was shown as follows:

$$n = \frac{v}{60k \cdot s} \text{ [r/min]} \quad (2)$$

where:

n is the speed of disk, [r/min];

v is the forward speed of planter, [m/s];

k is the number of seed holes on the disk;

s is the plant spacing of sowing and the plant spacing of soybean is designed as 0.05m.

Seeds accumulated under the action of gravity in the seed chamber and it was easily to form a nearly linear force chain at the bottom of the seed group. The force chain was linked to each other and generated arching. This reduces the activity of the seed group and easily leads to miss filling (*Ding et al., 2018*).

To activate the seed group, an agitator was designed on the inner side of the hole in the disk to break the force chain of the seed group. At the same time, the agitator was used to guide the seeds above the hole to the direction of the hole, so as to increase the probability of seed filling.

Two kinds of seed agitator were designed (Fig. 2). The first was concave type, which was lower than the inner surface of disk. The second was convex type, which was higher than the inner surface of disk. The number of two kinds of seed agitator were the same as the number of seed holes. The position was one-to-one corresponding to the seed taking hole. The preset length l_1 of the seed stirring structure was 20 mm, the depth or height h was 2 mm, and the inclination angle β was 60°.

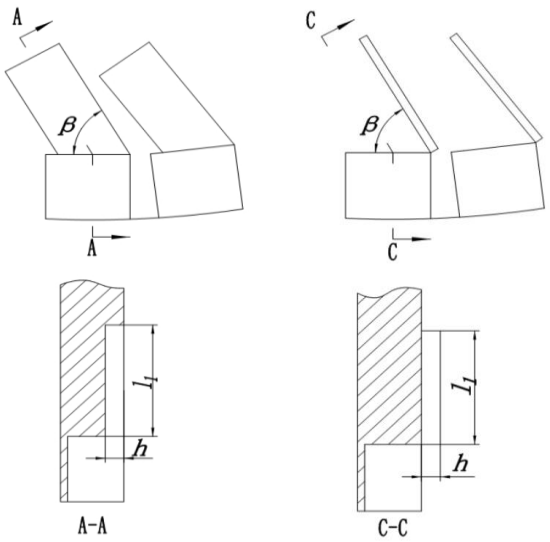

a. Concave type *b. Convex type*

Fig. 2 - Schematic diagrams of concave and convex agitators

Discrete element simulation design

Seed is a typical discrete material. Discrete element method is widely used in the research of seed metering device (*Khatchatourian, Binelo, & Lima, 2014; Yu et al., 2014*).

EDEM is a mature commercial discrete element simulation software (*Wang et al., 2015*) and version 11.0 of EDEM was used for virtual simulation test in this paper.

During the simulation, the seed metering device was simplified by removing the shaft and flexible seed cleaning part, and only the disk and shell were remained. The disk and shell were made of PMMA (polymethyl methacrylate), a transparent material.

Soybean used in this paper was Jiyu202 (Table 1), which was widely planted in Northeast the major soybean production region of China.

Table 1

Physical properties of soybean

Physical property	Mean	Standard error
L [mm]	7.21	0.32
W [mm]	6.11	0.31
T [mm]	6.32	0.44
D [mm]	6.52	
Φ [%]	91.88	
Thousand seed mass (g)	180.55	0.21

Note: L average length; W average width; T average Thickness; D means of geometrical diameter and calculated as $D=(LWT)^{1/3}$ respectively. ϕ means of sphericity and calculated as $\phi=\frac{(LWT)^{1/3}}{L}\times 100$.

The discrete element simulation model of soybean seed consisted of three spherical particles with a diameter of 6.0 mm (Fig. 3). According to the measured values of triaxial size of seeds, the length, width and thickness were set to 7.2 mm, 6.1 mm and 6.3 mm, respectively.

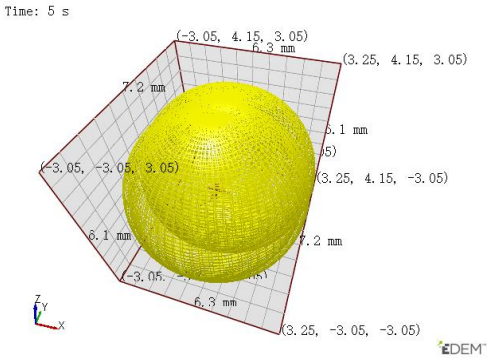

Fig. 3 - Discrete element simulation model of soybean seed

Since there was no adhesion on the surface of soybean seeds, the Hertz-Mindlin non-sliding contact model was adopted. The global parameters used in the simulation were obtained by reference (*Li et al., 2013; Zhang et al., 2017*) (Table 2).

Table 2

Parameters used in simulation

Property	Soybean	PMMA	Property	Soybean-Soybean	Soybean-PMMA
Poisson's ratio	0.4	0.33	Collision recovery coefficient	0.6	0.5
Shear modulus [Pa]	1.1×10^7	8×10^7	Static friction coefficient	0.5	0.3
Density [kg/m^3]	1053	1190	Rolling friction coefficient	0.01	0.09

Through the simulation test, the better agitator was selected, and the simulation optimization design was carried out on the depth or height and inclination angle of the agitator. The simulation test adopts two factors and five levels orthogonal rotation combination central composite design (Table 3) (*Yazgi, & Degirmencioglu, 2007*). To meet the requirements of high-speed operation, the tests were carried out when the forward speed was 10 km/h.

Table 3

Factors and codes of orthogonal rotation combination test

Code	Factors	
	***H* [mm]**	***B* [°]**
-1.414	1.6	45.9
-1	2	50
0	3	60
1	4	70
1.414	4.4	74.1

Prototype experiment

The simulation test results were verified by the indoor test bench (*Karayel et al, 2006; Zhao et al, 2010*〉. The physical prototype seed metering performance test was carried out on JPS-12 seed metering device performance test system (Fig. 4).

The test system is composed of seed metering device, conveyor belt, industrial camera, fuel injection device, computer, electronic control system and two frequency modulation motors.

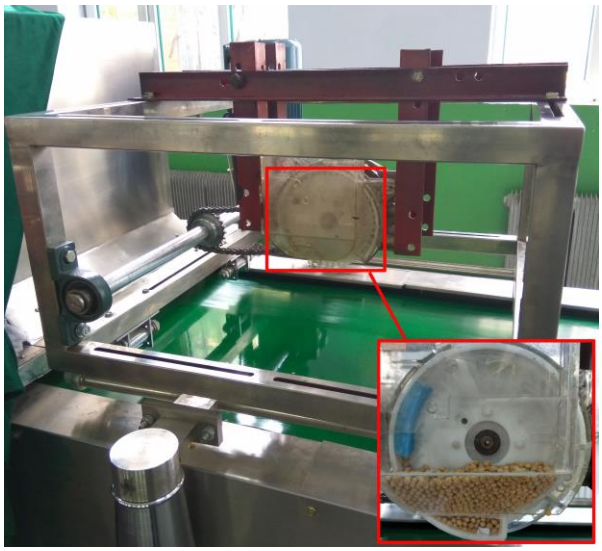

Fig. 4 - Physical prototype

Evaluating indicator

According to GB / T 6973-2005 test methods for single seed (precision) planter, 250 seeds were collected for statistics in each group of experiments, and the test was repeated for 3 times, and the seed metering performance evaluation indexes were MUL (multiple index), MIS and QFI (*Mao et al, 2015; Zhang et al, 2015*).

$$MUL = N_1 / N \times 100\% \tag{3}$$

$$MIS = N_2 / N \times 100\% \tag{4}$$

$$QFI = (1 - MIS - MUL) \times 100\% \tag{5}$$

where:

N_1 is the number of seed holes containing multiple seeds in the simulation test, and the number of seeds whose distance between adjacent seeds is less than 0.5 times the theoretical spacing in physical test.

N_2 is the number of seed taking holes that are not filled in the simulation test, and the number of seeds whose distance between adjacent seeds is greater than 1.5 times of the theoretical spacing in the physical test.

N is the total number of seed holes recorded in the simulation test, and the total number of seeds in the physical test.

RESULTS AND ANALYSIS

Optimization test of seed agitator device

The simulation experiments were carried out under three conditions of concave type agitator, convex type agitator, and without agitator. The filling conditions were recorded. Since the leakage of filling was the biggest impact on the sowing effect, this paper mainly studies the MIS (Fig. 5a).

Under three different conditions, the MIS increases significantly with the increase of rotating speed. When the speed was 16.7 r/min, the difference of the *MIS* under the three kinds of agitator was not significant. With the increase of the speed, the MIS of without agitator increases significantly at the speed of 16.7 and 33.3 r/min, which was significantly higher than that of the concave and convex type.

When the speed reached 66.7 r/min, the *MIS* of convex type increased significantly, and it was significantly higher than that of concave type.

To further analyse the influence of the seed agitator on the seed movement, the seed velocity near the agitator was recorded (Fig. 5b).

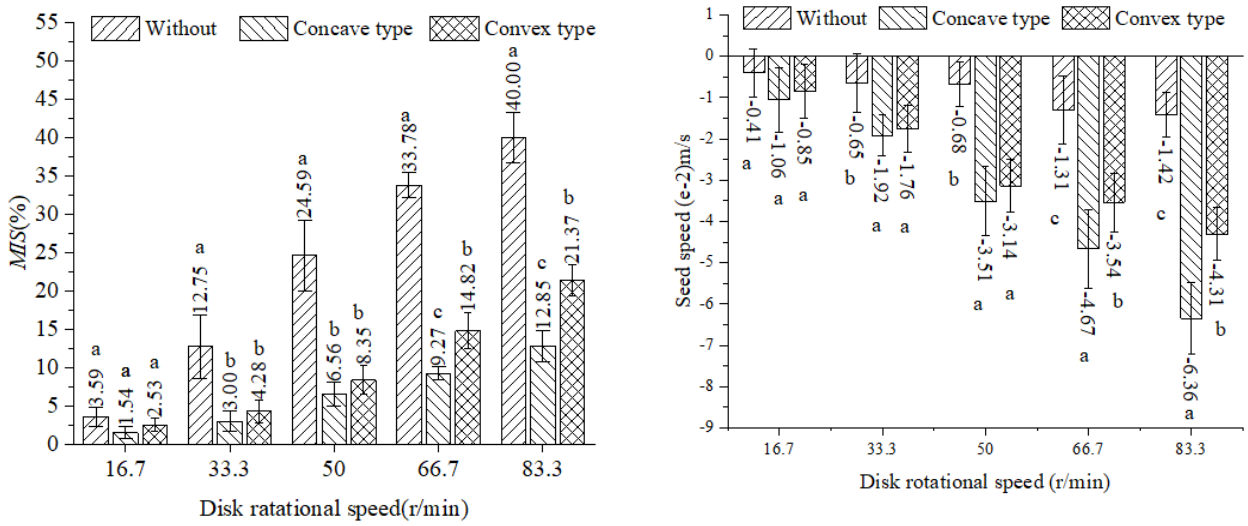

a) The influence of agitators on MIS

b) The influence of agitators on seed speed

Fig. 5 - The influence of agitators on *MIS* and seed speed

Note: At the same speed, different lowercases indicate that agitators have significant influence on MIS and seed speed ($p<0.05$).

It can be concluded that the seed stirring mechanism has a significant inhibitory effect on the *MIS*. With the increase of rotating speed, the decreasing trend was more and more significant. The concave type agitator has little difference with the convex seed stirring mechanism at low speed. With the increase of speed, the advantage of concave seed filling was more significant.

Therefore, the concave type was selected as the seed stirring mechanism, and its structure was further optimized.

The depth and angle of the concave type agitator were taken as experimental factors.

The simulation experiment of two factors and five levels orthogonal rotation combined central composite design tests was carried out (Table 4).

Table 4

Results of quadratic regression orthogonal rotating experiment

	h / x_1 [mm]	B / x_2 [°]	*QFI* [%]	*MIS* [%]	*MUL* [%]
1	2	70	84.9	15.1	0
2	3	60	98.9	1.1	0
3	4.4	60	83.3	0	16.7
4	3	60	97.3	0.5	2.2
5	3	74.1	92.4	2.2	5.4
6	3	60	98.4	0	1.6
7	3	45.9	90.5	2.5	7
8	4	50	85.1	1.1	13.8
9	4	70	89.1	0	10.9
10	1.6	60	81.1	18.9	0
11	3	60	97.3	0.5	2.2
12	3	60	98.2	0	1.8
13	2	50	89.7	10.3	0

The regression analysis of central composite design test results showed that the regression model was as follows.

$$QFI = -7.82x_1^2 - 0.03x_2^2 - 0.22x_1x_2 + 34.04x_1 + 3.19x_2 - 50.04 \quad (6)$$

$$MIS = 4.69x_1^2 + 0.01x_2^2 - 0.15x_1x_2 - 25.71x_1 - 0.89x_2 + 74.08 \quad (7)$$

$$MUL = 3.12x_1^2 + 0.02x_2^2 - 0.07x_1x_2 - 8.33x_1 - 2.30x_2 + 75.96 \quad (8)$$

Analysis of variance and significance test of regression coefficient were carried out for the above quadratic regression model.

The F-value of the QFI regression model was 125.84, and the corresponding P<0.0001.

Results indicate that the regression model was extremely significant. The F-value of lack of fit was 2.24, and the corresponding P >0.05, indicating that the lack of fit was not significant. For QFI, there was interaction between depth and angle.

The F -value of the regression model of MIS was 144.93, and the corresponding P <0.0001, indicating that the regression model was extremely significant. The F-value of lack of fit was 6.30, and the corresponding P >0.05, indicating that the lack of fit was not significant. P <0.0001 for x_1, P =0.2022>0.05 for x_2, but P =0.0079<0.01 for x_2^2, indicating that the depth and angle have significant effects on the MIS. P =0.0089<0.01 for x_1x_2, indicating that there was interaction between depth and angle for the MIS.

The F-value of the MUL regression model was 90.66, and the corresponding P<0.0001, which indicates that the regression model was extremely significant. The F-value of lack of fit was 1.05, and the corresponding P >0.05, indicating that the lack of fit was not significant. P <0.0001 for x_1, P >0.05 for x_2, but P =0.0006<0.01 for x_2^2, so the depth and angle have significant effects on the MUL; P =0.15912>0.05 for x_1x_2, indicating that the interaction between depth and angle was not significant for the MUL.

The results of significance analysis showed that the equation fitted by the quadratic regression model was consistent with the actual situation, which can correctly reflect the relationship between seed metering performance index and depth and angle of agitator. The regression model can predict the test results well.

According to the change law of seed metering performance index (Fig. 6), with the increase of depth, the QFI first increases and then decreases, and the maximum value appears at about 3mm.

With the increase of angle, the QFI increased first and then decreased, and the maximum value was about 60°. For the MIS, it decreased significantly with the increase of depth. When the depth was 3.5mm, the MIS was close to zero. With the increase of the angle, the MIS gradually increased, but the increase range was small.

For the MUL, with the increase of depth, the rebroadcast rate increased significantly, when the depth was 2mm, the rebroadcast rate was close to zero; with the increase of the angle, the MIS changed slightly.

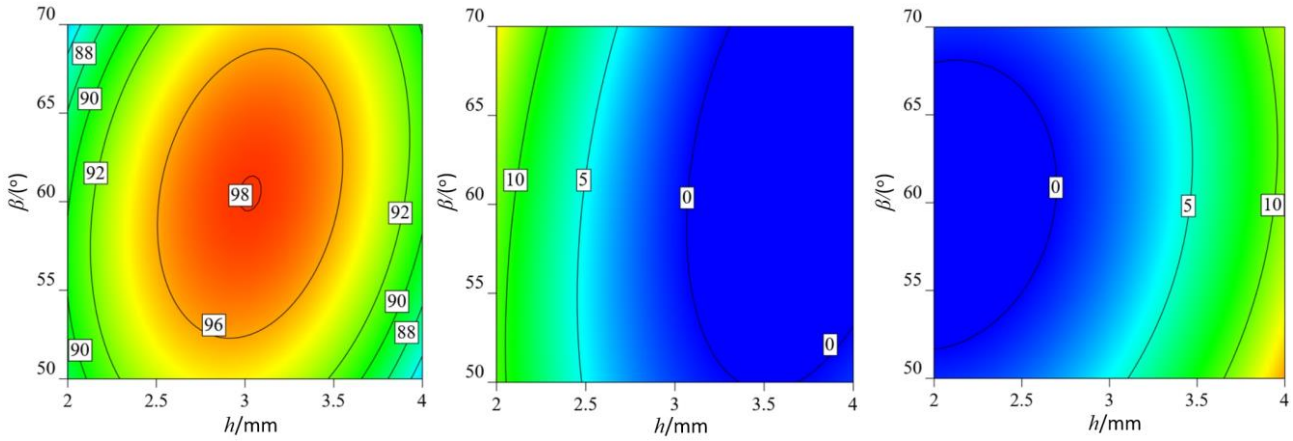

a. Contour of QFI *b. Contour of MIS* *c. Contour of MUL*

Fig. 6 - Effects of factors on the performance indexes

Taking the highest *QFI* and the minimum *MIS* as the optimization conditions, the optimal depth and inclination angle of agitator were 3.1 mm and 60.5° respectively.

Physical prototype test

Taking the optimal value of simulation test as the design parameters, the disk was made, and the physical test was carried out on the test bench (Fig. 7).

The tests were conducted at 16.7, 33.3, 50.0, 66.7 and 83.3 r/min, and the corresponding forward speed were 2, 4, 6, 8, 10 km/h respectively.

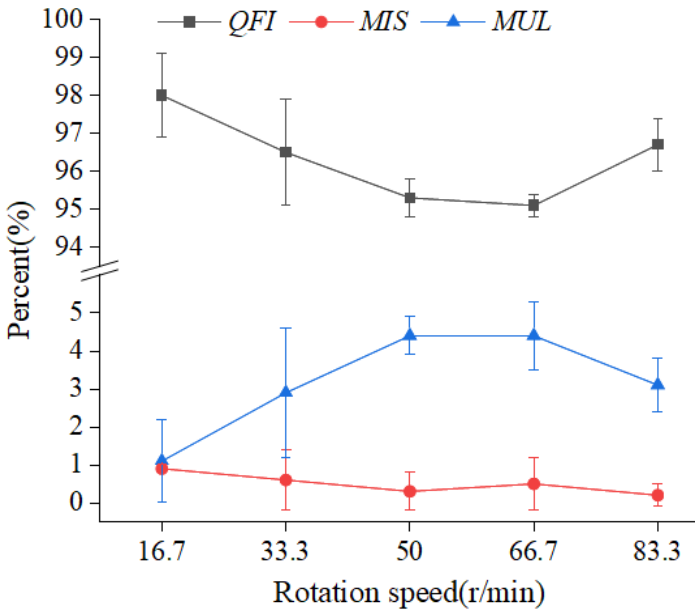

Fig. 7 - The results of physical prototype test

The *QFI* fluctuated with the increase of rotating speed. The highest *QFI* was 98.0% when the speed was 16.7r/min. The *MIS* and *MUL* were low, 0.9% and 1.1% respectively. With the increase of rotating speed, the *QFI* decreased. When the speed was 66.7 r/min, the *QFI* was the lowest (95.1%), and the *MUL* was the highest (4.4%), the *MIS* changed slightly, which was 0.5%. When the speed increased to 83.3 r/min, the *QFI* increased, which was 96.7%, the *MUL* was reduced to 3.1%. In the process of speed change, the *MIS* did not change significantly, and was always less than 1%.

Under the optimal parameters, the performance of the seed metering device with concave type agitator was excellent and met the requirements of precision seeding.

CONCLUSIONS

(1) In the speed range of 2-10 km/h, the *MIS* of concave type agitator was significantly lower than that of convex type and non-type.

(2) The depth and angle had significant influence on the *QFI*, and there was interaction effect. The depth and angle had significant influence on the *MIS*, and there was interaction effect. The depth and angle had significant influence on the *MUL*, but the interaction was not significant. The optimal depth and angle were 3.1 mm and 60.5° respectively.

(3) The results of physical prototype test showed that the *QFI* was more than 95.1% and the *MIS* was less than 1% in the speed range of 2-10 km/h, and the seed metering performance of the metering device was excellent.

ACKNOWLEDGEMENT

This work was supported by the National Natural Science Foundation of China (Grant No. 51905318), Key R&D Project of Shandong Province, China (Grant No. 2019JZZY010734), Shandong Provincial Colleges and Universities Youth Innovation Talent Induction Program (Smart Agriculture Research and Innovation Team), and Zibo School City Integration Project (Grant No. 2019ZBXC200).

REFERENCES

[1] Ding, L., Yang, L., Liu, Sh., Yan, B., He, X., & Zhang, D. X. (2018), Design of air suction high speed precision maize seed metering device with assistant seed filling plate（辅助充种种盘玉米气吸式高速精量排种器设计）, *Transactions of the Chinese Society of Agricultural Engineering*, vol.34, issue 22, pp.1-11, Ed. Chinese Society of Agricultural Engineering, Beijing/P.R.C.; https://doi.org/10.11975/j.issn.1002-6819.2018.22.001;

[2] Du, X., Liu, C., Jiang, M., Zhang F., Yuan H., & Yang, H. (2019), Design and experiment of self-disturbance inner-filling cell wheel maize precision seed-metering device（自扰动内充型孔轮式玉米精量排种器设计与试验）, *Transactions of the Chinese Society of Agricultural Engineering*, vol.3, issue.13, pp.23-34;

[3] Karayel, D., Wiesehoff, M., Ozmerzi, A., & Muller, J. (2006), Laboratory measurement of seed drill seed spacing and velocity of fall of seeds using high-speed camera system, *Computers and Electronics in Agriculture*, vol.50, issue.2, pp. 89-96; https://doi.org/10.1016/j.compag.2005.05.005;

[4] Khatchatourian, O., Binelo, M., & Lima, R. (2014), Simulation of soya bean flow in mixed-flow dryers using DEM, *Biosystems Engineering*, vol. 123, pp. 68-76; https://doi.org/10.1016/j.biosystemseng.2014.05.003;

[5] Li, Z., Yu, J., Feng, Z., Fu, H., Zhang, L. & Fei, X. (2013), Simulation and performance analysis of a soybean seed metering device using discrete element method, *Sensor Letters*, vol.11, issue 6-7, pp.1217-1222; https://doi.org/10.1166/sl.2013.2897;

[6] Liu, C., Du, X., Zhang, F., Ma, T., Zhang, H. & Li, Y. (2018), Design and test of cone diversion type horizontal plate wheat precision seed-metering device（锥面导流水平盘式小麦精量排种器设计与试验）, *Transactions of the Chinese Society for Agricultural Machinery*, vol.49, issue 12, pp.56-65; https://doi.org/10.6041/j.issn.1000-1298.2018.12.007;

[7] Liu, H., Guo, L., Fu, L., & Tang, S. (2015), Study on multi-size seed-metering device for vertical plate soybean precision planter, *International Journal of Agricultural and Biological Engineering*, vol.8, issue 1, pp.1-8; https://doi.org/10.3965/j.ijabe.20150801.001;

[8] Mao, X., Yi, S., Tao, G., Yang, L., Liu, H., & Ma, Y. (2015), Experimental study on seed-filling performance of maize bowl-tray precision seeder, *International Journal of Agricultural and Biological Engineering*, vol.8, issue 2, pp.31-3; https://doi.org/10.3965/j.ijabe.20150802.1809;

[9] Shi, S., Zhou, J., Liu, H., H., Jian, S., & Zhang, R. (2019), Design and experiment of pneumatic precision seed-metering device with guided assistant seed-filling（驱导辅助充种气吸式精量排种器设计与试验）, *Transactions of the Chinese Society for Agricultural Machinery*, vol.50, issue 5, pp.61-70;

[10] Singh, R., Singh, G., & Saraswat, D. (2007), Design and operational parameters of a pneumatic seed metering device for planting of groundnut (*Arachis hypogaea*) seeds, *Indian Journal of Agricultural Sciences*, vol.77, issue 1, pp.40-42;

[11] Vianna, L., Reis, A., & Machado, A. (2014), Development of a horizontal plate meter with double seed outlets, *Revista Brasileira de Engenharia Agricola e Ambiental-Agriambi*, vol.18, issue 10, pp.1086-1091; https://doi.org/10.1590/1807-1929/agriambi.v18n10p1086-1091;

[12] Wang, J., Tang, H., Wang, J., Li, X., & Huang, H. (2017), Optimization design and experiment on ripple surface type pickup finger of precision maize seed metering device, *International Journal of Agricultural and Biological Engineering*, vol.10, issue 1, pp. 61-71; https://doi.org/10.3965/j.ijabe.20171001.2050

[13] Wang, J., Tang, H., Wang, Q., Zhou, W., Yang, W., & Shen, H. (2015), Numerical simulation and experiment on seeding performance of pickup finger precision seed-metering device based on EDEM (基于EDEM软件的指夹式精量排种器排种性能数值模拟与试验), *Transactions of the Chinese Society of Agricultural Engineering*, 31(21), 43-50, https://doi.org/10.11975/j.issn.1002-6819.2015.21.006;

[14] Yang, L., Yan, B., Yu, Y., He, X., Liu, Q., Liang, Zh., Yin, X., Cui, T., & Zhang, D. (2016), Global overview of research progress and development of precision maize planters, *International Journal of Agricultural and Biological Engineering*, vol.9, issue 1, pp. 9-26;

[15] Yazgi, A., & Degirmencioglu, A. (2007), Optimisation of the seed spacing uniformity performance of a vacuum-type precision seeder using response surface methodology, *Biosystems Engineering*, vol.97, issue 3, pp. 347-356; https://doi.org/10.1016/j.biosystemseng.2007.03.013;

[16] Yi, S., Liu, Y., Wang, C., Tao, G., Liu, H., & Wang, R. H. (2014), Experimental study on the performance of bowl-tray rice precision seeder, *International Journal of Agricultural and Biological Engineering*, vol.7, issue 1, pp. 17-25; https://doi.org/10.3965/j.ijabe.20140701.002;

[17] Yu, J., Liao, Y., Cong, J., Yang, S., & Liao, Q. (2014), Simulation analysis and match experiment on negative and positive pressures of pneumatic precision metering device for rapeseed, *International Journal of Agricultural and Biological Engineering*, vol.7, issue 3, pp 1-12;

[18] Zhang, G., Zang, Y., Luo, X., Wang, Z., & Li, Z. (2014), Line-churning tooth design and metering accuracy experiment of rice pneumatic precision hill-drop seed metering device on pregnant Japonica rice seed(粳稻穴播排种器直线型搅种装置设计及排种精度试验), *Transactions of the Chinese Society of Agricultural Engineering*, 30 (17), 1－9; https://doi.org/10.3969/j.issn.1002-6819.2014.17.001;

[19] Zhang, G., Zang, Y., Luo, X., Wang, Z., Zhang, Q., & Zhang, S. (2015), Design and indoor simulated experiment of pneumatic rice seed metering device, *International Journal of Agricultural and Biological Engineering*, vol.8, issue 4, pp. 10-18; https://doi.org/10.3965/j.ijabe.20150804.1626;

[20] Zhang, T., Liu, F., Zhao, M., Liu, Y., Li, F., Ma, Q., Zhang, Y., & Zhou, P. (2017), Measurement of physical parameters of contact between soybean seed and seed metering device and discrete element simulation calibration(大豆种子与排种器接触物理参数的测定与离散元仿真标定), *Journal of China Agricultural University*, vol.22, issue 9, pp. 86-92;

[21] Zhao, Z., Li, Y., Chen, J., & Xu, L. (2010), Numerical analysis and laboratory testing of seed spacing uniformity performance for vacuum-cylinder precision seeder, *Biosystems Engineering*, vol.106, issue 4, pp. 344-351; https://doi.org/10.1016/j.biosystemseng.2010.02.012.

DESIGN OF AN INTELLIGENT IRRIGATION SYSTEM FOR A JUJUBE ORCHARD BASED ON IoT
/
基于物联网的枣园智能灌溉系统设计

Tan Kun, Sun Sanmin*), Du Liangzong, Zhou Shaoliang [1]
College of Water Conservancy and Architecture Engineering, Tarim University, Alar, Xinjiang/ China
Tel: +8609974680383; E-mail: ssmaqx@126.com
Corresponding author: Sanmin Sun
DOI: https://doi.org/10.35633/inmateh-63-19

Keywords: *IoT, smart irrigation, 4G network, human–computer interaction*

ABSTRACT
This research aimed to develop an information acquisition and intelligent irrigation decision system based on the agricultural Internet of Things (IoT). The system consists of a field control terminal and a remote client, realizing control, real-time display, alarm, and other functions. The user may apply the upper and lower limit of soil relative water content as the irrigation decision threshold. The system automatically controls irrigation according to the threshold. In the calculation and analysis part of the system, the programming software Keil 5 was used for data collection and monitoring, database comparison, calculation and analysis, irrigation decision, and other functions.

摘要
本研究旨在开发一套基于农业物联网的枣园信息获取与智能灌溉决策系统。该系统由现场控制终端和远程客户端组成，实现控制、实时显示、报警等功能。用户可将适宜枣树生长的根区土壤相对含水量上下限值作为灌溉决策的阈值，系统根据其阈值自动控制灌溉，该系统计算分析部分采用编程软件 Keil 5 来实现数据采集监测、模数转换、数据库对比、计算分析与灌溉决策等功能。

INTRODUCTION
There is a lack of water resources in the arid regions of western China. Additionally, existing water resources are unevenly distributed. Agricultural water consumption accounts for a total amount of 0.6 and the utilization rate is only about 0.4 *(Feng et al., 2018).* Further, traditional irrigation methods, such as flood irrigation, waste a lot of water and may negatively affect crop yield and quality *(Li et al., 2017).* Therefore, methods for efficient water saving are a regional research focus since the 1980s.

In recent years, the rapid development of Internet of Things (IoT) has brought the social development into the Era of the IoT. As the third wave of world information industry after the wave of computer and the internet, the IoT has penetrated into various industries and led a new trend of water-saving agriculture *(Han et al., 2017; Mason el al., 2019; Mendes et al., 2019; Yu et al., 2016; Jia et al., 2015).* In 2013, an intelligent crop water allocation method suitable for active irrigation scheme was proposed, and the results of the irrigation control model were compared with those of the classical irrigation control model. The results show that the fuzzy intelligent state descending (ISD) mechanism can produce appropriate irrigation control decisions *(Ganji et al., 2013).* At the same time, the energy saving and water saving effect and gross profit rate of intelligent sorghum surface drip irrigation were studied. Combined with new technology, total output and profit can be increased and resources can be fully utilized *(Papanikolaou et al., 2013).* In 2014, from the perspective of water saving and information collection, the idea of rotation irrigation improvement was designed to improve the response time of irrigation system and the security and reliability of irrigation system *(Li et al., 2014; Lv et al., 2014).* In 2018, combined with drip irrigation technology, the greenhouse automatic monitoring system was developed to monitor various plant growth parameters, optimize the utilization of agricultural water resources, and improve the water use efficiency of crop production *(Sivagami et al., 2018).* In 2019, an intelligent water-saving irrigation monitoring system based on LoRa technology was developed to improve agricultural irrigation efficiency and reduce water resource waste, combining automatic irrigation with water price reform to realize

[1] *Kun Tan, M.S. Stud. Eng.; Sanmin Sun, Prof. Ph.D. Eng.; Liangzong Du, M.S. Stud. Eng.; Shaoliang Zhou, Lecturer M.S. Eng.*

water-saving irrigation *(Song et al., 2019).* In addition, a low-cost intelligent irrigation system has been developed, which can be connected to devices connected to the Internet of Things. The main advantages of the system are intelligence, low cost and portability. Suitable for greenhouses and farms *(Nawandar et al., 2019).* With the development of science and technology, a set of sensor network acquisition system for automatic irrigation and fertilization has been developed, which can reduce water consumption by 74.92% *(Karunanithy et al., 2020).* Recently, a prototype of an efficient irrigation system composed of ARM microcontroller and GSM module has been developed, which can detect rainfall, inform farmers of rainfall levels and automatically adjust irrigation water quantity *(Barkunan et al., 2020).* At present, capacitive soil moisture sensor is often used to monitor soil moisture content in drip irrigation system. The difference between capacitive soil water sensor and traditional resistance soil moisture sensor is that it is not easy to be corroded *(Domínguez-Niño et al., 2020).*

In summary, current IoT irrigation control systems have achieved remarkable results in terms of intelligence and water saving. However, they still have some defects, such as weak remote and on-site integration performance, tedious human-computer interaction operation, and difficulties in secondary development. To more effectively implement precise irrigation, this study used a STM32F103ZET6 single-chip computer as the core control processor and a 4G module to connect the sensor system to the remote server. The current mature 4G network makes remote connections more rapid and stable. System design human-computer interaction interfaces enhance the scene of the remote and interactive, making monitoring and control more convenient and intuitive, and realizes the remote integration of field monitoring and control. This independent drip irrigation system implements real-time monitoring of soil temperature and relative water content, to provide technical support for the future of intelligent agriculture.

MATERIALS AND METHODS

System architecture

The system is divided into two plate assemblies, a field terminal, and a remote client. The system's overall framework is shown in Fig. 1, and its appearance is shown in Fig. 2.

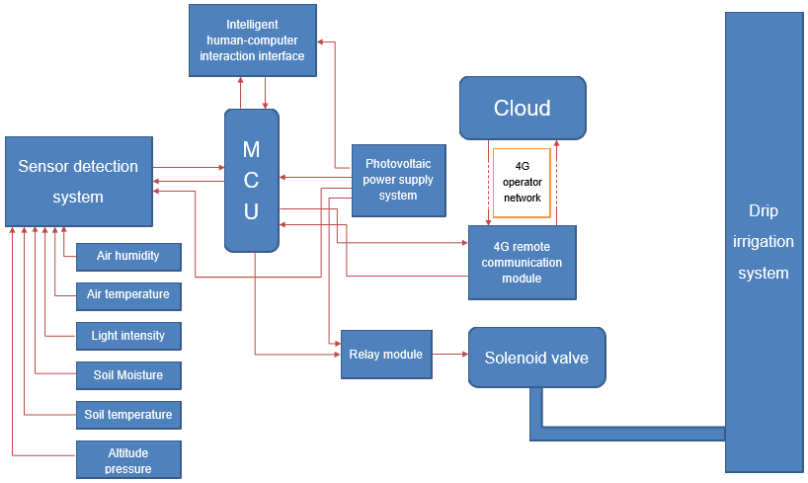

Fig. 1 – Overall system architecture

Fig. 2 – Appearance

The field control terminal comprises a core control system, a sensor monitoring system, a photovoltaic power supply system, an irrigation system, and a human-computer interaction interface. The core control system is composed of the STM32F103ZET6 microcontroller. This processor has become one of the most popular processors of the ARM company due to its low cost, fast operation speed, and rich interface. Our design adopts this chip as the core controller to achieve short time delays and high stability. The sensor system measures air temperature, relative humidity, atmospheric pressure, altitude, light, soil temperature, soil moisture, and other variables to monitor crop environmental information in real-time. The photovoltaic power supply system is composed of a solar panel, a constant voltage charger, and a new type of lead-acid battery, which can provide more stable outdoor power for the system and improve hardware life. The irrigation system is composed of a relay, a solenoid valve, and a drip irrigation system. An advanced indirect subsurface drip irrigation system is used to improve the water use efficiency. The human-computer interaction interface uses a serial touch screen. The HCI programming software was used to write the serial touch screen program, integrating control, real-time display, and alarm functions to ensure its practicability.

The remote client uses a 4G module to build the connection between the site and the remote. At present, the 4G network has been popularized worldwide, featuring high efficiency, strong flexibility, and good compatibility (*Tian et al., 2019).* This 4G module used for the data interaction is a WH–LTE–7 S4 V2, a pin type 4G module, with the function of UART turn 4G two-way passthrough 5 die 13 frequency, high speed, and low latency. It supports two online links at the same time and has support for TCP, UDP, a support registration mechanism/heartbeat package, support network passthrough mode, HTTPD, UDC, and a support basic instruction set. It supports FOTA difference for upgrades and stable operation. The system response speed and accuracy are much improved, and multi-terminal control is realized. The functional structure of the 4G module is shown in Fig. 3.

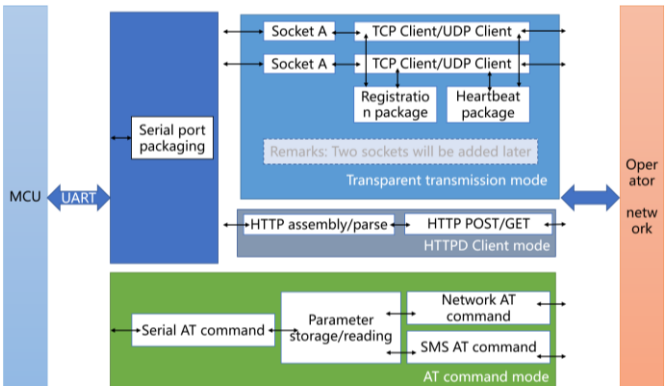

Fig. 3 – 4G module functional structure

Principle of system operation

The system field control terminal is divided into the acquisition and the control process. The system acquisition process collects data through the sensor system and sends the collected data to the core control system MCU, which processes the data. It sends it to the remote client and the human-computer interaction interface, which can display real-time data, system working status, charts, historical data, and alarm information. The system control process works as follows: when the system detects a water shortage signal in the crop root area, it sends the irrigation signal to the relay to control the solenoid valve to open for irrigation. When the irrigation amount reaches the upper limit of the set irrigation threshold, the system will stop irrigation and wait for the next water shortage. The system uses capacitive moisture sensors to measure soil relative water content. The sensor specifications are: 114 mm effective length, 19 mm width, 1.6 mm thickness. sensors have a large induction area, high precision, and high stability, to solve the problems of traditional sensors with small detection areas, and improve the accuracy of the response.

The remote client is divided into the PC terminal and mobile terminal, and the system remote client can realize remote data acquisition and control functions. The sensor acquisition system packages the acquired information through the MCU. It sends the packaged data to the remote client through the 4G module, thereby achieving efficient and orderly data exchange.

With the IoT system working principle as shown in Fig. 4, the sensor acquisition system connects through the I/O bus terminal with the control, human-computer interaction interface by the MCU UART connection site. Hereby data collected in the Modbus protocol are transmitted by 4G operators network transmission to the cloud server, and from the cloud server – via the Internet TCP/IP protocol to realize remote data conversion – to the mobile terminal and PC.

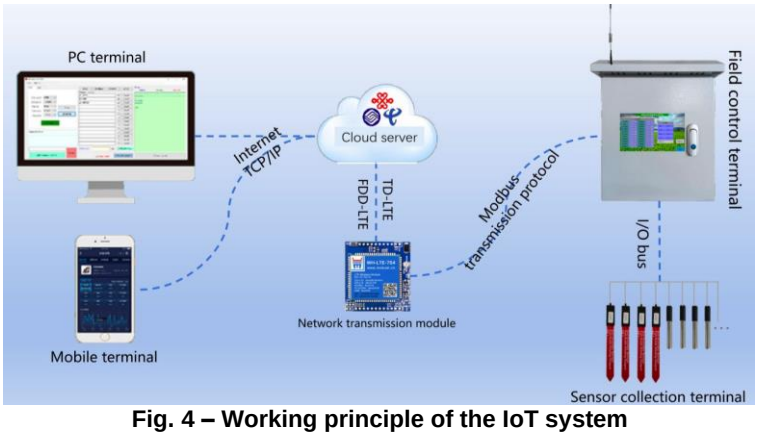

Fig. 4 – Working principle of the IoT system

Design of the core control system

The core control system, also known as MCU, collects soil moisture, soil temperature, air temperature, relative humidity, light intensity, and other data in an orderly manner through the sensor. It completes A/D conversion through the A/D conversion unit in the MCU and sends it to the remote client and human-computer interaction interface after the completion of the A/D conversion, and automatically records and stores it. The stored historical data contains crop information of different periods. Users can execute queries in the form of a graph or download data in Excel format to the user's computer for crop data analysis.

Irrigation process

First, the system is powered up and connected to the server. Second, the system can be run in manual mode and automatic mode. The default setting is the automatic mode that is used when the system uses crop root zone water information. The irrigation system alarm is transmitted by the bus transmission signal to the relay, and the relay controls the solenoid valve to open for irrigation. Then, the irrigation system sends a stop command after irrigation, waiting for the next irrigation cycle, and records the irrigation data at a time. The irrigation flow of the system is shown in Fig. 5.

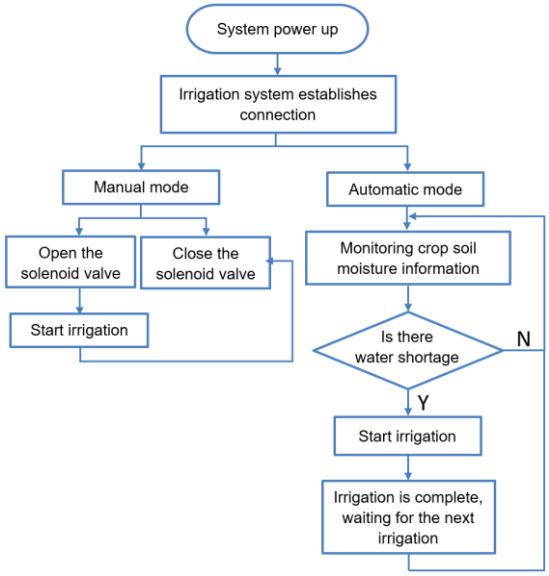

Fig. 5 – System irrigation process

Design of the human–computer interaction interface

Traditional screen programming is challenging and difficult to redevelop, and screens with touch functions tend to be more expensive. Therefore, this system adopts an HCI serial port screen and a screen integration HCI statement. The basic idea of HCI is to send relevant commands and requirements through HCI to complete the execution work of relevant equipment *(Xu et al., 2020).* This function is convenient to realize, and the development is strong. Our initial interface is shown in Fig. 6a, and the main interface is shown in Fig. 6b. The human-computer interaction interface is designed for user login, real-time data display, graph display, irrigation record table, irrigation threshold setting, historical data record table, as well as other functions.

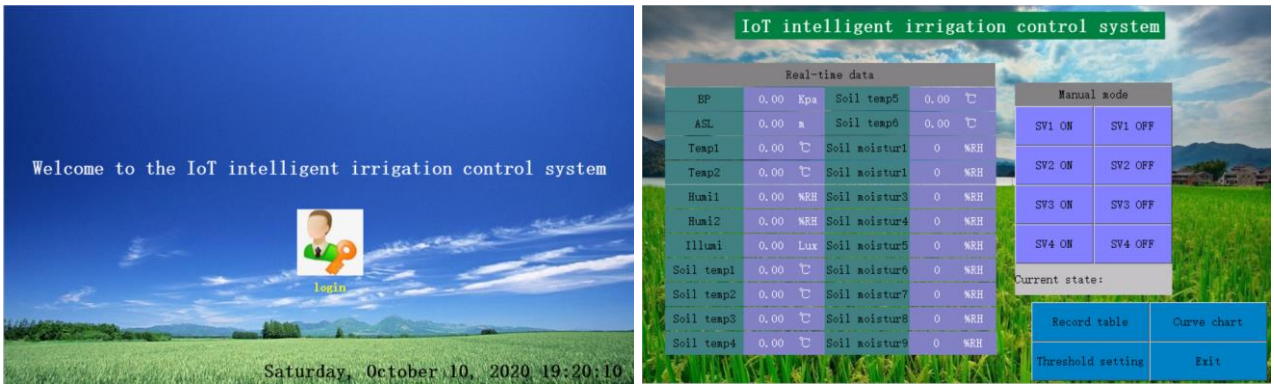

a) *b)*

Fig. 6 – User interface

a) Initial; b) Main

Photovoltaic power supply system

Considering that the system is used in remote and challenging areas, a photovoltaic power supply system was designed. The power supply system provides stable voltage and current output with a strong anti-interference performance. The integrated board uses the new polysilicon solar panel, whose service life is long. It can be used with a variety of batteries. The system may use the new lead-acid battery, ABS shell, and a lead-calcium-alloy grid that has a long service life, stable power supply, and high safety characteristics. The photovoltaic power supply system is shown in Fig. 7.

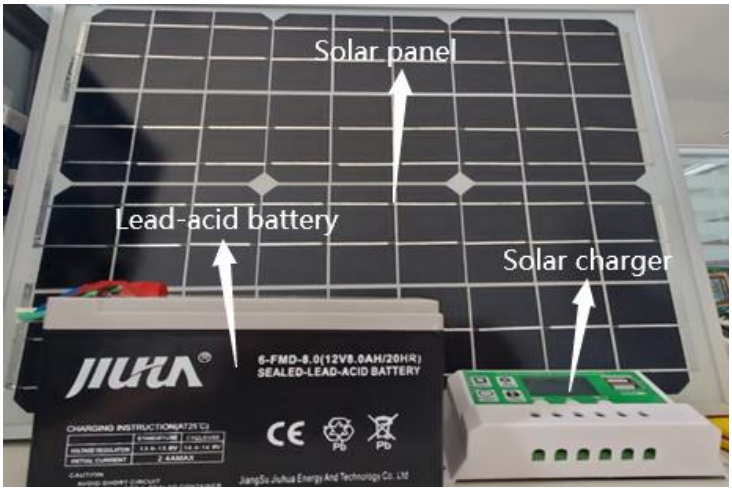

Fig. 7 – Photovoltaic power supply system

Remote control system design

To facilitate the software design, this system adopts the business's cloud programming system, which avoids challenges with APP software development. The monitoring interface of the remote PC terminal is shown in Fig. 8, and that of the mobile terminal is shown in Fig. 9. The configuration interface between the remote PC monitoring terminal and the mobile monitoring terminal is designed. The PC terminal displays real-time crop information, alarm information, and historical data through the cloud monitoring large screen. The mobile terminal mainly guarantees the simplicity of mobile operation and realizes status display, real-time data display, alarm, etc.

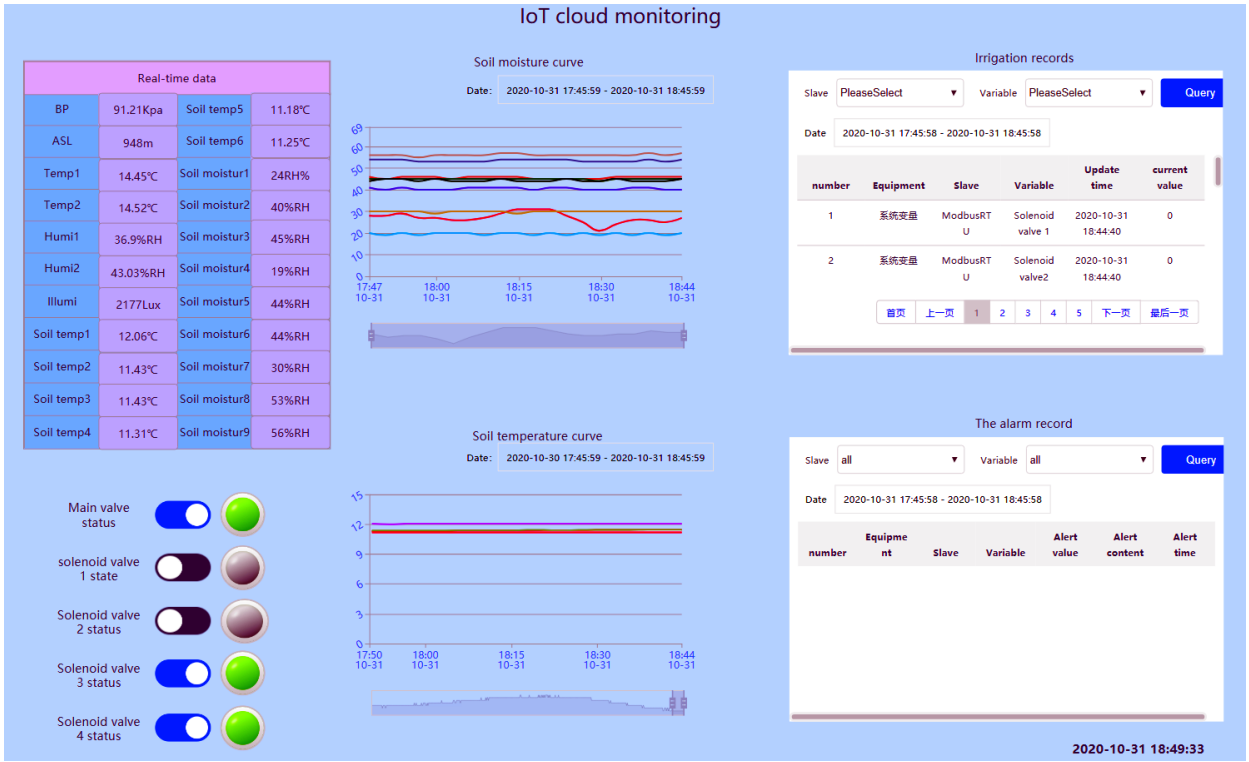

Fig. 8 – Remote PC monitoring interface

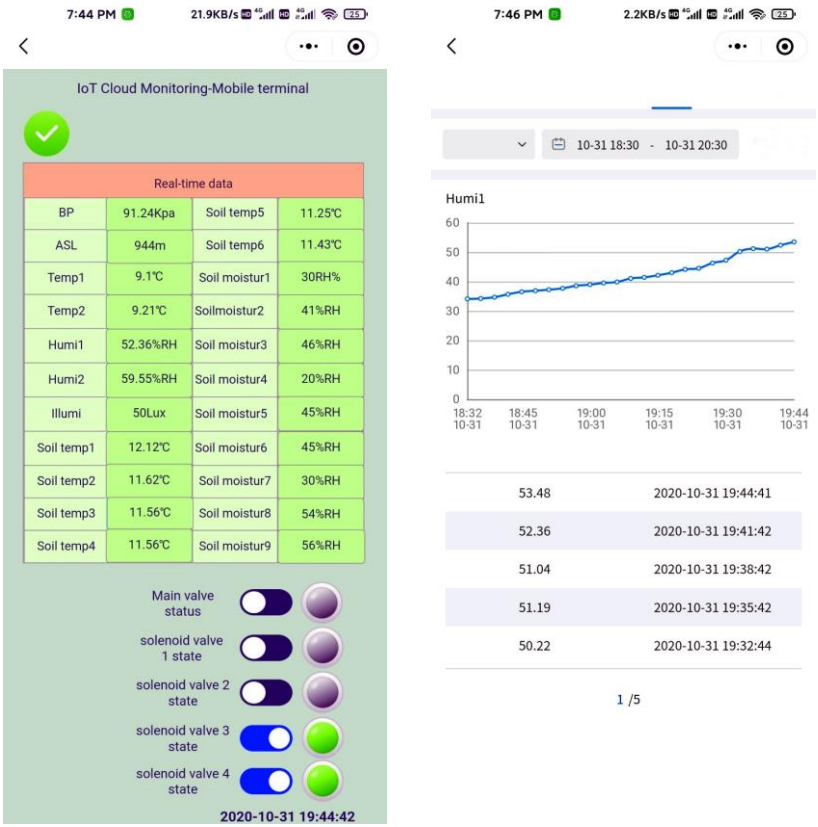

Fig. 9 – Mobile monitoring interface

Programming

The calculation and analysis part of the system is implemented in the C language, and the programming software is Keil 5. Data acquisition and monitoring, analog-digital conversion, database comparison, calculation and analysis, irrigation decision-making, and other functions were programmed. Example programs are shown in Fig. 10.

```
51  unsigned int  Get_Adc(unsigned char ch)
52  {
53
54    ADC_RegularChannelConfig(ADC1, ch, 1,  ADC_SampleTime_239Cycles5);
55
56    ADC_SoftwareStartConvCmd(ADC1, ENABLE);
57
58    while(!ADC_GetFlagStatus(ADC1, ADC_FLAG_EOC));
59
60    return ADC_GetConversionValue(ADC1);
61  }
62  unsigned int Get_Adc_Data(unsigned char ch)
63  {
64  unsigned int addat,res;
65  addat=Get_Adc(ch)>>4  ;
66        if(addat<35)
67          res=100;
68        if(addat>=222)
69          res=0;
70        if(addat>= 35 && addat<58)
71          {res=100 - 20*(addat-35)/(58-35);}
72        if(addat>= 58 && addat<85)
73          {res=80- 20*( addat-58)/(85-58);}
74        if(addat>= 85 && addat<137)
75          {res=60-20*( addat-85)/(137-85);}
76        if(addat>= 137 && addat<178)
77          {res=40-20*( addat-137)/(178-137);}
78        if(addat>= 178 && addat<222)
79          {res=20-20*( addat-178)/(222-178);}
80            return res;
81        }
82
```

```
452   if(ucRegCoilsBuf[4]==1)
453   {
454    if(ucRegCoilsBuf[0]==1)
455   {GPIO_SetBits(GPIOG,GPIO_Pin_2);
456   }
457    else if(ucRegCoilsBuf[0]==0)
458   {GPIO_ResetBits(GPIOG,GPIO_Pin_2);
459    }
460
461    if(ucRegCoilsBuf[1]==1)
462   {GPIO_SetBits(GPIOG,GPIO_Pin_3);
463   }
464    else if(ucRegCoilsBuf[1]==0)
465   {GPIO_ResetBits(GPIOG,GPIO_Pin_3);
466    }
467
468    if(ucRegCoilsBuf[2]==1)
469   {GPIO_SetBits(GPIOG,GPIO_Pin_4);
470   }
471    else if(ucRegCoilsBuf[2]==0)
472   {GPIO_ResetBits(GPIOG,GPIO_Pin_4);
473    }
474
475    if(ucRegCoilsBuf[3]==1)
476   {GPIO_SetBits(GPIOG,GPIO_Pin_5);
477   }
478    else if(ucRegCoilsBuf[3]==0)
479   {GPIO_ResetBits(GPIOG,GPIO_Pin_5);
480   }
481  }
```

a) ***b)***

Fig. 10 – A part of the program:
a) Water collection; b) Automatic irrigation

RESULTS

System accuracy test

The system was tested at the water-saving irrigation test base of the Tarim University in Aral, Xinjiang Province, China, and the following functions were verified: air temperature, relative humidity, soil relative water content, soil temperature, and light intensity. The system used the Chinese sea library union HKSHC03S soil moisture sensor that measures soil relative water content (± 2% accuracy), the Dallas DS18B20 digital temperature sensor (± 0.5°C), the Swiss sensirion SHT31 air temperature and humidity sensor (± 0.3 °C) for temperature, ± 2% for relative humidity). A US american Max44009 digital ambient light sensor (maximum gain error of 15%) was used to measure the light intensity in the Jujube orchard. We used the following instruments to assess the accuracy of the system and we ensured that the measuring instruments and the measurement system was at the same position of the sensors at the same time: the Chinese Ji Tai FD–T soil moisture meter (± 0.5% accuracy), the Chinese Huashengchang DT-321S temperature and humidity meter (temperature accuracy of ± 0.5 °C), relative humidity accuracy of ± 2%), and the Chinese Taiwan's Tai Shi TES1330A light intensity tester (± 0.5% FS precision). System data accuracy tests are shown in Fig. 11.

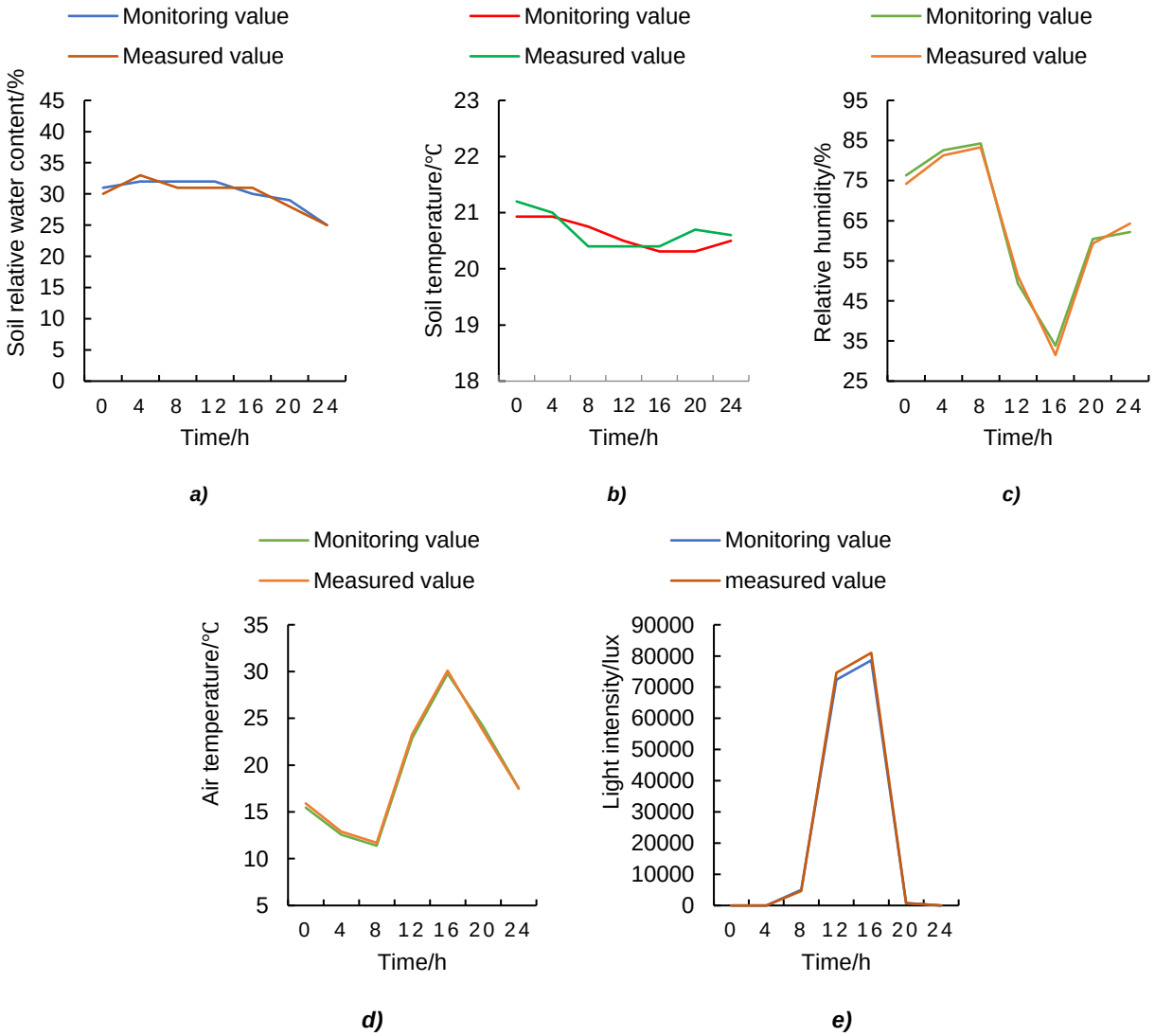

Fig. 11 – Monitored values of the information acquisition module and the measured values of the instrument on September 13, 2020

In the test data in Fig. 11, sensor and instrument data were in good agreement. Relative errors were within ± 3% for relative humidity. Soil temperature and air temperature relative errors were within ± 0.5℃. Light intensity relative errors were within ± 10% and show that the sensor monitoring values were more accurate and stable.

Intelligent irrigation accuracy test

The tested crops were jujube trees in the mature stage. The IoT monitoring system was set for irrigation, and indirect underground drip irrigation technology was adopted *(Sun et al., 2016).* According to Xu Rong et al., two groups of repeated experiments were set to 14 d test system. Research shows that dwarf close planting jujube under subsurface drip irrigation is indirect, with the water content of the soil in a maximum of 15 ~ 30 cm. Therefore, the soil moisture sensors are embedded in a depth of 10 cm, 25 cm, and 40 cm *(Xu et al., 2014).* The soil temperature sensors are buried in 15 cm and 25 cm depth, and 10 cm away from the trunk. Under the condition of highest water use efficiency, the soil water content in a 10 ~ 40cm soil layer change range is about 7% ~ 14% (dry soil weight %). Since the soil moisture sensor's measured value is the relative water content of soil, the volumetric water content of soil should be obtained first to obtain the soil's relative water content. The formula of the volumetric water content of the soil is:

$$\theta_\omega = \frac{\rho_d}{\rho_\omega} \cdot \omega \quad (1)$$

where:

θ_ω is the volumetric soil water content, [%]; ρ_d is the dry density, [g/cm³]; ρ_ω is the soil water density, [g/cm³]; ω is the soil weight water content, [%]. The calculated soil volumetric water content varied from 9.8% to 19.6%. The formula of soil relative water content is:

$$\textit{Relative water content of dryland soil (\%) = soil water content/field water holding capacity} \times 100 \quad (2)$$

The soil surface texture of the Jujube orchard was sandy loam, the soil density was 1.42g/cm³, and the field water holding rate was 29.1% (volume) *(Ye et al., 2012).* After conversion, the soil water content was 34%~72% (% of the soil mass), and this threshold was set for autonomous irrigation. The system irrigation test is shown in Table 1, and the change curve of soil relative water content is shown in Fig. 12.

Table 1

System irrigation tests

Test type	Date	Threshold set up [%]	Irrigation interval [d]	Irrigation trigger value of soil relative water content [%]	Irrigation stop value of soil relative water content [%]	Whether irrigation is completed	Whether to send manual irrigation instructions	Whether to alarm
Automatic irrigation test	September 11, 2020	34%~72	0	≤33~34	≥72~73	Yes	No	No
	September 15, 2020		3	≤33~34	≥72~73	Yes	No	No
	September 19, 2020		3	≤33~34	≥72	Yes	No	No
Manual irrigation test	September 20, 2020					Yes	Yes	No

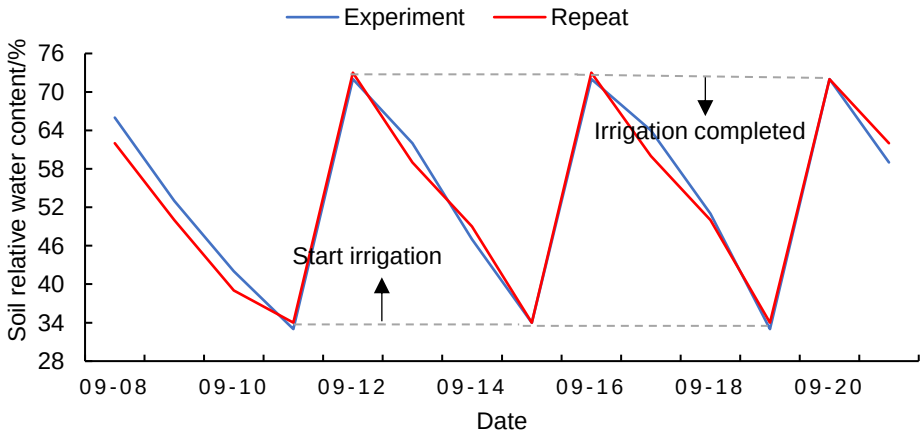

Fig. 12 – Soil relative water content change curve

According to Table 1, the system can report the completion and alarm information of irrigation in real-time while automatically irrigating using the set irrigation threshold. Manual control can be effectively implemented without conflicts with the automatic irrigation. As shown in Fig. 12, when the soil water content was lower than 34%, the system automatically irrigated when it alarmed. When it was higher than 72%, the system stopped irrigation, indicating that it could carry out stable irrigation according to the set water content.

CONCLUSIONS

Using IoT and HCI technology, we designed an intelligent irrigation system of a Jujube orchard, which realized the integration of remote monitoring and field monitoring and increased the diversity of intelligent irrigation system monitoring. During our experiment in the Jujube orchard air temperature, relative humidity, illumination, and soil water content was monitored in real-time. Accuracy tests showed that the data this system produced during the monitoring process were realistic and associated with low measurement uncertainties. Intelligent irrigation could be realized automatically and timely by setting an irrigation threshold according to soil water content change in the crop root area. Finally, our work provides a technical and theoretical basis for the intelligent irrigation of other crops.

ACKNOWLEDGEMENT

The authors were funded for this project by the National Natural Science Foundation of China (NSFC) (No.51869030) and science and technology project of Xinjiang Production and Construction Corps (No.2021CB021).

REFERENCES

[1] Barkunan, S. R., Bhanumathi, V., Balakrishnan, V. (2020). Automatic irrigation system with rain fall detection in agricultural field. *Measurement*, Vol. *156*, Netherlands.

[2] Domínguez-Niño, J. M., Oliver-Manera, J., Girona, J., Casadesús, J. (2020). Differential irrigation scheduling by an automated algorithm of water balance tuned by capacitance-type soil moisture sensors. *Agricultural Water Management*, *228*, Netherlands.

[3] Feng, Z., Cui, T., Zhang Z., Wang, R., Liu, C., Wang, L., (2018). Calculating Irrigation Schedule for Rice in Temperate Regions Using a Combination of Grey Neural Network and Fuzzy Control (基于灰色神经网络与模糊控制的寒地水稻灌溉制度). *Journal of Irrigation and Drainage*, Vol. 37, pp. 71-79, Henan/China.

[4] Ganji, A., & Shekarrizfard, M., (2012). A simple model of fuzzy irrigation depth control: An application of an intelligent state dropping (ISD) mechanism. *Irrigation and Drainage*, Vol. 61, pp. 596-603, United States.

[5] Han, G., C, Z., (2017). Design of Intelligent Irrigation Water Saving System Based on PLC and Internet of Things (基于 PLC 和物联网感应的智能灌溉节水系统设计). *Journal of Agricultural Mechanization Research*, Vol. 39, pp. 215-218, Heilongjiang/China.

[6] Jia, Y., Liu, S., (2015). Design of vineyard intelligent irrigation system based on ZigBee technology (基于 ZigBee 技术的葡萄园智能灌溉系统设计). *Jiangsu Agricultural Sciences*, Vol. 43, pp. 383-385, Jiangsu/China.

[7] Karunanithy, K., & Velusamy, B. (2020). Energy efficient Cluster and Travelling Salesman Problem based Data Collection using WSNs for Intelligent Water Irrigation and Fertigation. *Measurement*, Vol. 161, Netherlands.

[8] Li, D., Xu, C., Song, J., Tian, M., Xing, X., (2017). Development of Remote Intelligent Irrigation Control System Based on IOT (基于物联网的远程智能灌溉控制系统的开发). *Water Saving Irrigation*, Vol. 1, pp. 87-91, Hubei/China.

[9] Li, J., Lan, Z., Wang, Y., Wu, G., Li, P., (2014). Design and Realization of Photovoltaic Intelligent Irrigation System for Greenbelt on Freeway (高速公路绿化带光伏智能灌溉系统设计与实现). *Water Saving Irrigation*, Vol. 1, pp.79-82, Hubei/China.

[10] Lv, X., Lu, W., Wang, Y., Song, Z., Jia, B., Qian, C., … Liu, S., (2014). Study on Intelligent Irrigation Control System for Cucumber in Greenhouse Based on Internet of Things (基于物联网技术的日光温室黄瓜智能灌溉控制系统研究). *Tianjin Agricultural Sciences*, Vol. 20, pp. 34-37, Tianjin/China.

[11] Mason, B., Rufí-Salís, M., Parada, F., Gabarrell, X., & Gruden, C. (2019). Intelligent urban irrigation systems: Saving water and maintaining crop yields. *Agricultural Water Management*, Vol. *226*, Netherlands.

[12] Mendes, W. R., Araújo, F. M. U., Dutta, R., & Heeren, D. M. (2019). Fuzzy control system for variable rate irrigation using remote sensing. *Expert systems with applications*, Vol. *124*, pp. 13-24, United Kingdom.

[13] Nawandar, N. K., & Satpute, V. R., (2019). IoT based low cost and intelligent module for smart irrigation system. *Computers and Electronics in Agriculture*, Vol. 162, pp. 979-990, Netherlands.

[14] Papanikolaou, C., Sakellariou-Makrantonaki, M., (2013). The effect of an intelligent surface drip irrigation method on sorghum biomass, energy and water savings. *Irrigation Science*, Vol.31, pp. 807-814, Germany.

[15] Sivagami, A., Hareeshvare, U., Maheshwar, S., & Venkatachalapathy, V. S. K., (2018). Automated irrigation system for greenhouse monitoring. *Journal of The Institution of Engineers (India): Series A*, Vol. 99, pp. 183-191, India.

[16] Song, X., Zhou, Y., (2019). Application of Intelligent Irrigation Monitoring System Based on LoRa in Irrigation Area (基于 LoRa 的智能灌溉监控系统在灌区中的应用). *Yellow River*, Vol. 41, pp. 157-162, Henan/China.

[17] Sun, S., An, Q., Yang, P., Lu, X., Gu, K., (2016). Effect of Irrigation Depth on Root Distribution and Water Use Efficiency of Jujube under Indirect Subsurface Drip Irrigation (间接地下滴灌灌溉深度对枣树根系和水分的影响). *Transactions of the Chinese Society for Agricultural Machinery*, Vol. 47, pp. 81-90, Beijing/China.

[18] Tian, T., (2019). Design and Implementation of Remote Monitoring System for Farmland Irrigation Based on 4G Network (基于 4G 网络的农田灌溉远程监控系统设计与实现). *Journal of Shandong Agricultural University (Natural Science Edition)*, Vol. 50, pp. 977-979, Shandong/China.

[19] Xu, R., Sun, S., Wang, L., (2014). The Effect of Irrigation Amount on Physiological Characteristics and Quality of Fruit of Jujube under Indirect Subsurface Drips (间接地下滴灌下灌水量对枣树生理特征及果实品质的影响). *China Rural Water and Hydropower*, Vol. 1, pp. 50-53, Hubei/China.

[20] Xu, X., Sui, L., Zhao, Y., Li, Y., (2020). Advances in human-computer interaction system based on electrooculogram (基于眼电信号的人机交互系统研究进展). *Chinese Journal of Medical Physics*, Vol. 37, pp. 629-634, Guangdong /China.

[21] Ye, H., Yao, B., Wang, X., Sun, S., (2012). Transportation Law of Soil Water and Salt under Different Irrigation Frequencies and Quota for Dwarf Close Planting Red Jujube (不同灌溉制度对矮化密植红枣土壤水盐分布的影响研究). *Journal of Irrigation and Drainage*, Vol. 31, pp. 118-122, Henan/China.

[22] Yu, G., Wang W., Xie, J., Lu, H., Lin, J., Mo, H., (2016). Information acquisition and expert decision system in litchi orchard based on internet of things (基于物联网的荔枝园信息获取与智能灌溉专家决策系统). *Transactions of the Chinese Society of Agricultural Engineering*, Vol. 32, pp. 144-152, Beijing/China.

ON-LINE DETECTION OF CERASUS HUMILIS FRUIT BASED ON VIS/NIR SPECTROSCOPY COMBINED WITH VARIABLE SELECTION METHODS AND GA-BP MODEL

/

基于可见/近红外光谱技术结合变量选择和GA-BP模型的欧李果实在线分类检测

Wang Bin [1)], He Junlin *[1)], Zhang Shujuan *[1)], Li Lili [2)]

[1)] College of Agricultural Engineering, Shanxi Agricultural University, Taigu/China

[2)] College of Information Science and Engineering, Shanxi Agricultural University, Taigu/China

Tel: +86-0354-6288400; E-mail: hejunlin26@126.com

DOI: https://doi.org/10.35633/inmateh-63-20

Keywords: *fresh cerasus humilis fruit, detection, visible-near infrared spectroscopy, genetic algorithm, neural network, characteristic wavelengths*

ABSTRACT

In order to realize the rapid and non-destructive detection of fresh Cerasus Humilis' (CH) classification, and promote the deep-processing of post-harvest fresh fruit and improve market competitiveness, this study proposed a nonlinear identification method based on genetic algorithm (GA) optimized back propagation (BP) neural network of different varieties of fresh CH fruit. "Nongda-4", "Nongda-5", and "Nongda-7" fresh CH fruit were selected as research objects to collect their visible/near-infrared spectral data dynamically. The original spectra were preprocessed by moving smoothing (MS) and standard normal variate (SNV) methods, for the characteristic wavelengths were extracted with four dimension-reducing methods, namely principal components analysis (PCA), competitive adaptive reweighed sampling (CARS), CARS-mean impact value (CARS-MIV), and random frog (RF) algorithm. Finally, the BP prediction models were established based on full-spectrum and characteristic wavelengths. At the same time, the GA optimization was used to optimize the initial weight and threshold of the BP neural network and compared with the partial least squares' discrimination analysis (PLS-DA) linear model. Through comparing the MS (7)+SNV was proved to be the best preprocessing method, the CARS-MIV-GA-BP model had the best discriminant accuracy, the prediction set accuracy was 98.76%, of which the variety "Nongda-4" and "Nongda-5" recognition rate were 100%, the variety "Nongda-7" recognition rate was 96.29%. The results show that the GA can effectively optimize the initial weights and threshold randomization of the BP neural network, improve the discrimination accuracy of CH varieties, and the CARS-MIV algorithm can effectively reduce the number of input nodes of the BP neural network model, simplify the structure of BP neural network. This study provides a new theoretical basis for the detection of fresh CH fruit classification.

摘要

为了实现欧李鲜果分类的快速无损检测，推动采后鲜果的精深加工及提高市场竞争力。本研究提出基于遗传算法（GA）优化BP神经网络欧李鲜果品种的非线性判别方法。以产自同一地区的农大4号、农大5号和农大7号欧李果为研究对象，动态采集光谱数据。采用移动平滑法（MS）和标准正态变量（SNV）方法对原始光谱进行预处理，分别选用主成分分析（PCA）、竞争性自适应重加权算法（CARS）、竞争性自适应重加权-平均影响值算法（CARS-MIV）、随机蛙跳算法（RF）算法对光谱数据降维，将全波段和优选出的特征波长数据作为BP神经网络输入变量，采用GA优化BP神经网络的权值和阈值，建立BP、GA-BP神经网络非线性判别模型，并与偏最小二乘判别分析（PLS-DA）线性模型比较。分析得出，MS (7)+SNV为最佳预处理方法，CARS-MIV-GA-BP判别模型最佳，预测集总正确判别率为98.76%，其中"农大4号"和"农大5号"识别率均为100%，"农大7号"识别率为96.29%。研究表明，通过GA算法能有效地优化BP神经网络初始权值和阈值随机化，可提高欧李果品种判别精度，同时CARS-MIV算法可有效减少BP神经网络模型的输入节点数，简化BP神经网络结构。该研究为欧李果在线分类检测提供了新的理论基础。

INTRODUCTION

Cerasus humilis (Bge.) Sok. (CH) is a kind of Rosaceae cherry, it is not only a unique fruit plant resource in China, but also the most dwarf fruit tree in the world. CH has the characteristics of drought-resistance, cold-resistance, barren-resistance, strong root system, soil consolidation, and water conservation. CH fruit is a new kind of fruit, which contains many kinds of nutrients and mineral elements that are beneficial to the human body. The content of calcium in CH fruit is four times as high as that of Citrus Sinensis, Tangerine and Plum, more than 5 times higher than other fruits, so it is also called “fruit rich in calcium”, which is the third generation exclusive in China, and honoured as one of the three high-end fruits with American blueberry and Russian sea-buckthorn, at the same time, CH’s seed kernels are the main source of Yu Li Ren (Semen Pruni).

Therefore, as a "homology of medicine and food", CH fruit can be used as both fruit and medicinal material. With the continuous updating of CH varieties and the increase of yield year by year, the intensive processing of fresh fruits of CH has attracted more and more attention, from fresh food, fruit juice, fruit wine, fruit vinegar, fruit jam, preserved fruit to further extraction of a variety of physiologically active substances, the market prospects and its broad. However, the internal and external quality of different varieties are different, the products that can be further processed and the market price are also quite different.

Therefore, grading and sorting CH fruit according to its quality is essential in post-production processing, which is of great significance to the storage and sale of CH fruit. How to establish a rapid, non-destructive, and effective classification method of fresh CH fruit varieties has become an urgent problem.

In recent years, near-infrared spectroscopy has been widely used in agriculture and food as a rapid, non-destructive *testing method (Li et al., 2019; Du et al., 2020; Firmani et al., 2019)*. Near-infrared spectral modeling is based on multivariate statistical analysis, and an artificial neural network is one of the most widely used techniques. The back propagation (BP) network was proposed by *Rumelhart* in 1986. It is a multi-layer feedforward network trained by error back propagation theory. BP Neural Network has a strong ability of nonlinear mapping, self-learning, self-adaptation, generalization, and fault-tolerance. It is one of the most widely used neural network models, the method has been applied to improve the convergence speed and prediction accuracy of the model *(Xie et al., 2019; Yang et al., 2013; Lu et al., 2018; Wu et al., 2013)*.

At the same time, combining neural network with intelligent algorithms such as genetic algorithms (GA) *(Sun et al., 2016)*, particle swarm optimization (PSO) *(Chen et al., 2016; Mohamad et al., 2018)*., krill herd algorithm (KH) *(Liu et al., 2018)* and bird swarm algorithm (BSA) *(Xiang et al., 2019)* can improve the prediction accuracy, the BP neural network optimized by GA has been applied to the prediction and discrimination of walnut shell breaking *(Zhang et al., 2014)*, leaf chlorophyll *(Chen et al., 2018)*, soil moisture *(Liang et al., 2019)*, and red bean variety *(Sun et al., 2016)*.

For example, *Zhang et al., (2017)* put forward a method of tea leaf spot recognition based on hyperspectral image technology, and optimized BP neural network modeling independent variables by GA, which improved the spot recognition rate from 85.59% to 94.17%, the establishment time was also shortened from 6.6 seconds to 1.7 seconds before optimization. *Gu et al., (2017)* used a genetic algorithm to optimize the initial parameters of the BP neural network, which can effectively improve the prediction accuracy of corn yield and the convergence speed of the network.

Tan et al., (2019) identified soybean seed varieties using hyperspectral imaging and machine learning. It is concluded that the texture feature parameters are extracted from the three images by principal component analysis, and the prediction accuracy of the established GA-BP neural network model is 92%. *Yan et al., (2020)* by using the hyperspectral imaging technique and Chemometrics method, three kinds of identification models for fresh tea, which are GA optimized BP neural network, traditional BP neural network, and support vector machines (SVM), are established. The results show that the improved BP neural network based on GA can improve the performance of the model and has 100% prediction accuracy by combining the spectral preprocessing with the multiplicative scatter correction (MSC) and the standard normal variant (SNV). The studies above show that GA can effectively improve the predictive ability of the BP neural network, but there is little application in variety identification of fresh CH fruit based on Vis/NIR spectroscopy.

“Nongda-4”, “Nongda-5”, and “Nongda-7” CH fresh fruit were selected as research objects to collect their visible/near infrared spectral data dynamically. The raw spectral data is pre-processed by different pre-processing methods, combined with various wavelength extraction methods to downscale the pre-processed spectral data, and the downscaled data is used as the input of the model to build the traditional BP neural network and GA-BP neural network classification model for prediction and discrimination, and combined with

the linear model partial least squares discriminant analysis (PLS-DA), the predictive discriminatory effects of PLS-DA method were compared.

MATERIALS AND METHODS

Research samples

Test fresh CH fruit samples (Nongda-4, Nongda-5 and Nongda-7) were picked on 1 September 2019 at the Agricultural High-Tech Industry Demonstration Zone Cerasus Humilis Planting Demonstration Base in Taigu County, Shanxi Province, China (112°29'E, 37°23'N). The fruits were cleaned and dried in the laboratory (3 hours), and then the fruits with external defects and rot diseases were removed, and 80 each of "Nongda-4", "Nongda-5" and "Nongda-7" were screened for good maturity and basic consistency in physical properties. (240 in total), and the selected samples were numbered. According to the Kennard-Stone (K-S) algorithm *(Galvão et al., 2005)*, the three experimental samples were divided in a 2:1 ratio, and "Nongda-4", "Nongda-5" and "Nongda-7" were obtained, the sample sizes of the calibration set for the three species varieties were 53, 54, and 53 (160 samples in total), and the sample sizes of the prediction set were 27, 26, and 27 (80 samples in total).

The weight and fruit diameter (maximum diameter at the equatorial part of the fruit) were weighed and measured using a high-precision electronic balance (FA1004N, Shanghai) and a vernier calliper (Mitutoyo, Japan) for each variety of fresh CH fruit samples, and SPSS17.0 was used to calculate the parameters of the three different varieties of fresh CH fruit samples, as shown in Table 1.

Table 1

Data statistics of three different varieties of CH fruit samples

Cultivar	Sample parameters	Min.	Max.	Mean	S.D.	Variable coefficient (%)
Nongda-4	**Fruit diameter [mm]**	20.72	25.15	23.02	1.09	4.74
	Weight [g]	5.92	7.26	6.57	0.47	7.15
Nongda-5	**Fruit diameter [mm]**	15.48	28.66	24.72	3.62	14.64
	Weight [g]	7.47	16.18	11.39	1.76	15.45
Nongda-7	**Fruit diameter [mm]**	21.54	28.98	25.27	1.56	6.17
	Weight [g]	10.32	17.58	13.93	1.97	14.14

S.D.=Standard deviation.

Experimental system and data acquisition

The Field Spec3 spectrometer produced by ASD (Analytical Spectral Device) and the self-developed dynamic spectral acquisition system was used to achieve the spectral acquisition of fresh CH fruit samples, the schematic diagram of the online Vis-NIR spectroscopy detection device is shown in Fig.1.

Spectral data acquisition interval is 1nm, the wavelength range is 350～2500nm, the resolution is 3.5nm, the probe field of view angle is 20°, the light source is 14.5V halogen lamp, the probe of the spectrometer is perpendicular to the upper surface of the sample, 90mm away from the upper surface of the sample, the sample is placed between the two rollers.

To minimize the errors, the spectrometer was switched on for 0.5 hours for system configuration optimization and whiteboard calibration, and after the performance test, the sample was sampled by diffuse reflection.

For data collection, three kinds of CH fruit samples were rotated at a speed of 5 r/min and spectral data of the samples were collected at 120° intervals for a total of three times, and the average value was taken as the final spectral data of the test samples. When the CH sample enters the spectral scanning range, a proximity switch is triggered, the large sprocket stops moving, the small sprocket continues to move to ensure that the CH sample rotates under the probe, and after the spectral data is collected, the large sprocket continues to move and the CH sample is transported away until the next CH sample enters the spectral scanning range and begins scanning.

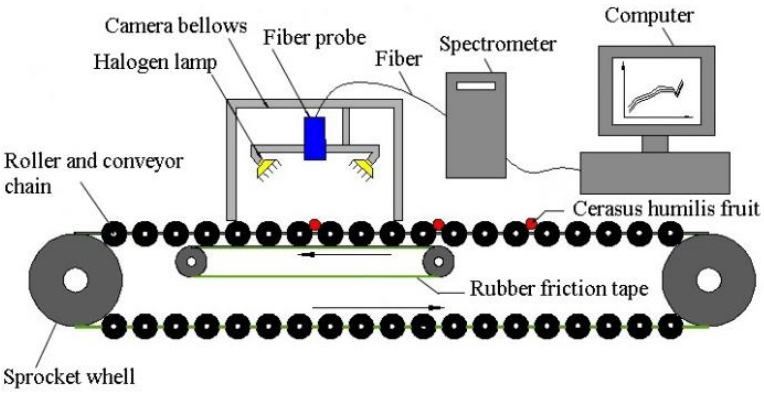

Fig. 1 - Schematic diagram of online Vis-NIR spectroscopy detection device

Data analysis and models establishment

Spectral data preprocessing

Due to the influence of the external environment and random errors during the spectral acquisition process, there are random noise and baseline drift in the spectral data, and the noise and background interference can be removed by appropriate spectral preprocessing methods, which is expected to improve the performance of the discriminant model. In this paper, moving smoothing (MS) and standard normal variate (SNV) are used to remove the noise and background interference.

Effective variable selection algorithms

There is a large amount of data redundancy in the original spectral information collected, the strong correlation among the wavelengths, and a large number of wavelength dimensions, which can affect the accuracy and prediction speed of the calibration model prediction classification. In order to solve these problems, several methods of extracting characteristic wavelengths are usually used to downscale the original spectral matrix. In this paper, we choose the feature extraction method of principal components analysis (PCA), feature selection method of competitive adaptive reweighed sampling (CARS), mean impact value (MIV), random frog (RF) and their combination algorithms are used to downscale the spectral data, screen the characteristic wavelengths that can reflect all the spectral information, and optimize the input variables of the model.

BP neural network

BP neural network is a kind of multi-layer feedforward network trained by back propagation of errors algorithm, with local search capability, it is a very mature regression analysis method, it can establish a non-linear model for classification and prediction, it is the most widely used back propagation artificial neural network, BP neural network contains input layer, implicit layer and output layer, if the input layer has X neurons, the output layer has Y neurons, there are P neurons in the hidden layer, and the weights are denoted by W. Then the basic structure of the BP neural network is shown in Fig.2, where X_1, X_2, ..., X_n are the input values, Y_1, Y_2, ..., Y_m are the predicted output values, and W_{ij} and W_{jk} are the weights of the BPNN.

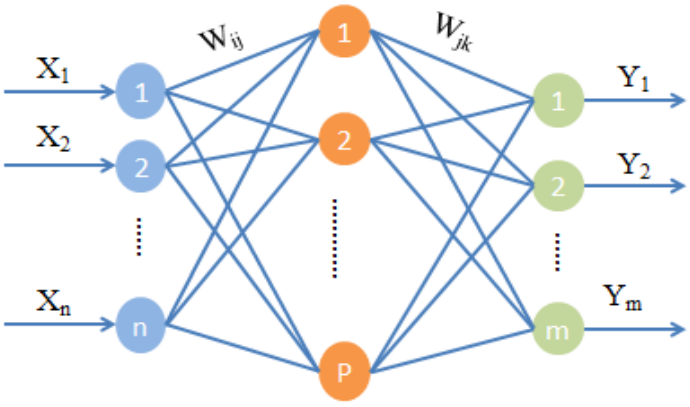

Fig. 2 - The basic principle of BP neural network

For the general pattern recognition problem, a three-layer network can be a good solution. In this study, a three-layer BP neural network is used, i.e., input layer, implicit layer and output layer, in which the number of nodes in the input layer is determined by the input data dimension, and the number of nodes in the output layer is determined by the sample characteristics, assuming that the number of neurons in the input layer is N_1 and the number of neurons in the implicit layer is N_2, and there is an approximate relationship between them: $N_2=2N_1+1$. The transfer function of the implicit layer neurons of the neural network adopts S-type tangent The function tansig( ), the transfer function of the output layer neurons uses the S-type logarithmic function logsig( ), this is because the output mode is 0-1, which exactly satisfies the output requirements of the network.

However, there are some shortcomings in the BP neural network, such as the network structure, the choice of initial connection weights and thresholds, which have a great influence on the network training, and the weights and thresholds are usually randomly initialized to random numbers in the interval of [-0.5,0.5]. To address these shortcomings this paper uses a genetic algorithm to optimize the BP neural network.

Genetic algorithms

In 1962, Professor Holland of the University of Michigan proposed the GA. The algorithm is a parallel random search that simulates the natural genetic mechanism and biological evolution, with excellent global search capabilities. According to the principle of the selection function, through a series of selection, intersection and variation screening of the population, the variables of the input population can be trained and optimized, and then continuously optimized according to the principle of "survival of the fittest", and finally better adapted. The GA can effectively optimize the BP neural network by randomizing the initial weights and thresholds, easily falling into local extremes and slow convergence, and locate the ideal search space for it. Searching for the optimal individual through selection, crossover and variation operations and assigning the optimized weights and thresholds parameters to BP neural networks not only exerts the powerful nonlinear mapping ability of neural networks, but also gives the neural networks faster convergence and stronger learning ability, which enables the optimized BP neural networks to make better sample predictions.

The idea of GA optimization of BP neural network can be divided into: (1) BP neural network structure determination; (2) GA optimization weights and thresholds; (3) BP neural network training and prediction. The flow of the GA to optimize the BP neural network is shown in Fig.3.

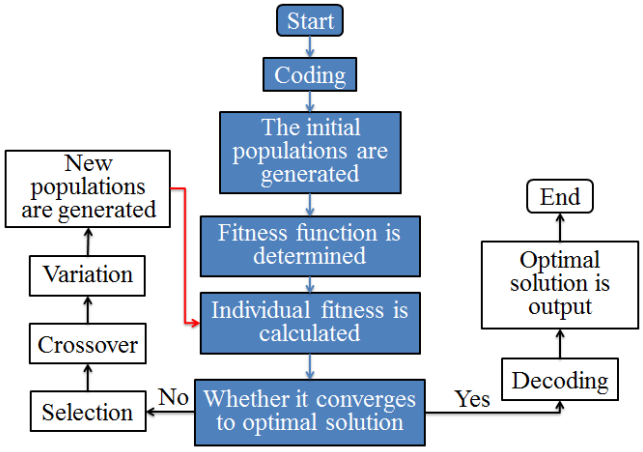

Fig. 3 - The optimization process of genetic algorithm

RESULTS

Spectral analysis of samples

The original spectra of three cultivars of CH fruit are shown in Fig.4(a). There were some crossovers and overlapping among these spectra, however, the trends of spectra were quite similar. Fig.4(b) shows the averaged reflectance spectra of three cultivars of CH fruit in the spectral region of 350-2500 nm, in the spectral region of 900-2500 nm, the average reflectivity of "Nongda-5" and "Nongda-7" is lower than that of "Nongda-4". In the visible spectral region of 500-700 nm, there were some differences that might have a direct correlation with the peel colour variances due to different CH fruit cultivars, there is an obvious peak around 680 nm which may be related to chlorophyll absorbance of CH's peel. In the near-infrared spectral

region, there are three obvious absorption peaks around 980 nm, 1190 nm and 1450 nm, the first two were assigned to second overtones of band O-H and band C-H, respectively *(Hideyuki et al., 2011)*.

The third may be associated with the first overtone of bond O-H. Three CH species have distinct absorption peaks at 1660nm, which is the second overtone of band C-H. It can be observed that the original spectra have obvious sample inhomogeneity, high-frequency random noise and light scattering. Therefore, the preprocessing of moving smoothing (7 points) transformation was filtered for random noise and high-frequency noise, standard normal variate transformation (SNV) was applied for light scatter correction. Reflectance spectra after the preprocessing is shown in Fig.4(c). From Fig.4(c), it can be seen that there was large noise at the beginning part (350-450nm) of spectra and the end of the spectral curve (2400-2500nm), which will directly affect the accuracy of the experiment. Therefore, only the spectral ranges of 450–2400nm were used for this study.

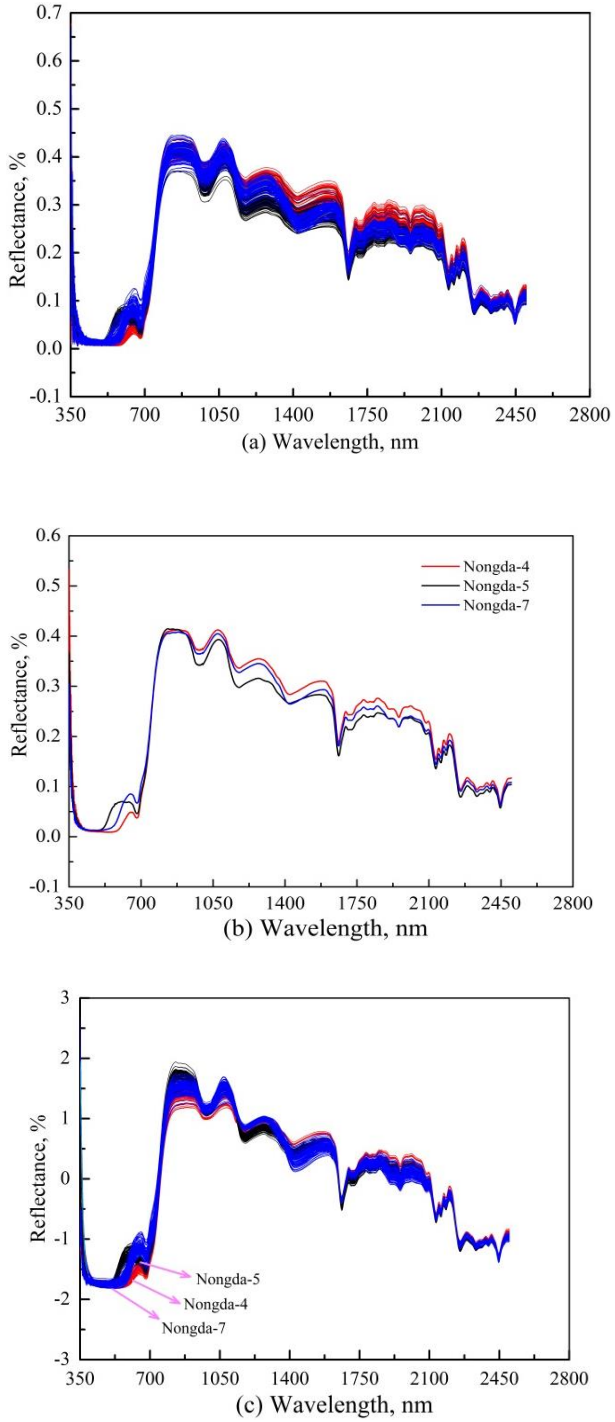

Fig. 4 - (a) Original spectra of 240 samples of three cerasus humilis varieties; (b) Average spectra of each cultivar; (c) Spectra after pre-treatment by moving average（7 points）and SNV

Selection of effective variables

Extraction of principal components

The main purpose of PCA is to extract variables and achieve the classification of the original large number of spectral variables into a few comprehensive indicators, which not only eliminates the overlap between the numerous information and extracts the most representative subset of variables but can also characterize the main features of the original data, as shown in Table 2.

Table 2

The accumulated contribution rate of the first 9 principal components

No. of principal components	PC 01	PC 02	PC 03	PC 04	PC 05	PC 06	PC 07	PC 08	PC 09
Cumulative contribution [%]	67.05	90.14	95.84	97.68	98.71	99.24	99.51	99.66	99.78

From Table 2, we can see that the cumulative contribution of the first six principal components has reached 99.24%, which contains more than 99% of the feature information of the spectral data, the cumulative contribution does not change much as the number of principal components increases, and the first six principal components do not affect each other. The first six principal components were selected to represent the main information of the original visible/near-infrared spectra. A total of 240 samples of the three species of CH were clustered by PCA, and the scatter plots of the first three principal components are shown in Fig.5.

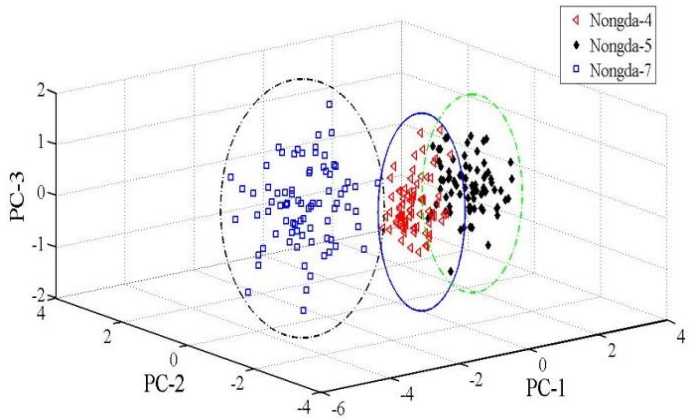

Fig. 5 - Scatter plots of cerasus humilis samples of the first three principal components

From Fig.5, it can be seen that there is a clear difference in characteristics between Nongda-4, Nongda-5 and Nongda-7, indicating that the first three principal components have a better clustering effect on the three species of CH. Nongda-4 and Nongda-5 had better aggregation, with some samples intersecting between them, with almost no overlap, and could be relatively distinguished; Nongda-7 had 80 samples less aggregated than the other two, but had no overlap with the other two, and was closely located on one side. The analysis showed that the first three principal components had a good clustering effect on the three species of CH, which provided a basis for qualitatively differentiating the different varieties of CH.

Competitive adaptive reweighted sampling (CARS)

CARS is a variable selection algorithm that employs the simple but effective principle “survival of the fittest” originating in Darwin's Evolution Theory. The adaptive reweighted sampling (ARS) technique is used to build the PLS model, and the wavelengths with larger absolute values of the regression coefficients are selected from the built model, the wavelength points with smaller weights are removed, and cross-validation selected the optimal subset of variables with the smallest root mean squares error of cross-validation (RMSECV) in the PLS model.

The process of CARS screening characteristic wavelengths is shown in Fig.6. The number of Monte Carlo sampling runs was set to 100 and the final variable number to be selected was determined by 10-fold cross-validation. Fig.6(a), (b) and (c) show the changing trend of the number of the sampled variables, RMSECV values and the regression coefficient path of each variable with the increase of Monte Carlo sampling runs in terms of running one CARS.

As shown in Fig.6(a), the number of wavelengths gradually decreases and finally stabilizes as the number of sampling runs gradually increases, which verified the rough and fine selection during wavelength screening. Fig.6(b) shows that the cross-validation RMSECV gradually decreases when the number of sampling runs increases to 67, and then shows an increasing trend; when RMSECV gradually decreases, it means that the useless information in the spectral information was eliminated; when RMSECV increases, it means that the valid info among spectral info was eliminated. In Fig.6(c), each curve represents the changing trend of the regression coefficient of each spectral variable with the number of sampling, when the position of the line of "*" indicated the runs were 67, RMSECV was minimized (RMSECV=0.2678). The 20 characteristic wavelengths selected by CARS are 455, 483, 575, 647, 648, 649, 650, 670, 671, 918, 919, 1105, 1106, 1322, 1324, 1325, 1326, 1327, 1916 and 1917nm, respectively.

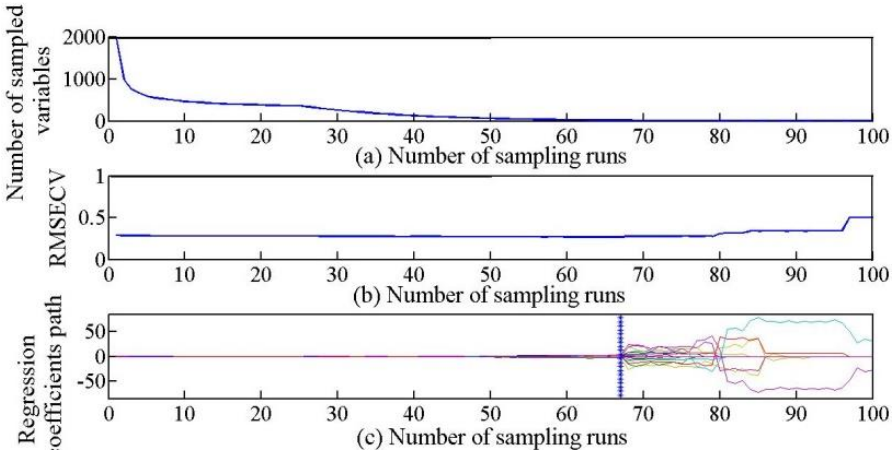

Fig. 6 - Process of selecting wavelength variables by the CARS method. (a) Number of Sampled variables; (b) The changes of RMSECV; (c) Paths of Regression coefficients

Effective variable selection by CARS-MIV

The MIV is an important index for evaluating the influence of input variables on output variables in neural networks *(Zhu et al., 2019)*. The number of Monte Carlo sampling times and the number of cross-validation groups are set randomly when the CARS algorithm is used to extract the characteristic wavelength, which makes the regression coefficient of the selected variables change with the random sampling times, the importance of characteristic variables can't be reflected comprehensively, which affects the robustness of prediction model. To reduce this effect, this study uses the MIV algorithm for secondary selection of the characteristic wavelengths extracted by the CARS algorithm to obtain the corresponding MIV values for 20 characteristic wavelengths, as shown in Fig.7(a). The MIV numerical values are arranged in descending order to analyse the cumulative MIV contribution rate of 20 feature wavelengths, as shown in Fig.7(b).

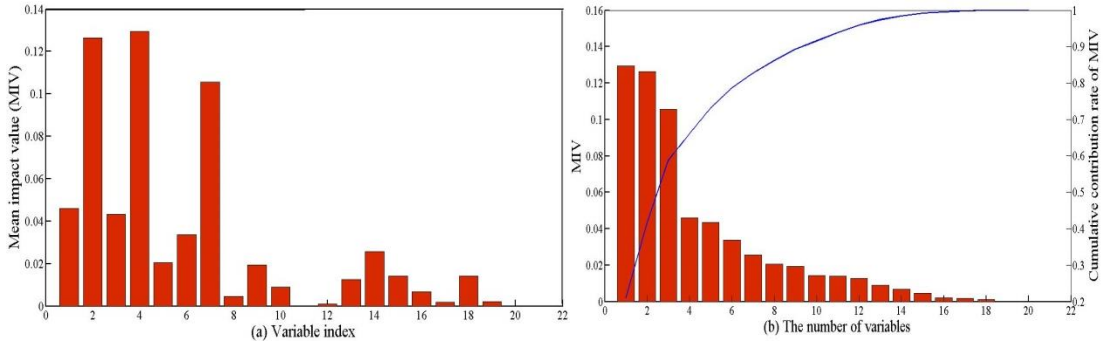

Fig. 7 - (a) Mean impact value of selected variables; (b) cumulative contribution rate of MIV

It can be found from Fig.7(a) that the 11th, 12th, 17th and 20th feature wavelengths correspond to smaller MIV values, which will affect the prediction accuracy of the calibration model. As shown in Fig. 7(b), the curve stands for the cumulative contribution of n(1≤n≤20) characteristic wavelengths, combined with Figure 8(a), the number of characteristic wavelengths after secondary selection of the MIV algorithm is 16.

Effective variable selection by RF

The RF method is similar to the reversible jump Markov chain Monte Carlo algorithm, it can iterate on multidimensional data variables and calculate the weight of each variable. The higher the value, the greater the probability of being selected, and the more important the corresponding wavelength. Therefore, the selection probability of all variables can be sorted, and the variables with higher probability can be selected as the characteristic wavelength.

In order to reduce the influence of random factors, it is necessary to run multiple times and calculate the results. In this study, the RF algorithm was run 2000 times, the selected threshold value was 0.4, and the top 10 wavelengths above the threshold were selected as characteristic wavelengths, which are 1011, 2326, 2397, 979, 2426, 2341, 2327, 2270, 1380, and 1056nm in descending order according to the probability of being selected, respectively. Most of the characteristic wavelengths were concentrated in the range of 2200-2450, which may be related to the region of the combined NIR spectral bands of C-H, N-H, and O-H bonds insoluble solids of CH. The process of filtering characteristic wavelengths using the RF algorithm is shown in Fig.8.

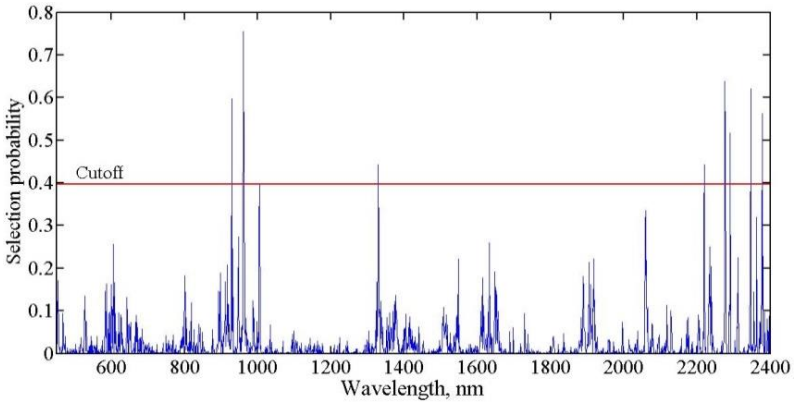

Fig. 8 - Effective variable selection by RF

Optimization of BP discriminant model

The weights and thresholds of traditional BP neural networks are generally random numbers in the interval of [-0.5,0.5], which makes the models have poor generalization ability and low prediction accuracy. In this study, GA is used to optimize the weights and thresholds of the BP neural network. After repeated tests, the initial population size is 40, the maximum number of genetic algebra is 50, the number of a binary number of the variable is 10, the crossover probability is 0.7, and the variation probability is 0.01.

In order to compare the modeling performance of BP before and after GA optimization, based on the spectral data in the range of 450-2400 nm, the full spectrum (FS) data and the preferred characteristic wavelength data are taken as input variables, where the number of input nodes of the BP neural network is determined by the respective input data dimension and the number of output nodes is determined by the variety number of CH. That is, the number of output nodes of the model is all 3, “Nongda-4”, “Nongda-5” and “Nongda-7” are represented by 100, 010 and 001, respectively, and different discriminant models are established. The discriminant results of the BP model before and after GA optimization is shown in Table 3.

Table 3

Comparison of discriminant results of BP model before and after GA optimization

Variable selection methods	No. of wavelength	BP				GA-BP			
		Prediction set accuracy [%]	Number of errors			Prediction set accuracy [%]	Number of errors		
			A	B	C		A	B	C
FS	1951	82.53	4	4	6	84.99	3	4	5
PCA	6	90.03	3	2	3	91.26	3	2	2
CARS	20	85.04	4	3	5	93.73	1	2	2
CARS-MIV	16	88.79	3	2	4	98.76	0	0	1
RF	10	83.76	4	4	5	86.22	3	4	4

Notes: A=Nongda-4, B=Nongda-5, C=Nongda-7

Looking at Table 3, the accuracy of the prediction set was increased using the feature extraction method of PCA, feature selection method of CARS, CARS-MIV and RF, compared with the FS-BP neural network and FS-GA-BP neural network models. Among the pre-optimized BP neural network models, the FS-BP model has a low discrimination accuracy of 82.53% and the PCA-BP identification model performed best, with a recognition rate of 90.03%.

The GA-BP neural network model built with FS data as input to the BP neural network model improved the recognition accuracy of the prediction set from 82.53% to 84.99%.

The recognition accuracy of the GA-BP neural network model based on the first six principal components extracted by PCA was improved from 90.03% to 91.26%.

The recognition accuracy of the GA-BP neural network model established for the 20 feature wavelengths screened by CARS improved from 85.04% to 93.73% for the prediction set. The recognition accuracy of prediction set by the GA-BP neural network model based on 16 characteristic wavelengths screened by CARS-MIV is improved from 88.79% to 98.76%.

The recognition accuracy of the GA-BP neural network model established for the 10 feature wavelengths screened by RF improved from 83.76% to 86.22% for the prediction set.

It is known that the CARS-MIV-GA-BP discriminant model is the best and the RF-GA-BP discriminant model is the worst. This is related to the fact that the characteristic wavelength extracted by the CARS-MIV algorithm contains information on the CH fruit visible and NIR spectral bands, whereas the characteristic wavelength extracted by the RF algorithm contains information only on the NIR spectral bands. The correct recognition rate of “Nongda-4”, “Nongda-5” and “Nongda-7” by CARS-MIV-GA-BP was 100%, 100% and 96.29%, respectively, and the total correct recognition rate was 98.76%. The results show that the characteristic wavelengths filtered by the CARS-MIV algorithm can effectively respond to the full-band spectral information, CARS-MIV-GA-BP identification model performed best, with a recognition rate of 98.76%. Fig.9 shows the GA optimized BP model of CARS-MIV screening variables, and Fig.10 shows the discriminant result of the CARS-MIV-GA-BP model.

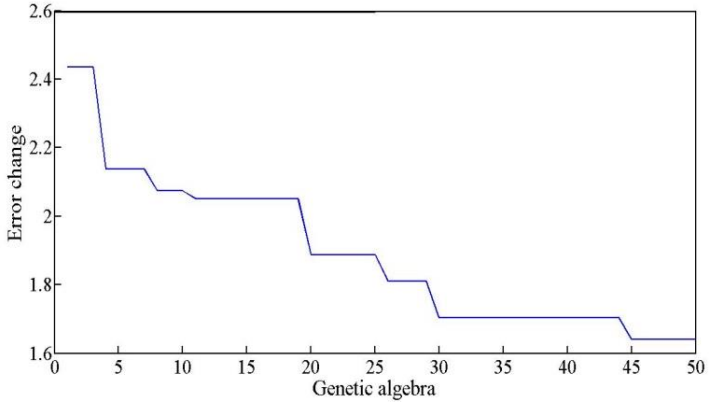

Fig. 9 - GA optimized BP model of CARS-MIV screening variables

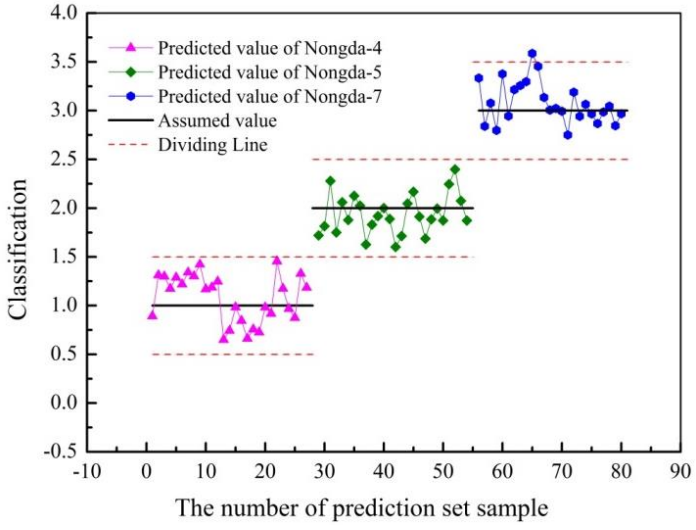

Fig. 10 - The discriminant result of CARS-MIV-GA-BP model

Comparison of optimum GA-BP model and PLS-DA discriminant model

PLS-DA is a multivariate statistical analysis method for discriminant analysis, which can reduce the influence of multicollinearity among variables, and has the characteristics of stable modeling performance and good prediction effect. In order to verify the prediction and discrimination effect of the CARS-MIV-GA-BP model built in this experiment, the characteristic wavelength variable extracted by CARS-MIV Algorithm is used as input of the PLS-DA linear model, and the prediction and discrimination model of CARS-MIVP-LS-DA is established, the discriminant results of the prediction set of CH samples are shown in Table 4.

Table 4

Discrimination of three cerasus humilis varieties by CARS-MIV-PLS-DA models

Cultivar	No. of predicted samples	No. of false positives	Correct discrimination rate [%]	Total [%]
Nongda-4	27	2	92.59%	
Nongda-5	26	1	96.15%	93.78%
Nongda-7	27	2	92.59%	

It can be seen from Table 4 that the CARS-MIV-PLS-DA model has a good discriminant effect on the sample of prediction set. The correct classification rate of “Nongda-4”, “Nongda-5” and “Nongda-7” are 92.59%, 96.15% and 92.59%, respectively, the total correct recognition rate was 93.78%. However, the correct recognition rate of “Nongda-4”, “Nongda-5” and “Nongda-7” by CARS-MIV-GA-BP were 100%, 100% and 96.29%, respectively, and the total correct recognition rate was 98.76%. Thus, the CARS-MIV-GA-BP discriminant model achieved better discriminatory results for CH fruit samples in this study.

CONCLUSIONS

In this study, the dynamic detection of classification discriminatory models of three fresh CH fruit samples was established based on Vis/NIR spectroscopy and GA-BP neural network, the original spectra were pre-processed using different kinds of pre-processing methods, Four different variable selection methods, PCA, CARS, CARS-MIV and RF, were used for variable optimization of the whole spectrum data, and the classification model established by different variable selection methods was discussed, and compared with traditional BP neural network and PLS-DA model.

The results show that, moving smoothing (7 points) and SNV were used to process original Vis/NIR spectral data, the GA-BP neural network based on 16 characteristic wavelengths extracted by the CARS-MIV algorithm has the best discrimination effect on prediction set, the CARS-MIV-GA-BP model total correct discrimination rate of prediction set was 98.76%, among them, the identification rates of “Nongda-4”, “Nongda-5” and “Nongda-7” were 100%, 100% and 96.29%, respectively.

Therefore, the on-line detection of fresh CH fruit based on Vis/NIR spectroscopy combined with variable selection methods and the GA-BP model is an effective method. Also, in later studies, more intelligent algorithms can be selected to optimize the model and further improve the accuracy and versatility of the model.

ACKNOWLEDGEMENT

This work was supported by National Natural Science Foundation of China (31271973); Key Research and Development Program of Shanxi Province, China (201703D221029-1)

REFERENCES

[1] Chen C. L., Jin Y., Cao Y. L., et al., (2018), Analysis of chlorophyll contents in maize leaf based on GA-BP neural network hyperspectral inversion model, *Journal of Shenyang Agricultural University,* Vol.49, Issue 5, pp.626-632, Shenyang/China;

[2] Chen X., Wang H. Y., Kong D. D., et al., (2016), Quality prediction model of pellet feed basing on BP network using PSO parameters optimization method, *Transactions of the Chinese Society of Agricultural Engineering,* Vol.32, Issue 14, pp.306-314, Beijing/China;

[3] Du X. B., He J. L., He Y. Q., et al., (2020), Design and experiment of eccentric swing combing device for cerasus humilis, *INMATEH-Agricultural Engineering,* Vol.60, Issue 1, pp.89-98, Bucharest/ Romania;

[4] Firmani P. , Bucci R., Marini F., et al., (2019), Authentication of “Avola almonds” by near infrared (NIR) spectroscopy and chemometrics, *Journal of Food Composition and Analysis,* Vol.82, pp.103235, San Diego /United States;
[5] Gu J., Yin G. H., Huang P. F., et al., (2017), An improved back propagation neural network prediction model for subsurface drip irrigation system, *Computers & Electrical Engineering,* Vol.60, pp.58-65, Oxford/England;
[6] Galvão R. K. H., Araujo M. C. U., José G. E., et al., (2005), A method for calibration and validation subset partitioning, *Talanta,* Vol.67, Issue 4, pp.736-740, Amsterdam/Netherlands;
[7] Hideyuki S., Pitiporn R., Yukihiro O. , (2011), Kernel analysis of partial least squares (PLS) regression models, *Applied spectroscopy,* Vol.65, Issue 5, pp.549-556, New York/United States;
[8] Li X., Liu Y. D., Ouyang A. G., et al., (2019), A general model for judging and brix detection of grapefruit variety based on near infrared, *Chinese Journal of Luminescence,* Vol.40, Issue 6, pp.808-814, Changchun/China;
[9] Liang Y., Ren C., Wang H. et al., (2019), Research on soil moisture inversion method based on GA-BP neural network model, *International Journal of Remote Sensing,* Vol.40, Issue 5-6, pp.2087-2103, Oxford/England;
[10] Liu D., Li S., Fu Q., et al., (2018), Comprehensive evaluation method of groundwater quality based on BP network optimized by Krill Herd algorithm, *Transactions of the Chinese Society for Agricultural Machinery,* Vol.49, Issue 9, pp.275-284, Beijing/China;
[11] Lu M. Y., Yang K., Song P. F., et al., (2018), The study of classification modeling method for near infrared spectroscopy of tobacco leaves based on convolution neural network, *Spectroscopy and Spectral Analysis,* Vol.38, Issue 12, pp.3724-3728, Beijing/China;
[12] Mohamad E. T., Armaghani D. J., Momeni E., et al., (2016), Rock strength estimation: a PSO-based BP approach, *Neural Computing and Applications,* Vol.30, Issue 5, pp.1635-1646, New York/USA;
[13] Sun J., Lu X. Z., Zhang X. D., et al., (2019), Identification of red bean variety with probabilistic GA-PNN based on hyperspectral imaging, *Transactions of the Chinese Society for Agricultural Machinery,* Vol.47, Issue 6, pp.215-221, Beijing/China;
[14] Sun J., Lu X. Z., Zhang X. D., et al., (2016), Identification of red bean variety with probabilistic GA-PNN based on hyperspectral imaging, *Transactions of the Chinese Society for Agricultural Machinery,* Vol.47, Issue 6, pp.215-221, Beijing/China;
[15] Tan K., Wang R., Li M., et al., (2019), Discriminating soybean seed varieties using hyperspectral imaging and machine learning, *Journal of Computational Methods in Sciences and Engineering,* Vol.19, Issue 4, pp.1001-1015, Amsterdam/Netherlands;
[16] Wu J., Huang F. R., Huang C., et al., (2013), Study on near infrared spectroscopy of transgenic soybean identification based on principal component analysis and neural network, *Spectroscopy and Spectral Analysis,* Vol.33, Issue 6, pp.1537-1541, Beijing/China;
[17] Xiang L., Deng Z. Q., Hu A. J., (2019), Forecasting short-term wind speed based on IEWT-LSSVM model optimized by bird swarm algorithm, *IEEE Access,* Vol.7, pp.59333-59345, New York/USA;
[18] Xie H., Chen Z. G., Zhang Q. H., (2019), Rapid discrimination of japonica rice seeds based on near infrared spectroscopy, *Spectroscopy and Spectral Analysis,* Vol.39, Issue10, pp.3267-3272, Beijing/China;
[19] Yan L., Pang L., Wang H., et al., (2020), Recognition of different Longjing fresh tea varieties using hyperspectral imaging technology and chemometrics, *Journal of Food Process Engineering*, Vol.43, Issue 4, pp.1-9, New York/United States;
[20] Yang D. F., Zhu H. D., (2013), Recognition of soybean varieties based on near infrared transmittance spectroscopy and BP neural network, *Soybean Science,* Vol.32, Issue 2, pp.249-253, Haerbin/China;
[21] Zhang H., Ma Y., Li Y., et al., (2014), Rupture energy prediction model for walnut shell breaking based on genetic BP neural network, *Transactions of the Chinese Society of Agricultural Engineering,* Vol.30, Issue 18, pp.78-84, Beijing/China;
[22] Zhang S. T., Wang Z. Y., Zou X. G., et al., (2017), Recognition of tea disease spot based on hyperspectral image and genetic optimization neural network, *Transactions of the Chinese Society of Agricultural Engineering,* Vol.33, Issue 22, pp.200-207, Beijing/China;
[23] Zhu X. L., Li G. H., Zhang M., (2019), Prediction of soluble solid content of Korla pears based on CARS-MIV, *Spectroscopy and Spectral Analysis,* Vol.39, Issue11, pp.3547-3552, Beijing/China.

DESIGN AND IMPLEMENTATION OF PIG INTELLIGENT CLASSIFICATION MONITORING SYSTEM BASED ON CONVOLUTION NEURAL NETWORK (CNN)

/

基于CNN猪只智能分类监控系统的设计与实现

Ziwei Wang, Yiming Hou*, Kai Xu，Lifeng Li [1]

College of Information Science and Engineering, Shanxi Agricultural University, Taigu / China

Tel:13233448152; E-mail: h13233448152@sina.com

DOI: https://doi.org/10.35633/inmateh-63-21

Keywords: *Convolution neural network(CNN), Pig classification, Monitoring system, Image recognition*

ABSTRACT

With the development of agricultural information technology, the intelligent monitoring system applied in pigsty can alert people when domestic pigs and wild boars jump into each other's pigsty, and bring convenience to breeding staff. The system uses convolution neural network as the core algorithm to realize the function of real-time monitoring and reminding users. Using Spring MVC framework technology, a pig intelligent classification monitoring system based on C/S architecture is developed. Three layer architecture model of presentation layer, business layer and persistence layer is used. Neural network algorithm is embedded in the image processing module, and Netty framework is used to maintain the connection between each module. Field experiments show that the recognition accuracy of the system can reach 97.08%. This system can be used as a reference for the design of pig intelligent classification monitoring system, and provide a reference for the design of related systems.

摘要

随着农业信息技术的发展，智能化的监控系统应用于猪场中可以对猪场中家养猪和野猪相互蹿窝起到警报作用，为养殖人员带来便利。该系统以卷积神经网络为核心算法，实现了对猪场实时监控并提醒用户的功能。利用Spring MVC框架技术，开发一套基于采用 C/S架构的猪只智能分类监控系统，用展现层、业务层、持久层 3 层架构模型，神经网络算法嵌入于图像处理模块中，采用 Netty 框架去维护各个模块之间的连接。经现场实验表明，系统识别准确率可达97.08%。本系统可以作为猪舍智能分类监控系统设计的参考，为相关系统设计提供参考。

INTRODUCTION

In recent years, with the rapid development of agricultural information technology, people have higher and higher requirements for agricultural technology and equipment. Among them, the breeding industry is developing in the direction of intelligence, and precision management has become more important. It is found that in the process of pig breeding, wild boar and domestic pig often jump to each other's pigsty, which brings great harm to the growth of pigs. *Weller et al (2019)* put forward that when the pigs are mixed with strange individuals, aggressive behaviour is easy to occur; In order to effectively prevent the occurrence of snatching food and fighting between wild boar and domestic pig, a real-time and accurate monitoring system for pig jumping behaviour is designed, which is of great significance to ensure the healthy growth of pigs and improve the breeding welfare.

Using monitoring system to monitor the behaviour of livestock has become an important auxiliary means of pig breeding. With the progress of technology, the related design innovation is constantly improved, but the ordinary monitoring system can only play the role of real-time monitoring. For example, *Wu et al, (2013),* designed a cattle farm remote monitoring system by using RFID technology and ZigBee technology, the system is simple in layout, low in cost and high in stability, however, the monitor only plays the role of monitoring and does not achieve intelligence. *Zeng et al, (2016),* designed a cowshed environmental parameters monitoring system using ARM technology and WiFi wireless transmission technology, which can accurately monitor the environmental parameters of the cowshed, however, when the temperature in the cowshed is unstable, the system cannot maintain the gas concentration in the cowshed within the appropriate range, and the monitor only plays a monitoring role.

[1] *Ziwei Wang, undergraduate; Yiming Hou*, undergraduate; Kai Xu , undergraduate; Lifeng Li, undergraduate.*

Zeng et al, (2020), designed a wireless multi-point and multi-source remote monitoring system for pigsty environment by using ZigBee network topology and other technologies.

The system can quickly sense the distribution characteristics of pigsty environment parameters, but the equipment continuous working time of the system needs to be improved, and the monitor is not intelligent. However, this paper designs a pig intelligent classification monitoring system, which can not only play the role of real-time monitoring, but also identify and classify pigs, prevent pig jumping each other's behaviour, and effectively apply to agriculture. The pig intelligent classification monitoring system embedded image recognition algorithm in the image processing module, although there are many technologies applied to the detection and recognition of animal behaviour, they are not applied to the monitoring system.

Yan et al, (2020), used the improved Alexnet model for pig face recognition, which can achieve a high accuracy rate, and the recognition accuracy rate can reach 98.11%, but it has not been applied to the monitoring system, which is lack of practical application.

Zhao et al, (2018), used image processing technology to analyse the leg swing behaviour of dairy cows, and developed a limp detection system based on vision technology, which was also not used in the monitoring system and needs further exploration.

Porto S et al, (2013), used computer vision technology to study the lying behaviour of dairy cows, which showed good robustness and can accurately classify, but at the same time, it lacks the application in the monitoring system, cannot monitor in real time, and does not bring too much convenience for users. This system takes convolution neural network algorithm as the core, which has the advantages of high recognition accuracy and less time-consuming. Compared with *Wang et al, (2020),* who use multi-scale convolution network for pig individual recognition, they can only recognize the pig individual according to the facial features. When the face is completely occluded, they cannot accurately recognize the identity, and the accuracy is not high.

Li et al, (2019), use computer vision technology to recognize the pig behaviour and individual, and capture the essential features of the pig individual, which is inefficient; Based on the principle of binocular vision, *Li et al, (2018*), designed a pig size detection system. Due to the pigs' active nature, their postures often change, and the measured data have a large error. Based on this, the neural network algorithm has good feasibility.

To sum up, this paper designs a pigs intelligent classification monitoring system with convolution neural network algorithm as the core, install monitors near in the domestic pig and wild boar to each other's channel, whenever the monitor detects that a wild boar is on the way to the nest of domestic pig, our mobile phone will send out a No.1 alarm sound and mark the wild boar. At this time, it will remind the breeders to pay attention to the track of the wild boar and prevent the wild boar from entering the nest of domestic pig. In the same way, when the domestic pig is on the way to the nest of wild boar, our mobile phone will send out No.2 alarm sound and mark the domestic pig, and the breeders will pay attention to the tracks of the pig. The creation of the system to a certain extent played a role in the prevention of domestic pig and wild boar fighting, snatching food and other phenomena, even when the breeders are busy with other things, they can also know the situation of pigs in real time, which not only provides convenience for the breeders, but also ensures the healthy growth of pigs.

MATERIALS AND METHODS

EXPERIMENTAL MATERIALS

The pig intelligent classification monitoring system was tested in January 2021 at Tang County pig farm, Baoding City, Hebei Province, China. The pig farm covers an area of 6000 square meters and is divided into 22 pigsties, including 6 wild boar pigsties and 16 domestic pigsties. The wild boar breed is the second generation boar, hereinafter referred to as boar (as shown in Figure 1).

There are two kinds of domestic pigs, namely Dabai and Beijinghei, hereinafter referred to as domestic pig (as shown in Figure 2).

Wild boar nest is not far from domestic pig nest. After half a month field investigation, it is found that when the breeders do not pay attention, the wild boar will leave their own pigsty to look for food. Because the domestic pig pigsty is not far from the wild boar pigsty, it is possible that the wild boar will enter the domestic pig pigsty. At this time, there will be a fight between the wild boar and the domestic pig. To prevent this phenomenon, we installed a monitor on the channel from pigs to each other's pigsty (as shown in Figure 3).

Fig. 1 - Wild Boar Sample

Fig. 2 - Domestic Pig Samples

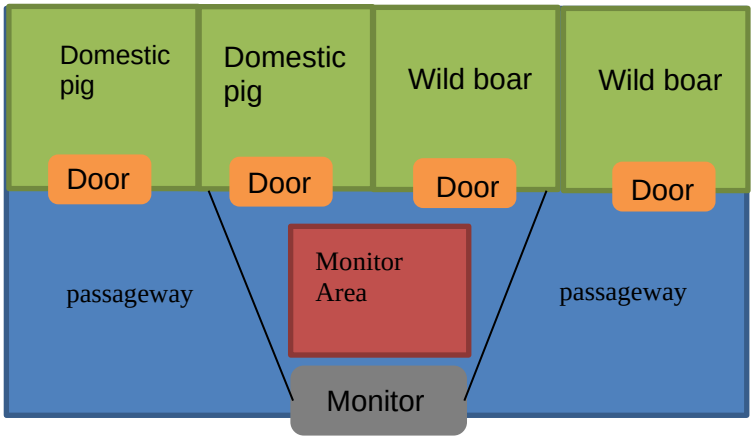

Fig. 3 - Image of Pigsty

SYSTEM DESIGN SCHEME

Overall system architecture

The overall structure of the pig intelligent classification monitoring system is shown in Figure 4. The system consists of three parts: monitoring and detection unit, information transmission system and information processing system. Among them, the monitoring and detection unit are used for image acquisition and image transmission of the channel where pigs lead to each other's pigsty. The data transmission subsystem is used to realize the transmission of network layer signal. The wired long-distance Internet communication is selected. Specifically, the embedded server is used to complete the network transmission of the data from the monitor. The information processing subsystem carries out image recognition and intelligent classification for the received image information, and specifically uses convolution neural network algorithm for pig identification, then the analysis results are transmitted to the client.

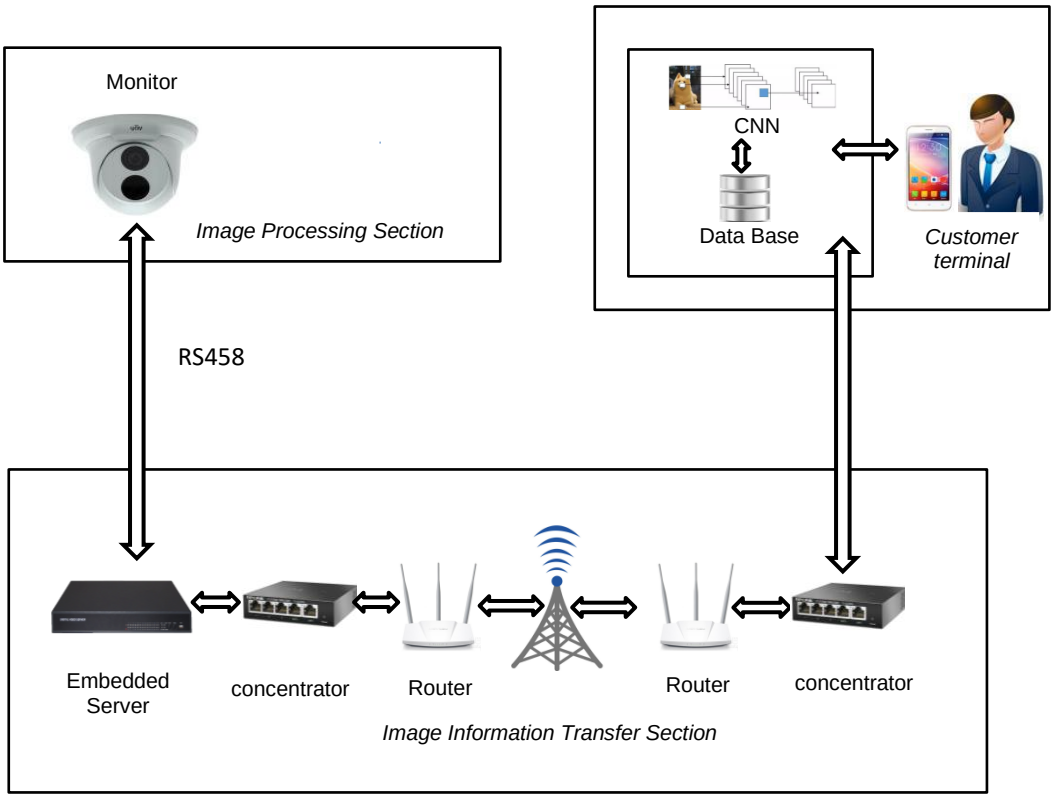

Fig. 4 - Overall Structure of Pig Identification and Classification System

System software architecture

According to the design of the software architecture of the system, the overall architecture is divided into three layers: presentation layer, business layer, data connection layer*(Lv et al, 2020).* As shown in Figure 5. The display layer is composed of front-end, and the user mobile interface is built by H5 technology; the business layer includes image recognition and processing module, alarm module and database module; the data connection layer is responsible for signal connection.

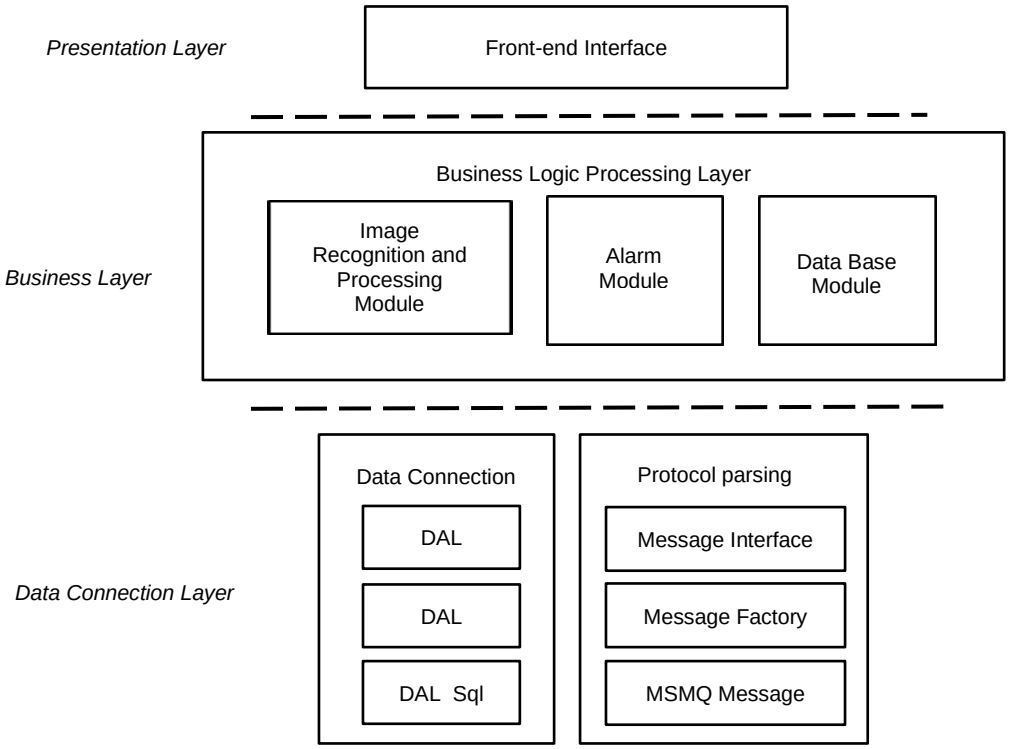

Fig. 5 - Software Overall Architecture Level

Front-end and rear-end design

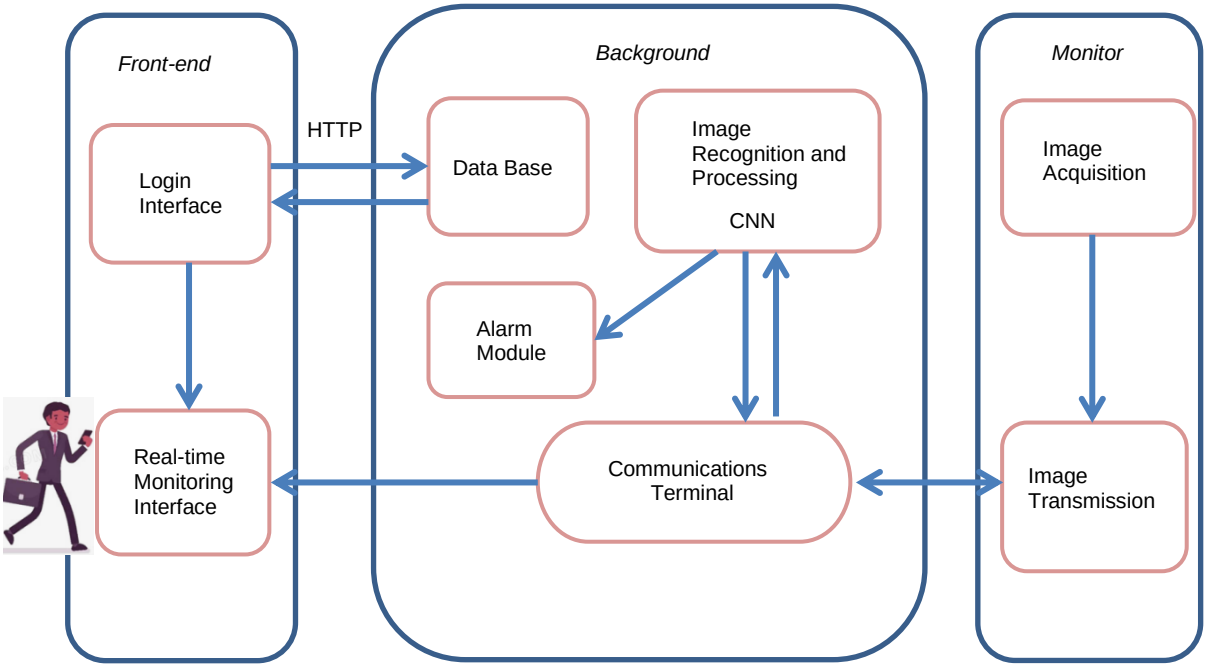

Fig. 6 - System Module Division Diagram

The system adopts C/S architecture, and the embedded server is a web server based on the embedded system, which can be accessed directly through IE browser, with slightly lower hardware requirements *(Zang et al, 2021).*

The front-end is mainly composed of login module and real-time monitoring module. The login module is presented to users in the form of login interface. The login interface is built with H5 technology, and the page layout is carried out. Elements are added to the interface to design a login interface, which includes account, password, password recovery, login and registration buttons. When the registration button is triggered, the registration interface will be presented. New users can register an account for themselves, and then the message will be sent to the database module. The real-time monitoring interface is mainly composed of channel image information from the monitor, opening the camera and closing the camera.

The back end is mainly composed of database module, image processing module and alarm module. The database module detects the data from the login module, and then feeds it back to the login interface. The user's registered account and password are stored in the database. When the user's account cannot be queried in the database, it cannot be logged in. The image processing module is based on convolution neural network algorithm, which can recognize the image information of the real-time monitoring module, and then feed back the recognition results to the alarm module. The alarm module is composed of No.1 alarm sound and No.2 alarm sound. It responds to the results processed by the image processing module and uses two kinds of alarm sound to distinguish two kinds of recognition results.

Communication between modules

This pig intelligent classification monitoring system establishes socket connection between background modules, and the background adopts Netty framework to maintain this connection *(Lv et al, 2020).* Netty is a NIO based client-side and server-side programming framework. At the same time, Netty is a high-performance event driven, asynchronous non-blocking IO (NIO) Java open source framework, which is provided by JBoss for establishing TCP and other underlying connections. Based on Netty, high-performance HTTP server can be established to rapidly develop high-performance, high reliability network server and client programs. It supports fast development, maintainable, high performance, protocol oriented server and client, avoids using the underlying API directly, and reduces the complexity of network programming *(Huang et al, 2021).* When a connection interruption is detected, the background can automatically initiate a reconnection to ensure the continuity of the connection *(Wei et al, 2020).*

SYSTEM WORKFLOW

System process overview

The pig intelligent classification monitoring system is different from the ordinary monitoring system. The system is based on CNN algorithm, so that the monitoring system can not only monitor in real time, but also remind users, which brings great convenience to users. When the monitor senses the light source, it firstly converts the light into electric charge, and then converts it into digital signal through the analog-to-digital converter chip. After compression, the digital signal is stored in the internal memory of the monitor, and then the image information can be transmitted to the embedded server through the serial port according to a certain data frame format. Finally, the embedded server is used to complete the transmission of the monitor. After the image data is transferred to the background, the background calls the image processing module to identify the image data, and returns the processed data to the front end for display *(Guo et al, 2020)*. The working process of the whole system is shown in Figure 7.

The working process of the system is as follows: firstly, the monitor collects the image of the pig's access to the other pigsty; secondly, the server pre-processes the collected image and randomly selects samples to form a random sample to ensure the credibility of the experiment *(Zhang et al, 2021)*. Thirdly, the server transfers the processed samples into the convolution neural network model for calculation and analysis to obtain the classification of the samples. Finally, when the classification is wild boar, the background is pushed to the front interface, which marks the wild boar on the channel leading to the pigsty and sends out No.1 alarm sound; When it is calculated and classified as a domestic pig, the background is pushed to the front interface, which marks the domestic pig on the channel leading to the pigsty and sends out No.2 alarm sound.

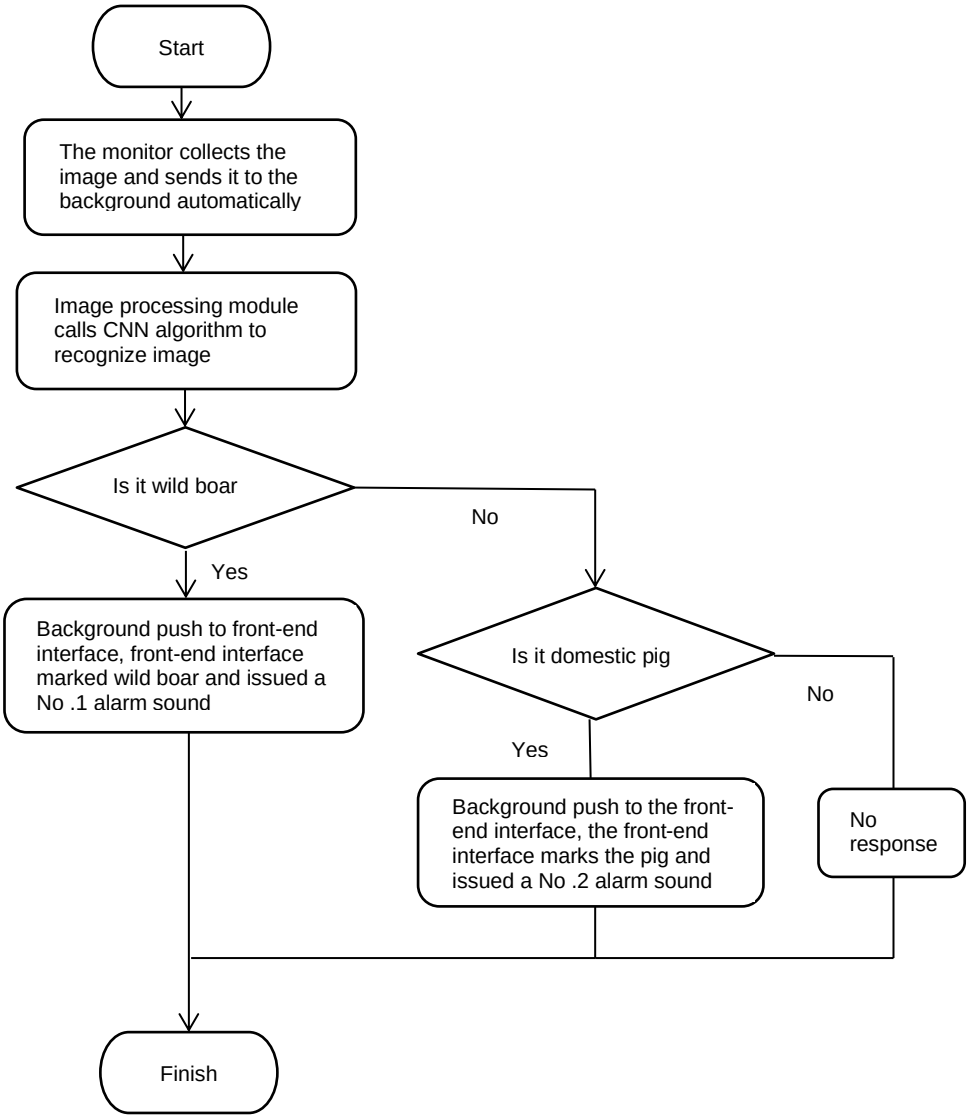

Fig. 7 - System Workflow

Core algorithm principle

In this experiment, convolution neural network algorithm is used to identify and classify wild boar and domestic pig, as shown in Figure 8. The model includes two layers of convolution layer, two layers of pooling layer, two layers of full connection layer, one layer of dropout layer and one layer of softmax layer.

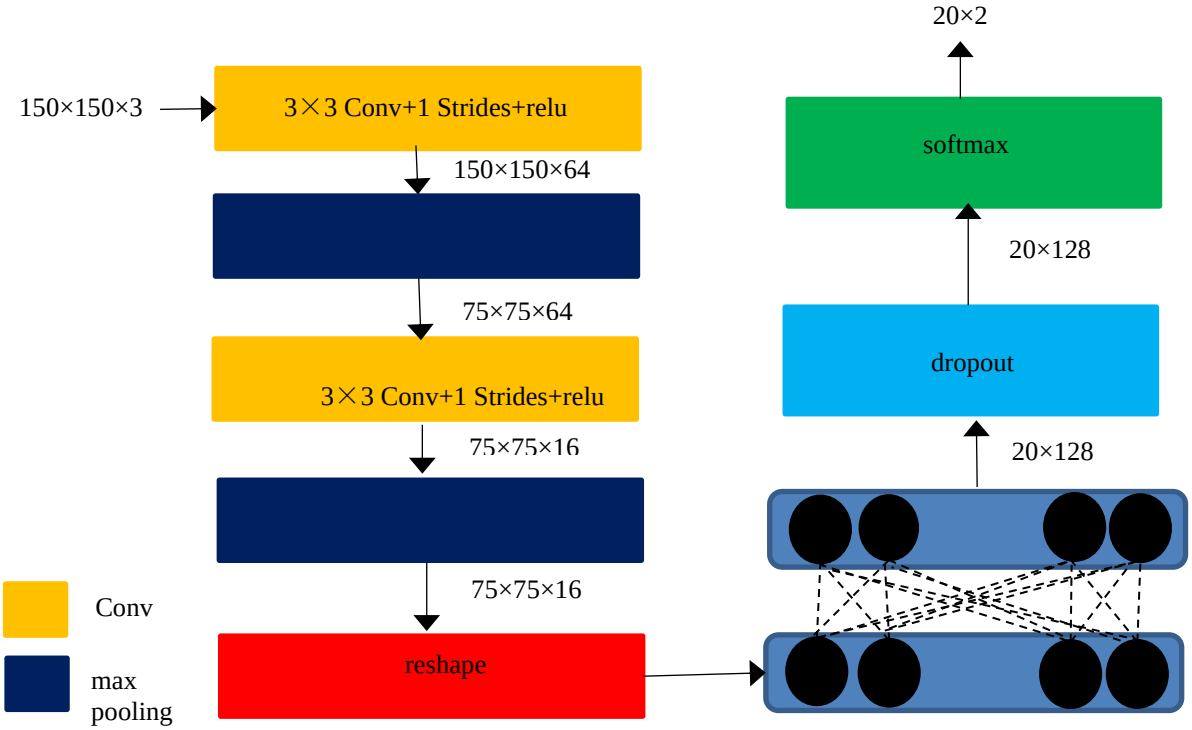

Fig. 8 - Algorithm model diagram

Convolution layer is the core of convolution neural network algorithm. In convolution layer, the preprocessed image can be extracted by the corresponding operation between filter and preprocessed image. In this model, 64 filters with 3×3 channels are set in the first layer of convolution layer, strides is 1, padding is "same", and 16 filters with 3×3 channels are set in the second layer of convolution layer, strides is 1, padding is "same".

In the two-layer convolution layer of the model, strides is set to 1 and padding is set to same. According to the parameters, the calculation formula for the size of the output image feature graph is as follows:

$$Sizeoutput = \left\lceil \frac{Sizeinput}{strides} \right\rceil \quad (1)$$

$Sizeinput$ represents the size of the input image of the convolution layer, $strides$ represents the step size, $Sizeoutput$ represents the size of the output image feature map after the convolution layer.

In the pooling layer, the max pooling method is used to extract more important features than objects. In this model, a 3×3 pooling window is selected for the first pooling layer, and the strides is 2; a 3×3 pooling window is selected for the second pooling layer, and the strides is 1.

The full connection layer is set with weight parameters, the feature can be further extracted by weight parameter. In order to ensure the nonlinearity of the model, the data is ReLU operated after each calculation to ensure that each parameter can be changed when training the model, which feature will not be biased, and the gradient will not disappear. In the full connection layer, the number of neurons will affect the quality of the trained model. Too many neurons will cause over fitting, and too few neurons will cause under fitting. In this model, 128 neurons are selected in the two full connection layers, at this time, the best model can be obtained.

The weight parameters are set in the full connection layer to further extract features. The calculation formula is as follows:

$$A = W \times X + b \quad (2)$$

A is the size of the feature map after the output of the full connection layer, W is the weight parameter, and X is the size of the feature map when the input of the full connection layer, b is the offset term.

The softmax layer sets the parameter 128×2 (in this model, the wild boar and domestic pig are identified and classified, so the category is divided into two categories). The score of each category is obtained by calculating the input data.

Algorithm workflow

The process of recognition and classification model of wild boar and domestic pig based on convolution neural network is as follows:

Set BATCH_SIZE is 20 in the model, and each time 20 images with size of 150×150 and channel of 3 are input into the convolution neural network model. In the first layer of convolution layer, the corresponding operation is performed with 64 filters with size of 3×3 and channel of 3, and the strings is set to 1. For the sake of fairness, the model can extract the features of each part of the image, using the filling model, setting padding to "same", which can make the size of the output image consistent with the size of the input image. The output data can be operated by ReLU (linear rectification function), which can ensure the nonlinearity of the model, reduce the interdependence between parameters and prevent over fitting. After the first layer of convolution, the size of the feature map is 150×150, and the channel is 64. At this time, the output image feature map is too large. In order to reduce the amount of parameters, we need to go through the pooling layer, compress the size of the feature map, and select more important features. Through the first pooling layer, the sliding window is 3×3, and the strides is 2. Through this layer, the output feature map size is 75×75, and the channel is 64. After entering the second layer of convolution layer, 16 filters with 3×3 channels and 64 channels are set up to carry out corresponding operation, and then the output data is operated by ReLU (linear rectification function). The size of the output feature map is 75×75 and the channel is 16. For the same reason, it also needs to pass through the pooling layer. In the second pooling layer, the sliding window is 3×3, and the strides is 1. In the same way as the first pooling layer, the more important features of the image are selected. Through this layer, the output feature map size is 75×75, and the channel is 16. In the full connection layer, 90000×128 weight parameters and 128 offset terms are set. At this time, the size of the output feature map is 75×75×16, and each feature map needs to be stretched into a size of 1×90000 by reshape operation. Since 20 images are input each time, the size of all feature maps is 20×90000. After the first layer of full connection layer, the size of feature map is 20×128. In order to ensure the nonlinearity of the model, after each full connection operation, it is necessary to carry out the ReLU (linear rectification function) operation. Then, a full connection operation is performed, 128×128 weight parameters and 128 offset terms are set, and the size of the output feature map is 20×128. A dropout operation of the output feature map is needed to prevent overfitting of the model, which can make the trained model have strong generalization ability. Finally, the score of each category is obtained through softmax layer.

After judging the category of pigs, the algorithm can frame the pigs in the image and locate the pigs. When it is detected that the pig is a wild boar, it will send out No.1 alarm sound, and the boar will be circled with a red box; When it is detected that the pig is a domestic pig, it will send out No.2 alarm sound, and the black domestic pig will be circled with a yellow box, and the white domestic pig will be circled with a green box. In the training model, each training can calculate the loss value of the training, optimize the loss value, make the loss value as small as possible. In this model, through the experiment, it is found that when the learning rate is set to 0.0001, after multiple training, we can get a high accuracy model.

RESULTS

Implementation of core algorithm

Figure 9 shows the change of the loss value in the process of training the model. With the increase of the number of iterations, the loss value generally changes in the direction of decreasing. By analysing the data, when the number of iterations is 641, the loss value is only 0.02, and then with the increase of the number of iterations, the loss value will not fluctuate too much.

Figure 10 shows the change of the accuracy in the process of training model. With the increase of the number of iterations, the accuracy generally changes in the direction of increase. When the number of iterations is 221, the accuracy reaches the highest. When the number of iterations increases by 511, the accuracy rate remains at 100%.

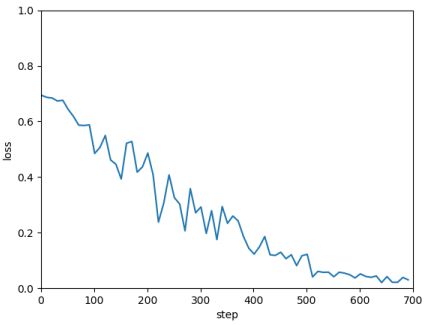

Fig. 9 - Loss-step Graph

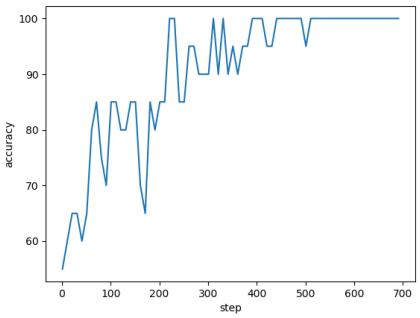

Fig. 10 - Accuracy-step Graph

Table 1

Pig identification results of test samples

Pig category	Number of test sets piece	Correctly identify quantity piece	Accuracy %
Wild boar	120	117	97.50
Domestic pig	120	116	96.67

A number of 240 randomly selected test sets (120 domestic pig test sets and 120 wild boar test sets) were input into the pig recognition and classification network. The trained pig recognition and classification network is used to detect the accuracy of the test set, and the results show that the accuracy of the network reaches 97.08%. The data show that the network has a good effect on pig recognition and classification under different light intensity.

User interface display

This pigsty intelligent classification monitoring system has good practicability, the monitor is installed near the channel that the domestic pig and the wild boar often lead to each other's pigsty, so the area irradiated by the monitor plays an important role in judging whether the wild boar and the domestic pig are likely to jump into each other's pigsty. When the breeder is indoors, he can open the mobile phone to watch whether there are pigs walking in the channel at any time.

When a black domestic pig leaves its own pigsty and goes to the direction of the wild boar house, the black domestic pig will inevitably pass through the area illuminated by the monitor. At this time, the mobile phone will send out No.2 alarm sound to remind the breeder to pay attention to the tracks of the domestic pig. At this time, the breeders can open their mobile phone and see the black domestic pig walking in the shooting channel of the monitor through their mobile phone, as shown in Figure 11, the black domestic pig is marked by a yellow box. At this time, the breeder needs to be alert to the black domestic pig, and prevents the black domestic pig from going to the wild boar's pigsty. Similarly, when a white domestic pig leaves its own pigsty and goes to the direction of the wild boar pigsty, it will send out No.1 alarm sound, as shown in Figure 12. The breeder can see the white domestic pig marked by a green box through the mobile phone.

When a wild boar leaves its own pigsty and goes to the direction of the domestic pig pigsty, as long as it passes through the area illuminated by the monitor, the mobile phone will give out No.1 alarm, and the interface shown in Figure 13 will appear on the mobile phone. The wild boar is marked with a red box. At this time, the breeders should be more vigilant, the wild boar is more ferocious and faster, so the breeders should pay more attention to it. Before the wild boar had the tendency to go to the pigsty at home, breeders arrived at the scene in advance to prevent the occurrence of pig fighting.

Fig. 11 - Black Domestic Pig

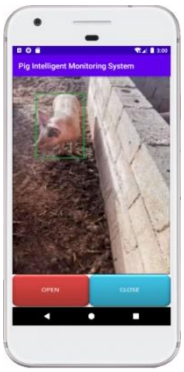

Fig. 12 - White Domestic Pig

Fig. 13 - Wild Boar

CONCLUSIONS

Aiming at the problem that the behaviour of pigs in pigsty will affect the growth of pigs, this paper studies a system based on convolution neural network algorithm to identify and detect the behaviour of pigs. The convolution neural network algorithm and the monitoring system cooperate for target recognition and detection, which can achieve the demand of accurate recognition and classification. The convolution neural network algorithm is integrated into the image processing module of the client, which can monitor the behaviour of pigs in real time and give an alarm. In addition, the system also expands other functions of the client to meet the needs of the market. Compared with the traditional method of distinguishing domestic pig and wild boar by naked eye, this method has faster detection speed, higher accuracy and greatly saves human resources. Experiments show that the accuracy can reach 97.08%. The system is of great significance to the research of real-time detection of pigs.

ACKNOWLEDGEMENT

This paper is supported by the research project of Shanxi Province excellent doctor work Award Fund (Research on model detection technology of Agricultural Internet of things, No: SXYBKY201721).

REFERENCES

[1] Guo X.L, Tao Z.J., (2020), Design of Electrical Fire Alarm Control System Based on Internet of Things. *Electronic world*, 21, 173-174.

[2] Huang Y.Z., Liu Z.Y., Qian R.X., Gu W.K., Guo Z.Y., (2021), A File Distribution Mechanism based on Netty Communication Framework. *IOP Conference Series: Materials Science and Engineering*, 1043(3).

[3] Li D., Chen Y.F., Li X.J., Pu D., (2019), Research Advance on Computer Vision in Behavioural Analysis of Pigs. *Journal of Agricultural Science and Technology*, 21, 07, 59-69.

[4] Li Z., Du X.D., Mao T.T., Teng G.H..,(2018), Pig Dimension Detection System Based on Depth Image. *Journal of Agricultural Machinery*, 4, 26-32.

[5] Lv X.D., Jiang G.H., Wang H.J., (2020), A Software Architecture Design of Intelligent Diagnosis System for Train Control Operating Data. *Technological innovation*, 17(10), 7-10+18.

[6] Porto S., Arcidiacono C., Anguzza U., Cascone G., (2013), A computer vision-based system for the automatic detection of lying behaviour of dairy cows in free-stall barns. *Biosystems Engineering*, 115, 2, 184-194.

[7] Wang R., Shi Z.F., Gao R.H., Li Q.F., (2020). Individual Identification of Pigs based on Multi-scale Convolutional Network in a Variable Environment. *Journal of Jiangxi Agricultural University*, 42, 2, 391-400.

[8] Wei J.H., Lv M., (2020), Design and Implementation of Message Push System Based on Netty Communication. *Industrial Control Computer*, 12, 33, 57-59.

[9] Weller E.J., Camerlink I., Turner P. S., Farish M. & Arnott G., (2019), Socialisation and its effect on play behaviour and aggression in the domestic pig (Sus scrofa). *Scientific Reports*, 9, 2.

[10] Wu C.H., He H.J., Xiong H.L., Xiong H.D., (2013), Design of Remote Monitoring System of Dairy Farm Based on RFID and Zigbee CC2430 Technology. *Journal of Agricultural Mechanization Researc*h, 02, 017.

[11] Yan H.W., Cui Q.L., Liu Z.Y., (2020), Pig face identification based on improved Alexnet model. *INMATEH - Agricultural Engineerin*g, 61, 2, 97-104.

[12] Zeng C., Wang C., Zhao Q.M., Wu X.H., (2016), Cowshed environment parameters monitoring system based on embedded. *Journal of Chinese Agricultural Mechanization,* 84-87.

[13] Zang S.Y., Kong L.D.,(2021), Interactive Design of Embedded System Based on Three-tier C/S Mode. *Modern electronic technology*, 1, 44, 10-13.

[14] Zeng Z.X., Dong B, Lv E.L., Xia J.J., Wu P., Shen H., (2020), Design and Experiment of Wireless Multi-point and Multi-source Remote Monitoring System for Pig House Environment. *Transactions of the Chinese Society for Agricultural Machinery*, 332-340+349.

[15] Zhang J., Dong L.Y., (2021), Image Monitoring and Management of Hot Tourism Destination Based on Data Mining Technology in Big Data Environment. *Microprocessors and Microsystems*. 80.

[16] Zhao K., Bewley J.M., He D., Jin X., (2018). Automatic lameness detection in dairy cattle based on leg swing analysis with an image processing technique. *Computers and Electronics in Agriculture*, 148, 226-236.

A GENERAL MODELLING APPROACH FOR COATED COTTON-SEEDS BASED ON THE DISCRETE ELEMENT METHOD
/
基于多目标优化的包衣棉种离散元接触参数标定

Wang Long[1, 2, 3], Hu Can[1, 2, 3], He Xiaowei[1, 2, 3], Guo Wensong[2, 3], Wang Xufeng[2, 3], Hou Shulin[1*] [1]

[1)] College of Engineering, China Agricultural University, Beijing, 100083 / China;

[2)] College of Mechanical and Electronic Engineering, Tarim University, Alar Xinjiang, 843300 / China;

[3)] Key Laboratory of Colleges & Universities under the Department of Education of Xinjiang Uygur Autonomous Region, Alar Xinjiang 843300/ China

Tel: +86 13581711364; E-mail: hsl010@126.com

DOI: https://doi.org/10.35633/inmateh-63-22

Keywords: *coated cotton seeds; discrete element; parameter calibration; optimal design*

ABSTRACT

In the current paper, a coated cotton-seed discrete element model was established. Furthermore, we designed a device for the simultaneous determination of the repose and accumulation angles, and Plackett–Burman and central composite design (CCD) tests were performed with the repose and accumulation angles as the test indexes. The static friction coefficient between seeds (SFCC) and the dynamic friction coefficient between seeds (DFCC) were observed to have a significant influence on the indexes and were thus selected for the subsequent analysis ($P < 0.05$). Analysis of variance revealed the terms of these two parameters to have a significant effect on the relative error of the repose angle (RERA) and the relative error of accumulation angles (REAA) ($P < 0.05$). A solution to the proposed mathematical model was determined via the NSGA-Ⅱ genetic algorithm and the Pareto optimal solution set was obtained. Based on multi-objective optimization, the SFCC and DFCC were determined as 0.174 and 0.068, for RERA and REAA values of 1.715% and 1.712%, respectively. Simulations were then performed using the optimal parameters. Results of the T-test demonstrated that there were no significant differences between the simulated and physical test results.

摘要

本文基于 EDEM 软件建立了包衣棉种离散元模型，设计了一种可以对物料休止角与堆积角同时进行测定的装置，通过物理试验与仿真试验对棉种接触参数进行了标定。首先，利用 Plackett-Burman 试验筛选出了对棉种休止角和堆积角有显著性影响的接触参数，为种间静摩擦系数和种间动摩擦系数；然后以休止角和堆积角相对误差为指标，对这两个参数进行最陡爬坡试验，优化其取值范围，并基于中心组合试验建立了指标与显著性参数的回归数学模型，数学模型的拟合度较好；进而采用遗传算法(NSGA-Ⅱ)进行多目标寻优，得到当种间静摩擦系数为 0.174，种间动摩擦系数为 0.068 时，棉种离散元模型的数学模型最优解较好；最后利用 T 检验得到休止角和堆积角的 P 值均大于 0.05，表明仿真试验与物理试验值差异不显著，验证了最优参数组合的可靠性。

INTRODUCTION

The rapid development of computer technology has facilitated the application of the discrete element method (DEM) in the study of agricultural bulk material. In particular, DEM can intuitively and quantitatively analyse the force and movement law of agricultural materials (*Liang et al., 2020*). For example, in the application of seed metering devices, DEM is employed to reveal the movement process and mechanisms, as well as to optimize the corresponding parameters and performance (*Gao et al., 2020; Hou et al., 2020*). The northwest region of China has become the principal cotton producing area in China, due to its special natural environment and soil conditions, obviously characterized by an arid climate, low rainfall, evaporation, and temperature difference between day and night, and long hours of sunshine. Existing cotton precision seed metering devices are prone to miss and repeat sowing, requiring farmers to supplement or thin the

[1] *Wang Long, Ph.D. Stud.; Hu Can, Ph.D. Stud.; He Xiaowei, Ph.D. Stud.; Guo Wensong, A. Prof. Ph.D.; Wang Xufeng, Prof. Ph.D.; Hou Shulin, Prof. Ph.D.;*

seedlings following sowing. In order to improve the performance of seed metering devices, several studies have adopted the discrete element method to analyse the mechanisms underlying the seed metering process and to subsequently optimize the structure (*Binelo et al., 2019*). The parameter and model accuracies play a crucial role in these studies. Previous research generally includes three-dimensional models and the characteristic and contact parameters of the material. Thus, it is necessary to reconstruct the material shape and calibrate and optimize the corresponding parameters prior to simulations (*Xue et al., 2019*).

Numerous scholars have performed research on the three-dimensional modelling and parameter calibration of crop seeds. Such work initially requires the establishment of an accurate three-dimensional seed model. This can be determined via three-dimensional software based on the seed shape and size, or reconstructed using reverse engineering technology, with the latter option proving to be more accurate and is thus widely used (*Zhou et al., 2020; Qi et al., 2019*). As the discrete element method is based on spherical particles, the discrete element seed particle model must be determined with spherical particles. The bonded particle and multi-sphere methods are commonly employed to establish discrete element particle models. The more spherical the particles, the closer the model is to the physical structure, irrespective of the method used (*Zhang et al., 2020; Yan et al., 2020*). Once the particle model is established, the parameters need to be calibrated to ensure that the simulation can truly reflect the movement process of the material and the underlying mechanisms, such that it can directly be used in simulation research. Physical and simulation tests are generally combined for the parameter calibration (*Ghodki et al., 2019; Wang et al., 2020*).

The long-term planting of cotton increases the amount of germs in the crop, while low temperatures are critical for seedling emergence. Due to this, cotton seeds in northwest China need to be coated in order to improve the germination and seedling preservation rate and to control bacteria (*Li et al., 2018*). More specifically, a seed coat agent is typically coated on the cotton seed surface. Commonly used seed coat agents include carboxin, thiram and salicylic acid. Such agents alter the surface characteristics of the cotton seeds (*Furuhata et al., 2011*). Simulation errors are typically a function of the accuracy of the model and parameters. The accurate calibration of the cotton seed model and its related parameters can greatly improve the accuracy of simulations (*Liu et al., 2016*).

In the current paper, we design a device to measure the repose and accumulation angles of coated cotton seeds, and establish a discrete element model for coated cotton seeds. A Plackett-Burman design was adopted to identify which contact parameters had a significant influence on the indexes based on the repose and accumulation angles. The steepest ascent and central composite design (CCD) were used to reduce the range of parameters. The regression mathematical model between the contact parameters and the index was then established and a genetic algorithm was employed to optimize the mathematical model, thus obtaining the optimal contact parameters. The optimal contact parameters were then used for simulation testing and the results were compared with the real physical test values to verify the simulations. The results of this paper can provide a reference for future DEM-based research on the material contact parameter settings during the movement process and mechanism of coated cotton seeds using a seed metering device.

MATERIALS AND METHODS

The test materials were selected from Zhongmian-96A coated cotton-seeds produced by Zhongmian Seed Industry in Akesu city, China in 2019. The effective components of the seed coating agent were carboxin and thiram, with a content of 200 g/L used for both agents. The density, 1,000 seed weight and average moisture content of the cotton seeds were 0.9793 g/ml, 88.14 g, and 7.3 % (w.b.), respectively.

A total of 200 cotton seeds with a regular shape were randomly selected, and the three-axis dimension was measured using a digital explicit vernier caliper (BK-318 with a 0.01 mm precision) (Figure 1). The length L, width W and thickness T of the cotton seeds were determined as 9.04±0.48 mm (mean ± standard deviation), 4.66±0.28 mm and 4.06±0.29 mm, respectively. The cotton seed volume V was determined as follows (*Baryeh and Mangope, 2003*):

$$V = \frac{\pi B^2 L^2}{6(2L - B)} \quad (1)$$

where $B=(WT)^{1/2}$, V is the volume of cotton seed (mm^3), L is the length of cotton seed (mm), W is the width of cotton seed (mm), T is the thickness of cotton seed. The volume distribution of cotton seeds is essentially normal, with mean and standard deviation values of 59.15±7.69 mm^3 (Figure 2).

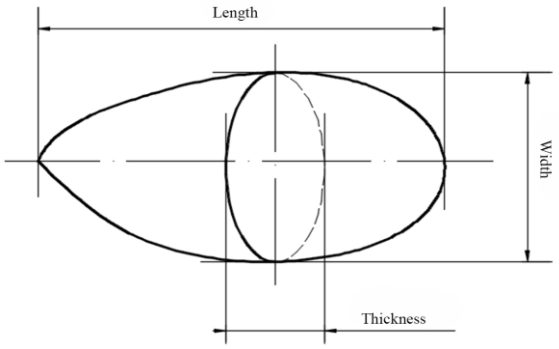

Fig. 1 - Three-dimensional dimension of cotton seed

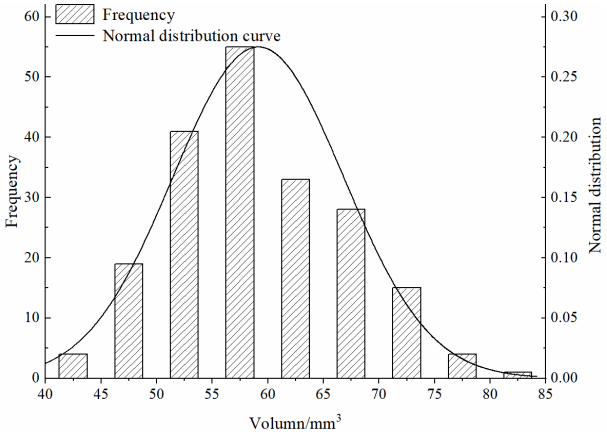

Fig. 2 - Distribution of cotton seed volume

Figure 3 presents the device used for the seed drop testing. The device is made of transparent plexiglass with a Poisson's ratio of 0.5, a density of 1180 kg/m^3, and a shear modulus of 177 MPa (*Han et al., 2018*) and is composed of a seed box, baffle, funnel and disk. The seed storage chamber is of dimensions 150 x 50 x 200 (length x width x height) and the inner diameter and height of the disc are 62 mm and 20 mm, respectively. The testing procedure can be described as follows. The baffle was inserted into the seed box prior to testing. Cotton seeds free from damage and defects were then selected and added into the seed box, filling 3/4 of the box. The upper surface of the seed layer was maintained as close to the horizontal plane as possible. The baffle was then removed, allowing the cotton seeds to slide down the opening, through the funnel and into the disc. Once the cotton population in the seed box and disk was stable, the angle between the inclined and horizontal planes in the seed box and the disk were measured, and denoted as the repose angle β and accumulation angle φ, respectively.

Fig. 3 - Experimental equipment

In order to reduce errors in the artificial measurement process, MATLAB 7.2 (MathWorks) was adopted to process the acquired images (Figure 4) using a median de-noising filter, gray processing and binary processing. The population boundary curve was obtained by extracting the population boundary contour and the least squares method was used to fit the boundary curve. The slope of the straight line was equal to the tangent value of the repose and accumulation angles, and was determined based on the slope of the straight line. The average values and variance of the actual repose angle and angles of the cotton population were determined as 34.70±0.49° and 29.05±0.32°, respectively, following 10 repetitions. The results reveal a significant difference between the repose and accumulation angles (P = 0.552), and thus they can be used as analysis indexes for the subsequent analysis.

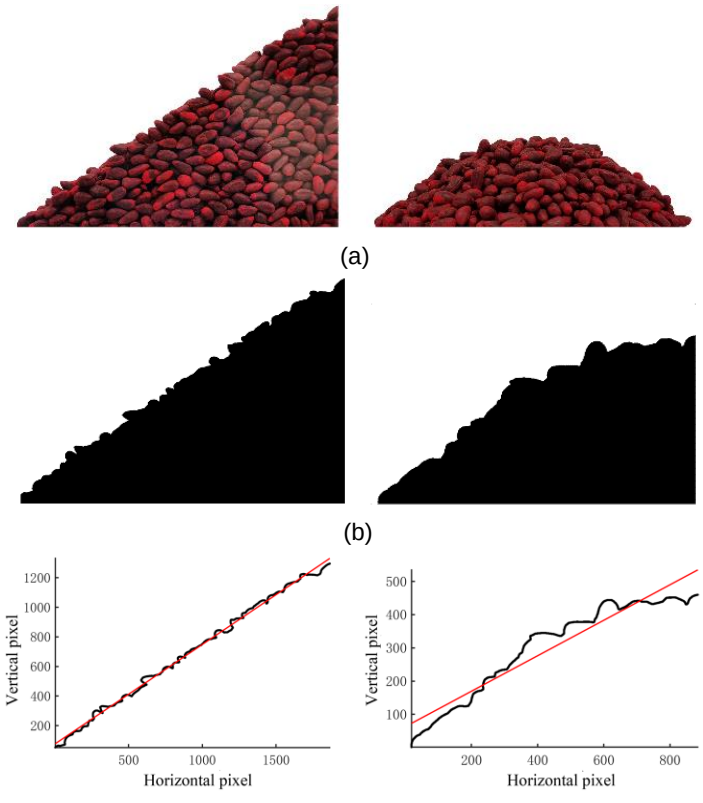

Fig. 4 - Image processing of the repose and accumulation angles

(a) image acquisition; (b) binary processing; (c) the contour curve is fitted as a straight line

The Herz-Mindlin contact model was selected for the simulation process. In order to realistically simulate the actual test process, the cotton seed particle model volume was generated according to the normal distribution of the actual cotton seed volume. The cotton seed particle quantities and test process follow those of the physical testing. The total number of cotton seed particles was 5,272, which reached a stable state in the seed box at 0.24 s. The baffle was then removed and the cotton seed particles fell into the disk through the funnel. Following the simulation test, images of the repose and accumulation angles were acquired (Figure 5) and processed in MATLAB to obtain the repose angle β' and accumulation angle φ' of the population simulation.

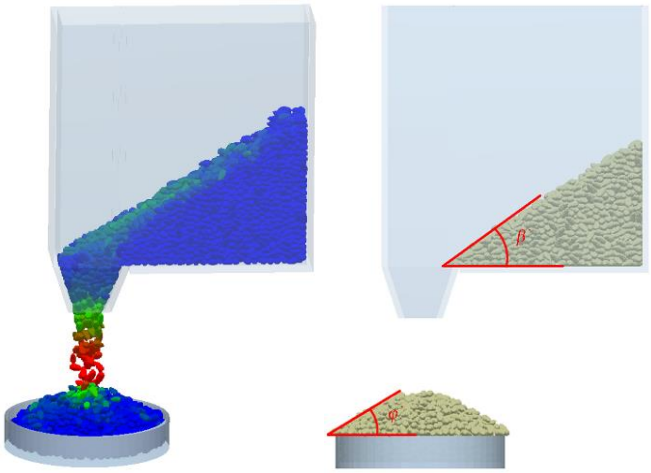

Fig. 5 - Simulated seed dropping test

The Plackett-Burman experiment was designed in Design-Expert V8.0 (Stat-Ease) and the repose and accumulation angles of the cotton population were used as the response values to identify the simulation parameters with a significant influence on the response value. A total of 8 (X_1-X_8) parameters were calibrated in the simulation test, as well as 3 virtual parameters (X_9-X_{11}).

In particular, parameters X_1-X_8 represent the high and low levels of each parameter in the form of 1 0, and - 1, are selected. A total of 12 simulation test groups were performed. Based on extensive preliminary testing and related references, 8 cotton seed simulation parameters were selected. Table 1 reports the ranges of the parameters that were calibrated.

Table 1

Parameters used in the Plackett Burman tests

Symbol	Parameter	Level		
		-1	0	1
X_1	Poisson's ratio	0.10	0.30	0.50
X_2	Shear modulus/MPa	5	9	14
X_3	Collision recovery coefficient between cotton-seed and plexiglass	0.10	0.40	0.70
X_4	Static friction coefficient between cotton-seed and plexiglass	0.30	0.50	0.70
X_5	Dynamic friction coefficient between cotton-seed and plexiglass	0.15	0.25	0.35
X_6	Collision recovery coefficient between cotton-seeds	0.20	0.40	0.60
X_7	Static friction coefficient between cotton-seeds	0.10	0.30	0.50
X_8	Dynamic friction coefficient between cotton-seeds	0.01	0.09	0.17
X_9、X_{10}、X_{11}	Virtual parameters			

Table 2 reports the design scheme and simulation results of the Plackett-Burman screening test. Design-Expert was used to analyse the variance of the simulation test results in order to obtain the influence of each calibration parameter on the simulation (Table 3). Static friction coefficient between cotton-seeds (SFCC) and dynamic friction coefficient between cotton-seeds (DFCC) are the only parameters observed to have a significant effect on the repose and accumulation angles. These two parameters were thus selected for optimization in the steepest climb and the CCD tests.

Table 2

Design scheme and results of the Plackett Burman test

No.	X_1	X_2	X_3	X_4	X_5	X_6	X_7	X_8	X_9	X_{10}	X_{11}	Repose angle / °	Accumulation angle / °
1	1	-1	-1	1	-1	-1	-1	1	-1	1	-1	29.16	22.64
2	1	1	1	-1	1	-1	-1	-1	-1	-1	1	21.18	17.62
3	-1	-1	1	1	-1	1	-1	-1	-1	-1	-1	21.08	16.27
4	1	1	-1	1	1	-1	1	-1	1	-1	-1	40.66	34.34
5	1	-1	1	-1	1	1	-1	1	1	1	-1	29.11	22.28
6	1	-1	1	1	-1	1	1	-1	1	1	1	39.06	35.55
7	-1	1	1	1	1	-1	1	1	-1	1	1	61.09	42.14
8	-1	1	-1	1	1	1	-1	1	1	-1	1	30.32	26.02
9	-1	1	-1	-1	1	1	1	-1	1	1	-1	30.90	26.80
10	1	-1	-1	-1	-1	1	1	1	-1	1	1	51.72	40.95
11	-1	1	1	-1	-1	-1	1	1	1	-1	1	52.87	44.22
12	-1	-1	-1	-1	-1	-1	-1	-1	-1	-1	-1	18.63	17.86

Table 3

Significance analysis of the Plackett-Burman test parameters

Parameter	Repose angle				Accumulation angle			
	df	Sum of square	F-value	P-value	df	Sum of square	F-value	P-value
X_1	1	3.97	0.19	0.6941	1	1.76	0.14	0.7358
X_2	1	3.32	0.16	0.7186	1	5.16	0.40	0.5710
X_3	1	44.09	2.08	0.2447	1	7.47	0.58	0.5013
X_4	1	23.98	1.13	0.3653	1	4.35	0.34	0.6013
X_5	1	2.60	0.12	0.7494	1	10.49	0.82	0.4327
X_6	1	37.17	1.76	0.2771	1	1.62	0.13	0.7463
X_7	1	957.47	45.22	0.0067**	1	509.29	39.66	0.0081**
X_8	1	570.59	26.95	0.0139*	1	206.83	16.11	0.0278*

*Note:** and * indicate significance at P < 0.01 and P < 0.05, respectively.*

Following the Plackett-Burman screening test results, the relative errors of the repose angle (RERA) and the relative errors of the accumulation angle (REAA) were taken as the objectives. Moreover, during the simulation tests, SFCC X_7 and DFCC X_8 were gradually increased based on a predetermined step size, while the remaining parameters were set as intermediate values.

RERA Y_1 and REAA Y_2 were obtained as follows:

$$Y_1 = \frac{|\beta_0 - \beta'|}{\beta_0} \times 100\% \quad (2)$$

$$Y_2 = \frac{|\varphi_0 - \varphi'|}{\varphi_0} \times 100\% \quad (3)$$

Figure 6 presents the experimental scheme and results of the steepest ascent experiment. The RERA and REAA are observed to initially decrease and subsequently increase with increasing SFCC X_7 and DFCC X_8, respectively. The RERA and REAA values determined in the test, when the SFCC and DFCC were 0.2 and 0.05 respectively, exhibit the lowest relative errors. Thus, test was selected as the central point and set as the medium level, while tests 1 and 3 were set as the low and high levels, respectively for the CCD simulation test.

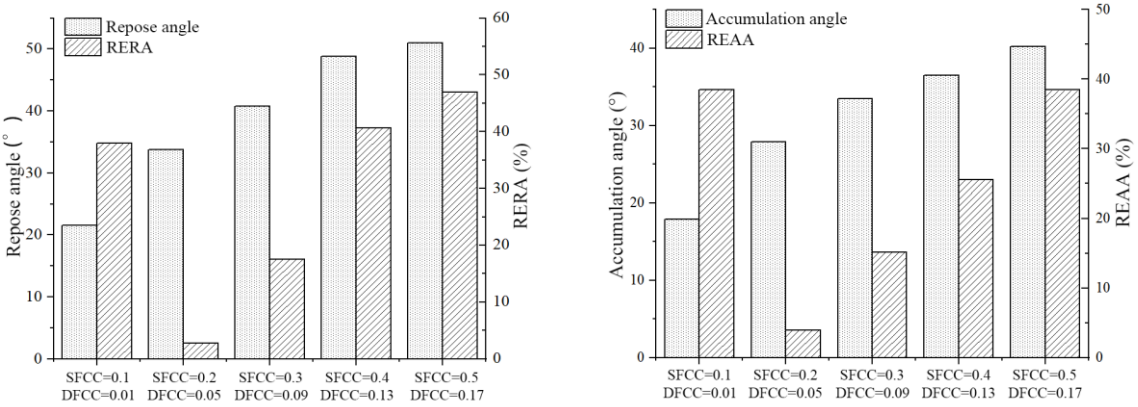

(a) (b)

Fig. 6 - Design scheme and results of the steepest ascent experiment under different parameters.
(a) Repose angle and RERA; (b) Accumulation angle and REAA.

Table 4

Simulation test factor code

Code	SFCC X_7	DFCC X_8
-1.4142	0.1	0.01
-1	0.13	0.02
0	0.2	0.05
1	0.27	0.08
1.4142	0.3	0.09

The results of the steepest climbing test (Figure 8) determined SFCC X_7 and DFCC X_8 as the experimental factors for the CCD, and RERA and REAA as the experimental indexes. Table 4 presents the test factor coding. A total of 13 tests were performed, with the details reported in Table 5.

Table 5

Design scheme and results of the central composite test

Test No.	X_7	X_8	Repose angle/°	RERA/%	Accumulation angle /°	REAA/%
1	1(0.27)	1(0.08)	37.66	8.53	31.44	8.23
2	1.414(0.3)	0(0.05)	38.29	10.36	31.75	9.32
3	1	-1	37.34	7.61	30.60	5.36
4	0(0.2)	0	35.22	1.52	29.77	2.51
5	0	1.414(0.09)	36.02	3.81	29.74	2.38
6	0	0	35.45	2.16	29.41	1.24
7	0	0	35.14	1.28	28.22	2.85
8	-1(0.13)	-1(0.02)	31.90	8.07	26.77	7.84
9	-1.414(0.1)	0	32.79	5.48	27.50	5.32
10	0	-1.414(0.01)	33.00	4.88	27.92	3.89
11	-1	1	33.72	2.82	28.40	2.24
12	0	0	33.81	2.56	28.50	1.89
13	0	0	34.17	1.53	28.41	2.18

Note: Bracketed numbers denote the test factor level values

Thus far, we selected RERA Y_1 and REAA Y_2 as the response values, and SFCC X_7 and DFCC X_8 as the variables, resulting in a multi-objective constrained optimization problem. In contrast to single-objective optimization problems, multi-objective optimization problems do not have a unique solution, but rather an optimal solution set denoted as the Pareto optimal solution. The NSGA-Ⅱ genetic algorithm is a popular multi-objective genetic algorithm (GA) that employs a fast non-inferior hierarchical sorting mechanism. Its advantages include a fast running speed and the ability to accurately approximate the Pareto optimal solution. Furthermore, by introducing the congestion degree and congestion degree comparison operator, the uniformity of the Pareto optimal solution dispersion is guaranteed. In this paper, the GA Pareto score, initial population size and genetic algebra were set to 0.3, 200, and 600, respectively.

RESULTS AND DISCUSSION

Multiple regression fitting was performed based on the test results and the test data (Table 5). The regression models of the effect of SFCC X_7 and DFCC X_8 on RERA Y_1 and REAA Y_2 are described as follows:

$$Y_1=36.50-277.17X_7-329.45X_8+734.52X_7X_8+655.36X_7^2+1581.94X_8^2 \quad (4)$$

$$Y_2=35.20-262.40X_7-301.24X_8+853.57X_7X_8+587.09X_7^2+1038.06X_8^2 \quad (5)$$

Table 6 reports the significance test results of the regression models. The fitting degrees of both models are observed to be highly significant ($P < 0.01$). The first term (X_8) of DFCC exerts a significant effect on RERA ($P < 0.05$), while the other terms have a highly significant effect on RERA ($P < 0.01$). The first (X_8) and quadratic (X_8^2) terms of DFCC X8 have a significant effect on REAA ($P < 0.05$), while the remaining terms have a highly significant effect on REAA ($P < 0.01$). This indicates that the primary, interaction and quadratic terms of SFCC X_7 and DFCC X_8 exert a significant influence on RERA and REAA. Furthermore, a quadratic relationship is identified by the influence of test factors on the response value. The *P*-values of the loss fitting item are determined as 0.2197 and 0.3690 for RERA and REAA respectively, revealing the lack of significance between these two variables. This demonstrates that there are no other factors affecting the indicators for both models. The goodness of fit (R^2) of the two regression equations were determined as 0.95 and 0.97, respectively. This indicates the strong fit between the predicted and actual values and the ability of the independent variable to explain the dependent variable to a higher degree.

Table 6

Regression analysis of variance for models RERA and REAA

Source	RERA				REAA			
	Sum of square	df	F-value	P-value	Sum of square	df	F-value	P-value
Model	111.12	5	47.98	< 0.0001**	85.29	5	38.68	< 0.0001**
X_7	18.46	1	39.85	0.0004**	10.50	1	23.82	0.0018**
X_8	4.27	1	9.21	0.0190*	2.96	1	6.71	0.0359*
X_7 X_8	9.52	1	20.55	0.0027**	17.94	1	40.66	0.0004**
X_7^2	71.74	1	154.88	< 0.0001**	53.20	1	120.63	< 0.0001**
X_8^2	14.10	1	30.44	0.0009**	3.15	1	7.14	0.0319*
Residual	3.24	7			3.09	7		
Lack of fit	2.11	3	2.50	0.2197	1.57	3	1.38	0.3690
Pure Error	1.13	4			1.51	4		
Cor Total	114.37	12			88.38	12		

*Note: ** and * indicate significance at P < 0.01 and P < 0.05, respectively*

The experimental data was then processed by Design-Expert V8.0 to determine the response surface of the effect of SFCC X_7 and DFCC X_8 on RERA Y_1 and REAA Y_2. Figure 7 presents the interaction effect between the two influence parameters via the response surface. Stronger effects of SFCC X_7 and DFCC X_8 resulted in an initial decrease and subsequent decrease in the RERA Y_1 of the REAA Y_2. In addition, SFCC X_7 and DFCC X_8 values between 0.15-0.23 and 0.04-0.07 resulted in relatively small values of RERA and REAA.

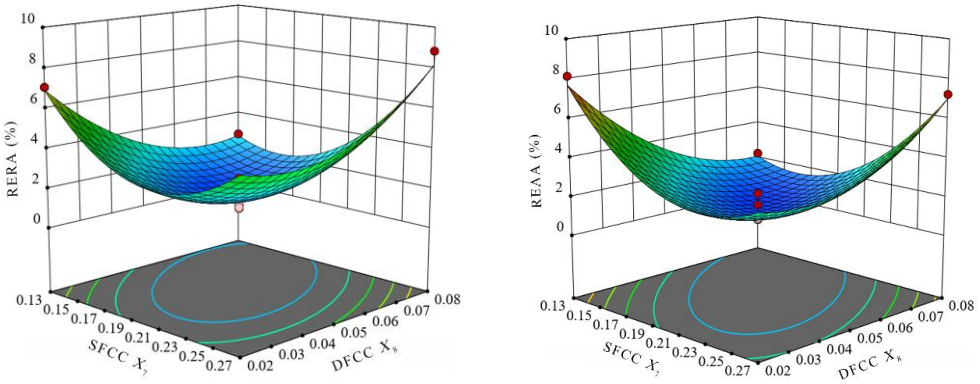

Fig. 7 - Influence of interaction between SFCC and DFCC on RERA and REAA

(a) Influence of interaction between SFCC and DFCC on RERA; (b) Influence of interaction between SFCC and DFCC on REAA

In order to minimize RERA and REAA, SFCC and DFCC were taken as the optimization objects based on the climbing test results (Table 3), with values of 0.1-0.3 and 0.01-0.09, respectively. The objective and constraint functions of the final optimization problem are described as follows:

$$\begin{cases} \min(Y_1(X_7, X_8), Y_2(X_7, X_8)) \\ \text{s.t.} \begin{cases} 0.1 \le X_7 \le 0.3 \\ 0.01 \le X_8 \le 0.09 \end{cases} \end{cases} \quad (6)$$

Figure 8 presents the Pareto optimal solution set obtained by NSGA - II. It is impossible to simultaneously achieve the optimal solution for each objective under the multi-objective optimization problem. Therefore, REAA increases as RERA is reduced. Under the condition of two objectives, SFCC is determined as 0.174 and DFCC as 0.068, with RERA and REAA as 1.715% and 1.712%, respectively.

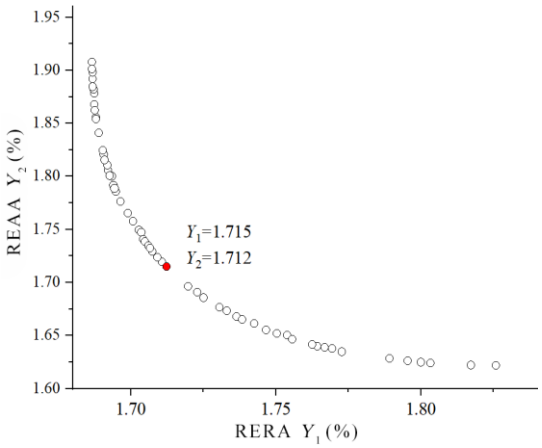

Fig. 8 - Pareto optimal solution set curve, the red data point is the optimal solution

We then verified that the optimal parameters satisfy the test results. SFCC and DFCC were set as 0.174 and 0.068, respectively and the other non-significant parameters were taken as intermediate levels. Poisson's ratio, the shear model, and the recovery coefficient of collision between cotton-seeds were set as 0.3, 9 MPa and 0.4, while the recovery, friction and dynamic friction coefficients of cotton-seed and plexiglass were set as 0.4, 0.5 and 0.25, respectively. These parameters were imported into EDEM for the simulations in order to obtain the contour comparison of the repose and accumulation angles between the simulation and actual tests (Figures 9 and 10, respectively). The contour lines of the simulation and actual tests are in agreement. The average repose and accumulation angles were determined as 34.07° and 28.55°, respectively. The T-test results of the test samples determined P-values of 0.5516 and 0.7432 for the repose and accumulation angles respectively, both of which are greater than 0.05. Furthermore, the results demonstrate that the repose and accumulation angles derived via the simulation are not significantly different to the actual physical test values.

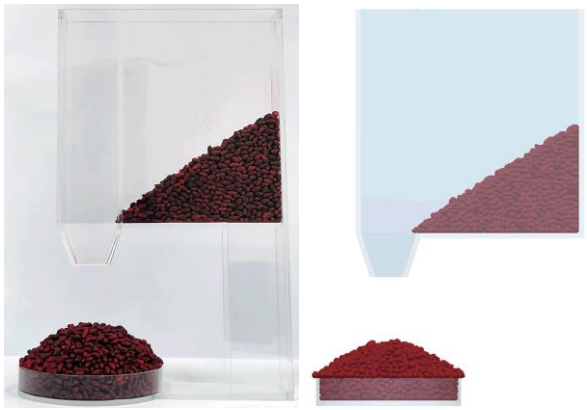

(a) (b)

Fig. 9 - Experimental results

(a) Physical experiment; (b) Simulation experiment

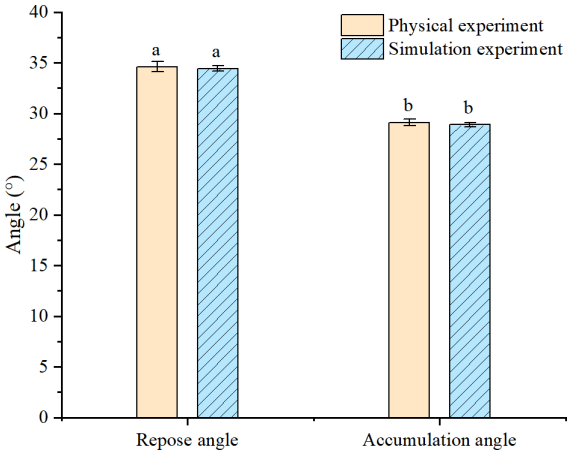

Fig. 10 - Verification of discrete element simulation

CONCLUSIONS

A device was designed to obtain the repose and accumulation angles of particle materials. The actual repose and accumulation angles of the Zhongmian-96A coated cotton seed were measured as 34.70° and 29.05°, respectively. A Plackett-Burman screening test was carried out with the repose and accumulation angles as the test indexes. The parameters SFCC and DFCC were observed to have a significant influence on the index. The CCD was then adopted by taking these two parameters as the experimental factors and RERA and REAA as the indicators. Analysis of variance revealed the first, interaction and quadratic terms of the two test parameters to have significant effects on RERA and REAA ($P < 0.05$). Multiple regression fitting of the test data was applied to determine the regression equation of the two indexes, with goodness of fit (R^2) values of 0.95 and 0.97, respectively. This reveals the strong fitting degree for both equations. The minimum values of RERA and REAA were taken as the optimization objectives, and SFCC and DFCC as the optimization objects. The NSGA - Ⅱ genetic algorithm was employed to solve the multi-objective optimization of the mathematical model, outputting the Pareto optimal solution set. Considering the two optimization objectives, SFCC, DFCC, RERA and REAA were determined as 0.174, 0.068, 1.715% and 1.712%, respectively. A simulation test was performed to verify the test results based on the parameters of the optimal solution. The results demonstrate that there are no significant differences between the repose and accumulation angles of the simulation and physical test results, indicating the high reliability of the optimal combination of the discrete element simulation parameters.

It should be noted that the DEM parameters of coated cotton seeds obtained in this study were calibrated for specific moisture content and under laboratory conditions. In further research, the relationship between DEM parameters of coated cotton seed and moisture content should be established, the contact parameters of cotton seed and different materials should be researched, and the influence of agricultural granule materials under actual working conditions should be considered. By exploring the contact behaviour between particle flow and mechanical parts, the DEM input parameters calibrated in this study can provide a reference for the design and development of cotton seeder.

ACKNOWLEDGEMENT

This research was supported by the National Natural Science Foundation of China funded by the Chinese government (11562019); and the President fund by the Tarim University (TDZKQN201803).

REFERENCES

[1] Baryeh, E., Mangope, B. (2003). Some physical properties of QP-38 variety pigeon pea. *Journal of Food Engineering*, 56: 59-65.

[2] Binelo, M., Delima, R., Khatchatourian, O., et al, (2019). Modelling of the drag force of agricultural seeds applied to the discrete element method. *Biosystems Engineering*, 178: 168-175.

[3] Furuhata, M., Ohsumi, A., & Chosa, T. (2011). Hardness, colour and germination characteristics of rice seed iron-coated to avoid bird damage-seed pretreatment, type and amount of coating material. *Japanese Journal of Crop Science*, 80: 302-311.

[4] Gao, X., Zhou, Z., Xu, Y., et al, (2020). Numerical simulation of particle motion characteristics in quantitative seed feeding system. *Powder Technology*, 367, 643-658.
[5] Ghodki, B., Patel, M., Namdeo, R., et al, (2019). Calibration of discrete element model parameters: soybeans. *Computational Particle Mechanics*, 6: 3-10.
[6] Han, D., Zhang, D., Jing, H., et al, (2018). DEM-CFD coupling simulation and optimization of an inside-filling air-blowing maize precision seed-metering device. *Computers and Electronics in Agriculture*, 150: 426-438.
[7] Hou, Junming, Zhu, Hongjie, Li, J., et al, (2020). Analysis and optimization on the process of adjustable double drum castor shelling based on discrete element method. *INMATEH-Agricultural Engineering*, 62(3), 289-298.
[8] Li, X., Yan, Q., Li, C., et al, (2018). Seed coating on cotton seedling cold tolerance control and screening of cold resistant seed coating agent. （种衣剂对棉花幼苗耐寒性的观测及耐寒种衣剂筛选）*Journal of China Agricultural University*, 23: 38-47.
[9] Liang, R., Chen, X., Jiang, P., et al, (2020). Calibration of the simulation parameters of the particulate materials in film mixed materials. International *Journal of Agricultural and Biological Engineering*, 13: 29-36.
[10] Liu, F., Zhang, J., Li, B., et al, (2016). Calibration of parameters of wheat required in discrete element method simulation based on repose angle of particle heap. （基于堆积试验的小麦离散元参数分析及标定）*Transactions of the Chinese Society of Agricultural Engineering*, 32: 247-253.
[11] Qi, X., Hu, T., Wang, Y., et al, (2019). Physical characteristics analysis and discrete element modelling of carrot seeds. *International Agricultural Engineering Journal*, 28: 236-243.
[12] Wang, S., Hu, J., Ji, J., et al, (2020). Experimental Study and Computer Simulation of Compression Characteristics and Crushing of Chinese Cabbage Seeds. *Applied Engineering in Agriculture*, 36: 815-828.
[13] Xue, P., Xia, X., Gao, P., et al, (2019). Double-setting seed-metering device for precision planting of soybean at high speeds. *Transactions of the ASABE*, 62: 187-196.
[14] Yan, D., Yu, J., Wang, Y., et al, (2020). A general modelling method for soybean seeds based on the discrete element method. *Powder Technology*, 372: 212-226.
[15] Zhang, H., Li, Y., Xu, C., et al, (2020). Optimization research of fertilizer guiding mechanism based on the discrete element method. *INMATEH-Agricultural Engineering*, 60(1), 275-286. doi:10.35633/inmateh-60-31
[16] Zhou, L., Yu, J., Wang, Y., et al, (2020). A study on the modelling method of maize-seed particles based on the discrete element method. *Powder Technology*, 374: 353-376.

EFFECTIVE PROFILE ESTIMATION FOR TRACTOR DYNAMICS ON AGRICULTURAL TERRAINS
/
基于拖拉机动力学特性的农田地面有效不平度估计

Wang Lijuan, Yan Jianguo*, Xie Shengshi, Wang Chunguang
Inner Mongolia Agricultural University, College of Mechanical and Electrical Engineering, Hohhot, China
Tel: +86 13624713647; E-mail: yanyjg@126.com
DOI: https://doi.org/10.35633/inmateh-63-23

Keywords: *Effective profiles, Independent component analysis, Agricultural terrain roughness, Tractor dynamics*

ABSTRACT

For tractor operation on deformable terrains, accurate terrain profiles are critically needed to determine the dynamic tractor response, which is affected by the terrain roughness. Effective profiles for tractors operating on agricultural terrains were identified in this study. A novel technique, called independent component analysis (ICA), was used to estimate the effective profiles. ICA can use a known system dynamic response (observed signals) to identify road-induced excitation. In this context, tractor wheel vibration signals were used as observed signals, and the ICA method was used to estimate the source signals, which are the effective profiles of the terrain. The proposed approach was validated by comparing the estimated profiles with those measured by a profiling apparatus in the time and frequency domains. The calculated root mean square error RMSE and the relative error E_f between the measured and estimated profiles showed that the proposed approach can be used to accurately estimate road profiles. A group of grass-field roughness data was taken as an example to compare the characteristics of the original and effective profiles, and the parameters of the effective profiles, such as the RMS, roughness index C and waviness W were found to noticeably change during the interaction between the tractor wheel and the terrain soil.

摘要

拖拉机在可变形地面上运行时，准确了解地面不平度特征是研究受地面不平激励的拖拉机动态响应的关键因素。本文研究拖拉机在农田地面上作业过程中地面有效不平度的识别问题，采用独立分量分析（ICA）这种新方法来估计农田地面的有效不平度，通过系统的动态响应（观测信号），ICA 可识别路面的不平激励源。为此，以拖拉机车轮振动信号为观测信号，采用 ICA 方法对地面有效不平度的源信号进行估计，为了验证该方法的有效性，在时域和频域将估计的不平度与通过不平度测试装置实测的不平度进行了比较，计算实测不平度与估计不平度之间的均方根误差 RMSE 和相对误差 E_f，结果可知该方法能很好地估计地面不平度。以一组田间草地不平度数据为例，通过比较草地原始不平度与有效不平度特征可知，在拖拉机车轮与地面土壤相互作用过程中，有效不平度特征参数 RMS、不平度系统 C 和频率指数 W 均发生了明显的变化。

INTRODUCTION

Agricultural tractors typically operate on rough field terrain, and the terrain roughness generates particularly noticeable vibrations. Severe vibration affects the work efficiency and service life of a tractor, increases the compaction of agricultural field soil, and gravely endangers the health of the tractor driver (*Becker et al, 2014; Cutini et al, 2017; Gialamas et al, 2016*). Therefore, a slow velocity is typically used in the design of agricultural tractors to reduce the magnitude of vibrations and thereby improve ride comfort and handling. To analyse terrain surface roughness as an excitation source for tractor dynamics, the surface profiles on which agricultural tractors usually operate need to be investigated. However, measured surface profiles usually cannot be directly used as the input excitations in a tractor vibration analysis. The vibration from tractors travelling on soft terrain surface may be significantly modified by the dynamic interaction between the tractor with the soil, mainly because of energy losses from soil compaction and elastic waves (*Hildebrand et al, 2008*).

Determining the tractor dynamic response on deformable terrain requires accurate terrain profiles. Previous studies have shown that the displacement excitations of tractor vibration while traversing soft terrain are not original, but effective profiles of the terrain surface that is, the equivalent excited displacements of the terrain that cause the tractor wheels to jump up and down along the longitudinal plane (*Fassbender et al, 1997;*

Liu et al, 1999). The effective profile is an intermediate variable in the interaction process between tractor the wheel and the terrain soil. Therefore, a considerable number of studies have been performed to develop terramechanics models considering the terrain surface roughness, soil properties, wheel load, tire size and pressure, tread pattern and other factors for off-road applications (*Taheri et al, 2015; He et al, 2018*).

A framework for terrain profile estimation is developed in this study for tractors operating on agricultural terrains. Previous studies have been based on steady-state tire operation, linearized classical terramechanics models, or on computationally expensive algorithms that are not suitable for real-time estimation (*Dallas et al, 2020*). To address these shortcomings, a novel technique called independent component analysis (ICA) is used in this study to extract effective profiles for terrains that affect tractor dynamics. The ICA does not require a long computation time and is easy to use. This technique only requires the dynamic responses of the studied system, as collected by sensors, such as accelerometers and the suspension deflections. A related study was carried out to estimate the road profiles that affect vehicles by using the ICA technique, showing that the ICA can adequately identify road disturbances (*Ben Hassen et al, 2017*). Another study showed that the ICA can be used to accurately estimate road profiles both in the time and frequency domains, even in the presence of payload or speed variations (*Chaabane et al, 2019*). However, no studies have been performed thus far on identifying effective profiles for vehicles operating on deformable terrains. Experimental validation of application of the ICA technique to this research field is essential.

MATERIALS AND METHODS

Independent component analysis (ICA)

The Independent component analysis (ICA) is based on blind source separation (BSS). This method consists of recovering source signals knowing based only on a mixture of observed signals (*Ben Hassen et al, 2017*). The ICA uses the dynamic responses of the system (observed signals) to identify road excitation. In this paper, the tractor wheel response (vibration) signals are regarded as observed signals, and the effective terrain profiles produced by the interaction between the tractor wheel and the terrain soil are regarded as the source signals. The problem of using response signal analysis to determine the effective profiles of the terrain is equivalent to using ICA to extract the source signals from the observed signals.

Figure 1 is a schematic of the ICA procedure.

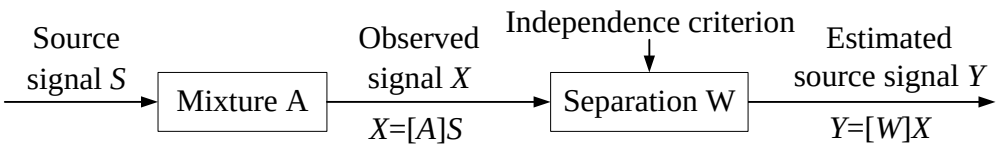

Fig. 1 - Schematic of ICA procedure

Within the ICA method, the observed signals $\{X(t)\}$ can be described as follows:

$$\{X(t)\} = [A]\{S(t)\} \tag{1}$$

where $\{X(t)\}$ and $\{S(t)\}$ represent signals observed by sensors and the source signals, respectively, and $[A]$ is the mixing matrix.

$$\{X(t)\} = \begin{bmatrix} x_1(t) \\ x_2(t) \\ \text{M} \\ x_n(t) \end{bmatrix},\ A = \begin{bmatrix} a_{11} & a_{12} & \text{L} & a_{1n} \\ a_{21} & a_{22} & \text{L} & a_{2n} \\ \text{M} & \text{M} & \text{O} & \text{M} \\ a_{n1} & a_{n2} & \text{L} & a_{nn} \end{bmatrix},\ \{S(t)\} = \begin{bmatrix} s_1(t) \\ s_2(t) \\ \text{M} \\ s_n(t) \end{bmatrix}$$

The source separation principle consists of determining a separating matrix $[W]$ to estimate the source signals $\{Y(t)\}$ as follows:

$$\{Y(t)\} = [W]\{X(t)\} \tag{2}$$

where $[W]$ denotes the separating matrix and $\{Y(t)\}$ denotes the vector of source signals.

$$\{Y(t)\} = \begin{bmatrix} y_1(t) \\ y_2(t) \\ \text{M} \\ y_n(t) \end{bmatrix}, \; W = \begin{bmatrix} w_{11} & w_{12} & \text{L} & w_{1n} \\ w_{21} & w_{22} & \text{L} & w_{2n} \\ \text{M} & \text{M} & \text{O} & \text{M} \\ w_{n1} & w_{n2} & \text{L} & w_{nn} \end{bmatrix}$$

The key task in the ICA method is to identify the separating matrix $[W]$ to estimate the source signals $\{Y(t)\}$.

Assumptions and pretreatments of ICA

To find the estimated sources, some assumptions must be satisfied to ensure that the source separation procedure is effective (*Akrout et al, 2012*).

The first hypothesis is that the components of source signals are statistically independent of each other. In fact, the source signals must be uncorrelated since the hypothesis is respected. Two signals s_1 and s_2 are uncorrelated if and only if their covariance is equal to zero. Then, the following relation can be written (*Hyvärinen and Oja, 2000*):

$$Cov(s_1, s_2) = E(s_1, s_2) - E(s_1)E(s_2) = 0 \tag{3}$$

where:

$Cov(s_1, s_2)$ is the covariance of signals s_1 and s_2. $E(s)$ denotes the variance of the variable s.

The second hypothesis required by the ICA is the non-Gaussianity of the sources. The normalized kurtosis function is commonly used to measure the non-Gaussianity and can be expressed as follows (*Akrout et al, 2012*):

$$Kurt(s) = E\{s^4\} - 3(E\{s^2\})^2 \tag{4}$$

When $Kurt(s) > 0$, the signal s is super-Gaussian; when $Kurt(s) < 0$, the signal s is sub-Gaussian; when $Kurt(s)=0$, the signal s is Gaussian; the stronger the non-Gaussianity of the signal s is, the farther the value of $Kurt(s)$ is from 0.

The final hypothesis is that the number of observed signals is more than or equal to the number of source signals.

To extract different sources from an unknown mixture, pretreatments of the observed signals is required for the ICA. These pretreatments are centering and whitening. Centering corresponds to subtracting the mean vector $E(X)$ of a signal and is expressed as follows:

$$\bar{X} = \{X\} - E(X) \tag{5}$$

The ICA algorithm exhibits higher convergence for whitened observations. The measured signals $\{X\}$ are transformed to white signals $\{\tilde{X}\}$ with uncorrelated components and a variance of unity (*Hyvärinen and Oja, 2000*):

$$\{\tilde{X}\} = [M]\{X\} \tag{6}$$

Here, $[M]$ is the whitening matrix determined by the eigenvalue decomposition of the observed signal covariance matrix:

$$\{M\} = [D]^{-1/2}[U]^T \tag{7}$$

where $[U]$ is the orthogonal eigenvector matrix and $[D] = \text{diag}(d_1, d_2, ..., d_n)$ is the eigenvalue diagonal matrix.

ICA algorithm

After the necessary pretreatments have been performed, the recovered signal can be separated. Note that the separating matrix $[W]$ must satisfy the criterion of following a non-Gaussian distribution.

Therefore, the kurtosis function defined by Zarzoso and Comen must be maximized as the normalized fourth-order marginal cumulates (*Zarzoso and Comon, 2010*):

$$K(w)=\frac{E\left\{|y|^4\right\}-2E^2\left\{|y|^2\right\}-\left|E\left\{y^2\right\}\right|^2}{E^2\left\{|y|^2\right\}} \quad (8)$$

After the first column of the separating matrix $[W]$ has been determined, the ICA uses deflation to extract the estimated sources. Therefore, each source is selected once by multiplication by the exact factor (*Zarzoso and Comon, 2010*).

Application of the ICA for the estimation of effective profiles

The ICA analysis is used in this paper is to identify effective profiles for tractors operating on agricultural terrains. The original surface profiles of nondeformable roads are considered effective profiles in vehicle dynamic analysis (*Pacejka, 2012*). Therefore, the proposed approach can be validated by comparing the estimated profiles identified by the ICA method with the profiles measured by a profiling apparatus during tractor travel on hard roads.

Previous studies have laid a foundation for the validating the approach proposed in this study. A profiling apparatus for measuring agricultural terrain profiles was designed in a previous study (*Yan et al, 2019*). The profiling apparatus was mounted on the front counterweight of a tractor, as shown in Figure 2, and the terrain surface profiles were measured dynamically for parallel tracks during tractor driving. Details on the testing and analysis of agricultural terrain profiles can be found in *Wang et al (2020*), in which the profiling tests were carried out in a field road, a grass field and a corn stubble field, as shown in Figure 2.

a) Profiling apparatus *b) Field road*

c) Grass field *d) Corn stubble field*

Fig. 2 - Profiling apparatus and agricultural terrain profiling measurement

RESULTS AND ANALYSIS

Assumption judgment of the ICA for road profile estimation

As previously mentioned, some hypotheses must be satisfied for ICA application. First, the components of the source signals must be statistically independent of each other. Considering the excitation of the vehicle dynamic response, the independence of the terrain profiles have mainly been tested by investigating the correlation between the left- and right-wheel profiles that the tractor wheels are subjected to. Profiling tests were carried out on three types of agricultural terrains: grass fields, corn stubble fields and field roads. Figure 3 shows the statistical results obtained from a data analysis of the covariance of the profiles for the left- and right-wheel tracks calculated using Eq. (3). Among the 30 groups of covariance data, the maximum and minimum values were 7.51×10^{-4} and 4.7×10^{-4}, respectively, and the mean value was 1.92×10^{-4}, which is close to 0. Therefore, the source signals of the terrain profiles on the left- and right-wheel tracks can be considered to be independent of each other.

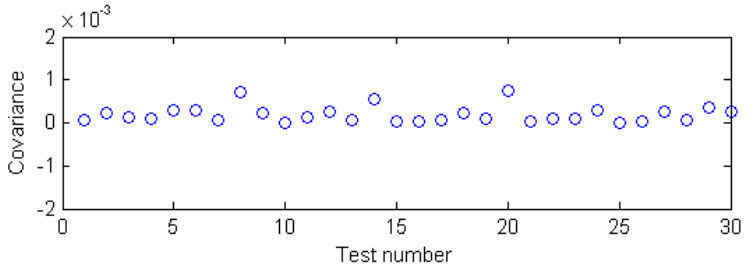

Fig. 3 - Statistical results for profile covariance on left- and right-wheel tracks

Figure 4 shows the statistical results obtained from a data analysis of the Kurt values of the measured agricultural terrain profiles calculated using Eq. (4). Figure 4 a) shows that the Kurt values for all 30 measured profiles of agricultural terrains (grass and corn stubble fields) are less than 0.

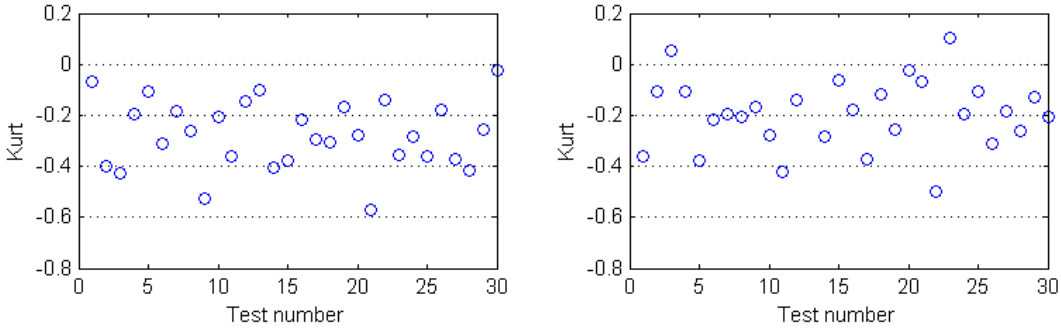

a) Grass and corn stubble fields *b) Field road*

Fig. 4 - Statistical results for Kurt values of terrain profiles

In Figure 4 b), the Kurt values of two of the 30 field road profiles are greater than 0, and the Kurt values of the other 28 profiles are less than 0. Figure 5 presents the probability densities of one group of profiles measured for grass and corn stubble fields, showing that agricultural terrain profiles follow a sub-Gaussian distribution and meet the non-Gaussianity of the sources required for the ICA method to be applicable.

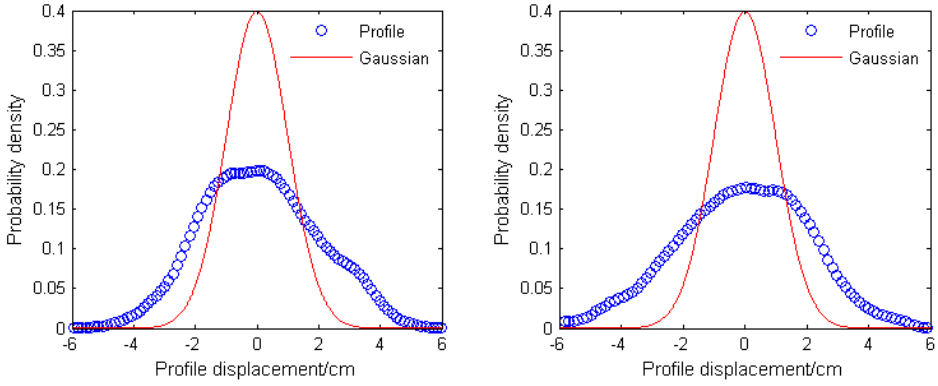

a) Left track of grass field *b) Right track of grass field*

Fig. 5 a,b - Probability density distribution of agricultural terrain profiles

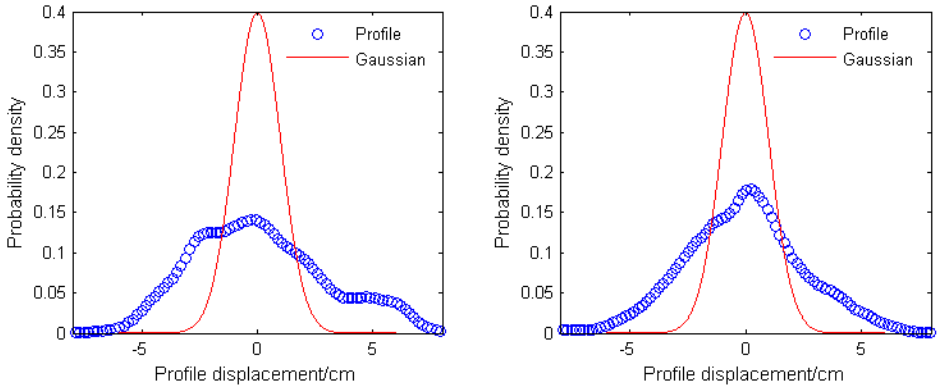

c) Left track of the corn stubble field *d) Right track of the corn stubble field*

Fig. 5 c,d - Probability density distribution of agricultural terrain profiles

Figure 6 shows the probability densities of one group of field road profiles. Therefore, it can be considered that the field road profile signals generally obey a sub-Gaussian distribution and meet the non-Gaussianity of the sources required by the ICA method.

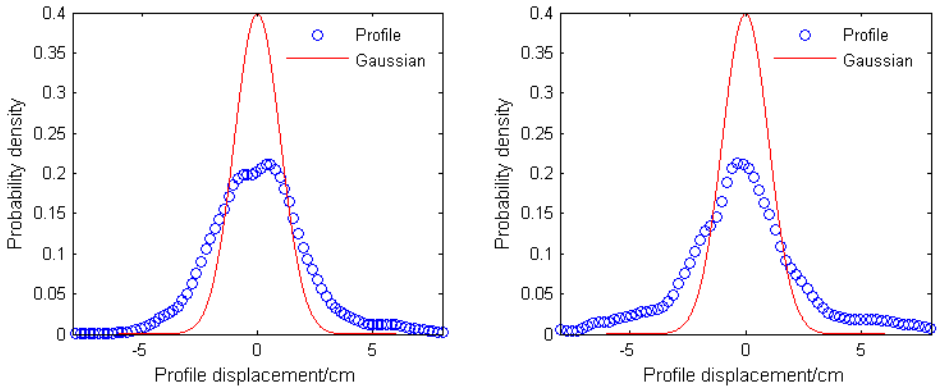

a) Left track *b) Right track*

Fig. 6 - Probability density distribution of field road profiles

Road profile estimation using the ICA

As the tractor travels along a terrain, the terrain profile excites the tractor wheel and generates wheel vibrations. Therefore, the tractor wheel vibration signals are used as the observed signals in the ICA method to estimate the source signals, which are the effective profiles of the terrain. The proposed approach is validated by comparing the estimated profiles with the profiles measured by a profiling apparatus during tractor travel on hard field roads.

Two accelerometers were attached to the ends of the front axle at the centres of the tractor's front wheels to measure the vertical acceleration of each front wheel and one accelerometer was attached at the midpoint of the front axle to measure the axle vertical acceleration for use as comprehensive background noise in the ICA analysis. The terrain profiles traversed by the tractor wheels were measured synchronously by the profiling apparatus mounted on the front counterweight of the tractor.

The obtained results are presented by the following Figures 7, 8 and 9 for tractor speeds of 2.56 km/h, 3.58 km/h and 5.41 km/h, respectively. Figures 7-9 show there is good agreement at each tractor speed between the estimated profiles identified by the ICA and the profiles measured by the profiling apparatus.

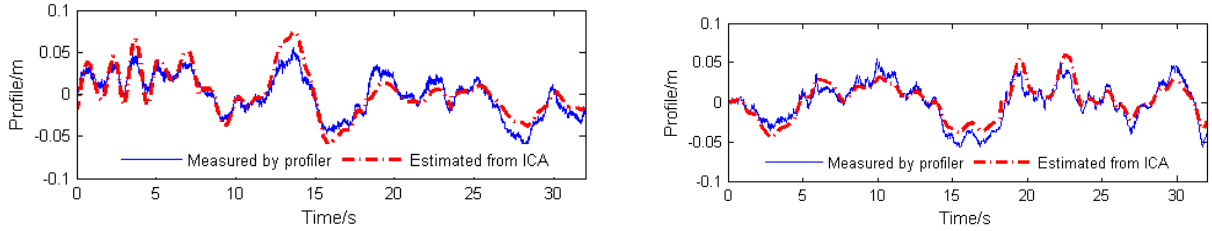

a) Left track *b) Right track*

Fig. 7 - Profiles of hard field roads measured at a speed of 2.56 km/h and obtained by ICA analysis

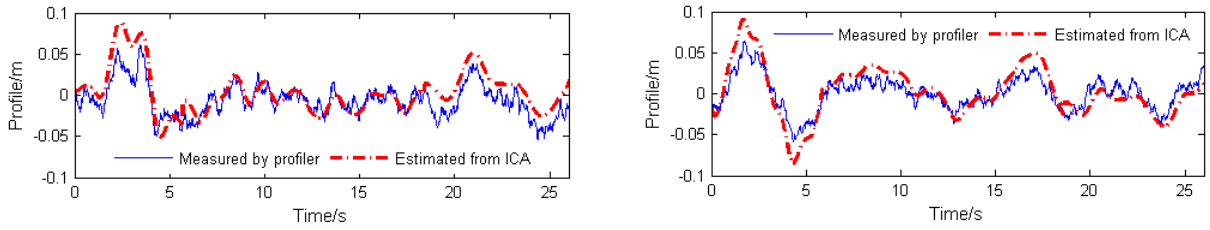

a) Left track *b) Right track*

Fig. 8 - Profiles of hard field roads measured at a speed of 3.58 km/h and obtained by ICA analysis

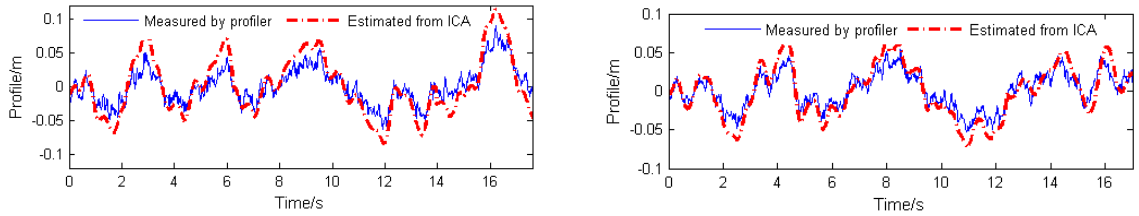

a) Left track *b) Right track*

Fig. 9 - Profiles of hard field roads measured at a speed of 5.41 km/h and obtained by ICA analysis

Figures 10, 11 and 12 are the power spectral density curves corresponding to the measured and ICA analysis results of the field road profiles shown in Figures 7, 8 and 9, respectively. The PSD spectrum clearly shows a loss of content for the high-frequency band using the ICA method. This result is obtained because that the measured profiles reflect the up-and-down motions of the profiler wheels on the road, where the profiler wheels are considerably smaller than the tractor tires and can sense the relatively high-frequency components of the terrain profile. Nevertheless, there is good agreement between the measured profiles and the profiles estimated by the ICA. The small discrepancy between the measured and estimated profiles in the low-frequency band does not affect the vehicle response (*Fauriat et al, 2016*).

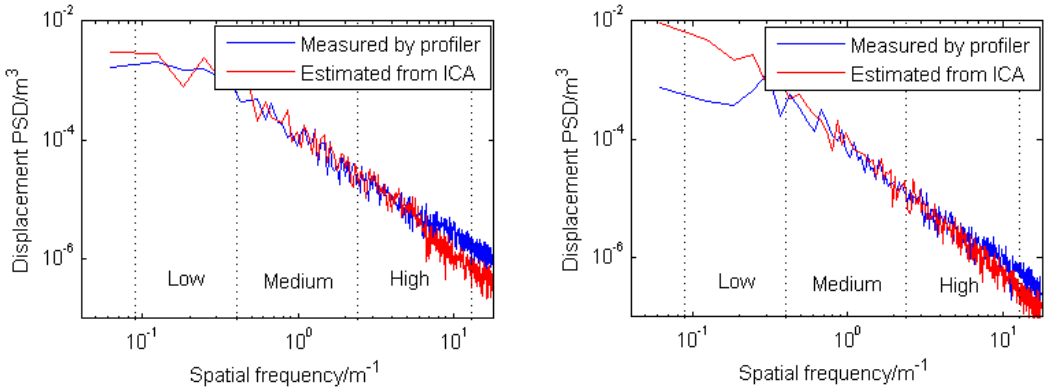

a) Left track *b) Right track*

Fig. 10 - Power spectral density of field road profiles measured at a speed of 2.56 km/h and estimated by the ICA

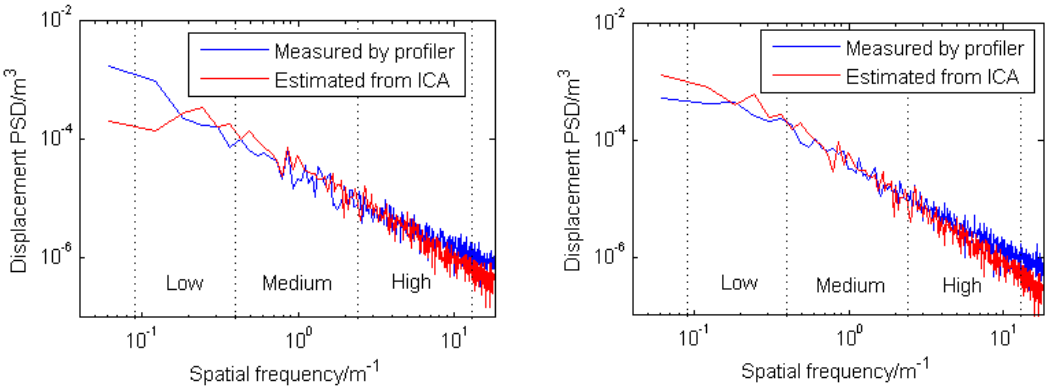

a) Left track *b) Right track*

Fig. 11 - Power spectral density of field road profiles measured at a speed of 3.58 km/h and estimated by the ICA

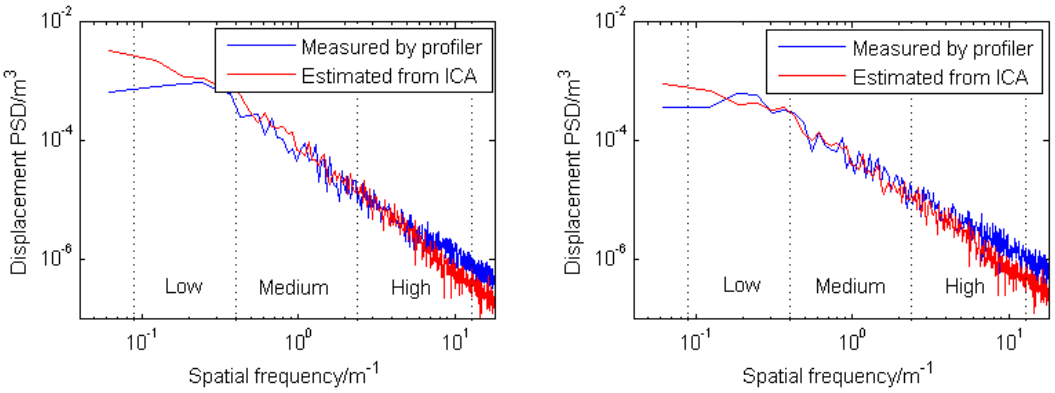

a) Left track *b) Right track*

Fig. 12 - Power spectral density of field road profiles measured at a speed of 5.41 km/h and estimated by the ICA

The ICA efficiency was analysed by calculating the root mean square error $RMSE$ and the relative error E_f between the measured and estimated profiles. These error measures are defined as follows:

$$RMSE = \sqrt{\frac{\sum_{i=1}^{N}(y_i - s_i)^2}{N}} \tag{9}$$

$$E_f = \frac{1}{N}\sum_{i=1}^{N}\frac{y_i - s_i}{s_i} \times 100\% \tag{10}$$

where: y_i is the profile estimated using the ICA at time instance i; s_i is the profile measured by the profiler for time instance i; and N is the number of measured points for the terrain profiles.

The calculated $RMSE$ and E_f for Figures 7-9 are shown in Table 1.

Table 1

***RMSE* and E_f between the measured and estimated profiles**

Test speed (km/h)	*RMSE* (m)		E_f (%)	
	Left track	Right track	Left track	Right track
2.56	0.0038	0.0046	5.6	8.1
3.58	0.0042	0.0045	7.7	7.2
5.41	0.0054	0.0037	8.9	6.8

The results in Table 1 show that the $RMSEs$ range from 3.8 mm to 5.4 mm, and E_f values range from 5.6% to 8.9%. The E_f values for the profiles estimated by the ICA in this paper are close to the obtained using the Kalman filtering theory in reference (*Fauriat et al, 2016*). Therefore, the proposed approach was validated, showing that the ICA is adequate for effective profile estimation.

Comparison of original and effective profiles for deformable terrain

One group of grass field roughness data was taken as an example to investigate the relationship between the original and the effective profiles for deformable terrain. The original profile of the grass field measured by the profiler was compared with the effective profile identified by the ICA method.

Figure 13 shows the original and effective profiles of a group of grass fields for left- and right-wheel tracks. The figure shows that the terrain profiles were flattened and filtered by the tractor wheel during the interaction between the wheel and the soil.

In Figure 13, the calculated *RMS* values of the original profiles of the grass field on the left- and right-wheel tracks are 24.7 mm and 26 mm, respectively, whereas the corresponding values for the effective profiles are 19.8 mm and 20.7 mm, respectively.

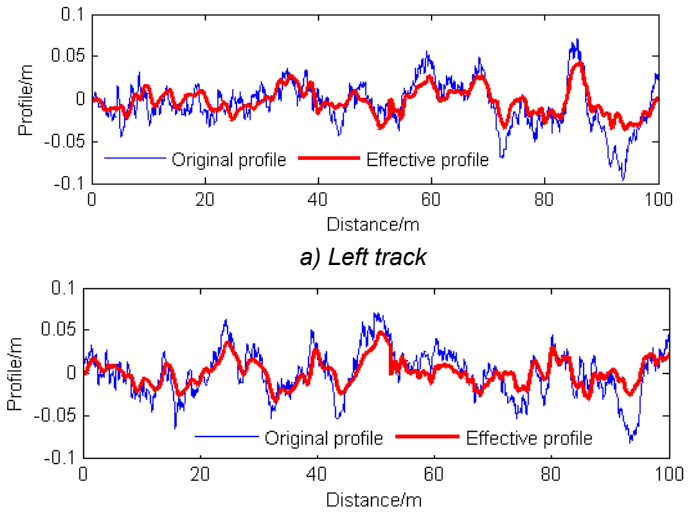

a) Left track

b) Right track

Fig. 13 - Profiles of agricultural grass field

Figure 14 shows the *PSD*s of the original and effective profiles presented in Figure 13. In Figure 14, the roughness index *C* of the original profiles for the left- and right-wheel tracks are 1182×10^{-8} and 1254×10^{-8}, respectively, and the corresponding waviness *W* values are 1.78 and 1.95, respectively. The roughness index *C* of the effective profiles for the left- and right-wheel tracks are 438×10^{-8} and 452×10^{-8}, respectively, and the corresponding waviness *W* values are 1.91 and 2.01, respectively. This result indicates a higher ratio of the shortwave energy to all the wavelength energies for the original profile than for the effective profile.

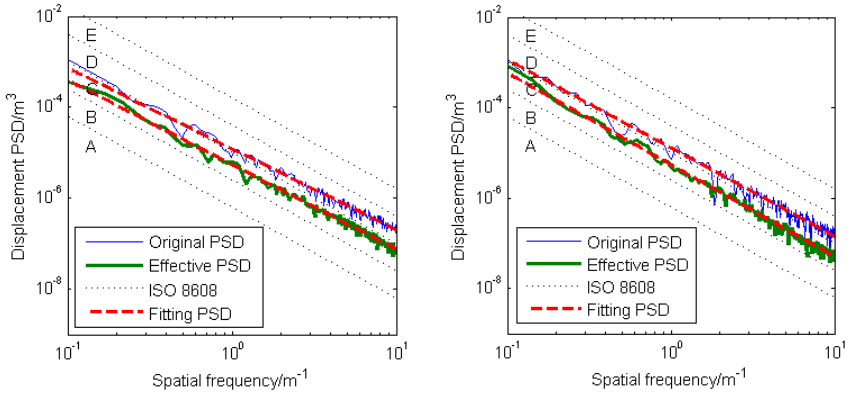

a) Left track *b) Right track*

Fig. 14 - Power spectral density of grass field profiles

CONCLUSIONS

The obtained results show that the ICA is suitable for estimating a true road profile. The proposed approach can be used to identify the effective profiles of a deformable field terrain as the ground excitation sources of vehicle dynamics without using complex terramechanics models and field soil parameters. Therefore, the ICA technique exhibits considerable potential for the dynamic analysis of agricultural tractors and implements. A comparative analysis of the characteristics of the original and effective profiles in both the time and frequency domains showed that the parameters of the effective profiles, such as the *RMS*, roughness index *C* and waviness *W* changed noticeably during the interaction of the tractor wheel and the terrain soil. Therefore, the effective profiles should be used instead of using the original profiles to analyse the dynamic response of vehicles excited by a deformable terrain.

ACKNOWLEDGEMENT

Special thanks are due to the Research Program of Science and Technology at Universities of Inner Mongolia Autonomous Region (NJZY20046), the National Natural Science Foundation of China (31901409), and the Natural Science Foundation of Inner Mongolia Autonomous Region (2019BS05012) for supporting authors' research.

REFERENCES

[1] Akrout A., Tounsi D., Taktak M., et al, (2012), Estimation of dynamic system's excitation forces by the independent component analysis, *International Journal of Applied Mechanics, 4*(03), 1-26. https://doi.org/10.1142/S1758825112500329

[2] Becker C. M., Els P. S., (2014), Profiling of rough terrain, *International Journal of Vehicle Design, 64*(2-4), 240-261. https://doi.org/10.1504/IJVD.2014.058500

[3] Ben Hassen D., Miladi M, Abbes M. S., et al, (2017), Road profile estimation using the dynamic responses of the full vehicle model, *Applied Acoustics, 12*, 1-13. https://doi.org/10.1016/j.apacoust.2017.12.007

[4] Chaabane M. M., Ben Hassen D., Abbes M. S., et al, (2019), Road profile identification using estimation techniques: comparison between independent component analysis and Kalman filter, *Journal of Theoretical and Applied Mechanics, 57*(2), 397-409. https://doi.org/10.15632/jtam-pl/104592

[5] Cutini M., Deboli R., Calvo A., et al, (2017), Ground soil input characteristics determining agricultural tractor dynamics, *Applied Engineering in Agriculture, 33*(4), 509-519. https://doi.org/10.13031/aea.11979

[6] Dallas J., Jain K., Dong Z., et al, (2020), Online terrain estimation for autonomous vehicles on deformable terrains, *Journal of Terramechanics, 91*,11-22. https://doi.org/10.1016/j.jterra.2020.03.001

[7] Fassbender F. R., Fervers C. W., Harnisch C., (1997), Approaches to predict the vehicle dynamics on soft soil, Vehicle System Dynamics: *International Journal of Vehicle Mechanics and Mobility, 27*, S1, 173-188. http://dx.doi.org/10.1080/00423119708969653

[8] Fauriat W., Mattrand C., Gayton N., et al, (2016), Estimation of road profile variability from measured vehicle responses, *Vehicle System Dynamics, 54*(5), 585-605. https://dx.doi.org/10.1080/00423114.2016.1145243

[9] Gialamas T., Gravalos I., Kateris D., et al, (2016), Vibration analysis on driver's seat of agricultural tractors during tillage tests, *Spanish Journal of Agricultural Research, 14*(4), 1-10. https://doi.org/10.5424/sjar/2016144-9664

[10] He R., Sandu C., Khan A. K., et al, (2018), Review of terramechanics models and their applicability to real-time applications, *Journal of Terramechanics, 81*(2), 3-22. https://doi.org/10.1016/j.jterra.2018.04.003

[11] Hildebrand R., Keskinen E., Navarrete J. A. R., (2008), Vehicle vibrating on a soft compacting soil half-space: Ground vibrations, terrain damage, and vehicle vibrations, *Journal of Terramechanics, 45*(4), 121-136. https://doi.org/10.1016/j.jterra.2008.09.003

[12] Hyvärinen A., Oja E., (2000), Independent Component Analysis: algorithms and applications, *Neural Networks Research Centre Helsinki University of Technology, 13*(4-5), 411-430. https://doi.org/10.1016/S0893-6080(00)00026-5

[13] Liu M. S., Zheng L. Z., Zhang Y. K., (1999), Research on effective roughness of terrain surface (软路面有效不平度的理论研究), *Transactions of The Chinese Society of Agricultural Machinery, 30*(5), 1-4. https://doi.org/10.3969/j.issn.1000-1298.1999.05.001

[14] Pacejka H. B., (2012), Dynamic tire response to short road unevennesses, *Tire and Vehicle Dynamics (Third Edition),* Pages: 475-504. https://doi.org/10.1016/B978-0-08-097016-5.00010-3

[15] Taheri S., Sandu C., Taheri S., et al, (2015), A technical survey on Terramechanics models for tire-terrain interaction used in modeling and simulation of wheeled vehicles, *Journal of Terramechanics, 57*(2), 1-22. https://doi.org/10.1016/j.jterra.2014.08.003

[16] Wang L. J., Yan J. G., Xie S. S., et al, (2020), Testing, analysis and comparison for characteristics of agricultural field and asphalt road roughness, *INMATEH Agriculture Engineering, 62*(3), 147-154. https://doi.org/10.35633/inmateh-62-15

[17] Yan J. G., Wang C. G., Xie S. S., et al, (2019), Design and validation of a surface profiling apparatus for agricultural terrain roughness measurements, *INMATEH Agriculture Engineering, 59*(3), 169-180. https://doi.org/10.35633/inmateh-59-19

[18] Zarzoso V, Comon P., (2010), Robust independent component analysis by iterative maximization of the kurtosis contrast with algebraic optimal step size, *IEEE Transactions on Neural Networks, 21*(2),248-61. https://doi.org/10.1109/TNN.2009.2035920

NUMERICAL SIMULATION AND EXPERIMENTAL STUDY OF INNER FLOW FIELD OF SEED PELLETING PREMIXER IN SPOUTED FLUIDIZED BED
/
喷动式流化床种粉丸化预混合装置内流场数值模拟与试验

Qiu Yi[1]; Dai Xiaofeng[1]; Chen Zhi[2*]; Dai Nianzu[2]; Mi Longkai[2]
[1] Yangzhou Polytechnic Institute, College of Transportation Engineering, Jiangsu, China
[2] Inner Mongolia Agricultural University, College of Mechanical and Electrical Engineering, Inner Mongolia, China
Tel: 04714309215; [*]Corresponding author E-mail address: sgchenzhi@imau.edu.cn
DOI: https://doi.org/10.35633/inmateh-62-24

Keywords: *Agropyron seeds; Pelleting; CPFD, Spouted fluidized bed; Pelleting qualified rate*

ABSTRACT
In order to explore the temporal and spatial distribution and motion state of the grains of wheatgrass (Agropyron) seeds and powder in pelleting process, and to find the optimal inlet air speed of pelleting premixer, the pelleting forming mechanism was revealed. Based on Herz-Mindlin contact theory, the contact mechanics model of seed and powder was established. Besides, CPFD software was used to model and simulate the pelleting premixer, and the contact, collision and friction rules among particles were analysed. The simulation and experimental results show that with the increase of inlet wind speed, the bed expansion increases and the unit volume particle concentration decreases, while the air pressure difference only slightly increases. When the inlet wind speed is set at 3.5 m/s, the atomizing nozzle velocity is set at 4.1 m/s, and the seed coating agent flow rate is 0.36 L/min, the particles are suspended due to air isolation, forming a spouted fluidized bed. It is good for seed and powder contact and rapid prototyping. In this time, the pelleting qualified rate was 95.8%. The results provide theoretical basis and technical support for the research of small irregular seeds pelletizing technology.

摘要
为了探究冰草种子与丸化粉料在丸化过程中的颗粒时空分布、运动状态以及寻找丸化预混合装置最优的进气速度，揭示丸化成型机理。基于Herz-Mindlin接触理论，建立了种粉丸化接触力学模型；采用CPFD软件对丸化预混合装置进行建模与仿真分析，分析颗粒间的接触、碰撞、摩擦规律。仿真与试验结果表明：随着风速增加床体膨胀升高，床体内单位体积颗粒浓度下降，而气压差仅略微增加，当入口风速设为 3.5 m/s、雾化喷头速度设为 4.1 m/s、种衣剂流量 0.36 L/min时，颗粒间因被空气隔离而悬浮，形成喷动式流化床，有利于种粉接触、快速成型，该风速下丸化合格率为 95.8%。研究结果为小粒不规则种子丸化技术的研究提供理论基础和技术保障。

INTRODUCTION

Seed pelleting technology is the use of specific powder through mechanical processing methods, made of uniform size, regular shape of small spheres. The core problem of pelleting technology is whether the particle size increases evenly. The seeds with increased particle size are conducive to mechanized precision sowing, increase the fluidity of seeds, and achieve the purpose of saving seeds and improving sowing efficiency (*Shao, 2018*). Therefore, high quality pelleting technology has become an urgent demand. In addition to the need of drought resistance, cold resistance, saline alkali resistance and soil borne diseases control, the diversification and functional specialization of grass seed pelleting has become a novel development trend (*Qiu, 2017*).

The function of pelleting premixer is to promote the full mixing of seed and powder, and its mixing effect is directly related to the quality of pelleting (*Jiang, 2019*). At present, domestic and foreign scholars have studied the motion law of materials in the drum and the mixing effect between materials (*Yang, 2003; Koteswara, 2013*). Christodoulou studied the hydrodynamic behaviour model of film coated suspension in the process of tablet coating (*Christodoulou, 2020*). Computational fluid dynamics (CFD) method was used to simulate the solid-liquid mixing process in stirred tank (*Xu, 2019*). Liu Wenjun used discrete element theory to simulate and analyse the mixing characteristics of materials in coal mine rotary kiln (*Liu, 2017*). Liu used discrete element method to simulate the radial mixing process and motion law of particles in U-mixer (*Liu, 2019*).

Hou Zhanfeng optimized the process parameters of vibration pelleting machine (*Hou, 2020*). Throughout the above research, it is found that the mixing between materials is a very complex physical behaviour, and the mixing uniformity cannot be expressed quantitatively.

Therefore, this paper designed a spouted fluidized bed Agropyron seeds pelleting premixer. The Agropyron seeds were suspended in the mixing chamber in a spouted fluidized bed, and the atomized pelleting agent was sprayed on the outer surface of the seeds to achieve the ideal pelleting effect.

MATERALS AND METHODS

Test Equipment

The spouted fluidized bed pelleting premixing device is mainly composed of gas predistribution chamber *10*, seed and liquid mixing chamber *7* and settling chamber *4*, as shown in Fig. 1.

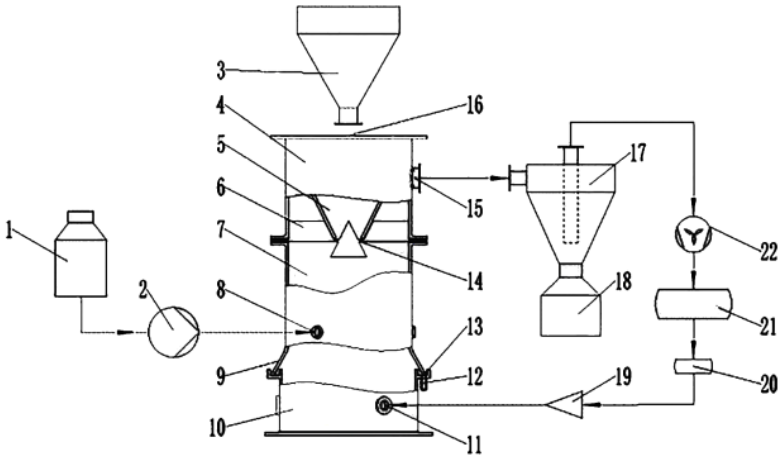

Fig. 1 - Pelleting pre-mixing equipment
Schematic diagram of overall structure of pelletizer for Agropyron seeds

1. Seed coating box; 2. Liquid supply pump; 3. Seed supply hopper; 4. Settling chamber; 5. Conical guide bucket; 6. Gas solid isolation plate; 7. Seed and liquid mixing chamber; 8. Adhesive supply port; 9. Liquid guide plate; 10. Gas predistribution chamber; 11. Air supply port; 12. Adhesive guide tube; 13. Annular seal; 14. Conical feeder; 15. Exhaust port; 16. Seed feeding port; 17. Dust removal device; 18. Recovery device; 19. Pressure relief valve; 20. Air purification device; 21. Air compression tank; 22. Air compressor

Working principle of spouted fluidized bed

As shown in Fig. 1, the purified air is compressed into the air compression tank *21* through the air compressor *22*, and then enters the gas predistribution chamber *10.* The seeds in the seed hopper *3* enter the conical guide bucket *5* through the seed feeding port *16*, and then enter the seed and liquid mixing chamber *7*. The adhesive in the seed coating box *1* is pressurized by the liquid supply pump *2* and then enters the seed and liquid mixing chamber *7*. With the increase of the air flow through the predistribution chamber *10*, the lifting force of the seeds in the seed and liquid mixing chamber *7* will also increase. When the lifting force received by the particles is just equal to their own weight, the particles will move violently in the bed to form fluidization. At this time, the adhesive is sprayed into the seed and liquid mixing chamber *7* through the adhesive supply port *8* to contact with the suspended seeds for adhesion. When the air flow continues to increase, the seeds will continue to rise to the gas solid isolation plate *6*, and the seeds collide with the spoiler to reduce the speed. At the same time, the air flow enters the settling chamber *4* after passing through the gas solid isolation plate 6, and then enters the seed feeding port *17* through the exhaust port *15*. Besides, the light weight seeds mixed in the air flow are collected into the recovery device *18* after passing through the cyclone separator. After mixing, the seeds fall into the coater for the next pelleting work.

NUMERICAL SIMULATION

Seed and powder contact mechanics model

During the pelleting process, when the outer surface of Agropyron seeds contacts with the adhesive, the interaction force between the seed and powder is far less than the adhesive force, which realizes the pelleting process. However, the interaction between the seed of Agropyron and powder during the rotation of the coater is mixing in most cases, and the next step of bonding will be conducted only after the mixture is even. In this way, the process of mixing and bonding is repeated until the ideal pelleting effect is achieved.

Based on Herz-Mindlin contact theory, it is assumed that the force between the seed and powder is a small deformation and recoverable collision force, that is, the impact force of the elastic sphere on the seed surface. The impact process of the powder particles and the Agropyron seeds is shown in Fig. 2.

In the discussion of contact problems, it is generally assumed that:

1. The contact system is composed of two objects in contact with each other, and there is no rigid body motion between them.
2. The deformation of the contact object is small, the contact point can be determined in advance, and the contact or separation is only carried out at the corresponding point where two objects may contact.
3. The medium of contact surface and the influence of dynamic friction are not considered.
4. The seeds were oval in shape and distributed evenly.
5. The powder is approximately a sphere with uniform size and mass distribution.

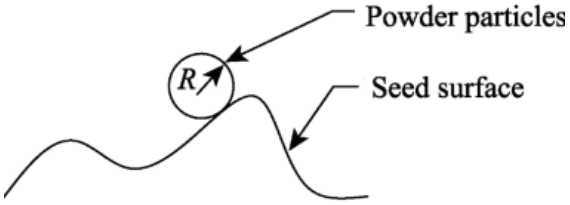

Fig. 2 - Figure of powder impact on seed surface

As shown in Fig. 2, the radius of the elastic ball is setting at R, and impacts the Agropyron seeds at the speed V. according to the Hertz contact theory, the penetration depth of the elastic ball impacting the seed surface is as follows:

$$\lambda = \left[\frac{9}{10}\frac{P^2}{R}E^2\right]^{\frac{1}{3}} \tag{1}$$

Therefore, the pressure P can be obtained as follows:

$$P = \frac{4}{3}E^{-1}R^{\frac{1}{2}}\lambda^{\frac{3}{2}} \tag{2}$$

$$\frac{1}{E} = \frac{1-\mu_1^{\ 2}}{E_1} + \frac{1-\mu_2^{\ 2}}{E_2} \tag{3}$$

Where: E_1, μ_1 and E_2, μ_2 are the elastic modulus and Poisson's ratio of the elastic ball and seed respectively.

According to Newton's second law:

$$m\frac{d^2\lambda}{dt^2} = -P \tag{4}$$

By substituting the calculated pressure P into the above formula and integrating λ, the following results can be obtained:

$$\frac{1}{2}\left[v^2 - (\frac{d\lambda}{dt})^2\right] = \frac{8}{15}\frac{R^{\frac{1}{2}}E}{m}\lambda^{\frac{3}{2}} \tag{5}$$

Where V is the initial velocity of the elastic ball impacting the seed. When the maximum impact velocity λ_1 is reached, $d\lambda/dt$ = 0. It is concluded that:

$$\lambda_1 = \left[\frac{5\pi}{4}\rho(\frac{1-V_1^{\ 2}}{E_1} + \frac{1-V_2^{\ 2}}{E_2})^{\frac{2}{5}}\right]^{\frac{2}{5}} RV^{\frac{4}{5}} \tag{6}$$

At this time, the maximum load P_1 between seed and powder is:

$$P_1 = \frac{4}{3}(\frac{5\pi}{4}\rho)^{\frac{2}{5}}(\frac{1-V_1^{\ 2}}{E_1} + \frac{1-V_2^{\ 2}}{E_2})^{\frac{-3}{5}} R^{\frac{3}{2}}V^{\frac{6}{5}} \tag{7}$$

Where: ρ - density of elastic sphere, [kg/m^3];

At this time, increasing the impact force can improve the turbulence degree of powder flow. The impact force can be expressed as:

$$P_1 = m_1 \frac{V'_1 - V_1}{t} = m_2 \frac{V'_2 - V_2}{t} \quad (8)$$

Where: V_1, V_1', V_2, V_2' - the velocities of seeds and powders before and after collision, [m/s].

It can be seen that the impact force is mainly related to the speed difference from equation (8). Therefore, the introduction of pelleting premixing chamber can increase the speed difference between the seed and powder, promote the seed and powder to "boiling" state, and improve the pelleting quality of pelleting seeds.

Simulation analysis of premixing chamber

Model import and mesh generation

The premixing chamber model established in Creo software is imported into CPFD simulation software, and the imported model is meshed. The number of meshing is 150000. Because the finer the meshing is, the higher the accuracy of simulation is. Therefore, under the condition of ensuring the processing speed, the number of meshing is set higher, as shown in Fig. 3.

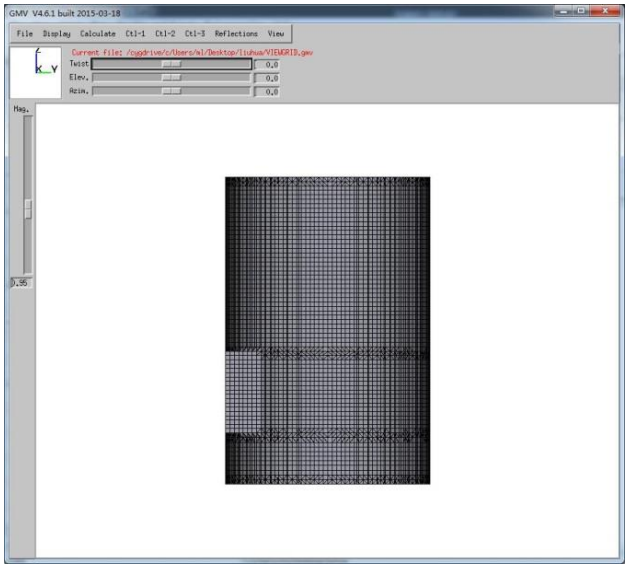

Fig. 3 - Mesh generation

Simulation results analysis of powder mixing

In order to study the mixing of Agropyron seeds and powder in premixing chamber under different inlet wind speed, the temporal and spatial distribution of Agropyron seeds and powder were studied. When the inlet wind speed is set at 0.5 m/s, 1 m/s, 1.5 m/s, 2 m/s, 2.5 m/s, 3 m/s, 3.5 m/s, 4 m/s, 4.5 m/s and 5 m/s, the temporal and spatial distribution of particles is shown in Fig. 4. The orange particles in the figure are pelleting powder, and the blue particles are Agropyron seeds.

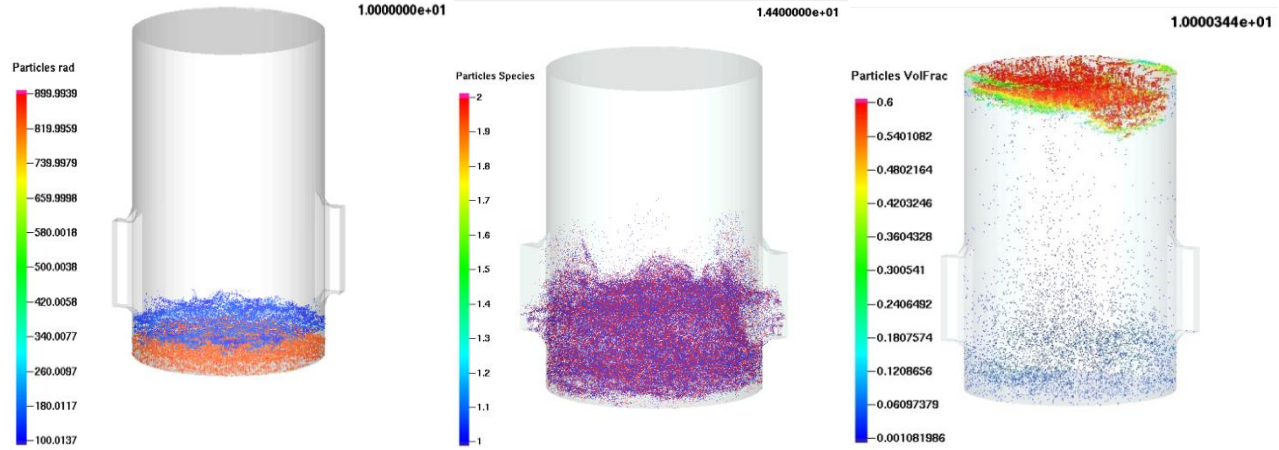

a. Particle distribution at inlet wind speed of 0.5m/s *b. particle distribution at inlet wind speed of 3.5m/s* *c. Particle distribution at inlet wind speed of 5 m/s*

Fig. 4 - Contrast diagram of particle distribution in different inlet wind speed

In order to determine the optimal inlet wind speed, three kinds of wind speed were selected from the set 9 kinds of wind speed to study the temporal and spatial distribution of particles. The inlet wind speed was 0.5m/s, 3.5 m/s and 5m/s respectively. As shown in Fig. 4a, when the inlet wind speed is 0.5 m/s, the movement between Agropyron seeds and powder is not obvious, and it is difficult to roll, jump and disperse. The mixing effect of pelleting is poor. However, when the wind speed is 3.5 m/s in Fig. 4b, the movement of particles is more intense, and the particles are in a "boiling" state, which increases the chances of contact, collision, friction and rolling between Agropyron seeds and powder, which is conducive to improving the pelleting quality. Besides, Fig. 4c shows the distribution of particles when the inlet wind speed is 5 m/s. It can be seen that too high inlet wind speed will cause most particles to concentrate on the top of the premixing chamber, which is not conducive to the mixing of Agropyron seeds and powder. The space utilization rate of the premixing chamber is poor, resulting in the increase of multi-seed rate and seedless rate, and the decrease of pelleting qualified rate. Therefore, the initial simulation results show that when the inlet speed is 3.5 m/s, the mixing effect of Agropyron seeds and powder is better, and can reach the ideal premixed state.

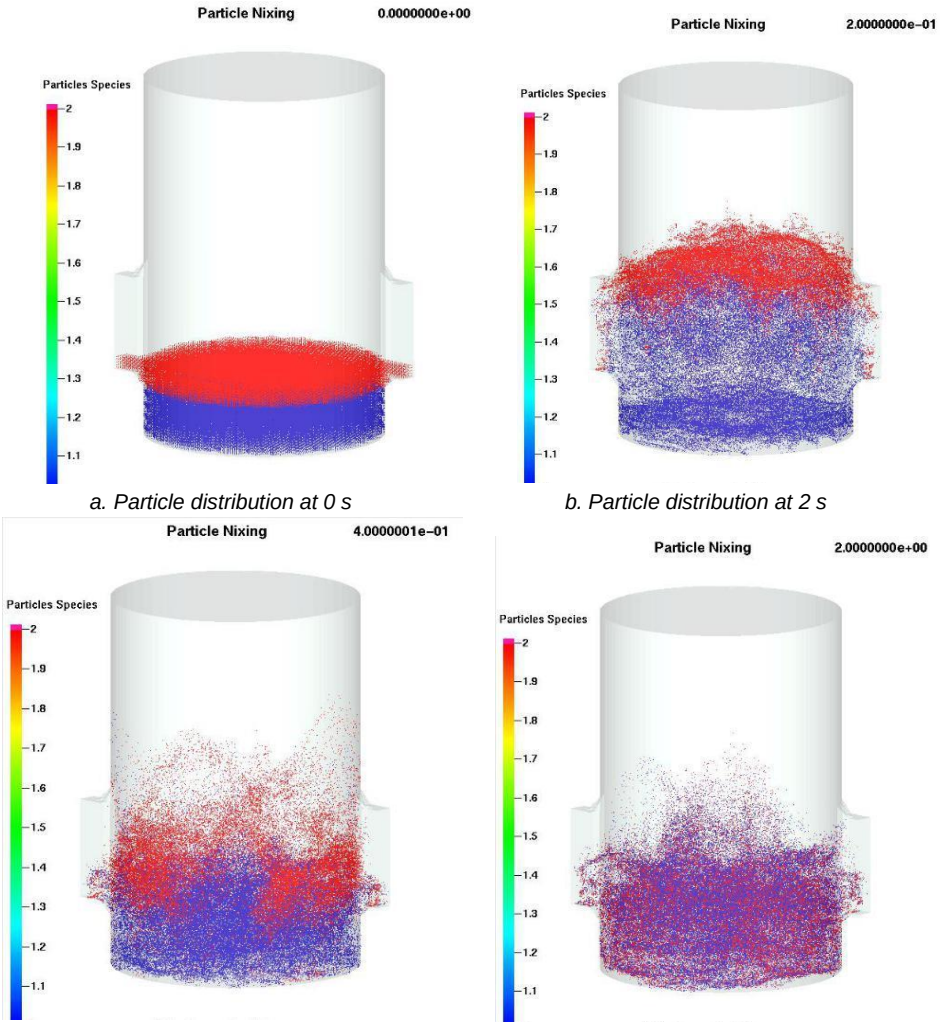

a. Particle distribution at 0 s *b. Particle distribution at 2 s*

c. Particle distribution at 4 s *d. Particle distribution at 20 s*

Fig. 5 - When the inlet wind speed is 3.5m/s, the distribution of particles in different times

Fig. 5a shows the initial state of Agropyron seeds and powder in simulation 0 s. The seeds of Agropyron seeds and powder are independent of each other when they are put into the premixing chamber initially, and they have obvious moving boundary, so it is difficult to achieve the ideal mixing state. Fig. 5b shows the temporal and spatial distribution of Agropyron seeds and powder when the simulation time is 2 s. It can be seen from this process that the moving boundary between Agropyron seeds and powder is shrinking, and there is a relative moving trend. This process is the initial state of particle mixing. Fig. 5c shows the state of population movement when the simulation duration is 4 s. Under the action of air flow, there is an obvious relative movement trend between Agropyron seeds and powder, which is conducive to the good mixing of Agropyron seeds and powder. Fig. 5d shows the population distribution when the simulation duration is 20s.

At this moment, the population has formed a good solid fluidized bed under the action of pneumatic force, which can achieve the ideal purpose of seeds and powder mixing, and is conducive to improving the qualified rate and quality of Agropyron seeds pelleting.

RESULTS AND DISCUSSION

Orthogonal test

Taking the pelleting qualified rate as the test performance index, taking the inlet wind speed, atomizing nozzle velocity and seed coating agent flux as the test factors, the orthogonal test with 3 factors and 3 levels was conducted. The factor level code is shown in Tab. 1.

Table 1

Factors and levels encode table

Level	Inlet wind speed A/ [m/s]	Atomizing nozzle velocity B/ [m/s]	Seed coating agent flux C/ [L/min]
1	2.5	2	0.25
0	3.5	4	0.35
-1	4.5	6	0.45

Each group of tests were conducted 3 times, with an interval of 10 min, and the average test results were taken. Take three samples randomly from each test sample, and observe them with a 5-fold magnifying glass. Then separate out the completely coated seeds of Agropyron and determine them as qualified for pelleting. Calculate the pelleting qualified rate according to formula (9) and then take the average value. The statistical results are shown in Tab. 2.

$$J = \frac{Z_d}{Z_d + Z_f} \times 100\% \quad (9)$$

In formula (9), J-the pelleting qualified rate, [%];

Z_d - the number of seeds completely coated Agropyron seeds, [-];

Z_f - the number of seeds of incompletely coated Agropyron seeds, [-];

Table 2

Quadratic regression orthogonal test scheme and experimental results

Test No.	Inlet wind speed A [m/s]	Atomizing nozzle velocity B [m/s]	Seed coating agent flux C [L/min]	Pelleting qualified rate [%]
1	0	0	0	84.2
2	-1	-1	0	75.1
3	0	1	-1	76.5
4	0	0	0	83.9
5	0	0	0	83.8
6	-1	0	-1	76
7	1	1	0	75.6
8	1	0	-1	76.5
9	0	-1	-1	75.9
10	0	0	0	84.1
11	-1	1	0	73.2
12	0	1	1	76.2
13	0	0	0	83.7
14	0	-1	1	74.9
15	1	0	1	76.8
16	1	-1	0	76.5
17	-1	0	1	75.8

Analysis of pelleting qualified rate

According to the quadratic regression orthogonal test scheme and test data in Tab. 2, the quadratic regression method was used to analyse the pelleting qualified rate. First, Design-expert was used for variance analysis (see tab. 3) and the regression mathematical model was established.

$$J=95.62+1.24A+0.14B-0.56C+0.075A \bullet B-0.025A \bullet C-0.050B \bullet C-1.43A^2-1.91B^2-1.55C^2 \quad (10)$$

A is the inlet wind speed, [m/s]; B - the atomizing nozzle velocity, [m/s]; C - the seed coating agent flux, [L/min].

The absolute value of each factor in the regression mathematical model determines the influence on the pelleting qualified rate. Therefore, the influence of each factor on the pelleting qualified rate can be determined by the regression model as inlet wind speed > seed coating flux > atomizing nozzle velocity.

Table 3

Variance analysis of test result of pelleting qualified rate

Origin	Squares	Df	SD	F Value	P Value
Mode	273.894	9	30.433	202.788	**
A	0.911	1	0.911	6.072	**
B	0.001	1	0.001	0.008	
C	0.125	1	0.125	0.833	*
A•B	0.090	1	0.090	0.600	*
A•C	0.063	1	0.063	0.416	
B•C	0.202	1	0.202	1.349	*
A^2	82.818	1	82.818	551.856	**
B^2	80.961	1	80.961	539.483	**
C^2	80.040	1	80.040	533.349	**
Residua	1.365	7	0.195		
Lack of Fit	0.313	3	0.104	0.396	
Pure Error	1.052	4	0.073		
R^2	0.9669				
Adequate Precision	11.362				

The *F* value of the model is 202.8 and the *P* value is less than 0.01 in tab. 3. The *P* value of the model is extremely significant and the mismatch term is not obvious, which proves that the regression equation (10) has high fitting accuracy with the actual results. Therefore, the model can be used to analyse and predict the pelleting qualified rate.

According to the regression mathematical model (10), the response surface of inlet wind speed, seed coating agent flux and atomizing nozzle velocity to the pelleting qualified rate was obtained (Fig. 6).

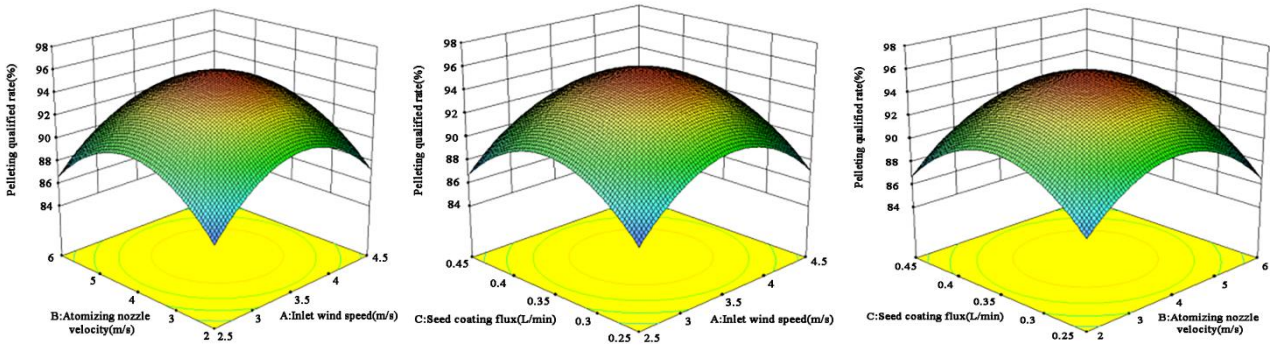

a) J=(A,B,0) *b) J=(A,0,C)* *c) J=(0,B,C)*

Fig. 6 - Response surface of pellet rate

According to the corresponding surface of pelleting qualified rate, with the increase of inlet wind speed, pelleting qualified rate first increases and then decreases. With the increase of atomizing nozzle velocity, pelleting qualified rate first increases and then decreases. With the increase of seed coating flux, pelleting qualified rate first increases and then decreases.

Optimisation and experimental verification

According to the fitting factor and response value of quadratic regression equation, the optimal parameters were obtained by using Design-expert software.

$$\begin{cases} \max J \\ 2.5 \le A \le 4.5 \\ 2 \le B \le 6 \\ 0.25 \le C \le 0.45 \end{cases} \quad (11)$$

Through the analysis of Design-expert software, when *A*=3.5, *B*=4.1, *C*=0.36, the optimal value *J*= 95.8%, that is, when the inlet wind speed is 3.5 m/s, the atomizing nozzle velocity is 4.1 m/s, and the seed coating flux is 0.36 L/min, the pelleting qualified rate is 95.8%.

CONCLUSIONS

1) The law of contact, collision and friction between Agropyron seeds and powder in pelleting process was analysed theoretically, and the pelleting mechanism was revealed.

2) CPFD software was used to model and simulate the premixing chamber. The results showed that with the increase of inlet wind speed, the bed expansion increased, the particle concentration per unit volume in the bed decreased, while the pressure difference only increased slightly. When the inlet wind speed reached 3.5 m/s, the particles suspended due to air isolation, forming a spouted fluidized bed, which was conducive to seeds and powder contact and rapid prototyping.

3) Response surface methodology was used to analyse the test, and the main and secondary factors affecting the pelleting qualified rate of Agropyron seeds were determined as inlet wind speed > seed coating flux > atomizing nozzle velocity. When the inlet wind speed was 3.5 m/s, atomizing nozzle velocity was 4.1m/s, and seed coating flux was 0.36 L/min, the pelleting qualified rate was 95.8%.

ACKNOWLEDGEMENTS

We acknowledge that this work was financially supported by National Natural Science Foundation Project "Research on soil wind erosion monitoring system based on wireless sensor network and its key technologies (41361058)" and "Research on seed pelleting parameters and coating mechanism under the vibration force field (2018MS05023)".

REFERENCES

[1] Christodoulou C., Sorensen E., Khair A.S., (2020), A model for the fluid dynamic behaviour of a film coating suspension during tablet coating, *Chemical Engineering Research and Design,* Volume 160, Issue 3, pp. 301-320, University College London/UK;

[2] Hou Z., Qiu Y., Chen Z., Liu H., Guo F., Mi L., (2020), Optimization of process parameters of pelletizer for Agropyron seeds under vibration force field, *INMATEH-Agricultural Engineering*, Vol 60, Issue 1, pp. 147-154, Bucharest/Romania;

[3] Jiang S., Ye Y., Yang E., (2019), Numerical simulation of mixing uniformity of sand and gravel materials in rotary cylinder, *Journal of Computational Mechanics*, Vol 36, Issue 5, pp. 603-609, Xiangtan University/China;

[4] Koteswara R., Fabian H., Eckehard S., Jochen M., (2013), Influence of flight design on the particle distribution of a flighted rotating drum, *Chemical Engineering Science*, Vol 90, Issue 1, pp.101-109, Otto von Guericke University Magdeburg/Germany;

[5] Liu W., Liu Y., Zhang Y., Tang Y., Lan H., Zhang H., Ma J., (2019), Discrete element simulation of particle mixing motion in u-mixer. *Feed industry*, Vol 40 Issue 3, pp. 10-14, Tarim University/China;

[6] Liu Wenjun, (2017), Simulation analysis of material mixing characteristics in coal mine rotary kiln based on discrete element method, *Coal Technology*, Vol 36 Issue 11, pp. 320-322, Xuzhou Institute of Technology/China;

[7] Qiu Y., Chen Z., Hou Z.F., Song T., Mi L.K., Shao Z.W., (2017), Numerical simulation and experiment on improving pelleted coating of forage grass seeds by vibration force field. *Transactions of the CSAE*, Vol 33, Issue 19, pp. 86–93, Inner Mongolia/China;

[8] Shao Z., Chen Z., Hou Z., Mi L., Qiu Y. (2018). Analysis of pelleting movement characteristics of BYW-400 type vibrating seed coating machine for wheatgrass. *Transactions of the CSAE*, Vol 34, Issue 3, pp. 57-64, Inner Mongolia/China;

[9] Xu Y., Liu Y., Hui H., Yu Y. (2019), Numerical simulation and experimental study on solid liquid mixing process, *Journal of East China University of science and technology*, Vol 45, Issue 4, pp. 675-680, East China University of science and technology/China;

[10] Yang R., Zou R., Yu A., (2003), Microdynamic analysis of particle flow in a horizontal rotating drum, *Powder Technology*, Vol 130, Issue 1, pp. 138-146, The University of New South Wales/Australia.

SIMULATED ANNEALING GENETIC ALGORITHM-BASED HARVESTER OPERATION SCHEDULING MODEL
/
基于模拟退火遗传算法的收割机作业调度模型

Zhang Qingkai [1,2], Cao Guangqiao [2], Zhang Junjie [1], Huang Yuxiang *[1], Chen Cong [2], Zhang Meng [2]
[1]College of Mechanical and Electronic Engineering, Northwest A&F University, Yangling 712100, China
[2] Nanjing Research Institute for Agricultural Mechanization, Ministry of Agriculture and Rural Affairs, Nanjing 210014, China
Correspondent author: Tel: +86-1510294917; E-mail: hyx@nwsuaf.edu.cn
DOI: https://doi.org/10.35633/inmateh-63-25

Keywords: *harvester, operation, scheduling model, optimization*

ABSTRACT

To address problems involving the poor matching ability of supply and demand information and outdated scheduling methods in agricultural machinery operation service, in this study, we proposed a harvester operation scheduling model and algorithm for an order-oriented multi-machine collaborative operation within a region. First, we analysed the order-oriented multi-machine collaborative operation within the region and the characteristics of agricultural machinery operation scheduling, examined the revenue of a mechanized harvesting operation and the components of each cost, and constructed a harvester operation scheduling model with the operation income as the optimization goal. Second, we proposed a simulated annealing genetic algorithm-based harvester operation scheduling algorithm and analysed the validity and stability of the algorithm through experimental simulations. The results showed that the proposed harvester operation scheduling model effectively integrated the operating cost, transfer cost, waiting time cost, and operation delay cost of the harvester, and the accuracy of the harvester operation scheduling model was improved; the harvester operation scheduling algorithm based on simulated annealing genetic algorithm (SAGA) was able to obtain a global near-optimal solution of high quality and stability with high computational efficiency.

摘要

针对农机作业服务供需信息匹配能力弱、调度方式落后的问题，该文针对区域内面向订单的多农机协同作业模式，建立了收割机调度模型及算法。首先对区域内面向订单的多农机协同作业模式进行了明确，并建立了以机收作业总收益为优化目标的收割机作业调度模型；其次，设计了基于模拟退火遗传算法的收割机作业调度算法，并通过相关仿真实验对算法的有效性、稳定性及计算效率进行了分析。研究结果表明：建立的收割机作业调度模型有效整合了使用成本、转移成本、等待时间成本、延误作业损失成本信息，提高了收割机作业调度模型的准确性；基于模拟退火遗传算法的收割机作业调度算法可以获得质量较高的全局近优解，具有较高的计算效率。

INTRODUCTION

With the improvement of agricultural machinery social service systems, agricultural machinery social services are becoming increasingly popular in rural China *(Dong and Li, 2015)*. Faced with the expanding scope of agricultural machinery services and the informationisation needs of agricultural machinery operations, traditional scheduling management techniques such as manual scheduling and telephone scheduling can no longer meet the needs of social services at this stage. Problems such as the poor matching efficiency of supply and demand information for agricultural machinery services and untimely updates of operation information can waste agricultural machinery resources or delay agricultural production *(Wu et al., 2013; Zhou et al., 2014)*. Establishing an agricultural machinery operation scheduling model, suitable for the collaborative operation of agricultural machinery entities, is the key to realizing agricultural machinery scheduling information management and is of great significance for improving agricultural machinery use efficiency and benefits *(Luo and Zhang, 2016; Zhang, 2020)*.

Agricultural machinery operation scheduling and planning have been extensively investigated, and typical operational research formulations for industrial manufacturing and logistics transportation have been applied in this area *(Bochtis et al., 2014)*. By drawing from ideas for vehicle scheduling, *Guan et al. (2018)* proposed a two-stage metaheuristic algorithm for mechanized harvesting on sugarcane farms, in which the initial job scheduling scheme was generated based on the priority rules and then optimized using a genetic algorithm. *He et al. (2018)* constructed a scheduling model with the total operation time as the optimization goal and the operation time of each harvester as a constraint while considering the effects of different machine

models and soil types on scheduling. *Thuankaewsing et al. (2015)* proposed a sugarcane harvester operation scheduling model with the highest yield as the optimization goal and the proportion to which each sugarcane field is harvested at the time of the highest yield as a constraint. *Edwards et al. (2015)* proposed an agricultural machinery scheduling model that considered farmland operating conditions and solved it with an improved tabu search algorithm, which is suitable for scenarios where multiple operations are performed sequentially. However, the existing agricultural machinery scheduling and operating models have not fully considered the timeliness cost derived from the time requirements of field operation on agricultural machines, while the performance of the solving algorithms of the current model needs to be improved.

Based on the existing studies, we analysed the costs and benefits of mechanized harvesting scheduling to address various aspects of cereal crop harvesting using an order-oriented multi-machine collaborative operation as the subject, established a harvester operation scheduling model using the maximum operation income as the optimization goal, and proposed a simulated annealing genetic algorithm-based harvester operation scheduling algorithm to generate a reasonable agricultural machinery scheduling plan, improve the benefits and efficiency of agricultural machinery use, and provide a rational decision-making basis for agricultural machinery management.

MATERIALS AND METHODS

ANALYSIS AND ESTABLISHMENT OF THE HARVESTER OPERATION SCHEDULING MODEL

Analysis of the mode of harvester operation scheduling

In view of the characteristics and trends of agricultural machinery operation scheduling, this paper took the regional order-oriented multi-agricultural machinery cooperative scheduling model as the research object, and took the grain harvester as an example. The process of harvester operation scheduling under this model can be described as follows:

There is an agricultural machinery scheduling centre in a certain area, which has the functions of gathering statistics for agricultural machinery operation orders and coordinating the allocation of agricultural machinery resources within the region. During the harvest season, the centre collects agricultural machinery operation orders from farmers, including the type of operation, location coordinates of the operation, operation area, the earliest harvest time, and the latest harvest time, generates a harvester operation schedule for the region, and matches an appropriate harvester to each farm field according to the distance between each harvester and the field, the productivity and operation status of the harvester, etc.

Due to the complexity of the agricultural production environment, the research in this paper was based on the following assumptions:

(1) Information on farm operation orders and information on the location, operation capacity and status of harvester are clear, and the harvesters are not faulty during operation;

(2) Because the area of farmland is small and the distribution of farmland is scattered, the position information of farmland orders is represented by the latitude and longitude coordinates of the position where the harvester enters and exits the farmland;

(3) Single farm operation orders can be operated by one or more harvesters. When multiple harvesters work together, the agricultural machinery may come from different cooperatives. The harvesting time window required for the farmland operation order is the best harvest period of the grain;

(4) The harvester can reach the farmland operation point in advance, and the time for completing all the work in the farmland can slightly exceed the latest completion time specified in the order; However, it is necessary to calculate the cost loss caused by not operating in the time window specified by the order;

(5)The start time of each harvester in the same farmland is not necessarily the same, but the end time should be the same, and each harvester returns to the original hangar after completing all the order tasks.

Establishment of the harvester operation scheduling model

- **Model variables and parameter settings**

To analyse the harvester operation scheduling problem, it is necessary to mathematically describe the main variables and parameters involved in the scheduling process.

We defined the set $Ord=\{ord_1,ord_2,...,ord_M\}$ to represent M farmland order operation information, and single order operation information can be expressed as $ord_j=\{\{longitude_j, latitude_j\}, A_j, T_{sj}, T_{ej}\}, j=1,2,...,M$. Among them, $\{longitude_j, latitude_j\}$ represents the latitude and longitude position information of the order; A_j is the area of the field (hm^2); The operation time window starts from T_{sj} to the end of T_{ej}.

We defined the set $M_a=\{m_1,m_2,...,m_N\}$ to represent N harvesters, and each harvester can be expressed as $m_i=\{\{longitude_i, latitude_i\}, w, v\}$, i=1, 2,...,N. $\{longitude_i, latitude_i\}$ refers to the current location information of i harvester, including the parking locations in cooperative and operation point in farmland; w is the productivity of the harvester (hm²/h); v is the transfer speed (km/h).

We defined the set $P_r=\{V_s, G, D_{(g,h)}\}$ to represent the actual traffic road network information in reality. Among them, the set $V_s=\{V_{mo}, V_f\}$ represents all the path nodes in the traffic road network, $V_{mo}=\{V_{m1}, V_{m2}, \ldots, V_{mK}\}$ represents the set of K cooperative location nodes, $K \leq N$; $V_f=\{V_{f1}, V_{f2}, ..., V_{fM}\}$ is the set of M farmland location nodes; the set $G=\{(g,h)/g, h \in V_s, g \neq h\}$ represents the linking arcs of all path nodes. The set $D_{(g,h)}=\{dist.(g,h)/g, h \in V_s\}$ represents the actual distance of the linking arc (g,h), calculated by the geographic coordinates of g and h.

The scheduling plan given by the scheduling centre includes the number of harvesters ordered by Field j (M_j), the ID number of each harvester, the time taken by Harvester i to reach Field j through Node g ($t_{i(g,j)}$), where $g, j \in V_s$, the actual starting time of Harvester i in Field j (t^i_{sj}), and the actual ending time of Harvester i in Field j (t_{ej}).

In addition, the following variables and parameters are included: F is the total income of the scheduling scheme (yuan); c_h is the revenue of the harvesting operations per unit area (yuan); c_{wj} is the cost of the harvester operations per unit area of Field j (yuan/hm²); c_d is the waiting time cost of the harvester per unit time (yuan/h); c_y is the harvester transfer cost per unit distance (yuan/km); c_s is the timeliness loss per unit area (yuan/hm²/h); x_{ij} is the flag of the harvester operation (when Harvester i operates in Field j, x_{ij} = 1, otherwise, x_{ij} = 0); $p_{i(g,h)}$ is the flag of harvester transfer (when Harvester i is transferred to Field h from Field g, $p_{i(g,h)}$ = 1, otherwise, $p_{i(g,h)}$ = 0).

- **Scheduling goals and constraints**

Through analysis of order-oriented multi-machine coordination scheduling, we constructed a harvester operation scheduling model with the operation income as the optimization goal, as follows:

$$\max F = (c_h - c_{wj})\sum_{j=1}^{M} A_j - c_y \sum_{i=1}^{N}\sum_{g\in Vs}\sum_{h\in Vs} p_{i(g,h)} D_{(g,h)} - c_d \sum_{i=1}^{N}\sum_{j=1}^{M} x_{ij} \max\left\{t_{i(g,j)} - T_{sj}, 0\right\} - c_s w \sum_{i=1}^{N}\sum_{j=1}^{M} x_{ij} \max\left\{t_{ej} - T_{ej}, 0\right\} \quad (1)$$

Equation (1) is the objective function of the model, which calculates the income of the machine-harvesting operation in the area by subtracting the total cost from the total revenue of the machine-harvesting service. The total cost includes the operating cost, the transfer cost, the waiting time cost and the operation delay cost of the harvester.

By combining the production reality and relevant assumptions about the scheduling process, we placed the following constraints:

$$M_j = \left\lfloor \frac{A_j}{w[T_{ej} - T_{sj}]} \right\rfloor + 1 \quad (2)$$

$$\sum_{i=1}^{N}\sum_{j=1}^{M} x_{ij} w(t_{ej} - t^i{}_{sj}) = A_j \quad (3)$$

$$t_{i(g,h)} = t_{eg} + \frac{D_{(g,h)}}{v} < t_{eh} \quad (4)$$

$$\sum_{k\in V_{mo}}\sum_{g\in V_s} p_{i(k,g)} - \sum_{k\in V_{mo}}\sum_{g\in V_s} p_{i(g,k)} = 0 \quad (5)$$

Equations (2)-(5) are the constraints of the model, of which equation (2) indicates the minimum number of harvesters required to complete the operation load of harvesting Field j; Equation (3) indicates the constraint that the operation load of harvesting Field j must be completed, in which t^i_{sj} is the time when Harvester i starts to operate in Field j; Equation (4) indicates that the time when Harvester i arrives at Field h is the sum of the

time taken to complete operation in Field g and that taken for transfer from Field g to Field h and that this time should be earlier than the latest time that Field h needs to be harvested; Equation (5) indicates the constraint that Harvester i must return to its original garage.

SIMULATED ANNEALING GENETIC ALGORITHM-BASED HARVESTER SCHEDULING ALGORITHM

Selection of the harvester operation scheduling algorithm

The harvester operation scheduling problem can be regarded as a special case of a multi-parking lot vehicle scheduling problem with a time window, which is a rather complicated combinatorial optimization problem *(Santoro et al., 2017)*. Intelligent heuristic algorithms such as Genetic algorithm (GA) *(Gholami et al., 2018)*, Simulated Annealing algorithm (SA) *(Cruz-Chávez et al., 2017)*, Ant Colony Optimization *(Engin and Güçlü, 2018)* and Tabu Search algorithms *(Dabah et al., 2019; Qiu et al., 2018)* have been widely used to solve similar large-scale scheduling problems. Among them, simulated annealing genetic algorithm is a hybrid optimization algorithm that combines genetic algorithm and simulated annealing algorithm. It adopted the original genetic algorithm coding method, which can keep the original global parallel search ability of genetic algorithm *(Liu et al., 2014; Song et al., 2020)*. The simulated annealing operation in the algorithm can give full play to the excellent local search ability of simulated annealing algorithm, overcome the disadvantage of poor local search ability of genetic algorithm, make the algorithm jump out of the local optimal solution region and search for the global optimal solution *(Zheng et al., 2020)*; Therefore, we designed a harvester operation scheduling algorithm based on simulated annealing genetic algorithm, in order to improve the responsiveness of the harvester scheduling system while increasing income of the machine-harvesting operation.

Coding for the solution

By combining the characteristics of the harvester operation scheduling problem and the results of related studies, we used a two-layer coding method for the solution, as shown in Fig.1.

F_1		F_2			F_3			F_4		F_5	
m_1	m_2	m_3	m_4	m_5	…	…	…	…	…	m_{k-1}	m_k

Fig. 1 - Coding structure

The first layer of the coding is to sort the fields, in which the order of the fields is the service order of the field operation orders; in Fig. 1, F_1 - F_5 are field operation orders. The second layer of the coding sorts the harvesters in the fields, e.g., in Fig. 1, harvesters m_1 and m_2 are operating in Field F_1.

Generation of the initial solution based on scheduling rules

In traditional genetic algorithm, the initial population is mostly constructed by random generation, which may produce a large number of poor-quality solutions or illegal solutions for scheduling problems with time windows. In order to avoid the generation of invalid solutions and improve the efficiency of the algorithm, the initial solution is generated based on scheduling strategy.

- **scheduling strategy**

According to production experience, prioritizing the service to fields that have an approaching harvesting time window and a large area can lower the loss caused by harvesting delay, and reasonably allocating harvesters for different fields can reduce production cost. Therefore, we used the following strategies when coding:

Strategy 1: The priority function was designed with the weighting method using the field time window and field area as variables, and the field operation order was decided based on the priority.

Assuming that the weight of the time window factor is w_1, that of the field area is w_2, and t and a are the normalized data of the field time window and field area, respectively, we obtained the priority function as shown in Equation (6).

$$f = w_1 t + w_2 a \tag{6}$$

Strategy 2: The field is matched with the minimum amount of agricultural machinery resources that can meet the production needs. The number of harvesters assigned to a field is determined by the area of the field and the harvesting time window, using Equation (2).

Strategy 3: When matching the field operation order with harvesters, the harvester with the lower absolute difference between the arrival time and the earliest harvesting time of the field is preferentially scheduled.

- **Initial population generation algorithm**

Based on the above coding strategies, the initial solution of the simulated annealing genetic algorithm was generated, with the following steps:

Step 1: Establish a field operation set and rank the operation order according to Strategy 1; establish the operating harvester set;

Step 2: Determine whether the field operation set is empty. If the set is empty, go to Step 4, otherwise, go to Step 3;

Step 3: Assign harvesters to field operation orders according to Strategies 2 and 3; go to Step 2;

Step 4: The matching for the initial scheduling scheme is completed. The initial population with a certain number of chromosomes is generated by random variation of genes in the initial scheme.

Fitness function

Since the optimization goal of the harvester scheduling model is to maximize the operation income of harvesters, the Equation (1) can be directly used to calculate the fitness of each chromosome.

Genetic manipulation

- **Selection operator**

The selection operation in the algorithm adopted the roulette method. The greater the fitness of the individual is, the greater the probability of each chromosome being selected, which ensures that good individuals have a greater chance of being retained and participating in evolution.

- **Crossover operator**

We used the mutated partially mapped crossover to cross the selected parent individuals to increase the proportion of feasible solutions. The basic operation is as follows: two crossover points are randomly generated in the upper farmland code, and then the agricultural machinery codes of the lower layer corresponding to the two crossing points in the parent individuals A1and A2 are exchanged to generate new individuals B1 and B2. The specific cross processing is shown in Fig.2:

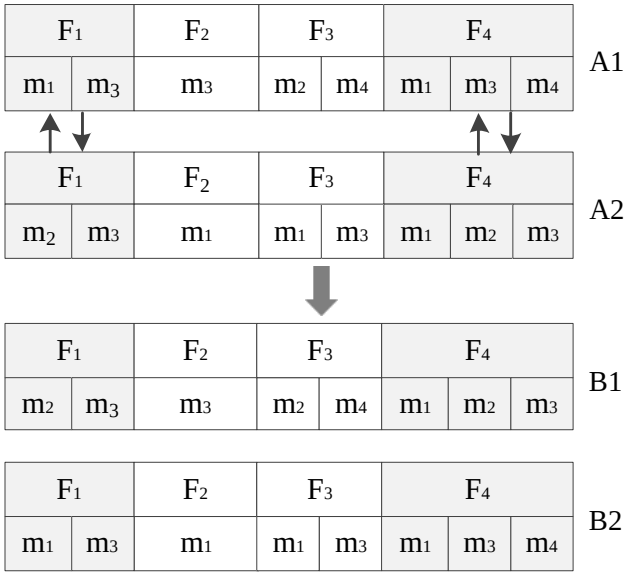

Fig. 2 - Chromosome crossover

- **Mutation operator**

Mutation operation is an important means to ensure the diversity of population. The basic operation of mutation operator in this paper was as follows: randomly generated a mutation point in the selected individual farmland code, and randomly mutated an agricultural machinery code in the lower layer of the selected farmland code to generate a new individual.

Simulated annealing operation

- **Cooling function**

Simulated annealing operation is the simulation of thermodynamic annealing process. In the simulated annealing process, every time the temperature is lowered, the algorithm completes an optimization, and the number of iterations is equal to the number of temperature drops. The simulated annealing cooling formula is:

$$T_k = r^k \cdot T_0 \tag{7}$$

In Equation (7), T_k is the current temperature; r is the cooling coefficient, $0 < r < 1$; k is the number of cooling; T_0 is the initial temperature; all variables in this equation are dimensionless. The number of cooling times k is the current iteration number of the algorithm.

- **New solution acceptance criteria**

In the iterative process of the algorithm, new solutions are generated through the crossover and mutation operations mentioned above. The objective function values of the new solution X_2 and the old solution X_1 are $F(X_2)$ and $F(X_1)$ respectively, and the difference between $F(X_2)$ and $F(X_1)$ is defined as $\Delta E = F(X_1) - F(X_2)$. The probability of accepting the new solution is calculated using Metropolis criterion:

$$P_{T_k} = \min\{1, e^{-\frac{\Delta E}{T_k}}\} \tag{8}$$

In Equation (8), P_{T_k} is the probability of accepting the new solution; T_k is the current temperature, and all variables are dimensionless.

Overall algorithm steps

The overall process of the simulated annealing genetic algorithm-based harvester operation scheduling algorithm is as follows:

Step1: Read the order information of the farmers and the position coordinate information of the harvesters; initialize the distance matrix; establish the field operation task set and prioritize the tasks; establish the harvester set.

Step2: Initialize the parameters. Parameters include annealing initial temperature T_0, termination temperature T_{min}, cooling rate r, population size S_{pop}, evolution termination algebra M_{gen}, crossover probability P_c, mutation probability P_m, etc.

Step3: According to the various parameters in the scheduling model: order information of farmland, initial state information of each harvester, distance matrix of each coordinate point and other information, use priority rules to generate the initial population, and calculate the fitness value of each individual X_i, i= 1, 2, ... , S_{pop}. Record the global optimal solution as X_{best}=maxX_i; set the current temperature T=T_0;

Step4: Set the genetic loop count variable gen=0.

Step5: Perform selection, crossover, and mutation operations on the population to form a new population individual and calculate the fitness value X_i, i=1,2,..., S_{pop}, and record the current optimal solution X_{new}=maxX_i.

Step 6: calculateΔE=X_{best} − X_{new}, if ΔE<0, X_{best}=X_{new}; otherwise, calculate the acceptance probability P_{tk} of new solution X_{new} according to the new solution acceptance criteria in 2.6 and judge whether to make X_{best} = X_{new} .

Step 7: judge whether $gen < M_{gen}$ is true, if yes, then gen = gen + 1 and go to step 5; otherwise, go to step 8.

Step 8: judge whether $T < T_{min}$ is true, if so, the algorithm will terminate and get the global optimal solution X_{best}; otherwise, execute the cooling operationT_{k+1}=$T_k r$, and turn to step 4 until T<T_{min} holds.

RESULTS

Case information

In this paper, four agricultural machinery cooperatives in Wuchang City, Heilongjiang Province, China were selected as the analysis objects, numbered O1-O4. The cooperatives had 10 harvesters. The Agricultural Machinery Operation Scheduling Centre received a total of 20 farmland rice harvesting orders during the harvest season, and all orders were completed by four cooperatives. The specific information of farmland orders and harvesters are shown in Tables 1 and 2.

Table 1

Farmland job order information

Farmland number	East longitude [°]	North latitude [°]	Area [hm^2]	Time window
1	127.1594	45.1222	34.20	10.1-10. 4
2	127.1750	44.5621	16.40	10.1-10. 3
3	126.8755	44.4111	27.87	10.2-10.5
4	127.7832	45.2904	23.60	10.2-10. 5
5	126.7959	44.9090	30.67	10.2-10. 6
6	127.1191	44.5549	22.80	10.3-10.6
7	126.7471	45.1648	31.07	10.3-10.7
8	126.9162	44.3555	36.13	10.3-10.7
9	127.5360	44.9858	24.20	10.4-10.7
10	127.2267	44.9844	25.40	10.5-10.8
11	127.0565	44.8796	39.67	10.5-10.9
12	126.9382	45.0852	25.47	10.5-10.9
13	126.9322	45.0250	19.80	10.6-10.10
14	127.4192	44.6940	37.80	10.6-10.10
15	126.8195	45.1222	33.53	10.7-10.11
16	127.5845	45.2773	14.73	10.7-10. 10
17	127.2102	44.8170	32.40	10.8-10. 12
18	127.0675	44.7754	30.40	10.8-10. 12
19	127.2927	44.8396	21.07	10.9-10. 14
20	127.6055	45.1611	35.73	10.9-10. 14

Table 2

Agricultural machine descriptions

Harvester number	East longitude [°]	North latitude [°]	Transfer speed [km/h]	Productivity [hm^2/h]
M1	127.0841	45.0843	35	0.45
M2	127.0841	45.0843	35	0.45
M3	127.1765	44.8246	35	0.45
M4	127.1765	44.8246	35	0.45
M5	127.1765	44.8246	35	0.45
M6	127.4425	45.0242	35	0.45
M7	127.4425	45.0242	35	0.45
M8	127.4425	45.0242	35	0.45
M9	127.5586	44.9168	35	0.45
M10	127.5586	44.9168	35	0.45

Through relevant research and data review, the service price of Wuchang City is 900 yuan/hm^2, and the Kubota 4LBZ-172B semi-feeding harvester was used for operation. The operating cost of the harvester was 720 yuan/hm^2 (excluding fuel cost), the harvester can work for 12 hours a day, the transfer speed was 35 km / h, the transfer cost was 4 yuan/km, the waiting cost was 42 yuan/h, harvester hourly productivity was 0.45 hm^2/h, the operation delay cost of the harvester was 10.8 yuan/hm^2/h, and the actual transfer distance between each coordinate point was obtained through the Baidu map API interface.

RESULTS AND DISCUSSION

The proposed simulated annealing genetic algorithm-based harvester operation scheduling algorithm was implemented using MATLAB R2019a software on a PC with Windows10. In the experiment, the parameters of the simulated annealing genetic algorithm were as follows: initial temperature T_0 = 100, termination temperature T_{min} =10^{-20}, cooling rate r = 0.85, population size S_{pop}=30, evolution termination algebra M_{gen}=20, crossover probability P_c=0.8, mutation probability P_m=0.2.

This example was solved using the proposed simulation annealing genetic algorithm with MATLAB software to obtain the scheduling scheme, as shown in Figs. 3 and 4.

Fig. 3 shows the transfer paths of harvester operation, the locations of the agricultural machinery centres and fields were described through coordinates, in which the abscissa is the longitude, and the ordinate is the latitude. The harvester transfer path of each harvester of each centre can be obtained using the proposed algorithm.

For example, Fig. 3a shows that the harvester transfer path of Harvester M1 from Centre O1 was 8-2-6-10-13. It can be seen from the Fig. 3 that all the orders were serviced and there was spatial proximity between the order tasks assigned to each harvester, which indicated the rationality of the experimental results.

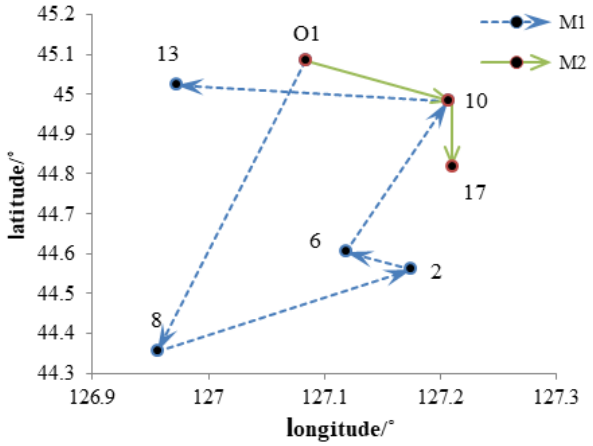

a) Transfer path of O1 cooperative harvester

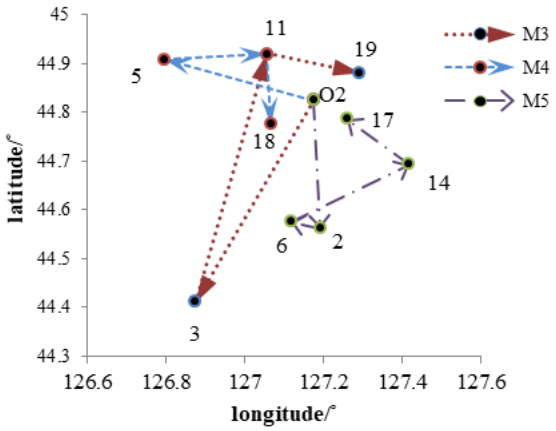

b) Transfer path of O2 cooperative harvester

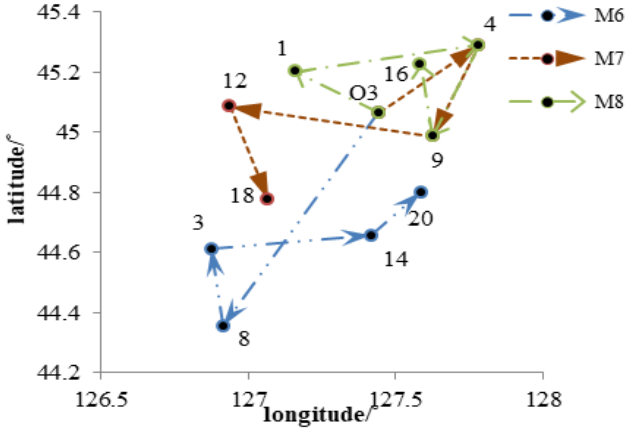

c) Transfer path of O3 cooperative harvester

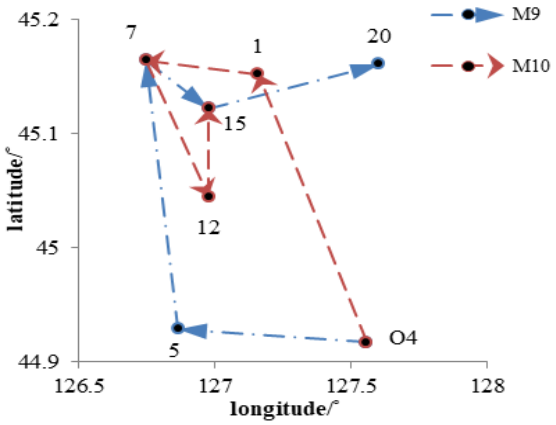

d) Transfer path of O4 cooperative harvester

Fig. 3 - Diagram of each harvester's job transfer path

Figure 4 shows the harvester operation scheduling Gantt chart, in which:

- the abscissa is time;
- the ordinate is the harvester ID number;
- the bar represents the operation plan of each harvester in the field, including the order number, the operation start time, and the operation end time.

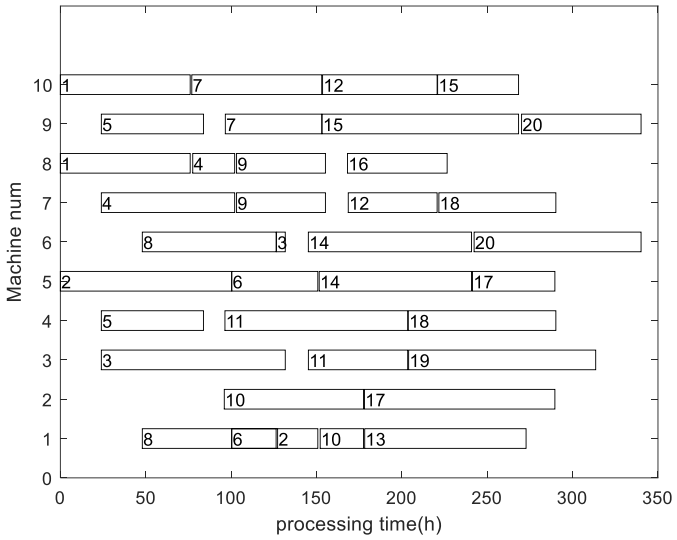

Fig. 4 - Deployment of Gantt chart

To further illustrate the validity of the algorithm, we ran 20 iterations using SA, GA and SAGA respectively, and compared each of the variable cost indicators of the scheduling schemes obtained. The results are shown in Table 3.

Table 3

The comparison of 3 algorithms scheduling results

Income and cost indicator	SA	GA	SAGA
The operation income (yuan)	94027.40	92816.07	94414.73
The transfer distance (km)	1669.81	1728.13	1602.92
The waiting time cost (yuan)	0	456.12	0
The operation delay cost (yuan)	671.07	1234.73	541.70

Table 3 shows that the operation income of the scheduling scheme generated using the proposed algorithm increases by 387.33 yuan and 1598.66 yuan on average compared with SA and GA alone, indicating that the SAGA was superior in improving the income from the harvesting operation. Compared with those of the scheme obtained through the SA and GA, the transfer distance of the scheme obtained through the SAGA decreased by 4.0% and 7.25% on average. SA and GA can obtain the scheduling scheme with a waiting time of 0 hours. In addition, the scheduling scheme calculated by SAGA also had the minimum average operation delay cost, which were 19.28% and 56.1% lower than those of SA and GA respectively. The experimental results showed that the harvester scheduling algorithm based on SAGA can better meet the constraints of time window, and reduce the costs related to scheduling, so as to obtain the highest operation income.

Algorithm performance analysis

To further evaluate the stability, search performance and running efficiency of the harvester operation scheduling algorithm designed in this paper, based on the cases obtained from the investigation, five calculation examples with different numbers of farmland were constructed. We used simulated annealing algorithm, genetic algorithm and simulated annealing genetic algorithm to conduct 20 simulation tests for 5 cases respectively. The experimental results are shown in Fig. 5 and Fig. 6.

Fig. 5 shows the average operation income and standard deviation of the scheduling scheme obtained by three algorithms for five different calculation examples. The SAGA can obtain the maximum average operation income in all the calculation examples, and in the first four examples, SA obtained better average operation income than genetic algorithm. Among the three algorithms, the standard deviation of the operation income calculated by genetic algorithm was the largest in all calculation examples, which proved that the solution of genetic algorithm had greater fluctuation. When SAGA was used to solve the calculation examples of 20, 60, 100 farmland, the standard deviation of the operation income was the smallest.

The experiment confirmed that the proposed algorithm had good stability and can obtain high-quality solutions for various examples, with only small fluctuations.

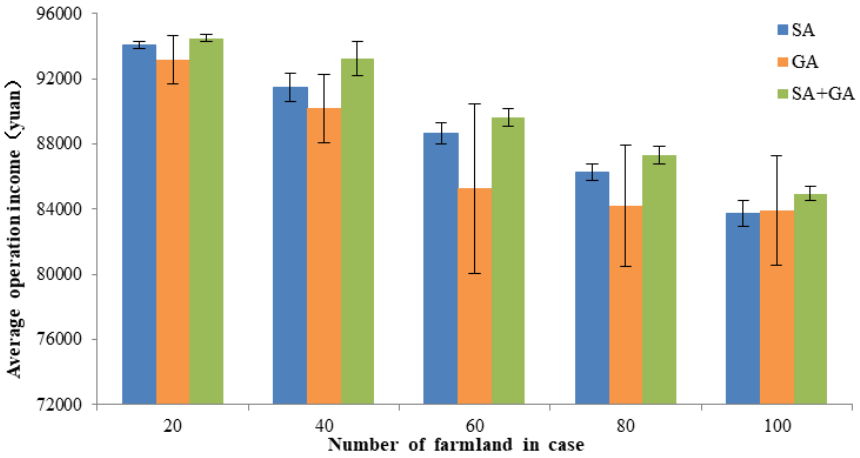

Fig. 5 - The average and variance of operation income

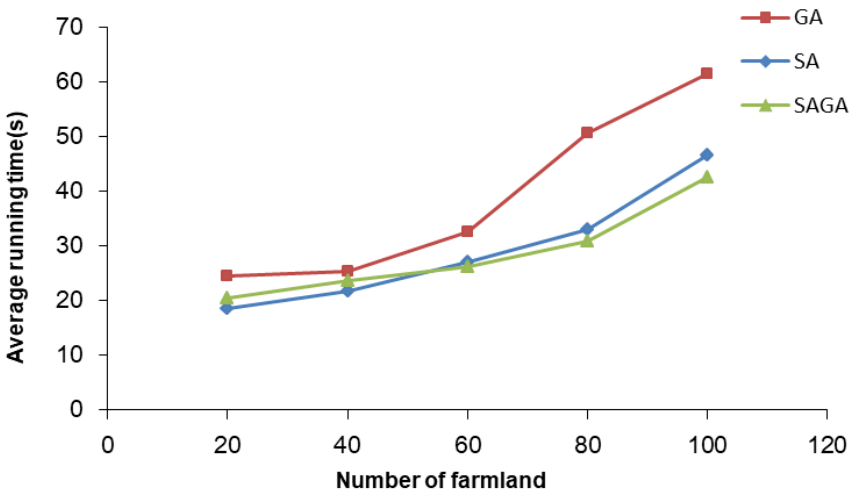

Fig. 6 - The average running time of three algorithms

Fig. 6 shows the average running time of the scheduling scheme obtained by three algorithms for five different calculation examples. With the increase of the number of farmlands in the calculation examples, the average running time of the three algorithms increased, which was caused by the increase of the complexity of the problem. GA had the longest running time, which may be related to its use of randomly generated initial population as the starting point of evolution. The SA and SAGA use the rule-based initial solution algorithm to obtain the initial solution which is a better beginning of optimization and greatly shorten the running time of the algorithm. In the last three calculation examples, the average running time of SAGA is less than that of using SA only, and the time saved was increasing, which showed that the genetic operation introduced in SAGA can improve the search efficiency of the algorithm in large-scale cases. At the same time, when the number of farmlands in the case was 100, the running time of the SAGA was only 42.55 s, which can meet the demand of large-scale farmland case scheduling in reality.

CONCLUSIONS

(1) In this study, we analysed each cost item generated in harvester operation scheduling using order-oriented multi-machine collaborative operation scheduling as the subject and constructed a harvester operation scheduling model using the total income of the harvesting service as the optimization goal. This model effectively integrated the information about the operating cost, transfer cost, waiting time cost, and the operation delay cost of the harvesters and improved the accuracy of the harvester operation scheduling model.

(2) By analysing and comparing the advantages and disadvantages of existing vehicle scheduling algorithms, combining with the characteristics of harvester scheduling, we combined genetic algorithm with simulated annealing algorithm and proposed a simulated annealing genetic algorithm-based heuristic harvester operation scheduling algorithm.

(3) We performed example simulations and related experimental analyses using MATLAB software to analyse the effectiveness, stability, search performance and running efficiency of the proposed harvester operation scheduling algorithm. The experimental results showed that the proposed harvester operation scheduling algorithm effectively combined the good global search performance of the GA and the strong local search capability of SA, and can be superior to the existing algorithm in meeting the demand of farmland time window and increasing operation income. Moreover, the proposed algorithm had higher stability, less fluctuation of solution quality and faster running efficiency, which made it possible to solve large-scale farmland scheduling problems.

ACKNOWLEDGEMENT

This work was funded by the National Key Research and Development Program of China (Grant No.2017YFD0700601-2), Humanities and Social Sciences Foundation of the Ministry of Education of China (Grant No. 14YJCZH06), Science and Technology Innovation Project of the Chinese Academy of Agricultural Sciences (Office of CAAS (2014) No. 216).

REFERENCES

[1] Bochtis, D. D., Sørensen, C. G., & Busato, P. (2014). Advances in agricultural machinery management: A review. *Biosystems Engineering*, vol. 126, pp. 69-81.

[2] Cruz-Chávez, M. A., Martínez-Rangel, M. G., & Cruz-Rosales, M. H. (2017). Accelerated simulated annealing algorithm applied to the flexible job shop scheduling problem. *International Transactions in Operational Research*, vol. 24, issue. 5, pp. 1119-1137.

[3] Dabah, A., Bendjoudi, A., AitZai, A., & Taboudjemat, N. N. (2019). Efficient parallel tabu search for the blocking job shop scheduling problem. *Soft Computing*, vol. 23, issue. 24, pp. 13283-13295.

[4] Dong, J., & Li, S. (2015). Analysis of status and developing trend for service principal of agricultural machinery operations in China. *Journal of Chinese Agricultural Mechanization*, vol. 36, issue. 6, pp.308-314.

[5] Edwards, G., Sørensen, C. G., Bochtis, D. D., & Munkholm, L. J. (2015). Optimised schedules for sequential agricultural operations using a tabu search method. *Computers and Electronics in Agriculture*, vol. 117, pp. 102-113.

[6] Engin, O., & Güçlü, A. (2018). A new hybrid ant colony optimization algorithm for solving the no-wait flow shop scheduling problems. *Applied Soft Computing*, vol. 72, pp. 166-176.

[7] Gholami, O., Sotskov, Y. N., & Werner, F. (2018). A genetic algorithm for hybrid job-shop scheduling problems with minimizing the makespan or mean flow time. *Journal of Advanced Manufacturing Systems*, vol. 17, issue. 4, pp. 461-486.

[8] Guan, S., Shikanai, T., Nakamura, M., Fukami, K., & Takahashi, K. (2018). Practical scheduling problem for sugarcane-farming corporations and its solution. *Engineering in Agriculture, Environment and Food*, vol. 11, issue. 4, pp. 211-219.

[9] He, P., Li, J., & Wang, X. (2018). Wheat harvest schedule model for agricultural machinery cooperatives considering fragmental farmlands. *Computers and Electronics in Agriculture*, vol. 145, pp.226-234.

[10] Liu, M., Liu, C., Xing, L., Zhang, X., Wang, Q., & Wang, X. (2014). Quality oriented assembly grouping optimal allocation method for remanufactured complex mechanical products. *Journal of Mechanical Engineering*, vol. 50, issue. 8, pp. 150-155.

[11] Luo, X., & Zhang, L. (2016). The optimal scheduling model for agricultural machinery resources with time-window constraints. *International Journal of Simulation Modelling*, vol. 15, issue. 4, pp. 721-731.

[12] Qiu, M., Fu, Z., Eglese, R., & Tang, Q. (2018). A Tabu Search algorithm for the vehicle routing problem with discrete split deliveries and pickups. *Computers & Operations Research*, vol. 100, pp.102-116.

[13] Santoro, E., Soler, E. M., & Cherri, A. C. (2017). Route optimization in mechanized sugarcane harvesting. *Computers and Electronics in Agriculture*, vol. 141, pp. 140-146.

[14] Song, Z., Zang, L., & Zhu, W. (2020). Study on minimum emission control strategy on arterial road based on improved simulated annealing genetic algorithm. *Physica A-Statistical Mechanics and its Applications*, vol. 537, 122691.

[15] Thuankaewsing, S., Khamjan, S., Piewthongngam, K., & Pathumnakul, S. (2015). Harvest scheduling algorithm to equalize supplier benefits: A case study from the Thai sugar cane industry. *Computers and Electronics in Agriculture*, vol. 110, pp. 42-55.

[16] Wu, C., Cai, Y., Luo, M., Su, H., & Ding, L. (2013). Time-windows based temporal and spatial scheduling model for agricultural machinery resources. *Transactions of the Chinese Society for Agricultural Machinery*, vol. 44, issue. 5, pp. 237-241, 231.

[17] Zheng, X., Bao, J., Ma, Q., Zhou, H., & Zhang, L. (2020). Spinning workshop collaborative scheduling method based on simulated annealing genetic algorithm. *Journal of Textile Research*, vol. 41, issue. 6, pp. 36-41.

[18] Zhou, K., Jensen, A. L., Sørensen, C. G., Busato, P., & Bochtis, D. D. (2014). Agricultural operations planning in fields with multiple obstacle areas. *Computers and Electronics in Agriculture*, vol. 109, pp.12-22.

[19] Zhang, Z. (2020). Optimal Analysis of farm agricultural machinery equipment based on mathematical modelling. *INMATEH - Agricultural Engineering*, vol. 62, issue. 3, pp. 333-340.

DESIGN AND EXPERIMENTAL STUDY OF THE COMB-TYPE HARVESTING TEST BENCH FOR CERASUS HUMILIS
/
梳脱式钙果采收试验台设计与试验

Shaohua Liu, Junlin He*), Nan Wu [1]
College of Agricultural Engineering, Shanxi Agriculture University, Taigu/China;
Tel: +86-0354-6288400; E-mail: hejunlin26@126.com
DOI: https://doi.org/10.35633/inmateh-63-26

Keywords：*agricultural machinery, comb-type test bench, simulation experiment, design, Cerasus humilis*

ABSTRACT
A comb-type harvesting test bench was designed to address low fruit collection rate and theoretical analysis and simulation analysis of the harvesting process were carried out in this work. Single factor simulation experiment and bench experiment were carried out, and fruit collection rate was used as the evaluation index. The motor speed, bending angle of comb teeth and radial diameter of comb teeth arrangement were selected as the experimental factors. Results showed that the collection rate decreased with the increase of motor speed; and increased with the increase of the bending angle of comb teeth or the radial diameter of comb teeth arrangement. The orthogonal experiment of three-factor and three-level quadratic rotation centre combination was performed. The results showed that motor speed had the largest effect on collection rate, followed by radial diameter of comb teeth arrangement and bending angle of comb teeth. The optimal parameter combination was predicted by the response surface model as follows: motor speed of 25 r/min, bending angle of comb teeth of 120°, radial diameter of comb teeth arrangement of 868.45 mm and correspondingly the collection rate reached 91.51%. Based on actual harvesting efficiency and the machining problems of the test bench, the bench experiment was performed with the motor speed of 25 r/min, the bending angle of comb teeth of 120°, the radial diameter of comb teeth arrangement of 900 mm, and the collection rate was 93.82%. The relative error with the predicted optimal result was 2.48%, achieving the purpose of improving the collection rate.

摘要
针对钙果采收要求，本文设计了梳脱式钙果采收试验台，并对采收过程进行了理论分析与仿真分析。以采收率为评价指标，以电机转速、梳齿弯曲角度和梳齿排布弧度的直径为影响因素，进行单因子仿真试验与台架试验，试验结果表明采收率随着电机转速的增大而逐渐降低，随着梳齿弯曲角度或梳齿排布弧度直径的增大而逐渐升高。进行了三因素三水平二次旋转中心组合正交试验，结果表明各因素对采收率影响的主次顺序是电机的转速、梳齿排布弧度和梳齿弯曲角度。由响应面模型预测最优梳脱参数组合为：电机转速 25 r/min、梳齿弯曲角度 120°、梳齿排布弧度直径 868.45 mm，在此参数下模型预测最大采收率为 91.51%。结合实际采收效率以及试验台加工等问题，用试验台以电机转速 25 r/min、梳齿弯曲角度 120°、梳齿排布弧度直径 900 mm 进行试验，得到采收率为 93.82%，与预测最优结果相对误差为 2.48%，达到了提升采收率的目的。

INTRODUCTION

In recent years, with the popularization and development of breeding experts on *Cerasus humilis*, the planting area of *C. humilis* in China has been increasing year by year. As *C. humilis* is gradually recognized by the Chinese market, people attach great importance to the development of *C. humilis* industry (*Wang et al., 2016*). *C. humilis* is soft and easy to be damaged, and artificial harvesting efficiency is low, which seriously harms the economic benefits for the *C. humilis* industry. Therefore, the realization of mechanized harvesting of *C. humilis* is an urgent problem to be solved in the development of *C. humilis* industry.

The performances of the air shaking, trunk shaking, limb shaking and canopy shaking mechanical harvesting systems are briefly summarized (*Sanders., 2004*). The traction force of the fruits, the percentage of fruit removed, the detachment point and the tree damage were evaluated (*Torregrosa et al., 2009*).

[1] *Shaohua Liu, As. M.S. Stud. Eng.; Junlin He, Prof. Ph.D. Eng.; Nan Wu, M.S. Stud. Eng.*

A research aimed at assessing the effect of excitation position on fruit removal efficiency and fruit damage using a hand-held limb shaker for harvesting sweet cherry (*Zhou et al., 2014*). A study aimed to evaluate the feasibility of a mechanical-assist shake-and-catch system to harvest sweet cherries in a large range of commercial orchards (*Zhou et al., 2016*).

In China, some scholars have done the following relevant studies on the mechanized harvesting of *C. humilis*. A rotating wire collision *C. humilis* picking device was developed (*Liu et al., 2013*). The material properties and biomechanical properties of *C. humilis* were measured (*Sun et al., 2016*). An intermittent comb - brush *C. humilis* picking device was proposed and developed (*Zhang et al., 2018*).

The relationship between comb teeth of different shapes and the collision force of *C. humilis* was analysed based on the principle of comb brush (*Kang et al., 2017*). An eccentric swing combing device for *C. humilis* was designed aiming at the low removal rate of *C. humilis* (*Du et al., 2019; Du et al., 2020*). The finger-type lifter test bench, the continuous *C. humilis* picking test bench and a self-moving electric harvester for *C. humilis* were developed. (*He et al., 2018; He et al., 2019; Fang et al., 2019*), realizes the specific planting agronomic harvest of *C. humilis*, but the collection rate remains to be improved.

To improve the collection rate, a comb-type harvesting test bench for *C. humilis* was designed and the fruit shedding track was analysed in this paper. The experimental study was carried out with fruit collection rate being used as the evaluation index, the motor speed, bending angle of comb teeth and radial diameter of comb teeth arrangement were selected as the experimental factors, to explore the optimal parameter combination of test bench and improve collection rate.

MATERIALS AND METHODS

Experiment *C. humilis* variety: 'Nongda 4'. Sampling location: Juxin Modern Agriculture Base in Taigu County, Shanxi Province, China (E 112°29′, N 37°23′). Sampling time: September 7, 2019. The growth status of 'Nongda 4' as shown in Fig. 1a. Due to the different effects of field environmental differences on the growth status of fruit, 5 different sampling sites were set in the experimental field of 'Nongda 4' to sample the fruit, so as to minimize the influence of individual differences on the experimental results.
Fig. 1b shows the hanging fruit branches samples of 'Nongda 4' *C. humilis*.

'Nongda 4' Cerasus humilis sampling

a) Growth state of 'Nongda 4' *b) Sample of hanging fruit branches*

Fig. 1 - 'Nongda 4' Cerasus humilis branches

Design of comb-type test bench

The combing and stripping mechanism was the core component of the *C. humilis* harvester; the design must be optimized to improve the collection rate of *C. humilis* harvester. In this paper, a comb-type harvesting test bench for *C. humilis*, as shown in Fig. 2, was designed on the basis of the characteristics of *C. humilis* plants and previous studies. It was mainly composed of a frame, combing and stripping mechanism, baffle, clamping conveying mechanism, control system, fruit-collecting box and transmission system. The combing and stripping mechanism was composed of rotating disk, comb teeth carrier plate and comb teeth, which was mainly used to separate branches and fruits. Branches could pass through the comb teeth, and fruits were blocked by the comb teeth and took off. The comb teeth could be replaced to facilitate the experiment with different parameters of comb teeth (*Zhang et al., 2014*).

The clamping conveying mechanism and control system were composed of controller, guide rail and branch fixing clamp, it mainly transported the hanging fruit branches to the combing and stripping mechanism. The transmission system was composed of motor, synchronous pulley, belt and transmission shaft, which provided the turnover power for the test bench. Fruit-collecting box served as a fruit gatherer.

Before the experiment, the number of fruits on the hanging fruit branches was counted, and the hanging fruit branches was fixed on the branch fixing clamp of the clamping conveying mechanism. The electromagnetic speed-regulating motor was started to provide turnover speed for the combing and stripping mechanism by the transmission system.

The control system controlled the branch fixing clamp to feed the hanging fruit branches into the combing and stripping mechanism, under the action of the motor, the combing and stripping mechanism performed continuous rotation movement to remove the fruits. After, the fruit finally fell into the fruit-collecting box to complete the harvesting process under the joint action of the initial collision velocity, gravity, and the comb teeth back pull and baffle.

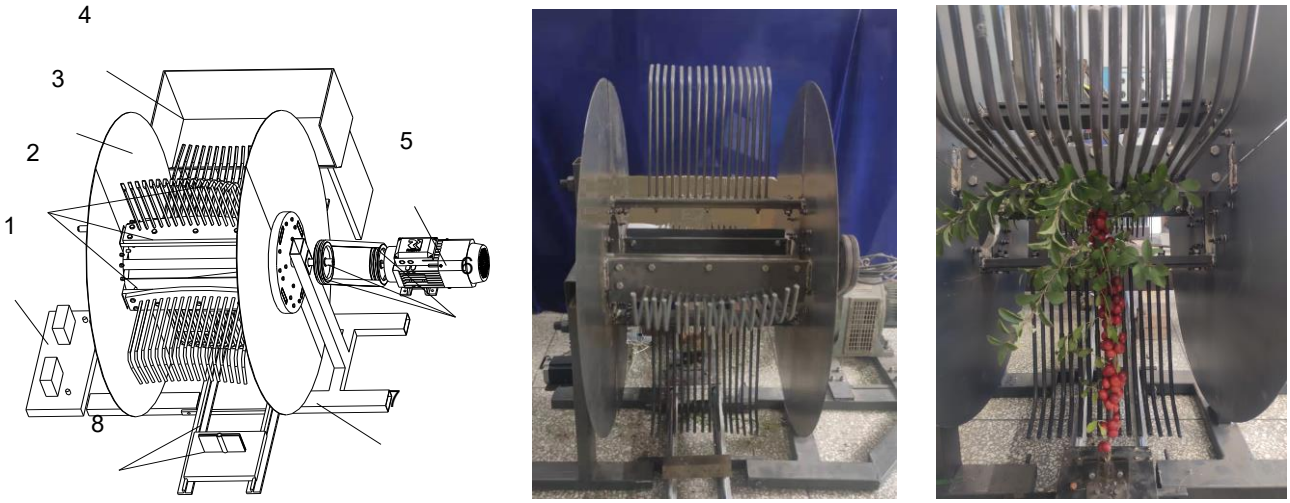

Fig. 2 - Comb-type harvesting test bench for Cerasus humilis

1- Control system；2- Combing and stripping mechanism；3- Baffle；4- Fruit-collecting box；5- Electromagnetic speed-regulating motor；6- Transmission system；7- Frame；8- Clamping conveying mechanism

Experiment factor analysis confirmed

Theoretical analysis of *Cerasus humilis* shedding track

The comb teeth would collide with the fruit when the Comb-type harvesting test bench for *C. humilis* is working, according to colliding situation in mechanics; the collision was accompanied by a change in energy from kinetic energy to potential energy to kinetic energy, so that after the collision, the speed of the test bench would give the fallen fruit an initial impact speed, the direction and size of this speed determined the range of fruit shedding, which would directly affect the fruit collection rate.

The previous experiment and research showed that the direction of fruit shedding was uncertain (*Liu et al., 2020*). If we assume that the fruit of shedding is a two-dimensional motion in a plane from which are detached, there would be two situations after shedding. When the position of *C. humilis* is lower than the rotating centre of the comb-type test bench, the *C. humilis* would finally fall to the front of the test bench. When the position of *C. humilis* is higher than the rotating centre of the comb-type test bench, the *C. humilis* would finally fell into the fruit-collecting box behind the test bench, as shown in Fig.3a. When the comb teeth were bent at a certain angle, some fruits below the rotating centre would be pushed back by the curved comb teeth, as shown in Fig.3b. With the constant turnover of the test bench, the fruit eventually fell into the fruit-collecting box under the action of comb teeth and baffle, and the proportion of fruit falling into the fruit-collecting box behind the test bench would increase, as shown in Fig. 3c.

Theoretically, the lower rotating centre of the test bench is the better, but if the centre is too low, it will limit the length of the comb teeth. If the length of the comb teeth is less than half of that of the branches, it is easy to cause branches winding. Therefore, bending the comb teeth angle was preferred to improve the collection rate.

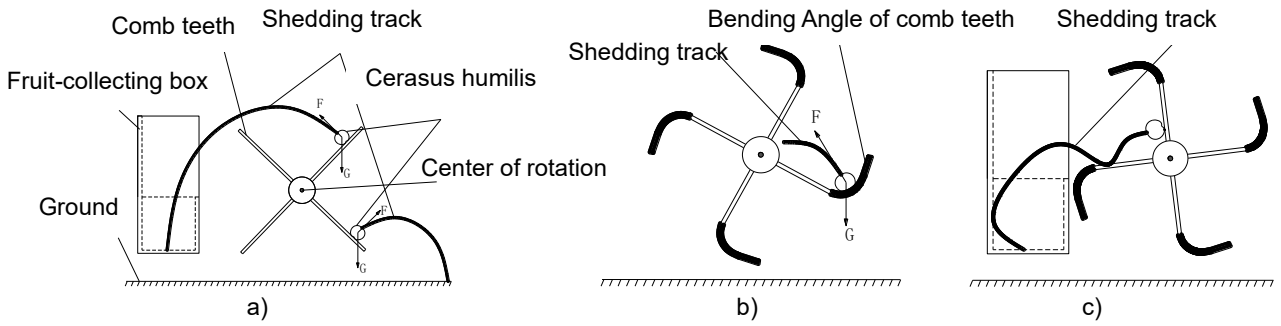

Fig. 3 - Fruit shedding track in two - dimensional plane

In fact, the branches of *C. humilis* are soft and pliable, and the fruit grows in different directions, hence some of the fruit bounce left or right after shedding off. In order to improve the collection rate, this paper combines the design of left and right baffles to arrange the comb teeth in a certain radian, which would give the fruit a left or right orienting force, so that fruit fell off in accordance with the predetermined direction, and the fruit fell into the fruit-collecting box under the action of baffle and comb teeth, which improved the collection rate of the test bench.

The above analysis showed that the motor speed determined the initial speed of the fruit after collision, which determined the range of the fruit falling off. The bending angle of comb teeth would increase the proportion of *C. humilis* falling into the fruit-collecting box. The comb teeth arrangement radian combined the design of baffle and test bench could improve the collection rate. These three factors would affect the collection rate of *C. humilis*.

Simulation analysis of *Cerasus humilis* shedding track

Based on PROE and ADAMS, this paper carried out dynamic simulation analysis on harvesting process of *C. humilis* (*He et al., 2020*). The 3D model of the test bench was established by PROE, and the simplified model was imported into ADAMS. The branch model of *C. humilis* hanging fruit was established in ADAMS, the number of *C. humilis* was set at 80, and the mechanical characteristics of *C. humilis* plant were simulated by flexible treatment of the branches. The harvesting of fruit was simulated by combining sensor and script simulation. The dynamic simulation model is shown in Fig. 4a. The shedding track diagram of No. 35～50 *C. humilis*, under the conditions of the motor speed 25 r/min, the bending angle of comb teeth 60°, and radial diameter of comb teeth arrangement 900 mm, is shown in Fig. 4b.

Fig. 4b shows that the direction of fruit shedding was random. Due to the blocking and combing effect of baffle and test bench, most fruits were collected in the fruit-collecting box with the movement of comb teeth, but some fruits still fell from the front, the left and right. The simulation result was basically consistent with the fruit shedding track results in the theoretical analysis, which further verified that the three experimental factors in the theoretical analysis, namely motor speed, bending angle of comb teeth and radial diameter of comb teeth arrangement, would have a certain influence on the collection rate of C. humilis.

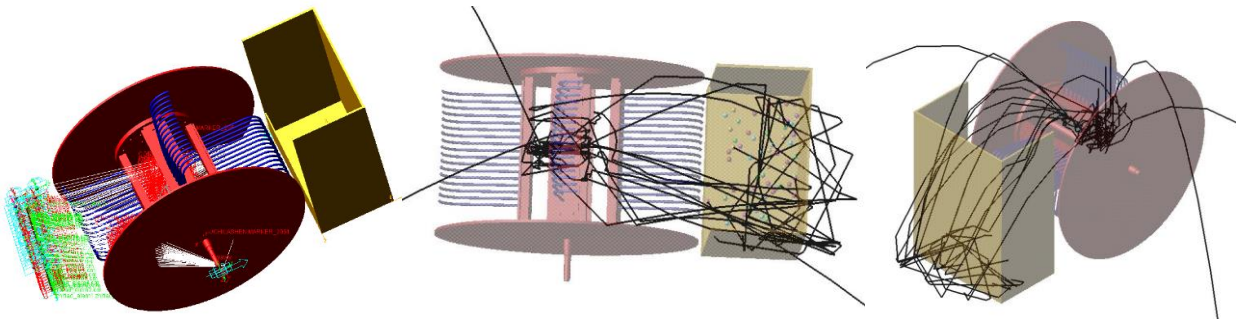

a) three-dimensional model of test bench b) *Cerasus humilis* shedding track

Fig. 4 - Dynamic simulation model

Experiment design

To clarify the effects of motor speed, bending angle of comb teeth and radial diameter of comb teeth arrangement on the collection rate, this paper took the collection rate as the evaluation index and carried out single factor dynamic simulation experiment, single factor bench experiment and the orthogonal experiment of three-factor and three-level quadratic rotation center combination. The calculation formula of collection rate is shown in Equation (1). Three times tests were conducted for each group, and the results were averaged. The design of each experiment scheme was as follows:

$$Y = \frac{G_1}{G} \times 100\% \quad (1)$$

Where

Y is the fruit collection rate, [%];

G_1 is the total number of *Cerasus humilis* on the branches;

G is the number of *Cerasus humilis* in the fruit-collecting box.

Design of single factor simulation experiment

Taking motor speed, bending angle of comb teeth and radial diameter of comb teeth arrangement as experimental factors, a single-factor dynamics simulation experiment was designed, with five levels for each factor. The experiment design is shown in Table 1.

Table 1

Single factor simulation experiment scheme

Item	1	2	3	4	5	1	2	3	4	5	1	2	3	4	5
Motor [r/min]	20	25	30	35	40	30					30				
Bending angle [°]	60					60	75	90	105	120	60				
Radial diameter [mm]	900					900					600	700	800	900	1000

Design of single factor bench experiment

The simulation experiment basically proved that the collection rate of *Cerasus humilis* was affected by the motor speed, bending angle of comb teeth and radial diameter of comb teeth arrangement. In order to further confirmed the accuracy of the simulation experiment results, the single factor bench experiment was used to verify the experiment results in this paper. Considering the machining problem of the test bench, each factor of the bench experiment was set at three levels, and the experiment scheme was consistent with the simulation experiment.

Design of orthogonal experiment

To study the influence of interactive factors on fruit collection rate, the orthogonal experiment of three-factor and three-level quadratic rotation center combination was designed in this paper. The experimental factors and levels are shown in Table 2.

Table 2

Coding schedule of experimental factors

Coded value	Motor speed	Bending angle	Radial diameter
	[r/min]	[°]	[mm]
	A	B	C
Lower level（-1）	25	60	600
Middle level（0）	30	90	750
Upper level（1）	35	120	900

If all the experimental schemes of orthogonal experiment were conducted, it would be too complicated. In order to improve the experiment efficiency and ensure the accuracy, the experiment scheme was designed by box-Behnken module in the Design-Export, with a total of 17 experiment points. The Design does not require multiple consecutive experiments and could assess the nonlinear influence of factors.

RESULTS

Simulation experiment results and quadratic regression analysis

Origin 2018 was used for fitting analysis of single-factor simulation experiment data, and the results are shown in Fig. 5.

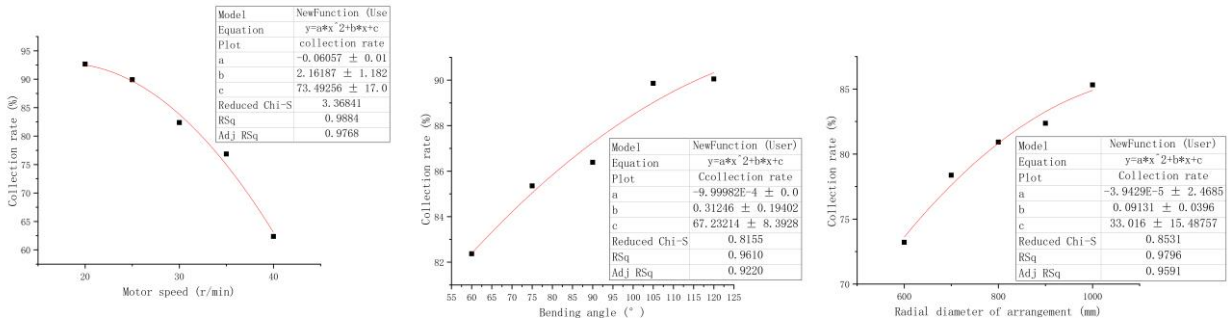

a) Motor speed fitting diagram b) Bending angle fitting diagram c) Radial diameter fitting diagram

Fig. 5 - The result of single factor simulation experiment

Fig. 5a shows the influence of motor speed on the collection rate, the quadratic polynomial parameters are shown in the figure, the determination coefficient (R^2) up to 0.9884, the adjusted determination coefficient (Adj R^2) up to 0.9768, it indicated that the predicted value of the regression model was well fitted to the actual value thus can be used in the prediction and analysis of the influences of the motor speed on the collection rate in the harvesting process. With the motor speed increased from 20 r/min to 40 r/min, the collection rate decreased from 92.65% to 62.37%.

Fig. 5b shows the influence of the bending angle of comb teeth on the collection rate, the quadratic polynomial parameters are shown in the figure, the determination coefficient (R^2) up to 0.9610, the adjusted determination coefficient (Adj R^2) up to 0.9220, it indicated that the predicted value of the regression model was well fitted to the actual value thus can be used in the prediction and analysis of the influences of the bending angle of comb teeth on the collection rate in the harvesting process. With the bending angle of comb teeth increased from 60° to 120°, the collection rate increased from 82.37% to 90.05%.

Fig. 5c shows the influence of the radial diameter of comb teeth arrangement on the collection rate, the quadratic polynomial parameters are shown in the figure, the determination coefficient (R^2) up to 0.9796, the adjusted determination coefficient (Adj R^2) up to 0.9591, it indicated that the predicted value of the regression model was well fitted to the actual value thus can be used in the prediction and analysis of the influences of the radial diameter of comb teeth arrangement on the collection rate in the harvesting process. With the radial diameter of comb teeth arrangement increased from 600 mm to 1000 mm, the collection rate increased from 73.18% to 85.32%.

Analysis of single factor bench verification experiment

Table 3 shows the comparison between the bench experiment and the simulation experiment, Table 3 showed that with the motor speed increased from 25 r/min to 35 r/min, the collection rate decreased from 88.65% to 78.86%; with the bending angle of comb teeth increased from 60° to 120°, the collection rate increased from 83.23% to 89.32%; with the radial diameter of comb teeth arrangement increased from 600 mm to 900 mm, the collection rate increased from 75.21% to 83.23%.

The maximum relative error between the bench and the simulation experiment is 3.09%, and the influence of the motor speed, the bending angle of the comb teeth and the radial diameter of the comb teeth arrangement on the collection rate are basically consistent with the conclusions from the simulation experiment. This shows that the simulation results are reliable, and the conclusion and regression model can be adopted.

Table 3

Comparison of experimental data

Item		Motor speed [r/min]			Bending angle [°]			Radial diameter [mm]		
		25	30	35	60	90	120	600	750	900
Collection rate [%]	Bench experiment	88.65	83.23	78.86	83.23	86.19	89.32	75.21	81.29	83.23
	Simulation experiment	89.92	82.37	76.42	82.37	86.39	90.05	73.18	79.32	82.37
Relative error [%]		1.43	1.03	3.09	1.03	0.23	0.82	2.70	2.42	1.03

Results of orthogonal experiment and ANOVA

The experiment points and experiment results designed by box-Behnken module in design-Export are shown in Table 4.

Table 4

Orthogonal experiment points and experiment results

No.	Motor speed A	Bending angle B	Radial diameter C	Collection rate Y
	[r/min]	[°]	[mm]	[%]
1	-1	-1	0	87.30
2	1	-1	0	75.83
3	-1	1	0	94.78
4	1	1	0	81.66
5	-1	0	-1	85.32
6	1	0	-1	73.27
7	-1	0	1	92.25
8	1	0	1	81.02
9	0	-1	-1	75.21
10	0	1	-1	79.63
11	0	-1	1	83.23
12	0	1	1	89.32
13	0	0	0	85.38
14	0	0	0	85.12
15	0	0	0	86.09
16	0	0	0	84.96
17	0	0	0	85.89

The results of variance analysis are shown in Table 5.

Table 5

The results of ANOVA

Item	Degree of freedom	Mean square	*F Value*	*P Value*
Model 1	9	58.55	124.50	< 0.0001**
A	1	286.44	609.08	< 0.0001**
B	1	70.92	150.81	< 0.0001**
C	1	131.14	278.85	< 0.0001**
AB	1	0.68	1.45	0.2681
AC	1	0.17	0.36	0.5688
BC	1	0.70	1.48	0.2628
A^2	1	0.29	0.61	0.4604
B^2	1	3.09	6.57	0.0374*
C^2	1	32.63	69.39	< 0.0001**

Note: P < 0.01 (extremely significant, **), P < 0.05 (significant, *).

The regression equation as shown in Equation (2).

ANOVA in Table 4 showed that the motor speed, the bending angle of the comb tooth and the radial diameter of the comb tooth arrangement all have extremely significant impact on collection rate (P<0.01). The quadratic regression model of fruit collection rate Y was extremely significant (P<0.01), with determination coefficient (R^2) was 0.9938, the adjusted determination coefficient (Adj R^2) was 0.9858, and the predicted determination coefficient (Pred R^2) was 0.9265, the difference between adjusted determination coefficient and the predicted determination coefficient was not more than 0.2. These results indicated that the quadratic regression fitting model has a high fitting precision, which can be used to predict and analyze the influence of motor speed, the bending angle of comb teeth and the radial diameter of comb teeth arrangement on the collection rate.

$$Y = 85.49 - 5.98 \cdot A + 2.98 \cdot B + 4.05 \cdot C - 0.41 \cdot AB + 0.20 \cdot AC + 0.42 \cdot BC + 0.26 \cdot A^2 - 0.85 \cdot B^2 - 2.78 \cdot C^2 \quad (2)$$

Where:

A is the motor speed, [r/min];

B is the bending angle of the comb teeth, [°];

C is the radial diameter of the comb teeth arrangement, [mm];

Y is the fruit collection rate, [%].

Analysis of the influence of interaction factors on the collection rate

In order to more visually see the interactive effect of motor speed, bending angle of comb teeth and radial diameter of comb teeth arrangement on collection rate, the 3D response surface was generated according to the Box-Behnken Centre combination method, as shown in Fig. 6a-6c.

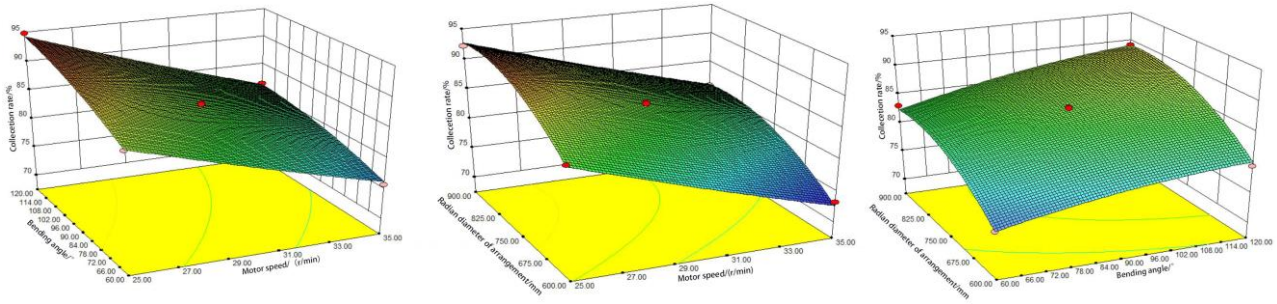

a. Y (A, B, 750) b. Y (A, 90, C) c. Y (25, B, C)

Fig. 6 - Response surface of various factors on fruit collection rate

Fig. 6a shows the interaction of motor speed and bending angle of comb teeth on the collection rate. Under the condition that the radial diameter of comb teeth arrangement was 750 mm, the collection rate decreased with the increase of motor speed, and increased with the increase of the bending angle of comb tooth. But when both the motor speed and the bending angle of comb teeth increased, the collection rate decreased gradually. When the motor speed increased, and the bending angle of comb teeth decreased, the collection rate declined significantly, indicating that the influence of the motor speed on the collection rate is more significant.

Fig. 6b shows the interaction of motor speed and radial diameter of comb teeth arrangement on the collection rate. Under the condition that the bending angle of comb teeth was 90°, the collection rate decreased with the increase of motor speed, and increased with the increase of the radial diameter of comb teeth arrangement. But when both the motor speed and the radial diameter of comb teeth arrangement increased, the collection rate decreased gradually. When the motor speed increased and the radial diameter of comb teeth arrangement decreased, the collection rate declined significantly, indicating that the influence of the motor speed on the collection rate is more significant.

Fig. 6c shows the interaction of bending angle of comb teeth and radial diameter of comb teeth arrangement on the collection rate. Under the condition that the motor speed was 30 r/min, the collection rate increased with the bending angle of comb teeth, and increased with the increase of the radial diameter of comb teeth arrangement. But when the bending angle of comb teeth increased and the radial diameter of comb teeth arrangement increased, the collection rate increased significantly. When the bending angle of comb teeth increased and the radial diameter of comb teeth arrangement decreased, the collection rate decreased gradually, indicating that the influence of the radial diameter of comb teeth arrangement on the collection rate is more significant.

As indicated by above analysis of the response surface, the priority of motor speed, bending angle of comb teeth and radial diameter of comb teeth arrangement for the collection rate was motor speed A, radial diameter of comb teeth arrangement C and bending angle of comb teeth B in turn.

Selection of optimal combination parameters

By analyzing above experiments and data, we found that interaction among factors, including the motor speed, bending angle of comb teeth and radial diameter of comb teeth arrangement, has influence on the collection rate, and the influence from each factor varies. To obtain the best combination of parameters, the Optimization module in design-Export was used to predict the optimal value of response surface test.

Considering mechanical efficiency in field work, the optimal range of each factor were determined as follows: motor speed A: 25-35 r/min, bending angle of comb teeth B: 60-120°, radial diameter of comb teeth arrangement C: 600-900 mm, the fruit collection rate Y was set to its maximum value.

The optimal parameters were motor speed A: 25 r/min, bending angle of comb teeth B: 120°, radial diameter of comb teeth arrangement C: 868.45mm. The comprehensive response value of the model surface was optimal, and the collection rate was 91.51%.

The optimized parameters were applied in test bench. Due to the constraints of processing accuracy and experiment materials, the experimental parameters in this paper were as follows: motor speed: 25 r/min, bending angle of comb teeth: 120°, radial diameter of comb teeth arrangement 900 mm. The average collection rate taken from three experiments was 93.82%. The relative error between the experiment results and the model prediction is 2.48%, indicating that the model prediction is highly accurate and the prediction is reliable, thus, the goal of improving the collection rate is achieved.

CONCLUSIONS

1) To increase fruit collection rate, this paper offers a comb-type harvesting test bench. It is mainly composed of a frame, combing and stripping mechanism, baffle, clamping conveying mechanism, control system, fruit-collecting box and transmission system, among which the comb teeth parts in the combing and stripping mechanism can be replaced to conduct experiments with different parameters.

2) Through theoretical and simulation analysis of Cerasus humilis shedding track, it was determined that the main factors affecting the fruit collection rate were motor speed, bending angle of comb teeth and radial diameter of comb teeth arrangement. Single factor simulation experiment and bench experiment showed that the collection rate decreased gradually with the increase of motor speed, and increased gradually with the increase of the bending angle of comb teeth or the radial diameter of comb teeth arrangement. The orthogonal experiment showed that motor speed had the largest effect on collection rate, followed by radial diameter of comb teeth arrangement and bending angle of comb teeth.

3) Based on the quadratic response surface model， the optimal combined parameters of motor speed, bending angle of comb teeth and radial diameter of comb teeth arrangement were predicted, and the optimal parameters were motor speed: 25 r/min, bending angle of comb teeth: 120°, and radial diameter of comb teeth arrangement: 868.45mm, the corresponding maximum collection rate was 91.51%.

The bench experiment was carried out with parameters as follows motor speed: 25 r/min, bending angle of comb teeth: 120°, radial diameter of comb teeth arrangement 900 mm, and the collection rate was 93.82%. The relative error with the predicted values was 2.48%, and the goal of improving the collection rate is achieved.

ACKNOWLEDGEMENTS

This research titled ‘Design and experimental study of the comb-type harvesting test bench for Cerasus humilis’ was funded by the Key Research and Development Plan of Shanxi Province, China (201703D221029-1) and Science and Technology Innovation Fund Project of Shanxi Agricultural University (Zdpy201802, Zdpy201906). The authors are grateful and honoured to have obtained support from the Laboratory of Key Technology and Equipment for Dry Farming Machinery.

REFERENCES

[1] Du X.B., He J.L., He Y.Q., et al., (2019), Parameter optimisation and experiment on the combing of cerasus humilis. *INMATEH-Agricultural Engineering*, Vol.57, issue 1, pp.103−114, Bucharest / Romania.

[2] Du X.B., He J.L., He Y.Q., et al., (2020), Design and experiment of eccentric swing combing device for Cerasus humilis. *INMATEH-Agricultural Engineering*, Vol.60, issue 1, pp.89−98, Bucharest / Romania.

[3] Fang D.W., He J.L., He Y.Q., et al., (2019), Design and experimental of comb - tooth Cerasus humilis picking test bench. *Journal of Gansu Agricultural University*, Vol.54, Issue 5, pp. 212−218+231, Gansu / P.R.C.

[4] He Y.Q., He J.L., Du X.B., et al., (2018), Design and experimental study of the finger-type lifter test bench for Cerasus humilis branches. *INMATEH- Agricultural Engineering*, Vol.56, issue 3, pp.147−154, Bucharest / Romania.

[5] He Y.Q., He J.L., Fang D.W., et al., (2019), Collision injury assessment of mechanical harvesting cerasus humilis fruit based on deformation energy. *Agriculture Engineering*, Vol.9 (3), pp.67−72, P.R.C.

[6] He Y.Q., He J.L., Fang D.W., et al., (2019), Experimental design and evaluation of the finger-type lifter bench for cerasus humilis branches, *Journal of Shanxi Agricultural University* (*Natural Science Edition*), Vol.39, issue.2, pp.105−112, Jinzhong / P.R.C.

[7] He Y.Q., He J.L., Fang D.W., et al., (2020), Dynamic simulation experiment and analysis of lifter for Cerasus humilis branches based on ADAMS. *Agricultural Engineering*, Vol.10, Issue 2, pp. 72−75, Beijing / P.R.C.

[8] Jianfeng Zhou; Long He; Qin Zhang; Manoj Karkee, (2014), Effect of excitation position of a handheld shaker on fruit removal efficiency and damage in mechanical harvesting of sweet cherry. Biosystems Engineering, Vol.125, pp.36−44, Washington / USA.

[9] Jianfeng Zhou; Long He; Matthew Whiting; Suraj Amatya; Peter A. Larbi; Manoj Karkee; Qin Zhang, (2016), Field evaluation of a mechanical-assist cherry harvesting system. Engineering in Agriculture, Environment and Food, Vol.9, issue 4, pp.324−331, Washington / USA.

[10] Kang S.L., He J.L., (2017), Design and finite element analysis of harvesting device for the Cerasus humilis. *Journal of Shanxi Agricultural University (Natural Science Edition)*, Vol.37, Issue 6, pp.439-443, Jinzhong/P.R.C;

[11] Liu H.F., He J.L., Min J.J., et al., (2013), Experimental study on technical parameters of Cerasus Humilis picking device. *Journal of Shanxi Agricultural University (Natural Science Edition)*, Vol.33, issue 4, pp.342−345, Jinzhong / P.R.C.

[12] Liu S.H., He J.L., Wu N., et al., (2020), Design and optimization of comb-type harvesting test bench for Cerasus humilis. Agricultural Engineering, Vol.10, Issue 3, pp. 81−85, Beijing / P.R.C.

[13] Sun Z.B., He J.L., Du J.J., et al., (2016), Experiment on physical parameter and biomechanical properties of Cerasus humilis 5. *Agricultural Engineering*, Vol.6, Issue 2, pp. 1−4, Beijing / P.R.C.

[14] Sanders K.F., (2004), Orange harvesting systems review. Biosystems Engineering, Vol.90, issue 2, pp.115−125, Trangie / Australia.

[15] Torregrosa A., Ortí E., Martín B., Gil J., Ortiz C., (2009), Mechanical harvesting of oranges and mandarins in Spain. Biosystems Engineering, Vol.104, issue 1, pp.18−24, Valencia / Spain.

[16] Wang Y.X., He W.J., (2016), Discussion on the industrialization development of Cerasus humilis. *Fruit Growers' Friend*, Issue 9, pp. 1−3, Henan / P.R.C.

[17] Zhang Z.L., Zhang D.X., Cui T., et al., (2014), Design and experiment of corn stripping monomer mechanism, *Transactions of the Chinese Society of Agricultural Engineering (Transactions of the CSAE*), Vol.30, issue 20, pp.1−9, Beijing / P.R.C.

[18] Zhang W., Du X.B., He J.L., et al., (2018), Simulation analysis and experiment of combing pluck of cerasus humilis. *Agriculture Engineering*, Vol.8, issue 5, pp.89−94, Beijing / P.R.C.

A RELIABILITY TEST METHOD FOR AGRICULTURAL PADDY FIELD INTELLIGENT ROBOT

/

一种农业水田智能机器人可靠性测试的方法

Xuefeng Deng *), Bingqian Zhou, Yiming Hou [1]
College of Information Science and Engineering, Shanxi Agricultural University, Taigu / China
Tel: 13546632115; E-mail: dxf@sxau.edu.cn
DOI: https://doi.org/10.35633/inmateh-63-27

Keywords: *Agricultural paddy field intelligent robot, Reliability, Timed automata, Model checking*

ABSTRACT

With the development of artificial intelligence technology, in order to alleviate the labour intensity of agricultural paddy field production and improve production efficiency, the development of robot used in paddy field production has been a hot research in the field of agricultural production. Different from the industrial environment, the agricultural production environment is complex, and there are many interference factors to the intelligent robot. Therefore, ensuring the reliability of the robot in the operation has become an important index in the production process. The model checking technique can evaluate the reliability of the system when designing the system. In this paper, timed automata is used to model the agricultural paddy field intelligent robot, and the environmental influence factor model is introduced, so as to evaluate the reliability of the system qualitatively and quantitatively in the design of the agricultural paddy field robot. Finally, the control prediction of the system safety is carried out, and to provide a definite basis for the actual engineering design.

摘要

随着人工智能技术的发展，为了缓解农业水田生产作业的劳动强度，提升生产效率，用于水田生产的机器人的研制一直是农业生产领域的热点研究。与工业环境不同，农业生产环境复杂，对智能机器人的干扰因素较多，因此，保证作业中机器人的可靠性成为生产过程中的重要指标。模型检测技术可以在系统设计时对系统的可靠性做评估，本文采用时间自动机对农业水田智能机器人进行建模，引入环境影响因素模型，从而在农业水田机器人的设计时对系统的可靠性进行定性与定量的评价。最后对系统安全进行控制预测，并且为实际工程中设计提供确定的依据。

INTRODUCTION

With the development of artificial intelligence technology, intelligent agricultural machinery design has become a hot issue of the new generation of agricultural machinery research.

In China, as a big agricultural country, “smart agriculture” has always been the most sought after goal of people. At the same time, it is also an advanced stage of agricultural development, which includes the integration of Internet of things, cloud computing, automatic control and other technologies. Finally, the intelligent perception of agricultural production environment, intelligent early warning, intelligent analysis is realized, which provides accurate planting, visual management, intelligent decision making and so on for agricultural production. Intelligent agricultural machinery and equipment (currently called "intelligent agricultural machinery" by agricultural machinery management departments in some provinces and cities) is not only an important part of intelligent agriculture, but also an important material means for the development of Intelligent Agriculture. Although most of the current agricultural machinery has information-based operation, its efficiency is still low, cannot liberate human and material resources, waste of human resources and other problems, the design of agricultural machinery integrated with artificial intelligence control is gradually making agricultural machinery more capable of executing instructions automatically, such as *Zhang et al. (2021)* designed based on STM32F7 agricultural machinery automatic navigation operation controller. The controller uses STM32F7 as the main control chip, which is composed of wireless data transmission module, wheel angle sensor, filter circuit and so on. It can realize the path tracking control of agricultural machinery and the control of operation parts according to the control instructions, and complete the combination of automatic navigation and automatic operation.

[1] *Xuefeng Deng*, PhD; Bingqian Zhou, undergraduate; Yiming Hou, undergraduate.*

Paddy field production has high labour intensity and low production efficiency, so there is a great demand for the development of intelligent robot for paddy field production. At present, there are many applications in the development of intelligent robot for paddy field operation, such as *Zhang et al. (2013)* developed a mechanical weeding robot - a small stampede weeding robot. The use of the robot not only does not cause pollution to the environment, but also because of its small size can meet the requirements of those engaged in agricultural production at this stage. DSP is the main control chip of the robot, and motion control module, data communication module and image acquisition module are designed around the robot. This method is not only flexible and convenient to develop, but also greatly enhances the modifiability and portability, which can realize real-time image acquisition, processing and recognition, so as to achieve the purpose of weeding in paddy field.

Yang et al. (2021) designed and built a robot mobile platform with electric drive, which mainly includes walking chassis and control system. The walking chassis is composed of main frame, electric drive system, walking assembly, steering assembly and lifting mechanism. The control system uses STM32F407IGT6 as the main controller, and realizes remote driving control of robot platform by using speed measuring encoder, angle sensor, AT9S remote controller and R9D wireless module etc. *Zhang et al. (2013)* designed the conventional path planning method of rectangular field for automatic rice transplanter, and then extended it to trapezoidal field, and further designed the path planning method of rectangular field according to the mechanical characteristics and agronomic requirements of cultivated land tractor. This method can not only obtain the optimal path, improve the efficiency of paddy field operation, but also reduce the production cost, which makes the automatic agricultural robot practical, and can control the automatic operation of rice transplanter in any quadrilateral field. *Zhu et al. (2018)* established the single leg finite element model and soil finite element model of foot robot through ABAQUS to explore the influence of typical gait (rectangle, modified cycloid, ellipse, zero impact) and its parameters on unit energy consumption of foot robot in paddy soil environment. Based on C8051F340 single chip microcomputer, *Qi et al. (2013)* and others designed a control system of weeding robot platform suitable for paddy field operation environment. The system is mainly composed of vehicle control module, PC translation and transmission module, and remote control module. It realized two functions of automatic navigation control and manual remote control.

In the design of many paddy field robots, the general robot test method mainly uses the means of field test, the main test indicators include reliability, robustness and other performance indicators. When the robot is in an unstable environment or under certain business pressure, the robot is required to run for a period of time without the influence of the outside world, so as to determine whether the robot can run well. Therefore, it is necessary to observe the running state and resource index of the robot to carry out reliability test; robustness test is the key to judge whether the system can continue to operate normally when the robot is in abnormal or dangerous situation; the test is to test the function of each module and the fault tolerance of the system. The accuracy test requires that the robot can make a more accurate judgment in route planning, image recognition, obstacle avoidance and tracking, and then issue instructions to ensure that the system can run accurately; feasibility test is required to judge whether the robot meets the purpose of project development, whether it is suitable for most people, whether its price is moderate, and whether the allocation of resources is appropriate. For example, *Zheng. (2020)* proposed a method to test the imaging performance of ground mobile robot visual system. It includes resolution, colour difference, distortion and other basic imaging performance, frame frequency, delay, bit rate, video defects and other video quality performance detection methods. It provides a test basis for the inspection of visual imaging performance of ground mobile robot, and provides a theoretical basis for the formulation of inspection method standard of visual system imaging performance of ground mobile robot. The field test of robot paddy field, due to the complex actual working conditions, is greatly affected by environmental factors, and the specific working environment cannot test all the working scenes, resulting in incomplete test. After the test, the system is officially put into use. If the reliability cannot be fully evaluated, the production will be lost.

This paper presents a reliability testing method of paddy field intelligent robot based on timed automata, which can be used to evaluate its reliability in the design process of paddy field intelligent robot, so as to meet the design requirements and ensure the correctness of the system in the model design, so as to reduce the problems in the field test. The model checking technique based on timed automata is a mathematical based method. Therefore, the evaluation process is mainly based on theoretical testing, which has the characteristics of accurate testing and high efficiency. It can be used as an effective means to ensure the rationality of design.

ANALYSIS OF WORKING ENVIRONMENT OF PADDY FIELD

The paddy field environment is different from the industrial environment. In the industrial environment, robots are less affected by uncertain factors. In the paddy field environment, for example, to overcome the problem that the silt block below the water surface may hinder the robot movement, because the obstacle detection module installed on the robot cannot detect the potential obstacles under the water surface. In the long run, it will inevitably cause problems to the operation of the robot, and even lead to idling phenomenon. In the paddy field, weeds are also a common problem, because when the robot is running, weeds are likely to be rolled into the wheels. If this problem occurs, the wheels will be restricted, and eventually the motor will be damaged. For a robot, when it moves in water, the first thing is to prevent water ingress, because the robot is an electronic device after all. When the robot moves in the water, it will inevitably cause water spray. Once the robot enters the water, it will cause the robot to burn to a great extent. In addition, when the robot encounters silt and weeds, it will inevitably lead to the shaking of the paddy field intelligent robot, which will interfere with the signal returned by the intelligent robot, resulting in the signal not being sent back in time and weakening the signal. As shown in Figure 1, the paddy field simulation environment of intelligent robot is as follows:

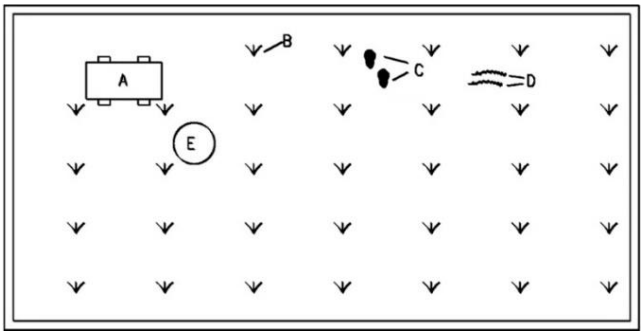

Fig. 1 - Paddy Field Simulation Environment of Intelligent Robot

A - stands for paddy field intelligent robot;
B - stands for crops;
C - stands for silt block;
D - stands for water grass;
E - stands for the sunken part of the paddy field.

The area around Figure 1, where the double solid lines are drawn, is the field ridge of paddy field.

It can be seen from the above figure that if the paddy field intelligent robot wants to realize its basic functions, the first thing it should do is to recognize the crops and not damage the seedlings in the process of movement. If one wants to make the intelligent robot walk according to the predetermined route and not damage the crops, the robot needs to have the functions of image recognition, tracking and obstacle avoidance. When the car moves forward, it will encounter C (silt block). If it wants to cross the silt block, it will need to increase the power, which will make the intelligent robot vibrate, and if the power is too large, the damage to the motor cannot be underestimated.

When the robot is lucky enough to cross the C (silt block), it will encounter D (water grass) when it continues to move forward. Once the water grass is involved in the wheel of the robot, it is bound to have an impact on the movement of the robot. The control centre outputs signals, but the rotation of the motor is not enough to drive the wheel to get rid of the control of the water grass, so there will be machine jam or idling, but no matter what kind of phenomenon, we don't want to see. When the robot is lucky to get rid of the control of D (water grass), it will go to the edge of the paddy field, that is the field ridge. At this time, the intelligent robot needs to have the function of judging whether the road ahead can be carried out. Obstacle avoidance is the basic requirement to realize this function. When completing obstacle avoidance (bypassing the ridge), the robot needs to plan its next route, that is, turn left or right. When the car is lucky enough to bypass the ridge, it will encounter E (the sunken part of the paddy field). Once it enters the sunken area, there will be three problems. Firstly, the rise of the water level is a problem, because the robot is always in the safe water level range when it does not enter the sunken part, but when the robot falls into E (the sunken part of the paddy field), its water level is bound to rise; secondly, when the robot is trapped in E (the sunken part of the paddy field), the vision of the robot will be affected, which makes the signal sent back by the robot unstably; thirdly, if the robot wants to run out of E (the sunken part of the paddy field), it needs to increase the power of the motor, which will cause the robot to shake and have the influence to the signal return.

MATERIALS AND METHODS

Design framework of paddy field intelligent robot

Paddy Field Intelligent Robot generally completes the agricultural production operation in the paddy field. In order to make it work normally, the general design structure of the intelligent robot in the paddy field is shown in Figure 2. It is mainly composed of central control module, camera module, motor drive module, power module, sensor module, display module and wireless module. The central control module mainly processes the images and data uploaded by camera module and sensor module, and turns the processing results into instructions to drive the motor. The camera module is to obtain the external environment in real time, to detect the path visually, and uploads the collected information back to the central control module. The motor driving module is used to drive the motor, which mainly receives the information from the central control module to realize the basic movement of the robot, such as turn left, turn right, straight travel and so on. The power module is used to supply power to the central control module and motor drive module. The sensor module is mainly used to achieve the basic obstacle avoidance or tracking function, which can be used with the camera to improve its stability, reliability and other performance. The display module is used to display the image or video information captured by the camera in real time. The wireless module uploads the information to the computer, which is convenient for the user to monitor the working state of the robot in real time, and the user can judge whether the robot has problems through the uploaded information, which is convenient for timely maintenance.

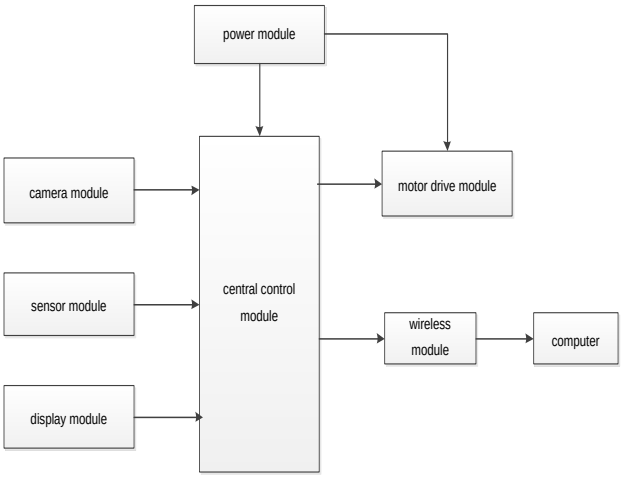

Fig. 2 - Framework of Paddy Field Intelligent Robot

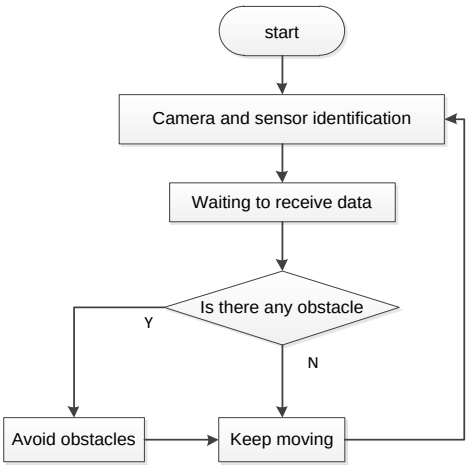

Fig. 3 - Flow Chart of The Paddy Field Intelligent Robot

Figure 3 shows the flow chart of the paddy field intelligent robot system: when the paddy field intelligent robot starts to work, its central control module will wait for the data from the camera module and the sensor module.

Once the data is sent back to the central control module, the central control module will process the signal. For the image or video sent back by the camera, the central control module will carry on the image recognition, and carries on the vision plan to its path, and can effectively avoid the obstacle to a certain extent. For the sensor module, the central control module calculates the distance according to the data sent back, so as to avoid obstacles. The use of camera module and sensor module at the same time will increase the robustness of paddy field intelligent robot to a certain extent. However, after the data returned by the system is processed, if the central control module finds that there is an obstacle in front of it, the control module will send a command to the motor drive module to avoid the obstacle, and the motor drive module will control the wheel of the intelligent robot to wake up the function of turning left or right, so that the intelligent robot can be used normally and efficiently.

The design framework of the paddy field intelligent robot can be widely used in various fields of paddy field, as long as a little change on this basis can achieve a variety of effects, such as the use of weeding in farmland. We all know that there are two traditional weeding methods: the first method is to employ a lot of human resources, and use a lot of weeding tools (hoes, sickles, etc.) to achieve the purpose of weeding by hand. This practice is obviously a waste of human and material resources, employers will also bear a large amount of employment costs, and the efficiency of weeding is low. And the second method is to rely on spraying pesticides to achieve the purpose of weeding. Although this method liberates human and material resources to a certain extent, its disadvantages are still very obvious, that is, a large number of pesticide spraying will

cause damage to the environment, and in the long run will cause soil hardening, which is not conducive to the growth of plants. However, if we can add a rotating blade on the basis of the paddy field intelligent robot, and use our camera module to recognize and process the images, we can achieve the effect of weeding specific weeds. Compared with the traditional manual weeding operation mode, the farmland weeding robot can well liberate human and material resources, and greatly improve the agricultural production efficiency, and greatly reduce the harm to the environment. As we all know, the traditional agricultural planting method mainly relies on employing a lot of manpower to carry out manual transplanting. This transplanting method has very high requirements for technical personnel. It not only requires that the transplanter's transplanting force is appropriate enough; if the force is too large, it will damage the root of the seedling, but if the force is too small, it may lead to the impossibility for the seedling to be really inserted into the soil, and finally cause the seedling to be damaged-death. For the traditional transplanting method, people will plan the farmland before transplanting in order to get enough sunshine in the process of seedling growth, but only by visual observation, it is inevitable that there will be errors. But if on the basis of the paddy intelligent robot described in this paper, we add a mechanical arm, use its mechanical arm to carry out rice transplanting, and use the camera of the robot to carry out path recognition and paddy field planning, which not only liberates human and material resources, speeds up the production efficiency, but also ensures the survival rate of seedlings to a great extent. It can be seen that the applicability of the paddy field intelligent robot is very considerable.

Introduction of timed automata and model checking technique

Model checking is a technology of testing and analysing design based on mathematical method. It was first proposed by Clarke and Emerson, Quelle and Sifakis, It is a formal verification method. It analyses system attributes by exploring all reachable states (state space) of system model *(Einollah Pira., 2021)*.The model detection is mainly based on explicit state search or implicit fixed point calculation to verify the modal or propositional properties of concurrent systems in finite state. The model checking method can be executed automatically to determine the correctness, validity and reliability of the system model, and the model checking method can put forward the counterexample path when the system does not meet our proposed properties. Model checking consists of three parts: one is the canonical temporal logic propositional language; the second is the method of coding state machine; the third is the verification method of intelligently searching the state space to determine whether the specification is true or false. Model checking has attracted the attention of academia and industry since it came into being, and its application fields are very wide, for example, it can be used in the analysis and verification of computer hardware, communication protocol, control system, security authentication protocol. A new technique to reduce the explosion state in model checking is proposed in the paper written by *Aung et al. (2021).* This technique, called divide and conquer, is used for the final model checking. As the name suggests, the technology is dedicated to the final attribute. This technique divides the original final model checking problem into several smaller model checking problems, and solves each smaller model checking problem.

Feng et al. (2021) proposed a class of graphical and numerical techniques using model simulation to check the overall fit of the marginal additional hazard model to the current state data of multivariable, the test method is based on the maximum value of the random process, which is based on the cumulative sum of time and covariant residuals. *Baouya et al. (2021)* introduces a novel deployment decision method based on prism probabilistic model checker, which uses software components and physical platform to generate a group of candidate deployment. Starting from system modelling language (SysML), the process includes the mechanism of extracting hardware and software functions and executing a set of candidate deployment. Each candidate should satisfy the reliability attributes written in probabilistic tree logic. Thus, model detection is still a hot issue.

Timed automata is proposed by Alur and Dill. They point out that if A has two clocks, the problem of universality cannot be determined. However, when A has a single clock, their problem states are still unresolved. *Sproston et al. (2021)* closed the gap between infinite word timed automata by proving the uncertainty of the universality of a clock. For timed automata overrun words, this paper proves that a clock universality problem is decidable and has non-primitive recursive complexity. This reveals the surprising divergence between finite words and infinite words in timed automata theory. If ϵ transition or nonsingular postposition condition is allowed, then a clock universality problem cannot be determined in finite words and infinite words. Timed automata is a set of theory for modelling and verifying real-time systems. A timed automaton A is a tuple <N,l_0,E,I>where

- N is a finite set of locations (or nodes),
- $l_0 \in$ N is the initial location,

• $E \subseteq N \times B(C) \times \Sigma \times 2^C \times N$ is the set of edges and

• $I : N \rightarrow B(C)$ assigns invariants to locations

We restrict location invariants to constraints that are downwards closed, in the form: $x \leq n$ or $x < n$ where n is a natural number. *(David Al. et al., 2015)*. A lot of validation tools (such as Uppaal) we know are based on time automata theory. It is easy to guess from the name that timed automata is a finite automata with clock set. When a finite number of clocks are set together, a clock set is formed, and each clock is a variable with a value greater than 0. When the timed automata satisfies certain clock constraints, certain transitions can occur between its states. If the state of timed automata is attached with the property of "position invariance", this property is also equivalent to a clock constraint, so as to ensure that the state will not stay in place. This kind of automata is also called “Timed Safety Automata". Timed automata not only has several real valued variables, but also is an abstract model of time series system. Only when the clock satisfies the clock constraint (guard), its state can jump.

DESIGN AND MODELING OF PADDY FIELD INTELLIGENT ROBOT

Paddy field environment and paddy field operation robot constitute the paddy field production system. On this premise, this paper introduces the paddy field environment model, abstracts the complex environmental factors of paddy field into event input state machine, and then tests and simulates the model. The modelling and analysis process consists of the following steps:

Modelling: the paddy field environment and robot system are described by timed automata tools to make them into discrete and continuous environmental conditions. For example, in the design of paddy field robot, the normal operation of the robot will not be affected when passing through the silt area within a certain length. If the silt area does not exceed the safe range that the robot can bear, it is considered that the robot will be in normal driving state, otherwise it will be considered as abnormal state, and necessary treatment should be carried out;

Model qualitative detection: verify the nature of the model through the given condition, check whether the design model has deadlock and other problems, so as to ensure the correctness of the system design;

Instantiation model: by introducing specific design requirement, the model is instantiated to provide basis for quantitative evaluation of design;

Quantitative analysis of the model: quantitative analysis of the working state of the model through the simulation method, giving the reference of the change of the working state of the model.

System modelling

The description of paddy field environment is introduced into the modelling of paddy field intelligent robot, so the system modelling is divided into two parts: paddy field environment modelling and robot system.

Paddy field environment modelling: the influence of paddy field environment on intelligent robot is composed of many factors, such as weeds, silt, etc. Formal modelling tools such as timed automata are based on discrete event modelling, so continuous events should be discretized first. In the model of paddy field influencing factors, the abnormal continuous events will be quantized and discretized. For example, driving in the mud for a certain time does not affect the robot's moving. When the driving distance reaches a certain range, the output power will be increased to ensure the robot's continuous operation.

Here, the timed automata model as shown in Figure 4 (a) is established. In the model, it is advisable to set that when a certain kind of event is encountered, it will not affect the operation of the system within a certain period of time [I, J]. When such event exceeds the reliability design requirements of the system, the system will produce emergency measures such as error reporting. The event was initiated by E_ S_ Start state to E_ S_ T state and indicates the range of events that the system can process automatically. After exceeding the range, it is judged whether there is still such event influence. In some cases, taking the equal probability model as an example, such events can continue to occur or not. Therefore, there are two branches of event processing. In the model, E_ S_ D() and E_ S_ Er() are used for recording the frequency of the above two situations.

Robot system modelling: intelligent robot system consists of sensor elements which can perceive environmental factors, peripheral equipment of actual operation and core control module. Therefore, these components are modelled respectively.

In general, the core processor of the robot system has a fixed clock cycle. When the system is running, the core control chip is used as the minimum unit of the system running cycle. For this, the model as shown in Figure 4 (b) is established, where M_ S_ start state is the start state of each clock cycle. In each clock cycle, the MS signal is used as the clock cycle signal, and the model uses M_ S_ D () function to record the running time.

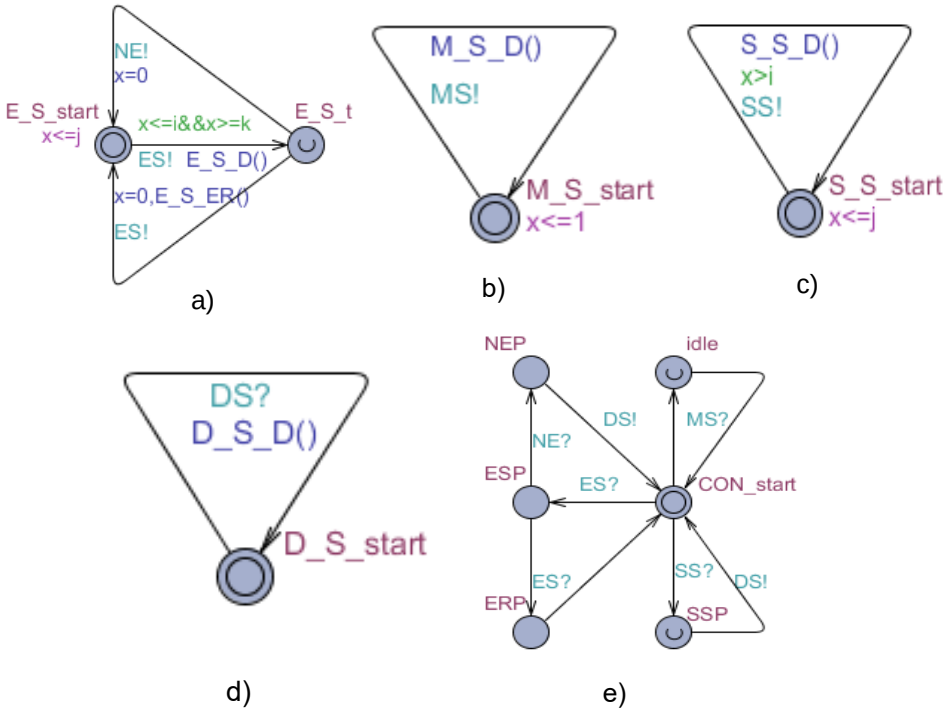

Fig. 4 - Timed Automata Model of Paddy Field Robot System

The sensor in the system is used to collect data at a fixed time interval, and its model is shown in Figure 4 (c), where S_ S_ Start is the initial state of data acquisition, and it is specified to complete data acquisition in time interval [I, J], and send synchronous signal SS, in which the S_ S_ D () function be used for recording the amount of data collected.

The execution device in the system is used to receive signals and perform corresponding work, and its model is shown in Figure 4 (d), where D_ S_ Start is the initial state of the device. After receiving the signal DS, the device performs the corresponding operation. The model uses D_ S_ D () to record the operation of the equipment.

The core control module in the system is used to process corresponding data and send control information. Its model is shown in Figure 4 (E), where CON_ Start is the initial state of the control module. If there is no data input, the system will enter idle state.

If there is a sensor transmitting data, it will be disposed, and then it will enter SSP state. After that, it will send DS information to the device. If there is an abnormal state in the external environment, it will enter ESP state. If there is no impact on the system operation within the scope of reliability design, it will enter ESP state. If the system cannot automatically handle, it will enter ERP state, which is used to alarm or for manual intervention processing.

Case analysis

The model of paddy field intelligent robot system is established by timed automata, which can be used to check the correctness and evaluate the reliability of the model. This paper uses UPPAAL timed automata tool to verify.

Example description

This section takes the paddy field weeding robot as an example to illustrate the process of model verification and analysis. In order to explain the problem conveniently, only verify the visual recognition process. Paddy field weeding robot uses machine vision module to identify weeds. The vision module uses OpenMV camera to collect data, and the recognition time is 12ms. The core microcontroller uses STM32, and the speed is about 13.2MHz. For external events, the passing of silt is regarded as an external abnormal event, and it takes about 3.5 seconds for the design to pass 5cm silt.

The model variables are initialized according to the above data, as shown in Table 1. The running speed of the core is very fast compared with the acquisition speed and the initialization unit 1 is 0.01ms in the M_S model, so the running rate controlled by the core should be about 104 times in this time interval. According to this standard, the parameters i and j in S_S model are about i = 15, j = 18. In E_ S model i and j are initialized as i = 460 and j = 500, where k is set 480, which means that the interval between 460 and 480 is the interval

where the abnormal event occurs but does not affect the operation of the system. If the abnormal event continues to occur after that, the system cannot automatically handle it.

After the model is instantiated, the effect displayed by the timed automata tool UPPAAL simulator is shown in Figure 5.

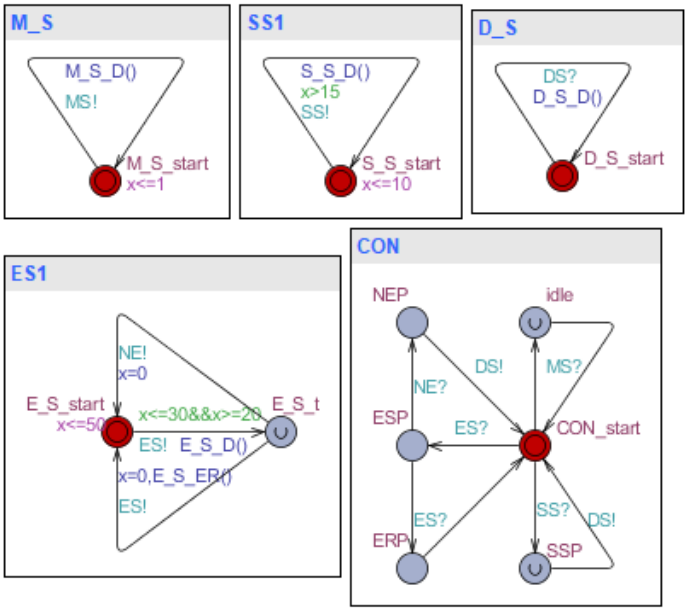

Fig. 5 - Example Model of Paddy Field Intelligent Robot System

Verification of model properties

The properties of system design model can be used to test the correctness of system design and provide theoretical evidence for the guarantee of system reliability. In this example, we can verify whether the execution logic of the system is correct and reliable through reachability. It can be verified by inputting the corresponding BNF expression in the model verifier of the timed automata tool UPPAAL. Such as, whether the sensor signal can be correctly processed, E < > CON.SSP imply D_ S.D_ S_ Start, Table 1 lists the expressions of model correctness verification, and the results verified by the verifier.

For other properties in the system, UPPAAL can be used to verify the relevant characteristics according to the engineering needs.

Table 1

Examples of Paddy Field Intelligent Robot Model Verification

EXPRESSION	EXPLANATION	RESULT
E<> CON.SSP imply D_S.D_S_start	Verification of the correctness of the signal sent by the sensor which is processed by the controller	Satisfied
E<> CON.ESP imply ES1.E_S_t	Whether the controller can handle verification when an exception occurs	Satisfied
E<> CON.NEP||CON.ERP imply ES1.E_S_start	The processor can handle verification normally in two cases of abnormal events	Satisfied
E<>D_S.D_S_start imply ES1.E_S_t ||SS1.S_S_start	The execution device performs verification caused by signals collected by sensors or abnormal events	Satisfied
E<> CON.idle imply M_S.M_S_start	Controller standby state verification	Satisfied

Simulation analysis

The nature of the model can qualitatively verify the model, but it cannot give quantitative data simulation. The dynamic simulation of the model can be carried out by using the simulator, and the quantitative evaluation of the model can be given by analysing the relevant simulation data. This example model uses the simulator to carry on the simulation operation, and can carry on the quantitative research to the related indexes, such as the utilization rate of the microcontroller and other indexes, which can be used to optimize the system design. The experiment simulates the microprocessor running about 2500 cycles.

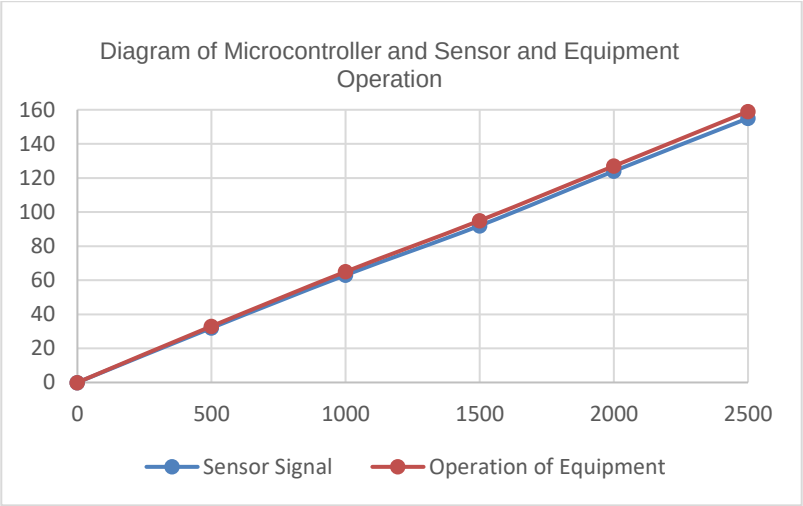

Fig. 6 - Simulation Diagram of Running Relationship between Microcontroller, Sensor and Equipment

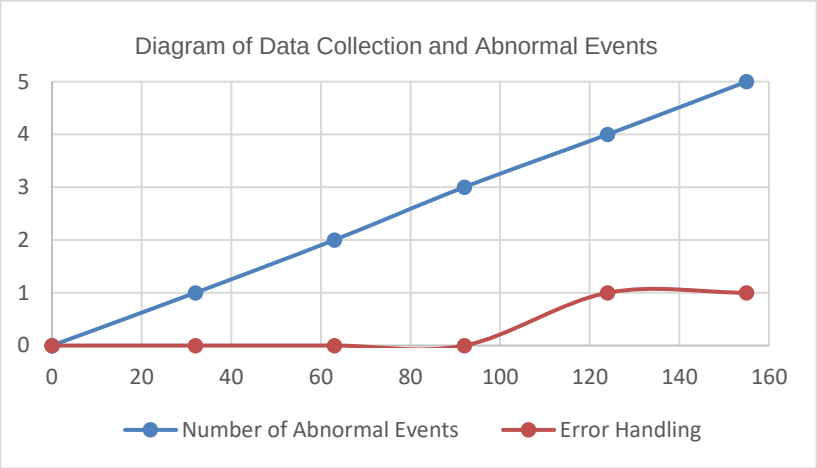

Fig. 7 - Simulation Diagram of Corresponding Relationship between Microcontroller Running Time and Abnormal Events

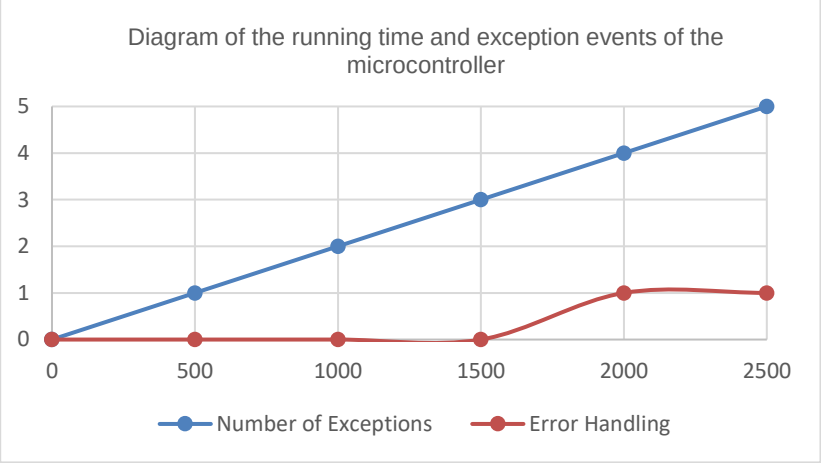

Fig. 8 - Simulation Diagram of Corresponding Relationship between Collected Data and Abnormal Events

Figure 6 shows the simulation results of the running relationship between the microcontroller, sensor and equipment. Corresponding to the microcontroller, the sensor takes a long time to collect data. From the data in the figure, it can be seen that the microcontroller has a lot of standby time. Therefore, the microcontroller can run more modules to make full use of its processing capacity.

Figure 7 shows the simulation data results corresponding to the running time of the microcontroller and the abnormal events, in which the abnormal events appear in a periodic manner to complete the test of whether

the system can stably handle the abnormal events. As shown in Figure 6, when the abnormal events accumulate to a certain length of time, the system fails to handle the situation and enters into the error handling phase.

Figure 8 shows the simulation results of the corresponding relationship between the collected data and the abnormal events. In the relationship of Figure 8, it can be seen that the occurrence of abnormal events is similar to that in Figure 7. Since the collection data is approximately linear with the operation time of the microcontroller, the situation shown in Figure 8 is similar to figure 7, and the correctness of the system operation state is verified. It can be seen that the system abnormal error is a small probability event compared with the system operation cycle. It can be used to calculate whether the system meets the reliability requirements of the design requirements.

CONCLUSIONS

Aiming at the analysis of paddy field intelligent robot system and its running environment, this paper puts forward a model checking method based on timed automata for the design of paddy field intelligent robot system. Using this method, the correctness of the system design can be verified by formal method, and the designed model can be simulated and analysed by relevant model checking tools, so as to provide basis for system design optimization and ensure the reliability of system design.

ACKNOWLEDGEMENT

This research, titled ‘A Reliability Test Method For Agricultural Paddy Field Intelligent Robot’ , was funded by the research project of Shanxi Province excellent doctor work Award Fund (Research on model detection technology of Agricultural Internet of things, No: SXYBKY201721), Scientific Research Start of Doctor of Shanxi Agricultural University (Research on Detection Technology of Agricultural Internet of Things Model, 2017YJ30). The authors are grateful and honoured to receive this support.

REFERENCES

[1] Aung M N, Phyo Y, Do C M, Ogata K., (2021), A Divide and Conquer Approach to Eventual Model Checking. *Mathematics*, 4, 9.

[2] Baouya A, Mohamed O A, Ouchani S, Bennouar D., (2021), Reliability-driven Automotive Software Deployment based on a Parametrisable Probabilistic Model Checking. *Expert Systems with Applications*, (prepublish).

[3] David Al., Larsen K., Legay A., Mikučionis M., Bøgsted Poulsen D., (2015), Uppaal SMC tutorial. *International Journal on Software Tools for Technology Transfer*, 4, 17.

[4] Einollah P., (2021), Using knowledge discovery to propose a two-phase model checking for safety analysis of graph transformations. *Software Quality Journal*, prepublish.

[5] Feng Y.Q., Zhang C., Ding J.L., (2021), A model checking method for the additive hazards model with multivariate current status data. *Statistics and Its Interface*, 3, 14.

[6] Qi L., Liao W.Q., Ma X., (2013) Design and test of control system for small weeding robot platform in paddy field. *Journal of Jilin University (Engineering Edition)*, 4, 43, 991-996.

[7] Sproston J, Hague M, Potapov I., (2021), Probabilistic Timed Automata with Clock-Dependent Probabilities. *Fundamenta Informaticae*, 1-2, 178.

[8] Yang G.Y., Ni B.W., Li J., (2021), Design of agricultural robot platform for paddy field operation. *Research on Agricultural Mechanization*, 7, 43, 51-57.

[9] Zhang B., (2013) Research and implementation of control system for paddy field weeding robot. *South China University of Technology*, 1.

[10] Zhang F.M., Cheng S.J., (2013), Path planning method for paddy field wheeled automatic agricultural robot. *The 10th Yangtze River Delta science and Technology Forum agricultural mechanization sub Forum*.

[11] Zhang J., Guo S.J., Yang R.B., (2021), The automatic navigation operation controller of agricultural machinery based on stm32f7. *Research on Agricultural Mechanization*, 5, 43, 73-78.

[12] Zheng G.F., (2020), Imaging performance detection method of ground mobile robot vision system. *Mass standardization*, 24, 253-254.

[13] Zhu P., Zhang Y.L., He C.X., (2018), Influence of typical gait and its parameters on energy consumption of foot robot in paddy soil. *China Mechanical Engineering*, 12, 29, 1485-1491.

STUDY ON THE RAPE POD SHATTER RESISTANCE SUITABLE FOR LOW-LOSS HARVESTING OF HARVESTER REEL
/
适宜收获机拨禾轮低损失收获的油菜角果抗裂角性研究

Qing Yiren, Li Yaoming*, Xu Lizhang, Ma Zheng [1]
School of Agricultural Engineering, Jiangsu University, Zhenjiang, Jiangsu, 212013, China
*Tel: +86-18851400010; *E-mail: ymli@ujs.edu.cn*
DOI: https://doi.org/10.35633/inmateh-63-28

***Keywords**: Rape pod, Shatter resistance, Harvesting, Impact force.*

ABSTRACT

During the mechanical harvesting of rapeseed, the impact of the rotating reel tine on rape can easily cause the pods to burst and seeds drop. However, the specific size of the pod shatter resistance suitable for mechanical harvesting is unsure. In this paper the impact force on the rape was analysed through the measurement and wireless transmission of stress change of the tine. A two-degree-of-freedom (2-DOF) collision tester of pod resistance for field testing was used. The results of the shatter resistance index (SRI) under 2-DOF method and the cracking force under ripping method were compared. According to the results of SRI, cracking force and tine impact force, the expected field SRI was determined. The results show that the tine impact forces at the low reel speed of 18 revs min^{-1} was 1.76 N. The 2-DOF method results are reliable and the SRI is significantly correlated with the cracking force. The SRI should be over 0.576 to be greater than the impact force under the low reel speed, however, only 14.8% of the tested varieties could satisfy. It indicates the resistance of the commercial varieties is generally poor and need to strengthen.

摘要

油菜机械联合收获中，拨禾轮弹齿对油菜造成的打击很容易使角果炸裂和种子掉落，但是适于机械收获的角果抗裂角性具体大小一直是未知的。本文通过对收获过程中弹齿应力变化的测量和无线传输，分析了其对油菜的碰撞力；使用便于田间检测角果抗裂角性的二自由度随机碰撞仪，并将该方法测得的抗裂角指数（SRI）与拉裂法下的开裂力结果进行了比较；根据 SRI、开裂力和碰撞力结果，得到机械收获期望的 SRI 大小。结果表示，在拨禾轮低速旋转 18 rev min^{-1} 下，对应的弹齿碰撞力为 1.76N；SRI 结果与开裂力间有显著的相关性，说明两自由度碰撞方法结果可靠；满足拨禾轮 18 rev min^{-1} 下收获要求的角果抗裂角指数应大于 0.576，所测品种中仅有 14.8%满足此要求，这说明目前市场油菜品种的抗裂角性还是普遍较差，需加强品种的选育。

INTRODUCTION

Rapeseed (*Brassica napus*), which is an important oil crop, is an essential raw material in not only edible but also industrial applications (*Btluri et al.,* 2013*; Delgado et al., 2018; Shubert, 2018*). However, rape pods have the characteristic of easy cracking, that is, the pods in the mature stage are easy to crack under external forces, which lead to large losses of mechanized harvesting, especially the header losses that can account for more than half of the total losses (*Shim et al.,* 2017*; Bruce et al., 2002; Cavalieri et al., 2014*). The main reason for the above problem is the mismatch between the rape combine harvester requirement and the pod shatter resistance. When the rape combine harvester is working, the reel placed horizontally in front of the header is the first component that contacts with the rape directly. Its rotary movement cans easily attacks the pod burst quickly and causes extensive seed falling losses, which is the main source of the header losses (*Cavalieri et al.,* 2016*; Pari et al., 2012*).

In order to reduce the losses and screen the varieties with strong pods that are suitable for mechanized harvesting, many researches have been done on the evaluation methods of pod shatter resistance. These methods can be divided into two categories in terms of testing principle.

One is to measure the magnitude of bending moment or the ripping force when the pod is bent or cantilevered tearing by using an experimental device indoor, including the ripping method developed (*Hobson et al., 2002*), and the ripping method has been improved (*Kadkol et al., 1985*). In addition, a three-point bending fracturing method has also been designed (*Tan et al., 2006*).

[1] *Qing Yiren, Ph.D. Stud.; Li Yaoming, Prof. Ph.D.; Xu Lizhang, Prof. Ph.D.; Ma Zheng, Ph.D.*

However, these methods were carried out under the static or quasi-static conditions without considering the pod resistance under dynamic harvesting conditions. The other is to adopt the principle of random collision, which applies the collision between metal balls and pods to test the shatter resistance. This principle was first proposed by *(Morgan et al., 1998*), which takes into account the dynamic conditions and has a good repeatability of test results. Therefore, this principle is generally accepted by researchers, including the (*Morgan et al., 2000*) and (*Summers et al., 2003*), all applied this principle and improved the test method. However, all of them were tested under laboratory conditions, and the pod shatter resistance of varieties can only be roughly divided into two categories, namely, cracking resistance and easy fragile. It is impossible to know the specific value of pod shatter resistance that meets the requirements of mechanical harvesting. The main reason for the above phenomenon is that few scholars have researched the impact force of the harvester reel on the rapeseed pod in the actual harvesting process, the relationship between the impact force and pod resistance has not been established.

Considering the above mentioned problems, from the perspective of integrating agricultural machinery and agronomy, this paper analysed and measured the impact force between the combine harvester and the rape in the working process. In addition, a two-degree-of-freedom (2-DOF) random collision method was used. The results of ripping method and the 2-DOF method were analysed and compared, and combined with the tested impact force of the reel, the expected value of the pod shatter resistance for the mechanized harvesting was determined. Moreover, the pod resistance of typical rape varieties was investigated, and resistance varieties for harvesting were screened.

MATERIALS AND METHODS

2.1 Working principle and movement of harvester reel

The main function of the reel is to push the crops to be harvested towards the cutter, and then cooperate with the cutter to cut the stalks and push the cut crops to the auger to avoid stalk accumulation on the cutter and header (*Peng et al, 2013; Moses et al, 2012*). The trajectory analysis of the reel is shown in Figure 1. The rectangular coordinate system is established as shown in the figure. The machine's forward direction is forward right, and the reel rotates counterclockwise, the trajectory equation of a certain point A_0 on the reel can be expressed as:

$$\begin{cases} x = V_m + R\cos\omega t \\ y = H - R\sin\omega t + h \end{cases} \quad (1)$$

Where, V_m is the forward speed of harvester, m s^{-1}; t is the working time of reel, s; R is the reel radius, m; ω is reel angular speed, rad s^{-1}, H is the vertical distance between horizontal central axis of reel and main cutter, m; h is the cutting height of the main cutter, m.

The horizontal and vertical speeds of the reel can be obtained by deriving equation (2):

$$\begin{cases} V_x = \dfrac{d_x}{d_t} = -R\omega sin\omega t + V_m \\ V_y = \dfrac{d_y}{d_t} = -R\omega\cos\omega t \end{cases} \quad (2)$$

Suppose the circumferential speed of the reel is V_b, the combine forward speed is V_m and the reel speed ratio is $\lambda = V_b / V_m$. Different λ values have different forms of reel trajectories as shown in Fig. 1 (a). When $\lambda = 0$, the trajectory of the reel is a straight line, when $0 < \lambda < 1$, the trajectory is a curtate cycloid with no buckle and when $\lambda > 1$, the trajectory is a prolate cycloid with a buckle ring. Because the reel needs to support the crops to be cut into the header, the reel motion should have a backward horizontal velocity. Only when $\lambda > 1$, in the lower part of the buckle in the trajectory curve, that is, below the longest horizontal chord A_1A_3, the point on the reel has a backward horizontal speed, which can meet the working requirements. When the reel is working, the horizontal position point A_0 moves to point A_1, its absolute moving speed direction is vertical downward without horizontal sub-velocity V_x. At this condition, the impact of the reel tine is the least when it enters the crop, so theoretically it is required that it is the best entry point for the reel.

In the harvesting process of the combine, the operation process of the reel tine is shown in Fig. 1(b). It mainly includes three stages. The first is entering the crop, whose function is to support the crop to be cut; the second is the feeding, which pushes the cut crops into the auger; and the last is the releasing stage, the tine leaves the crop to prepare for the next round of work.

Except for the three stages, the rest of the reel's rotation cycle is empty stroke without any contact with the crop. Among them, the stage of entry is the main reason for the loss of the header. The impact force direction of the tine is shown as F in the graph. Because the reel tines are a little outside of the header bottom plate at this stage, this leads to the burst pods and seeds cannot fall inside the header. Therefore, the study of the impact force between the reel tine and the rape pod at the early stage of entering the crop is the key to reduce the loss.

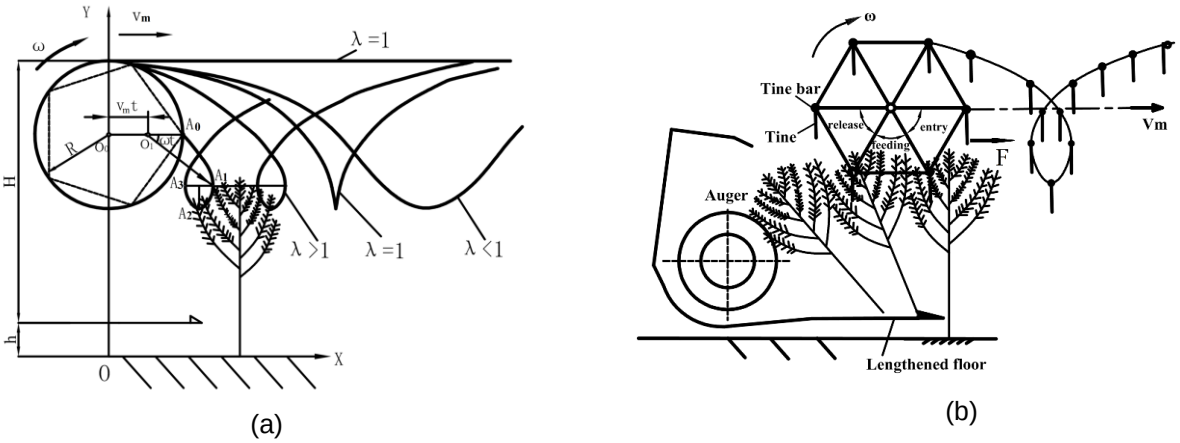

Fig. 1 - Analysis of the trajectory and working process of the reel
(a) Theoretical analysis of the trajectory of reel;
(b) Schematic diagram of the working process of the harvester reel.

2.2 Tests of the impact force of the reel tine on rape pod

2.2.1 Static calibration test of force on the tine

The reel tine that direct contact with the pod was selected as the monitoring object, by collecting the signal change of the force on the tine calculating the impact force on the pod. The DH5905 dynamic signal acquisition and analysis system (Donghua Testing Co., Ltd., Taizhou, China) is selected for testing. Since the reel tine is slender cylindrical, the surface of the tine needs to be ground flat when attaching the strain gauges. The strain gauge is connected in a half bridge circuit (two working pieces), which is suitable for measuring bending strain. The contact lead of strain gauge was connected with the acquisition module of DH5905 strain test system, and the static calibration of strain test part was carried out, and the test device is shown in Fig. 2. Since the initial stage of entering the crop is the main stage that causes the header loss, at this time the collision position between the reel tine and the pod is at the tine end mainly, thus, it was selected as the loaded position on the calibration test bench. In the test, different weights were added sequentially on the tine end. The average value of the stabilized stress collected in the computer was recorded as the tine stress value; each group was repeated 3 times. The least square method was used to fit the data measured in the calibration test.

The proportional coefficient *b* and the intercept *a* in the regression equation is obtained by formula (3) and (4).

$$b = \frac{\sum_{i=1}^{n}(T_i - \bar{T})(U_i - \bar{U})}{\sum_{i=1}^{n}(T_i - \bar{T})^2} \tag{3}$$

$$a = \bar{y} - b\bar{x} \tag{4}$$

where:

b is proportional coefficient, MPa N^{-1};

T_i is the force loaded at the *i*-th time, N;

U_i is the corresponding output stress of the *i*-th load acquisition module, MPa;

$\bar{T}$ is the arithmetic mean of loading force for all times, N;

$\bar{U}$ is the arithmetic mean value of the corresponding output stress of all load times acquisition modules, MPa;

n is all load times for a set of test.

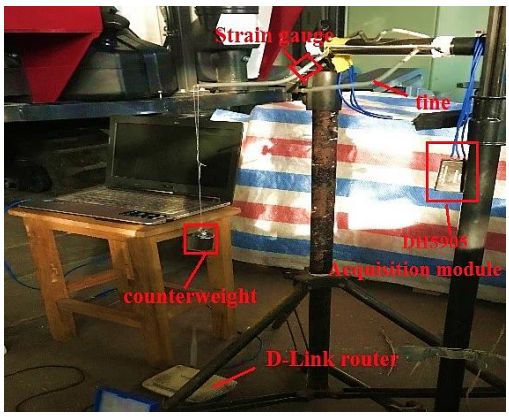

Fig. 2 - Static calibration test bench for force and stress of reel tine

2.2.2 Field experiment on the impact force of the tine

The field test of the impact force of the reel tine on the pod in the working state of the combine harvester was conducted in Dafeng farm in Yancheng City, Jiangsu Province, China in June 2018. The harvest rape cultivar was Zheyou 51, the yield was 2258 kg ha^{-1}, and the average plant height was 1186 mm. The same strain gauge connection method with the indoor calibration was used in the field test. The strain gauges are attached to the front and back sides of the tine of the rape combine, and the DH5905 dynamic signal acquisition device was fixed on the harvesting frame. In the experiment, as the height of the harvested rape plant is constant in the field, the reel height and the horizontal displacement relative to the cutter were set as 1000 mm and 300mm respectively. The stresses of the tine under the reel speeds of 18, 24 and 30 rev min^{-1} were tested with three replicates and the frequency of stress acquisition was 2 kHz.

2.3 Comparative experiments of pod shatter resistance in different methods

2.3.1 Ripping method

Fig. 3 - Measurement of the rape pod ripping force using a texture analyser

Ripping method is an available method that can directly quantitatively measure the force of separate layer cracking in the lab. The Texture analyser (TA.XT Plus, Stable Micro Systems, UK) was used to measure the force. The test operation is shown in Fig. 3. Before testing, the pod was tangled at a distance of 25mm from the peduncle with a wire to ensure that the arm of force was consistent for different pods ripping. A L-hook was used to hook the pod stalk and was pulled by the texture probe at a speed of 10 mm/min, the force of the probe was recorded on the computer in real time. During the test, the tensile force increased continuously before the pod cracking, and when the force reached a certain value, it decreased instantly, and the peak value was the pod cracking resistance force. The experiment was repeated 5 times for each variety.

2.3.2 Two-degree-of-freedom (2-DOF) random collision method

The object of mechanical harvesting is the natural growing pods in the field; in order to reduce the influence of human interference on the pod characteristic and reflect the resistance exactly, it is necessary to develop a method and an instrument that are convenient for field testing. To solve the above problem, a two-degree-of-freedom collision tester was designed by our research team, as shown in Fig. 4 (*Qing et al., 2019*).

The principle of random collision was applied in this method, a two-stage motion mechanism was proposed. The first-level is reciprocating vibration mechanism, and the second-level is swing mechanism. The controller can separately control the speed and working time of motor *1* and motor *2*, and set different motion frequencies. During the test, 20 intact pods of the same variety and maturity and 12 steel balls with a diameter of 13mm were placed in the material box at the same time. The stepper motor controller would stop automatically every 1min. Then the broken pods were taken out and their number was recorded. Repeat the above operation no more than 10 times, and calculate the pod shatter resistance according to formulas (5) and (6). Each group of tests was repeated three times, and the formula of pod shatter resistance index is as follows:

$$SI = \frac{\sum_{i=1}^{10} x_i(10-i+1)}{n_1 \cdot n_2} \quad (5)$$

$$SRI = 1 - SI \quad (6)$$

where: SI is the pod shatter index;

x_i is the number of broken pods at time i;

n_1 is the total number of pods, which is 20 here;

n_2 is the specified total number of collision repetitions, which is 10 here;

SRI is pod shatter resistance index.

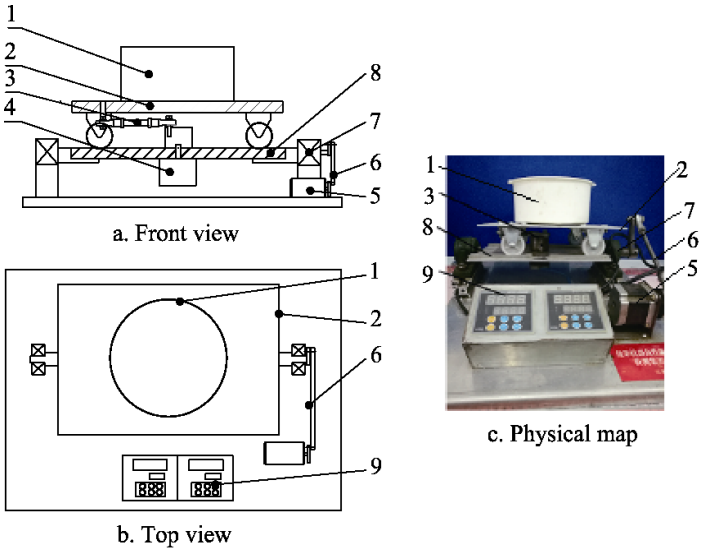

Fig. 4 - Structure and physical diagram of the 2-degree-of-freedom collision tester

1. Material box; 2. Upper plate; 3. Crank slide mechanism; 4. Motor 2; 5. Motor 1; 6. Crank rocker mechanism; 7. Bearing; 8. Lower plate; and 9. Controller.

2.3.3 Test materials and program

A total of 15 varieties that related to the pod resistance were planted in the Experimental field of Agricultural Equipment Engineering College of Jiangsu University. In the two years of 2018 and 2019, during the yellow ripening period of rapeseed in May, 5 plants of the same growth and colour of plants were selected from each variety randomly. The main inflorescences of the plants were cut and marked, and then were placed in a room at 25°C under constant temperature and humidity to dry naturally for 25 days to ensure that the moisture content of different varieties was consistent. After drying, the intact pods with the same growth rate and without diseases and insect pests in the middle of the main inflorescence were cut for experiment. Then the shatter resistance of these pods was tested by the ripping method and 2-DOF random collision method.

The test results of the two methods were compared and analysed, and the linear relationship between the cracking force and the SRI was found. Combined with the test results of the impact force between the reel tine and the rape during the field mechanized harvest, the range of the SRI suitable for mechanized harvest was obtained. In addition, the 2-DOF tester was moved to the field, and 12 rape varieties were randomly selected from the experimental field of Jiangsu Academy of Agricultural Sciences on May 25, 2018. The pod shatter resistance of varieties on the market was investigated for surveying whether the field pod resistance meets the needs of mechanical harvesting.

RESULTS

3.1 Impact force of reel tine on the rape during harvesting

After processing the test data collected by the calibration, it is found that there is a significant linear relationship between the internal stress signal and the load on the tine. The load size and the corresponding average stress measured in the test are shown in Table 1. According to the formula (3) and (4), the scale coefficient *b* of the tine calibration is 0.0797, and the intercept *a* is 0.042. Therefore, the relationship model between the force *y* and the internal stress *x* of the tine collected by the system is obtained as follows:

$$y=0.0797x+0.042\ (R^2=0.993) \tag{7}$$

Table 1

Results of the load size and the average stress measured in the static calibration test of the reel tine

Load (N)	0.1	0.2	0.3	0.4	0.5	0.75	1.0	2.0
Measured stress (MPa)	1.126	2.261	3.275	4.687	5.532	8.278	11.531	24.942

The operating parameters of the highest harvesting efficiency with the reel speed of 30 rev min^{-1} were taken as a typical example to analyse the field test results in detail. Fig. 5 shows the measured stress change curve of the reel tine at the reel speed of 30 rev min^{-1}. Fig. 5(a) is the general diagram of the tine stress from the harvester start up; it can be seen from it that the stress variation of the whole curve can be divided into three areas A, B and C.

The amplitude of the stress curve change in the period of 'A' is very small and has certain regularity, generally not more than 5 MPa. During this period, the machine had just started up without moving, and the reel had not been running, so the tine stress change was caused by machine vibration.

At the beginning of period 'B', the tine stress increased instantaneously, and the overall showed a cyclical change trend of first increasing and then decreasing. Because during this stage, the harvester stayed at the edge of the field and had not yet moved forward, but the reel had started to operate, when the tine hit the rape on the edge of the field, the stress measured increases instantly, and when the tine separated from the rape plant, the stress began to decrease. During the period of 'C', the stress increased sharply, and it was found that the stress in empty stroke stage 'C' was significantly higher than that of 'B' at the same stage. This is because of vibration increase caused by uneven field when the machine started to go forward for harvesting, which means that the machine walking has a great influence on the tine stress and the vibration will significantly increase the impact force. In order to judge the cycle easily in the curve, the moment of the stress value increased instantaneously, that is the moment when the tine attacked the pod, which was selected as the starting point of the cycle. In the graph, the two blue dot sliding lines are the tine stress changes of one revolution from the contact, among them, the period 'a' is the working stroke of contact with the rape, and the period 'b' is the empty stroke period without contact.

Fig. 5(b) shows a complete cycle of stress variation collected after the harvesting operation is stable. It can be seen that the stress curve fluctuates greatly due to the uneven ground, machine vibration and impact force. In the design of the rape harvester, in order to reduce the seed falling loss, the harvester bottom plate will be lengthened. For the later stage of entering, the feeding and the releasing stages, the burst pods will directly fall into the inside of the header, so the impact force causing the header loss is only affected by the early stage of feeding. In the calculation of the impact force, the maximum stress within 0.1s after the start of one cycle of rotation was selected as the effective conversion stress value. The stress values of three cycles were randomly selected for each test and averaged, with three replicates for each group of parameters, and then the impact force was calculated according to formula (7).

The results of converted contact force were showed in Table 2. This illustrates that the reel speed has a significant influence on the force.

Theoretically, the pod cracking resistance force should be greater than the tine impact force, which can reduce the pod burst and decrease the header loss. Therefore, the pod resistance force would be best greater than 3.85 N and at least over 1.76 N for the selection of rape varieties that are suitable for mechanized harvesting.

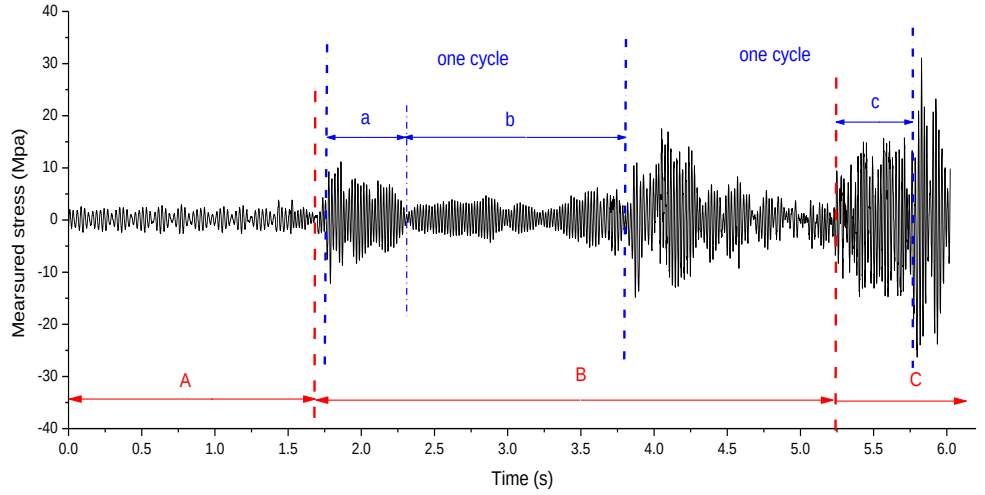

(a)

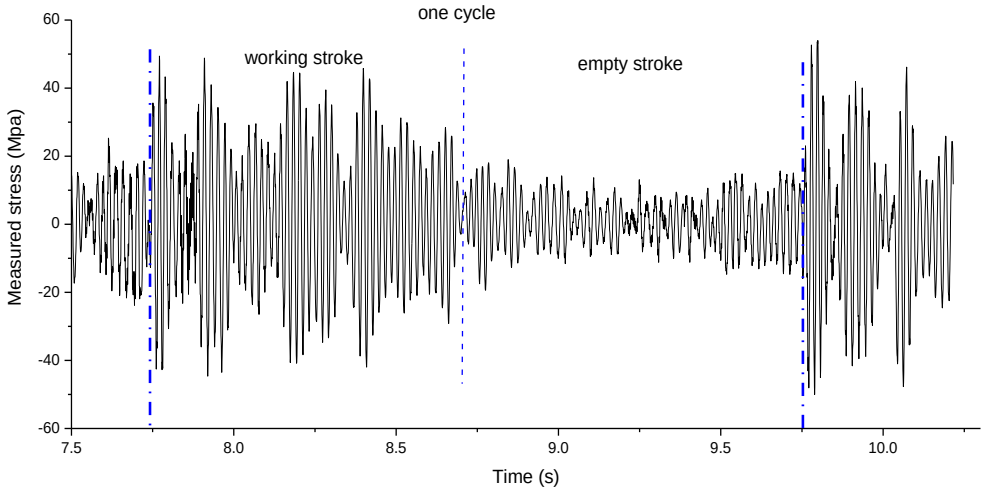

(b)

Fig. 5 - The measured stress change curve of the reel tine with the reel speed of 30 rev min^{-1}

(a) General diagram of the tine stress collected during the harvesting period from the harvester start up;

(b) The tine stress variation collected after the harvesting operation.

Table 2

Machine operation parameters and conversion results of the tine impact force in field test

Reel speed (rev min^{-1})	Reel height (mm)	Harvester forward speed (m s^{-1})	Reel speed ratio λ	Converted tine contact force (N)
18	1000	0.6	1.41	1.76
24	1000	0.8	1.41	2.82
30	1000	1.0	1.41	3.85

3.2 Comparison results of pod shatter resistance by two methods

The results of pod shatter resistance of different varieties by ripping method and 2-DOF collision method are shown in Fig. 6. There was a significant correlation between the two results with the Pearson correlation coefficient being 0.937 ($P < 0.01$). This reflects that the test results of 2-DOF collision method are reliable. The results of pod resistance of other varieties under the two methods were similar in two years, therefore, it is concluded that the genotype is the main factor to determine the pod resistance. Among them, C6009 had the strongest pod with the highest shatter resistance.

A linear regression model was established for the data results of the two methods, and the following relationship was found between the cracking force resistance F and the SRI:

$$F=2.186\cdot SRI+0.501 \ (R^2=0.890,\ P<0.001) \quad (8)$$

Two varieties 15w2130-20 and F17W82-n747 are used for verification test. The SRI measured by the test were 0.275 and 0.358 respectively, and the ripping force was 0.975 N and 1.135 N respectively. The results are similar to the theoretical values 1.102 N and 1.284 N, which justifies that the model is reliable. The tine impact force at the reel speed of 18 rev min^{-1} is 1.76 N. In order to reduce the header loss caused by reel tine attack, the pod cracking resistance force should be greater than the value theoretically. According to the model relationship, it can be concluded that the pod shatter resistance index (SRI) should be greater than 0.576 under the same resistance.

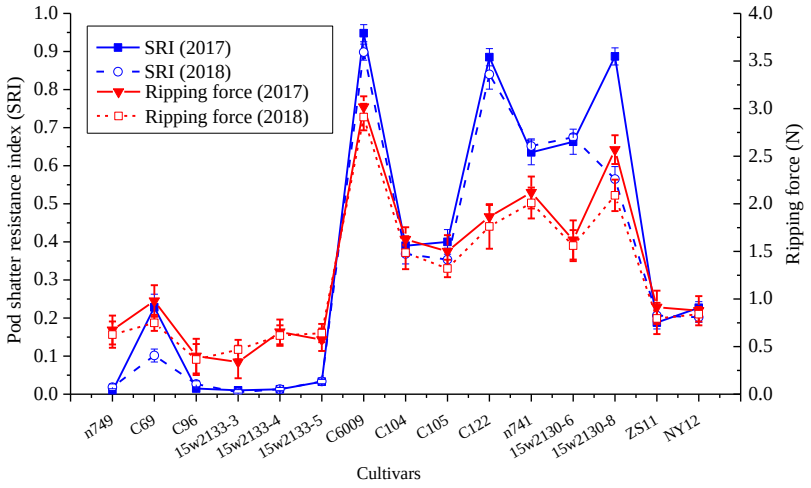

Fig. 6- Results of pod shatter resistance of different varieties by ripping method and 2-DOF collision method

3.3 Investigation results of rape pod resistance planted in the field

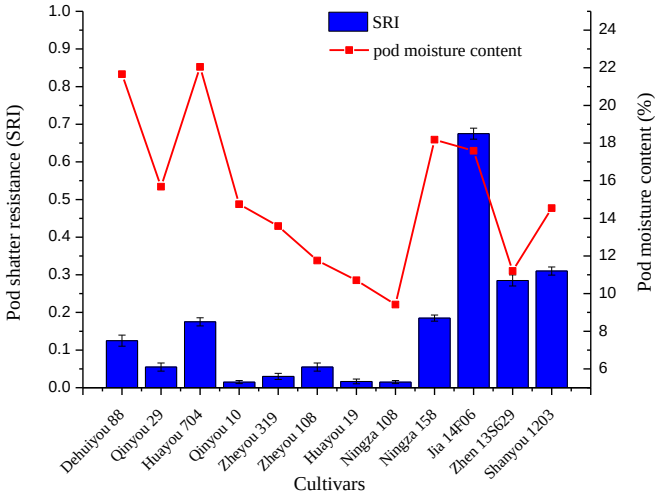

Fig. 7 - The investigation results of pod shatter resistance of the field-grown rape varieties

The investigation results on pod shatter resistance of twelve randomly selected field-grown rape varieties are shown in Fig. 7. During the test, the Sfy-20 infrared rapid moisture tester (Haibin Instrument Co., Ltd., Shenzhen, China) was used to measure the moisture content of all varieties of pods in the field site test. The variation range of the SRI of all varieties was 0.015-0.675, and the water content of pod varied from 11.20% to 22.05%. Among them, the variety with the strongest resistance was Jia14F06. In addition, it was found that the pod moisture content was not the most important factor influencing the resistance. For example, Huayou704 had the highest moisture content of 22.05%, but its pod resistance index was not the largest, only 0.175. This indicates that the genotype of rapeseed has a greater influence on the resistance, and it is reliable to select varieties with high shatter resistance to reduce the harvest loss.

3.4 Current varieties situation of rape pod shatter resistance

A total of 27 rape varieties measured in all tests were classified by the value of SRI, and the distribution of the varieties number in different SRI ranges are shown in Fig. 8.

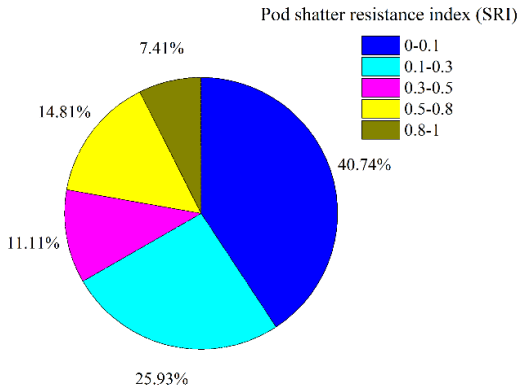

Fig. 8 - Distribution diagram of the number of rape varieties in different pod shatter resistance index (SRI) ranges

It can be seen from the distribution pie chart that the number with the SRI < 0.1 accounted for the largest proportion of 40.74 %, and there are 11 varieties in total, which are very easy to burst and cause large losses in the harvesting process. There are only 6 rape varieties with the SRI greater than 0.5, in which only 4 varieties can meet the required SRI of 0.576 of the low reel speed, accounting for 14.8%. There is no cracking resistance force in the tested varieties that can be greater than the impact force at the reel speed of 30 rev min^{-1}. That indicates that the crack resistance of rapeseed varieties in the market is generally poor, which doesn't not satisfy the harvesting requirement of combine harvesters.

CONCLUSIONS

When rape pods have poor shatter resistance, the impact of the rotation movement of the reel on rape will make the pod crack rapidly and cause the drop loss of rapeseed, which is the main reasons for header loss. In this paper, the signal acquisition and analysis of the internal stress caused by the impact between the tine and the rape under different reel rotation speeds of 18, 24, and 30 rev min^{-1} during the mechanical harvesting was carried out, the corresponding sizes being 1.76, 2.82 and 3.85 N.

The developed two-degree-of-freedom (2-DOF) collision tester has the advantages of easy to move, simple operation, and can be used for field test of pod shatter resistance, which can reflect the true characteristics of the pod grown in the field object during the harvesting period and be more conducive to screen reliable and suitable rape varieties for mechanical harvesting. The expected SRI value of 0.576 that meets the harvesting requirements of the reel at low speed was determined. There was no variety of all the tested pods in this paper whose pod resistance could satisfy the requirement of the tine impact force at the reel high-speed, and only 14.8% of the tested varieties had it greater than the standard. Therefore, the current commercial and researched rape varieties are generally poor in pod resistance, which does not match the harvesting requirements of combine harvesters.

For the rape pods of the same variety, the higher the water content, the better the cracking resistance. Therefore, for the varieties with stronger resistance, it is recommended to continuously test the pod resistance during their maturity stage and choose the appropriate harvesting time to improve the pod resistance to meet the harvesting requirements. However, the moisture content of pods during harvesting should not be too high to avoid excessive load and loss in the threshing and cleaning process. On the other hand, it is suggested to improve the reel tine material and develop the flexible tine, increasing the use of flexible materials to reduce the impact force of the tine. This study provides a reliable screening standard for selecting rape varieties suitable for mechanical harvesting, and promotes low-loss rapeseed harvesting.

ACKNOWLEDGEMENT

This research was funded by National Natural Science Foundation of China, grant number 31671590.

REFERENCES

[1] Bruce D.M., Farrent J.W., Morgan C.L., Child R.D. (2002). Determining the oilseed rape pod strength needed to reduce seed loss due to pod shatter. *Biosyst. Eng.,* vol. 81, no. 2, pp. 179–184. doi:10.1006/bioe.2001.0002.

[2] Btluri S. M., Han S., Shen S. (2013). Meshless Bocal SPatrov-Galerkin (MLPG) approaches for weakly singular traction & approach in dompusational integral equations. *Computers in Engineering*, vol. 22, no. 5, pp. 507-517.

[3] Cavalieri A., Harker K.N., Hall L.M., Willenborg C.J., Haile T.A., Shirtliffe S.J., Gulden R.H. (2016). Evaluation of the causes of on-farm harvest losses in canola in the northern Great Plains. *Crop Sci.*, vol. 56, no. 4, pp. 2005-2015. doi: 10.2135/cropsci2013.09.0624

[4] Cavalieri A., Lewis D.W., Gulden R.H. (2014). Pod drop and pod shatter are not closely related in canola. *Crop Sci.*, vol. 54, no. 3, pp. 1184–1188. doi:10.2135/cropsci2013.09.0624

[5] Delgado M., Felix M., Bengoechea C. (2018). Development of bioplastic materials: From rapeseed oil industry by products to added-value biodegradable biocomposite materials. *Ind. Crops Pro.*, vol.125, pp. 401-407. doi: 10.1016/j.indcrop.2018.09.013

[6] Hobson R.N., Bruce P.M. (2002). PM—Power and Machinery: Seed Loss when Cutting a Standing Crop of Oilseed Rape with Two Types of Combine Harvester Header. *Biosyst. Eng.*, vol. 81, no. 3, pp. 281-286. doi: 10.1007/BF00022751

[7] Kadkol G. P., Halloran G. M., Macmillan R. H. (1985). Evaluation of brassica genotypes for resistance to shatter. II. variation in siliqua strength within and between accessions. *Euphytica*, vol. 34, no. 3, pp. 915-924. doi:10.1007/BF00035431

[8] Li Y.M., Zhu J.Q., Xu L.Z. (2012). Experiment on strength of rapeseed pod dehiscence based on impending fracturing method (基于悬空压裂法的油菜角果抗裂角力测试试验). *Transactions of the CSAE*, vol. 28, pp. 111-115. doi: 10.3969/j.issn.1002-6819.2012.08.017

[9] Morgan C.L., Ladbrooke Z.L., Bruce D.M., Child R., Arthur A.E. (2000). Breeding oilseed rape for pod shattering resistance. *J. Agri. Sci.*, vol. 135, no. 4, pp. 347-359. doi:10.1017/S0021859699008424

[10] Moses F.O., Thomas O.M., Jun S. (2012). Kinematics of the tined combine harvester reel. Agric. Eng. Int: CIGR J. vol. 14, no. 3, pp. 53-60.

[11] Pari L., Assire A., Alessandro S., Vincenzo C. (2012). The harvest of oilseed rape (Brassica napus L.): The effective yield losses at on-farm scale in the Italian area. *Biomass Bioenerg.*, vol. 46, pp. 453-458. doi: 10.1016/j.biombioe.2012.07.014

[12] Qing Y.R., Li Y.M., Xu L.Z., Ma Z., Yang Y. (2019) Technology of 2-DOF collision testing for rape pod shatter resistance (油菜角果抗裂角性二自由度碰撞测试方法的研究). *Trans. CSAE*, 35, 33-40. Doi: 10.11975/j.issn.1002-6819.2019.05.005

[13] Peng P.F., Li Y.C., Mei D.S., Liu D.M., Fu L., Wang H., Sang S.F., Chen Y.F., Hu Q. (2013). Optimization and experiment of assessment method for pod shatter resistance in Brassica napus L. (油菜抗裂角性鉴定方法的改进及试验). *Transactions of the CSAE*, vol. 29, pp. 19-25. doi: 10.3969/j.issn.1002-6819.2013.21.003

[14] Shim Y.Y., Falk K., Ratanapariyanuch K., Reaney M.J.T. (2017). Food and fuel from Canadian oilseed grains: Biorefinery production may optimize both resources. *Eur. J. Lipid Sci. Technol.*, vol.119, no. 9, 1438-7697. doi:10.1002/ejlt.201600358

[15] Shubert K. (2018). Synthesis of organofunctional silane from rapeseed oil and its application as a coating material. *Cellulose*. pp. 6269-6278. doi: 10.1007/s10570-018-2018-6

[16] Summers J. E., Bruce D. M., Vancanneyt G., Redig P., Werner C. P., Morgan C. (2003). Pod shatter resistance in the resynthesized brassica napus line dk142. *J. Agr. Sci.* vol. 140, no. 1, pp. 143-52. doi:10.1017/s002185960200285x

[17] Tan X.L., Zhang J.F., Yang L. (2006). Quantitative determination of the strength of rapeseed pod dehiscence (油菜角果裂角力的定量测定). *Transactions of the CSAE*, vol. 22, pp. 40-43. doi: CNKI:SUN:NYGU.0.2006-11-009

MODELING AND ANALYSIS OF AN AGRICULTURAL VEHICLE CROSS-BOUNDARY WARNING SYSTEM
/
农业车辆田间作业越界预警系统建模与分析

Guangrui Hu, Chuang Qi, Weiyu Kong, Jun Chen*, Yu Chen, Shuo Zhang, Hongling Jin
College of Mechanical and Electronic Engineering, Northwest A&F University, Yangling 712100, China;
Tel: +86 13572191773; E-mail: chenjun_jdxy@nwsuaf.edu.cn
DOI: https://doi.org/10.35633/inmateh-63-29

Keywords: *Electronic fence; Cross-boundary model; GNSS; Robot Operating System (ROS)*

ABSTRACT
In order to improve the safety of agricultural vehicle in the field, we established a vehicle kinematics model for hanging agricultural tools, and comprehensively considered driving speed, the agricultural tool rotation radius, and vehicle movement trend to propose an agricultural vehicle field operation cross- boundary warning method based on a Robot Operating System (ROS). Furthermore, we designed a set of agricultural vehicle safety warning systems and employed Qt Creator to develop the agricultural vehicle warning system operation interface. Following this, a test platform was built based on the Oubao 4040 tractor and unilateral cross-boundary warning tests were conducted. Test results demonstrate the ability of the proposed cross-boundary warning system to: i) correctly determine the warning area at different speeds (low (3.6km/h±0.5km/h), medium (10.8km/h±1.0km/h) and high (18.0km/h±1.5km/h)) and driving paths ("V" and "U"-shaped routes); ii) and to prompt the operator in a timely manner. The proposed framework exhibits strong applicability and improves the safety of agricultural vehicle hanging agricultural tools.

摘要
为提高农业机械田间作业的安全性，本研究建立了悬挂农具的车辆运动学模型，综合考虑了行驶速度、农具旋转半径与车辆运动趋势，提出了一种农业机械田间作业越界预警方法，并基于 ROS 系统设计了一套农业机械安全预警系统，使用 Qt Creator 开发了农业机械预警系统操作界面，搭建了以欧豹 4040 型拖拉机为基础的试验平台，进行了单边越界预警试验。试验结果表明，本研究设计的越界预警系统在不同速度（低速（3.6km/h±0.5km/h），中速 （10.8km/h±1.0km/h）和高速（18.0km/h±1.5km/h）)与不同行驶路径（“V”和“U”型路线）下均能正确判断预警区，并能够及时提示操作人员，具有良好的适用性，具有提高悬挂农具的农业车辆田间作业安全性的潜力。

INTRODUCTION

The agricultural sector field is currently experiencing a rapid development in the field of intelligence, particularly the navigation technology of agricultural vehicles. The safety of agricultural vehicles in the field has always been the concern of researchers and farmers (*Khorsandi F, et al., 2019; Latorre-Biel J A, et al., 2019*). *Weichelt and Gorucu* (2018) report that All-Terrain Vehicle (ATV) accidents were the second most common injury source in US agriculture, causing 190 injuries or deaths (63% fatal). Safety warnings are crucial for the safe and reliable independent running of agricultural vehicles (*Mousazadeh H, 2013*). Agricultural vehicle safety warnings typically includes vehicle rollover warnings, wheel slip warnings, obstacle warnings and cross boundary warnings (*Hickman J S et al., 2015; Tian Y, 2018; Vidoni R, et al, 2015; Zhu B, et al., 2016; Zhao T, et al. 2016; Zhu T, et al, 2011*). The theory of cross-boundary warning has continuously developed over the recent years, resulting in an increase in its applications. However, despite the recent progress, research cross-boundary warnings based on satellite positioning in agricultural vehicle navigation is relatively limited (*Guo et al., 2019*).

Traditional methods generally regard the farmland road marking line and crop boundary as the operation boundary of agricultural vehicles. Farmland imagery, which is typically obtained by one or two cameras, is used to extract farmland road signs and navigation lines via segmentation, clustering, and the Hough transformation (*Bonadies S and Gadsden S A, 2019; Li X, et al., 2020; Song Y, et al., 2017; Zeng H, et al., 2020; Zhao T, et al. 2016*). These extracted features are combined with deep learning methods to prevent agricultural vehicles from crossing the boundary.

Traditional cross-boundary warning technology is largely dependent on the sensor's perception of the surrounding environment, yet complex farmland environments increase the amount of computing resources consumed by the sensing algorithms (*Zhang M, et al., 2020*).

The development of Global Navigation Satellite Systems (GNSS) has increased the applications of electronic fence technology in security, railway, aviation, etc. (*Figueiras J, et al., 2012; Cheng H, et al., 2017; Hsu C, et al., 2019; Hu J, et al, 2018; Monod M O, et al., 2008; Yuan Z, et al., 2017*). In particular, electronic fence technology is able to employ satellite positioning coordinates to set the working area, install GNSS signal receiving equipment on the working device to locate position, and determine whether the working device is in the working area via its coordinates. *Yang et al. (2016)* employed an electronic fence to set the plant protection operation area of unmanned aerial vehicles (UAVs) and was able to find out whether the UAV crossed the boundary in real time via a ray detection algorithm. Results demonstrated the ability of electronic fence technology to reliably monitor UAV plant protection operations. *Zhao (2019)* designed an earthing warning system for tractors based on the Beidou System (BDS), but failed to employ electronic fences to the cross-boundary warning of agricultural vehicles.

In the current study, in order to improve the safety of agricultural vehicle field operations, we employ electronic fence technology to limit the operational range of agricultural vehicles. A field operational cross-boundary warning framework for agricultural vehicles based on satellite positioning is proposed by integrating the speed of agricultural vehicles, the rotation radius of agricultural tools, the movement trend of vehicles, and the vehicle kinematics model of hanging agricultural tools. The front wheel angle encoder and BDS are installed on an Oubao 4040 tractor and the agricultural vehicle safety warning system is designed based on a Robot Operating System (ROS).

MATERIALS AND METHODS

Mathematical modeling of vehicle kinematics and the warning system

We selected the agricultural tractor as the research object and established a kinematic model for the tractor (Fig. 1). Note that we did not consider the influence of factors such as slip, side deviation and ground flatness during the tractor driving process. The model is expressed as equation 1, while equation 2 represents the relationship between turning radius R_2 of the agricultural tools and turning radius R_1 of the tractor.

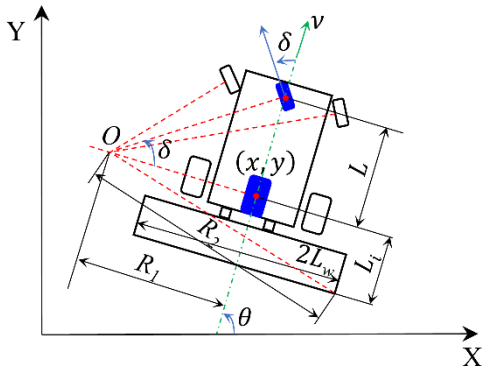

Fig. 1 - Proposed kinematics model of tractor-mounted farm tools

$$\begin{aligned} \dot{x} &= v\cos\theta \\ \dot{y} &= v\sin\theta \\ \dot{\theta} &= \omega = \frac{v}{L}\tan\delta \end{aligned} \tag{1}$$

$$\begin{aligned} R_1 &= L/\tan\delta \\ R_2 &= \sqrt{(R_1 + L_w)^2 + L_i^2} \end{aligned} \tag{2}$$

where: x and y – the global coordinates of the tractor rear axle centre (m);

θ – The heading angle of the tractor in the global coordinate system (°);

ω – The angular speed of the tractor (rad/s);

v – The driving velocity of the tractor, $v \in (0, v_{max}]$ (m/s);

δ – The steering angle of the tractor's front wheels (°);

L – The distance between the front and rear wheels of the tractor (m);

L_i – The distance between the farm tool and the rear wheel axis of the tractor (m);

L_w – Half of the total width of the farm tools (m);

R_1 – The turning radius of the tractor (m);

R_2 – The rotation radius of the tractor-mounted farm tools (m).

The operation boundary of the agricultural vehicles refers to the boundary of the electronic geofence preset by the operator via the latitude and longitude and is based on the size of the farmland. Agricultural vehicles perform field operations within an electronic geofence and cannot go beyond the geofence. When the agricultural vehicles approaches the boundary, a warning is required in order to alert the operators.

Fig. 2 presents the proposed cross-boundary warning model. Straight line MN denotes the operation boundary in terms of the latitude and longitude. $Q(x_k,y_k)$ are the GNSS-determined tractor coordinates at time k, and point $Q'(x_{k+1}, y_{k+1})$ represents the position of the tractor following time ΔT, which is predicted by the kinematic model via equation 4.

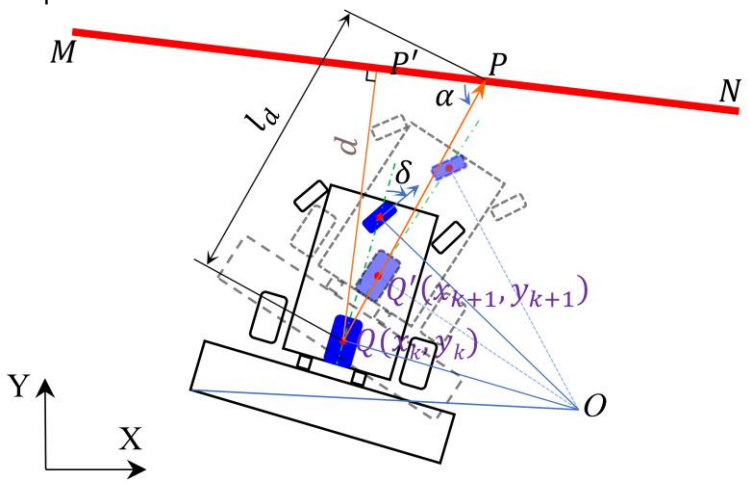

Fig. 2 - Schematic diagram of cross-boundary warning model

$$\begin{aligned} A_1x + B_1y + C_1 = 0 \\ A_2x + B_2y + C_2 = 0 \end{aligned} \tag{3}$$

$$\begin{bmatrix} x_{k+1} \\ y_{k+1} \end{bmatrix} = \begin{bmatrix} x_k \\ y_k \end{bmatrix} + v_k \Delta T \begin{bmatrix} \cos\delta_k \\ \sin\delta_k \end{bmatrix} \tag{4}$$

$$\lambda = \frac{\sqrt{|A_1x_k + B_1y_k + C_1|}}{\sqrt{|A_1x_{k+1} + B_1y_{k+1} + C_1|}} \tag{5}$$

$$\alpha = \arccos \frac{A_1A_2 + B_1B_2}{\sqrt{A_1^2 + B_1^2}\sqrt{A_2^2 + B_2^2}}, \alpha \in [0, \pi/2] \tag{6}$$

$$d = \frac{|A_1x_k + B_1x_k + C_1|}{\sqrt{A_1^2 + B_1^2}} \tag{7}$$

$$l_d = \frac{d}{\sin\alpha} \tag{8}$$

where:

A_1, B_1 and C_1 – The parameters of operation boundary line *MN*;

A_2, B_2 and C_2 – The parameters of ray *QQ´*;

λ – the cross-boundary trend parameter, where λ>1, and λ<1 indicate a tendency of the vehicle to drive to and leave the specified boundary, respectively, and λ=1 indicates a direction of travel that is parallel to the specified boundary or at rest;

d – The vertical distance between the vehicle coordinate point and boundary line (m);

α – The angle between ray *QQ´* and operation boundary line *MN* (°).

Agricultural vehicles operate parallel and close to the boundary line, which consequently introduces a cross-boundary risk that must be assessed by the cross-boundary warning model in order to warn the operator. Therefore, parameter ξ was introduced to broaden the range used to determine whether the vehicle was stationary or parallel. The distance between the vehicle and the boundary was then determined via equation 9.

$$\begin{cases} dist = l_d, \lambda > 1+\xi \\ dist = d, 1-\xi \le \lambda \le 1+\xi \\ dist = \infty, \lambda < 1-\xi \end{cases} \quad (9)$$

The cross-boundary warning was divided into three levels: i) green indicates that it is safe to drive at this time; ii) yellow specifies that the tractor is gradually approaching the boundary of the driving direction and warns the operator to leave the warning state via steering; and iii) red warns the operator that the steering operation is no longer able to take the vehicle out of the warning state at this time, and the vehicle must leave the warning state. We determined the warning distance by taking into account the minimum turning radius of the vehicle as follows:

$$l_t = \mu(Av^2 + Bv) + \tau C \quad (10)$$

where: A=1/2 a_{max}, a_{max} – the maximum braking acceleration of agricultural vehicles, 7 m/s;

B – The operator response time, 0.7 s;

μ – The vehicle speed safety factor, μ >1;

C – The minimum turning radius of the tractor-mounted agricultural tools, R_{2min}, m;

τ – The safety factor of vehicle turning, τ >1.

In the first quadrant of the v-l coordinate system, the quadratic curve l_t=$\mu(Av^2$+$Bv)$+λC, the straight lines v=v_{max}, and l_c=λC divide the coordinate system into the green, yellow and red regions. The warning level was evaluated by comparing the actual distance between $dist$, l_t and l_c during the driving process (Fig. 3). For v=v_1, $dist$=l_1∈[0, l_c], $dist$=l_2∈(l_c, l_t] and $dist$=l_3∈(l_t,+∞) denote red, yellow and green.

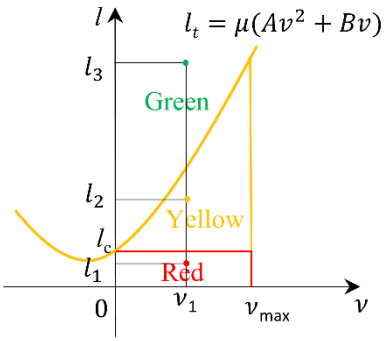

Fig. 3 - Schematic diagram of the cross-boundary warning level classification

Hardware and software

In order to test the proposed cross-boundary warning model, we established a test platform using a Oubao 4040 tractor with front-wheel steering and rear-wheel driving (Fig. 4).

Tab. 1 reports the key parameters of the test platform.

Table 1

Key performance parameters of the test platform

Type	Length, width and height (mm)	Front wheel track (mm)	Rear wheel track (mm)	Engine power (kW)	Speed range (km/h)
Oubao 4040	3200×1800×2110	1320	1300	29.40	2.65～34.78

We employed Raspberry Pi 4B and Ubuntu 18.04LTS as the controller and operating system, respectively, as well as XW-GI5610 (sampling frequency: 10Hz; manufactured by StarNeto Co., Ltd., China) as the positioning equipment. The mobile station GNSS antenna was fixed on the top of the test platform in order to set the base station XW-GPS1060 coordinate information.

The base station and the mobile station were integrated with GE MDS EL-7052 series data transmission radio communication system to form an RTK-GNSS (real time kinematic-global navigation satellite system), allowing for centimetre-level positioning accuracy.

The test platform was centred around a ROS-based software system. More specifically, ROS Melodic was installed under the Ubuntu 18.04 LTS operating system to obtain GNSS positioning data through the serial port. In order to detect the front wheel angle, the Wittower absolute rotary encoder (±45° detection range, 11 bit detection accuracy and 12 bit resolutions) was placed on the steering column of the front left wheel. Based om the calibration results, the ROS node Arduino was used to collect and convert the encoder output voltage into the front wheel angle. Arduino then published the front wheel angle through the serial port to the ROS at a frequency of 50 Hz.

Fig. 4 - Cross-boundary warning test platform

Fig. 5 presents the proposed agricultural vehicle warning system operation interface developed by Qt Creator. The interface was divided into two components: the agricultural vehicle obstacle warning and agricultural vehicle cross-boundary warning. In the current study, we focused on the latter, reserving the former for future research. The frequency of warning information released by the agricultural vehicle cross-boundary warning was consistent with the sampling frequency of GNSS (10Hz).

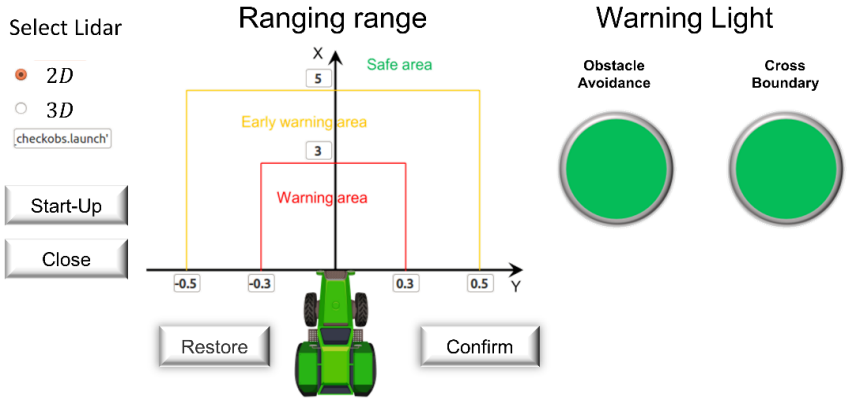

Fig. 5 - Operational interface of the agricultural vehicle warning system

Experiment methods

- **Calibration test of the tractor front wheel angle**

Once the encoder was installed on the front wheel column, the line drawing method was applied to calibrate the front wheel angle and the encoder output value. In particular, the front wheel turned left to positive and right to negative. The front axle of the tractor was then held via a jack, raising the front wheels off the ground to place the A0 drawings below them. Following this, the steering wheel was turned such that the front wheels faced parallel to the body. The front wheel angle was recorded as 0° and the encoder was returned to 0. The steering wheel was then turned from left to right to determine whether the encoder output voltage exceeded the range. When the range was not exceeded in both directions, calibration was subsequently performed (Fig. 6).

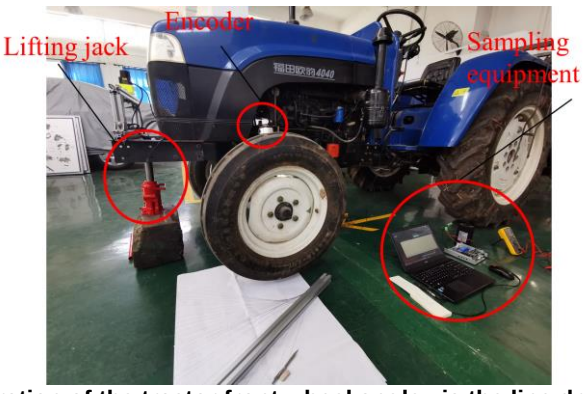

Fig. 6 - Calibration of the tractor front wheel angle via the line drawing method

- **Agricultural vehicle boundary warning experiment**

The single-boundary cross-boundary warning test simulated the process of the agricultural vehicle in the field, warning the agricultural vehicle of cross-boundary behaviour, and detecting the warning level of the cross-boundary warning model.

A GNSS device initially set two boundary points, which were then connected to form a working boundary. Low (3.6km/h±0.5km/h), medium (10.8km/h±1.0km/h) and high (18.0km/h±1.5km/h) speeds were used for the agricultural vehicle when driving to the operating boundary via "V" and "U"-shaped routes (Fig. 7). We monitored the state of the cross-boundary warning lights and the actual cross-boundary status of the agricultural vehicle in order to determine the accuracy of the warning. The agricultural vehicle traversed the "V" and "U" routes and record the state of the cross-boundary warning lights. We assumed that the tractor hung a farm tool with a width and installation distance of 4 m and 1 m, respectively. We chose point *M* (506313.000, 3795910.000) and *N* (506313.000, 3795960.000), *MN* as boundary line. According to the previous test, we set ξ=0.01, μ=2 and τ=1.5. The experiment was performed on the lawn on the west side of the School of Mechanical and Electronic Engineering, Northwest A&F University, Yangling, China (Fig. 8).

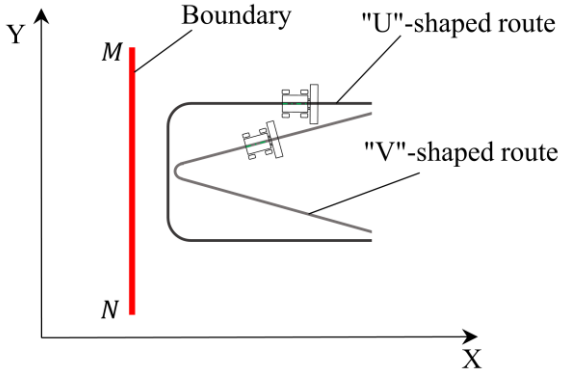

Fig. 7 - Route map of test vehicle

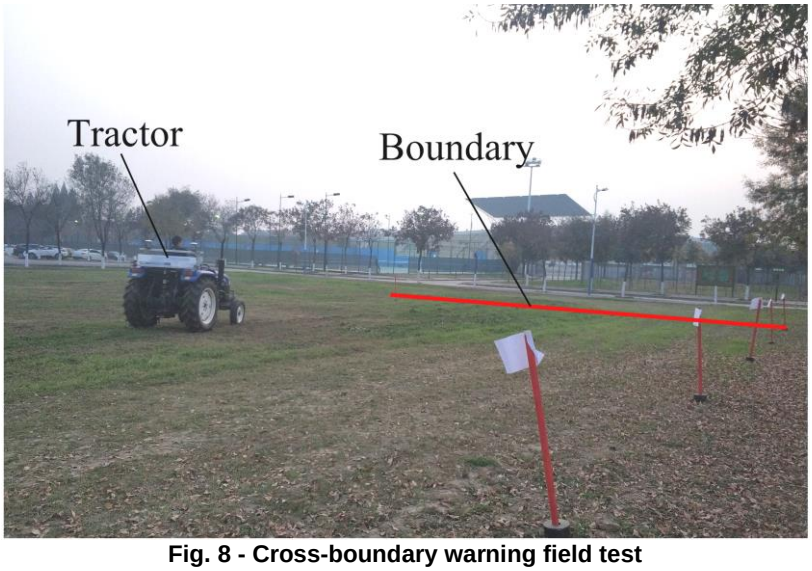

Fig. 8 - Cross-boundary warning field test

The implementation steps of the algorithm are as follows: i) obtain the operation boundary based on GNSS coordinates; ii) obtain the position, speed and front wheel angle data of agricultural machinery; iii) calculate *dist* according to the algorithm proposed in this study, compare *dist*, l_t and l_c, and send out warning signal.

RESULTS AND DISCUSSION

A total of 33 datasets were recorded during the front wheel angle calibration test, and calibrated using Origin (2018, OriginLab) (Fig. 9). The results were fit with a straight line with R^2 = 0.99975, demonstrating the strong linearity between the front wheel angle value and the encoder output value. Thus, the encoder output value can be employed to calculate the front wheel angle.

The proposed cross-boundary warning model of the agricultural vehicle was tested on the tractor testing platform. Raspberry Pi 4B was used for the data processing and display terminal. We performed the cross-boundary warning tests in order to comprehensively analyse the cross-boundary warning model. The point locations and warning level data were exported and visually analysed via Python. Fig. 10, Fig. 11 and Fig. 12 present the scatter plots of the exported data, where the colour of the point indicates the warning level. Fig. 10, 11 and 12 show that the system will correctly determine the warning area at different speeds (low (3.6 km / h ± 0.5 km / h), medium (10.8 km / h ± 1.0 km / h) and high (18.0 km / h ± 1.5 km / h)) and different driving paths ("V" and "U"-shaped routes). The yellow warning zone is (6.74m, 8.28m], (6.74m, 12.20m] and (6.74m, 17.24m] respectively for low, medium and high-speed, which indicates that the yellow warning zone is observed to be shorter for agricultural vehicles driving at lower speeds, and subsequently increases with speed. The expansion of the yellow warning zone aids operators in determining warning signs in order to take timely preventive measures. Compared with the cross-boundary warning algorithm proposed by Yang et al. (2016), the proposed algorithm reduces the steps of generating safe operation boundary, simplifies the complexity of the algorithm, and improves the response speed of the algorithm.

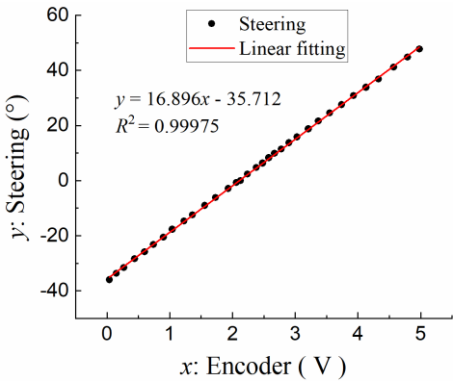

Fig. 9 - Calibration results of the front wheel angle

The red warning zone was determined via the minimum turning radius of the agricultural vehicles and the size of the suspended agricultural vehicle. As the driving speed increased, the collected location points became sparser. This is not conductive to the accurate determination of out-of-bounds warnings due to the dependence of the out-of-bounds warning system on positioning data.

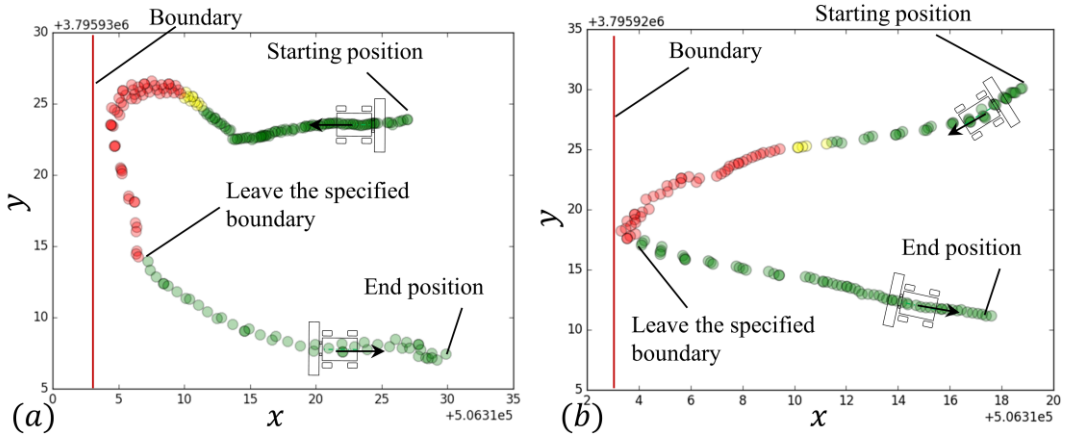

Fig. 10 - Agricultural vehicles driving at low speed for the (a) "U"-shaped route and (b) "V"-shaped route Red warning zone [0.00m, 6.74m], yellow warning zone (6.74m, 8.28m] and green zone (8.28m, + ∞)

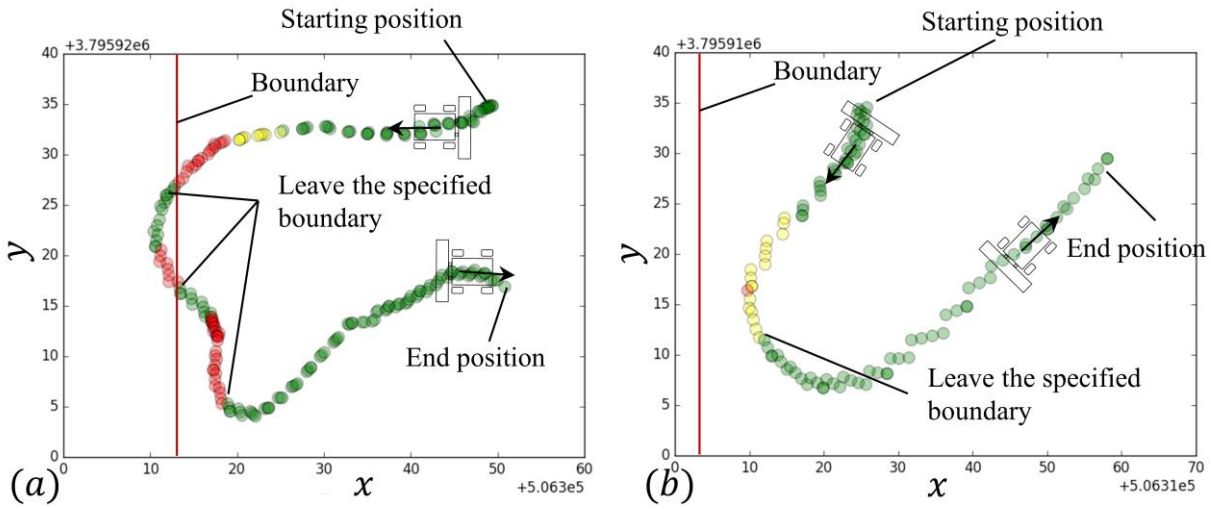

Fig. 11 - Agricultural vehicles driving at medium speed for the (a) "U"-shaped route and (b) "V"-shaped route Red warning zone [0.00m, 6.74m], yellow warning zone (6.74m, 12.20m] and green zone (12.20m, + ∞)

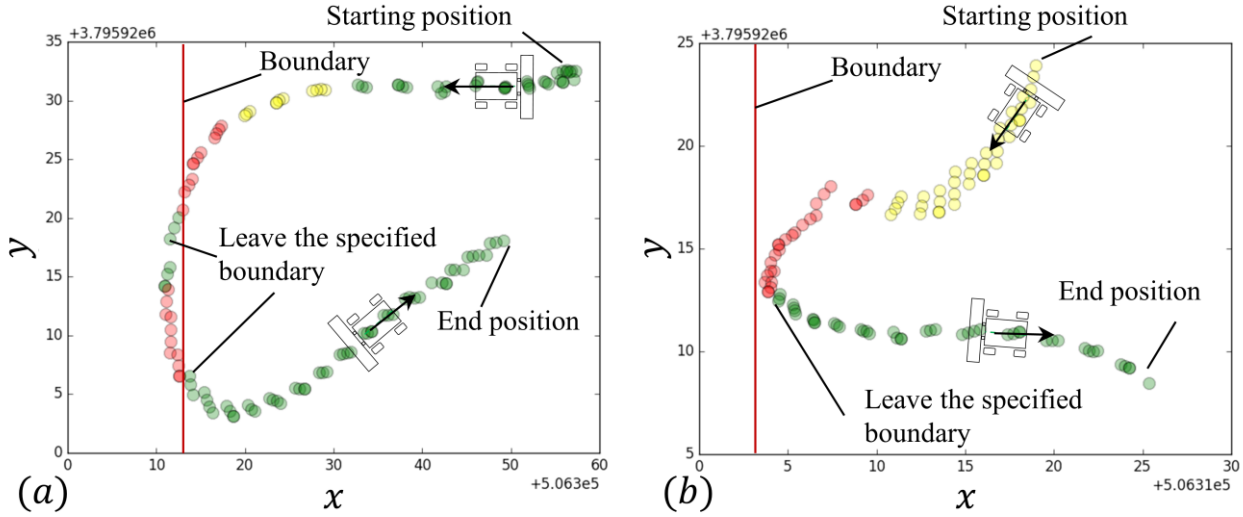

Fig. 12 - Agricultural vehicles driving at high speed for the (a) "U"-shaped route and (b) "V"-shaped route Red warning zone [0.00m, 6.74m], yellow warning zone (6.74m, 17.24m] and green zone (17.24m, + ∞)

Agricultural vehicles driving close to the boundary are located in the yellow and red warning zones. In contrast, for agricultural vehicles driving away from the boundary, the cross-boundary risk is limited and no warning is given. Thus, in the proposed warning model, driving away from the boundary is regarded as the safest situation. The results demonstrate that for agricultural vehicles driving close to the boundary, the system is able to output the correct warning. Figures 11 (a) and 12 (a) reveal that agricultural vehicles still use the previous crossing warning rules after crossing the boundary, which is not conducive to the field operation of agricultural vehicles. Therefore, it is necessary to judge whether the agricultural vehicle is inside the polygon boundary when we conduct the polygon boundary warning test.

CONCLUSIONS

(1) In the current study, we focused on the problem of cross-boundary risk for agricultural vehicles by comprehensively considering the driving speed, the rotation radius of farm tools and the movement trend of the vehicle. We proposed a warning framework for cross-boundary farming machinery based on the kinematics model of hanging farm tools.

(2) The proposed cross-boundary warning system can correctly determine the warning zone at different speeds and driving paths, demonstrating good applicability and reliability. For agricultural vehicles with a tendency to cross the boundary, the system will warn the operator, which improves the safety of agricultural vehicles in the field.

(3) The detection method of the agricultural vehicle cross-boundary warning system is simple, computationally inexpensive and has limited performance requirements. It can accurately determine whether the agricultural vehicle crosses the boundary in real time in order to prompt the operator in a timely manner, effectively improving the safety of agricultural vehicle operations. However, in the current study, only a single boundary was tested.

In order to further develop the proposed model, future research will test polygon boundaries to detect the effectiveness of cross-boundary warnings and equip emergency braking device on agricultural vehicles to avoid the operator neglecting the warning signal.

ACKNOWLEDGEMENT

The authors thank the editing team of EditorBar for improving the English language fluency of our paper. The work in this paper was supported by the National Key Research and Development Program (No. 2017YFD0700402) and the China Postdoctoral Science Foundation (No. 2017BSHEDZZ138).

REFERENCES

[1] Bonadies S., & Gadsden S A. (2019). An overview of autonomous crop row navigation strategies for unmanned ground vehicles. Engineering in Agriculture, *Environment and Food*, vol.12, pp.24-31.

[2] Cheng H, Yun L, Chen K, et al. (2017). A real-time electronic fence monitoring algorithm based on Baidu maps. *The 13th IEEE International Conference on Electronic Measurement & Instruments (ICEMI)*, Yangzhou / P.R.C.

[3] Figueiras J., GrønbæK J., Ceccarelli A. et al. (2012). GPS and Electronic Fence Data Fusion for Positioning within Railway Worksite Scenarios. *The IEEE 14th International Symposium on High-Assurance Systems Engineering*, Omaha / USA.

[4] Guo C., Zhao X., Zhang S. et al. (2019). Design of a cross-boundary warning system for soil preparation based on BDS. *INMATEH - Agricultural Engineering*, vol.58, pp.59-68.

[5] Hickman J.S., Guo F., Camden M.C. et al. (2015). Efficacy of roll stability control and lane departure warning systems using carrier-collected data. *Journal of Safety Research*, 52, 59-63.

[6] Hsu C., Chiu Y., Wu K. et al. (2019). Design and Implementation of Image Electronic Fence with 5G technology for Smart Farms. *The IEEE VTS Asia Pacific Wireless Communications Symposium (APWCS)*, Singapore.

[7] Hu J., Li J., & Nawaz S.A. (2018). The design of a reminder device for placing shared bikes neatly based on attitude sensors. *The IEEE International Conference on Advanced Manufacturing (ICAM)* Yunlin / Taiwan.

[8] Khorsandi F., Ayers P.D., & Fong E.J. (2019). Evaluation of Crush Protection Devices for agricultural All-Terrain Vehicles. *Biosystems Engineering*, vol.185, pp.161-173.

[9] Latorre-Biel J.I., Benito-Amurrio M., Perez-Ezcurdia A. et al. (2019). Characterisation of mechanical energy absorbers developed to complement of roll-over protection structures in agricultural vehicles. *Biosystems Engineering*, vol.188, pp.40-56.

[10] Li X., Peng X., Fang H. et al. (2020). Navigation Path Detection of Plant Protection Robot Based on RANSAC Algorithm（基于RANSAC算法的植保机器人导航路径检测）. *Transactions of the Chinese Society for Agricultural Machinery*, vol.51, pp.40-46.

[11] Monod M.O., Faure P., Moiroux L. et al. (2008). A virtual fence for animals management in rangelands. *The MELECON 2008 - The 14th IEEE Mediterranean Electrotechnical Conference*, Ajaccio/France.

[12] Mousazadeh H. (2013). A technical review on navigation systems of agricultural autonomous off-road vehicles. Journal of Terramechanics, vol.50, pp.211-232.

[13] Song Y., Liu Y., Liu L. et al. (2017). Extraction Method of Navigation Baseline of Corn Roots Based on Machine Vision（基于机器视觉的玉米根茎导航基准线提取方法）. *Transactions of the Chinese Society for Agricultural Machinery*, vol.48, pp.38-44.

[14] Tian Y. (2018). *Study on the Slip Warning System of Wheeled Vehicle*（轮式车辆陷车预警系统研究）. (Master's dissertation), Northwest A&F University, Yangling Shaanxi.

[15] Vidoni R., Bietresato M., Gasparetto A. et al. (2015). Evaluation and stability comparison of different vehicle configurations for robotic agricultural operations on side-slopes. *Biosystems Engineering*, vol.129, pp.197-211.

[16] Weichelt B., & Gorucu S. (2019). Supplemental surveillance: a review of 2015 and 2016 agricultural injury data from news reports on AgInjuryNews.org. Injury prevention, vol.25, pp.228-235.
[17] Xu Y., Jin S., Zhong C. et al. (2017). High accuracy virtual electronic fence management technique based on GNSS. *The 13th IEEE International Conference on Electronic Measurement & Instruments (ICEMI)*, Yangzhou/ P.R.C.
[18] Yang Z., Zheng L., Li M. et al. (2016). Design of Electronic Fence of UAV for Plant Protection Assignment Based on Ray Method（基于射线检测算法的无人机植保作业电子围栏设计）. *Transactions of the Chinese Society for Agricultural Machinery*, vol.47, pp.442-448.
[19] Zeng H., Lei J., Tao J. et al. (2020). Navigation line extraction method for combine harvester under low contrast conditions（低对比度条件下联合收割机导航线提取方法）. *Transactions of the Chinese Society of Agricultural Engineering*, vol.36, pp.18-25.
[20] Zhang M., Ji Y., Li S. et al. (2020). Research Progress of Agricultural Machinery Navigation Technology（农业机械导航技术研究进展）. *Transactions of the Chinese Society for Agricultural Machinery*, vol.51, pp.1-18.
[21] Zhao X. (2019). *Study on the Cross-boundary Warning System of Soil Preparation Based on BDS*（基于BDS的整地作业越界预警系统研究）. (Master's dissertation), Northwest A&F University, Yangling Shaanxi.
[22] Zhao T., Noboru N., Yang L. et al. (2016). Development of uncut crop edge detection system based on laser rangefinder for combine harvesters. *International Journal of Agricultural and Biological Engineering*, vol.9, pp.21-28.
[23] Zhao T., Chen J., & Mu J.Y. (2013). Boundary of crop detection using a laser scanner. *Advanced Materials Research*, vol.710, pp.542-545.
[24] Zhu B., Piao Q., Zhao J. et al. (2016). Integrated chassis control for vehicle rollover prevention with neural network time-to-rollover warning metrics. *Advances in Mechanical Engineering*, vol.8, pp.1-13.
[25] Zhu T., Zong C., Wu B. et al. (2011). Rollover warning system of heavy duty vehicle based on improved TTR algorithm（基于改进TTR算法的重型车辆侧翻预警系统）. *Journal of Mechanical Engineering*, vol.47, pp.88-94.

ANALYSIS OF THE FIELD EFFICIENCY OF SUGARCANE HARVESTERS / *ANÁLISIS DE LA EFICIENCIA DE CAMPO DE COSECHADORAS DE CAÑA DE AZÚCAR*

González-Cueto O.[1)], Castillo-Rodríguez J.A. [2)], Ávalos-Clavelo, J.L. [2)], López-Bravo E.[1)], Herrera-Suárez, M.[3)], Salcerio Salaberry[1)] [1]

[1)] Universidad Central "Marta Abreu" de las Villas, Faculty of Agricultural and Animal Sciences / Cuba;
[2)] Empresa Azucarera Villa Clara / Cuba;
[3)] Universidad Técnica de Manabí, Faculty of Mathematical, Physical and Chemical Sciences
Tel: 05342222875; E-mail: omar@uclv.edu.cu
DOI: https://doi.org/10.35633/inmateh-63-30

Keywords: *time efficiency, fuel efficiency, throughput capacity, furrow length*

ABSTRACT

Field efficiency is a main factor for obtaining high productivity of agricultural machinery. The aim of this paper was to determine the field efficiency of KTP 2M and CASE IH 8000 sugarcane harvester machines, working with different lengths of cutting fronts. The research was carried out in the Panchito Gómez Toro area of production, belonging to Sugar Enterprise, Villa Clara, during February and March 2020. The main movement times of the harvester inside the field was obtained by stop watch, as well as the fuel consumption during the works. The influence of the length of the cutting fronts on the turning time, time for completing the task and field efficiency were determined according to the sugarcane yield. The results show that lengths of cutting front less than 300 m, represent greater losses in time and higher rate of fuel consumption.Lengths of cutting fronts greater than 500 m, do not represent an increase in field efficiency.

RESUMEN

La eficiencia de campo es un factor principal para la obtención de alta productividad de maquinaria agrícola .El presente trabajo se realizó con el objetivo de determinar la eficiencia de campo de cosechadoras de caña de azúcar KTP 2M y CASE IH 8000 durante el trabajo en frentes de corte de diferentes longitudes. La investigación se llevó a cabo en áreas de producción de APA Panchito Gómez Toro de la Empresa Azucarera Villa Clara, durante los meses de febrero y marzo de 2020. Se obtuvieron mediante cronocartas los principales tiempos que componen el movimiento dentro de los campos de las cosechadoras; así como, el consumo de combustible durante la realización de los trabajos. Se determinó la influencia de la longitud de los frentes de corte en el tiempo de viraje, el tiempo para la realización de la tarea y la eficiencia de campo en función del rendimiento agrícola de la caña de azúcar. Los resultados del trabajo muestran que longitudes de frente de corte inferiores a 300 m representan mayores pérdidas de tiempo y mayor tasa de consumo de combustible. Longitudes de frentes de corte superiores a 500 m no representan incremento en la eficiencia de campo.

INTRODUCTION

In Cuba, the mechanized harvesting with harvester machines reaches 96% of the total sugarcane amount that goes to the factories for the production of sugar and other derivatives. The harvesters used are from different manufacturers and different models, such as the Cuban harvesters KTP 2M and other imported harvesters as the machines from CAMECO, AUSTOFF and the CASE IH series 7000, 8000 and 8800.

The economic technical index, that most widely characterizes the agricultural machinery performance is the direct operating cost per unit of time (*Jrobostov, 1977*). Among the factors that determine this index and determine the lower direct operating costs is the field capacity of agricultural machines. Field capacity is an index used to evaluate the performance of agricultural machinery (*Adamchuk et al., 2004*); it is also identified as the productivity of agricultural machinery. Hunt (1999), defines the field capacity as the work done by the machinery in the unit of time, it is expressed in surface such as m^2 or hectare per units of time. Theoretical field capacity *(TCC)* is the amount of work that a machine realizes by working without interruption, at its normal speed *(v)* and using its entire theoretical width *(a)*. It can be expressed by the following equation $Cct = v * a$.

[1] *González-Cueto O., Prof. Ph.D. Eng.; Castillo-Rodríguez J.A., Eng.; Ávalos-Clavelo, J.L., Eng.; López-Bravo E., Prof. Ph.D. Eng.; Herrera-Suárez, M., Prof. Ph.D. Eng.; Salcerio Salaberry, R.A.*

Several factors modify the ability of machines to perform at their theoretical field capacity. In soil preparation, the theoretical width of the implement is generally not reached. During the work, part of the implement overlaps previous pass, to avoid leaving spaces unworked, which makes the effective width of the implement less than the theoretical one. During operation with grain or fodder harvesters, even with experienced operators, they are seldom handled at the designed cutting width. During open row operation, the effective width is the same as the designed width, depending on the spacing of the current pass with respect to the previous one. The non-equidistant spacing of the furrows during sowing are later reflected in difficulties during the travel of the machines in the work of cultivation and harvesting (*Hunt, 1999*). Furthermore, the forward speed cannot be kept constant depending on the soil conditions.

The theoretical field capacity can be reached by a combine harvester over short distances, it is expressed in ha h^{-1} or also in Mg of product per hour (*Ortiz-Cañavate et al., 2012*). When the machine works at its designed width and travels at constant speed without interruption, it works at 100% of field capacity; interruptions in machine operations reduce the field capacity. These interruptions can be generated by turns at the end and beginning of the fields, unproductive stops waiting for transport, unloading and filling the hopper with seeds or fertilizers, etc. When the loss of field capacity due to insufficient width or speed of the machinery is taken into account, and also the time losses due to turns or other causes in the fields, the parameter is called effective field capacity (Cce).

The relation between theoretical field capacity and effective field capacity is called *field efficiency coefficient (e)* (****ASABE D497.7, 2011*). This term takes into account the working width, advance speed and time losses of the machine in the field. Travel to and from a field, major repairs, preventive maintenance, and daily service activities are not included in field time or field efficiency (*Topakci et al., 2010*). ****ASABE D497.5 (2006*) shows ranges of average and typical field efficiency for different implements, agricultural machines, and self-propelled harvesters. Field efficiency is calculated by the equation $e = (Cce/Cct) * 100$ and takes into account the time lost during operation, influenced by parameters such as: operator skills, machine operation mode, movement method and types of turns, size and shape of the fields, crop agricultural yield, and moisture and soil conditions.

For sugarcane harvesting machines the advance speed and the effective width are equal for effective and theoretical field capacity. This happen because the width is given by the distance between rows, which in the Cuban fields of sugarcane is mostly 1.6 m. Therefore, both capacities are calculated as a function of the operation times. On the other hand, the theoretical field capacity is determined by the theoretical time, necessary to realize all the work, if the theoretical field capacity could be reached. This, would be expressed as $e = (Te/(Te + Tp)) * 100,$ so this indicator coincides with the time efficiency that *Grisso et al.* (*2004)* defined as a ratio of the time a machine is effectively operating to the total time the machine is committed to the operation. The time when the operator is in the machine and not actually working the field is counted as lost time. *Topakci et al. (2010)* and *Carroll (2015)*, propose time efficiency as the effective time worked by the machine, between the total theoretical time worked.

The field capacity and field efficiency are essential indicators for evaluating the performance of agricultural machines and implements. Several researches have been carried out on this subject, such as those by *Grisso et al. (2013*) on fodder packing machines, *Carroll (2015*) on combined soybean harvester, *Baio (2012*), *Ma et al. (2018*), *Santos et al. (2018)* in sugarcane harvesters.

The evaluation of the productivity of agricultural machines in Cuba is carried out by the stop watch method. The times in which the production process is carried out, and the productivity indicators are calculated. Several researches have been carried out with this objective, highlighting those carried out by *Betancourt et al.* (2016), *Diego et al. (2015*), *González-Cueto et al. (2017*), *Ramos and Lora (2013)*. Specifically, in sugarcane harvesters, researches have been conducted by *Daquinta et al. (2014), De la Rosa et al. (2014), Martinez et al. (2020)*. However, no research has been carried out, to establish the influence of the field conditions and machine movement methods in field efficiency. In this sense, the present paper aims to determine the field efficiency of KTP 2M and CASE IH 8000 sugarcane harvesters, working on different lengths of cutting fronts.

MATERIALS AND METHODS

Data on the field was measured by timing the different operations of KTP 2M and CASE IH 8000 harvester machines at the Panchito Gómez Toro farm, in Villa Clara, Cuba. By this procedure were obtained the cutting time, turning time and fuel consumption per Mg of sugarcane.

The agricultural yields (*Ra*) for KTP 2M were established: 40; 50 and 60 Mg ha^{-1}; for CASE IH 8000 were: 50 70 and 90 Mg ha^{-1}. The advance speed of KTP 2M was 5, 4.6 and 4.1 km h^{-1} for each yield, and the advance speed of CASE IH 8000 was 5.1, 4.3 and 3.7 km h^{-1} respectively. The effective field capacity of each machine was established based on the daily cutting tasks (Tc), 100 Mg for KTP 2M and 400 Mg for CASE IH 8000. The lengths of cutting front were from 100 to 1000 m with intervals of 100 m.

The effective working time was determined by means of the equation.

$$Te = \frac{Lc}{v} \quad (1)$$

where:

Te - effective working time (h);

Lc - length to harvest for the task (km);

v – advance speed (km h^{-1}).

$$Lc = Tac\,(6250/1000) \quad (2)$$

Tac - total area to be harvested (ha).

$$Tac = \frac{Tc}{Ra} \quad (3)$$

Tc - cutting task (Mg)

Ra – crop yield (Mg ha^{-1})

The time lost in cutting task, due to turning time, was determined from the result of the measurements of turning time by means of the stopwatch method.

$$Tp = \frac{Lc * 1000}{L_{fc}} * Tv \quad (4)$$

where:

Tp - time lost in cutting task (h);

Tv – turning time (h);

L_{fc} - length of the cutting front (m)

The time necessary to carry out the cutting task is the sum of the effective working time and the time lost in the cutting task.

RESULTS

Time lost in the cutting task

In the paper, reference is made to length of cutting front, however, in many occasions this term is confused with the furrows' length. Length of cutting front refers to the longitude of one or more furrows located in the same direction in adjacent fields that are being cut one after other. As result of the stop watch it was obtained that turning time average of the KTP 2M was 0,026 h and of the CASE IH 8000 was 0.0173 h. The Figures 1 and 2 show the results of time lost in the cutting task, due to turning time, for both harvesters, working on three sugarcane yields and different lengths of the cutting front.

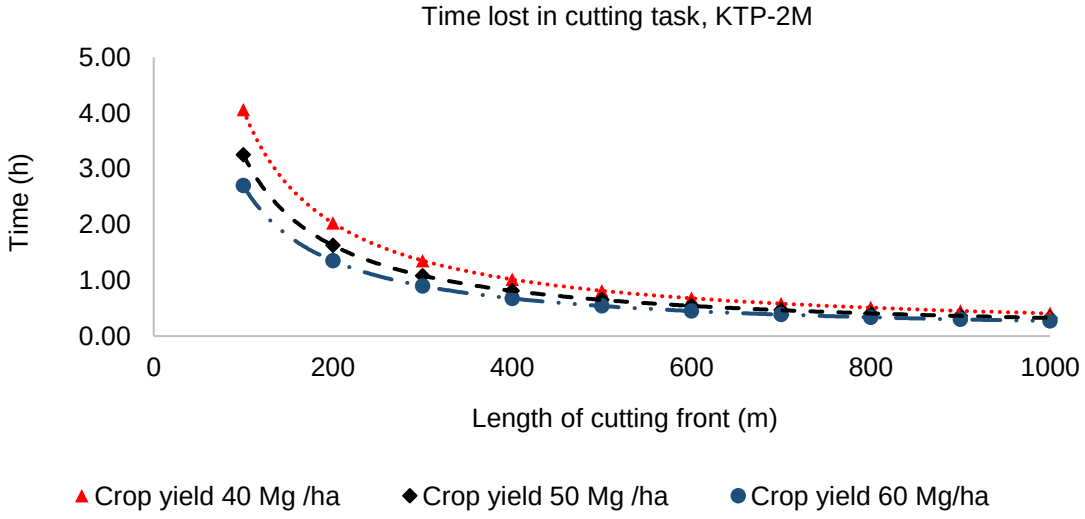

Fig. 1 - Time lost in cutting task for KTP 2M harvester, working on three sugarcane yields and different lengths of the cutting front

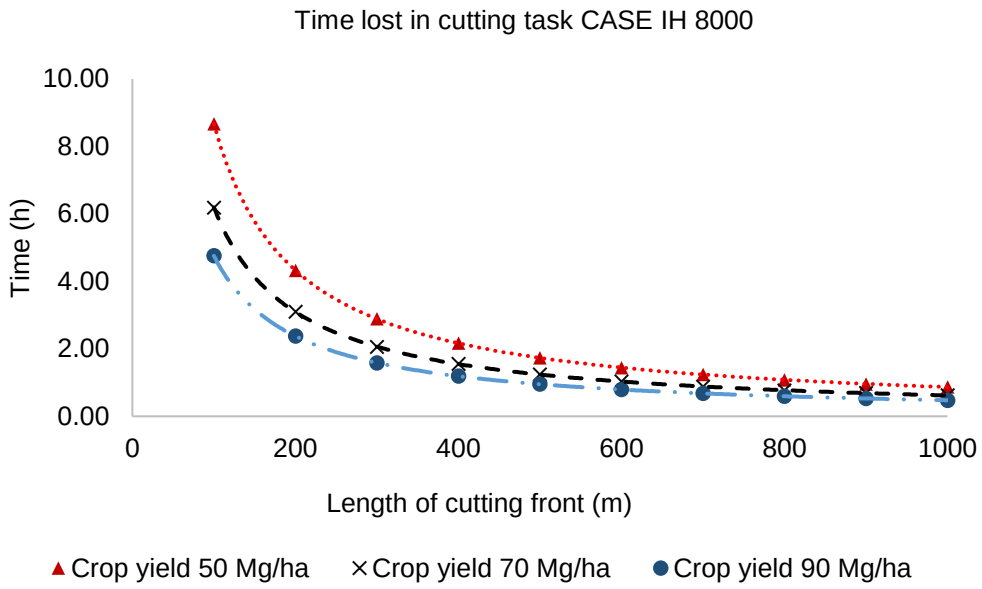

Fig. 2 - Time lost in cutting task for CASE IH 8000 harvester, working on three sugarcane yields and different lengths of the cutting front

As the Fig. 1 and 2 show, the time lost in cutting task decreases as increases the length of the cutting front independently of the agricultural yield. For small lengths of cutting fronts a significant increment of time lost in cutting task takes place. The equation of the curves of the tendency lines are of the potential type. The potential equation curves: $y = ax^{-n}$, describe the behaviour of the time lost in cutting task (y) to respect the length of cutting front (x) and agricultural yield (n). Table 1 shows the prediction equations obtained from the trend curves fits and the R^2 for time lost in cutting task in KTP 2M and CASE IH 8000 harvester machines.

Table 1

Prediction equations for time lost in cutting task for both harvester machines.

Crop yield Mg ha^{-1}	KTP 2M Equation	R^2	CASE IH 8000 Equation	R^2
40	$Y = 401.38x^{-0.998}$	1	-	
50	$Y = 325x^{-1}$	1	$Y = 867.96x^{-1}$	1
60	$Y = 269.75x^{-1}$	1	-	
70	-		$Y = 620.78x^{-1.001}$	1
90	-		$Y = 475.75x^{-1}$	1

The field dimension is one of the main factors that modify time lost due to turning time of the harvesters as shown in several researches (****SASA, 1998; Meyer, 1999; Ma et al., 2015*). The efficiency of harvesters must be taken into account for the right design of the fields during soil preparation before sugarcane plantation. The geometry of the field should offer as long as possible cutting fronts up to 500 m. As shown in Fig. 1 and 2, from 500 m the time lost during turning has an asymptotic behaviour up to 1000 m. Therefore, extremely long cutting fronts are not recommended because of the difficulty to change transport, increasing travelled distance and consequently fuel consumption.

The design of the harvester also affects the capacity to reduce time lost during turning. The harvester CASE IH 8000 has 2.96 m wheelbase, being more compact and shorter than the KTP 2M who has 3.5 m wheelbase, making the CASE IH 8000 more manoeuvrable. The turning radius of self-propelled machines depends on the wheelbase and the KTP 2M is 0.54 m higher than the CASE. Another factor that affects the manoeuvrability of the combines is the expertise of the operator (Meyer, 1999). Regarding this parameter, it should be noted that, due to the high level of automation, the training of operators of CASE machines is generally better.

The efficiency of the harvester also depends on the infield transport, because it needs to wait for the turn of the tractor with trailer or truck. As the infield transport is heavier, the trailer's wheelbase is greater, thus the turning radius is bigger and there is more time lost waiting for turning infield transport.

The preparation of the headlands to carry out the turns and the conformation of a turning strip are essential to reduce the time lost during the turn in the harvest.

The turning strip widths should be taken into account during field design, because it modifies the turning times. The study found that turning strips do not have adequate size, being a common factor in the fields of the researched area. De la Rosa *et al* (2014) found a similar result in areas of the farm Arquímedes Colina, although it is known that this situation is common in almost all fields, in Cuba.

Time for cutting task

Fig. 3 and 4 show the behaviour of the times for cutting task, this including time lost in cutting task due tuning and effective work times. The trends of the curve in the figure look similar to those of the time lost in cutting task, time for cutting increases when lengths of the cutting front are shorter. Cutting time decreases for cutting front between 400 and 500 m, after that it remains asymptotic. These results are independent of crop yield. As shown in Table 2, prediction equations from the trend of cutting time curves are potential too. The adjustments R^2 indicated that equations can be used with good results to make predictions of timing cutting task.

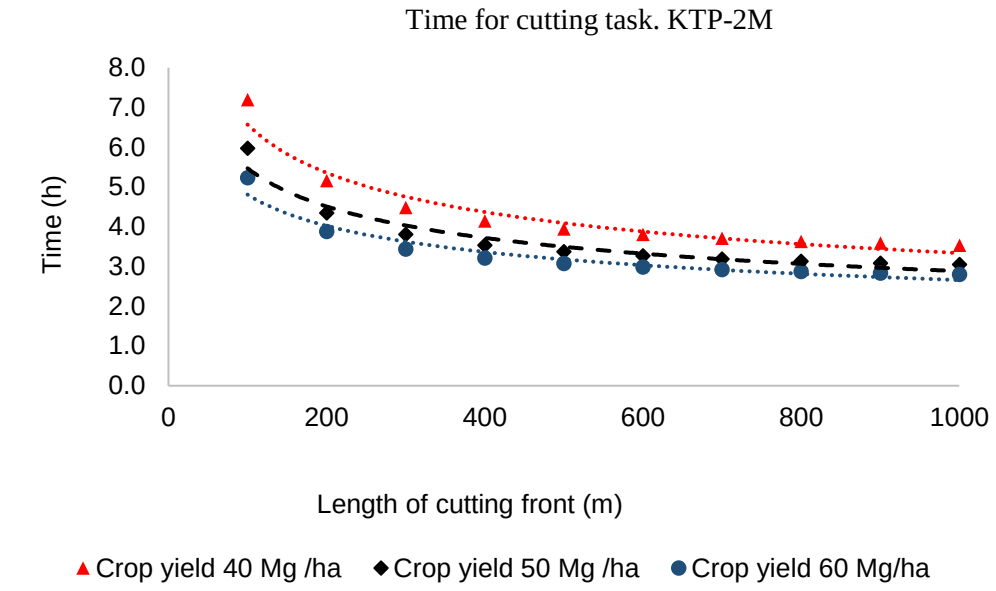

Fig. 3 - Times for cutting task for KTP 2M harvester, working on three sugarcane yields and different lengths of the cutting front.

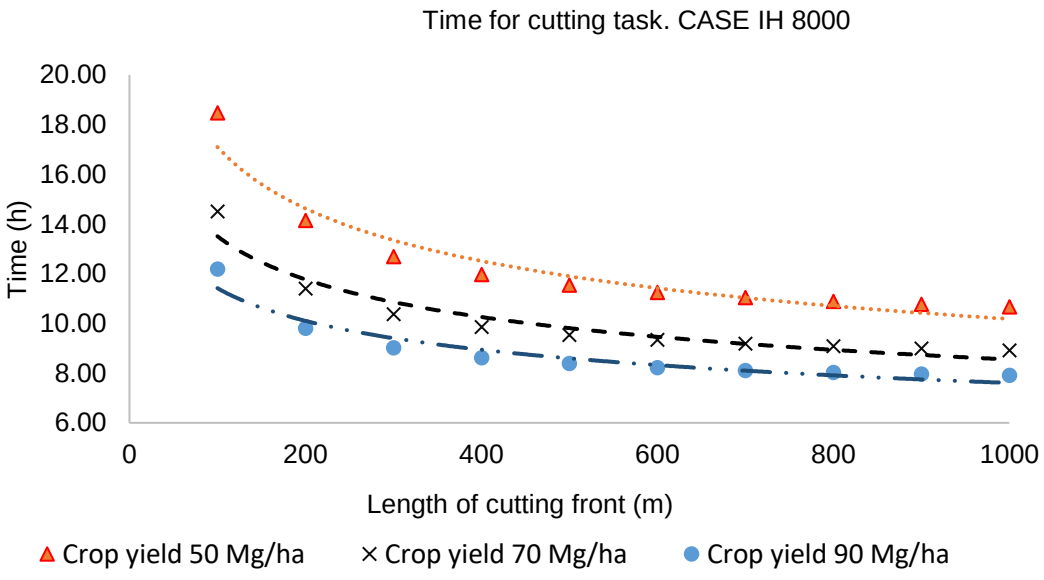

Fig. 4 - Times for cutting task for CASE IH 8000 harvester, working on three sugarcane yields and different lengths of the cutting front

Table 2

Prediction equations for time cutting task for both harvester machines.

Crop yield Mg ha^{-1}	KTP 2M Equation	R^2	CASE IH 8000 Equation	R^2
40	$Y = 25.439x^{-0.294}$	R^2 = 0,9476	-	
50	$Y = 19.695x^{-0.278}$	R^2 = 0,9457	$Y = 48.235x^{-0.225}$	R^2 = 0,9374
60	$Y = 15.727x^{-0.257}$	R^2 = 0,9425	-	
70	-		$Y = 33.72x^{-0.199}$	R^2 = 0,9331
90	-		$Y = 25.752x^{-0.177}$	R^2 = 0,9294

Field efficiency

As shown in Figure 5, for KTP 2M, at cutting lengths of 300 m, for the three yields, the harvester has a field efficiencies of approximately 70% or less. Only the time losses per turning time will be 30%, when adding the other time losses that always occur in the field, the efficiency will be less than 70%. In fields with cutting fronts of 200 m or less, the efficiency is below 60%. The behaviour is the same for CASE IH 8000 (Figure 6) at cutting lengths less than 200 m.

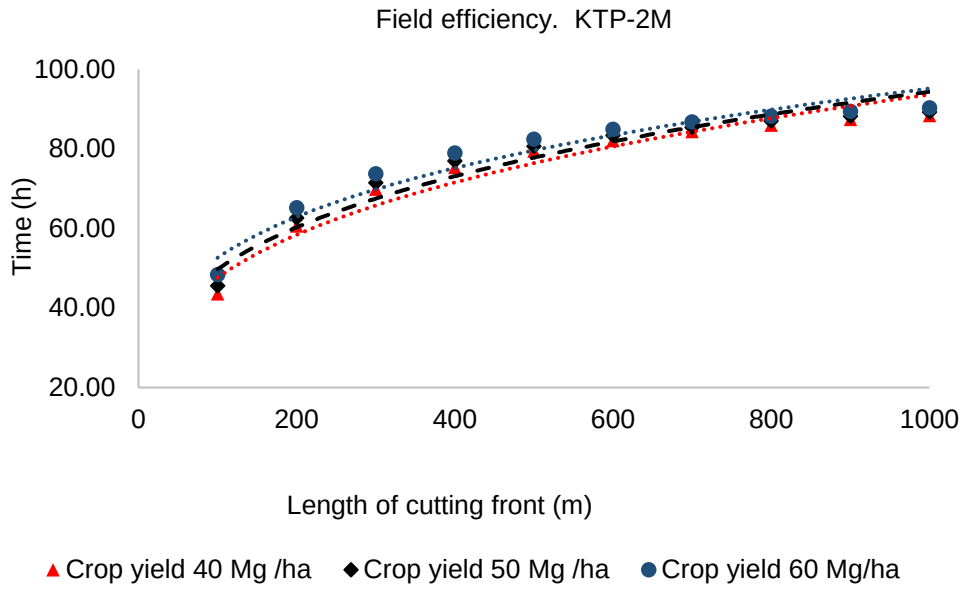

Fig. 5 - Field efficiency for KTP 2M harvester, working on three sugarcane yields and different lengths of the cutting front

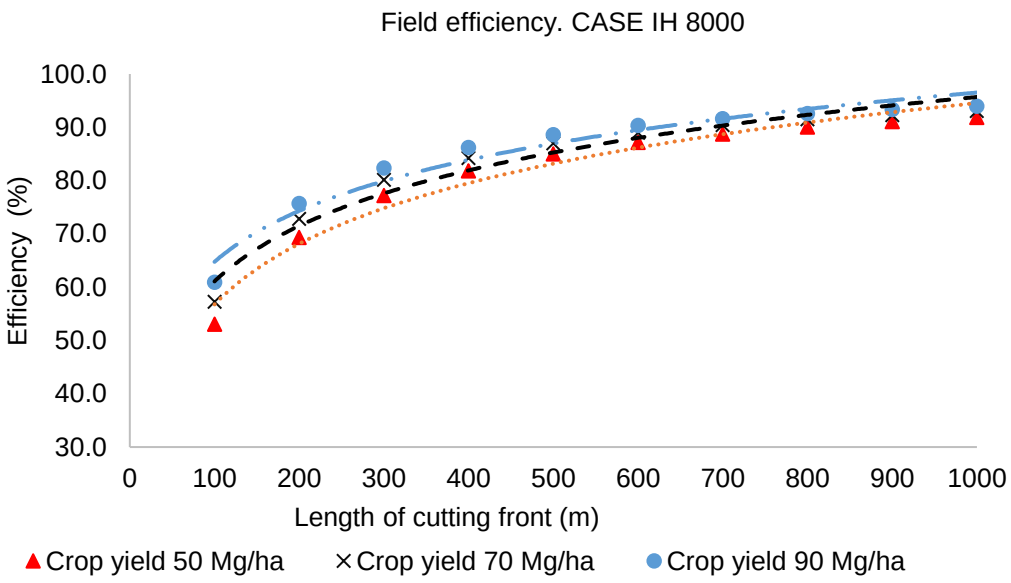

Fig. 6 - Field efficiency for CASE IH 8000 harvester, working on three sugarcane yields and different lengths of the cutting front

For both harvesters, the increases in crop yield modify field efficiency a little; this result could be explained by the narrow range of agricultural yield researched. Although, the greatest difference is found in cutting front lengths up to 400 m, in longer lengths the difference in field efficiency decreases. The length of cutting front increases field efficiency more than agricultural yield. The logarithmic prediction equations were obtained from the trend curves (Table 3), also R^2 of each curve is bigger than 96%, showing excellent fit between measurements and prediction. The typical values of field efficiency in harvesting machines have a range between 65 and 80% (*ASABE D497.5, 2006*). In a review by *Abd-El Mawla and Hemeida (2015)* of sugarcane harvesters, the KTP-1 reported field efficiency of 80%; *Ma et al. (2015)* in harvester John Deere 3522 obtained field efficiencies of 86.2% in energy cane, 80.6% harvesting banagrass, and 59.6% harvesting sugar cane. *Baio (2012)* determined field efficiencies of 80% in a CASE 7700. The authors coincide on the relation of field efficiency with factors such as: manoeuvrability of the machines, skills of the operators and turn time at the headlands. Other factors are the organization of the machines in the field, minimum distance travelled during the turns, the design of the fields, length of the cutting front, irregularly in shape of the fields and low crop yield.

Table 3

Equation of prediction curves for field efficiency

Crop yield Mg ha^{-1}	KTP 2M Equation	R^2	CASE IH 8000 Equation	R^2
40	$Y = 19.279\ln(x) - 42.19$	0,9824	-	
50	$Y = 18.725\ln(x) - 37.431$	0,9797	$Y = 16.41\ln(x) - 18.806$	0,9687
60	$Y = 17.873\ln(x) - 30.458$	0,9757	-	
70	-		$Y = 15.029\ln(x) - 8.1295$	0,9624
90	-		$Y = 13.794\ln(x) + 1.228$	0,9566

CONCLUSIONS

The time lost in cutting task, for harvesters under investigation decreases as increases yield and the length of cutting front up to 500 m, from this length the time lost during turning has an asymptotic behaviour. Similar behaviour was found in time for cutting task; it increases when lengths of the cutting front are shorter. The time for cutting task is also affected by the organization of the harvest and shape of the field. For both harvesters increases in agricultural yield have low impact on field efficiency. On the other hand, the length of the cutting front increases field efficiency more than agricultural yield. The length of the cutting front in a field of sugarcane is a fundamental parameter to achieve high field efficiency of the harvesters. Lengths of cutting front less than 500 m increase time losses. At cutting lengths of 300 m or less, the combines showed a field efficiency less than 70%, reaching 50% in fields of 100 m, which shows the importance of shaping fields with lengths of up to 500 m. Prediction equations were obtained from the trend curves with R^2 greater than 96%, showing excellent fit between measurements and prediction.

REFERENCES

[1] Abd-El Mawla, H. A., Hemeida, B. E. (2015). "Sugarcane mechanical harvesting-evaluation of local aplications", J.Soil Sci. And Agric. Eng., 6 (1): 129-141. https://doi.org/10.21608/jssae.2015.41814.

[2] Adamchuk, V. I., Grisso, R., Kocher, M. F. (2004). Machinery performance assessment based on records of geographic position. *Proceedings of ASAE / CSAE Annual International Meeting*.

[3] Baio, F. H. R. (2012). "Evaluation of an auto-guidance system operating on a sugar cane harvester", *Precision Agriculture*, 13: 141-147. https://doi.org/10.1007/s11119-011-9241-6

[4] Betancourt, Y., Rodríguez, M., Churches C. E., Gómez, J. R., García, I. (2016). "Indexes of three primary tillage implements in soil with mound surface and covering of vegetables residues", *Revista Ciencias Técnicas Agropecuarias*, 25(1): 17-22.

[5] Carroll, J. (2015). *Using Precision Agriculture Field Data to Evaluate Combine Harvesting Efficiency,* Agricultural Education, Communications and Technology Undergraduate Honours Theses. 4.

[6] Daquinta, A., Dominguez, J., Pérez, C., Fernández, M. (2014). "Operating technical indicators for the sugar cane harvesting machines CASE-IH 7000 & 8000 in Ciego de Avila province", *Revista Ingeniería Agrícola*, 4(3): 3-8.

[7] De la Rosa, A. A, Ventura, L., Calzada, I., Suárez, O. (2014). "Valuation of mechanized harvests of the sugar cane process, by means of the harvesters, CASE IH (A 7000), in the Sugar Mill “Arquímedes Colina Antunez", *Revista Ingeniería Agrícola*, 4(4): 30-34.

[8] Diego, F., Herrera, M., González, O. García de la Figal, A. E. (2015) "Performance assessment of two animal traction plough in Oaxaca milpa environment", *Revista Ingeniería Agrícola*, 5(1): 46-51.

[9] González-Cueto, O., Machado-Trujilllo, N., González-Álvarez, J. A., Acevedo-Pérez, M., Acevedo-Darias, M., Herrera-Suárez, M. (2017). "Technological and economical evaluation of the tractor XTZ-150K-09 during soil tillage", *Revista Ingeniería Agrícola*, 7(1): 49-54.

[10] Grisso, R. D., Kocher, M. F., Adamchuk, V. I., Jasa, P. J., Schroeder, M. A. (2004). "Field efficiency determination using traffic pattern indices", *Applied Engineering in Agriculture*, 20(5): 563−572.

[11] Grisso, R. D., Webb, E. G., Cundiff, J. S., Sokhansanj, S. (2013). Parametric Study of Machinery Management Relationships on Forage Equipment. *Proceedings of ASABE Annual International Meeting*.

[12] Hunt, D. R. (1999). "2.5. Cost Analysis", in *CIGR Handbook of Agricultural Engineering Volume III. Plant Production Engineering*. American Society of Agricultural Engineers, St. Joseph.

[13] Jrobostov, S. N. (1977). Operation of the fleet of tractors and machines (Explotación del parque de tractores y máquinas). MIR, Moscú.

[14] Ma, S., Karkee, M., Scharf, P. A., Zhang, Q. (2018). “Adaptability of chopper harvester in harvesting sugarcane, energy cane, and banagrass”. Transactions of the ASABE, 61(1), 27-35. https://doi.org/10.13031/trans.12038

[15] Martínez, R., Acevedo, M., Yanes, M. R., González-Cueto, O. (2020). “Operation Indicators of the CASE IH Austoft 8800 sugar cane harvest”. *Revista Ingeniería Agrícola,* 10**,** 28-32.

[16] Meyer, E. (1999). Some measurements of mechanical sugarcane harvester performance. *Proceedings of South African Sugar Technology Association*.

[17] Ortiz-Cañavate, J., Barreiro, P., Diezma, B., Garcia, F. J., Gil, J., Moya, A., Ortiz, C., Ruiz, M., Ruiz, L., Valero, C. (2012). *Agricultural machines and their application* (Las máquinas agrícolas y su aplicación). Mundi-Prensa.

[18] Ramos, R., Lora, D. (2013)." Determination of operating and economic parameters in cutting different forage harvesters", *Revista Ingeniería Agrícola*, 3(2): 31-38.

[19] Santos, N. B., Teixeira, M. M., Fernandes, H. C., Gadanha Júnior, C. D. (2018). “Analysis of times and efficiencies of the mechanized harvest of sugarcane (Saccharum spp.)”, Nucleus, 15(1), 181-188. https://doi.org/10.3738/1982.2278.2794

[20] Topakci, M., Unal, I., Canakci, M., Yigit, M., Karayel, D. (2010). "Improvement of field efficiency measurement system based on GPS for precision agriculture applications", *Journal of Food, Agriculture & Environment*, 8(3&4): 288-292.

[21] ***ASABE D497.5. (2006). *Agricultural Machinery Management Data,* American Society of Agricultural and Biological Engineers, St. Joseph. Michigan.

[22] ***ASABE D497.7. (2011). *Agricultural machinery management data.* American Society of Agricultural and Biological Engineers, St. Joseph. Michigan.

[23] ***SASA. (1998). Factors to consider when implementing a mechanised cane harvesting system, Information sheet, South African Sugar Association, Durban, SA.

DYNAMICS OF SEEDLING PLANTING MACHINE EQUIPPED WITH VERTICAL DISTRIBUTOR AND ARTICULATED BUCKETS PLANTING UNIT

/

DINAMICA MAŞINII DE PLANTAT RĂSADURI ECHIPATĂ CU APARAT DE PLANTAT CU DISTRIBUITOR VERTICAL ŞI CUPE ARTICULATE

Mitrache P.M.[1)], Bularda M.[*2)], Ciuperca R.[3)], Saracin I.[1)]
[1)] University of Craiova / Romania; [2)]Univ. Dunărea de Jos Galaţi / Romania;
[3)]National Institute of Research Development for Machines and Installations Designed to Agriculture and Food Industry – INMA Bucharest/ Romania
E-mail: marcelbularda@yahoo.com
DOI: https://doi.org/10.35633/inmateh-63-31

Keywords: *dynamic, bucket planting, efficiency*

ABSTRACT

In this work we make a comparative analysis of the dynamics for two variants of seedling planting machines equipped with distributors and articulated buckets respectively: with the seedlings being placed in the furrow opened by a coulter; with the seedling being planted directly into the ground. The dynamics of the seedling planting machine equipped with vertical distributors and articulated buckets is seen from the perspective of the working process involving the placement of the seedling in the ground, its release, its covering with earth and its additional compaction. In principle, furrow opening is performed by a coulter and the vertical distributor with articulated buckets places and releases the seedling in the furrow, in the first variant, and in the second one, the seedling is inserted and released directly into the ground. In the paper are written the mathematical relations describing the dynamics of the seedling planting machine, in the two variants, and we perform their testing, make recordings, interpret the results, reach conclusions and make recommendations on the optimum variant. The agro-technical parameters and tensile strength of the planting machine are analysed in the two functional variants. The experiments were performed under the same working conditions for both variants analysed.

REZUMAT

În lucrarea de faţă s-a efectuat o analiză comparativă a dinamicii pentru două variante de mașini de plantat răsaduri echipate cu distribuitoare și cupe articulate respectiv: cu plasarea răsadului în rigola deschisă de un brăzdar; cu plasarea răsadului direct în sol. Dinamica mașinii de planta răsaduri echipată cu distribuitoare verticale si cupe articulate, este privită din perspectiva procesului de lucru care presupune plasarea răsadului in sol, eliberarea acestuia, acoperirea cu pământ si tasarea suplimentară a acestuia. In principiu, deschiderea rigolei este realizat a de către un brăzdar iar distribuitorul vertical cu cupe articulate plasează și eliberează răsadul în rigolă, în prima variantă, iar în varianta a doua, răsadul este introdus și eliberat direct in sol. În lucrare s-au scris relațiile matematice ce descriu dinamica mașinii de plantat răsaduri, in cele două variante, testarea acestora, efectuarea înregistrărilor, interpretarea rezultatelor, concluzii și recomandări privind varianta optimă. S-au analizat parametrii agrotehnici și rezistența la tracțiune realizați de mașina de plantat răsaduri in cele două variante funcționale. Experimentările s-au efectuat în aceleași condiții de lucru pentru ambele variante analizate.

INTRODUCTION

The advantages of seedling planting technology produced in nutrient pots led to its adoption by more and more vegetable growers, sufficient motivation for manufacturers of technical equipment for planting seedlings to develop and make such types of equipment in more varied dimensions and technical solutions.

On the basis of studies carried out by various authors (*Mitrache et al., 2020; Ciuperca et al., 2012, Poenaru, 2014; Voicu, 2014*), which analysed most of the types of equipment for planting seedlings produced, in which the technical solutions, advantages and disadvantages of each were presented, it was concluded that planting equipment equipped with disk planter and articulated buckets, is the simplest from a constructive point of view and achieves the working parameters, specific to the seedling planting work, in accordance with the agro-technical requirements.

This type of equipment has been made by many companies, more or less famous, which have adopted solutions from the simplest and with low working capacity, intended for small producers, to medium and large capacity types, semi-automatic and culminating with high capacity machines, whose working process is automated and electronic.

In an interesting study *(Ciuperca et al., 2012; Muraru-Ionel, 2009)* two of the most used types of vegetable seedling planting machines were compared, respectively: with section equipped with rotary bucket distributor and with section equipped with feeding chain with clamps and flexible discs for planting. The study unequivocally concluded the advantages of articulated bucket equipment.

A planting machine equipped with a relatively cheap planting device with discs and articulated buckets, designed especially for small areas, which is now on the market, is the Checchi & Magli planting machine - Wolf model (*www.checchiemagli.com/en/transplanting-machines.).* This machine model can be equipped with one or two planting sections. There is also the Wolf Compact model in which the number of planting sections can be increased to 6, and the distance between rows can be reduced to 30 cm.

As there are several planting machine manufacturers on the market, there is also a wide variety of planting machines that operate based on the planting system, with articulated bucket distributor, to which small aesthetic or functional changes have been made *(https://www.duijndam-machines.com/en/machines/2318/hortech-over-1-row-planting-machine/#; https://autoline.ro/-4-rijige-plantmachine-Duijndam-Machines--17090611134281090900)*.

A semi-automatic planting machine, for planting in two rows, equipped with disc and articulated buckets was made at the National Institute of Research Development for Machines and Installations Designed to Agriculture and Food Industry - INMA Bucharest and tested with very good results in Romania, thus demonstrating the viability of these types of equipment.

Many authors have done research over time to continuously improve the working process of seedling planting equipment, both in terms of kinematics and dynamics, as well as working capacity or process control.

An automatic machine for planting potted tomato seedlings was designed *(Xin et al., 2018);* this machine is composed of a horizontal and vertical seedling supply mechanism, a planting part featured with an eccentric disk, parallelogram and a control system. The control system included position sensors, stepper motor, variable-frequency motor and program controller. The result demonstrated that the machine was feasible to transplant the potted tomato seedlings efficiently.

Research has also been carried out to solve functional synchronization problems when the seedling stem describes a circular arc in the area where it falls into the furrow. This is done by a special rotating mechanism (*Nakanishi et al., 2007).*

Given the high intensity of current work on planting seedlings with low efficiency, a machine was designed based on a motion controller. Tests have shown that it can perform the planting process automatically and can improve efficiency and reduce the cost of the process *(Zhao and Liu, 2015).*

Besides the realization of the agro - technical working parameters, specific to the planting operation of the vegetable seedlings, of great importance are also the qualitative working indices *(Popescu V., and Popescu A., 2006; SR 13215:1994).*

MATERIALS AND METHODS

To identify and quantify the energy indices, it is necessary to know the dynamics of this equipment in order to adopt the optimal constructive and functional solutions.

From this perspective, in order to approach in terms of work dynamics, a planting machine with two-row planting, was used, equipped with a vertical distributor and articulated buckets, made at INMA Bucharest in 2018, in two working variants, namely:

- with a planting device which places the seedling in a furrow made by a coulter, followed by the covering of the nutritious bale with earth, by two paddles and the additional fixing by means of two compaction wheels, called **Variant I**;

- with a planting machine which places the seedling directly in the ground followed by an additional fixing of it by means of two compaction wheels, called **Variant II**.

Planter with vertical distributor with buckets, Variant I, fig. 1 - consists mainly of an assembled frame (1) in the shape of a deformable parallelogram, a rotary distributor with buckets (2) and a coulter for furrow opening (3).

The working depth is adjusted by means of a screw mechanism (4) which ensures the adjustment of the position of the ground copying wheel (6), mounted articulated on the frame of the section, with respect to the bottom of the coulter. Keeping the working depth constant is achieved by means of a tension spring (5) mounted on the deformable parallelogram.

The opening of the buckets, in order to place the seedling in the furrow, is made by means of a mechanism with adjustable cam. The transmission is a kinematic mechanism consisting of two chain transmissions that ensure the transmission of movement from the drive wheel axle to the axle of the rotary distributor with buckets.

The dynamics of the planting machine is seen from the perspective of the work process which involves the performance of two main operations, namely the opening of the furrow by the coulter and the effective planting of the seedling by the bucket planter, acted by the drive wheel. These two operations generate the tensile strength of the planting machine.

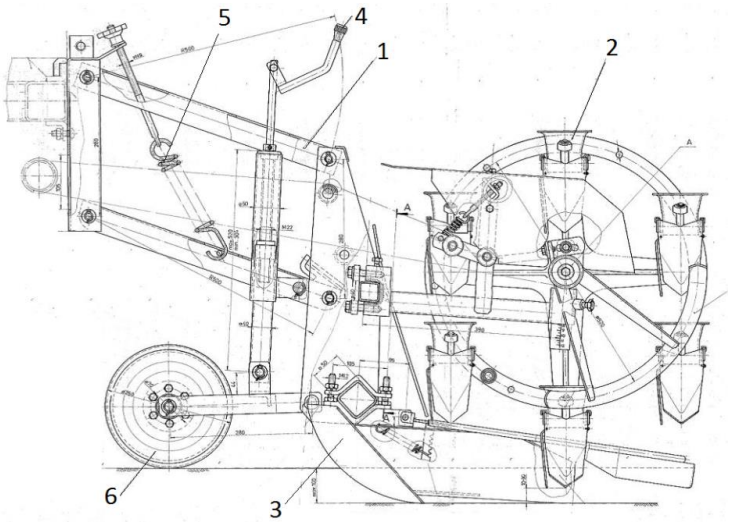

Fig. 1 - Planter with vertical distributor and articulated buckets equipped with coulter - Variant I

a) Dynamics of furrow opening

The opening of the furrow, by the coulter, involves cutting the soil vertically at a set depth and width, deforming and moving the soil cut horizontally in order to make the furrow.

Along with the deformation of the soil, a slight upward movement is made, at a volume equal to the difference between the volume of the furrow and the deformed soil.

The tensile strength R_{tr} at the opening of the furrow is determined by the relation (1):

$$R_{tr} = R_r + R_{td} + R_f \quad (1)$$

where:

R_r - resistance to the own movement of the machine at work [daN];

R_t - resistance to cutting and soil deformation [daN];

R_f –resistance caused by the friction between coulter and the soil [daN].

Replacing in relation (1) the terms with their expressions, relations (2) result:

$$\begin{aligned} R_r &= f \cdot G_b \\ R_{td} &= k_0 \cdot a \cdot b \\ R_f &= \mu \cdot G_b \end{aligned} \quad (2)$$

where:

f - rolling resistance coefficient;

G_{mb} - the weight of the planting machine, less weight taken over by the coulter [daN];

k_0 - specific resistance of the soil to cutting and deformation [daN/cm^2];

a - working depth of the coulter [cm];

b - working width of the coulter [cm];

μ - the coefficient of friction between the coulter and the soil;

G_b - weight taken by the coulter [daN].

The relation (1) becomes (3):

$$R_{tr} = f \cdot G_b + k_0 \cdot a \cdot b + \mu \cdot G_b \quad (3)$$

In the working process of the planting equipment, the parts, in the form of paddles, for covering the nutrient bale with soil, which offer an additional resistance to the movement of the equipment, R_{ac}, according to the relation (4), also intervene.

$$R_{ac} = k_{ac} \cdot a_a \cdot b_a \quad (4)$$

in which:

R_{ac} - the result of elementary resistance to covering the nutrient bale with soil [daN];

k_{ac} - specific resistance of the soil to the lateral displacement of the paddles left-right [daN/cm^2];

a - working depth of the paddle [cm];

b- working width of the paddle [cm].

b. Planter drive wheel dynamics

The moment of rolling resistance acts on all the drive, the torque transmitted to the active parts, respectively the bucket disc, this moment being transmitted by means of two chain transmissions, fig. 2.

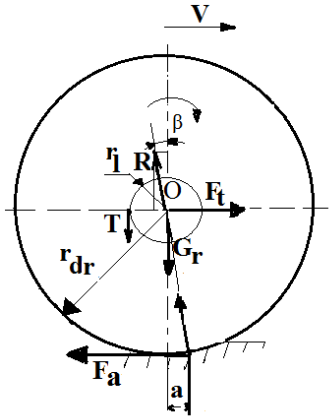

Fig. 2 - Drive wheel dynamics

The moment of friction in the wheel bearings has a negligible value and the moment of inertia of the wheel is zero, considering the movement with constant speed.

Under these conditions, the equilibrium equations are according to the relations (5):

$$\begin{gathered} F_t - R \cdot sin\,\beta - F_a = 0 \\ G_r - R \cdot cos\beta = 0 \\ F_a \cdot r_{dr} - R \cdot cos\beta \cdot r_{dr} - T \cdot r_l = 0 \end{gathered} \quad (5)$$

where:

F_t- tangential traction force at the drive wheel [daN];

R - the result of the soil reactions in the contact surface [daN];

F_a - the adhesion force of the drive wheel on the soil [daN];

T - tangential force developed in the transmission chain [daN];

r_{dr} - dynamic radius of the drive wheel [m];

r_l- splitting radius of the chain wheel [m].

The adhesion force of the drive wheel and the rolling resistance force are considered as shown in relation (6).

$$F_a = f_a \cdot G_r$$

$$F_f = R \cdot sin\,\beta = \frac{a}{r_{dr}} \cdot G_r = f \cdot G_r \quad (6)$$

where:

f_a - adhesion coefficient;

f- rolling resistance coefficient;

G_r - the weight of the machine taken over by the drive wheel [daN].

By replacing in the relation (6) the forces F_a and F_f with their expressions, the relations (7) result.

$$\begin{gathered} F_t - f \cdot G_r - f_a \cdot G_r = 0 \\ G_r - R \cdot cos\beta = 0 \\ f_a \cdot G_r \cdot r_{dr} - R \cdot cos\beta - T \cdot r_l = 0 \end{gathered} \quad (7)$$

For normal, non-slip operation, the traction force must satisfy the relation (8):

$$F_t \geq f \cdot G_r + f_a \cdot G_r \quad (8)$$

On the other hand, the moment generated by the force of adhesion to the drive wheel must overcome the resistance of the rotating moment M_{rd} of the bucket distributor, having its own weight G_d according to relation (9) and the force necessary to open the bucket F_{dc} which is equal to the force of the two traction springs arranged on it.

$$\begin{gathered} M_{rd} = f_a \cdot G_r \cdot r_{dr} = \frac{G_d}{g} \cdot \frac{r_{cd}^2}{2} \\ F_{dc} = k_a \cdot f_a \end{gathered} \quad (9)$$

where:

G_d - the weight of the bucket disc [daN];

r_{cd} - radius of the centre of gravity of the bucket disc [m];

k_a - stiffness of the traction spring of the bucket [daN/cm^2];

f_a - the working arrow of the bucket spring [m].

Thus, the relation (8) becomes (10).

$$F_t \geq f \cdot G_r + \frac{\frac{G_d}{g} \frac{r_{cd}^2}{2}}{r_{dr}} \quad (10)$$

In conclusion, for the Variant I of planting, the total traction force, F_{tI} necessary for the operation of the planting machine with the placement of the seedling in the furrow, is according to the relation (11).

$$F_{tI} = f \cdot G_{m_b} + k_0 \cdot a \cdot b + \mu \cdot G_b + k_{ac} \cdot a_a \cdot b_a + \frac{\frac{G_d}{g} \frac{r_{cd}^2}{2}}{r_{dr}} + k_a \cdot f_a \quad (11)$$

Planter with vertical distributor with buckets Variant II - for variant II, from a constructive and functional point of view, the planting machine, according to fig. 1, is no longer equipped with a coulter for opening the furrow and the covering paddles, fig. 1 item 3.

Considering those mentioned above, in the case of planting variant II, the resistance of the coulter at the opening of the furrow and the resistance to covering the seedling with soil no longer appear, but the resistance to the penetration of the bucket into the soil appears. Also, the total weight of the machine intervenes when calculating the resistance when moving the car. The other resistance are the same as for variant I.

The relations written for variant I are valid for the common resistances of the two variants, when moving the machine under operation.

Dynamics of bucket penetration into the soil, Variant II

The resistance to the penetration of the bucket into the soil and to the opening of the bucket for releasing the seedling, in the case of Variant II, in which we have the situation of planting the seedling directly in the soil and not in the furrow, is according to relation (12).

$$R_{pc} = k_0 \cdot a_c \cdot b_c \quad (12)$$

where:

R_{pc} - resistance to penetration of the bucket into the soil [daN];

k_0 - soil resistance to cutting and deformation [daN/cm^2];

a_c - the depth of penetration of the bucket into the soil [cm];

b_c - working width of the bucket [cm].

Taking into account those mentioned, the total traction force F_{tII} necessary for the operation of the planting machine with the placement of the seedling directly in the soil, Variant II, is according to relation (13).

$$F_{tII} = f \cdot G_t + k_0 \cdot a_c \cdot b_c + \frac{\frac{G_d \cdot r_{cd}^2}{g}}{r_{dr}} + k_a \cdot f_a \quad (13)$$

where: G_t - the total weight of the planting machine [daN].

The experimental research was carried out with the planting equipment in the two variants in aggregate with a 45 HP agricultural tractor, New Holland TCE 50. To perform the measurements for the traction force, strain gauges were mounted on the frame and on the frame of the equipment coulter.

To perform the experiments, inductive displacement system, MGC plus data acquisition - HBM (Hottinger-Baldwin-Messtechnik), Catman DAQ data acquisition software, data processing software nCode were used. Images during the experiments are shown in fig. 3.

Fig. 3 - Aspects during the experiments of the aggregate New Holland TCE50 tractor + MPA planting machine

RESULTS AND DISCUSSIONS

The experiments were carried out at planting tomato and pepper seedlings for working speeds ranging from 1.46 to 1.61 km/h, for working depth of a=70 mm and a=100 mm, in the two variants.

The traction forces calculated according to the relations (11) and (13) are:

- Variant 1: For a = 70mm, F_{t1} = 171.8 daN and for a = 100 mm, F_{t1} = 182.8 daN;
- Variant 2: For a = 70mm, F_{t2}= 135.4 daN and to a = 100 mm, F_{t2} = 155.5 daN.

After the experiments were carried out, the traction forces were obtained when moving the machine tested under operation, the comparative diagram for the two variants tested being presented in fig. 4 and fig. 5.

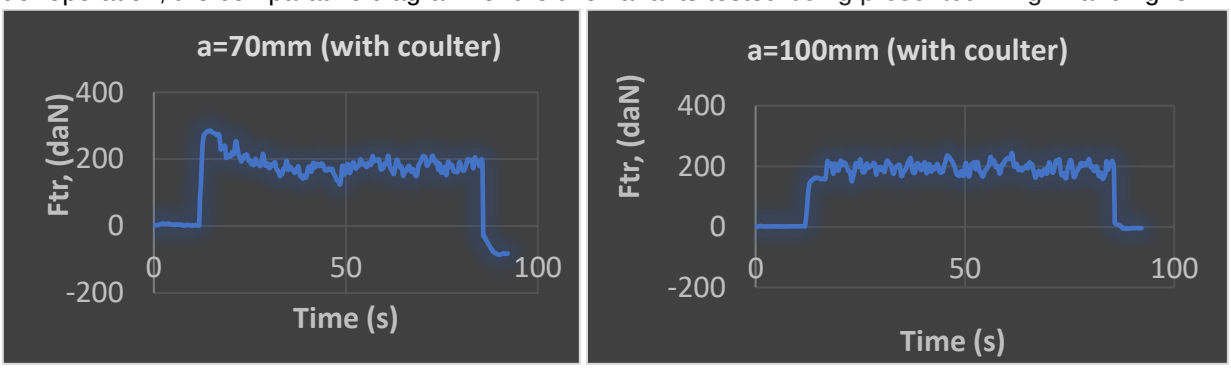

Average value for traction force = 180.74 daN Average value for traction force = 195.83 daN

Fig. 4 - Traction force diagrams for seedling planter, for working depth of 70 mm, respectively 100 mm, Variant I

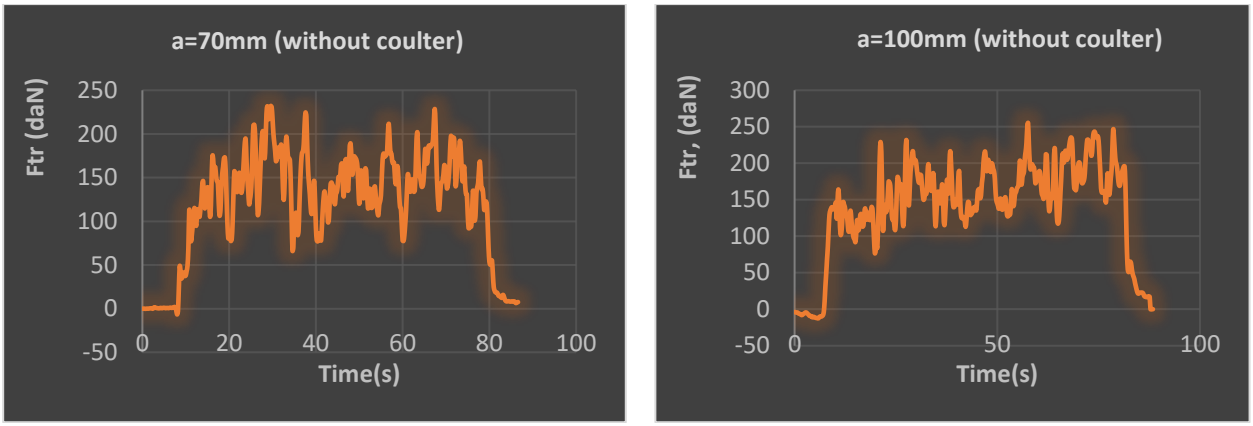

Average value for traction force = 145.7 daN

Average value for traction force = 165.1 daN

Fig. 5 - Traction force diagrams for seedling planter, for working depths of 70 mm, respectively 100 mm, Variant II

The tests performed found a slip of the drive wheel of 7-10%, although from a numerical check of the mathematical relations presented in the chapter Material and method, it resulted that the adhesive force developed at the drive wheel level is sufficient to drive the disc with buckets, in both equipped variants.

The variation of the traction forces with the working speed, for the two experienced variants, is presented in fig. 6.7.

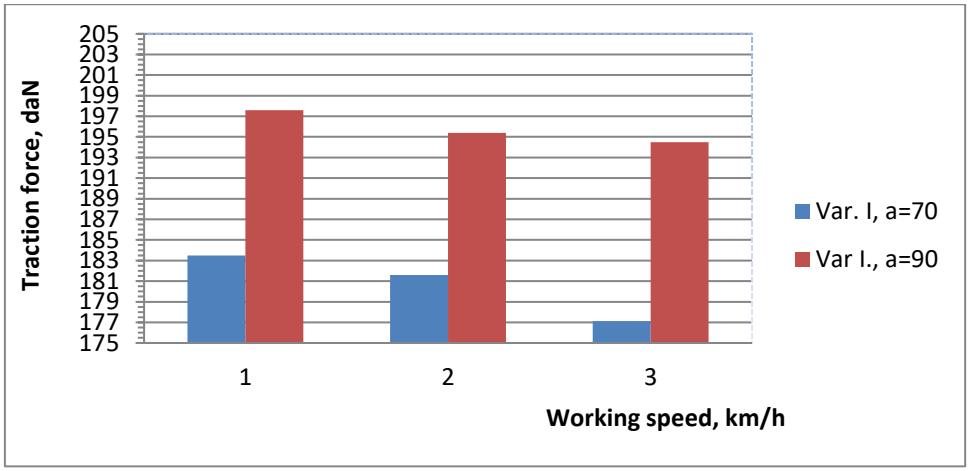

Fig. 6 - The variation of the traction forces with the working speed, Variant I

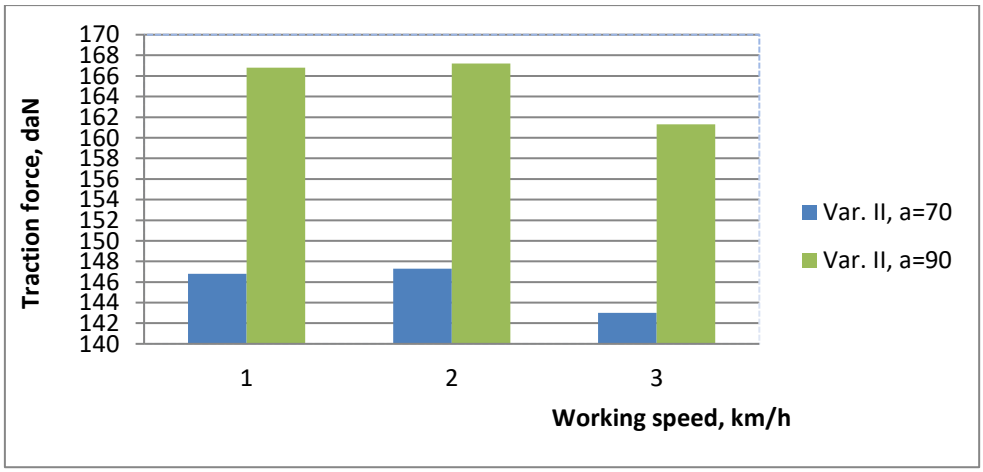

Fig. 7 - The variation of the traction forces with the working speed, Variant II

CONCLUSIONS

After the experiments were carried out, the following conclusions can be drawn:

1. From the multitude of studied bibliographic references, it resulted that the seedling planting equipment, equipped with planting machines with bucket distributors is, by far, the most used at present, this being distinguished by constructive simplicity and high efficiency in achieving qualitative working indices;

2. Traction forces when moving the tested machine, equipped with a planting equipment which places the seedling in a furrow made by a coulter, followed by the covering of the nutritious bale with soil by two paddles and the additional fixing by means of two compaction wheels, Variant I, have significantly higher values than those obtained with the machine equipped with a planting equipment that places the seedling directly in the soil followed by an additional fixing of it with the help of two compaction wheels, called, Variant II, in a percentage of 18-24%,depending on the working depth;

3. The traction forces determined in experiments differ by an additional 5 to 7% from those calculated in theory.

4. The variation of traction forces, with working speed, is insignificant. It was observed a decrease of this, once with the increase of the working speed, in a percentage of 2-3%.

REFERENCES

[1] Ciuperca R., Popa L. et. al, (2012), Comparative study on mechanized process of planting vegetable seedlings, *INMATEH - Agricultural Engineering*, vol. 37, No. 2, pp.61-68, Bucharest / Romania.

[2] Gui-Zhi Zhao, Da-Peng Liu, (2015), Design of seedling transplanting machine based on motion controller*, International Conference on Computational Science and Engineering- ICCSE*, pp.556-560.

[3] Jin Xin, Zhao Kaixuan, Ji Jiangtao, (2018), Design and Experiment of Automatic Transplanting Device for Potted Tomato Seedlings, *Proceedings of the Institution of Mechanical Engineers, Part C: Journal of Mechanical Engineering Science,* pp.1054-1065.

[4] Mitrache P.M, Sărăcin I., Ciupercă R., (2020), Comparative research on the realization of agro-technical indices by seedlings planting machines with bucket dispensers, *19th International Scientific Conference Engineering for Rural Development*, ISSN 1691-5976, pp. 549-554, Jelgava / Latvia.

[5] Muraru-Ionel C., (2009), *Machines with flexible disks for planting vegetable seedlings*, *(Maşini cu discuri flexibile pentru plantat răsaduri legumicole)* Terra Nostra Publishing House, ISBN 978-973-1888, pp.50-62, Iasi / Romania.

[6] Nakanishi Y., Kusamoto H., Fukui S. et al, (2007), *Seedling Planting Tine of Seedling Planting Machine,* Abstract of JP2007037444 (A), Japan.

[7] Poenaru I., Paraschiv G., Voicu Gh., Moiceanu G., Biriş S.S., Vlăduţ V. (2012), Studies regarding the working process executed on ploughshare of planting machines, *11th International Scientific Conference "Engineering for Rural Development"*, 24, 25.05.2012, pp. 22-26, vol. 11, ISSN 1691-5976, Jelgava / Latvia.

[8] Popescu V., Popescu A., (2006), *Vegetable crop in field and solariums*, (*Cultura legumelor din camp şi solarii)*, MAST Publishing House, pp. 256, Bucharest / Romania.

[9] SR 13215(1994), *Seedling planting machines. Quality technical conditions* (*Maşini de plantat răsaduri. Condiţii tehnice de calitate*), ASRO, Romania.

[10] Voicu Gh., Poenaru I.C., Paraschiv G., Dincă M., Vlăduţ V. (2014), Theoretical modeling of working process of covering devices to miscanthus rhizomes planters, *Proceedings of the 42 International Symposium on Agricultural Engineering "Actual Tasks on Agricultural Engineering"*, pag. 139-148, ISSN 1333-2651, Opatija / Croatia.

[11] *** www.checchiemagli.com/en/transplanting-machines.

[12] *** https://www.duijndam-machines.com/en/machines/2318/hortech-over-1-row-planting-machine/#.

[13] *** https://autoline.ro/-4-rijige-plantmachine-Duijndam-Machines--17090611134281090900.

OPTIMIZATION TECHNIQUE OF DRIVING DISC PARAMETERS
/
МЕТОДИКА ОПТИМИЗАЦИИ ПАРАМЕТРОВ ДИСКА-ДВИЖИТЕЛЯ

Konstantinov Yu.V. [1], Akimov A.P. [1], Medvedev V.I. [1], Terentyev A.G. [1,2]
[1] Chuvash State Agrarian University, Cheboksary / Russia;
[2] Chuvash State University named after I. N. Ulyanov, Cheboksary / Russia
E-mail: konstantinov@polytech21.ru
DOI: https://doi.org/10.35633/inmateh-63-32

Keywords: *tillage units, powered disc knife, driving force, kinematic parameter, relative depth, specific energy consumption*

ABSTRACT
Flat circular discs in powered operation mode create driving forces. These forces enable to decrease the wheel slippage of the energy saturated tractor of tillage unit and to reduce the specific energy consumption. The objective of this study was to develop a technique that enables to determine the driving disc optimal parameters for maximum efficiency criterion. The earlier developed mathematical model of soil-disc interaction was used for this purpose. Soil properties in the model are characterized by means of two empirical constants. The relative depth and the kinematic parameter determine the disc operation mode. It was shown that the driving disc can operate with high efficiency, if the disc operates at the optimal values of the parameters. The driving disc efficiency can achieve the value about fifty percent. The experimental results confirmed the adequacy of the technique. The discrepancy between the predicted and field experimental values of driving forces and applied moments was about 25%. The proposed technique can be modified to optimize the parameters of other powered rotary tools of tillage machines and units.

РЕЗЮМЕ
Плоские круглые диски в приводном режиме создают движущие силы. Эти силы позволяют уменьшить буксование колес энергонасыщенного трактора почвообрабатывающего агрегата и снизить удельные энергозатраты. Целью данного исследования явилась разработка методики определения оптимальных параметров диска-движителя по критерию максимального коэффициента полезного действия. Для этого использовалась математическая модель взаимодействия диска с почвой, построенная ранее. Свойства почвы в ней характеризовались двумя эмпирическими постоянными, а режим работы диска определялся его относительным заглублением и кинематическим параметром. Было показано, что КПД диска-движителя составляет около 50% при оптимальных режимах работы. Результаты экспериментов подтвердили адекватность предложенной методики. Расхождение между предсказанными и экспериментальными значениями движущих сил и приложенных моментов составило около 25%. Эта методика может быть модифицирована для оптимизации параметров приводных ротационных рабочих органов почвообрабатывающих машин и агрегатов.

INTRODUCTION

The analysis of proposed designs of primary tillage tools showed that, in terms of the quality indicators, the ordinary share plough is still the best. At the same time, ploughing is the most energy-intensive process in the plant growing. Its implementation takes about 30-40% of all energy consumption for field works. In this regard, conservation of energy resources in ploughing acquires the special importance, in particular, by reducing the power losses of the tractor drive wheels due to slippage (*Misuno, 2018*).

About 20–55% of all tractor power is lost due to the slippage of the tractor driving wheels and to the tire and soil deformation (*Eto et al., 2018; Janulevicius et al., 2019*). Wheeled tractors work with the greatest efficiency if the slippage of the driving wheel is in the optimal range, namely, in the range of 8–12% (*Zoz, 1972; Battiato et al., 2017*). In order for the slippage of the tractor drive wheel to correspond to this range it is necessary to reduce the traction resistance of tillage implements.

There are many ways to reduce the traction resistance of tilling implements, which can be divided into three main groups (*Akimov & Medvedev, 2004*). The first group is the improvement of passive tillage tools (coating the mouldboard surface with polymers, plastics, watering of the plough mouldboard, vibration of

plough bottom, as well as using a plough bottom with variable geometry). The second group is the setting of additional active tillage tools (a vertical rotor instead of mouldboard wing, a rotary tiller section instead of skimmer, flat discs in front of each plough bottom, etc.). The third group is characterized by the creation of new type implements, which do not have share-mouldboard tillage bottoms. This group includes rotary ploughs of various designs, screw ploughs, blade ploughs, etc.

Energy saturation growth predetermines an increase in operating speed of tractors and an intensive increase in plough resistance. The increasing of the energy capabilities of the tractors must correspond to the technological plough capabilities at higher speeds. Therefore it is necessary to find ways to significantly reduce the soil resistance to plough movement. Ploughs in combination with driving discs (DDs) well satisfied this requirement (*Akimov & Medvedev, 2004*). A plough in combination with DDs (flat discs set in the plane of the field cutoffs of the plough bottoms and operating in the mode of movers) can operate at the forward speeds 2–3 times higher than the fastest rotary plough. At the same time it has the significant advantages in productivity and specific energy consumption with the good quality work compared to conventional share ploughs.

Ploughs with DDs enable to use efficiently the energy saturated wheeled tractors for ploughing. In this case the slippage of tractor drive wheels decreases significantly, productivity increases, fuel consumption per hectare decreases, the possibility of full engine loading and further energy saturation of tractors appears. The active discs are used in forced rotation mode not only in combination with plough, but in other various tillage units to create an additional driving force.

A flat disc coulter is the simplest rotary tool, which is widely used in various tillage implements. Disc coulters are used in different modes in ploughs, seeders and planters to cut crop residues (*Morrison & Allen, 1987*). In addition, the active discs are used in a forced rotation mode in various tillage units to create an additional driving force. This enables to reduce the specific energy consumption for soil cultivation by decreasing the wheel slippage at the soil-tyre interface of energy saturated tractor (*Medvedev, 1972*). The use of driven discs also makes it possible to increase the directional stability of the tillage units (*Musin et al., 2011*). With the help of such discs, it is possible to significantly reduce the traction resistance of the row cultivator and to increase its directional stability (*Serguntsov, 2017*). In the forced rotation mode, the disc coulters of seeders better cut crop residues (*Sarauskis et al., 2013*).

Adequate mathematical model of the disc coulter-soil interaction makes it possible to create low-power-consuming tillage units by modeling technological processes with carrying out numerous calculations on a computer. For applications of this model, it is necessary to choose reasonably the criteria of optimality. The mathematical model of the interaction of a disc coulter with a soil was being developed firstly only for a freely rotating (passive) disc (*Nerli 1929–1930a, 1929–1930b; Sineokov, 1949; Skakun & Flaischer, 1981*). And then it was developed for the powered (active) disc (*Akimov & Konstantinov, 2017*).

The objective of this article is to develop a technique that enables to determine the driving disc (DD) optimal parameters for maximum efficiency criterion by using the previously developed mathematical model of soil-disc interaction. This technique enables the combination of ploughs with DDs to use the energy resources more efficiently.

MATERIALS AND METHODS

We suppose that the flat DD of radius r [m] moves with a constant forward velocity $\boldsymbol{v_f}$ [m/s] and simultaneously rotates with an angular velocity ω [rad/s], cutting the soil to a depth h [m]. The disc operation mode is determined by its kinematic parameter $\lambda = \omega r/v_f$ and the relative depth $\xi = h/r$. The experiments show (*Akimov & Konstantinov, 2017*) that the soil pressure p on the lateral surfaces of disc in the soil and the cutting resistance Q of a unit length of its blade are practically constant and do not depend on λ and ξ. The empirical constants p and Q can be determined from simple experiments.

Let us direct the Ox axis of the coordinate system moving together with the disc in the direction of the movement of the DD, and direct the Oz axis vertically downward (Fig. 1). An elementary soil friction force $\boldsymbol{dF}_f$ acts on an arbitrary elementary area $dS = dxdy$ of the lateral surface segment of the disc in the soil. This force is directed opposite to the absolute velocity vector of a point $M(x; z)$ of this area. Therefore, its projection onto the Ox axis is equal to:

$$dF_{fx} = dF_f \cdot \cos\varphi = fpdxdy \cdot \cos\varphi \quad (1)$$

where:

f is the soil-steel surface friction coefficient;

φ is the angle between CM segment and Oz axis (Fig. 1(a)).

If the point *M* is located below the point *C*, then the projection of the force $\boldsymbol{dF}_f$ onto the *Ox* axis is positive, that is, the component of the force $\boldsymbol{dF}_f$ relative to the *Ox* axis is the driving force.

The value of the total driving force created by the frictional forces of the soil on the lateral surfaces of the disc is equal to the doubled double integral of the elementary projection of the force $\boldsymbol{dF}_f$ onto the *Ox* axis over the segment *S* immersed in the soil of one of the two lateral disc surfaces

$$F_{sx} = 2fp\iint_S \cos\varphi \, dx dz. \tag{2}$$

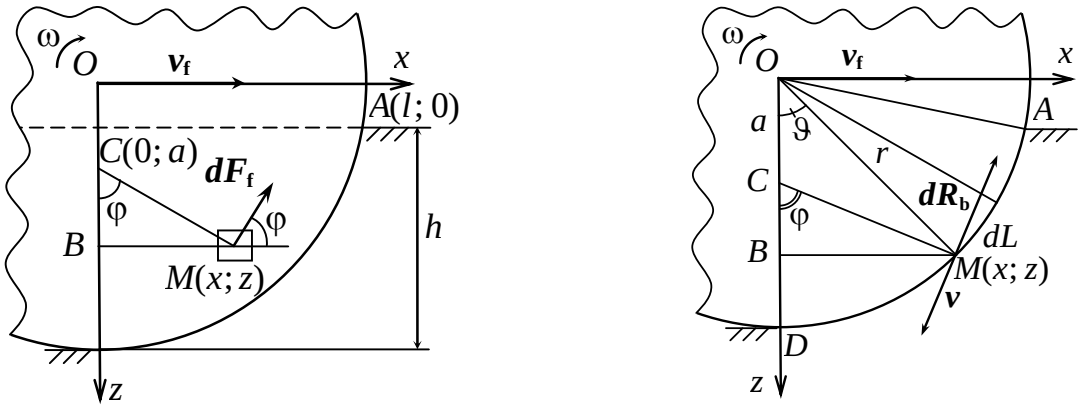

(*a*) (*b*)

Fig. 1 - The scheme of interaction with the soil of an elementary part of
(a) the disc side surface and (b) the disc blade

From a right triangle MBC we have:

$$\cos\varphi = (z - a)/((z - a)^2 + x^2)^{0.5}, \sin\varphi = x/((z - a)^2 + x^2)^{0.5}. \tag{3}$$

Substituting the first of these expressions into the integral (1) and representing the double integral as an iterated integral, we obtain the formula:

$$F_{sx} = 4fp\int_0^{l\cdot r} dx \int_{r-h}^{\sqrt{r^2-x^2}} \frac{(z-a)}{\sqrt{(z-a)^2 + x^2}} dz \tag{4}$$

where: $l = (2\xi - \xi)^{0.5}$.

Calculating the inner definite integral in the iterated one and changing the integration variable to $t = x/r$ in the outer integral, we obtain the final expression for the magnitude of the total driving force created by the friction forces on the lateral surfaces of the DD:

$$F_{sx} = 4fpr^2\int_0^l \left[\left(\mu^2 - 2\mu\sqrt{1-t^2} + 1\right)^{0.5} - \left((1-\xi-\mu)^2 + t^2\right)^{0.5}\right] dt \tag{5}$$

We consider as the positive direction of the moments of forces the direction coinciding with the direction of rotation of the DD.

It follows from Figure 1(b) that the moment of the elementary frictional force $\boldsymbol{dF}_\mathbf{f}$ about point C (instantaneous centre of velocities) is equal to:

$$dm_C = -dF_f \cdot CM = -fpdxdy((z - a)^2 + x^2)^{0.5} \tag{6}$$

The value of the total moment about point C, created by the frictional forces of the soil on the lateral surfaces of the disc, is equal to the doubled double integral of the moment of the elementary force $\boldsymbol{dF}_\mathbf{f}$ with respect to this point along the immersed in the soil segment *S* of one of the two lateral surfaces

$$m_C = -2fp\iint_S \sqrt{x^2 + (z-a)^2} \, dx dz \tag{7}$$

Representing the double integral as an iterated one, we obtain:

$$m_C = -4fp \int_{r-h}^{r} dz \int_{0}^{\sqrt{r^2-z^2}} \sqrt{x^2+(z-a)^2}\,dx \tag{8}$$

Calculating the inner definite integral in the iterated one and changing the integration variable to $t = x/r$ in the outer integral, we obtain the final expression for the total moment about point C of elementary friction forces of soil on the lateral surfaces of the disc:

$$m_C = -2fpr^3 \int_{1-\xi}^{1} \left(\sqrt{1-t^2}\sqrt{\mu^2-2\mu t+1} + (\mu-t)^2 \ln \frac{\sqrt{1-t^2}+\sqrt{\mu^2-2\mu t+1}}{|\mu-t|} \right) dt \tag{9}$$

If we shall simplify the system of elementary friction forces to the point *C*, we shall get the system principal vector $\boldsymbol{F_s}$ acting at this point and the couple with the principal moment m_C. In order to simplify the simplified system to the new point O (the disc centre), it is necessary to move the principal vector of the system from the point C to the point O, and add a couple with a moment equal to the moment of the moving principal vector with respect to the point O (theorem of parallel translation of a force).

So, the moment about the point O of the system of elementary soil friction forces on the sidewalls of the disc is:

$$m_O = m_C - F_{sx} \cdot a \tag{10}$$

Let us consider an arbitrary elementary segment of the blade $dL = r \cdot d\vartheta$ with a point $M'(r\sin\vartheta; r\cos\vartheta)$ on it (Fig. 1 (b)). The elementary reaction of the soil resistance to penetration (wedging) by this elementary segment of the disc blade $\boldsymbol{dR_b}$ is directed against the vector of the absolute velocity of the point M', that is, perpendicular to the segment CM′ (Fig. 1 (b)).

Therefore, its projection onto the *Ox* axis is equal to:

$$dR_{bx} = Qrd\vartheta\cos\varphi \tag{11}$$

If the point M' is located below the point *C*, then the projection of the force $\boldsymbol{dR_b}$ onto the *Ox* axis is also positive, that is, the component of the force $\boldsymbol{dR_b}$ relative to the *Ox* axis is the driving force too.

From the equality (3) we find that:

$$\begin{aligned} \cos\varphi &= \frac{r\cos\vartheta - a}{\sqrt{(r\cos\vartheta - a)^2 + r^2\sin^2\vartheta}} = \frac{\lambda\cos\vartheta - 1}{\sqrt{(1+\lambda^2-2\lambda\cos\vartheta}}, \\ \sin\varphi &= \frac{r\sin\vartheta}{\sqrt{(r\cos\vartheta - a)^2 + r^2\sin^2\vartheta}} = \frac{\lambda\sin\vartheta}{\sqrt{(1+\lambda^2-2\lambda\cos\vartheta}}. \end{aligned} \tag{12}$$

By substituting the first of the two last equalities in the equality (11) and integrating the result we find the value of the total driving force created by the reaction forces of the soil on the blade of the disc which is equal to the curvilinear integral of the elementary projection of the force $\boldsymbol{dR_b}$ onto the *Ox* axis over the immersed in the soil segment *L* of the blade:

$$R_{bx} = Qr \int_{0}^{\vartheta_0} \frac{(\lambda\cos\vartheta - 1)d\vartheta}{\sqrt{1+\lambda^2-2\lambda\cos\vartheta}}, \tag{13}$$

where $\vartheta_0 = \arccos(1-\xi)$.

It follows from Figure 1 (b) that the moment of the elementary soil reaction $\boldsymbol{dR_b}$ about point O (the disc centre) is equal to:

$$dM_O = -Qrd\vartheta r\cos(\varphi - \vartheta) = -Qr^2(\cos\varphi\cos\vartheta - \sin\varphi\sin\vartheta) \tag{14}$$

Substituting the equalities (12) into the last equality and finding the curvilinear integral of dM_O over the immersed in the soil segment *L* of the blade we obtain the principal moment M_O of the soil reactions to the DD blade about the disc centre:

$$M_O = Qr^2 \int_{0}^{\vartheta_0} \frac{(\cos\vartheta - \lambda)d\vartheta}{\sqrt{1+\lambda^2-2\lambda\cos\vartheta}}. \tag{15}$$

In order to reduce the number of independent parameters, we introduce the dimensionless force characteristics of the DD:

$$F_{sx}^{*} = \frac{F_{sx}}{4fpr^2},\ R_{bx}^{*} = \frac{R_{bx}}{Qr},\ m_O^{*} = \frac{m_O}{4fpr^3},\ M_O^{*} = \frac{M_O}{Qr^2}. \tag{16}$$

To find the total driving force of DD we add the driving force of the disc surfaces and the driving force of the blade

$$R_x = QrR_{bx}^{*} + 4fpr^2F_{sx}^{*} = Qr(R_{bx}^{*} + nF_{sx}^{*}), \tag{17}$$

where $n = 4fpr/Q$ is the dimensionless coefficient ($n \geq 0$).

In a steady motion mode the moment applied to the powered disc from the PTO is equilibrated with the principal moment M_p of all soil reactions, which is equal to:

$$M_p = Qr^2M_O^{*} + 4fpr^3m_O^{*} = F_{sx}^{*} = Qr^2(M_O^{*} + nm_O^{*}). \tag{18}$$

The field unit was created for experimental investigations of the DD operation mode influence on energy characteristics of tillage unit. This unit allowed to vary the λ parameter in a wide range.

During the test, the torsion torque on the shaft of driving discs, the horizontal and vertical soil reaction forces on the DDs, and the rotation frequency of DDs were synchronously measured and recorded. The torsion torque transmitted to the shaft with discs was measured with the help of rotational dynamograph, the forces acting on the discs were measured with the help of strain gauge dynamometers, and the rotation frequency was measured with the help of the inductive sensor. The oscillograph was used for recording the measured values.

The tests were performed on the wheat field after harvesting. At the soil depth ranges of 0.10–0.20 m the average soil cone index was 2.95 MPa. At the soil depth ranges of 0–0.10 m the soil moisture content was 13.6%, and at the soil depth ranges of 0.10–0.20 m the soil moisture content was 16.1%.

A series of tests were conducted with discs of radius r = 0.25 m at constant depth h = 0.1 m, and their operation mode was varied at the expense of peripheral rotational velocity. As a result of the treatment of oscillograms the experimental values of the driving forces of the driving discs and moments applied to discs were determined. The experimental points with theoretical curves for f = 0.5, Q = 440 N/m and p = 34.4 KPa drawn by formulas (11), (12) are shown in Figure 2.

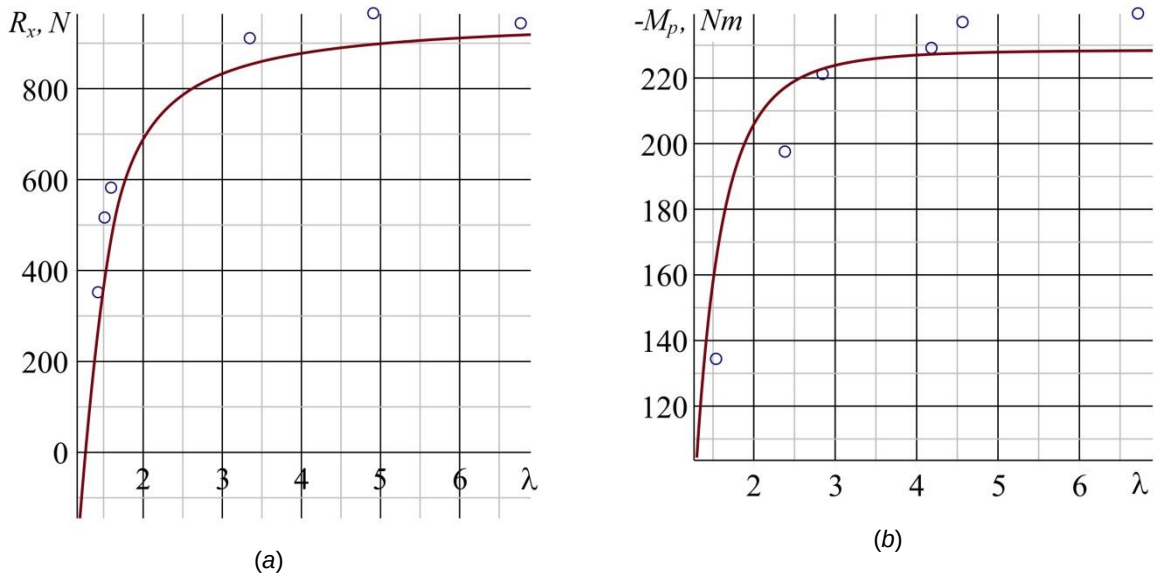

(*a*) (*b*)

Fig. 2 - Comparison of the theoretical and the experimental driving disc force characteristics

(a) for the driving force and (b) for the modulus of principal moment of soil reactions

As one can see from Figure 2, the maximum relative error for the driving force is equal to 24.6%, and for the modulus of principal moment of soil reactions it is equal to 25.4%. Such errors are acceptable for field measurements, so the mathematical model adequately describes the driving disc-soil interaction.

In accordance to the classical definition, the efficiency of a tool is the ratio of the useful tool power (work or energy) to the total one supplied to it.

The useful power developed by the DD is $P_1 = R_x v_f = (R_{bx}^* + nF_{sx}^*)Qrv_f$, and the total power supplied to the disc is $P_2 = -M_O\omega = -(M_O^* + nm_O^*)Qr^2\omega$.

By the definition, the efficiency of the drive disc is $\eta = P_1/P_2$, that is:

$$\eta = -\frac{R_{bx}^* + nF_{sx}^*}{(M_O^* + nm_O^*)\lambda} > 0. \quad (19)$$

We notice that, in active operation mode $R_{bx}^* + nF_{sx}^* > 0$ and $(M_O^* + nm_O^*)\lambda < 0$, that is the soil reaction forces push the DD and slow down its rotation.

In the formulas (5)–(10) and (13)–(15), the definite integrals parametrically depend on the quantities λ and ξ. Therefore, these formulas and formulas (16), (19) make it possible to analyse the dependence of the coefficient η on the parameters. These integrals are expressed in terms of Legendre elliptic integrals in normal form (*Akimov & Konstantinov, 2017*), but they are not expressed in terms of elementary functions. Therefore, the integrals were calculated numerically in the Maple package.

RESULTS

We also introduce the two dimensionless power characteristics of the active disc:

$$P_1^* = \frac{P_1}{Qrv_f} = R_{bx}^* + nF_{sx}^*,\ P_2^* = \frac{P_2}{Qrv_f} = -(M_O^* + nm_O^*)\cdot\lambda, \quad (20)$$

where P_1^* is the dimensionless useful power developed by the DD, and P_2^* is the dimensionless total power supplied to the disc.

The graphs of the resultant side friction force projection onto the *Ox* axis versus λ parameter are shown in Figure 3(a), and such graphs of the projection of the resultant soil reaction to the blade – in Figure 3(b).

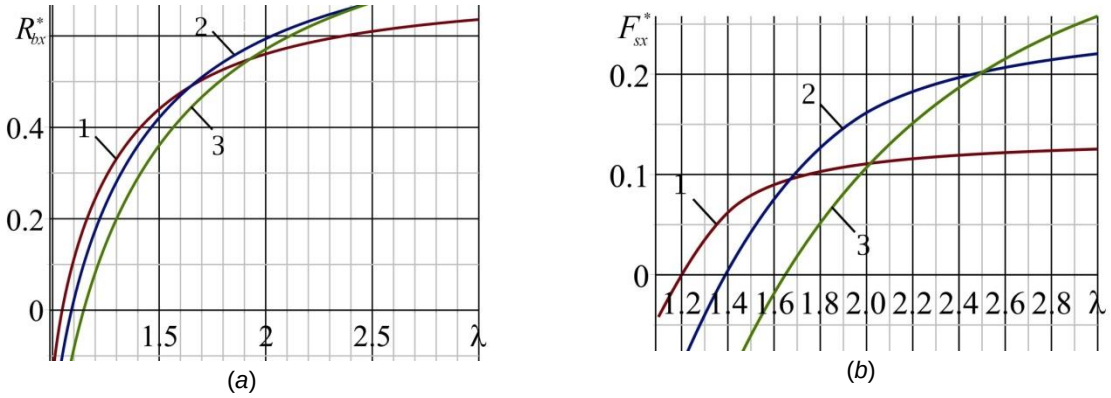

Fig. 3 - The graphs of the dimensionless projections of the soil resultant reactions versus λ

(*a*) R_{bx}^* (*on the disc blade*) *and* (*b*) F_{sx}^* (*on the disc sides*)

The graphs in Figure 3 were plotted for the following three ξ values: 0.3 (curve 1), 0.5 (curve 2), and 0.7 (curve 3).

For any given ξ there exists a value $\lambda_1^* = \lambda_1^*(\xi)$ such that at $\lambda = \lambda_1^*$, $R_{bx}^* = 0$, and there exists a value $\lambda_2^* = \lambda_2^*(\xi)$ such that at $\lambda = \lambda_2^*$, $F_{sx}^* = 0$ (Fig.3). Both projections are positive for values $\lambda > max(\lambda_1^*, \lambda_2^*)$, hence the sum $R_{bx}^* + nF_{sx}^*$ is positive too, and the powered disc can perform the moving function in the corresponding operation modes. The projections decrease with increase in ξ for small λ parameter values and increase for the larger values of this parameter. The increase rates of the projections decrease with λ increase, therefore operation modes with small λ parameter values are more effective for the moving function.

Theoretically, the dimensionless coefficient *n* is in the range from 0 to ∞. For *n* = 0, there are no friction forces on the lateral surface of the disc and one can easily obtain from the formulas (20) that $P_1^* = R_{bx}^*$, $P_2^* = -M_O^*\lambda$. The graphs of these power characteristics versus λ parameter are shown in Figure 5(a). For λ ≈ 1.1 the useful power $P_1^* \approx 0$, and it increases with the increase in λ. For λ values greater than 1.5 with the λ increase the supplied power P_2^* increases almost linearly, but the power P_1^* tends to some limit (Fig. 4(a)).

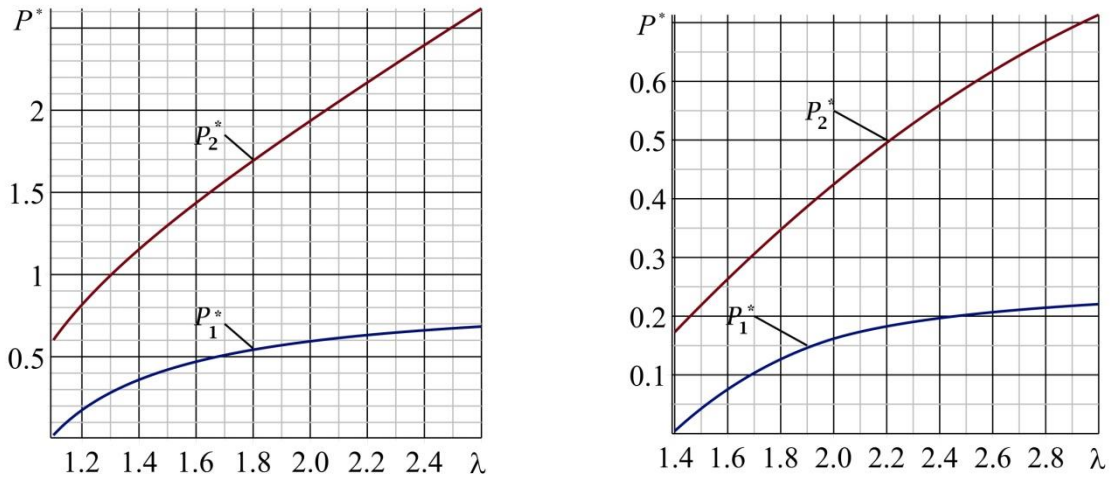

(*a*) (*b*)

Fig. 4 - The graphs of the dimensionless powers P_1^* and P_2^* versus λ

(a) for n = 0 (the disc blade) and (b) for n = ∞ (the disc sides)

In the case *n* = 0 the expression for the efficiency of the DD is also simplified:

$$\eta_0 = -\frac{R_{bx}^*}{M_O^*\lambda}. \tag{21}$$

This formula can be used to calculate the efficiency of the DD when the disc operates in light soils, for which friction forces on the lateral surfaces of the disc can be neglected in comparison with the cutting resistance forces on the disc blade (*n* << 1).

Value *n* = ∞ corresponds to the case when there are no soil resistance to cutting, so *Q* = 0, *Q*·*n* = 4*fpr*, and $P_1 = 4fpr^2 v_f F_{sx}^*$, $P_2 = 4fpr^3 m_O^* \omega$. In this case, the dimensionless powers are equal to $P_1^* = P_1 / (4fpr^2 v_f) = F_{sx}^*$, $P_2^* = P_2 / (4fpr^2 v_f) = -m_O^*\lambda$. The graphs of these power characteristics versus λ parameter are shown in Figure 4(b).

One can see from Figure 4(b) that again with the λ increase the supplied power P_2^* increases almost linearly, but the power P_1^* tends to some limit.

If we substitute *n* = ∞ into the formula (5), we obtain one more simple expression for the driven disc efficiency:

$$\eta_1 = -\frac{F_{sx}^*}{m_O^*\lambda}. \tag{22}$$

The latest formula can be used to calculate the efficiency of the DD when the disc operates in hard soils, for which cutting resistance forces on the disc blade can be neglected in comparison with the friction forces on the disc lateral surfaces (*n* >> 1).

Calculations show that in the general case the efficiency satisfies the following inequality: $min(\eta_0, \eta_1) \le \eta \le max(\eta_0, \eta_1)$. For the calculation of DD efficiency by the formulas (19), (21) or (22), several formulas (16) are used, as well as the formulas (5)–(10), (13), and (19).

The results of calculations on a personal computer are shown in graphical form in Figure 5. The DD efficiency dependences on λ have the graphs which are shown in Figure 5(a).

They were plotted for the value of ξ = 0.4 and for three values of *n* = 0 (curve 1), *n* = 3 (curve 2), and *n* = ∞ (curve 3). The presence of the DD efficiency maximum is explained by the earlier discussed changes of the P_1^* and P_2^* powers with the λ increase.

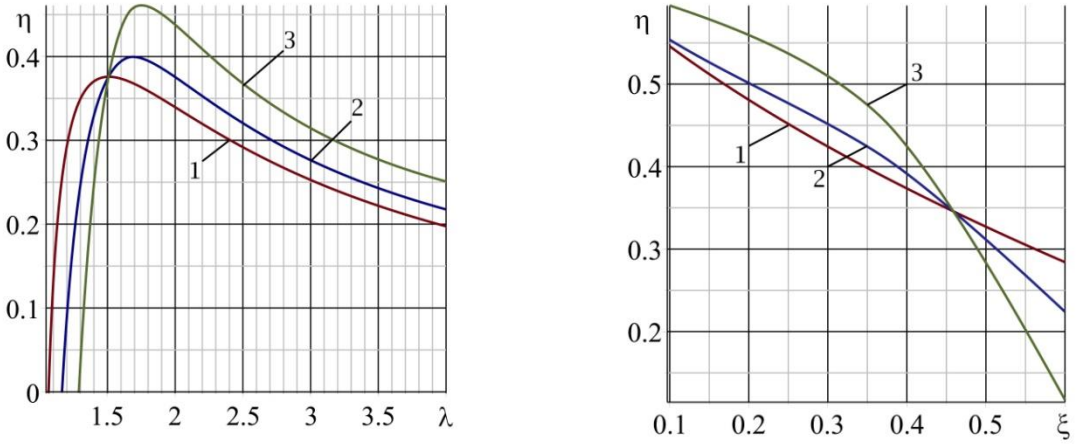

(*a*) (*b*)

Fig. 5 - Dependence of the driving disc efficiency η
(a) on the kinematic coefficient λ; (b) on the relative depth ξ

The driving force of the disc knife is vanished at the λ values close to one. One can see from the graphs that at these λ values the DD efficiency is too close to zero. Already at relatively small λ values the η coefficient sharply increases to its maximum value 0.38 – 0.51 at some optimal value λ^* from the range $1.5 \le \lambda \le 1.75$ (depending on soil properties). Then it gradually and almost uniformly decreases to $\eta \approx 0.2$ at the point λ = 5.

The result is in good agreement with the field experimental data (*Akimov, 1976*), according to which the maximum value of the efficiency of a tillage unit with the driving disc with radius of 25 cm and a cutting depth of 9 – 10 cm (ξ = 0.36 – 0.4) corresponded to $\lambda \approx 2$.

The Figure 5(b) shows the graphs of the DD efficiency dependence on ξ at λ = 1.6 for the same values of *n*. It follows from them that the efficiency of the disc decreases monotonically with an increase in the relative depth ξ, and almost linearly at *n* = 0 and 3, and at *n* = ∞ the graph of η versus λ is close to a parabola. With an increase in the depth of the location of the knife part interacting with the soil, the projections of elementary cutting resistance forces and elementary friction forces on the direction opposite to the direction of disc movement increase. A decrease in the relative depth of the disc (i.e., an increase in its diameter) at the given operating depth leads to an increase in the DD efficiency. However, the increase in diameter is limited by the requirement of low material consumption. Therefore, a reasonable compromise is required when we choose the disc diameter.

Comparative tests of a ploughing unit with the DDs and a conventional ploughing unit (without driving discs) directly confirmed the effectiveness of using DDs to reduce slippage of an energy saturated tractor. The tests have shown that the slippage of the driving wheels of the tractor with DDs does not exceed 22%, and for the control unit it reaches 35%. In addition, the acceptable slippage was observed for the control unit already at a speed of 4 km/h, while for the experimental unit only at a speed of 7.5 km/h.

CONCLUSIONS

The technique has been developed to determine the optimal parameters of the driving disc for maximum efficiency criterion. The experimental results confirmed the adequacy of the technique. The discrepancy between the predicted and field experimental values of driving forces and applied moments was about 25%.

The numerical simulation showed, that:

- the position of the point of the DD maximum efficiency weakly depends on the parameter *n*, therefore the optimal modes are quite close even for different types of soils;

- the values of the efficiency of the discs-movers at the maximum points are quite high, so the powered discs can effectively perform the function of movers;

- an increase in the diameter of the discs with their constant deepening leads to an increase in the efficiency of the DD;

- for the constant depth of the disc equal to *h* = 10 cm, with an increase in its diameter from 50 to 75 cm and a simultaneous decrease in the kinematic parameter from 2 to 1.4–1.5, the efficiency of the DD increases from 37 to 48%.

The developed technique for optimizing the parameters of the DD can be modified to optimize the parameters of other powered rotary tools of tillage machines and units.

REFERENCES

[1] Akimov A. P. (1976), Influence of the operation mode of discs-movers on the energy characteristics of tillage unit (Влияние режима работы дисков-движителей на энергетические показатели почвообрабатывающего агрегата), *Transactions of the Izhevsk Agricultural Institute, Questions of Theory and Exploitation of Tractors and Cars (Труды Ижевского сельскохозяйственного института, Вопросы теории и эксплуатации тракторов и автомобилей)*, 33–37.

[2] Akimov A. P., & Konstantinov Yu. V. (2017), *Optimization of parameters and operation modes of discs of tillage machines and implements (Оптимизация параметров и режимов функционирования дисков почвообрабатывающих машин и агрегатов)*. Chuvash State Agricultural Academy pbl, ISBN 978-5-906305-24-4, 108 p.

[3] Akimov A. P., Medvedev V. I. (2004), *Rotary operating tool-movers (Ротационные рабочие органы-движители),* Moscow State Open University pbl., 233 p.

[4] Battiato A., & Diserens E. (2017). Tractor traction performance simulation on differently textured soils and validation: A basic study to make traction and energy requirements accessible to the practice. *Soil & Tillage Research,* 166, 18–32.

[5] Eto R., Sakata K., & Yamakawa J. (2018). Driving force distribution based on tyre energy for independent wheel-drive vehicle on rough ground. *Journal of Terramechanics*, 76, 29–38.

[6] Janulevicius A., Juostas A., & Pupinis G. (2019). Estimation of tractor wheel slippage with different tire pressures for 4wd and 2wd driving systems. *Proc. Int. Conf. Engineering for rural development, Jelgava, Latvia*, 18, 88-93.

[7] Medvedev V. I. (1972), *Power engineering of machine units with tools-movers (Энергетика машинных агрегатов с рабочими органами-движителями),* Chuvash Book Publishing House, 180 p.

[8] Misuno O. I. (2018). Reducing power losses due to slipping of a wheeled tractor on ploughing. *Proc. Int. Conf. Technical support of innovative technologies in agriculture*, *Minsk*, 229–231.

[9] Morrison J., Allen J. (1987). Planter and drill requirements for soils with surface residues. *Proc. No-till Conf. Conservation Tillage: Today and Tomorrow Southern Region, College Station, Texas, USA*, 44–58.

[10] Musin R. M., Mingalimov R. R., Gashenko A. A. (2011). Influence of driven discs on the movement stability of the cultivator unit in the horizontal plane and its comparative assessment with the serial unit. *Tidings of the Samara State Agricultural Academy*, 3, 79–82.

[11] Nerli N. (1929–1930a), On the dynamic advantage of the rotating coulter (Sul vantaggio dinamico del coltro rotante), Pubblicazioni della R. *Scuola d'ingegneria di Pisa*, 3 (127).

[12] Nerli N. (1929–30b). On the dynamic problem of the plough disc (Sul problema dinamico dell' aratro a disco), Annali delle Università Toscane. *Sezione delle Scienze Mediche, Fisiche, Matematiche e Naturali, Nuova Serie*, 48 (14), 51–78.

[13] Sarauskis E., Masilionyte L., Romaneckas K., Kriauciuniene Z., Jasinskas A. (2013). The effect of the disc coulters forms and speed ratios on cutting of crop residues in no-tillage system. *Bulg. J. Agric. Sci.*, 19 (3), 620–24.

[14] Serguntsov A. S. (2017). Traction resistance reduction of row cultivator. *Proc. Conf. Scientific support of the agroindustrial complex*, *Krasnodar*, *Russia*, 460–461.

[15] Sineokov G. N. (1949). *Disc tools of tillage machines (Дисковые рабочие органы почвообрабатывающих машин)*. Mashgiz, 86 p.

[16] Skakun T. S., Flaischer N. M. (1981). To the dynamics of the disc coulter. *Transactions of the VIM: Parameters of promising tillage tools and machines* 90, 138–145.

[17] Zoz F. (1972). Predicting tractor field performance. *Trans. ASAE*, 15, 249–255.

OPTIMIZATION OF THE DESIGN AND OPERATIONAL PARAMETERS OF PLANTER FOR VEGETABLE PIGEON PEA (*CAJANUS CAJAN* L. MILLSP.) SEED

/

सब्जी अरहर (*CAJANUS CAJAN* L. MILLSP.) को बोने के मशीन के लिए डिज़ाइनर और परिचालन पैरामीटर का चयन

Patel S.K.[1], Bhimani J. B.[2], Yaduvanshi B.K.[3], Gupta P.[4]
[1)] Dr. Rajendra Prasad Central Agricultural University, Pusa, Samastipur, Bihar, India
[2)]Polytechnic in Agril. Engg., Anand Agricultural University, Dahod, Gujarat, India
[3)]Polytechnic in Agril. Engg., Anand Agricultural University, Dahod, Gujarat, India
[4)]Anand Agricultural University, Dahod, Gujarat, India
Corresponding Authors: S.K. Patel, E-mail: sppiari@gmail.com
DOI: https://doi.org/10.35633/inmateh-63-33

Keywords: *Planter; RSM; Optimization; Picking type mechanism; CCD, vegetable pigeon pea*

ABSTRACT

Precision machinery is one of the most important technology in the recent decades in respect to judicious use of resources. In precision machinery one of the most important machine is seeding machines because it picks the seed from the hopper and individually placed in field. An effort has been made to optimize the operational (forward speed and vacuum pressure) and design (nozzle diameter) parameters of the precision seed drill. For optimizing the metering mechanism three parameters i.e. nozzle diameters: 2.00, 2.50, 3.00, 3.50 and 4.0 mm; forward speed: 0.27, 0.55, 0.83, 1.11 and 1.38 m/s and vacuum pressure: 19.33, 39.32, 43.98, 58.64 and 68.63 kPa were selected. The seed to seed spacing was 300 mm. The RSM technique was used to optimize the above parameters. The machine was evaluated on the basis performance parameters like miss index, multiple index, quality of feed index and precision. The optimum value for forward speed, vacuum pressure and the nozzle holes diameter was 0.83 m/s, 43.98 kPa and 3.50 mm, respectively. The most important variable that governs planting phenomenon for vegetable pigeon pea seed is nozzle diameter as well as vacuum pressure.

सार

संसाधनों के विवेकपूर्ण उपयोग के संबंध में हाल के दशकों में सटीक मशीनरी सबसे महत्वपूर्ण प्रौद्योगिकी में से एक है। सटीक मशीनरी में, सबसे महत्वपूर्ण मशीन में से एक बोने की मशीन है क्योंकि यह हॉपर से बीज को उठाती है और व्यक्तिगत रूप से क्षेत्र में रखा जाता है। सटीक बीज ड्रिल के संचालन (आगे की गति और वैक्यूम दबाव) और डिजाइन (नोजल व्यास) मापदंडों को अनुकूलित करने का प्रयास किया गया है। पैमाइश तंत्र के अनुकूलन के लिए तीन पैरामीटर यानी नोजल व्यास: *2.00, 2.50, 3.00, 3.50* ***और*** *4.0* ***मिमी; आगे की गति:*** *0.27, 0.55, 0.83, 1.11* ***और*** *1.38* ***मीटर / से और वैक्यूम दबाव:*** *19.33, 39.32, 43.98, 58.64* ***और*** *68.63 kPa* ***चुने गए। बीज से बीज की दूरी*** *300* ***मिमी रखी गई थी। आरएसएम तकनीक का उपयोग उपरोक्त मापदंडों को अनुकूलित करने के लिए किया गया था। मशीन को मिस इंडेक्स, मल्टीपल इंडेक्स, क्वालिटी ऑफ फीड इंडेक्स और प्रिसिजन जैसे आधार परफॉर्मेंस पैरामीटर पर आंका गया। आगे की गति, वैक्यूम दबाव और नोजल के छेद के व्यास के लिए इष्टतम मूल्य क्रमशः*** *0.83* ***मीटर / सेकंड,*** *43.98* ***केपीए और*** *3.50* ***मिमी था। सबसे महत्वपूर्ण चर जो वनस्पति कबूतर के बीज के लिए रोपण घटना को नियंत्रित करता है, नोजल व्यास के साथ-साथ वैक्यूम दबाव भी है।***

---

[1] *Patel S.K., Assoc. Prof. (FMPE), CAE;*
[2] *Bhimani J. B., RA;*
[3] *Yaduvanshi B.K., Asst. Prof.;*
[4] *Gupta P., Professor & Head, Dept. of FMPE, CAET.*

INTRODUCTION

Precision agriculture, which grew up with the help of remote sensing and on-line sensing technology in the middle of the 1980s, made agricultural production and agricultural management more accurate and effective (*Balafoutis et al, 2017*).

Precision seeding is one of the important parts of precision agriculture. Precision sowing is the preferred method at present, since it provides more uniform seed spacing than other methods. Precision seeding by planter requires single seeds to be picked from the hopper and individually placed in each cell. Singulation of seeds has been investigated extensively by researchers all over the world and a large number of precision seeding systems with design variations have been developed for different crops (*Gaikwad and Sirohi, 2008; Jin et al, 2019; Minfeng et al, 2018*).

Among precision seeders, those with vacuum plates are widely used in agriculture for sowing seeds of various plants. Many studies in the past were conducted in order to determine the performance of precision seeders (*Singh et al.* 2005). These studies revealed information about how a metering system of a precision seeder performed in the laboratory or in the field. The studies on the performance of a precision seeder mostly focused on vacuum pressure applied to the vacuum plate, the most common metering system in precision seeders *(Panning et al, 1999; Panning et al, 2000*).

There are many factors that contribute to the accuracy of seed spacing in precision spacing. In the design process, it is assumed that the spacing between seeds will be uniform but the uniformity may change depending on soil conditions, machine-related properties and the most important among them is seed properties (*Srivastava et al, 1993*). The mean particle diameter, geometry and mass of the seeds determine the level of vacuum, the diameter of holes and the peripheral speed of the vacuum plate (*Karayel et al, 2004; Moody et al, 2003*).

Optimum values of these parameters are very useful to the manufacture as well as researches for design of new planters for different crops (*Patel et al, 2019; Yazgi et al, 2010*). Very little techniques and information are available in the literature. Hence, a study was conducted on a planter with single seed picking technique for planting radish seeds and response methodology principles were applied to the physical system. The objective of this study was to optimize the performance of a precision seed metering unit for planting pigeon pea seed using response surface methodology (RSM).

MATERIALS AND METHODS

The laboratory study of picking type of seed metering mechanism was carried out at department of Processing and Food Engineering, College of Agricultural Engineering & Technology, Anand Agricultural University, Godhra. This consists of a vacuum pump which exhausts air from a reservoir that maintained below atmospheric pressure. A distributor connects the reservoir with a designed vacuum pick-up device, provided with an interchangeable nozzle. The vacuum is blocked as the hole reach a point above the seed hole and the seeds fall into the port knocking system under gravity. The vegetable pigeon pea seed (Anand Vegetable Pigeon pea-1) was used in the experiment for the tests and the physical properties of the seeds are given in Table 1.

Table 1

Mean values of physical properties of vegetable varieties

Crt. No.	Parameters	Mean Value
1	Length (*l*) (mm)	6.436
2	Width (w) (mm)	5.837
3	Thickness (t) (mm)	4.470
4	Equivalent diameter (D_e) (mm)	5.502
6	Sphericity (φ)	0.850
7	1000 seed weight (g)	117.748
8	Bulk Densities (g/cc)	0.781
9	Porosity (%)	39.882
10	Moisture Content (%)	7.747
11	Angle of repose (deg.)	21°

The three parameters were selected for the study. The parameters are, operational speed 5 levels: 0.27, 0.55, 0.83, 1.11 and 1.38 m/s, vacuum pressure 5 levels i.e. 19.33, 29.32, 43.98, 58.64 and 68.63 kPa and nozzle diameter 5 levels: 2.00, 2.50, 3.00, 3.50 and 4.00 mm, respectively. The optimization of above parameters was based on the performance of picking type planter metering mechanism considering the values of miss index, multi index, quality feed index and precision.

Seed metering mechanism

In seed metering mechanism 1/2.88 rpm was available for seed picking and the rest 2/3.06 rpm was for the movement of nozzle from seed hopper to port knocking system, releasing of seed and again return back to the seed hopper. In the port knocking system 4 ports were used for desired seed placement. In this system one port was always open and remaining three ports were closed. First seed was directly dropped in the furrow remaining three seeds held in the three closed ports. After 90^0 revolute of port opening shaft second port was opened, dropped the seed in the furrow and closed the port, then next 90^0 revolute the third port was opened, dropped the seed in the furrow and closed the port, then next 90^0 fourth port was opened, dropped the seed in the furrow and closed the port. These processes repeated for every revolution of cam shaft. This process was calculated considering release of a seed from each row in one revolution of cam shaft (Fig. 1). Provisions were also provided for changing the vacuum nozzle, suction pressure and seed pickup height.

Experimental procedure

The test was carried out on 600 mm wide belt with a 3.3 m long horizontal belt having picking type metering mechanism arrangement. An electric motor having fan was used to create vacuum at different levels. The belt was driven separately and special care was given to provide the synchronization of the travel speed associated with the movement of the metering mechanism and belt speed. The metering mechanism used in this study (Fig.1) had a ground-driven wheel that transfers the motion to the movable shaft with a combination of gears available. The seed metering mechanism was mounted on the greased belt as close as possible to eliminate the seed bouncing. Grease was spread on belt so that seed was stick on the belt and sowing uniformity of each seed at the different operational speeds, vacuum pressures and nozzle diameters were determined. The metering mechanism was operated at five different operational speeds. These were 0.27, 0.55, 0.83, 1.11 and 1.38 m/s with the centre point of 0.83 m/s of belt speed corresponding to 0.83 m/s of operational speed. The selection of the belt speed was achieved by considering the travelling speed of the planter in the field. The theoretical seed to seed spacing of vegetable pigeon pea seed was 300 mm. The metering mechanism was operated (run number one) as per central composite design and data were collected. After each run, seeds on grease belt were collected and spacing from seed to seed was measured. At the same speed, experiments were replicated three times. The seeding uniformity performance of the precision planter was defined using measures based by *Kachman and Smith (1995)*. The performance or uniformity parameters miss index, multi index, quality feed index and precision were determined. This was followed by run no 2 to 20 as per CCD (Table 2) with three replications. The observations were analysed and collated to draw inferences about the responses in operational speed, vacuum pressure, nozzle diameter and their interactions.

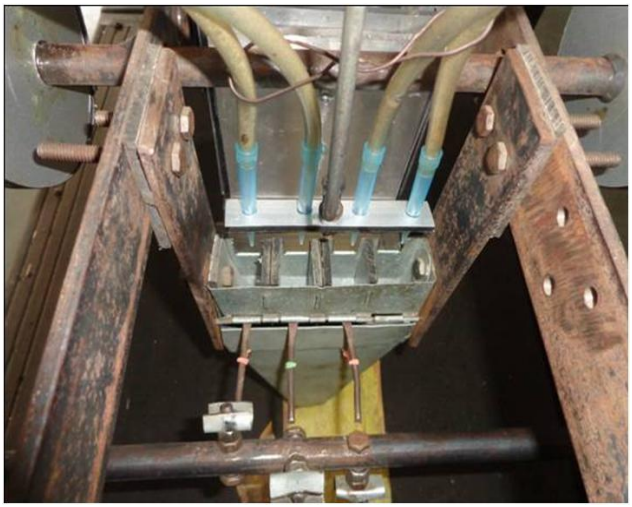

Fig. 1 - Metering mechanism

Models development and optimization procedure

A statistical and mathematical technique, Response Surface Methodology (RSM) (*Box and Draper, 1987*) was used to optimize the operating (forward speed and vacuum pressure) and constructional variables (nozzle diameter). The RSM designs are used for understanding the mechanism of the system to determine the optimum operating conditions of a system. It is less laborious and time-consuming than other approaches. It is an effective technique for optimizing complex processes since it reduces the number of experiments needed to evaluate multi parameters and their interactions.

The response surface problem usually centres on an interest in some response y, which is a function of k independent variables $x_1, x_2, ..., x_k$, that is,

$y = f(x_1, x_2, .., x_k)$

and response surface can take the different forms according to the function types of response and usually response function is defined in the quadratic polynomial form as follows:

$$Y = \beta_0 + \sum_{i=1}^{k} \beta_i \cdot X_i + \sum \beta_{ii} \cdot X_i^2 + \sum \beta_{ij} \cdot X_i \cdot X_j + e \quad \text{....(1)}$$

where:

Y is the response;

β_0 is the intercept;

$\beta_i, \beta_{ii}, \beta_{ij}$ are the regression coefficients;

$X_i\ X_j$ are the coded variables;

e is the error.

The coding of independent variables into X_i is expressed by the following equation:

$$X_i = \frac{x_1 - x^*}{d_S} \quad \text{... (2)}$$

where:

x_i is the actual value in original units;

x^* is the mean value (centre point) and

d_s is the step value.

The determination of the centre point for each independent variable was based on field conditions and the physical properties of the seed used. The design of such experiments special care has to be given for the selection of centre point as well as the minimum and maximum levels in order to construct polynomial functions from which the optimum levels of the independent variables are to be calculated.

The design used in this study is a rotatable CCD and it requires five levels for each independent variable. These levels were coded, -1.682, -1, 0, 1 and 1.682, respectively.

The different nozzle diameters were used. These were determined based on the CCD principles. The centre point in this design is coded as zero and as a centre point for the nozzle diameter was 3.00 mm. A step value of 0.50 mm was selected and as a result of this, the selected nozzle diameters became 2.00, 2.50, 3.00, 3.50 and 4.00 mm. The determination of the range for nozzle diameter was based upon the physical properties of seeds.

The vacuum at five levels was provided by the vacuum regulating valve of the vacuum pump. The vacuum level was centred at 43.98 kPa while the other levels were calculated based on the CCD principles at a step value of 19.33 kPa as 19.33, 39.32, 43.98, 58.64 and 68.63 kPa. Table 2 gives a list of independent variables and the coded factor levels.

The performance data were then transferred into a design expert statistical package program for further analysis. The response surface functions were developed for each performance criteria. The functions developed were defined as full quadratic polynomials in design expert, a statistical package program and stepwise procedure used for the selection of the variables as they enter the model in linear, interaction and quadratic form. The planter was then operated at optimum levels to verify the results from each model.

Table 2

Coded level for independent variables used in developing response surface functions

Variables	Code	Coded level				
		-1.682 (-α)	-1	0	+1	+1.682 (+α)
Operating speed, m/s	X_1	0.37	0.56	0.83	1.11	1.30
Vacuum pressure, kPa	X_2	19.33	29.32	43.98	58.64	68.63
Nozzle diameter, mm	X_3	2.00	2.50	3.00	3.50	4.00

α is defined as $[2^k]^{1/4}$ and k is the number of factors (independent variables).

RESULTS AND DISCUSSION

Optimization of design parameters of metering mechanism

The experimental results were carried out in the laboratory experiment based on Central Composite Design (CCD) are given in Table 3. It was observed that the planter operated at run no. 12, 17 and 20 gave satisfactory results in terms of miss index, multi-index, quality of feed index and precision. This result could be explained as the good selection of the ranges for the design and operational parameters and their step values. The stepwise multi second order model was tested for its adequacy to describe the response surface.

The effect of operational speed (speed of operation), vacuum pressure and constructional variables (nozzle diameter) of planter are described below.

Table 3

Central composite design (CCD) with coded and un-coded independent variables

Run no.	Independent variables			Run no.	Independent variables		
	X_1 [x_1] m/s	X_2 [x_2] kPa	X_3 [x_3] mm		X_1 [x_1] m/s	X_2 [x_2] kPa	X_3 [x_3] mm
1	0 [0.83]	0 [43.98]	-1.682 [2.0]	11	0 [0.83]	0 [43.98]	0 [0.83]
2	1 [1.11]	1 [58.64]	-1 [2.5]	12	0 [0.83]	0 [43.98]	0 [0.83]
3	0 [0.83]	1.682 [8.63]	0 [3.0]	13	0 [0.83]	-1.682 [19.33]	0 [0.83]
4	-1 [0.56]	0 [43.98]	-1 [2.5]	14	0 [0.83]	0 [43.98]	0 [0.83]
5	-1 [0.56]	1 [58.64]	-1 [2.5]	15	1.682 [1.30]	0 [43.98]	1.682 [1.30]
6	0 [0.83]	0 [43.98]	0 [3.0]	16	0 [0.83]	0 [43.98]	0 [0.83]
7	1 [1.11]	-1 [29.32]	1 [3.5]	17	-1 [0.56]	-1 [29.32]	-1 [0.56]
8	1 [1.11]	1 [58.64]	1 [3.5]	18	0 [0.83]	0 [43.98]	0 [0.83]
9	-1 [0.56]	1 [58.64]	1 [3.5]	19	-1.682 [0.37]	0 [43.98]	-1.682 [0.37]
10	1 [1.11]	-1 [29.32]	-1 [2.5]	20	0 [0.83]	0 [43.98]	0 [0.83]

Effect of design parameters of metering mechanism on performance

Stepwise multiple quadratic models were tested for its adequacy to describe the response surface of miss index, multi-index, quality feed index and precision. The analysis of variance shows the model for vegetable pigeon pea seeds were significant. There is only a 0.013 % chance that this large "model F value" could occur due to noise. It was observed that significant miss index model factor was X_2X_3, X_2^2 and X_1X_3. From the model factor, it is clear that nozzle diameter along with pressure is the most important factor for miss index followed by nozzle diameter and vacuum pressure. Values greater than 0.100 indicate the model terms are significant. The lack of fit was not significant (Table 4).

The coded and un-coded factor models are given in Eqs. 1 & 2. The results from stepwise regression analysis for each function are given in Table 4. The "Pre R-squared" of miss index, quality feed index and precision were 0.78, 0.75 and 0.54, respectively. A "Pre R-squared" implies that the overall mean is a better predictor of response than the current model and it has reasonable agreement with the "Adj R-squared" of 0.67, 0.66, and 0.52, respectively for same order (Table 5). Pred R-squared and Adeq precision for different performance models are given in Table 5. No relation was observed for multi-index. This model can be used to navigate the design space (*Montgomery, 2001*).

Based on the results obtained from the stepwise regression analysis, the most important variable that governs seeding phenomenon for vegetable pigeon pea crop was the combination of nozzle diameter and vacuum pressure accounting for 62.23%.

Graphical view of some response surfaces as drawn using polynomial functions are depicted in Fig. 2. The figure shows the consistent behaviour of the metering unit as response to constructional and operating parameters.

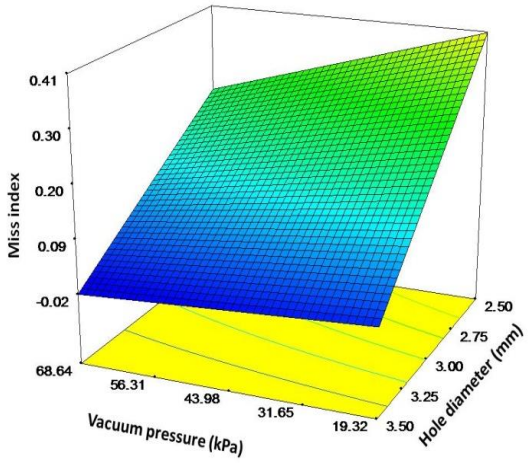

(a)

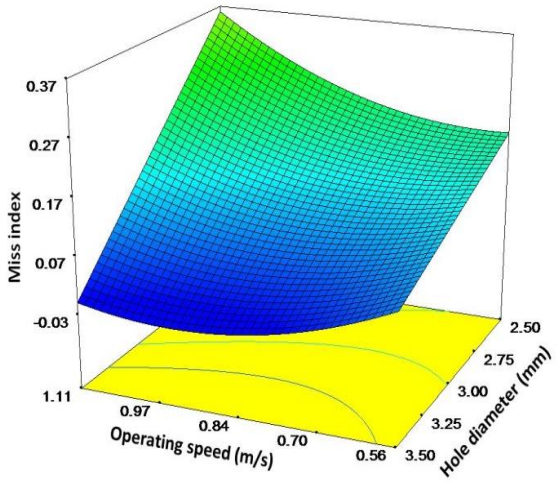

(b)

Fig. 2 - Miss index as a function of (a) vacuum pressure and hole diameter (b) operating speed and hole diameter

Miss index model in terms of un-coded factors

$$I_{miss} = 0.8712 + 0.3384x_1 - 0.0110x_2 - 0.0801x_3 - 0.4413x_1x_3 + 2.9283 \times 10^{-3}x_2x_3 + 0.6402{x_1}^2 \quad \ldots (3)$$

Miss index model in terms of coded factors

$$I_{miss} = 0.47 + 0.023X_1 - 0.24X_2 + 0.26X_3 - 0.061X_1X_3 + 0.16X_2X_3 + 0.048{X_1}^2 \quad \ldots (4)$$

Table 4

Results from the stepwise regression analysis for the miss index model

Variable	Coefficient	Standard error	Probability (P)	Coefficient of determination (R^2), %
Constant	0.160	0.028	-	-
X_2X_3	0.062	0.010	<0.0001	62.23
${X_1}^2$	0.048	0.025	0.0882	68.32
X_1X_3	-0.061	0.034	0.0946	73.54

Table 5

Coefficient of determination and precision adequacy of miss index, multi-index, quality feed index and precision model

Seeds	R-square	Adj R-square	Pred R-square	Adeq precision
Miss index	0.78	0.67	0.51	10.52
Quality feed index	0.75	0.66	0.47	10.06
Precision	0.54	0.52	0.44	13.33

No model for multi-index I_{multi} was obtained from the analysis of the data. Graphical view of some response surfaces as drawn using polynomial functions are depicted in Fig. 3.

It is interesting to observe that the multi-index surfaces are very different in shape for all the seeds.

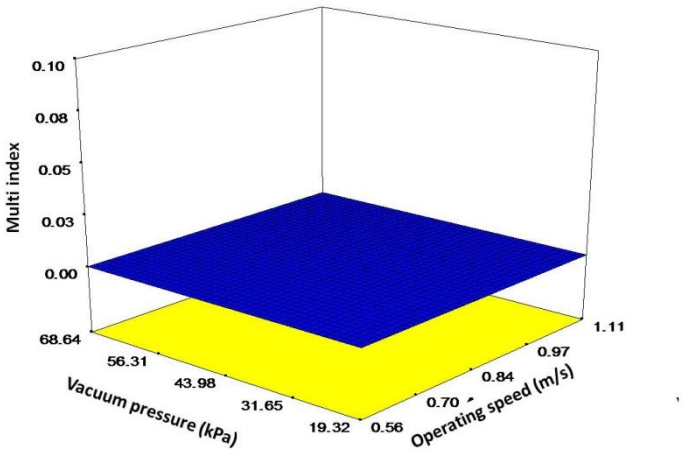

Fig. 3 - Multi index as a function of nozzle diameter

The coded and un-coded models for quality feed index are given in Eqs. 5 and 6. The results from the stepwise regression analysis for each function are given in Table 7. The entire model is significant at the 99% probability level. The lack of fit was significant. The "Pre R-squared" and "Adj R-squared" are given in Table 5. Graphical view of some response surface as drawn using polynomial functions are depicted in fig. 4. This could be considered to be a consistent behaviour of the metering unit as a response to constructional and operating condition.

Quality feed index model in terms of un-coded factors

$$I_{qf} = 0.81352 + 1.06260 * x_1 + 5.1479 \times 10^{-3} x_2 + 0.38597 x_3 - 1.1598 \times 10^{-3} x_2 x_3 - 0.6698 {x_1}^2 \quad \ldots (5)$$

Quality feed index model in terms of coded factors

$$I_{qf} = 1.32 - 0.015 X_1 + 0.18 X_2 + 1.62 \times 10^{-3} X_3 - 0.064 X_2 X_3 - 0.051 {X_1}^2 \quad \ldots (6)$$

Table 7

Results from the stepwise regression analysis for the quality feed index model

Variable	Coefficient	Standard error	Probability (P)	Coefficient of determination (R^2), %
Constant	0.840	0.028	-	-
X_2X_3	-0.064	0.010	<0.0001	66.26
${X_1}^2$	-0.051	0.025	0.0599	72.77

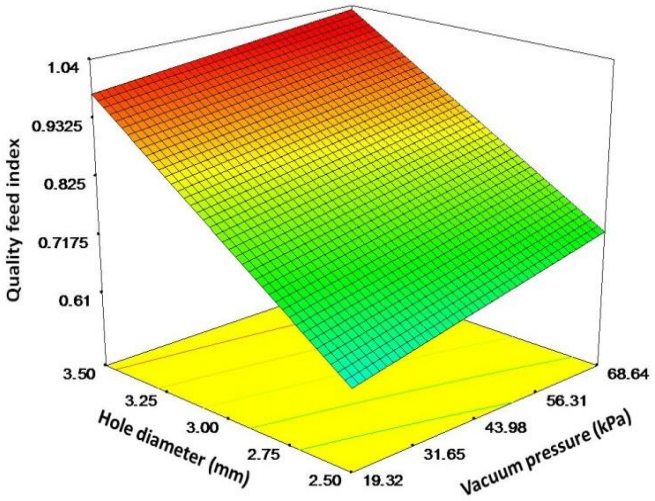

Fig. 4 - Quality feed index as a function of hole diameter and vacuum pressure

Akin to above response, the precision of metering mechanism depends on nozzle diameter. There is only a 0.01% chance that this "model F-value" could occur due to noise. This means the operational parameters, i.e. speed of the planter, had no effect on quality feed index.

A stepwise quadratic multiple regression was developed. The developed model was highly significant. The results of the models are given in Table 8. The highest coefficient of determination was observed 0.54. The coded and un-coded factor models for different seeds are given in Eq. 7 & 8. The major contributing factor is nozzle diameter i.e. 54.40%.

Graphical view of some response surfaces is drawn using polynomial functions as depicted in Fig 5.

Precision model in terms of un-coded factors

$$I_{prec} = 2.91738 - 0.79117x_3 \quad \ldots (7)$$

Precision model in terms of coded factors

$$I_{prec} = 0.54 - 0.40X_3 \quad \ldots (8)$$

Table 8

Results from the stepwise regression analysis for the precision model

Variable	Coefficient	Standard error	Probability (P)	Coefficient of determination (R^2) %
Constant	0.54	0.071	-	-
X_3	-0.40	0.085	0.0002	54.40

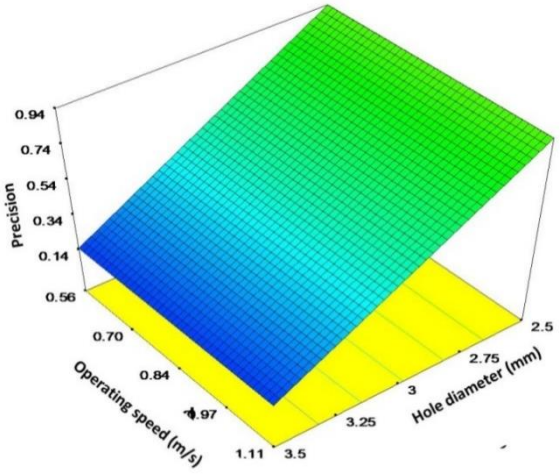

Fig. 5 - Precision as a function of vacuum pressure and nozzle diameter

Optimum Value of the Design

Based on the results from the stepwise quadratic regression analysis, the models are valid for the following conditions:

0.56 m/s < v > 1.11 m/s

29.32 kPa < p > 68.63 kPa

1.50 mm < d > 4.00 mm

The partial derivatives of Eq. 3 to 8 with respect to each independent variable have been considered to obtain the optimum value of operating speed, vacuum pressure and nozzle diameter for vegetable pigeon pea crop. The optimum levels of the nozzle diameter i.e. 3.50 mm, vacuum pressure i.e. 43.98 kPa and operating speed i.e. 0.83 m/s were obtained from different models.

CONCLUSIONS

Based on the present study the main conclusions are:

- Response surface methodology (RSM) is a useful tool for optimizing the performance of a picking type pneumatic planter.
- The coefficient of determination of miss index, quality feed index and precision adequacy are 0.78, 0.75 and 0.54, respectively.
- The nozzle diameter is the most important factor of seed metering mechanism of precision planter for deciding the performance of pigeon pea seed.
- The optimum values of nozzle diameter, vacuum pressure and operating speed are 3.50 mm, 43.98 kPa and 0.83 m/s, respectively.

REFERENCES

[1] Bhimani, J.B., Patel, S.K., Yaduvanshi, B.K., Gupta P. (2019). Optimization of the operational parameters of a picking-type pneumatic planter using response surface methodology. *Journal of AgriSearch*, 6(1): 38-43.

[2] Gaikwad, B. B. & Sirohi N. P. S. (2008). Design of a low-cost pneumatic seeder for nursery plug trays. *Biosystem Engineering*, 99, 322-329.

[3] Jin, X., Li, Q., Zhao, K., Zhao, B., He, Z. & Qi, Z. (2019). Development and test of an electric precision seeder for small-size vegetable seeds. *J Agric & Biol Eng*. 12 (2), 75-81.

[4] Karayel, D., Wiesehoff, M., Ozmerzi, A. and Muller, J. (2006). Laboratory measurement of seed drill seed spacing and velocity of fall of seeds using high-speed camera system. *Computers and Electronics in Agriculture*, 50, 89–96.

[5] Minfeng, J., Yongqian, D., Hongfeng, Y., Haitao, L., Yizhuo, J. & Fu Xiuqing (2018). Optimal Structure Design and Performance Tests of Seed metering Device with Fluted Rollers for Precision Wheat Seeding Machine. *IFAC PapersOnLine*, 51-17, 509–514.

[6] Moody, F. H., Hancock, J. H. and Wilkerson, J. B. (2003). Evaluating planter performance-cotton seed placement accuracy. *Transactions of the ASAE,* Paper No. 03 1146, St Joseph, Michigan, USA.

[7] Panneton, B., Philion, H., Dutilleul, P., Theriault, R. and Khelifi, M. (1999). Full factorial design versus central composite design: Statistical comparison and implications for spray droplet deposition experiments. *Transactions of the ASAE*, 42(4):877–883.

[8] Panning, J. W., Kocher, M. F., Smith, J. A. and Kachman, S. D. (2000). Laboratory and field testing of seed spacing uniformity for sugar beet planters. *Applied Engineering in Agriculture,* 16(1), 7-13.

[9] Singh, R. C., Singh, G. and Saraswat, D. C. (2005). Optimization of design and operational parameters of a pneumatic seed metering device for planting cottonseeds. *Biosystems Engineering*, 92(4), 429-438.

[10] Srivastava, A. K., C. E. Goering, R. P. Rohrbach. 1993. Engineering Principles of Agricultural Machines. *American Society of Agricultural Engineers: ASAE*, St. Joseph-Michigan.

[11] Yazgi, Degirmencioglu & Bayram (2010). Optimization of the Seed Spacing Uniformity Performance of a Precision Seeder Using Spherical Materials and Response Surface Methodology. *Paper presented in ASABE conference*, ASABE Paper 1008560.

MULTI-SENSOR SIGNAL ACQUISITION AND DATA PROCESSING ANALYSIS OF COMBINE HARVESTER

/

联合收割机多传感器信号采集与数据处理分析

Wang Li [1)]*, Li Shuo [1)], Lv Dianji [1)], Ekhlo Ghay [2)]
[1)] Beijing Institute of Economic and Management, Beijing / China
[2)] Exor Group, Amsterdam / Netherlands
**Tel: 18330614933; E-mail: nw9836377laic@163.com*
DOI: https://doi.org/10.35633/inmateh-63-34

Keywords: *combine harvester, multi-sensor, signal acquisition, data processing*

ABSTRACT

In recent years, combine harvesters are increasingly developing in the direction of large-scale, technology, automation and intelligence, and more and more electrical equipment is installed on combine harvesters. The electrical system of combine harvester is prone to failure when it works in high temperature, high humidity, dusty and strong vibration environment. Parameters to be adjusted in the header system of combine harvester include header height, drum height, drum front and back position, cutting frequency and drum speed. Aiming at the inconvenience of debugging and testing the measurement and control system of combine harvester in the field operation environment, an intelligent control test bed of combine harvester was designed. The test bed can simulate various intelligent control algorithms of combine harvester in laboratory environment, control the forward speed of combine harvester according to data processing results, classify faults, and send and print stored data through serial communication. Experiments show that the system works stably and reliably, and can realize the integration of the monitoring system of combine harvester operation process. It can save costs and improve efficiency in the application of the monitoring system of combine harvester.

摘要

近年来，联合收割机日益向大型化、技术化、自动化和智能化方向发展，联合收割机上安装的电气设备越来越多。联合收割机在高温、高湿度、多灰尘和强振动环境中工作，其电气系统容易出现故障。联合收割机割台系统中需要调整的参数包括割台高度、滚筒高度、滚筒前后位置、滚筒速度、切割频率和滚筒速度。针对联合收割机测控系统在田间作业环境下调试和测试的不便，设计了一种联合收割机智能控制试验台。该试验台可以在实验室环境下模拟联合收割机的各种智能控制算法，根据数据处理结果，控制联合收割机的前进速度，进行故障分类处理，并通过串行通信发送和打印存储的数据。实验表明，该系统工作稳定可靠，能够实现联合收割机作业过程监控系统的一体化，在联合收割机测控系统的应用中能够节约成本，提高效率。

INTRODUCTION

As an important tool of modern agriculture and an important material basis of agricultural mechanization, combine harvester has been rapidly developed and widely applied in recent years, and its development degree is related to the enhancement of agricultural productivity and the advancement of agricultural modernization in China *(Chen X et al., 2019)*. At the same time, there are many problems in the actual use of the combine harvester *(Chen Z et al., 2018).* For example, when the forward speed of the combine harvester is not in harmony with the feeding amount, the threshing drum and the conveying trough are easy to be blocked. China is a big agricultural country with a long farming civilization, with a wide grain planting area. The rice planting area is nearly 33,000 square kilometres, accounting for about 1/4 of the total rice planting area in the world, which provides an important opportunity for the automatic harvest of agricultural machinery *(Jhih Y C et al., 2021)*. At present, the degree of automation and intelligence of the combine harvester in China is relatively low. Compared with the advanced combine harvester developed by foreign companies, there are still many problems and shortcomings.

Obtaining the yield information of crop plot and establishing the spatial distribution map of plot yield are the basis for realizing scientific control and investment and making management decision-making measures in the process of crop production *(Yang Y et al., 2021).*

Most of the models of combine harvesters developed in China at present are mainly small and medium-sized ones, which are suitable for local operation, but the automation degree of combine harvesters is increasingly difficult to meet the operation and use requirements of operators. In the process of combine harvester operation in China, the artificial subjective judgment is strong, the operation is cumbersome, and it depends on the daily accumulated experience and training technology of operators for adjustment and control, and the automation and intelligence are low, which seriously restricts the operation efficiency and development of combine harvester *(Jin C et al., 2019).*

In this paper, a multi-sensor signal acquisition and processing system based on microprocessor C8051F020 is designed with a brand of tangential flow combine harvester as the experimental prototype. By analysing the working characteristics of the combine harvester and the working characteristics of each part, the monitoring objects of the system are selected, including cab, granary, header and threshing drum. On this basis, the software and hardware architecture is designed, including the selection of airborne front-end hardware platform and operating system, the selection of peripheral hardware modules, the implementation method of each software module and the design of information processing program, etc., which is used for simulating various intelligent control algorithms of the combine harvester.

Jeong et al *(Jeong W et al., 2020)* analysed the factors of header loss of combine harvester, and put forward a broken grain loss model based on linear statistical model. Based on theoretical mechanical analysis, the model function relationship between reel parameters and crop characteristics was constructed, and the header loss was collected through field experiments, which verified that the data fitting degree of the model was good. Hwang et al. *(Yi Q et al., 2021)* used computer communication technology to package the traveling speed, grain yield, humidity, header lifting state, position information and other data acquired by the onboard data acquisition and processing unit of the harvester and transmit them to the monitoring centre through GSM terminal. Yuan C et al. *(Ng K A et al., 2019)* measured the vibration of the bottom floor of the cab with YE6261B dynamic data acquisition tester to check the vibration resistance of instruments and meters. Japan Kubota Company has done a lot of research on small-sized combine harvesters, and designed an intelligent monitoring and control system by using sensing technology, display device and geographic information system, which was put into use on PRO208 combine harvester *(Ryoei I et al., 2021).* In addition, Shuenn-Yuh et al. *(Shuenn Y and Lee C. 2019)*, a foreign research scholar, designed an agricultural machinery telemetry application system based on OPC-UA standard, which used GPS, CAN-Bus and 3G technology to remotely obtain information such as driving speed, fuel oil, heading direction, crop moisture content and yield of the combine harvester.

MATERIALS AND METHODS

Overall design scheme

When the combine harvester operates in the field, the operators need to adjust the joystick constantly due to the harsh field environment, the fluctuation of terrain and the inconsistent crop growth. Most operators judge and adjust the joystick according to the harvest experience accumulated all the year round. Many mechanical joysticks are a severe test for the operators *(Tasanai P J S et al., 2021)*, so it is necessary to study and improve the control mode of the combine harvester.

The video monitoring system of combine harvester operation site is mainly composed of embedded airborne monitoring front-end system, remote indoor large-screen monitoring centre or hand held mobile monitoring terminal, and Internet of Things platform, as shown in Figure 1.

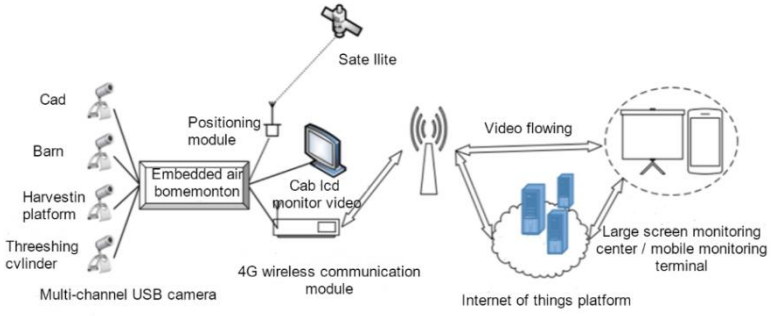

Fig. 1 - Overall scheme of system

The embedded airborne monitoring front-end system is installed and deployed on the combine harvester, which uses GPS module to locate the real-time position of the combine harvester, extracts, calculates and analyses the information of the positioning module, transmits the video image information to the remote indoor large-screen monitoring centre through 4G wireless network, and uploads the positioning information and image data to the Internet of Things platform. Users can log in to the internet of things platform through the mobile app or PC Web, access the image data of the job site of the combine harvester and know its geographical location in time.

Hardware construction

The visual navigation t platform is based on that hardware architecture of the USB bus structure of the vehicle-mounted computer (fig. 2), including the high-speed data collector N I 2 USB6211.

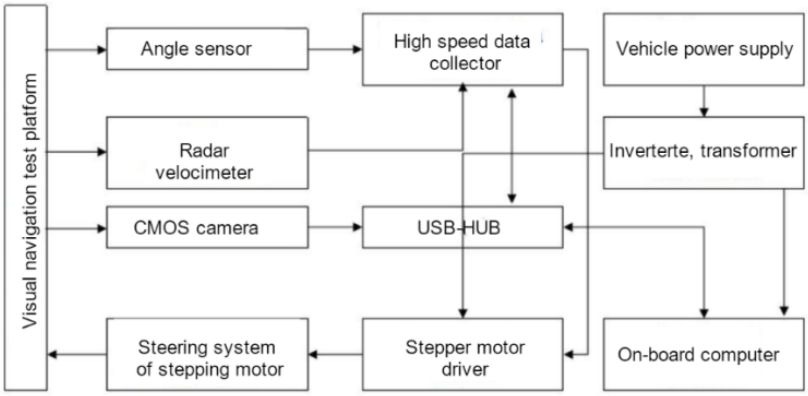

Fig. 2 - Hardware structure of visual navigation control system of combine harvester

The vehicle-mounted power supply is used to invert AC220V, boost voltage to obtain 24V, and DC2DC conversion to obtain 5V, which is convenient for the control system. NI2USB6211 provides 12 channels of A/D conversion, 2 channels of timers to generate pulses or count, and 4 channels of TTLI/O, which are mainly used to collect angular displacement voltage and radar velocimeter speed signals, and generate pulse signals with specified frequency for stepper motor drivers *(Moreno E et al., 2020) (Ng K A et al., 2019)*. All expansion circuits and boards are packaged in anti-interference metal box, and the interface adopts unified aviation plug mode, which is convenient for use in harsh environment to improve the stability of the system.

The control system is mainly used to control the forward speed of the test trolley, collect multi-channel rotational speed signals such as simulated roller and screw conveyor, and give alarm and display. FX3U-64MT PLC (Programmable Logic Controller) is selected as the intelligent control module, which integrates almost all analog and digital peripherals and other functional components required by the control system, and it also has powerful communication function. In the signal acquisition module, a plurality of corresponding multisensors are input into the controller through corresponding conditioning circuits to complete signal acquisition; The LCD (Liquid Crystal Display) module adopts HD104MK type display, and the acousto-optic alarm module prompts the fault type through the blinking of buzzer and LED (Light-Emitting Diode) lamp. The parameter setting module sets the parameters by 6 buttons: "Automatic", "Manual", "Screen Control", "+","-"and "Confirm" *(Jin C et al., 2018)*.

The detection of the speed and forward speed of the reel of the combine harvester belongs to the field of speed measurement. Commonly used speed measurement methods are: magnetoelectric speed measurement method, magnetic sensitive speed measurement method, capacitive speed measurement method, pulse number speed measurement method, etc. Considering the harsh working environment of the combine harvester, which is affected by water, grease, dust and vibration, the photoelectric and capacitive multi-sensors are easy to bring measurement errors. In this paper, the magnetoelectric multi-sensors are selected for speed measurement.

The main working principle of magnetoelectric Haldore sensor is to detect the magnetic field with polar magnetic steel and send out pulse signals, which are sent to the controller for subsequent processing after being shaped *(Qiao N et al., 2020).*

Because the controller adopts PLC, which has high anti-interference ability, the signal at the input end is connected to the internal LED lamp of the photoelectric coupler, and the photoelectric tube of the photoelectric coupler receives the input signal, which can realize reliable transmission with external signals *(Rahman M et al., 2019).* The detection principle is shown in Figure 3.

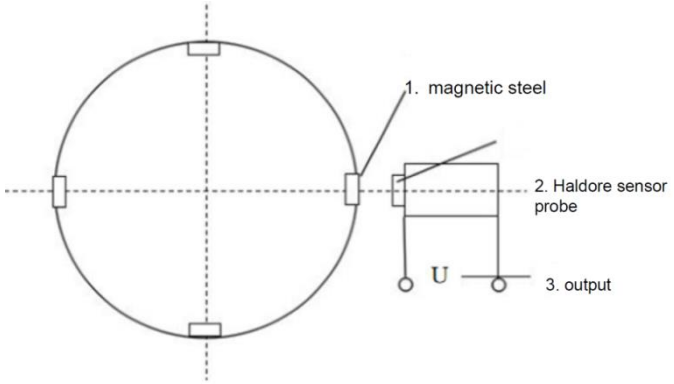

Fig. 3 - Detection principle of Haldore sensor

The pulse signal sent by Haldore sensor has poor waveform edge in actual acquisition. In order to better acquire the signal waveform of Haldore sensor, filter and shape the signal, the circuit design is shown in Figure 4.

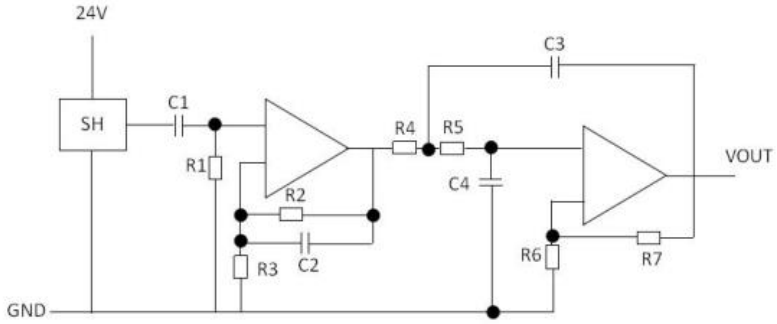

Fig. 4 - Design drawing of Haldore sensor signal acquisition circuit

Fuzzy PID algorithm

The working condition of combine harvester is complex, and the adjustment of reel speed is easily affected by machine vibration and inertia. The stability of control system constructed by conventional PID control method is poor. The three coefficients of conventional PID controller need to be adjusted manually, and it is difficult to meet the system control requirements with strong time variability. To obtain satisfactory control effect, it is necessary to continuously adjust the three coefficients of PID controller online.

PID control, also known as PID regulation, is a mature and widely used control system with simple principle, convenient structure, flexibility, high efficiency and easy adjustment. It consists of three parts: proportional control unit (P), integral control unit (I) and differential control unit (D).

Fuzzy PID controller is composed of fuzzy controller and PID regulator. Deviation e and deviation change rate $\triangle e$ are the input variables of fuzzy controller. Then, according to fuzzy control rules, logic reasoning and defuzzification are carried out, and three adjustment coefficients $k_{p,}k_{i,}\,k_d$ of the controller are adjusted online. The linear combination of them constitutes the actual control quantity, which controls the output of the controlled object.

Set $u(t)$ as the output during t sampling, $e(t)$as the deviation during t sampling period, T as the sampling period, and the calculation formula of output control quantity is:

$$u(t)=k_p e(t_i)+k_i T\sum_{i=1}^{t} e(t_i)+k_d\left[e(t_i)-e(t_{i-1})\right] \quad (1)$$

The formula for calculating the speed deviation $e(t)$ of reel at time t and the rate of deviation change $\triangle e$ is as follows:

$$e(t_i) = n_i - n_i' \tag{2}$$

$$\Delta e = \frac{e(t_i) - e(t_{i-1})}{t_i - t_{i-1}} \tag{3}$$

Where n_i is the target value of reel speed n_i is the current sampling value of reel speed.

Control quantity of navigation controller

In order to make the navigation controller speed adaptive, the influence of driving speed on the control quantity u must be considered. Therefore, through the preliminary road test research, the control gain K of the controller, a control period T, the distance ζ travelled in the control period, the relationship between the processing frame number Γ and the driving speed v in the control period are analysed.

In order to improve the rapid response capability of the controller, the PD controller is designed, and the calculation formula of the control quantity u_k of the computer control system is *(Cai H Y et al., 2021):*

$$u_k = K(\zeta_p e_k + \zeta_d \bar{e}_k) \tag{4}$$

Where:

e_k, $\bar{e}_k$———Current navigation path deviation and deviation change rate;

ζ_p, ζ_d———Proportional coefficient and differential coefficient;

K———Scale factor, which is equivalent to the gain of the system.

Setting $\zeta_p+\zeta_d=1$, these two coefficients directly determine the effect of deviation and deviation change rate. Based on the experience of manual driving, fuzzy design method is adopted, which is described in detail in reference *(Song X.J. 2019)* and will not be repeated.

The navigation path parameters detected by vision are converted into the current heading deviation θ_k and dead-end deviation d_k. According to the analysis of navigation path detection error in literature *(Xu L et al., 2019)*, when the angle is small, the angle detection error is better than the intercept detection error, so the deviation e_k is:

$$e_k = \begin{cases} (\theta_k - \theta_o)/\theta_m & (\theta_k \geq \delta \text{ or } \theta_k \leq -\delta) \\ (d_k - d_o)/d_m & (-\delta < \theta_k < \delta) \end{cases} \tag{5}$$

Where:

θ_o, d_o———Target heading angle and target dead position deviation;

θ_m, d_m———Maximum value of heading deviation and dead position deviation;

δ———The allowable threshold of course deviation is obtained from the test.

Software design

Collection and processing of feeding amount and loss amount are completed in serial port interrupt 0. The baud rate of serial port initialization configuration is 115 200 b/s, and the serial port sending protocol is shown in Figure 5.

Preamble	MID	LEN	DATA	Checksum

Description of the agreement:

Field	Field width	Discription
Preamble	1 Byte	Instruct development to send one frame of data (0xFA)
MID	1 Byte	The frame information ID indicates the transmitted frame type
LEN	1Byte	Data length (fixed at 8 bytes in case of double)
DATA	LEN Byte	Data (the number of data sent depends on the size of LEN)
Checksum	1 Byte	Check bit: subtract all transmissions except the frame header with zeroSum of bytes

Fig. 5 - Serial port sending protocol

At first, the received byte is judged by serial port interruption, if it is 0xFA, then 11 bytes of DATA received subsequently are put into the array R Data *(Yan L et al., 2021)*, and these 11 bytes of data are summed and verified. After the verification is passed, the MID bit is judged, if MID is 0x00, it is the feeding amount signal, and the data is processed, and the result is put into the global variable; If MID is 0x01, it is a loss signal. Data is processed, and the result is put into the global variable. The dynamic digital display subroutine in the main program realizes the dynamic refresh of feeding amount and loss amount by processing these two global variables.

The test bed adopts different algorithms for different tests, which can optimize the selection of algorithms. Fig. 6 is the subroutine flow of multi-information fusion fuzzy control algorithm for controlling forward speed *(Zhang Z G et al., 2019)*.

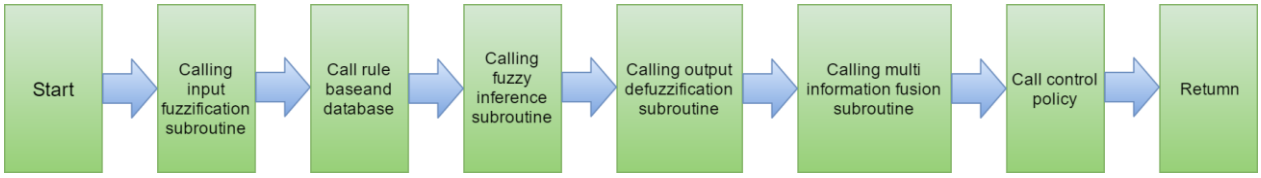

Fig. 6 - Multi-information fusion fuzzy control algorithm subroutine flow chart

The subroutines of multi-information fusion fuzzy control algorithm are as follows: calling input fuzzification subroutine, calling rule base and database, calling fuzzy inference subroutine, calling output fuzzification subroutine, calling multi-information fusion subroutine and calling control strategy. Then, according to the algorithm results, it is judged whether the forward speed needs to be adjusted, and if so, the stepper motor control subroutine is called to reasonably adjust the forward speed, thus completing the intelligent control of the forward speed of the combine harvester. At the same time, the test bench can adopt different control algorithms for the same test, for example, the forward speed can also adopt grey prediction fuzzy control algorithm *(Chavdar V et al., 2021)*.

RESULTS

Data acquisition experiment

Table 1 shows the parameters such as forward speed, conveying trough rotation speed, drum rotation speed, header screw conveyor rotation speed, feed rate and loss rate collected under normal working conditions of the test bench. The results show that the data collected by the test bed is accurate and reliable.

Table 1

Data acquisition results

Time (s)	Speed of advance ($r \cdot min^{-1}$)	Rotating speed of drum ($r \cdot min^{-1}$)	Rotating speed of conveying trough ($r \cdot min^{-1}$)	Rotating speed of header auger ($r \cdot min^{-1}$)	Feeding amount ($kg \cdot s^{-1}$)	Loss rate (%)
0	0.3	720	336	155	4.2	0.41
1	0.3	720	320	160	4.0	0.44
2	0.3	720	305	140	4.3	0.39
2	0.3	714	307	150	3.9	0.45
4	0.3	711	325	152	3.8	0.41
5	0.3	696	310	145	4.0	0.41
6	0.3	716	327	161	4.2	0.50
7	0.4	682	311	153	3.8	1.46
8	0.4	693	308	155	3.9	0.44
9	0.4	701	317	140	4.1	0.51
10	0.3	708	303	146	4.0	0.46

Error analysis of cutting width setting

When setting the cutting width, if the set value is larger than the actual value, the calculated plot area is larger than the actual harvest area, which further leads to the output value of this point being smaller than the actual value, and the low-yield point will appear on the output map.

If it is less than the actual value, the high-yield point will appear on the yield map. In this way, the cutting width is set according to the observation of the harvester operator, and the operator must modify the cutting width according to the actual situation. The usual method is to eliminate these data which are not satisfied with the cut width records, because the data points collected by the harvester are very dense, it will not have much influence on the final yield distribution map.

Table 2

Comparison of data column of cutting width setting error with data of adjacent columns

Data column	Number of Production points	Maximum output (kg·hm^{-2})	Minimum yield (kg·hm^{-2})	Average output (kg·hm^{-2})
1	80	5532	778	4120
2	79	4780	2566	3860
3	36	8933	1890	6250
4	69	3560	2310	3571
5	70	3917	2428	3690

In the harvesting process, a series of high-yield points appeared in the original data table because the cutting width set by visual inspection at that time was smaller than the width of crops actually entering the header. In Table 2, the data in this column is compared with the adjacent columns, and the output varies greatly. The average output of this column is 6250 kg·hm^{-2}, while the average output of adjacent columns is less than 412 kg·hm^{-2}. The header width of the combine harvester is 6m, so the interval between two adjacent columns of data is about 6m. However, the output data cannot change greatly in a small range, so there are errors in this column of data.

Vibration acceleration

Test 1

Install acceleration multi-sensors in horizontal direction, vertical direction and axial direction in the middle frame position of the header of the combine harvester, and start collecting and saving data after the engine of the combine harvester accelerates to run stably, as shown in Table 3.

Table 3

Test 1 - Vibration acceleration

Condition	Direction	Experiment serial number				
		1	2	3	4	5
Working condition 1	Horizontal direction	0.124	0.178	0.171	0.169	0.166
	Normal direction	0.141	0.122	0.142	0.138	0.130
	Axial	0.136	0.130	0.133	0.136	0.134
Working condition 2	Horizontal direction	2.150	2.514	2.529	2.551	2.530
	Normal direction	2.036	1.948	2.014	2.058	2.026
	Axial	1.966	1.902	1.963	1.984	1.985

The two working conditions of this test are: only the engine rotates at the big throttle (working condition 1), and the big throttle of the engine runs together with the cutter transmission system (working condition 2). Judging from the data, the vibration of the header in the horizontal direction is the largest. The maximum acceleration in horizontal direction is 0.178 when the big throttle engine rotates, and 2.551 when the big throttle engine runs together with the cutter transmission system.

Test 2

In this test, the horizontal vibration conditions of the three positions near the cutter, the frame above the header shield and the header bridge at the same time are measured, and the data under different working conditions are shown in Table 4. The working conditions are small throttle rotation (working condition 1), middle throttle rotation (working condition 2), big throttle rotation (working condition 3), big throttle rotation, cutter transmission system (working condition 4) and middle throttle 2-gear traveling transportation state (working condition 5).

Table 4

Test 2 - Vibration acceleration

Location	Experiment serial number	Working condition				
		1	2	3	4	5
Near the cutter	1	0.022	0.021	0.428	1.569	0.033
	2	0.011	0.024	0.021	1.669	0.043
	3	0.025	0.026	0.368	1.718	0.039
Frame above shield	1	0.145	0.139	0.166	2.556	0.203
	2	0.106	0.120	0.184	2.690	0.196
	3	0.151	0.137	1.77	2.714	0.188
The harvesting platform crosses the bridge	1	0.081	0.162	0.225	2.512	0.223
	2	0.096	0.177	0.206	2.501	0.310
	3	0.088	0.180	0.329	2.886	0.281

Through data analysis, it is concluded that the vibration of the header is the largest at the bridge position, with the maximum horizontal acceleration of 2.886, followed by the frame above the header shield and the smallest near the cutter.

Study on the correlation between manual determination of particulate impurities and multi-sensor determination of particulate impurities

By adjusting the advancing speed, calibration experiments were carried out in the field, and different rheological properties of materials were obtained. The test temperature is 18℃ and the ambient humidity is 68%. Experiments were carried out at three different forward speeds of 0.6, 1.0 and 1.3 m/s, which were related to the feed speeds of 1.5, 2.0 and 2.3kg/s, respectively. The quantity and discharge speed of grain and non-grain materials discharged from grain box auger are affected by their rheological properties, which largely depend on the output of combine harvester. Therefore, the forward speed of the combine harvester is set to three levels to obtain different rheological properties of materials, and the sampling device is installed below the outlet of the diversion tunnel of the granary.

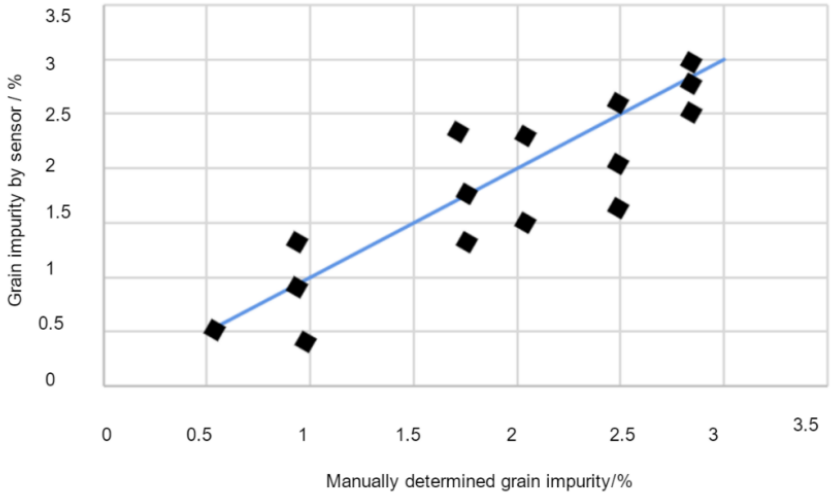

Fig. 7 - Correlation between manual determination of grain impurities and multi-sensor determination of grain impurities

In order to verify the influence of different grain impurities on the image, the same event was shot at different straw levels. It is observed that with the control of grain impurities, the average number of straw in the visual window increases; However, because the clarity of the image depends on the brightness of the image, the influence of illumination is easily ignored. By analysing the relationship between multi-sensor and manual determination of impurities, a correlation was found, as shown in Figure 7.

CONCLUSIONS

This paper designs the overall scheme of combine video monitoring system, analyses the working process of combine, and selects the monitoring object of the system. According to the overall scheme of the system, the appropriate embedded hardware and software platform and peripheral hardware modules are selected, and the overall hardware architecture and software architecture of the system are designed completely. The designed double closed-loop PD controller can effectively change the control parameters dynamically according to the change of driving speed. The motor module is used to simulate the rotation speed of the combine drum, conveyor trough, header screw conveyor and other rotating parts, and the simulation module is used to simulate the feeding process and loss process. The intelligent control algorithm of the forward speed of the test bed is tested, and the expected effect is achieved. Although the anti-interference measures such as filtering and shaping are used in the circuit design, it will still interfere with the signal acquisition of the whole system. We can consider sending information to the controller through the industrial bus to improve the anti-interference and stability of the whole system.

REFERENCES

[1] Cai H.Y., Li F.Z., Lv P., Ran L.J., Zou L.D., (2021). Intelligent aquaculture environment monitoring system based on lora communication technology. *INMATEH Agricultural Engineering*, Vol.63, Issue 01, pp.107-118. Romania;

[2] Chavdar V., Atanas A., Valentin V., (2021), Calculation of field capacity and fuel consumption of mobile machinery with bunkers, tanks or other containers for agricultural goods. *INMATEH Agricultural Engineering,* Vol.63, Issue 01, pp.19-28. Romania;

[3] Chen X., Wu C.Y, Sharla C., (2019). Design and research of grain combine harvester yield measurement system. *Chinese Journal of Agricultural Machinery Chemistry,* Vol.40, Issue 308-10, pp.26-30. China;

[4] Chen Z., Wu H.C., Zhang Y.H., (2018), Development of automatic depth limiting system for semi-fed four-row peanut combine harvester. *Journal of Agricultural Engineering,* Vol.34, Issue 15, pp.18-26. China;

[5] Jeong W., Tsingas C., Almubarak M.S., (2020). A numerical study on deblending of land simultaneous shooting acquisition data via rank-reduction filtering and signal enhancement applications. *Geophysical Prospecting*, Vol.68, Issue 6. United Kingdom;

[6] Jhih Y.C., Hsin C.C., Chih W.C., Kai M.Y., (2021), Relationship between Antioxidant Components and Oxidative Stability of Peanut Oils as Affected by Roasting Temperatures. *MDPI (Agriculture)*, Vol. 11, Issue 004, pp. 300. Switzerland;

[7] Jin C., Lian Y., Li Y.M., (2019). Design of sampling box for rice impurity rate sensor in grain bin of combine harvester. *Journal of Agricultural Engineering,* Vol.035, Issue 005, pp.18-25. China

[8] Jin C., Wang Y.H., Lian Y., (2018). Development of on-line monitoring device for grain moisture content of high-frequency capacitive combine harvester. *Journal of Agricultural Engineering,* Vol.34, Issue 10, pp.36-45. China;

[9] Tasanai P.J.S., Maliwan N., Somjit H., Phithak I., Anupan K.K., (2021). Production and Molecular Identification of Interspecific Hybrids between Phaius mishmensis (Lindl. and Paxton) and Phaius tankervilleae (Banks) Blume. MDPI (Agriculture), Vol. 11, Issue 004, pp. 306. Switzerland;

[10] Moreno E., Jess J., Morales M.O., Tejeida P.R., (2020). Biomedical Signal Acquisition Using Sensors under the Paradigm of Parallel Computing. *Sensors,* Vol.20, Issue. 23, p.6991. Switzerland;

[11] Ng K.A., Yuan C., Rusly A., (2019), A Wireless Multi-Channel Peripheral Nerve Signal Acquisition System-on-Chip. *IEEE Journal of Solid-State Circuits,* Vol.54, Issue 99, pp.2266-2280. United States;

[12] Ng K.A., Yuan C., Rusly A., (2019), A Wireless Multi-Channel Peripheral Nerve Signal Acquisition System-on-Chip. *IEEE Journal of Solid-State Circuits,* Vol.54, Issue 99, pp.2266-2280. United States;

[13] Qiao N., Wang L., Zhu W., (2020). An improved path-tracking controller with mid-angle adaptive calibration for combine harvester. *Journal of Instrumentation*, Vol.15, Issue 01, P01025. United Kingdom;

[14] Rahman M.M., Ishii K., Noguchi N., (2019), Optimum harvesting area of convex and concave polygon field for path planning of robot combine harvester. *Intelligent Service Robotics*, Issue 24, pp.1-13. Germany;

[15] Ryoei I., Takamitsu K., (2021), Development of paddy-field water level gage corresponding to a sensor-network. *INMATEH Agricultural Engineering,* Vol.63, Issue 1, pp.129-134. Romania*;*

[16] Shuenn Y., Lee C., (2019). Ultra-High-Frequency Radio-Frequency-Identification Baseband Processor Design for Bio-Signal Acquisition and Wireless Transmission in Healthcare System. *IEEE Transactions on Consumer Electronics,* Vol.66, Issue 1, pp.77-86. United States;

[17] Song X.J., (2019), A brief description of multi-sensor data processing and fusion. *Science and information technology,* Vol.000, Issue 003, pp.21-21. China;

[18] Xu L., Wei C., Liang Z., (2019), Development of rapeseed cleaning loss monitoring system and experiments in a combine harvester - ScienceDirect. *Biosystems Engineering,* Issue 178, pp.118-130. United States;

[19] Yang Y., Chun R.Q., Wan R.G., Cai F.L., (2021), Responses of root characteristic parameters and plant dry matter accumulation, distribution and transportation to nitrogen levels for spring maize in Northeast China. *MDPI(Agriculture)*, Vol.11, Issue 4, p.308. Switzerland;

[20] Yi Q., Dai X.F., Chen Z., Dai N.Z., Mi L.K., (2021). Numerical simulation and experimental study of inner flow field of seed pelleting premixer in spouted fluidized bed. *INMATEH Agricultural Engineering,* Vol.63, Issue 1, pp.239-246. Romania;

[21] Yan L., Xiao D.S., Jin W., Qiang D., Chao Y.W., Chun B.D., Tian L., (2021). Effects of nitrogen application rate on protein components and yield of low-gluten rice. *MDPI(Agriculture),* Vol.11, Issue 4, pp.302. Switzerland;

[22] Zhang Z.G., Peng C., Sun Y.F., (2019). Signal analysis and processing of feed monitoring system of combine harvester. *Journal of Agricultural Machinery*, Vol.50, Issue S1, pp.80-85. China.

ANALYSIS OF ELECTRIC CONTROL SYSTEM OF RICE TRANSPLANTER UNDER WSN (WIRELESS SENSOR NETWORK)
/
WSN (WIRELESS SENSOR NETWORK)主导下的水稻插秧机电控系统分析

Ruibin Niu[1)]*, Hongwei Yao[1)], Xindi Tong[1)], Asmat Algabri[2)]
[1)]Department of Electronic Information, Xinxiang Vocational and Technical College, Xinxiang, Henan, 453006, China
[2)]Trafigura Group, Singapore
** E-mail: sqr7210698shi@163.com*
DOI: https:// doi.org/10.35633/inmateh-63-35

Keywords: *WSN, rice transplanter, electromechanical control system, optimize*

ABSTRACT

In rice planting technology, the planting depth of seedlings has high requirements for transplanters, which directly determines the survival rate and tillering effect of seedlings. Aiming at the problems of low automation degree and low working efficiency of rice transplanter, the rice transplanter is designed under WSN (Wireless Sensor Network) technology, and its electric control system is optimized and analysed. In this paper, in order to optimize the overall working performance of the electronic control mechanism system of adjustable width and narrow row high-speed rice transplanter, the discipline analysis of the electronic control mechanism system is carried out based on WSN (Wireless Sensor Network) technology. Combined with the working characteristics of electronic control mechanism and the influence index of design parameters, the multidisciplinary design optimization framework of electronic control mechanism is established, and the optimization objectives, design variables and constraints at system level and discipline level are determined, and the multidisciplinary design optimization mathematical model of electronic control mechanism is constructed. Finally, the optimization results are analysed. The results show that the optimized design variable value can significantly improve the overall working performance of the adjusting mechanism of the electronic control system.

摘要

在水稻种植技术中，秧苗的栽插深度对插秧机有很高的要求，直接决定着秧苗的成活率及分蘖效果。针对水稻插秧机自动化程度不高、工作效率较低的问题，在 WSN 技术下对水稻插秧机进行了设计，并对其电控系统进行优化并分析。本文以优化可调宽窄行高速水稻插秧机电控调节机构系统整体工作性能最优为目的。基于 WSN(Wireless Sensor Network) 技术对电控调节机构系统进行了学科分析，结合电控调节机构的工作特性和设计参数的影响指数，建立电控调节机构的多学科设计优化框架，确定了系统级和学科级的优化目标、设计变量和约束条件，构建出电控调节机构多学科设计优化数学模型。最后对优化结果进行了分析，结果表明，优化所得的设计变量值使得电控系统调节机构的整体工作性能显著提高。

INTRODUCTION

China has a vast territory and the largest rice planting area in the world, with an area of about 27 million hectares. The rice planting area in China has a very large span, and there are many types and varieties of rice. The development type of rice transplanting technology determines the development mode of rice transplanting mechanization *(Chaitanya D.N.V. et al., 2018; Feng X.T. et al., 2018)*. Wide-narrow row rice planting mode promoted in recent years is a direct embodiment of the idea of combining transplanting density. Wide-narrow row rice planting is a new planting mode put forward by agricultural researchers in China. Practical research shows that this planting mode can effectively improve the ventilation and light transmission characteristics and photosynthesis of rice, reduce the humidity between plants, effectively reduce the occurrence of rice diseases and insect pests, and is beneficial to the later field management, prevent lodging and increase the yield per unit area *(He J. et al., 2020).*

With the promotion and popularization of agricultural mechanization, the proportion of mechanized rice transplanting has been increasing, and the transplanter industry in China is also developing rapidly *(Jiangtao J. et al., 2020).* The front wheel positioning parameters of rice transplanter are important performance parameters of the steering system of rice transplanter.

Whether these parameters are designed reasonably or not is directly related to the steering performance of rice transplanter and the whole vehicle. For example, the reversibility of vehicles, the stability of straight running, the stability of braking and the portability of steering are mainly affected by the caster angle. However, there is still a big gap between China's agricultural mechanization level and Europe and America in rice planting, high efficiency work and intelligent control level *(Jin X. et al., 2018; Lee P.U. et al., 2018)*, so it is of great significance to develop intelligent rice transplanter for the development of China's agriculture. With the development of microelectronic system, system-on-chip and wireless communication technology, WSN (Wireless Sensor Network), which integrates sensing technology, microprocessor technology, embedded operating system, modern network, wireless communication technology and distributed information processing technology, has developed rapidly and significantly in recent years *(Li G. et al., 2018)*. Its development and application will bring far-reaching influence to all fields of human life and production. The research and application of WSN is an inevitable trend, and its appearance will bring great changes to human society, so it has been paid attention to by scientific research and commercial institutions in various countries. The electric control system is one of the key components to ensure the reliable and stable operation of rice transplanter. In order to make the rice transplanter work intelligently and efficiently, WSN technology was applied to the rice transplanter, and the electric control system was optimized and improved.

In the research of reference *(Li G. et al., 2020)*, the co-simulation optimization method is applied to the optimization design of the controlled rotating arm, and the mechanism system and the control system of the research object are simulated in parallel, and the design parameters of the two systems are optimized cooperatively. The parameter results obtained by the joint simulation optimization method can reduce the deformation energy of the rotating arm mechanism in the working process, and obviously improve the overall working stability of the system. Literature *(Peng H.H. and Shang Y.C., 2021)* puts forward a cooperative optimization method, which is different from the cooperative optimization algorithm in that there is no transmission of coupled design parameter data flow between each subsystem discipline, and it is a relatively completely independent space, and the constraints of subsystem discipline only assist the process of solving and optimizing this discipline. Literature *(Putri R.E. et al., 2020)* takes the manipulator as the research object, adds simulated stress and boundary conditions to its finite element model, and uses Shape Finder to optimize the structure of the research object. On the premise that the working strength of the manipulator system is taken as the constraint condition, the structural weight is reduced and the first-order natural frequency of the optimization target is effectively improved, and the working performance of the manipulator system is significantly improved. In the process of structural optimization design of the manipulator, this method is feasible and efficient.

Literature *(Samal P. et al., 2018)* studies the influence of front wheel alignment parameters on vehicle shimmy. The curves of camber angle and front wheel shimmy amplitude and the relationship between kingpin caster angle and front wheel shimmy amplitude are obtained through experiments. This experiment shows that kingpin caster angle and front wheel camber angle have great influence on front wheel shimmy. Literature *(Siddique A.A. et al., 2020)* designed the row spacing of wide row planting to be 297mm and that of narrow row planting to be 198 mm. Investigation after harvesting shows that: Compared with equal row spacing planting, the number of effective ears per hole increased by 0.96, the number of grains per ear increased by 10.7, the weight of 1000 grains increased by 0.5g, and the yield per mu increased by 50.06 kg and 9.1%. In reference *(Siddique M.A.A. et al., 2020),* planting with equal row spacing and planting with wide and narrow rows were carried out respectively (the width and narrow rows increased or decreased by 50mm respectively compared with the equal row mode). The results showed that the actual yield of wide and narrow row planting mode per hectare was 400 ~ 500 kg more than that of equal row spacing planting mode *(Sun X.Z., 2018)* Based on the riding type, the transplanting mechanism was improved, and the world's first wide and narrow row transplanter was born. The row spacing of the transplanter was 400mm and 200mm, and the field experiment was successful.

MATERIALS AND METHODS

WSN architecture

The system architecture of WSN is shown in Figure 1, which includes sensor nodes, coordinator nodes (also called aggregation nodes), monitoring stations and network protocols. The data monitored by sensor nodes are transmitted along other sensor nodes in multi-hops.

During the transmission, the monitoring data may be processed by multiple nodes, routed to the coordinator nodes in multi-hops, and finally sent to the monitoring station through the Internet or wireless network *(Ahn T.I. et al., 2020; Tong X.F., 2020).* Users configure and manage the sensor network, send monitoring tasks and receive monitoring data by giving operation instructions to nodes.

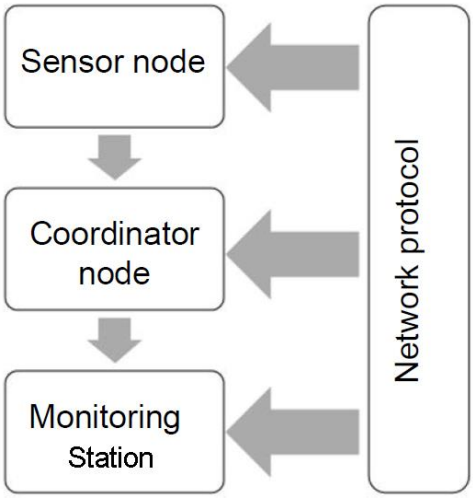

Fig. 1 - WSN system architecture diagram

Sensor network node is a miniaturized embedded system, which constitutes the basic support platform of WSN. The node part consists of four parts: sensor module, processor module, wireless communication module and power supply module *(Wang X.Z. and Li Y.D., 2018)*, as shown in Figure 2.

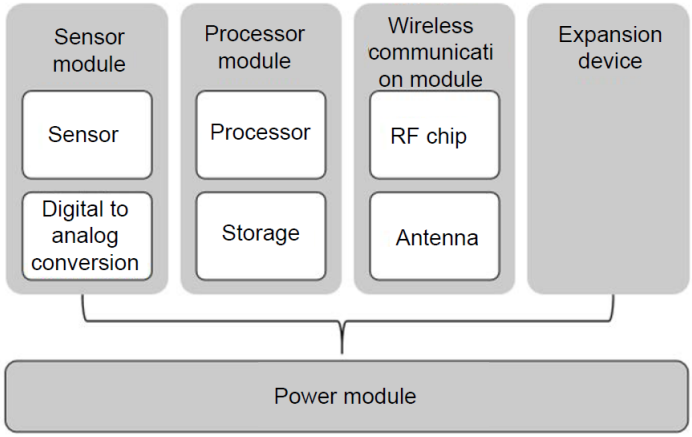

Fig. 2 - Composition of WSN nodes

They are responsible for their own work:

(1) The data acquisition module of sensor module is composed of sensor and A/D converter, which is responsible for collecting information in the monitoring area, converting data format, converting original analog signals into digital signals, and converting AC signals into DC signals for subsequent modules to use *(Wen C.J. et al., 2018; Wen F. and Fu K., 2019);*

(2) The processor module is divided into two parts, processor and memory, which are responsible for the control of processing nodes and data storage. The data processing and control module includes memory and microprocessor, which controls the operation of the whole sensor node, processes and stores the data collected by itself and the data sent by other nodes.

(3) The wireless communication module is composed of radio transceiver devices such as radio frequency chips and antennas, and is specially responsible for the mutual communication between nodes *(Xinchun Y. and Meihua, 2018).*

(4) The power supply module is used to provide energy for the sensor nodes, which is generally powered by miniature batteries.

Establishment of mathematical model for design optimization of electric control adjusting mechanism

The structure of mechatronics system is complex, especially that the mechanical subsystem has many design variables, complex constraints, complex mathematical models, and it is difficult to get effective and comprehensive objective functions.

The optimization analysis process is slow, the efficiency is low, and the decoupling effect is not necessarily ideal, which cannot meet the requirements of optimal design.

In the process of designing and optimizing the electric control mechanism of the adjustable wide and narrow row high-speed rice transplanter, the discipline analysis of the structure is needed first. According to the different characteristics of the research object, the system is decomposed into several independent sub-discipline systems, and all the subsystems obtained by decomposition can be analysed and optimized based on the existing mature basic theory of disciplines. Combined with the working characteristics of the electronic control mechanism and the corresponding design theory knowledge, the decomposed subsystems are divided into four relatively independent subsystems for discipline analysis: structural mechanics system, dynamics system, kinematics system and control system.

Therefore, considering the stability of components and the overall energy consumption, the smaller the weight of the adjusting mechanism, the smaller the inertia and energy consumption of the structure.

Therefore, it is necessary to analyse the static strength of the structure, and the structure should be as light as possible while satisfying the deformation and strength.

The installation position of the electric control adjusting mechanism is the middle and upper part of the seedling box. The seedling box moves back and forth at high speed in the process of transplanting rice, and at the same time, the transplanting arm is in a working state of rotating at high speed, so the whole unit of the seedling box in operation is always in a vibrating state. In the process of rotation adjustment, the unbalanced balance of inertia force will lead to the vibration of the mechanism itself. In order to avoid the resonance between the adjusting mechanism and the seedling box unit, it is necessary to analyse the structural vibration of the mechanism to minimize the vibration influence of the adjusting mechanism in operation. Reasonable structural design and optimal optimization scheme are to ensure that the high-speed rice transplanter can stably, effectively and accurately adjust the row spacing of rice transplanter under the action of the electronic control mechanism. The transmission efficiency of the mechanism system can be maximized under different working environments and working conditions.

Multidisciplinary design optimization method is derived from the theoretical basis of traditional optimization design method. Compared with traditional optimization design method, multidisciplinary design optimization method has more optimization strategies, and there will be a most suitable optimization scheme for different optimization objectives. The serial optimization method of traditional optimization design method will be developed into a parallel method for simultaneous optimization of multiple subsystems, which will more effectively decompose complex large modules into special small modules, and solve the highly coupled system-level optimization problem with effective subsystems and optimization strategies.

The optimization model of traditional optimization design method is as follows *(Yang X.D. and Zhang S.X., 2019)*:

$$Min: f(x) \tag{1}$$

$$s.t.: \begin{cases} g_i(x) \geq 0 \quad (i = 1,2,\cdots,m_1) \\ h_i(x) = 0 \quad (j = 1,2,\cdots,m_2) \\ x_{\min} \leq x \leq x_{\max} \end{cases} \tag{2}$$

In formulas (1) and (2), f is an objective function, x is a design variable, $g_i(x)$ is an inequality constraint, and $h_i(x)$ is an equality constraint.

It is necessary to separate the traditional optimization model from multiple subsystems when the traditional optimization design method is derived and developed into multidisciplinary optimization design.

The multidisciplinary design optimization model after separating the optimization model in the above formula from subsystems is as follows:

$$Min: f(x) = f\left(f_1(x, x_1, y_1), f_2(x, x_2, y_2), \cdots, f_n(x, x_n, y_n)\right) \tag{3}$$

$$s.t.: \begin{cases} g_i(x, x_i, y_i) \geq 0 \\ h_i(x, x_i, y_i) = 0 \\ E_i\left(x, x_i, y_i, y_{i1}(x, x_1, y_1), \cdots, y_{ij}(x, x_i, y_i), \cdots, y_{in}(x, x_n, y_n)\right) = 0 \end{cases} \tag{4}$$

In formulas (3) and (4), $i,j=1,2,...,n,i\neq j$; $f_1,...,f_n$ is the objective function of each subsystem level, x is the system level design variable, x_i is the subsystem level design variable, y_i is the subsystem level state variable, and y_{ij} is the coupling state variable between each subsystem level. $g_i(x,x_i,y_i)$ is an inequality constraint; $h_i(x,x_i,y_i)$ is the equality constraint and the system state equation. E_i the basic flow of multidisciplinary design optimization system is shown in Figure 3.

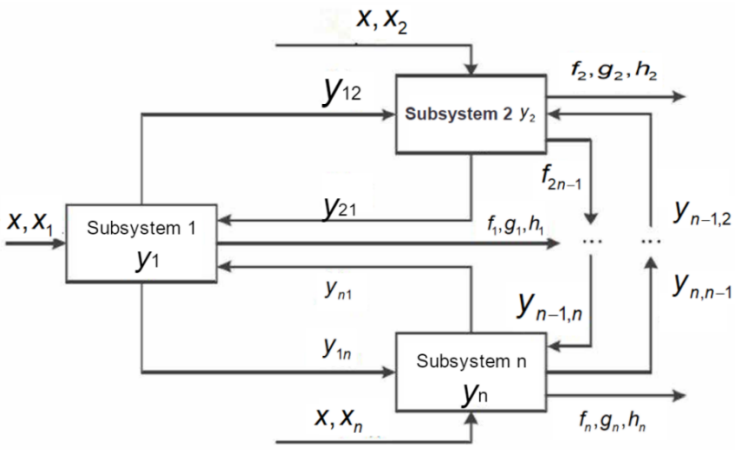

Fig. 3 - Typical multidisciplinary design optimization system

In the multidisciplinary design optimization system shown in fig. 3, the system-level design variable x is in n subsystems at the same time, and the state variables of each subsystem will become the input variables of other subsystems at the same time, thus forming a complete system-level framework by data transmission of coupling parameters among subsystems. The input variables of subsystem 1 include not only system-level design variables x and discipline design variables x_1, but also state variables y_{21}, y_{31}, ..., y_{n1} from subsystem 2 to subsystem n. It reflects the modular analysis of multidisciplinary design optimization, and there are certain coupling variables among subsystems, so parallel optimization can get more effective optimization results.

Optimal design of steering trapezium

After the overall basic parameters of rice transplanter are determined, such as kingpin inclination angle α, kingpin inclination angle β, wheelbase L, kingpin centre distance B and steering gear forward extension distance, trapezoidal bottom angle φ_0, φ_1, steering tie rod l_1 and trapezoidal arm length m can be determined. In this paper, m and l_1 are taken as optimization variables.

In view of the steering trapezoidal structure itself, it is impossible to absolutely guarantee that the steering trapezoidal structure can meet the requirements of theoretical turning characteristics at any turning angle. Therefore, the objective function takes the minimum difference between the actual trapezoidal characteristics and the theoretical trapezoidal characteristics. It is hoped that the deviation will be as small as possible in the small angle range near the middle position which is often used, so as to reduce the wear of tires at high speed.

However, when it is not used frequently and the vehicle speed is slow, the requirements can be relaxed appropriately *(Zha X., Zhang G. and Zhang S., 2020).* Therefore, the weighting factor $\omega(\theta_1)$ is introduced, and this article $\omega(\theta_1)=-\theta/\theta_{1max}+1.5$ usually takes $\theta_{1max}=90°$.

For the overall structure layout, if the m value, that is, the size design of the steering knuckle arm is too large, the size of the whole trapezoid will also become larger, and it will be difficult to adjust the overall structure; If the value of m is designed too small, the axial force on the steering cross-pull will be increased, and the cross-pull may contact the front axle of the front axle during the movement of the whole steering system, thus causing motion interference. If the steering trapezoid is closer to the rectangle *(Zhang C.Z., 2021)*, the value of $F(X)$ will be larger. Because the optimization in this paper is to find the minimum value of $F(X)$, the upper limit can be ignored.

The two constraint values mentioned in the plane constraint, in the spatial model, in order to make the optimal solution within the constraint range, the range of statistical values is generally relaxed, and the relaxed expression is as follows:

$$g_1=(x_1=m)=m-0.10K=0 \tag{5}$$

$$g_2=(x_1=m)=m-0.16K=0 \tag{6}$$

In addition, according to the understanding of mechanical principle, the minimum transmission angle constraint condition of the four-bar mechanism can be obtained by cosine theorem when the vehicle turns left to the limit position *(Zhang X S. 2018)*; δ should not be too small, generally take $\delta\geq\delta_{min}=40°$. When δ reaches the minimum value. Combined with cosine theorem, the following constraint relation of minimum transmission angle can be obtained through a certain mathematical relationship:

$$g_3=(x_1=m,x_2=\phi)$$

$$\cos^{-1}\frac{2(B+2l_2\sin\alpha)\cos\phi-(B+2l_2\sin\alpha)\cos(\phi+\theta_2\max)-2m\cos^2\phi}{B+2l_2\sin\alpha-2m\cos\phi}+40=0 \tag{7}$$

RESULTS

Automatic navigation test

A piece of cement pavement and farmland were selected as the test site, and the transplanter was driven by the driver, and the driving routes were straight and turning. The electric control system records the driving route as the preset route, so that the transplanter can automatically navigate and drive according to the preset route; The electronic control system automatically records the heading deviation and lateral deviation during driving. The test results are shown in Table 1.

Table 1

Automatic navigation test results

Situation	Drive straight		Turn and drive	
	Maximum deviation of course/ (°)	Maximum lateral deviation/ (°)	Maximum deviation of course/ (°)	Maximum lateral deviation/ (°)
Cement pavement	6.3	4.2	5.2	4.3
Farmland pavement	7.1	4.7	7.3	4.6

It can be seen from table 1 that the deviation results of rice transplanter running on farmland pavement and cement pavement are similar, and the straight running is less than the maximum deviation value of turning; However, the heading deviation and lateral deviation of straight driving and turning are small, which can meet the requirements of automatic navigation.

Analysis of multidisciplinary design optimization results of electronic control mechanism system

Sequential Quadratic Programming NLPQL, pp. This algorithm is mostly used in nonlinear optimization systems with constraints, and the objective function is assumed to be continuously differentiable. The basic step is to expand the objective function by the second-order Taylor series, and then linearize the constraint conditions, so that it can be transformed into a quadratic programming problem. The second-order equation is improved by quasi Newton formula, and straight line search is added as an aid to enhance the stability of the algorithm.

Multi-island Genetic Algorithm MIGA, pp. In multi-island genetic algorithm, like other genetic algorithms, each design point has a fitness value, which is based on the cardinality of objective function and constraint penalty function value. If an individual has a good objective function value, the penalty function will have a higher fitness value.

Combined with the analysis of optimization strategy selection, the combination optimization algorithm of MIGA and NLPQL is selected for multidisciplinary design optimization of electronic control adjusting mechanism. Based on the established collaborative optimization platform, the electronic control adjusting mechanism is optimized and analysed. The numerical changes of system-level design variables before and after optimization are shown in Table 2.

Table 2

Optimization result of electric control adjusting mechanism

Design variable	Initial value	Optimization result	Optimization increment (%)
Adjust the total length of the lead screw	1820	1802.32	-0.97
Adjust the length of screw thread section	140	133.63	-4.6
Adjust the lead screw diameter	17	16.20	-4.71
Height of screw thread	1.3	1.21	-6.92
Adjust the lead screw pitch	2.5	1.97	-2.12
Adjust the screw speed	0.6	0.57	-0.05
Proportional control coefficient	5.6	4.33	-22.68
Integral regulation coefficient	10.2	13.02	27.65
Differential regulation coefficient	5.9	0.77	-86.95

The optimization results in Table 2 show that the overall performance of the system-level optimization target mechanism system based on the collaborative optimization method is optimal when the design variables of the electronic control mechanism system are above the design values. The final solution of the optimization objectives of each subsystem discipline is not necessarily the optimal solution within the constraints of the current discipline, but under the influence of cross-coupling design variables among subsystem disciplines, different subsystem disciplines restrict and adjust each other in a balanced way, which makes the system-level optimization objectives achieve the best under the premise that the optimization objectives of this discipline are as close as possible to the optimal solution.

In this paper, the four subsystem-level optimization objectives of structural mechanics, dynamics, kinematics and control of the electronic control mechanism system are: minimum weight, minimum vibration, maximum transmission efficiency and minimum adjustment response error, and the optimization results are shown in the following figure 4:

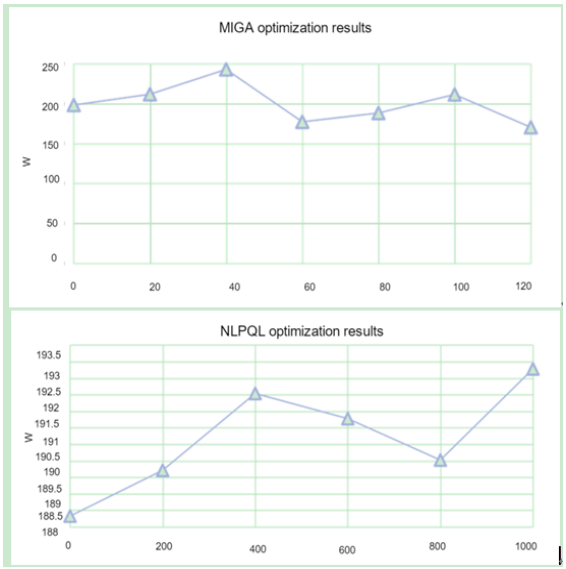

Fig. 4 - Optimization results of dynamic subsystem

It can be seen from fig. 4 that, in the structural mechanics subsystem, the weight of the optimization target electronic control adjustment mechanism is optimized from 2.617kg in the initial state to 2.453kg by MIGA algorithm, and then the final optimization solution is 2.214kg by NLPQL algorithm. On the premise of satisfying the working performance, the weight of the rod is reduced by 12.36% after optimization.

Significance analysis

In scientific experiments and production practice, things are affected by many factors, and if the factors change, they will have a certain impact on products, such as the quantity and quality of products. There will be many differences in the degree of influence, such as some factors causing great influence, some causing little influence or even ignoring it. In this paper, in order to ensure high quality and high output, and make the production process of enterprises stable, the factors affecting products are analysed with mathematical significance. The analysis uses mathematical variance analysis, which is mainly to further calculate and analyse the experimental results. This analysis can further compare the influence degree of each factor on the experiment, which is an effective method in a short time.

The primary and secondary relationship of the influence of factors on the experiment is judged by the magnitude of the extreme value, and the primary and secondary relationship is:

A→B→D→C, Corresponding relationships are kingpin inclination angle, steering knuckle arm and tie rod. Although the extreme value can reflect the primary and secondary relationship of the factors, it cannot reflect the influence of the factors on the experiment. Because there is no standard for the degree of influence on the experiment, it is impossible to scientifically judge whether all factors have significant influence.

Let F ratio F_j of factor j be:

When $F_j > F_{0.01}(2,2)$, it shows that the change of this factor level has a significant impact on the experimental results, which is denoted as * *.

When $F_j > F_{0.05}(2,2)$, it shows that the change of this factor level has a significant impact on the experimental results, which is denoted as *.

When $F_j > F_{0.1}(2,2)$, it shows that the change of this factor level has a certain influence on the experimental results, which is recorded as 0.

Table 3

Significance analysis

Variance source	Sum of squares S	Freedom f	Mean square $\bar{S}$	F value	Significance
A	12.01	3	6.20	27.21	*
B	10.24	3	5.63	24.06	*
$\triangle C$	0.44	3	0.20	2	
D	5.36	3	2.71	12.50	0
e	0.41	3	0.22		

It can be seen from Table 3 above that factors A and B are significant, factor D has certain influence, and factor C is not significant and can be ignored. From this conclusion, we can see that among the four parameters of front wheel alignment and steering trapezoid, kingpin inclination and kingpin caster angle have great influence on the whole steering system.

However, the influence of tie rod and knuckle arm in trapezoidal structure on the whole system is not great, and the influence of tie rod on trapezoidal structure is greater than that of knuckle arm, which is also consistent with the production practice. The above conclusions provide a certain reference for the improvement of steering system structure.

In order to show the change results of the curves before and after optimization more clearly, we draw the curves of the actual rotation angle and the ideal rotation angle with the input angle before and after optimization, as shown in Figure 5 below.

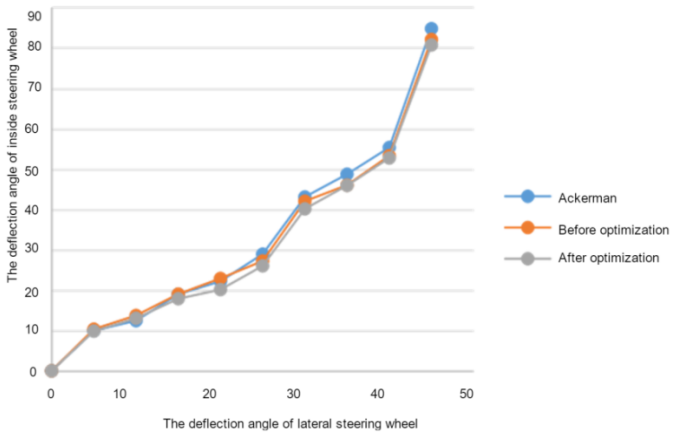

Fig. 5 - Theory and curve before and after optimization

As shown in Figure 5, the theoretical Ackermann curve is closer to the optimized curve when the outer wheel angle is in the range of 0° to 25°, but when the outer wheel angle is greater than 25°, the optimized curve is farther and farther away from the theoretical Ackermann curve, while the curve before optimization is closer to the Ackermann curve. Although this situation occurs, it does not affect the work of the transplanter in the field. Because the speed of the transplanter in the field is relatively small, the work site is limited, and the corner of the field work is mostly in a small angle range, it shows the scientificity of the optimization method to a certain extent.

CONCLUSIONS

Mechatronics system is a nonlinear complex system integrating mechanics and control, in which mechanical system includes many different disciplines such as statics, structural mechanics, dynamics and kinematics. In this paper, the multidisciplinary design optimization of adjustable wide and narrow row high-speed rice electric control mechanism is discussed and studied by analysing the research status of multidisciplinary design optimization of wide and narrow row rice transplanter and mechatronics system at home and abroad. The hybrid algorithm based on WSN technology, which uses MIGA algorithm to determine the optimal value range, and then uses NLPQL algorithm to find the optimal value within the range, shortens the calculation time and ensures the accuracy and global optimality of the final optimized value. The results show that the hybrid optimization algorithm has high computational efficiency and good optimization effect, and is suitable for multidisciplinary design optimization of mechatronics system.

REFERENCES

[1] Ahn T.I., Yang J.S., Park S.H., (2020), "Translation of Irrigation, Drainage, and Electrical Conductivity Data in a Soilless Culture System into Plant Growth Information for the Development of an Online Indicator Related to Plant Nutritional Aspects." *Agronomy,* Vol. 10, Issue 9, pp. 1306. USA;

[2] Chaitanya D.N.V., Arunkumar S., Akhilesh G.B., (2018), Design of Rice Transplanter. *Iop Conference,* p. 377. United Kingdom;

[3] Feng X.T., Hu H.H., Chen R., (2018), Electric Drive Automatic Control System "Engineering Quality Teaching Reform. *Journal of Electrical and Electronic Teaching*, Vol. 040, Issue 003, pp. 47-49, 114. China;

[4] He J., Luo X., Zhang Z., (2020), Positioning correction method for rice transplanters based on the attitude of the implement. *Computers and Electronics in Agriculture*, Issue 176, p. 105598. Netherlands;

[5] Jiangtao J., Kaikang C., Xin J., (2020), High-efficiency modal analysis and deformation prediction of rice transplanter based on effective independent method. *Computers and Electronics in Agriculture,* Issue 168:105126. Netherlands;

[6] Jin X., Chen K.K., Ji J.T., (2018), Modal analysis and structural optimization of support arm of rice transplanter based on modal confidence criterion. *Transactions of the Chinese Society of Agricultural Engineering (Transactions of the CSAE)*, Vol. 34, Issue 18, pp. 93-101. China;

[7] Lee P.U., So J.H., Nam Y.S., (2018), Power analysis of electric transplanter by planting distances. *Korean Journal of Agricultural Science,* p. 45. Korea;

[8] Li G., Wang Y., Guo L.F., (2018), Improved pure tracking algorithm for transplanter navigation path tracking. *Journal of Agricultural Machinery*, Vol. 049, Issue 005, pp. 21-26. China;
[9] Li G., Xia P.S., Yu C., Li X., (2020), Investigation and analysis on the quality of rice transplanters in Chongqing. *Agricultural Machinery Quality and Supervision*, Vol. 191, Issue 11, pp. 19-20. China
[10] Peng H.H., Shang Y.C., (2021), Fixed optimization analysis of a power steering pipeline system. *Power system and control,* Vol. 10, Issue 1, pp. 7. China;
[11] Putri R.E., Fadhilah R., Cherie D., (2020). Analysis of Energy Consumption and Performance Test on Rice Planting Using Rice Transplanter: A Case Study in West Sumatera Province, Indonesia. *Journal of Applied Agricultural Science and Technology*, Vol. 4, Issue 1, pp. 12-25. China;
[12] Samal P., Din M., Mondal B., (2018), Promotion of Self-propelled Rice Transplanters in Odisha state of India. *Agricultural mechanization in Asia, Africa and Latin America*, Vol. 49, Issue 1, pp. 28-35. Japan;
[13] Siddique A.A., Kim Y.J., Kim W.S., (2020), Analysis of the Axle Load of a Rice Transplanter According to Gear Selection. *Journal of Drive and Control,* Vol. 17, Issue 4, pp. 125-132. China;
[14] Siddique M.A.A., Kim W.S., Kim Y.S., (2020). Effects of Temperatures and Viscosity of the Hydraulic Oils on the Proportional Valve for a Rice Transplanter Based on PID Control Algorithm. *Agriculture*, pp. 10. Switzerland;
[15] Sun X.Z., (2018), Optimization design analysis of PLC automation control system. *Computer nerd,* Issue 02, p. 31. China;
[16] Tong X.F., (2020), Design Analysis of Optimizing PLC Automation Control System. *Information Recording Materials,* Vol. 21, Issue 11, pp. 128-129. China;
[17] Wang X.Z., Li Y.D., (2018), Optimization design analysis of electrical control system based on PLC technology. *Times Agricultural Machinery,* Vol. 45, Issue 10, pp. 242. China;
[18] Wen C.J., Wang H.L., Wang M., (2018), Transplanting mechanism for rice transplanter. *Journal of Physics Conference Series,* pp. 1087. United Kingdom;
[19] Wen F., Fu K., (2019), Simulation analysis and optimization design of transplanting mechanism of rice transplanter. *China plant engineering,* Vol. 000, Issue 007, pp. 167-168. China;
[20] Xinchun Y., Meihua, (2018), Development and Experiment of 2ZB-79 Shallow Rice Seedling Transplanter. *Asian Agricultural Research,* Vol. 10, Issue 06, pp. 90-92. China;
[21] Yang X.D., Zhang S.X., (2019), Analysis of technical status and existing problems of rice transplanter. *Agricultural machinery use and maintenance,* Vol. 279, Issue 11, pp. 114-114. China;
[22] Zha X., Zhang G., Zhang S., (2020). Design and experiment of centralized pneumatic deep precision fertilization device for rice transplanter. *International Journal of Agricultural and Biological Engineering,* Vol. 13, Issue 6, pp. 109-117. China;
[23] Zhang C.Z., (2021), Optimization analysis of electric control system of rice transplanter under WSN. *Research on agricultural mechanization*, Vol. 43, Issue 09, pp. 111-114+126. China;
[24] Zhang X.S., (2018), Analysis of factors affecting the operation effect of rice transplanter. *Agricultural Equipment Technology,* Vol. 044, Issue 006, pp. 32-33. China.

OBTAINING "ORGANIC SEEDS" OF VEGETABLE AND INDUSTRIAL PLANTS USING THE AERODYNAMIC PROPERTIES OF THE SEEDS

/

OBŢINEREA DE "SEMINŢE ECOLOGICE" DE PLANTE LEGUMICOLE ŞI TEHNICE UTILIZAND PROPRIETĂŢILE AERODINAMICE ALE SEMINŢELOR

Paun A[1)]., Stroescu Gh[1)]., Zaica Al.[1)], Ştefan V[1)]., Olan M[1)]., Yasbeck Khozamy S.[2)]
[1)] National Institute of Research-Development for Machines and Installations designed to Agriculture and Food Industry – INMA / Bucharest, Romania;
[2)] Schneider Electric / Romania
ani_paun@yahoo.com
DOI: https://doi.org/10.35633/inmateh-63-36

Keywords: *seed, conditioning, aerodynamic properties, vegetable species, impurities, floating velocity*

ABSTRACT

The production and quality of any agricultural crop is determined both by the factors acting from the moment of sowing until harvesting, as well as by those that directly influence the seeds before sowing. In the organic cultivation of cereals, industrial plants, vegetables, medicinal plants, the seeds must be clean without any impurities because the maintenance of these crops does not allow using chemicals. There is a number of technologies and pieces of equipment for separating impurities. In case of separating impurities from the mass of small seeds, especially vegetable and flower seeds, the use of separation on sieves is very expensive because compared to other crops, vegetable seeds are produced in small quantities (except for beans, peas, lentils, etc.) and have a wide variety of characteristics. Vegetables belong to a large number of plant families. This is why their seeds have a very different structure, shape, size and chemical composition. To overcome these challenges, the experimental model Seed conditioning module for vegetable species – MCSL, which separates impurities by using the aerodynamic properties of the seeds was developed. Seed conditioning module for vegetable species is designed to improve the technologies of organic seed production for vegetable seeds, flowers, industrial plants, cereals and to solve practical problems regarding seed production in the case of vegetable crops. Starting from these considerations, the paper will present theoretical and experimental information on the influence of some factors on the aerodynamic properties of cereal seeds, vegetables and industrial plants. The quality of seed separation in this module depends on the degree of uniformity of the air velocity field in the working area, on the stability of this field and on its extent.

REZUMAT

Producția și calitatea oricărei culturi agricole este determinată atât de factorii care acționează din momentul însămânțării până la recoltare, precum și de cei care influențează direct asupra semințelor înainte de însămânțare. În cultura ecologica de cereale, plante tehnice, legume, plante medicinale, semințele trebuie să fie curate fără nici o impuritate deoarece întreținerea acestor culturi nu permite utilizarea substanțelor chimice. Pentru separarea impurităților există o serie de tehnologii și echipamente. În situația separării impurităților din masa de semințe mici, in special semințe de legume si flori, utilizarea separării pe site este foarte costisitoare deoarece în comparație cu alte culturi de legume semințele se produc în cantități mici (excepție fasolea, mazărea, lintea etc.) și au caracteristici foarte variate. Legumele aparțin unui număr mare de familii botanice. Din această cauză semințele lor au o structură, formă, mărime și compoziție chimică foarte diferite. Pentru a răspunde acestor provocări a fost realizat modelul experimental Modul de condiționat semințe pentru speciile legumicole - MCSL care realizează separarea impurităților utilizând proprietățile aerodinamice ale semințelor. Modul de condiționat semințe pentru speciile legumicole este conceput în vederea perfecționării tehnologiilor de producere de sămânță ecologică la semințelor de legume, flori, plante tehnice, cereale, pentru rezolvarea unor probleme practice privind producerea de sămânță la culturile din legumicultură. Pornind de la aceste considerente în cadrul lucrării sunt prezentate informații teoretice și experimentale privind influența unor factori asupra proprietăților aerodinamice ale semințelor de cereale, legume și plante tehnice. Calitatea separării semințelor în acest modul depinde de gradul de uniformitate a câmpului vitezelor aerului din zona de lucru, de stabilitatea acestui câmp și de întinderea lui.

INTRODUCTION

Vegetable growing is a synthetic discipline, integrated in agricultural science and practice, with a well-defined field of activity. It is one of the most complex branches of specialization of plant production due to the great diversity of cultivated plants and with a permanent dynamism following the change of species and hybrids but also the emergence of new technologies and equipment related to specific crops, (*Jadhav et al., 2017*). Seed production for leguminous plants is of great importance, as the vast majority of species propagate this way, (*Panasiewicz et al., 2008*). Due to the fact that the production obtained depends on the quality of the seeds, seeds from varieties and hybrids with superior properties and from superior biological categories without foreign bodies (impurities) must be used (*Stroescu et al., 2019*). Through its position in the national economic system, vegetable growing is a determining factor for the creation or development of productive units that operate both downstream (for the production of construction elements of greenhouses and solarium, installations for heating, ventilation, watering, soil disinfection, chemical fertilizers and pesticides, production of specific machines and tractors, etc.) as well as upstream (design and manufacture of machinery and installations for sorting, calibration, conditioning of vegetables and seeds, production of specific packaging, transport machinery and equipment, storage facilities, canneries, vegetable markets). Quality seeds form the basis of the vegetable production system. Seed quality, in terms of viability and vigour, depends mainly on harvesting, extraction conditions, cleaning, transport and storage (*Stroescu et al., 2020*).

Seed production for vegetable species requires special attention due to the different types of seeds, their corresponding shapes and sizes. The conditioning of small vegetable seeds requires a high level of precision, therefore, cleaning must be performed in stages, paying special attention to the quality performance of each component equipment of the conditioning plants. (*Păun et al., 2018)*. A considerable increase of productivity in vegetable growing can be ensured only through increased efforts to mechanize and automate production processes, ensuring a very good quality seed material and reducing manual labour consumption (*Ciobanu et al., 2015*). The paper presents some theoretical aspects and experiments under operating conditions for the conditioning of mixtures of cereal seeds, vegetables and industrial plants based on the aerodynamic principle, *(Norkulova et al., 2016).*

MATERIALS AND METHODS

Because vegetable seeds have a wide variety of shapes and sizes, it is preferable to use, in the conditioning process, equipment that works on the principle of separation by aerodynamic properties, because separation by size using sieves requires a great financial effort (sieves with holes suitable for each species are necessary), (*Stroescu et al., 2018*). In order to meet the requirements of vegetable growing stations, in particular, but also of individual producers of vegetable seeds and not only, INMA Bucharest created within a complex project, in partnership with vegetable growing stations, a seed conditioning module for vegetable species - MCSL, which works on the principle of separation by aerodynamic properties of the seeds (fig.1). The seed conditioning module for vegetable species MCSL (figure 1, a) consists of the following main parts: 1 - aerodynamic sorter MCSL 1.0; 2 - sorts discharge system MCSL 2.0; 3 - working platform MCSL 3.0; 4 - electrical installation MCSL 4.0. (From: *Test report Seed conditioning method for vegetable species, 2020).*

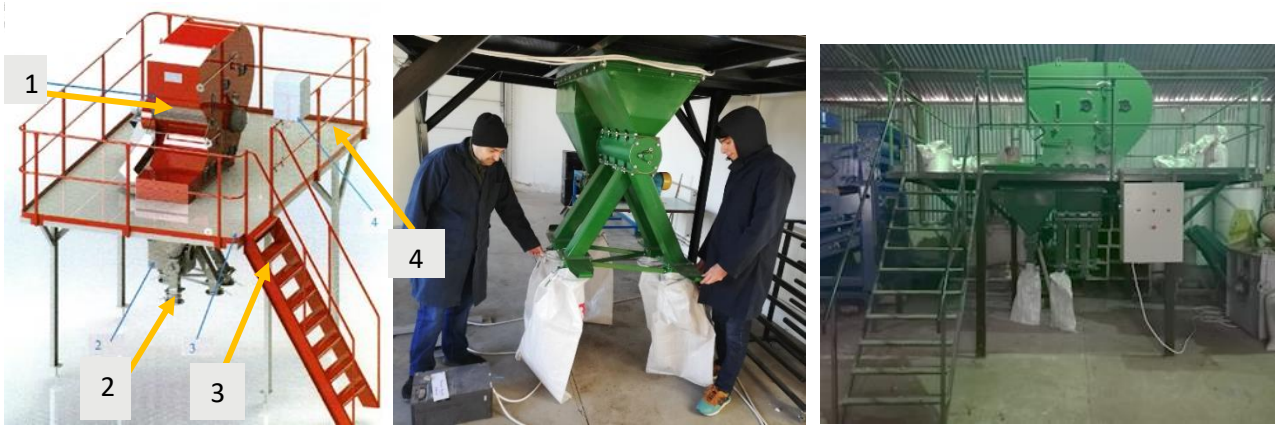

a b c

Fig. 1 - Seed conditioning module for vegetable species: a – MCSL 3 D; b, c – MCSL operating

This module can be used with good results also for separating impurities from cereal seeds. The MCSL module sorts seeds of the same size, but with different shapes, weights and roughness in three fractions, while removing light impurities in two fractions. For a uniform distribution of the seed layer that is subjected to air flow, MCSL is equipped with a feed cylinder. Depending on the shape and size of the seed, one of the three variants of grooved jackets will be mounted on the feed cylinder shaft. Depending on the degree of infestation with impurities, pre-cleaning and destination of the seeds, one or more passes of the resulted useful fractions through the equipment can be performed. The foreign bodies that frequently appear in the seed mass are:

- inert organic foreign bodies (chaff, chopped stems and leaves, dead insects, etc.);
- inert mineral foreign bodies (lumps, loose or sticky dust on seeds, sand, gravel, metal pieces of various sizes;
- weed seeds;
- seeds from the basic crop degraded by various diseases such as: smut, bunt;

It should be emphasized that the separation processes in agriculture and the food industry are much more complicated than in other branches of the economy, because the material is very biologically diversified. These materials (cereal seeds, industrial plants, etc.) are characterized by high variability and low reproducibility (even within the same variety or species of grains) (*Brăcăcescu et al., 2016*).

From the analysis of the specialized literature, of the studies and experiments carried out by various researchers from universities, research centres or private companies, regarding the factors that influence the process of separation of impurities from the mass of vegetable seeds (cereals, industrial plants), it is found that often addressed factors such as: humidity, density, relative to the speed of floating in the situation of an air flow at a well-determined height in a vertically oriented pipe, which blows the mixture of seeds and impurities, (fig.2), (*Stroescu et al., 2019*).

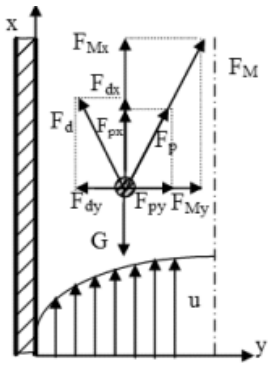

Fig. 2 - Distribution of forces acting on solid particles (seed assimilated to spherical shape) in turbulent vertical air flow: G – weight force; Fd – frontal dynamic pressure force; Fp – bearing force; FM – Magnus force

In the case of technical equipment using as a principle of separation the difference between the aerodynamic properties of the components, one must take into account the floating velocities of the seeds and impurities, but also the aerodynamic coefficient, respectively:

$$v_p = \sqrt{\frac{\rho_p \frac{\pi d^3}{6}}{0.124 k \frac{\pi d^2}{4}}} \quad (1)$$

$$v_p = 2{,}4\sqrt{\frac{\rho_p}{k}\, d} \quad (2)$$

where:

v_p -floating velocity, m/s;

ρ_p - specific mass of the particle (spherical seed), kg/m^3;

d - particle diameter, m;

k - aerodynamic drag coefficient (depends on the condition of the particle surface).

The seed conditioning module for vegetable species MCSL sorts seeds of the same size, but with different shapes, weights and roughness in three fractions, while removing light impurities in two fractions. Depending on the degree of infestation with impurities, pre-cleaning and destination of the seeds, the passes of the seeds through the equipment can be repeated (fig.3). Under the influence of the ascending air flow, within the limits of floating velocities, the seeds fall to the bottom obtaining the fraction F_1, the others go up to the first hole where the fraction F_2 is separated, to the second hole where the fraction F_3 is separated, or leave the column at the top entering the settling chamber where the fraction F_4 of light bodies (impurities) is deposited.

The air sucked from the settling chamber is expelled by the fan into the second settling chamber where the dust and other very light impurities that form the sort (fraction) F_5 are separated. The five fractions (of which three are useful) pass through the discharge hoppers and the two locks into the exhaust pipes and then into the bags.

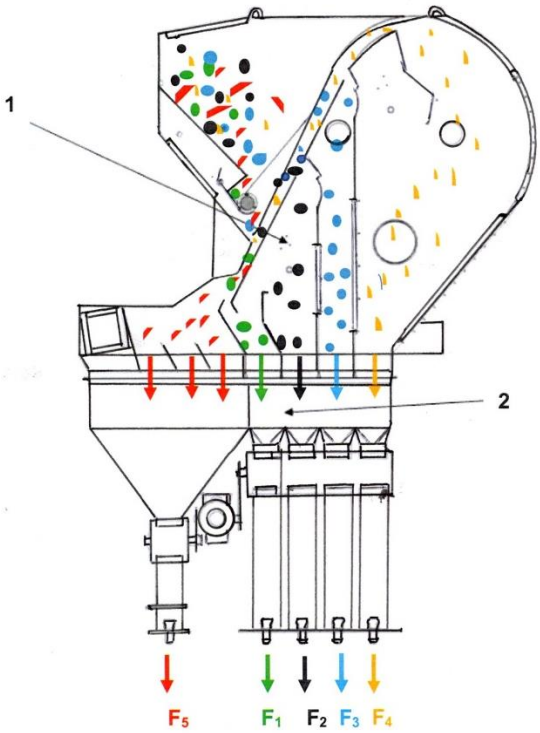

Fig. 3 - Technological flow scheme of seed conditioning module MCSL ***(Păun A., 2018)***

In order to verify the functional parameters of the Seed Conditioning Module MCSL and to analyse the aerodynamic properties of vegetable seeds, experiments were performed under operating conditions. The test of the Seed Conditioning Module for Vegetable Species MCSL was carried out within INMA under operating conditions and processed sorghum, wheat and sunflower seeds purchased on the market.

The technological effect of seed pre-cleaning module MCSL was analysed compared to the product standards and assessed on the basis of the results obtained in a single pass through the installation of the product to be processed.

The following determinations were made:

- E_{csM} - large foreign bodies removed, *%;*
- E_{csm} - small foreign bodies removed, *%;*
- E_{csu} - light foreign bodies removed, *%;*
- C_{ps}- good seeds of the product to be processed lost in by-products, *%.*

The calculation formulas for determining the technological effect of the pre-cleaning group used were:

$$E_{csM} = [(C_{sMi} - C_{sMe}) / C_{sMi}] \times 100 \ [\%] \quad (3)$$

$$E_{csm} = [(C_{smi} - C_{sme}) / C_{smi}] \times 100 \ [\%] \quad (4)$$

$$E_{csu} = [(C_{sui} - C_{sue}) / C_{sui}] \times 100 \ [\%] \quad (5)$$

$$C_{ps} = (\Sigma m_k / M) \times 100 \ [\%] \quad 6)$$

where:

C_{sMi} – content of large foreign bodies at the module input, (%);
C_{sMe} – content of large foreign bodies at the module output, (%);
C_{smi} - content of small foreign bodies at the module input, (%);
C_{sme} - content of small foreign bodies at the module output, (%);
C_{sui} - content of light foreign bodies at the module input, (%);
C_{sue} – content of light foreign bodies at the module output, (%);
Σm_k – sum of good seed masses, in the products collected at the module outputs, during the entire test and determined by laboratory analysis, based on the samples taken separately from each by-product, reported to the total mass of analysed sample, expressed as percentage;
M – good seed mass at module input, determined by laboratory analysis based on the samples taken at the module input of product to be processed and expressed as percentage reported to the total mass of samples, (*Păun et al., 2017*).

RESULTS

The results obtained from the experimental research activities carried out under MCSL Module operating conditions are presented in tables 1, 2, 3, 4. During the laboratory analyses, the moisture and impurity of the samples extracted from the supply and evacuation seed material were obtained, and their image is presented in figures 4, 5, 6, 7 and 8 (From: *** *Test report Seed conditioning method for vegetable species, 2020*).

Table 1

Determining the quality of the processed product

Measured parameter	Sample no.	Sorghum seeds		Wheat seeds		Sunflower seeds	
		Product inlet	Product outlet	Product inlet	Product outlet	Product inlet	Product outlet
Humidity [%]	S I	16.42	16.19	7.6	7.4	9.6	9.3
	S II	16.40	16.20	7.4	7.3	9.4	9.1
	S III	16.48	16.19	7.7	7.35	9.7	9.3
	Average value	**16.43**	**16.19**	**7.56**	**7.35**	**9.56**	**9.23**
Physical purity [%]	S I	*95.2*	97.45	*96.2*	98.9	*96.2*	98.30
	S II	*91.8*	97.35	*94.8*	99.1	*95.8*	97.85
	S III	94.1	97.28	95.1	97.7	95.7	98.32
	Average value	**93.7**	**97.36**	**95.37**	**98.56**	**95.90**	**98.15**
Light foreign bodies (weeds, dust, husks, plant debris, peels + dry seeds less than 1.5 mm thick) *(Csui and Csue)* [%]	S I	2.42	1.1	0.72	0.19	1.10	0.56
	S II	3.43	1.15	0.68	0.20	1.20	0.90
	S III	2.34	0.86	0.65	0.17	1.33	0.77
	Average value	**2.73**	**1.05**	**0.68**	**0.19**	**1.21**	**0.74**
	Ecsu	**61.5**		**72.05**		**39.1**	
Small foreign bodies(C*smi and Csme*), [%]	S I	0.42	0.15	0.22	0.04	0.32	0.10
	S II	0.45	0.25	0.25	0.04	0.25	0.11
	S III	0.43	0.33	0.23	0.06	0.33	0.15
	Average value	**0.43**	**0.24**	**0.23**	**0.047**	**0.30**	**0.12**
	Ecsm*	**41.77**		**85.87**		**57.69**	
Large foreign bodies*(CsMi and CsMe)*, [%]	S I	1.66	1.15	1.7	0.2	2.19	0.84
	S II	3.93	1.05	2.27	0.28	2.51	1.05
	S III	2.73	1.2	2.19	0.3	2.40	0.83
	Average value	2.77	1.13	2.05	0.26	2.37	0.91
	EcsM	**59.20**		**87.31**		**47.36**	

Table 1
(continuation)

Determining the quality of the processed product

Measured parameter	Sample no.	Sorghum seeds		Wheat seeds		Sunflower seeds	
		Product inlet	Product outlet	Product inlet	Product outlet	Product inlet	Product outlet
Sharps, [%]	S I	0.30	0.15	1.16	0.2	0.19	0.1
	S II	0.39	0.20	2,0	0.25	0.23	0.09
	S III	0.40	0.33	1.83	0.21	0.24	0.1
	Average value	0.36	0.22	1.66	0.22	0.22	0.1
Hectolitre mess, kg/hl	S I	14.3	14.1	74.3	80.1	74.3	80.1
	S II	14.3	13.6	79.3	79.05	79.3	79.05
	S III	14.5	13.9	79.1	78.95	79.1	78.95
	Average value	14.36	13.86	79.56	79.36	79.56	79.36

Ecsm* *includes sharps.*

Table 2

Determination of good seed loss coefficient in by-products in the case of sorghum

Measured parameter	Characteristic value/ Test determinations					Air flow speed, m/s
	F_1	F_2	F_3	F_4	F_5	
Good seed mass / at equipment outlet (M) / in fractions, [%]	78.4/79.8/83.2	14.6/13.6/11.28	1.8/1.6/1.3	-	-	3.5/5.5/ 8.2
Mass of good seeds in light and small foreign bodies (m_1) , [%]	-	-	-	1.4/1.2/0.9	-	
Mass of good seeds at the exit of the fan(m_2) , [%]	-	-	-	-	1.2/1.1/0.6	
The sum of good seed masses *(Σmk)*, [%]	97.45 / 97.35 / 97.28					
Good seed loss coefficient in by-products, *Cps* [%]	4.51 /4 / 2.8					

Table 3

Determination of good seed loss coefficient in by-products in the case of wheat

Measured parameter	Characteristic value/ Test determinations					Air flow speed, m/s
	F_1	F_2	F_3	F_4	F_5	
Good seed mass / at equipment outlet (M) / in fractions, [%]	79.2/81.4/85.2	14.2/13.6/11.8	1.6/1.5/1.1	-	-	9 /10.2/11.3
Mass of good seeds in light and small foreign bodies (m_1) , [%]	-	-	-	1.5/1.4/0.7	-	
Mass of good seeds at the exit of the fan(m_2) , [%]	-	-	-	-	1.2/1.0/0.3	
The sum of good seed masses *(Σmk)* , [%]	97.7/98.9/ 99.1					
Good seed loss coefficient in by-products, *Cps* [%]	2.76/2.42/1					

Table 4

Determination of good seed loss coefficient in by-products in the case of sunflower

Measured parameter	Characteristic value / Test determinations					Air flow speed, m/s
	F_1	F_2	F_3	F_4	F_5	
Good seed mass / at equipment outlet (M) / in fractions, [%]	84.1/85.85/91.2	10.6/8.98/5.12	1.5/1.2/0.9	-	-	5.5/7.5/10
Mass of good seeds in light and small foreign bodies (m_1) , [%]	-	-	-	1.2/1.02 /0.7	-	
Mass of good seeds at the exit of the fan(m_2) , [%]	-	-	-	-	0.9/0.8/0.4	
The sum of good seed masses (Σmk) , [%]	98.30/97.85/98.32					
Good seed loss coefficient in by-products *Cps* [%]	3.66/3.08/2.03					

F1 ***F2*** ***F3*** ***F4*** ***F5***

Fig. 4 - Samples collected during sorghum seed conditioning (air flow speed 5.5 m/s)

F1 ***F2*** ***F3*** ***F4*** ***F5***

Fig. 5 - Samples collected during wheat seed conditioning (air flow speed 9 m/s)

F1 ***F2*** ***F3*** ***F4*** ***F5***

Fig. 6 - Samples collected during sunflower seed conditioning (air flow speed 7.5 m/s)

Analysing the collected samples, but also the results obtained from the table above, we notice the existence of good seeds within the fractions F2 and F5. To reduce the good seed mass in these fractions we have the possibility to adjust the feed flow (for a uniform distribution of the seed layer) with a feed cylinder. Depending on the shape and size of the seeds, one of the three variants of grooved jackets can be mounted on the feed cylinder shaft. Another solution is to modify the section of the sorting column.

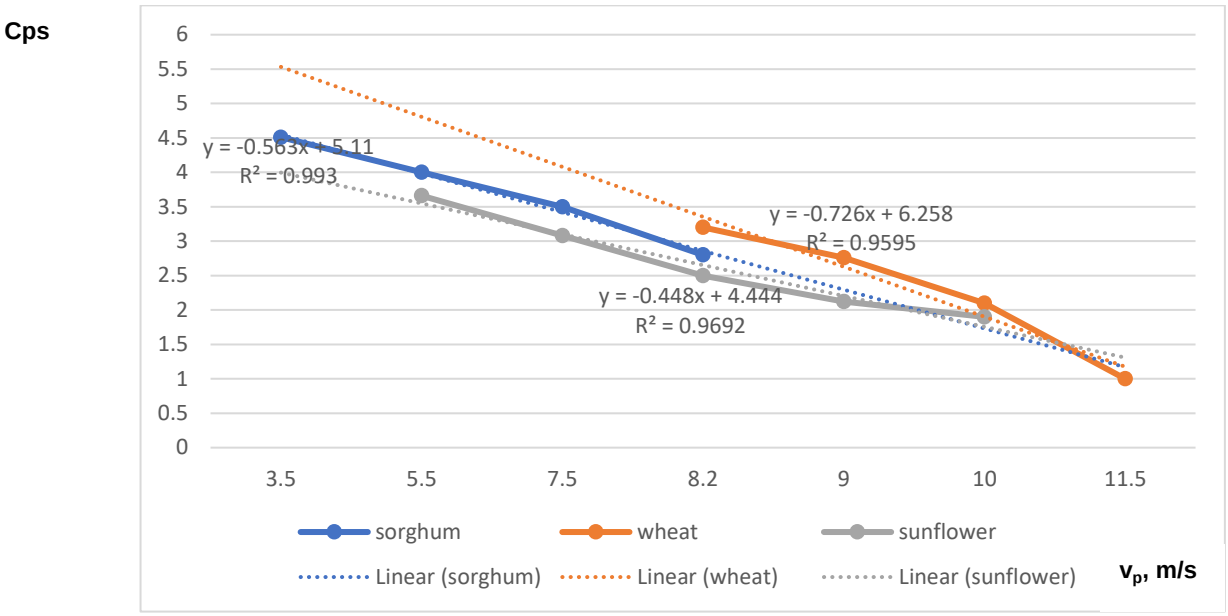

Fig. 7 - Variation of loss coefficient Cps depending on the floating velocity

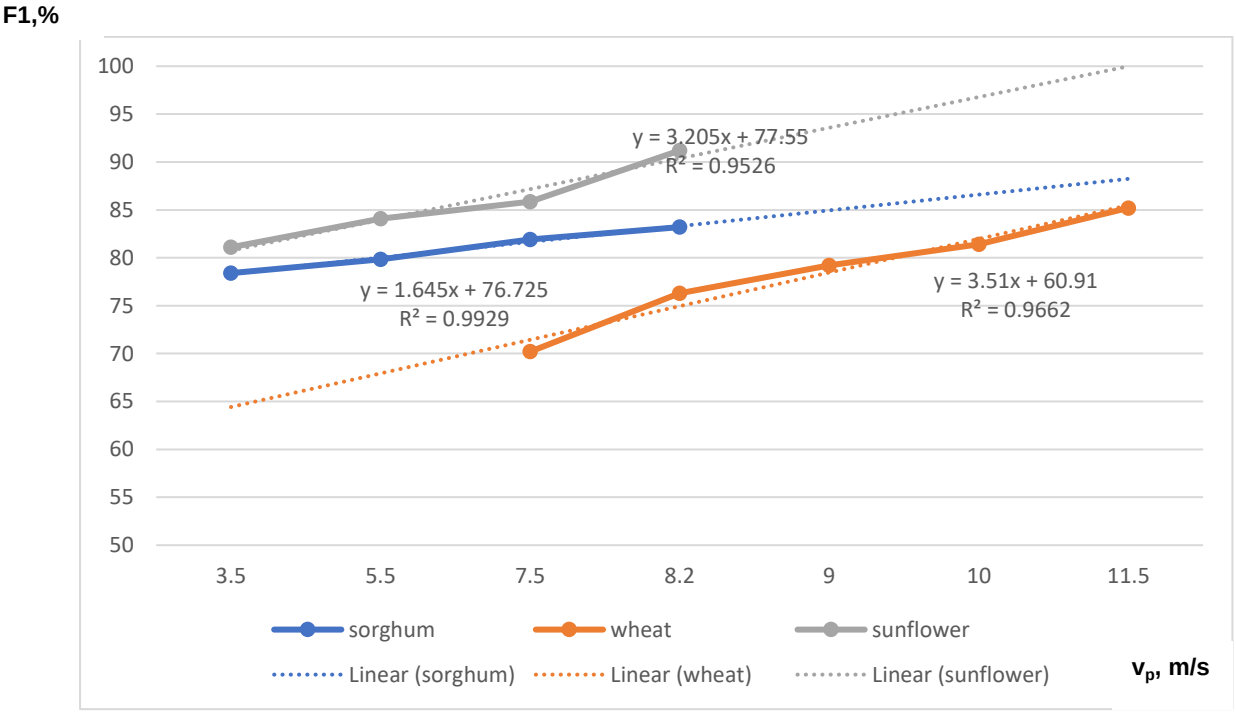

Fig. 8 - Good seed mass F1 at the equipment outlet depending on the floating velocity

From the analysis of the results presented in the tables and figures above, obtained during the experiments, the following phenomena were found:

- the pre-cleaning capacity and the technological effect are influenced by the floating velocity, the degree of impurities and the feed cylinder of the equipment by the type of jacket and the speeds used;
- the humidity of the processed product influences the aerodynamic properties of the seeds (*Stroescu et al., 2020*).
- there are situations when the degree of impurities existing in the seed mass leads to the pass of the seeds through the separator twice;
- the appearance of good seeds in fractions F3, F4 and F5 is due to the fact that these seeds were not threshed, detached from the husks.
- the increase of the air flow speed leads to the decrease of the good seeds in by-products;

- the increase of the air speed in the sorting column over the floating velocity of the seeds has a negative effect because in by-products a higher percentage of good seeds appears

CONCLUSIONS

An analysis of the results obtained led to the conclusions:

- it was found that both the intensity of the air flow and the mode and speed of the seed mixture supply in the working area of the separator had the greatest influence on the separation of the components;

- precise regulation of the air flow rate led to good results in the separation process;

The quality of seed separation in these systems depends on the degree of uniformity of the air speed field in the working area, the stability of this field and its extent.

From the experiments performed under operating conditions it was found that: the coefficient of good seed losses in by-products *Cps* decreases from 4.5% to 2.8% with the increase of the floating velocity v_p from 3.5 m/s to 8.2 m/s for sorghum; *Cps* decreases from 3.2% to 1% for v_p increase from 8.2 m/s to 11.5 m/s for wheat; *Cps* decreases from 3.66% to 2.03% for v_p increase from 5.5 m/s to 10 m/s for sunflower.

The separation module has the possibility to regulate the flow rate of the air flow from the sorting column by modifying the geometry of its cross section by actuating some control flaps.

ACKNOWLEDGEMENTS

This paper was financed with the support of National Agency for Scientific Research and Innovation, Farming Tomorrow - Ensuring Environmental Sustainability by Increasing Competitiveness of Improvement for Organic Agriculture Programme (UEFISCDI PN-III-P1-1.2-PCCDI-2017- 0850, Contract: 14PCCDI/06.03.2018), project component 4 “Making efficient the technology of producing organic seeds for vegetable species by creating a seed conditioning module”.

REFERENCES

[1] Brăcăcescu C., Găgeanu I., Popescu S., Kemal C.S., (2016), Researches concerning impurities separation process from mass of cereal seeds using vibrating sieves in air flow currents, in *Proceedings of 5th International Scientific Conference "Engineering for rural development 2016*”, Jelgava/ Latvia, ISSN1691-5976, pp.364-370;

[2] Ciobanu V.G., Vişan A.L., Păun A, Nedelcu A., (2015), Comparative study regarding seed sorting equipment and the importance of implementing smart systems within the working process, *JoKULL Journal*, vol.64, no.9, ISSN 0449-0576, pp.91-100;

[3] Jadhav M.L., Pramod M., Shelake P.S. (2017), Investigation of Engineering Properties of Vegetable Seeds Required for the Design of Pneumatic Seeder, *International Journal of Current Microbiology and Applied Sciences*, Vol. 6 No. 10, Journal homepage: http://www.ijcmas.com, ISSN: 2319-7706, pp. 1163-1171;

[4] Norkulova K., Safarov J., Sultanova S., (2016), Research on Aerodynamics Separator for Medicinal Plants, *Journal of Food Process Technol* 7:5, vol.7, Issue 5, 1000586, Tashkent State Technical University, Republic http://dx.doi.org/10.4172/2157-7110.1000586, ISSN: 2157-7110 JFPT;

[5] Panasiewicz M., Zawiślak K., Kusińska E., Sobczak P., (2008), Purification and separation of loose materials in a pneumatic system with vertical air stream, *Department of Food Engineering and Machines, TEKA Kom. Mot. Energ. Roln. – OLPAN*, pp. 171–176, University of Life Sciences / Lublin;

[6] Păun A., Stroescu Ghe., Bogdanof G., Vlăduţ V., (2018), *Module to clean vegetable seeds*, Patent application no. A 0986, RO;

[7] Păun A., Brăcăcescu C., Milea D., Bunduchi G. (2017), Researches in producing organic certified seeds and planting material, *Proceedings of 16th International Scientific Conference “Engineering for Rural Development*”, Jelgava, Latvia, ISSN1691-5976, pp.503-508;

[8] Păun A., Stroescu Gh., Vişan A., Olan M., Zaica A., Moiceanu G., (2018) - Researches regarding the optimization of impurities removal technology from the cereal and industrial plant seeds for establishing ecological crops, *INMATEH - Agricultural Engineering*, vol. 56, no.3, pag.83-91;

[9] Stroescu Gh., Păun A., Matache A., Persu C., Dumitraşcu A., Dumitru I., Iuga D., Epure M., Fătu V., (2018). Technology for obtaining environmentally-friendly seeds and sowing material for vegetable species, *Proceedings of International Symposium ISB-INMA TEH’ 2018 “Agricultural and Mechanical Engineering”,* pp. 467-472, http://isb.pub.ro/wp-content/isbinmateh/2018/Volume_Symposium_2018.pdf

[10] Stroescu Gh., Păun A., Brăcăcescu C., Olan M., (2019), Streamlining organic seed production technologies for vegetable species by making seed conditioning module, *Proceedings of 18th International Scientific Conference "Engineering for Rural Development",* Jelgava, Latvia, ISSN 1691-5976, pp. 34-38, http://www.tf.llu.lv/conference/proceedings2019/Papers/N026.pdf

[11] Stroescu Ghe., Păun A., Voicu Ghe., Brăcăcescu C., Popa R., Popa V., (2019), Researches on the separation of impurities from a seed flow based on the aerodynamic principle, *The 8th International Conference on Thermal Equipment, Renewable Energy and Rural Development, TE-RE-RD*, vol. 112. https://doi.org/10.1051/e3sconf/201911203011

[12] Stroescu Gh., Paun A., Voicea I., Persu C., Matache A., Bunduchi G., (2020) - Influence of moisture content on aerodynamic properties of agricultural products in separation of impurities process, Engineering for Rural Development Jelgava, pp. 1277 – 1283, DOI:10.22616/ERDev.2020.19.TF315;

[13] *** Test report Seed conditioning method for vegetable species, (2020). *National Institute of Research – Development for Machines and Installations Designed for Agriculture and Food Industry – INMA Bucharest*.

SIMULATION ANALYSIS AND CONSTRUCTION OF MAIZE SEEDER MODEL BASED ON EDEM (EM SOLUTIONS EDEM)

/

基于 EDEM 的玉米排种器模型构建与仿真分析

Shuanglin Jia[1,2], Jianqun Yu[1*], Torsten Ghayekhloo[3]

[1]College of Biological and Agricultural Engineering, Jilin University, Changchun 130022, Jilin / China

[2]Mechanical Engineering College, Beihua University, Jilin 132021, Jilin / China

[3]Berkshire Hathaway, Omaha / United States of America

** E-mail: w2515970tongjia0@163.com*

DOI: https://doi.org/10.35633/inmateh-63-37

Keywords: *maize seeder, EDEM technology, watershed algorithm, RTM model*

ABSTRACT

In order to improve the large-scale production efficiency of corn and realize the intellectualization and automation of corn seed metering technology, it is necessary to combine modern computer technology with intelligent algorithm to establish a feasible model suitable for corn seed metering device. In this paper, watershed algorithm and EDEM (EM Solutions EDEM) algorithm are used to establish an efficient corn particle recognition model. Watershed algorithm is used for image matching and recognition, EDEM algorithm is used for simulation and processing of corn particles. Twenty corn seeds were selected, and the proportion and volume fraction of seeds with different shapes were calculated by using the model. The parameters needed for simulation were calibrated to verify the reliability of corn sowing accuracy. Through the credibility evaluation of RTM (Resin Transfer Moulding) model in maize seed metering model, it can be seen that the model has credibility, and the variance test result P = 0.662 > 0.10 shows that the credibility of the model meets the requirements. The results show that the model can be applied to the large-scale production of corn seed metering device, greatly improve the production efficiency, has high reliability, and is worthy of practical application and promotion. In this paper, the model construction and Simulation of corn planter based on EDEM are deeply studied and analysed, and the related processes are improved, so as to comprehensively improve the work efficiency of corn planter and improve the quality of planter.

摘要

为了提高玉米规模化的生产效率，实现玉米排种技术的智能化和自动化，需要基于现代计算机技术和智能算法结合，构建出可以应用于玉米排种器的可行模型。此次选取 Watershed 算法及 EDEM (EM Solutions EDEM) 算法来构建一个高效的玉米颗粒识别模型，通过 Watershed 算法进行图像的匹配和识别，利用 EDEM 算法进行玉米颗粒的模拟和处理操作。选取 20 粒玉米种子，利用该模型对玉米种子进行不同形状种子的比例及体积分数的计算，对模拟所需要的各项参数进行试验标定，并对玉米种排种的精度进行可信性检验。通过 RTM (Resin Transfer Moulding) 模型对玉米种子排种模型的可信性评估可以看出，该模型具有可信性方差齐性检验结果为 P=0.662>0.10，说明该模型的可信性满足要求。研究显示，此次提出的模型能够应用于玉米规模化的排种生产之中，能够极大提升生产效率，具有很高的可靠度，值得进行生产实践应用和推广。本文对基于 EDEM 的玉米播种机模型构建与仿真进行了深入的研究与分析，并对相关流程进行了改进，以全面提高玉米播种机的工作效率，提高播种机的质量。

INTRODUCTION

At present, China has a large area of corn planting, the planting area and yield of corn has ranked second in the world, and the planting area and yield are increasing year by year. In China, corn is widely used and the social demand is strong, so the stability and high yield of corn planting must be guaranteed to ensure the stable supply of domestic grain *(Gultyaeva E., Shaydayuk E., Gannibal P., 2021).* Based on the analysis of various technologies in current corn planting and production, although the quality of seeds and subsequent cultivation stages will directly affect the final yield of corn planting, the most critical factor in these planting stages is the quality of seed row *(Wang G.P. et al., 2018).* With the development of agricultural industrialization, various kinds of planting techniques are born.

Corn seeding is no longer the traditional manual seeding, but more mechanized equipment such as corn seeder, to carry out more efficient seeding operations. Therefore, the rationality of the design of corn seeder is directly related to the quality of corn seeder *(Dong J., 2018).* Excellent corn seeding machinery can achieve confidential seeding *(Cheng R. and Jin Y., 2018)*. It can ensure that seed row amount, spacing between seeds and planting depth of seeds are in an optimal state at all times and ensure the growth and development space of each seed to the maximum extent, thus usable areas of land are used to the maximum extent *(Wang B. et al., 2020)*. Only in this way can the yield per unit area reach the maximum and the yield of corn crop can be increased across the board *(Gross G. and Hoffmann A., 2018; Martínez-Moreno F. et al., 2021)*. At the same time, with the addition of corn seeding machinery, manual labour is greatly released and the efficiency of corn seeding is increased exponentially, making large-scale corn planting and centralized and unified management possible. However, due to the special seasonality of corn planting, the research cycle of corn seeder becomes longer and its research work is more difficult *(Kang D., 2018)*.

Although a large number of excellent research results have been achieved and corn seeder has been improved for several generations after its development to date, the research on the model construction and simulation of EDEM-based corn seeder is still in a short period of time, and there are still many deficiencies *(Nouiri M. et al., 2018)*. With the increase of social demand for the quality of corn seeding, how to prompt the quality and efficiency of corn seeding is an urgent matter. Only by further research on the corn seeding device, can the basic needs of the public be fundamentally satisfied *(Wu M.Y. et al., 2018)*. Therefore, the EDEM-based model construction and simulation of corn seeder are deeply studied and analysed, and relevant processes are improved to comprehensively improve the working efficiency of corn seeder and improve the quality of seeder *(Lan Y. et al., 2021)*.

Watershed algorithm and EDEM technology are used to create a corn seed row model by taking the corn seed row problem as an example. Watershed algorithm is a data operation algorithm that uses iterative random sampling to extract and filter abnormal data to obtain the mathematical model. The algorithm needs to acquire necessary image data information first, such as the edge of the object and the gray level information. The accuracy of these two information acquisition will directly affect the accuracy of detection *(Tai J J et al., 2020)*. According to the different fields used, it can be divided into two types; one is spatial processing and frequency domain processing *(Wei W et al., 2021)*. The former is directly processed on the image itself, the latter is to carry out various calculation and analysis on the image after special processing. EDEM technology mainly includes pre-processor, solver and post-processor. The main functions of the preprocessor are to set up analytical geometry model, cut and analyse grid elements and nodes, set element types and material parameters, set and analyse boundary conditions, etc *(Jensen R., 2021)*. The solver reads the result file of the preprocessor and the numerical method is used to solve the answer according to the input conditions. The post-processor will process a large amount of data into interface graphics in a regular way and make analysis animation, so that the analysis data result is convenient for the user to interpret the answer. Watershed algorithm and EDEM technology are the mainstream trend in maize seeding in the future *(Fan et al., 2021)*.

Aspects of innovation are as follows: 1) EDEM is used to build and simulate the model of corn seeder, and targeted structural optimization is carried out according to the simulated seeding data in reality. Simulation model is established by combining with different parameters such as rotational speed and air pressure. (2) RTM model is used to evaluate the credibility of maize seed seeding model, and the actual effect of theoretical model is verified by real data.

The structure is as follows: the first section mainly describes the research background and the organizational structure. The second section mainly describes the research status of Watershed algorithm and EDEM technology in the corn seeder. The third section mainly describes the design process of the algorithm model. The fourth section mainly describes the practical experimental research of maize seed - discharging model. The fifth section mainly summarizes the research results.

MATERIALS AND METHODS

Watershed algorithm

Watershed algorithm is a data operation method that uses iterative random sampling to extract and filter abnormal data to obtain the mathematical model. Watershed algorithm is mostly applied to image processing in engineering (as shown in figure 1). The basic implementation process is as follows:

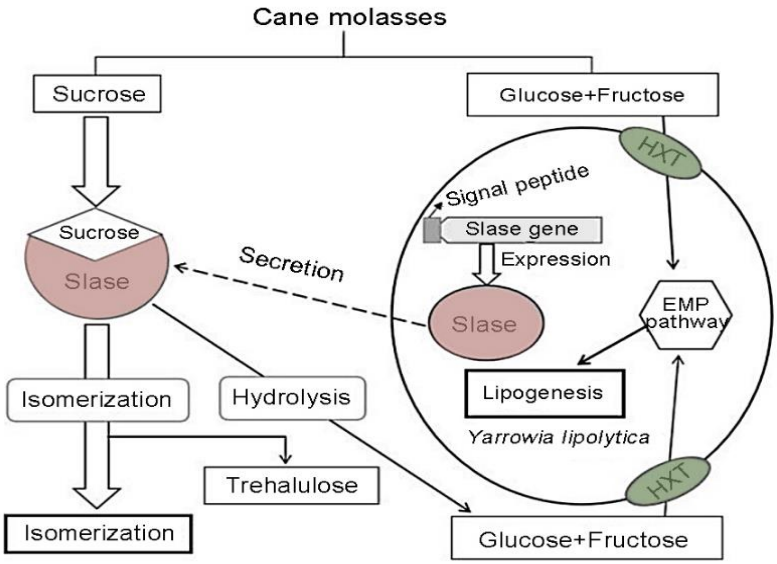

Fig. 1 - Watershed algorithm is mostly applied to image processing in engineering

Necessary image data information, such as object edge and gray level information should be acquired. The accuracy of these two information acquisition will directly affect the accuracy of detection. According to the different fields used, it can be divided into two types. One is spatial processing and frequency domain processing. The former is directly processed on the image itself, the latter is to carry out various calculation and analysis on the image after special processing. The spatial processing formula is as follows:

$$g(x, y) = EH[\, f(x, y)] \tag{1}$$

Where $f(\cdot)$ is the image before enhancement. $g(\cdot)$ is the image after enhancement, and EH represents the enhancement operation. The edge information of the image can directly reflect the shape of the object, and its importance is self-evident. It can project most of the information of the item only by the local image information. However, there are many difficulties in its acquisition. The data obtained by the edge in the system is presented as discontinuous gray value, which requires special algorithm to calculate its edge (as shown in figure 4). It is usually calculated using the first and second derivatives. The gradient corresponds to the first derivative, and the gradient operator is the first derivative operator. For a continuous function $f(x,y)$, its gradient at the position (x,y) can be expressed as:

$$\nabla f(x, y) = G(x, y) = \left[G_x\, G_y\right]^T = \left[\frac{\partial f}{\partial x}\, \frac{\partial f}{\partial y}\right]^T \tag{2}$$

Generally, in order to reduce the amount of calculation, the absolute value approximate gradient amplitude is used to calculate.

$$|\, G(x, y)\,| = |\, G_x\,| + |\, G_y\,| \tag{3}$$

Then corner point extraction is carried out for the image content which has been preliminarily processed. Suppose there is a variable I_x and a variable I_y to represent the first partial derivative of the graph I in two different ways, the Cartesian axis of x and the axis of y. Then the function $w(x,y)$ can be used to represent the two-dimensional Gaussian smooth function in Cartesian coordinates. The calculation process of this function is shown in the following two formulas.

$$M = \sum_{x,y} w(x, y) \tag{4}$$

$$R = \det M - k \cdot (traceM)^2, k = 0.04 \sim 0.2 \tag{5}$$

The specific number of each corner point R on the image can be obtained by solving formula (5). Then the corner points calculated by the normalization method are matched to obtain the value of the corner points. The matching calculation equation is shown as follows:

$$\frac{\partial(H_z u)}{\partial t}+\frac{\partial(uH_z u)}{\partial x}+\frac{\partial(vH_z u)}{\partial y}+\frac{\partial(\Omega H_z u)}{\partial s}-fH_z v= \\ -\frac{H_z}{\rho_0}\frac{\partial p}{\partial x}-H_z g\frac{\partial \eta}{\partial x}-\frac{\partial}{\partial s}\left(\overline{\overline{uw}}-\frac{\nu}{H_z}\frac{\partial u}{\partial s}\right)-\frac{\partial\left(H_z S_{xx}\right)}{\partial x}-\frac{\partial\left(H_z S_{xy}\right)}{\partial y}+\frac{\partial S_{px}}{\partial s} \quad (6)$$

$$\frac{\partial(H_z C)}{\partial t}+\frac{\partial(uH_z C)}{\partial x}+\frac{\partial(vH_z C)}{\partial y}+\frac{\partial(\Omega H_z C)}{\partial s}=-\frac{\partial}{\partial s}\left(\overline{\overline{cw}}-\frac{\nu_\theta}{H_z}\frac{\partial C}{\partial s}\right)+C_{source} \quad (7)$$

$$NCC=\frac{\sum_i (I_1(x_i,y_i)-u_1)(I_2(x_i,y_i)-u_2)}{\sqrt{\sum_i (I_1(x_i,y_i)-u_1)^2 \sum_i (I_2(x_i,y_i)-u_2)^2}} \quad (8)$$

It is worth noting that the results obtained by using the idea of normalization are often mixed with some singularities. These singularities are the abnormal data that belong to the image corner point values with noise and cannot be described by the mathematical model. Therefore, Watershed algorithm needs to be used to purify the image corner point value, the algorithm is a mathematical morphology segmentation method based on topological theory. The basic idea is to treat the image as a geodesic topological landform. The gray value of each pixel in the image represents the altitude of the point. Each local minimum and its affected area is called a catchment basin, and the boundary of the catchment basin forms a watershed. In the purification process, the image should be considered separately according to the three colour channels of red, green and blue. Thus, the following linear algebraic equation is obtained:

$$\begin{pmatrix} R_2 \\ G_2 \\ B_2 \end{pmatrix}=\begin{pmatrix} c_r & 0 & 0 \\ 0 & c_g & 0 \\ 0 & 0 & c_b \end{pmatrix}\cdot\begin{pmatrix} R_1 \\ G_1 \\ B_1 \end{pmatrix}+\begin{pmatrix} d_r \\ d_g \\ d_b \end{pmatrix} \quad (9)$$

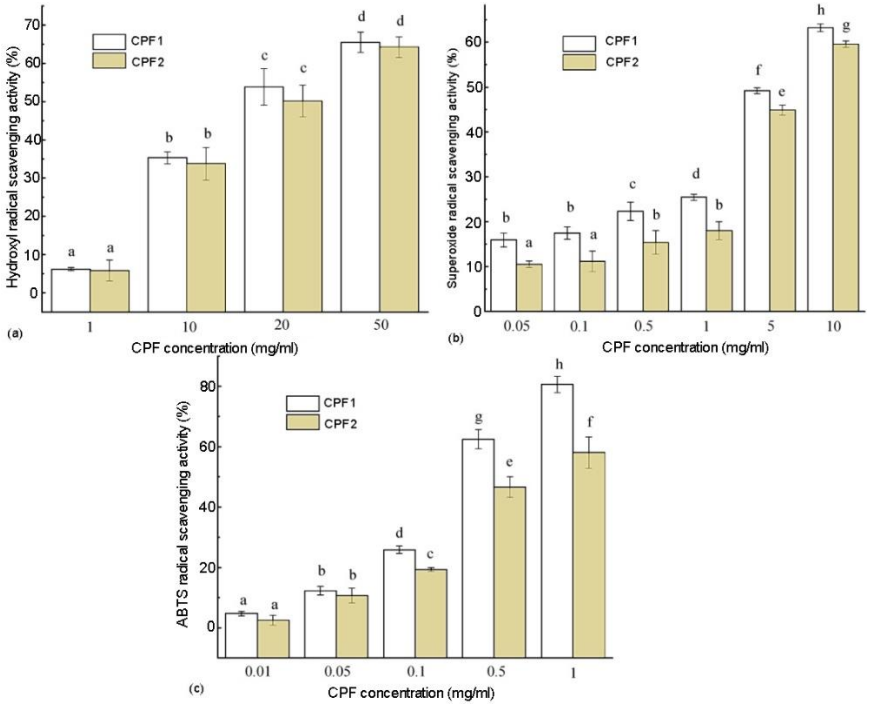

Fig. 2 - In the process of purification, the image should be considered separately according to the red, green and blue colour channels

In the above formula, variable R_2, variable G_2 and variable B_2 respectively represent the red, green and blue colour channels of the image. The variable (c,d) is mainly used to represent the transformation parameters of the linear equation.

The red channel is taken as an example to calculate. First, suppose that there is n group of different image corner point data, and the variable d_n represents the absolute value distance between different data points (R_1,R_2) and line (c,d). At this point, it is purified by iterative summation as shown below:

$$E = \sum T(d_n^{\,2}) \tag{10}$$

In the above formula, when the condition satisfies $d_n^2 < Thre^2$, then $T(d_n^2) = d_n^2$. And the other way around is $T(d_n^2) = Thre^2$. The corners of the image that meet the requirements are filtered out and the iterative calculation is continued. The whole purification process is completed until there is no significant change in the value. At this time, all data points belong to the data that can be normally described by the mathematical model. Finally, the image needs to be segmented. The effect of image segmentation will directly determine whether the image analysis is in place.

After the image is segmented, the similarity between the image and the established image in the database is calculated and matched according to the calculated results.

The image matching result is extremely its characteristic result. The following functions are used to measure the similarity between T and f:

$$SE(x,y) = \sum_{i=1}^{N}\sum_{j=1}^{N}[f(x-i,y-j) - T(i,j)]^2 \tag{11}$$

In the above formula, the matching degree between image T and sub-image f at the (x,y) coordinate is provided.

Matching results can be calculated by expanding the above formula:

$$SE(x,y) = \sum_{i=1}^{N}\sum_{j=1}^{N} f^2(x-i,y-j) - 2\sum_{i=1}^{N}\sum_{j=1}^{N} f(x-i,y-j)T(i,j) + \sum_{i=1}^{N}\sum_{j=1}^{N} T^2(i,j) \tag{12}$$

$$\frac{\partial(H_z u)}{\partial t} + \frac{\partial(uH_z u)}{\partial x} + \frac{\partial(vH_z u)}{\partial y} + \frac{\partial(\Omega H_z u)}{\partial s} - fH_z v = -\frac{H_z}{\rho_0}\frac{\partial p}{\partial x} - H_z g\frac{\partial \eta}{\partial x} - \frac{\partial}{\partial s}\left(\overline{\tilde{u}\tilde{w}} - \frac{v}{H_z}\frac{\partial u}{\partial s}\right) - \frac{\partial\left(H_z S_{xx}\right)}{\partial x} - \frac{\partial\left(H_z S_{xy}\right)}{\partial y} + \frac{\partial S_{px}}{\partial s} \tag{13}$$

$$\frac{Dk}{Dt} = P_k + \frac{\partial}{\partial x_j}\left(\left(v + \frac{v_t}{\sigma_k}\right)\frac{\partial k}{\partial x_j}\right) \tag{14}$$

EDEM technology

EDEM is the world's most professional simulation and analysis of particle processing operation of the standard computer-aided engineering analysis software. The visual modeling of the particle processing process can help designers to complete the processing of different bulk materials. CAE (Computer-aided engineering) is an innovative research and application technology for industrial design and production technology development in addition to computer-aided design CAD (Computer-aided design) and computer-aided manufacturing CAM (Computer-aided manufacturing). It is an auxiliary research technology that assists in the creation, design, modification, analysis and optimization of design by making use of the powerful computing functions of computer.

The introduction of CAE technology makes the related research and industry personnel on the computer possible. Results are predicted and verified by the computer analysis of the original design CAD geometric model and combined with various physical problems analysis technology and operations to reduce the cost of loss caused by the test errors. It can shorten product design and development schedules, and points out the design by scientific data analysis results and potential risks and problems in the process of production; CAE design application benefits include the following : (1) design changes that assist in optimization, (2) assist in the understanding and elimination of problems, (3) rapidly accumulate application knowledge, systematize data and establish design criteria (as shown in figure 3).

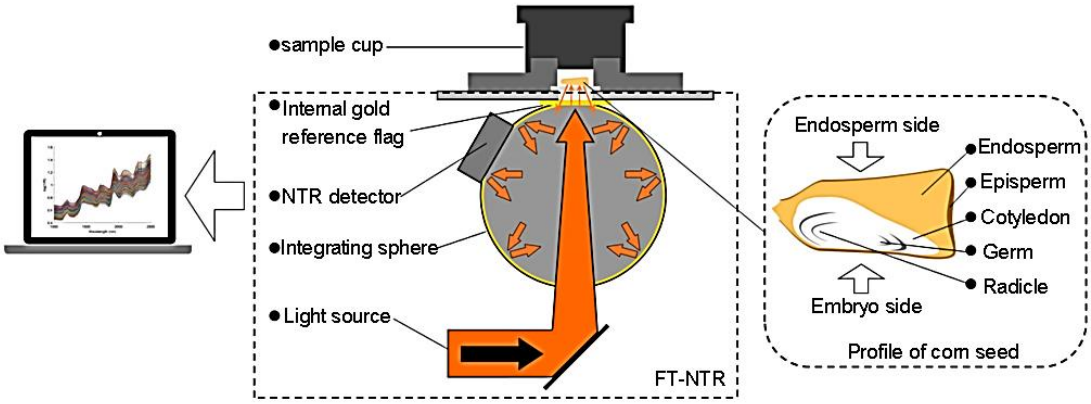

Fig. 3 - Multicast is the sending of data packets to a host group represented by a unique IP address

At present, in engineering application, relatively mature CAE technology fields include: structure analysis, sound field analysis, vibration analysis, optical design analysis, fluid analysis, heat transfer analysis, electromagnetic analysis, mechanism motion analysis and plastic injection moulding mould flow analysis, etc. The development of engineering design CAE has been quite mature in practicality, reliability and computational efficiency, and has a fairly basic theory of analysis and accurate analysis results. CAE analysis software includes two categories: generic and proprietary. General CAE software provides a wide range of selectivity and software expansion application scope, but the software system is usually large, easy to consume a lot of computer resources. It is difficult to operate due to the lack of targeted use, and different general software has its own advantages and characteristics. Special-purpose analysis software provides the most professional results in specific engineering fields. The software system is small, the system resources required for calculation are less, and the practical application and operation are simpler (as shown in figure 4).

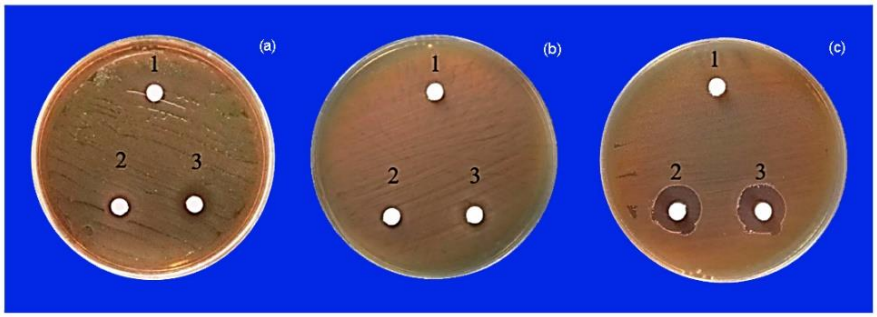

Fig. 4 - The independent Mrouter is responsible for multiple propagation

The industrial application of CAE analysis software are already quite mature, and other kinds of special software, verification through constantly update analysis parameters, thus the reliability of the software applications is enhanced. The product development design process is greatly shortened by combining with computer-aided design CAD and powerful computer aided manufacturing engineering CAM, thus trustworthiness is increased. For industrial application and development, CAE has advantages of cost reduction, high speed and quality. Through the accumulation of continuously updated application material database, CAE simulation analysis results are closer to the real situation. In combination with the efficient solution algorithm that has been gradually improved in recent years, the calculation efficiency and accuracy are growing exponentially. This also lays a more indispensable link for CAE in engineering development and application. In terms of calculation technology, CAE analysis technology uses approximate numerical methods to calculate and solve, instead by the traditional mathematical solution method. Numerical methods can solve many problems that cannot be solved correctly in pure mathematics, and its application level is more extensive.

RESULTS

Experiment overview

Watershed algorithm and EDEM technology are used to create a corn seed row model by taking the corn seed row problem as an example.

First, buy corn seeds of different varieties (3-5 varieties) and classify them by shape (trapezoid, four-pyramid, and spheroid) to determine the proportion or volume fraction of seeds of various shapes. The size of three axes is measured, and the shape of different seeds with a large proportion is scanned by 3d scanner, and the particle model is established. The parameters needed for simulation (static friction coefficient, rolling friction coefficient, collision recovery coefficient) are tested and calibrated. Required parameters are obtained; routine testing of corn seeds (accumulation Angle, resting Angle, etc.) is done; then, RTM model is used to verify the credibility of maize seed scheduling model (as shown in figure 5).

Fig. 5 - The expert model of building energy intelligent management is applied to the energy management of the building garden

Experimental process

The test equipment mainly uses the seed adsorption needle grinded and processed by the injection needle of adsorption, and installs on the seed arranging machine in the way of vertical adsorption. The seed adsorption needle of different specifications can be replaced according to the need. The cursor calliper made by Japanese Mitutoyo Company is used to measure the geometric characteristics of seeds with the measuring range of 0-50mm and precision up to 0.05mm. The electronic balance produced by Japanese AND（ Android）company is used to measure the average distribution of seed quality AND to establish the parameters of seed physical characteristics. The MPS 2.3 Series LED（Light Emitting Diode） Digital Pressure Sensor v3rc-g-m produced by CONVUM Company is used to manually set the high and low Pressure parameter values. The high Pressure is mainly used to determine whether the adsorption needle has absorbed the seeds, and the low Pressure is used for reserve. Parameter setting mode: vacuum suction value not adsorbed to seeds < high pressure parameter value in the sensor < vacuum suction value adsorbed to seeds. Judgment mode: when the vacuum suction value of the adsorption needle is higher than the high pressure parameter value in the sensor, the seed is adsorbed. The pressure range is -100 kPa ~ 0 kPa, and the reaction time is below 1msec. Vacuum voltage valve can be used to fine adjust the size of the vacuum suction to avoid the influence of too much or too little vacuum suction adsorption force. The vacuum filter can prevent the dirty things or seeds from accidentally running into the pipeline in the seeding operation. It can filter in the filter to avoid pipeline obstruction. FX2N-48MR Mitsubishi programmable controller is used. Output/input (Y/X) contacts have 24 points with FX2N-1PG uniaxial NC module controlling servo motor.

The FX2N-232BD communication substrate produced by twin image Company is connected with the RS232 through jumper to enable the computer to communicate with PLC（Programmable Logic Controller）. The experimental materials are mainly purchased from the seedlings planted by ordinary farmers.

They are mainly spherical corn seeds and flat corn seeds, respectively. 128 lattices of round seedling tray are used with a pore diameter of 4.2cm and a depth of 3.5cm.

Experimental steps: (1) measure the length and diameter of spherical corn seeds, the thickness and length and axle diameter of flat corn seeds, and record them. After measuring 20 corn seeds, take their average length. (2) Before starting the experiment, machine vacuum MPS 2.3 Series of LED Digital Pressure Sensor V3Rc - G - M operates for a period of time, let the vacuum suction tend to be stable. And then Pressure Sensor of high Pressure parameter value is adjusted. The parameter value ranges from the vacuum suction value not adsorbed to the seed < the high pressure parameter value within the sensor < the vacuum suction value adsorbed into seed, so as to ensure that the misjudgement of the computer monitoring system and avoid no seed metering. (3) The man-machine interface statistics and operation of the computer monitoring system are recorded. The error between the control and manual operation statistics after each experiment is analysed and discussed by using EDEM technology. (4) The 128-cell-acupoint disc is used as the experimental material, and different parameter factors are changed as follows: 1) different seeds: spherical corn seeds and flat corn seeds, respectively, affect seed arrangement accuracy. 2) Seed adsorption needles of different types: the numbers are 22, 23, 24 and 25, respectively. 3.) Different oscillation degrees: 1.5, 2.0 and 2.5, respectively. 4) Rotation times of rotary cylinder: once, twice and three times, which affect the precision of seed arrangement. 5) Repeat each experiment 3 times.

The experimental results are shown in figure 6 below:

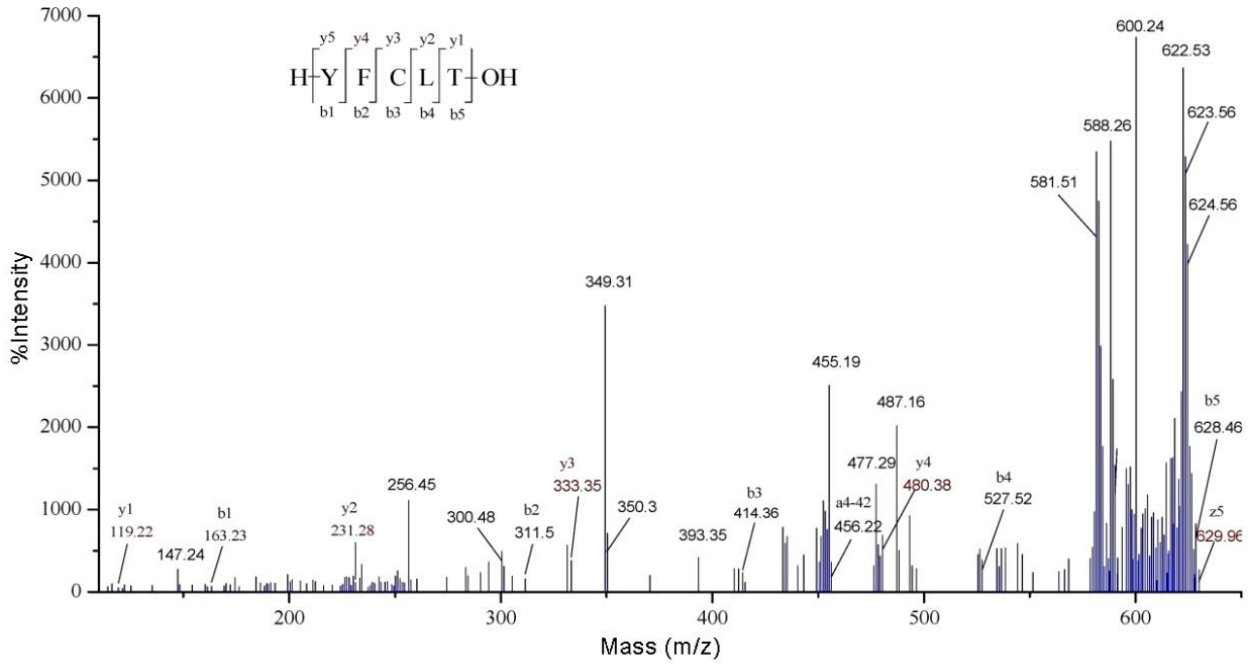

Fig. 6 - Actively issue abnormal energy consumption and alert to reduce wrong energy consumption

Experimental evaluation

After the experiment, RTM model is used to evaluate the credibility of maize seed seeding model. The steps are as follows: Find out the different evaluation indexes of the evaluated object and establish an evaluation weight matrix R, calculate the product of each row element of the judgment matrix R, and get the actual weight values of the different indexes of the evaluated object. Then, calculate the evaluation score by computing the weight values and evaluation content data. The evaluation results can be obtained by calculating the data information recorded in the experiment in accordance with the above calculation method (as shown in figure 7).

The data in the figure shows that the test result of homogeneity of variance for the credibility of the maize seed row model designed is $P=0.662>0.10$. Since the result is much larger than 0.10, it can be inferred that the credibility of the maize seed row model has reached the requirements.

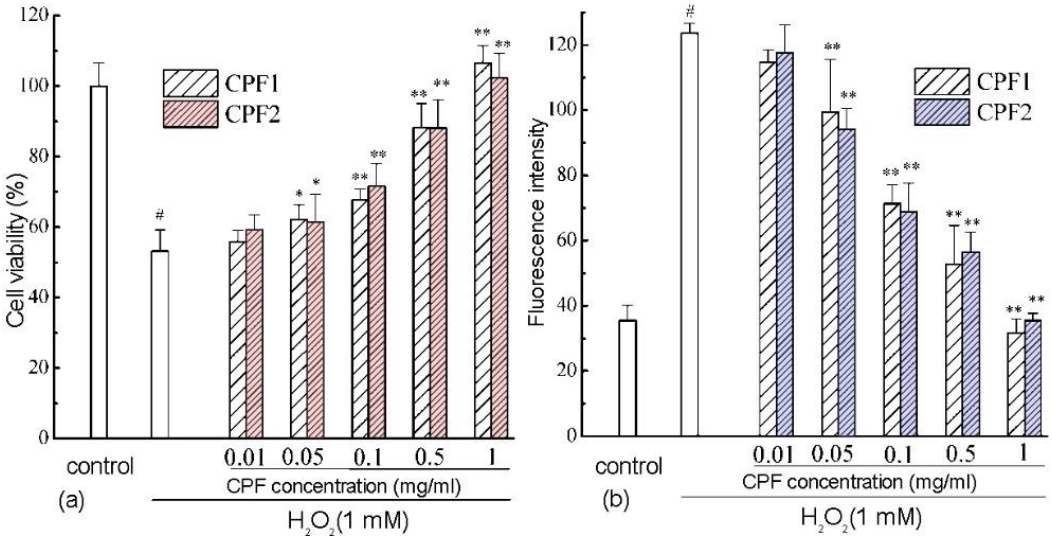

Fig. 7 - Precision instrument of watt-hour meter tester with fault in transmission system

CONCLUSIONS

The watershed and EDEM algorithm were used to solve the corn seed row problem. First of all, buy different varieties (3-5 varieties) of corn seeds, according to the shape (trapezoid, pyramid, sphere) classification, determine the proportion or volume fraction of various shapes of seeds. The size of three axes was measured, and the shape of different seeds was scanned by a three-dimensional scanner. The length and diameter of spherical corn seeds were measured by vernier calliper, and the thickness, length and shaft diameter of flat corn seeds were recorded. After measuring 20 pieces, take the average length. Before the start of the experiment, turn on the vacuum mps2.3 series LED digital pressure sensor v3rc-g-m of the planter for a period of time, stabilize the vacuum suction, and adjust the high-pressure parameters in the pressure sensor. The statistics and calculation of man-machine interface of computer monitoring system are recorded. By using EDEM technology, the error of statistical calculation is compared with that of manual calculation at the end of each experiment. 128 grid tray was used to change the influence of different parameters on the precision of corn seed metering. At the end of the experiment, RTM model was used to evaluate the reliability of maize seed sowing model. The evaluation data showed that the homogeneity of variance test result of the credibility of the designed maize seed row model was $p = 0.662 > 0.10$. As the result is much larger than 0.10, it can be inferred that the credibility of maize seed row model meets the requirements. However, there are some defects in the designed structure of corn seeder, which is not conducive to the popularization and application of this method. In addition, there are some conclusions error in the selection of seed quantity or due to the insufficient quantity. Therefore, the structure of top part of corn sowing will be improved in the future. The pattern selection of seeds will adopt more cardinality. The deficiencies in this area will be improved in future studies.

REFERENCES

[1] Cheng R, Jin Y., (2018), A social learning particle swarm optimization algorithm for scalable optimization. *Information Sciences,* Vol. 291, Issue 6, pp. 43-60. Netherlands;

[2] Dong J., (2018), Biomedical materials for adhesion repair after tendon injury. *Journal of Clinical Rehabilitative Tissue Engineering Research,* Vol. 15, Issue 47, pp. 8899-8902. China;

[3] Gultyaeva E., Shaydayuk E., Gannibal P., (2021), Leaf Rust Resistance Genes in Wheat Cultivars Registered in Russia and Their Influence on Adaptation Processes in Pathogen Populations. *MDPI.* Vol. 11, Issue 4, pp. 319. Switzerland;

[4] Martínez-Moreno F., Giraldo P., del Mar Cátedra M., Ruiz M., (2021), Evaluation of leaf rust resistance in the Spanish core collection of tetraploid wheat landraces and association with ecogeographical variables. *MDPI (Agriculture),* Vol. 11, Issue 4, pp. 277. Switzerland;

[5] Gross G, Hoffmann A., (2018), Therapeutic strategies for tendon healing based on novel biomaterials, factors and cells. *Pathobiology,* Vol. 80, Issue 4, pp. 203-210. Switzerland;

[6] Jensen R., (2021), The Restless and Relentless Mind of Wes Jackson: Searching for Sustainability. University Press of Kansas. *JSTOR*. USA;
[7] Kang D., (2018), Anti-adhesion effect of absorbable biomaterials during tendon reconstruction. *Chinese Journal of Tissue Engineering Research,* Vol. 12, Issue 2, pp. 23-24. China;
[8] Nouiri M., Bekrar A., Jemai A., (2018). An effective and distributed particle swarm optimization algorithm for flexible job-shop scheduling problem*. Journal of Intelligent Manufacturing,* Vol. 2, Issue 3, pp. 11-13. Netherlands;
[9] Fan P., Lang G., Guo P., Liu Z., Yang F., Yan B., Lei X., (2021) Multi-feature patch-based segmentation technique in the gray-centred RGB colour space for improved apple target recognition. *MDPI (Agriculture),* Vol. 11, Issue 3, pp. 273. Switzerland;
[10] Lan Y., Sui X., Wand J., Duan Q., Wu C.Y., Ding C.B., Li T., (2021). Effects of nitrogen application rate on protein components and yield of low-gluten rice. *MDPI (Agriculture),* Vol.11, Issue 4, pp.302. Switzerland.
[11] Tai J.J., Li H.T., Du Y.F., Mao E.R., Zhang J.N., Long X.J., (2020), Rapid design of maize ear harvester header based on knowledge engineering. *INMATEH Agricultural Engineering*, Vol.61, Issue 2, pp. 263-272, Romania;
[12] Wang B., He J.L., Zhang S.J., Li L.L., (2020), Nondestructive testing of soluble solids content in cerasus humilis using visible / near-infrared spectroscopy coupled with wavelength selection algorithm. *INMATEH Agricultural Engineering,* Vol.61, Issue 2, pp.251-262, Romania;
[13] Wang G.P., Zhang K.F., Chen G.F., (2018), Application of artificial biomaterials for the treatment of tendon injury. *Journal of Clinical Rehabilitative Tissue Engineering Research,* Vol. 13, Issue 47, pp. 9345-9348. China;
[14] Wei W., Yuan J.G., Xue W.B., (2021), Detection system for feeding quantity of mobile straw granulator based on power of screw conveyor. *INMATEH Agricultural Engineering*, Vol.63, Issue 1, pp. 9-18, Romania;
[15] Wu M.Y, Lin Y.H., Ke C.K., (2018), WSN-based Automatic Monitoring Management Platform for Plant Factory. *International Journal of Digital Content Technology & Its Applications,* Vol. 8, Issue 6, pp. 303-311. South Korea.

ANALYSIS OF CRANKSHAFT MECHANISM OF AGRICULTURAL ENGINE UNDER THE APPLICATION OF COMPOUND SUPERCHARGING TECHNOLOGY
/
复合增压技术应用下的农用发动机曲轴机构分析

Xu Ran[1)]*, Chandra Mathkour[2)]
[1)]Water Conservancy of Shandong Technician College, Zibo, Shandong, 255130 / China
[2)]Amerisourcebergen, Chesterbrook / United States of America
**E-mail: fi5619552biwensho@163.com*
DOI: https://doi.org/10.35633/inmateh-63-38

Keywords: *crankshaft mechanism, optimization, agriculture, tractor engine*

ABSTRACT

With the development of engine supercharging technology and the application of in-cylinder direct injection technology, engines with high power and torque have become a trend. Crankshaft, as one of the most important and expensive parts in tractor engine, plays the role of transforming linear motion into circular rotation. The damage and destruction of crankshaft will lead to the damage of other parts of the engine, which makes the engine unable to work normally, and its stability affects the reliability of the whole engine to a great extent. The main failure form of tractor engine crankshaft is bending fatigue failure, so alternating bending stress occurs in crankshaft, which may cause fatigue failure of crankshaft. Crankshaft is one of the important components of tractor engine, and its stress is complex, which is the key and difficult point of engine design. In this paper, the crankshaft of tractor engine is analysed and studied based on compound supercharging technology, so that the dynamic characteristics of the engine are deeply understood, the action law of dynamic working load is mastered, the response analysis and evaluation of the system are carried out, and the optimization method of crankshaft mechanism of agricultural tractor engine is found out.

摘要

随着发动机增压技术的发展和直喷技术的应用，大功率大扭矩发动机已成为一种发展趋势。曲轴作为拖拉机发动机中最重要、最昂贵的零件之一，起着将直线运动转化为圆周运动的作用。曲轴的损坏和破坏会导致发动机其他部件的损坏，使发动机不能正常工作，其稳定性在很大程度上影响到整个发动机的可靠性。拖拉机发动机曲轴的主要失效形式是弯曲疲劳失效，曲轴产生交变弯曲应力，可能导致曲轴疲劳失效。曲轴是拖拉机发动机的重要部件之一，其受力复杂，是发动机设计的重点和难点。本文以复合增压技术为基础，对拖拉机发动机曲轴进行了分析和研究，以便深入了解发动机的动态特性，掌握动态工作载荷的规律，分析和评价系统的响应，并找出了农用拖拉机发动机曲轴机构的优化方法。

INTRODUCTION

Crankshaft is one of the important components of engine, and its stress is more complex, which is the key and difficult point of engine design. Traditional design methods can't meet the actual needs, and the bearing capacity of crankshaft can be accurately analysed by using 3D solid modeling software and finite element software *(Wei W. et al., 2021)*. The research on structural strength of engine is first carried out on large heavy-duty diesel engine, because this kind of diesel engine usually not only bears large load, but also has small batch size, long manufacturing cycle and high cost *(Deng D.W. et al., 2019)*. Among all parts of tractor engine, the core position of crankshaft is self-evident. Its performance directly affects the reliability and life of the engine. The evaluation of crankshaft also represents the evaluation of the whole engine. Crankshaft is one of the most important parts of the engine. It has the characteristics of complex structure, rapid structural change and extremely complex working conditions. It bears the alternating stress of torsion and bending under the periodically changing gas force. In the process of engine operation, the explosion pressure and inertia load of gas are transmitted, and then the torque is transmitted to the flywheel end, which is the output power of the engine *(Chen Y.M. et al., 2021)*. The main failure mode of tractor engine crankshaft is bending fatigue failure, so alternating bending stress in crankshaft may lead to fatigue failure of crankshaft, and other parts may be damaged once crankshaft fails.

In the working process of tractor crankshaft, it bears complex loads, including reciprocating mass inertia force, rotating mass inertia force, inertia force caused by dead weight and counterweight *(Shu P.P., 2019)*. Furthermore, due to the periodicity of the internal combustion engine, the magnitude and direction of these loads on the crankshaft will change periodically *(Yu L.C. et al., 2021)*. In the past, generally speaking, for the large-scale production of small and medium-sized internal combustion engines, the degree of strengthening was not high, and the design could be based on experience. However, with the continuous development of small and medium-sized internal combustion engines to high speed and high power, this situation has undergone major changes *(Qiuju X. et al., 2021)*. With the development of engine supercharging technology and the application of in-cylinder direct injection technology, engines with high power and high torque have become a trend. With the continuous increase of the maximum explosion pressure in the cylinder, the reliability requirements of the engine are continuously improved, the working conditions of the crankshaft are worse, and the strength requirements of the crankshaft are also higher *(Jhih Y.C. et al., 2021)*. Modal analysis is used to determine the vibration characteristics of design mechanism or mechanical components, that is, the natural frequency and mode shape of structure, which are important parameters in structural design under dynamic load. If improving its dynamic characteristics is an important goal of dynamic design and structural optimization, engine design can be changed from experience, analogy and static design method to dynamic and optimal design method, thus improving the design level of products.

Crankshaft is the key component of diesel engine. The quality characteristics of crankshaft directly affect the service life, safety and reliability of diesel engine. Strength analysis and finite element analysis of crankshaft have become an indispensable link in new product development and design *(Dong J.H. et al., 2018)*. Therefore, the multi-body dynamics analysis of diesel engine has certain guiding significance for the development and design of new products. The problems are always complicated for medium and small supercharged engines with high heat load and mechanical load *(Liu Y.W. et al., 2020)*. As in the past, it is impossible to study the crankshaft directly through the comprehensive test of prototype. The results of finite element static analysis and dynamic analysis can truly and effectively obtain the stress distribution of crankshaft under all dangerous working conditions. Through this result, the danger can be predicted, which can reveal the mechanism and provide basic data for optimizing the crankshaft strength *(Meng R.G. et al., 2018)*. It is of great significance to study the dynamic performance of crankshaft and master the vibration law and load change law of crankshaft in the working process for improving the reliability and service life of the crankshaft. Through the analysis and research of crankshaft, we can deeply understand the dynamic characteristics of tractor engine, master the law of dynamic workload, analyse and evaluate the response of the system, and find out the problems in dynamic performance.

In the aspect of crankshaft research, *Yuan Z.Y. et al.* used simulation technology to analyse the static strength of crankshaft *(Yuan Z Y et al., 2019)*. *Peng F. et al.* carried out finite element analysis on fatigue strength of 368Q engine crankshaft *(Peng F., 2020)*. *Cai Y.Q. et al.* used the experimental method to study the crankshaft modal of small diesel engine *(Cai Y.Q. et al., 2018)*. *Liu Z.T.* used finite element analysis technology to analyse the strength of X6135 diesel engine crankshaft, thus exploring a new method combining continuous beam method and finite element method *(Liu Z.T. et al., 2020)*.

Yang Z.L. studied that the bending stress of crankshaft is affected by the change of its structural parameters *(Yang Z.L. et al., 2019)*. At this time, the finite element method has been applied, but the method of measuring stress with strain gauge is still applied at the same time, which is used to compare with the results of finite element. Because the load of crankshaft changes violently in the actual working condition, in order to obtain the stress distribution as detailed as possible, a lot of working condition calculation must be done. However, due to the large structure of crankshaft, the number of three-dimensional nodes needed to be divided is very large *(Hong W.L. et al., 2021)*.

MATERIALS AND METHODS

Parametric model and finite element static analysis of crankshaft

Crankshaft is the core component of the engine group, which is constantly affected by the interaction of cylinder, piston, body and other parts in the working process. Before the analysis of crankshaft, the matching engine must be analysed theoretically, including the selection of dangerous working conditions and the calculation of cylinder aerodynamics.

Crank and connecting rod mechanism is one of the main motion mechanisms of the engine group. It can transform the reciprocating linear motion of the piston into the rotary motion of the crankshaft around the rotation centre, so as to output the explosive force of the cylinder to the transmission system in the form of torque. The core theory of virtual prototyping technology is multi-body system dynamics. Multi body system is a complex mechanical system connected by multiple objects through motion pairs. Multi body system dynamics is composed of multi rigid body system dynamics and multi flexible body system dynamics. As one of the important moving parts of engine, piston works under severe conditions, such as high temperature, high pressure, high speed and poor lubrication. Therefore, it is necessary to require the piston to have enough stiffness and strength, reliable force transmission *(Li J.J., 2020)*. Although solid mechanics and structural mechanics have developed quite well, when it is necessary to analyse complex structural analysis problems such as crankshafts, the classical methods are still powerless. However, the finite element method can overcome this difficulty well, and it has developed into a powerful and practical general numerical analysis method in structural analysis.

Crankshaft dynamic model mechanism is mainly crank connecting rod mechanism, including piston connecting rod group, crankshaft flywheel group and other main operating components of internal combustion engine. Its function is to convert the reciprocating motion of the piston into the rotary motion of the crankshaft, and convert the air pressure acting on the piston into torque. Among all the loads on the crankshaft, the thrust from the connecting rod is the largest, which will directly affect the peak stress. Therefore, the analysis of crank and connecting rod mechanism is very important. The application of displacement boundary conditions is usually based on the actual support of crankshaft. The interaction between automation objects and automation customers is shown in Figure 1.

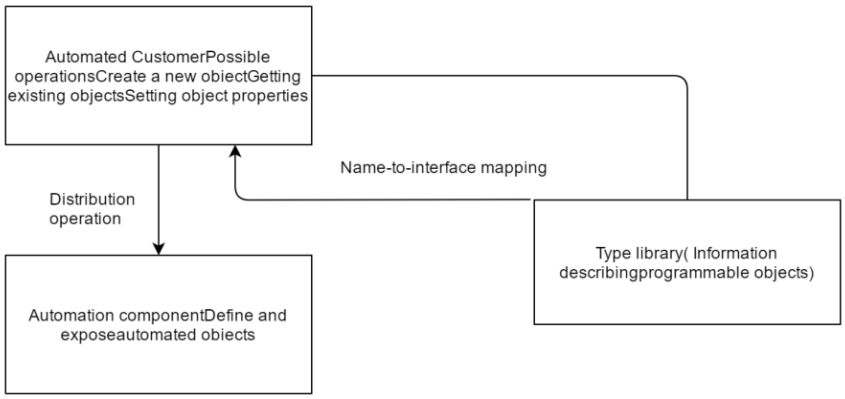

Fig. 1 – Interaction between automated customers and automated components

The crankshaft of multi cylinder tractor diesel engine is supported by several main bearings. Therefore, in the process of analysis, more than one main journal support should be set according to the actual situation. The static analysis of crankshaft is to calculate the displacement and stress of crankshaft under fixed load. Because the influence of inertia and damping is not considered, the static analysis can provide an important reference for the structural optimization of crankshaft.

Now, with the rapid development of computer, the configuration of computer hardware is higher and higher, and the calculation speed reaches trillions of times, which makes the application scope of finite element analysis more and more widely. Three dimensional finite element method can accurately determine the stress of any part. Before determining how to simplify the model, firstly, under the same working conditions, loading mode and mesh accuracy division method, the full axis model with oil hole and without oil hole is compared and analyzed.

From the cloud diagram, the maximum stress values and stress distribution of the two structures are similar, and the peak stress of the oil hole model does not appear in the oil hole position. The boundary element method (BEM) is a common method to analyze the internal combustion engine related problems. However, for parts with complex geometry and loads, such as crankshafts. In order to obtain accurate results, the mesh should have accurate shape, appropriate density and small distortion. However, such a grid is not only difficult to partition, but also has a large number of nodes, long solving time and consumes a lot of computing resources.

Using the existing technology to establish a multi-mode collaborative work environment, the operation process of collaborative design is shown in Figure 2.

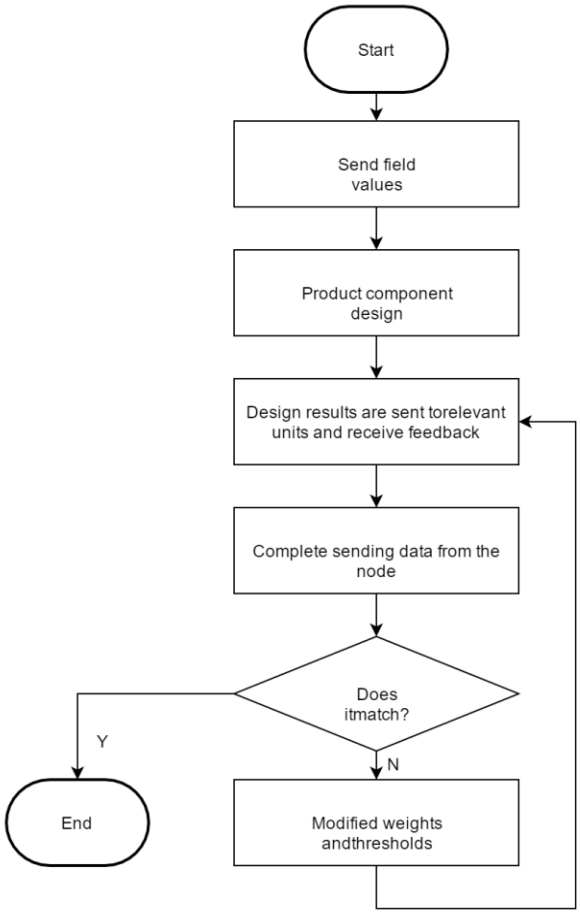

Fig. 2 – The operation process of mechanical processing cooperative design

As the gas pressure gradually rises to the highest value, the gas force will far exceed the inertial force. Because the pressure in the cylinder is higher than atmospheric pressure, the direction of gas force is vertically downward, and because the direction of inertia force is always opposite to the direction of mass movement, the inertia force is also vertically upward. For the local areas with serious stress concentration, smaller elements are used, and the rest areas are larger elements, which realizes a rapid transition between grid density and mesh density.

The finite element method is a discrete numerical method. The discrete elements are only connected by nodes, and all forces and displacements are calculated by nodes. For each cell, an appropriate interpolation function is selected, so that the function satisfies certain conditions in the subdomain, the inner boundary on the subdomain interface and the outer boundary between the subdomain and the external interface. Forged steel crankshafts with high tensile strength and high elongation are generally selected for the crankshafts of traditional supercharged direct injection engines to meet the performance requirements of high power and high torque.

For crankshafts, stress concentration is often concentrated in areas with irregular geometric shapes such as oil holes and transition fillets.

The fundamental purpose of multibody system dynamics is to apply computer technology to dynamic analysis and simulation of complex mechanical systems. To study the dynamics of these systems, it is necessary to establish nonlinear motion equations, energy expressions, kinematic expressions and other quantitative formulas. Through the use of network technology, workers can quickly understand the demand of automation market, the development direction and the information of product feedback, so as to provide reference direction for the design work of related mechanical design and manufacturing enterprises.

Figure 3 is an example of communication in a three-dimensional network.

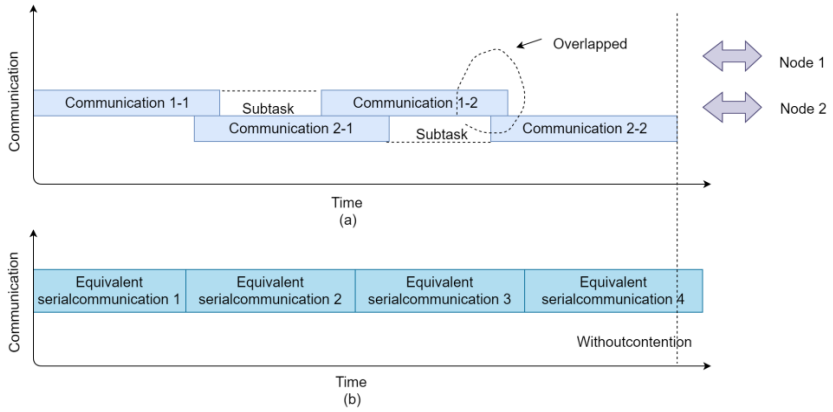

Fig. 3 – Communication example in a three-dimensional network

Project quality control refers to the control of the progress of each stage and the final completion period of the project in the process of project implementation. In which the process duration obeys lognormal distribution. Figure 4 shows the planning results of critical chain method.

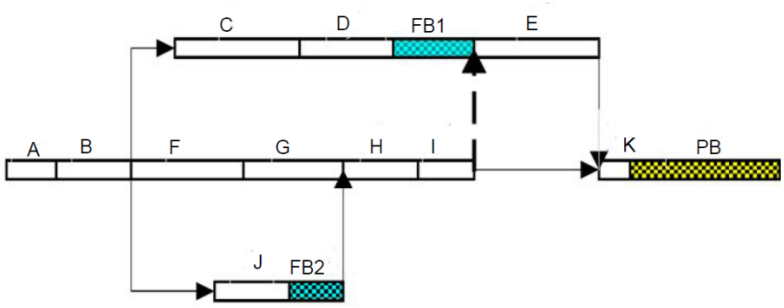

Fig. 4 – Critical chain method planning results

The traditional calculation method generally determines the stress concentration coefficient through experiments. However, most of the stress concentration coefficients are empirical formulas, and some related test conditions and parameter conditions must be considered when using them. Discretization is the basis of finite element method. The type, number, shape, size and arrangement of units must be determined according to the actual situation of the structure. The purpose is to divide the structure into small enough units, so that the simple displacement model can represent the exact solution approximately enough. Due to the complexity of the shape and the sharp change of the structure of the tractor crankshaft, serious stress concentration will occur at the transition fillet from crank arm to main journal and from crank arm to connecting rod journal, so it is necessary to adopt appropriate technology to strengthen the strength of the excessive fillet. The stress situation of crankshaft mainly refers to the stress analysis of crank-connecting rod mechanism. During the working stroke, the crank connecting rod bears both bending force and torsion force. It can be said that the working environment of crankshaft is extremely harsh and complex. Piston is the “heart” of tractor engine, which bears alternating mechanical load and thermal load, and is one of the key components in the engine with the worst working conditions. The function of the piston is to bear the gas pressure and inertia force, and transmit the gas pressure to the connecting rod through the piston pin, so as to drive the crankshaft to rotate and do work externally.

RESULTS

Dynamic analysis of crank and connecting rod mechanism

Because of the characteristics of finite element technology, the pre-and post-processing software of finite element software becomes a relatively independent and very important part. Optimum size sensitivity analysis is to use the change of sensitivity value to reflect the degree of influence of each parameter on the target value, so as to optimize the design of crankshaft according to the size and positive and negative of sensitivity value.

Pretreatment is an important link in finite element analysis and calculation, and the quality of pretreatment will directly affect the accuracy of calculation results and the scale of calculation. The discretization of computational objects divides the computational model to be analysed into finite elements, and sets connection nodes between the elements, so that the relevant parameters of adjacent elements have certain continuity, and then forms a collection of elements to replace the original computational objects, and replaces the elastic body boundary constraint with the node constraint on the boundary. Multi-body dynamics has something in common with classical mechanics. For example, the simplest system free particle in multi-body dynamics is also the research object of classical mechanics. The task of multibody system dynamics is to establish a mathematical model that can be identified and solved by computer for the dynamics and operational analysis of complex multibody systems, and on this basis, to seek an accurate and stable numerical solution method.

Rod force is the most critical of all loads borne by tractor crankshaft. It is the combination of cylinder burst pressure and piston reciprocating mass inertia force, and its magnitude will directly affect the maximum stress value. In most cases, pre-processing software has a good interface with CAD software, and can be combined with numerous finite solution software, so that users can solve problems faster and more conveniently. The parametric model of crankshaft is shown in Figure 5.

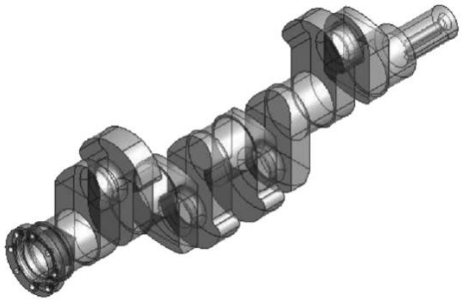

Fig. 5 – Parametric model of crankshaft

Aiming at the medium access constraint of wireless communication network, the agent node scheduling protocol is designed by using binary sequence. And the scheduling protocol is used to schedule the qualified agent nodes to access the network at the sampling time. Figure 6 shows the structure of agent nodes.

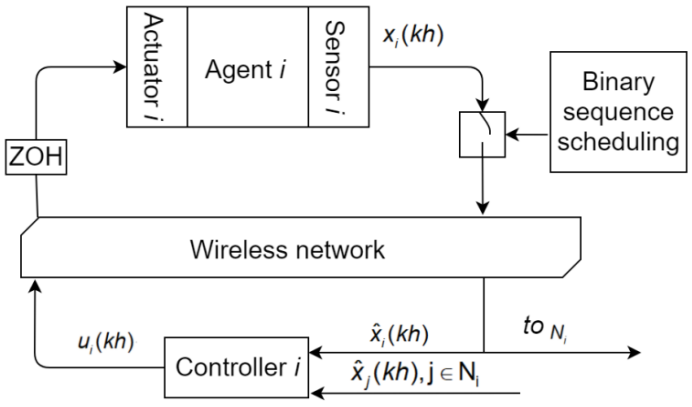

Fig. 6 – The structure of the agent node

The finite element static analysis of the crankshaft model was carried out, and the stress results under various working conditions were calculated. In the preprocessing step, the same simplified model, meshing accuracy and material parameters are used to accurately compare and summarize the results.

Establishment of finite element model

Before meshing, the geometric model should be processed, for example, some features which have little influence on the results of structural analysis and greatly increase the workload should be simplified, such as chamfers, local holes, etc. In the research of this subject, the oil holes of crankshaft have been cleaned. Assembled parts of mechanical products are often connected with each other by fastening bolts, bearings, pins and supports. This is completely different from the connection mode between general structural members. The two members in contact with each other are neither rigid connection which can transmit torque nor hinge which can transmit tensile force. Only pressure and friction force can be transmitted between two contact surfaces, and the tension force can be transmitted. Adjacent parts are either separated or contacted and cannot penetrate. Polynomials are usually chosen as the displacement mode, because the mathematical operation of polynomials is convenient, and all local functions can be approximated by polynomials. As for the choice of terms and order of polynomial, the degree of freedom of element and the convergence of solution should be considered. Because the contact force between contact pairs varies with the degree of compression deformation of the parts in contact with each other, and the deformation displacement of the structure is determined by the structural load including the contact force, the structural analysis of the structure with contact pairs by calculating the displacement through the load is no longer a general linear analysis problem, but a contact nonlinear analysis problem requiring iterative calculation.

In order to reduce the cost of crankshaft and improve the cost performance and competitiveness of engine, it is an effective method to change the blank and process of crankshaft from non quenched and tempered steel and forging process to ductile iron and casting process. In order to describe the displacement of any point in the element, it is necessary to assume that the displacement distribution in the element is a simple coordinate function, i.e. displacement mode or interpolation function. After determining the input vector of the finite element optimization model, the distribution of variables is checked, and these data are transformed to facilitate network learning. For continuous variables, the common normalization methods are as follows:

$$\frac{Y(s)}{N(s)} = \frac{G_D(s)G(s)}{1+\mathrm{C}(s)H(s)} \tag{1}$$

The network convergence time is greatly shortened and the performance of the network is improved. The transformation method is:

$$\frac{I(s)}{U(s)} = \frac{Js+b}{JLs^2+(bL+JR)s+bR+K^2} \tag{2}$$

Find the heat transfer coefficient:

$$f(x) = \sum_{j=1}^{n} \alpha_j N\left(\mu, \sigma_j^2\right) \tag{3}$$

Under the joint action of machining control law and multi-machining control law, multi-system successfully realized machining treatment and machining control in the machining process. There are many cognitive radio networks, and each cognitive spectrum is allocated by the cognitive base station. The change of success rate with cycle times is shown in Table 1.

Table 1

Success rate varies with the number of cycles

Number of calculations	Success rate of prompt function (%)
2000	80.97
2800	81.33
6000	81.78
9000	87.65

Calculate the activation value of the output layer unit:

$$BH(p,q) = \sum_{u=1}^{n} \sqrt{p_u(f)q_u} \tag{4}$$

The sample is sent to the hidden layer unit through the connection weight, and a new activation value of the hidden layer unit is generated:

$$E(x,y,z)=\frac{xL_{LED}A_{LED}}{\left[(x-x_0)^2+(y-y_0)^2+(z-z_0)^2\right]^{3/2}} \quad (5)$$

The change of success rate with cycle times is shown in Table 2.

Table 2

The success rate varies with the number of cycles

Number of calculations	Prompt function success rate (%)
3000	80.75
3700	81.11
7000	81.58
8000	87.43

Improve and meet the performance requirements of machining from four aspects: solidity, economy, energy saving and coordination. The relation number, overall density and degree centre potential are analysed, as shown in Table 3. With the increase of node relations, the shortest path between nodes decreases, as shown in Figure 7.

Table 3

Analysis of processing material network structure

Network	Number of relationships	Overall density	Degree central potential
Meet information	413	388	0.871
Mutual information	455	372	0.798
Weighted summation	346	365	0.842

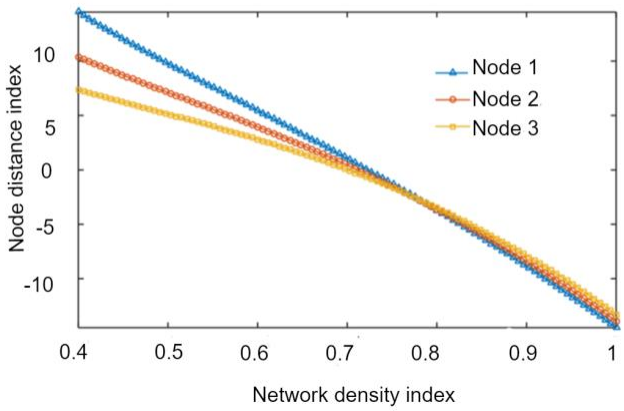

Fig. 7 - Distance analysis of network nodes during processing

According to the crankshaft of small displacement supercharged direct injection engine, on the premise of meeting the requirements of crankshaft strength and reliability, the design concept of changing crankshaft from non-quenched and tempered steel to nodular cast iron and optimizing tractor crankshaft structure to improve the fatigue strength of crankshaft is adopted for design optimization. In order to meet different analysis needs, different cell types should be selected. When selecting the element type, the selected element can simulate the shape of the geometric model to be analysed more accurately, and avoid causing larger calculation errors.

Under the same cell density, tetrahedral elements are not as accurate as hexahedron elements, while pentahedral elements are used as transitional elements. The emergence of computational multibody system dynamics has completely changed the traditional mechanism dynamics analysis method, so that engineers no longer need to carry out complicated manual calculations, only need to establish appropriate mathematical models according to engineering problems, and the next work can be handed over to computers. After the solution is completed, the post-processing program provided by computer software is used to provide various output modes of the solution results, which can help engineers to process the calculation results and realize automation and intelligence.

CONCLUSIONS

Crankshaft is one of the most important parts in agricultural tractor diesel engine, and its fatigue strength and safety factor directly affect the safe operation of the whole diesel engine. Different from the single-throw model analysis of crankshaft, the analysis of the whole shaft can not only get the value of the maximum stress on the crankshaft under a certain dangerous working condition, but also get the distribution law of the maximum stress on the whole shaft. The maximum stress of the whole crankshaft model is in the limit range under all dangerous working conditions. Although the maximum stress of crankshaft under various dangerous conditions is less than the limit value, the maximum stress distribution often appears in several fillets near the output end in a working cycle. It is an economic and effective scientific method to analyze the key parts of the mechanism by combining the digital prototype simulation technology with the finite element analysis. Using finite element analysis method to predict crankshaft strength can effectively save sample production and test time, reduce cost and improve product reliability.

REFERENCES

[1] Cai Y.Q., Zhao C., (2018), Finite element modal analysis of a V12 engine crankshaft based on Workbench. *Journal of North China University of Technology: Natural Science Edition*, Vol. 40, Issue 04, pp. 82-87. China;

[2] Chen Y.M., Song H.Y., Zhao R., Su Q., (2021), CFD-based simulation and model verification of peaches forced air cooling on different air supply temperatures. *INMATEH Agricultural Engineering*, Vol. 63, Issue 001, pp. 59-70. Romania;

[3] Deng D.W., Zheng Y.N., Nie J. Y., (2019), Research on low-speed performance of gasoline engine two-stage compound supercharging system. *Small Internal Combustion Engine and Vehicle Technology*, Vol. 48, Issue 02, pp. 18-21. China;

[4] Dong J. H., Li W., Yang Z. R., (2018), Analysis and optimization of torsional vibration of 3-cylinder engine crankshaft system based on virtual prototype. *Automotive Engine*, Vol. 235, Issue 02, pp. 64-70. United Kingdom;

[5] Hong W.L., Qing J.W., Jin H., Caiyun L., Qinglu Y., Peng L., (2021), Experiment and parameters optimization of seed distributor of mechanical wheat shooting seed-metering device. *INMATEH Agricultural Engineering*, Vol. 63, Issue 001, pp. 29-40. Romania;

[6] Jhih Y.C., Hsin C.C., Chih W. C., Kai M. Y., (2021), Relationship between Antioxidant Components and Oxidative Stability of Peanut Oils as Affected by Roasting Temperatures. *MDPI (Agriculture)*, Vol. 11, Issue 004, pp. 300. Switzerland;

[7] Li J.J., (2020), Research on Bearing Lubrication of Three-cylinder Naturally Aspirated Gasoline Engine. *Times Auto*, Vol. 334, Issue 10, pp. 149-151. China;

[8] Liu Y.W., Ye F.H., Chen H., (2020), Optimization of engine crankshaft friction torque monitoring system. *Modular Machine Tool and Automatic Manufacturing Technology*, Vol. 553, Issue 03, pp. 100-103+107. China;

[9] Liu Z.T., Wei H.L., Xu Q.Z., Song G.Y., (2020), Analysis of engine crankshaft timing phase air gap optimization based on virtual assembly technology. *Internal Combustion Engine and Power Plant*, Vol. 179, Issue 05, pp. 82-87+102. China;

[10] Meng R.G., Zhang C.H., Liang J.C., (2018), Application of improved particle swarm optimization-Elman algorithm in engine crankshaft pulse width prediction. *China Mechanical Engineering*, Vol. 29, Issue 007, pp. 766-770. China;

[11] Peng F., (2020), Analysis of engine crankshaft strength and fatigue based on ANSYS Workbench. *Mechanical Engineering and Automation*, Vol. 219, Issue 02, pp. 89-90+93. China;

[12] Qiuju X., Fanyi L., Ming J. Y., Jun L., Shang H. Y., Shou Y. X., (2021), DEM simulation and evaluation of well cellar making performance of opener with large socket. *Machine Design*, Vol. 63, Issue 01, pp. 41-50. Romania;

[13] Shu P.P., (2019), Numerical simulation and die optimization of automobile engine crankshaft die forging based on Deform. *Hot Working Technology*, Vol. 48, Issue 03, pp. 180-182. China;

[14] Wei W., Yuan J.G., Xue W.B., (2021), Detection system for feeding quantity of mobile straw granulator based on power of screw conveyor. *INMATEH Agricultural Engineering*, Vol. 63, Issue 001, pp. 09-18. Romania;

[15] Yu L.C., Meng Z.L, Yu B.L., Li L.Y., Qiang J.P., Xiang Y., (2021), Design and experiment of seed agitator for vertical disk seed metering device. *INMATEH Agricultural Engineering*, Vol. 63, Issue 01, pp. 177-186. Romania;
[16] Yang Z.L., Hu B., Jia H.X., (2019), Natural frequency optimization of engine crankshaft based on topology optimization. *Journal of Anyang Institute of Technology*, Vol. 018, Issue 004, pp. 19-23. China;
[17] Yuan Z.Y., Gu T.C., Wang B., (2019), The influence of main journal cylindricity on the lubrication characteristics of engine bearings. *Mechanical Design and Research*, Vol. 35, Issue 01, pp. 113-117+125. China;

RESEARCH ON A GRAIN CULTISEEDER FOR SUBSOIL-BROADCAST SOWING
/
ДОСЛІДЖЕННЯ ЗЕРНОВОЇ СІВАЛКИ-КУЛЬТИВАТОРА ДЛЯ ПІДҐРУНТОВО-РОЗКИДНОЇ СІВБИ

Rogovskii I.L.[1)], Titova L.L.[1)], Trokhaniak V.I.[1)], Borak, K.V.[1,2)], Lavrinenko, O.T.[1)], Bannyi, O.O.[1)] [1]
[1)] National University of Life and Environmental Sciences of Ukraine / Ukraine;
[2)] Zhytomyr Agrotechnical College / Ukraine.
Tel: +380673513082; E-mail: Trohaniak.v@gmail.com
DOI: 10.35633/INMATEH-63-39

Keywords: *cultivator, optimization, mathematical modelling, seeds, sowing.*

ABSTRACT

The paper presents the results of theoretical and experimental studies on determining process efficiency of subsoil-broadcast sowing by means of improving the diagram and determining the technological parameters of a cultiseeder tined coulter / opener. The design of a tined coulter, where seeds are fed to its right and left sub-coulter spaces through various seed pipes, has been suggested. A simulation model of the process of seed movement and deflection in the sub-coulter space has been suggested. As a result of the conducted experimental studies, the statistics of the air drag coefficient and the recovery coefficient, the deviation angle of a seed flight operating trajectory after its divergence from the theoretical one, have been found. Rational parameters of a separator-distributor have been determined. Field experiments have been conducted in order to compare agro-technical performance indices of the experimental coulter and a commercial one.

РЕЗЮМЕ

В статті наведены результати теоретичних та експериментальних досліджень зі встановлення ефективності технологічного процесу підґрунтово-розкидної сівби шляхом вдосконалення схеми та визначення раціональних параметрів лапового сошника сівалки-культиватора. В результаті узагальнення запропоновано конструкцію лапового сошника, до якого у правий та лівий підлапові простори насіння подається різними насіннєпроводами. Запропоновано імітаційну модель процесу відбивання та руху насіння у підлаповому просторі. За результатами експериментальних досліджень встановлено статистичні характеристики коефіцієнта опору повітря та коефіцієнта відновлення, кута відхилення реальних траєкторій польоту насіння після відбивання від теоретичної. Визначено раціональні параметри відбивача-розподільника. У виробничих умовах проведено експериментальні дослідження з порівняння агротехнічних показників роботи для експериментального і серійного сошників.

INTRODUCTION

One of the main indicators of sowing quality is the uniform distribution of plants by feeding area (*Zhai C., et al., 2019*). Until now, the most common method of sowing cereals is ordinary, in which plants occupy only about 30% of the field area. Agrotechnical science has established that the necessary factors for the growth and development of cereals – light, water and nutrients can be rationally used only with a uniform distribution of seeds over the field area (*Vlăduţ D.I. et al., 2018*). The plants closest to the optimal feeding area are obtained by applying the soil-spreading method of sowing (*Jha A. & Kewat M., 2013*), which is performed by a seeder-cultivator. In addition to increasing yield capacity, this method allows you to combine pre-sowing tillage with sowing, which reduces the time of sowing, operating costs and causes less loss of soil moisture (*Rogovskii I. et al., 2020*).

In order to provide high accuracy of seed distribution on a field surface, a great number of coulter designs has been suggested. Coulters with passive seed distributors, which are simply engineered and more reliable compared to active distributors (mechanical and pneumatic ones), are considered to be more advanced.

[1] *Rogovskii I.L., Prof. Ph.D. Eng.; Titova L.L., Assoc. Prof. Ph.D. Eng.; Trokhaniak V.I., Assoc. Prof. Ph.D. Eng.; Borak K.V., Assoc. Prof. Ph.D. Eng.; Lavrinenko, O.T., Assoc. Prof. Ph.D. Eng.; Bannyi O.O., Assoc. Prof. Ph.D. Eng.*

In order to change the direction of seed movement in passive distributors and maintain the necessary speed of seed distribution across the width of gripping, kinetic energy obtained from falling from a certain height is used. The change of movement directions in the existing distributors can be made in the process of oblique impacting or in the process of sliding on a curvilinear surface.

The advantages of seeder-cultivators can be especially effective when it is used in farms, in most of which energy resources are represented by one or two tractors of traction class no more than 14 kN. Pre-sowing tillage and sowing are performed by one tractor (*Voicea I. et al., 2020*). This causes a significant gap between the implementation of pre-sowing cultivation and sowing, which negatively affects the yield.

Analysing the results of research on mechanization of subsoil-spreading sowing method, it should be noted: all studies confirm the high efficiency of this method (*Farooq M. et al., 2011*), which is performed by seeder-cultivators (*Turan J. et al., 2015*); reasonable advantage of passive distributors in comparison with mechanical and pneumatic active distributors (*Jin H. et al., 2014*); change of the direction of movement of seeds by passive distributors can be carried out in two ways – sliding on a curved surface or reflection (*Verma A. & Guru P., 2015*). The method of sliding is more studied, but it has a number of disadvantages. It requires vertical feeding of seeds, which is not always possible; distributors operating on the principle of reflection are studied superficially (*Saitov V.E., 2014*); most studies have not taken into account the randomness of the physical and mechanical properties of seeds (*Abbaspour-Gilandeh Y. et al., 2018*).

Given the above, we can assume that a promising tendency is the development of openers for subsoil-spreading sowing with distributors operating on the principle of reflection (oblique impact). To implement this direction, it is necessary to study the process in detail, taking into account the statistical characteristics of seed properties (*Rogovskii I.L. et al., 2020*).

Thus, it is to the point to develop a cultiseeder. Here, the operating elements of cultiseeders should be maximally reliable.

The purpose of the study is to increase the efficiency of the process of subsoil spreading by improving the scheme and determining the rational parameters of the opener of the seeder-cultivator.

MATERIALS AND METHODS

Constructive Elements

The method of determining the statistical characteristics of the coefficient of air resistance K was, as follows: using the installation (Fig.1), the time of fall of series of seeds t_i from a given height H was determined; according to the graphical dependences $K=f(t)$ for different values H, provided $x=H$, for each t_i, the corresponding values K_i were determined, which were processed statistically.

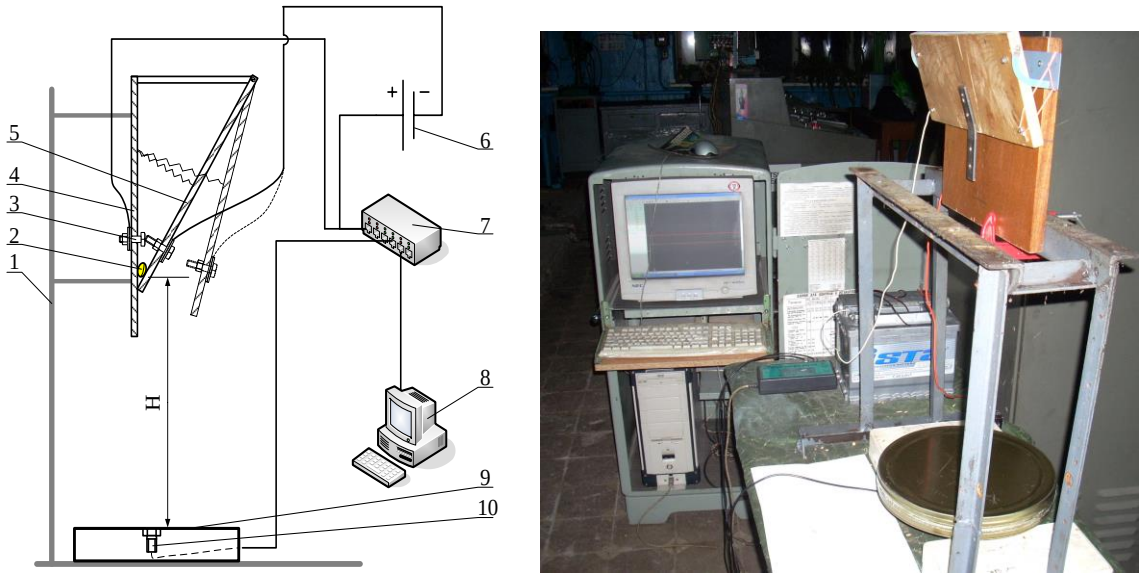

Fig. 1 – The scheme of the installation for defining seed falling time

1 – support; 2 – seeds; 3 – contact; 4, 5 – fixed and movable valve surface; 6 – current source; 7 – USB oscilloscope; 8 – PC; 9 – site; 10 – vibration sensor.

Statistical characteristics of the recovery factor K_b were determined by the flight range of the seed L_i after falling from a fixed height on an inclined reflector. According to graphic dependencies $K_b=f(L)$, a corresponding value L_i was determined for each value K_{bi}. The obtained values K_{bi} were processed statistically. The speed of seeds after climbing from the curved part of the seed line was determined by the flight range of the seed L_k after passing through the seed line of a certain radius. The method of multivariate testing is used to substantiate the optimal values of angles $\alpha_1(x_1)$ and $\gamma(x_2)$ and the height of the sub-blade area $h(x_3)$. The results of the implementation of the planning matrix of the experiment are presented in table 1.

According to the indicators of lateral scattering of seeds, due to the oblique impact, the angles τ between the central plane and the plane of the seed trajectory, flight range l and lateral deviation from the central plane c were taken (Fig.2). After the seeds fall from a fixed height H without initial velocity and reflection by the reflector *2*, the values l and c are measured. According to the obtained data, the statistical characteristics of the studied parameters are determined. Studies to determine the uniformity of seed distribution across the width of the seeding strip were performed on the installation, the scheme of which is shown in Fig.2.

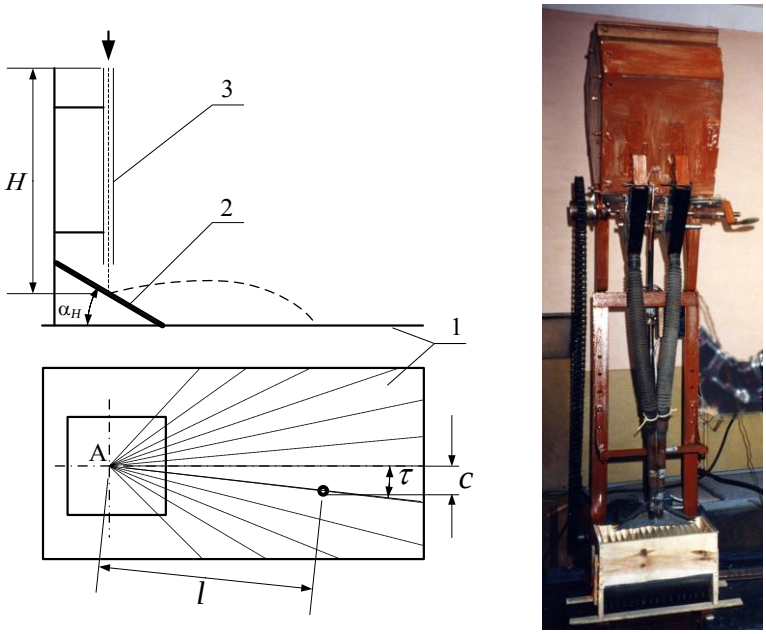

Fig. 2 – Scheme and general view of the of installation for defining seed distribution uniformity on seeding strip width

1 – platform; 2 – reflector-distributor; 3 – guide.

The grain of each cell was weighed. The average mass of seeds in the cells was taken as a number of random variables. After statistical processing, the coefficient of variation was obtained, which was taken as an estimate of uniformity (*Rogovskii I.L.. et al., 2019*).

Optimization criterion of the broadcasting process is the uniformity of seed distribution across the operating element width, which is characterized by the variation coefficient V.

Table 1

Levels of factor variation when determining optimal parameters of distributors

№	Factors		Levels of variation:		Interval of variation
	Title	Symbols	upper +	lower -	
1	Angle between deflecting and horizontal surfaces α_1, (deg.)	x_1	88	68	10
2	Angle between the intersection line of deflective and horizontal surfaces and the direction of movement γ, (deg.)	x_2	65	45	10
3	Height of sub-coulter space h, (m)	x_3	0.04	0.02	0.01

The Box-Behnken plan matrix for three factors was used in the planning of the experiments (Table 2).

The main parts of the cultivator blade opener are (Fig. 3a): two seed ducts *1*, which have rectilinear inclined cylindrical sections *2* and *4*, and torus-like upper *3* and lower *5* sections; the reflector-distributor *6* and the cultivator blade *7* with the shield *8*. The reflector-distributor is a prism, the two working borders of which (right and left) are installed at certain angles to the horizon and the direction of movement. During the movement of the drill-cultivator by the sowing machine *9*, the seed drill is fed into the seed lines, from which it enters the reflector-distributor 6 at a certain angle (Fig. 3b). After reflection, the seed flies in the sub-blade area for some distance.

Table 2

The results of the implementation of the planning matrix of the experiment (Box-Behnken plan)

Codes			Codes and natural values			y (v, %)
x_1	x_2	x_3	x_1 (α_1, deg.)	x_2 (γ, deg.)	x_3 (h, m)	
+1	+1	0	88	65	0.030	60
+1	-1	0	88	45	0.030	54
-1	+1	0	68	65	0.030	40
-1	-1	0	68	45	0.030	48
+1	0	+1	88	55	0.040	38
+1	0	-1	88	55	0.020	62
-1	0	+1	68	55	0.040	36
-1	0	-1	68	55	0.020	60
0	+1	+1	78	65	0.040	26
0	+1	-1	78	65	0.020	53
0	-1	+1	78	45	0.040	41
0	-1	-1	78	45	0.020	60
0	0	0	78	55	0.030	29

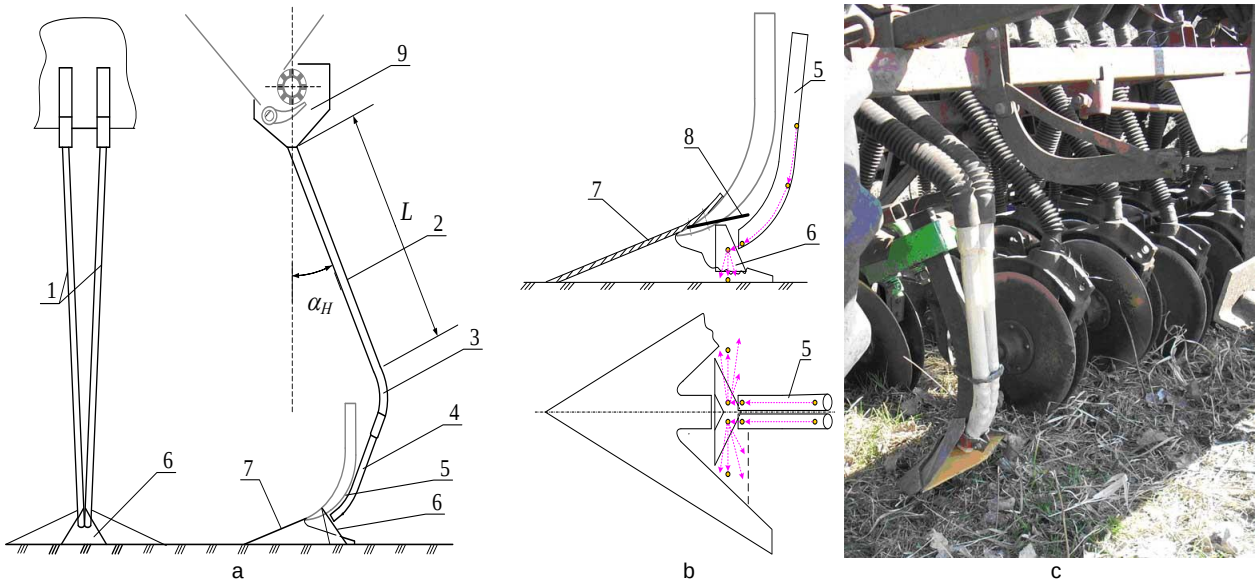

Fig. 3 – Cultivator blade of drill coulter

a – scheme; b – reflector-distributor in the sub-blade area; c – general appearance

Due to the different physical and mechanical properties of some seeds (coefficients of recovery and air resistance), the flight distances are different, which determines the distribution of grain along the bottom of the furrow. An important feature of the proposed opener is that in the right and left sub-blade area the seeds are fed by different seed ducts, which eliminates the divider of the seed flow.

Field research was conducted at the NULES of Ukraine "Agronomic Research Station" on winter wheat. A serial cultivator blade 33 cm wide with a special riser and a reflector-distributor with reasonable parameters was installed instead of the disk opener of the John Deere N542C seeder.

Theoretical Elements

The coefficient of speed change K_{zV2} is defined as the ratio $K_{zV2}=(K_b \times \cos\alpha_2/\cos\beta)$, where K_b – the coefficient of recovery, α_2 and β – the angles between the direction of speed before and after the impact and the normal, respectively. The process of seed movement along the lower section of the torus-shaped seed line is considered as the movement of a material particle along a cylindrical surface with a horizontal axis. In this case, the following forces act on the seed: the component of gravity $F_1=m \times g \times \cos\alpha_4$; friction force due to gravity $F_2=f \times m \times g \times \sin\alpha_4$; friction force due to centrifugal force $F_3=f \times m \times V^2/R$; air resistance force $F_4=K \times m \times V$, (where R – the radius of curvature). The process of motion along the arc of a cylinder with radius R is considered. The change in velocity is determined by the loss of kinetic energy E. In this case, the speed V_2 after passing the seed arc Δl will be determined by the equation:

$$V_2 = \sqrt{V_1^2 + 0.0348 \cdot \Delta\alpha \left(g \cdot \cos\alpha_4 \cdot R - f \cdot g \cdot \sin\alpha_4 \cdot R - f \cdot V_1^2 - K \cdot V_1 \cdot R \right)}. \quad (1)$$

From the lower torus-like section of the seed line, the seed enters the prismatic reflector-distributor. The process of reflection is reduced to oblique impact (Fig.4). For this case, the coefficient of speed change K_{zV} and speed after impact V_2 will be defined as:

$$K_{zV} = V_2/V_1 = \cos\alpha \sqrt{K_b^2 + \mathrm{tg}^2\alpha}\ ,\ V_2 = V_1 \cdot \cos\alpha \cdot \sqrt{K_b^2 + \mathrm{tg}^2\alpha} \quad (2)$$

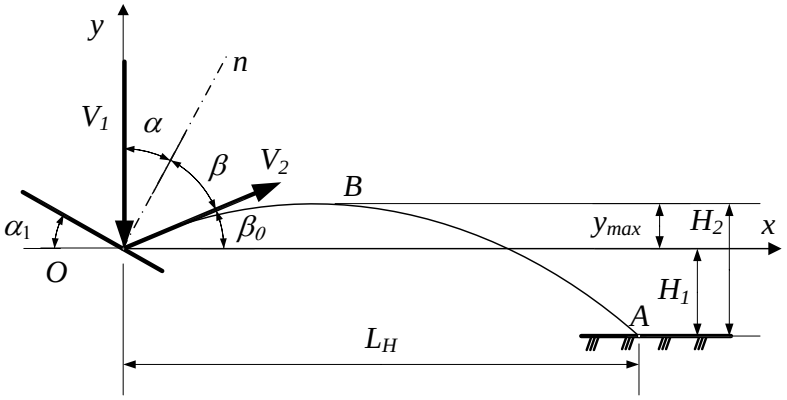

Fig. 4 – The scheme of seed movement after reflection without taking into account air resistance

Using dependences (2) it is seen that the change of angle α is within 20 - 70° and causes a change in K_{zV} from 0.48 to 0.95 (at K_b=0.35). The effect K_b on K_{zV} decreases with increasing α. The speed after reflection V_2 and the angle β_0 determine the parameters of the flight trajectory of the seeds in the sub-blade area, which are the flight range L_H and the height of the trajectory above the bottom of the furrow H_2. These parameters are determined by the equations:

$$L_H = g^{-1} \cdot V_2^2 \cdot \sin\beta_0 \cdot \cos\beta_0 + V_2 \cdot \cos\beta_0 \cdot \sqrt{V_2^2 \cdot \sin^2\beta_0 + 2 \cdot g \cdot H_1} \cdot g^{-1},\ H_2 = V_2^2 \cdot \sin^2\beta_0 \cdot (2 \cdot g)^{-1} + H_1 \quad (3)$$

where H_1 – the height of the reflection point above the bottom of the furrow.

Listed in Fig.4. The scheme provides for the vertical supply of seeds to the reflector-distributor, which makes it impossible to place the seed line outside the cultivator blade. And such placement significantly increases the reliability of the cultivator blade opener.

To simplify, we consider the process by which it is conventionally assumed that the cultivator blade is stationary and the soil moves with speed V_r. Then the basic L_2 and z_3 are determined by equations (3), respectively, with $V_2=V_r$, $\beta_0=\varphi$, $H_2=z_3$, $H_1=z_1$. So:

$$L_2 = g^{-1} \cdot V_r^2 \cdot \sin\varphi \cdot \cos\varphi + V_r \cdot \cos\varphi \cdot \sqrt{V_r^2 \cdot \sin^2\varphi + 2 \cdot g \cdot z_1} \cdot g^{-1},\ z_3 = V_2^2 \cdot \sin^2\varphi \cdot (2 \cdot g)^{-1} + z_1 \quad (4)$$

where $z_1=l_c \times \sin\beta$.

The movement of the soil under the action of the cultivator blade opener was studied in order to determine the length L_2 and height z_3 of the sub-blade area (Fig.5). Considering the wing of the cultivator blade as a wedge and taking into account the scientific positions on the laws of interaction of the triangular wedge with the soil, the dependences between the speed of the operating device (wedge) V_b and the relative speed of soil seam V_r are used.

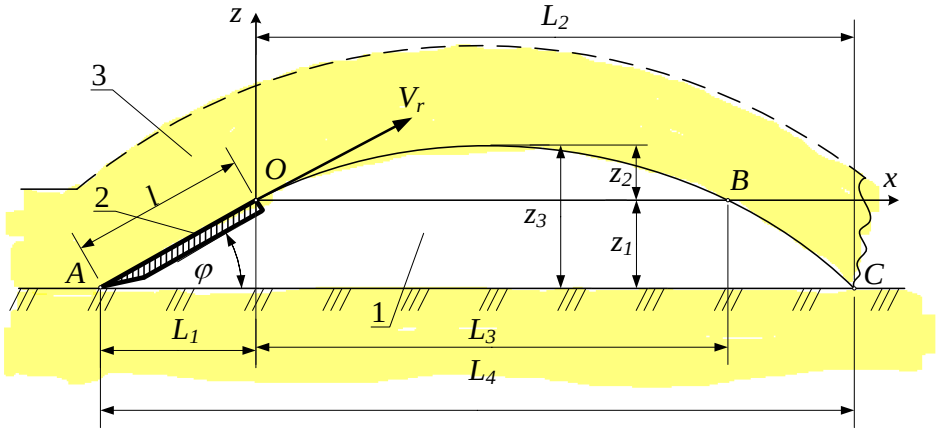

Fig. 5 – The main parameters of the sub-blade area
1 – sub-blade area; 2 – wing of blade; 3 – soil seam

Estimated increase in yield – 21.6%, when calculating the specific energy consumption, the equation for determining the power on the tractor hook N_w will look like this:

$$N_w = N_{eH} \cdot \eta_N \cdot \eta_{mT} \cdot \left[1 - A_\delta + \left(B_\delta - f \cdot g \cdot \left\{3.6 \cdot \eta_N \cdot \eta_{mT} \cdot W_e\right\}\right) \cdot V_P\right], \quad (5)$$

where N_{eH} – rated effective engine power of the tractor, kW; η_N – coefficient of use of the engine nominal effective power; η_{mT} – efficiency of tractor transmission; A_δ, B_δ – factors that determine the dependence of the skid coefficient δ on the operating speed V_p (subject to constant engine load) dependence $\delta = A_\delta - B_\delta \times V_p$ (based on the results of the analysis of traction characteristics for tractors John Deere 3071 A_δ=20.6 and 18.5; B_δ=0.99 and 0.90 respectively); f – coefficient of resistance to tractor rolling; W_e – energy saturation of the tractor, kW/t.

To determine the specific resistance of the working machine K_V (kN/m) used the dependence $K_V = K_0 + K_0 \times K_s \times (V_p - V_0)$, where K_0 – specific resistance at $V_p = V_0$=5 km/h, kN/m; K_s – the rate of increase of traction resistance with increasing speed by 1 km/h (in fractions of a unit); V_p – working speed of the unit, km/h. Before determining the energy-saving working speed of the sowing unit, combined graphs of dependences of the width of capture B_p, specific resistance K_V and productivity on the working speed V_p were constructed under the condition of using 90% of the effective power of the tractor engine, when plotting the factors of formula (16) are taken as follows: N_{eH}=58 kW; η_N=0.9; η_{mT}=0.9; f=0.18; W_e=18 kW/t; A_δ=0.206; B_δ=0.99; K_s=0.045.

RESULTS

The main evaluation characteristic of seed movement through the seed duct and in the process of reflection is the coefficient of speed change K_{zv}, which is defined as the ratio of speed after passing the operating device V_2 (or its section) to the input or potential (maximum possible) speed V_1. The process of movement of seeds by the seed duct, which has the form of an inclined cylinder, is considered as the movement of a material point on an inclined plane. The seed is affected by gravity $G = m \times g$, friction $F = f \times m \times g \times \sin\alpha_H$ and air resistance $R = K \times m \times V$, where m – seed mass, kg; g – acceleration of free fall, m/s^2; f – friction coefficient; α_H – angle of inclination of the seed line; K – coefficient of air resistance. After solving the differential equation, the velocity V_2, without taking into account the air resistance (K=0), will be determined by the dependence $V_2 = (2 \times g \times L_H \times n)^{1/2}$, where L_H – length of seed duct; $n = \cos\alpha - f \times \sin\alpha_H$. It is advisable to take the potential speed V_1, speed of falling from a height $L_H \times \cos\alpha_H$, which is determined by the dependence $V_1 = (2 \times g \times L_H \times \cos\alpha_H)^{1/2}$.

With the following initial parameters, the coefficient of speed change will be determined:

$$K_{zV_1} = V_2 \cdot V_1^{-1} = \sqrt{(\cos\alpha_H - f \cdot \sin\alpha_H) \cdot (\cos\alpha_H)^{-1}} = \sqrt{1 - f \cdot \mathrm{tg}\alpha_H}\ . \quad (6)$$

Taking into account the air resistance ($K \neq 0$), the solution of the differential equation will look like:

$$V_2(t) = n \cdot g \cdot K^{-1} \cdot \left(1 - e^{-K \cdot t}\right),\ x(t) = n \cdot g \cdot K^{-1} \cdot t - n \cdot g \cdot K^{-2} \cdot \left(1 - e^{-K \cdot t}\right) \quad (7)$$

In this case, the coefficient of speed change is determined by the equation:

$$K_{zV_1} = V_2 \cdot V_1^{-1} = n \cdot g \cdot K^{-1} \cdot \left(1 - e^{-K \cdot t}\right) \cdot \left(2 \cdot g \cdot L_H \cdot \cos\alpha_H\right)^{-1/2}. \quad (8)$$

The dependences of the coefficient of speed change K_{zV1} during the movement of seeds in an inclined cylindrical seed line, taking into account the air resistance from the path L_H and K (at $\alpha_H=20°$; $f=0.25$) are shown in Fig.6. From the figure we see that at $L_H=1.0$ m, $K=1.0$ sec^{-1} (close to real conditions) $K_{zV1}=0.81$, i.e. the speed decreases by 19%. Under such conditions $K=0$, $K_{zV1}=0.93$. That is, air resistance causes a decrease in speed by 14%. The process of movement of seeds on the upper torus-like section of the seed line is reduced to a single oblique impact.

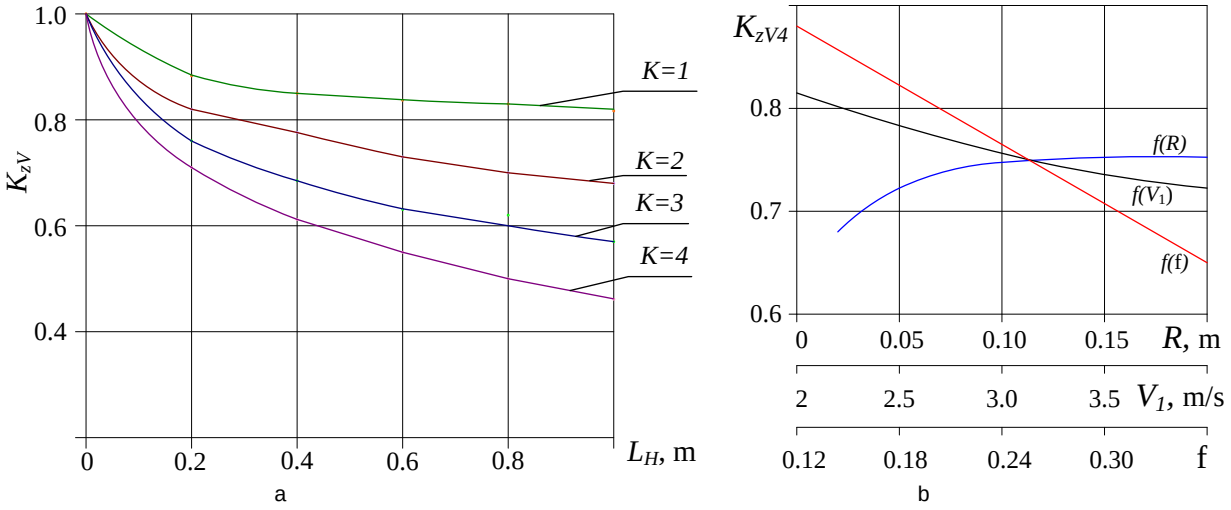

Fig. 6 – Dependence of the coefficient of speed change K_{zV}
a – on length of the seed line L_H and the coefficient of air resistance K; b – on the initial speed V_1, the radius of the arc R and the coefficient of friction f

According to the calculations, the output speed V_2 of the previous arc Δl is taken as the input V_1 for the next. The influence of the main factors of the process on the coefficient of speed change K_{zV4} can be seen from Fig.6. It is worth noting that at a speed $V_1>1.5$ m/s, the radius of curvature R has little effect on the rate of speed change K_{zV4}. This is explained by the fact that the main loss of kinetic energy (up to 90%) through the friction, is due to centrifugal force, the magnitude of which (energy) does not depend on the radius. The analysis of the process established that within the velocities of 2.0 m/s and 23.2 m/s the speed losses caused by the acting forces are distributed as follows: by the force of gravity of the seed (7 - 13%); centrifugal (71 - 82%); air resistance force (12 - 17%).

The working surface of the reflector x, y, z is inclined to the horizontal plane at an angle α_1, and the line of its intersection with the horizontal plane is an angle γ with an axis $0y$ that is parallel to direction of movement. The seeds are fed in a longitudinal vertical plane at an angle to the horizontal. The option when $\varepsilon=90°-\alpha_1$ was researched. This condition guarantees the normal position of the reflection plane relative to the reflection plane. Flight range L_H and trajectory altitude H_2 are determined under the conditions: $\beta_0=\varepsilon$, $\alpha=90°-\gamma$. The width of the capture L_b is related to the range L_H by the ratio $L_b=L_H\times\cos\psi$, where ψ – the angle between the speed V_2 and the transverse direction). In this case, the angle β will be defined as $\beta=arctg(tg\gamma/K)$. Graphic dependence of the main characteristics of the process of reflection and movement of seeds in the sub-blade area on the angle γ (provided V_1=1.5 m/s; $\varepsilon=12°$; H_1=0.02 m) is shown in Fig.7.

As the angle γ increases, all characteristics decrease; when increasing γ from 40 to 70° the average value of the recovery factor (K_b=0.33), the speed V_2 decreases from 1.04 to 0.761 m/s; angle ψ – from 35° to 0; seed flight distance in the transverse direction L_b – from 0.091 to 0.052 m; height of the flight trajectory of seeds H_2 – from 23.3 to 20.1 mm. According to the analysis of the results of previous experimental studies, the most uniform distribution of seeds occurs under the condition $L_b=0.5\times b$, where b – the working width of the blade wing. We take the working width of the blade wing $b=0.15$ m, so the desired flight range is 0.07 - 0.08 m. From the Fig.7 we see that values L_b correspond to the angle γ in the range of 55 - 60°. At values γ from Fig.7 we have: $\psi=14°$ - 0; H_2 – from 0.0233 to 0.0216 m. Therefore, according to the results of theoretical analysis at V_1=1.5 m/s; $\varepsilon=12°$; H_1=0.02 m the optimal value of the angle γ is in the range of 55 - 60°.

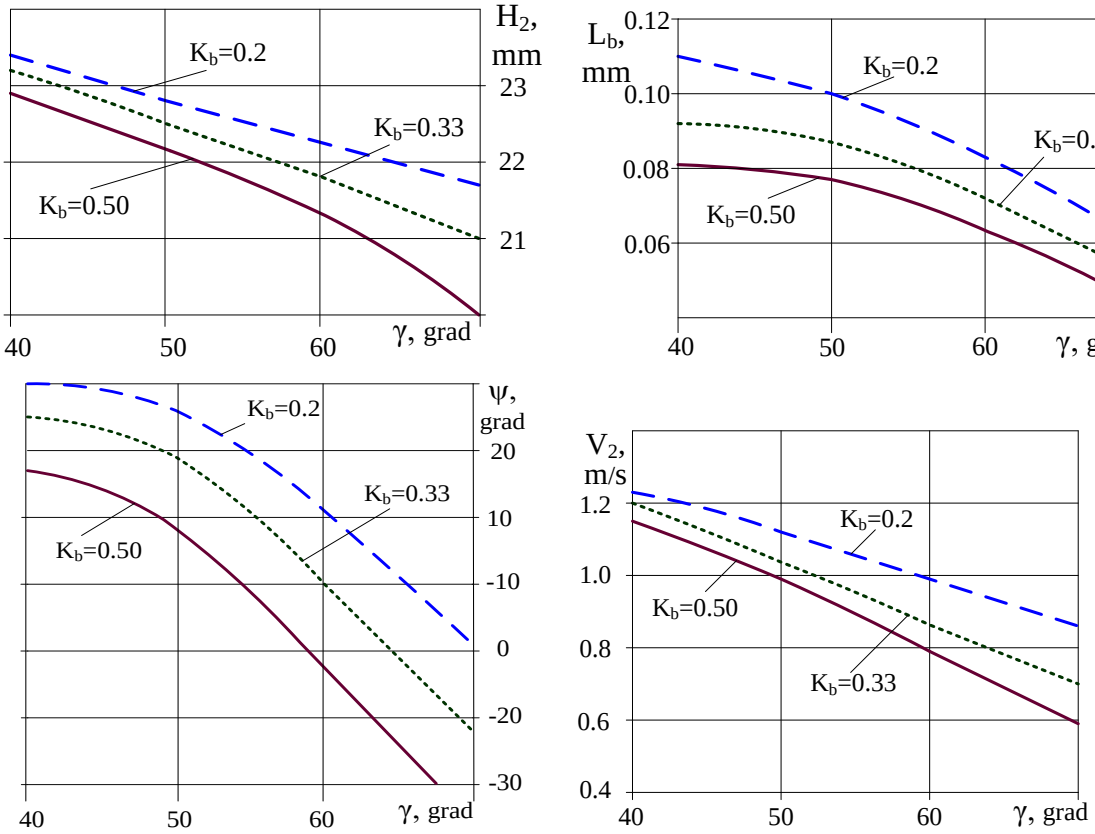

Fig. 7 – Graphic dependence of the main characteristics of the process of reflection and movement of seeds in the sub-blade area on the angle γ

According to the results of calculations for the cultivator blade with a width of 0.33 m (β=28°; γ=32.5°; l_1=0.054 m; l_2=0.031 m; l_c=0.042 m; φ=16°) for V_e within 2 - 2.5 m/s (7.2 - 9 km/h) L_2 from 0.17 to 0.26 m, and z_3 from 0.031 to 0.036 m. The value z_3 is slightly larger than the theoretical height of the trajectory H_2, which is 0.022 - 0.023 m (H_2 Fig.7). Statistical characteristics of the coefficient of air resistance K are given in table 3. Clear patterns of the influence of height of falling on K are not revealed. As the value K for each crop varies considerably, the speed of the seed before hitting the distributor also changes, which contributes to the quality of seed distribution along the bottom of the furrow. Statistical characteristics of the recovery factor K_b were determined for wheat seeds, barley and peas. The experiments were performed at height of fall of 0.5 m and angles of inclination of the reflective plane to the horizon of 20° and 30°. The obtained values of statistical characteristics are given in table 4.

Table 3

Statistical characteristics of air resistance coefficient *K*

Culture	Value of characteristics			
	K_{min}	K_{max}	m_K	ν, %
Wheat	0.307	3.59	1.09	45.3
Barley	0.460	2.30	1.24	27.5
Peas	0.425	2.64	1.03	55.6

Table 4

Statistical characteristics of the recovery rate K_b

Characteristic	Value of characteristics at an angle of inclination α_b					
	20°			30°		
	wheat	barley	peas	wheat	barley	peas
The minimum value	0.02	0.02	0.02	0.10	0.10	0.10
The maximum value	0.55	0.55	0.51	0.64	0.66	0.64
The arithmetic mean	0.33	0.31	0.26	0.41	0.38	0.34
Coefficient of variation, %	36.4	42.1	34.9	32.0	38.0	34.8

Analysing the data in table 4 it should be noted: the recovery factor is a random variable and varies for different cereals within significant limits (0.1 - 0.66). The average value K_b varies from 0.26 to 0.41, and the coefficient of variation from 32 to 42%. Fluctuations in the value cause variation in the flight range of the seeds, which contributes to better distribution of seeds in the transverse direction. The coefficients of speed change during the movement of seeds along the curved lower part of the seed line are determined in order to establish the reliability degree of the regularities of the process main factors influence of the, obtained by theoretical calculations.

The research results are given in table 5: V_K – input speed taking into account air resistance (K=1.0), m/s; V_{2T} – theoretical input speed, m/s; V_{2E} – experimental input speed, m/s.

From the table 5 we see that the difference between the theoretical and experimental values of the coefficient of speed change does not exceed 10%. Therefore, we can assume that the reliability of theoretical calculations is quite high. Experiments to determine the parameters of lateral scattering of seeds were carried out at heights of the fall H (0.5 and 1.0 m), and angles α (20 and 30°) (Fig.2). According to the results of processing the corresponding measurements (Fig.8), the following characteristics were obtained for winter wheat: the average value of the angle $\tau(m_\tau)$ 18.1 - 22.1°; coefficient of variation (60 - 64%); the average value of the flight range $l(m_l)$ (0.13 - 0.16 m); coefficient of variation (34 - 37%). As the angle of installation of the plane to the horizon α and the height of the fall H increases, there is a tendency to decrease the value of m_τ and m_l. Characteristic values for some crops vary from 7 to 11%. The deviation of the plane of the flight trajectory of the seed from the central contributes to a more uniform distribution of seeds at the bottom of the furrow.

Table 5

Comparison of theoretical K_{zVT} and experimental K_{zVE} values of speed coefficients

H, m	V_K, m/s	V_{2T}, m/s	V_{2E}, m/s	K_{zVT}	K_{zVE}	ΔK_{zV}, %
0.5	2.82	2.22	2.19	0.787	0.777	-1.2
0.75	3.37	2.57	2.68	0.764	0.795	3.9
1.0	3.72	2.80	3.11	0.753	0.836	9.9

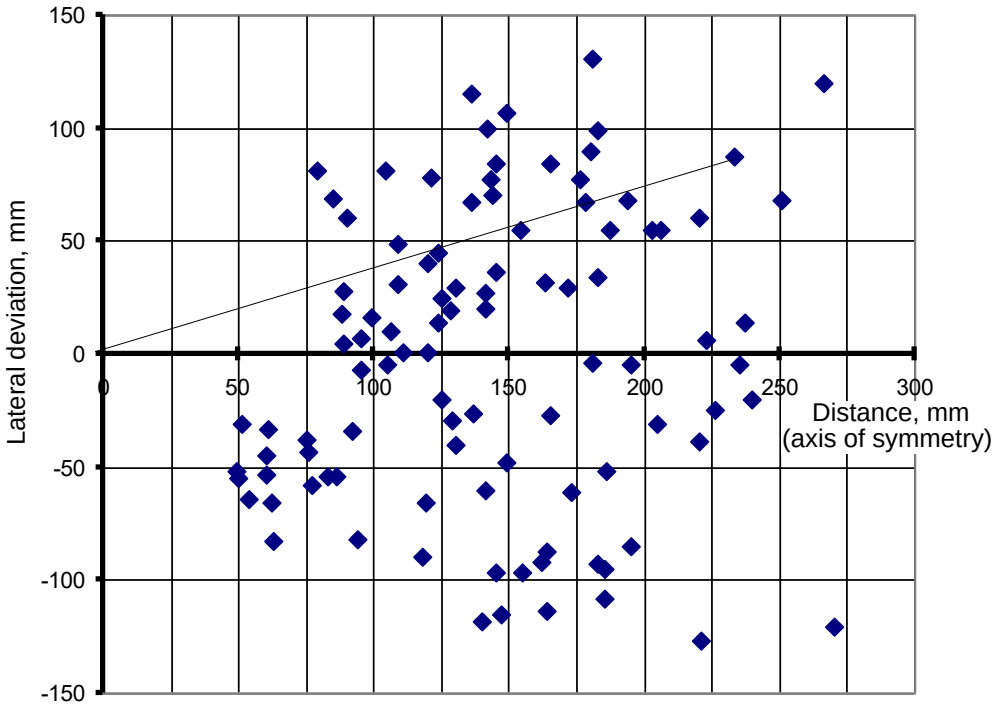

Fig. 8 – The nature of the placement of seeds after reflection

The main parameters of the reflector-distributor with a flat reflection surface are: the height of the reflection point above the bottom of the groove – H_1; the angle between the direction of the speed V_1 at which the seed is fed to the reflector and the horizontal plane – ε; the angle between the reflective and horizontal planes – α_1; the angle between the line of intersection of the reflective and horizontal planes and

the direction of movement – γ, height of sub-blade area – h. According to the results of previous research, we accept H_1=0.02 m. According to our reasonable scheme of the reflection process $\varepsilon=90°-\alpha_1$. To substantiate the optimal values α_1, γ and h the method of planning a multifactorial experiment is applied. After processing the experimental data, we obtained the regression equation of the coefficient of variation of the distribution of seeds along the width of the cultivator blade wing, which will look like this:

$$\nu = 29 + 3.875\cdot\alpha_1 - 2.875\cdot\gamma - 11.75\cdot h + 12.65\cdot\alpha_1^2 + 8.65\cdot\gamma^2 + 7.40\cdot h^2 + 3.25\cdot\alpha_1\cdot\gamma - 2\cdot\gamma\cdot h\,. \quad (9)$$

At fixed values h, the regression equations will look like this:

- at $h = 0.02$ m: $\nu = 1193 - 21.134\cdot\alpha_1 - 12.14\cdot\gamma + 0.0325\cdot\alpha_1\cdot\gamma + 0.127\cdot\alpha_1^2 + 0.0865\cdot\gamma^2$, (10)

- at $h = 0.03$ m: $\nu = 1185 - 21.134\cdot\alpha_1 - 12.34\cdot\gamma + 0.0325\cdot\alpha_1\cdot\gamma + 0.127\cdot\alpha_1^2 + 0.0865\cdot\gamma^2$, (11)

- at $h = 0.04$ m: $\nu = 1191 - 21.134\cdot\alpha_1 - 12.54\cdot\gamma + 0.0325\cdot\alpha_1\cdot\gamma + 0.127\cdot\alpha_1^2 + 0.0865\cdot\gamma^2$. (12)

The corresponding response surfaces are shown in Fig.9. From the figure we see that depending on the angles α_1 and γ there are minimum values of the coefficient of variation ν of seed distribution, which correspond to the optimal values of α_1 and γ. As the value h increases, ν decreases (the indicator improves) to a certain value h, and then it does not change. For example, at α_1=78° and γ=55° for h=0.02 m, ν=48.2% and for h=0.04 m, ν=24.7%. Given the fact that when increasing h by more than 0.03 m value ν decreases slightly, it is advisable to consider the condition h=0.03 m. The optimal value of the angle γ at h=0.03 m is determined by equation (11) under the condition $d\nu/d\gamma=0$. Then at α_1=78° value γ_{opt}=56.6°. As well as according to theoretical researches (Fig.1) at α_1=78°, optimum values of an angle γ are within 55 - 60° which coincides with experimental data. Thus, the following parameters of the prismatic reflector-distributor are substantiated by experimental research: $\varepsilon=90°-\alpha_1=12°$; α_1=78°; γ=56.6°; h=0.03 m; H_1=0.02 m.

The following agrotechnical indicators of work for experimental and serial openers, respectively, were obtained: average depth of wrapping – 3.8 and 4.1 cm; coefficient of variation – 15.3 and 19.7%; number of spikelets per 1 m^2 – 612 and 496; grain weight of one spikelet – 1.54 and 1.48 g. The quality index of seed distribution in the transverse direction (coefficient of variation) for the experimental opener – 28.6%.

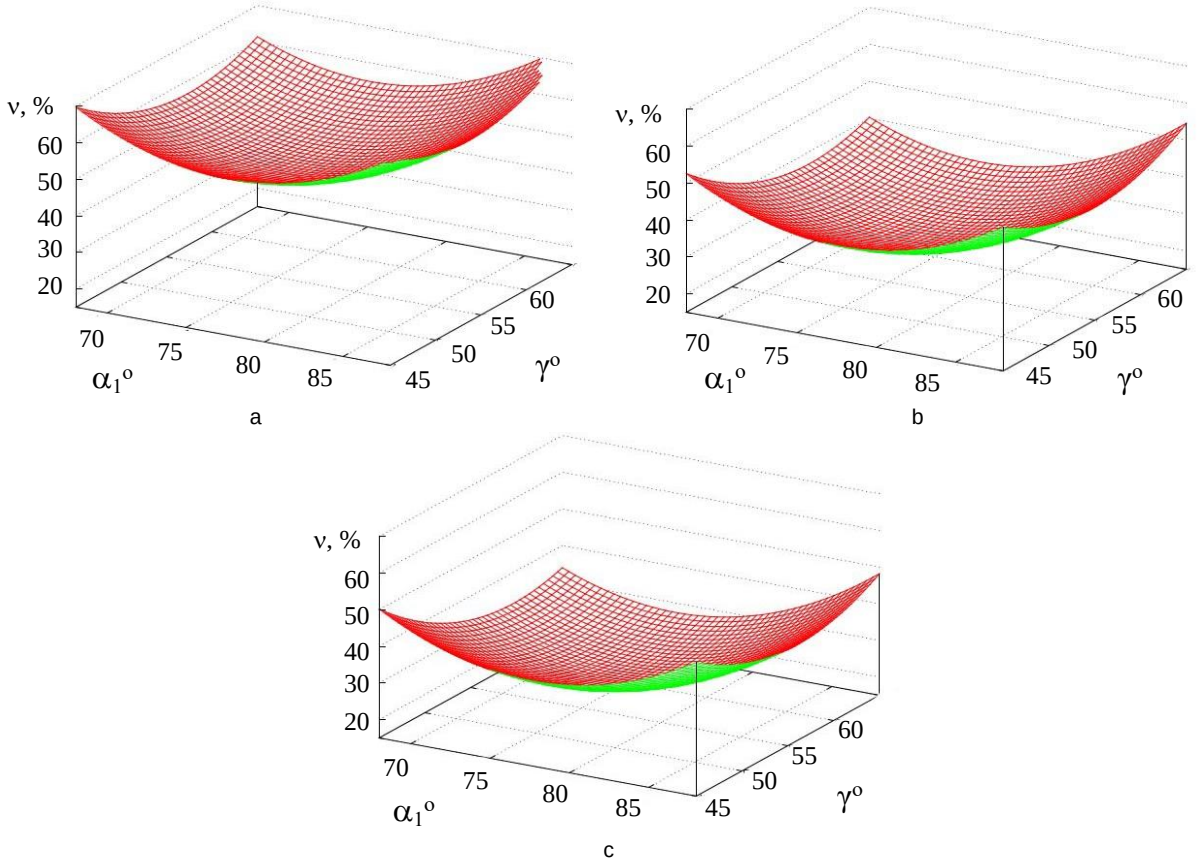

Fig. 9 – Graphs of the dependence of the coefficient of variation ν on the angles γ and α_1
a – h=0.02 m; b – h=0.03 m; c – h=0.04 m

It was found that for John Deere 3071 more energy-saving operating speed was of 8.4 km/h with a width of B_p=5.4 m.

CONCLUSIONS

It is established that neglect of air resistance in the seed line leads to an error of more than 15%. In the process of movement of seeds on the lower curvilinear section at the input speed of 1.5 - 3 m/s speed losses are distributed as follows: due to the force of friction from the gravity of the seeds (7 - 13 %); friction force from the centrifugal force (71 - 82%); air resistance (12 - 16%).

The dependences of the length L_2 and height z_3 of the sub-blade area on the cultivator blade parameters and the seeder-cultivator speed V_e were performed analytically according to the calculations made for a typical cultivator blade (b=0.33 m) at V_e from 2.0 to 2.5 m/s (7.2 - 9.0 km/h), L_2 from 0.17 to 0.26 m; z_3 from 0.031 to 0.036 m.

Field tests of the experimental cultivator blade opener show that the coefficient of variation of the depth of seed earning decreases compared to the serial disc opener, by 4% (from 15.3 to 19.3%); the uniformity of seed distribution in the transverse direction is 28.6%; the number of spikelets per 1 m^2 increases by 23% (from 496 to 612 pcs.) with a grain weight of one spikelet of 1.48 - 1.54 g, which allows us to predict an increase in yield by 22%.

REFERENCES

[1] Abbaspour-Gilandeh Y., Hasankhani-Ghavam F., Shahgoli G., Shrabian V., Abbaspour-Gilandeh M., (2018), Investigation of the effect of soil moisture content, contact surface material and soil texture on soil friction and soil adhesion coefficients, *Acta Technologica Agriculturae*, vol. 21, no. 2, pp. 44−50, https://doi.org/10.2478/ata-2018-0009, Nitra/Slovak;

[2] Farooq M., Siddique K., Rehman H., Wahid A., (2011), Rice direct seeding: experiences, challenges and opportunities, *Soil and Tillage Research*, vol. 111, no. 2, pp. 87-98, https://doi.org/10.1016/j.still.2010.10.008, Helsinki, Finland;

[3] Jha A. and Kewat M. (2013), Weed composition and seed bank as affected by different tillage and crop establishment techniques in rice-wheat system, *Weed Science*, vol. 45, no. 1, pp. 19-24, https://doi.org/10.20546/ijcmas.2018.703.357, Washington/USA;

[4] Jin H., Zhang Z., Hongwen L., Qihgjie W., (2014), Development of small/medium size no-till and minimum-till seeders, *International Journal of Agricultural and Biological Engineering*, vol. 7, no. 4, pp. 1-12, https://doi.org/10.3965/j.ijabe.20140704.001, Beijing/China;

[5] Rogovskii I.L., Titova L.L., Trokhaniak V.I., Rosamaha Yu.O., Blesnyuk O.V., Ohiienko A.V., (2019), Engineering management of two-phase coulter systems of seeding machines for implementing precision farming technologies, *INMATEH-Agricultural Engineering*, vol. 58, no. 2, pp. 137-146, https://doi.org/10.35633/inmateh-58-15, Bucharest/Romania;

[6] Rogovskii I.L., Titova L.L., Trokhaniak V.I., Haponenko O.I., Ohiienko M.M., Kulik V.P., (2020), Engineering management of tillage equipment with concave disk spring shanks, *INMATEH-Agricultural Engineering*. vol. 60, no. 1, pp. 45-52. doi:10.35633/inmateh-60-05, Bucharest/Romania;

[7] Rogovskii I.L., Titova L.L., Trokhaniak V.I., Marinina L.I., Lavrinenko O.T., Bannyi O.O., (2020), Engineering management of machine for formation of artificial shell on seed vegetable cultures, *INMATEH-Agricultural Engineering,* vol. 61, no. 2, pp. 165-174, https://doi.org/10.35633/inmateh-61-18, Bucharest/Romania;

[8] Saitov V.E., (2014), Analysis of energy-efficient designs seeders, *International Journal of Applied and Fundamental Research*, vol. 8, no. 4, pp. 85-98, Neu-Isenburg/Germany;

[9] Turan J., Visacki V., Sedlar A., Jan Mareček J., (2015), Seeder with different seeding apparatus in maize sowing, *Acta Universitatis Agriculturae et Silviculturae Mendelianae Brunensis*, vol. 63, no. 1, pp. 137-141, https://doi.org/10.11118/actaun201563010137, Brno/Czech Republic;

[10] Vlăduţ D.I., Biriş S., Vlăduţ V., Cujbescu D., Ungureanu N., Găgeanu I., (2018), Experimental researches on the working process of a seedbed preparation equipment for heavy soils, *INMATEH-Agricultural Engineering*, vol. 55, no. 2, pp. 27-34, Bucharest/Romania;

[11] Verma A., Guru P., (2015), Development and evaluation of cultivator cum seed drill, *Ecology, Environment and Conservation*, vol. 21, no. 3, pp. 1359-1364, Balewadi/India;

[12] Voicea I., Dumitru, D., Vladut V., (2020), Experimental research regarding influence of soil electrode conductivity and pH data on productivity of agricultural cereal crops, *Engineering for Rural Development*, vol. 19, pp. 1674-1679, https://doi.org/10.22616/ERDev.2020.19.TF434, Jelgava/Latvia;

[13] Zhai C., Long J., Taylor R., Weckler P., Ward N., (2019), Field scale row unit vibration affecting planting quality, *Precision Agriculture*, vol. 21, pp. 589-602, https://doi.org/10.1007/s11119-019-09684-4, Friesach/Austria.

IMPACT OF VENTILATIONS IN ELECTRONIC DEVICE SHIELD ON MICRO-CLIMATE DATA ACQUIRED IN A TROPICAL GREENHOUSE

/

PENGARUH JUMLAH VENTILASI PADA PELINDUNG PERANGKAT ELEKTRONIK TERHADAP HASIL AKUISISI DATA IKLIM MIKRO DALAM RUMAH KACATROPIS

Irfan Ardiansah[*1)], Nurpilihan Bafdal[2)], Awang Bono[3)], Edy Suryadi[2)], Ramadhoni Husnuzhan[1)]

[1)] Department of Agro-Industrial Technology, Faculty of Agro-Industrial Technology, Padjadjaran University / Indonesia

[2)] Department of Agriculture Engineering and Biosystem, Faculty of Agro-Industrial Technology, Padjadjaran University / Indonesia

[3)] Department of Chemical Engineering, Faculty of Engineering, Universiti Malaysia Sabah / Malaysia

Tel: +62 227798844; e-mail: irfan@unpad.ac.id

DOI: 10.35633/INMATEH-63-40

Keywords: *greenhouse; micro-climate; monitoring device; shield; Duradus Junction Box*

ABSTRACT

The greenhouse which is a building used to manipulate the micro-climate is an essential building for plant growth. Greenhouses have one or more devices that are used to monitor their internal environments against changes in micro-climate. The problem is that some devices are metal-based devices and plastics that can be deformed, such as electronic devices, one of which is a micro-climate monitoring device, so a shield that can protect the device but does not interfere with the sensor readings is needed. The purpose of this study was to make and test a plastic-based container called Duradus Junction Box, which has six removable ventilation openings to measure the micro-climate data. This study uses five Duradus Junction Boxes with different numbers of ventilation openings, a micro-controller connected to the air temperature and relative humidity sensor, and a MicroSD module to record all micro-climate data, all devices being then tested simultaneously for 30 days. Statistically, after using One Way ANOVA, this study found that micro-climate measurements result for actual devices data can be considered similar because the P-value for temperature (0.886) and relative humidity (0.917) is greater than alpha level of 0.05. However, when reading the recorded data for both parameters, it can be seen that micro-climate data inside all shields are slightly higher than actual microclimate data ranging from 1 to 2°C for air temperature and 1 to 3% for air relative humidity.

ABSTRACT

Rumah kaca yang merupakan bangunan yang digunakan untuk mengatur iklim mikro adalah sebuah bangunan yang sangat penting untuk pertumbuhan tanaman. Pada rumah kaca umumnya terpasang satu atau lebih perangkat yang digunakan untuk memantau lingkungan internalnya terhadap perubahan iklim. Masalahnya beberapa perangkat tersebut berbahan metal atau plastik yang dapat berubah bentuk dan rusak bila terpapar air dan sinar matahari terus menerus, terutama perangkat pemantauan iklim mikro, sehingga diperlukan pelindung yang dapat melindungi perangkat dari kondisi lingkungan tanpa mengganggu pembacaan sensor. Tujuan penelitian ini adalah menguji kontainer yang disebut Duradus Junction Box, yang memiliki enam buah ventilasi yang dapat dibuka tutup. Pengujian dilakukan pada lima buah Duradus Junction Box dengan jumlah bukaan ventilasi yang berbeda yang didalamnya sudah terpasang mikrokontroler, sensor temperatur dan kelembaban relatif udara, dan modul MicroSD sebagai perekam data iklim mikro, dan semua perangkat dalam Duradus diujikan bersamaan selama 30 hari. Perhitungan dengan ANOVA Satu Arah menunjukkan bahwa hasil pengukuran dapat dikatakan serupa antara data iklim mikro aktual dan kelima perangkat uang diujikan walau jumlah bukaannya berbeda mengacu pada nilai P temperatur (0.886) dan kelembaban relatif (0.917) yang lebih besar dibandingkan tingkat alfa 0.05. Walaupun secara kasat mata data kedua parameter terlihat berbeda dengan data aktual, dengan perbedaan berkisar antara 1 sampai 2 °C untuk temperatur, dan 1 sampai 3 % untuk kelembaban relatif udara.

INTRODUCTION

In recent years, some tropical countries farmers have changed the way they manage their agriculture, from using agricultural land to indoor farming; the cause of this trend is high rainfall and humidity, which can cause crops damage and crops are more easily exposed to pests and diseases, leading to increased use of pesticides, of crops failure (*Akpenpuun & Mijinyawa, 2018; Shamshiri & Ismail, 2014*), with the same thing also happened in Indonesia, a tropical country in Southeast Asia.

Indoor agricultural management is usually carried out in a building called a greenhouse (*Bafdal & Ardiansah, 2020)*. In the four-season country, this greenhouse is used in fall or winter, so that plants can grow even though the temperature outside the greenhouse is shallow *(Lim et al., 2020*).

Greenhouses are used to control several environmental conditions in plant growth ecosystems such as temperature, relative humidity and sunlight, which is referred to as microclimate. The reason crops are grown in this way is to extend the crop productivity period, change the cropping cycle to increase yields and crop quality, and to produce a sustainable harvest (*Sahdev et al., 2017*). In Indonesia, the temperature inside the greenhouse is always higher than the outside temperature, which can lead to spending up evapotranspiration and plant wilting (*Ardiansah et al., 2020; Bafdal et al., 2019*).

Academic Leadership Grant Universitas Padjadjaran (ALG Unpad) Greenhouse is a research greenhouse used to grow tomato plants, also has the same problem where air temperature which can reach 40^{o}C in the dry season whereas the air temperature should be between 28^{o}C to 32^{o}C to optimize tomato plants growth (*Bafdal & Dwiratna, 2018*), so that the Greenhouse is now integrated with several automatic devices to monitor and manage micro-climate condition based on Arduino NANO, using air temperature and relative humidity sensor, and a misting system (*Hafiz et al., 2020*). All devices are placed inside the Greenhouse and not protected from moisture and sunlight exposure, which makes all devices vulnerable.

Devices that are expected to detect micro-climate condition accurately require a cover or shield that can protect it from direct sunlight but still have a ventilation opening capable of circulating air because poor ventilation conditions will cause the shield inside became warmer than the actual data and result in inaccurate measurements *(Buisan et al., 2015; Harrison, 2010*). A commonly used protector to cover the microclimate measurement device is called Stevenson Screen, which is made from painted white wood, although there is still a difference of 0.5 to 2.5^{o}C between outside and inside of it (Harrison, 2010). The problem with the Stevenson screen is that it is large, heavy, and permanently installed, so it is not suitable for greenhouses with limited space (*Li & Song, 2017*).

The need for accurate micro-climate data measurements became an idea to seek a shield that could protect micro-climate measurement devices, could circulate air, be water-resistant and tinted white to reflect light *(Ma et al., 2019*).

MATERIALS AND METHODS

This study was conducted for thirty days using an experimental design with a randomized design (CRD) method inside Research Greenhouse (Figure 1), a greenhouse with a size of 14.5 x 9 x 3 m^3 which has been built and is ready to use in the research premise with a table placed in the greenhouse centre to place all monitoring devices. Five monitoring devices were made with different numbers of ventilations ranging from two to six ventilations coded A, B, C, D, E to determine the effect of the number of ventilations on sensor data reception. A Thermo hygrometer coded (Q) is used to measure actual micro-climate data inside the Greenhouse.

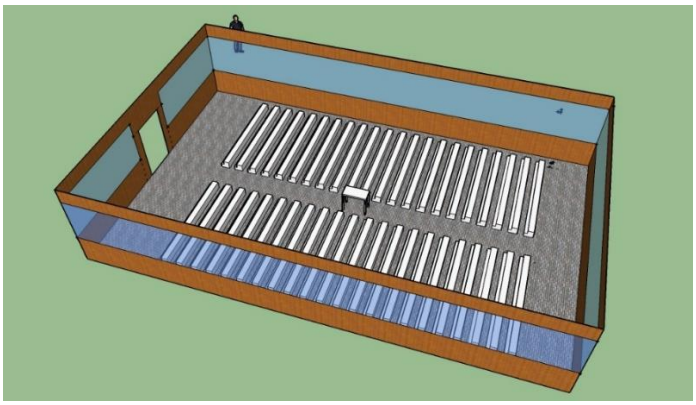

Fig. 1 - Research Greenhouse Layout

Components Selection

These micro-climate data monitoring devices are placed on a table and positioned in the centre of the Greenhouse. The table itself has a height of 75 cm. For portability, all devices must be capable of running on batteries, capable of storing thousands of micro-climate data, and easy to move to download stored data.

Based on these specifications, Arduino Nano is selected as a processing unit, which has a size of 1.8 cm to 4.5 cm, has an operating voltage of 5V with pin current requirement of 40 mA; Arduino Nano is a variant of the Arduino micro-controller board product. The Arduino Nano is the smallest Arduino board, using the ATMega328 micro-controller for Arduino Nano version 3 and ATMega168 for the Arduino Nano version 2. This variant has the same circuit as the Arduino UNO, but with a different PCB size and design. Arduino Nano is not equipped with a power socket, but there is a pin for the external power supply or you can use the power supply from the Mini or Micro USB port. *(Bt Mohd Shuib et al., 2018; Kumar et al., 2019*). With specifications like this, the power supply can be fulfilled by using a 10000mAh power bank.

The MicroSD card is then connected to record measured micro-climate data; those data are retrieved from sensors every 20 minutes. The sensors used are DHT22, which have a digital output and require 1.5mA current. DHT22 detects temperature in Celsius units with a range of -40°C to 80°C and relative humidity between 0 and 100% (Bogdan, 2016; Koestoer et al., 2019). These components are assembled using a breadboard and jumper cables, as shown in Figure 2a, with all sensors already tested and calibrated before use. Meanwhile, the data traffic flow starting from micro-climate detection to data recording can be seen in Figure 2b.

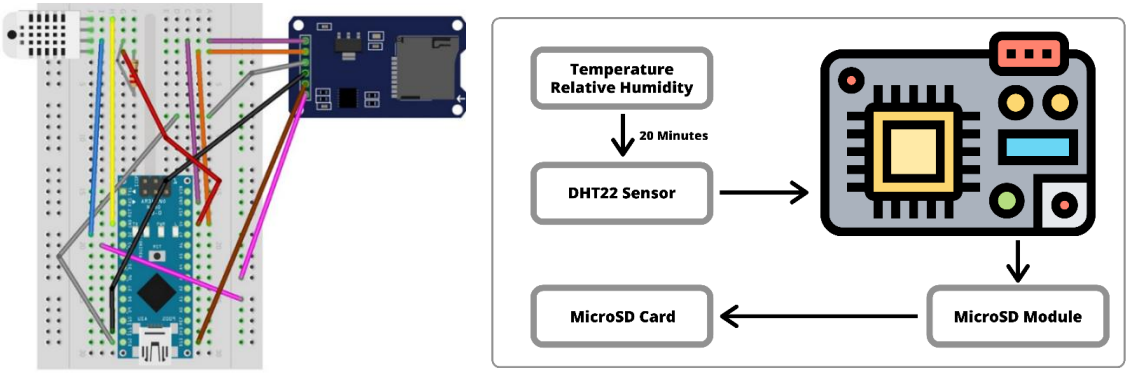

(a) **(b)**

Fig. 2 - (a) Device Component Layout; (b) Device Flow Diagram

Five devices are built using the same specifications, and then those devices are inserted into the shield by positioning the sensor towards the ventilation openings (*Astutik et al., 2019*) to make it easier for the sensor to detect micro-climatic conditions and not degraded by the heat generated by the micro-controller. All devices are then connected to the power bank using 5 ports USB Hub (Figure 3).

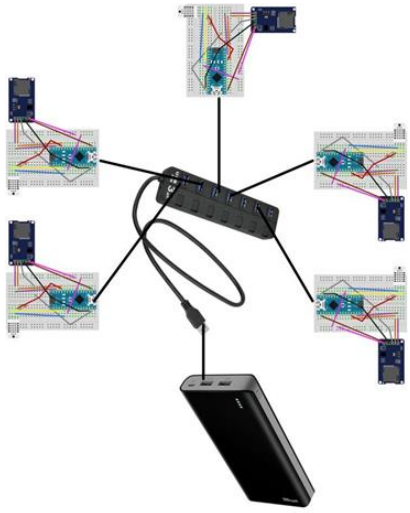

Fig. 3 - Devices Connected to Power Bank

Shield Options

All monitoring devices must be protected from direct sunlight exposure and water droplets coming from the misting system, so it is necessary to choose a shield that is designed to be enclosed, watertight but has sufficient ventilation openings to avoid hot air caught inside the shield (*Burt & de Podesta, 2020*). Based on a market survey, one suitable material called Duradus Junction Box is then selected because it is made of thick white plastic, has lids that can be removed on each side with its shape, as it can be seen in Figure 4.

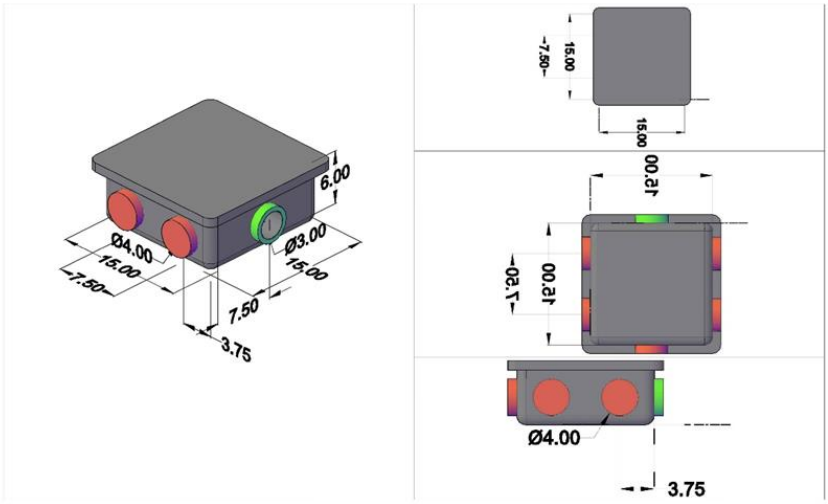

Fig. 4 - Duradus Junction Box Dimension

Experiment Procedure

Each monitoring device is put inside the shield with a different number of ventilation openings coded Shield A (2 ventilations) to Shield E (6 ventilations) then placed on the table as in Figure 1.

Data were monitored every day from 07.00 to 17.00 and recorded every 20 minutes using Comma-Separated Values (CSV) format for more accessible data processing and were downloaded at the end of every day. The power bank is replaced every other day to avoid running out of power when collecting data. Data series collected were plotted based on mean values, variance and standard deviation using a spreadsheet application based on their average.

The research was conducted for 9 hours (540 minutes), which produced 27 data per device every day which was guided by the research conducted by (*Hoover & Yao, 2018*), where the researcher took data every 30 minutes, and the research carried out by (*Strangeways, 2019*) using the same sensor but with 10-minute intervals. The two previous researches conclude that there is no definite determination about the amount of data and the interval used for data retrieval with the DHT22 sensor; therefore, this study takes the middle value of the two studies using an interval of 20 minutes.

RESULTS AND DISCUSSION

The study was carried out inside Research Greenhouse in December 2019 for thirty days, by measuring micro-climate data for each shield and simplifying it to 27 data. The hypothesis used in this study is that the more ventilations the shield has, the more accurate the reading of micro-climate data and closer to the actual data measurement. Shield E, which has six vents, is considered the best model for use as a shield.

The statistical analysis used is One Way Analysis of Variance (ANOVA). ANOVA is a statistical analysis that examines the mean differences between groups. The group here can mean a group or type of treatment with a test procedure similar to the t-test, but the advantage of ANOVA is that it can test the difference of over two groups. In contrast to the independent sample t-test, which can only test the mean difference between the two groups. The result of the ANOVA analysis is the P-value or F-value, if the p-value is smaller than the 5% error rate, it can be concluded that H1 is accepted and H0 is rejected, meaning that there is a significant difference in the mean in all groups. ANOVA analysis is often used in experimental research where there are several treatments and is used to test whether there are significant differences between these treatments (*Wahid et al., 2018*), (*Pujar et al., 2020*), (*Hong & Hsieh, 2016*).

This study will compare two groups of data, viz.:

1) Actual air temperature data (Q) against air temperature detected inside shields A to E using the following hypothesis:
   H0: A = B = C = D = E
   H1: A ≠ B ≠ C ≠ D ≠ E
2) Actual air relative humidity data (Q) against air relative humidity detected inside shields A to E using the following hypothesis:
   H0: A = B = C = D = E
   H1: A ≠ B ≠ C ≠ D ≠ E

Air Temperature

ANOVA calculations for temperature data Q and shield A to E can be seen in Table 1; also, this table displays all average calculation results, which show that the difference in the average temperature of each shield is only less than 1°C even though it has a different number of ventilation openings, and the actual temperature having only 1.1°C difference when compared to the average temperature of shield (A), which has the least ventilation. Table 1 also shows that the actual temperature (Q) has an average temperature value lower than all shields temperature and is more stable than shielded devices. This happens because the shielded devices have a slower response, according to the statement given by (*Harrison, 2010; Li & Song, 2017*; *Benyezza et al., 2018*).

Table 1

One Way ANOVA for 20 Minutes Temperature using 0.05 Alpha Level

Groups	*Count*	*Sum*	*Average*	*Variance*	*STDev*
Q	27	915.5867	33.91062	9.798062	3.130186
A	27	945.42	35.01556	15.57806	3.946905
B	27	941.2033	34.85938	14.66141	3.829022
C	27	940.9633	34.85049	15.62036	3.95226
D	27	932.2267	34.52691	15.89865	3.987311
E	27	925.02	34.26	13.02072	3.608424

ANOVA

Source of Variation	*SS*	*df*	*MS*	*F*	*P-value*	*F crit*
Between Groups	24.12934	5	4.825869	0.342352	0.886531	2.272137
Within Groups	2199.009	156	14.09621			
Total	2223.138	161				

Based on the P-value listed in Table 1, it can be concluded that H0 is accepted, and H1 is rejected for 27 gained data; this means that the results of measuring the actual temperature Q and the temperature inside shield A to E can be said to be the same based on ANOVA, although visually, in Figure 5, it can be seen that the line temperature values for shields A to E only approach the temperature Q and rarely touch the Q line.

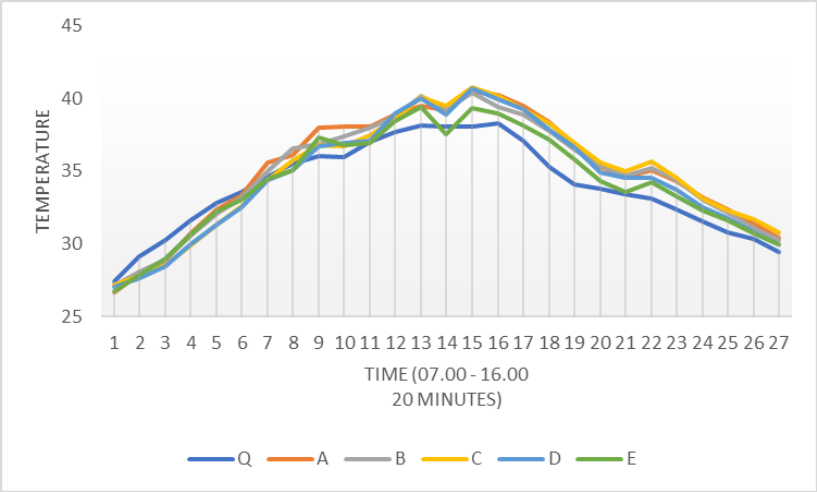

Fig. 5 - Comparison of Devices Temperature Values every 20 Minutes

Figure 5 also noted that the actual temperature value (Q) is lower than the temperature value inside all shields for the average data; this happens because the air inside all shields does not completely circulate (*Benyezza et al., 2018*).

Air Relative Humidity

ANOVA calculations for air relative humidity data Q and shield A to E can be seen in Table 2; it also displays the average calculation results similar to air temperature, which show that the difference in the average relative humidity of each shield is only less than 3% even though it has a different number of ventilation openings, as well as the actual relative humidity which has only 3% difference when compared to the average relative humidity of shield (A) which has the least ventilation. This means that the actual relative humidity (Q) average also has a slightly lower value, which shows that the air in all shields has more water, which can happen because of minimal air exchange (*Acquah et al., 2018*).

Table 1

One Way ANOVA for 20 Minutes Relative Humidity using 0.05 Alpha Level

Groups	*Count*	*Sum*	*Average*	*Variance*	*STDev*
Q	27	1311.867	48.58765	87.93454	9.377342
A	27	1387.9	51.4037	110.6763	10.52028
B	27	1378.947	51.0721	89.23243	9.446292
C	27	1378.187	51.04395	102.284	10.11356
D	27	1373.033	50.85309	106.7055	10.32983
E	27	1372.127	50.81951	83.40752	9.132772

ANOVA

Source of Variation	*SS*	*df*	*MS*	*F*	*P-value*	*F crit*
Between Groups	141.0016	5	28.20031	0.291607	0.917056	2.272137
Within Groups	15086.25	156	96.70671			
Total	15227.25	161				

Like the ANOVA test for temperature, the P-value for air relative humidity in Table 2 also has a value higher than 0.05; this result indicated that hypothesis H0 is accepted, and H1 is rejected for the total 27 data, and actual relative humidity (Q) data has the same value as data that comes from Shield A to E.

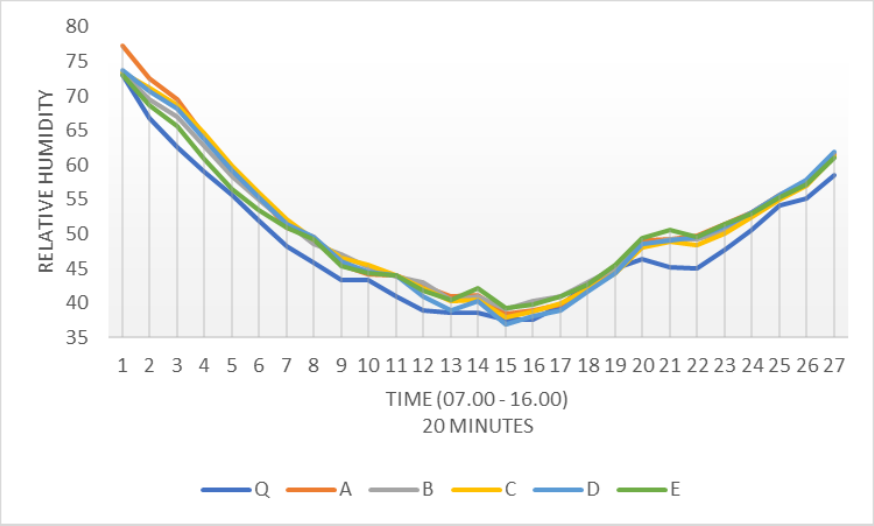

Fig. 6 - Comparison of Devices Relative Humidity Values every 20 Minutes

In contrast to the ANOVA calculation results, Figure 6 above shows that the actual relative humidity value (Q) is lower than that of shield A to E. This shows that shield humidity is slightly higher than relative humidity inside the greenhouse, this happens because more vapour is trapped inside shields *(Benyezza et al., 2018*).

CONCLUSIONS

In the course of developing greenhouse automation device using Arduino UNO, DHT22 sensor and MicroSD module, it is discovered that the instruments used have material that rusts easily, so it is important to utilize a piece of equipment that can protect all instruments from water and sunlight exposure. Duradus Junction Box made of plastic is one option to protect those instruments, especially because Duradus has six removable ventilation openings that can be used as means for air circulation. The study was conducted by developing five microclimate monitoring devices with the same specifications and placed in five Duradus Junction Boxes with different numbers of ventilation openings, then placed in the same place inside the greenhouse. Sensor acquired data then stored them in the form of a CSV file which is then processed statistically.

Based on statistical value, there was no significant difference between the real microclimate data (Q) and those measured in shield A to E because One Way ANOVA gave results that H_0 was accepted and H_1 was rejected after comparing the P-value to an alpha level of 5%. Also, based on collected data, it can be seen that the air temperature data in shields A to E is slightly higher than the real temperature, with a difference of 1.1^{o}C, The same thing happens in shields A to E air relative humidity data, which was also higher than the real (Q) data although the difference is less than 3%. These results showed that the Duradus Junction Box could be a shield for micro-climate monitoring devices in tropical greenhouses while considering that the differences in recorded data, although minimal, may affect plant growth.

ACKNOWLEDGEMENTS

The authors would like to acknowledge the contributions of Ramadhoni Huznuzhan, Muhammad Hafiz, Endryaz Vergian and the technical working group for their contributions to this project. Thanks to Direktorat Riset dan Pengabdian Masyarakat Universitas Padjadjaran (DRPM Unpad), and Badan Riset dan Inovasi Nasional (BRIN) for funding this project. We also thank the reviewers for their insightful comments and suggestions.

REFERENCES

[1] Acquah, S. J., Yan, H., Zhang, C., Wang, G., Zhao, B., Wu, H., & Zhang, H. (2018). Application and evaluation of Stanghellini model in the determination of crop evapotranspiration in a naturally ventilated greenhouse. *International Journal of Agricultural and Biological Engineering*, *11*(6), 95–103. https://doi.org/10.25165/j.ijabe.20181106.3972

[2] Akpenpuun, T. D., & Mijinyawa, Y. (2018). Evaluation of a Greenhouse under Tropical Conditions Using Irish Potato (Solanum Tuberosum) as the Test Crop. *Acta Technologica Agriculturae*, *21*(2), 56–62. https://doi.org/http://dx.doi.org/10.2478/ata-2018-0011

[3] Ardiansah, I., Bafdal, N., Suryadi, E., & Bono, A. (2020). Greenhouse Monitoring and Automation Using Arduino: a Review on Precision Farming and Internet of Things (IoT). *International Journal on Advanced Science Engineering Information Technology*, *10*(2).

[4] Astutik, Y., Murad, Putra, G. M. D., & Setiawati, D. A. (2019). Remote monitoring systems in greenhouse based on NodeMCU ESP8266 microcontroller and Android. *AIP Conference Proceedings*, *2199*, 030003 (14 pp.). https://doi.org/10.1063/1.5141286

[5] Bafdal, N., & Ardiansah, I. (2020). *Smart Farming Berbasis Internet of Things dalam Greenhouse* (T. Perdana (ed.); 1st ed.). Unpad Press.

[6] Bafdal, N., & Dwiratna, S. (2018). Water Harvesting System As An Alternative Appropriate Technology To Supply Irrigation On Red Oval Cherry Tomato Production. *International Journal on Advanced Science, Engineering and Information Technology*, *8*(2), 561–566.

[7] Bafdal, N., Dwiratna, S., & Sarah, S. (2019). Impact of Rainfall Harvesting as a Fertigation Resource using Autopot on Quality of Melon (Cucumis melo L). *International Conference on Food Agriculture and Natural Resources (FAN)*, *194*(FANRes 2019), 254–257.

[8] Benyezza, H., Bouhedda, M., Zerhouni, M. C., Boudjemaa, M., & Dura, S. A. (2018). *Fuzzy Greenhouse Temperature and Humidity Control based on Arduino BT - 2018 International Conference on Applied Smart Systems, ICASS 2018, November 24, 2018 - November 25, 2018*. et al.; IEEE; IEEE Algeria Section; Laboratoire d'. https://doi.org/10.1109/ICASS.2018.8652017

[9] Bogdan, M. (2016). How to Use the DHT22 Sensor for Measuring Temperature and Humidity with the Arduino Board. *Acta Universitatis Cibiniensis. Technical Series*, *68*(1), 22–25. https://doi.org/10.1515/aucts-2016-0005

[10] Bt Mohd Shuib, F. M., Abd Wahab, S. B., Mat Sulaiman, A. H. B., Ibrahim, M. N. I. B., Othman, M., Md Ali, S. H., & Hamzah, A. A. (2018). Performance comparison on current consumption between arduino nano and arm coretex M3 for portable dialysis system BT - 13th IEEE International Conference on Semiconductor Electronics, ICSE 2018, August 15, 2018 - August 17, 2018. *IEEE International Conference on Semiconductor Electronics (ICSE)*, *2018-Augus*, 148–151. https://doi.org/10.1109/SMELEC.2018.8481308

[11] Buisan, S. T., Azorin-Molina, C., & Jimenez, Y. (2015). Impact of two different sized Stevenson screens on air temperature measurements. *International Journal of Climatology*, *35*(14), 4408–4416. https://doi.org/10.1002/joc.4287

[12] Burt, S., & de Podesta, M. (2020). *Response times of meteorological air temperature sensors*. https://doi.org/10.1002/qj.3817

[13] Hafiz, M., Ardiansah, I., Bafdal, N., Info, A., & Control, M. (2020). Website Based Greenhouse Microclimate Control Automation System Design. *JOIN (Jurnal Online Informatika)*, *5*(1), 105–114. https://doi.org/10.15575/join.v5i1.575

[14] Harrison, R. G. (2010). Natural ventilation effects on temperatures within Stevenson screens. *Quarterly Journal of the Royal Meteorological Society*, *136*(646), 253–259. https://doi.org/10.1002/qj.537

[15] Hong, G. Z., & Hsieh, C. L. (2016). Application of Integrated Control Strategy and Bluetooth for Irrigating Romaine Lettuce in Greenhouse. *IFAC-PapersOnLine*, *49*(16), 381–386. https://doi.org/10.1016/j.ifacol.2016.10.070

[16] Hoover, J., & Yao, L. (2018). Aspirated and non-aspirated automatic weather station Stevenson screen intercomparison. *International Journal of Climatology*, *38*(6), 2686–2700. https://doi.org/10.1002/joc.5453

[17] Koestoer, R. A., Pancasaputra, N., Roihan, I., & Harinaldi. (2019). A simple calibration methods of relative humidity sensor DHT22 for tropical climates based on Arduino data acquisition system. *AIP Conference Proceedings*, *2062*, 020009 (7 pp.). https://doi.org/10.1063/1.5086556

[18] Kumar, N. K., Vigneswari, D., & Rogith, C. (2019). An Effective Moisture Control based Modern Irrigation System (MIS) with Arduino Nano. *5th International Conference on Advanced Computing & Communication Systems (ICACCS)*, 70–72. https://doi.org/10.1109/ICACCS.2019.8728446

[19] Li, Z., & Song, Y. (2017). Optimization for Low Cost and Handmade Radiation Shields in Tests of Outdoor Air Temperature. *Construction Conserves Energy*, *45*(2). https://search-proquest-com.aurarialibrary.idm.oclc.org/docview/1891877229?accountid=14506

[20] Lim, T., Baik, Y.-K., & Kim, D. D. (2020). Heating performance analysis of an air-to-water heat pump using underground air for greenhouse farming. *Energies*, *13*(15). https://doi.org/10.3390/en13153863

[21] Ma, D., Carpenter, N., Maki, H., Rehman, T. U., Tuinstra, M. R., & Jin, J. (2019). Greenhouse environment modeling and simulation for microclimate control. *Computers and Electronics in Agriculture*, *162*, 134–142. https://doi.org/10.1016/j.compag.2019.04.013

[22] Pujar, P. M., Kenchannavar, H. H., Kulkarni, R. M., & Kulkarni, U. P. (2020). Real-time water quality monitoring through Internet of Things and ANOVA-based analysis: a case study on river Krishna. *Applied Water Science*, *10*(1). https://doi.org/10.1007/s13201-019-1111-9

[23] Sahdev, R. K., Kumar, M., & Dhingra, A. K. (2017). A comprehensive review of greenhouse shapes and its applications. *Frontiers in Energy*, *13*(3), 427–438. https://doi.org/10.1007/s11708-017-0464-8

[24] Shamshiri, R., & Ismail, W. I. W. (2014). Investigation of Climate Control Techniques for Tropical Lowland Greenhouses in Malaysia. *Journal of Applied Sciences (Faisalabad)*, *14*(1), 60. https://search-proquest-com.aurarialibrary.idm.oclc.org/docview/1534843183?accountid=14506

[25] Strangeways, I. (2019). The replacement of mercury thermometers in Stevenson screens. *Weather*, *74*(4), 145–147. https://doi.org/10.1002/wea.3443

[26] Wahid, Z., Latiff, A. I., & Ahmad, K. (2018). Application of one-way ANOVA in completely randomized experiments BT - 4th International Conference on Mathematical Applications in Engineering 2017, ICMAE 2017, August 8, 2017 - August 9, 2017. *4th International Conference on Mathematical Applications in Engineering 2017 (ICMAE'17)*, 949(1).

EXPERIMENT AND PARAMETER OPTIMIZATION OF ROOT-CUTTING FOR TRIMMING POSTHARVEST CABBAGE
/
甘蓝采后整修切根试验与参数优化

Cui Gongpei [1,2], Wei Yongzhe, [1,2]; Wen Shuangtao [1,3], Zheng Xinmeng [1], Wang Jingzheng [1], Cui Yongjie *[1,3] [1]

[1] College of Mechanical and Electronic Engineering, Northwest A&F University, Yangling / China;
[2] Key Laboratory of Agricultural Internet of Things, Ministry of Agriculture and Rural Affairs, Yangling / China;
[3] Shaanxi Key Laboratory of Agricultural Information Perception and Intelligent Service, Yangling / China
Tel: +86 13720581232; E-mail: agriculturalrobot@nwafu.edu.cn
DOI: https://doi.org/10.35633/inmateh-63-41

Keywords: *postharvest cabbage, trimming, root-cutting, morphology, parameter optimization*

ABSTRACT
Trimming for postharvest cabbage is useful to increase its economic value added. For obtaining the optimal root-cutting parameters, a root-cutting test platform based on universal testing machine was designed. Then shear contrast test and orthogonal test were carried out respectively, and shear properties were explained according to root morphology obtained by scanning electron microscope (SEM). The results showed that the effect of sliding-cutting with single-edged cutter was the best. The optimal parameters of cutter thickness, shear position, shear speed and sliding-cutting angle were respectively 0.89 mm, 0.00 mm, 388.94 mm/min and 34.84°, and the shear stress was 28.02 kPa.

摘要
采后甘蓝整修有利于提升其经济附加值。为了获得采后甘蓝较佳的切根参数，本文基于万能试验机设计了一种切根试验平台。分别进行了剪切对比试验和正交试验，并根据扫描电子显微镜获取的根部形貌对剪切特性进行了分析。结果表明：单平刃滑切作业效果最佳；最优参数组合为刀具厚度 0.89 mm，剪切位置 0.00 mm，剪切速度 388.94 mm/min，滑切角 34.84°，剪切应力为 28.02 kPa。

INTRODUCTION
Efficiency and performance of existing cabbage harvesters have basically met the requirements of husbandmen *(Toncheva et al., 2017; Zhou et al., 2017; Du et al., 2019)*. But the root of harvested cabbage is too long, which seriously affects the appearance of cabbage products and easily causes economic losses *(Du, 2017)*. Thus root-cutting and other operations of postharvest trimming are needed to enhance the economic value added of cabbage products *(Cui et al., 2019)*.

At present, the reported studies on the root-cutting of cabbage mainly focus on the harvesting in the field. Li, X. Q. et al. determined the optimal cutting position was 5~40 mm from the top leaf *(Li et al., 2013)*. Du, D. D. et al. determined that the preferred cutting area was 30~35 mm in root diameter, and the test results were analysed by combining the average moisture content and crude fibre content *(Du, Wang and Qiu, 2014)*. Subsequently, the splitting of root-cutting was analysed through a mechanical model *(Du, Wang and Qiu, 2015)*. Li, T. H. et al. designed an adjustable device for root cutting, and a mathematical model between the maximum root cutting reaction force and various factors was established to obtain the optimal parameter combination *(Li et al., 2020)*.

Above researches of the root-cutting near top leaf during harvesting cannot be applied to trimming closer to the cabbage head during postharvest treatment. Therefore, this paper designs a root-cutting test platform based on the universal testing machine, according to the achievement of our research team on the automatic orientation of postharvest cabbage *(Zheng et al., 2021)*. Then shear contrast test and orthogonal test are carried out, and the optimal shear form and operating parameter combination are obtained, which provides a theoretical basis for designing and improving the root-cutting device of the postharvest cabbage automatic trimming equipment.

[1] *Gongpei Cui, Ph.D. Stud. Eng.; Yongzhe Wei, M.S. Stud. Eng.; Shuangtao Wen, M.S. Stud. Eng.; Xinmeng Zheng, M.S. Stud. Eng.; Jingzheng Wang, M.S. Stud. Eng.; Yongjie Cui, Prof. Ph.D. Eng.*

MATERIALS AND METHODS

Samples

Fresh "Zhonggan No.15" cabbages cultivated at Taibai Vegetable Experiment and Demonstration Station of Northwest A&F University (Shaanxi Province, China) were used for the root-cutting experiment in this study. Outer leaves and roots of all cabbage samples were preserved during harvesting in order to maintain the mechanical properties. A total of 172 cabbage samples were collected in July 2019, and these cabbages were checked again to ensure that they were not infested or infected after being properly transported to the laboratory. Then, the outer leaves of cabbage were removed manually and the surface was cleaned. The physical parameters of postharvest cabbage are reported in Table 1. All samples were stored in a refrigerator with a temperature of about 3℃, and the relevant tests were completed within 72 hours at room temperature (24 ±1℃, 50~55% Rh).

Table 1

Physical parameters of postharvest cabbage

	Cross diameter	Longitudinal diameter	Height	Root diameter
	[mm]	[mm]	[mm]	[mm]
Maximum	143.48	138.75	170.49	34.05
Minimum	106.37	96.99	126.01	28.26
Mean	129.27	119.10	149.02	31.43
Standard deviation	9.45	9.40	11.39	1.72

Root-cutting test platform

To further study the shear properties of root, a root-cutting test platform for cabbage based on the universal testing machine (HY-0230, Hengyi, Shanghai) was designed, consisting of adjusting mechanism for cutter, cutter, gripper, support, etc. The structure is shown in Fig. 1.

(a) Structure *(b) Actual prototype*

Fig. 1 - Root-cutting test platform for cabbage

1 - universal testing machine; 2 - adjusting mechanism for cutter; 3 - cutter; 4 - gripper; 5 – cabbage; 6 – support; V_s - shear speed, mm/min; A_s - sliding-cutting angle,°; L_s - shear position, mm.

Specifically, the postharvest cabbage was fixed by two 3D-printed profile modeling grippers, and the root was exposed to outside the gripper. The gripper was connected to the support fixed on the universal testing machine, and the shear position (L_s) can be changed by adjusting the positional relationship between the gripper and support. At the same time, the adjusting mechanism for cutter was connected to the chuck of force sensor on the universal testing machine, and the shear speed (V_s) was controlled by changing the parameter of loading speed. The cutter and the root of cabbage formed an angle of 90° to ensure the flatness of root-cutting surface *(USDA, 1997)*. One side of the cutter was hinged with the adjusting mechanism for cutter, and the other side was connected with a sliding pair to adjust the sliding-cutting angle (A_s). The root diameter has been measured to be 31.43±1.72 mm (shown in Table 1), thus the horizontal spacing of the adjusting mechanism for cutter was determined to be 55 mm to ensure the successful root-cutting.

In this study, shear stress was used as the test index to avoid the influence of individual differences on results *(Ghahraei et al., 2011; Ma et al., 2019)*, which can be calculated by equation (1) and equation (2).

Here, the value of the highest point of root-cutting curve was selected as the maximum root-cutting force (F_{max}), and the area of shear cross-section (S) was calculated from the diameter of shear cross-section (D_T).

$$\begin{cases} P_s = \dfrac{F_{\max}}{S} \\ S = \dfrac{\pi D_T^2}{4} \end{cases} \quad (1)$$

$$P_s = \frac{4F_{\max}}{\pi D_T^2} \quad (2)$$

where: P_s is the shear stress, [Pa]; F_{max} is the maximum root-cutting force, [N]; S is the area of shear cross-section, [m²]; D_T is the diameter of the shear cross-section, [m].

The specific steps of the root-cutting test are as follows: When the cutter approached the root with a constant loading speed, the signal of force sensor was reset. Then the cutter displacement and root-cutting force were measured by displacement sensor and force sensor respectively, and the root-cutting curve was obtained. The test was repeated three times for each group, and the mean value was taken as the test result. Among them, 72 cabbages were used for shear contrast test, 90 cabbages were used for shear orthogonal test, and 10 cabbages were used for verification test.

Shear contrast test

In order to obtain optimal shear form, the shear contrast test was carried out, and it provided a theoretical basis for subsequent shear orthogonal test. The specific test factors are described in Table 2. The thickness of cutter was 1mm, and the angle of sliding-cutting was selected as 40° *(Du, Wang and Qiu, 2015)*. The shear position refers to the distance from the cutter to the joint of the root and the head, and the longest length of root met trimming requirement was 20 mm *(MOA, 2002)*. In addition, the loading speed of the universal testing machine was consistent in each group of tests, all of which were 300 mm/min.

Table 2

Factors of shear contrast test

Cutter type	Sliding-cutting angle	Shear position
	[°]	[mm]
Single-edged cutter	0 (Flat cutting)	20
		16
		12
Double-edged cutter	40 (Sliding cutting)	8
		4
		0

Shear orthogonal test

In order to obtain the optimal parameter combination for root-cutting of postharvest cabbage, a shear orthogonal test was conducted. The cutter thickness (T_c), shear position (L_s), shear speed (V_s) and sliding-cutting angle (A_s) were used as the test factors, and the shear stress (P_s) was used as the test index. According to the results of the shear contrast test, the cutter type of this test was selected as a single-edged cutter, and the range of shear position was from 0 mm to 12 mm. At the same time, the ranges of other test factors were determined by trial tests. The factor codes of the shear orthogonal test are shown in Table 3.

Table 3

Factor codes of shear orthogonal test

Code	Cutter thickness	Shear position	Shear speed	Sliding-cutting angle
	[mm]	[mm]	[mm/min]	[°]
2(r)	1.4	12	500	50
1	1.2	9	400	40
0	1.0	6	300	30
-1	0.8	3	200	20
-2(-r)	0.6	0	100	10

Morphology analysis of root by SEM

In order to explain the root-cutting properties better, the microscopic morphology of the root tissue was achieved by SEM (Nano SEM-450, FEI, USA). Firstly, the samples of cambium and xylem were taken from the shear cross-section of root, and prepared into 6×6 mm slices with a thickness of 1 mm. Subsequently, the critical-point drying method *(Xu and Yang, 2008)* was used to fix, rinse, dehydrate, do critical-point drying and gold spraying, etc. Finally, the samples were observed under the SEM with 200 times magnification.

RESULTS

Analysis of shear properties by root morphology

The typical curve of root-cutting force with cutter displacement is shown in Fig. 2(a). Which was bimodal and could be divided into three stages (D_1, D_2 and D_3). Specifically, the root-cutting force at stage D_1 increased linearly with cutter displacement until it reached the first peak P_1. In the stage D_2, the root-cutting force fell from the peak value and remained stable within certain displacement range, and then increased linearly to the second peak P_2. Finally, the root-cutting force at stage D_3 decreased approximately linearly with cutter displacement until the end of root-cutting.

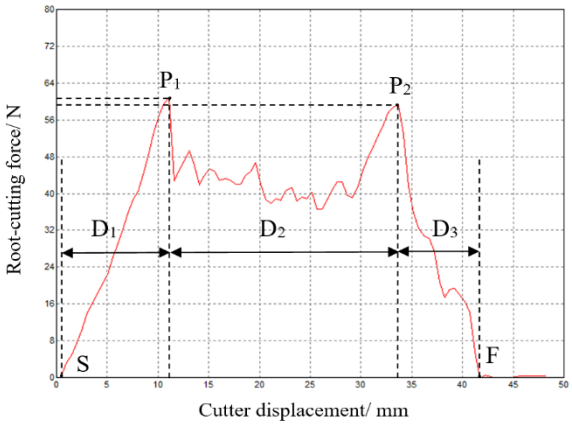

(a) Typical root-cutting curve

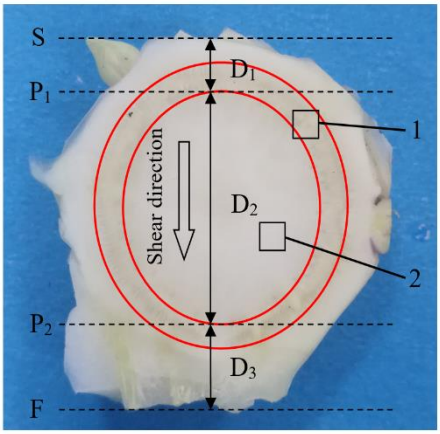

(b) Shear cross-section of root

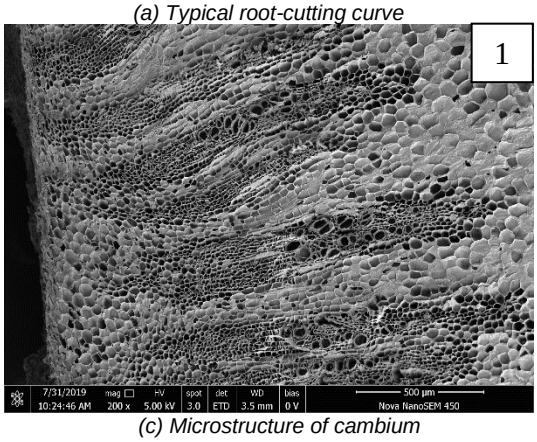

(c) Microstructure of cambium

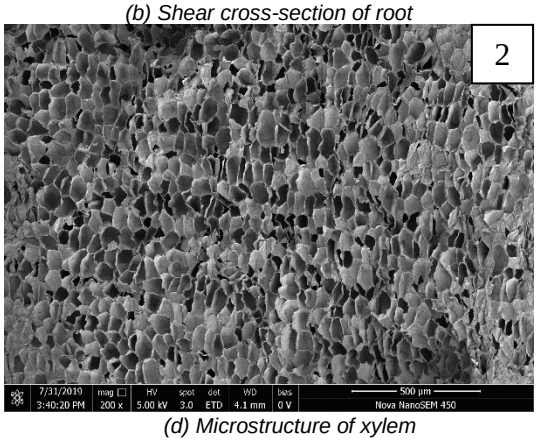

(d) Microstructure of xylem

Fig. 2 - Analysis of shear properties

S - start of root-cutting; P_1, P_2 - peaks of root-cutting; F - end of root-cutting; D_1, D_2, D_3 - different stages of root-cutting; 1 - cambium; 2 - xylem.

The shear properties were explained according to the root morphology of postharvest cabbage. As shown in Fig. 2(b), the contact area between cutter and root gradually increased with the increase of cutter displacement in stage D_1, resulted in the linear growth of root-cutting force. The cambium of root was annular and its cells were relatively small and dense (shown in Fig. 2(c)). The shear area of annular cambium at peak P_1 was the largest, so the root-cutting force was the greatest. In stage D_2, the shear area of annular cambium decreased to a stable state, and the shear area of the xylem relatively increased. Because the xylem cells were relatively larger and looser than cambium cells (shown in Fig. 2(d)), the root-cutting force at this stage was relatively reduced. With the cutter gradually approached peak P_2, the root-cutting force reached the peak again. The shear area at stage D_3 gradually decreased with the increase of the cutter displacement. In a similar way, the root-cutting force in this stage also decreased linearly. In addition, it doesn't matter if it's flat-cutting

or sliding-cutting, the curve of root-cutting force with cutter displacement was always similar to the Fig. 2(a), only the total cutter displacement increased with the increase of sliding-cutting angle.

Analysis of shear form on shear stress

The variation of root diameter with shear position is described in Fig. 3. In general, the root diameter increased with the decrease of shear position. The difference of root diameter was small and the increase tended to be gentle at range of shear position from 0 mm to 12 mm. But the increase trend of root diameter was obvious when the shear position was within 12~20 mm.

The variation of shear stress with shear position is shown in Fig. 4. The results showed that at all shear positions, the shear stress was the maximum when the double-edged cutter was used for flat cutting, and the shear stress was the second when the single-edged cutter was used for flat cutting. However, when double-edged cutter and single-edged cutter were used for sliding cutting respectively, the shear stress appeared alternating in the range from 8 mm to 12 mm. The shear stress of sliding cutting with single-edged cutter was lower than that of sliding cutting with double-edged cutter within 0~8 mm of shear position.

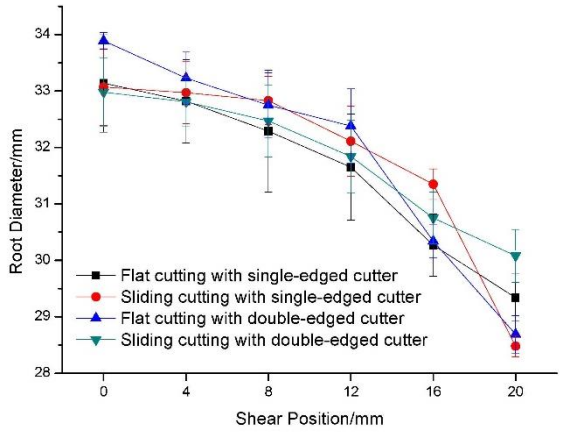

Fig. 3 - Variation of root diameter with shear position

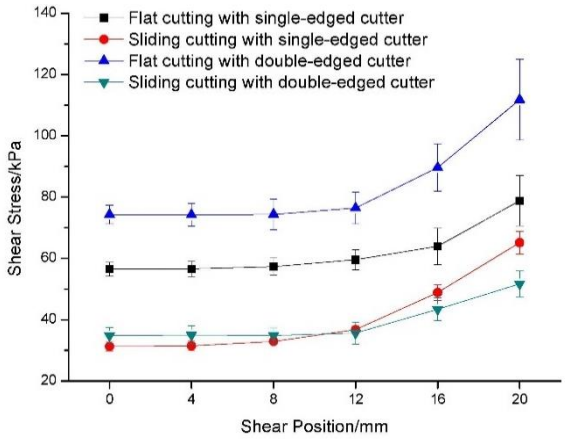

Fig. 4 - Variation of shear stress with shear position

Further analysis indicated that the shear stress gradually decreased with the decrease of shear position, regardless of the shear form. The shear position ranged from 0 mm to 12 mm was suitable for root-cutting of postharvest cabbage, the root diameter changed a little, and the shear stress tended to be stable during this range. In addition, compared with the shear stress of different shear forms, the shear stress of sliding cutting was far lower than that of flat cutting. The minimum shear stress of sliding cutting was 31.27±1.43 kPa when the shear position was 0 mm. Therefore, sliding cutting with single-edged cutter was selected as shear form of the orthogonal test to optimize the operation parameters of root-cutting.

Effect of test factors on shear stress

The results of shear orthogonal test are reported in Table 4. The shear stress of 23rd test (63.93 kPa) was the maximum and that of 13rd test (30.28 kPa) was the minimum. Regression analysis was carried out by Design Expert 10 software.

Table 4

Results of shear orthogonal test

Number	*A*	*B*	*C*	*D*	Shear stress [kPa]	Number	*A*	*B*	*C*	*D*	Shear stress [kPa]
1	-1	-1	-1	-1	44.49	16	1	1	1	1	46.54
2	1	-1	-1	-1	43.78	17	-2	0	0	0	41.41
3	-1	1	-1	-1	60.15	18	2	0	0	0	41.92
4	1	1	-1	-1	58.78	19	0	-2	0	0	32.37
5	-1	-1	1	-1	43.28	20	0	2	0	0	54.67
6	1	-1	1	-1	42.2	21	0	0	-2	0	48.05
7	-1	1	1	-1	60.46	22	0	0	2	0	46.24
8	1	1	1	-1	57.76	23	0	0	0	-2	63.93
9	-1	-1	-1	1	39.63	24	0	0	0	2	42.05

Table 4 (continuation)

Number	A	B	C	D	Shear stress	Number	A	B	C	D	Shear stress
					[kPa]						[kPa]
10	1	-1	-1	1	40.13	25	0	0	0	0	35.86
11	-1	1	-1	1	48.13	26	0	0	0	0	33.23
12	1	1	-1	1	43.97	27	0	0	0	0	37.65
13	-1	-1	1	1	30.28	28	0	0	0	0	39.73
14	1	-1	1	1	31.64	29	0	0	0	0	38.22
15	-1	1	1	1	48.54	30	0	0	0	0	41.58

A - cutter thickness; B - shear position; C - shear speed; D - sliding-cutting angle.

The regression equation of shear stress by dimensionless coded values is shown in equation (3):

$$P_s = 37.71\text{-}0.38A\text{+}6.40B\text{-}0.92C\text{-}5.24D\text{-}0.64AB\text{+}0.083AC\text{+}0.097AD\text{+}1.43BC\text{-}1.12BD\text{-}0.71CD\text{+}0.97A^2\text{+}1.44B^2\text{+}2.34C^2\text{+}3.80D^2 \quad (3)$$

The regression equation of shear stress by actual values is shown in equation (4):

$$P_s = 122.42\text{-}46.79T_c\text{+}0.98L_s\text{-}0.16V_s\text{-}2.42A_s\text{-}1.07T_cL_s\text{+}4.13\times10^{-3}T_cV_s\text{+}0.05T_cA_s\text{+}4.77\times10^{-3}L_sV_s\text{-}0.04L_sA_s\text{-}7.10\times10^{-4}V_sA_s\text{+}24.31T_c^2 \quad (4)$$
$$\text{+}0.16L_s^2\text{+}2.34\times10^{-4}V_s^2\text{+}0.04A_s^2$$

The adjusted determination coefficient (R^2) was 0.9642, and Pred R-Squared and Adj R-Squared were 0.8735 and 0.9307 respectively, the difference between them was less than 0.2. Therefore, the factors in regression analysis could explain the test indexes well. The analysis of variance (ANOVA) of the results is shown in Table 5, the model was extremely significant ($P<0.0001$), and the lack of fit was not significant ($P=0.8557>0.1$). The significance order of single factor was $B>D>C>A$, and the significance order of interaction was $BC>BD>CD>AB>AD>AC$. Shear position (*B*), shear speed (*C*) and sliding-cutting angle (*D*) had significant effects on shear stress, while interaction between shear position and shear speed (*BC*) and interaction between shear position and sliding-cutting angle (*BD*) had significant effects on shear stress.

Table 5

ANOVA of the results

Source	Sum of squares	Freedom	Mean square	*F* value	*P* value
Model	2233.19	14	159.51	28.84	<0.0001 ***
A	3.48	1	3.48	0.63	0.4400
B	981.76	1	981.76	177.48	<0.0001 ***
C	20.13	1	20.13	3.64	0.0758 *
D	659.40	1	659.40	119.20	<0.0001 ***
AB	6.63	1	6.63	1.20	0.2909
AC	0.11	1	0.11	0.020	0.8903
AD	0.15	1	0.15	0.027	0.8705
BC	32.78	1	32.78	5.92	0.0279 **
BD	20.03	1	20.03	3.62	0.0765 *
CD	8.07	1	8.07	1.46	0.2459
A^2	25.94	1	25.94	4.69	0.0469 **
B^2	56.58	1	56.58	10.23	0.0060 ***
C^2	150.51	1	150.51	27.21	0.0001 ***
D^2	396.85	1	396.85	71.74	<0.0001 ***
Residual	82.98	15	5.53		
Lack of Fit	40.16	10	4.02	0.47	0.8557
Pure Error	42.81	5	8.56		
Total	2316.17	29			

In order to further study the effect of both *BC* and *BD* on shear stress, the response surface analysis was conducted by dimensionality reduction, as reported in Fig. 5. The effect of *BC* on shear stress is shown in Fig. 5(a), where the cutter thickness was 1 mm and the sliding-cutting angle was 30°. When the shear speed was constant, the shear stress decreased with the decrease of shear position. But the shear stress decreased firstly and then increased with the increase of shear speed while the shear position was constant. Among them, when the shear position was less than 6 mm and the shear speed was greater than 180 mm/min, the shear stress was relatively small.

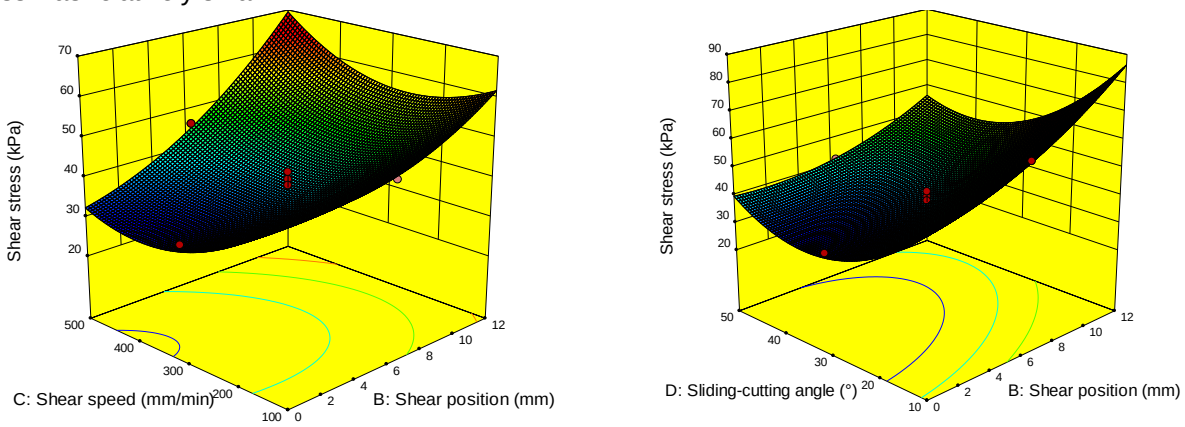

(a) Effect of BC on shear stress *(b) Effect of BD on shear stress*

Fig. 5 - Response surface between interaction term and shear stress

Fig. 5(b) shows the effect of *BD* on shear stress, where the cutter thickness and the shear speed were 1 mm and 300 mm/min respectively. When the sliding-cutting angle was constant, the shear stress decreased with the decrease of shear position. The shear position ranged from 8 mm to 12 mm, the shear stress decreased with the increase of sliding-cutting angle. The shear position was in the range of 0~8 mm, the shear stress firstly decreased rapidly and then increased slowly with the increase of sliding-cutting angle. Among them, when the shear position was less than 4 mm and the sliding-cutting angle was greater than 18°, the shear stress was relatively small and tended to be stable.

Optimization of root-cutting parameters

Aiming at the minimum shear stress, the parameters were optimized by Design Expert 10 software. The results showed that when the cutter thickness was 0.89 mm, the shear position was 0.00 mm, the shear speed was 388.94 mm/min, and the sliding-cutting angle was 34.84°, the shear stress was the minimum, which was 28.02 kPa.

Based on the above optimal parameter combination, the verification test was carried out. The parameters were rounded in order to facilitate practical operation. That is, the cutter thickness was 0.9 mm, the shear position was 0.00 mm, the shear speed was 390 mm/min, and the sliding-cutting angle was 35 °. On this condition, the average shear stress was 28.62±0.34 kPa, and the deviation from theoretical value of orthogonal test was 2.14%.

It could be seen from Table 4 that the results of 13rd and 14th tests were also acceptable, differed little from the shear stress on the condition of optimal parameter combination. At the same time, the shear position of 3.00 mm selected for the above tests was more practical, which could not only meet the requirements of postharvest trimming, but also avoid the damage of the head or scattering of leaf. In other words, the above combination could be selected as the parameters flexibly in the actual root-cutting operation.

CONCLUSIONS

1) The curve of root-cutting force with cutter displacement was bimodal, and the peak force appeared at the maximum shear area of annular cambium, where its cells were relatively small and dense.

2) Shear contrast test showed that the effect of sliding-cutting with single-edged cutter was the best. The shear position ranged from 0 mm to 12 mm was suitable for root-cutting operation.

3) Shear orthogonal test showed that the optimal parameters of cutter thickness, shear position, shear speed and sliding-cutting angle were respectively 0.89 mm, 0.00 mm, 388.94 mm/min and 34.84°, and shear stress was 28.02 kPa. On the condition of the optimal parameters, the actual average shear stress was 28.62±0.34 kPa by verification test, and the deviation from the theoretical value was 2.14%.

ACKNOWLEDGEMENT

The research was supported by research grants from Shaanxi Key Research and Development Program of China (2018TSCXL-NY-05-04, 2019ZDLNY02-04), and the Scientific and Technological Achievements Promotion Program of Experiment and Demonstration Station of Northwest A&F University (TGZX2018-28).

REFERENCES

[1] Cui, G. P., Zheng, X. M., Wang, J. Z., Yang, C., Liu, Z. H., & Cui, Y. J. (2019). Physical and mechanical experiments for designing cabbage precision trimming device. *The 2019 ASABE Annual International Meeting*, Boston, MA, United States. https://doi.org/10.13031/aim.201901420

[2] Du, D. D., Wang, J., & Qiu, S. S. (2014). Optimization of cutting position and mode for cabbage harvesting (甘蓝根茎部切割部位及方式优化试验研究). *Transactions of the CSAE*, *30*(12), 34-40. https://doi.org/10.3969/j.issn.1002-6819.2014.12.004

[3] Du, D. D., Wang, J., & Qiu, S. S. (2015). Analysis and test of splitting failure in the cutting process of cabbage root. *International Journal of Agricultural and Biological Engineering*, *8*(4), 27-34. https://doi.org/10.3965/j.ijabe.20150804.1723

[4] Du, D. D. (2017). *Research on crawler self-propelled cabbage harvesting equipment and development of its weighing system (履带自走式甘蓝收获机研究及称重系统开发)* [Doctoral dissertation, Zhejiang University]. CNKI.

[5] Du, D., Wang, J., Xie, L., & Deng, F. (2019). Design and field test of a new compact self-propelled cabbage harvester. *Transactions of the ASABE*, *62*(5), 1243-1250. https://doi.org/10.13031/trans.13327

[6] Ghahraei, O., Ahmad, D., Halina, A., Suryanto, H., & Othman, J. (2011). Cutting tests of kenaf stems. *Transactions of the ASABE*, *54*(1): 51-56. https://elibrary.asabe.org/abstract.asp?aid=36252

[7] Li, T. H., Meng, Z. W., Ding, H. H., Hou, J. L., Shi, G. Y., & Zhou, K. (2020). Mechanical analysis and parameter optimization of cabbage root cutting operation (甘蓝切根作业力学分析与参数优化). *Transactions of the CSAE*, *36*(07): 63-72. https://doi.org/10.11975/j.issn.1002-6819.2020.07.007

[8] Li, X. Q., Wang, F. E., Guo, W. J., Gong, Z. W., & Zhang, J. (2013). Influencing factor analysis of cabbage root cutting force based on orthogonal test (甘蓝根茎切割力影响因素分析). *Transactions of the CSAE*, *29*(10): 42-48. https://doi.org/10.3969/j.issn.1002-6819.2013.10.006

[9] Ma, Y. D., Xu, C., Cui, Y. J., Fu, L. S., Liu, H. Z., & Yang, C. (2019). Design and test of harvester for whole hydroponic lettuce with low damage (水培生菜整株低损收获装置设计与试验). *Transactions of the Chinese Society for Agricultural Machinery*, *50*(01):162-169. https://doi.org/10.6041/j.issn.1000-1298.2019.01.017

[10] Toncheva, N., Samsonov, A., Yegorov, V., & Lebedev, V. (2017). Results of laboratory studies of device for transporting heads to the elevator of cabbage harvest machine. *The 16th International Scientific Conference Engineering for Rural Development*, Jelgava, Latvia. https://doi.org/10.22616/ERDev2017.16.N040

[11] Xu, B. S., & Yang, J. (2008). *Practical electron microscope technology (实用电镜技术)*. vol.1, Southeast University Press, Nanjing/ China, ISBN 9787564114596

[12] Zheng, X. M., Cui, G. P., Wang, J. Z., & Cui, Y. J. (2021). Design and Experiment of Automatic Orientation Device for Post-harvest Cabbage Trimming System (甘蓝采后整修系统自动调向装置设计与试验). *Journal of Agricultural Mechanization Research*, *43*(02): 64-70. https://doi.org/10.13427/j.cnki.njyi.2021.02.011

[13] Zhou, C., Luan, F., Fang, X., & Chen, H. (2017). Design of cabbage pulling-out test bed and parameter optimization test. *Chemical Engineering Transactions*, 62, 1267-1272. https://doi.org/10.3303/CET1762212

[14] *** MOA. (2002). *NY/T 583-2002 Cabbage (结球甘蓝)*. The Ministry of Agriculture, China. https://kns.cnki.net/kcms/detail/detail.aspx?dbcode=SCHF&dbname=SCHF&filename=schf201909205

[15] *** USDA. (1997). *United States Standards for Grades of Cabbage for Processing*. United States Department of Agriculture, United States. https://www.ams.usda.gov/grades-standards/cabbage-processing

USING THE DISCRETE ELEMENT METHOD TO ANALYZE AND CALIBRATE A MODEL FOR THE INTERACTION BETWEEN A PLANTING DEVICE AND SOIL PARTICLES
/
栽植器与土壤相互作用离散元模型参数标定及分析

Zeng Fandi, Li Xuying *, Zhang Yongzhi, Zhao Zhiwei, Cheng Cheng [1]
Inner Mongolia Agricultural University, College of Mechanical and Electrical Engineering, Hohhot/China;
Tel: +86-0471-4309215; E-mail: zfd19508@163.com
DOI: https://doi.org/10.35633/inmateh-63-42

Keywords: *Soil, Duckbilled planter, Hertz-Mindlin model, Parameter calibration, Dynamic changes*

ABSTRACT
Dynamic soil behaviour at the contact interface during transplanting makes it difficult to ensure transplanting quality. To solve this problem, the Hertz-Mindlin with bonding contact model was used to calibrate the parameters of soils in Inner Mongolia. Based on the response surface design principle, *four-factor and three-level tests were performed using the repose angle as an evaluation index, and the following influence factors were considered: the soil-soil restoration coefficient, the soil-steel restoration coeficient, the soil-steel static friction coefficient and the soil-steel static friction coefficient. A regression model was analysed, and an optimization procedure yielded the following optimum combination of parameters: a soil-soil restoration coefficient of 0.45, a soil-steel restoration coefficient of 0.35, a soil-steel static friction coefficient of 0.85 and a soil-steel rolling friction coefficient of 0.13. This optimal combination was used to simulate the soil at the contact interface. The particle dynamic behaviour and soil particle mass flow were used to analyse the soil dynamic behaviour, showing that the average mass flow during the gradual opening of the* duckbilled planter *tends to increase over time; when the* duckbilled planter *gradually leaves soil, the contact interface of soil particles in the corner of the* duckbilled planter *unit causes a reduction in the fluctuation range of the soil mass flow, which exhibits a wave-like change. After the duckbilled planter has left soil, the contact interface of the soil changes tends to stabilize. The duckbilled planter-soil discrete element simulation model was verified. The results of this study provide a reference for the optimal design of a duckbilled planter structure.*

摘要
为解决栽植器与接触界面土壤的动态行为造成土壤回流，使栽植质量难以保证等问题，利用 Hertz-Mindlin with Bonding 模型对内蒙地区移栽环境下田间土壤进行参数标定，基于响应面法，分别以土壤-土壤恢复系数、土壤-钢恢复系数、土壤-钢静摩擦系数和土壤-钢滚动摩擦系数为试验因素，进行四因素三水平的正交试验，对回归模型进行了分析，最终得到最佳参数组合为土壤-土壤恢复系数 0.45、土壤-钢恢复系数 0.35、土壤-钢静摩擦系数 0.85 和土壤-钢滚动摩擦系数 0.13；根据最优组合，模拟栽植状态下接触界面的土壤颗粒动态变化行为，进行土壤颗粒质量流量分析，结果表明鸭嘴式栽植器逐渐打开过程中的平均质量流量随着时间的增加呈逐渐增加的趋势，当鸭嘴式栽植器逐渐离开土壤时，鸭嘴式栽植器单位转角内与不同土壤颗粒接触界面变化，土壤质量流量的波动范围较小，呈现波浪式的变化，最终当鸭嘴式栽植器离开土壤，接触界面的土壤质量变化趋于稳定。验证了鸭嘴式鸭嘴式栽植器-土壤离散元仿真模型的正确性，并研究栽植过程中接触土壤的动态变化，为鸭嘴式栽植器结构的优化设计提供参考。

INTRODUCTION

The interaction between a duckbilled planter and the soil is a challenging problem at the contact interface. The discrete element method is used to numerically simulate discrete materials (*Mustafa Ucgul et al., 2014; Lenaerts B. et al., 2014; Li et al., 2016*). The soil particles are modeled as a series of independent motion units; a simulation is performed to obtain the dynamic change law of the soil particles by determining the velocity

[1] *Fandi Zeng, Ph.D. Stud. Eng.; Xuying Li*, Prof. Ph.D. Eng.; Yongzhi Zhang, Lec. Ph.D. Eng.; Zhiwei Zhao, M.S. Eng.; Cheng, M.S. Eng.*

and a force distribution cloud diagram of the interaction between particles and implements; and the motion law of the implements is analysed to provide a reference for the optimal design of agricultural implements (*Fang et al., 2016; Wang et al., 2018*).

Current transplanter research is mostly focused on motion analysis and the working performance of the duckbilled planter. For example, the relationship among the tractor forward speed, the number of cups, the rotational speed of the cups and the planting spacing has been studied by analysing the trajectory of the cups (*Feng et al., 2002*). A 2-row fully automatic vegetable transplanter was developed considering the available power. Test results showed that the field capacity of the transplanter was 0.026 ha h-1, saving 68% of labour and 80% of time compared with traditional manual transplanting, while providing satisfactory transplanting quality (*Kumar et al., 2011*). A semiautomatic tomato transplanter was designed and built with conical distribution cups to increase the speed and precision of cultivation. Test results showed an optimum advance speed and a planting depth of 2 km h^{-1} and 5 cm, respectively. (*Seyed Mohamad Javidan et al., 2019*). The contact interface between the duckbilled planter and soil exhibits complex dynamic behaviour because of the spatial variability of the soil, dynamic factors and soil motion and fragmentation. Many studies on soil discrete element modeling have been carried out in China and abroad: for example, Mustafa used the Hertz-Mindlin and hysteretic spring contact models to analyse the plastic deformation of soil particles with and without cohesive forces (*Mustafa et al., 2015*). Ying Chen used discrete element software to analyse sandy soil mobility (*Ying et al., 2019*). Studies on soil motion in specific situations have shown that the forward speed of tillage implements affects horizontal and lateral soil displacement (*Liu et al., 2010*). Rahman measured the velocity of and disturbance to soil in troughs during various agricultural tillages (*Rahman et al., 2005*). Although the dynamic behaviour of soil during transplanting can deteriorate planting quality, the discrete element model for the interaction between a duckbilled planter and soil has been applied in few studies.

Therefore, the discrete element method was used to calibrate a model of a duckbilled planter and soil particles. The Hertz-Mindlin with bonding contact model was used to carry out soil repose angle tests, and the optimum combination of contact model parameters was determined using the Box-Benhken test. Mass flow was analysed to determine the motion of soil particles from the entry of the duckbilled planter into soil until the planter exits soil; the duckbilled planter-soil discrete element model was verified; and the dynamic changes in the duckbilled planter-soil system during transplanting were elucidated. The research results provide a reference for the optimal design of a duckbilled planter structure.

MATERIALS AND METHODS

- **Basic soil particle parameters**

Soil was selected from the experimental field of the Inner Mongolia Agricultural University in China: the soil had a water content of 14.52% and a density of 1450 kg/m^3, and large particle impurities, such as grass roots, were removed prior to the test. The soil physical parameters were determined in a laboratory at the Institute of Mechanical and Electrical Engineering of the Inner Mongolia Agricultural University. The soil particle size distribution was determined by the sieving method. The soil particle size distribution showed that the soil was a sandy loam.

- **Test method**
- **Soil shear test**

A ZJ-type strain-controlled straight shear instrument is commonly used to determine the shear strength of a soil. This instrument was used to perform experiments on four groups of samples under different vertical pressures (100, 200, 300 and 400 kPa), where the handwheel was gradually rotated to apply a shear force at a speed of 6 r/min until the soil in the shear box was damaged; the soil parameters were then determined using Coulomb's law, which is given by formula (1):

$$\tau = C + \sigma \times tan\varphi \quad (1)$$

Where:

C - Soil cohesion, [kPa];

σ - Normal stress on shear surface, [kPa];

φ - Soil internal friction angle, [°];

The shear strength curve presented in Fig.1 shows that the soil cohesion was 20.46 kPa and the internal soil friction angle was 15.64°.

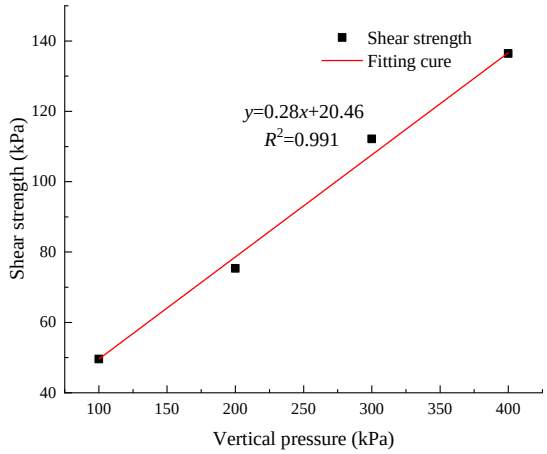

Fig. 1 - Shear strength and vertical load curve

- **Other soil characteristic parameters**

The shear modulus of soil can be approximated using the elastic modulus and Poisson's ratio, where the shear modulus is calculated using formula (2):

$$G=\frac{E}{2(1+\upsilon)} \tag{2}$$

Where:

E - Elastic modulus, [Pa];

υ - Poisson's ratio;

The Poisson's ratio of a soil is the ratio of the lateral expansion strain to the vertical compression strain when the soil is compressed without lateral limits and is typically estimated using formula (3):

$$\upsilon=\frac{K_0}{1+K_0} \tag{3}$$

Where:

K_0 - Side pressure coefficient.

The soil lateral pressure coefficient is the ratio of the lateral pressure to the vertical pressure under lateral pressure conditions and can be approximated using formula (4):

$$K_0=1-\sin\varphi \tag{4}$$

Where:

φ - Soil internal friction angle, [°].

- **Parameter calibration process and analysis**

DEM model of soil particles

An accurate soil particle model ensures the validity of the simulation results. The soil basic structure consists of a block, a nucleus, and column particles (*Zhang et al., 2005*).

The soil particle model is shown in Fig. 2: the model particles in EDEM are spherical, and the spherical filling unit radius is set to 1 mm.

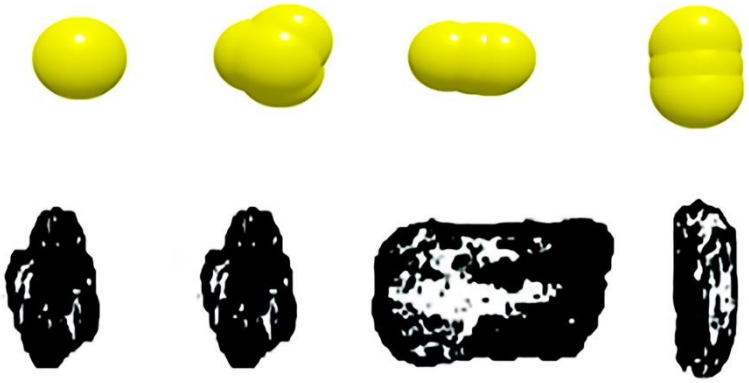

a） lump1 b） lump2 c） nuclei d） columnar

Fig. 2 - Sketch of soil particle model

Contact between soil particles produces a certain degree of bonding that significantly impacts planting resistance and the dynamics of the soil contact interface. The Hertz-Mindlin with bonding contact model was used to decompose the collision forces between soil particles into normal and tangential components, where the particles were bonded together by adding an "adhesive" to prevent relative motion between particles (*Li et al., 2014; Hang et al., 2017*).

When the bonding begins to act on the soil particles, the force Fn and the moments Mn and $M\tau$ of the soil particles increase with the time step, starting from zero, as given in formula (5):

$$\begin{cases} \delta F_{\mathrm{n}} = -V_{\mathrm{n}} S_{\mathrm{n}} A \delta_{\mathrm{t}} \\ \delta F_{\tau} = -V_{\mathrm{r}} S_{\tau} A \delta_{\mathrm{t}} \\ \delta M_{\mathrm{n}} = -\overline{w_n} S_{\mathrm{n}} J \delta_{\mathrm{t}} \\ \delta M_{\tau} = -\overline{w}_{\mathrm{r}} S_{\mathrm{r}} \dfrac{J}{2} \delta_{\mathrm{t}} \\ A = \pi R^2 \\ J = \dfrac{1}{2} \pi R_{\mathrm{b}}^4 \end{cases} \tag{5}$$

Where:

A - Contact area; J- cross-sectional moment of extreme inertia;

S_{n} -Normal stiffness of the bonded particles;

S_{τ} - Tangential stiffness of the bonded particles;

v_{n} - Normal component of the velocity of particle motion;

v_{τ} - Tangential component of particle velocity;

$\overline{w_{\mathrm{n}}}$ - Tangential component of particle angular velocity;

$\overline{w_{\tau}}$- Normal component of particle angular velocity.

The bonding constraint fails when the particle interaction force exceeds a maximum value, as given in formula (6).

$$\begin{cases} \sigma_{\max} < -\dfrac{\mathrm{F_n}}{A} + \dfrac{2M_{\mathrm{t}}}{J} R \\ \tau_{\max} < -\dfrac{F_{\mathrm{t}}}{A} + \dfrac{M_{\mathrm{t}}}{J} \mathrm{R} \end{cases} \tag{6}$$

The Hertz-Mindlin with bonding contact model used in this paper includes five microscopic parameters, namely the normal stiffness S_{n}, the tangential stiffness $S_{\tau,}$ the critical normal stress $\sigma_{\max}$, the bonding tangential critical stress $\tau_{\max}$, and the particle bonding radius R_{b}. The calculations were performed using results from the literature (*Hang et al., 2017*), as shown in Table 1.

Table 1

Contact model parameters

PARAMETER	Value
The normal stiffness	2400000 N/m
The tangential stiffness	1700000 N/m
The critical normal stress	235000 Pa
The bonding tangential critical stress	186000 Pa
Starting time	0.2 s
The particle bonding radius	1.5 mm

- **Simulation parameters**

Existing characteristic material parameters of the soil particles were used in conjunction with measured parameters; the duckbilled planter material is 20 steel with the following parameters: a density of 7850 kg/m^3, a Poisson's ratio of 0.3, and a shear modulus of 7×10^{10}Pa; the remaining parameters were determined using values in the literature (*Dun et al., 2016*), as shown in Table 2. During the simulation, 28% of the Rayleigh time step and the grid size were set to three times the minimum spherical element size.

Table 2

Discrete element simulation parameter table

Simulation parameters	Value
Density of soil particles[kg/m^3]	1452
Poisson's ratio of soil	0.42
Young's modulus of soil [MPa]	1×10^6
Density of steel [kg/m^3]	7850
Poisson's ratio of steel	0.3
Young's modulus of steel [MPa]	7×10^{10}
Soil-soil restitution coefficient	0.15~0.75^a
Soil-soil static friction coefficient	0.4
Soil-soil rolling friction coefficient	0.3
Soil-steel restitution coefficient	0.2~0.5^a
Soil-steel static friction coefficient	0.5~1.2^a
Soil-steel rolling friction coefficient	0.05~0.2^a

Note: a show the term is variable

- **Simulation model for repose angle**

The Hertz-Mindlin with bonding contact model was implemented using the EDEM software and identical inner diameters and heights of the funnel and the cylinder chassis as those used in the repose angle test, as shown in Fig. 3. The particles formed a particle plant at the top of funnel. The particle radius was set to 1 mm, and the simulation generation time was set to 2s. As the lower end of the hopper drop opening remained open, the soil particles continued to fall until all the soil particles stopped moving: a stable particle heap was then formed, and the repose angle was measured.

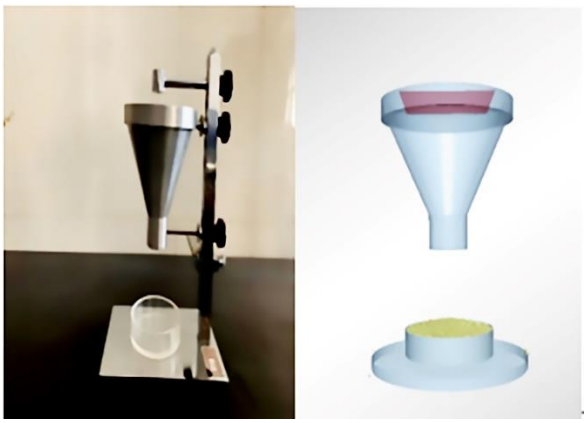

a) Physical test ***b) Simulation test***

Fig. 3 - The repose angle test

- **Response surface design for simulation parameters**

The repose angle parameters were accurately calibrated by determining the contact characteristic parameters (the soil-soil restitution coefficient, the soil-steel restitution coefficient, the soil-steel static friction coefficient and the soil-steel rolling friction coefficient). Based on the response surface design principle, Box-Behnken test was performed and three levels, i.e. low (-1), medium (0) and high (1), was chosen for each parameter. The parameters are shown in Table 3.

Table 3

Factors and levels of the repose angle test

Levels	Soil-soil restitution coefficient A	Soil-steel restitution coefficient B	Soil-steel static friction coefficient C	Soil-steel rolling friction coefficient D
-1	0.15	0.2	0.5	0.05
0	0.45	0.35	0.85	0.13
1	0.75	0.5	1.2	0.2

RESULTS

- **Test results and analysis**

The test scheme consisted of 29 groups of tests, in which each group was repeated three times. The average values were taken as the test results. The results are shown in Table 4.

Table 4

Test scheme and results of repose angle

No.	Soil-soil restitution coefficient A	Soil-steel restitution coefficient B	Soil-steel static friction coefficient C	Soil-steel rolling friction coefficient D	Angle of repose
	/	/	/	/	[°]
1	0.15	0.35	0.85	0.20	26.13
2	0.15	0.20	0.85	0.13	28.31
3	0.45	0.35	0.50	0.05	30.39
4	0.45	0.35	1.20	0.05	26.59
5	0.75	0.35	0.85	0.20	30.26
6	0.45	0.35	0.85	0.13	34.03
7	0.45	0.35	0.85	0.13	33.93
8	0.15	0.50	0.85	0.13	29.69
9	0.45	0.35	1.2	0.20	31.23
10	0.45	0.35	0.85	0.13	34.66
11	0.45	0.35	0.85	0.13	33.76
12	0.45	0.35	0.85	0.13	34.49
13	0.75	0.35	0.50	0.13	26.56
14	0.45	0.20	0.85	0.20	30.43
15	0.15	0.35	1.20	0.13	28.96
16	0.75	0.35	0.85	0.05	30.29
17	0.15	0.35	0.85	0.05	28.49
18	0.75	0.20	0.85	0.13	25.96
19	0.75	0.35	1.20	0.13	30.59
20	0.45	0.50	1.20	0.13	29.36
21	0.45	0.50	0.85	0.05	30.13
22	0.15	0.35	0.5	0.13	28.80
23	0.45	0.35	0.5	0.20	30.96
24	0.45	0.20	0.5	0.13	28.59
25	0.45	0.20	1.2	0.13	32.26
26	0.45	0.50	0.5	0.13	30.23
27	0.45	0.20	0.85	0.05	28.89
28	0.75	0.50	0.85	0.13	29.83
29	0.45	0.50	0.85	0.20	31.46

- **Analysis of variance and the regression model**

The test results were analysed using design-expert 8.0.6, and the ANOVA results are shown in Table 5. The regression model for the repose angle is shown in formula (7). The letters *A*, *B*, *C* and *D* correspond to parameters with a highly significant effect on the repose angle, where the order of influence on the repose angle was soil-steel restitution coefficient *B*<soil-steel static friction coefficient *C*<soil-steel rolling friction coefficient *D*<soil-soil restitution coefficient *A*. The interaction terms *AB*, *AD*, *BC* and *CD* were found to have an important effect on the repose angle. The analysis of variance results show that the model was extremely significant (*P*<0.01).

$$\theta=34.17+1.48A+0.57B-0.88C+1.30D+0.62AB+0.47AC+0.58AD-0.64BC-0.052BD+1.02CD$$
$$-3.50A^2-2.06B^2-2.50C^2-1.88D^2-0.75A^2B+2.43A^2C-1.90A^2D-2.03AB^2$$
$$-1.14AC^2+1.08B^2C-0.59B^2D-0.38BC^2-0.16A^2B^2+0.053A^2C^2$$

Table 5

ANOVA of soil repose angle model of Box-Benhken test

Source	DF	MS	F Value	P Value
Model	24	6.98	47.52	< 0.0001**
A	1	8.79	59.83	0.0015
B	1	1.29	8.77	0.0415
C	1	3.12	21.20	0.0100
D	1	6.79	46.19	0.0024
AB	1	1.55	10.55	0.0314
AC	1	0.87	5.95	0.0713
AD	1	1.36	9.24	0.0384
BC	1	1.61	10.98	0.0296
BD	1	0.011	0.075	0.7977
CD	1	4.14	28.19	0.0061
A^2	1	25.12	170.97	0.0002
B^2	1	17.95	122.14	0.0004
C^2	1	26.31	179.03	0.0002
D^2	1	14.91	101.50	0.0005
A^2B	1	1.11	7.55	0.0514
A^2C	1	11.81	80.38	0.0009
A^2D	1	7.22	49.14	0.0022
AB^2	1	8.28	56.37	0.0017
AC^2	1	2.58	17.54	0.0138
B^2C	1	2.34	15.95	0.0162
B^2D	1	0.68	4.66	0.0971
BC^2	1	0.29	1.99	0.2310
A^2B^2	1	0.026	0.18	0.6934
A^2C^2	1	2.756E-003	0.019	0.8977
Pure Error	4	0.15		
Cor Total	28			
R^2=0.996; R^2_{adj}=0.975; CV=1.28%; Adeq-Precision=23.08				

*Note: P < 0.01 (extremely significant, **),P < 0.05 (significant, *).*

- **Analysis of influences of interaction factors on productivity**

The optimized regression equation was solved using the actual repose angle of the soil particles as a target. The ANOVA results of the regression model indicated that parameter interaction terms, i.e. AB, AD, BC and CD, had a significant effect on the repose angle of the soil particles (*P*<0.05). The response surfaces of the four considered parameters under the interactions of AB, AD, BC and CD were plotted using design expert software, as shown in Fig. 4, to analyse the effect of the interaction terms on the repose angle.

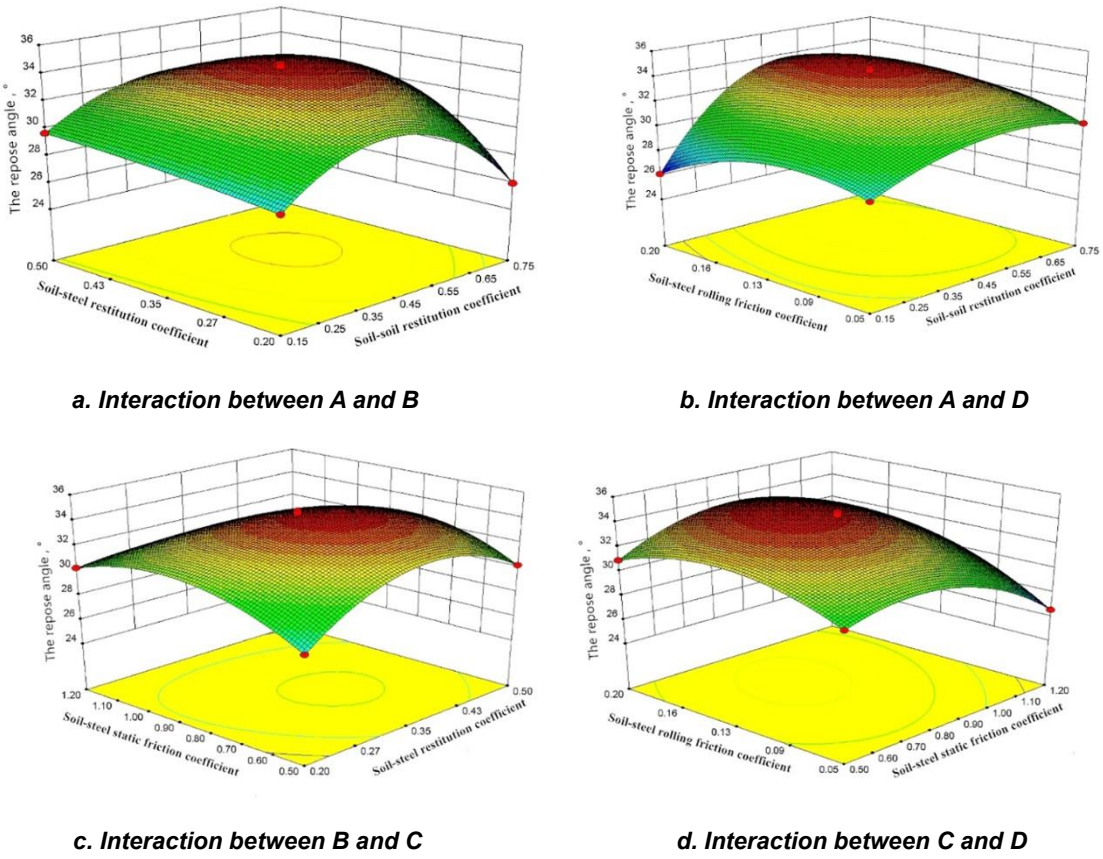

a. Interaction between A and B *b. Interaction between A and D*

c. Interaction between B and C *d. Interaction between C and D*

Fig. 4 – Interaction effect diagram of response surface results

Fig. 4a-4d show the response surfaces of the soil-soil restitution coefficient, the soil-steel restitution coefficient, the soil-steel static friction coefficient and the soil-steel rolling friction coefficient with respect to the repose angle: when the soil-steel rolling friction coefficient and the soil-steel static friction coefficient were at the zero position, the soil-steel recovery coefficient and the soil-soil recovery coefficient increased, whereas the repose angle first increased and then decreased (Fig. 4a); when the soil-steel restitution coefficient and the soil-steel static friction coefficient were at the zero position, the soil-soil restitution coefficient and the soil-steel rolling friction coefficient increased, whereas the repose angle first increased and then decreased (Fig. 4b); for a soil-steel restitution coefficient of 0.35, the repose angle slowly increased (Fig. 4c). For a soil-steel rolling friction coefficient of 0.13, the repose angle decreased with the soil-steel static coefficient (Fig. 4d).

- **Parameter optimization and verification**

To obtain the optimal parameters of the repose angle, the regression equation was solved using design-expert 8.0.6 software. The objective function and constraints are given in formula (7).

$$\begin{cases} max\theta \\ 0.15 \le A \le 0.75 \\ 0.2 \le B \le 0.5 \\ 0.5 \le C \le 1.2 \\ 0.05 \le D \le 0.2 \end{cases} \quad (7)$$

The optimization procedure yielded the following optimum combination of parameters for the repose angle: a soil-soil restitution coefficient of 0.45, a soil-steel restitution coefficient of 0.35, a soil-steel static friction coefficient of 0.85 and a soil-steel rolling friction coefficient of 0.13. The predicted repose angle was 34.71°. The reliability of the prediction was verified by carrying out a physical test: the measured repose angle of 36.23° showed that the prediction model was reliable.

- **Dynamics of soil particles at contact interface during planting**
- **Simulation model for transplanting**

The dynamic changes in soil at the contact interface were determined by using EDEM in the simulation. The transplanting depth for tomatoes and other agricultural crops was generally 60 ~ 100 mm, and a prism-type duckbilled planter was selected, as shown in Fig. 5. Considering that the soil surface in an actual field is uneven, the soil particle was set to 3 mm, and the final plane of naturally fallen soil particles was regarded as flat soil in the simulation, thereby increasing the calculation speed and saving computing time.

Taking λ = 1.068 as an example, the transplanting operation was set to begin at 5 s, and the angular velocity of the duckbilled planter was set at 1.57 rad/s; the dynamic simulation of soil particles at the contact interface under the operation state of the transplanter was then carried out. The simulation model is shown in Fig. 6, where the simulation was completed in 8 s: information about the soil mass flow was collected using the mass flow sensor during post-processing.

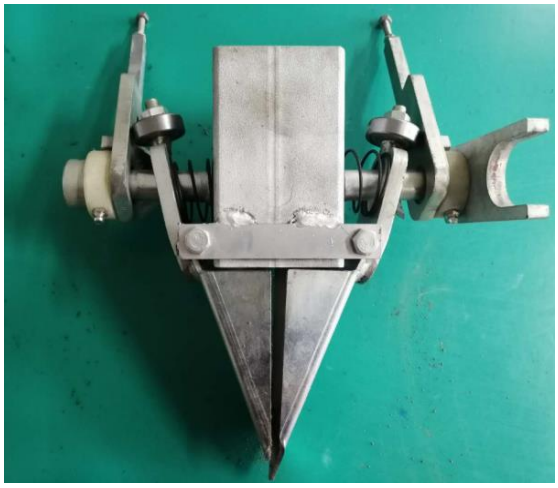

Fig. 5 - A prism-type duckbilled planter

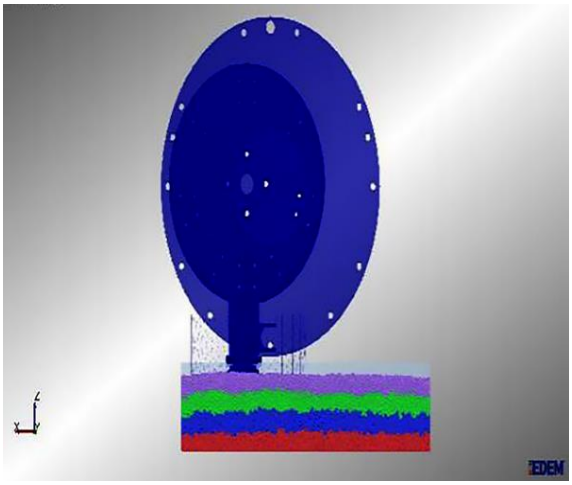

Fig. 6 - Mass flow statistics diagram

- **Velocity analysis of soil movement at contact interface**

A simulation time of 8 s was used. After the simulation was completed, a post-processing colouring function was used to mark the speed of the soil particles to determine the dynamic changes of the particles, where the colours were set to black, red and gray.

Soil particle velocity cloud maps and vector cloud maps at two points were used in the simulation: the lowest position that the duckbilled planter penetrates to and the position at which the duckbilled planter is maximally open, as shown in Figs. 7 and 8.

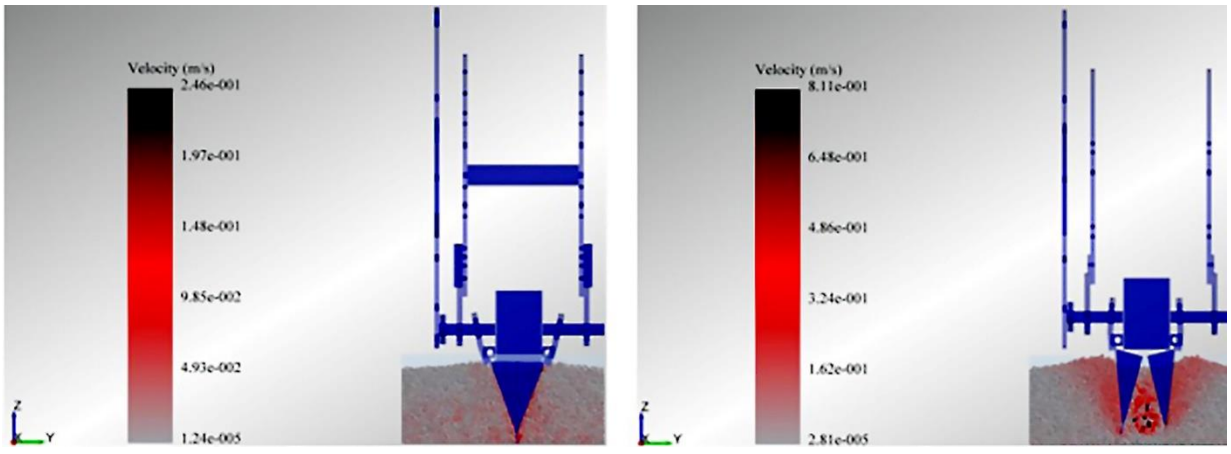

a. The duckbilled planter reaches the lowest point ***b. The duckbilled planter is maximally open***

Fig. 7 - Soil particle velocity cloud maps

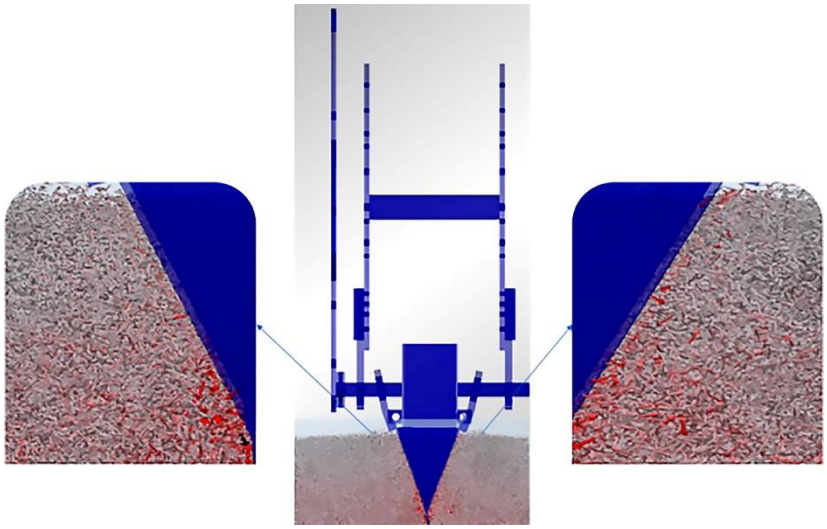

a. The duckbilled planter reaches their lowest point

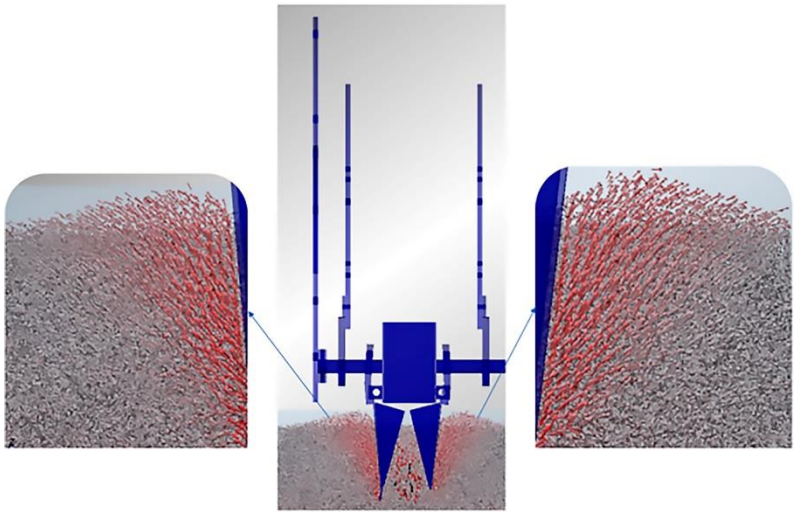

b. The duckbilled planter is maximally open

Fig. 8 - Soil particle velocity vector cloud maps

The velocity of soil particles close to the squeezing action of the duckbilled planter after the planter has reached its lowest point of penetration is smaller than the velocity of soil particles away from the duckbilled planter. As shown in Fig. 7a and 7b, the maximum velocity of soil particles at the contact interface is 0.10279 and 0.26138 m/s at the lowest point of the duckbilled planter and at the maximum opening of the duckbilled planter, respectively. Fig. 8a and 8b clearly shows that the velocity vector of the soil particle population at the contact interface points away from the duckbilled planter and outward towards the outer wall of the beak. As the duckbilled planter gradually opens, soil particles gather around the planter beak. When the duckbilled planter is at its maximum opening during transplanting, the soil at the contact interface is clearly moving opposite to the direction of the transplanting speed, indicating reflux and flow into the bottom of the hole.

- **Soil particle mass flow analysis at contact interface**

The opening and closing of the duckbilled planter during transplanting significantly affects soil dynamics. Thus, the motion of the entire soil particle system, from the duckbilled planter to the soil discharge process, must be simulated and analysed, where the mass flow is used to describe the dynamics of the soil particles. The reference surface level in the simulation is taken to be the final stable surface of the falling particles after the filling phase of the soil particles, where the mass flow is 0 kg/s. The mass flow sensor is used during post-processing of the discrete element software to collect data on the average mass flow rate of the soil particles at the contact interface, which is then used to derive the variation curve for the average mass flow shown in Fig. 9.

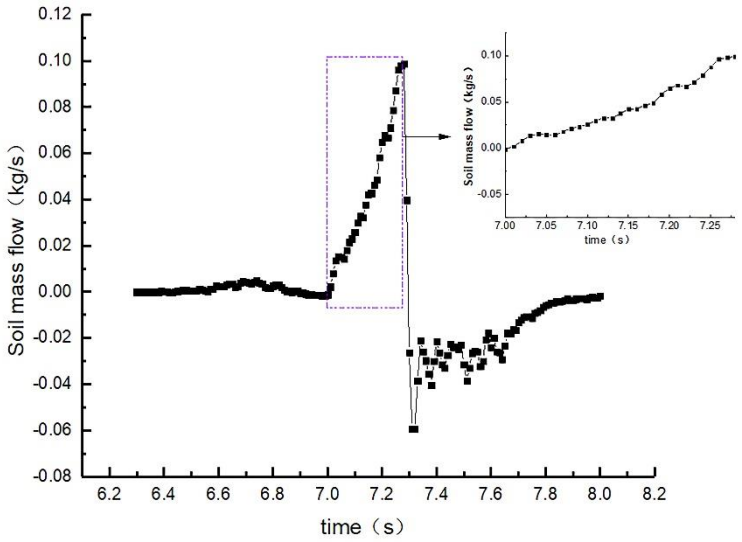

Fig. 9 - Soil mass flow versus time curve

The mass flow of soil particles at the contact interface changes slightly between when the duckbilled planter first touches the soil and the duckbilled planter reaches its lowest point of penetration; when the duckbilled planter completes drilling and the seedlings are planted, the soil particles at the contact interface are affected by the rotational motion of the duckbilled planter with a rotating spindle and the forward speed of the tractor, as well as by the opening motion of the duckbilled planter at the lowest point of penetration. The enlarged diagram shows different effective depths of the duckbilled planter in contact with the soil for different positions of the planter during the opening of the planter; the change in the contact space between the duckbilled planter and the contact interface of soil particles results in different soil particle masses per unit corner. As the duckbilled planter opens, the mass flow of soil particles at the contact interface increases over time. When the duckbilled planter opens to its maximum extent, as shown in Fig. 9, the soil particles at the contact interface are in contact with the bulk soil. At this time, the duckbilled planter gradually leaves the soil in this maximally open state because the soil particles at the contact interface are subjected to the effect of the rotational motion of the duckbilled planter, which acts in conjunction with the rotating spindle and the tractor traction to produce a flattening motion; however, the soil particles at the interface on both sides of the planter are no longer subjected to the planter opening motion, and the opening of the duckbilled planter exerts a force on the soil on both sides of the planter to change the dynamics of the surface soil particles. This force causes the curve to change abruptly, such that the soil mass flow at the contact interface exhibits a wave-like change under the movement and inertia of the soil. The duckbilled planter eventually leaves the soil, and the soil mass flow at the contact interface stabilizes at -0.00187 kg/s.

CONCLUSIONS

1. A straight shear test was used to determine the soil characteristics of a field in Inner Mongolia: the soil cohesion was 20.46kPa and the friction angle was 15.64°, which provided an empirical basis for a discrete element model of the interaction between soil and a duckbilled planter.

2. An optimization procedure was performed to determine the following optimum combination of parameters: a soil-soil recovery coefficient of 0.45, a soil-steel recovery coefficient of 0.35, a soil-steel static friction coefficient of 0.85 and a soil-steel rolling friction coefficient of 0.13; the simulation model was found to accurately reflect the physical characteristics of the soil in the Inner Mongolia field environment.

3. EDEM software was used to analyse the soil dynamics at the contact interface. The mass flow of soil changed slightly during transplanting. At the seedling stage, the soil mass flow trended upwards with time. When the duckbilled planter opened to its maximum extent and then gradually left the soil, the soil mass flow exhibited a wave-like change. After the duckbilled planter left the soil, the soil mass flow tended to stabilize.

ACKNOWLEDGEMENTS

This project was funded by the National Natural Science Foundation of China (NSFC) (51465048) and the Natural Science Foundation of the Inner Mongolia Autonomous Region of China (2019MS05031 and 2020MS05055).

REFERENCES

[1] Dun, Guoqiang, Chen, Haitao, Feng, Ying et al. (2016). Parameter optimization and experiment of key components of fertilizer blending device based on EDEM software. *Transactions of the Chinese Society of Agricultural Engineering*, 32(7), 36-42. https://doi.org/ 10.11975/j.issn.1002-6819.2016.07.005

[2] Fang, Huimin, Zhang, Qingyi, Farman, Ali Chandio et.al. (2016). Effect of straw length and rotavator kinematic parameter on soil and straw movement by a rotary blade. *Engineering in Agriculture, Environment and Food*, 9(3), 235-241. https://doi.org/10.1016/j.eaef.2016.01.001

[3] Feng, Jun, Qin, Gui, Song, Weitang et al. (2002). Analysis and design criteria of hanging cup movement of transplanting machine. *Transactions of the Chinese Society of Agricultural Machinery*, 33(5), 48-50. https://doi.org/10.3969/j.issn.1000-1298.2002.05.015

[4] Hang, Chengguang, Huang, Yuxiang, Zhu, Ruixiang, (2017). Analysis of the movement behaviour of soil between subsoilers based on the discrete element method. *Journal of Terramechanics*, 74(12), 35-43. https://doi.org/10.1016/j.jterra.2017.10.002

[5] Hang, Chengguang, Gao, Xijie, Yuan, Mengchang et al. (2017). Discrete element simulations and experiments of soil disturbance as affected by the tine spacing of subsoiler. *Biosystems Engineering*, 168, 73-82. https://doi.org/10.1016/j.biosystemseng.2017.03.008

[6] Kumar, G. V. P., Raheman, H., (2011). Development of a walk-behind type hand tractor powered vegetable transplanter for paper pot seedlings, *Biosystems Engineering*, 110(2), 189-197. https://doi.org/10.1016/j.biosystemseng.2011.08.001.

[7] Lenaerts, B., Aertsen, T., Tjskens, E. et al. (2014). Simulation of grain-straw separation by discrete element Modelling with bendable straw particles. *Computers & Electronics in Agriculture*, 101, pp.24-33. https://doi.org/10.1016/j.compag.2013.12.002

[8] Li, Bo, Liu, Fanyi, Mu, Junying et al. (2014). Distinct element method analysis and field experiment of soil resistance applied on the subsoiler. *International Journal of Agricultural and Biological Engineering*, 7(1), 54-59. https://doi.org/10.3965/j.ijabe.20140701.006

[9] Li, Bo, Chen, Ying, Chen, Jun (2016). Modelling of soil–claw interaction using the discrete element method (DEM). *Soil & Tillage Research*, *158*(1), 177-185. https://doi.org/10.1016/j.still.2015.12.010

[10] Liu, J., Chen, Y., Kushwaha, R. L., (2010). Effect of tillage speed and straw length on soil and straw movement by a sweep. *Soil & Tillage Research*, 109(1), 9-16. https://doi.org/10.1016/j.still.2010.03.014

[11] Qi Long, Chen Ying, Sadek, Mohammad, (2019). Simulations of soil flow properties using the discrete element method (DEM). *Computers and Electronics in Agriculture*, 157, 254-260. https://doi.org/10.1016/j.compag.2018.12.052

[12] Ucgul, M., Fielke, J. M., Saunders, C. (2014). 3D DEM tillage simulation: validation of a hysteretic spring (plastic) contact model for a sweep tool operating in a cohesionless soil. *Soil & Tillage Research*, 144, 220-227. https://doi.org/10.1016/j.still.2013.10.003

[13] Ucgul, M., Fielke, J. M., Saunders, C., (2015). Defining the effect of sweep tillage tool cutting edge geometry on tillage forces using 3D discrete element modelling. *Information Processing in Agriculture*, *2*(2), 130-141. https://doi.org/10.1016/j.inpa.2015.07.001

[14] Rahman, S., Chen, Y., Lobb, D. A., (2005). Soil movement resulting from sweep type liquid manure injection tools. *Biosystems Engineering*, 91(3), 379-392. https://doi.org/10.1016/j.biosystemseng.2005.04.002

[15] Seyed Mohamad Javidan, Davood Mohammadzamani, (2019). Design, construction and evaluation of semi-automatic vegetable transplanter with conical distributor cup. *SN Applied Sciences*. 1(9). https://doi.org 10.1007/s42452-019-1034-y

[16] Wang, Xuezhen, Yue, Bin, Gao, Xijie et al. (2018). Simulation and experiment of soil disturbance behaviour of deep loose shovel with different wing shovel installation heights. *Journal of Agricultural Machinery*, vol.49 (10), pp.124-136. https://doi.org/10.6041/j.issn.1000-1298.2018.10.014

[17] Zhang, Rui, Li, Jiangqiao, (2006). Simulation on mechanical behaviour of cohesive soil by distinct element method. *Journal of Terramechanics*, *43*(3), 303-316. https://doi.org/10.1016/j.jterra.2005.05.006

REAL TIME SEARCH OF AGRICULTURAL MACHINERY BASED ON MATRIX SEQUENCE SENSOR

/

基于矩阵序列传感器的农业机械实时搜索

Zheng Jiaxin [1)]*, Gao Yanyu [1)], Lei Zhengdong [1)], Yang Changhu [1)], Wang Chongjin [1)], Oderman Gary [2)]

[1)]College of Electrical and Mechanical Engineering, Yunnan Agricultural University, Kunming, 650201, Yunnan / China

[2)]Legal & General Group, London / UK

**E-mail: ys30454442hangsi@163.com*

DOI: https://doi.org/10.35633/inmateh-63-43

Keywords: *matrix sequence, agricultural machinery, search algorithm*

ABSTRACT

Omni-directional vision sensor can provide information within the sensor range, and the directional angle of an object can be accurately obtained through omni-directional images. Based on this characteristic, an automatic navigation and positioning system for agricultural machinery is developed, and a three-dimensional positioning algorithm for agricultural wireless sensor networks based on cross particle swarm optimization is proposed. The method mainly includes three stages: convergence node selection, measurement distance correction and node location. Using the idea of crossover operation of genetic algorithm for reference, the diversity of particles is increased, and the influence of ranging error and the number of anchor nodes on positioning results is effectively improved. The location algorithm has the ability of global search. On the positioning node, the symmetric bidirectional ranging algorithm based on LFM (Linear frequency modulation) spread spectrum technology is used to calculate the distance between the positioning node and each beacon node, and the trilateral centroid positioning algorithm is used to calculate the coordinate position information of unknown nodes. Finally, the Kalman filter algorithm is used to superimpose the observed values of the target state to solve the influence of measurement noise on the positioning accuracy.

摘要

全向视觉传感器可以提供传感器范围内的信息，通过全向图像可以准确获得物体的方向角。研究基于这一特点，开发了农业机械自动导航定位系统，并提出一种基于交叉粒子群优化的农业无线传感器网络三维定位算法。该方法主要包括收敛节点选择、测量距离校正和节点定位三个阶段。研究借鉴遗传算法交叉运算的思想，增加了粒子的多样性，有效地改善了测距误差和锚节点数目对定位结果的影响。定位算法具有全局搜索能力。在定位节点上，采用基于LFM（线性调频）扩频技术的对称双向测距算法计算定位节点与各信标节点之间的距离，采用三边质心定位算法计算未知节点的坐标位置信息。最后，利用卡尔曼滤波算法对目标状态的观测值进行叠加，解决测量噪声对定位精度的影响。

INTRODUCTION

In recent years, the automation and intelligence of agricultural machinery is a hot spot in the field of agricultural engineering in the world *(Hu Z. et al., 2020)*. Agricultural machinery automation is one of the key technologies to realize modern precision agriculture, improve productivity and reduce fertilization and pesticide application *(Gao L. et al., 2020)*. Data fusion needs to reason based on these uncertain information to achieve target identification and attribute determination. This kind of uncertain reasoning constitutes the basis of sensor data fusion *(Mugandani R. et al., 2020)*. An evidence theory is a typical method in solving this uncertainty reasoning method. Location information plays an important role in the monitoring activities of agricultural wireless sensor networks. Location or access information node location is important information that must be included in the sensor node monitoring message *(Butts T.R. et al., 2019)*. Monitoring information without location information is often meaningless, and limited by resources, cost and application environment. Facility agriculture is the growing demand for people's lives *(Qin J. et al., 2020; Yudao L. et al., 2020; Joppa M. et al., 2018)*. Developed at the same time. Facility agriculture is a new mode of production to obtain fast-growing, high-yielding, high-quality and high-efficiency agricultural products, and is the main technical measure to provide fresh agricultural products in the world *(Li Y. et al., 2020)*.

Wireless sensor network extends people's information acquisition capability, links physical information of the objective world with network transmission, provides people with the most direct, effective and real information, has a very broad application prospects, and can be widely used in military defense, industrial and agricultural control, urban management, biomedical treatment. Environmental monitoring, disaster relief, anti-terrorism, remote control of dangerous areas and many other areas *(Wang B. et al., 2020).*

Traditional agricultural production can no longer meet people's growing demand for the quantity and quality of various agricultural products. Node localization in wireless sensor networks refers to the process that sensor nodes determine the location information of other nodes in the network through certain positioning technology according to the location information of a few known nodes in the network. Node positioning technology is one of the important supporting technologies in agricultural wireless sensor network applications *(Wang J. et al., 2019)*. The so-called node location problem is to use the nodes of known locations to obtain the location information of other nodes, that is, to use the position information of the reference nodes to establish a coordinate system, and to determine the position information of the pending nodes in the coordinate system by different methods *(Musiu E.M. et al., 2019).* There are certain restrictions depending on the application of GPS in agricultural machinery navigation. In farmland operation, especially in mountainous areas, GPS can not be used in greenhouses, and greenhouse agriculture is an important part of modern agriculture. In practical applications, a sensor network is composed of several sensors, and the sensor network constructs the corresponding basic credibility assignment of propositions by using these evidences. However, as the amount of data increases, the amount of calculation flips exponentially, resulting in huge data flow and increasing the pressure of sensor networks *(Kooij S. et al., 2018).* Wireless sensor networks involve many research fields, including network routing, data fusion, positioning technology, time synchronization, security management and so on. The research and development of wireless sensor networks is driven by practical application requirements, and has become a research hotspot of the next generation network.

Sensor is a knowledge-intensive, technology-intensive, interdisciplinary, very complex Mechatronics system. Besides rich image information, omnidirectional vision sensor has another characteristic: when acquiring omnidirectional image, the direction angle of space object relative to sensor is fixed and unchanged *(Geng L. et al., 2020)*. Farmland or greenhouse varies with seasons. Different colored crops are planted, but the same kind of crops are often planted in the same area, which is not conducive to the use of natural markers to extract image features *(Naveeninder K. S. et al., 2019)*.

The research of point localization mainly focuses on two-dimensional plane, but the environmental factors of three-dimensional space are more complex. The computational complexity of refinement problem increases greatly, so it is difficult to apply two-dimensional localization algorithm directly to three-dimensional space. Space position, based on the development of safety management technology, must be three-dimensional positioning of nodes. Machine vision can provide all or part of the image information for relative positioning *(Soponpongpipat N. et al., 2020)*. The positioning accuracy is high, but the positioning accuracy and stability of machine vision are greatly affected by environmental factors such as weather and light, and its edges. Image processing methods such as edge sharpening and feature extraction are computations with large amount and poor real-time performance *(Muzylyov D. et al., 2020).* The academician's research team has been working on the research of agricultural machinery automatic navigation system for many years, and developed a GPS-based agricultural machinery automatic navigation system that can reach the centimeter accuracy level. The initial basic reliability distribution of the target, data fusion, and the goal of advanced basic Credibility is assigned to obtain target identification and attribute determination *(Zheng Y. et al., 2020)*. The sensor and agricultural machinery are closely combined to facilitate the discovery and treatment of potential problems in agricultural machinery, promote the development of agricultural machinery automation, and the application of sensors in agricultural machinery is very extensive. The transformation of traditional agricultural machinery is inseparable from sensors.

MATERIALS AND METHODS

According to the different reflective surfaces, the omnidirectional vision sensor is mainly divided into three kinds of surfaces: spherical, parabolic and hyperbolic; its main features are: low price, single viewpoint, wide viewing angle, 360° information, and the image does not rotate with the sensor. Change the relative angle between the image and the two objects on the ground.

Even in the case of convergence, since all the particles fly in the direction of the optimal solution, the particles in the latter stage tend to be the same, which makes the convergence speed slower.

When the number of anchor nodes in agricultural wireless sensor networks is small and the search range is large, the problem of locating unknown nodes using this algorithm is more prominent, which will limit the improvement of location accuracy.

CSS technology (Cascading Style Sheets) has the characteristics of reliable communication, good stability, long transmission distance and low power consumption, so CSS technology is very suitable for indoor positioning by a large number of resource-constrained sensor nodes composed of Ad hoe mode of self-organizing multi-hop wireless communication network, a combination of sensor technology, embedded computing technology, sub-system Distributed processing technology and communication technology', through collaborative operation, real-time monitoring, perception and collection of various monitoring object information and processing and transmission to the destination node.

The trend prediction method is carried out and compared with the actual data according to the data of the past years. The results show that the prediction accuracy is high. It is the primary task of the sensor to accurately convert the seed flow signal of the seed guide tube into the signal accepted by the single chip microcomputer. The performance of the method directly affects the whole system. The overall performance. The photoelectric sensor has the advantages of simple structure, low price, strong anti-electromagnetic interference ability, and has no effect on the movement of seeds. Therefore, at present, the application is the most extensive and mature.

A new matrix can be obtained by multiplying the transposition of one row in the matrix with another row. First, the omnidirectional vision sensor is corrected to obtain the inner and outer parameters of the vision system and the projection center of the USB camera. Second, the input image, Extracting the identification feature, estimating the position of the center of gravity of the feature pixel as the position in the image; and then calculating the angle between the four directions of the marker relative to the projection center, according to the circumferential theorem, if the arc is formed by the direction angle, if there is no error, 4 arcs should intersect at the same intersection, but in general, due to the existence of errors such as measurement and identification, the probability of this situation is small and no positioning is required. Only rely on information such as network connectivity for positioning. Generally, there are centroid algorithm, approximate trigonometric point test method, vector jump moment, convex plan and so on.

Compared with the positioning algorithm without ranging, the positioning algorithm based on ranging has the disadvantages of high energy consumption, large amount of calculation and large amount of communication, but the positioning accuracy of the former is generally higher than that of the latter; The latter is less affected by environmental factors, but the positioning error is larger, and the density of anchor nodes is required higher. infrared has relatively high indoor positioning accuracy, but its linear sight distance and transmission distance are shorter these two major drawbacks make the indoor positioning effect is very poor. The overall positioning accuracy of ultrasonic positioning is higher and the structure is simple, but the ultrasonic is greatly affected by multipath effect and non-line-of-sight propagation, and the cost is higher. Modern control theories and methods, such as optimal estimation, optimal control, adaptive control and fuzzy control, are adopted. Prospects for the future development of agricultural machinery navigation technology are made. Communication security is an important part of this technology. Privacy protection is becoming more and more important, while authorization is becoming less important. It needs to be based on wireless. According to the characteristics of sensor networks, a new type of security protocol and security strategy are studied in view of its unique security threats.

Table 1 shows the static positioning coordinates and error data of indoor nodes. Figure 1 shows the static positioning coordinates and errors of indoor nodes.

Table 1

Static positioning coordinates and error of the indoor node

Numbering	Actual coordinates	Positioning coordinates	Error
1	(2,3.1)	(2.7,2.6)	0.1
2	(2,3.1)	(3,2.5)	0.1
3	(2,3.1)	(3.1,2.8)	0.1
4	(2,3.5)	(3.9,4,6)	0.2

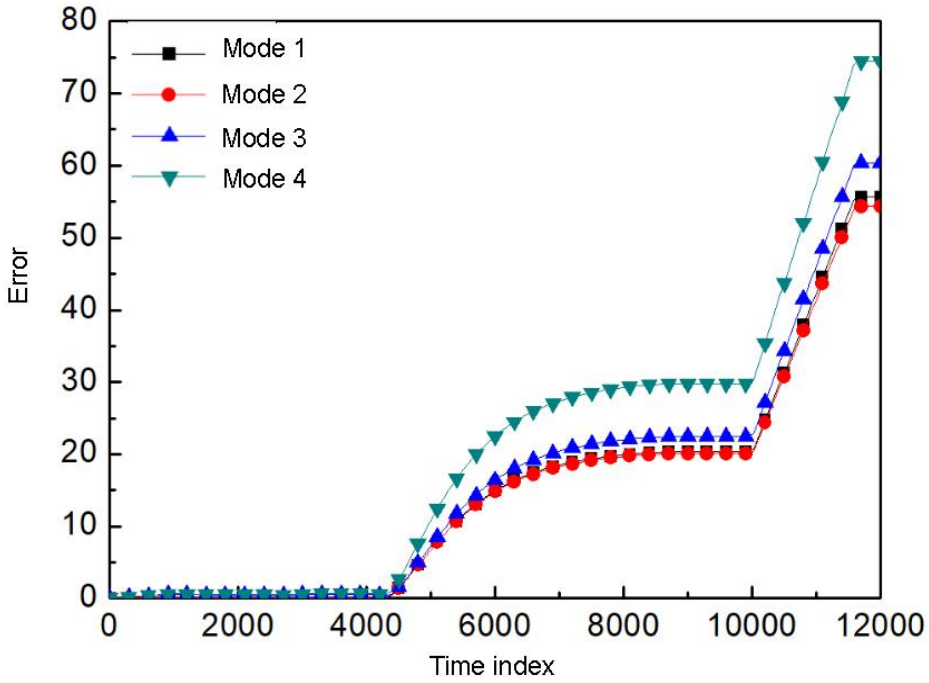

Fig. 1 - Static positioning coordinates and error of the indoor node

RESULTS

The development of modern agricultural machinery requires more sensors. It can be seen that modern agricultural machinery is equipped with various sensors, which improves trilateral localization he automation control performance, thereby reducing the mechanical power loss and saving energy. Reduce energy consumption and save investment in human and material resources. Therefore, sensors have a very important position and role in agricultural machinery. Figure 2 is a modern agricultural sensor.

Fig. 2 - Modern agricultural sensors

The study of single-component force sensors focuses on improving the accuracy of measurement. The research of multi-component force sensor includes various structural forms. The main problems to be solved by different structural forms are to improve the mutual interference between the natural frequency and the component force.

Positioning technology is a low-cost, low-power, short-distance wireless communication technology, but it is very sensitive to environmental impacts and easily deviates from the computational model. In the identification process, there is a certain error between the average value of the extracted pixels and the actual center of the identification. The transmission range of the RF positioning technology is large, the cost is relatively low, and the positioning accuracy is high, but its action distance is short and communication capability is not available.

Originally used primarily for Internet network multicast authentication. It solves the problem of high information load in asymmetric MAC protocol (Multiple Access Control Protocol) by introducing time synchronization mechanism. But this agreement needs another agreement to ensure the authenticity of time synchronization.

As a big agricultural country, one of the magic weapons to solve people's livelihood problems is the popularization of scientific modernization. Selecting suitable pressure sensors can significantly improve the reliability and life of agricultural machinery and equipment. Location technology based on wireless sensor network has the characteristics of non-contact and non-line-of-sight, and has become one of the preferred indoor positioning methods. It can be used not only in navigation and positioning system, but also in sensor information transmission and automatic monitoring system of facility agricultural environment. A cross-Particle swarm optimization based three-dimensional localization method for agricultural wireless sensor networks is proposed. By introducing cross-factor into the algorithm searching process, a new population is generated through cross-operation, and the diversity of particles is increased.

This method not only enhances the global searching ability of particles, but also speeds up the convergence speed of particle swarm optimization and effectively improves the efficiency of particle swarm optimization. Positioning accuracy. The automatically enhanced autonomous key scheme mainly includes two pairs of asymmetric key protocols and group key protocols. Both are based on asymmetric public key technology, which combines the security information of a group of nodes to determine the key, independent of trusted third parties. However, the computational overhead of such schemes is too high and is not applicable in most wireless sensor networks. Like most sensors, the force sensor needs to be calibrated. If the sensor is designed and manufactured, the interference coefficient can be made small, negligible, and only six calibration coefficients can be used. This method is called direct decoupling.

The initial basic credibility of the target is assigned in the sensor network, and the high-level basic credibility of the target is assigned through data fusion, so as to get the target recognition and attribute determination. Particle swarm optimization algorithm has the characteristics of high positioning accuracy, few parameters and simple implementation, which is very suitable for agricultural wireless sensor. This paper proposes a clock synchronization algorithm to locate the time of bidirectional transmission and obtain the distance between nodes. The ranging process includes two symmetrical measurements. The first measurement sends a packet from node 1 to node 2 and receives an automatic response from node 2. Node 1 calculates the propagation delay time, and node 2 calculates its own processing delay.

It detects the shape, mechanical and optical characteristics of the tested objects in the process of robot work, and guides the robot to walk, classify and pick agricultural products automatically. This not only enhances the perception ability of the agricultural robot to the environment, but also directly improves the intelligent degree of the agricultural robot. After deployment, it can establish shared key with neighboring nodes independently. The scheme is based on a probability model, and its secure connection probability is related to the key pool and its proportion.

The model node coefficient table is shown in table 2 and figure 3.

Table 2

Model node coefficient table

	A->A	B->C	C->B
Model 1	1.02	0.21	0.85
Model 2	0.35	0.01	0.31
Model 3	0.4	0.01	0.64

Sensors are the core components of the whole engine and chassis control system. They can be used to realize steering lightly, improve response characteristics, reduce engine loss, increase output power, save fuel and so on.

After sorting the fitness of the particles, the first N/2 particles with good fitness enter the next generation directly. The latter N/2 particles are paired in the particle selection pool, and a crossover position is randomly generated (i.e. a crossover point is randomly set, and some structures of the two particles before or after the crossover point are interchanged, and two new particles are generated) to produce the same offspring as the parent number. Identification and location determination are extremely important for positioning.

People usually plant the same plants in the same field, which exhibit roughly the same color characteristics, which is very disadvantageous for positioning systems that are identified by natural environmental features. In addition, it is difficult to calibrate to get an accurate coefficient. It is in this situation that the study of multi-component force sensors has important practical significance for scientific research. This optimization of the sensor can be classified as virtual prototype technology. The biggest advantage is that the probability of secure connectivity is always 1, but usually the computation and communication overhead is large. Later, some people improved on this basis and proposed several improvements.

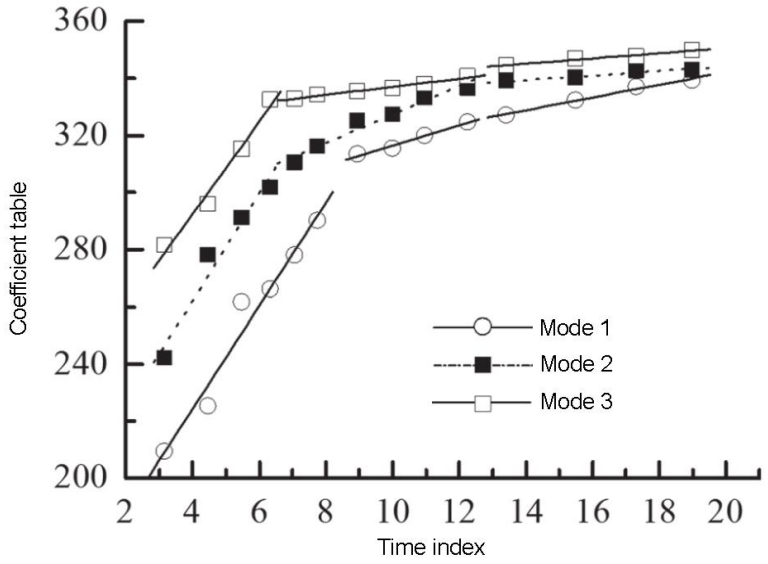

Fig. 3 - Model node coefficient table

The indoor dynamic positioning coordinates and node errors are shown in Table 3

Table 3

Indoor dynamic positioning coordinates and errors in nodes

Numbering	Actual coordinates	Positioning coordinates	Error
1	(1,1.5)	(1.2,2.5)	0.3
2	(1,1.2)	(1.8,2.8)	0.6
3	(1,2)	(0.7,1.7)	0.3
4	(1,3)	(1.8,2.8)	0.8

The indoor dynamic positioning coordinates and errors are shown in figure 4. Because wireless sensor networks may be deployed in hostile environments, in order to prevent malicious nodes from injecting illegal information, forging and tampering with data, information authentication technology must be used to confirm that information originates from legitimate nodes and ensure data integrity. Different authentication methods are different for different communication modes.

Multipoint data source broadcasting authentication and low energy consumption multi-hop authentication path are the focus of research. With the further development and integration technology of modern physics, such as nanotechnology, laser, infrared, ultrasound, microwave, optical fiber, strong magnet, radioisotope, etc., the integration of sensors has opened up a broad front.

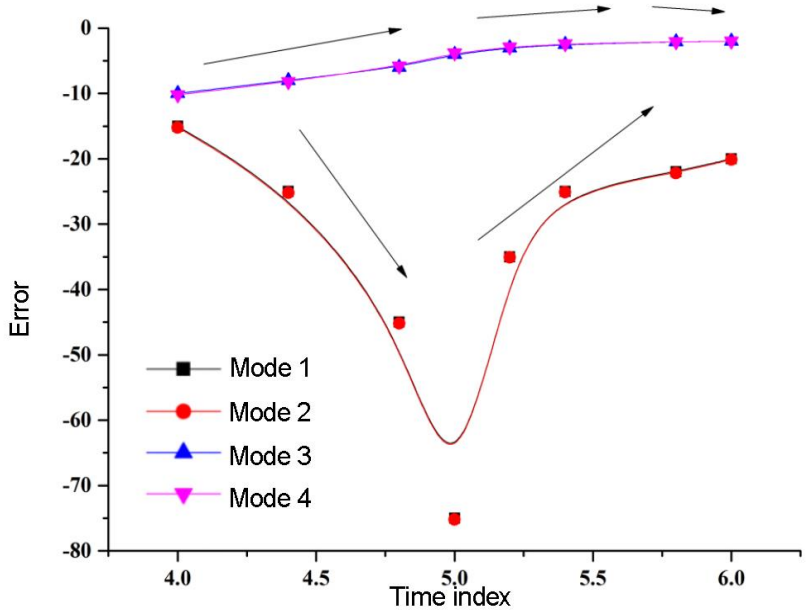

Fig. 4 - Indoor dynamic positioning coordinates and error

The development of sensors with small size, easy encapsulation, wider application range, high reliability, long service life and stronger function is also the trend of sensor development in facility agriculture. The material delivery vehicle and 3 beacon nodes are used to realize data communication and ranging and positioning functions. In the positioning node, the trilateral positioning algorithm in the common WSN positioning method is adopted and used in conjunction with the centroid estimation method. Finally, the Kalman filtering algorithm is used to improve the positioning accuracy. In the positioning calculation, the unknown node optimizes the calculation of the normal anchor node information and the corrected distance input cross particle swarm optimization algorithm. Therefore, whether it is outdoors or indoors, it is completely feasible to ensure that the location of the logo is appropriate. Then, since the visual range of the omnidirectional vision sensor currently used is about 120°, the height range of the marker setting position is large; and the setting of the height of each marker position can be arbitrary as long as the camera imaging requirements are satisfied. The node positioning effect is shown in figure 5.

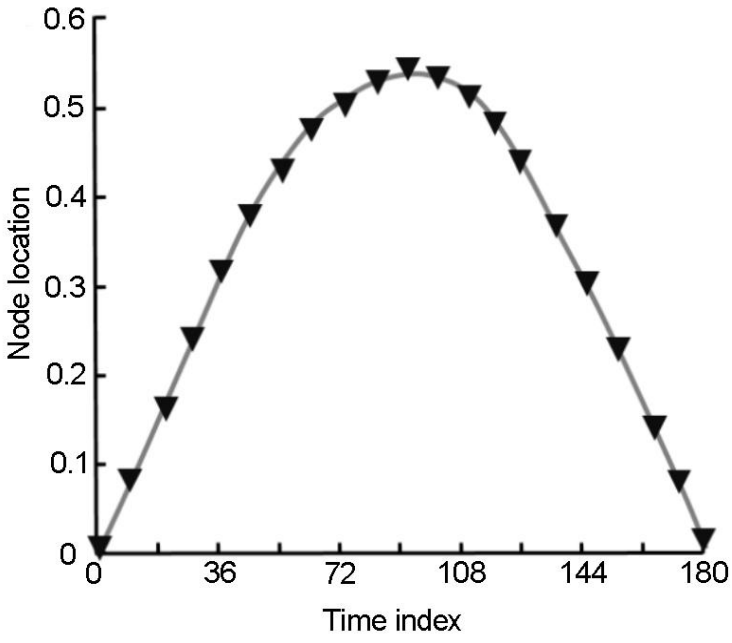

Fig. 5 - Node positioning effect diagram

When the size of network nodes is adjusted, when the dimensions of matrix M and VD are m, the formula is:

$$M(w) = \frac{w}{D} R_{ON} + (1 - \frac{w}{D}) R_{OFF} \tag{1}$$

$$v_D = \eta \frac{u_D R_{ON}}{D} i(t) \tag{2}$$

When the number of matrices is expanded, the following formula is established:

$$v_D = \frac{dw}{dt} \tag{3}$$

$$D_k(x,y) = \begin{cases} 255 & \left|P_k(x,y) - B_k(x,y)\right| > T_h \\ 0 & else \end{cases} \tag{4}$$

In contrast with the polynomial mentioned above, the directional quantity is:

$$D_k(x,y) = \left| f_{k-1}(x,y) - f_k(x,y) \right| \tag{5}$$

$$B_k(x,y) = \left| f_k(x,y) - B(x,y) \right| \tag{6}$$

Since Rk is the network capacity, the storage of this scheme has the following formula:

$$R_k(x,y) = \begin{cases} 1, \text{target}, & if\ T_k(x,y) > Th \\ 0, \text{background}, & if\ T_k(x,y) \le Th \end{cases} \tag{7}$$

Combining matrix decomposition and polynomial schemes:

$$P_d = N_i v_i \left(\frac{M_i v_i^2}{2} + Zeu(t) \right) \tag{8}$$

$$N_i = N_{i0} \exp(-\frac{t - t_0}{\tau})(\frac{D_{amp} l^2}{D_{gap}^2} + 1) \tag{9}$$

$$U_0 = \frac{M_i}{2e}(v_i + \frac{dl}{dt})^2 \tag{10}$$

$$i(t) = \frac{\pi D^2 Z N_i e}{4}(v_i + \frac{dl}{dt}) \tag{11}$$

$$R = \omega L + \frac{1}{\omega C} \tag{12}$$

CONCLUSIONS

Compared with the location results, the algorithm mainly calculates the direction angle formed by the mark and the projection center of the camera. It is very important to find the correct position of the mark in the image. Therefore, in the next step, we will focus on the feature extraction of the mark. If we want to further improve the location accuracy, we need to change the location node. The method based on multi-point three-dimensional space positioning can be studied, even if the best ultra-wide band sensor series products are used as positioning nodes. Although its price is very expensive, its positioning stability is good, the precision is very high, and the theoretical positioning accuracy can reach the centimeter level. It better overcomes the negative impact of the standard particle swarm optimization algorithm on the slow convergence, easy to fall into the local minimum point and premature convergence in the late stage of evolution. It not only improves the positioning accuracy, but also optimizes the performance.

The matrix scheme combines matrix multiplication and polynomial-based key pre-allocation schemes, and is extended on the multi-dimensional key space to meet the needs of larger network capacity with lower storage, communication, and computational overhead. Network positioning applications have certain value.

ACKNOWLEDGEMENTS

The study was funded by 2018 Yunnan Education Department Scientific Research Fund. Topic: Polygonatum kingianum Coll. et Hemsl Adaptive Seedbed Establishment Technology for High-Altitude Hilly Areas (NO. 2018JS272), Yunnan Province College Students Innovative Entrepreneurship Training Program: Limin Agricultural Machinery Service Company.

REFERENCES

[1] Butts T.R., Luck J.D., Fritz B.K., (2019), Evaluation of spray pattern uniformity using three unique analyses as impacted by nozzle, pressure, and pulse‐width modulation duty cycle. *Pest Management Science*, Vol. 75, Issue 7, pp. 1875-1886. England;

[2] Gao L., Zhao P., Kang S., (2020), Comparison of evapotranspiration and energy partitioning related to main biotic and abiotic controllers in vineyards using different irrigation methods. *Frontiers of Agricultural Science and Engineering*, Vol. 7, Issue 4, pp. 490-504. China;

[3] Geng L., Wang Y., Wang J., (2020), Numerical simulation of the influence of fuel temperature and injection parameters on biodiesel spray characteristics. *Energy Science & Engineering*, Vol. 8, Issue 2, pp. 312-326. United States;

[4] Hu Z., Li R, Xia X., (2020), A method overview in smart aquaculture. *Environmental Monitoring and Assessment*, Vol. 192, Issue 8, pp. 1-25. Netherlands;

[5] Joppa M., Köhler H., Kricke S., (2018), Simulation of jet cleaning diffusion model for swellable soils. *Food and Bioproducts Processing,* Vol. 113, pp. 168-176. United Kingdom;

[6] Kooij S., Sijs R., Morton M.D., (2018), What determines the drop size in sprays? *Physical Review X*. Vol. 8, Issue 3. United States;

[7] Li Y., Li H., Guo X., (2020), Online parameter identification of rice transplanter model based on IPSO-EKF algorithm. *INMATEH-Agricultural Engineering*, Vol. 61, Issue 2. Romania;

[8] Mugandani R., Mafongoya P., (2020), The 5As: assessing access to animal-drawn conservation agriculture planting equipment by smallholder farmers. *Environment, Development and Sustainability*, pp. 1-18. Netherlands;

[9] Musiu E.M., Qi L., Wu Y., (2019), Evaluation of droplets size distribution and velocity pattern using Computational Fluid Dynamics modelling. *Computers and Electronics in Agriculture*, Vol. 164. United Kingdom;

[10] Muzylyov D., Shramenko N., Shramenko V., (2020), Integrated business-criterion to choose a rational supply chain for perishable agricultural goods at automobile transportations. *International Journal of Business Performance Management*, Vol. 21, Issue 1-2, pp. 166-183. United Kingdom;

[11] Naveeninder K.S., (2019). A comparative study of organic agriculture (traditional agriculture) and inorganic agriculture (conventional agriculture). *IASET,* Vol.08, Issue 05, pp.09-18. Germany;

[12] Qin J., Yin Y., Liu Z., (2020), Optimisation of maize picking mechanism by simulation analysis and high-speed video experiments. *Biosystems Engineering*, Issue 189, pp. 84-98. United Kingdom;

[13] Soponpongpipat N., Nanetoe S., Comsawang P., (2020), Thermal and Torrefaction Characteristics of a Small-Scale Rotating Drum Reactor. *Processes*, Vol. 8, Issue 4, pp. 489. Switzerland;

[14] Wang B., He J., Zhang S., (2020), Non-destructive testing of soluble solids content in cerasus humilis using visible/near-infrared spectroscopy coupled with wavelength selection algorithm. *INMATEH Agricultural Engineering*, Vol. 61, Issue 2, pp. 251-262. Romania;

[15] Wang J., Zhou G., Wei X., (2019), Experimental characterization of multi-nozzle atomization interference for dust reduction between hydraulic supports at a fully mechanized coal mining face. *Environmental Science and Pollution Research*, Vol. 26, Issue 10, pp. 10023-10036. United States;

[16] Yudao L., Xuezhen S., (2020), Design and Experimental Study of a Combined Pneumatic Plot Seed-metering Device for Cotton. *International Journal of Engineering,* Vol. 33, Issue 8, pp. 1652-1661. United Kingdom;

[17] Zheng Y., Lu G.H., Shao P.W., (2020), Source Tracking and Risk Assessment of Pharmaceutical and Personal Care Products in Surface Waters of Qingdao, China, with Emphasis on Influence of Animal Farming in Rural Areas. *Archives of environmental contamination and toxicology*, Vol. 78, Issue 4, pp. 579-588. United States.

RESEARCH ON DESIGN AND EXPERIMENT OF MULTIFUNCTIONAL VEGETABLE FIELD MACHINE
/
多功能蔬菜田间作业机械设计与试验研究

Shuo Zhang[1)], Qingyu Chen[1)], Jinyi Liu[2)], Yu Chen*[1)], Jun Chen[1)], Hongling Jin[1)], Tongyun Luo[1)]
1) College of Mechanical and Electronic Engineering, Northwest A&F University, Yangling 712100, China;
2) College of Mechanical and Electronic Engineering, Hainan University, Haikou 570000, China
Tel: +86 13810248046; E-mail: jdxy73@nwafu.edu.cn
DOI: https://doi.org/10.35633/inmateh-63-44

Keywords: *Vegetable, Frame-type, Multi-function power machine, Hitch mechanism*

ABSTRACT
Vegetable industry occupies a significant position in the world agricultural production, China has been the largest vegetable producing country in the world. However, the mechanization of vegetable production is still in the initial stage. There are many problems such as complex environment, non-uniform agronomy, various kinds of agricultural machinery etc. In order to meet the varied requirements of vegetable field work, in this paper, a new type of high-efficiency vegetable field operation power equipment was developed by adopting the idea of "frame-type", and the key components are developed. They include ground gap adjusting mechanism, wheel spacing adjusting mechanism, inter-axle hitch mechanism, the rear hitch mechanism and frame. The vibration modal analysis and stiffness analysis of the frame are carried out by ANSYS, which proves that the frame design is reasonable and meets the use requirements. Finally, a prototype was made and field experiments were carried out. The results showed that the maximum running speed of the multifunctional vegetable field machine was 16 km/h, the maximum operating speed was 8 km/h, the maximum gradient was 20, and the adjustable range of ground clearance was 400~800 mm. The adjustable range of wheel spacing was 1600-2000 mm.

摘要
蔬菜产业在世界农业生产中占有重要地位,中国已成为世界上最大的蔬菜生产国。然而，蔬菜生产机械化程度仍旧很低，存在着田间环境复杂、农艺不统一、农机具种类繁多等诸多问题。为满足蔬菜田间作业农艺需求多样化的要求，本文采用"框架式"结构设计思想，开发了一种新型多功能高效蔬菜田间作业动力设备，并对其关键部件进行设计，包括地隙调节机构、轮距调节机构、轴间悬挂机构、后悬挂机构和车架。利用 ANSYS 对车架进行振动模态分析和刚度分析，证明车架设计合理，能够满足使用要求。最后，试制样机并进行田间试验。结果表明，多功能蔬菜田间作业机的最高运行速度为 16 公里/小时；最大运行速度 8Km/h，最大坡度 20°，离地间隙可在 400 ~ 800 mm 范围内调节；轮间距可调范围为 1600-2000 毫米。

INTRODUCTION

Vegetable industry occupies a significant position in the world agricultural production. In recent years, with the development of agricultural science and technology, the yield of vegetable products has increased. According to FAO statistics, from 2009 to 2018, Asia had the largest vegetable yield and area. In the meantime, China has been the largest vegetable producing country in the world, and its output has accounted for more than half of the world's output since 2015. However, at present, the mechanization of vegetable production is still in the initial stage. The comprehensive mechanization level of the whole vegetable production process is lower than 25%, and the vegetable production efficiency is far lower than that of developed countries. At the same time, there are some problems such as insufficient productivity, high cost and low benefit, etc. *(He C.X. and Yu X.C., 2012; Xiao T.Q. et al., 2015; Li X.R. et al., 2021; Yang et al., 2020).*

At present, vegetable production can be divided into two types: one uses large fields to produce vegetables, and the other uses artificial facilities to produce vegetables efficiently. The two production modes have basically the same mechanized production process.

According to the vegetable production process, the mechanization process can be divided into three types: pre-harvest mechanization, harvest mechanization and postharvest operation. Among them, the mechanization of vegetable pre-harvest operation mainly includes: soil preparation, seedling raising, transplanting, grafting, sowing, field management and other processes; vegetable harvest mechanization mainly includes: rhizome vegetables, leafy vegetables, melon, fruit and other categories; vegetable postharvest operation mechanization mainly includes: waste film recovery, vegetable residue treatment, etc. Vegetable field machine plays a very important role in vegetable mechanization production.

For vegetable production, with the development of trenchers, graders, rotary tillers, subsoilers, rakes, two-way ploughs and other agricultural machinery, mechanized operations can basically be realized *(Mi N.H. et al., 2014)*. However, agricultural machinery usually needs to be used with tractors. *Kumar and Raheman, (2011)* developed a walk-behind type hand tractor powered 2-row fully automatic vegetable transplanter for individual paper pot seedlings by considering the power availability. *Dihingia et al. (2018)* developed a vegetable transplanter for transplanting soil block seedlings which can cooperate with local power machinery. *Raja et al., (2019)* developed a precision weed control equipment for vegetable fields with high crop and weed densities. Because of the variety of field operations, different agricultural machinery have different characteristics, and they will also change for different vegetable objects, so it is difficult to achieve universal and accurate matching between agricultural machinery and tractors to realize mechanized operation. Therefore, it is urgent to apply the operation machinery suitable for multi agricultural tools.

At present, the phenomenon of field crop damage and soil compaction caused by the operation of field power machinery is receiving widespread attention. *Materechera S., (2009),* discover that conventional tillage practices with tractors limit the performance of vegetable crops and affect the quality of water resources. *Pedersen et al., (2013),* proposed a wide span tractor which is designed to optimise the Controlled Traffic Farming (CTF) system, and *Bulgakov et al., (2019)* had determined the quantitative effect of transverse displacements of the working implements and the suitable size of the safeguard zone. However, wide span tractor can only be used in specific scenes and it is not suitable for small plots and greenhouse operations. Therefore, it is more common to design tractors with small size and light weight to reduce soil compaction.

In addition, the research on tractors now also focuses on safety reliability and hitch mechanism of the tractor. *Hui W.D. et al., (2018),* established the security frame prototype geometric model and applied with MIDAS software to verify the accuracy and effectiveness of analysis model. *Shao M.X. et al., (2019)* designed a tractor system with force adjustment function based on the traditional tractor hydraulic hitch system. *Yang Q.Z. et al., (2020)* proposed a tractor three degree of freedom of agricultural implement hitch mechanism which can be used for the operation of the tractor and farm implement set with automatic chassis levelling on the slope.

Based on previous research, in order to break through the limitation that traditional vegetable field operation power machinery uses small tractors as power machinery, this paper studies the structural design scheme of multifunctional vegetable field machine, develops the power machinery with inter-shaft hitch system and rear hitch system for different agricultural machinery, adopts frame structure to replace the traditional agricultural machinery chassis, so as to provide 100% visual inter-axle working space. In the meantime, in order to ensure reliability and reduce soil compaction, the key components are developed and improved, including ground clearance adjustment and wheel spacing adjustment mechanism, hitch mechanism and frame structure. The strength and stiffness of the frame are analysed by using ANSYS software.

MATERIALS AND METHODS

Structure design of multifunctional vegetable field machine

Multifunctional vegetable field machine is mainly used in the vegetable field production process including fertilization, weeding, sowing, spraying, intertillage, etc. There are various kinds of vegetables, complicated working environment, various kinds of supporting agricultural machinery, and different requirements in different areas. Therefore, the design should be considered from many aspects at the beginning *(Wang Z.Y., 2010)*.

According to the working characteristics and requirements of multifunctional vegetable field machine, the layout scheme of the machine structure is proposed, because the working environment of multifunctional vegetable field machine requires that the machine can withstand various bending moments and torques stably under various working conditions. In this paper, the "frame-type" structure is adopted, and the inter-

shaft hitch system is developed to enable the driver have a good visual field for agricultural machinery. Therefore, the driver can operate accurately in the working process, so as to improve the final yield of vegetables. The structure of multifunctional vegetable field machine is shown in Fig.1.

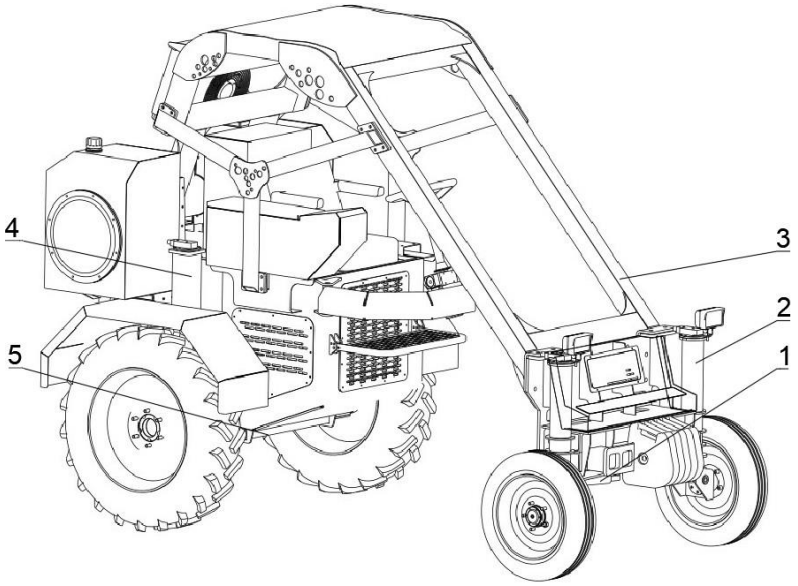

Fig. 1 – Structural design scheme of the whole machine

1. Front wheel spacing adjustment mechanism; 2. Front ground clearance adjustment; 3. Frame; 4. Rear ground clearance adjusting mechanism; 5. Rear wheel spacing adjustment mechanism

Key component design

- **Ground clearance adjustment and wheel spacing adjustment mechanism**

The ground clearance adjustment mechanism and wheel spacing adjustment mechanism work together to make the multifunctional vegetable field machine adapt to the different flatness of field, the mechanized production methods and planting agronomy of different vegetable varieties *(Du X.X., 2014; Shen T.L.F. et al., 2016)*. Combined with the actual situation and requirements, the minimum ground clearance of multifunctional vegetable field machine is selected to be 400mm, the minimum wheel spacing is 1600mm, the adjustable range of the ground clearance is 400mm, and the adjustable range of the wheel spacing is 400mm. The front ground clearance adjustment mechanism, the rear ground clearance adjustment mechanism, front wheel spacing adjustment mechanism and rear wheel spacing adjustment mechanism are shown in Fig. 2.

The ground clearance adjustment mechanism in front of the machine is composed of hydraulic cylinder block, end cap, piston rod and hydraulic cylinder block sleeve. The hydraulic cylinder block is fixed with the front wheel steering mechanism. Piston rod drives the hydraulic cylinder block sleeve move. Because the sleeve and the frame form a whole in the direction perpendicular to the ground, so it can drive the machine movement, the purpose of changing the clearance from the ground is achieved.

The ground clearance adjusting mechanism at the rear of the machine body is composed of independent hydraulic cylinder and guide device. The piston rod of the hydraulic cylinder is firmly connected to the motor cover of the wheel part, the cylinder block is connected to the guide mechanism, and the guide mechanism is connected to the spacing adjustment device of the rear wheel, so as to form a whole with the frame in the direction of the vertical ground. When the cylinder block moves, the movement of the whole machine is driven to achieve the purpose of changing the clearance from the ground.

The front wheel spacing adjustment mechanism is composed of the left and right frame, the beam sleeve and the hydraulic cylinder. The adjustment frame for single wheel spacing is composed of four 5 mm thick steel plates and 100×100×10 mm square pipes, and the beam sleeve is composed of 120×120×10 mm square pipes. The frame is fixed with the sleeve of the ground gap adjustment mechanism, and the force of vertical movement is transmitted through the beam sleeve which is fixed with the frame. The cylinder body is firmly connected with the beam sleeve. Through the connection of the hydraulic rod and the adjustment frame on both sides, the left and right motion stroke can be synchronously adjusted to avoid the vehicle centre of gravity be too high, which will lead to the increase of the vehicle risk.

The structure and working principle of the rear wheel spacing regulating mechanism is similar to that of the front wheel spacing regulating mechanism. The hydraulic cylinder is a two-way piston cylinder with a rod cavity as the working chamber when the wheel spacing is reduced.

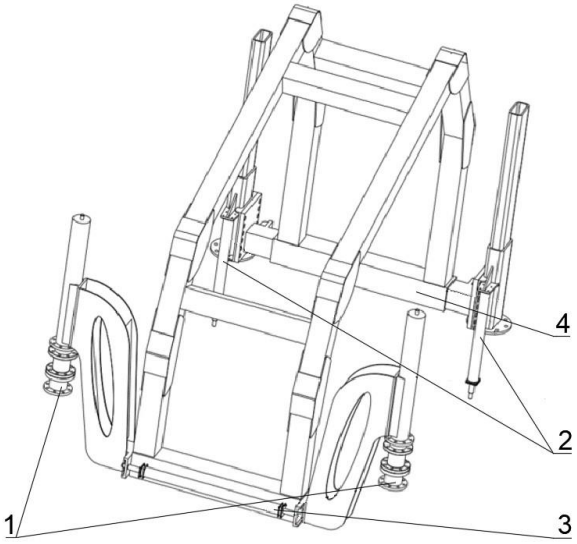

Fig. 2 – The ground clearance adjustment and wheel spacing adjustment mechanism

1. Front wheel gap adjustment mechanism; 2. Rear wheel gap adjustment mechanism;
3. Front wheel spacing adjustment mechanism; 4. Rear wheel spacing adjustment mechanism

- **Hitch mechanism design**

At present, most agricultural machinery is driven by tractors or has its own power source, and most agricultural machinery and tools used in vegetable production are hooked up by traction or three-point hitch *(Xue C.S., 2018)*. In the process of agricultural machinery operation, drivers need to constantly look back to observe the operation situation. It is difficult to ensure the accuracy of the operation and it may bring danger. Therefore, a non-standard three-point inter-shaft hitch system is developed. The height adjustment function is realized by hydraulic power, and the width of the hitch system can be adjusted manually. It can make the working state of agricultural machinery completely within the driver's visual field, thus ensuring the accuracy of the operation process and improving the driver's safety.

As shown in Fig. 3, the transverse part of the inter-shaft hitch mechanism is square sleeve beam, which is similar to the wheel spacing adjustment mechanism.

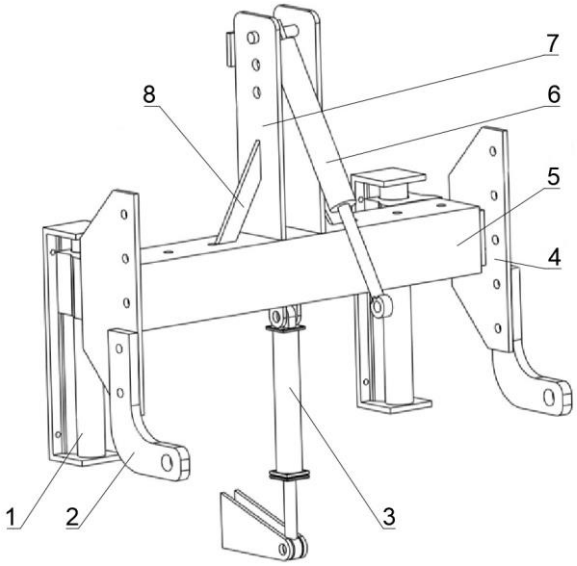

Fig. 3 – Inter-shaft hitch mechanism

1. Slide rail; 2. Lifting arm; 3. Height adjusting hydraulic cylinder; 4. Stretching beam; 5. Stretching beam sleeve;
6. Lifting hydraulic cylinder; 7. Longitudinal beam; 8. Reinforcing plate.

It adopts the structure of two telescopic sleeves, but the width adjustment here needs to be completed manually. The sliding guide rail can adjust the height of the hanging position of agricultural machinery, and the lifting arm machine can change the height of hanging agricultural tools, which can increase the height adjustment range, match more agricultural machinery and better control the working depth of agricultural machinery in the soil. The mechanism has a maximum width adjustment capacity of 300 mm and a maximum height adjustment distance of 150 mm. The rear hitch of this machine adopts the traditional three-point hitch mechanism, which can match more agricultural machinery. Because of multifunctional vegetable field machine having two hitch structures, it can install multiple machines for simultaneous operation which can reduce soil compaction and crop damage.

- **Frame mechanism design**

The frame is one of the most important parts of the multifunctional vegetable field machine, which mainly plays the following roles: connects the front and rear parts of the whole machine, bears various forces and torques brought by the front and rear wheels, reduces the vibration of the whole machine caused by uneven road surface, so that the tractor can have good driving stability *(Zhang L., 2018)*.

The multifunctional vegetable field machine adopts "frame-type" structure. The front end is welded and fixed with the crossbeam and crossbeam sleeve which can adjust the distance between front wheels, and the rear end is similar to the front end. When designing the frame, it is necessary to ensure its safe rigidity and strength.

The material selection and cross-section shape of the frame directly affect the performance of the tractor. Reasonable selection can effectively ensure the strength and rigidity of the frame, and can also help the subsequent processing and manufacturing. The main material of the frame structure use 100×100×10 mm square tube. The frame is welded by 13 square tubes with different lengths and 24 steel plates with 10 mm thickness. Its structure is shown in Fig.4, its length is 1900mm, the width is 800mm, and the height is 1534 mm. Among them, the wide steel plate can connect all parts of the frame and strengthen the moment bearing capacity.

As the main load-bearing component, the rigidity of the frame directly affects the safety performance, service performance, stability performance and service life of the multifunctional vegetable field machine. In this paper, the finite element analysis software ANSYS is used to carry out linear static analysis on the frame, so as to understand its stress and strain under the statics condition, which provides a certain theoretical design basis for the structural design and will play a certain reference role for the subsequent design improvement of related models.

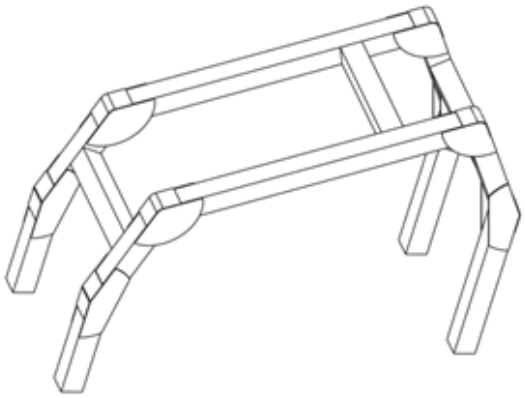

Fig. 4 – Frame

- **Frame analysis**

In this paper, CREO software is used to carry out 3D model of the frame. After simplifying some features of the 3D model that are not applicable for finite element analysis, it is converted into the available model of ANSYS. The frame is made of carbon structural steel Q345B, and its material performance is shown in Tab.1. The grid division has a great impact on the quality of analysis. In order to make the grid division reasonable, the automatic grid division application of ANSYS software is adopted in this analysis, and on this basis, the larger grid is refined, and a total of 214270 dividing nodes and 49976 body units are obtained. In order to facilitate calculation, each part is integrated into a solid, and the default SOLID186 unit type of the system is selected.

Table 1

Q345B material properties

Name of the material	Elastic modulus/(kg·cm^{-2})	Poisson's ratio	Yield strength (MPa)	Tensile strength (MPa)	Density (Kg·m^{-3})
Q345B	2.06·e^{5}	0.280	345	470~630	7.85·e^{3}

In ANSYS, Block Lanczos is used as the mode extraction method, and free boundary modal analysis is used as the analysis method. The vibration source of the frame is mainly from two different aspects. One is the vibration generated by the ground when moving. Due to the low motion speed of the machine, the frequency is generally less than 30Hz. And the other is the excitation source from the interior of the vehicle, such as the engine and internal friction, whose excitation frequency is generally less than 100Hz. Therefore, the range of calculated frequency band is determined as 0Hz-100Hz. The first 10 modes are shown in Fig.5, and the analysis results are shown in Tab.2.

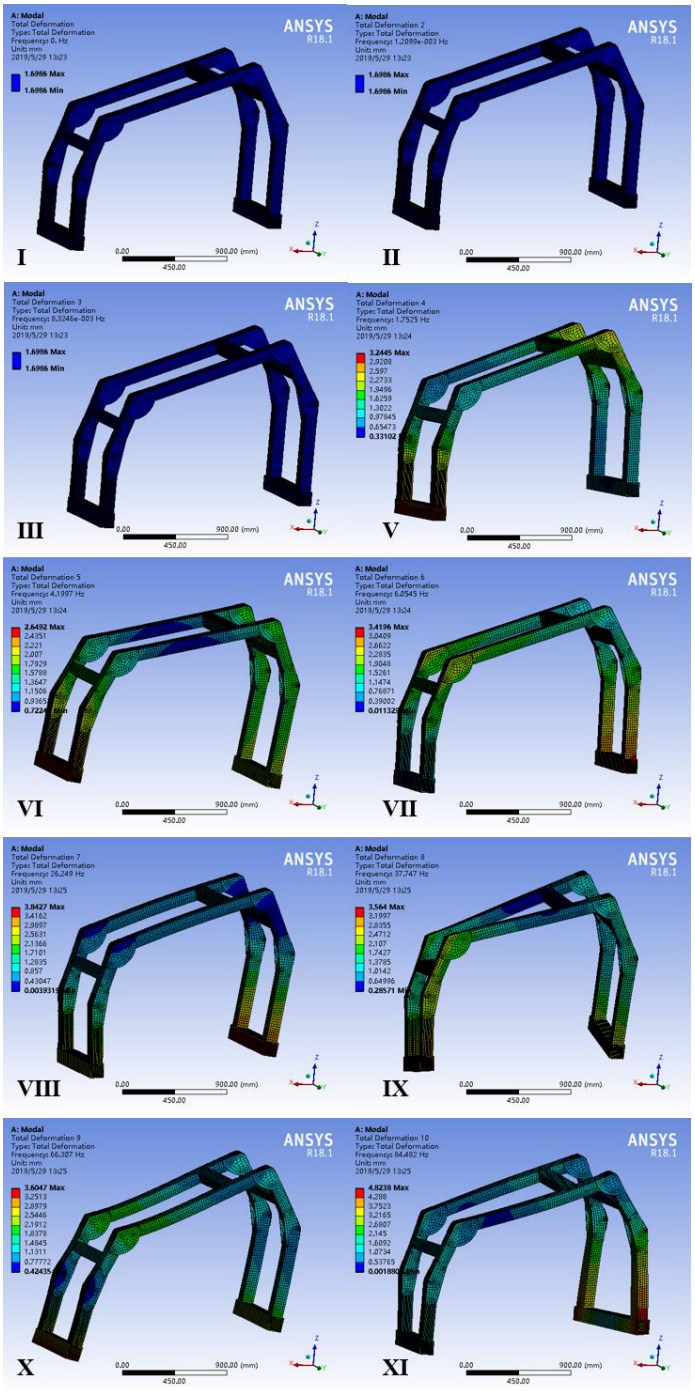

Fig. 5 – The first ten natural frequencies of the frame correspond to the mode diagram

According to the results of the frame free boundary modal analysis, the frame deformation is mainly in the form of bending, torsion and bending. From first to the third order modal of ultra-low frequency almost no effect is shown, four order shows the state of local bending vibration mode, five order modal and ten order modal show the local torsional vibration mode, the six order modal and nine order modal show the overall longitudinal bending vibration mode, combination of seven order modal show the local bending and twisting vibration mode, the combination of eight order modal show the overall bending and twisting vibration mode. The deformation of the beam is relatively small.

Table 2

The first ten natural frequencies and modes of vibration of the frame

Modal order time	Modal frequency (Hz)	Maximum displacement (mm)	Vibration performance
1	0	1.6986	No obvious vibration
2	$1.2099 \cdot e^{-3}$	1.6986	No obvious vibration
3	$8.3245 \cdot e^{-3}$	1.6986	No obvious vibration
4	1.7525	3.2445	Local bending
5	4.1997	2.6492	Local bending
6	6.0545	3.4196	Overall longitudinal bending
7	26.249	3.8427	Local bending and twisting
8	37.747	3.564	Overall bending and twisting
9	66.307	3.6047	Overall longitudinal bending mode
10	84.482	4.8238	Partially reversing

In addition, the stiffness of the frame is analysed. Taking the right front wheel of the vehicle impacted by the road as an example, the frame is deformed due to the deformation of the front axle. The dynamic load of the front axle is taken as 1.14MPa through searching literature and calculation, which simulates the impact of a single wheel on the road, and the other three tires are used as fixed in homeostatic position. The stress and strain of the frame under impact are shown in Fig.6.

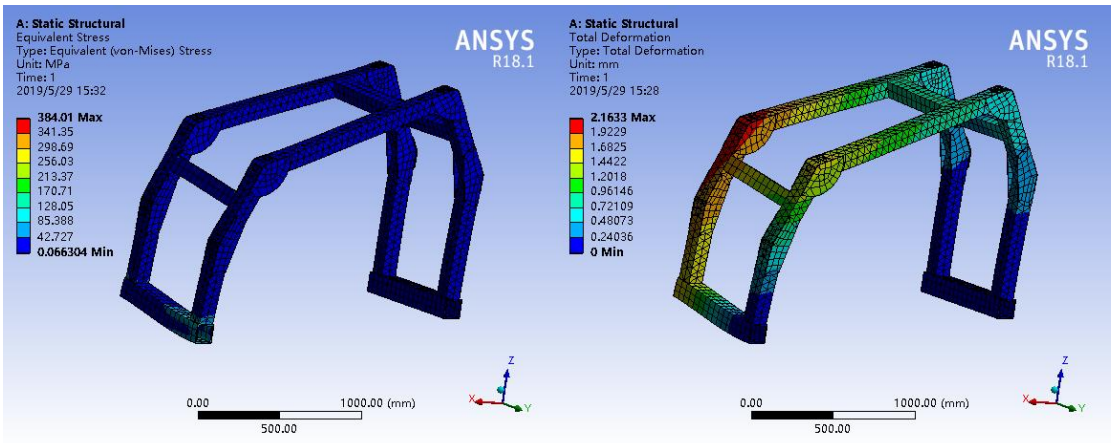

Fig. 6 – The Stress and strain of frame under impact

It can be seen from the analysis results that the maximum stress of the frame does not exceed 200 MPa under the impact action, so the frame material meets the use requirements. The maximum deformation displacement of the frame is about 2.17 mm.

RESULTS

At present, there are many problems in vegetable mechanized production, such as complex environment, non-uniform agronomy, different production processes, various kinds of vegetables, and many supporting agricultural machinery. In this paper, the multifunctional vegetable field machine is developed, and its key components are designed, including the ground clearance adjustment and wheel spacing adjustment mechanism, the inter-axle hitch mechanism, the rear hitch mechanism and the frame.

The multifunctional vegetable field machine can adapt to different production conditions, adjust chassis levelling and reduce soil compaction.

Through the finite element analysis, the vibration modal analysis and stiffness analysis of the frame are carried out, which proves that the frame design is reasonable and meets the requirements. Finally, a prototype was made and its parameters were measured in the Mechanical and Electrical College of Northwest A&F University. The prototype of multifunctional vegetable field machine is shown in Fig. 7.

Fig. 7 – Multifunctional vegetable field machine

The measure results are shown in Tab.3.

Table 3

Main structure parameters of precise and efficient vegetable field operation management machine

Name	Parameter
Length × width × height（mm）	2580×1914×2115
Wheelbase length（mm）	1800
Minimum wheel track length（mm）	1600
Minimum ground clearance（mm）	400
Quality（kg）	1600
Power source	ZN385Q Diesel engine

CONCLUSIONS

In order to realize efficient, intelligent and environment-friendly full-cycle field operation management of vegetables, a new type of high-efficiency multifunctional vegetable field machine was developed by adopting the idea of "frame-type" mechanism design.

The whole machine structure, ground clearance adjustment and wheel spacing adjustment mechanism, the inter-axle hitch mechanism, the rear hitch mechanism and frame are developed and optimized, especially the vibration modal analysis and stiffness analysis of the frame are carried out.

The trial production and experiment of the equipment have been completed. The test results show that the maximum running speed of the vegetable field machine is 16 km/h.

The maximum operating speed is 8 Km/h, the maximum gradient is 20^{o}, and the adjustable range of ground clearance is 400 ~ 800 mm. The adjustable range of wheel spacing is 1600-2000mm. It can improve the efficiency and quality of vegetable field operation.

ACKNOWLEDGEMENT

The authors appreciate the financial support provided by the China Postdoctoral Science Foundation (No. 2019M653764), the Key Research and Development Program of Shaanxi Province (No. 2019ZDLNY02-01), the Shaanxi Province Postdoctoral Science Foundation (No. 2017BSHEDZZ138) and Hainan University Scientific Research Project (No. Hnky2018-8).

REFERENCES

[1] Bulgakov V., Pascuzzi S., Adamchuk V. et al. (2019). Theoretical Study of Transverse Offsets of Wide Span Tractor Working Implements and Their Influence on Damage to Row Crops, *Agriculture*, vol.9;

[2] Dihingia P.C., Kumar G V P, Sarma P.K. et al. (2018). Hand-Fed Vegetable Transplanter for Use with a Walk-Behind-Type Hand Tractor, *International Journal of Vegetable Science*, vol.24, pp.254-273;

[3] Du X.X. (2014). Retrofit design of tractor with high clearance and wide track (高地隙、宽轮距拖拉机改装设计), *Transactions of the Agricultural Engineering*, vol.4, pp.129-134+96;

[4] He Chaoxin, Yu Xianchang. (2012). Development trend and prospect of main vegetable production in the world (世界主要蔬菜生产的发展趋势与展望), *Transactions of the Vegetables*, pp.1-6;

[5] Hui Weidong W.C., Ben Nengjun, Gu Qi. (2018). Research of strength and stiffness performance analysis of tractor safety frame, *Modern Manufacturing Engineering*, vol.456, pp.62-65;

[6] Kumar G.V.P. and Raheman H. (2011). Development of a walk-behind type hand tractor powered vegetable transplanter for paper pot seedlings, *Biosystems Engineering*, vol.110, pp.189-197;

[7] Li X.R., Zhang Y.P., Diao P.S., et al. (2021). General situation of vegetable production in China and research status of precision seeder (我国蔬菜生产概况及精量播种机研究现状), *Transactions of the Journal of Agricultural Mechanization Research*, vol.43, pp.263-268;

[8] Materechera S.A. (2009). Tillage and tractor traffic effects on soil compaction in horticultural fields used for peri-urban agriculture in a semi-arid environment of the North West Province, South Africa, *Soil and Tillage Research*, vol.103, pp.11-15;

[9] Mi N.H., Zhao Y., Qing G.M. et al. (2014). Present situation and countermeasures of vegetable mechanization in the whole process (蔬菜全程机械化研究现状与对策), *Transactions of the Journal of Chinese Agricultural Mechanization*, vol.35, pp. 66-69;

[10] Pedersen H.H., Grøn Sørensen C., Oudshoorn F.W. et al. (2013). A Wide Span Tractor concept developed for efficient and environmental friendly farming*, Land, Technik, Proceedings of Ageng 2013*, pp.47-53;

[11] Rajaa R, Slaughter D.C., Fennimore S et al. (2019). Precision weed control robot for vegetable fields with high crop and weed densities, *ASABE*, pp.1;

[12] Shao M., Zhang X. and Xin Z. (2019). Research on hilly mountain tractor based on adaptive, *IOP Conference Series: Materials Science and Engineering*, vol.612, pp.032070;

[13] Shen T.L.F., Zhang Y., Tang L.J. et al. (2016). Design and Experiment of Rice Seedling Field Conveyor (水稻秧苗田间运输机的设计与试验), *Transactions of the Journal of Chinese Agricultural Mechanization*, vol.37, pp.36-40;

[14] Wang Z.Y. (2010). Design of general chassis of tea garden management machine (茶园管理机通用底盘的设计), *Transactions of the Nanjing Agricultural University*;

[15] Xiao T.Q., He C.X., Cao G.Q. et al. (2015). Study on the Development Status of Vegetable Industry in China and Foreign Models from the Perspective of Mechanized Production (机械化生产视角下我国蔬菜产业发展现状及国外模式研究), *Transactions of the Research of Agricultural Modernization*, Vol.36, pp.857-861;

[16] Xue C.S. (2018). Working principle and maintenance of tractor hydraulic suspension mechanism (拖拉机液压悬挂机构工作原理与使用维护), *Transactions of the Farm Machinery Using & Maintenance*, pp.42;

[17] Yang H., Xia C., Han J. et al. (2020). Model and dynamic performance analysis of mountain tractor suspension implements, *IOP Conference Series: Earth and Environmental Science*, vol.508, pp.012194;

[18] Yang Q., Huang G., Shi X. et al. (2020). Design of a control system for a mini-automatic transplanting machine of plug seedling, *Computers and Electronics in Agriculture*, vol.169, pp.105226;

[19] Zhang L. (2018). Design analysis and optimization of box frame through connection structure (箱型车架贯通连接结构设计分析及优化), *Transactions of the Special Purpose Vehicle*, pp.94-97.

ANALYSIS ON INCLINATION MONITORING OF ONLINE AGRICULTURAL MACHINERY EQUIPMENT BASED ON WSN (WIRELESS SENSOR NETWORK)

/

基于无线传感器网络的在线农机设备倾斜度监测研究

Gui Jinyao [1)]*, Hu Xiaoning [2)], Hu Guohua [1)], Hudgens Lucia [3)]

[1)]Electronic Information and Electrical Engineering Department, Hefei University, Hefei, 230601, Anhui / China

[2)]Anqing Branch of China Mobile Communications Group Anhui Co., Ltd., Anqing, 246005, Anhui / China

[3)]Royal Dutch Shell, the Hague / Netherlands

**E-mail: ys30454442hangsi@163.com*

DOI: https://doi.org/10.35633/inmateh-63-45

Keywords: *wireless sensor, agricultural machinery equipment, tilt monitoring research*

ABSTRACT

The shell of inclined conveyor of combine often has the defect of serious vibration. In order to solve this problem, this study uses the dynamic signal test and analysis system and control the electromagnetic directional valve to realize the horizontal stability control of agricultural machinery. In order to improve the bearing accuracy, this paper designs a bearing tilt detection device. When the tilt reaches its set point, an alarm can be issued to initiate an emergency response. Taking tractor as the object, the application of real-time tilt angle measurement algorithm on three-axis multifunctional turntable is tested. At the same time, the automatic leveling system of agricultural machinery was tested in the field, and the minimum inclination angle of the chute conveying all kinds of grain and oil materials was obtained. The image collected by AGV has the characteristics of high speed, high efficiency and small resolution error. It can also correct the tilt image in real time. This study is helpful to adapt to the new requirements of modern agricultural large-scale agricultural machinery or production facilities. The monitoring system has practical guiding significance in the construction process, and has a certain promotion value.

摘要

联合收割机倾斜输送机机壳经常存在振动严重的缺陷。为了解决这一问题，本研究采用动态信号测试分析系统和控制电磁换向阀来实现农业机械的水平稳定性控制。为了提高轴承精度，本文设计了一种轴承倾斜检测装置。当倾斜达到其设定点时，可以发出警报以启动紧急响应。以拖拉机为对象，测试了实时倾角测量算法在三轴多功能转台上的应用。同时，对农机自动调平系统进行了田间试验，得出了输送各种粮油物料的溜槽的最小倾角。AGV 采集的图像具有速度快、效率高、分辨率误差小的特点。它还可以实时校正倾斜图像。该研究有助于适应现代农业对大型农业机械或生产设施的新要求。该监测系统在施工过程中具有实际指导意义，具有推广价值。

INTRODUCTION

With the implementation of the national agricultural side supply structural reform strategy, the production efficiency of agricultural machinery put forward higher and newer requirements. Nowadays, high efficiency and compound modern agricultural machinery and equipment are constantly emerging *(Adloff C. et al., 2013)*. Large-scale agricultural production will make the whole process of mechanization inevitable. But the measurement technology of bearings in China is still relatively backward, especially the lack of measuring equipment for measuring bearing inclination angle and related measurement methods because of the complex farmland environment, unstructured characteristics are obvious *(Krawczyk A.I. et al., 2020); (Geng L. et al., 2020).* After the development of navigation methods such as range estimation and inertial navigation, the current research on agricultural machinery navigation mainly focuses on the way of machine vision. The suitable inclination angle of material conveyed by chute is determined by the characteristics of material, the material and shape of chute and the use conditions of combine harvester. Complex structure, multiple transmission components, heavy workload, strong continuity of operation, bad working environment, cannot control the balance of the whole machine in the left and right horizontal direction, resulting in the operation, cannot meet the predetermined requirements *(Boesch A. et al., 2020)*.

If the paddy field is accurate and flat, the bottom of the paddy field is uneven, and the failure rate is much higher than in the case of other machinery. In the paddy field levelling operation, the laser control system can only control the height of the level shovel to adjust, but cannot guarantee that the level of the shovel can be controlled, which makes it difficult to meet the planting requirements *(Moczkowska M. et al., 2020)*. Compared with technology, the substantial difference in design is that the use of scientific measuring instruments replaces the traditional detection of the bearing inclination angle by subjective judgements, so that the bearing inclination angle is more accurate *(Joppa M. et al., 2018)*.

In the installation stage of equipment, the inclination must be controlled immediately to ensure the verticality, so as to meet the installation accuracy. However, there is no clear national standard and means for monitoring installation inclination. Traditional methods include observation method and inclination method, which can only reflect the influence of deformation indirectly, not directly by on-line measurement. At present, the detection of the tilt angle in China is mostly done manually by humans *(Musiu E.M. et al., 2019).* First, place the inner and outer rings of the bearing on the water platform, hold the inner ring with one hand, lift the outer ring with the other hand, and measure the height of the outer ring gear by the dial gauge to calculate the inner ring and the outer sleeve *(Goswami M. et al., 2020).*

The amount of tilt between the circles, and with the maturity of computer image processing technology, the cost performance of related hardware has been continuously improved, and has become a navigation method with more research at home and abroad. The harvester header is generally located in front of the whole machine *(Li Y.B. et al., 2020; Krishnamurthy S.L. et al., 2020).*

In the working process of the harvester, the imbalance of harvesting, threshing, cleaning and conveying devices, engine operation and unevenness of road surface will cause violent vibration of the cutting table and inclined conveyor, resulting in cracks and wear on the cover of the cutting table and the shell of inclined conveyor, thus affecting the normal operation of various components; The transplanter is composed of dynamic balancing device. In order to realize the horizontal control of manual transplanter, the principle of gravity and balance lever is applied. The level of the transplanter is realized by the automatic balance of the weight hammer of the sensor, and the control hydraulic system is used to drive the relevant components.

Although the non-contact measurement angle has gradually become the mainstream in recent years, in order to obtain high-precision angle measurement values, contact measurement is still required. It directly affects the service life of the reserve materials, and its primary problem is to strengthen the monitoring of temperature and humidity *(Francois J.M. et al., 2020; Teshome F B et al., 2019)*. The traditional method is time consuming and laborious, and the temperature and humidity errors of the test are large. The contact type measurement is that the measuring head is in contact with a certain point on the surface of the workpiece for measurement, and scanning along the shape of the workpiece can obtain a large number of points at a high density in a short time. The more the number of measuring points, the more accurate shape parameters can be obtained. The tilt of mechanical equipment is monitored in real time. Through the preset alarm threshold, the real-time measured values are compared and judged to determine whether to alarm. (*Sevast'yanov V.D. et al., 2018*).

Research on vision navigation technology of agricultural machinery mainly focuses on the acquisition of navigation parameters, navigation control methods and algorithms, vision hardware system and so on. However, the image acquisition deviation caused by uneven ground or tilt of agricultural vehicles has a great impact on the final navigation parameters obtained by subsequent image processing *(Wang J. et al., 2019)*. The vibration intensity, energy distribution and frequency structure of the inclined conveyor shell midpoint under four working conditions of harvester idling, field operation, engine idling and highway transportation were measured by dynamic signal test and analysis system *(Ting N.C. et al., 2020)*. Therefore, in order to improve the working quality of agricultural machinery and realize the automatic levelling control of agricultural machinery, a kind of automatic levelling control system suitable for agricultural machinery is designed by using sensor technology and control technology, and the system is analysed by three-axis multi-function turntable test and field test *(Yang H. et al., 2019).*

MATERIALS AND METHODS

The most intuitive feature in crop images is the colour feature. Plants are green and the soil is yellowish brown, and their colour is very different. For this reason, colour features can be used to distinguish.

Through visual inspection, the maintenance personnel can directly judge whether the guide wheel in the casing rotates, so as to promptly find problems and repair in time, thereby prolonging the service life of key components such as guide wheels and chains in the slag machine.

Installed on the top surface of large agricultural machinery, it uses a solid pendulum sensor. The project test uses a dual-axis tilt sensor with a test accuracy of 0.1°, which mainly completes the measurement and transmission of the inclination data. The control principle of agricultural machinery automatic leveling control system: the agricultural machinery rotating mechanism on the tractor is connected with the agricultural machinery.

Agricultural machinery can be driven by hydraulic cylinder to adjust the relative angle with the tractor around the rotating mechanism. In addition to the rotation direction of agricultural tools, the connection between agricultural machinery rotating mechanism and tractor is considered as rigid connection.

Dynamic signal acquisition and analysis system software and socket driver, check the working condition of data acquisition and sensor. After debugging the working state of the wheat combine, the measuring points are selected, the sensors are fixed and connected to the relevant lines. All channels must be cleared before sampling. With the introduction of network technology, sensors become an organism that can realize the interconnection between objects, not just being independent perception units.

This feature of Wireless Sensor Networks (WSN) has made it play an important role in many fields. WSN technology that combines sensor technology, information processing technology and network communication technology has emerged. This kind of network is a new field in information technology.

The tube shape coefficients of different sliding tubes are shown in Figure 1.

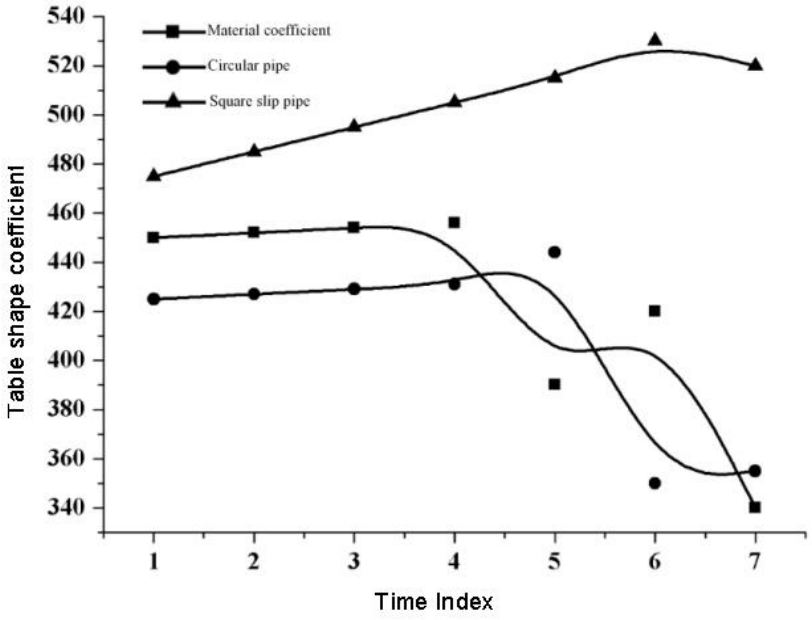

Fig. 1 - Tube shape coefficient of different slide tubes

The transformation test data are shown in Table 1 and Figure 2.

Table 1

Transformation test data

Image serial number	Actual inclination	Calculate the inclination	Difference
1	8	15	7
2	20	23	3
3	40	43	3

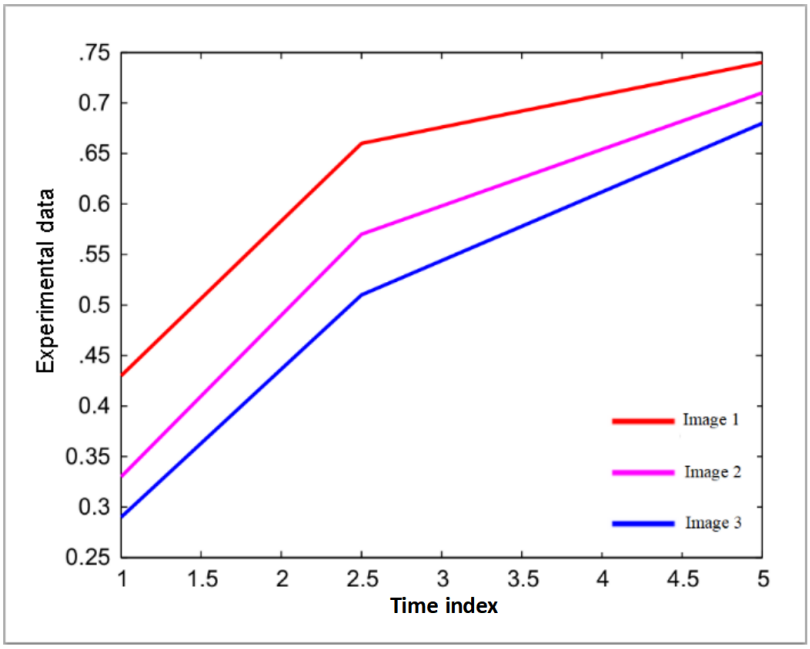

Fig. 2 - Transformation test data

To analyse the characteristics of an image, it is necessary to separate the object from the image, thereby using the graphic and the background as separate binary images. It is critical to choose the appropriate threshold to separate the crop area from the non-crop area. The tractor roll angle sensing system measures the lateral tilt angle of the tractor body and uses algorithms to fuse the data of the accelerometer sensor and the gyro sensor to obtain an accurate roll angle and the engine is idling.

The engine is initially operated at the lowest speed after starting, and then is gradually increased to the rated speed. The vibration acceleration of the measuring point is collected under the rated speed of the engine. The tensioning mechanism of the device is mounted on the head casing.

The disadvantage of this type of structure is that the tension adjustment cannot be synchronized. When the chain wear on both sides is inconsistent, the drag mechanism is caused. Tilting on both sides, it is easy to damage the bearing seat at the end of the drag mechanism and drag the sprocket, which will endanger the safe operation of the equipment. The inclination of the measuring equipment of the distributed biaxial inclination sensor is tested by the scientific experiment method, the embedding mode of data transmission between the biaxial inclination sensor and the wireless sensor through the serial port and the networking mode are built, so that the sensor measurement data can be modulated into wireless signals and sent to the monitoring centre to maintain the network topology routing information.

Because of the limitation of size, price and power supply, the node can only exchange data with its neighbours in the communication range. To access nodes outside the scope of communication, multihop routing must be used. In order to ensure that most nodes in the network can establish wireless links with the gateway, the distribution of nodes should be quite dense.

The convergence of the distributed algorithm under different network sizes is shown in Table 2 and figure 3.

Table 2

Convergence of distributed algorithms under different network sizes

Network size	Convergence to the optimal value 110% Average number of iterations required	Convergence to the optimal value 105% Average number of iterations required
30	900	1700
40	990	1782
50	1800	2300
60	1850	2800

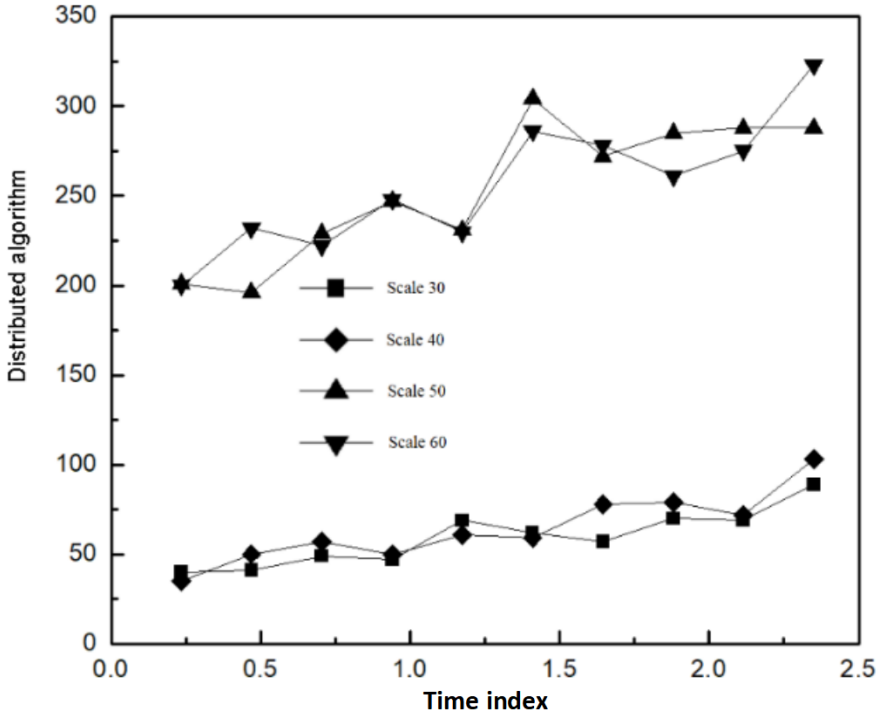

Fig. 3 - Convergence of distributed algorithms under different network sizes

Since the number of nodes is on the order of 110, 105 in the network scenario under consideration, the total amount of data generated by the iterative process is small relative to the long-term operation of the network.

RESULTS

The field test platform of automatic levelling control system for agricultural machinery adopts the paddy field laser levelling machine matched with transplanter. The levelling shovel of the levelling machine is designed for paddy field in South China. The wear of the chain in the operation of the slag machine is manifested as the overall elongation of the chain. A stable and reliable tensioning device is necessary. Intelligent wireless gateway and Ethernet switch are the main components, mainly responsible for data exchange with the monitoring centre. The paddy field laser leveler is shown in Figure 4.

Fig. 4 - Paddy field laser levelling machine

Direct Sequence Spread Spectrum (DSSS) is a digital modulation method, which directly uses the spread spectrum code series with high bit rate to spread the spectrum of the signals. Firstly, the nodes of the sensor network fail due to physical damage, battery depletion, environmental shielding and so on. The remaining sensor nodes will be reconstructed. Network is represented by node addition or deletion, which results in network topology reconfiguration. How to design a data-centric, energy-efficient and highly scalable routing protocol is the key to routing design. Algorithms to achieve optimal performance are often centralized, while operations on real nodes are based on local information, so designing distributed and efficient algorithms to support is a future research direction. The simulation parameters in one dimension are shown in Table 3 and figure 5.

Table 3

Simulation parameters in one-dimensional case

Sensor node	Coordinate	Data collection rate
1	7.8124	0.8045
2	14.5412	0.1240
3	22.4510	0.9124
4	30.4653	0.1156

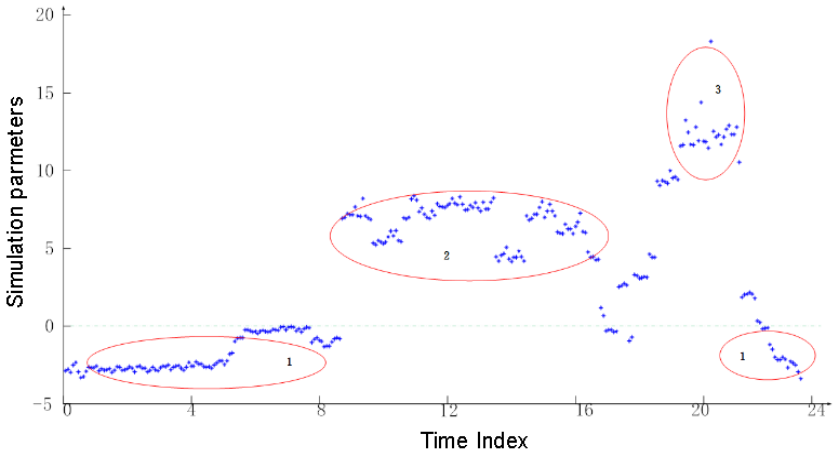

Fig. 5 - Simulation parameters in one-dimensional case

Considering the data collection scenario, there are often multiple data collection centres in the network to collect information from other nodes and transmit it to base station nodes. In clustering networks, nodes are divided into clusters, and some nodes act as cluster heads. Ordinary nodes in the cluster send data to cluster head nodes, and cluster head nodes aggregate the received data to reduce the energy consumption caused by packet head, and transmit it to base station nodes. And a query processing system is constructed to facilitate the acquisition of information in the database.

Data management involves data storage technology, data query technology, data analysis technology and data mining technology. In order to ensure the normal operation of the sensor network, redundant node deployment and even redundant links should be considered to make the sensor network data highly redundant.

The axis inclination sensor and the wireless sensor do the embedded experiment combination of data transmission through the serial port, set up the network experiment environment, set up the wireless network management, complete the hardware integrity test. The sealing structure of the new structure adopts a multi-layer sealing structure; a high wear-resistant sleeve is adopted between the sealing member and the shaft to prevent the guide shaft from being damaged due to the damage of the sealing member; the mechanical multi-groove labyrinth ring is selected as the first-stage sealing method. It is difficult to enter the sealed circuit with grey water.

In digital image processing, convolution is often performed with a small area template to approximate the gradient. The mathematical basis for constructing the edge detection operator is the first-order and second-order derivative changes, and the derivative change in the direction of the two-dimensional image is represented by a gradient. The vibration frequency and amplitude are both large. This vibration acts directly on the frame and propagates through the rack.

The comparison of hardware node platforms of wireless sensor networks is shown in Table 4.

Table 4

Comparison of WSN hardware node platforms

Platform	Mica2	Telos
cpu@/MHZ	8bit Atmel@8	16bit TI@8
SRAM/KB	5	10
Flash/KB	134+540	55+1108

The accelerometers and gyroscopes of the tractor roll angle sensor system adopt our own DOF inertial sensors. The vibration from the engine to the measuring point mainly comes from the overturning torque produced by reciprocating parts, rotating parts and pressurized gas. This should be taken into account when calculating angles. In addition, the inclination angle of the slide pipe should be determined and the movement of the material into the slide pipe should be considered.

The network communication subsystem transmits the collected data to the base station node through wireless sensor network. In the process of completing the same operation, the node needs to wake up many times to forward the data of other nodes, which leads to the increase of energy consumption and delay. Compared with the sinusoidal motion angle data of the turntable, the tractor rolling angle sensor system has a certain delay time of 0.057 s. The error shows that the fusion algorithm of tractor rolling angle sensor system effectively improves the accuracy of rolling angle. The main reason is that the original data of accelerometer and gyroscope are smoothed.

Due to the change of sensor network applications and the difficulty of deployment, wireless sensor network operating system must have the ability of remote wireless upgrade, which is one of its indispensable functions. It simplifies the management of sensor node system and improves the efficiency of wireless sensor network.

The FSG tilt sensor is shown in Figure 6.

Fig. 6 - FSG tilt sensor

Along the gradient of the B and Y directions, the gradient vector can be expressed as:

$$\begin{cases} \omega^T x_i + b \geq 1, & y_i = +1 \\ \omega^T x_i + b \leq -1, & y_i = -1 \end{cases} \quad (1)$$

Let it indicate the gradient direction:

$$i_t = (1-\rho)\left[r^* + \pi_t + \alpha(\pi_t - \pi^*) + \beta(y_t - y_t^*) + \gamma e_t + \delta m_t\right] + \rho i_{t-1} + \xi_t \quad (2)$$

Stay the rate of change in direction θ(P) is the magnitude of the gradient:

$$\theta(P) = Logit(P) = Ln(\frac{P}{1-P}) \quad (3)$$

$$\theta(P) = Ln(\frac{P}{1-P}) = \alpha + \sum \beta_i X_i + \xi \quad (4)$$

The above differential is often replaced by a differential, which is defined in the form of:

$$NDVI = \frac{P4-P3}{P4+P3} \quad (5)$$

$$MNDWI = \frac{P2-P5}{P2+P5} \quad (6)$$

Then the average value can be calculated as follows:

$$\frac{Y(s)}{R(s)} = \frac{G(s)\mathrm{C}(s)}{1+G(s)\mathrm{C}(s)H(s)} \quad (7)$$

$$\frac{Y(s)}{N(s)} = \frac{G_D(s)G(s)}{1+\mathrm{C}(s)H(s)} \quad (8)$$

Since the tractor roll angle sensing system also has a pitch angle error during installation, the pitch angle of the turntable is set at an angle during the turntable test, and the sinusoidal motion amplitude is 10° and the centreline coincidence condition is tested. The test results show that the initial pitch angle of the sensor installation has no effect on the measurement accuracy of the tractor roll angle sensing system. A capacitive sensor is equivalent to a capacitive device in circuit configuration, and its capacitance increases as the measured humidity of the air increases. The humidity sensitive capacitor is placed in the oscillating circuit, and the change of the capacitance value is converted into a voltage frequency signal inversely proportional thereto, which can be directly collected by the computer. The first-level port is mainly based on the function and design structure of the target chip, as well as the function definition and level output of the pin, modifying or rewriting the corresponding files in the two directories, completing the definition of the pin function package function, and modifying the level. When calculating the coverage rate, the whole area is divided into several unit areas.

Suppose there is a transaction in each unit. If a transaction can be perceived by a certain working node, the transaction is said to be perceived in a small area. The final coverage rate is 100% of all transactions that can be perceived. The cluster head node assigns the current slot to the independent set with high priority, and judges the node which does not belong to the independent set. If the node does not conflict with the currently scheduled node, the scheduling of the node will be adjusted. At the same time, the cluster head node determines the unique encoding used by the cluster head to communicate with the base station, so that the cluster head node or intra-cluster node will not be disturbed by other intra-cluster communication when transmitting information. The centre line of the sensor system coincides with the centre line of the turntable, and the centre line of the roll angle sensor system deviates from the centre line of the turntable as shown in Figure 7:

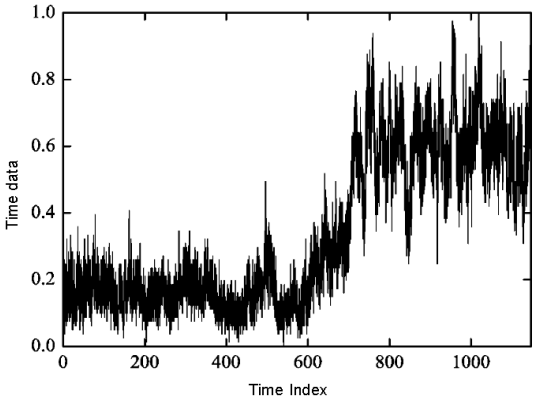

Fig. 7 - Turntable test data

CONCLUSIONS

An automatic levelling control system for agricultural machinery is designed. The real-time roll angle of the tractor is measured by using the algorithm of integrating accelerometer and gyroscope data, and the elongation of hydraulic cylinder is measured by linear displacement sensor.

The tilt correction of the image captured by the agricultural automatic navigation vehicle has the characteristics of high speed, high efficiency and small discrimination error, and it can correct the tilt image in real time. The protocol code distributes the range of nodes to reduce the consumption of node resources, and shortens the time of code distribution. Wireless sensor technology, modern detection technology and simplified mechanical mechanism are used to replace manual operation. It can not only realize the accurate detection of bearings, but also improve the efficiency of post-point scheduling and has more data. Priority scheduling can reduce the network data acquisition time and reduce the latency. The cluster head node calculates the priority and adjusts it for the independent set within the cluster according to the local conflict information. In addition, in order to meet the new requirements of modern agriculture for large-scale agricultural machinery or production facilities, such as adding, shifting, lifting or falling, the monitoring system has practical guiding significance in the construction process, and has the value of popularization.

ACKNOWLEDGEMENTS

The study was funded by 2018 Yunnan Education Department Scientific Research Fund. Topic: Polygonatum kingianum Coll. et Hemsl Adaptive Seedbed Establishment Technology for High-Altitude Hilly Areas (NO. 2018JS272), Yunnan Province College Students Innovative Entrepreneurship Training Program: Limin Agricultural Machinery Service Company.

REFERENCES

[1] Boesch A, de Montmollin A., (2020), Indicators for assessing the sustainability of cities. *Sustainability Assessments of Urban Systems*, pp. 311. Poland;

[2] Francois J.M., Alkim C., Morin N., (2020), Engineering Microbial Pathways for Production of Bio-Based Chemicals from Lignocellulosic Sugars: Current Status and Perspectives. *Biotechnology for Biofuels,* Vol. 13, Issue 1, pp. 1-23. England;

[3] Geng L., Wang Y., Wang J., (2020), Numerical simulation of the influence of fuel temperature and injection parameters on biodiesel spray characteristics. *Energy Science & Engineering,* Vol.8, Issue 2, pp.312-326, USA;

[4] Goswami M., Suresh D., (2020), Plant growth-promoting rhizobacteria—alleviators of abiotic stresses in soil: a review. *Pedosphere*, Vol. 30, Issue 1, pp. 40-61. China;

[5] Joppa M., Köhler H., Kricke S., (2018), Simulation of jet cleaning diffusion model for swellable soils. *Food and Bioproducts Processing*, Vol.113, pp. 168-176, Netherland;

[6] Krawczyk A.I., Van Duijvendijk G.L.A., Swart A., (2020), Effect of rodent density on tick and tick-borne pathogen populations: Consequences for infectious disease risk. *Parasites & Vectors*, Vol. 13, Issue 1, pp. 1-17. England;

[7] Krishnamurthy S.L., Pundir P., Warraich A.S., (2020), Introgressed saltol QTL lines improves the salinity tolerance in rice at seedling stage. *Frontiers in plant science*, Issue 11, pp. 833. Switzerland;

[8] Li Y.B., Li H., Guo X., (2020). Online Parameter Identification of Rice Transplanter Model Based on Ipso-Ekf Algorithm. *INMATEH Agricultural Engineering*, Vol.61, Issue 2, pp.25-34, Romania;

[9] Moczkowska M., Karp S, Horbanczuk O.K., (2020), Effect of rosemary extract addition on oxidative stability and quality of hemp seed oil. *Food and Bioproducts Processing*, Issue 124, pp. 33-47. England;

[10] Musiu E.M., Qi L., Wu Y., (2019), Evaluation of droplets size distribution and velocity pattern using Computational Fluid Dynamics modelling. *Computers and Electronics in Agriculture*, Vol.164, pp.104886, England;

[11] Sevast'yanov V.D., Kovalenko O.I., (2018). System of Standard Neutron Sources on Neutronic Setups for Monitoring, Certification, and Calibration of Apparatus and Equipment. *Atomic Energy*, pp. 1-5. Germany;

[12] Teshome F.B., Degu Y.M., (2019), Design of Combined Press Tool for the Manufacturing of Rice Thresher Blade (Case Study at Amhara Agricultural Mechanization and Food Science Research Centre-Ethiopia). *International Journal of Engineering Science*, Vol.3, Issue 4, pp.90-107, England;

[13] Ting N.C., Sherbina K., Khoo J.S., (2020), Expression of fatty acid and triacylglycerol synthesis genes in interspecific hybrids of oil palm. *Scientific reports*, Vol. 10, Issue 1, pp. 1-15. England;
[14] Wang J., Zhou G., Wei X., (2019), Experimental characterization of multi-nozzle atomization interference for dust reduction between hydraulic supports at a fully mechanized coal mining face. *Environmental Science and Pollution Research*, Vol.26, Issue 10, pp.10023-10036, Germany;
[15] Yang H., Gao L., Tang N., (2019), Experimental Analysis and Evaluation of Wide Residual Networks Based Agricultural Disease Identification in Smart Agriculture System. *EURASIP Journal on Wireless Communications and Networking*, Vol.1, pp.292. USA.

PIG FACE DETECTION ALGORITHM AND SUPPLEMENTARY LIGHT SYSTEM DESIGN BASED ON OPEN MV3

/

基于 open mv3 猪脸检测算法与补光系统设计

Yan Hongwen *, Liu Zhenyu, Cui Qingliang [1]
College of Information Science and Engineering, Shanxi Agricultural University, Taigu/China
Tel: +86-0354-6288165; E-mail: yhwhxh@126.com
DOI: https://doi.org/10.35633/inmateh-63-46

Keywords: *pig face detection, open mv3, supplementary light system, data acquisition*

ABSTRACT

Individual pig recognition is an essential step for accurate breeding and intelligent management of pigs. To realize individual pig identification, applicable dataset of pigs needs to be built. For pigs' behaviour is difficult to control, the data acquisition is of great difficulty and low efficiency. In addition, few reports on pig face detection are there at home and abroad, thus, face data acquisition faces more difficulty. In this study, double open mv3 digital cameras were adopted, and the approach of starting the pig face acquisition program by acquiring pig figure with a vertical camera to calculate the slope of their back before sending a signal to the horizontal camera was adopted. The image brightness was calculated based on RGB function: when the value was less than 90, the supplementary light system would be started by L298 module, and when the value was more than 120, the acquisition system would be restarted. This study provides a reference for solving the key problem of automatic acquisition of pig face data for pig face detection.

摘要

生猪个体识别是生猪的精准养殖与智能管理的必要步骤，为实现生猪个体识别需构建适用的生猪数据集，由于生猪行为难于控制，数据采集难度大、效率低且关于生猪脸部检测的国内外研究鲜有报道，脸部数据的采集难度更大，本研究中采用双 open mv3 数字摄像头，提出由垂直摄像头采集到生猪身影计算背部区域斜率并发送信号给水平摄像头启动猪脸采集程序的方法，并基于 RGB 函数计算图像亮度，当值低于 90 时由 L298 模块启动补光系统，当值大于 120 时重新启动采集系统，为解决猪脸数据自动采集的关键问题猪脸检测提供了参考。

INTRODUCTION

In the field of animal individual identification research, as the image data of animals are difficult to acquire, few animal image datasets are provided for researchers to make classification and identification research under restricted and non-restricted conditions. At present, the animal datasets with research value include KTH-ANIMALS constructed by Afkham et al. *(Afkham et al., 2009)*, in which a total of 1,900 images of 19 kinds of animals were acquired, with about 100 images contained for each kind of animals, and Oxford-iiiT Parkhi animal datasets constructed by Parkhi *(Parkhi et al., 2012)* et al., in which images of two categories, a total of 37 varieties of cats and dogs are included, with 200 images contained for each variety. These kinds of datasets are suitable for species taxonomy, yet datasets for the research of individual species need to be newly constructed. In recent years, researchers have begun to construct datasets suitable for individual identification. The red-bellied monkey dataset constructed by David Crouse *(Crouse et al., 2012)* is small, which is easy to cause overfitting; though the gorilla dataset constructed by Alexander Freytag *(Freytag et al., 2012)* is of a large scale, though the blocking is serious, thus the data availability is poor; the golden monkey face identification database constructed by Fang Nan *(Fang N., 2017; Hu X., 2019; Fan Y. Y., 2018)* includes 80 individual golden monkeys of 4 varieties; datasets of other animals are there, though they are in secrecy, so they are not suitable for study *(Pérezluque et al., 2017; Hughes et al., 2015)*. However, few reports on datasets of individual pig identification are there. *Ma et al., (2016), Nasirahmadi et al. (2016), Chen et al., (2017)* used machine learning method to conduct target extraction and behaviour judgment on pigs, and many

[1] *Hongwen Yan*, As. Ph.D. Lect. Eng.; Zhenyu Liu, Prof. Ph.D. Eng.; Qingliang Cui, Prof. Ph.D. Eng.*

researchers have studied pig behaviour and health status *(Kim et al., 2017; Haladjian et al., 2017; Ahrendt et al., 2011; Guo et al., 2014; Guo et al., 2015; Li et al., 2017)* from different points of view. In a lot of studies, manually self-constructed datasets are adopted, for which not only the workload is huge but also the generalization performance is poor. With individual pig identification becoming a hot spot, having study of data acquisition methods of pigs is imperative. At present, both at home and abroad, reports on the construction of pig datasets are few, that is why double open mv3 digital cameras were adopted in this paper to design the pig face detection algorithm and supplementary light system, so as to provide reference for pig data acquisition.

MATERIALS AND METHODS

DESIGN OF DATA ACQUISITION SYSTEM FOR PIG FACE DETECTION BASED ON OPEN MV3

In this paper, double open mv3 digital cameras were adopted for pig face detection, which helped realize the pig body detection, acquirable pig face area detection and acquisition, as well as a supplementary light system for solving the problem of uneven light intensity. The core functions included a pig face detection module and a supplementary light module. The overall process and functional modules of the system were as shown in Fig. 1.

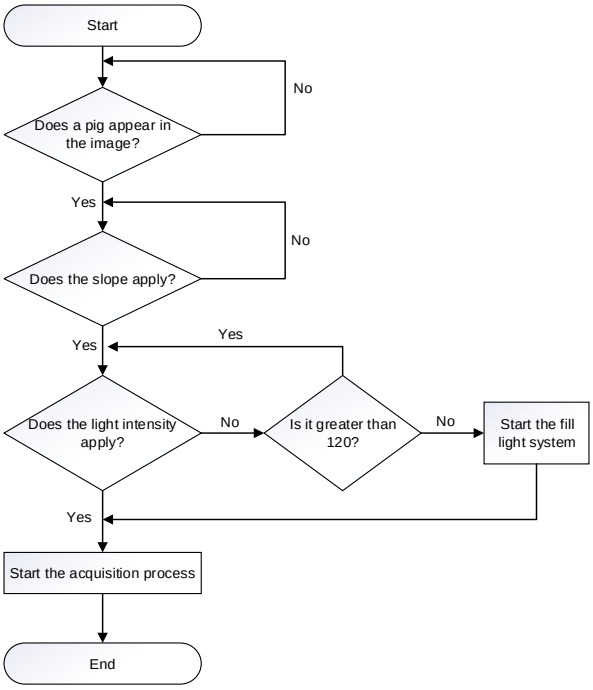

Fig. 1 - Overall Design of Pig Face Acquisition System

The open mv3 digital camera used in the study was as shown in Fig. 2. The main control chip of open mv3 digital camera was STM32F7, with basic frequency of 216 MHZ, 2M flash and 512 KB RAM, colour limp frame rate of 85~90 frames, photosensitive element OV7725, and optional modes of gray (640×480) and RGB565 (320×240), WiFi module of atwinc1500, and transmissibility reaching 48 Mbps. With IP address input in the PC terminal, images could be viewed at real time. With SD card equipped, images and videos could be saved or matching algorithm could be invoked for match identification. With M12 lens base configured, distortion-free viewing angle reached 90 degrees, and standard viewing angle reached 120 degrees. The focal length of lens was 2.8mm and that of a distortion-free lens was 3.6mm.

Fig. 2 - Open mv3 Digital Camera

The acquisition equipment set up in a single piggery management unit was as shown in Fig. 3.

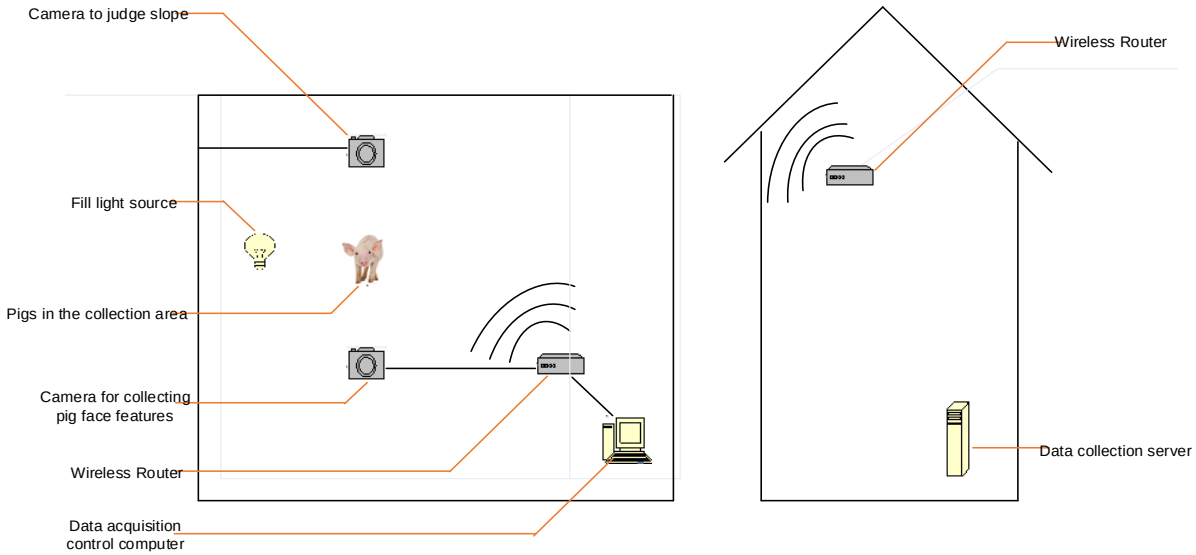

Fig. 3 - Simulated Diagram of Data Acquisition in a Piggery Unit

PIG FACE DETECTION ALGORITHM AND SUPPLEMENTARY LIGHT SYSTEM

Pig face detection module

Principle of pig face detection

The pig face trigger detection system was equipped with two open mv3 cameras, which was able to automatically acquire pig faces when they appeared in the acquisition range. The schematic diagram of the trigger acquisition system was as shown in Fig. 4. The first camera was installed 1.5m directly above the pig body at pigs' activity area. When the pigs entered the camera area, the image of the back of pig body was able to be acquired, and the pixel values of the two centre points selected at back of pigs could be calculated. With the point-point slope k calculated, the pig face samples could be acquired with range of k determined.

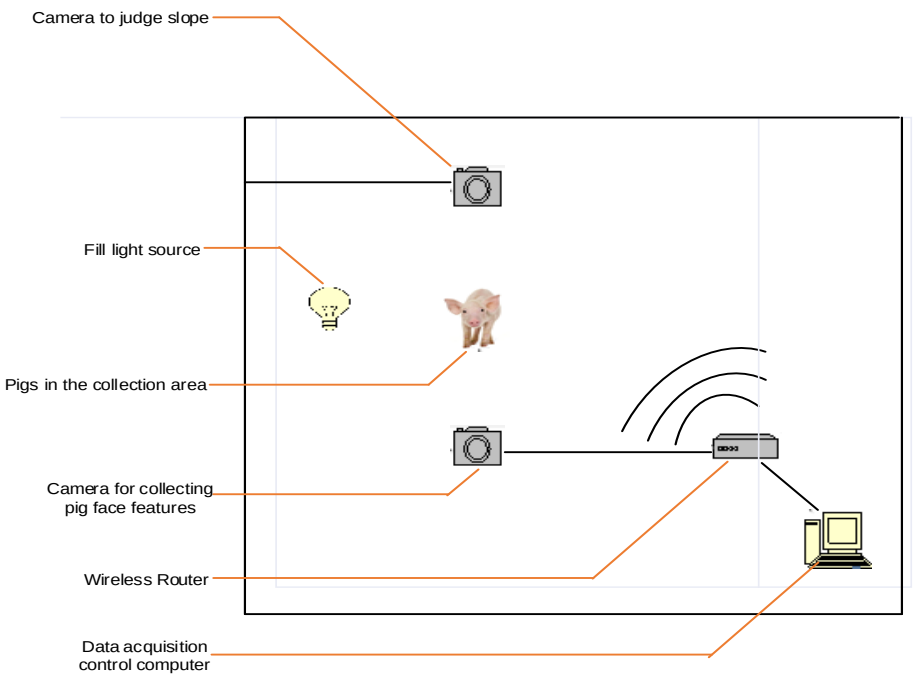

Fig. 4 - Trigger Acquisition Structure Chart

The second camera installed in the front of the pigs' activity area could acquire the image of pig face. When the pig face faced the camera, it was the best time to acquire the image. The timing of pig face acquisition could be determined by judging the value of slope k. There were several representative images of the pigs' back as captured by the vertical camera.

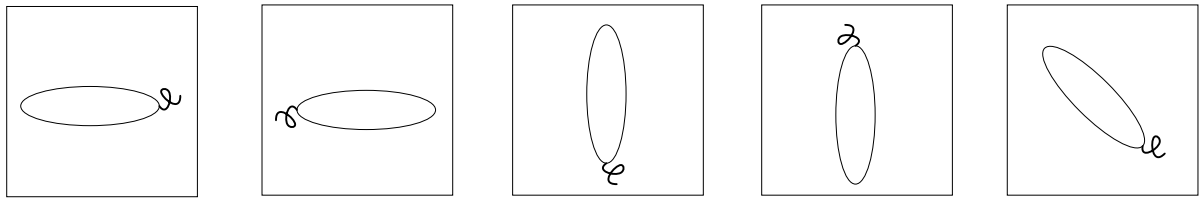

a.Pig face facing the camera b.Pig hips facing the camera c.Pig sideways facing the camera d.Pig sideways facing the camera e.Pig side face to the camera

Fig. 5 - Diagram of the Back of Pigs

How to judge whether the image in Fig. 5 was able to acquire pig face? The oval in Fig. 5 that represents the pigs was divided into two areas, as shown in Fig. 6, and the horizontal line in the middle was taken as the boundary to divide the oval into two areas of A and B, then the centre points a and b were found out before their coordinate values were calculated, finally, the slope k of the ligature between a and b was calculated. As can be seen in Fig. 5, when k was of infinity, it meant that pig face or buttock was just facing the camera, while when k was less than infinity and activates within a certain range, the pig face image could be acquired; when k was less than a certain value, the pig face image acquired would be with a slope that was too large, which was not suitable for subsequent identification. In this study, it was set that pig face acquisition procedure could be started when the slope angle was within a range of 30 degrees. In this way, it was OK to have the calculated value of k be larger than $\sqrt{3}$.

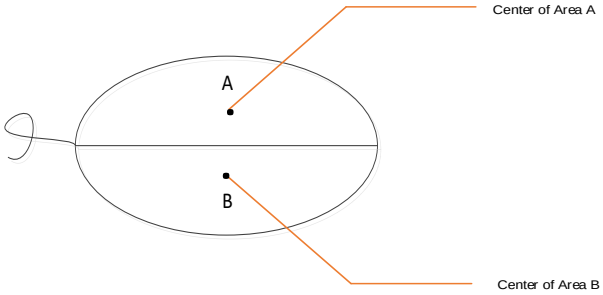

Fig. 6 - Two Areas on the Back Image of Pigs

When k met the requirement, some non-pig face samples could also be acquired. In Fig. 5 (b), (c) and (d), the buttock, left side and right side of the pig body were acquired. At present, such images can be excluded manually. When the slope was of infinity, the pig face samples of the best quality could be acquired, at this time, images of the buttocks and sides of pigs might also be acquired, for which the reason was that when the slope was of infinity, the vertical camera could capture the samples as in the four conditions of Fig. 5 (a)-(d). In Fig. 5 (a) and (b), pig face, pig buttock were directly facing the lens, at this time, images of pig face and buttock were acquired, and in Fig. 5 (c) and (d), sides of pigs were directly facing the lens, at this time, images of sides of pigs were acquired.

Procedures of pig face detection algorithm

The procedures of pig face detection algorithm were as follows.

(1) All the pixel differences of adjacent frames transmitted by the vertical camera were calculated to judge whether pigs had entered the acquisition area;

(2) If the judgment result was true, the adjacent frames were extracted, and then the difference values of all pixel points were calculated, thus the pig body was determined. The theoretical value of pixel points outside the area was 0, with small fluctuations;

(3) The RGB value of each pixel of the pig body was extracted to get the sum, and then it was assigned to the variable r;

(4) The pixels were confirmed to be within the threshold value t of pig body;

(5) Pig body area could be determined when r was larger than the threshold value t;

(6) The pixel points were traversed, and the row and column coordinates (i, j) of the pixels of the pig body area and count s were saved in the array m;

(7) The row coordinates i_1, i_2 and column coordinates j_1, j_2 of the center points a and b of each of the s/2 pixel in the front and at the back were calculated;

(8) The slope k of ligature between a and b was calculated;

(9) Whether the slope k was within the threshold of acquirable slope was judged, and if the result was true, then the pig face was acquired; if the result was false, no operation would be done.

In pig face detection algorithm, the slope k needed to be determined, and its calculation formula was

$$k = \frac{y_2 - y_1}{x_2 - x_1} \quad (1)$$

where: x_1 represents value of row-coordinates of the pixels in the centre point of the s/2 figure in the front of the pig figure, [pixel];

x_2 represents value of row-coordinates of the pixels in the centre point of the s/2 figure at the back of the pig figure, [pixel];

y_1 represents value of column-coordinates of the pixels in the centre point of the s/2 figure in the front of the pig figure, [pixel];

y_2 represents value of column-coordinates of the pixels in the centre point of the s/2 figure at the back of the pig figure, [pixel].

The coordinates of the centre point on the back of the pig body were calculated according to the following formula

$$x = \sum_{i=0}^{s/2} I_i / s/2 \quad (2)$$

$$y = \sum_{i=0}^{s/2} j_i / s/2 \quad (3)$$

where: x represents row-coordinate of the centre point of the pig figure, [pixel];

y represents column-coordinate of the centre point of the pig figure, [pixel];

i represents serial number of pixel points in the front half of the pig figure, [a];

I_i represents row-coordinate of the pixel point i in the pig figure, [pixel];

J_i represents column-coordinate of the pixel point i in the pig figure, [pixel];

s represents total number of pixels in the front half of the pig figure, [a].

As for determination of threshold t in pig body area, the values of the pixels outside the pig figure were 0 in ideal conditions, and when the t value determined in the test was between 90 and 120, signals of pig figures that met the test requirements could be received. The effect of pig face acquired was as shown in Fig. 7. When k was of infinity, the following categories could be obtained: Fig. 7(a), (b) and (c) show the pig face image, the pig buttock image and the pig side image, respectively. When $\sqrt{3} < k < \infty$, the pig face sample acquired was tilted at a certain angle from the camera at the horizontal level, as seen in Fig. 7(d). When $k < \sqrt{3}$, the detection program would not start, and no pig face image would be acquired.

a) Pig front view *b) Pig buttocks photo* *c) Pig side view* *d) Pig side face photo*

Fig. 7 - Right Face, Lateral Face and Non-face Acquisition Conditions of Images for Pig Samples

Supplementary light system module

Structural design for supplementary light mode

Under the influence of weather and other factors, the images acquired were not with even light intensity, but the phenomenon of uneven light intensity could be eliminated by supplementary light. The structure diagram of the supplementary light system was as shown in Fig. 8. The supplementary light bulb was controlled by the output signal of L298 double-bridge module which sent high and low level according to the signals transmitted from the open mv3 digital camera. If the I/O port received a high level, it would control the L298 double-bridge module to turn on the supplementary light bulb; if the low level was received, it would not turn on the supplementary light bulb. The value of the image brightness was calculated according to the pixel information of the pig face image transmitted by the camera, and it was compared with the set threshold value to judge whether the high level or low level would be sent to the L298n double-bridge module.

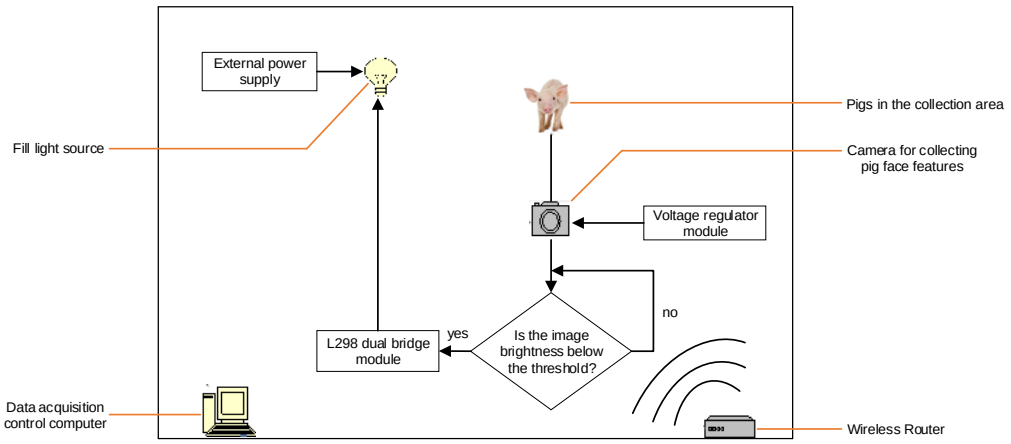

Fig. 8 - Structure Diagram of the Supplementary Light System

Design principle of supplementary light mode and its realization

After samples were acquired by the digital cameras, to obtain uniform brightness values, the values of four thousand pixels evenly distributed in the image of samples were calculated. When the value was less than the threshold value of brightness, high level signals were transmitted. The I/O port received the high level signal to control the switch controller of the supplementary light bulb and start the light source before continuing to acquire images and save them in the frame sequence.

As to the determination principle of the brightness of pig face samples, the pig images were transmitted to the image sensor, and each image point of the image sensor corresponded to a photosensitive element. After receiving the light, the element could generate an electric current. The current intensity was linearly related to the intensity of the light. The induced current converted the digital signal of the output image via the signal amplifier and A/D converter. The RGB value of image points with different light intensity was different, and the value of high intensity was larger than that of ordinary intensity and low intensity. By comparison, it was found that the value of pixels was around 90 under low light intensity, while the value was around 120 under high intensity. Samples acquired in this range was applicable, therefore, the supplementary light threshold was set to be 90. All the digital signals generated by all the photographic units of the camera were all the data of the image. The calculation formula for image brightness was

$$r = \sum_{i=0}^{h} i \sum_{j=0}^{w} j \, RGB(R, 0, 0) \tag{4}$$

where: r represents brightness value of pixels, [pixel];
h represents height of image, [pixel];
w represents width of image, [pixel];
RGB represents colour function.

Fig. 9 (a), (b) and (c) show pig face samples acquired in conditions of r<90, r>120 and 90< r<120, respectively. After supplementary light treatment, the brightness of pig face samples was uniform and the applicability was strong.

a. Light intensity is less than the threshold b. Light is stronger than the threshold c. Normal light intensity

Fig. 9 - Samples with Different Light Intensity

RESULTS AND DISCUSSION

In order to test the effect of this algorithm and system, the face data of pigs were collected in three breeding places, and the results were as shown in Table 1. The calculation formula for image collection efficiency was:

$$e = \frac{a+b}{a+b+c} \times 100\% \quad (5)$$

where: a represents the number of frontal pictures of pig faces, [a];
b represents the number of side pictures of the pig's face, [a];
c represents the number of pictures of pig buttocks, [a];
$a+b$ represents the number of pictures of valid picture, [a].

Table 1

Pig face data collection results

Breeding base	a [a]	b [a]	c[a]	a+b [a]	e [%]
The College of Animal Science	968	2903	111	3,871	97.21
Wujiazhuang	377	2061	205	2,438	92.24
Dongsongjiazhuang	1099	2117	199	3,216	94.17

The algorithm and system as used to collect live pig face data with the data collection equipment on three pig farms. A total of 3,982 pieces of live pig face data were collected at the Pig Breeding Experimental Base (112º57′E, 37º42′N) of the College of Animal Science, Shanxi Agricultural University, Shanxi Province, China, among which 3,871 were suitable for follow-up research (live pig face detection, live pig face recognition), with an effective rate reaching 97.21%; a total of 2,643 pieces of live pig face data were collected on the small pig farm in Wujiazhuang (112º53′E, 37º38′N), Taigu District, Jinzhong City, Shanxi Province, China, among which 2,438 were suitable for follow-up research, with an effective rate reaching 92.24%; at the same time, a total of 3,415 pieces of live pig face data were collected in Dongsongjiazhuang (111º95′E, 37º26′N), Jicun Town, Fenyang City, Shanxi Province, China, among which 3,216 were suitable for follow-up research, with an effective rate reaching 94.17%. With the total effective rate of data collected on the three farms reaching 94.54%, it is indicated that the algorithm and system has positive significance for the automatic construction of data sets on live pig face.

CONCLUSIONS

In this study, double open mv3 digital cameras were adopted to conduct pig face detection, which has certain universality and provides certain reference for solving the data acquisition problem in the field of animal individual recognition. Moreover, a supplementary light system was designed to solve the problem of uneven light intensity in the image acquisition process. The conclusions of the study are as follows:

(1) Double open mv3 digital cameras can be adopted to detect pig faces, and the vertical camera can be used to obtain the slope of the back area of the pig body to judge whether the pig faces are in the acquirable range. The test shows that when the slope is more than $\sqrt{3}$, pig faces meeting the requirement can be acquired.

(2) The threshold value of pig body figure can be set between 90 and 120. If it is less than 90, the image acquired will be dim, at this time, the supplementary light system can be started for supplementing the light. If it is more than 120, the image acquired will be bright, and at this time, the images shall be discarded and image acquisition shall be restarted.

(3) Open mv3 and L298 can be adopted to control the supplementary light system. When the brightness value of the pig face sample is less than 90, open mv3 will send high level to the L298 module to start the supplementary light system, which can solve the problem of low brightness of the sample image.

ACKNOWLEDGEMENTS

This research, titled ‘Pig Face Detection Algorithm and Supplementary Light System Design Based on Open mv3’, was funded by the National Key Research and Development Plan of China (2016YFD0701801), the National Natural Science Foundation of China (31772651), the Doctor Scientific Research Foundation of Shanxi Agricultural University (2020BQ14). The authors are grateful and honoured to have obtained support from the Key Laboratory of Biomechanics.

REFERENCES

[1] Afkham H.M., Targhi, A.T., Eklundh, J.O. et al., (2009), A*nimal Recognition using Joint Visual Vocabulary*, pp. 2019-2022, IEEE, New York /USA;

[2] Ahrendt P., Gregersen T., Karstoft H., (2011), Development of a real-time computer vision system for tracking loose-housed pigs, *Computers and Electronics in Agriculture*, Vol.76, Issue 2, pp.169-174, Elsevier, Oxford/England;

[3] Chen C., Zhu W.X., Ma C.H. et al., (2017), Image motion feature extraction for recognition of aggressive behaviours among group-housed pigs, *Computers and Electronics in Agriculture*, Vol.142, pp.380-387, Elsevier, Oxford/England;

[4] Crouse D., Jacobs R.L., Richardson Z. et al., (2017), LemurFaceID: a face recognition system to facilitate individual identification of lemurs, *BMC Zoology*, Vol.2, Article Number: UNSP 2, BMC, CAMPUS, 4 CRINAN ST, London/ England;

[5] Fan Y.Y., (2018), *Design and Implementation of Facial Recognition of Gold Monkey based on Attention Mechanism*, MSc thesis, Xidian University, Xi'an/China;

[6] Fang N., (2017), *Research and Implementation of Gold Monkey Recognition based on Convolutional Neural Network*, MSc thesis, Xidian University, Xi'an/China;

[7] Freytag A., Rodner E., Simon M. et al., (2016), Chimpanzee faces in the wild: Log-Euclidean CNNs for predicting identities and attributes of primates, *German Conference on Pattern Recognition*, pp. 51-63, Springer, Hannover/Germany;

[8] Guo Y.Z., Zhu W.X., Jiao P.P. et al., (2015), Multi-object extraction from topview group-housed pig images based on adaptive partitioning and multilevel thresholding segmentation, *Biosystems Engineering*, Vol.135, pp.54-60, Elsevier, San Diego/USA;

[9] Guo Y.Z., Zhu W X., Jiao P.P. et al., (2014), Foreground detection of group-housed pigs based on the combination of Mixture of Gaussians using prediction mechanism and threshold segmentation, *Biosystems Engineering*, Vol.125, pp.98-104, Elsevier, San Diego/USA;

[10] Haladjian J., Ermis A., Hodaie Z. et al., (2017), iPig: Towards Tracking the Behaviour of Free-roaming Pigs, *ACI2017 Proceedings of the Fourth International Conference on Animal-Computer Interaction*, pp.10.1-10.5, ACM, Milton Keynes/UK;

[11] Hu X., (2019), *Research and Implementation of Gold Monkey Face Recognition Software based on Deep Learning*, MSc thesis, Xidian University, Xi'an/China;

[12] Hughes B., Burghardt T. (2015), Automated Identification of Individual Great White Sharks from Unrestricted Fin Imagery, *Proceedings of the British Machine Vision Conference 2015*, pp:92.1-92.14, BMVA Press, Swansea/UK;

[13] Kim J., Choi Y., Ju M. et al., (2017), Lying-Pig Detection using Depth Information, *ICACS '17 Proceedings of the International Conference on Algorithms*, *Computing and Systems*, ,pp.40-43, ACM, New York/USA;

[14] Li Y., Sun L.Q., Zou Y.B. et al. (2017), Detection method of moving object pig based on difference method and energy minimization, International Agricultural Engineering Journal. Vol.26, Issue 3, pp.428-438, AAAE, Beijing/China;

[15] Ma C.H., Li M., Zhu W.X. et al., (2016), Pig target extraction based on adaptive elliptic block and wavelet edge detection. *ICSPS 2016 Proceedings of the 8th International Conference on Signal Processing Systems*, pp.11-15, ACM, New York/USA;

[16] Nasirahmadi A., Hensel O., Edwards S.A. et al., (2016), Automatic detection of mounting behaviours among pigs using image analysis, *Computers and Electronics in Agriculture*, Vol.124, pp.295-302, Elsevier, Oxford/England;

[17] Parkhi O.M., Vedaldi A., Zisserman A., Jawahar C.V., (2012), Cats and dogs, *Computer Vision and Pattern Recognition (CVPR)*, pp. 3498-3505, IEEE Computer Society, RI/USA;

[18] Pérezluque A.J., Bareaazcón J.M., ÁlvarezRuiz L. et al., (2016), Dataset of Passerine bird communities in a Mediterranean high mountain (Sierra Nevada, Spain), *Zookeys*, Issue 552, pp.137-154, Pensoft Publ, 12 Prof Georgi Zlatarski ST, Sofia/Bulgaria.

MAIZE STRAW CUTTING PROCESS MODELLING AND PARAMETER CALIBRATION BASED ON DISCRETE ELEMENT METHOD (DEM)
/
基于离散元法的玉米秸秆切断模型构建及参数标定

Zhiqi Zheng[1)], Hongbo Zhao[1)], Peng Liu [2)], Jin He[*2)] [1]
[1)] College of Mechanical and Electronic Engineering, Northwest A&F University, Yangling 712100, China;
[2)] College of Engineering, China Agricultural University, Beijing 100083, China;
Tel: +8610 62737300; E-mail: hejin@cau.edu.cn
DOI: https://doi.org/10.35633/inmateh-63-47

Keywords: *maize straw, DEM, cut, parameter calibration, cohesion*

ABSTRACT

In order to simulate straw cutting process, this paper established a maize straw cutting model with discrete element method (DEM) based on straw cutting experiment. Firstly, maize straw model consisting of several small particles was established by DEM. Then, a straw cutting experiment was conducted and the maximum straw cutting resistance was 199 N for straw with 15 mm diameter. Then, single-factor experiment was conducted to analyze the effect of DEM parameters on straw cutting effect and the max straw cutting resistance F_{max}. The normal stiffness between particles and blade (ball-facet-kn) and shear stiffness between particles and blade (ball-facet-ks) were found to be the significant factors affecting F_{max}, and the value of the parameters that has no significance was determined. The optimum combination of the significant parameters was 17662 $N \cdot m^{-1}$ of ball-facet-kn and 52499 $N \cdot m^{-1}$ of ball-facet-ks. The verification test results showed that the maize straw model was cut off, thus it could simulate the real straw cutting effect, and the relative error of max straw cutting resistance F_{max} between the simulation and the experiment was below 9.1%. Thus, it could be concluded that the established maize straw cutting model was accurate and reliable.

摘要

玉米秸秆切断是秸秆粉碎还田、少免耕播种等作业中重要的技术环节之一，对玉米秸秆进行离散元建模及参数标定，有利于更好地理解分析玉米秸秆切断行为。本文首先利用万能材料试验机进行秸秆切断试验，测得秸秆最大切断力。其次通过单因素试验，分析不同离散元模型参数对玉米秸秆切断效果及最大切断力的影响，筛选出对玉米秸秆模型最大切断力有显著影响的参数为颗粒墙体间法向刚度 ball-facet-kn 与切向刚度 ball-facet-ks，并确定了其他非显著因素的值。通过最陡爬坡试验确定了这两个关键参数的最优区间，在此基础上，根据中心旋转组合试验建立了最大切断力与显著性参数的二阶线性回归模型。通过 Design-Expert 优化模块，以最大切断力为目标，得出显著性参数的最佳组合为：颗粒墙体间法向刚度和切向刚度分别为 17662 和 52499 $N \cdot m^{-1}$。最优参数组合验证试验表明，秸秆模型和秸秆颗粒之间粘结键被从中间切断，所校核参数模型可模拟真实切断效果，且不同直径秸秆最大切断力仿真值与试验值误差不超过 9.1%，所建立秸秆模型准确可靠。研究结果可为少免耕播种、秸秆还田中玉米秸秆切断过程研究提供参考。

INTRODUCTION

Straw returning is a technology that returns the post-harvest straw into field directly or indirectly. Straw returning could improve soil structure, enhance soil fertility, reduce straw burning, etc. (*Wang et al., 2017; Liu et al., 2019; Gao et al., 2004; Yu et al., 2014*). In straw returning, the straw touching parts of the straw smashing or no/minimum till seeding machinery, such as rotary blades and smashing blades interact with straw, so as to cut them off into small pieces (*Zhang et al., 2018*). Therefore, it is necessary to investigate the straw cutting process to improve straw returning quality.

The traditional straw cutting experiment is restricted by farming season and high economic cost. The discrete element method (DEM), a computer simulation technology which is used to analyze the dynamic characteristics of the target through discrete particles, has been more and more popular in agricultural machinery research. It is fast, economic and convenient to record minor behaviour of agricultural materials (*Shmulevich, 2010*).

[1] *Zhiqi Zheng, Ph.D.; Hongbo Zhao, Ph.D.; Peng Liu, Ph.D. Stud.; Jin He, Prof.*

Modelling the straw cutting process by DEM could help to understand the straw cutting behavior and provide theory basis for the development of straw returning machine and no/minimum till seeders.

A set of research were conducted on the DEM modelling of crop straw, *Zhang et al. (2018)* and *Huo et al. (2011)* calibrated repose angle and restitution coefficient of straw model; *Bart Lenaerts et al. (2016), Leblicq et al. (2014)* and *Liu et al. (2018)* established bendable straw model with flexibility to simulate the straw deformation process. *Liao et al. (2020)* simulated the chopping process of fodder rape crop straw in bolting stage. *Zhang et al. (2019)* modelled the straw kneading and crushing process. However, seldom research was done on the maize straw cutting process and the calibration of relevant parameters.

Therefore, this paper intended to establish a straw cutting model based on DEM, and simulate the straw cutting process, analyze the key parameters' effect on straw cutting effect and straw cutting force, and calibrate the DEM parameters.

MATERIALS AND METHODS

Basic parameters of the maize straw

The straw sample (Fig.1) was taken right after maize harvesting from an experiment station of China Agricultural University located at Zhuozhou city, Hebei province (115°56′E, 39°28′N), the maize variety Huaiyu 20 was commonly planted around Zhuozhou city. The average water content of the straw sample was 17.2%, and the average diameter was 15mm.

Fig. 1 - Straw samples to be tested

Establishment of the straw DEM model

The straw model was established with the DEM software PFC^{3D}5.0 (*Itasca, 2017*). In PFC^{3D}5.0, there were two major elements: balls and walls. Agricultural materials can be modeled by balls or ball agglomerates, agricultural machinery or its components can be modeled by combination of walls. Considering the complexity of straw physical composition, it is difficult to establish model in real structure. According to the previous literature, the DEM straw model was established in isotropy with small particles. The contact model between straw particles adopted the parallel bond model, which could bond the adjacent particles together when their distance is in a limited range. And only if the stress exceeds the default value, the bond breaks and particles separate, which could simulate the straw cutting behaviour. Firstly, a cylinder wall with 15mm diameter and 120mm length was established, then the cylinder wall was filled up with particles having 1.8mm diameter. After the initial unbalance force of the particles dissipated, the cylinder wall was deleted and cohesion was endowed between particles to bond together, then the straw model was established as shown in Fig.2.

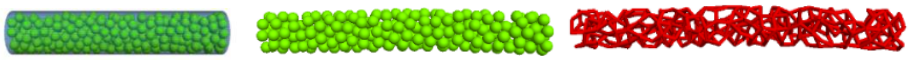

a) *b)* *(c)*

Fig.2 - Establishment of DEM cutting straw model

a) generation of particles in the cylinder to model the straw; b) straw model with cohesion; c) the parallel bond between particles

Experiment methods

Firstly, the universal material test machine was used to conduct the straw cutting experiment, in order to observe the straw cutting process and determine the straw cutting force. Secondly, single factor simulation experiment was conducted to screen out the DEM parameters preliminarily, calibrate the parameters with no significance and find the parameters that have significant influence on straw cutting forces and effect (*Mak et al., 2012*), then the steepest ascent test was conducted to find out the appropriate range for the significant parameters (*Yuan et al., 2018; Liu et al., 2016*). After that, regression model between max straw cutting force and the significant parameters was confirmed by a Box-Behnken test. At last, the best fit value of the key parameters was archived by finding out the optimum outcome of the regression model. Then, a comparison experiment was carried out to compare the max straw cutting force and straw cutting effect between the simulation and physical experiment, to verify the accuracy of the calibrated parameters' values.

Basic parameters of the DEM straw model

As listed in Table 1, 12 parameters are concluded in this parallel bond DEM model. The friction coefficient between straw and wall, straw density, normal and shear damping coefficient index, bond radius were taken from previous literatures (*Fang et al., 2016; Lu et al., 2016; Li et al., 2016*). Through preliminary experiment, it was found that the other 8 parameters may influence straw cutting force and straw cutting effect, so single factor experiment was done and their values are presumed at a large range.

Table 1

Key parameters of maize straw model

Parameters	Value
Density /(kg/m^3)	243
Shear stiffness of the particle ball-ball-kn/ (N·m^{-1})	5~5e5
Normal stiffness of the particle ball-ball-ks/ (N·m^{-1})	5~5e5
Friction coefficient between straw and wall μ	0.35
Shear critical damping coefficient βn	0.5
Normal critical damping coefficient Bs	1
Tensile strength of the bond pb_ten / Pa	5e2~5e6
Cohesion strength of the bond pb_coh/ Pa	1e3~1e7
Normal stiffness of the bond pb_kn/ (N·m^{-1})	2e5~2e9
Shear stiffness of the bond pb_ks/ (N·m-1)	2e5~2e9
Shear stiffness between particle and wall ball-facet-kn/ (N·m^{-1})	2e2~2e6
Normal stiffness between particle and wall ball-facet-ks/ (N·m^{-1})	1e3~1e7
Bonding radius index	0.5

Straw cutting experiment

The straw cutting experiment was conducted using a universal material testing machine (Fig.3). It is developed by Ruigeer Technology Company in Shenzhen and it is a RGM4005 type digital electronic universal material testing machine. To start the experiment, the straw sample was fixed in the fixture first and loaded on the blade, then the blade moved downward and the straw sample was cut off. The straw cutting force can be obtained in the universal material testing machine. The blade material was normal steel with 3mm thickness and 30° throat angle; it moved 60mm/min. The experiment was replicated 30 times.

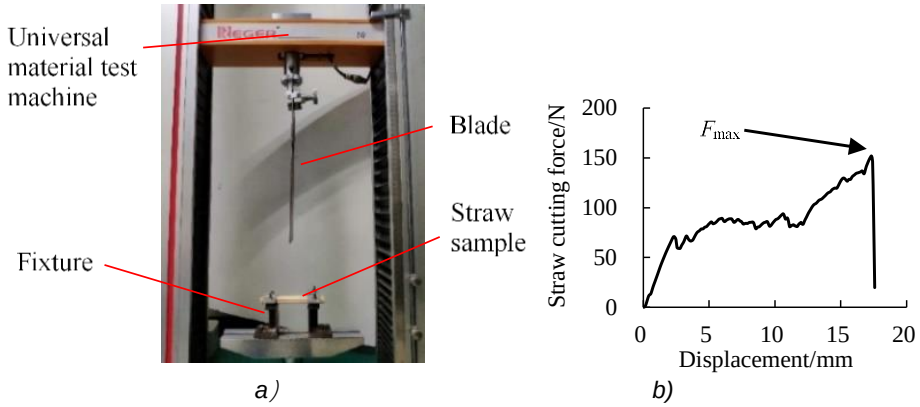

Fig. 3 - Straw cutting experiment

a) Universal material testing machine; b) Real-time straw cutting force

Observing the straw cutting process, the typical resistance variation of the blade can be drawn as Fig.3. The displacement of the blade when it interacted with straw was 0, with the blade moved downward, the blade resistance increased along to the maximum value, when the straw was cut off. Then the blade resistance decreased dramatically and the universal material testing machine stopped operating. The average maximum straw cutting force was 199N from the 30 times experiment.

Establishment of the straw cutting model to calibrate DEM parameters

In order to mimic the straw cutting process and the blade resistance, a straw cutting model was established as shown in Fig.4.

The blade model was first established in SolidWorks software and then imported into DEM software to generate the DEM blade model, its thickness and angle of throat were kept the same within the experiment. The straw model established in chapter 1.1 was fixed by four walls, certain velocity was given to the walls to fix the straw. Then the blade model moved downward in a velocity of 60mm/min to cut off the straw, during which the straw cutting process could be monitored and the straw cutting force could be recorded.

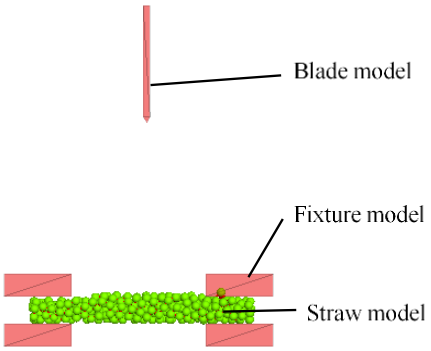

Fig. 4 - DEM simulation of straw cutting

RESULTS AND DISCUSSION

The selection of significant factor by single factor experiment

In order to analyze the effect of the 8 DEM parameters on straw cutting performance and pick out the factors with significant influence, single factor experiment with DEM simulation was conducted. In the simulation experiment, the test factor was changed with different values while the other factors' value was fixed, and the effect on maximum straw cutting force and straw cutting effect of the 8 DEM parameters were examined. The initial factor value of the ball-ball-ks was 500 N·m-1, ball-facet-kn was 2×10^4 N·m^{-1}, ball-facet-ks was 1×10^5 N·m^{-1}, pb_kn was 2×10^7 N·m-1, pb_ks was 2×10^7 N·m^{-1}, pb_ten was 1×10^5 Pa, pb_coh was 5×10^4 Pa. Via the built-in command, random seed can be changed to generate three straw model so that 3-time replicate simulation experiment can be conducted to eliminate experiment error. The effect of these 8 factors on straw cutting force was shown in Fig.5, and the significance analysis was listed in table 2.

Table 2

Significance analysis of different DEM parameters

Simulation factors	F	P value	Significance
Ball-ball-kn	0.12	0.97	
Ball-ball-ks	0.18	0.94	
Ball-facet-kn	23.27	4.7E-05	**
Ball-facet-ks	65.82	3.8E-07	**
Pb_kn	0.17	0.95	
Pb_ks	0.07	0.99	
Pb_ten	0.02	0.99	
Pb_coh	0.02	0.99	

**indicates significant, p<0.05, ** indicates highly significant, p<0.01*

The normal stiffness of the particle ball-ball-kn and shear stiffness of the particle ball-ball-ks represent normal and shear stiffness between the particles which consist in the straw model. During the experiment, the ball-ball-kn value from 5 to 5×10^4 N·m^{-1} was increased while other factors were kept unchanged. Results showed that with the increase of ball-ball-kn, the maximum straw cutting force increased slowly with no significance. It can be observed that the straw cutting effect at 5×10^3 N·m^{-1} was closer to the real experiment than that at 500 N·m^{-1}, thus the value of ball-ball-kn was chosen 5×10^3 N·m^{-1}. The ball-ball-ks value had no significant influence on maximum straw cutting force either, and had similar influence on straw cutting effect, so its value was chosen 5×10^3 N·m^{-1} with synthesis analysis.

Normal stiffness between particle and wall and shear stiffness between particle and wall represent the contact parameters between blade and straw particles in the straw cutting process, both of which have vital influence on the contact force between blade and straw model. Both of the two parameters had highly significant influence on maximum straw cutting force ($p<0.01$). With ball-facet-kn increased from 200 to 2×10^6

N·m-1, the maximum straw cutting force displayed an exponential growth from 9N to 16412N, so ball-facet-kn had the greatest influence among the 8 parameters. The maximum straw cutting force was 203N when the ball-facet-kn value was 2×10^4 N, which was the closest to the target value.

With the increase of ball-facet-ks from 1×10^3 N·m^{-1} to 1×10^7, the maximum straw cutting force increased from 169N to 775N, the maximum straw cutting force reached 203N when ball-facet-ks was 1×10^5. These two parameters had the biggest influence on maximum straw cutting force; it is necessary to calibrate them further.

Having the other factors fixed, with the increase of pb_kn, the maximum straw cutting force fluctuated in a small range with no significance. When it was at low value of 2×10^5 or 2×10^6 N·m^{-1}, the straw model could not be cut off, and when the value was bigger than 2×10^8 N·m^{-1}, the straw cutting effect was different from the real situation. With the increase of pb ks, the maximum straw cutting force increased first and then decreased in a small range with no significance. When the pb_ks value was low 2×10^5 N·m^{-1}, straw could be cut off, but when it was bigger than 2×10^9 N·m^{-1}, it seemed unreal. By synthesis analysis, the values of the two factors were both set as 2×10^7 N·m^{-1} which could ensure a straw cutting effect close to the real experiment.

With the other factors fixed, neither pb_ten, nor pb_coh had significant influence on the maximum straw cutting force. It can be observed from the straw cutting process that when the pb_ten value was too low (500 or 5×10^3 Pa) or when the pb_coh value was too low (1×10^3 or 1×10^4 Pa), the straw cutting effect could not be simulated. When the pb_ten was too high, the straw model could not be cut off, but when the pb_coh value was too high, the straw model could still be cut off. By synthesis analysis, the pb_ten and pb_coh were set as 5×10^4 Pa and 1×10^5 Pa respectively.

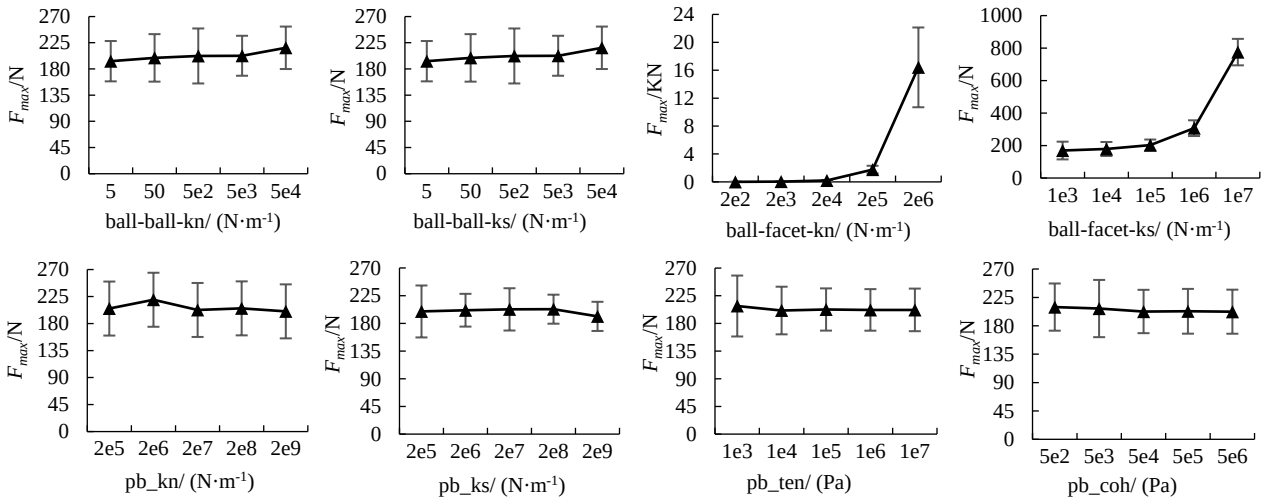

Fig. 5 - Effect of different DEM parameters on the max cutting force

The steepest ascent test to determine the optimum range of the factor value

The steepest ascent test was conducted to determine the optimum range of the significant factors of ball-facet-kn and ball-facet-ks. During the simulation experiment, the value of the two factors was increased step by step, the experiment scheme and results were shown in Table3. With the increase of ball-facet-kn and ball-facet-ks, the maximum straw cutting force increased gradually, the relative error between the simulation value and experiment value of the maximum straw cutting force decreased first and increased after. The smallest relative error of 10.4% occurred in the third simulation experiment, so the optimum range of the factor value was around the third simulation experiment. Therefore, central composite experiment was conducted in the next chapter with the second to fourth experiment factor values, and regression equation would be established to solve the optimum value of these two significant factors.

Table 3

Scheme and results of steepest ascent test

No	ball-facet-kn	ball-facet-ks	F_{max}/N	Relative error /%
1	1e4	5e4	111	79.3
2	1.5e4	7.5e4	167	19.2
3	2e4	1e5	222	10.4
4	2.5e4	1.25e5	278	28.4
5	3e4	1.5e5	327	39.1

Central composite experiment and regression model

Based on the result of the steepest ascent test, central composite experiment was conducted through Design-Expert 8.0 software and the regression model was established. 5 values were set for each factor, and 5 central points were adopted to estimate the error; coding of central composite design factors was shown in Table4. 13-time experiment repetitions were conducted totally.

Table 4

Coding of central composite design factors

Factors	Level				
	1.414	1	0	-1	-1.414
Ball-facet-kn	27071	25000	20000	15000	12929
Ball-facet-ks	135355	125000	100000	75000	64645

The experiment scheme and results were shown in Table 5. Design-Expert 8.0 software was used to do the variance analysis (Table 6). It can be seen that both ball-facet-kn and ball-facet-ks had highly significant influence on the maximum straw cutting force ($P < 0.01$), and the linear regression model was also highly significant. So the experiments were reasonable and effective, with all relative significant factors considered. After eliminating the factors with no significance, a well matching regression equation with practical analysis meaning can be drawn. In the regression equation, R represents the maximum straw cutting force, A and B represents ball-facet-kn and ball-facet-ks respectively. The final regression equation after being optimized was

$$R = 188.5652174 + 45.2006403 \times A + 7.424621202 \times B - 6 \times A \times B + 4.456521739 \times A^2 - 6.924621202 \times A^2 \times B$$

Through the optimization module of Design-Expert 8.0 software, the maximum straw cutting force Fmax was set as the target (199N), the optimized regression equation was put into the optimization module of Design-Expert, the best combination value of ball-facet-kn and ball-facet-ks was 17662 $N \cdot m^{-1}$ and 52499 $N \cdot m^{-1}$, respectively.

Table 5

Scheme and results of central composite design

No.	Ball-facet-kn	Ball-facet-ks	F_{max}
1	-1	1	176
2	0	0	189
3	-1.414	0	133
4	-1	-1	189
5	0	0	245
6	0	0	155
7	1	-1	260
8	0	-1.414	197
9	0	1.414	234
10	0	0	189
11	1	1	189
12	1.414	0	142
13	0	0	189

Table 6

ANOVA of central composite design quadratic model

Source	Freedom	mean sum of square	P value
Model		16851	< 0.0001
Ball-facet-kn	1	16345	< 0.0001
Ball-facet--ks	1	221	< 0.0001
AB	1	144	< 0.0001
A^2	1	141	0.0001/
B^2	1	-	-
A^2B	1	96	0.0003

The verification results

Aiming to verify the accuracy of the value of the two significant factors and other factors determined with the single factor experiment, a verification experiment was conducted. Three straw models with diameter of 13, 15 and 17mm were established and straw cutting process was simulated to compare with the real experiment. The final parameters' values of the DEM model were listed in Table 7.

Table 7

Final parameters of DEM maize straw model

Parameters	Value
ball-ball-kn/ (N·m^{-1})	5×10^3
ball-ball-ks/ (N·m^{-1})	5×10^3
pb_ten / Pa	5×10^4
pb_coh/ Pa	1×10^5
pb_kn/ (N·m^{-1})	2×10^7
pb_ks/ (N·m^{-1})	2×10^7
ball-facet-kn/ (N·m^{-1})	17662
ball-facet-ks/ (N·m^{-1})	52499

The cutting process of the real straw, the DEM straw model and the bond between straw particles were shown in Fig.6. The straw cutting process showed great resemblance between the simulation and the real experiment. The maximum straw cutting forces of the simulation and the experiment were shown in Table 8.

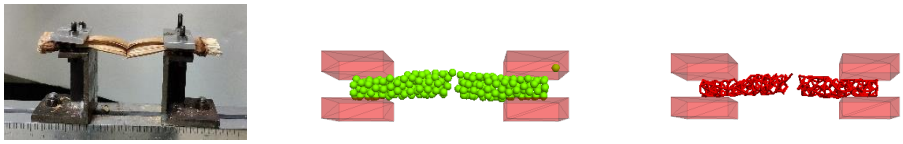

a) b) c)

Fig.6 - Comparison on the straw cutting effect of experiment and simulation

a) Real straw cutting process b) Simulation of straw cutting process c) Simulation of bond cutting process

The relative error of the maximum straw cutting force with different diameters between the simulation and the experiment was below 9.1%, and the maximum straw cutting force showed good linear relation with straw diameter, indicating the accuracy and reliability of the established DEM straw cutting model.

Table 8

Blade resistance in straw cutting simulation

Parameters	Straw diameter /mm		
	13	15	17
The maximum straw cutting force of experiment /N	151	199	241
The maximum straw cutting force of simulation/N	146	184	219
Relative error/%	3.3	7.5	9.1

CONCLUSIONS

A DEM straw model was established based on straw cutting experiment. Firstly, the maximum straw cutting force of the 15mm straw was determined as 199N. Secondly, single factor experiment was used to confirm the factors with significant influence on the maximum straw cutting force namely ball-facet-kn and ball-facet-ks, while other parameters' value was determined, 5×10^3 N·m^{-1} of ball-ball-kn and ball-ball-ks, 2×10^7 N·m^{-1} of pb_kn and pb_ks, 1×10^5 Pa of pb_coh and 5×10^4 Pa of pb_ten.

Regression model was established between the maximum straw cutting force and the significant factors and the regression model was also significant. The best combination value of ball-facet-kn and ball-facet-ks was 17662 N·m^{-1} and 52499 N·m^{-1}. Straw cutting verification experiment was conducted with different straw diameters; the results showed that the established DEM straw model could simulate the straw cutting effect, and the relative error of the maximum straw cutting force between the simulation and the experiment was below 9.1%. So, the conclusion can be drawn that the established DEM straw model was accurate and reliable.

ACKNOWLEDGEMENT

This work was supported by the grant of China Postdoctoral Science Foundation (No. 2020M683578), the National Natural Science Foundation of China (No. 31971803) and the grant of the Fundamental Research Funds for the Central Universities (No. 2452016079).

REFERENCES

[1] Fang H.M., Ji C.Y., Ahmed A.T., Zhang Q.Y., Guo J. (2016). Simulation analysis of straw movement in straw-soil-rotary blade system (秸秆-土壤-旋耕刀系统中秸秆位移仿真分析)[J]. *Transactions of the Chinese Society for Agricultural Machinery*, 47(1): 60-67.

[2] Gao H.W. (2004). *The conservation tillage technology and machinery* (保护性耕作技术与机具)[M]. The Chemical Industry Press, 2004.
[3] Huo L.L., Tian Y.S., Zhao L.X., Yao Z.L., Hou S.L., Meng H.B. (2011). Research on physical property of crop straw and test methods (农作物秸秆原料物理特性及测试方法研究) [J]. *Renewable Energy Resources*, 29(6):86-92.
[4] Itasca. (2017). *User's manual for PFC3D version PFC5.0*. Minneapolis. USA: Itasca consulting Group
[5] Lenaerts B., Aerstsen T., Tijskens E., Ketelaere B., Ramon H., Baerdemaeker J., Saeys W. (2014). Simulation of grain-straw separation by a discrete element approach with bendable straw particles [J]. *Computers and Electronics in Agriculture*, 101(7441): 24-33.
[6] Leblicq T., Smeets B, Ramon H., Saeys W. (2016). A discrete element approach for modelling the compression of crop stems [J]. *Computers & Electronics in Agriculture*, 123(C): 80-88.
[7] Liu F.Y., Zhang J., Chen J. (2018). Modelling of flexible wheat straw by discrete element method and its parameters calibration [J]. *International Journal of Agricultural & Biological Engineering*, 11(3):42-46.
[8] Liu P., He J., Li H.W., Wang Q.J., Lu C.Y., Zheng K., Liu W.Z., Zhao H.B., Lou S.Y. (2019). Effect of Straw Retention on Crop Yield, Soil Properties, Water Use Efficiency and Greenhouse Gas Emission in China: A Meta-Analysis [J]. *International Journal of Plant Production*, 13(71):347-367.
[9] Liao Y.T., Liao Q.X., Zhou Y., Wang Z.T., Jiang Y.J., Liang F. (2020). Parameters Calibration of Discrete Element Model of Fodder Rape Crop Harvest in Bolting Stage (饲料油菜薹期收获茎秆破碎离散元仿真参数标定) [J]. *Transactions of the Chinese Society for Agricultural Machinery*, 51(6):73-82.
[10] Liao Y.T., Wang Z.T., Liao Q.X., Wan X.Y., Zhou Y., Liang F. (2020). Calibration of Discrete Element Model Parameters of Forage Rape Stalk at Early Pod Stage (果荚初期饲料油菜茎秆离散元接触模型参数标定) [J]. *Transactions of the Chinese Society for Agricultural Machinery*, 51(s1):236-243.
[11] Lu C. Y., Zhao C.J., Meng Z.J., Wang X., Wu G.W., Gao N.N. (2015). Straw friction characteristic based on rotary cutting anti-blocking device with slide plate pressing straw (基于滑板压秆旋切式防堵装置的秸秆摩擦特性研究) [J]. *Transactions of the CSAE*, 31(9): 13－18.
[12] Li B., Chen Y., Chen J. (2016). Modelling of soil-claw interaction using the discrete element method (DEM). *Soil Till. Res*. 158, 177-185.
[13] Liu F.Y., Zhang J., Li B., Chen J. (2016). Calibration of parameters of wheat required in discrete element method simulation based on repose angle of particle heap (基于堆积试验的小麦离散元参数分析及标定 [J]. *Transactions of the CSAE*, 32(12): 247－253.
[14] Mak, J., Chen, Y., Sadek, M.A. (2012). Determining parameters of a discrete element model for soil–tool interaction [J]. *Soil and Tillage Research*, 118:117–122.
[15] Shmulevich I. (2010). State of the art modelling of soil-tillage interaction using discrete element method. *Soil Tillage Research*. 111, 41-53.
[16] Wang J.W., Tang H., Wang J.F. (2017). Comprehensive utilization status and development analysis of crop straw resource in Northeast China (东北地区作物秸秆资源综合利用现状与发展分析) [J]. *Transactions of the Chinese Society for Agricultural Machinery*, 48(5):1-21.
[17] Yu K., Feng H., Li Z.P., Wang Z.L. (2014). Effects of different pretreated straw on soil water content and water consumption characteristics of winter wheat (秸秆还田对农田土壤水分与冬小麦耗水特征的影响) [J]. *Transactions of the Chinese Society for Agricultural Machinery*, 45(10):116-123.
[18] Yuan Q.C., Xu L.M., Xing J.J., Duan Z.Z., Ma S., Yu C.C., Chen C. (2018). Parameter calibration of discrete element model of organic fertilizer particles for mechanical fertilization (机施有机肥散体颗粒离散元模型参数标定) [J]. *Transactions of the CSAE,* 34(18): 21－27.
[19] Zhang Z.Q. (2018). *Research on corn straw chopping and spreading machine design and dynamic characteristic of straw* (玉米秸轩粉碎抛撒还田机的设计与秸秆运动特性研究) [D]. China Agric.Univ.
[20] Zhang F.W., Song X.F., Zhang X.K., Zhang F.Y., Wei W.C., Dai F. (2019). Simulation and experiment on mechanical characteristics of kneading and crushing process of corn straw (玉米秸秆揉丝破碎过程力学特性仿真与试验) [J]. *Transactions of the Chinese Society of Agricultural Engineering*, 35(9): 58-65.
Zhang T., Liu F., Zhao M.Q., Ma K., Wang W., Fan Q., Yan P. (2018). Determination of corn stalk contact parameters and calibration of Discrete Element Method simulation (玉米秸秆接触物理参数测定与离散元仿真标定) [J]. *Journal of China Agricultural University*, 23(4): 120-127.

NUMERICAL SIMULATION AND EXPERIMENT OF VIBRATION PELLETIZER BASED ON EDEM

/

基于 EDEM 振动丸化包衣机的数值模拟与试验

Nianzu Dai[1)]; Zhanfeng Hou[1*)]; Yi Qiu[2)]; Xiwen Zhang[1)]

[1)]Inner Mongolia Agricultural University, College of Mechanical and Electrical Engineering, Inner Mongolia, China

[2)]Yangzhou Polytechnic Institute, College of Transportation Engineering, Jiangsu, China

*Tel: 04714309215; *)Corresponding author E-mail: njauhzf@163.com*

DOI: https://doi.org/10.35633/inmateh-63-48

Keywords: *Vibration; Pelleting; Coating machine; Mixing uniformity; EDEM*

ABSTRACT

In order to quantitatively describe the influence between the mixing process and the pelleting quality of the vibration pelletizer, this paper uses EDEM to conduct a numerical simulation study on the uniformity of the seeds and powder mixing of the pelleting machine under vibration force field. Meanwhile, a single factor test was established to verify the feasibility of numerical simulation. The results show that the coefficient of variation CV is the smallest and the mixing uniformity between the seeds and powder is the highest when the vibration frequency is 20Hz, the rotation speed is 45r/min, the tilt angle is 40° during numerical simulation. The pelleting qualified rate J and single seed rate P as the test index of the mixing uniformity of seed pelleting shows the optimum value in the single factor test, EDEM can be used to analyse the mixing uniformity and pelleting quality in pelletizer. The results of orthogonal experiment indicated that the best combination of parameters was obtained as follows: vibration frequency of 20Hz, rotation speed of 45r/min and tilt angle of 40°, the mixing uniformity of seeds and powder and the pelleting quality of Agropyron seeds are the highest. This study can effectively provide reference for design of pelleting machine of small seeds under vibration force field.

摘要

为了定量描述振动丸化包衣机混合过程与丸化包衣质量间的影响规律，本文采用EDEM对丸化包衣机在振动力场作用下的种、粉混合均匀度进行数值模拟研究，同时利用单因素试验验证数值模拟的可行性。结果表明：当丸化包衣机的振动频率、包衣锅转速、包衣锅倾角分别设定为 20Hz 、45r/min、40°时，变异系数Cv在数值模拟过程中均出现最小值，表明种、粉颗粒间达到较优的混合均匀度；丸化合格率J和单籽率P作为种子丸化包衣混合程度的试验评价指标在单因素试验中均表现出最佳值，EDEM可以用于丸化包衣机混合均匀程度及丸化质量的数值模拟分析。正交试验结果得到振动丸化包衣机最优工作参数组合：振动频率 20Hz、包衣锅转速为 45r/min、包衣锅倾角为 40°，在此工作参数组合下种子与粉料能达到较为理想的混合均匀度，冰草种子丸化包衣质量较高，研究结果可为振动作用下小粒种子的丸粒化包衣机设计提供参考依据。

INTRODUCTION

Seed pelleting is a novel type of seed processing technology that uses pelleting equipment to uniformly apply powder, seed coating agent and other additives with specific functions to the surface of seeds to form pelleted seeds, which improved the germination rate and survival rate of seeds (*Wang, 2011; Lei, 2010*). The key to the quality of pelleting depends on the pelleting performance of the pelleting equipment, which is also a significant issue for scholars at home and abroad. The research focus of domestic and foreign scholars on the coating machine is mainly concentrated in the development of pelleting equipment suitable for different types of seeds. However, there are few researchers on the content of pelleting qualified rate, optimization of coating mechanism and working parameters of rotary equipment (*Sang, 2015*).

The main function of the pelleting equipment is to promote the mixing uniformity of materials. Its mixing effect is directly related to the pelleting quality, pelleting qualified rate and single seed rate. Therefore, it is of great significance to study the mixing uniformity between seeds and powder in the coater to improve the quality of the pelleting (*Yang, 2015*).

At present, some scholars have studied the movement law of materials in the drum and the mixing effect between the materials (*Su, 2014; Jiang, 2019*). Due to the complexity of the mixing movement of materials, the special characteristics and opacity of the mixing equipment such as pelleting drums and coaters, it is impossible to dynamically track and detect the mixing process of materials by means of experiments (*Koteswara, 2013*). Therefore, the method of computer numerical simulation is used to study the mixing effect and movement law between materials by many researchers. Discrete Element Method (DEM) proposed by Cundall in 1971 is the most widely used. You Ying established a discrete droplet spray analysis model based on DEM to simulate the effects of working parameters on particle motion and tablet coating uniformity (*You, 2019*). Liu Wenjun used discrete element theory to simulate and analyse the mixing characteristics of materials in coal mine rotary (*Liu, 2017*). Dun Guoqian conducted EDEM simulation on the filling characteristics of different varieties of soybean seeds (*Dun, 2019*). Zhang Tao used DEM theory to study the movement law of the corn population in the seed metering chamber (*Zhang, 2016*). Throughout the above studies, it was found that the mixing between materials is a very complicated physical behaviour, and it is impossible to express the quantitative uniformity of the mixing uniformity. In this paper, the coefficient of variation CV is used as the evaluation index of the mixing uniformity. Besides, the EDEM is used to conduct a numerical simulation study for the mixing uniformity of Agropyron seeds and powder in the vibrating coater. In addition, the mixing effect and law between seeds and powder under different working conditions were compared by simulation and verification experiments, in order to obtain the best combination of parameters of pelleting machine.

MATERIALS AND METHODS

Pelleting machine structure and principle

The pelletizer for Agropyron seed overall structure is shown in Fig.1. It contained seed supply system, powder supply system, liquid supply system, pelleting device, vibration system, and control system. When the pelleting machine is working, seeds and powder are lifted up to the respective hoppers. The seed agent is mixed according to a certain proportion, and is atomized into the coater by high-pressure pump. The coater starts to rotate under the drive of a rotating motor, which drives the Agropyron seeds and powder in the coater to rotate, and there are other complex movements under the action of friction. In this time, the powder is adhered to the surface of the seed due to seed coating agent. Furthermore, powder and seed coating agent continue to be added until the desired seed size is reached, and the whole pelleting process is ended. The driving motor, tilt angle adjustment mechanism and vibration exciter are used to adjust the rotation speed, tilt angle and vibration frequency of the coater respectively.

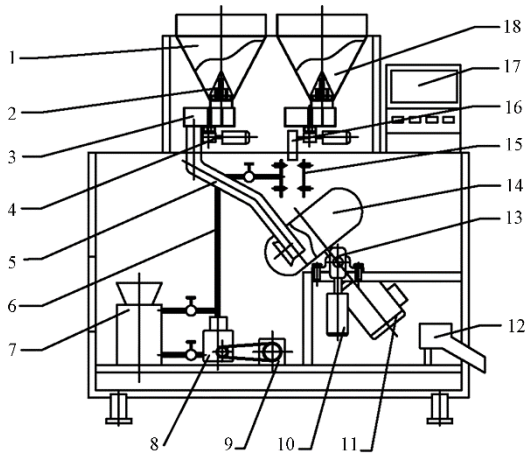

Fig. 1 – Structure figure of the pellet coating machine

1. Powder feed inlet 2. Feed inlet valve 3. Weighing system 4. Step motor 5. Powder conveying pipeline 6. Liquid medicine pipe 7. Liquid medicine storage tank 8. High pressure pump 9. Motor 10. Rotary stepper motor 11. Coater motor 12. Outlet port 13. Electric vibration exciter 14. Coater 15. Nozzles 16. Seed diffuser 17. Controller 18. Seed feed inlet

Basic principles of Discrete Element Method

The force of pelleted seed includes the force between seed and seeds or between seeds and coater. If the coater is equivalent to seeds of infinite diameter, the force between seeds and coater can be uniformly regarded as the force between the seeds and the analysis of force is shown in Fig.2.

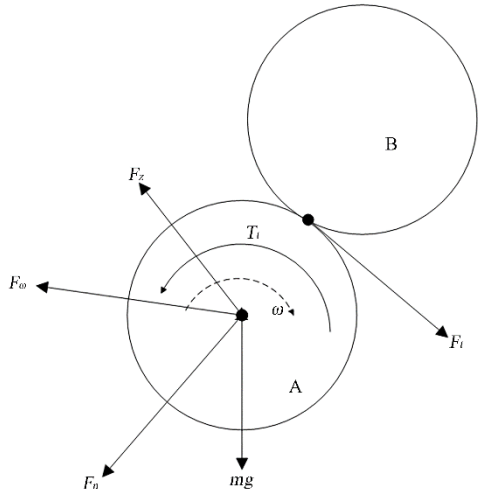

Fig. 2 – Force analysis diagram between the seeds and between the seeds and the coater

It can be seen from Fig.2 that the combined external force ΣF and the combined external moment ΣM of seed i can be expressed by the following equation:

$$\begin{aligned} m_i u_i &= \sum F \\ I_i \alpha_i &= \sum M \end{aligned} \tag{1}$$

where:

u_i - the acceleration of seed particle i, [m/s^2];

α_i - the angular acceleration of seed particle i, [rad/s];

m_i - the mass of seed particle i, [g];

I_i - the rotational inertia of seed particle i, [kg·m^2].

$$\begin{cases} \sum F = F_g + F_r + F_z + \sum_{j=1}^{n_i} \left(F_{n,ij} + F_{t,ij} \right) \\ \sum M = \sum_{j=1}^{n_i} \left(M_{t,ij} + M_{r,ij} \right) \end{cases} \tag{2}$$

In equations (2): F_g - gravity, [N]; F_r - centrifugal force, [N]; F_z-excitation force, [N]; $F_{n,ij}$ - the normal contact force of particle i subjected to particle j, [N]; $F_{t,ij}$ - the tangential contact force of particle i subjected to particle j, [N]; $M_{t,ij}$ - the tangential contact torque of particle i subjected to particle j, [N·m]; $M_{r,ij}$ - the friction torque of particle i subjected to particle j, [N·m]; n_i - the total number of particles in contact with particle i.

Discrete element simulation

Simulation parameter settings

This paper aims at the research of natural Agropyron seeds suitable for growing in arid and semi-arid areas. The intrinsic physical parameters and contact parameters of Agropyron seeds were measured by means of stacking and kinematic experiments. The measurement results are shown in Table 1. The seed particles are modelled and analysed using discrete element simulation software EDEM for three-dimensional solid modelling, and the Agropyron seeds are created by the overlapping of multiple spheres (ellipsoid with a long semi-axis a=2.5mm, short semi-axis b=1.2mm, and a thickness of 2.4mm). The three-dimensional solid model is shown in Fig.3.

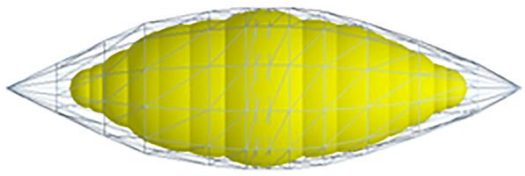

Fig. 3 – Simulation model of Agropyron seeds

EDEM simulation parameters of Agropyron seeds Table 1

Test object	Simulation parameters	Value
Agropyron seed	Density / [kg·m^{-3}]	763
	Shear modulus / [Pa]	1.08×10^{7}
	Poisson's ratio	0.28
Coater	Density / [kg·m^{-3}]	7890
	Shear modulus / [Pa]	7.0×10^{10}
	Poisson's ratio	0.28
Powder	Density / [kg·m^{-3}]	978
	Shear modulus / [Pa]	1.1×10^{7}
	Poisson's ratio	0.25
Seeds and seeds	Coefficient of static friction	0.5
	Coefficient of collision recovery	0.3
Seeds and coater	Coefficient of static friction	0.4
	Coefficient of collision recovery	0.4
Seeds and powder	Coefficient of static friction	0.25
	Coefficient of collision recovery	0.25
Powder and coater	Coefficient of static friction	0.3
	Coefficient of collision recovery	0.3
Powder and powder	Coefficient of static friction	0.25
	Coefficient of collision recovery	0.25

Simulation model of coater

The geometric model of the coater of the Agropyron seed was established using CATIA 3D modelling software in Fig.4. The main parameters of the coater are shown in Table 2.

Basic parameters of pelleting coater Table 2

Item	Units	Parameters
Maximum diameter of coater	mm	400
Calibre of coater	mm	200
Vibration acceleration of coater	m/s^2	9.81

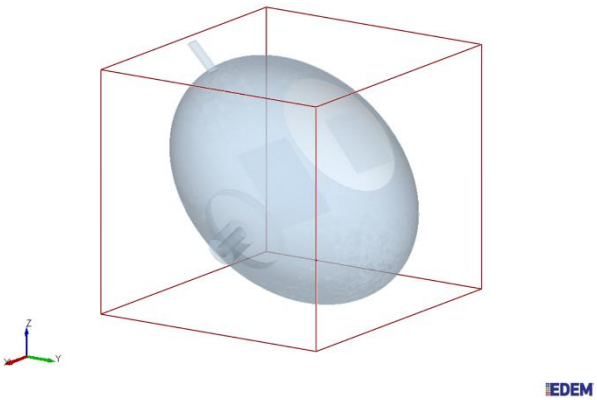

Fig. 4 – The geometric model of Agropyron seed coater

Simulation and experiment of mixing process between seeds and powder

Evaluation parameters of mixing uniformity

In order to be able to quantitatively analyse the mixing uniformity between seeds and powder, the coefficient of variation is used as an evaluation parameter to measure the mixing degree between seeds and powder.

Through the Grid Bin Group module in the selection function in the EDEM post-processing, the entire mixed simulation of seeds and powder is divided into square grids of equal size, as shown in Fig.5. The entire simulation time is set to 15s, the number of seeds and powder particles in each grid is output at a time interval of 3s, and the coefficient of variation of powder particles is calculated.

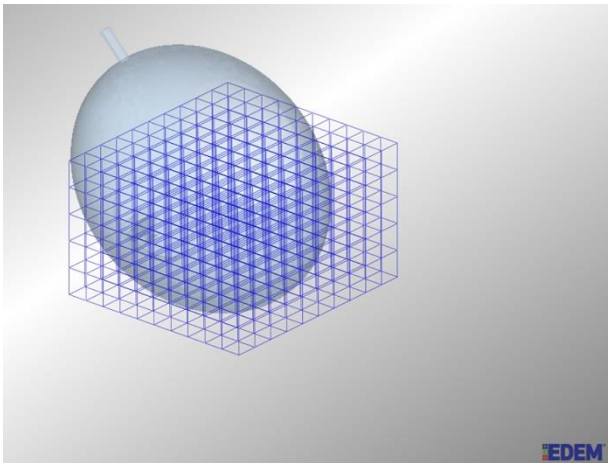

Fig. 5 – Schematic diagram of meshing of EDEM simulation model

Assuming that the total number of divided grids is m, the number of powder particles in the k^{th} grid is b_k, and the total number of seeds and powder particles in the grid is d_k, then the percentage of powder particles in each grid is:

$$g_k = \frac{b_k}{d_k} \tag{3}$$

The theoretical optimal mixing degree ε is:

$$\varepsilon = \frac{\sum_1^m b_k}{\sum_1^m d_k} \tag{4}$$

The dispersion X_k of the powder particles in the *k-th* grid is:

$$X_k = \frac{g_k}{\varepsilon} \tag{5}$$

Then the standard deviation S_x is:

$$S_x = \sqrt{\frac{\sum_1^m \left(X_k - \bar{x}\right)}{m-1}} \tag{6}$$

In equations (6): $\bar{x} = \sum_1^m \frac{X_k}{m}$

Then the coefficient of variation Cv of the powder particles is:

$$C_v = \frac{S_x}{\bar{x}} \tag{7}$$

The coefficient of variation can objectively reflect the degree of mixing uniformity between particles. The smaller the coefficient of variation, the better the mixing uniformity. It has been used to evaluate the axial mixing degree of particles in a rotating device.

In order to verify the reliability of the simulation analysis, the pelleting qualified rate J and the single seed rate P were used as the test evaluation index of the mixing degree of seeds and powder. The coating agent was completely coated on the surface of the seed as pelleting qualified. Only one particle of Agropyron seeds in the pelleted seeds accounted for a percentage of the total number of pelleted seeds tested is called single seed rate.

$$J = \frac{Z_h}{Z_b + Z_h} \times 100\% \tag{8}$$

$$P = \frac{D_d}{D_d + D_f} \times 100\% \tag{9}$$

where:

J - pelleting qualified rate, [%];

Z_h - the number of particles completely coated with Agropyron seeds, [-];

Z_b - the number of particles incompletely coated with Agropyron seeds, [-];

P - single seed rate, [%];

D_d - the number of single seed of Agropyron seeds in the total of pelleted seeds, [-];

D_f - the number of multi-seeds of Agropyron seeds in the total of pelleted seeds, [-].

Simulation and test analysis

Effect of vibration frequency on mixing uniformity

In order to study the effect of vibration on the mixing uniformity, the discrete element software EDEM was used to set the rotation speed of the coater, the tilt angle of the coater, and the amplitude of vibration to 45 r/min, 45°, and 2 mm, respectively, and the vibration frequency was set to 10 Hz, 15Hz, 20Hz, 25Hz, 30Hz to simulate and analyse the effect of vibration frequency on the uniformity of seeds and powder mixing. The simulation results are shown in Fig.6, and the test verification results are shown in Fig. 7.

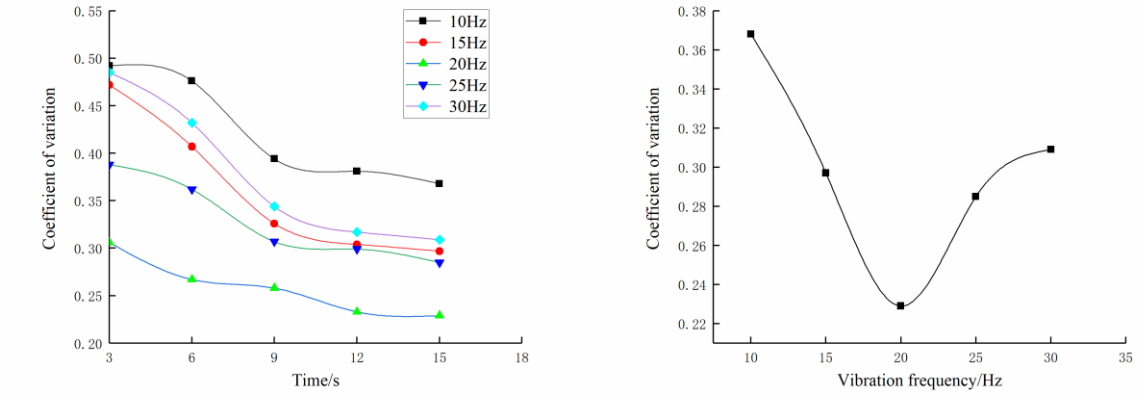

(a) Variation coefficient of powder particles under different vibration frequencies

(b) Variation coefficient of powder particles at different vibration frequencies at 15s

Fig. 6 – Effect of vibration frequency on mixing uniformity

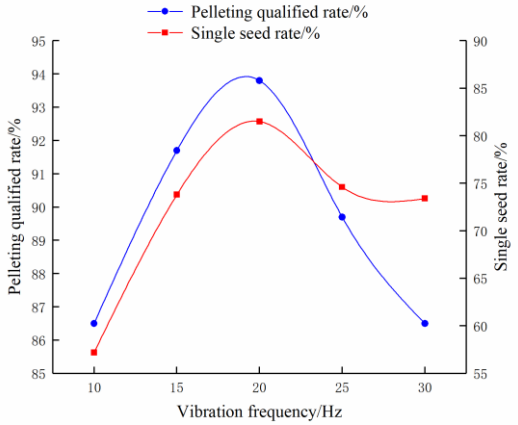

Fig. 7 – Experimental verification of the effect of vibration frequency on mixing uniformity

It can be seen from Fig.6 (a) that when the vibration frequency is 10 Hz, 15 Hz, 20 Hz, 25 Hz, and 30 Hz, the variation trend of the coefficient of variation during the mixing process decreases with the increase of time, and tends to be stable at 12 s. When the time is from 3s to 9s, the variation coefficients of the vibration frequency of 15Hz and 30Hz vary greatly, which is not conducive to the uniform mixing of seeds and powder. When the vibration frequency is 10Hz, 20Hz, 25Hz, the whole mixing process is relatively stable, and the variation range of the coefficient of variation is small. In general, when the vibration frequency is 20Hz, the time required is shorter, the coefficient of variation is smaller, and the mixing uniformity is better than other

vibration frequencies. As can be seen from Fig.6 (b), the vibration frequencies are 10Hz, 15Hz, 20Hz, 25Hz, and 30Hz, respectively, the coefficient of variation tends to decrease first and then increase. When it is 20Hz, the coefficient of variation reaches the minimum value of 0.229, and the seeds and powder can reach a uniform state faster and have a better mixing uniformity. It can be seen from the test results in Fig. 7 that both the pelleting qualified rate and the single seed rate have a tendency to increase first and then decrease. At 20 Hz of vibration frequency, both the pelleting qualified rate and single seed rate reach the maximum, indicating that when the vibration frequency is at 20Hz, the mixing uniformity of seeds and powder is the best, and the quality of the pelleting is high.

Effect of coater rotation speed on mixing uniformity

The discrete element software EDEM was used to set the tilt angle of the coater to 45°, the vibration frequency to 20 Hz, and the amplitude to 2 mm. The rotation speed of the coater was set to 30 r/min, 35 r/min, 40 r/min, 45 r/min, 50 r/min to simulate and analyse the effect of the coater speed on the mixing uniformity of seeds and powder. The simulation results are shown in Fig. 8, and the test verification results are shown in Fig. 9.

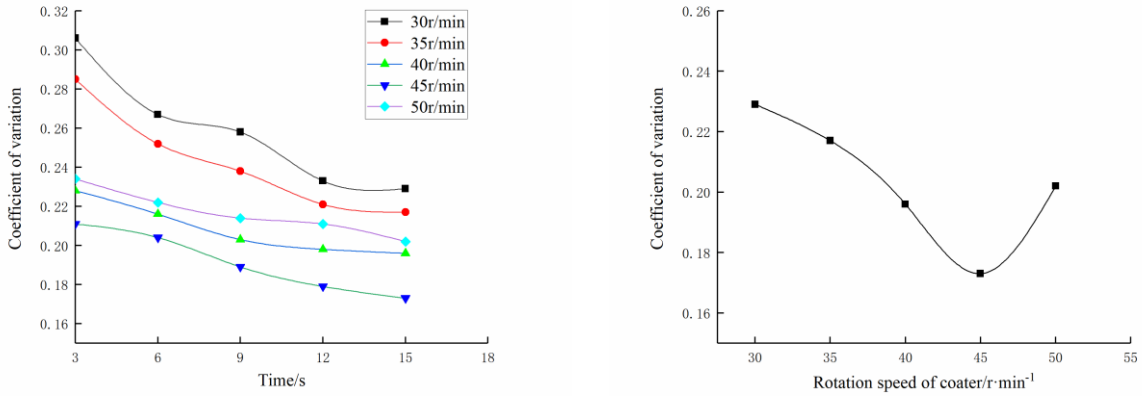

(a) Variation coefficient of powder particles at different rotation speeds of coater

(b) Variation coefficient of powder particles at different rotation speeds of coater at 15s

Fig. 8 – Effect of coater rotation speed on mixing uniformity

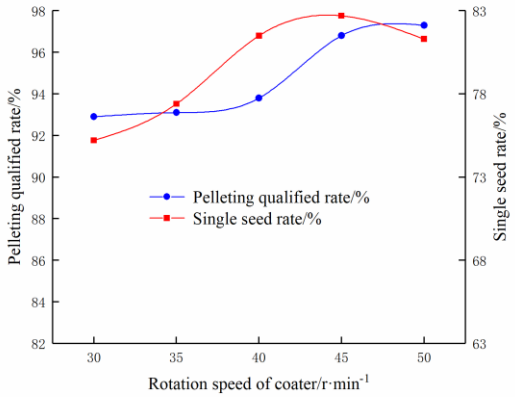

Fig. 9 – Experimental verification of the effect of coater rotation speed on mixing uniformity

It can be seen from Fig. 8 (a) that when the rotation speed is 30r/min, 35r/min, 40r/min, 45r/min, 50r/min, the variation trend of the coefficient of variation in the mixing process decreases with the increase of time. When the rotation speed is 30r/min, 35r/min, the coefficient of variation at 3s is much greater than 40r/min, 45r/min, 50r/min, and gradually stabilizes at 12s, the variation range of the coefficient of variation in the whole mixing process is large and has poor mixing stability. When the rotation speed is 40r/min, 45r/min, 50r/min, the whole mixing process is relatively stable and the variation coefficient variation range is small. Overall, when the speed is 45r/min, the time required is shorter and the mixing degree is better than other speeds, the coefficient of variation is smaller.

As can be seen from Fig. 8(b), when the rotation speed of the coater is 30r/min, 35r/min, 40r/min, 45r/min, 50r/min, the coefficient of variation is 0.229, 0.217, 0.196, 0.173, 0.202, which shows that when the speed of the coater is 45r/min, the coefficient of variation is small. It can be concluded that the seeds and powder can reach a uniform state faster and have a better mixing uniformity. It can be seen from the test results in Fig. 9 that when the speed of the coater is 45r/min, the pelleting qualified rate and the single seed rate reach the maximum, indicating that the mixing uniformity of seeds and powder is the best and the quality of pelleting seeds is higher.

Effect of the coater tilt angle on mixing uniformity

The discrete element software EDEM was used to set the rotation speed, vibration frequency and amplitude of the coater to 45r/min, 20Hz and 2mm respectively. The tilt angle of the coater was set to 25°, 30°, 35°, 40° and 45° to simulate and analyse the effect of the coater tilt angle on the mixing uniformity of seeds and powder. The simulation results are shown in Fig. 10, and the test verification results are shown in Fig. 11.

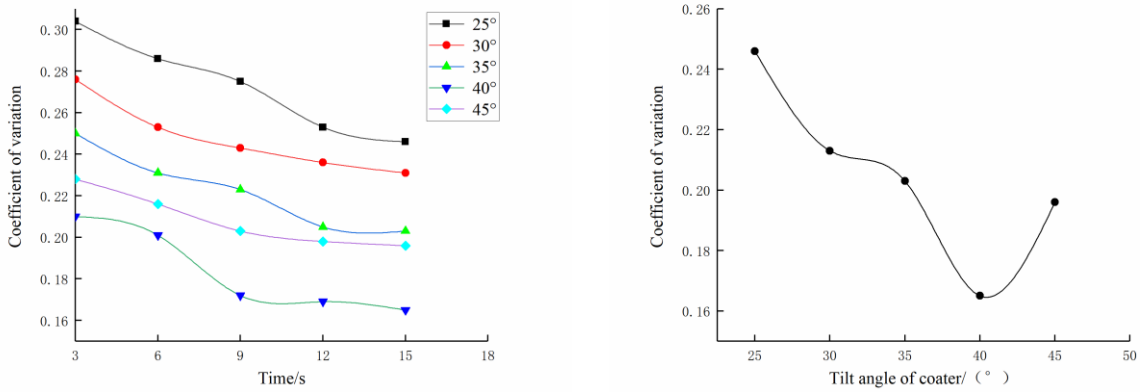

(a) Variation coefficient of powder particles under different tilt angle of coater

(b) Variation coefficient of powder particles under different tilt angle of coater at 15s

Fig. 10 - Effect of coater tilt angle on mixing uniformity

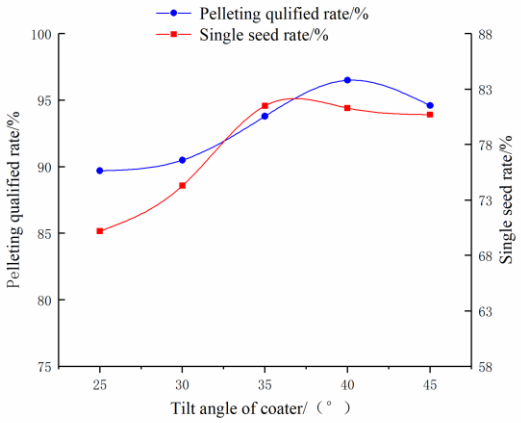

Fig. 11 – Experimental verification of the effect of the coater tilt angle on the mixing uniformity

It can be seen from Fig. 10 (a) that when the coater tilt angle is 25°, 30°, 35°, 40°, and 45°, the variation trend of the coefficient of variation during the mixing process decreases with time. When the tilt angle of the coater is 25°, 30°, 35°, 45°, the variation coefficient and the change range of the whole mixing process is stable and gradually stabilizes in 12s. When the tilt angle of the coater is 40°, the coefficient of variation has a small amplitude change during the period of 6s to 9s. In general, when the tilt angle of the coater is 40°, the time required is shorter and the coefficient of variation is smaller, it can be concluded that the mixing degree is better than other tilt angles. As can be seen from Fig. 10 (b), when the tilt angles of the coater are 25°, 30°, 35°, 40°, and 45° , the coefficient of variation are 0.246, 0.231, 0.203 , 0.165, 0.196. It shows that when the tilt angle of the coater is 40°, the coefficient of variation is small, the seeds and powder not only can reach a

uniform state faster but also have a better mixing degree. It can be seen from the test results in Fig. 11 that during the entire test, the pelleting qualified rate has a tendency to increase first and then gradually stabilizes with the increase of the tilt angle, the single seed rate increases first and then increases with the increase of the tilt angle. The results shows that when the pelleting qualified rate and the single seed rate reached the maximum, the tilt angle of the coater is 40°, which verifies the authenticity and feasibility of the simulation results.

Orthogonal test

In order to determine the optimal working parameters combination of Agropyron seeds pelleting machine, the orthogonal test of 3 factors and 3 levels was conducted with pelleting qualified rate and single seed rate as evaluation indexes. L_9 (3^2) orthogonal table was selected, and the test results are shown in Table 3. The experiment was carried out on a self-designed vibrating pelleting machine. The ratio of seed to powder was 1:50, and the ratio of seed to binder was 3.5:1.

Table 3

Orthogonal test plan and results

Test number	Coater rotation speed [r/min]	Coater vibration frequency [Hz]	Coater tilt angle [°]	Pelleting qualified rate [%]	Single seed rate [%]
1	40	10	35	93	75
2	40	15	40	95	76
3	40	20	45	91	73
4	45	10	45	95	78
5	45	15	35	94	74
6	45	20	40	98	82
7	50	10	40	96	78
8	50	15	45	93	73
9	50	20	35	97	81

Range analysis and determination of optimal working parameters combination

According to the results of orthogonal test, the range analysis of pelleting qualified rate and single seed rate was conducted. The results are shown in Table 4.

Table 4

Range analysis of the pelleting qualified rate and single seed rate

	Parameters	Coater rotation speed A [r/min]	Coater vibration frequency B [Hz]	Coater tilt angle C [°]
Pelleting qualified rate	X_{1n}	279	284	284
	X_{2n}	287	282	289
	X_{3n}	286	286	279
	R_n	2.7	1.3	3.3
Single seed rate	X_{1n}	224	231	230
	X_{2n}	234	223	236
	X_{3n}	232	236	224
	R_n	3.3	4.3	4.0

Note: X_{1n} is the sum of test indexes of level i corresponding to the factors in column n (i = 1,2,3)

The calculation formula of range is as follows: $R_n = \max(\overline{X}_{1n}, \overline{X}_{2n}, \overline{X}_{3n}) - \min(\overline{X}_{1n}, \overline{X}_{2n}, \overline{X}_{3n})$.

It can be seen from table 4 that the range values under each factor are not equal, which indicates that the influence of the change of corresponding level of each factor on the test results is not the same. According to the range values in Table 4, the order of importance of three factors (rotation speed of coater, vibration frequency of coater and tilt angle of coater) on pelleting qualified rate is C > A > B. The order of importance to single seed rate was B > C >A.

Considering the two evaluation indexes, the optimal combination of working parameters is A2B3C2. The results showed that the optimal working parameters of the pelleting machine of Agropyron seeds were as follows: the rotation speed of the coater was 45r/min, the vibration frequency of the coater was 20Hz, and the tilt angle of the coater was 40 °. Under this working parameter combination, the mixing uniformity of the seed and the powder material, the qualified rate of pelleting and the single seed rate were higher.

CONCLUSIONS

1) The discrete element simulation model of Agropyron seeds pelleting machine was established by using EDED simulation software. The variation coefficient CV was used as the evaluation index to determine the influence of the vibration frequency, rotation speed and tilt angle on mixing uniformity. According to the simulation results, when the vibration frequency of coater is 20Hz, the rotation speed of coater is 45r/min, and the tilt angle of coater is 40 °, the best mixing state and high mixing uniformity can be achieved.

2) When the coefficient of variation is at the minimum value, the corresponding test indexes of pelleting qualified rate and single seed rate reach the highest value, with high pelleting quality and the best mixing uniformity. The feasibility of single factor numerical simulation is verified.

3) Taking the pelleting qualified rate and single seed rate as evaluation indexes, the orthogonal test of 3 factors and 3 levels was conducted. The results showed that the optimal working parameters of the pelleting machine for Agropyron seeds was A2B3C2.

ACKNOWLEDGEMENTS

We acknowledge that this work was financially supported by National Natural Science Foundation Project "Research on soil wind erosion monitoring system based on wireless sensor network and its key technologies (41361058)" and "Research on seed pelleting parameters and coating mechanism under the vibration force field (2018MS05023)".

REFERENCES

[1] Dun G., Yang Y., Guo Y., (2019), EDEM simulation analysis of seed filling characteristics of different soybean varieties. *Journal of Henan Agricultural University*, Vol 53, Issue 1, pp. 93-98, Northeast Forestry University/China;

[2] Jiang S., Ye Y., Yang E., (2019), Numerical simulation of mixing uniformity of sand and gravel materials in rotary cylinder. *Acta computational mechanics*, Vol 36, Issue 5, pp. 603-609, Xiangtan University/China;

[3] Koteswara R., Fabian H., Eckehard S., Jochen M., (2013), Influence of flight design on the particle distribution of a flighted rotating drum. *Chemical Engineering Science*, 2013,90;

[4] Lei J., (2010), Vegetation restoration effect after aerial seeding and enclosure in Alxa Plateau. Inner Mongolia Forestry Science and technology, Vol 36, Issue 1, pp. 27-29, Alxa/China;

[5] Liu W. (2017), Simulation analysis of material mixing characteristics in coal mine rotary kiln based on discrete element method. *Coal technology*, Vol 36, Issue 11, pp. 320-322, Jiangsu/China;

[6] Sang J., Zhao C., Zhu C. (2015), Design of detection and control system for BY-150 seed coating machine. Agricultural Mechanization Research, Vol 37, Issue 3, pp. 83-86, Shanghai /China;

[7] Su T., (2014). *Experimental and Simulation Study on Influencing Factors of binary particles mixing in roller*, Master Dissertation, Northeast University China;

[8] Wang W., Hao X. (2011), Study on aerial seeding effect in Kubuqi Desert. Resources and environment in arid area, Vol 25, Issue 11, pp. 193-198, Inner Mongolia/China;

[9] You Y. (2019). *Numerical simulation of coating process of ellipsoidal tablet*. Master Dissertation, Zhejiang University/China;

[10] Yang E., (2015), Experimental study on mixing uniformity of bulk materials in rotary drum and discrete element simulation, Master Dissertation, Xiangtan University/China;

[11] Zhang L., Cheng S., Li S., (2018), Numerical analysis of mixing characteristics of binary particles in rotating drum with variable speed. *Journal of Northeast Electric Power University*, Vol 38, Issue 3, pp. 39-45, Northeast Electric Power University/China;

[12] Zhang T., Liu F., Zhao M., (2016), Dynamic law of maize population in seeding chamber based on discrete element [J]. *Transactions of the Chinese Society of Agricultural Enginee*ring, Vol 32, Issue 22, pp. 27-35, Inner Mongolia Agricultural University/China.

EXPERIMENTAL STUDIES OF THE PROCESS OF LOOSE MATERIAL TRANSPORTATION BY A PNEUMATIC-SCREW CONVEYOR
/
ЕКСПЕРИМЕНТАЛЬНІ ДОСЛІДЖЕННЯ ПРОЦЕСУ ПЕРЕМІЩЕННЯ СИПКИХ МАТЕРІАЛІВ ПНЕВМО-ШНЕКОВИМ ТРАНСПОРТЕРОМ

Hevko R.B.[1)], Lyashuk O.L.[1)], Dzyura V.O.[1)], Dovbush T.A.[1)], Trokhaniak O.M.[2)], Liashko A.P.[2)] [1]
[1)]Ternopil Ivan Puluj National Technical University / Ukraine;
[2)]National University of Life and Environmental Sciences of Ukraine / Ukraine;
E-mail: oleglashuk@ukr.net
DOI: https://doi.org/10.35633/inmateh-63-49

***Keywords*:** *pneumatic-screw conveyor, loose material, screw feeder, air pressure, productivity, displacement forces*

ABSTRACT

The article presents the developed design of the pneumatic-screw conveyor, as well as its experimental installation. The method of conducting experimental researches to determine force indicators at movement of different types of loose materials under the influence of air pressure and their volume of various types of bulk materials. Based on the conducted experimental studies, the response surfaces and two-dimensional cross-sections of the pneumatic-screw conveyor productivity when the material passes from the whole area in the hopper transition zone to the screw feeder, its rotation frequency and the working air pressure in the process line have been constructed.

РЕЗЮМЕ

У статті представлено розроблену конструкцію пнемо-шнекового транспортера, а також його експериментальну установку. Наведено методику проведення експериментальних досліджень для визначення силових показників при переміщенні різних типів сипких матеріалів від впливу тиску повітря та їх об'єму різних видів сипучих матеріалів. На основі проведених експериментальних досліджень побудовані поверхні відгуку та двомірні перерізи продуктивності пнемо-шнекового транспортера від зміни площі отвору в зоні переходу бункера на шнековий живильник, частоти його обертання та величини робочого тиску повітря в технологічній магістралі.

INTRODUCTION

Based on the analysis of the patent literature, well-known theoretical and experimental studies, it has been established that mechanical screw conveyors are characterized by low productivity and energy consumption for the process of loose materials transportation. At the same time, pneumatic conveyors, unlike screw ones, have much higher productivity, but also the energy to perform the same manufacturing process is significantly higher.

The modeling of loose materials movement processes in vertical and horizontal mechanical conveyors with definition of their rational parameters and operating modes has been outlined in several studies (*Pylypaka S.F., et al., 2019; Qi J., Meng H., et al., 2017*). Filling the technological route of the conveyor with loose materials heavily depends on design perfection and selection of screw feeder parameters, and the research to substantiate the structural and kinematic parameters which have been given in the articles (*Lyashuk O.L., et al., 2018; Mondal D., 2018*).

Improving the quality indicators during transportation of agricultural production materials, particularly seeds, can be provided by screw conveyors, the working surfaces of which are made elastic. The results of such studies have been presented in the works (*Tian Y., et al., 2018; Hevko R.B., et al., 2019*).

Screw conveyors can also move loose materials along curved paths in elastic casings. Theoretical and experimental studies of these types of conveyors have been discussed in the researches (*Trokhaniak O.M., et al., 2020*).

[1] *Hevko R.B., Prof. DSc. Eng.; Lyashuk O.L., Assoc. Prof. Ph.D. Eng.; Dzyura V.O., Assoc. Prof. Ph.D. Eng.; Dovbush T.A., Assoc. Prof. Ph.D. Eng.; Trokhaniak O.M., Assoc. Prof. Ph.D. Eng.; Liashko A.P., Ph.D. Eng., Senior Lecturer*

The choice of optimal parameters of screw and scraper conveyors with a general assessment of the efficiency of their operation has been given in the articles (*Yao Y.P., et al., 2014, Roberts Alan W., Bulk Solids, 2015, Wang D.-X., 2012*).

The current study presents the design and the evaluation of a laboratory device, which combines mechanical motion of wheat grain and turbulent air streaming inside a positive pneumatic conveyor system *(Buteler M. et.al., 2020)*. Our experimental results, which were conducted under laboratory conditions, show that the recovery efficiency of the prototype was equal to 98.0% (±1.4) on average.

The work written by *de Freitas A.G. et.al., (2020),* presents the experimental characterization of industrial bulk solids feeder, named Batchpump, and validates the performance in terms of transport capacity and compressed gas consumption of an unconventional compact pressure vessel, used as a feeding device for dense phase pneumatic conveying. The developed device was shown to have similar performance parameters (transport rate and gas consumption) when compared to conventional versions of blow tanks operating at 4 bar pressure and conveying powder material at about 9 t/h rate, albeit the smaller dimensions and simplification in operation, resulting in significant advantages in retrofits and in the implement of a new conveyor line.

The paper of *Gao X.M. et.al., (2020),* covers critical speed of pneumatic transport for conveying materials and measuring the angle of friction and the coefficient of restitution of materials on a variety of material surfaces. With the help of a machine verification test it was proved that the optimal parameters for the pneumatic transportation of Baisha peanut pods with a moisture content of 7.24% was a fan speed of 2700 r/min and a cushioning/anti-obstruction layer thickness of 6 mm.

The use of pneumatic conveyors and selection of options when moving various loose materials for rectilinear and curvilinear process routes has been described in the works (*Manjula E.V.P.J., et al., 2017; Naveen Tripathi, et al., 2015*).

In general, the disadvantage of pneumatic screw mechanisms is that screw conveyor flights provide not only translational axial material movement, but also its rotary motion, which results in both material damage and decrease in mechanism efficiency (*Hevko R.B., et al., 2014; Baranovsky V.M. et al., 2018*). As a result, it is not possible to reach the highest economic effectiveness and the maximum efficiency of a pneumatic screw conveyor in general.

When optimizing the parameters of transportation-technical systems equipped with the operating elements of screw mechanisms and at the stage of their development, it is to the point to build a mathematical technological model of a screw feeder of a pneumatic screw conveyor (*Hevko R.B. et al., 2014*) in order to obtain the performance pattern of a screw feeder, which is cantilevered on its support depending on its main design and kinematic parameters.

The aim of experimental studies of these types of conveyors is to select the optimal parameters and modes of their operation for efficient movement of loose materials on technological routes of different spatial configuration using mechanical material feed by a screw feeder and further enhance the flow of loose material with compressed air.

MATERIALS AND METHODS

In order to understand the process flow of a screw feeder operation when transporting loose materials and further substantiation of the rational parameters of the operating elements of a pneumatic screw conveyor, it is important to consider its functional diagram, which is presented in figure 1.

The pneumatic-screw conveyor consists of a frame *1*, inside of which there is an electric motor *2* with a speed regulator *3*. In the screw body *4* there is a screw feeder *5*. The pneumatic system is connected to a central opening *7*, which is made in the slotted shaft *8* of the screw feeder. The slotted shaft of the screw feeder has the possibility of angular deflection in bearing units *9* and is biased by a pressure spring *10*. On the left end of the slotted shaft, there is a pressure disk *11*, which is rigidly fixed and makes contact with the feeder of the pneumatic distributor *12* of the pneumatic system. Here, a slotted shaft of the screw feeder is mounted with the possibility of axial deflection with the help of a ball slotted joint *13*. The helix *14* of the screw feeder is multifillar and the pneumatic-operated valve *16* is arranged in the area of material output from hopper *15*.

During the operation, loose material moves through the hopper and gets into the screw body through the screw feeder, which rotates and executes loose material feed in the output area. When there is overload, caused by accumulation of a certain amount of loose material in the working space of the screw body, due to its spiral surface, the screw feeder deflects axially against the direction of loose material transportation by

means of the ball slotted joint and compresses the spring. Here, a pressure disk contacts the pneumatic distributor, which admits high-pressure air from the pneumatic system. The air enters the central opening in the slotted shaft, which causes softening of pressed loose material mass and its further transportation.

The pneumatic-operated valve, which blocks the outlet of the hopper and seals the working space of the screw body, is automatically disengaged.

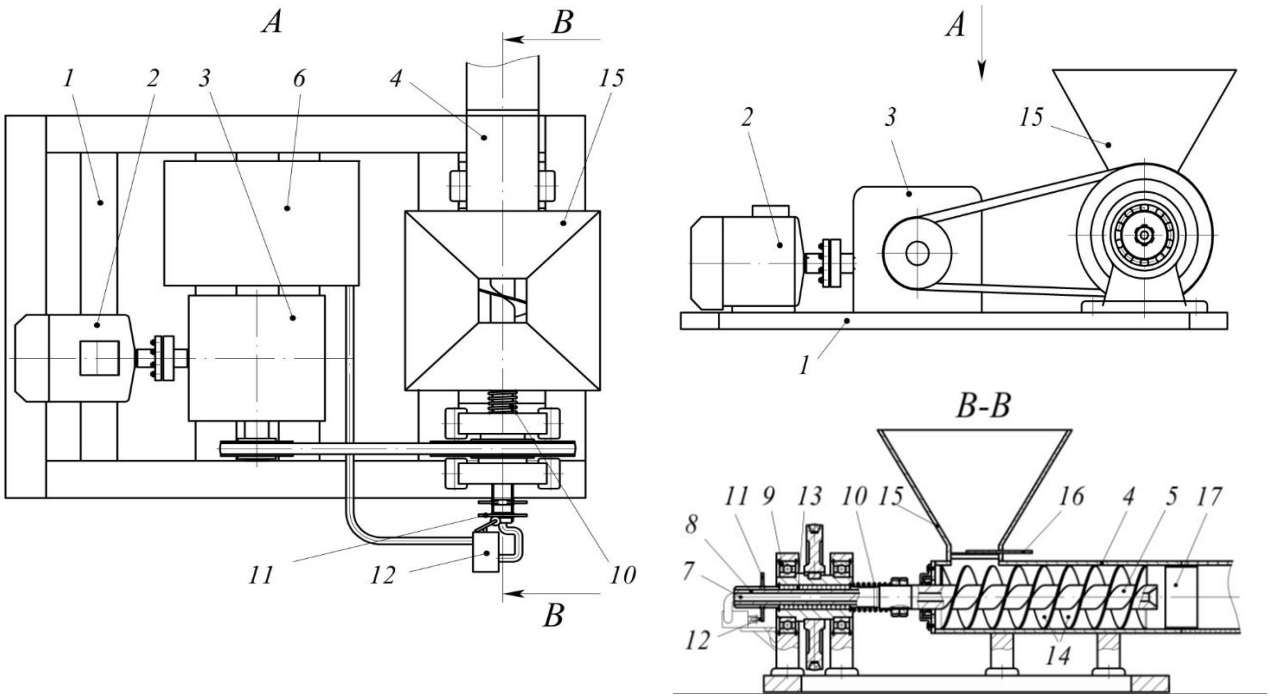

Fig. 1 – Design concept of the pneumatic-screw conveyor

1 – frame; 2 – electric motor; 3 – speed regulator; 4 – screw body; 5 – screw feeder; 6 – pneumatic system; 7 – central opening; 8 – slotted shaft; 9 – bearing units; 10 – pressure spring; 11 – pressure disk; 12 – pneumatic distributor; 13 – ball slotted joint; 14 – screw helix; 15 – hopper; 16 – pneumatic-operated valve, 17 – air circuit.

When the material is transported, axial pressure on the screw feeder is reducing and it is drawn toward the direction of loose material transportation by pressure spring force and this causes shifting of the pressure disk, which engages the pneumatic distributor that, in its turn, shuts off air feeding from the pneumatic system.

In the course of implementing loose material transportation performed by the screw, the value of the coefficient of pressure screw space filling was non-constant and depended mostly on the uniformity of loose grain material that was fed from the loading hopper as well as on other factors such as material size specifications, its moisture, material particle compacting capability in the process of their transportation by the screw etc.

The efficiency of the pneumatic screw conveyor Q was determined according to the known equation, which characterizes calculation of the necessary diameter of the pressure screw of pneumatic screw conveyor, taking into account the volumetric efficiency of the last pressure flight of the pneumatic screw conveyor feeder (*Hevko R.B. et al., 2018)*, thus:

$$D = 0.29\sqrt[3]{\frac{Q}{\left(1-a_1^2\right)a_2\rho k_k \eta_t n}} \quad (1)$$

where Q – pneumatic screw conveyor efficiency, t/h; $a_1 = d/D$; $a_2 = \pi a_1 f_1 = \pi f_1 d/D$;

η_t - volumetric efficiency of the last pressure flight of the pneumatic screw conveyor feeder.

The efficiency Q (t/h) of the pneumatic screw conveyor was determined according to the formula:

$$Q = \frac{\left(D^2 - d^2\right)}{0.024}\pi d f_1 \rho k_k \eta_t n \quad (2)$$

According to *Hevko R.B. et al., (2018)*, the coefficient of sliding k_k was determined from the following formula:

$$k_k = k_\beta k_y (10 p_k)^{\lambda_D} \quad (3)$$

where p_k – excess pressure in the mixing chamber of the screw feeder, MPa; λ_D – the coefficient that shows the degree of impact of the coefficient of screw compacting capability k_y and screw diameter D on k_k.

Power dependence of the excess pressure in the mixing chamber and the coefficient λ_D $(10 p_k)^{\lambda_D}$ represent the degree of the influence of the reverse pressure and the diameter of the screw D on the value of the sliding coefficient k_k, taking into account material compacting in the screw space due to the excess pressure. The volumetric efficiency was determined according to the dependence (*Baranovsky V.M., et al., 2018*):

$$\eta_t = 1 - \frac{0.6\sqrt{10 p_k}}{n\sqrt{\rho k_y}} \sqrt{\frac{D_{cm} f_1}{f_2 (D - d f_1)}} 10^3 \quad (4)$$

where D_{cm} – average diameter of loose material friction along the screw flight, m; f_1 – internal friction coefficient $f_1 = tg^2 \left(45^0 - 0.5\alpha_k\right) = tg^2 \beta$

The efficiency of the pneumatic screw conveyor Q was determined according to the know equation:

$$Q = \frac{\pi d \left(D^2 - d^2\right)}{0.024} \left(1 - \frac{\delta_n z_n}{D tg\beta} \cos arctg \frac{2\pi D tg\beta}{D + d}\right) \times \rho \varphi_k k_\beta k_y^2 \left(n - 0.6 tg\beta \sqrt{\frac{10 p_k D_{cm}}{\rho k_y f_2 \left(D - d tg^2 \beta\right)}} 10^3\right) \quad (5)$$

Based on (5), graphic representation of the dependency of the change in pneumatic screw conveyor efficiency Q on diameter D and the frequency of screw rotation n as a functional $Q = f(D, n)$ at the following values φ_k = 1.0 *(Wang D.X., 2012)*, k_β=0.8; k_y=1.3 (*Yao Y.P., et.al., 2014*); d= 0.5D, p_k=0.15 MPa (*Trokhaniak O.M. et.al., 2020*), β= 20.0 deg, f_2=0.7 (*Buteler M., et.al., 2020*), z=1, δ=0.02 m, ρ=1.3 t/m^3 and on the bulk material weight ρ and the frequency of screw rotation n as a functional $Q = f(\rho, n)$ at D =0.15m in the form of surfaces and their two-dimensional sections presented in figure 2 and figure 3, respectively, were built.

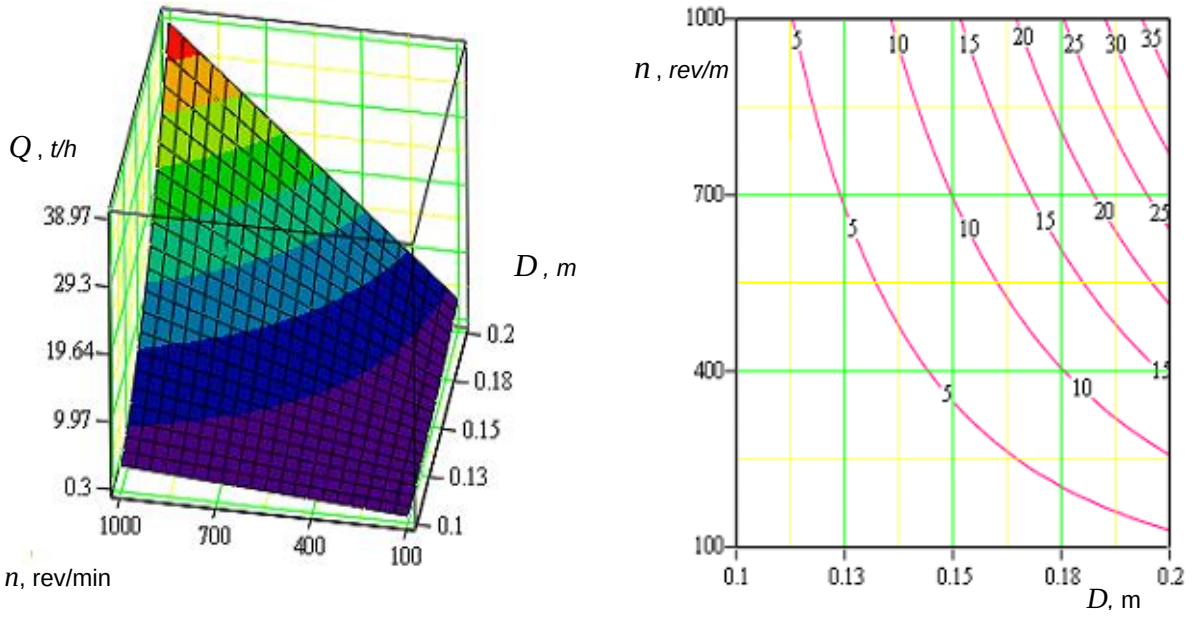

Fig. 2 – Change dependency of pneumatic screw conveyor efficiency Q on the diameter D and the frequency of screw rotation n as a functional $Q = f(D, n)$

The analysis of the presented surfaces shows that the pneumatic screw conveyor efficiency Q changes within the range of 0.3…39 t/h, depending on the change of screw design-kinematic and technological parameters and the properties of loose material within the following ranges: screw diameter D=0.1…0.2 m; frequency of screw rotation n = 100…1000 rev/min volumetric loose material weight

ρ=0.9…1.5 t/m^3 and characterizes the increase in the efficiency Q compared to the efficiency of the feeding screw approximately by 1.3 times.

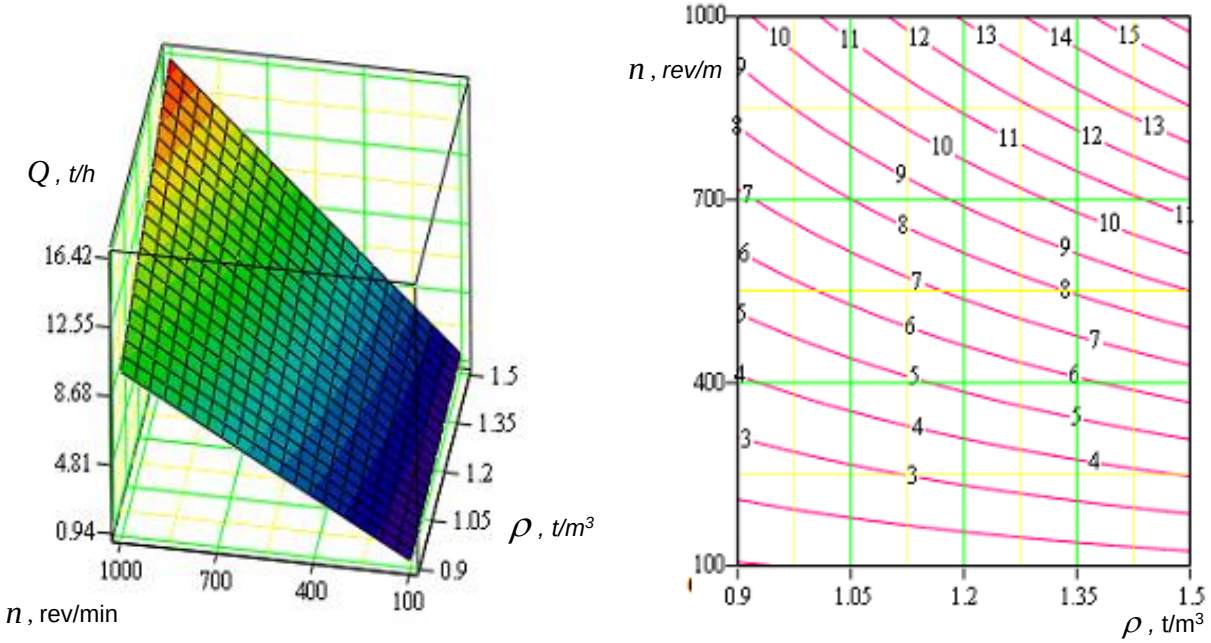

Fig. 3 – Change dependency of pneumatic screw conveyor efficiency Q on bulk material weight ρ and the frequency of screw rotation n as a functional $Q = f(\rho, n)$

Based on the design concept of the pneumatic-screw conveyor, a laboratory-scale plant (Fig.4) has been developed. Its main units are: compressor *1* with electric drive *2*, drive motor of the screw operating element *3*, control unit *4*.

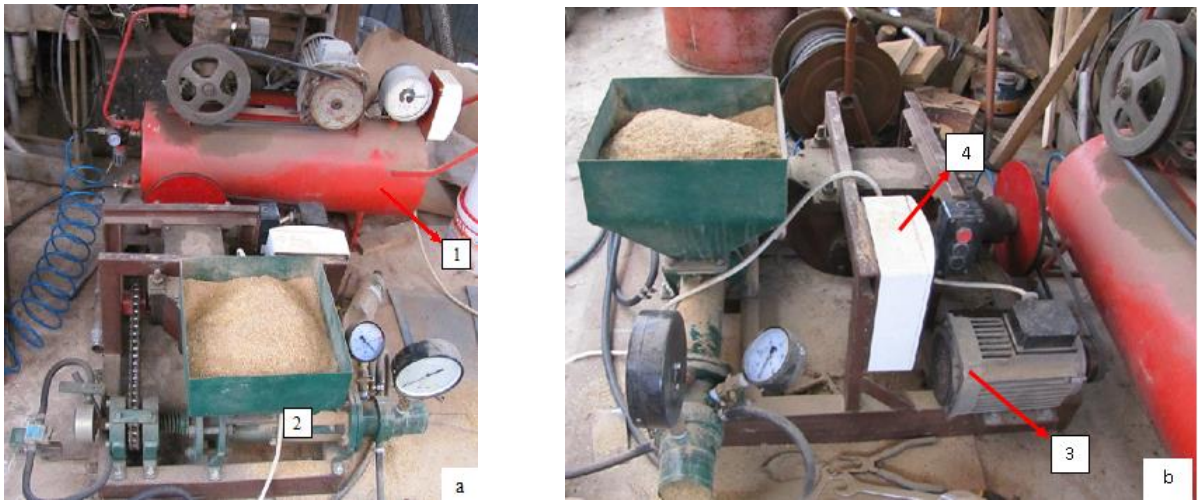

Fig. 4 – Overall view of the laboratory-scale plant

a – side view; b – front view; 1 – electrically driven compressor; 2 – pneumatic-screw conveyor; 3 – drive motor of operating elements; 4 – control unit.

One of the main mechanisms of a pneumatic screw conveyor is the mechanism of pneumatic distributor engagement (Fig.5). This mechanism allows compressed air automatically feed along hoses to nozzles (*Hevko R.B. et al., 2018*).

When there is an accumulation of loose material at the point of its feeding by the feeder, flight screw loading increases, but at first stages of transportation pressure spring *1* force is able to deal with this load. A feeder valve is connected to the slotted shaft *3*, which is fixed in the body *2* by means of balls and its axial deflection is possible when loading increases. When flight loading reaches its critical value, the axial component of which exceeds compressed spring force, the valve begins to bias in the direction opposite to material movement. Here, the rotary pneumatic junction *5* engages the pneumatic distributor *4* and ingoing compressed air begins to move along air-lines in the direction of material unloading area.

Such mechanism gives the opportunity to regulate torque value when a pneumatic distributor is engaged for various loose materials transportation and to control the distance of their movement.

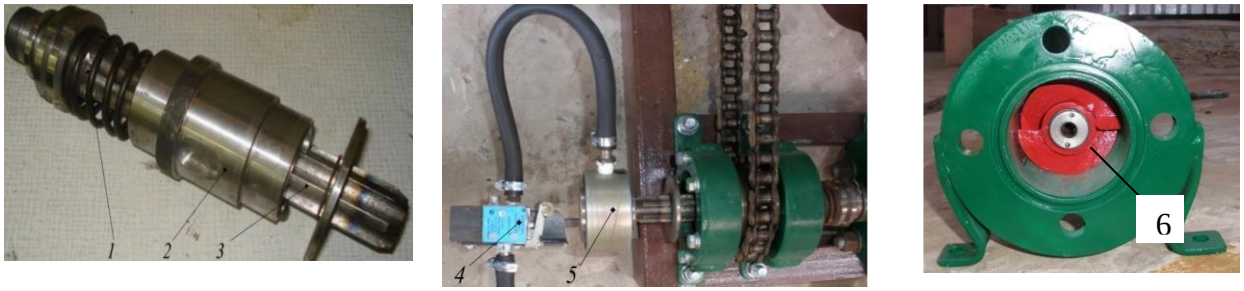

Fig. 5 – Mechanism of pneumatic distributor engagement and its connection to a tri-linear switch
1 *– spring; 2– body; 3 – slotted shaft with half slots; 4 – pneumatic distributor; 5 – pneumatic junction; 6 – nozzle.*

In order to conduct experimental studies, a pneumatic screw conveyor plant with air-powered transportation flow has been designed and it is presented in figure 6.

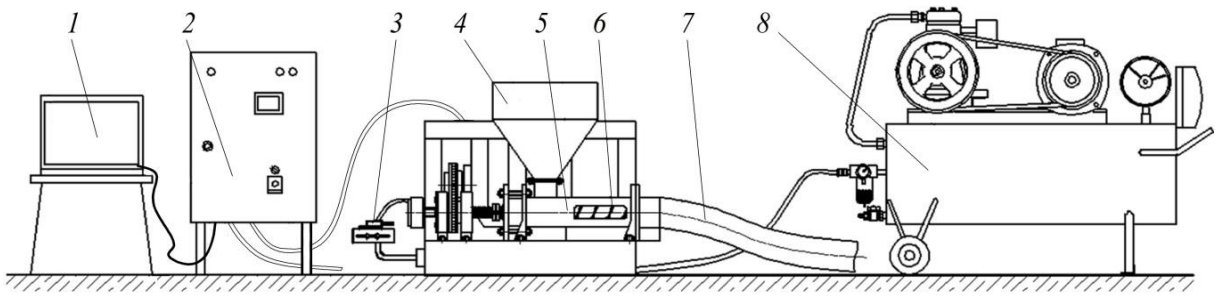

Fig. 6 – The lay-out of the pneumatic screw conveyor plant with air-powered material flow
1 – computer; 2 – «Altivar-71»; 3 – pneumatic distributor; 4 – hopper; 5 – feeder body;
6 – screw feeder; 7 – flexible transportation pipe; 8 – compressor.

In order to determine real power parameters of the process of loose material transportation, a frequency control drive Altivar-71 with Power Suite v.2.5.0 software has been used in the process of experimental studies. Altivar-71 system is connected to the network and to a computer. While setting the required rotation frequency with the help of a computer, there is a command transfer to the electric motor by means of Altivar-71 system and it begins to rotate the screw feeder valve with pre-set parameters.

By changing certain parameters, it is possible to determine the influence of torque value T and engine power N depending on the rotation frequency of the operating element n at its overload and the beginning of reverse movement of the slotted shaft with the screw feeder in order to feed the air from the pneumatic system. In addition, the obtained data are the initial ones in order to choose spring stiffness.

RESULTS

Based on the results of experimental studies, graphical dependences of the force F_T of load transportation on the air pressure P are constructed (Fig.7a) and the displacement forces of different loose materials from their volume V at a constant air supply pressure P = 0.6 MPa (Fig.7b).

The bulk density of loose material also has a significant effect on the magnitude of the F_T force. Thus, for wheat with a bulk density of 720 kg/m^3 and bran with a bulk density of 250 kg/m^3, the F_T force is significantly higher for a material with a higher bulk density.

Experimental research on the efficiency of the pilot pneumatic screw conveyor unit at high-pressure air feeding was conducted based on implementing a multifactorial experiment of FFE 3^3 type. The efficiency of the pilot pneumatic screw conveyor unit Q at high-pressure air feeding, which was experimentally observed, was found in the form of a mathematical model:

$$Q = -4.33 + 7.34\ln(S_c - 24) + 2.26\ln(n - 300) + 2.97\ln(20P - 5) \quad (6)$$

The conducted experimental research on the pilot unit resulted in obtaining the dependencies of pneumatic screw efficiency on the change in the area of the hopper discharge hole $12.10^{-4} \leq S_c \leq 36.10^{-4}$ m^2, the frequency of feeder rotation $150 \leq n \leq 450$ rev/min and the value of operating air pressure $0.2 \leq P \leq 0.3$ MPa in a technological line, which are presented in the form of response surfaces (a) and their two-dimensional sections (b), as a functional $Q = f(S_c, P)$ at n = 300 rev/min (Fig.8a) and $Q = f(n, P)$ at S_c = 24 10^{-4} m^2 (Fig.8b).

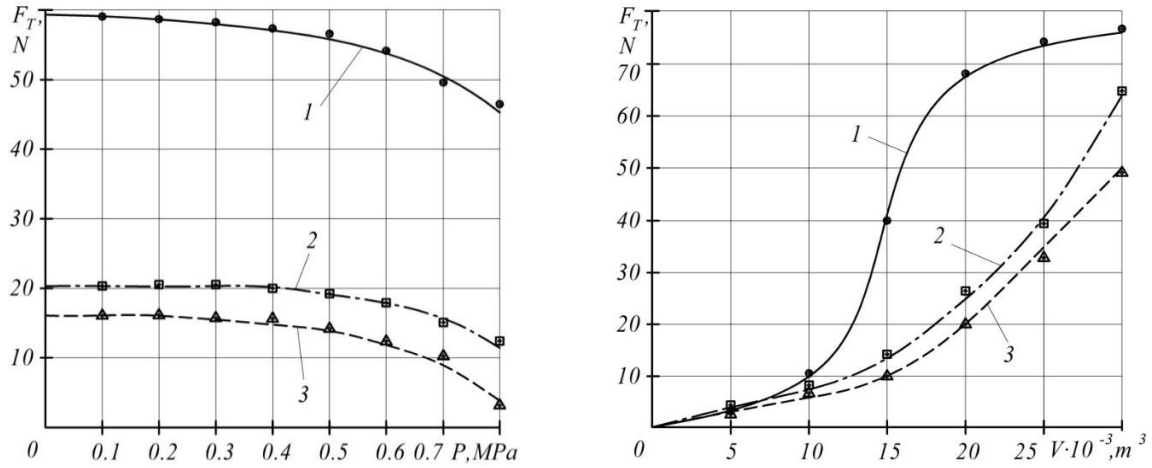

Fig. 7 – Graphic dependencies: effort of load transportation on one running meter F_T
a – on air pressure P; b – on the volume V of different loose materials; 1 – wheat; 2 – saw dust; 3 – bran.

The graphs show that the effort F_T of transporting loose materials decreases with increasing air pressure P in the pneumatic system and increases with increasing volume V of loose material.

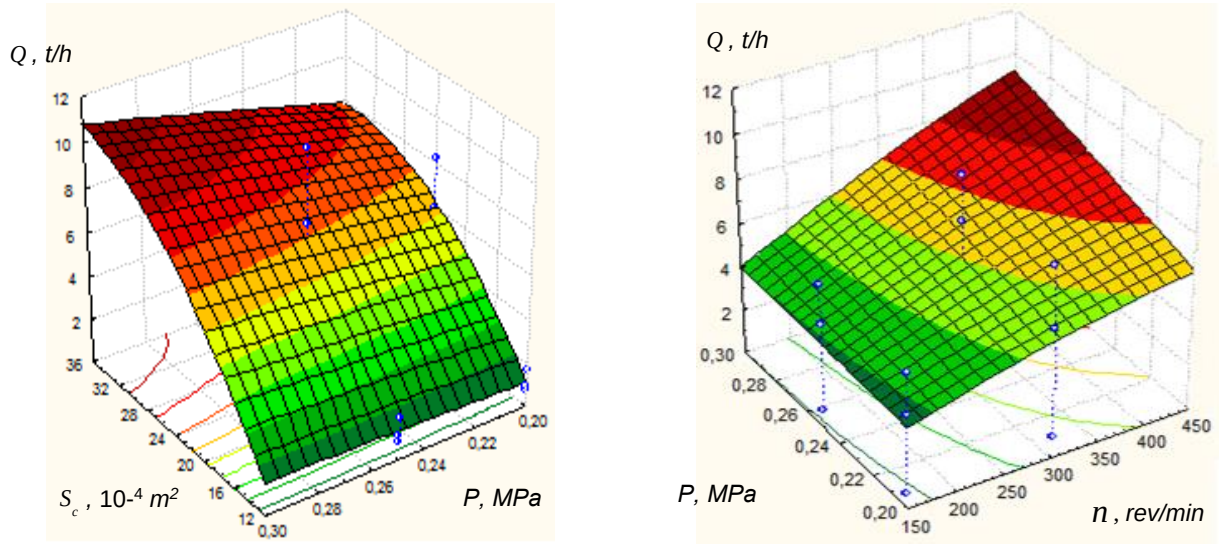

Fig. 8 – Response surfaces of pneumatic screw conveyor efficiency as a functional
a – Q = f(Sc, P) at n = 300 rev/min; b – Q = f(n, P) at Sc = 24 10-4 m^2.

The obtained regression dependence (6) can be used for determining the efficiency of the pilot pneumatic screw conveyor unit with high-pressure air feed depending on the change in the area of a hopper discharge hole S_C, the frequency of screw rotation n and the value of the operating air pressure P within the following limits: 12. $10^{-4} \leq S_C \leq 36. 10^{-4}$ m^2; $150 \leq n \leq 450$ rev/min; $0.2 \leq P \leq 0.3$ MPa.

The analysis of graphical dependences shows that the productivity Q of the pneumatic screw conveyor increases with increasing magnitude of the active factors. The most significant influence on the value Q has the value S_c, then the value n. It should be noted that increasing the area of the discharge hole of the hopper S_c over $36 \cdot 10^{-4}$ m^2 does not increase the productivity of Q, because the excess loose material is not included in the housing of the screw feeder, and is thrown back into the hopper.

The minimum influence on productivity Q, in the given range of variable values of factors, has the size of air pressure P in the technological line.

CONCLUSIONS

The article presents the developed design of the pneumatic screw conveyor as well as experimental installations and research methods for determining the force indicators for the movement of loose load under the influence of air pressure and the volume of different types of loose materials. It is established that transportation efforts F_T of bulk materials decreases with increasing air pressure in the pneumatic system. The bulk density of loose material has a significant effect on the amount of the effort F_T. Thus, for wheat with a bulk density of 720 kg/m^3 and bran with a bulk density of 250 kg/m^3, the effort F_T at a pressure P of up to 0.8 MPa and V = (20…25) 10^{-3} m^3 is by 3.5…5 times larger for a material with a larger bulk density.

Based on the manufactured installation of pneumatic-screw conveyor with feeding the flow of material by air jets, the dependences of productivity Q of pneumatic-screw conveyor on the change of the area of the eastern opening of the hopper, the speed of the screw feeder and the working air pressure in the process line have been established. The value S_c, then the value n has the most significant influence on the value Q. Increasing the area of the discharge hole of the hopper S_c over 36·10^{-4} m^2 does not increase the productivity Q, because the excess material does not enter the housing of the screw feeder, and is thrown back into the hopper.

The minimum influence on the productivity Q of the pneumatic-screw conveyor, in this range of variable values of factors, has the value of air pressure P in the process line.

REFERENCES

[1] Baranovsky V.M., Hevko R.B., Dzyura V.O., Klendii O.M., Klendii M.B., Romanovsky R.M., (2018), Justification of rational parameters of a pneumoconveyor screw feeder, *INMATEH-Agricultural engineering*, Vol. 54, no. 1, pp. 15-24, Bucharest/Romania;

[2] Buteler M., Gitto J.G., Stadler T., (2020), Enhancing the potential use of microparticulate insecticides through removal of particles from raw grain, *Journal of Stored Products Research,* Vol. 89, 101707, Oxford/England;

[3] De Freitas A.G., De Oliveira V.F., Lima Y.O., dos Santos R.B., Riascos L.A.M., (2020), Energy efficiency in pneumatic conveying: performance analysis of an alternative blow tank, *Particulate Science and Technology*, pp. 1-8, London/England;

[4] Gao X.M., Xie H.X., Gu F.W., Wei H., Liu M.J., Yan J.C., Hu Z.C., (2020), Optimization and experiment of key components in pneumatic peanut pod conveyor, *International Journal of Agricultural and Biological Engineering*, vol. 13, no. 3, pp. 100-107, Beijing/China.

[5] Hevko R.B., Zalutskyi S.Z., Hladyo Y.B., Tkachenko I.G., Lyashuk O.L., Pavlova O.M., Pohrishchuk B.V., Trokhaniak O.M., Dobizha N.V., (2019), Determination of interaction parameters and grain material flow motion on screw conveyor elastic section surface, *INMATEH-Agricultural Engineering,* vol. 57, no. 1, pp. 123-134, Bucharest/Romania;

[6] Hevko R.B., Dzyura V.O., Romanovsky R.M., (2014), Mathematical model of the pneumatic-screw conveyor mechanism operation, *INMATEH-Agricultural Engineering*, Vol. 44, no. 3, pp. 103-110, Bucharest/Romania;

[7] Hevko R.B., Baranovsky V.M., Lyashuk O.L., Pohrishchuk B.V., Gumeniuk Y.P., Klendii O.M., Dobizha M.V., (2018), The influence of bulk material flow on technical and economical pereformance of a screw conveyor, *INMATEH-Agricultural Engineering*, Vol. 56, no. 3, pp. 175-184, Bucharest/Romania;

[8] Hevko R.B., Strishenets O.M., Lyashuk O.L., Tkachenko I.G., Klendii O.M., Dzyura V.O., (2018), Development of a pneumatic screw conveyor design and substantiation of its parameters, *INMATEH-Agricultural Engineering*, Vol. 54, no. 1, pp. 153-160, Bucharest/Romania;

[9] Lyashuk O.L., Sokil M.B., Klendiy V.M., Skyba O.P., Tretiakov O.L., Slobodian L.M., Slobodian N.O., (2018), Mathematical model of bending vibrations of a horizontal feeder-mixer along the flow of grain mixture, *INMATEH-Agricultural Engineering*, vol. 55, no. 2, pp. 35-44, Bucharest/Romania;

[10] Mondal D., (2018), Study on filling factor of short length screw conveyor with flood-feeding condition, *Materials Today: Proc*eedings, vol.5, no.1, pp.1286–1291. https://doi.org/10.1016/j.matpr.2017.11.213,

[11] Manjula E.V.P.J., Hiromi W.K. Ariyaratne, Ratnayake Chandana, Morten C. Melaaen, (2017), A review of CFD modelling studies on pneumatic conveying and challenges in modelling offshore drill cuttings transport, *Powder Technology*, Vol. 305, pp. 782-793, United Kingdom;

[12] Naveen Tripathi, Atul Sharma, S.S. Mallick, P.W. Wypych, (2015), Energy loss at bends in the pneumatic conveying of fly ash, *Particuology*, vol. 21, pp. 65-73, Netherlands;

[13] Pylypaka S.F., Nesvidomin, V.M., Klendii M.B., Rogovskii I.L., Kresan T.A., Trokhaniak V.I., (2019), Conveyance of a particle by a vertical screw, which is limited by a coaxial fixed cylinder*, Bulletin of the Karaganda University. «Mathematics» series*, vol. 95, no. 3, pp. 129-139, Karaganda/Kazakhstan;

[14] Qi J., Meng H., Kan Z., Li C., Li Y., (2017), Analysis and test of feeding performance of dual-spiral cow feeding device based on EDEM, *Transactions of the Chinese Society of Agricultural Engineering*, vol. 33, no. 24, pp.65-71, Beijing/Chines;

[15] Roberts Alan W., Bulk Solids, (2015), Optimizing Screw Conveyors, *Chemical engineering*. vol. 122(2), pp.62-67, New York/USA;

[16] Tian Y., Yuan P., Yang F., Gu J., Chen M., Tang J., Su Y., Ding T., Zhang K., Cheng Q., (2018), Research on the Principle of a New flexible screw conveyor and its power consumption, *Applied Sciences*, vol. 8, no. 7, Basel/Switzerland

[17] Trokhaniak O.M., Hevko R.B., Lyashuk O.L., Dovbush T.A.; Pohrishchuk B.V.; Dobizha N.V., (2020), Research of the of bulk material movement process in the inactive zone between screw sections, *INMATEH/Agricultural Engineering,* vol. 60, no. 1, pp. 261-268, Bucharest/Romania;

[18] Wang D.-X., (2012), Research on numerical analysis and optimal design of the screw conveyor, *Univ. Technol*., vol. 27, pp.32–36;

[19] Yao Y.P., Kou Z.M., Meng W.J., Han G., (2014), Overall Performance Evaluation of Tubular Scraper Conveyors Using a TOPSIS-Based Multiattribute Decision-Making Method, *Scientific World Journal*, vol. 2014, 753080, https://doi.org/10.1155/2014/753080, London/United Kingdom.

RELATIVE ORDERING TESTS FOR DRAFT FORCE MODELS IN SOIL TILLAGE
/
TESTE DE ORDONARE RELATIVA PENTRU MODELE ALE FORTEI DE REZISTENTA LA TRACTIUNE IN LUCRARILE SOLULUI

Cardei P.[1)], Muraru V.[1)], Muraru S.[1)], Sfaru R.[1)], Muraru-Ionel C.[1)] [1]
[1)] National Institute of Research – Development for Machines and Installations designed to Agriculture and Food Industry – INMA Bucharest, Romania
Tel: 0744357250; E-mail: vmuraru@inma.ro
DOI: https://doi.org/10.35633/inmateh-63-50

Keywords: *draft, tillage, soil, test, models, ordering, physical laws*

ABSTRACT
The article presents results of some test sketches - validation and ordering - of the mathematical models proposed for the physical law rank on soil tillage draft force. The results constitute the continuation and partial completion of a method of testing - validation and ordering - the models proposed and published by researchers in the specialized literature of the last seventy years. The material defines and completes the method (initially only a validation method), up to a method of ordering the models according to their accuracy in relation to the experimental results. The proposed tests are intended to increase the coherence of research in the field of searching for a physical law of soil tillage draft force, assuming that it exists. The method can also be applied in case of other physical laws in research, construction or improvement stage.

REZUMAT
Articolul prezintă rezultatele unor scheme de testare - validare și ordonare ale modelelor matematice propuse pentru clasa de legi fizice referitoare la forța de rezistenta la tracțiune în lucrările solului. Rezultatele constituie continuarea și completarea parțială a unei metode de testare - validare și ordonare - a modelelor propuse și publicate de cercetători în literatura de specialitate din ultimii șaptezeci de ani. Materialul definește și completează metoda (inițial doar o metodă de validare), până la o metodă de ordonare a modelelor în funcție de precizia acestora în raport cu rezultatele experimentale. Testele propuse sunt menite să crească coerența cercetărilor în domeniul căutării unei legi fizice a forței rezistenta la tracţiune a solului, presupunând că aceasta există. Metoda poate fi aplicată și în cazul altor legi fizice aflate în stadiul de cercetare, construcție sau perfecționare.

INTRODUCTION

The results presented in this article constitute a continuation and, to a large extent, a completion of those set out in (*Cardei et al., 2020*). Finding and defining a physical law of the soil tillage draft force is a very complex experimental and theoretical research activity, due, first of all, to the large number of parameters involved in the process of interaction of the working bodies and, generally, of the machines with the soil. Also the random character of many parameters and characteristics of the soil constitutes an element of high difficulty. The hope that a physical law of soil tillage draft force exists, involves a large number of researchers in experimental and theoretical research. Most likely, if it exists, the law will materialize in one or more mathematical relationships that will form the mathematical model that will express the sought law. Currently, there are a relatively large number of mathematical relationships that want a place in the hierarchy of claimants to the title of law of the soil tillage draft force. However, despite the large number of such relationships, they can be grouped into several simple categories. An important observation is required here. Validation in the sense of *(Cardei et al., 2020*) refers to the positivity of the coefficients of the terms, but not to the exponents determined by the method of the smallest squares, exponents that, in general, can have a positive or negative sign.

[1] *Cardei P, Math., Muraru V., PhD.Eng.; Muraru S., PhD.Eng.Stud.; Sfaru R., Eng.; Muraru-Ionel C., PhD.Eng.*

The observation refers, especially to formulas produced by factors with various exponents, formulas obtained correctly from a dimensional point of view, for example *Moenifar & al., (2014*). From the point of view of the physical sense, the formulas leading to parameters with an uncertain physical dimension are invalidated (*Cardei and Gageanu, 2017*). In *Cardei and Gageanu (2017)* is showed how such situations can be remedied. The mathematical models are comparable by means of precision in report to the experimental data, thus resulting a hierarchy of them. In this article, according to *Cardei et al., (2020)*, by validation is understood first of all the physical consistency of the model expression, in the sense of the two criteria set out by (*Cardei et al., 2020)*. The validation in the classical sense, is made in the ordering stage. The ordering stage also includes what the literature understands by comparing models (*Dadu, 2012*). Often, the authors understand by testing even the experimental validation (comparing the model results with the experimental results (*Marion, 2008*).

Generally, mathematical models are divided into two broad categories: deterministic and stochastic (*Dadu, 2012; Marion, 2008*). In this article only deterministic mathematical models will be considered. Obviously, the usefulness of these tests consists primarily in the validation and ranking of the models in an order according to the accuracy achieved by experimental data. Validation using experimental data causes the ordering to become relative to a batch of experimental data.

Proceeding in this way there will be orders of the batch of proposed formulas, but relative to certain experimental data. Therefore, it is very likely that the order of accuracy of the formulas will differ for different experimental data sets. This is normal, primarily because both mathematical models (formulas) and experimental data neglect many parameters that influence the soil tilling processes. Another usefulness of these tests is the elimination of those formulas that have no physical meaning (due to the physical dimension of their terms) or present negative terms in an additive representation of the soil tillage draft force. *Cardei et al., (2020*) explains why this requirement of theoretical validation is included in tests. For example, we sought to avoid classical formulas as they appear in *Ion and Ion, (2019*).

MATERIALS AND METHODS

The working material of this article consists of three basic mathematical models for the draft force, of which the first two, each together with three variants, altogether nine models or nine formulas for testing. The first two basic models, together with their variants, are among the most used in the literature, for example: *Letosnev, (1959); Krasnicenco, (1964); Scripnic and Babiciu, (1979); ASAE, (2003); Ranjbarian et al., (2017); Askari and Khalifahamzehghasem, (2006); Ormenisan, (2014); Cardei et al., (2019)*.

In the paper of *Cardei et al., (2019)*, it was showed that there is a formula for the draft resistance force to tillage that generally includes the most commonly used formulas today. A generalization was given in *Cardei et al., (2020)*. The third basic model tested is taken from *Moenifar et al., (2014)*, which is very interesting, especially for dynamic reasons, but it can be a very good competitor to the best coverage of all the considered experimental cases.

Table 1 lists the parameters that appear in the formulas (mathematical models) analysed in this paper.

Table 1

Parameters of the process: notations, significance and units of measurement

Notation	Name	Unit
F	Draft force	N
F_i	The values of the interpolated force in the experimental points	N
A	The static coefficient of the draft force term	N
B	The coefficient of the draft force term that depends on the working speed	kg/s
C	The coefficient of the draft force term that depends on the square of the working speed	kg/m
φ	Dimensionless factor describing the influence of soil texture: φ = 1 fine, φ = 2 average, and φ = 3 coarse	-
v	Working speed	m/s
b	Working body width	m
a	Working depth	m
k	Coefficient that characterizes specific soil deformation resistance	MPa
ε	Coefficient which depends on the shape of the active surface of the body and the soil properties (*Letosnev, 1959*)	kg/m^3
f	Coefficient analogous to friction coefficient	-

Table 1

(continuation)

Notation	Name	Unit
G	Plough weight	N
g	Gravitational acceleration	m/s^2
ρ	Soil mass density	kg/m^3
α	Horizontal blade angle (rake angle)	rad
n	Number of working bodies	-
φ_s	The lateral displacement angle of the furrow	rad
δ	Coulter sharpening angle	rad
G_A	The degree of dislocation of the soil	-
a_i	Working depth, experimental data	m
b_i	Working body, width experimental data	m
v_i	Working speed, experimental data	m/s
$\mathcal{F}_i$	Draft force, experimental data	N
$\bar{\mathcal{F}}$	The average value of the forces determined experimentally	N
i	Index of the experimental data	-
$\mathbf{e_x}$	The set of experimental data	-
N	The number of experiences in the experimental data set	-
ε_{rel}	global relative error	%
ε_{max}	maximum relative error	%
R^2	Coefficient of determination	-
c	Soil cohesion	Pa
c_a	Soil – working body adhesion	Pa
x	Model parameter - coefficient	-
y, z, t	Model parameters -exponents	-

For working body definition see paper of *Singh, (2017*). If there are n working bodies, each one with working width b', is considered the relation for the total working width: $b = nb'$.

The method of evaluating the mathematical models proposed in the specialized literature, used to obtain the results presented in this article, has been set out and exemplified in *Cardei et al., (2019)*. In short, this method consisted in identifying model parameters using the least squares method. Validation, $\mathbf{V}$, was done demanding the fulfilment of the criteria:

C1 - formulas must have a physical meaning, in the sense of dimensional correctness;

C2 - in the additive composition of the formulas, generally negative terms will not be accepted because the negative components would have the meaning of some components that lead to the decrease of the draft tillage resistance.

Criterion C1 is reflected in the physical dimension of the model parameters and in their physical unit (see table 1). Criterion C2 will be generally supplemented with the indication that the values of the model parameters should be included in the intervals specified by the literature, if any. In addition to the model validation, a proposal for precision test of approximation was added to this paper, $\mathbf{P}$. This test proposes an ordering of the tested formulas, according to the accuracy that they perform in relation to the experimental data relative to which the validation is performed (identifying the parameters model). In order to estimate the accuracy of a model against a batch of experimental data, $\mathbf{e_x}$, two variants are proposed in this article.

The first precision estimator is based on the average value of the sum of the squares of the data errors calculated by interpolation, relative to the experimental data, relative to the average value of the experimental data:

$$\varepsilon_{rel} = \frac{\sqrt{\sum_{i=0}^{N-1}(F_i - \mathcal{F}_i)^2}}{N\bar{\mathcal{F}}} \cdot 100 \quad (1)$$

and it will be called *global relative error*.

Another precision evaluator starts from the definition of the infinite or maximum norm (*Trench, 2013; En.wikipedia.org; Colojoara, 1983*):

$$\mathcal{E}_{max} = \frac{\max\limits_{i=0...N-1} |F_i - \mathcal{F}_i|}{\bar{\mathcal{F}}} \cdot 100 \quad (2)$$

ε_{max} is the maximum relative error (it receives relative character by dividing by the average value of the force). Both operators are given as a percentage.

With these definitions, the testing process can be synthetically presented as a process:

$$\mathbf{T}=\mathbf{T}(\mathbf{V},\mathbf{P},\mathbf{e_x},\mathbf{m}) \quad (3)$$

where $\mathbf{m}$ is a model set, and the result of this process is:

$$\mathbf{R_T}=(\mathbf{m_v},\mathbf{t_m}) \quad (4)$$

A couple of results, the first consisting of validated mathematical models (formulas), $\mathbf{m_v}$, and the second, $\mathbf{t_m}$, in a ranking of the validated models depending on the accuracy achieved for the batch of experimental data that was worked on.

The experimental data for which, the candidate formulas for the title of draft force law are tested, come from six papers that have been freely accessed: *Akbarnia et al., (2014)*, *Ranjbar et al., (2013)*, *Naderloo et al., (2009), Fechete-Tutunaru et al., (2018), and Moenifar et al., (2014)*. This set of experimental data forms in our case the ex-set of experimental data, from the definition (3). In general, the data from the sources above contain working depth and width, working speed and draft force. Some also contain soil moisture, the type of plough or different angles characteristic of the working bodies. For the latter, separate tests were performed on each additional process characteristic compared to the basic ones (depth, width and working speed and draft force). In some reasonable cases a global validation can be done over a number of additional parameters.

The mathematical models of the tillage draft force, whose results of the qualitative and quantitative evaluation are presented in this paper, are the following:

$$F = fG + kabn + \varepsilon abv^2 \quad (5)$$

$$F = fG + kab \quad (6)$$

$$F = kab \quad (7)$$

$$F = kab + \varepsilon abv^2 \quad (8)$$

$$F = \varphi(A + Bv + Cv^2)ab \quad (9)$$

$$F = \varphi(A + Bv)ab \quad (10)$$

$$F = \varphi(A + Cv^2)ab \quad (11)$$

$$F = \varphi(Bv + Cv^2)ab \quad (12)$$

The set of nine formulas (5) - (13) forms the set of mathematical models, $\mathbf{m}$, from the definition of the test process (3). For the moment, the models of the soil tillage draft force that depend on the second power of the working depth, as in *Okoko, et al., (2018); Kushwaha, et al., (1993)*, have not been considered.

In addition to models (5) - (12), for the soil tillage draft force, an example of a model which is established using the dimensional analysis is considered in *Moenifar et al., (2014).*

Dimensional analysis is used for the same purpose by *Larson, (1964)*. In order to test the model in *Moenifar et al., (2014)*, it is necessary to know the cohesion, adhesion and density of the soil, in addition to the experimental data used in the presented tests.

The model (5) is known as Goriacikin's formula, and (9) as ASABE Universal Draft Equation (*Tewari, 2018*). With this all the working data are presented, that is, all the components of the test process $\mathbf{T}$, (3) are known.

Before proceeding with the presentation of the results, it should be specified that:
- we do not consider before or after testing, that any model is true or false;
- we consider that all experimental results are correct.

With these two working principles, the conclusions of the tests can state whether a model is valid for an experimental data set or not and, from the valid models, a model will be a model will be selected in the desired order according to their accuracy. Thus, the validation and precision of a model will become a notion relative to a certain set of experimental data. Under such conditions, there is the possibility that certain models may be statistically significant.

These will be the models that must be followed and studied in order to reach a hypothetical convergence to an existing hypothesis of a physical law of soil tillage draft force. Of course, there is the possibility that that

law will depend on the particular conditions of experimentation. Then, fundamental problems of human thought arise in relation to the laws of nature and their perception by man.

RESULTS AND DISCUSSION

We now proceed to the presentation of the results of the T test, respectively the system of test results, (4), R_T, that is, to specify the validated models and to order them in the descending order of accuracy (the option of the descending order is not mandatory). In order to select valid models, and order them, one can proceed by eliminating the models with negative model parameters (terms), respectively by manual or automatic ordering, using a norm composed of one or both errors (1) and (2), and correlation, and the index of determination, which forms the group of quality parameters.

In order to obtain a mixed, qualitative and quantitative measure of each model, it is recommended the ratio between quality factors (correlation and / or determination index) and errors (one or both). This ratio must be maximized. A typical result for this analysis shows that in table 2. By applying the least squares method to the models (5) - (12), we obtain values of the model parameters as in table (2), columns 2-7.

The quality and quantitative estimators of the interpolations performed are grouped in columns 8-11 of table 2. A table of the type of table 2 results by processing each set of experimental data, relative to the batch of formulas or models tested and specified on the first column of the table 2.

The results from the table 2 are obtained by applying the least squares method for formulas (5) - (12) and experimental data from *Ranjbarian et al., (2017),* for soil moisture with a value of 22%.

Table 2

The values of the models parameters and estimators of quality and precision

For-mula	fG	k	ε	φA	φB	φC	correlation	R^2	ε_{rel}	ε_{max}
(5)	2413.484	14576.06	9547.043				0.944	0.891	2.414	15.17
(6)	2413.484	22997.6	0				0.818	0.669	4.201	38.861
(7)	0	36952.22	0				0.818	0.387	5.715	40.779
(8)	0	28530.67	9547.043				0.929	0.609	4.565	33.369
(9)				39636.86	-27465.7	24936.03	0.927	0.599	4.626	33.755
(10)				21488.63	17208.32	0	0.929	0.609	4.563	33.881
(11)				36821.081	0.000	148.66	0.82	0.394	5.683	40.664
(12)				0.000	793440.95	-718326	-0.29	-226.67	110.155	711.706

The values of the parameters for the formula (13), in the case of the experiments (*Ranjbar et al., 2013*) at 22% soil moisture, are found in *Cardei et al., (2020)*.

The quantitative estimators reduced to the unit are calculated below, that is, each of the columns (9) and (10) are reduced to unit by dividing by the maximum value. Also, the correlation and the index of determination are reported to the absolute maximum value, for a more compact graphical representation. We also add a validation estimator that has a positive value if the model parameters are strictly positive and a negative one otherwise. The absolute value of the validation estimator is chosen so that it can be represented graphically together with the values of the other estimators (we have chosen 0.1). This last group of estimators is given in table 3.

Table 3

Selection parameters obtained from the parameters and estimators calculated in table 2
All estimators are reduced to one unit

Formula	ε_{rel}	ε_{max}	correlation	R^2	validation
(5)	1.000000	1.000000	0.422397	0.372005	0.100000
(6)	0.866525	0.750842	0.735083	0.952966	0.100000
(7)	0.866525	0.434343	1.000000	1.000000	0.100000
(8)	0.984110	0.683502	0.798775	0.818289	0.100000

Table 3
(continuation)

Formula	ε_{rel}	ε_{max}	correlation	R^2	validation
(9)	0.981992	0.672278	0.809449	0.827754	-0.100000
(10)	0.984110	0.683502	0.798425	0.830844	0.100000
(11)	0.868644	0.44220	0.994401	0.997180	0.100000
(13)	0.958686	0.815937	0.667892	0.720665	0.100000

The material presented in the Results chapter is produced for each set of experimental data.

For the purpose of qualitative and quantitative selection will be presented validations and classifications for an example of the norm considered.

The validation operator will be considered compulsory for ordering. In the example, it was used only the maximum error (the product between the validation estimator value and the inverse of the maximum error).

The results given in the Table 4 are obtained for the batch (1)-(8) of mathematical models of the tillage draft force and for the data the experiences provided in *Akbarnia et al., (2014).*

Table 4

Synthesis of validation and of the modelling performances

Model / Experimental data	(5)	(6)	(7)	(8)	(9)	(10)	(11)	(12)	(13)
Akbarnia et al., (2014)	0.000	0.000	0.271	0.349	0.000	0.354	0.273	0.000	0.152
Ranjbar et al., (2013), soil moisture 16.1%	0.464	0.257	0.176	0.215	0.000	0.215	0.177	0.000	0.268
Ranjbar et al., (2013), soil moisture 22.0%	0.414	0.238	0.175	0.219	0.000	0.219	0.176	0.000	0.262
Ranjbar, Rashidi, Najjarzadeh, & Niyazadeh, (2013), soil moisture 25.4%	0.427	0.245	0.177	0.22	0.000	0.221	0.178	0.000	0.257
Ranjbar et al., (2013), all soil moisture	**0.732**	**0.435**	**0.315**	**0.387**	**0.000**	**0.388**	**0.315**	**0.000**	**0.463**
Naderloo et al., (2009), mouldboard plough	0.284	0.094	0.09	0.213	0.000	0.192	0.093	0.000	0.145
Naderloo et al., (2009), disk plough	0.000	0.000	0.058	0.085	0.000	0.084	0.059	0.000	0.072
Naderloo et al., (2009), chisel plough	0.515	0.141	0.122	0.223	0.000	0.229	0.125	0.000	0.089
Naderloo et al., (2009), all ploughs	**0.8**	**0.235**	**0.27**	**0.521**	**0.000**	**0.504**	**0.277**	**0.000**	**0.305**
Fechete-Tutunaru et al., (2018), angle of cutting 30, rake 25	0.000	0.000	0.076	0.076	0.000	0.076	0.076	0.000	0.605
Fechete-Tutunaru et al., (2018), angle of cutting 30, rake 35	0.000	0.000	0.087	0.087	0.000	0.087	0.087	0.000	0.618
Fechete-Tutunaru et al., (2018), angle of cutting 30, rake 50	0.000	0.000	0.094	0.094	0.000	0.094	0.094	0.000	0.592
Fechete-Tutunaru et al., (2018), angle of cutting 45, rake 25	0.000	0.000	0.076	0.076	0.000	0.076	0.076	0.000	0.597
Fechete-Tutunaru et al., (2018), angle of cutting 45, rake 35	0.000	0.000	0.083	0.083	0.000	0.083	0.083	0.000	0.603
Fechete-Tutunaru et al., (2018), angle of cutting 45, rake 50	0.000	0.000	0.101	0.101	0.000	0.101	0.101	0.000	0.612

Table 4 (continuation)

Model / ***Experimental data***	**(5)**	**(6)**	**(7)**	**(8)**	**(9)**	**(10)**	**(11)**	**(12)**	**(13)**
Fechete-Tutunaru, Gaspar, & Gyorgy, (2018), angle of cutting 60, rake 25	0.000	0.000	0.072	0.072	0.000	0.072	0.072	0.000	0.571
Fechete-Tutunaru, Gaspar, & Gyorgy, (2018), angle of cutting 60, rake 35	0.000	0.000	0.083	0.083	0.000	0.083	0.083	0.000	0.599
Fechete-Tutunaru, Gaspar, & Gyorgy, (2018), angle of cutting 60, rake 50	0.000	0.000	0.094	0.095	0.000	0.095	0.094	0.000	0.676
Fechete-Tutunaru et al., (2018), all bodies type	**0.000**	**0.000**	**0.765**	**0.767**	**0.000**	**0.767**	**0.765**	**0.000**	**5.474**
Cardei et al., (2017) Optimum working conditions for variable width ploughs,	1.357	1.203	0.166	0.170	0.000	0.17	0.166	0.000	0.214
Total	**4.193**	**2.613**	**2.317**	**2.849**	**0.000**	**2.838**	**2.329**	**0.000**	**7.395**
Total percent	**17.092**	**10.651**	**9.444**	**11.611**	**0.000**	**11.569**	**9.492**	**0.000**	**30.141**

The following observations resulting from table 4 are:

O1) - for the experimental data from *Akbarnia et al., (2014),* variant (10), which is a linear velocity dependence in the set of formulas suggested by ASAE, (2003), is the most appropriate, followed by formula (8), of Goriacikin inspiration, variant which excludes the term of friction given by the weight of the tillage machine;

O2) - the three experimental datasets offered by *Ranjbar et al., (2013),* are best modelled, all, regardless of soil moisture, even the Goriacikin variant, (5), followed by (13), then by variants (6) and (8) of the formula (5);

O3) - the results of the processing of the experimental data from *Naderloo et al., (2009)*, show that the Goriacikin model (5) better models the soil tillage draft force in the case of the mouldboard plough and chisel plough, while the variant (8) of the same model is better for the plough disk;

O4) - the experimental data series presented in *Fechete-Tutunaru et al., (2018)*, by processing according to the test presented in this article, shows that, for the experimental device used in *Fechete-Tutunaru et al., (2018),* the best theoretical model, without exception, is given by the formula (13);

O5) - the experimental data are most efficiently modelled by the original Goriacikin model, (5), together with all its variants, in particular (6);

O6) - an observation of structure is found by comparing the Modified ASABE Universal Draft Equation formula, (*Tewari, 2018*), with formula (5), namely that both contain two constant terms in relation to the speed of movement.

The observations **O1) - O5)** can be used for the selection of the most exacting mathematical model claimant to the title of law of soil tillage draft force, for each set of experimental data.

If instead of the maximum error, relation (2), the relative global error, relation (1), is used for selection, the situation does not change. Moreover, the estimators are well correlated with each other. Also in table 4, invalid formulas or models are those that have in their cell the number 0.000, according to the validation operator value, conventionally chosen value.

For an example of applying the method in the case of a mathematical model of the soil tillage draft force as a product, the formula proposed in *Moenifar et al., (2014)*, is taken:

$$F = x\rho b^2 v^2 \left(\frac{c + c_a}{\rho v^2}\right)^y \left(\frac{a}{b}\right)^z (\sin\alpha) \tag{13}$$

Formula (13) is deduced using dimensional analysis and considering ten parameters that influence the process. Finally, only seven of the parameters appear in the soil tillage draft force formula.

For formulas of type (13), the dimensionality condition of the parameters x, y, z, t is not required because they are dimensionless by the correct construction mode (dimensional analysis).

However, the condition of positivity is valid for the coefficient x, considering the positive values of the other factors (the angle of position within the constructive and technological limits, has the positive sine). The exponents y, z and t can be negative.

An important mention to be made in the case of model (13) of the draft force is that, if the model parameter, y is positive, then the traction force is zero as long as the speed is not strictly positive.

This behaviour makes it easy to use this model in dynamic calculations, which does not happen with the models that contain term independent of speed, constant, zero (possible in models (5) - (11)).

For testing this formula, the value of soil cohesion and density from *Moenifar et al., (2014)* was used, also there where the experimental data did not specify them, and for estimating the adhesion we used the relation from (*https://www.finesoftware.eu*). This may explain any errors that occur in the results.

Results of the tests of formula (13) on the experimental data from *Akbarnia et al., (2014), Ranjbar et al., (2013), Naderloo et al., (2009), Fechete-Tutunaru et al., (2018)*, are given in the article of *Cardei et al., (2020).*

CONCLUSIONS

The validation and ordering test, of a mathematical model applying for the title of physical law of the draft force generated by the soil working machines is useful for selecting the best model, from a collection of tested models and relative to a lot of experimental data. The validation is conventional and can be ignored, obviously with the price of increasing the risk of some theoretical disadvantages.

The validation and ordering test presented in this article shows that, for now, if we give priority to the accuracy of the mathematical models in relation to the experimental data, then the physical law of the soil tillage draft force has a relative character.

Different models are performing for different experimental data. Acceptance of this situation is a common attitude in the practice of designing and operating machinery for soil works. But, from a theoretical point of view, the situation can be uncomfortable.

Theoretically, one can accept the explanation that if the above law exists, then we are in an intermediate stage of construction. This explanation is likely to be accepted, considering that in the formulas used in current practice, less than one-fifth of the physical parameters involved in the process (known) appear explicitly.

On the other hand, even if we were to build formulas with a large number of parameters, experiences that would sweep all these parameters would be very expensive, almost impossible to achieve.

Under these conditions, it is possible that we will never reach a formula (mathematical model) that bears the name of physical law of the soil tillage draft force, which is not a problem, at least from a practical point of view. Theoretically, however, this situation shows the inability of science to solve complex multi-parametric phenomena. The situation is not new, since such problems arise for well-known mathematical models such as the force of gravitational attraction. Modern physics knows that the same natural phenomenon can be described by different models, with the same precision, but it is difficult to answer for current science when we discover that phenomena apparently belonging to the same category develop or can be developed according to different laws.

From a formal point of view, the notion of physical law can be enforced in the sense of giving the classic form of physical law expressible through an elementary functional relation, a non-elementary expression, practically admitting more relations for a notion of physical law, that becomes so, a collection of relationships, each valid in well-defined fields or intervals of some of the parameters that influence the phenomenon.

For future attempts to formulate a law of draft force, remember that most of the current forms have the following characteristics:

- are additive formulas of polynomial form in relation to the speed of advancement (with certain exceptions), containing also one or two constant terms;
- the model parameters that appear as coefficients of the terms in the formulas, are dependent on: soil moisture and texture, soil density and degree of compaction, the geometrical characteristics of the working bodies and the interaction characteristics between the working parts and soil;
- the basic parameters retained by almost all formulas, are: working width and depth, working speed;
- there can also be considered formulas produced by parameters (possibly deductible by dimensional analysis) and which can be extended by summing with model parameters;
- soil characteristics (moisture, texture, density, compaction etc.) are very numerous and have a random character in space and time, so we must expect the "law" of variation of the draft force to change from place to place and in time.

The only certainties, for the time being, that the research can give to the design and manufacture of agricultural machines for soil tillage, are the upper limits of the draft force, sufficient information for the machines to work safely.

ACKNOWLEDGEMENTS

This work was supported by a grant of the Romanian Research and Innovation Ministry (RRIM), through Programme 1 – Development of the national research-development system, subprogramme 1.2 – Institutional performance – Projects for financing excellence in RDI, contract no. 16PFE, and was done by "NUCLEU" Programme, developed with the support of the RRIM, project PN 19 10 01 02.

REFERENCES

[1] Akbarnia, A., Mohammadi, A., Farhani, F., Alimard, R. (2014). Simulation of draft force of winged share tillage tool using artificial neural network model, *Agric Eng Int: CIGR , 16*(4), 57-65.

[2] American Society of Agricultural Engineers [ASAE], (2003), *Agricultural machinery management data.* Saint Joseph: ASAE.

[3] Askari M, & Khalifahamzehghasem, S. (2006), Draft Force Inputs for Primary and Secondary Tillage Implements in a Clay Loam Soil, *World Applied Sciences Journal , 21*(12), 1789-1794.

[4] Canarache, A., Vintila, I., & Munteanu, I. (2006). Elsevier's Dictionary of Soil Sciences*. Elsevier*.

[5] Cardei, P., Muraru S.L., Sfiru R., Muraru V., (2019). General structure of tillage draft force. Consequences in experimental and applicative researches, *INMATEH Agricultural Engineering*, 59(3), 253-262.

[6] Cardei, P., Condruz P., Sfiru R., Muraru C. (2020). Tests for physical laws of the draft force generated in the tillage operations, *Proceedings of 19th International Scientific Conference Engineering for Rural Development*, vol. 19, 1262-1269.

[7] Cardei, P., Gageanu, I. (2017). A critical analysis of empirical formulas describing the phenomenon of compaction of the powders, *Modern Technology & Engineering,* 2(1), 1-20.

[8] Colojoara, I. (1983). *Mathematical analyses.* Bucharest, Romania: Didactic and Pedagogical Printing House.

[9] Dadu, C. M. (2012). History of the use of computer-aided modeling and simulation in science. XI, 319-329.

[10] Fechete-Tutunaru, L. V., Gaspar, F., Gyorgy, Z., (2018), *Soil-tool interaction of a simple tillage tool in sand*, *E3S Web of Conferences , EENVIRO*, 85, p.08007. Cluj-Napoca. https://www.finesoftware.eu. (n.d.). (Fine) Retrieved from https://www.finesoftware.eu/help/geo5/en/adhesion-of-soil-01/

[11] Ion, S., Ion, A. V., (2019), *Mathematical Modelling of Soil Erosion Process, Technical Report.*

[12] Krasnicenco, A. V, (1964), *Farm Machinery Manufacturer's Manual,* Editura Tehnica, Bucuresti, Romania.

[13] Kushwaha, R. L., Chi, L., Shen, J., (1993), *Analytical and numerical models for predicting soil forces on narrow tillage tools* - A review, *Canadian Agricultural Engineering,* 35(3).

[14] Larson, L. W, (1964), *Predicting draft forces using model moldboard plows in agricultural soils, Retrospective Theses and Dissertations*, *Retrospective Theses and Dissertations*, 3863, Iowa, USA.

[15] Letosnev, M. N. (1959). Agricultural Machinery*. (S. Agro-Forestry, Ed.) Bucharest, Romania: Ministry of Agriculture and Forestry*.

[16] Marion, G. (2008). An Introduction to Mathematical Modelling, *Semantic Scholar*.

[17] Moenifar, A., Mousavi-Seyedi, S., Kalantari, D. (2014), *Influence of tillage depth, penetration angle and forward speed on the soil/thin-blade interaction force*, *Agric Eng Int: CIGR,* 16(1), 69-74.

[18] Naderloo, L., Alimadani, R., Akram, A., Javadikia, P., Khanghah, H. Z. (2009). *Tillage depth and forward speed effects on draft of three primary tillage implements in clay loam soil*, *Journal of Food, Agriculture & Environment,* 7(3&4), 382-385.

[19] Okoko, P., Ajav, E., Olosunde, W. A. (2018). *Draft and power requirements for some tillage implements operating in clay loam soil*, *AgricEngInt: CIGR,* 20, 95-102.

[20] Ormenisan, A. A. (2014). *Theoretical and experimental research concerning the influence of automatic control systems of the tractor linkage mechanisms on the dynamics and energetics of ploughing units*, Thesis. Brasov, Romania: Transilvania University of Brasov.

[21] Ranjbar, I., Rashidi, M., Najjarzadeh, I., Niyazadeh, M. (2013). Modeling of Moldboard Plow Draft Force Based on Tillage Depth and Operation Speed, *Middle-East Journal of Scientific Research,* 17(7), 891-897.
[22] Ranjbarian , S., Askari , M., Jannatkhah, J. (2017), Performance of tractor and tillage implements in clay soil, *Journal of the Saudi Society of Agricultural Sciences*, 16, 154-162. ro.wikipedia.org. (n.d.). *Modelul_unui_sistem*, https://ro.wikipedia.org/wiki/Modelul_unui_sistem
[23] Scripnic, V., Babiciu, P. (1979). *Agricultural machinery.* Ceres, Bucharest, Romania.
[24] Singh, T. P. (2017). *In Farm Machinery,* Delhi, India: PHI Lerning
[25] Tewari, V. K. (2018). Farm Machinery, *Lecture - 03, https://www.youtube.com/playlist?list=PLbRMhDVUMngfpJp_tkeFAy_qF20vlwn3k*
[26] Trench, W. F. (2013). *Introduction to real analysis,* Pearson Education.

WRITING INSTRUCTIONS

Article Types

Three types of manuscripts may be submitted:

1. **Regular articles:** These should describe new and carefully confirmed findings, and experimental procedures should be given in sufficient detail for others to verify the work. The length of a full paper should be the minimum required to describe and interpret the work clearly (max.10 pages, even number);
2. **Reviews:** Submissions of reviews and perspectives covering topics of current interest are welcome and encouraged (max.10 pages, even number).

Manuscripts should be written in English (American or British usage is accepted, but not a mixture of these) and submitted **electronically** at the following e-mail addresses: ***inmatehjournal@gmail.com***
Please be sure to include your full affiliation and e-mail address (see Sample manuscript)
The authors are responsible for the accuracy of the whole paper and references.
There are allowed 2 papers by each first author.
The text layout should be in single-column format. To avoid unnecessary errors, it is strongly advised to use the "spell-check" and "grammar check" functions of your word processor.

Review Process

All manuscripts are reviewed by 2 members of the Scientifically Review Office. Decisions will be made as rapidly as possible and the journal strives to return reviewers' comments to authors in approx.3 weeks.
The editorial board will re-review manuscripts that are accepted pending revision.

NOTE:

Submission of a manuscript implies: that the work described has not been published before (excepting as an abstract or as part of a published lecture or thesis) that it is not under consideration for publication elsewhere.

1. REGULAR ARTICLES

- Manuscripts should be concise, in ***1.15 line spacing***, and should have 2 cm all over margins. The font should be ***Arial 10 pt.*** Ensure that each new paragraph is clearly indicated, using **TAB at 1 cm**.
- Title will be ***Arial 12 pt***. and explicit figures will be ***Arial 9 pt***.
- Text will be written in English.
- Chapters' titles are written by ***Arial 10 pt, Bold, Uppercase*** (e.g. **INTRODUCTION, MATERIALS AND METHODS**), between chapters is left a space for 10 pt. At the beginning of each paragraph, TAB of 1 cm.
- The paper body will be written in ***Arial 10 pt., Justify alignment***.

TITLE ***Arial 12 pt., Uppercase, Bold, Center*** *(in English language)* and ***Bold Italic*** *(in native language).*
Should be a brief phrase describing the contents of the paper. Avoid long titles; a running title of no more than 100 characters is encouraged (without spaces).

AUTHORS ***ARIAL 9, Bold, Centre alignment***
Under the paper's title, after a space (enter) 9 pt., write ***authors' names*** and ***affiliations (Arial 8 pt.-Regular)***
When the paper has more than one author, their name will be followed by a mark (Arabic numeral) as superscript if their affiliation is different. Less than 6 authors.
Corresponding author's name (next row), ***(Arial 8 pt.)***. Should be added also: phone, fax and e-mail information, for the paper corresponding author (***font: 8 pt., Italic***).

KEYWORDS ***(In English)*** about 4 to 7 words that will provide indexing references should be listed (title: ***Arial 10pt, bold italic,*** text ***Arial 10 pt., Italic***).

A list of non-standard *Abbreviations* should be added. In general, non-standard abbreviations should be used only when the full term is very long and used often. Each abbreviation should be spelled out and introduced in parentheses the first time it is used in the text. Standard abbreviations (such as ATP and DNA) need not to be defined.

ABSTRACT ***(in English and Native language, Arial 10 pt.)***, the title ***bold***; the text of abstract: ***Italic*)** should be informative and completely self-explanatory, briefly present the topic, state the scope of the experiments, indicate significant data, and point out major findings and conclusions. The Abstract should be max.250 words. Complete sentences, active verbs, and the third person should be used, and the abstract should be written in the past tense. Standard nomenclature should be used and abbreviations should be avoided. No literature should be cited.

INTRODUCTION (***Arial 10 pt.***) should provide a clear statement of the problem, the relevant literature on the subject, and the proposed approach or solution. It should be understandable to colleagues from a broad range of scientific subjects. We should refer to the current stage of researches performed in the field of the paper to be published, by quoting up-to-date specialty studies, preferably published after 2006, excepting certain referential specialty books/studies, especially papers issued in magazines/journals/conferences/ISI quoted symposia or in other international data bases, which are well known and available.

MATERIALS AND METHODS (***Arial 10 pt.***) should be complete enough to allow experiments to be reproduced. However, only truly new procedures should be described in detail; previously published procedures should be cited, and important modifications of published procedures should be mentioned briefly. Methods in general use need not be described in detail.

RESULTS (***Arial 10 pt.***) should be clarity presented. The results should be written in the past tense when describing findings in the authors' experiments. Results should be explained, but largely, without referring to the literature. Discussion, speculation and detailed interpretation of data should not be included in the Results, but should be put into the Conclusions section.

CONCLUSIONS (***Arial 10 pt.***) The main conclusions drawn from results should be presented in a short Conclusions section. Do not include citations in this section.

Formulae, symbols and abbreviations: Formulae will be typeset in Italics (preferable using an Equation Editor) and should be written or marked as such in the manuscript, unless they require a different styling. They should be referred to in the text as Equation (4) or e.g. (4). The formulae should be numbered on the right side, between brackets ***(Arial 10 pt.)***:

$$P = F \cdot v \tag{1}$$

Terms of the equation and the unit measure should be explained, e.g.

P is the power, [W];

F – force, [N];

v – speed, [m/s]

SI units must be used throughout.

Tables should be self-explanatory without reference to the text. The details of the methods used in the experiments should preferably be described in the legend instead of in the text. The same data should not be presented both in table and graph form or repeated in the text.

Table's title will be typed ***Arial 9 pt, Bold, Centered***

In the table, each row will be written Arial 9 pt, single-spaced throughout, including headings and footnotes.

The table should be numbered on the right side, ***Arial 10 pt.*** ***(E.g.:*** **Table 1)**

Figures ***(Arial 9 pt., Bold, Center)*** should be typed in numerical order (Arabic numerals). Graphics should be high resolution (e.g.JPEG). Figure number is followed by what represent the figure or graph e.g.:

Fig.1 – Test stand

Legend: ***Arial 8 pt, Italic, Center,*** e.g.:

1 - plansifter compartments; 2- break rolls; 3 – semolina machines; 4 – reduction rolls; 5 – flour

ACKNOWLEDGMENTS (***Arial 10 pt.***) of people, grants, funds etc should be brief (*if necessarily*).

REFERENCES (***Arial 10 pt.***)

(In alphabetical order, in English and in the original publication language).

Minimum 10 references, last 10 years, minimum 3 references from the last 2 years

It can be used "***References***" tool from the ***Word Editor***. **APA Style (American Psychological Association)**
https://apastyle.apa.org/style-grammar-guidelines/references/examples

Authors are fully responsible for the accuracy of the references.

References should be **alphabetically**, with complete details, as follows:

Examples:

Books: https://apastyle.apa.org/style-grammar-guidelines/references/examples/book-references

Jackson, L. M. (2019). *The psychology of prejudice: From attitudes to social action* (2nd ed.). American Psychological Association. https://doi.org/10.1037/0000168-000

Kesharwani, P. (2020). *Nanotechnology based approaches for tuberculosis treatment*. Academic Press.

Sapolsky, R. M. (2017). *Behave: The biology of humans at our best and worst*. Penguin Books.

Torino, G. C., Rivera, D. P., Capodilupo, C. M., Nadal, K. L., & Sue, D. W. (2019). *Microaggression theory: Influence and implications*. John Wiley & Sons. https://doi.org/10.1002/9781119466642

In text:

- ***Parenthetical citations***: (Jackson, 2019; Sapolsky, 2017)
- ***Narrative citations***: Jackson (2019) and Sapolsky (2017)

Journal Article:
https://apastyle.apa.org/style-grammar-guidelines/references/examples/journal-article-references

Grady, J. S., Her, M., Moreno, G., Perez, C., & Yelinek, J. (2019). Emotions in storybooks: A comparison of storybooks that represent ethnic and racial groups in the United States. *Psychology of Popular Media Culture*, *8*(3), 207–217. https://doi.org/10.1037/ppm0000185

In text:

- ***Parenthetical citation***: (Grady et al., 2019)
- ***Narrative citation***: Grady et al. (2019)

Conference or Symposium:
https://apastyle.apa.org/style-grammar-guidelines/references/examples/conference-proceeding-references

Duckworth, A. L., Quirk, A., Gallop, R., Hoyle, R. H., Kelly, D. R., & Matthews, M. D. (2019). Cognitive and noncognitive predictors of success. *Proceedings of the National Academy of Sciences*, *USA*, *116*(47), 23499–23504. https://doi.org/10.1073/pnas.1910510116

In text:

- ***Parenthetical citation***: (Duckworth et al., 2019)
- ***Narrative citation***: Duckworth et al. (2019)

Dissertation / Thesis:
https://apastyle.apa.org/style-grammar-guidelines/references/examples/published-dissertation-references

Zambrano-Vazquez, L. (2016). *The interaction of state and trait worry on response monitoring in those with worry and obsessive-compulsive symptoms* [Doctoral dissertation, University of Arizona]. UA Campus Repository. https://repository.arizona.edu/handle/10150/620615

In text:

- ***Parenthetical citations***: (Kabir, 2016; Miranda, 2019; Zambrano-Vazquez, 2016)
- ***Narrative citations***: Kabir (2016), Miranda (2019), and Zambrano-Vazquez (2016)

https://apastyle.apa.org/style-grammar-guidelines/references/examples/unpublished-dissertation-references

Harris, L. (2014). *Instructional leadership perceptions and practices of elementary school leaders* [Unpublished doctoral dissertation]. University of Virginia.

In text:

- ***Parenthetical citation***: (Harris, 2014)
- ***Narrative citation***: Harris (2014)

Patents: Names and initials of authors, year (between brackets), patent title (Italic), patent number,country:
Grant, P. (1989). *Device for Elementary Analyses*. Patent. No.123456. USA.

Legal regulations and laws, organizations:
https://apastyle.apa.org/style-grammar-guidelines/references/examples/iso-standard-references

International Organization for Standardization. (2018). *Occupational health and safety management systems—Requirements with guidance for use* (ISO Standard No. 45001:2018). https://www.iso.org/standard/63787.html

Occupational Safety and Health Administration. (1970). *Occupational safety and health standards: Occupational health and environmental control: Occupational noise exposure* (OSHA Standard No. 1910.95). United States Department of Labor. https://www.osha.gov/laws-regs/regulations/standardnumber/1910/1910.95

In text:

- ***Parenthetical citations***: (International Organization for Standardization, 2018; Occupational Safety and Health Administration, 1970)
- ***Narrative citations***: International Organization for Standardization (2018) and Occupational Safety and Health Administration (1970)

Web references: The full URL should be given in text as a citation, if no other data are known. If the authors, year, and title of the documents are known and the reference is taken from a website, the URL address has to be mentioned after these data.

Citation in text

Please ensure that every reference cited in the text is also present in the reference list (and vice versa).
Do not cite references in the Abstract and Conclusions !.
Unpublished results, personal communications as well as URL addresses are not recommended in the references list.
Making personal quotations (one, at most) should not be allowed, unless the paper proposed to be published is a sequel of the cited paper. Articles in preparation or articles submitted for publication, unpublished, personal communications etc. should not be included in the references list.

Citations style

Text: All citations in the text may be made directly (or parenthetically) as bellow.

- ***single author:*** the author's name (without initials, unless there is ambiguity) and the year of publication:
  "as previously demonstrated *(Brown, 2010)*".
- ***two authors:*** both authors' names and the year of publication: *(Adam and Brown, 2008; Smith and Hansel, 2006; Stern and Lars, 2009)*
- ***three or more authors:*** first author's name followed by "et al." and the year of publication: "As has recently been shown *(Werner et al., 2005; Kramer et al., 2000)* have recently shown ...."

Citations of groups of references should be listed first alphabetically, then chronologically.

Units, Abbreviations, Acronyms

- Units should be metric, generally SI, and expressed in standard abbreviated form.
- Acronyms may be acceptable, but must be defined at first usage.

2. REVIEWS

Summaries, reviews and perspectives covering topics of current interest in the field, are encouraged and accepted for publication. Reviews do not have the requirements for regular articles. However, should include: (*) an introductory chapter, (**) a careful and critical presentation of the relevant aspects of the topic approached and (***) emphasis of the aspects that aren't known and require further research to progress. Reviews should be concise (max. 12 pages).

Edited by: INMA Bucharest
6, Ion Ionescu de la Brad Blvd., sect. 1, Bucharest, ROMANIA
Tel: +4021.269.32.60; Fax: +4021.269.32.73
https:// inmateh.eu/
e-mail: ***inmatehjournal@gmail.com***